NANOSTRUCTURES: PHYSICS AND TECHNOLOGY

18th International Symposium

St Petersburg, Russia, June 21–26, 2010

Co-Chairs
Zh. Alferov
L. Esaki

PROCEEDINGS

Saint Petersburg, 2010

Published by
Ioffe Physical-Technical Institute
26 Politekhnicheskaya, St Petersburg 194021, Russia
http://www.ioffe.ru/

Publishing license ΛP No 040971 of June 16, 1999.

ISBN 978-5-93634-045-1

The International Symposium "Nanostructures: Physics and Technology" is held annually since 1993. The first Symposium was initiated by Prof. Zh. Alferov and Prof. L. Esaki who are its permanent co-chairs. More detailed information on the Symposium is presented on the World Wide Web **http://www.ioffe.ru/NANO2010/**

The Proceedings include extended abstracts of invited talks and contributed papers to be presented at the Symposium. By tradition this book is published before the beginning of the meeting.

The volume was composed at the Information Services and Publishing Department of St Petersburg Academic University — Nanotechnology Research and Education Centre of the RAS from electronic files submitted by the authors. When necessary these files were converted into the Symposium style without any text revisions. Only minor technical corrections were made by the composers.

Design and layout: N. Vsesvetskii
Desk editor: E. Savostyanova

Information Services and Publishing Department
St Petersburg Academic University — Nanotechnology Research and Education Centre of the RAS
8, bld. 3 Khlopina, St Petersburg 194021, Russia
Phones: (812) 534-58-58
Fax: (812) 534-58-50

Printed in Russian Federation

The Symposium is held under the auspices of
the Russian Academy of Sciences

Organizers

St Petersburg Academic University — Nanotechnology Research and Education Centre of the RAS
Ioffe Physical-Technical Institute of the RAS
Submicron Heterostructures for Microelectronics, Research & Engineering Center RAS
Foundation for Support of Education and Science (Alferov's Foundation)

in association with

Branch of Physical Sciences of the RAS
Branch of Nanotechnologies, Information and Computer Sciences of the RAS
St Petersburg Scientific Center of the RAS
Karelian Research Centre of the RAS

Acknowledgments

The Organizers gratefully acknowledge the following
for their contribution to the success of the Symposium:

RUSNANO, Russian Corporation of Nanotechnologies
Russian Academy of Sciences
Russian Foundation for Basic Research
Ministry of Education and Sciences of Russian Federation
Foundation for Support of Education and Science (Alferov's Foundation)
JSC Mikron

Location and Date

Symposium is held in Saint Petersburg, Russia, June 21–26, 2010
and arranged as a river tour along a circular route
(St Petersburg–Petrozavodsk–Kizhi–Mandrogi village–St Petersburg).

Advisory Committee

G. Abstreiter (*Germany*)
Zh. Alferov (*Russia*)
Y. Arakawa (*Japan*)
A. Aseev (*Russia*)
G. Bastard (*France*)
D. Bimberg (*Germany*)
L. Eaves (*United Kingdom*)
L. Esaki (*Japan*)
S. Gaponov (*Russia*)
E. Gornik (*Austria*)
Yu. Gulyaev (*Russia*)
N. Holonyak, Jr. (*USA*)
L. Keldysh (*Russia*)
G. Landwehr (*Germany*)
J. Merz (*USA*)
M. Shur (*USA*)
M. Skolnick (*United Kingdom*)
R. Suris (*Russia*)

Programme Committee

R. Suris, Chair (*St Petersburg, Russia*)
V. Evtikhiev, Secretary (*St Petersburg, Russia*)
A. Andronov (*Nizhny Novgorod, Russia*)
N. Bert (*St Petersburg, Russia*)
C. Chang-Hasnain (*Berkeley, USA*)
A. Chaplik (*Novosibirsk, Russia*)
V. Dneprovskii (*Moscow, Russia*)
V. Dubrovskii (*St Petersburg, Russia*)
A. Egorov (*St Petersburg, Russia*)
A. Gippius (*Moscow, Russia*)
A. Gorbatsevich (*St Petersburg, Russia*)
S. Gurevich (*St Petersburg, Russia*)
S. Ivanov (*St Petersburg, Russia*)
P. Kop'ev (*St Petersburg, Russia*)
Z. Krasil'nik (*Nizhny Novgorod, Russia*)
V. Kulakovskii (*Chernogolovka, Russia*)
M. Kupriyanov (*Moscow, Russia*)
X. Marie (*Toulouse, France*)
I. Merkulov (*St Petersburg, Russia*)
V. Panov (*Moscow, Russia*)
O. Pchelyakov (*Novosibirsk, Russia*)
E. Poltoratskii (*Moscow, Russia*)
H. Sakaki (*Tokyo, Japan*)
N. Sibel'din (*Moscow, Russia*)
M. Stutzmann (*Garching, Germany*)
V. Timofeev (*Chernogolovka, Russia*)
V. Volkov (*Moscow, Russia*)
V. Ustinov (*St Petersburg, Russia*)
A. Zhukov (*St Petersburg, Russia*)

Organizing Committee

M. Mizerov *Chair* (Submicron Heterostructures for Microelectronics, Research & Engineering Center RAS)
M. Baranov *Vice-chair* (St Petersburg Academic University)
V. Okrepilov (St Petersburg Scientific Center of the RAS)
A. Titov (Karelian Research Centre of the RAS)
V. Vdovitsyn (Karelian Research Centre of the RAS)
E. Mozgovoy (Foundation for Support of Education and Science (Alferov's Foudation))
A. Egorov (St Petersburg Academic University)
N. Sibeldin (Lebedev Physical Institute of the RAS)
M. Sudenkova (St Petersburg Academic University)
A. Baranov (St Petersburg Academic University)
L. Grudnikova (Submicron Heterostructures for Microelectronics, Research & Engineering Center RAS)

This book is dedicated to 80th Anniversary
of Symposium Co-chair Zhores I. Alferov

Zhores I. Alferov

Zhores Ivanovich Alferov was born on March 15, 1930, in Vitebsk (USSR, now Belarus). In December 1952 graduated from LETI (Leningrad Electrotechnical Institute). In January 1953 became staff member of the Ioffe Institute, where defended his candidate (1961) and doctoral (1970) theses. Corresponding-member (1972), Academician of the Russian Academy of Sciences (1979). From 1987 till 2003 director of the Ioffe Institute.

In 2000, awarded (together with H. Kroemer) Nobel Prize in Physics *for basic work on information and communication technology particularly for developing semiconductor heterostructures used in high-speed- and opto-electronics*.

As shown theoretically and experimentally in the studies carried out by the laureate at the Ioffe Institute, it is possible to control in a novel way fluxes of electrons and photons in semiconductor heterostructures, artificial crystals grown from semiconductors with different chemical compositions. Lasers, light-emitting diodes, photodiodes, transistors and solar cells developed on the basis of heterostructures are universally used in modern systems for information transfer and storage and in space power engineering.

Alferov is one of the most prominent organizers of academic science in Russia and proponent of creation of educational centres at leading institutes of the RAS. Educational centre for physics and technology organized by him at the Ioffe Institute has been functioning since 1999, since 2004 — as an independent institution affiliated to the RAS, and since 2009 — as St Petersburg Academic University — Nanotechnology Research and Education Centre of the RAS.

At present, Vice-president of the RAS, Chair of the Presidium of St Petersburg Scientific Centre of the RAS, Rector of the St Petersburg Academic University.

Zh. Alferov is the author of four books, more than 500 scientific articles and 50 inventions in semiconductor technology.

Awards

- The Order «Sign of Honor» (USSR, 1959),
- Ballantyne Medal of the Franklin Institute (USA, 1971),
- Lenin Prize (USSR, 1972),
- The Order of Labor Red Banner (USSR, 1975),
- Hewlett-Packard Europhysics Prize (1978),
- The Order of the October Revolution (USSR, 1980),
- State Prize (USSR, 1984),
- The Order of Lenin (USSR, 1986),
- GaAs Symposium Award and H. Walker Medal (USA, 1987),
- Karpinskii Prize (FRG, 1989),
- Ioffe Prize, Russian Academy of Sciences (Russia, 1996),
- Foreign Member of the OSA (USA, 1997),
- The Order of Service to the Fatherland third degree (Russia, 1999),
- Demidov Prize (Russia, 1999),
- The Order of Service to the Fatherland second degree (Russia, 2000),
- The Medal of Alexander Popov, Russian Academy of Sciences (Russia, 2000),
- Nicholas Holonyak, Jr. Award (USA, 2000),
- The Nobel Prize for Physics (Sweden, 2000),
- Kyoto Prize — Advanced Technology (Japan, 2001),
- V.I. Vernadskiy Award, NAS (Ukraine, 2001),
- State Prize (Russia, 2001),
- The Order of Francis Skorina (Belarus, 2002),
- The Medal, «Marin Drinov» of the Bulgarian Academy of Sciences (Bulgaria, 2002),
- Gold Medal Award, SPIE (2002),
- Golden Plate Award, Academy of Achievement (USA, 2002),
- The Order of Prince Yaroslav the Wise (Ukraine, 2003),
- The Giorgi Nikoladze Medal (Georgia, 2005),
- The Order of Service to the Fatherland first degree (Russia, 2005),
- Global Energy Prize (Russia, 2005),
- The Medal of Friendship (Cuba, 2006),
- Brothers Karich Prize (Serbia, 2007),
- The Order of Frienship of Peoples (Belarus 2009),
- Wisdom Award of the University of Athens (Greece, 2009),
- The Order of Service to the Fatherland fourth degree (Russia, 2010).

Honorary Membership

— Life Fellow of the Franklin Institute (USA, 1971),
— Foreign Member of the German Academy of Sciences (GDR, 1987),
— Honorary Professor of the Havana University (Cuba, 1987),
— Foreign Member of the Polish Academy of Sciences (Poland, 1988),
— Foreign Associate of the National Academy of Engineering (USA, 1990),
— Foreign Associate of the National Academy of Sciences (USA, 1990),
— Honorary Member of the Metrological Academy, St Petersburg (Russia, 1994),
— Foreign Member of the National Academy of Sciences of Belarus (Belarus, 1995),
— Foreign Member of the Korean Academy of Science and Technology (Korea, 1995),
— Honorary Member of the Pakistan Society for Semiconductor Science and Technology (Pakistan, 1996),
— Fellow of the Leibniz Association (Germany, 1997),
— Honorary Academician of the International Academy of Refrigeration, St Petersburg (Russia, 1997),
— Academician of the International Academy of Ecology, Man and Nature Protection Sciences, St Petersburg (Russia, 1998),
— Honorary Doctor of the Humanity University, St Petersburg (Russia, 1998),
— Honorary Doctor of the Kurchatov Institute, Moscow (Russia, 1998),
— Honorary Professor of the Institute of Management and Economics, St Petersburg (Russia, 1999),
— Honorary Doctor of the State Technical University, St Petersburg (Russia, 2000),
— Academician of the Russian Academy of Natural Sciences (Russia, 2000),
— Academician of the International Higher Education Academy of Sciences (Russia, 2000),
— Foreign Member of the National Academy of Sciences (Ukraine, 2000),
— Fellow of the Optical Society of America (USA, 2000),
— Fellow and Charted Physicist of the Institute of Physics (United Kingdom, 2000),
— Honorary member of the European Academy of Sciences (EU, 2001),
— Honorary member of the European Academy of Sciences and Arts (EU, 2001),
— Honorary Doctor of Belarusian State University (Belarus, 2001),
— Honorary Doctor of Shota Rustaveli State University (Georgia, 2001),
— Member of the Russian Academy of Education (Russia, 2001),
— Honorary Doctor of the State Electrotechnical University (LETI), St Petersburg (Russia, 2001),
— Honorary Doctor of the Moscow State University (Russia, 2001),
— Doctor Honoris Causa by the Universidad Politecnica de Madrid (Spain, 2001),
— Foreign Member of the Spain Engineering Academy (Spain, 2001),
— Honorary Fellowship of the Institute of Physics (Singapore, 2001),
— Honorary Doctor of Belarusian State University of Informatics and Radioelectronics (Belarus, 2002),
— Doctor Honoris Causa of the National Institute for Applied Sciences,Toulouse (France, 2002),
— Foreign Member of the Azerbaijan National Academy of Sciences (Azerbaijan, 2002),
— Academician of the Academy of Sciences of Cuba (Cuba, 2002),
— Honorary Professor of the Moscow State Pedagogical University (Russia, 2002),
— Honorary Doctor of the Japan Advanced Institute of Science and Technology (Japan, 2002),
— Honorary Professorship at Nanjing University (China, 2002),
— Doctor Honoris Causa of the Plovdiv University (Bulgaria, 2002),
— Doctor Honoris Causa of the University of Turku (Finland, 2003),
— Honorary Doctor of the National Technical University of Ukraine «Kiev Polytechnic Institute» (Ukraine 2003),
— Honorary Doctor of the Tavrichesky University (Ukraine, 2003),
— Honorary Foreign Member of the Academy of Sciences of Moldova (Moldova, 2004),
— Honorary Professor of the Beijing University of Posts and Telecommunications (China, 2005),
— Honorary Professor of the Institute of Semiconductors, Chinese Academy of Sciences (China, 2005),
— Honorary Professor of the Ulyanovsk State University (Russia, 2005),
— Honorary Doctor of the University of St Andrews (United Kingdom, 2006),
— Honorary Doctor of the University of Dundee (United Kingdom, 2006),
— Doctor Honoris Causa of the University of Oulu (Finland, 2006),
— Foreign Member of the Chinese Academy of Sciences (China, 2006),
— Honorary Doctor of the Arkhangelsk State Technical University (Russia, 2006),
— Honorary Professor of Vitebsk State Technological University (Belarus, 2007),
— Honorary Doctor of the Donetsk National University (Ukraine, 2007),
— Doctor Honoris Causa of the Tampere University of Technology (Finland, 2007),
— Academician of the National Engineering Academy of the Republic of Kazakhstan (Kazakhstan, 2007),
— Honorary Professor of the Eurasian National University named after L.N. Gumilev (Kazakhstan, 2007),
— Professor of Konkuk University (South Korea, 2007),
— Honorary Doctor of the Novosibirsk State University (Russia, 2007),
— Member of the Mongolian Academy of Sciences (Mongolia, 2008),
— Honorary Doctor of the Far Eastern National University (Russia, 2008),
— Honorary Doctor of the Tomsk State University (Russia, 2008),
— Champion of Technology (United Kingdom, 2009),
— Honorary Doctor of the Technical University of Berlin (Germany, 2009),
— Honorary Member of the Montenegrin Academy of Sciences and Arts (Montenegra, 2009),
— Honorary Doctor of the Samara State Aerospace University named after academician S.P. Korolyov (Russia, 2009).

Eponymous asteroid is named after Zhores Alferov.

Contents

Lasers and Optoelectronic Devices

2D Electron Gas

Infrared and Microwave Phenomena in Nanostructures

Quantum Wells and Quantum Dots

Nanostructure Characterization

Si-Ge Based Nanostructures

Spin Related Phenomena in Nanostructures

Excitons in Nanostructures

Tunnelling Phenomena

Transport in Nanostructures

Metal Nanostructures

Microcavity and Photonic Crystals

Nanostructure Technology

Nanostructure Devices

Wide Band Gap Nanostructures

Plenary Session–III

Author Index 385

Unprinted Papers

The papers listed below are included in the Symposium Programme, but not printed in the Proceedings, as the authors had not submitted electronic files in due time.

18th Int. Symp. "Nanostructures: Physics and Technology"
St Petersburg, Russia, June 21–26, 2010

Intentional modification of quantum dot properties for laser applications

A. E. Zhukov[1,2]

[1] St Petersburg Academic University, St Petersburg, Russia
[2] Ioffe Physical-Technical Institute, St Petersburg, Russia

Abstract. Various intentional modifications of self-organized quantum dots intended for laser's active region are described. In particular, we discuss an effect on mean quantum dot size and luminescent peak position of InAs effective thickness and of compositional variation of a material which surrounds quantum dots. Additional broadening of quantum dot optical transitions by intentional disordering is also discussed.

Introduction

Device characteristics of a diode laser are tightly connected with band structure of the active medium. As compared to quantum wells, quantum dots may provide additional flexibility in controlling the properties of the laser's active region. This behavior is associated with a low surface density of quantum dots formed in Stranski–Krastanow mode, sensitivity of QD energy levels to variation of QD size, existence of several excited optical transitions in QDs, etc. In particular, variation of QD effective thickness in combination with changing the composition of surrounding matrix may tune the luminescence peak position in a wide spectral range. Important parameters, which affect optical gain of a QD laser, depend upon surface density of quantum dots. In its turn, QD density can be adjusted by changing the number of QD planes repeatedly deposited in the active region. For a number of applications including multi-channel optical data transmission, tunable lasers, optical coherence tomography and others, the gain spectrum has to be as broad as possible. Additional spectral broadening in a QD active region can be achieved by formation of several nonidentical QD planes, e.g. with different thickness or composition of surrounding InGaAs quantum well.

1. Effective thickness of strained material

The driving force for the self-organization process as well as for the misfit dislocation formation is the lattice mismatch between the epitaxial layer and the substrate (buffer layer). Possibility of partial relaxation of elastic strain in apical zones of three-dimensional islands is just the driving force for island formation. While weakly strained InGaAs layers ($x < 0.2$) being deposited on a GaAs surface predominantly accommodate lattice mismatch by misfit dislocations, highly strained InGaAs films ($x > 0.5$) grow in a three-dimensional mode prior to the dislocation formation. The critical thickness of three-dimensional growth is 1.7 monolayers (ML) for InAs and increases to 4 ML for the 50% content of InAs [1]. InAs QDs can remain dislocation-free in a relatively narrow interval of effective thicknesses (1.7–3.5 ML). Further deposition of InAs leads to partial strain relaxation.

A luminescence peak position of a QD array is primarily governed by the average island size, which increases with increasing Q_{InAs}. Formation of three-dimensional islands reveals itself in an intensive luminescence band strongly shifted to longer wavelengths with respect to the GaAs bandgap. The spectrum usually comprises two lines of which longer wavelength one originates from the ground state optical transition. A shorter wavelength line that appears in samples with higher Q_{InAs} is due to the excited state optical transition in islands of larger volume. Within the interval of the dislocation-free growth, the QD luminescence may cover the wavelengths from 1.05 to 1.24 μm.

In addition to the effective thickness of strained material, various growth parameters (such as growth rate, flux of group V atoms, growth interruptions, substrate temperature) exert influence on characteristics of QD arrays because of their effect on thermodynamic parameters as well as kinetic-related limitations [2]. In particular, rise of temperature leads to decrease of surface density which is accompanied by increase of QD lateral size and corresponding red shift of luminescence line. Increase of the deposition rate has opposite effect. For example, the density of an array deposited at 485 °C changes from 7×10^9 to 3×10^{10} cm^{-2} if InAs deposition rate changes from 0.01 to 0.1 ML/s. At the same time average lateral size of QDs decreases from 21 to 13 nm, while the luminescence peak position shifts to shorter wavelengths by approximately 70 nm. Deposition of quantum dots at 440 °C additionally shifts the wavelength by about 30 nm.

2. Atomic layer epitaxy, quantum dots in a quantum well

It is difficult to achieve the emission wavelength longer than 1.24 μm in In(Ga)As/GaAs quantum dots formed in Stranski–Krastanow growth mode on a GaAs substrate. A specific method of QD deposition has to be used to prolong dislocation-free growth and extend the longer wavelength border of QD luminescence. It was reported on growth of QD structures in a GaAs matrix with the ground state emission centered at 1.32 μm by using of atomic layer epitaxy (ALE), i.e. alternating deposition of the elements [3]. The larger migration distance due to the alternating sub-monolayer deposition cycles yields larger QD size (e.g., 20 nm in base, 10 nm in height for 24 ML of $In_{0.5}Ga_{0.5}As$) with improved uniformity. For example, FWHM as low as 33 meV was reported already in initial experiments [4]. On the other hand, QDs formed by ALE deposition method are characterized by a relatively low density of $\sim 1.3 \times 10^{10}$ cm^{-2}.

A low optical gain of ALE-formed quantum dots associated with their low surface density motivates a search for novel QD materials suitable for long-wavelength emission. An alternative approach utilizes a sensitivity of optical transition energy to variation of a bandgap of a surrounding matrix. This effect

is caused by penetration of wavefunctions into the barriers. The luminescence line of quantum dots shifts to shorter wavelengths when a GaAs matrix is replaced by a wider bandgap AlGaAs ternary alloy [5]. Similarly, the quantization energy can be decreased by placing quantum dots into a material with a narrower bandgap. It was proposed to cover QDs with a thin InGaAs layer, which acts as a narrow bandgap host [6]. It was shown that the QD line can be shifted up to 1.3 μm at room temperature by decreasing the bandgap of the surrounding material. It should be mentioned that the red shift of wavelength is also caused by certain modification of QD shape, size and strain which occurs upon their re-growth with the InGaAs layer.

3. Stacked quantum dot arrays

The saturated gain and the transparency current density are proportional to the quantum dot density. For a certain optical loss α threshold current density of a laser with N planes of QDs can be express as:

$$J_{\text{th}}(\alpha, N) \approx N j_0 \left(1 - \frac{1}{\gamma} \ln\left(1 - \frac{\alpha}{N g^{\text{sat}}}\right)\right), \qquad (1)$$

where j_0 and g^{sat} represents, respectively, the transparency current density and the saturated gain of a single quantum dot plane. For QD lasers operating in the 1.2–1.3 μm spectral range the following parameters [7] $g^{\text{sat}} = 4.6 - 6$ cm^{-1}, $j_0 = 5 - 9.5$ A/cm^2, non-ideality parameter γ usually ranges from 0.5 to 0.8.

Dependence of the threshold current density on number of QD planes is characterized by certain optimum surface density, which provides minimal threshold current density for a given level of optical loss. For typical optical loss the optimum QD density corresponds to about ten planes of QDs. If the surface density is lower than its optimum value, the threshold current density increases because of gain saturation. If the surface density is higher than its optimum value, increase of the threshold current density is caused by higher transparency current density.

Number of repeatedly deposited QD layers is limited by plastic relaxation of the strain and lateral association of neighboring QDs. On the one hand, strain relaxation may be prevented by sufficiently thick spacer layers. Quantum dots emitting in the 1.2–1.3 μm spectral range require thicker spacers as compared to shorter-wavelength QDs because of larger volume of lattice-mismatched material per layer. On the other hand, thicker spacers reduce the optical confinement factor since outer QD layers are situated far from a waveguide center. It is currently accepted that 30–35 nm thick spacers provide high structural quality and sufficient optical confinement in a laser with ten QD plane. As a result of thick spacers, effect of vertical coupling of islands of neighboring planes is usually not observed in long-wavelength QD lasers.

Relationship between modal gain and threshold current density is presented in Fig. 1 for several different laser structures based on multiply stacked quantum dots of the 1.3 μm spectral range. A modal gain of 41 cm^{-1} with a threshold current density of 622 A/cm^2 has been reported for a QD laser comprising seven InAs/InGaAs QD layers [8]. By using optical waveguide with high optical confinement factor, a modal gain of 10-times stacked QD active region has been increased

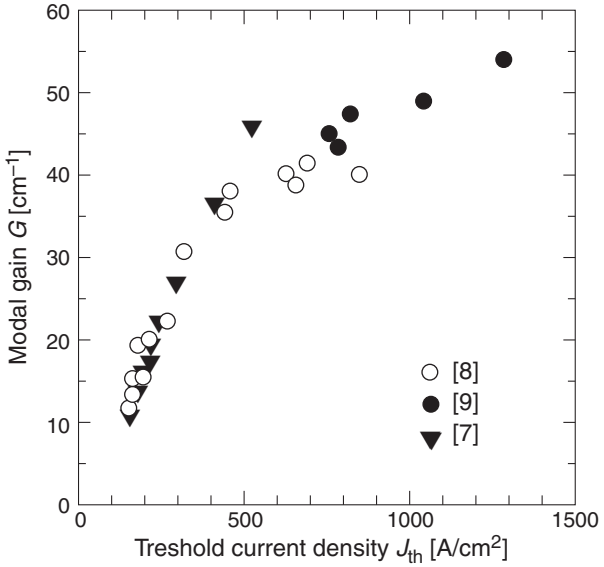

Fig. 1. Relationship between ground-state modal gain and threshold current density for 1.3 μm lasers based on multiply stacked quantum dots.

to 46 cm^{-1} (at ~500 A/cm^2) while the lasing wavelength exceeds 1.32 μm [7]. By using arrays of InAs/InGaAs QDs with a high surface density of 8×10^{10} cm^{-2} per plane and high uniformity synthesized under specific growth conditions, modal gain as high as 54 cm^{-1} was reported at a ground-state emission of nine-stacked QD laser [9]. However, in that reference the threshold current density is quite high (~1300 A/cm^2).

4. Chirped quantum dots

Side modes, which appear in lasing spectrum of a QD laser at moderate current densities, correspond to inhomogeneously broadened ground-state optical transition. Meanwhile, at sufficiently high currents those longitudinal modes are excited, whose spectral position corresponds to wavelengths of the first excited-state optical transition. In most cases spectral bands of the ground-state and first excited-state optical transitions are well separated from each other. As a result, a lasing spectrum comprises two distinguished maxima (Fig. 2). More uniform distribution of the spectral power density as desired for practical purposes can be achieved if the spectral bands of the GS and ES1 optical transitions notably overlap each other.

It was demonstrated that a periodic monolayer deposition of InAs/GaAs pairs results in formation of quantum dots with increased inhomogeneity [10]. The authors found that in a laser with QDs of this sort the laser emission is solely originated from the GS (ES1) level for long (respectively, short) cavities. These lasers exhibit a lasing FWHM of about 10 nm from single quantized states. However, at the intermediate lengths, very broad emission spectra of >20 nm are achieved. This broad spectral width is a result of the simultaneous emission of two states with strong spectral overlap owing to a close energy separation between GS and ES1 optical transitions and increased inhomogeneity.

Similar result can be achieved some parameter affecting a spectral position of a central wavelength is varied from one quantum dot layer to another. In particular, a width or a composition of an InGaAs layer that covers InAs/InGaAs QDs may be used as such parameter. Quantum dots formed in this way

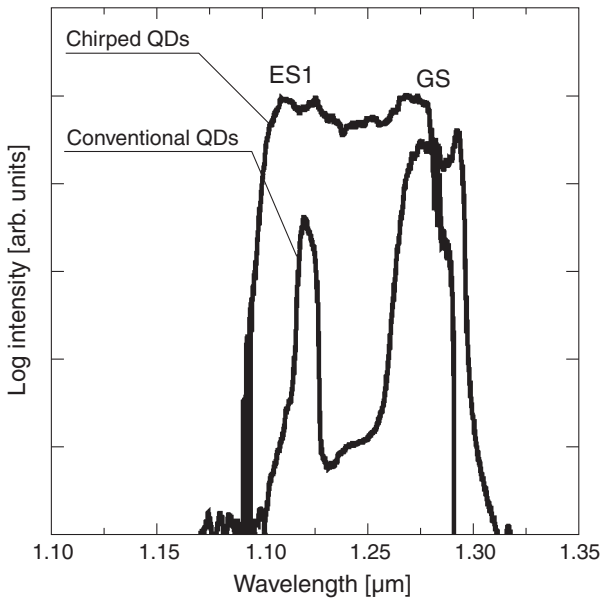

Fig. 2. Lasing spectra taken at high current densities from a conventional QD laser and a laser comprising nonidentical (chirped) QDs.

are often called as chirped QDs. Use of chirped QDs led to realization of a lasing spectral width of 75 nm [11]. A lasing spectrum of such QD laser (Fig. 2) comprises spectral components arisen from two quantized states. Overlap of these spectral components and approximate equalization of their intensities result in a large spectral width and a high degree of uniformity (4.5 dB) of a spectral power density. A total emission power is 750 mW corresponds to an average spectral power density of 10 mW/nm.

Owing to inhomogeneous line broadening and a plurality of excited-state optical transitions, self-organized quantum dots and, in particular chirped QDs, may be useful for realization of widely tunable laser diodes, which are highly desired for various application including spectroscopy, optical coherence tomography, optical communication, environmental monitoring, and direct frequency doubling. An external cavity grating-coupled laser comprising 10 nonidentical planes of InAs/InGaAs QDs was tuned in the 175 nm interval. Across the entire tuning range, a CW peak power exceeds the 150 mW level, while the maximum peak power was as high as 632 mW obtained at wavelength of the first excited-state optical transition [12]. To the best of our knowledge, these are the highest power levels ever reported for tunable lasers operating in this spectral range, as well as the highest ones for tunable QD lasers of any spectral range.

5. Conclusion

It is demonstrated that various methods of intentional modifications of QD properties may provide additional flexibility for their use in lasers. In particular, variation of QD effective thickness in combination with changing the composition of surrounding matrix may tune the luminescence peak position in a wide spectral range. Minimization of the threshold current density can be achieved by proper choice of number of QD planes repeatedly deposited in the active region. A requirement of broad emission spectra can be satisfied by use of nonidentical QD planes.

Acknowledgements

The work is supported in different parts by Russian Federal Agency of Education, Russian Federal Agency of Science and Innovations, Russian Foundation for Basic Research, Programs of Fundamental Studies of the Russian Academy of Sciences.

References

[1] A. Yu. Egorov *et al*, *Semiconductors* **28**, 809 (1994).
[2] N. N. Ledentsov *et al*, *Semicond. Sci. Technol.* **16**, 502 (2001).
[3] K. Mukai *et al*, *Jpn. J. Appl. Phys.* **33**, L1710 (1994).
[4] D. L. Huffaker *et al*, *Appl. Phys. Lett.* **73**, 520 (1998).
[5] A. E. Zhukov *et al*, *Semiconductors* **31**, 411 (1997).
[6] V. M. Ustinov *et al*, *Appl. Phys. Lett.* **74**, 2815 (1999).
[7] M. V. Maximov *et al*, *Semicond. Sci. Technol.* **23**, 105004 (2008).
[8] A. Salhi *et al*, *IEEE Photon. Tech. Lett.* **18**, 1735 (2006).
[9] T. Amano *et al*, *IEEE J. Selected Topics Quantum Electron.* **13**, 1273 (2007).
[10] H. S. Djie *et al*, *Optics Lett.* **32**, 44 (2007).
[11] A. Kovsh *et al*, *Optics Lett.* **32**, 793 (2007).
[12] A. E. Zhukov *et al*, *Quantum Electron.* **38**, 409 (2008).

18th Int. Symp. "Nanostructures: Physics and Technology"
St Petersburg, Russia, June 21–26, 2010

Maximum modulation bandwidth of a quantum dot laser

Levon V. Asryan[1] and Robert A. Suris[2]

[1] Virginia Polytechnic Institute and State University, Blacksburg, Virginia 24061, USA
[2] Ioffe Physical-Technical Institute, St Petersburg, Russia

Abstract. Modulation response of a quantum dot (QD) laser is studied as a function of injection current and parameters of the structure. The highest possible bandwidth is calculated and shown to increase with increasing overlap integral between the electron and hole wave functions in QDs, number of QD-layers and surface density of QDs in a layer, and with reducing QD-size dispersion.

Introduction

Due to the capability of direct modulation of the optical output by electric current, semiconductor lasers are extensively used in high-speed fiber networks. Whereas a discrete energy spectrum of carriers in quantum dots (QDs) enables low-threshold and temperature-stable lasing, the modulation bandwidth of QD lasers is still below that of quantum well (QW) lasers. In this work, the factors limiting the modulation bandwidth of a QD laser are identified and the highest possible bandwidth is calculated.

1. Theoretical model and discussion

The carrier injection into a quantum-confined active region of semiconductor lasers is an indirect process — carriers are first injected into the reservoir [optical confinement layer (OCL)] and then captured into the active region. Reservoir-mediated injection adversely affects the laser operating characteristics — the threshold current is increased and more temperature-sensitive [1], and the output optical power is decreased [2]. Due to a transport delay across the OCL and a capture delay from the OCL into the active region, the bandwidth of direct modulation of the output power by injection current is also reduced. The main objective of this work is to estimate the highest possible modulation bandwidth of a laser. For this purpose, we assume instantaneous carrier injection into the active region, i.e., we assume that both the transport across the OCL to the active region and exchange between the OCL and the active region are instantaneous. At the same time, our model includes the carrier population and recombination in the OCL. Although our analysis and derivations are general and apply also to QW and quantum wire lasers, our focus here is on QD lasers.

We use the small-signal analysis of rate equations [3–6]. The assumptions of no transport and capture delay effectively reduce the number of equations to two — for the total carrier density $n = n_{\rm act} + n_{\rm OCL}$ (including the active region and OCL) and the photon number N. Assuming small ac injection current density $\delta j = (\delta j_{\rm m})\exp(i\omega t)$, we calculate the small variations $\delta n = (\delta n_{\rm m})\exp(i\omega t)$ and $\delta N = (\delta N_{\rm m})\exp(i\omega t)$ and then the modulation response function $H(\omega) = |\delta N_{\rm m}(\omega)/\delta N_{\rm m}(0)|^2$.

Depending on the dc component of the current density, $H(\omega)$ may have a peak (Fig. 1), which is obtained at

$$\omega_{\rm peak} = \sqrt{\Omega_{\rm osc}^2 - \Gamma_{\rm dec}^2} = \sqrt{\omega_0^2 - 2\Gamma_{\rm dec}^2}\,, \qquad (1)$$

where $\Omega_{\rm osc}$ and $\Gamma_{\rm dec}$ are the frequency and decay rate of relaxation oscillations,

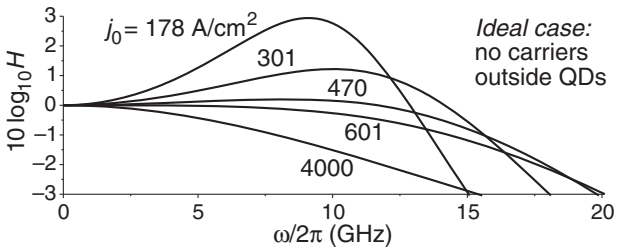

Fig. 1. Response function at different values of the dc injection current density. In Figs. 1–4, a GaInAsP structure of [6] lasing at $T = 300$ K near 1.55 μm is considered; $Z_{\rm L} = 1$, $\delta_{\rm RMS} = 0.05$ (10% QD-size fluctuations), $N_{\rm S} = 6.11\times10^{10}$ cm^{-2}, $I_{\rm overlap} = 1$; $g^{\rm max} = 29.52$ cm^{-1} and $G_{\rm act}^{\rm dif} = 1.36\times10^{-14}$ cm^2. At $L = 1.139$ mm, $\omega_{-3{\rm dB}}^{\rm max}/2\pi = 20$ GHz and $j_{\rm opt} = 601$ A/cm^2.

$$\Gamma_{\rm dec} = \frac{1}{2}\left(\frac{1}{\tau_{\rm spon}^{\rm dif}} + v_{\rm g}\frac{G_{\rm dif}}{V}N_0\right),\ \omega_0 = \sqrt{v_{\rm g}\frac{G_{\rm dif}}{V}N_0\frac{1}{\tau_{\rm ph}}}\,, \qquad (2)$$

N_0 is the dc number of photons in the lasing mode, $v_{\rm g}$ is the group velocity of light, $1/\tau_{\rm ph} = (v_{\rm g}/L)\ln(1/R)$ is the reciprocal of the photon lifetime in the cavity, L is the cavity length, and R is the mirror reflectivity.

The *effective differential gain* $G^{\rm dif}$ in (2) is calculated as the derivative of the modal gain g with respect to the *total carrier density*, $n = n_{\rm act} + n_{\rm OCL}$,

$$G^{\rm dif} = \partial g/\partial n = (\partial n_{\rm act}/\partial n)\,G_{\rm act}^{\rm dif} \ll G_{\rm act}^{\rm dif}\,, \qquad (3)$$

where $G_{\rm act}^{\rm dif} = \partial g/\partial n_{\rm act}$ is the differential gain calculated as the derivative with respect to the carrier density in the active region only. Since $\partial n_{\rm act}/\partial n \ll 1$, $G^{\rm dif} \ll G_{\rm act}^{\rm dif}$, and, as discussed below, the practically achievable modulation bandwidth of the laser can be significantly reduced.

In (2), $\tau_{\rm spon}^{\rm dif}$ is the effective differential spontaneous recombination time, which is expressed in terms of the differential recombination times in the active region and OCL.

The most important dynamic characteristic is the -3dB-bandwidth (referred to as the modulation bandwidth here) — the frequency, at which $H(\omega)$ is twice decreased compared to its dc ($\omega = 0$) value. The equation for $\omega_{-3{\rm dB}}$ is

$$\omega_{-3{\rm dB}} = \sqrt{\omega_{\rm peak}^2 + \sqrt{\omega_{\rm peak}^4 + (r-1)\omega_0^4}}\,, \qquad (4)$$

where $r = 10^{0.3} \approx 1.995$.

The relaxation oscillations are only possible [$\Omega_{\rm osc}$ should be real — see (1)] within a certain range of values of N_0, i.e.,

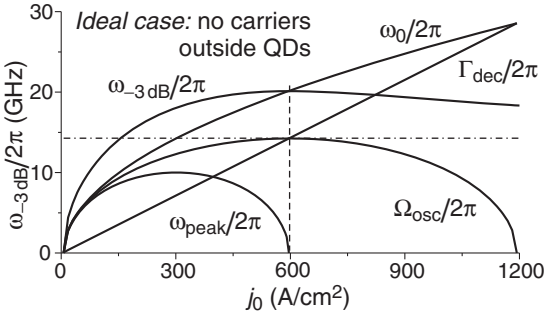

Fig. 2. Modulation bandwidth $\omega_{-3\mathrm{dB}}$, peak frequency of the response function ω_{peak}, relaxation oscillation frequency Ω_{osc}, and decay rate Γ_{dec} versus dc injection current density.

of dc component j_0 of the injection current density. Within this range, Ω_{osc} increases from zero, approaches its maximum value, and then decreases to zero (Fig. 2). The peak of $H(\omega)$ also exists within its own range of j_0 [ω_{peak} should be real — see (1)]; ω_{peak} behaves similarly to Ω_{osc} (Fig. 2). At j_0 value, at which the peak of $H(\omega)$ disappears [$\omega_{\mathrm{peak}} = 0$], Ω_{osc} becomes maximum (Fig. 2); although Ω_{osc} is maximum, the relaxation oscillations are strongly damped at this j_0 ($\Gamma_{\mathrm{dec}} = \Omega_{\mathrm{osc}}^{\mathrm{max}} = 1/\tau_{\mathrm{ph}}$).

As a function of j_0, $\omega_{-3\mathrm{dB}}$ also has a maximum, which is obtained at approximately the same value j_{opt} of j_0, at which Ω_{osc} is maximum and the peak of $H(\omega)$ disappears (Fig. 2); at $j_0 = j_{\mathrm{opt}}$, $H(\omega)$ is as flat as possible (Fig. 1). On further increase of j_0 beyond j_{opt}, $\omega_{-3\mathrm{dB}}$ decreases and asymptotically approaches its saturation value ($\approx 1/\tau_{\mathrm{ph}}$). The maximum values of ω_{peak}, Ω_{osc}, and $\omega_{-3\mathrm{dB}}$ are controlled by the reciprocal photon lifetime in the cavity,

$$\omega_{-3\mathrm{dB}}^{\mathrm{max}} \approx \sqrt{2}\Omega_{\mathrm{osc}}^{\mathrm{max}} \approx \sqrt{2}\left(\sqrt{2}\omega_{\mathrm{peak}}^{\mathrm{max}}\right) \approx \frac{\sqrt{2}}{\tau_{\mathrm{ph}}} = \sqrt{2}\frac{v_{\mathrm{g}}}{L}\ln\frac{1}{L}. \quad (5)$$

The shorter L, the higher $\omega_{-3\mathrm{dB}}^{\mathrm{max}}$. The shortest L is controlled by the maximum modal gain g^{max} through the lasing condition: $(1/L^{\mathrm{min}})\ln(1/R) = g^{\mathrm{max}}$. Using L^{min} in (5), we find that *the highest possible bandwidth increases directly with* g^{max} *and is not affected by the differential gain*,

$$\omega_{-3\mathrm{dB}}^{\mathrm{highest}} = \sqrt{2}\, v_{\mathrm{g}} g^{\mathrm{max}} \propto I_{\mathrm{overlap}} Z_{\mathrm{L}} N_{\mathrm{S}}/\delta_{\mathrm{RMS}}\,, \quad (6)$$

where we used the expression for g^{max} of a QD laser [6,13], and I_{overlap} is the overlap integral between the electron and hole wave functions in a QD, Z_{L} is the number of QD-layers, N_{S} is the surface density of QDs in one layer, and δ_{RMS} is the root mean square of QD-size fluctuations.

While $\omega_{-3\mathrm{dB}}^{\mathrm{highest}}$ is controlled by merely g^{max}, and $\omega_{-3\mathrm{dB}}^{\mathrm{max}}$ by L, the current densities, at which they are obtained, are controlled by G^{dif} as well. Consequently, a practically achievable bandwidth can be significantly reduced compared to (6) and even (5).

For the ideal case of no carriers in the OCL (direct injection into QDs), Fig. 1 shows $H(\omega)$, and Fig. 2 shows $\omega_{-3\mathrm{dB}}$ versus j_0. As seen from the figures, $\omega_{-3\mathrm{dB}}^{\mathrm{max}}$ [given by (5)] is easily attained at low j_{opt} (601 A/cm^2). This is because G^{dif} is high in this case: $G^{\mathrm{dif}} = G_{\mathrm{act}}^{\mathrm{dif}} = 1.36 \times 10^{-14}$ cm^2.

Fig. 3 shows $\omega_{-3\mathrm{dB}}^{\mathrm{highest}}$ versus g^{max} in a single QD-layer laser. The top axis illustrates the situation when g^{max} is varied through changing I_{overlap}. At 10% QD-size fluctuations

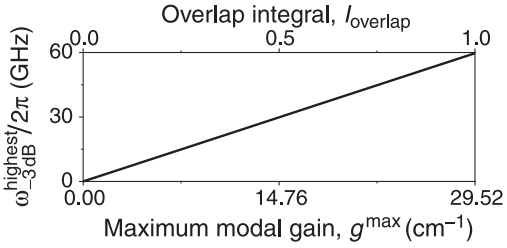

Fig. 3. Highest possible modulation bandwidth of a single QD-layer laser versus maximum modal gain and overlap integral between the electron and hole wave functions in QDs.

($\delta_{\mathrm{RMS}} = 0.05$), $N_{\mathrm{S}} = 6.11 \times 10^{10}$ cm^{-2}, and ideal overlap ($I_{\mathrm{overlap}} = 1$), the shortest cavity length is $L^{\mathrm{min}} = 386\ \mu$m, the maximum gain is $g^{\mathrm{max}} = 29.52$ cm^{-1}, and *the highest possible bandwidth in a single QD-layer laser* is

$$\omega_{-3\mathrm{dB}}^{\mathrm{highest}}/2\pi \approx 60\,\mathrm{GHz}\,. \quad (7)$$

If the overlap is poor, even $\omega_{-3\mathrm{dB}}^{\mathrm{highest}}/2\pi$ will be low — thus, $g^{\mathrm{max}} = 4.4$ cm^{-1} and $\omega_{-3\mathrm{dB}}^{\mathrm{highest}}/2\pi \approx 9$ GHz if $I_{\mathrm{overlap}} = 0.15$. One way of increasing I_{overlap} is the use of more symmetrical (e.g., truncated or disk-shape) QDs [7]. As seen from (6), the use of multiple layers with QDs can effectively enhance the modulation bandwidth thus compensating for a poor overlap or a large QD-size dispersion. The use of submonolayer QDs allowing for a higher surface density N_{S} of QDs in a layer [8] can also enhance the bandwidth.

In the presence of carriers in the OCL, all the above expressions hold. At the same time, G^{dif} [see (3)] is considerably reduced as compared to $G_{\mathrm{act}}^{\mathrm{dif}}$. Due to this, $\omega_{-3\mathrm{dB}}^{\mathrm{max}}$ (and the more so $\omega_{-3\mathrm{dB}}^{\mathrm{highest}}$) becomes unattainable at practical values of the current density in a single QD-layer laser. Indeed, the condition for the maximum bandwidth ($\omega_{\mathrm{peak}} = 0$) is obtained when $\omega_0^2 = 2\Gamma_{\mathrm{dec}}^2$ — see (1). As seen from (2), both ω_0 and Γ_{dec} are controlled by the product of the photon number N_0 and G^{dif}. In a single QD-layer laser considered here, $\partial n_{\mathrm{act}}/\partial n = 0.01$, i.e., G^{dif} is about two orders of magnitude lower than $G_{\mathrm{act}}^{\mathrm{dif}}$ [see (3)]: $G^{\mathrm{dif}} = 1.27 \times 10^{-16}$ cm^2. Hence, the photon number $N_0 = N_0^{\mathrm{opt}}$, at which $\omega_0^2 = 2\Gamma_{\mathrm{dec}}^2$, is two orders of magnitude higher than in the ideal case of no carriers in the OCL, and so is j_{opt} (64 kA/cm^2). Fig. 4 shows $j_0 = j_{\mathrm{opt}}$ maximizing $\omega_{-3\mathrm{dB}}$ versus number of QD-layers. While j_{opt} is very high even for $Z_{\mathrm{L}} = 2$, the use of 4 or 5 layers makes $\omega_{-3\mathrm{dB}}^{\mathrm{max}}$ practically attainable thus compensating for the adverse effect of carriers in the OCL.

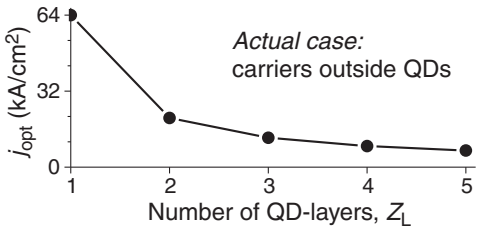

Fig. 4. Optimum dc current density maximizing $\omega_{-3\mathrm{dB}}$ versus number of QD-layers ($\omega_{-3\mathrm{dB}}^{\mathrm{max}}/2\pi = 20$ GHz at $L = 1.139$ mm).

2. Conclusion

Modulation response of a QD laser has been studied as a function of injection current density and parameters of the structure. The highest possible bandwidth has been calculated and shown to increase with increasing overlap integral between the electron and hole wave functions in QDs, number of QD-layers and surface density of QDs in a layer, and with reducing QD-size dispersion.

Acknowledgements

L.V.A. acknowledges the U.S. ARO (Grant No. W911-NF-08-1-0462) and R.A.S. acknowledges the RFBR for support of this work (Grant No. 08-02-01337).

References

[1] L. V. Asryan, R. A. Suris, *Sem. Sci. Technol.* **11**, 554 (1996).
[2] L. V. Asryan, S. Luryi, R. A. Suris, *APL* **81**, 2154 (2002).
[3] T. Ikegami, Y. Suematsu, *Proc. IEEE* **55**, 122 (1967).
[4] R. F. Kazarinov, R. A. Suris, *Sov. Phys.-JETP* **39**, 522 (1974).
[5] R. Olshansky *et al*, *IEEE J. QE* **23**, 1410 (1987).
[6] R. Nagarajan *et al*, *IEEE J. QE* **28**, 1990 (1992).
[7] L. V. Asryan *et al*, *J. Appl. Phys.* **90**, 1666 (2001).
[8] A. Mutig *et al*, *Proc. SPIE* **7615**, 76150N (2010).

18th Int. Symp. "Nanostructures: Physics and Technology"
St Petersburg, Russia, June 21–26, 2010

Mode-locked broadened-waveguide SQW GaInAs laser diode with improved stability

I. M. Gadzhiev, M. S. Buyalo, I. O. Bakshaev, S. O. Slipchenko, N. A. Pikhtin, A. Yu. Leshko, A. V. Lyutetskiy, I. S. Tarasov and E. L. Portnoi
Ioffe Physical-Technical Institute, St Petersburg, Russia

Abstract. It was shown for the first time that the waveguide broadening in a single QW laser diode improves the stability of the passive mode-locking regime. The increasing of the carrier transport time leads to suppression of the self-pulsation instability near threshold, and the reduction of the overlap integral decreases the width of the RF spectrum.

Introduction

Passively mode-locked semiconductor lasers, which include a monolithically integrated forward biased gain section with a reverse biased saturable absorber section, have been identified as promising optical pulse sources for communications and metrology [1] and, most recently, on-chip clock distribution in future computer systems [2]. To date, however, their behavior has been plagued with various instabilities; the most important of these are: 1) the self-pulsation instability, or passive Q-switching and 2) the fluctuations caused by the amplified spontaneous emission (ASE). The first one tends to happen precisely at the operating conditions (such as low operating current) corresponding to the shortest mode-locking pulses attractive for many applications. The second one increases the timing jitter and, consequently, widens the RF spectrum.

Recently, it was predicted theoretically that broadening of optical confinement layer (OCL) in single quantum well (SQW) monolithic mode-locked semiconductor lasers may suppress Q-switching instability by increasing the carrier transport time [3]. It can be expected also that very small optical confinement factor in such laser will reduce ASE.

In this report we present the first experimental results of passive mode locking received on separate confinement heterostructure described in [4]. The thickness of OCL was 1.7 μm, and the QW width — 9 nm (overlap integral $\Gamma < 1\%$), the cavity length — 3.3 mm, stripe width — 5 μm, the saturable absorber section length — 300 μm.

1. Experimental

The absorption spectra of the reverse biased saturable absorber section measured at different biases by the integrated optics absorption spectroscopy method [5] is submitted for consideration on the Fig. 1. The spectra demonstrate strong quantum confinement Stark effect (QCSE) at the whole range of applied reverse biases at room temperature.

The two section laser shows nonstandard laser generation behavior in wide range of reverse biases, from zero till -10 V: CW operation takes place, no Q-switching was observed. At the Fig. 1 the position of laser generation spectral line at zero reverse bias is shown. The band gap shrinkage of about 40 meV takes place at threshold current density 600 A/cm^2. At the bias below -10 V the reverse biased saturated absorber starts to work as nonlinear absorption element, providing the expected mode-locking regime. A small red shifting of laser generation spectral line occurs (Fig. 1). Autocorrelation functions at operating currents 175, 182 and 197 mA and reverse bias -12.5 V

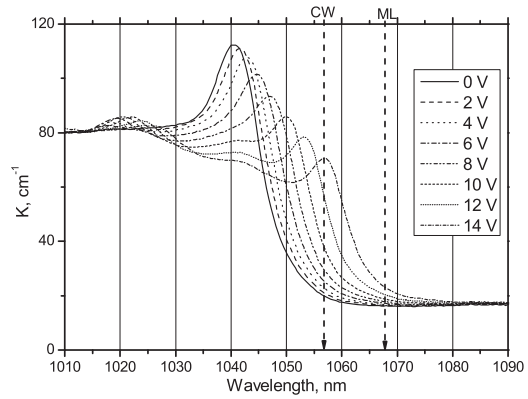

Fig. 1. Evolution of exciton edge absorption with reverse biases increasing and wavelength position of generation in CW and mode-locked (ML) regimes.

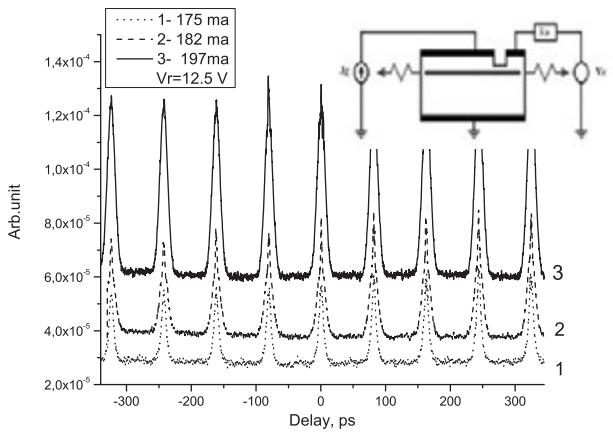

Fig. 2. Autocorrelation function of mode-locked laser at different currents.

is shown on Fig. 2. One can see stable mode-locking in the wide pumping range, starting from the threshold (in agreement with [3]). It should be mentioned that near the threshold the pulse duration is bandwidth limited. Typical RF-spectrum in considered regime is presented on the Fig. 3. The FWHM is near 20 kHz, that is significantly less than for the QW laser with narrow graded waveguide (2 MHz).

The increase of reverse bias results in an increase of the operating current and leads to low frequency modulation of high frequency mode-locked signal (Fig. 4). The RF spectrum of optical signal from the mode-locked laser diode at pumping current 210 mA and reverse bias -13.2 V is shown on Fig. 5. This RF spectrum demonstrates up/down conversion of

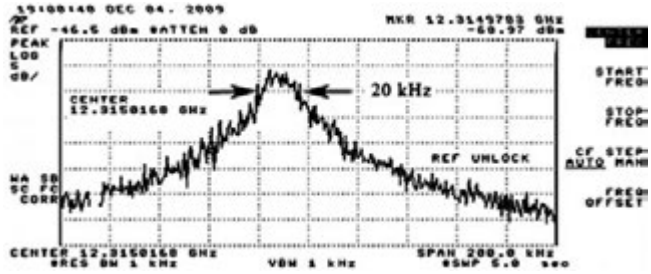

Fig. 3. RF-spectrum of mode-locked laser near threshold.

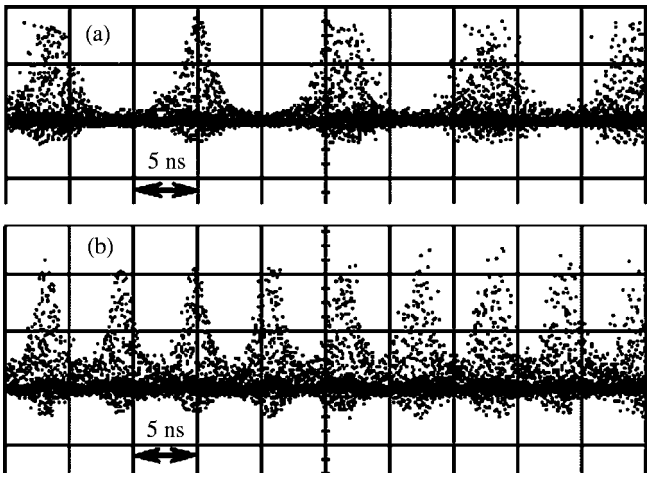

Fig. 4. Frequency increasing in mixed regime with current growth. $I_g = 204$ (a), 234 (b) mA, $V_r = -14$ V, $f_{\mathrm{SB}} = 90$ (a), 180 (b) MHz, $f_{\mathrm{ML}} = 12$ GHz.

the 12.315 GHz mode-locking frequency. The conversion frequency depends on the CW operating current (approximately 2 MHz/mA) (see Fig. 4). Theoretical calculation proved the feasibility of RF frequency conversion due to parametric effects in such LDs [6]. Frequency up/down conversion of optically transmitted RF signals may be useful for a number of microwave-over-fiber applications.

In conclusion, we would like to draw attention that the mode-locked generation wavelength is 1060–1070 nm. It opens the possibility to amplify the RF signal at the optical frequency by standard optical fiber amplifier.

Acknowledgements

This work has been supported in part by RFFI grant 08-02-12149-ofi and the programms of the Russian Academy of Science.

References

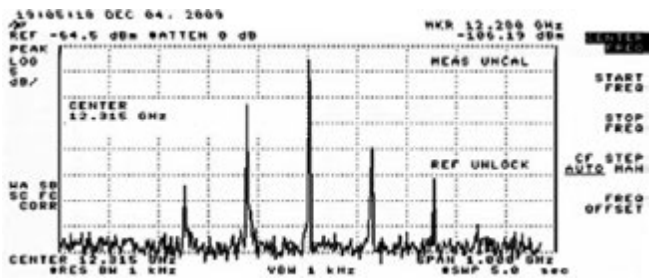

Fig. 5. RF-spectrum in mixed regime.

[1] E. A. Avrutin, J. H. Marsh and E. L. Portnoi, "Monolithic and multi-gigahertz mode-locked semiconductor lasers: constructions, experiment, models and applications" *IEE Proc. Optoelectron* **147**, 251–278 (2000).

[2] A. Gubenko, D. Livshits, I. Krestnikov, S. Mikhrin, A. Kozhukhov, A. Kovsh, N. Ledentsov, A. Zhukov and E. Portnoi, "High-power monolithic passively modelocked quantum-dot laser" *Electronic letters* **41**, 1124–1125 (2005).

[3] E. A. Avrutin and E. L. Portnoi, "Suppression of Q-switching instabilities in broadened-waveguide monolithic mode-locked laser diodes" *Optical and Quantum Electronics* **40**, 655–664 (2008).

[4] D. A. Vinokurov, S. A. Zorina, V. A. Kapitonov, A. V. Murashova, D. N. Nikolaev, A. L. Stankevich, M. A. Khomylev, V. V. Shamakhov, A. Yu. Leshko, A. V. Lyutetskiy, T. A. Nalyot, N. A. Pikhtin, S. O. Slipchenko, Z. N. Sokolova, N. V. Fetisova, I. S. Tarasov, "High power laser diodes based on asymmetric separate confinement heterostructure" *Semiconductors* **39**, 370–373 (2005).

[5] V. V. Nikolaev, N. S. Averkiev, M. M. Sobolev, I. M. Gadzhiyev, I. O. Bakshaev, M. S. Buyalo, and E. L. Portnoi, "Tunnel coupling in an ensemble of vertically aligned quantum dots at room temperature" *Phys. Rev. B* **80**, 205304 (2009).

[6] E. L. Portnoi, V. B. Gorfinkel, E. A. Avrutin, I. G. Thayne, D. A. Barrow , J. H. Marsh, and S Luryi, "Optoelectronic Microwave-Range Frequency Mixing in Semiconductor Lasers" *IEEE J. Select. Topics Quantum Electron.* **1**, 451–460 (1995).

18th Int. Symp. "Nanostructures: Physics and Technology"
St Petersburg, Russia, June 21–26, 2010

InGaN/GaN superlattices for high-power III–N light-emitting diodes

N. V. Kryzhanovskaya[1,2], W. V. Lundin[1,2], A. E. Nikolaev[1,2], A. F. Tsatsul'nikov[1,2], A. V. Sakharov[1,2], N. A. Cherkachin[3], M. J. Hytch[3], G. A. Valkovskiy[1], M. A. Yagovkina[1] and S. O. Usov[2]

[1] Ioffe Physical-Technical Institute, St Petersburg, Russia
[2] Submicron Heterostructures for Microelectronics, Research & Engineering Center RAS, St Petersburg, Russia
[3] Center for Material Elaboration & Structural Studies of the NCSR, 31055, Toulouse, France

Abstract. We present the results of the investigation of structural and optical properties of InGaN/GaN short-period superlattices (SPSL), grown by MOCVD on sapphire substrates using a method of periodical growth interruptions of InGaN layer in hydrogen atmosphere. Non-uniform In distribution and formation of the regions of the neighboring InGaN layers coalescence were revealed in the InGaN/GaN structures. These features of the structural properties result in modification of the emission spectrum in depend on the SL periods number. Improving of the light emitting diodes parameters with active region containing the SPSL was demonstrated.

Introduction

Relatively thick (quasi-bulk) InGaN layers are very attractive for a number of applications [1]. However, a tendency of InGaN alloy for phase separation in combination with fast morphology deterioration and dislocation generation during growth results in poor material quality of the layer. A well-known way of material quality improvement is a replacement of bulk alloy with a short-period superlattice with the same average composition. Recently we have developed a new method to grow short-period InGaN/GaN superlattice (SPSL) based on conversion of an InGaN layer to GaN in hydrogen atmosphere [2]. The SPSL was formed by applying the periodic growth interruptions in hydrogen atmosphere during growth of thick InGaN layer. Growth interruption in hydrogen atmosphere was applied after 2 nm-thick $In_{0.1}Ga_{0.9}N$ layer growth in nitrogen atmosphere during each period. Growth interruption leads to the conversion of the $\sim$1 nm thick InGaN surface layer into GaN. Periodic repetition of this procedure allows us to form 1 nm InGaN / 1 nm GaN SPSL. In this work we investigate structural and optical properties of the SPSLs in dependence on the number of the periods and develop a design of a deep green light emitting diode (LED) containing these SPSLs in the active region.

1. Experiment

Growth of the SPSLs was carried out on the Aixtron 2000HT MOCVD system on sapphire substrates followed by a 4 μm-thick buffer layer. Details of the growth procedure were presented in [2]. SPSLs containing 6, 30 and 60 periods (samples A, B and C correspondently) were grown. All the SPSL structures were capped by 2-nm-thick GaN layer. Structural properties of the grown SLSLs were investigated by x-ray diffraction and two-dimentional reciprocal space mapping using Bruker AXS diffractometer and by high-resolution transmission electron microscopy (HR TEM) using microscope Technai (200 kV). Optical properties were investigated by photoluminescence (PL) spectroscopy using standard PL setup based on He-Cd laser (325 nm) and closed-cycle He cryostat. LED structures for deep green optical range containing SPSL in active region were grown. In all structures the active region was deposited on a 4 μm thick n-doped GaN buffer layer. SPSL-based LEDs consist of active region containing 12-period SPSL followed by an active InGaN quantum well. After active region 2-nm GaN cap layer, 20-nm-thick p-AlGaN electron blocking layer and a 0.2-μm-thick p-GaN cap layer (p-doping $= 1.2 \times 10^{18}$ cm^{-3}), were deposited.

2. Discussion

Investigations of the structural properties of the SPSLs shown that applied method of the SPSL growth allowed us to realize heterostructures with periodical change of In concentration from 0 to 10% along the direction of growth. The measured diffraction curve for (0002) reflection of a typical InGaN/GaN SPSL exhibits peak of the GaN layer and the zero-order peak with satellite peaks associated with the SL. The (11–24) two-dimensional reciprocal space mapping shows that GaN maximum, zero-order and first-order SL satellites are along q_z direction for SPSL studied. It means that the InGaN/GaN SPSLs are grown coherently on GaN layer without relaxation even for 60-period SPSL (total thickness of the SPSL is 120-nm) (Fig. 1).

Fig. 2 shows geometric phase analysis of HRTEM image of 60-period SPSL: strain relative to GaN, (resolution 1 nm). One can see periodical change of contrast corresponding to the periodical change of lattice constant InGaN (bright regions) and GaN (dark regions) along the growth direction. In composition inside InGaN layers is inhomogeneous. Local (2–4 nm) regions with higher (up to 16%) In contents are observed along

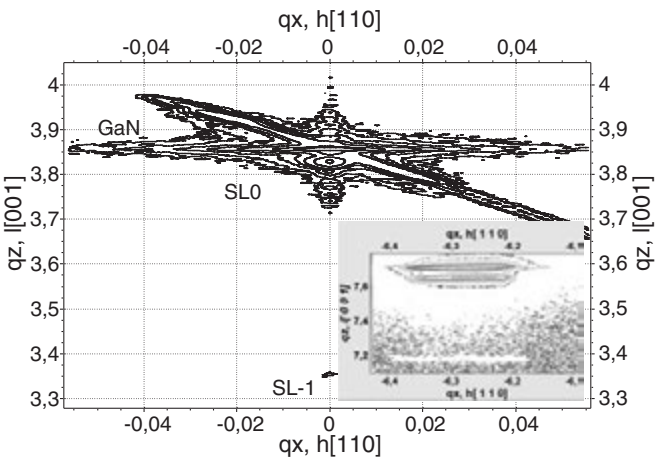

Fig. 1. The (11–24) two-dimensional reciprocal space mapping of InGaN/GaN SPSL (sample B).

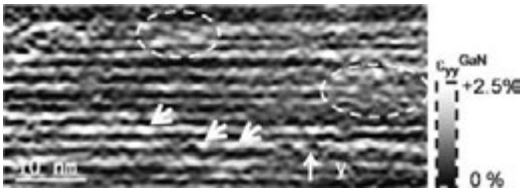

Fig. 2. Geometric phase analysis of HRTEM image along [−15 − 40]: deformation relatively to GaN.

the layers (marked by arrows). In addition, some adjacent InGaN layers lock together due to the inhomogeneous InGaN layer conversion during the growth interruption (marked by circles). This effect leads to formation of the local areas in which thickness of the InGaN is increased to 3 nm. TEM investigations have also shown that no additional dislocations were generated in SPSL in spite of relatively high thickness and lattice mismatch.

The presents of the local regions with higher In content

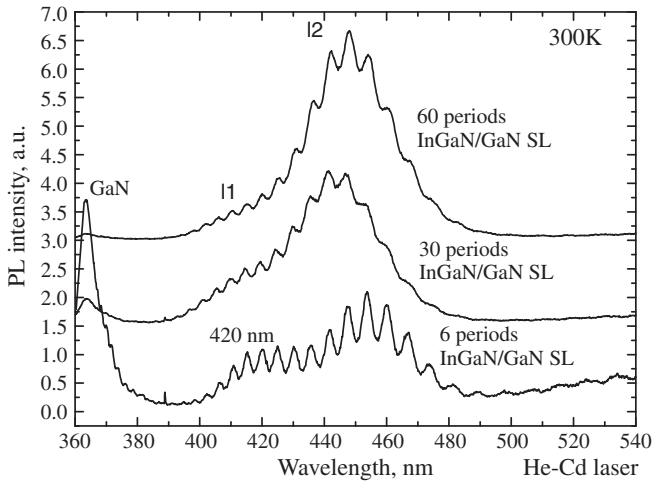

Fig. 3. PL spectra of the structures A, B and C.

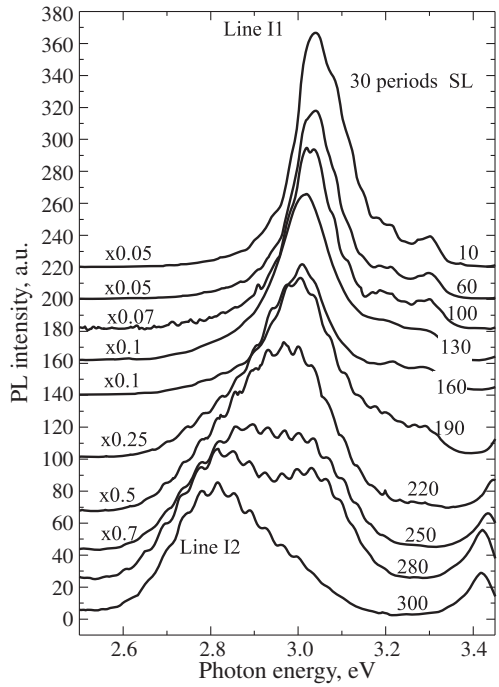

Fig. 4. PL spectra of the structures obtained at different temperatures.

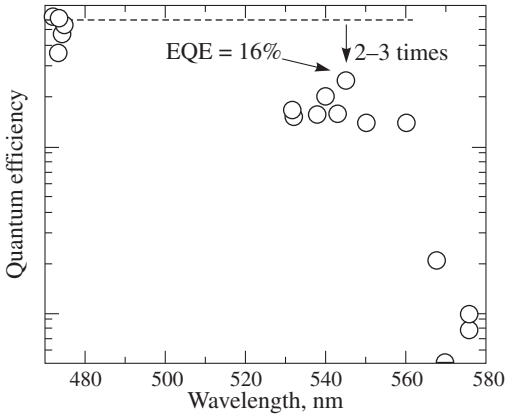

Fig. 5. Dependence of the quantum efficiency of the LED structures on emission wavelength (on-wafer measurements).

result in the formation of the potential minimums for the carriers. It is need to emphasize that non-uniformity of the small ∼1 nm thick InGaN layers is responsible for non-equilibrium broadening of the emission line whereas existence of the local 3 nm thick InGaN areas can leads to significant shift of the emission and formation of additional PL line in the spectrum. Fig. 3 shows PL spectra of the samples A–C at 300 K. PL line I1 at 2.95 eV (420 nm) corresponds to the transitions in the uniform $In_xGa_{1-x}N$ layers with $x \sim 0.1$. This result is in agreement with average In content obtained from structural analysis. Increase in temperature from 10 K to ∼190–220 K results in I2 line arising (Fig. 4). Position of this line does not depended on the number of periods in the SPSL. We propose that this line can be connected with recombination in the local ∼3 nm thick InGaN areas formation of which was described above. Increase in temperature leads to transport of carriers inside the SPSL that results in collection of carriers inside the local potential minima and increase in the I2 line intensity.

The developed SPSL were used to grow LED structures for deep green optical range (540–560 nm). Problems of the deep green LEDs growth are associated with a required high In content in the InGaN active region. We have proposed a design of an active region comprised a single InGaN quantum well (QW) deposited on the InGaN/GaN SPSL. The green InGaN QW and SPSL were separated by 20-nm-thick GaN barrier. The use of this active region design instead of the InGaN/GaN multi QW structure allows us to decrease the total In content in active region and to improve the emission efficiency. Dependence of the quantum efficiency of the developed green LED structures on the emission wavelength is shown at Fig. 5.

Acknowledgements

This work is supported by RFBR 09-02-12449, 08-02-01344, Ministry of education and science of the RF project P1219.

References

[1] Wu Junqiao *et al*, *Journal of Applied Physics* **106**, 011101 (2009).

[2] W. V. Lundin *et al*, 13th European Workshop on Metalorganic Vapour Phase Epitaxy (Ulm, Germany, 2009).

[3] A. F. Tsatsulnikov *et al*, *Proc. 7th All-Russian Conference Gallium, aluminum and indium nitrides*, (Moscow, Russia, 2010).

18th Int. Symp. "Nanostructures: Physics and Technology"
St Petersburg, Russia, June 21–26, 2010

Green lasers and laser converters based on II–VI nanoheterostructures

S. V. Ivanov[1], S. V. Sorokin[1], I. V. Sedova[1], E. V. Lutsenko[2], G. P. Yablonskii[2], N. A. Gamov[3], M. M. Zverev[3] and P. S. Kop'ev[1]

[1] Ioffe Physical-Technical Institute, St Petersburg, Russia
[2] Stepanov Institute of Physics of NAS Belarus, Independence Ave. 68, Minsk 220072, Belarus
[3] Moscow State Institute of Radio Engineering, Electronics and Automations, Moscow, 117454, Russia

Abstract. The paper presents and discusses the original results on molecular-beam epitaxy growth, design optimization, and studies of structural, optical and laser properties of low-dimensional wide-gap ZnCdSe/ZnMgSSe laser nanoheterostrucures emitting in the green spectral range (500–550 nm) under the optical and electron beam pumping.

Introduction

After the general cessation of research on II–VI laser diodes (LDs) in 1998 because of the heavy progress in III-nitride optoelectronics, the studies of the ZnSe-based LDs have been performed only in a few laboratories over the world in attempts to overcome the "slow" degradation problem arising from using the nitrogen-doped ZnSe-based layers. The N-acceptor is unstable under the light illumination with the quantum energy above 2.3 eV, i.e. under the intrinsic laser emission. This results in the onset of mobile defects accumulated in the LD active region [1].

The first demonstration of InGaN/GaN pulsed LDs with the wavelength at the edge of blue-green spectral range (λ = 500 nm, T = 80 °C) was reported only last year [2], i.e. after more than 10 years of active research in this field. The pulsed output power in this case was as high as ∼70 mW. However, the increase of In content to obtain emission in the green spectral range (above 515 nm) leads to a drastic increase in the threshold current density [3]. Nevertheless, the market needs the compact pulsed and cw green lasers due to a large number of potential applications like projection and 3D television, short-range fiber-optics communications with plastic fibers, location and navigation systems, fluorescent cell diagnostics etc.

We are developing the alternative approaches aimed to obtain degradation-stable II–VI based green lasers using undoped laser heterostructures pumped optically by the emission of a violet III-N LD or by electron beam. The active region of such ZnMgSSe/ZnCdSe laser heterostructure consists of single/multiple ZnCdSe QWs or self-organized quantum dots (QDs) sheets with the surface density and average lateral sizes of $\sim 10^{11}$ cm^{-2} and 5 nm, respectively. The waveguide comprises alternately strained ZnSSe/ZnSe superlattice (SL) with a period of 4 nm. Such structure design was used earlier in the first ZnSe-based LD with CdSe QDs [4].

1. II–VI/III–V laser diode converter

The research on optically pumped lasers is focused mainly on the adaptation of II–VI laser heterostructures for the design of the violet-to-green laser converter where the II–VI active element is pumped by the emission of the violet III-N-based LD [5]. The Cd(Zn)Se/ZnMgSSe nano-heterostructure optimized from the point of view of the maximum optical confinement factor has been grown by molecular-beam epitaxy on GaAs (001) substrates and involved of bottom and top $Zn_{0.9}Mg_{0.1}S_{0.15}Se_{0.85}$ cladding layers with the thickness of 1.1 μm and 20 nm, respectively, and asymmetric $ZnS_{0.15}Se_{0.85}$/ZnSe SL waveguide with the total thickness of 0.2 μm. The active region consisted of several CdSe QD sheets separated by 1 nm-ZnSe/3 nm-$ZnS_{0.15}Se_{0.85}$/1 nm-ZnSe barriers providing the tunneling of non-equilibrium carriers between the QD sheets for uniform active region pumping and also providing the partial compensation of compressive stress induced by the CdSe QD sheets.

The emission of the violet InGaN/GaN LD (λ = 416 nm, τ_p = 50 ns, $P_{\text{pulse max}}$ = 2 W) was collected and focused in a stripe via a system of lenses and then used for pumping of the II–VI active element. The resulting edge emission of the Cd(Zn)Se/ZnMgSSe laser was registered by a CCD camera. The green laser chips with various cavity lengths were studied, the laser with the cavity length of 139 nm showing best results. The laser spectra maximum was positioned at λ_{las} = 523 − 535 nm. Fig. 1 demonstrates the dependence of the external quantum efficiency of the converter on the power of the InGaN/GaN LD at room temperature. The excitation power at laser threshold is as low as 0.6–0.7 W. The emission power reached the maximum value of 65 mW at P_{exc} = 1.3 W (Fig. 2). The maximum value of the external quantum efficiency was as large as 8% at P_{exc} = 1.3 W.

It is expected that further decrease in the threshold power density of the Cd(Zn)Se/ZnMgSSe laser nanostructure can be achieved by optimizing its design and development of the re-

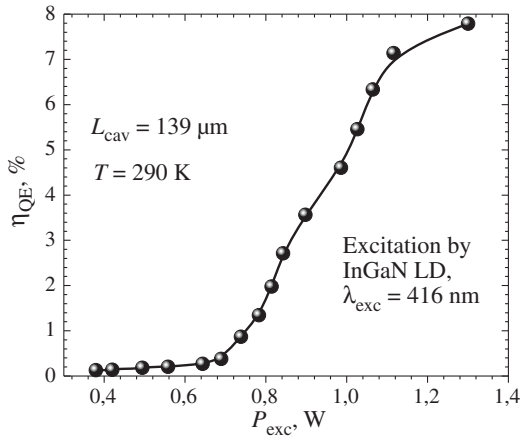

Fig. 1. External quantum efficiency of the convertor as a function of the excitation power of the InGaN/GaN LD at T = 290 K.

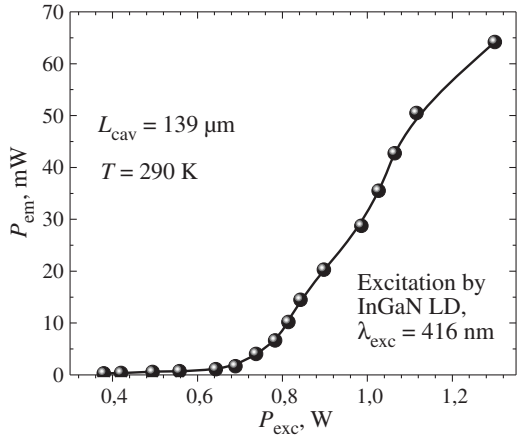

Fig. 2. Cd(Zn)Se/ZnMgSSe laser pulse power as a function of InGaN/GaN LD excitation power at $T = 290$ K.

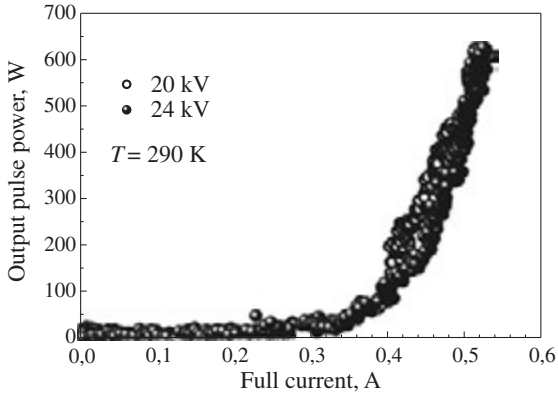

Fig. 3. The dependencies of pulse output power on electron beam current for electron beam of 20 and 24 keV. The laser wavelength is 535 nm.

spective microlens system. It will enable one to increase significantly the conversion efficiency and the output power of the injection converter as well as to provide the quasi-cw generation mode.

2. Lasers with transverse electron beam pumping (EBP)

The active elements of EBP lasers, based on the II–VI heterostructures with the active region containing a single QD sheet, have allowed us to achieve the ultra-low values of threshold current density (<0.5 A/cm^2 at 300 K) and accelerating voltage (<5 kV) of the electron beam at the output pulse optical power of ∼1 W [6]. The introduction of the SL waveguide with a built-in electric field and à graded variation of the effective refractive index has resulted in the increase in the output power up to 8.5 W at the accelerating voltage of 16 keV and an improvement of the degradation stability of EBP lasers.

The development of the multiwell heterostructures (10 ZnCdSe QWs or CdSe QD sheets) with an extended waveguide (1–2 μm) attracts special attention, since they are unique candidates for fabrication of high-power pulse EBP lasers demonstrating the output power above 12 W per facet of the laser crystal chip at the total efficiency of 17% (300 K) [7]. Optimization of the heterostructure design for matching the elastic stresses, decreasing the structural defect density, choosing appropriate thickness of the waveguide and a number of QWs has led to maximum pulse output power of 34 W per facet of the laser chip, the cavity length and width being 0.4 and 0.24 mm, respectively.

The employed values of the electron beam current and accelerating voltage were 19 A/cm^2 and 26 keV, respectively. The laser exhibited an efficiency of 7.5% per facet, while the specific linear power was 140 W/mm. These results were employed for the development of laser arrays with the pulse output power above 600 W. The laser array involves three linear sets arranged in a stepwise order. The size of each linear set is of ∼4 × 1.3 mm (1.3 mm is the cavity length). The width of each laser element is still rather large 0.5 mm, the total amount of elements in array — 26). The dependencies of pulse output power on electron beam current measured for two different energies of the electron beam are shown in Fig. 3. The maximum pulse output power (per facet) is as high as 630 W at the electron beam energy of 24 keV, and ∼500 W at the electron beam energy of 20 keV. The achieved parameters of laser and laser arrays enables one to obtain the pulse output power of 10–35 kW from 1 cm^2 laser array providing its pumping by an uniform electron beam. The achieved results have no analogues in the world.

Acknowledgements

The work was supported in part RFBR #09-02-12406-ofi-m and ISTC #3754 grants, as well as by Contract KAST-SIPH/2.

References

[1] D. Albert *et al*, *Appl. Phys. Lett.* **74**, 1957 (1999).
[2] D. Queren *et al*, *Appl. Phys. Lett.* **94**, 081119 (2009).
[3] T. Miyoshi *et al*, *Appl. Phys. Express* **2**, 062201 (2009).
[4] S. V. Ivanov *et al*, *Appl. Phys. Lett.* **74**, 498 (1999).
[5] S. V. Ivanov *et al*, *J. Cryst. Growth* **311**, 2120 (2009).
[6] M. M. Zverev *et al*, *Tech. Phys. Lett.* **33**, 1032 (2007).
[7] M. M. Zverev *et al*, *Semiconductors* **42**, 1440 (2008).

18th Int. Symp. "Nanostructures: Physics and Technology"
St Petersburg, Russia, June 21–26, 2010

Magnetic field assisted THz and sub-THz quantum cascade lasers

D. Smirnov[1], A. Wade[1], G. Fedorov[1], Y. Kim[1], B. S. Williams[2,3], S. Kumar[3], Q. Hu[3] and J. L. Reno[4]

[1] National High Magnetic Field Laboratory, Tallahassee, FL 32310, USA
[2] University of California at Los Angeles, CA 90095, USA
[3] Massachusetts Institute of Technology, Cambridge, MA 02139, USA
[4] Sandia National Laboratories, Albuquerque, NM 87185-0601, USA

Abstract. We demonstrate magnetic field assisted, (sub)THz quantum cascade laser operating above 200 K. This is achieved through the application of strong magnetic fields which provide an additional lateral confinement in order to suppress non-radiative intersubband scattering.

Introduction

A quantum cascade structure is a general concept of optoelectronic devices (laser, LED, frequency mixer, or detector) based on a cascade of radiative transitions between size-quantized energy levels in a multi-quantum-well structure. Today, Quantum Cascade Lasers (QCLs) are the only semiconductor devices operating from the midinfrared (MIR) to the THz range of frequencies. The motivation to push QCLs to longer wavelengths and to higher operational temperatures is driven by their potential for remote sensing and imaging, spectroscopy, and communications. THz QCLs now cover the frequency range from 1.2 to 5 THz, though cryogenic cooling is still required [1]. Progress towards the realization of sub-THz and/or high temperature QCLs operation becomes exceedingly difficult because it requires the necessary population inversion between closely spaced electronic subbands (1 THz $\sim$4 meV) to be achieved.

Recently there has been much focus on utilizing a magnetic field to create additional lateral quantization in QCLs. A sufficiently strong magnetic field breaks subbands in-plane continuum of states into a set of discrete, equidistant, 0D-like Landau levels (LLs) separated by the cyclotron energy. The similar energy and size scales of spatial and magnetic confinements allows the application of an external magnetic field to be an experimental tool to control processes that determine the performance of QCLs — quantum confinement and intersubband relaxation [2]. Here we exploit this field-controlled confinement in a threefold way. First, it allows suppressing LO phonon emission, thus increasing the electrons lifetime in the initial state of the laser transition. Second, by adjusting the magnetic field one can resonantly decrease the final state lifetime. Finally, making the LLs separation bigger than the emission energy eliminates the reabsorption of light, and opens up a possibility of achieving extremely low emission energies.

1. Experimental

We performed a systematic study of THz QCL structures based on a resonant-phonon design: 3 THz QCLs with a two-well injector and 1.9 THz QCL with a one-well injector. The GaAs/$Al_{0.15}Ga_{0.85}As$ structures were grown with typically 170–220 cascaded modules to form active regions approximately 10 μm thick. All studied structures were fabricated into a double-metal waveguide offering high-confinement, low-loss cavity for a wide THz range. Details on the QCL design, structure and zero-field charcterization can be found in Ref. 3,4.

QCL devices processed into striped ridges 40 to 150 μm wide and from 0.6 to 1.2 mm long were measured mounted in a variable-temperature cryostat inserted in the bore of a resistive magnet capable of producing fields up to 33 T such that the magnetic field lines were perpendicular to the plane of the quantum wells and parallel to the direction of the current. The QCLs were driven with 1–2 μs current pulses and repetition frequency up to 3 kHz. The optical power (P) is monitored using InSb hot-electron, inhomogeneously B-tuned bolometer, or a Ge:Ga photoconductor. The optical and electrical characteristics (current density J, voltage/period V, optical power P as well as emission spectra) were recorded as a function of the magnetic field applied perpendicular to the plane of the quantum wells.

2. Results and discussion

In a 3 THz QCL with a two-well injector, at $B = 0$ T and designed bias of $\sim$53 mV/period, the laser transition takes place between levels $|6\rangle$ and $|5\rangle$ ($E_{6,5} \approx 13$ meV or 3.1 THz) followed by a fast, LO-phonon assisted relaxation towards the triplet ground states: $|3\rangle$, $|2\rangle$, and $|1\rangle$ (Fig. 1a). At strong enough magnetic fields, it becomes possible to increase voltage bias above 60 mV/period. Here the separation of levels $|5\rangle$ and $|4\rangle$,and levels $|8\rangle$, $|7\rangle$, and $|6\rangle$ is possible while maintaining a large dipole-matrix element, resulting in the possibility for different laser transitions. Applying appropriate electrical bias and magnetic field, we achieved laser emission in an unprecedented range of frequencies from 0.68 to 3.33 THz (Fig. 1b). In a narrow range of magnetic fields about 20 T, we observed strong dual-frequency lasing (0.97 and 3 THz) that originates from the simultaneous emission from two cascaded optical transitions in each QCL period. Moreover, 1 THz laser action is observed at record high temperatures up to 215 K (19 T), and 3 THz lasing up to 225 K (31 T). The detailed description of different magnetic field assisted lasing regimes can be found in Ref. 5.

1.9 THz devices with a with a one-well injector also show multiple magnetic-filed assistant lasing regimes. At $\sim$17 T, we observed single-line lasing at 600 GHz, the lowest emission frequency ever recorded from a QCL. In this regime, a QCL operate without resonant tunneling injection into the upper lasing level.

In conclusion, we report strong, magnetic-field-assisted, multiwavelength emission in a QCL. We have demonstrated

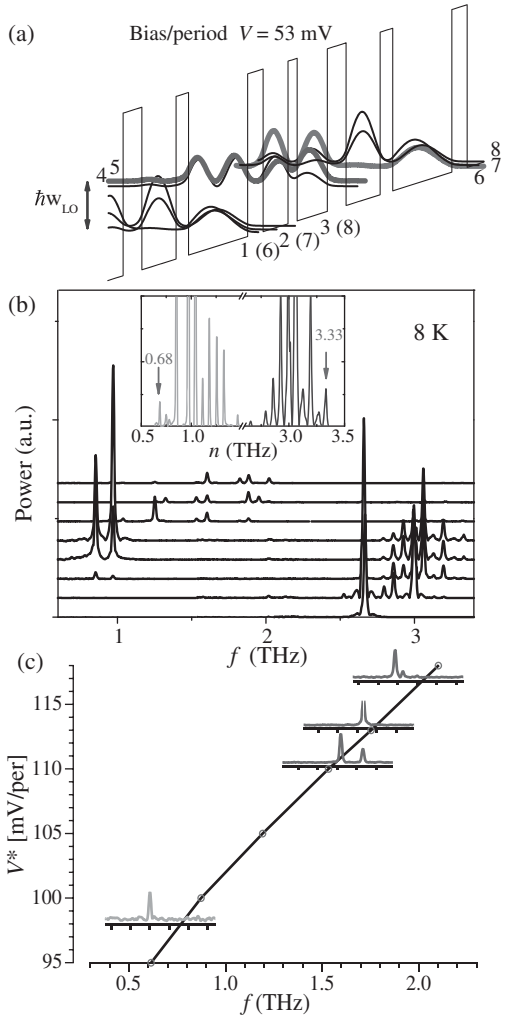

Fig. 1. QCL with a two-well injector: (a) Conduction band diagram and squared wavefunctions at 53 mV/period, zero B-field operational bias. Levels 3,2,1 are 8,7,6 for the next period. (b) Spectral coverage of the QCL device with increasing voltage bias and magnetic field (bottom curve 54.9 mV/period, 13 T; top curve 88.4 mV/period, 25 T). The inset shows the QCLs spectral extremes: 0.68 THz (69.9 mV/period, 31.2 T) and 3.33 THz (63.9 mV/period, 19 T). QCL with a one-well injector: (c) Field-assisted emission at different magnetic fields. Top curve 118 mV/per, 7.5 T; bottom curve 100 mV/per, 17.4 T.

the longest wavelength, the widest spectral coverage, and the highest operational temperatures in any single terahertz solid-state laser to date. Furthermore, these results demonstrate that additional lateral quantum confinement is a route to higher temperature operation for THz QCLs.

Acknowledgements

The National High Magnetic Field Laboratory is supported by NSF Cooperative Agreement No. DMR-0084173, by the State of Florida, and by the DOE. The work at MIT is supported by AFOSR, NASA and NSF. Sandia is a multiprogram laboratory operated by Sandia Corporation, a Lockheed Martin Company, for the United States Department of Energy under Contract DE-AC04-94AL85000.

References

[1] B. S. Williams, *Nature Photonics* **1**, 517 (2007).
[2] D. Smirnov *et al*, *Phys. Rev. B* **66**, 121305(R) (2002).
[3] B. S. Williams *et al*, *Opt. Express* **13**, 3331 (2005).
[4] S. Kumar *et al*, *Appl. Phys.Lett* **88**, 121123 (2006).
[5] A. Wade *et al*, *Nature Photonics* **3**, 41 (2009).

18th Int. Symp. "Nanostructures: Physics and Technology"
St Petersburg, Russia, June 21–26, 2010

Surface plasmon polariton modes versus modes of conventional layered waveguide in quantum cascade laser

A. A. Bogdanov[1,2] and R. A. Suris[1]

[1] Ioffe Physical-Technical Institute, St Petersburg, Russia
[2] St Petersburg Academic University, St Petersburg, Russia

Abstract. We analyze mode structure of quantum cascade laser (QCL) resonator taking into account surface plasmon polariton modes. Dielectric function of waveguide materials describes within Drude–Lorentz approximation. Dispersion law of eigen modes is obtained for different parameters of the resonator. Comparative analysis of optical losses on free carriers for different modes are presented.

Introduction

The idea of superlattice (SL) application to light amplification was put forward firstly in 1971 [1]. However, it was realized only two decades later in 1994 [2].

In order to extend lasing range toward a Terahertz (THz) region it is necessary to overcome some fundamental problems. It is minimization of the free carriers absorption. These loses increase with the wavelength roughly as $\sim \lambda^2$ [3]. In order to reduce them, one can, for example, reduce the optical confinement factor or suppress the electron motion along the SL layers of the active region. The last might be achieved in quantum dot cascade laser [4].

Owing to free carriers in the walls of QCL cavity, the eigenmodes like cavity eigenmodes of hollow waveguide with perfectly conducting walls, have a frequency cutoff [5]. The wavelength cutoff of a planar metallic waveguide is close to the double distance between the waveguide faces. Therefore, the long-wave QCL should be rather thick. It is a problem to fabricate QCL structures thicker than 10–15 μm through the MBE or MOCVD techniques.

Overcoming of these problems is possible especially owing to right laser resonator design and surface plasmon polariton (SPP) modes exploiting. Just such a solution was used to fabricate the first THz QCL in 2002 [6].

Here we give comprehensive mode structure analysis of QCL resonator taking into account SPP modes. For the analyze we consider reduced model of QCL resonator.

1. Model

We will believe that QCL resonator is a planar symmetric waveguide unbounded in y and z directions (Fig. 1) consisting of finite thickness lightly doped semiconductor waveguide core surrounded with two identical infinitely thick metallic or heavily doped semiconductor cladding layers.

Let us consider the dielectric functions of cladding layers and resonator core within Drude–Lorentz approximation: $\varepsilon_s(\omega) = \varepsilon_s^\infty(1 - \Omega_s^2/[\omega(\omega + i\gamma_s)])$. The s index is a medium number (see Fig. 1), ε_s^∞ is material permittivity at $\omega \to \infty$, γ_s is inverse electron transport scattering time. It is responsible for free electron losses. Ω_s is plasma frequency. It gives by expression [5]: $\Omega_s = \sqrt{4\pi n_s e^2/(m_s^* \varepsilon_s^\infty)}$, where n_s is free electron concentration, m_s^* is effective electron mass.

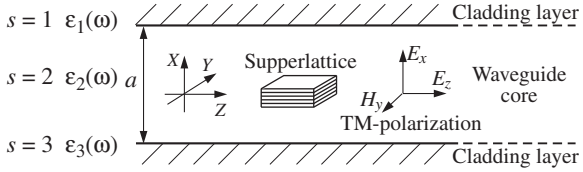

Fig. 1. A reductive QCL model. A planar symmetric waveguide.

We will look for Maxwell equations solutions as traveling waves propagating in the z-direction (Fig. 1) and localized in the x-direction. Then the electric and magnetic field depend on the coordinate z and time t through a factor $\exp(ik_z z - i\omega t)$, where $k_z = k_z(\omega)$.

We consider modes of TM polarization only (Fig. 1), because the QCL transitions are stimulated by electric field component normal to the SL layers[1]. This field component E_x is nonzero only for TM modes (see Fig. 1).

The waveguide symmetry assumes to divide the modes into two types: symmetric modes ($E_x(x)$ is even function and $E_z(x)$ is odd function) and antisymmetric modes ($E_x(x)$ is odd function and $E_z(x)$ is even function).

From now on we use these dimensionless quantities:

$$\widetilde{\omega} = \omega\frac{\sqrt{\varepsilon_2^\infty}a}{\pi c};\ \widetilde{\Omega}_s = \Omega_s\frac{\sqrt{\varepsilon_2^\infty}a}{\pi c};\ \widetilde{\gamma}_s = \gamma_s\frac{\sqrt{\varepsilon_2^\infty}a}{\pi c};\ \widetilde{k}_z = k_z\frac{a}{\pi}.$$

It is convenient, because dispersion law $\widetilde{k}_z(\widetilde{\omega})$ is determined by these dimensionless quantities only.

2. QCL mode structure

Keeping in the mind scalability of the problem, for clarity sake, let us consider mode structure of QCL with 8 μm-thick undoped GaAs waveguide core and heavily doped ($n_{1,3} = 5 \times 10^{18}$ cm^{-3}) GaAs cladding layers.

Calculated dispersion curves ($\widetilde{k}_z = \widetilde{k}_z(\widetilde{\omega})$) for the such waveguide are shown in Fig. 2. In the hatched area there is no localized modes.

As one can see in Fig. 2, dispersion curves of two first modes (0 and 1) differ from others qualitatively. These modes are SPP modes. For them $\widetilde{k}_z$ increases infinitely as $\widetilde{\omega} \to \widetilde{\Omega}_1\sqrt{2}$. The frequency $\widetilde{\Omega}_1/\sqrt{2}$ calls surface plasmon frequency ($\widetilde{\Omega}_{\rm sp}$) [7]. SPP modes are result of interference of two SPP localized at

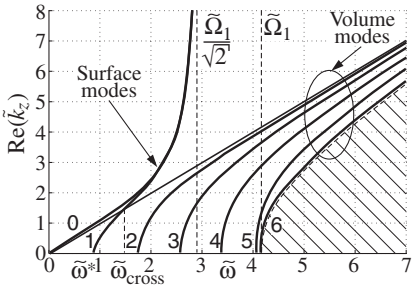

Fig. 2. $\mathrm{Re}(\widetilde{k}_z)$ versus $\widetilde{\omega}$. Waveguide parameters are $\widetilde{\Omega}_1 = 4.1$ and $\widetilde{\Omega}_2 = 0$. Gray curves are the symmetric modes, black curves are the antisymmetric modes.

interfaces separating cladding layers and waveguide core. Results of SPP interference are essential in thin waveguides.

The frequency cutoff of symmetric SPP mode is zero (see Fig. 2). Then this mode propagates at arbitrarily low frequency. This allows us to fabricate thin waveguides for long-wave, particulary THz, operating QCLs. In the general case frequency cutoff of this mode equal to $\widetilde{\Omega}_2$.

The others modes we will call volume modes (see Fig. 2) in contrast to the surface ones. Their properties are well studied in the theory of hollow metallic waveguide [5]. All of the volume modes have nonzero frequency cutoff. They propagate at arbitrary high frequency in contrast to the SPP modes.

Waveguide eigenmode number, N, increases in proportion to the waveguide core thickness a and plasma frequency of cladding layer Ω_1, i.e., in proportion to $\widetilde{\Omega}_1$. At arbitrary $\widetilde{\Omega}_1$ the waveguide always has three modes at least (two surface and one volume).

Consider waveguide mode structure at $\widetilde{\Omega}_1 \to \infty$. Then $\epsilon_1 \to -\infty$ at fixed $\widetilde{\omega}$. And so, we can consider waveguide as planar hollow waveguide with perfectly conducting metallic walls. It is why there is no wave field inside cladding layers. The total number of the modes, N, in this case tends to infinite. The volume mode dispersion characteristics coincide with dispersion characteristic of hollow waveguide with perfectly conducting walls [5].

At $\widetilde{\Omega}_1 \to \infty$, symmetric surface mode becomes transversal and absolutely confined in waveguide core. Its dispersion characteristic tends to the dispersion characteristic of light ($\widetilde{\omega} = \widetilde{k}_z$). Modes with above properties are called principal modes or TEM-modes [5].

At the $\widetilde{\Omega}_1 \gg 1$, symmetric surface mode has three essential advantages among others modes in QCL: (i) it has zero frequency cutoff;(ii) it is almost localized inside waveguide core and so there is no significant free carrier absorbtion in the cladding layers; (iii) this mode is nearly transversal ($E_z \approx 0$, $E_x \neq 0$). So the electric field does not stimulate energy dissipation due to electron motion parallel to the SL layers and stimulates laser transition only.

Dispersion curve for antisymmetric mode cuts the light dispersion curve ($\widetilde{\omega} = \widetilde{k}_z$) at frequency $\widetilde{\omega}_{\text{cross}}$ (see Fig. 2). At $\widetilde{\omega}_{\text{cross}}$ the field distribution has qualitative change (Fig. 3).

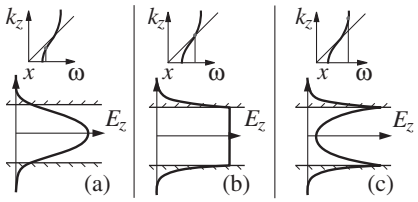

Fig. 3. The electric field distribution ($E_z(x)$) for the antisymmetric mode at: (a) $\widetilde{\omega} < \widetilde{\omega}_{\text{cross}}$, (b) $\widetilde{\omega} = \widetilde{\omega}_{\text{cross}}$, (c) $\widetilde{\omega} > \widetilde{\omega}_{\text{cross}}$.

At $\widetilde{\omega} < \widetilde{\omega}_{\text{cross}}$ field distribution is similar to that of the first hollow metallic waveguide mode, i.e. the first volume mode. At $\widetilde{\omega} < \widetilde{\omega}_{\text{cross}}$, the wave is represented by two overlap surface waves. So antisymmetric surface mode owns the volume and surface mode properties depending on $\widetilde{\omega}$.

Therefore, at $\widetilde{\Omega}_1 \to \infty$, antisymmetric surface mode transforms to the first hollow metallic waveguide mode.

3. Free carrier losses

Absorbtion coefficient $\widetilde{\alpha}_w$ is $2\text{Im}(\widetilde{k}_z)$. Let us consider the waveguide with the same parameters as in the previous section, but with n-doped core ($n_2 = 4.7 \times 10^{16}$ 1/cm^3). Let us put $\widetilde{\gamma}_s$ equal to the 10% of $\widetilde{\Omega}_s$ for $s = 1, 2, 3$. Dependence $\text{Im}(k_z(\widetilde{\omega}))$ is shown in Fig. 4.

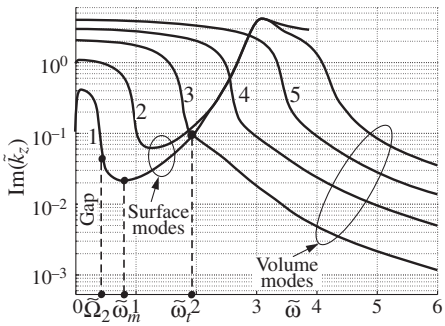

Fig. 4. Dependence $\text{Im}(\widetilde{k}_z)$ on $\widetilde{\omega}$. Waveguide parameters $\widetilde{\Omega}_1 = 4.1$, $\widetilde{\Omega}_2 = 0.4$, $\widetilde{\gamma}_s = 0.1\widetilde{\Omega}_s$, $s = 1, 2, 3$. Gray curves are the symmetric modes, black curves are the antisymmetric modes.

One can see that, at low frequencies, the losses are minimal for the symmetric surface mode. Out of the spectral gap the losses for this mode increase with frequency in opposite to the volume modes. At the frequencies higher then $\widetilde{\omega}_t$ (see Fig. 4) free carrier losses are minimal for the first symmetric volume mode. The frequency $\widetilde{\omega}_t$ corresponds to the wavelength 29 μm. Surface symmetric mode has a minimum of losses at the frequency $\widetilde{\omega}_{\text{m}}$. The frequency $\widetilde{\omega}_{\text{m}}$ corresponds to the wavelength of THz region 70 μm.

4. Conclusion

Complete set of QCL eigen modes consists of the volume and two SPP modes. Volume modes exist due to a total wave reflection from waveguide walls. SPP modes arises due to interference of two plasmon polaritons localized at the interfaces separated waveguide core and waveguide walls.

Optical losses due to free carrier absorbtion decrease for symmetric SPP mode with frequency decreasing in opposite to the volume modes. Owing to nearly complete confine of symmetric SPP mode inside waveguide core in THz region this mode has the least losses among others modes. Frequency cutoff for this mode does not depend on waveguide core thickness and determines only by free electron concentration in the core. In THz region this mode nearly transversal. Therefore electric field does not induce lateral losses in the SL layers, but stimulates laser transition only.

Acknowledgements

This work has been supported by RFBR 08-02-01337-a, by Dynasty foundation and RMSE 2.1.1/988.

References

[1] R. A. Suris and R. F. Kazarinov, *Sov. Phys. Semicond.* **5**, 707 (1971).
[2] J. Fais *et al*,*Science* **5**, 553 (1994).
[3] D. Marcuse, *Theory of Dielectric Optical Waveguides*, (New York: Academic Press) 253, 1974.
[4] I. Dmitriev and R. Suris, *Phys. Stat. Sol.* **202**, 987 (2005).
[5] L. D. Landau and E. M. Lifshitz *Electrodynamics Of Continuous Media*, (Oxford: Pergamon Press) 313, 1984.
[6] R. Kohler *et al*, *Nature* **417**, 156 (2002).
[7] V. M. Agranovich and D. L. Mills *Surface polaritons*, (Amsterdam: North-Holland) 38, 1982.

18th Int. Symp. "Nanostructures: Physics and Technology"
St Petersburg, Russia, June 21–26, 2010

Middle-IR whispering gallery mode lasers

Yu. P. Yakovlev[1], A. M. Monakhov[1], A. P. Astakhova[1], A. N. Baranov[2], G. Boissier[2], E. A. Grebenshchikova[1], S. S. Kizhaev[1], V. V. Sherstnev[1] and R. Teissier[2]

[1] Ioffe Physical-Technical Institute, St Petersburg, Russia
[2] P2IES, Universite Montpellier 2, UMR CNRS 5214, 34095 Montpellier, France

Abstract. WGM lasers operating at room temperatures in the 2–2.5 μm wave range was fabricated. The new type of WGM lasers — a laser with the sectorial disk resonator was supposed, fabricated and investigated both theoretically and experimentally.

Whispering gallery modes (WGM) are universal linear excitations of circular and annular resonators. They have been first observed in 1910 in form of sound wave travelling along the outer wall of a walk way in the circular dome of St Paul's Cathedral in London and were investigated by Lord Raylegh [1]. Referring to the acoustic phenomenon the name "whispering gallery modes" was also coined for electromagnetic eigenmodes of circular resonators. Dielectric rings, disks or spheres can be used as passive or optically pumped active resonators with integrated active media. Such phenomena was used for creation a new type of the disk WGM-lasers at the MID-Infared spectral range. In this talk we present design and electroluminescence properties of new disk WGM-Lasers for spectral range 2–2.4 μm. The whispering gallery effect is well-known for many years. As early as in 15-th century in China was built a Temple of Heaven, where this effect was deliberately used for improving the impression of this construction. The first explanation of the effect was done by Lord Rayleigh who explained the same acoustic phenomenon has been observed in St Paul Cathedral in London.

One of the distinctive features of a resonator operating on a whispering gallery mode (WGM) is high Q-factor and the idea to use WGM as an operating mode of a laser has been considered since 1960-th, but it is necessary to have not high but optimal Q-factor for the resonator. So, for visible and near-infrared semiconductor lasers WGM resonator is not an optimal choice, but for the MID-IR wave range, where the nonradiative recombination is high, WGM lasers seem to be a promising device. We have fabricated WGM lasers for 2–2.5 μm operating at room temperatures and for 3–4 μm operating at the liquid nitrogen temperature. The lasing spectra of these devices are

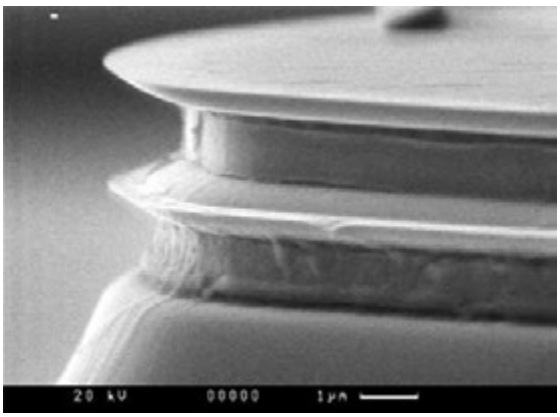

Fig. 1. Scanning electron microscope image of the mesa wall profile obtained using a our etching procedure. Mesa diameter: 200 μm.

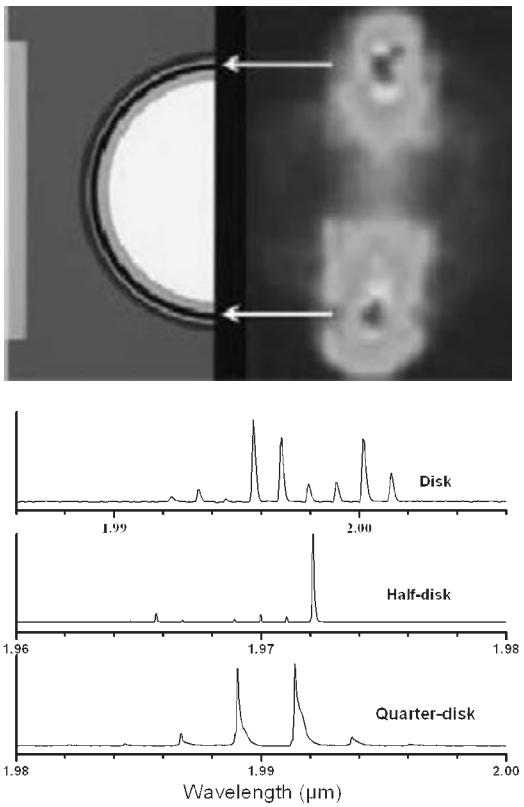

Fig. 2. Near field patterns of the half disk laser emission obtained using an IR camera and emission spectra.

in a good agreement with the theoretical predictions.

The main issue in the WGM laser applications is the light extracting from the laser resonator. We suppose a new solution of this problem. It was found that WGM exist not only in a whole disk but also in a sector of a disk, for example in a half-disk or quarter-disk resonator. For such a resonator one have a directed laser beam from the cleaved facets [2]. The specific spatial structure of output beams of sector lasers can certainly be used in some applications.

The experiment was performed on the laser structure has been grown on [100] n-GaSb substrates by molecular beam epitaxy (MBE) in a Riber Compact 21 solid source MBE machine. The undoped active zone of the structure consisted of two 10-nm-thick $Ga_{0.76}In_{0.24}Sb_{0.95}As_{0.05}$ quantum wells separated by a 30 nm $Ga_{0.75}Al_{0.25}Sb$(As) barrier lattice matched with GaSb and enclosed between 0.35-μm-thick spacer layers also made of $Ga_{0.75}Al_{0.25}Sb$(As). The $Ga_{0.1}Al_{0.9}Sb$(As) alloy was used in 1.5-μm-thick cladding layers doped with Te or Be

for n- and p-doping, respectively. The structure was finished by a 0.3-μm-thick heavily doped p-GaSb contact layer.

Emission spectra of the lasers with different geometries are shown in Fig. 2. Lasing modes of disk lasers appeared at 2.17 μm, in the long wavelength side of the spontaneous emission spectrum peaked at 2.12 μm (Fig. 2).

The lasers exhibited single mode emission in a large range of driving currents, several modes separated by 1.4 nm being visible at some conditions (Fig. 2). The emission lines can be attributed to WGMs since the mode spacing satisfies the theoretical estimations. Half-disk and quarter-disk lasers emitted at slightly higher energies, close to the maximum of the spontaneous spectrum (Fig. 2). The spectra were measured at conditions permitting to reveal several lasing modes. In agreement with the theoretical consideration the mode spacing for the half-disk laser was the same as for the full-disk laser, while the mode spacing for the quarter-disk device (2.8 nm) was doubled. In sector lasers the WGMs propagate along the disk edge reflecting from the cleaved facets. Figure 2 shows near field patterns of the half-disk laser measured using an InSb IR camera.

The smooth frequency tuning in the process of the flow of current pulse by duration to 1.2 μs was observed. It is shown that the increasing the pulse duration from 0.1 to 1.2 μs shifts the wavelength of the emission to the long-wave direction on 30 A.

Acknowledgements

The authors are grateful to the CNRS (France) and RFBR for the support of this work (Grant Nos. 10-02-93110 and 10-02-00548-a), to the Program of the presidium of RAS #27 and the State contract #02.740.11.0445.

References

[1] J. W. S. Rayleigh, *Phil. Mag.* **20**, 1001–1004 (1910).

[2] A. M. Monakhov, V. V. Sherstnev, A. P. Astakhova, Yu. P. Yakovlev, G. Boissier, R. Teissier, and A. N. Baranov, Applied Physics Letters **94**, 051102 (2009).

18th Int. Symp. "Nanostructures: Physics and Technology"
St Petersburg, Russia, June 21–26, 2010

Feasibility of terahertz lasing in optically pumped multiple graphene layer laser with vertical Fabri–Perot resonator

A. A. Dubinov[1], V. Ya. Aleshkin[1] and V. I. Ryzhii[2,3]

[1] Institute for Physics of Microstructures RAS, 603950 Nizhny Novgorod, Russia
[2] Computational Nanoelectronics Laboratory, University of Aizu, 965-8580 Aizu-Wakamatsu, Japan
[3] Japan Science and Technology Agency, CREST, 107-0075 Tokyo, Japan

Abstract. We propose and substantiate the concept of terahertz (THz) laser based on the optically pumped multiple graphene layers (MGL) and the resonant cavity of the Fabri–Perot type. The pumping scheme which corresponds to the optical interband excitation of graphene provides the population inversion for the interband transitions in a relatively wide range of THz frequencies. The dynamic conductivity of the MGL structure is calculated as a function of the signal frequency, the number of GLs, and the optical pumping intensity. The utilization of optically pumped MGL structures might provide the achievement of lasing with the frequencies of about 1 THz at room temperature due to a high efficiency of pumping.

Introduction

Under optical excitation, the interband population inversion in graphene can be achieved [1]. Due to the gapless energy spectrum of graphene, such a population inversion can lead to the stimulated emission of THz radiation. The results of recent experiments [2] confirm this. A THz laser based on optically pumped graphene with metal waveguide was considered and evaluated recently [3]. In this paper, we propose the concept of a THz laser based on an optically pumped multiple graphene layers structure with a Fabri–Perot type resonator and substantiate this concept.

1. Device structure

A laser with one or several optically pumped GLs serving as the active media placed in inside a Fabri–Perot resonator can have the structure shown in Figs. 1a and 1b. The graphene structure with the two GLs can be fabricated using a Si substrate covered by a 3C-SiC film (on both sides) and subjected to anneling [4]. It assumes that the electrons and holes generated by optical radiation with the photon energy $\hbar\Omega$ are accumulated in the energy range ε. The accumulation of the photogenerated electrons near the bottom of the conduction and holes near the top of the valence band results in the situation that the electron and hole distribution functions $f_e(\varepsilon) = f_h(\varepsilon) > 1/2$ in a certain range of energies, i.e., results in the population inversion and, consequently, in the negative absorption coefficient of THz photons. To overcome the losses associated with the absorption in the substrate, mirrors, and so on, as well as to enhance the pumping efficiency, the structures with MGL appear to be attractive. Recently, very perfect MGL structures (with the number of GLs up to 100) were fabricated using anneling of SiC substrates and studied [5]. A sketch of the laser with such a MGL structure is shown in Fig. 1c. However, these MGL structures as the active media exhibit the following two features. First, due to the absorption of optical pumping radiation in MGLs, the attenuation of this radiation, and consequently, marked difference in the population and the values of the quasi-Fermi energies $\varepsilon_F^{(k)}$ of different GLs occurs ($1 < k < K$ is the index of GL and K is the total number of GLs). Second, there is a buffer (BL) bottom GL between the SiC substrate and perfect GLs. The density of electrons in this BL is rather high and the electron Fermi energy in this BL ε_F^B is large. This can lead to undesirable absorption of THz photons in BL.

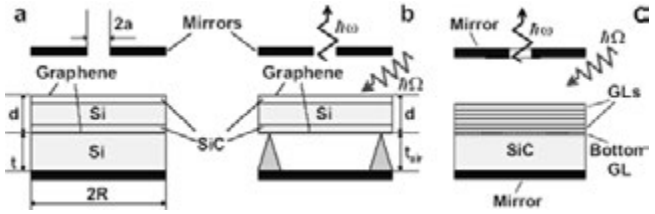

Fig. 1. Schematic view of a laser based on double-GL structures with Si separation layer (a) and with air separation layer (b), and a laser with a MGL structure (c).

2. THz absorption coefficient

To obtain the conditions of lasing one needs to find the GL absorption coefficient as a function of the photon frequency. This coefficient is proportional to the real part of the dynamic conductivity. For the real part of the dynamic conductivity of GLs in the structures under consideration with nonequilibrium electron-hole, generalizing formulas derived previously one can obtain for each GL [6,7]:

$$\mathrm{Re}\sigma_\omega^{(k)} = \left(\frac{e^2}{4\hbar}\right)\tanh\left(\frac{\hbar\omega - 2\varepsilon_F^{(k)}}{4k_BT}\right) + \left(\frac{e^2}{4\hbar}\right)\frac{8k_BT\tau}{\pi\hbar(1+\omega^2\tau^2)}\ln\left[1+\exp\left(\frac{\varepsilon_F^{(k)}}{k_BT}\right)\right]. \quad (1)$$

Here τ is the electron and hole momentum relaxation time in each GL, T is the electron and hole temperature, and $\hbar$ and k_B are the Planck and Boltzmann constants. The quasi-Fermi energy in the k-th GL $\varepsilon^{(k)}$ with $k \geq 1$ is mainly determined by the electron (hole) density in this GL $\sum_k$, and, therefore, by the rate of photogeneration $G_\Omega^{(k)}$ by the optical radiation (incident and reflected from the mirror) at the k-th GL plane. Using Eq. (1) for $\hbar\omega = \hbar\Omega > 2\varepsilon_F^{(k)}$, we obtain

$$G_\Omega^{(k)} = \frac{I_\Omega^{(k)}}{\hbar\Omega}\left(\frac{\pi e^2}{\hbar c}\right)\tanh\left(\frac{\hbar\omega - 2\varepsilon_F^{(k)}}{4k_BT}\right) \simeq \frac{I_\Omega^{(k)}}{\hbar\Omega}\beta, \quad (2)$$

where $I_\Omega^{(k)}$ is power density of the optical radiation at the k-th GL and $\beta = \pi e^2/\hbar c \simeq 0.023$. A relationship between $\varepsilon_F^{(k)}$

and $G_\Omega^{(k)}$ is determined by the recombination mechanisms. We assume that $\varepsilon_{\rm F}^{(k)} \propto \left[G_\Omega^{(k)}\right]^\gamma$, where γ is a phenomenological parameter. In this case,

$$\varepsilon_{\rm F}^{(k)} = \varepsilon_{\rm F}^T \left[(1-\beta)^{K-k} \frac{1+(1-\beta)^{2k+1}}{1+(1-\beta)^{2K+1}}\right]^\gamma, \qquad (3)$$

where $\varepsilon_{\rm F}^T = \varepsilon_{\rm F}^{(K)}$ is the quasi-Fermi energy in the topmost GL. To achieve lasing in the MGL structures under consideration, the following condition should be satisfied:

$$Q = \frac{(8\pi/c)\left|\sum_{k=0}^K {\rm Re}\sigma_\omega^{(k)} \left(E^{(k)}\right)^2\right|}{(1-r_1)E_1^2+(1-r_2)E_2^2+(a/R)^2\,E_1^2+E_{\rm S}^2} > 1. \qquad (4)$$

Here, $E^{(k)}$ is the amplitude of the THz electric field $E = E(z)$ at the the pertinent GL, E_1 and E_2 are the amplitudes of the THz electric field near the bottom and top mirrors, respectively, $E_{\rm S}^2 = (a_{\rm S} n_{\rm S}/2)\int_0^{t+d} E^2 dz$, $a_{\rm S}$ and $n_{\rm S}$ are the absorption coefficient of THz radiation in the substrate (Si or SiC) and real part of its refractive index, r_1 and r_2 are the reflection coefficients of THz radiation from the mirrors, and a/R is the ration of the diameters of the output hole a and the mirror R. The THz electric field is assumed to be directed along the GL plane (in the xy plane). In deriving inequality (4), we neglected the finiteness of the MGL thickness (in comparison with t and the THz wavelength) and disregarded the diffraction losses and reflection of THz radiation from the bottom GL.

The spatial distribution of the THz electric field can be found using the following equation:

$$\frac{d^2E}{dz^2} + \frac{\omega^2}{c^2}\xi_\omega(z)E = 0, \qquad (5)$$

where $\xi_\omega(z)$ is the permittivity at the THz frequency ω. The spatial dependence of $\xi_\omega(z)$ reflects a difference in its values in different layers of the resonator (in the air layer, substrate, GL structure, and in the depth of the metal mirrors). The boundary conditions for Eq. (5) correspond to the continuity of E and dE/dz, $E \to 0$ when $z \to \pm\infty$.

In the case of double-GL structure (no bottom GL and $K = 2$, see Figs. 1a and 1b) with relatively thick separation layer, and taking into account that $\varepsilon_{\rm F}^{(1)} \simeq \varepsilon_{\rm F}^{(2)} \simeq \varepsilon_{\rm F}^T$, $T = 77$ K, $\varepsilon_{\rm F}^T = 17$ meV, $\tau = 1$ ps, and $\omega/2\pi = 1.08$ THz, Eq. (1) yields ${\rm Re}\sigma_\omega^{(1)} \simeq {\rm Re}\sigma_\omega^{(2)} \simeq -5\times10^7$ cm/s. The thicknesses of the Si layers are chosen to be $t = 61$ μm and $d = 39$ μm to provide the maxima of the THz electric field modulus just at both GL planes: $E^{(1)} = E^{(2)} = E_{\max}$. At $r_1 = r_2 = 0.99$, $a/R = 0.1$, $a_{\rm S} \simeq 0.7$ cm^{-1} and $n_{\rm S} \simeq 3.42$ (for the Si separation layer and the substrate [8]), this, as follows from Eq. (4), provides the maximum value of $Q \simeq 2.16$, that corresponds to the condition of lasing. In the case of MGL structure, its net thickness is small in comparison with the wavelength of THz radiation (even if $K > 100$), so that the amplitudes of the THz electric field at all GLs is approximately equal to each other. When the thickness of the substrate t is chosen to provide the maximum value $E_{\max}$ at the GLs, Fig. 2b shows the frequency dependence of the real part of the net conductivity ${\rm Re}\sigma_\omega$ normalized by $e^2/4\hbar$ and calculated with different numbers of GLs ($K = 20$, 50, and 100) at different optical pumping intensities (i.e., different values of the quasi-Fermi energies in the topmost GL $\varepsilon_{\rm F}^{\rm T} = 30$ and 50 meV). As it seen from Fig. 2b, an increase in the number of GLs leads to markedly large absolute value of ${\rm Re}\sigma_\omega$ in the frequency range where it is negative. One can see that ${\rm Re}\sigma_\omega$ becomes negative at $\omega/2\pi > 1$ THz and its absolute value is fairly large. Indeed, if $K = 20$–100, $\varepsilon_{\rm F}^{\rm T} = 30$ meV, and $\omega/2\pi = 1.5$ THz, one obtains ${\rm Re}\sigma_\omega \simeq -(3$–$10)\times10^8$ cm/s. Assuming, that $r_1 = r_2 = 0.99$, $a/R = 0.1$, $a_{\rm S} \simeq 2$–4 cm^{-1} and and setting for SiC substrate [8] $n_{\rm S} \simeq 3$ and $t = 45$ μm, one obtains $Q \simeq 3.1$–$13.4 \gg 1$.

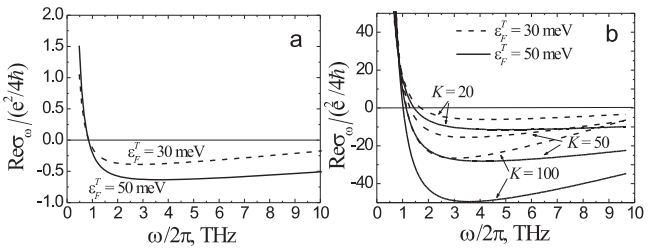

Fig. 2. Frequency dependences of the real part of dynamic conductivity ${\rm Re}\sigma_\omega$ normalized by quantity $e^2/4\hbar$ for dual-GLs (a) and MGL (b) structures with different number of GLs K at $\varepsilon_{\rm F}^{\rm T} = 30$ and 50 meV.

As follows from the results obtained above, when the quasi-Fermi energy in the topmost GL $\varepsilon_{\rm F}^{\rm T}$ is about 30–50 meV, the conditions of THz lasing in the MGL structures under consideration at the THz range of frequencies (even at the room temperature) can be well satisfied, particularly, if the momentum relaxation time τ is sufficiently long. At $T = 300$ K, $\varepsilon_{\rm F}^{\rm T} > 30$ meV corresponds to the electron and hole densities $\sum_n = \sum_p \simeq 2\times10^{11}$ cm^{-2} are achieved at the photogeneration rate $G > 10^{22}$ cm^{-2}s^{-1}. If $\hbar\Omega = 120$–920 meV, the above photogeneration rate corresponds to the optical power density $I_\Omega > 8$–64 kW/cm^2.

Acknowledgements

This work has been supported by the Federal special programm "Scientific, research and educational personnel of innovation Russia" for 2009–2013 yy. (#2289), and the RAS "Modern problems of radiophysics" and "Physical and technological investigations of semiconductor lasers for achievement of the maximum parameters" Programs.

References

[1] V. Ryzhii *et al*, *J. Appl. Phys.* **101**, 083114 (2007).
[2] T. Otsuji *et al*, *Proc. 17th Int. Symp. Nanostructures: Phys. and Technol.*, Minsk, Belarus, June 22–26, 2009, p. 66.
[3] V. Ya. Aleshkin *et al*, *JETP Lett.* **89**, 63 (2009).
[4] Yu. Miyamoto *et al*, *e-J. Surf. Sci. Nanotech.* **7**, 107 (2009).
[5] P. Neugebauer *et al*, *Phys. Rev. Lett.* **103**, 136403 (2009).
[6] A. A. Dubinov *et al*, *Appl. Phys. Express* **2**, 092301 (2009).
[7] V. Ryzhii *et al*, *J. Appl. Phys.* **106**, 084507 (2009).
[8] O. Madelung, *Semiconductors: Data Handbook.*, (New York: Academic Press, 1998).

18th Int. Symp. "Nanostructures: Physics and Technology"
St Petersburg, Russia, June 21–26, 2010

Frequency response of oxide-confined 850 nm VCSELs

S. A. Blokhin[1,2,3], A. Mutig[3], A. M. Nadtochiy[1,3], G. Fiol[3], J. A. Lott[4], V. A. Shchukin[4], N. N. Ledentsov[4] and D. Bimberg[3]

[1] St Petersburg Academic University, St Petersburg, Russia
[2] Connector Optics LLC, Shatelena 26, 194021, St Petersburg, Russia
[3] Institute of Solid-State Physics and Center of Nanophotonics, Technical University Berlin, EW 5-2, D-10623, Berlin, Germany
[4] VI Systems GmbH, Hardenbergstrasse 7, 10623 Berlin, Germany

Abstract. We perform, present, and analyze static and small signal modulation measurements on 850 nm-range vertical cavity surface emitting lasers (VCSELs). The key VCSEL parameters including relaxation resonance frequency, damping factor, and parasitic cut-off frequency are extracted. Small signal optical modulation bandwidths (BWs) larger than 22 GHz are measured. At larger bias currents we determine that the frequency response is limited primarily by thermal effects. We believe the VCSEL thermal properties may be further improved to realize current modulated VCSELs with a BW exceeding 30 GHz and with reliable and practical error-free operation at data transfer rates beyond 40 Gbit/s.

Introduction

The continuous growth of overall data traffic combined with the rapid substitution of copper links by optical interconnects requires a new efficient solution for short distance datacom networks. Vertical cavity surface emitting lasers (VCSELs) emitting at 850 nm are well established as reliable, low-cost, high performance light sources for local area and storage area networks applications as well as for active optical cables [1]. However, the development of current-modulated VCSELs that are reliable with degradation free operation at data transfer rates beyond 10 Gbit/s is challenging. Very recently 850 nm-range VCSELs exhibiting error-free operation up to 20 Gbit/s [2,3] and ∼40 Gbit/s [4] were reported.

In order to better understand and further improve a given VCSEL's dynamic performance it is very important to study, model, and characterize the physical processes that occur inside these micrometer-scale laser devices. Herein we present the results of static light power-current-voltage (L-I-V) and small signal modulation measurements up to 40 GHz on our state-of-the-art oxide-confined 850 nm VCSELs.

1. Design

The VCSEL structures are grown on n^+-GaAs {001} substrates by metal-organic vapour phase epitaxy. The structures consist of a 35.5-period n-doped AlGaAs bottom distributed Bragg reflector (DBR), an undoped AlGaAs-based microcavity with an InGaAlAs-based active region, and a 22-period p-doped AlGaAs top DBR. The thickness and composition are chosen in order to obtain an 850 nm etalon resonance wavelength. Selective wet oxidation of AlGaAs materials is applied to create lateral current and optical confinement. Planarization with bis-benzocyclobutene (BCB) is used to reduce the parasitic capacitance of the ground-source-ground (GSG) contact pads. The epitaxial and device designs are optimized to achieve a compromise between high-speed, thermal management and the highest possible processing Yield.

2. Static device characteristics

Figure 1 shows the temperature evolution of typical light power-current (L-I) characteristics for VCSELs with 6 μm-diameter oxide aperture. The threshold current remains below

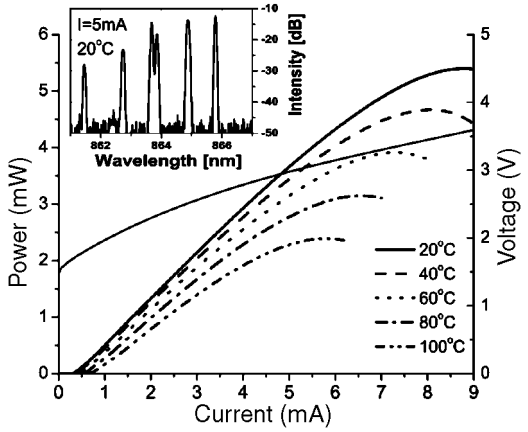

Fig. 1. L-I-V curves for a 6 μm-diameter oxide-confined InGaAlAs-based VCSEL in the temperature range 20–100 °C. Inset: emission spectrum at 20 °C and 5 mA forward bias current.

0.8 mA for temperatures from 20 to 100 °C . The maximum differential L-I slope efficiency is ∼60%. The differential series resistance and thermal resistance are ∼160 Ohms at 5 mA and ∼3.7 K/mW, respectively. The VCSELs exhibit high thermal stability that is extremely important for robust high-speed operation. The inset displays the emission spectrum at 20 °C and 5 mA indicating clear multimode operation at a peak emission wavelength of ∼865 nm.

3. Dynamic device characteristics

To analyze the dynamic behavior of the VCSELs, the small signal modulation response (S_{21}) and microwave reflection (S_{11}) magnitudes and phases are measured via scattering parameters using a network analyzer and a calibrated photodetector in the range from 50 MHz to 30 GHz. By accounting for both the intrinsic behavior of the resonant second order system and the effects of the electrical parasitics, the frequency response can be described by the three-pole transfer function [5]:

$$H(f) = \frac{f_R^2}{\left[\left(f_R^2 - f^2 + j\frac{\gamma}{2\pi}\right)\left(1 + j\frac{f}{f_P}\right)\right]}, \qquad (1)$$

where f_R is the relaxation resonance frequency, f_P is the parasitic cut-off frequency, γ is the damping factor. We fit an

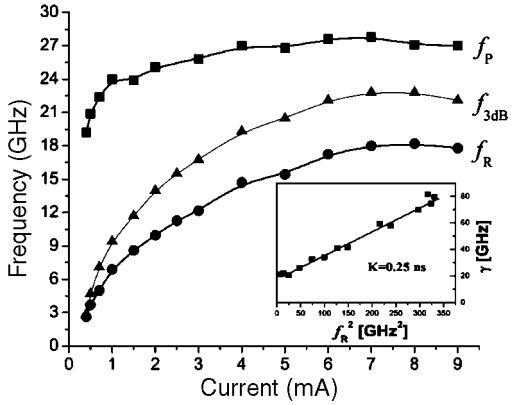

Fig. 2. Parasitic cut-off (black squares), relaxation resonance (black circles) and 3dB-(grey triangles) frequencies for a 6 μm-diameter oxide-confined InGaAlAs-based VCSEL. Inset: damping factor as a function of the squared relaxation resonance frequency.

equivalent electrical circuit (as described in Ref. [6]) to the measured 2-port s-parameters and obtain the VCSEL's intrinsic electrical parasitic resistances and capacities and f_P. Then, f_R and γ are extracted using the first part of the theoretical rate equation (1) without the parasitic low pass filter.

Figure 2 shows the relaxation resonance frequency f_R, parasitic cut-off frequency f_P, and 3dB-frequency f_{3dB} as extracted from the S_{21} and S_{11} measurements for a typical VCSELs with 6 μm-diameter oxide aperture. Note that the maximum 3dB-frequency is larger than 22 GHz at 6 mA, corresponding to a current density of only 7–8 kA/cm^2. Generally there are three physical limits that restrict the high-speed performance of VCSELs including thermal, damping and parasitic limits. As can be observed in Fig. 2 f_P is larger than f_R and thus the parasitic are not limiting the laser's data transfer rate.

Of further interest is the extracting of the K-factor from the damping factor as a function of the squared relaxation resonance frequency (see the inset in Fig. 2):

$$\gamma = K\, f_R^2 + \gamma_0\,. \tag{2}$$

Here the damping shows a weak nonlinear behavior because of heating and possibly due to gain compression. The best estimations for the K-factors are 0.25 ns, leading to an ultimate intrinsic bandwidth that is estimated to be as high as ~35 GHz ($f_{3dB,damping} = 2\pi\sqrt{2}/K$). The 3dB-frequency exceeds the relaxation resonance frequency by a factor ~1.4, which agrees well with the theoretical value of the maximum bandwidth limited by thermal effects only ($f_{3dB,thermal} = \sqrt{1+\sqrt{2}}\, f_{R,max}$). Hence, the increase of the relaxation resonance frequency with current above threshold increase is limited by thermal effects, so that the resonance frequency has a more clearly observed thermal roll-over behavior at bias currents above about 7 mA. a stronger impact of thermal roll-over at high currents.

By fitting a linear function to the extracted squared resonance frequencies as a function of the bias current above the threshold current, one can extract the important D-factor, which determines how efficient a laser can be directly modulated:

$$f_R^2 = D^2\ (I - I_{th})\ . \tag{3}$$

Figure 3 shows the D-factor and f_{3dB} as a function of the VCSEL's oxide aperture diameter. One clearly sees that the D-factor is inversely proportional to the diameter of the active

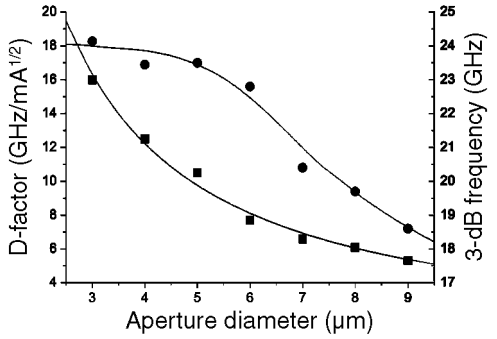

Fig. 3. The D-factor and 3dB-frequency of InGaAlAs-based VCSEL as a function of oxide aperture diameter.

region, while the maximum 3dB-frequency is saturated for oxide aperture diameters of less than 6 μm. This result is a striking performance feature for oxide-confined VCSELs wherewith a constant current density one may improve the reliability and data transfer rate by seemingly by employing a smaller oxide aperture diameter, at least down to about 5 μm where in Fig. 3 f_{3dB} begins to saturate.

To conclude, oxide confined InGaAlAs-based VCSELs emitting near 850 nm for future applications in short reach datacom systems are fabricated. Static and dynamic studies are performed. Small signal modulation bandwidths beyond 22 GHz are realized. The results indicate that further reductions in the electrical and thermal resistances will enable VCSEL bandwidths of 30 GHz for current densities not exceeding ~10 kA/cm^2 and ultimately practical and reliable 850 nm VCSELs for optical links able to operate error-free 40 Gbit/s or higher.

Acknowledgements

The research leading to these results has received funding from the European Community's Seventh Framework Programme (FP7/2007-2013) under grant agreement No. 224211. Our work is also supported by the 100 × 100 project of the Zukunftsfond Berlin, the ProFit project HiTrans, DFG (Sfb 787), RFBR, St Petersburg Scientific Centre RAS, a grant from the St Petersburg Government for the support of young scientists and by the Russian Federal Agency of Education.

References

[1] D. Collins *et al*, *Proc. SPIE* 6908, 690809-1 (2008).
[2] J. A. Lott *et al*, *Proc. SPIE* 7211, 721140P-1 (2009).
[3] P. Westbergh *et al*, *Electron. Lett.* **45**, 366 (2009).
[4] S. A. Blokhin *et al*, *Electron. Lett.* **45**, 501 (2009).
[5] L. A. Coldren and S. W. Corzine, *Diode Lasers and Photonic Integrated Circuits*, (New York: Wiley), 1995.
[6] A. Mutig *et al*, *J. Sel. Top. Quantum Electron.* **15**, 679 (2009).

18th Int. Symp. "Nanostructures: Physics and Technology"
St Petersburg, Russia, June 21–26, 2010

Superradiance and stimulated emission in active nanostructures: multiple scattering effects

V. V. Kurin

Institute for Physics of Microstrucures, 603950 GSP-105 Nizhny Novgorod, Russia

Abstract. It is shown that effects of multiple scattering in active nanostructures can considerably accelerate population inversion decay and radiation intensity due to enhancement of local field coupling to radiation. Linear theory of unstable leaky modes carried by active diffraction gratings is developed and possibility of superradiance in quantum dots array is predicted.

Introduction

It is well known that light scattering on diffraction gratings can entail by so called Wood's anomalies of two types [1]. One manifests in sharp change of light intensity of light reflected to some diffraction order when one of diffraction maximum become grazing. The other appears as a narrow resonance-like peculiarity in frequency or angle dependency of reflection and usually is related to interaction of incident light with quasi surface "leaky" mode originated from existence of local resonances. Theories exploiting ideas of multiple scattering [2] and diffraction on periodic impedance surface [3] yield reliable explanations of effects of such kind. Recent development in nanostructure fabrication renewed interest to optical properties of ordered arrays of nanoparticles and many effects, which is originated from Multiple Scattering were found experimentally. Thus, there was experimentally found collective enhancement of local field in array of golden disks [4] and amplification of magnetooptic Kerr effect in perforated Co films [5].

In this report we claim that effects of multiple scattering can strongly affect the coupling between matter and radiation and can qualitatively change accustomed picture of stimulated emission and superradiance. As a matter of fact the diffraction grating would represent a multiple element antenna providing effective matching of local field to radiation.

In the framework of semiclassic two level system we consider a simple problem of instability of coupled electromagnetic and polariton modes in active diffraction grating formed by long cylinders of dielectric with inverse population situated equidistantly in one plane as it is shown on Fig. 1.

1. Linear theory of active diffraction gratings

In geometry with preferred z axis all field components can be expressed via longitudinal H_z, E_z ones which obey scalar wave equations. Radiation field is represented by sum of fields

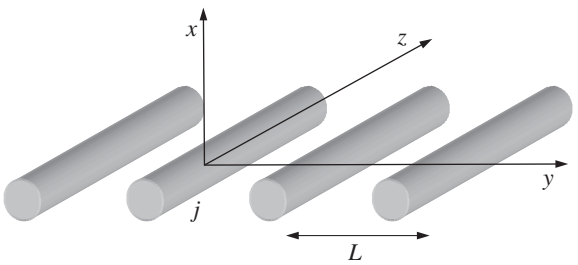

Fig. 1. Appearance of an example of active nanostructure and coordinate system used.

radiated by separate cylinders

$$\left\{ \begin{array}{c} H_z \\ E_z \end{array} \right\} = \sum_{m,j} i^m e^{im\varphi + ik_z z} \left\{ \begin{array}{c} D_m^{H,j} \\ D_m^{E,j} \end{array} \right\} H_m^1(k_\perp \rho_j)\,, \qquad (1)$$

where $H_m^1(k_\perp \rho_j)$ is Hankel function of the first kind, corresponding to running away field, k_z, $k_\perp = \sqrt{k_0^2 - k_z^2}$ are longitudinal and transverse wave numbers, $k_0 = \omega/c$-wave number in vacuum, $D_m^{E,H,j}$-are electric and magnetic multipole coefficients of j-th cylinder for scattering fields respectively. Internal field can be presented by analogous way

$$\left\{ \begin{array}{c} H_z \\ E_z \end{array} \right\} = \sum_{m} i^m e^{im\varphi + ik_z z} \left\{ \begin{array}{c} F_m^{H,j} \\ F_m^{E,j} \end{array} \right\} J_m(\chi_\perp \rho_j)\,, \qquad (2)$$

where now $F_m^{E,H,j}$ are multipole coefficients for internal fields and J_m is Bessel function, $\chi = \sqrt{k_0^2 \varepsilon - k_z^2}$ is a transverse wavenumber where ε is a dielectric permittivity of the material of cylinders. In linear problem it will be the function of frequency, but in general case it will be some operator of linear response acting on functions of time. Further we will assume the radii of cylinders to be small enough so that we can expand cylindrical functions to power series and bound by linear terms. In this approximation only dipole $m = \pm 1$ components would contribute to sums and electromagnetic fields would be homogeneous within cylinders. Using Graf's addition formula for Hankel functions we can transform representation of radiated field outside dielectric cylinders to the form convenient for matching boundary conditions on the surface of j-th cylinder

$$\left(\begin{array}{c} H_z \\ E_z \end{array} \right) = \sum_m i^m e^{im\varphi} \left\{ J_m(k_\perp \rho_j) \times \right.$$
$$\left[\sum_{n,l<j} \left(\begin{array}{c} D_{-n}^{H,l} \\ D_{-n}^{E,l} \end{array} \right) H_{n+m}^1(k_\perp L|j-l|) + \right.$$
$$\left. \left. \sum_{n,l>j} \left(\begin{array}{c} D_{-n}^{H,l} \\ D_{-n}^{E,l} \end{array} \right) H_{n+m}^1(k_\perp L|j-l|) \right] + \right.$$
$$\left. + \left(\begin{array}{c} D_m^{H,j} \\ D_m^{E,j} \end{array} \right) H_m^1(k_\perp \rho_j) \right\}. \qquad (3)$$

Matching boundary conditions of continuity of tangential electric and magnetic components on the surface of j-th cylinder we come to infinite set of homogeneous equations for multipole coefficients on each cylinder. Using translation symmetry of

the problem this set of equations can be diagonalized with respect to index of cylinder j by using Fourier transform defined as

$$D_m^j = \int_{-\pi/L}^{\pi/L} D_m(q)\exp\{iqLj\}\frac{Ldq}{2\pi}\,,$$
$$D_m(q) = \sum_j D_m^j \exp\{-iqLj\}\,,$$

and if we confine myself with dipole approximation we come to two independent pairs of equation for Cartesian dipole components D_x^E, D_y^H and D_y^E, D_x^H defined by standard way $D_{\pm1} = -i(D_x \pm iD_y)$. Solubility conditions for these two x, y subsystems yield two dispersion equations for hybrid H, E eigenmodes with two independent polarizations carried by diffraction grating. In the case of strict transverse propagation when $k_z = 0$ electric and magnetic waves splits and full dispersion equation become considerably simpler. Here, as an the most important example, we write down the dispersion equation for the pure x polarized H-mode

$$\frac{\varepsilon+1}{\varepsilon-1}+\frac{z^2}{2}\left[\ln\frac{ze^\gamma}{2}+\frac{\varepsilon+2}{8}\right]=i\frac{\pi z^2}{4}\left[1+G_x(k_0L,q)\right], \quad (4)$$

where $z = k_0a$, a — cylinder radius, $L_g = \ln(ze^\gamma/2)$, γ — Euluer constant. Renormalization factor G_x for x polarization

$$G_x(k_0L,q) = \sum_{j>0}\left[H_0^1(k_0Lj) - H_2^1(k_0Lj)\right]\cos qLj\,. \quad (5)$$

All terms now can be easily interpreted. The first term is responsible for quasistatic polarization of individual cylinder and describes local plasmon resonance lying at $\varepsilon = -1$. The rest ones proportional to z^2 give wave corrections. Imaginary part of the expression is responsible for damping due to ohmic and radiative losses, real part — for renormalization of local field. Factor G_x describes collective effects due to interaction of cylinders via radiation field. It has singularities at wave numbers corresponding to opening diffraction order. At these points, sometimes called Rayleigh's one, coupling to radiation field become anomalously large. In the vicinity of this singularity, factor G_x behave itself asymptotically as

$$G_x \sim 2\left[(k_0L)^2 - (qL+2\pi l)^2\right]^{-1/2}\,, \quad (6)$$

where l is integer number. Such Dielectric permittivity and renormalization factor G_x are meant as analytical functions in the upper half plane of complex frequency $\mathrm{Im}\omega > s > 0$, that provides definiteness and convergence of all expressions. The solutions of dispersion relation 4 for the case of passive media can give both true surface wave and so called leaky waves — the quasi surface waves coupled to radiation, depending on what sheet of multiple valued function, which contain square roots like 6, lies the root of Eq. 4. For unstable media, when the equation 4 will have a solution with $\mathrm{Im}\omega > 0$ leaky mode will turn into growing in time true surface wave.

Now we are able to consider the case of unstable media with inverse population. As we have already mentioned that when radii of cylinders are small compared with wavelength then dipole approximation is valid and ectromagnetic field and polarization to be homogeneous inside cylinders. Then we are able to write down equation for homogeneous polarization vector and population. Using semiclassical approach and two level approximation we have standard equation

$$\ddot{\mathbf{P}} + 2\nu\dot{\mathbf{P}} + (\omega_0^2+\nu^2)\mathbf{P} = -2N(\mathbf{Ed})\mathbf{d}\omega_0\hbar^{-1}\,,$$
$$\dot{N} + T_1^{-1}(N-N_0) = 2(\hbar\omega_0)^{-1}\mathbf{E}(\dot{\mathbf{P}}+\nu\mathbf{P})\,,$$

where $\nu = T_2^{-1}$. In linear approximation for fixed population density from these equations we come to expression for dielectric permittivity

$$\epsilon = 1 - \frac{\omega_c^2}{(\omega+i\nu)^2-\omega_0^2}\,, \quad (7)$$

where ω_c is a so called cooperative frequency defined as $\omega_c^2 = 8\pi d^2 N\omega_0\hbar^{-1}$. In inverted media $N > 0$ and $\omega_c^2 < 0$ Dispersion equation 4 with this expression for dielectric permittivity describes unstable leaky modes. Not so difficult to estimate maximal increment in the vicinity of Rayleigh frequency. If we assume that $cq \sim \sqrt{\omega_0^2 - |\omega_c|^2/2}$ and consider $\omega = cq + \delta\omega$ with $\delta\omega \ll cq$ the dispersion equation can be easily solved

$$\delta\omega \simeq \begin{cases} \frac{\sqrt{3}+i}{16}|\omega_c|\left(qa\frac{|\omega_c|a}{c}\frac{a^2}{L^2}\right)^{1/3}, & \delta\omega \gg \nu \\ \frac{1+i}{32\sqrt{2}}|\omega_c|\frac{|\omega_c|a}{c}\left(\frac{cq}{\nu}\right)^{1/2}\frac{a}{L} & \delta\omega \ll \nu \end{cases}. \quad (8)$$

The first solution describes the so-called dissipative instability of polariton mode, when polariton having negative self energy grows to dissipation due to radiation into open space. Evolution of instability of such kind leads to superradiance [6]. Due to strong enhancement of coupling to radiation caused by multiple scattering effects the increment found is much greater than for single cylinder. The second solution describes slower instability, which correspond to developing "laser" instability. This instability is also strongly modified by multiple scattering effects.

2. Conclusion

As it seen from Eq. 8 for developing of dissipative instability corresponding to superradiance one needs to have a sufficient large cooperative frequency in an active media. A good candidate for experimental realization of proposed generation scheme would be InAs/GaAs quantum dot active media [7]. Based on value of gain up to 6×10^4 cm^{-1} measured in [7] and corresponding value of inhomogeneous broadening it is easy estimate increment and show that condition $\delta\omega > \nu$ corresponding to developing of superradiance can be satisfied.

Acknowledgements

This work has been supported in part by Russian Foundation for Fundamental Research, by programs RAS and by Federal Program "Scientific personnel of innovative Russia"

References

[1] R. W. Wood, *Phil. Mag.* **4**, 396 (1902).
[2] V. Twersky, *J. App. Phys.* **23**, 1099 (1952); M. Meier *et al*, *J. Opt. Soc. Am. B* **2**, 931 (1985).
[3] A. A. Hessel, A. A. Oliner, *Applied Optics* **4**, 1275 (1965).
[4] Y. Chu *et al*, *Appl. Phys. Lett.* **93**, 181108 (2008).
[5] G. Ctitis *et al*, *Nano Lett.* **9**, 1 (2009).
[6] V. V. Zheleznyakov *et al*, *UFN* **159**, 193 (1989).
[7] N. Kirstaedter *et al*, *Appl. Phys. Lett.* **69**, 1226 (1996).

18th Int. Symp. "Nanostructures: Physics and Technology"
St Petersburg, Russia, June 21–26, 2010

Improvement of efficiency for red resonant-cavity light-emitting diodes using modified electron stopped layers

V. V. Lysak[1], C. Y. Park[2], K. W. Park[2] and Y. T. Lee[2,3]

[1] Chonbuk National University, Jeonju, Republic of Korea
[2] Gwangju Institute of Science and Technology (GIST), Gwangju, Republic of Korea
[3] Department of Nanobio Materials and Electronics, GIST, Gwangju, Republic of Korea

Abstract. The analysis of electro-optical properties of 635 nm InGaP/InGaAlP resonant-cavity light-emitting diodes (RCLED) with AlGaAs mirrors for compact projectrors is presented. We show that including the p-doped electron stop layer in both side of active layer improves the efficiency of such device due to increasing the electron capture efficiency in the quantum wells and decreasing the electrical field across the active layer. Also reflectivity spectra of both top and bottom DBRs at wavelength 635 nm was theoretically investigated including dispersion relation of refractive index. Theoretical analysis is proved by experimentally.

Introduction

MICRO-DISPLAY based projectors require projection lamps. Currently high intensity discharge (HID) lamps are used. They have a very high luminance, but limited life, and require a color wheel. Light-emitting diodes (LEDs) have a very long lifetime, and don't require a color wheel, which increases the acceptance and flexibility of a color sequential projection display considerably. The external quantum efficiency η_{ext} is the key performance figure for high-efficiency LEDs [1], which is limited to 2–4% by Snell's law for conventional planar LEDs due to the high refractive index contrast between the source material and the surrounding medium. Extraction efficiency can be increased when cavity optics entered the world of LEDs with the resonant-cavity LED (RCLED). In these devices, the active layer is embedded in a cavity with at least one dimension of the order of the wavelength of the emitted light. Under those circumstances, the spontaneous emission process itself is modified, such that the internal emission is no longer isotropic. Schubert et al. presented the RCLED as a conceptual novel LED in 1992 [2,3]. From this time the extraction efficiency was improved up to 50%. Like in standard red LEDs, the GaAsP material system is increasingly substituted by the high-quality AlGaInP for use as active medium. Devices in the 600- to 650-nm range are described by several research groups, showing η_{ext} up 10% [4,5].

1. Structure description

Red RCLED with 635 nm of emission wavelength (Fig. 1) consists of 2 $Al_{0.5}Ga_{0.5}As/Al_{0.95}Ga_{0.05}As$ distributed Bragg reflectors (DBR) with 22.5 pairs for bottom and 5 pairs for top DBR. The cavity consists 815 nm thickness $In_{0.498}Ga_{0.08}Al_{0.422}P$ cladding layers, 0.2% of compressive-strained InGaP 63 nm quantum wells and 0.1% tensile-strained InGaAlP 150 nm barrier due to the low conduction band offset [6–8]. The conduction band offset of lattice matched InGaP/InGaAlP material system as 165 meV is about a half of the conduction band offset of lattice matched InGaAs/AlGaAs material system 350 meV. Due to the low conduction band offset ($\Delta E_c/\Delta E_c \approx 0.4$), electrons in the quantum wells can easily escape from the well reducing internal quantum efficiency in the lattice-matched InGaP/InGaAlP material system. To reduce the electron leakage from active layer the 5 nm p-doped $In_{0.49}(Ga_{0.2}Al_{0.8})_{0.51}$ electron stopped layer (ESL) can be introduced in the cladding layer close to the active layer. Here three structures is compared. First structure does not contain ESL, in second structure ESL is placed on p-cladding and third structure contains ESLs on both p- and n- cladding layers.

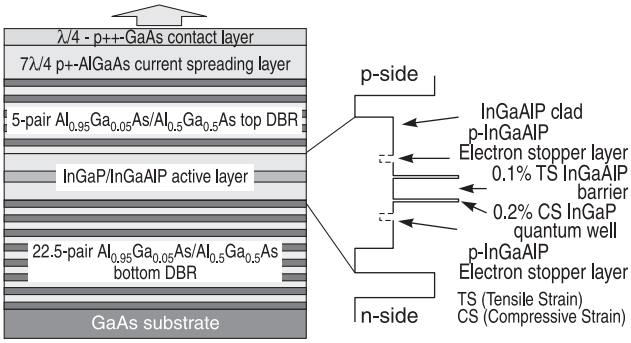

Fig. 1. Red RCLED structure with active layer details.

2. Numerical simulations models

Several software tools were used in the process of designing and optimizing the devices. Besides using the self-consistent model implemented in CrossLight's package APSYS. This software simulates a wide spectrum of electrical, optical and thermal characteristics with the ability to update to new material parameters and calculation algorithms. All important heat sources, i.e. non-radiative recombination, absorption of spontaneous radiation, are taken into account. The main material parameters can be found in the related literature [9]. Fast and flexible transfer-matrix-based calculations of the reflection coefficient dependencies (upon wavelength, incidence angle, polarization, layer contrast, layer thickness, number of DBR periods) and of the optical field distributions played an important role in the device development-mostly in the early design stages-and in understanding the angular emission of the RC-LEDs [10]. The refractive index of AlxGa1-xAs system can be given by the Adachi model [11].

3. Results and discussion

Figure 2 shows the calculation of conduction band distribution for structures without ESL (green line) compare to device with ESL in p-side (red line) and 2 ESLs in both sides of active layer (blue line). The material and doping concentrations for both layers are depicted on figure. Including the second stop layer to the n-side of structure increase the capture efficiency and makes the energy distribution in the active layer region more uniform.

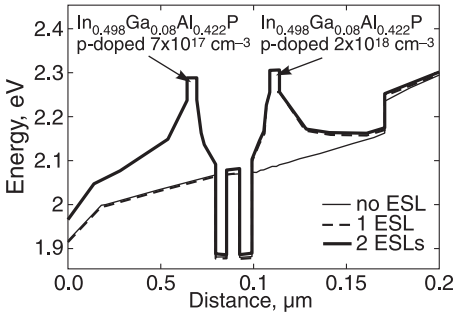

Fig. 2. Conduction band distribution without ESL (thin line), with 1 ESL (dashed line) and with 2 ESLs (thick lines).

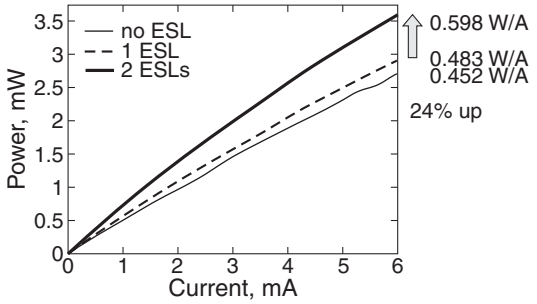

Fig. 3. L-I characteristics for RCLED without ESL (thin line), with 1 ESL (dashed line) and with 2 ESLs (thick lines).

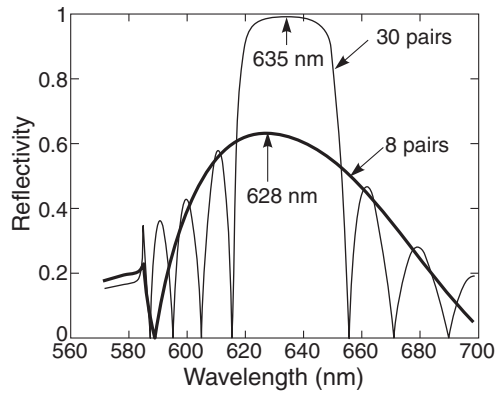

Fig. 4. Reflectivity spectra for top and bottom DBRs.

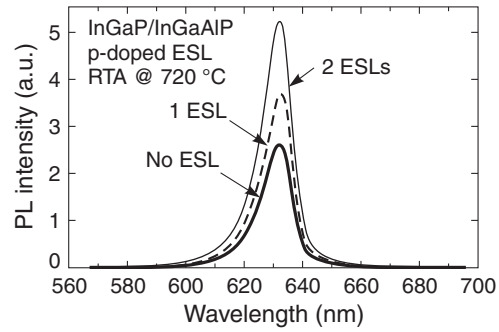

Fig. 5. Spontaneous emission spectra for RCLED without ESL (thick line), 1 ESL (dashed) and 2 ESLs (thin lines).

Such modification allows increasing the total efficiency of device as shown on Fig. 3. Figure shows slope efficiency (SE) for structure without ESL is equal to 0.452 W/A. If ESL on the p-side cladding layer is introduced SE increased up to 0.483 W/A. When we have a structure with 2 ESLs on both side of active layer SE increased up to 0.598 W/A or 24% improvement comparing to 1 ESL structure.

4. Mirror reflectivity analysis

Distributed Bragg reflector (DBR) was calculated with and without including wavelength dependency of refractive indices of materials. Results are shown on Figure 4 for top and bottom mirrors. Analysis shows a dependence of dispersive refractive indices on central wavelength of mirror with change of layer number.

Results shows decreasing the central wavelength then number of layers is decreased. To solve this problem the layer thicknesses should be slightly modified to get the same central wavelength for both mirrors.

5. Experimental verification

To verify theoretical data, the real device with structure shown on Fig. 1 was grown. Results show improvement of SE spectra with introducing the ESL on both sides of active layer that verify our theoretical calculations. The measured Spontaneous emission (SE) spectra are present on Fig. 5. The PL was measured by RPM2000 with using 532 nm laser diode which output power is 7 mW at room temperature.

6. Conclusions

The electrical and optical properties are analyzed for the 635 nm InGaAlP RCLED with different structures of active layer. Results show, inserting ESL layers in both sides of active layer increases the slope efficiency of L-I characteristic up to 24% due to increasing the electron capture efficiency in the quantum wells. Reflectivity spectra of both top and bottom DBRs at wavelength 635 nm was theoretically investigated including dispersion relation of refractive index. Results show decreasing the mirror stop-band for model with refractive index dispersion and blue shifting the central wavelength at decreasing the number of layers in the mirror. Comparing with grown mirrors allow receiving the proper thicknesses of layer for bottom mirror ($d_h = 457$ Å and $d_l = 502$ Å) and top mirror ($d_h = 464$ Å and $d_l = 509$ Å). Theoretical result was verified experimentally and shows the twice increasing the internal quantum efficiency between the structure without ESL and optimized 2 ESL structure.

Aknowledgement. This work was supported by IT RND program of MKE/IITA [2007-F-045-03].

References

[1] D. Delbeke *et al*, *IEEE JSTQE* **8**, 189 (2002).
[2] E. F. Schubert *et al*, *Applied Physics Letters* **60**, 921 (1992).
[3] M. R. Krames *et al*, *Applied Physics Letters* **75**, 2365 (1999).
[4] P. Modak *et al*, *Electronics Letters* **37**, 377 (2001).
[5] R. Wirth *et al*, *IEEE Phot. Tech. Letters* **13**, 421 (2001).
[6] P. Mackowiak and W. Nakwaski, *Journal of Physics D: Appl. Phys.* **34**, 954 (2001).
[7] M. Dumitrescu *et al*, *Microelectronics Engineering* **51–52**, 449 (2000).
[8] R. P. Schneider Jr. *et al*, *Int. J. of High Speed Electronics and Systems Devices* **5**, 625 (1994).
[9] *SimuApsys, User's manual and reference manual*, (Crosslight Inc.) 2008.
[10] P. Yen, *Optical waves in Layered Media*, (New York: Wiley) 1988.
[11] S. Adachi, *GaAs and Related Materials*, (World Scientific) 1995.

18th Int. Symp. "Nanostructures: Physics and Technology"
St Petersburg, Russia, June 21–26, 2010

Peculiarities of plasma-assisted molecular beam epitaxy of $Al_xGa_{1-x}N$ layers grown in the whole composition range

A. M. Mizerov, V. N. Jmerik, P. S. Kop'ev and S. V. Ivanov
Ioffe Physical-Technical Institute, St Petersburg, Russia

Abstract. The paper describes the growth kinetics of $Al_xGa_{1-x}N$ ($x = 0-1$) layers by plasma assisted molecular beam epitaxy. The growth of both metal- and nitrogen-polarity AlGaN films on different substrates or templates (c-Al_20_3, GaN/c-Al_2O_3, AlN/c-Al_20_3) has been demonstrated. The influence of residual strain on the growth rate of metal-polar $Al_xGa_{1-x}N$ layers was studied. A phase diagram for managing the surface morphology during growth of $Al_xGa_{1-x}N(0001)$/c-Al_2O_3 films at the relatively low substrate temperature $T_S \sim 700$ °C and group III to activated nitrogen flux ratio changing from 2 to 0.9 has been elaborated.

Introduction

Group III nitrides are of great importance for further progress in the solid-state deep UV optoelectronics with the minimum wavelength of 210 nm [1–4]. Among different technologies developed for the growth of AlGaN-based heterostructures plasma-assisted molecular beam epitaxy (PA MBE) provides the unique facilities. They concern the growth of AlGaN epilayers with a sub-monolayer resolution at the relatively low substrate temperatures $T_S < 800$ °C that suppresses the surface segregation and improves the sharpness of the heterostructure interfaces. Ultra-low nitrogen pressure in the growth chamber ($\leq 10^{-5}$ Torr) excludes any parasitic gas-phase reactions increasing the defect density in the layers. In addition, PA MBE enables one to grow the group III nitrides with well controllable rough nanocolumnar (3D) or atomically smooth (2D) surface morphology, anion (N) or cation (Al,Ga) surface polarity, depending on the growth conditions and a type of the substrate or buffer layer [5]. Thus PA MBE especially prospective for realization of the low-defect density AlGaN nanostructures with different design and morphologies.

However, information on the PA MBE growth kinetics of AlGaN layers is quite scarce and, to our knowledge, the only paper of Moustakas *et al* has been published so far [6]. We reported also the preliminary results on complex correlation between polarities of the AlGaN epilayers and kind of the substrate employed [7]. In addition, in contrast to Ref. [6] we found that highly metal-enriched stoichiometric conditions should be maintained for growing the atomically smooth AlGaN layers.

The paper reports on the growth of $Al_xGa_{1-x}N$ layers ($x = 0-1$) by PA MBE with different polarities and strain conditions. Special attention is devoted to peculiarities of the controllable variation of surface morphology from 2D to 3D and back for Ga-polar films with high Al-content ($x > 0.2$).

1. Experimental

$Al_xGa_{1-x}N$ epitaxial layers ($x = 0-1$) with a typical thickness of ~ 1 μm were grown using a PA MBE setup Compact 21T (Riber) equipped with a plasma source HD-25 (OAR). The layers were grown on annealed nitridated c-Al_2O_3 substrates using different buffer layers including GaN(000I)/c-Al_2O_3 and AlN(0001)/c-Al_2O_3 with the thickness varied from 0.2 to 1 μm. In addition, 3-μm-thick GaN(0001)/c-Al_2O_3 templates grown by MOVPE were used as substrates. Different substrate temperatures $T_S = 650-820$ °C, growth rates $v_g = 0.2-0.5$ μm/h and group III to activated nitrogen flux ratios $F_{III}/F_N = 0.8-2$ were employed.

The growth rate, Al-content and surface morphology were evaluated in-situ using the laser reflectometry (LR) and reflection high energy electron diffraction (RHEED), respectively. The surface polarity was determined by chemical etching of the films in a 2M NaOH solution. The morphologies of the films and existence of metal microdroplets were evaluated by using the scanning electron and optical microscopes.

2. Results and discussion

The was generally established that the usage of an AlN buffer layer on c-Al_2O_3 substrate in PA MBE results in growth of Ga-polar AlGaN films only. We have found that contrary to that the polarity of $Al_xGa_{1-x}N$ films ($x = 0-1$) grown atop of GaN buffer layers (or templates) with different polarities (Ga- or N-face) inherits its polarity even for a pure AlN. In the case of growth of the $Al_xGa_{1-x}N$ ($x = 0-1$) layers on c-Al_2O_3 substrates directly we have revealed that the film's polarity is changed from the nitrogen to metal one above the critical value of Al-content $x = 0.20 \pm 0.05$.

The effect of the strain on the AlGaN growth kinetics was evaluated from the temporal behavior of the growth rate of thick Ga-polar $Al_xGa_{1-x}N/0.3\mu$m-AlN/c-Al_2O_3 layers of different composition grown at other fixed parameters. Fig. 1 shows the change of growth rates versus thickness (growth time) for two layers grown at the same $F_{N^*} \sim 0.5$ μm/h, $F_{III}/F_{N^*} \sim 1$, $T_S \sim 700$ °C and different value of the F_{Al}/F_{N^*} flux ratio which define directly the alloy composition. The surface morphology starts with 2D following that of the AlN buffer, and transforms gradually to 3D one. According to x-ray diffraction data the AlN buffer is completely relaxed at a thickness below 0.25 μm. The AlGaN layer grown at $F_{Al}/F_{N^*} = 0.25$ demonstrates increasing of growth rate above the thickness of ~ 0.5 μm, while for the film with higher $F_{Al}/F_{N^*} = 0.5$ and smaller lattice mismatch the growth rate remains constant up to 1.6 μm. These results can be explained qualitatively by the enhancement of the critical thickness of compressive stress relaxation with the increase of Al content in the AlGaN/AlN heterostructures. The obtained results correlate well with previous observation of the higher growth rates for AlGaN films grown on GaN buffer layer in comparison with those grown on a c-Al_2O_3 substrate. This was interpreted by an existence of

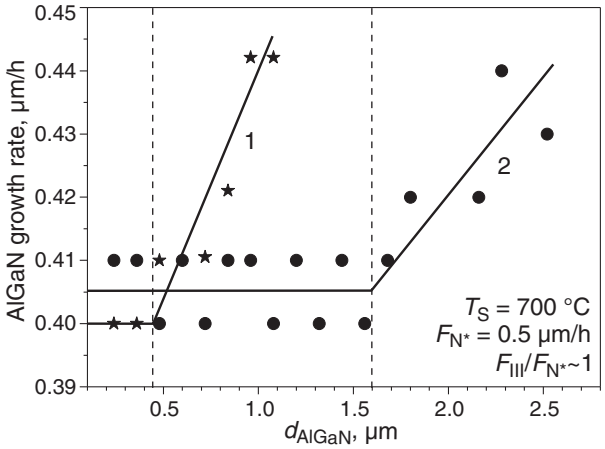

Fig. 1. Dependence of $Al_xGa_{1-x}N$/AlN/c-Al_2O_3 growth rate on d_{AlGaN} during growth at $T_S \sim 700$ °C, $F_{III}/F_{N^*} \sim 1$ and (1) $F_{Al}/F_{N^*} \sim 0.25$, (2) $F_{Al}/F_{N^*} \sim 0.5$.

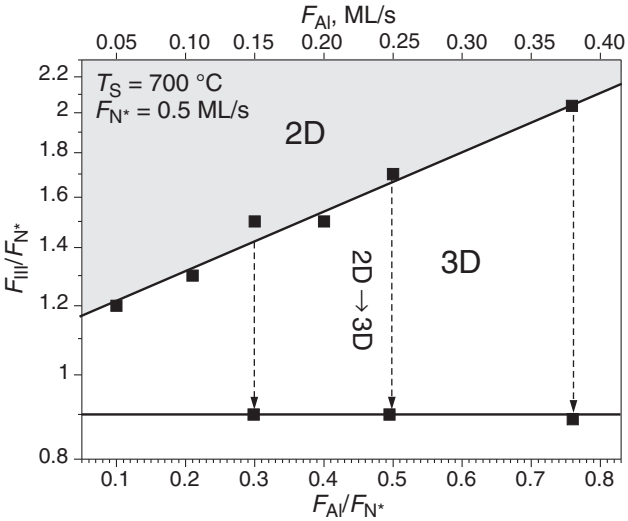

Fig. 2. F_{III}/F_{N^*} ratios which are necessary to recover 3D growth conditions of $Al_xGa_{1-x}N$/AlN/c-Al_2O_3 layers to 2D ones versus F_{Al}/F_N ratio at $T_S = 700$ °C and constant F_{N^*}.

the higher residual strain in the latter case, which facilitates the Ga-N bond breaking even at 700 °C, while the Al incorporation in AlGaN is not inhibited [7].

Fig. 2 shows a phase diagram of variation of the surface morphology of metal-polar $Al_xGa_{1-x}N$ (0001) layers by varying the F_{III}/F_{N^*} ratio at $T_S = 700$ °C. The upper slope solid line demonstrates the minimum F_{III}/F_{N^*} values necessary to recover the 3D growth mode of the AlGaN films to 2D one for different Al molar concentrations governed unambiguously by the equation $x = F_{Al}/F_{N^*}$. The F_{III}/F_{N^*} ratio regulated by Ga flux rises gradually with x and reaches 2.0 for $x \sim 0.75$. The surface morphology remains droplet-free up to $F_{III}/F_{N^*} = 1.6$ achieved for $Al_{0.5}Ga_{0.5}N$ films. In this case complete evaporation of the excessive Ga flux (~0.3 ML/s) corresponds to maximum possible Ga equilibrium evaporation rate from pure Ga melt at 700°C [8]. Rise of the growth temperature up to 710 °C results in possibility to grow droplet-free $Al_{0.75}Ga_{0.25}N$ layer at $F_{III}/F_{N^*} = 2.0$. Thus, during the growth of AlGaN films under the metal-rich conditions the excess of Ga evaporates from Ga-adlayer without Ga-droplets formation. The measurements of Al-content in the AlGaN films confirm the full Al flux incorporation. The vertical dashed lines in Fig. 2 demonstrate the necessary change of the F_{III}/F_{N^*} ratio down to ~0.9 (solid horizontal line) for the reverse 2D–3D transition of the growth mode of $Al_xGa_{1-x}N$ layers with different x, thus revealing a strong hysteresis of the growth conditions. Again to recover the 2D growth mode the values of F_{III}/F_{N^*} corresponding to the upper solid line must be restored. Such variation of growth conditions can be used to grow the 3D/2D AlGaN buffer structures intended for the efficient filtering of threading dislocations [2], as well as for generation of the localization sites of charge carriers in the active region of light emitting nanoheterostructures etc.

3. Conclusions

In conclusion, we have demonstrated the ability to grow $Al_xGa_{1-x}N$ films in the full composition range with both the nitrogen and metal polarities. The compressive strain in AlGaN films reduces partially the growth rate through facilitating the Ga-N bond breaking even at 700 °C. The plotted phase diagram for controlling the AlGaN surface morphology demonstrates that practically important atomically smooth droplet-free Ga-face $Al_xGa_{1-x}N$ ($x > 0.2$) layers can be grown on c-Al_2O_3 in a wide range of metal supersaturation ($F_{III}/F_{N^*} \sim 1.6$ and 2.0 at $T_S \sim 700$ and 710 °C, respectively). Strong hysteresis of the F_{III}/F_{N^*} ratios necessary for 3D–2D and reverse AlGaN growth mode transition has been found, with the amplitude depending on the Al mole fraction.

Acknowledgements

The work was supported in part by RFBR and Program "Novel materials" of RAS, as well as by St Petersburg high education and science committee.

References

[1] Y. Taniyasu, M. Kasu and T. Makimoto, *Nature* **441**, 325 (2006).
[2] H. Hirayama *et al*, *Proc. of SPIE* **7216**, 721621-1 (2009).
[3] S. Nikishin *et al*, *Jpn. J. Appl. Phys.* **44**, 7221 (2005).
[4] V. Jmerik *et al*, *J. Cryst. Growth* **311**, 2080 (2009).
[5] D. Huang *et al*, *Appl. Phys. Lett.* **78**, 4145 (2001).
[6] E. Iliopoulos and T. Moustakas, *Appl. Phys. Lett.* **81** 2, 295 (2002).
[7] A. M. Mizerov *et al*, *to be published in Phys. Stat. Sol. (c).*
[8] I. Grigorjev and E. Meoelikhov, *Physical Quantities*. The Handbook, (Energoatomizdat, Moscow, 1991), p. 255.

18th Int. Symp. "Nanostructures: Physics and Technology"
St Petersburg, Russia, June 21–26, 2010

AlGaN MQW optically pumped lasers at 300 nm

V. N. Jmerik[1], A. M. Mizerov[1], T. V. Shubina[1], K. G. Belyaev[1], A. A. Sitnikova[1], M. A. Yagovkina[1], P. S. Kop'ev[1], S. V. Ivanov[1], E. V. Lutsenko[2], N. P. Tarasuk[2], N. V. Rzheutskii[2] and G. P. Yablonskii[2]

[1] Ioffe Physical-Technical Institute, St Petersburg, Russia
[2] Stepanov Institute of Physics of NAS Belarus, Independence Ave. 68, Minsk 220072, Belarus

Abstract. We report on AlGaN multiple-quantum-well (MQW) separate confinement laser heterostructures grown by plasma-assisted molecular-beam epitaxy (PA MBE) directly on c-sapphire at low temperatures (<800 °C). Threading dislocation density was reduced down to 10^9–10^{10} m^{-2} owing to both intentionally introduced strained AlGaN/AlN superlattices and self-organized blocking structures in the AlGaN step-graded buffer layers. The optimization of the growth conditions and the design of the MQW structures fabricated by a sub-monolayer digital alloying technique enabled optically pumped UV lasing at 303 nm with the relatively low threshold excitation density of 0.8 MW/cm^2.

Introduction

AlGaN-based ultraviolet (UV) optoelectronic devices are very attractive for numerous applications in the bio-medical and environmental field, as well as in the UV-sensitive material processing. However, the poor structural quality of AlGaN-based heterostructures with high Al mole fraction (>20%) grown on lattice-mismatch substrates and the absence of strong enough localization effects in this material cause serious difficulties in fabrication of UV light emitting diodes (LED) and laser diodes (LD) for the deep UV range (<300 nm). As a result, a minimum emission wavelength for UV-LD is still restricted by a value of 336 nm [1] and only optically pumped lasing with the threshold power density above ∼1 MW/cm^2 has been achieved for AlGaN-based multiple-quantum well (MQW) structures emitting at shorter wavelengths down to 214 nm (AlN layer) [2,3]. To overcome this problem, different techniques have been proposed to decrease the threading dislocation (TD) density in the active region of laser structures [4], while the improving of the AlGaN MQW laser characteristics by means of optimization of the laser structure design has been proposed theoretically just in few papers [5].

We report on further development of the PA MBE technology of $Al_xGa_{1-x}N$-based structures ($0.4 < x < 1.0$) as well as of the laser structure design to reduce the threshold power density at a wavelength around 300 nm.

1. Experimental

AlGaN MQW laser structures were grown by PA MBE directly on a c-Al_2O_3 substrate, as described in detail previously [6]. In particular, the growth was initiated with the deposition of a two-step AlN buffer layer consisting of 30-nm-thick low-temperature (570 °C) and 250-nm-thick high-temperature (800 °C) layers. Then the substrate temperature was reduced down to 700 °C and kept constant till the end of the growth. The strained $\{AlGaN/AlN\}_{30}$ superlattice (SL) with a period of 10 nm and an average AlN mole fraction of 0.9 was grown atop the AlN layer. Both structures have three 3-nm-thick QWs with an average $x = 0.39$ separated by 7-nm-thick barriers layers with $x = 0.49$. The structures are differed mainly in a design of the top parts above the SL. In structure A, QWs were disposed in 1 μm-thick buffer layer $Al_{0.49}Ga_{0.51}N$ at a distance of 100 nm from surface. The structure B comprises stacked $Al_xGa_{1-x}N$ buffer, cladding, and waveguide layers with $x = 0.77$, 0.66, 0.49, respectively. An asymmetric waveguide has been used in this separate confinement (SC) heterostructure, as shown in Fig. 1a. All AlGaN layers in the both structures were grown under the metal-rich stoichiometric condition, and MQW were formed by using the sub-monolayer digital alloying (SMDA) technique described elsewhere [6].

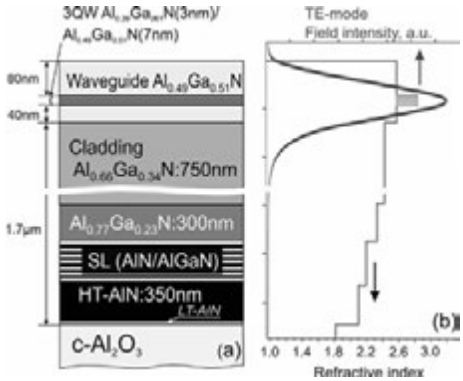

Fig. 1. Structure B for optically pumped AlGaN MQW laser: (a) schematic diagram of the SC heterostructure, (b) variation of the refractive index versus the thickness in the structure and the simulated near-field distribution of a fundamental mode supported by the laser waveguide.

The crystalline properties of the structures were studied by transmission electron microscopy and X-ray diffraction. Optical properties were investigated by measuring optical adsorption spectra and time-resolved photoluminescence (TR PL) spectra with excitation by the 3rd harmonic (266 nm) from a Ti:sapphire femtosecond pulsed laser. The 4th harmonic (266 nm) of a Nd-YAG laser was employed for optical pumping of stimulated emission.

2. Results and discussion

XRD study confirmed the values of Al-content in all the AlGaN layers, which were defined using a simple ratio of the calibrated aluminum flux to the measured total growth rate $x = F_{Al}/V_{AlGaN}$. The latter was determined by the calibrated active nitrogen flux under the metal-rich growth conditions used. TEM study of the structures revealed a decrease of the TD density from the values above 10^{11} cm^{-2} within the AlN buffer layers towards the 10^9–10^{10} cm^{-2} range within the top part of the MQW structures. In both structures, the TD filtering effect was observed initially within the intentionally grown strained AlN/AlGaN SL. Then, a sharp reduction of the TDs was de-

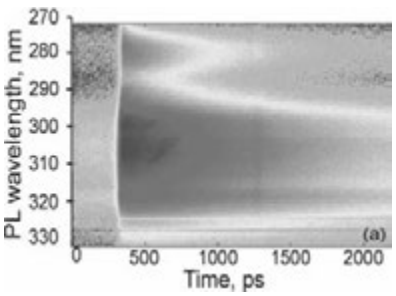

Fig. 2. Low temperature (1.8 K) time-resolved PL spectra of the structure B.

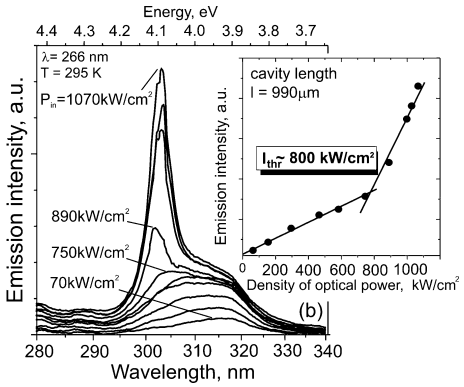

Fig. 3. Room temperature edge PL spectra of the structure below and above the lasing threshold. The insert shows the emission intensity versus the pumping power density.

tected in the AlGaN intermediate buffer layer of structure B at a distance of 180 nm above the AlN/AlGaN SL, where a dense defect network structure (DNS) with some ordering features was self-organized. Formation of such structure is observed for the first time and can be regarded as a new relaxation mechanism of the compressive stress in the $Al_{0.77}Ga_{0.23}N$ buffer layer. As a result, relatively small concentration $\sim 1.5 \times 10^9$ cm^{-2} of the screw-type TD has been found in the top region of structure B. This is only 5% of the total TD density $\sim 3 \times 10^{10}$ m^{-2} contributed by 55% of mixed and 40% of vertical edge TDs. Note also that structure B demonstrates twice as much reduction of TD density in the top active region in comparison with structure A (without DNS).

Three QWs are clearly observed in the TEM images; their thicknesses are well consistent with those calculated via growth parameters defined by the SMDA technique. The high efficiency of the dominant PL emission and its origin from the QWs has been confirmed by time-resolved PL spectroscopy. The PL spectra measured in both structures were very similar; they have complex shape with well-separated peaks. Fig. 2 demonstrates that presenting the spectra of structure B. Comparison with the absorption spectra has permitted us to attribute the higher-energy PL band to the barrier emission, whereas the lowest-energy band is related to the luminescence from QWs. These bands demonstrate different characteristic life times, which are usually longer for the latter. This reflects the effective carrier transfer to the QWs and rather small contribution of non-radiative recombination.

It is necessary to underline that the main difference between the structures is the design of their top regions, with structure B possessing the asymmetric MQW position in the optical cavity region along with the different composition and thickness of its cladding layers. As a result, this structure has the near-field distribution of the fundamental TE mode of electromagnetic field with the maximum laying at the center of the MQW active region, as shown in Fig. 1b. The calculations of the lasing parameters, taking into account these peculiarities, show the great increase of the optical confinement factor from 0.002 to 0.09 in structure B as compared to A. Parameters of optically pumped lasing observed in both structures confirm the results of the calculations. The high pumping density of about 12 MW/cm^2 was required for structure A to detect the onset of stimulated emission in the edge PL, namely the superlinear rising and weak sharpening of the emission spectrum at a wavelength of 300.4 nm. While the optimized structure B reveals the relatively low threshold power density of the laser emission $\sim$0.8 MW cm^{-2} which was derived from emergence of the fast growing higher energy narrow PL line at 303 nm with the increase in the pumping power, as shown in Fig. 3.

We believe that the main factor of lowering the laser threshold is the improvement of the laser structure design comprising the separate confinement double heterostructure with the asymmetric waveguide, which results in increasing the optical confinement factor for the fundamental mode at practically the same lasing wavelength. Additional factors promoting the lasing are (i) weaker sensitivity of the laser threshold to a quality of mirrors, (ii) increased radiative recombination efficiency by about 70% and decreased internal losses in the laser structure B owing to the multi-stage TD filtering, which resulted in lowering the TD density in the active region. The combined action of the factors results in the laser threshold being less or comparable to those in AlGaN MQW structures grown by MOVPE and emitting at the same wavelengths [2,7].

3. Conclusions

We have demonstrated a possibility to grow by PA MBE on c-Al_2O_3 substrates the AlGaN MQW structure exhibiting optically pumped lasing at 303 nm. Carefully chosen laser structure design and employing different ways of threading dislocation filtering led to the remarkably low value of laser threshold of 0.8 MW/cm^{-2} at room temperature.

Acknowledgements

We are grateful to B. Monemar for enabled TR PL characterization. The work was supported in part by RFBR and Program "Novel materials"of RAS.

References

[1] H. Yoshida *et al*, *Appl. Phys. Lett.* **93**, 241106 (2008).
[2] T. Takano *et al*, *Appl. Phys. Lett.* **84**, 3567 (2004).
[3] M. Shatalov *et al*, *Jpn. J. Appl. Phys.* **45**, L1286 (2006).
[4] W. H. Sun *et al*, *Appl. Phys. Lett.* **87**, 211915 (2005).
[5] W. W. Chow *et al*, *Appl. Phys. Lett.* **90**, 101116 (2007).
[6] V. N. Jmerik *et al*, *J. Crystal Growth* **311**, 2080 (2009).
[7] M. Kneissl *et al*, *J. Appl. Phys.* **101**, 123103 (2007).

18th Int. Symp. "Nanostructures: Physics and Technology"
St Petersburg, Russia, June 21–26, 2010

Two-parametric analysis of operation regimes of a dual-wavelength vertical external cavity surface-emitting laser

Yu. A. Morozov, M. Yu. Morozov and V. V. Popov
Kotelnikov Institute of RadioEngineering and Electronics (Saratov Branch) RAS, 410019, Saratov, Russia

Abstract. The two-parametric analysis of operation regimes of a dual-wavelength vertical external cavity surface-emitting laser is outlined. The areas of continuous wave operation as well as of time-periodic and quasi-periodic operation can be marked out in the map of dynamic regimes. A possible explanation of quite different laser behavior in those area is given.

Introduction

Now, vertical external cavity surface-emitting lasers (VECSELs) surely occupy a specific niche among other lasers [1]. As compared with their rare-earth counterparts, semiconductor VECSELs offer greater opportunities in achievable wavelength and bandwidth of emission. VECSELs lase low-divergence, circular, near-diffraction-limited beams what distinguish them favorably from edge-emitting semiconductor lasers. Besides, VECSELs have a great potential as regarding an intracavity non-linear frequency conversion of high efficiency. Such lasers emitting about 15 W at the second harmonic (488 nm) of fundamental wavelength are already demonstrated [2].

We believe that since the dual-wavelength VECSELs have been made [3,4], a realizable possibility for highly efficient frequency conversion (sum- and difference frequency generation) hopefully appears. These lasers generate two coaxial gaussian beams in the fundamental transverse modes of a high cross section and thus of a high power. Besides, the external cavities of the lasers have enough room for a nonlinear crystal to be placed thus providing an opportunity for an intracavity nonlinear optical interaction of high efficiency. In our opinion, prospects of a dual-wavelength VECSEL's application for a difference frequency generation corresponding to mid- and far infrared bands are very promising. Indeed, despite essential success of quantum-cascade lasers, the problem of making easy-to-use (with no cryogenic refrigeration), relatively simple and inexpensive lasers is still an item of the agenda.

The dual-wavelength VECSELs [3,4] demonstrate both a steady-state and a pulsed operation mode. One mode of operation transforms to another when pump power attains the bifurcation value. The pulsed regime of operation could even be more effective as compared with the continuous wave one provided a temporal overlap of pulses at both wavelengths is high enough. So, the goal of the paper is to study some features of the dual-wavelength VECSEL's pulsed operation, what we believe is of importance for applications to nonlinear frequency conversion in such the lasers.

1. Rate equations of laser dynamics

The rate equations for ordinary (single-wavelength) edge-emitting external cavity semiconductor laser with arbitrary value of feedback parameter $\chi = r_{\text{ext}}(1-r_f^2)/r_f$ have been formulated, e.g., in [5]. (Here r_{ext} and r_f are the reflection factors of an external mirror and an emitting facet of a structure, respectively). If $\chi \ll 1$ the system of rate equations transforms to the well-known Lang–Kobayashi equations [6]. Taking into account the features of the model imposed by vertical arrangement of the cavity and by presence of two sets of non-identical quantum-wells [7], the rate equations for the dual-wavelength VECSEL can be written as follows:

$$\dot{S}_i = v_g \left[\sum_{j=1}^{2} \Gamma_{ij} g_{ij} - \alpha_i + \frac{1}{2L_i} \ln\left(\frac{S_{i\tau}}{S_i}\right) \right] S_i,$$

$$\dot{N}_i = \frac{J_i}{t_w} - \frac{N_i}{\tau_r} - \frac{v_g}{m_i t_w} \sum_{j=1}^{2} \Gamma_{ji} g_{ji} L_j S_j, \qquad (1)$$

here i is the index corresponding to the short- ($i = 1$) and the long-wavelength ($i = 2$) radiation; S_i is the photon density, the quantity with index τ corresponds to the time moment $t - \tau_{\text{ext}}$; Γ_{ij} and g_{ij} are the confinement factor and the gain of the i-th optical field in the j-th equivalent QW; v_g is the light group velocity; L_i is the sub-cavity length; N_i is the carrier density in the i-th equivalent QW; τ_r and τ_{ext} are the carrier lifetime and the round-trip time in the external cavity, respectively; J_i is the pumping carrier flux density to the i-th equivalent QW; t_w is the width of QW; m_i is the number of QWs in the corresponding gain area; α_i is overall loss factor.

When deriving equations (1), a few simplifying assumptions have been adopted. First of all, we assumed that the gain coefficient of the i-th active region with m_i QWs can be lumped to a single equivalent QW. Second, we have taken into account an influence of radiation returning to the active region after just one round-trip in the external cavity (the term $S_{i\tau} = S_i(t - \tau_{\text{ext}})$ in equations (1)). As it was shown in [7], this assumption is valid for $\chi \gg 1$ what is the case for the laser concerned. Third, we neglect the effect of gain saturation and spontaneous emission to the laser modes.

Note, that the active areas appear to be uncoupled if the reciprocal confinement factors $\Gamma_{12} = \Gamma_{21} = 0$, the quantity Γ_{12} playing the main role in their coupling. The effect of Γ_{21} is negligible because of a small value of the gain coefficient g_{21} for the long-wavelength optical field in the shallow equivalent QW. To link the averaged carrier flux density J with pump power P_{in}, we used the approach that had been developed in [8].

2. Map of dynamic regimes of the dual-wavelength VECSEL

The steady-state operation point of the dual-wavelength VECSEL [3] and its stability have been studied in [9]. However, two-parameter analysis of nonlinear systems gives an idea of possible dynamic regimes in more clear and representative form. This method implies a construction of a dynamic regimes

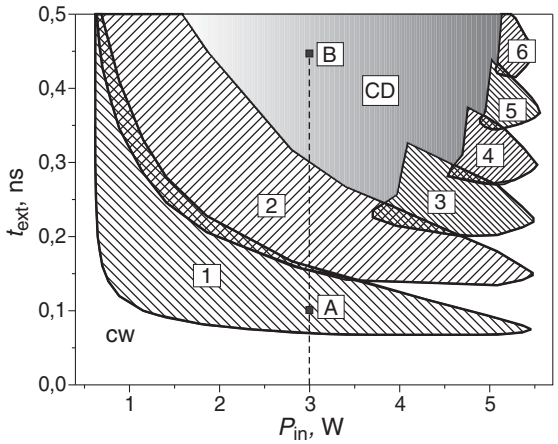

Fig. 1. Map of dynamic regimes for the dual-wavelength VECSEL: CW is the steady-state (continuous wave) operation; (1–6) are the time-periodic regimes with $T \approx \tau_{ext}/n$, where n is the number of the area; CD is the area of complex dynamics.

map, i.e. a diagram in a plane of two parameters, where regions of qualitatively different system's behavior are marked.

As the example of such a map, we present Fig 1 where the dynamic regimes of the dual-wavelength VECSEL are plotted in the plane of (τ_{ext}, P_{in}).

The simulation has been performed with the following parameters: $L_1 = L_2 = 10$ μm, $\Gamma_{11} = \Gamma_{22} = 0.0112$, $\Gamma_{12} = \Gamma_{11}/5$, $\Gamma_{21} = 0$, $\alpha_1 = \alpha_2 = 10$ cm^{-1}, $\tau_r = 2$ ns, $t_w = 7$ nm, $m_1 = m_2 = 8$, $r_{ext}^2 = 0.98$. $In_{0.14}Ga_{0.86}As/GaAs$ and $In_{0.25}Ga_{0.75}As/GaAs$ QWs are assumed to be used in the short-wavelength and the long-wavelength gain areas.

In Fig. 1, the origin of the abscissa corresponds to the value slightly exceeding the threshold pump power $P_{in_{th}}$. The area where the VECSEL operates in the continuous wave dual-wavelength regime is marked as CW. One can see that when pump power is increased, the CW operation mode transforms to a periodic solution provided the value of $\tau_{ext} \geq 0.07$ ns. As it has been shown before [8,9], the violation of the steady-state is due to some absorption of the short-wavelength emission in the deeper QWs. To compute the branches of periodic solutions emanating from a Hopf bifurcation point we have used the freely available DDE-BIFTOOL package [10]. There are six areas in the graph window where the VECSEL demonstrates the periodic solutions of different ratio as regards to the round-trip time τ_{ext}. The wide area labelled by 1 corresponds to periodic oscillations of the dynamic variables running with the time period $T \approx \tau_{ext}$; area 2 corresponds to the solutions with $T \approx \tau_{ext}/2$ and so forth. We believe an explanation of such the partitioning of the map could be as follows. The periodic solution occurs provided the intrinsic laser oscillations (the relaxation oscillations) are captured by harmonics of the intermode beating oscillations. In other words, the periodic regime of oscillations could possibly be treated as sinchronous mode-coupled regime of some kind. In the area marked as CD, complex dynamic exists that we plan to study in follow-up works at greater length. At first glance, the dynamic variables behaves quasi-periodically with the quasi-period $T_{qp} \approx \tau_{ext}$ in this area, the magnitude being modulated by multiple slow (on the time scale of microseconds) periodic functions. Most likely, this regime could be interpreted as non-sinchronous one concerning the relaxation and intermode beating oscillations.

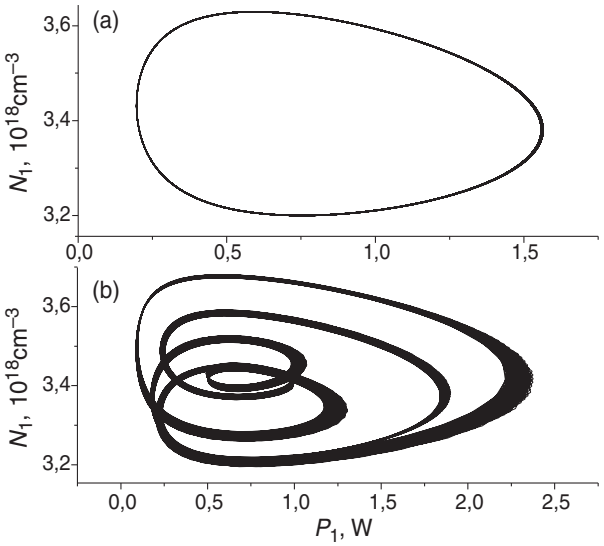

Fig. 2. Phase portraits of the VECSEL dynamics: graphs a,b correspond to points A,B in Fig. 1, respectively.

Fig. 2 displays the phase portraits of laser dynamics in the projection to the plane (N_1, P_1). Here P_1 is the power of the VECSEL's short-wavelength radiation. The graphs are plotted for the trailing part of the pulse realization, namely, at the time interval between 199.95 and 200 microseconds. One can see the attractor's projection in the form of single cycle (a) and multiple quasi-cycle with slowly varying magnitude (b).

It should be noted that the short-wavelength and the long-wavelength pulses of the VECSEL occur nearly simultaneously. This finding is of key importance for efficient intracavity nonlinear optical interaction that could be accompanied by difference frequency radiation.

References

[1] A. C. Tropper, H. D. Foreman, A. Carnache, K. G. Wilcox *et al*, *J. Phys. D* **37**, R75 (2004).

[2] G. Chilla, S. Butterworth, A. Zeitschel, J. Charles *et al*, *2004 Photonics West. Proc. SPIE.* **5332**, 143 (2004).

[3] T. Leinonen, Yu. A. Morozov, A. Härkönen, M. Pessa, *IEEE Phot. Techn. Lett.* **17**, 2508 (2005).

[4] T. Leinonen, S. Ranta, A. Laakso, Yu. Morozov *et al*, *Optics Express* **15**, 13451 (2007).

[5] J.-D. Park, D.-S. Seo, J. McInerney, *IEEE Journ. Quant. Electr.* **26**, 1353 (1990).

[6] R. Lang, K. Kobayashi, *IEEE Journ. Quant. Electr.* **16**, 347 (1980).

[7] Yu. A. Morozov, T. Leinonen, A. Härkönen, M. Pessa, *IEEE Journ. Quant. Electr.* **42**, 1055 (2006).

[8] M. Yu. Morozov, Yu. A. Morozov, V. V. Popov, *Semiconductors* **43**, 382 (2009).

[9] Yu. A. Morozov, M. Yu. Morozov, V. V. Popov, *Proc. of 17th International Symp. Nanostructures: Physics and Technology (Minsk, Belarus, 2009)*, Ioffe Phys.-Tech. Inst., 33, 2009.

[10] K. Engelborghs, T. Luzyanina, G. Samaey, *DDE-BIFTOOL v.2.00 user manual: a Matlab package for bifurcation analysis of delay differential equations. Tehnical Report TW-330*, (Leuven, Belgium), 60, 2001.

18th Int. Symp. "Nanostructures: Physics and Technology"
St Petersburg, Russia, June 21–26, 2010

Properties of non-diffracting (Bessel) beams generated from semiconductor lasers

G. S. Sokolovskii[1], S. N. Losev[1], V. V. Dudelev[1], A. G. Deryagin[1], V. I. Kuchinskii[1], E. U. Rafailov[2] and W. Sibbett[3]

[1] Ioffe Physical-Technical Institute, St Petersburg, Russia
[2] Carnegie Laboratory of Physics, Division of Electronic Engineering and Physics, University of Dundee, UK
[3] School of Physics and Astronomy, University of St Andrews, UK

Abstract. We report on research of non-diffracting beams generated from the broad-area semiconductor lasers. We believe that generation of Bessel beams will make it possible to overcome limitation on the gradient of light intensity and spatial power density for the multimode laser radiation with beam propagation parameter $M^2 \gg 1$. It is shown, that in the case of poor laser beam quality the propagation length of the Bessel beam can be limited by the divergence of the constituting quasi-Gaussian beam rather than the geometrical parameters of the optical scheme (i.e. aperture and the apex angle of the axicon) but still has practical value at power density exceeding achievable with "conventional" focusing.

Introduction

Propagation-invariant (non-diffracting) light beams, which are capable of retaining their intensity during propagation, have been described in 1987 by Durnin [1] (and by Zel'dovich *et al* and by McLeod as early as in 1950–60s [2]) and called Bessel beams because their amplitude profiles are described by a zero-order Bessel function of the first kind as illustrated in Fig. 1. In the projection onto a transverse plane (perpendicular to the propagation direction) such a beam appears as a bright spot surrounded by concentric fringes. The Bessel beams are generated via interference of convergent beams, which takes place when a collimated Gaussian beam passes via a cone-shaped lens (axicon). The central spot diameter of Bessel beam is determined by the axicon angle and can be of the order of a wavelength. In practice, Bessel beams exhibit a finite propagation distance, which depends on the cross-sectional diameter of the initial collimated beam. Another remarkable property of Bessel beams is the ability of the central ray to self-reconstruct its profile disturbed by an obstacle [3]. Non-diffracting beams are extremely important in biomedical research through applications in optical trapping and tweezing, microporation, Doppler velocity measurement and colloid research. Utilization of Bessel beams also opens new horizons in manipulation of micro-machines and micro-fabrication, as well as for frequency doubling and for other non-linear effects.

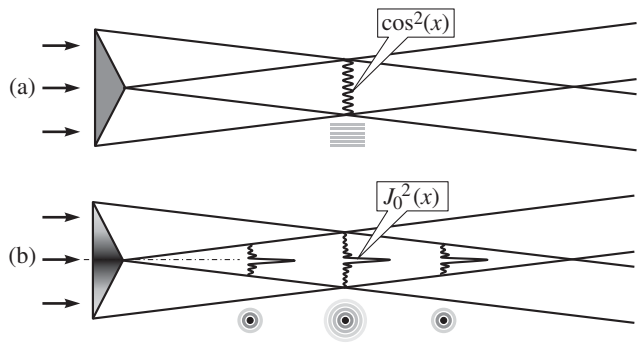

Fig. 1. Comparison of interference of plane wave on a prism (a) and formation of Bessel beam with axicon (b).

1. Generation of Bessel beams from laser diodes

To date, Bessel beams have generally been produced by reconfiguring the output beams from solid-state or gas lasers, but nowadays most of practical applications require the sources to be more compact, efficient and cost-effective. One of the main impediments to developing light sources that produce non-diffracting beams is the coherence of the generated light, but recently it was shown that Bessel beams can be formed from temporally incoherent light sources [4] and that the spatial rather than the temporal coherence of the light source plays the crucial role in formation of Bessel beams. This opens up new avenues for generation of Bessel beams from semiconductor lasers [5] which are by far the most compact, reliable and efficient laser sources. Unfortunately, the direct application of conventional semiconductor lasers for generation of practical Bessel beams is complicated due to either insufficient power level of the narrow-stripe diode lasers or due to low spatial quality of the beam of the broad-area devices.

In our research, it was found that the main difficulties of generation of non-diffracting beams from the broad-area laser diodes can be classified in three main categories: (i) Multimode generation prevents collimation of the laser beam and causes "washout" of the circles of Bessel beam [6] as shown in Fig. 2a. (ii) Astigmatism of the laser diode radiation (as well as filamentation) leads to degradation of the central lobe of Bessel beam (Fig. 2b). (iii) Oblique irradiation of the axicon can cause degradation of the central spot of the beam into diamond-shaped caustic (Fig. 2c) with size proportional to the angle of misalignment and beam propagation distance [7].

Let us consider normal incidence of the quasi-Gaussian beam with propagation (beam quality) parameter $M^2 \gg 1$ on the axicon. In this case, the divergence of the initial collimated beam can not be neglected as in the case of pure "geometrical" beam propagation (Fig. 1b) and the angle of interference of the beam components will increase with distance from the axicon causing increase of the period of the interference pattern and, hence, diameter of the central lobe, as shown in Fig. 3. Taking the "divergence-defined" propagation length z_B as the length of propagation of the Bessel beam to the point of the central lobe diameter increase by a factor of $\sqrt{2}$ and using paraxial approximation to utilize a direct proportion between the diver-

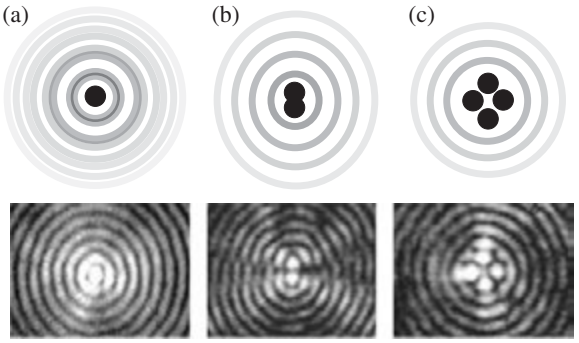

Fig. 2. Experiment and illustration of Bessel beam formed with a) multimode, b) filamented and c) oblique illumination. Radiation wavelength $\lambda = 1.06$ μm. Axicon apex angle 170°. Central lobe size of Bessel beams $d_0 = 10$ μm.

gence angle and interference period, we can derive the formula for z_B in the form:

$$z_B \approx \frac{2\omega_0^2}{M^2\lambda}, \tag{1}$$

where λ is the radiation wavelength and ω_0 is the focal diameter of the initial quasi-Gaussian beam with propagation parameter M^2. One can note strong similarity between this formula and Raleigh range of the initial quasi-Gaussian beam:

$$z_0 \approx \frac{\pi\,\omega_0^2}{M^2\lambda}. \tag{2}$$

It is very important to note that (1) does not substitute the Bessel beam "geometrical" propagation length z_{B0}. These parameters have to be used one at a time, to ensure utilization of the minimal value. Comparing z_B derived here and z_{B0} well known from the first works on Bessel beams [1,2]:

$$z_{B0} = \frac{\pi\,\omega_0\,d_0}{\kappa\lambda} \tag{3}$$

one can see that the "divergence-defined" propagation length of Bessel beam, in contrast to the "geometrical" counterpart, does not depend on the axicon apex angle through the central lobe diameter d_0 and geometrical parameter k. This difference is manifestation of the fact that z_B takes into account non-ideality of the initial beam while z_{B0} is the distance to the geometrical shadow of the ideal plane wave.

2. Gradient of intensity and spatial power density

In slow axis, the typical value of the beam propagation parameter M^2 for the broad-stripe laser diodes is few 10 s, thus making it fundamentally impossible "conventional" focusing of the IR laser beam to a spot of less than $10-20$ μm (Fig. 3a). For the Bessel beam, the central lobe originates from the self-interference of the modes-components, not from the refraction on the spherical surfaces as in the case of "conventional" focusing. Therefore, the size of the central lobe of the Bessel beam generated from the multimode radiation is not limited so dramatically comparing to the quasi-Gaussian counterpart. The ratio of power density in the central lobe of Bessel beam to the maximal quasi-Gaussian power density (i.e. at unity numerical aperture) can be approximated as:

$$BG = \frac{1}{m}\left(\frac{M^2\lambda}{2\,d_0}\right)^2, \tag{4}$$

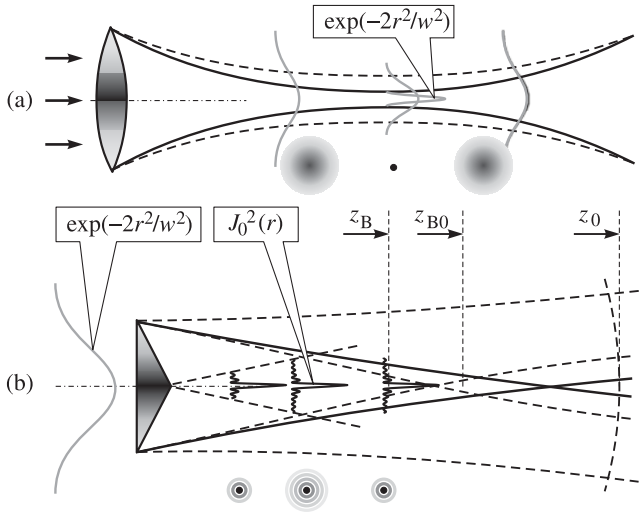

Fig. 3. a) Focusing of Gaussian beam (solid line) and illustration of focusing of quasi-Gaussian beam with $M^2 \gg 1$ (dashed line). b) Propagation of the Bessel beam formed from the diverging Gaussian beam. The drawing illustrates difference between Bessel propagation length limited by the initial beam divergence z_B and the "geometrical" propagation length z_{B0}. Raleigh range is denoted by z_0.

where m is the number of side rings of Bessel beam. From (4) one can see that for $\lambda \approx 1$ μm, feasible central lobe diameter $d_0 = 5$ μm and $M^2 = 50$ the ratio BG is greater than unity when the number of Bessel rings is 25 or below. It worth to note that even 5 rings of Bessel beam with $d_0 = 5$ μm (i.e. 25-fold maximal power density of quasi-Gaussian beam with $M^2 = 50$) correspond to still practical propagation length $z_B \approx 0.4$ mm.

3. Summary

In this paper, we report on research of non-diffracting beams generated from the broad-area semiconductor lasers. We believe that generation of Bessel beams will make it possible to overcome limitation on the gradient of light intensity and spatial power density for the multimode laser radiation with beam propagation parameter $M^2 \gg 1$. It is shown, that in the case of poor laser beam quality the propagation length of the Bessel beam can be limited by the divergence of the constituting quasi-Gaussian beam rather than the geometrical parameters of the optical scheme (i.e. aperture and the apex angle of the axicon) but still has practical value at power density exceeding achievable with "conventional" focusing.

References

[1] J. Durnin, *J. Opt. Soc. Am.* **A4**, 651 (1987).
[2] B. Ya .Zel'dovich and N .F. Pilipetskii, *Izvestia VUZov, Radiophysics*, **9**(1), 95 (1966); J. H. McLeod, *J. Opt. Soc. Am.*, **44**, 592 (1954).
[3] Z. Bouchal *et al*, *Opt. Commun.* 151, 207 (1998).
[4] P. Fischer *et al*, *Opt. Express* **13** (17), 6657 (2005).
[5] G. S. Sokolovskii *et al*, *Tech. Phys. Lett.* **34** (12), 1075 (2008).
[6] G. S. Sokolovskii *et al*, *Tech. Phys. Lett.* **36** (1), 9 (2010).
[7] Zh. Bin and Li Zhu, *Appl. Opt.* **37** (13), 2563 (1998).

18th Int. Symp. "Nanostructures: Physics and Technology"
St Petersburg, Russia, June 21–26, 2010

Mid-infrared difference frequency generation by intracavity mixing in optically pumped semiconductor lasers

D. E. Svjatoshenko

Lobachevsky State University of Nizhni Novgorod, Nizhni Novgorod, Russia
Institute for Physics of Microstructures RAS, Nizhni Novgorod, Russia

Abstract. A scheme of the phase-matched difference harmonic generation (DHG) in optically pumped semiconductor lasers is presented to derive a tuneable mid-infrared (mid-IR) radiation. For optically pumped vertical cavity surface emitting lasers in the well-developed near-infrared (near-IR) range (wavelength from 0.94 to 1.3 μm) and high-power pump laser diods (wavelength 0.808 μm) the difference harmonic about 1 mW can be obtained in wavelength range from 3 to 6 μm at room temperature.

Introduction

Achieving room-temperature, continuous-wave operation in the mid-IR range still remains one of the intensively developing spheres of interest in expanding the spectral range of semiconductor lasers [1,2]. Although significant progress has been made towards realizing the technological potential of quantum cascade lasers, high costs of their fabrication and difficulties in achiving room-temperature operation still stimulate a search for alternatives.

Frequency down-conversion in nonlinear semiconductor structures is suggested to be another possible way in producing the mid-IR radiation [3,4]. A method for the DHG in stripe geometry lasers is proposed by combining the counterpropagating phase matching scheme [2] with suggested idea of the optically pumped semiconductor lasers where pumping and laser waves result in a difference harmonic wave. This approach allows to adjust longitudinal phase matching condition with pump incidence angle setting. Phase matching condition in the epitaxial direction is not significant because of the high absorptance of the pumping wave. As it follows from the energy and momentum conservation, radiation in the range only shorter than 3 μm may be obtained theoretically. This restriction is due to the high mismatch in refractive indexes on air-semiconductor interface. Also, it is difficult to implement waveguiding propogation for both the near-IR and mid-IR radiation in the stripe geometry lasers.

A way to obtain radiation in the wavelength range above 3 μm discussing here can be realized in optically pumped vertical cavity surface emiting lasers (see Fig. 1) with both external (VECSEL) and coated dielectric (VCSEL) mirror designs. The laser and difference harmonic waves are propagated in transverse directions (transversal cavity for laser beam is longitudinal waveguide for difference harmonic) and longitudinal phase matching condition is also easily satisfied with pumping angle adjusting. In addition, the vertical cavity designs allow laser output power rising, by increasing the laser mode area at higher pump powers [5], which also result in increased nonlinear interacting length and higher magnitude of difference harmonic power.

1. Design consideration

The following principles must be taken into account during designing heterostructures for frequency down-conversion under the optical pumping: (1) it is necessary to optimize lasing power by maximazing an optical pumping efficiency (transversal cavity material would absorpt major of the pumping wave along absorpting length L_{abs} shown on Fig. 1) and choosing appropriate number of QW or QD layers and its favorable placing in cavity's nodes; (2) it is essential to optimaze nonlinear ovelaping to obtain a good conversion efficiency. To exploit non-zero second order nonlinearity in GaAs, polarizations of the pumping and difference harmonic beams must be TE-TM (or TM-TE) respectively. As it shown on Fig. 1 the laser beam is in-plane polarized.

In the present work, three alternative vertical cavity designs are considered. Common parameters for all of this schemes are pumping wavelength $\lambda_{\text{P}} = 0.808$ μm (available with a high-power semiconductor laser) and laser wavelength $\lambda_{\text{L}} = 1.064$ μm which can be obtained for a QW-based active layer grown on (100) GaAs substrate. Difference harmonic wavelength $\lambda_{\text{d}} = 3.36$ μm and phase matching pumping angle $\theta_{\text{air}} \approx 50^\circ$ results from the pumping and the laser wavelengths.

The first scheme is a VECSEL with a AlO/GaAs bottom distributed Bragg reflector (DBR) and a top external mirror with amplitude reflectance 98%. Due to refractive index contrast provided by AlO and GaAs materials, high (more than 99.9%) and stable to layer width fluctuation reflectance of the bottom mirror can be derived with only four AlO/GaAs pairs. Moreover, the scheme improves overlaping of the interacting waves due to a symmetric difference harmonic mode profile. The second design is a VECSEL with a AlAs/GaAs DBR bottom and the same external mirror as in the previouse case. The 19 pairs

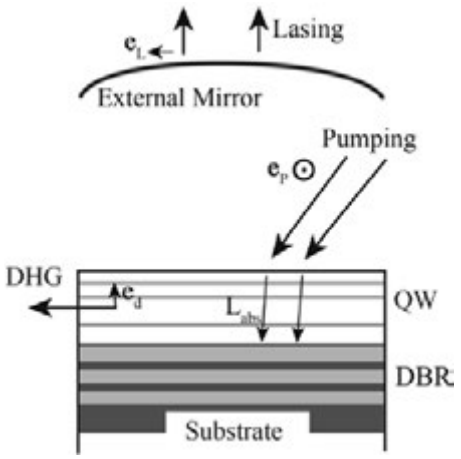

Fig. 1. The principle scheme of the DHG in the optically pumped VECSEL design. $\mathbf{e}_{\text{P}}$, $\mathbf{e}_{\text{d}}$ and $\mathbf{e}_{\text{L}}$ is the electric field polarizations of the pump, difference harmonic and laser waves involved in nonlinear interaction.

AlAs/GaAs bottom DBR yields the reflectance 99.54% which is in a accordance with a technologically availabel reflection coefficient evaluated for the similar DBR in VCSEL [6]. The last scheme of the VCSEL design with the same AlAs/GaAs bottom DBR and a ZrO_2/SiO_2 top dielectric mirror (reflectance is 98.78%) allows to apply an antireflection (AR) coating for pumping at the phase matching angle without laser treshold raising. However, high mismatch in refractive indexes of the top and the bottom "cladding" layers for the difference harmonic in the both last cases yields to wider waveguides and reduction of the overlap integral.

2. Result and discussion

To optimaze QW's number and the absorpting length for laser threshold reducing and increasing a slope efficiency resulting in maximum output power, effective pump intensity is taken into account as follow:

$$I_{\text{eff}} = I(1-R)\left[1-\exp\left(-\alpha_{\text{P}} L_{\text{abs}}\right)\right],$$

where I is the initial pump intensities; R is the pump reflectance on the air-semiconductor interface; α_{P} is the pump absorptance by the cavity material.

The threshold effective intensities and the laser output power ranges are given in the Table for 3-QW active layer under 9 kW/cm^2 initial optical pumping in 200 μm spot for the certain reasonable absorpting length. Major magnitude of the laser power in the VCSEL design is provided by the AR coating which assumes to have reflectance about 1%.

In order to illustrate the second criterion in designing, the difference harmonic power was estimated from the wave equation by the slowly varying amplitude method [7]:

$$P_{\text{d}} = \frac{2\pi^3 c n_{\text{d}}^2}{\lambda_{\text{d}}^2 n_{\text{d}}^{\text{eff}\ 3}} L_x L_z^2 \frac{\left|\int\limits_y \chi^{\text{GaAs}} E_{\text{L}}^* E_{\text{P}} E_{\text{d}}^0 dy\right|^2}{\int\limits_y \left|E_{\text{d}}^0\right|^2 dy}, \qquad (1)$$

where P_{d} is the difference harmonic power; c is the light velocity; χ^{GaAs} is the GaAs second order nonlinearity ($\chi^{\text{GaAs}} = 5\times10^{-7}$ CGSE^{-1} is typical); x, z are in-plane and y is epitaxial layer directions; E_{L}, E_{P} and E_{d}^0 are the laser, pumping and difference harmonic wave's y-profile respectively. The phase matching condition is suggested to be satisfied.

Since laser's mode profiles are similar in all cases, the laser power itself and the overlap of the pumping and difference harmonic waves simultaneously are the most significant in Eq. (1) for maximazing the difference harmonic power generated. The shorter the absorpting length the better the pumping and the diference harmonic waves interaction. However, the laser output power is diminished with shorter absorpting lengths. Fig. 2 reports the difference harmonic power for the zero difference harmonic mode being excited as a function of the absorpting length calculated using Eq. (1). For the proper difference harmonic power estimation it is considered that only a part of the pumping linewidth is involved in the nonlinear interaction with the resulting difference harmonic. Moreover, the reduction of the output harmonic power by about of factor of 3 [5] can be due to the effective laser linewidth.

Table 1.

Scheme	$I_{\text{eff}}^{\text{th}}$, kW/cm^2	P_{out}, W
AlO/GaAs VECSEL	0.90	0.50–0.70
AlAs/GaAs VECSEL	1.05	0.45–0.65
AlAs/GaAs VCSEL	1.00	1.00–1.40

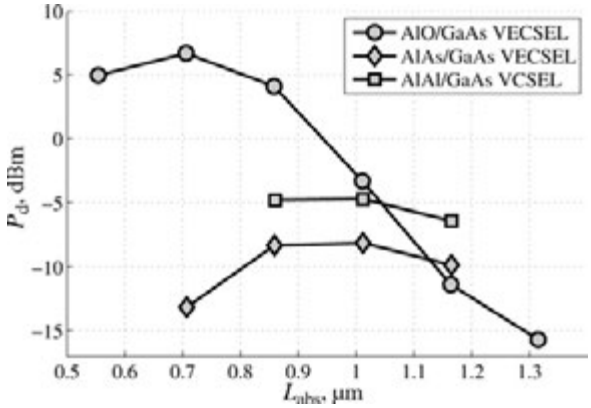

Fig. 2. Plot of the difference harmonic power as a function of the laser cavity length.

As it appears from Fig. 2, the difference harmonic output is considerable large for the AlO/GaAs VECSEL design. However the both AlAs/GaAs VECSEL and VCSEL designs with the noticeable difference harmonic power value are more easier fabricated because of the absence of problems with the oxidation processes for the large apertures.

The primary advantage offered by the approach considered is that the tunable (in the range of about 100 nm) radiation in the mid IR range is capable to be obtained (with 4 nm temperature's shifting of the pumping wavelength). Moreover, the usage of the optical pumping scheme results in an ability to grow dopant-free heterostructure's layers yielding to low free carrier absorption in the mid-IR range while absorption on carriers generated was estimated to be low to appreciably decrease the difference harmonic power.

Acknowledgements

I am indebted to my scientific adviser A. A. Andronov and A. V. Marugin for their fruitful discussions and assistanse. This work was supported by the Council on President's Grant of the Russian Federation for Leading scientific school (project No. NSh-2786.2008.2)

References

[1] A. Krier (ed.), *Mid-infrared Semiconductor Optoelectronics*, London: Springer, 2006.
[2] M. Ebrahim-Zadeh and I. T. Sorokina (eds.), *Mid-infrared Coherent Sources and Application*, Dordrecht: Springer, 2008.
[3] B. N. Zvonkov *et al*, *Appl. Phys. Lett.* **92**, 021122 (2008).
[4] E. Guillotel *et al*, *Appl. Phys. Lett.* **94**, 171110 (2009).
[5] M. Jacquemet *et al*, *Appl. Phys. B* **86**, 503–510 (2007).
[6] S. A. Blokhin *et al*, *Semiconductors*, **40**, 615–619 (2006).
[7] N. Bloembergen, *Nonlinear optics*, New York: Behjamin, 1965 (Russ. transl., Moscow: Mir, 424 p., 1966).

18th Int. Symp. "Nanostructures: Physics and Technology"
St Petersburg, Russia, June 21–26, 2010

Concentration and temperature of hot carriers in quantum wells under electrical and optical excitation

L. E. Vorobjev[1], *M. Ya. Vinnichenko*[1], D. A. Firsov[1], V. L. Zerova[1], V. Yu. Panevin[1], A. N. Sofronov[1], P. Thumrongsilapa[1], V. M. Ustinov[2], A. E. Zhukov[3], A. P. Vasil'ev[3], L. Shterengas[4], G. Kipshidze[4], T. Hosoda[4] and G. Belenky[4]

[1] St Petersburg State Polytechnical University, 195251 St Petersburg, Russia
[2] Ioffe Physical-Technical Institute, St Petersburg, Russia
[3] St Petersburg Academic University, St Petersburg, Russia
[4] State University of New York at Stony Brook, New York 11794, USA

Abstract. Carrier heating in doped GaAs/AlGaAs quantum wells is determined from the analysis of the spontaneous photoluminescence spectra at high excitation level. Experimental data are compared with the results of calculations. The lack of the concentration saturation in stimulated emission regime at pumping current exceeding threshold one is found in InGaAsSb/InAlGaAsSb quantum wells. The origin of this phenomenon is discussed.

Introduction

High level of the optical or electric excitation in the barrier region results in heating the carriers in quantum wells. This phenomenon can change significantly luminescence spectra and characteristics of semiconductor lasers. In the present paper we report the results of the investigations of these processes in nanostructures with GaAs/AlGaAs and InGaAsSb/InAlGaAsSb quantum wells.

1. Spontaneous luminescence spectra

Spectra of spontaneous luminescence under different levels of optical excitation were measured in nanostructure consisted of 100 pairs of double n-doped GaAs/$Al_{0.38}Ga_{0.62}As$ quantum wells ($n_s = 6 \times 10^{11}$ cm^{-2}). Design of the structure and electron energy levels are shown in Fig. 1. The depths of the wells for electrons and holes are 276 and 208 meV, respectively.

The main contribution to photoluminescence at low lattice temperature and relatively low pumping level is given by $e1 \to hh1$ electron transitions. This allows to determine the electron temperature T_e analyzing the shortwavelength decay of photoluminescence spectrum. This method of determination of T_e was used before (see, for example, [1]). The increase of carrier temperature results from the energy transferred from the injected carriers. Electrons and holes injected in barrier can transfer the energy approximately equal to the depth of quantum well either to the lattice with emission of optical phonons or to other electrons and holes located on the lowest levels of size quantization. The latter process dominates at high electron concentrations $n_s > 10^{11}$ cm^{-2} causing heating the carriers.

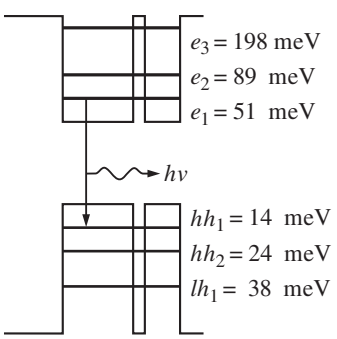

Fig. 1. Structure design and calculated carrier energy levels.

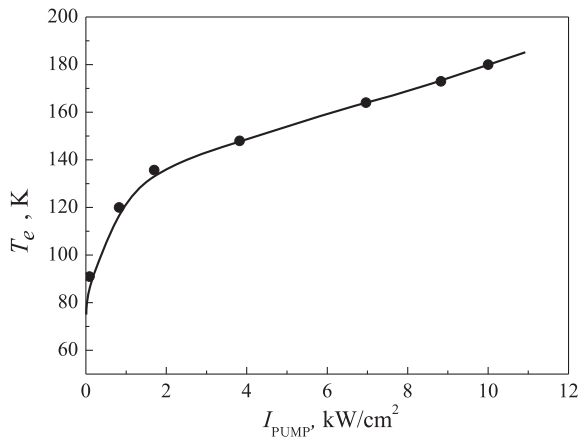

Fig. 2. Temperature of hot carriers in quantum well as a function of optical pumping level at $T = 77$ K.

Dependence of electron temperature on the pumping level J_{pump} determined from the photoluminescence spectra is shown in Fig. 2. Nonlinear character of this dependence is related to the different energy accumulation rate calculated per one electron for weak pumping level (concentration of nonequilibrium electrons and holes $\Delta n_s \ll n_s$) and at high levels of excitation ($\Delta n_s \gg n_s$). Results of the calculation of the dependence $T_e(J_{pump})$ from the rate equation for carrier concentration and energy balance equation taking into account accumulation of nonequilibrium optical phonons are in good agreement with experimental data.

The present results demonstrate the peculiarities of carrier heating in doped and undoped structures. The former case corresponds to low excitation level and the condition $\Delta n_s \ll n_s$ and latter one corresponds to $\Delta n_s \gg n_s$.

2. Spontaneous luminescence from laser structures in the regime of stimulated emission

We studied spectra of spontaneous electroluminescence from laser structures with InGaAsSb/InAlGaAsSb quantum wells under conditions of stimulated emission for different pumping current. In this case, the integral intensity of spontaneous electroluminescence gives the information about carrier concentra-

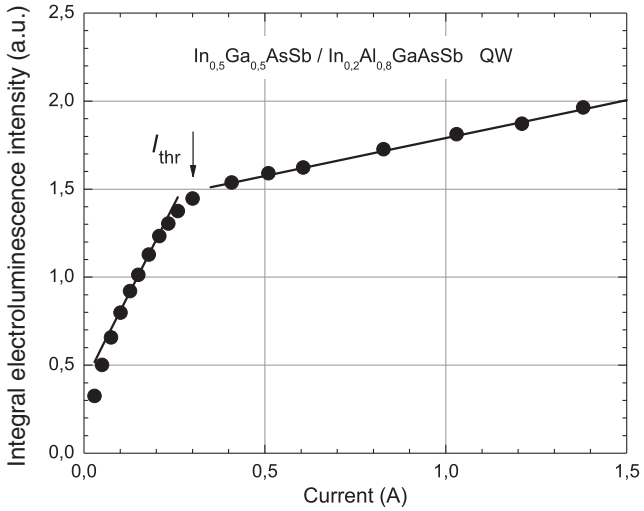

Fig. 3. Integrated spontaneous electroluminescence intensity from QW as a function of pumping current in the regime of stimulated emission at $T = 300$ K.

tion as a function of injecting current. Spontaneous emission was observed perpendicularly to the plane of the structure from the narrow 10 μm slot in the top layer. This window in the top contact was obtained by lift-off technology. Whole width of the laser strip was 100 μm. Integral intensity of electroluminescence was evaluated as a result of integrating electroluminescence spectrum. This technique allowed to exclude the contribution of scattered stimulated radiation to measured electroluminescence. The dependence of integral intensity of electroluminescence on the pumping current is shown in Fig. 3.

As it follows from the Fig. 3, electron concentration is not stabilized after starting the generation at $I > I_{\text{th}}$ but continues to grow with current. Analysis shows that the main reason of the increase of carrier concentration with current is carrier heating under e-h pair injection. We consider, the optical gain does not change, because increase of electron temperature is compensated by increase of carrier concentration. We can evaluate from Fig. 3, that electron temperature at current 1.5 A is 350 K. We can determine the electron temperature from power

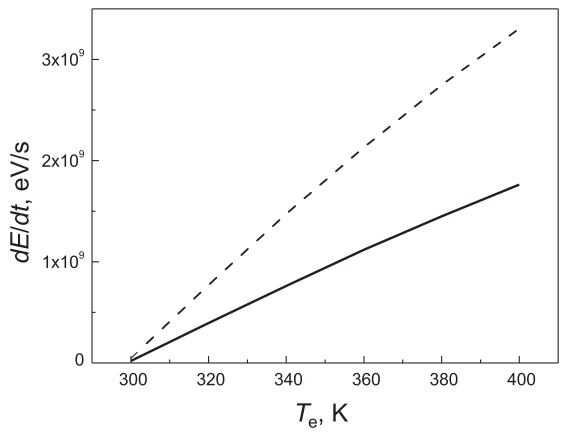

Fig. 4. Total energy-loss rate of electron and hole upon their interaction with polar optical phonons in QW at $T = 300$ K. Solid line represents the result for case of accumulation of phonons (lifetime of PO-phonons is $\tau_{\text{PO}} = 2$ ps), the dash line is for the case of $\tau_{\text{PO}} = 0$ (there is no accumulation phonons). The electron surface concentration ($n_s = 2 \times 10^{12}$ cm^{-2}).

balance equation taking into account accumulation of nonequilibrium polar optical phonons. The energy-loss rate of carriers is presented at Fig. 4. The calculated value of electron temperature is 400 K for the case of accumulation of phonons with $\tau_{\text{PO}} = 2$ ps and 350 K for the case, when accumulation is absent. We can assume from comparison with experimental data ($T_e = 350$ T), that lifetime of PO phonons is much less, than 2 ps due to phonon scattering on interface or/and there is additional process of energy scattering, for example with participation of interface phonons.

Acknowledgements

This work was supported with the grants of Russian Foundation of Basic Researches and Russian Ministry of Education and Science.

References

[1] "Spectroscopy of nonequilibrium electrons and phonons", volume editors C. V. Shank and B. P. Zakharchenya, 1992 North Holland; Amsterdam, London, N-Y, Tokyo, chapter 2 "Ultrafast Luminescence Spectroscopy of Semiconductors: Carrier Relaxation, Transport and Tunneling", J. Shah.

18th Int. Symp. "Nanostructures: Physics and Technology"
St Petersburg, Russia, June 21–26, 2010

States with zero differential resistance in high mobility quantum Hall systems driven by dc electric fields

M. A. Zudov[1], A. T. Hatke[1], H. -S. Chiang[1], L. N. Pfeiffer[2] and K. W. West[2]

[1] School of Physics and Astronomy, University of Minnesota, Minneapolis, Minnesota 55455, USA
[2] Princeton University, Department of Electrical Engineering, Princeton, NJ 08544, USA

Abstract. When a high-mobility two-dimensional electron system is subject to weak electric and magnetic fields, its current-voltage characteristics exhibit a plateau signaling a state characterized by zero differential resistance. This state emerges over a *continuous* range of magnetic fields extending well below the onset of the Shubnikov–de Haas oscillations. We find that the minimum current required to support this state is largely *independent* on the magnetic field, while the maximum current increases with the magnetic field and appears to correlate with the onset of inter-Landau level scattering.

Introduction

Over the past decade it was realized that high mobility two-dimensional electron systems (2DES) exhibit an array of fascinating phenomena occurring in very high Landau levels when the Shubnikov–de Haas oscillations are not yet resolved. Among these are several classes of magneto-oscillations such as microwave [1], phonon [2], and Hall field [3] induced resistance oscillations. Remarkably, the minima of microwave-induced oscillations can evolve into states with zero resistance [4, 5], which are currently understood in terms of the absolute negative resistance and its instability with respect to formation of current domains [6, 7, 8]. Unfortunately, experimental confirmation of predicted domain structure has proven difficult in microwave-irradiated samples and awaits future studies. It is therefore of great interest to see if other classes of magneto-oscillations might give rise to phenomenologically similar states.

Here we report on a state characterized by a *zero differential resistance* (a plateau in a current-voltage characteristic) which does not rely on microwave radiation. This state emerges from a minimum of Hall field-induced resistance oscillations (HIRO) in a high mobility 2DES subject to weak magnetic field and low temperatures. The focus of the present study is on some of the generic characteristics of this state such as the range of electric and magnetic fields within which it is supported.

Experimental details

Our experiment was performed on a Hall bar (width $w = 100\ \mu$m) etched from a symmetrically doped GaAs/AlGaAs quantum well. After a brief low-temperature illumination with visible light, density and mobility were $n_e \simeq 3.8\times10^{11}\,\mathrm{cm}^{-2}$ and $\mu \simeq 1.0\times10^{7}\,\mathrm{cm}^2/\mathrm{Vs}$, respectively. The sample was immersed in a ^{3}He coolant with $T \simeq 1.5$ K. Differential resistivity, $r_{xx} \equiv \mathrm{d}V_{xx}/\mathrm{d}I$, was measured using a quasi-dc (a few hertz) lock-in technique.

Results and discussion

Before presenting the experimental data, we briefly discuss the basic physical picture behind HIRO. According to the "displacement" model [9], HIRO originate from the impurity-mediated transitions between Landau levels tilted by Hall field $\mathcal{E}_{\mathrm{dc}}$. In this scenario, a dominant process involves an electron which is *backscattered* off an impurity. The guiding center of such an electron is displaced by a distance equal to the cyclotron diameter $2R_c$. When the cyclotron diameter matches an integral multiple of the real-space Landau level separation, the probability of such events is enhanced. This enhancement manifests as a maximum in the differential resistivity occurring whenever $\epsilon_{\mathrm{dc}} \equiv e\mathcal{E}_{\mathrm{dc}}(2R_c)/\hbar\omega_c$ is equal to an integer.

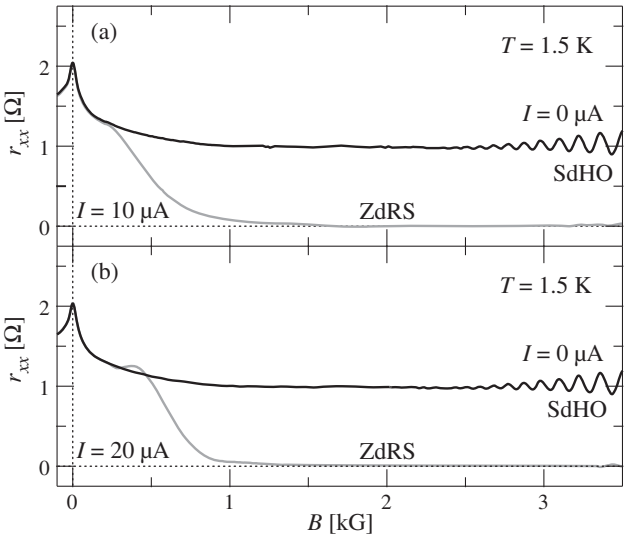

Fig. 1. Differential magnetoresistivity $r_{xx}(B)$ measured at $I = 10\ \mu$A [20 μA] and $T \simeq 1.5$ K. Magnetoresistivity $\rho_{xx}(B)$ at $I = 0$ is shown for comparison.

In Fig. 1(a) and (b) we present the longitudinal differential magnetoresistivity $r_{xx}(B)$ acquired under applied dc currents of 10 μA and 20 μA, respectively. For comparison, each panel also includes the linear response ($I = 0$) longitudinal magnetoresistivity $\rho_{xx}(B)$, which exhibits *only* the Shubnikov–de Haas oscillations (SdHO) starting to develop at $B \gtrsim 2.5$ kG. In contrast, the data obtained under finite dc currents show several distinct characteristics signaling strong non-linearities. First, the differential resistivities both at 10 and 20 μA reveal a HIRO peak at $B \simeq 0.2$ and $B \simeq 0.4$ kG, respectively [cf., ↓]. This peak occurs at $\epsilon_{\mathrm{dc}} \simeq 1$ and originates from the enhanced scattering due to electron transitions between neighboring Hall field-tiled Landau levels. However, the most remarkable characteristic of the data is a dramatic drop of the r_{xx} at higher B which extends *all the way to zero* at $B \gtrsim 1$ kG. This drop marks a transition to a zero-differential resistance state (ZdRS).

It is clear that the ZdRS presented in Fig. 1 is qualitatively different from that observed in microwave-irradiated 2DES [10] or in the regime of high magnetic fields where the linear response resistivity is dominated by the SdHO [11].

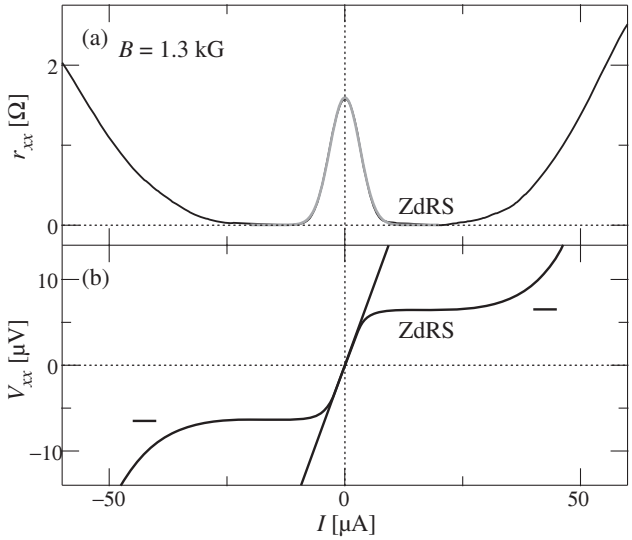

Fig. 2. (a) Differential magnetoresistivity $r_{xx}(I)$ and (b) voltage V_{xx} at $B = 1.3$ kG and $T \simeq 1.5$ K. Straight line represents Ohm's law which holds at small I.

First, the ZdRS shown in Fig. 1 extends over a *continuous* range of magnetic fields. This is in contrast to Ref. [11] where the ZdRS were formed at *discrete* values of the magnetic field corresponding to the SdHO maxima. Second, the ZdRS reported here clearly does not rely on the existence of the SdHO at all; similar to microwave-induced zero-resistance states, it persists to magnetic fields *much lower* than the onset of the SdHO. Finally, our data reveal neither negative spikes in differential resistance preceding ZdRS formation nor temporal fluctuations reported in Ref. [11].

To get further insight on the ZdRS we examine the characteristic currents at which it is formed. This is most conveniently achieved by using an alternative measurement technique in which a magnetic field B is held constant and a current I is varied. An example of such a measurement performed at $B = 1.3$ kG is presented in Fig. 2(a) showing differential resistivity r_{xx} as a function of applied current I. The data show a dramatic drop in the r_{xx} with increasing I which leads to a state with zero differential resistance (cf., "ZdRS"). Once formed, the ZdRS persists over a finite, continuous range of currents up to some critical current above which the differential resistivity starts to increase. This increase eventually terminates at the fundamental HIRO maximum.

Formation of the ZdRS can also be illustrated by a current-voltage characteristic which we present in Fig. 2 (b). Concurrent with the drop in the r_{xx}, the longitudinal voltage V_{xx} departs from the Ohm's law (cf., straight line) and saturates to *a plateau* extending over a finite current range. Inside this range, the voltage is independent of the applied dc current. To describe this range quantitatively, we introduce two critical currents, $I_{\rm min}$ and $I_{\rm max}$ between which the ZdRS is supported. The lower current $I_{\rm min}$ can be estimated by fitting the zero-bias peak, e.g. with a Gaussian, $r_{xx}(I) = r_{xx}(0)\exp(-I^2/\Delta_0^2)$, where $r_{xx}(0)$ is the linear response resistivity, and setting $I_{\rm min} = \Delta_0$. An example of such a fit over the current range from -20 to $+20$ μA is shown in Fig. 2 (a) by a dark line. The fit describes the experimental data remarkably well yielding $I_{\rm min} \simeq 4.5$ μA.

We have also examined the evolution of the ZdRS with the magnetic field up to 2.5 kG (not shown) and observed that the minimum current, $I_{\rm min}$, has a very weak dependence on the magnetic field. At the same time, we have found that the higher critical current $I_{\rm max}$ increases roughly linearly with B and appears to correlate with the position of the fundamental HIRO peak which occurs at $I = I_1$. One can obtain a measure of the $I_{\rm max}$ by fitting the differential resistivity with $r_{xx}(I) = r_{xx}(I_1)\exp[-(I - I_1)^2/\Delta_1^2]$. The higher critical current can then be estimated as $I_{\rm max} = I_1 - \Delta_1$. Similar to the width of the zero-bias peak Δ_0, we find that Δ_1 is roughly B-independent but is noticeably larger, about 20 μA.

Summary

In summary, we reported on a state with a zero differential resistance in a high mobility 2DES subject to low temperatures. Appearing in very high Landau levels, this unusual state exists over a *continuous* magnetic field range extending well below the onset of the Shubnikov–de Haas oscillations. The minimum current required to support this state is largely *independent* on the magnetic field and thus has no relation to the conventional parameter $\epsilon_{\rm dc}$ describing HIRO. On the other hand, the current describing the upper boundary relates to the current corresponding to the fundamental HIRO peak reduced by a roughly constant value. A state with zero-differential resistance is similar to a microwave-induced zero-resistance state in a sense that it can also be explained by the domain model [11] and, as such, offer exciting new research directions. For example, it provides an alternative playground to experimentally explore theoretically predicted instabilities leading to current domain formation. Finally, future temperature dependent studies of the phenomenon should provide further insight on the role of electron-electron interactions [12,13,14] and to distinguish between competing microscopic mechanisms [9] responsible for the strong nonlinearity leading to the ZdRS formation.

Acknowledgement

We thank I. A. Dmitriev and B. I. Shklovskii for useful discussions and remarks. This work was supported by the NSF DMR-0548014.

References

[1] Zudov *et al*, *Phys. Rev. B* **64**, 201311(R) (2001).
[2] Zudov *et al*, *Phys. Rev. Lett.* **86**, 3614 (2001).
[3] Yang *et al*, *Phys. Rev. Lett.* **89**, 076801 (2002).
[4] Mani *et al*, *Nature* **420**, 646 (2002).
[5] Zudov *et al*, *Phys. Rev. Lett.* **90**, 046807 (2003).
[6] Andreev *et al*, *Phys. Rev. Lett.* **91** 056803 (2003).
[7] Auerbach *et al*, *Phys. Rev. Lett.* **94** 196801 (2005).
[8] Finkler and Halperin, *Phys. Rev. B* **79**, 085315 (2009).
[9] Vavilov *et al*, *Phys. Rev. B* **76** 115331 (2007).
[10] Zhang *et al*, *Phys. Rev. Lett.* **98**, 106804 (2007).
[11] Bykov *et al*, *Phys. Rev. Lett.* **99**, 116801 (2007).
[12] Hatke *et al*, *Phys. Rev. Lett.* **102**, 066804 (2009).
[13] Hatke *et al*, *Phys. Rev. Lett.* **102**, 086808 (2009).
[14] Hatke *et al*, *Phys. Rev. B* **79**, 161308(R) (2009).

18th Int. Symp. "Nanostructures: Physics and Technology"
St Petersburg, Russia, June 21–26, 2010

Quantal heating of 2D electrons in strong magnetic fields

S. A. Vitkalov[1] and A. A. Bykov[2]

[1] The City College of New York, New York, NY 10031, USA
[2] Institute of Semiconductor Physics, Novosibirsk, Russia

Abstract. Usually heating of conducting electrons by dc electric field results in an increase of electron temperature. In this paper we show that the dc heating of 2D electrons, placed in quantized magnetic fields, results in a peculiar electron distribution, which has the same broadening or an effective "temperature" as the unbiased electron system. The quantal heating, however, violates strongly the Ohm's Law. In the conducting system with discrete electron spectrum the quantal heating results in a spectacular decrease of electron resistance and a transition of the electrons into a state with zero differential resistance (ZDR). Finally the heating leads to an apparent dc driven metal-insulator transition, which correlates with the transition into the ZDR state. The correlation is very unexpected and are not understood.

Introduction

The nonlinear properties of low-dimensional electron systems attract a great deal of attention for its fundamental significance as well as for potential applications in microelectronics. In this paper we report that a weak dc electric field applied to highly mobile 2D electrons, placed in quantized magnetic fields, produce spectacular, several fold decrease of the resistance. We have identified that the dominant mechanism of the dc nonlinearity is related to a peculiar, quantal heating. The heating occurs in conducting systems with discrete or quantized spectrum. It produces an exceptionally strong overheating inside the levels [1,2].

1. Experimental setup

Our samples are high-mobility GaAs quantum wells grown by molecular beam epitaxy on semi-insulating (001) GaAs substrates. The width of the GaAs quantum well is 13 nm. Two AlAs/GaAs type-II superlattices grown on both sides of the well served as barriers, providing a high mobility of 2D electrons inside the well at a high electron density. Two samples (N1 and N2) were studied with electron density $n_1 = 12.2 \times 10^{15}$ m^{-2}, $n_2 = 8.2 \times 10^{15}$ m^{-2} and mobility $\mu_1 = 93$ m^2/V s, $\mu_2 = 85$ m^2/V s at $T = 2.7$ K.

Experiments are done in a classically strong magnetic fields ($\omega_c \tau_{tr} \gg 1$), where the ω_c is cyclotron frequency and τ_{tr} is the transport scattering time. At this condition the electric current density $\vec{J} = (J_x, 0)$ directed along the x-axis is almost perpendicular to the total electric field $\vec{E} = (E_x, E_y)$, where $E_x \ll E_y$.

The differential resistance $r_{xx} = V_{ac}/I_{ac}$ is measured at a frequency of 77 Hz in the linear regime, using four probes method. In the experiment a dependence of differential resistance $r_{xx} = dV_{xx}/dI$ on the dc bias I_{dc} is recorded [1].

2. Results and discussion

Fig. 1 demonstrates dependencies of the longitudinal resistance of two dimensional electrons on the magnetic field in sample N2. Two upper curves present dependencies obtained at different temperatures $T = 2.16$ K (dotted curve) and $T = 4.2$ K (solid curve) at zero dc bias. At $B > 0.1$ T the electron spectrum is quantized and at temperature $T = 0.3$ K quantum oscillations of the longitudinal resistance are observed (not shown). An arrow marks the magnetic field $B = 0.1$ T.

At magnetic fields $B < 0.3$ T the two traces at $T = 2.16$ K and at $T = 4.2$ K are almost identical, indicating a very weak temperature dependence of the resistance ($dr_{xx}/dT > 0$). At stronger magnetic fields the quantum oscillations (Shubnikov–de Haas, SdH) are observed. At small magnetic fields $\hbar\omega_c \ll kT$ the amplitude of the SdH oscillations is small due to an effective averaging of the conductivity oscillations $\sigma(\epsilon)$ over the temperature interval kT. Fig. 1 shows that the increase of the temperature reduces the magnitude of the oscillations symmetrically in good agreement with existing theory.

In the presence of a dc bias the resistance demonstrates significantly different behavior. In Fig. 1 the lower curve shows a typical dependence of the differential resistance on magnetic field at $I_{dc} = 6$ μA. At $B > 0.1$ T the resistance shows a considerable decrease with the dc bias ($dr_{xx}/dI < 0$). The decrease of the resistance cannot be explained by a temperature increase due to the dc heating. The temperature increase raises the resistance ($dr_{xx}/dT > 0$). Moreover the quantum oscillations at the finite dc bias do not have the canonical shape, corresponding to the two upper curves at zero dc bias. Instead a strong increase of higher harmonics of the oscillations is obvious. The enhancement of the higher harmonic content is in apparent contradiction with the description of the dc biased electrons by an elevated temperature T_e: high temperature reduces exponentially the higher harmonic content of quantum

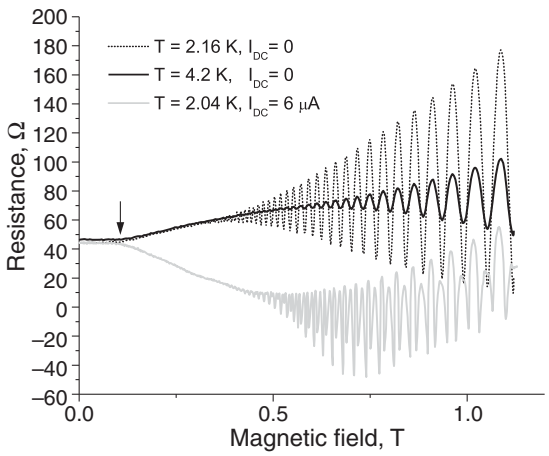

Fig. 1. Dependencies of resistance r_{xx} on magnetic field at different temperatures with no dc bias (black solid and dotted lines) and with applied dc bias $I_{dc} = 6$ μA at $T = 2.04$ K. Arrow marks magnetic field $B = 0.1$ T above which the electron spectrum is quantized.

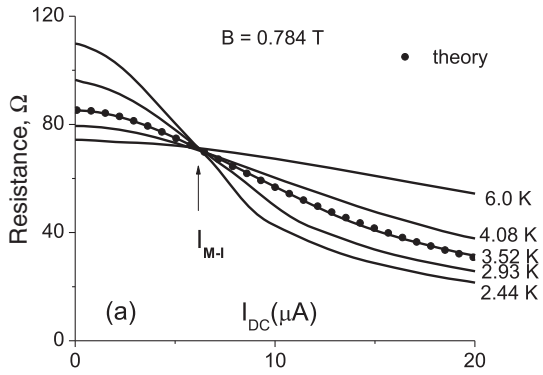

Fig. 2. Dependencies of resistance R_{xx} on current $I_{\rm dc}$ at different temperatures; $B = 0.784$ T. Circles present numerical calculations of the resistance, based on theory of spectral diffusion in strong magnetic field [5].

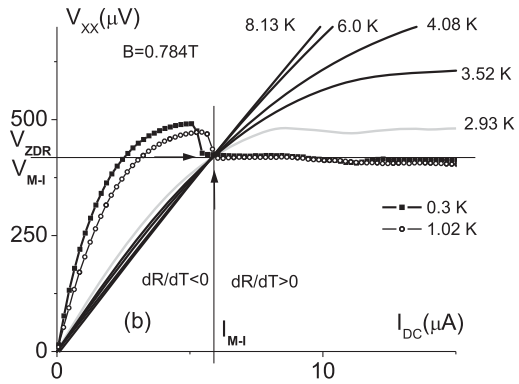

Fig. 3. Dependence of voltage V_{xx} on applied current $I_{\rm dc}$ at different temperature. $B = 0.784$ T. $I_{\rm M-I}$ marks current, at which a metal insulator transition occurs. $V_{\rm ZDR}$ is voltage at ZDR state [4] and $V_{\rm M-I}$ marks the voltage, at which metal insulator transition occurs.

oscillations [3].

Fig. 2 presents dependencies of the resistance on applied current $I_{\rm dc}$ at different temperatures. The dependencies are taken at a maximum of the quantum oscillations at which the density of states at Fermi level is high and the 2DEG is a good normal metal. Fig. 2 shows a strong reduction of the resistance with the current $I_{\rm dc}$. It is interesting that the set of curves demonstrates a dc driven metal-insulator transition (M-I) at $I = I_{\rm M-I}$. At $T < 2$ K the electron system undergoes a transition into the state with zero differential resistance $r_{xx} = dV_{xx}/dI_{\rm dc} = 0$ (ZDR). In this state the voltage is independent on the driving current: $V_{xx} = V_{\rm ZDR}$ [4]. It is even more fascinating that the voltage coincides with the voltage, at which the metal insulator transition occurs: $V_{\rm ZDR} = V_{\rm M-I}$. This is shown in Fig. 3. The correlation between M-I transition and the ZDR state is unexpected and is not understood.

The strong electron nonlinearity is result of peculiar, quantal dc heating, which occurs in system with discrete or quantized spectrum. The dc heating originates nonuniform spectral diffusion of electrons [5]. The spectral diffusion is strong inside Landau levels and is suppressed between them since there are no quantum states available. In result the dc heating stratifies electron distribution, creating very strong overheating inside the levels. The distribution is shown in Fig. 4 [1]. Due to the strong reduction of the spectral diffusion between Landau levels the overall broadening of the distribution function or an

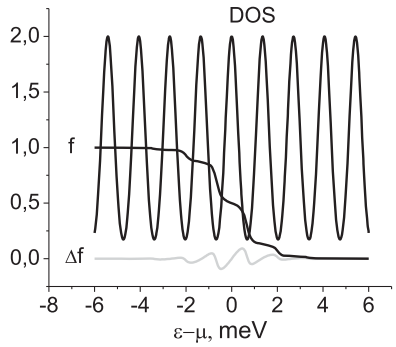

Fig. 4. Dependencies of density of states, distribution function F and non-equilibrium part of the function Δf on energy ϵ near Fermi level μ; $T = 8.13$ K, $I_{\rm dc} = 58.5$ μA).

effective "temperature" is preserved. The quantal heating produces exceptionally strong violation of Ohm's Law, which is unusual for normal metals [2].

Acknowledgements

This work was supported by NSF DMR N0349049 and by RBFR project 08-02-01051 and 10-02-00285.

References

[1] J.-Q. Zhang, S. A. Vitkalov and A. A. Bykov, *Phys. Rev. B.* **80**, 045310 (2009).
[2] S. A. Vitkalov, *Int. J. of Modern Physics B* **23**, 4727 (2009).
[3] N. Romero Kalmanovitz, A. A. Bykov, Sergey Vitkalov, and A. I. Toropov, *Phys. Rev. B* **78**, 085306 (2008).
[4] A. A. Bykov, Jing-qiao Zhang, Sergey Vitkalov, A. K. Kalagin, and A. K. Bakarov *Phys. Rev. Lett.* **99**, 116801 (2007).
[5] I. A. Dmitriev, M. G. Vavilov, I. L. Aleiner, A. D. Mirlin, and D. G. Polyakov, *Phys. Rev. B* **71**, 115316 (2005).

18th Int. Symp. "Nanostructures: Physics and Technology"
St Petersburg, Russia, June 21–26, 2010

Magnetoplasma oscillations of 2D electrons with SO interaction in a lateral superlattice

A. V. Chaplik[1,2], L. I. Magarill[1,2] and *R. Z. Vitlina*[1]

[1] Institute of Semiconductor Physics SB RAS, Novosibirsk, 630090, Russia
[2] Novosibirsk State University, Novosibirsk, 630090, Russia

Abstract. Low frequency magnetoplasma modes in 1D lateral superlattice are investigated with accounting for spin-orbit interaction in the Rashba form. Such modes correspond to the intra-Landau-level oscillations which become possible due to spreading of each Landau level into a band caused by the superlattice potential. The plasmon frequency dependence on the wave vector (for given filling factor) and on the filling factor (at given wave vector) are found.

Collective excitation of a 2D electron gas subjected to the magnetic field **B** (magnetoplasmons) have a gap in the dispersion law at zero momentum due to discrete character of the one particle energy spectrum. These excitations are similar to the intersubband plasmons in a quantum well at $\mathbf{B} = 0$. Even if some Landau level is not filled up transitions within this level do not generate a low frequency plasmon because degeneracy of the level results in zero contribution of such transitions into polarizability of the system. Any external potential, like disorder or periodic field of a superlattice lifts the degeneracy and each Landau level smears into a band. Then the intraband low frequency plasmons become possible.

In the present work we investigate intra-Landau-level plasma oscillations in a 1D lateral superlattice with account for spin - orbit (SO) coupling of 2D electrons. The magnetic field is supposed to be sufficiently strong: $\hbar\omega_c \gg V_0, \varepsilon_R$, where ω_c is the cyclotron frequency, V_0 is the amplitude of the superlattice potential, $\varepsilon_R = m\alpha^2$ is the characteristic SO energy, m is the effective mass, α is the Rashba SO coupling constant.

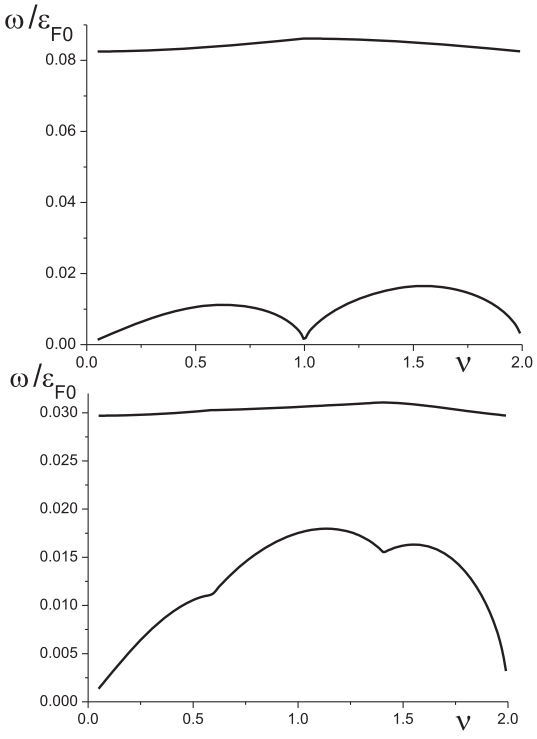

Fig. 1. Dependence of two lower branches of plasmon spectrum on filling factor at $q = 0.1k_F$, $k_F = \sqrt{2\pi n_s}$ is the Fermi wave number of the system in the absence of magnetic field, modulation and SO interaction. Upper: $\alpha = 2.4 \times 10^6$ cm/s (without overlapping of spin subbands). Lower: $\alpha = 1.44 \times 10^6$ cm/s (with overlapping).

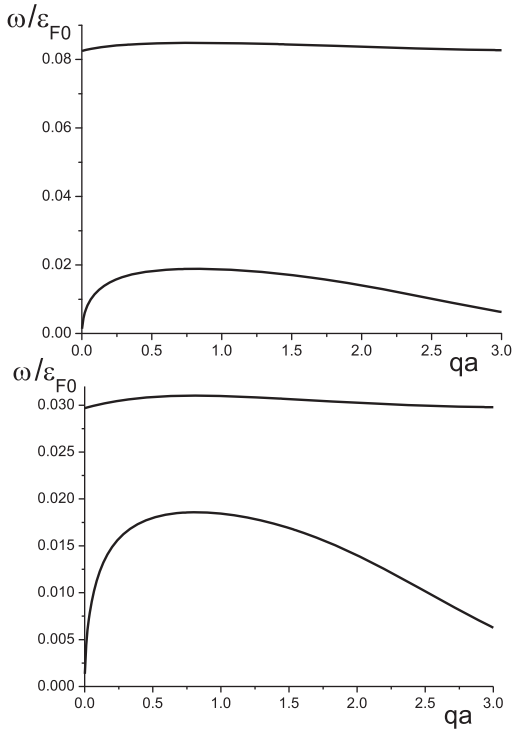

Fig. 2. Plasmon spectrum vs wave vector q at $\nu = 1.8$. Upper: $\alpha = 2.4 \times 10^6$ cm/s. Lower: $\alpha = 1.44 \times 10^6$ cm/s.

The two lower spin subbands arising from the zeroth Landau level describe the single-particle spectrum of the system:

$$\varepsilon_+(k) = \frac{\hbar\omega_c}{2} - 2\varepsilon_R + V\cos\left(\frac{2\pi k a^2}{d}\right),$$
$$\varepsilon_-(k) = \frac{\hbar\omega_c}{2} + V\cos\left(\frac{2\pi k a^2}{d}\right),$$

where $V = V_0 \exp(-2\pi^2 a^2/d^2)$, k is the electron momentum in y direction. The above formulas give the leading term of the electron energy in the limit $\hbar\omega_c \gg V_0$. The eigen function in the same approximation are the well known Bychkov-Rashba two component spinors.

We consider ultraquantum limit, i.e., the situation when only states of zeroth Landau level are filled: $0 < \nu \leq 2$ ($\nu \equiv 2\pi n_s a^2$ is the filling factor, n_s is the areal electron concentration, $a = \sqrt{c\hbar/|e|B}$ is the magnetic length). As the model of a lateral potential we use $V(x) = V_0 \cos(2\pi x/d)$, where d is the superlattice period.

We investigate the modes of 2D plasma in the framework of RPA approximation. The plasmon frequencies follow from the dispersion equation:

$$1 + \frac{2\pi e^2}{\kappa q}\Pi(\omega, q) = 0,$$

where κ is the background dielectric constant, $\Pi(\omega, q)$ is the polarization operator consisting of two parts $\Pi = \Pi_1 + \Pi_2$; Π_1 is diagonal in spin quantum numbers contribution to the polarizability, Π_2 accounts for spin-flip transitions. We have found analytical expressions for two lower branches of plasmon spectrum connected with intra-Landau-level transitions.

Fig. 1 shows the dependence of two lower plasmon frequencies on filling factor (magnetic dispersion). In Fig. 2 q-dispersion is depicted. In numerical calculation the following parameters were used: $n_s = 10^{11}$ cm^{-2}, $V_0 = 0.1$ meV, $m = 0.055m_0$, $\kappa = 12.9$, $d = 200$ nm. On pictures frequencies are normalized to the value $\varepsilon_{F0} = \pi\hbar^2 n_s/m$ which is the Fermi energy of unmodulated system in the absence of magnetic field and SO interaction.

It is worth to note that SO interaction without superlattice potential also generates a low frequency plasmon. The latter corresponds to the spin-flip transitions between two components of the zeroth Landau level and, as any interlevel plasmon, has gap in its dispersion law:

$$\omega = 2\varepsilon_R \sqrt{1 + \frac{qa^2}{a_B} \frac{\exp\left(-q^2a^2/2\right)(\nu_+ - \nu_-)}{F\left(q^2a^2/2\right)}},$$

where a_B is the effective Bohr radius, $\nu_\mp$ are the filling factors of upper (lower) spin sublevel, $F(u) = 1 + (\mathrm{Ei}(u) - C - \ln(u))e^{-u}$, $\mathrm{Ei}(u)$ is the exponential integral function, C is the Euler's constant.

Acknowledgements

Work was supported by RFBR grant No. 08-02-00152.

18th Int. Symp. "Nanostructures: Physics and Technology"
St Petersburg, Russia, June 21–26, 2010

Low-magnetic-field "non-Ohmicity" of the Hall resistance in disordered 2D electron gas

A. V. Germanenko[1], G. M. Minkov[1,2], O. E. Rut[1], A. A. Sherstobitov[1,2] and I. V. Soldatov[1]

[1] Ural State University, 620083 Ekaterinburg, Russia
[2] Institute of Metal Physics, 620041 Ekaterinburg, Russia

Abstract. The paper is devoted to study of the nonlinear behavior of the Hall resistance in the vicinity of zero magnetic field. Investigating the two-dimensional electron gas in strongly disordered GaAs/$In_xGa_{1-x}As$/GaAs quantum well we show that the anomaly of the Hall effect can be described by taking into account of the second order quantum correction to the conductivity originated from the interplay of the weak localization and electron-electron interaction contributions.

Introduction

The quantum corrections to the conductivity, namely the interference or weak localization (WL) correction and Aronov–Altshuler (AA) correction due to electron-electron (*e-e*) interaction, wholly determine the low temperature and magnetic field dependences of the conductivity under the conditions: $T/E_F \ll 1, T\tau \ll 1$, where E_F and τ are the Fermi energy and the transport relaxation time, respectively. The modern theory being elaborated since 1980 [1,2,3,4] allows ones to describe most of experimental results obtained on the well controlled semiconductor two-dimensional (2D) systems quantitatively. However, one peculiarity, namely, the nonlinearity or "non-Ohmicity" [5] of the magnetic field dependence of the Hall resistance $\rho_{xy}(B)$ remains a puzzle. Such a non-Ohmicity results in that the magnetic field dependence of the Hall coefficient $R_H(B) = \rho_{xy}(B)/B$ reveal a beak-like peculiarity centered at $B = 0$. Characteristic scale of the beak is close to the transport magnetic field $B_{tr} = \hbar/2el^2$, where l is the mean free path, i.e., close to the field, in which the main part of the interference correction is suppressed. As a rule, the Hall coefficient increases in absolute value with the growing magnetic field, and the magnitude of the beak is close to that of the negative magnetoresistivity caused by suppression of the weak localization: $|\delta R_H/R_H| \sim |\delta\sigma^{WL}|/\sigma$. The existence of low field anomaly of R_H was pointed out in the pioneering papers on the quantum corrections [5,6,7]. In the later papers the anomaly of R_H behavior is not mentioned, although the beak is observed practically in all the 2D structures [8,9,10].

Theories of the weak localization and interaction correction do not predict any low magnetic field dependence of the Hall coefficient. The WL theory claims that the quantum interference renormalizes the transport relaxation time and, consequently, does not lead to correction in the Hall coefficient. The *e-e* interaction within the diffusion regime, $T\tau \ll 1$, contributes to the longitudinal conductivity σ_{xx} only and this correction does not depend on the magnetic field while the Zeeman splitting is less than the temperature, $|g|\mu_B B < T$. So, this correction leads to the temperature dependence of the Hall coefficient, in the magnetic field domain R_H remains constant. Thus, the origin of the beak in the B dependence of the Hall coefficient remains enigmatic.

In this paper we try to understand the origin of the low-filed anomaly of R_H in strongly disordered structures in the diffusion regime. We show that the non-Ohmicity of the Hall effect comes from the interplay of the weak localization and interaction. This interplay term contributes to σ_{xx} only like the interaction correction and depends on the magnetic field like the WL correction.

1. Experimental

The structures investigated were grown by metal-organic vapor-phase epitaxy on a semiinsulating GaAs substrate and consist of 0.5-μm-thick undoped GaAs epilayer, a $In_xGa_{1-x}As$ quantum well with Sn or Si δ-layer situated in the well center and a 200 nm cap layer of undoped GaAs. The samples were mesa etched into standard Hall bars and then an Al gate electrode was deposited by thermal evaporation onto the cap layer through a mask. Varying the gate voltage V_g we were able to change the density and the conductivity of 2D electron gas in the quantum well. We studied samples prepared from four wafers with different well width, doping level and well composition. The results obtained were mostly analogous, therefore we will discuss the results for the structure 4261 studied more thoroughly. The quantum well width in this structure is 8 nm, indium content in the quantum well is 0.2 and tin density in δ layer is about 2×10^{12} cm^{-2}.

2. Results and discussion

Magnetic field dependences of ρ_{xx} and ρ_{xy} for $V_g = -1$ V taken at different temperatures are shown in Fig. 1. They are typical for such a type of systems. The sharp in the shape negative magnetoresistance at low B [Fig. 1(a)] results from suppression of the WL correction. A crossover to the parabolic-like behavior of ρ_{xx} at $B \geq 2$ T and the decrease of ρ_{xy} with the temperature increase come from the *e-e* interaction correction.

For the first sight, ρ_{xy} linearly depends on the magnetic field [Fig. 1(b)] as predicted theoretically. Let us, however, inspect the Hall coefficient, $R_H = \rho_{xy}/B$, which magnetic field dependences taken for different gate voltages at $T = 1.4$ K are plotted in Fig. 2(a). It is evident that R_H decreases in magnitude when B goes to zero for all the gate voltages. Comparing these dependences with that for magnetoresistance presented in Fig. 2(b), one can see that the characteristic scales in B domain for the R_H beak and for the interference induced negative magnetoresistance are close; the main changes happen at $B < B_{tr}$ in both cases. Moreover, both effects are close in the magnitude: $|\delta R_H/R_H| \simeq |\delta\rho_{xx}/\rho|$.

The following mechanisms for the beak are analyzed in the paper. Firstly, the simultaneous existence of the B dependent WL correction to σ_{xx} and to σ_{xy} and the *e-e* interaction

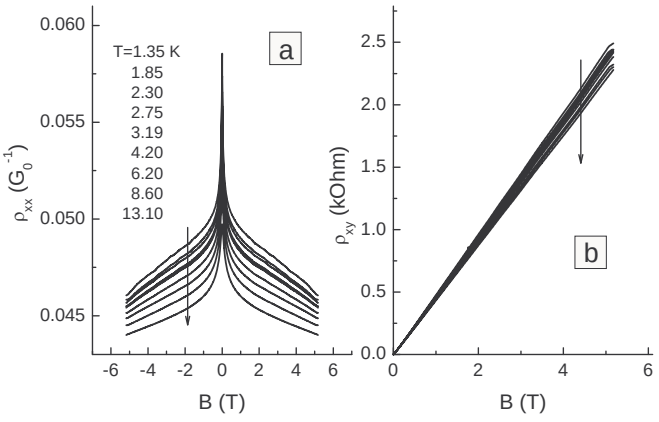

Fig. 1. The magnetic field dependences of ρ_{xx} (a) and ρ_{xy} (b) for $V_g = -1$ V taken at different temperatures. The arrows indicate the temperature growth. $G_0 = e^2/2\pi^2\hbar$.

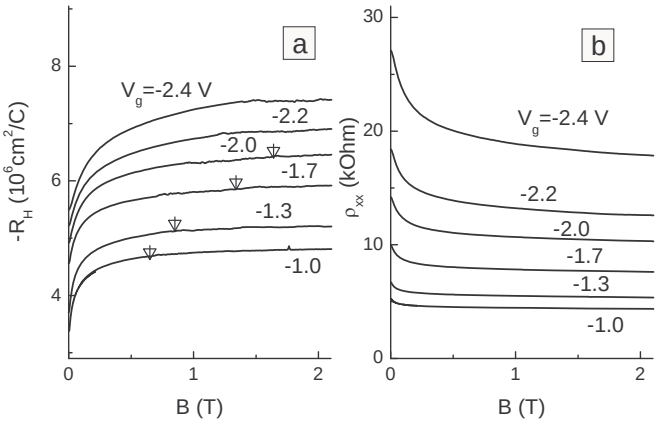

Fig. 2. The magnetic field dependences of R_H (a) and ρ_{xx} (b) taken for different gate voltages at $T = 1.4$ K. The arrows in (a) indicate $B_{\rm tr}$.

correction to σ_{xx}, which is independent of the magnetic field, should obviously lead to the low magnetic field dependence of $R_{\rm H}$. However, this effect is the next order of smallness as compared with the above corrections. Moreover, the Hall coefficient should decrease in magnitude with the B increase if the sign of the interaction correction is insulating. The experimental behavior is opposite, as seen from Fig. 2.

The second reason is the interaction corrections in the Cooper channel. Two terms contribute to the low-magnetic field magnetoconductance. They are the Maki–Thomson correction and correction to the density of states (DoS). The role of these terms in the low field magnetoconductivity is thoroughly considered in [11]. We merely mention that only DoS correction can in principle result in low-B dependence of $R_{\rm H}$, because it contributes to σ_{xx} and do not to σ_{xy} and its B-dependence is close in the shape to that of interference induced magnetoconductivity [1]. However our analysis of the data carried out within framework of the theory [12] shows that existence of DoS correction should result in drastic change of character of the temperature dependence conductivity of our samples at $B = 0$. It should be changed from the insulating to the metallic-like with decreasing temperature due to renormalization of the constants of the *e-e* interaction with changing conductivity. In systems investigated the conductivity is of insulating character, i.e., it decreases with decreasing temperature, under any conditions.

To proceed with the third reason we fix attention to that the non-Ohmic behavior of the Hall resistance coexists with the fact that the T dependence of the conductivity at $B = 0$ is weaker than it should be when one takes into account only the WL and AA contributions. It is natural to suggest that both effects of common reason. Because $\sigma_{xy} = 0$ at $B = 0$, it is reasonably to suppose that the effects mainly results from the existence of additional correction $\delta\sigma^{(2)}$ to σ_{xx}. In such a case, the temperature and magnetic field dependences of $\delta\sigma^{(2)}$ can be obtained using approach [13]. It turns out that the shape of the dependence $\delta\sigma^{(2)}(B)$ obtained in such a manner is very close to that of the WL quantum correction. Analysis of the data obtained over the wide conductivity range, $\sigma = (3\text{–}300)G_0$, where $G_0 = e^2/2\pi^2\hbar$, shows that at relatively low conductivity, $\sigma < (15\text{–}20)G_0$, the relationship between these two corrections is close to that observed in [11] for the second-order correction resulted from the interplay of the WL and interaction contributions. In the samples with the lower disorder strength, $\sigma > 20G_0$, the higher-order corrections become negligible, whereas the anomaly in the Hall effect is clearly observed. This points to the fact the nature of the beak in the dependence $R_{\rm H}(B)$ is different for dirty and clean systems.

Thus, the "non-Ohmicity" of the Hall resistance and impossibility of description of the temperature dependences of zero-field conductivity by taking into account only two first order quantum corrections (WL and AA) are explained by significant contribution of the second order interplay correction in disordered systems. The experimental results are satisfactorily interpreted under assumption that interplay contributes to diagonal component of the conductivity tensor σ_{xx} only, its magnetic field dependence is close to that of the weak localization correction, although the temperature dependence is metallic-like.

Acknowledgements

This work has been supported in part by the RFBR (Grant Nos. 08-02-00662, 09-02-00789, and 10-02-00481).

References

[1] B. L. Altshuler and A. G. Aronov, in *Electron-Electron Interaction in Disordered Systems*, edited by A. L. Efros and M. Pollak, (North Holland, Amsterdam, 1985) p. 1.
[2] I. L. Aleiner *et al*, *Waves Random Media* **9**, 201 (1999).
[3] Gabor Zala *et al*, *Phys. Rev. B* **64**, 214204 (2001).
[4] I. V. Gornyi and A. D. Mirlin, *Phys. Rev. B* **69**, 045313 (2004).
[5] E. Tousson and Z. Ovedyahu, *Phys. Rev. B* **17**, 12290 (1988).
[6] D. A. Poole *et al*, *J. Phys. C* **14**, L995 (1981).
[7] D. J. Newson *et al*, *J. Phys. C* **20**, 4369 (1987).
[8] G. M. Minkov *et al*, *Phys. Rev. B* **74**, 045314 (2006).
[9] A. Yu. Kuntsevich and V. M. Pudalov, private communication.
[10] V. A. Tkachenko and Z. D. Kvon, private communication.
[11] G. M. Minkov *et al*, *Phys. Rev. B* **70**, 245423 (2004).
[12] A. Punnoose and A. M. Finkel'stein, *Science* **310**, 289 (2005).
[13] G. M. Minkov *et al*, *Phys.Rev. B* **76**, 165314 (2007).

18th Int. Symp. "Nanostructures: Physics and Technology"
St Petersburg, Russia, June 21–26, 2010

The interference quantum correction to the conductivity in double quantum well structures

G. M. Minkov[1,2], A. A. Sherstobitov[1,2] A. V. Germanenko[2], O. E. Rut[2], I. V. Soldatov[2], D. V. Dmitriev[3] and A. I. Toropov[3]

[1] Institute of Metal Physics RAS, 620041 Ekaterinburg, Russia
[2] Ural State University, 620083 Ekaterinburg, Russia
[3] Institute of Semiconductor Physics RAS, 630090 Novosibirsk, Russia

Abstract. The interference quantum correction to the conductivity in double-well $Al_xGa_{1-x}As$/GaAs structures are studied experimentally. The gate voltage provides a way to change the relationship between electron density in the wells and trace a variation of the interference correction. It is shown that interwell transitions change the negative magnetoresistance noticeably, while the inelasticity of the electron-electron interaction of an electron in one well with electrons in another well does not contribute to the dephasing rate observably.

The low temperature and magnetic field dependences of the conductivity of 2D degenerated electron gas are determined by the quantum corrections — the interference correction and correction due to electron-electron interaction. The theoretical studies elaborated since 1980 and detailed experimental investigations on the well controlled semiconductor 2D systems made possible the quantitative comparison with theoretical results. The practically whole consistency was demonstrated for different structures with the simple one-valley parabolic spectrum. The more complex structures, namely, the structures with two-valley spectrum and double-well structures are studied significantly less. The manifestation of specific features of the quantum corrections in such a type of structures is determined by relationship between the following parameters: quantum and transport relaxation times τ_q and τ, respectively, the phase relaxation time τ_ϕ, interwell transition time τ_{ij}, temperature length $L_T = \sqrt{D/T}$ (where D is the diffusion coefficient), interwell distance d and screening length, which is about the Bohr radius a_B. There are two limiting cases, for which the situation looks simple. The first case is close and strongly interacting wells, when the quantum corrections are the same as for the single quantum well. The second one is the remote non-interacting wells. In this case the corrections are the additive sum of the corrections to the conductivity of each well. The intermediate cases are more interesting and diversified. The interference correction, even without inter-well transitions ($\tau_{ij} \gg \tau_\phi$), can differ from the case of non-interacting wells due to inelasticity of the electron-electron interaction of carriers in the different wells. The gain of the interaction in a triplet channel can be so significant that it leads to the change of the sign of the temperature dependence of the conductivity from dielectric ($d\rho/dT > 0$) to metallic ($d\rho/dT < 0$).

The structures investigated have two 8-nm-thick GaAs quantum wells separated by 10 nm $Al_{0.3}Ga_{0.7}As$ barrier. The main doping Si δ-layer was situated in the barrier center. Because the gate voltage can effectively only decrease the electron density, the additional doping δ layer was situated at 18 nm above the upper quantum well. Such structure design provides a way to have the close mobility values at equal electron densities in the wells. This fact is very important for reliable determination of the quantum corrections. To make sure that this condition is met, the Shublkov-de Haas oscillations at the gate voltages close to the "resonance" characterized by the equal electron density in the wells, $n_1 = n_2$, was studied in detail (see Fig. 1). When the splitting of symmetric and antisymmetric states in such double-well structures, Δ_{SAS}, is less than $\hbar/\tau_q$, that is fulfilled in our case, the oscillations are just the sum of the

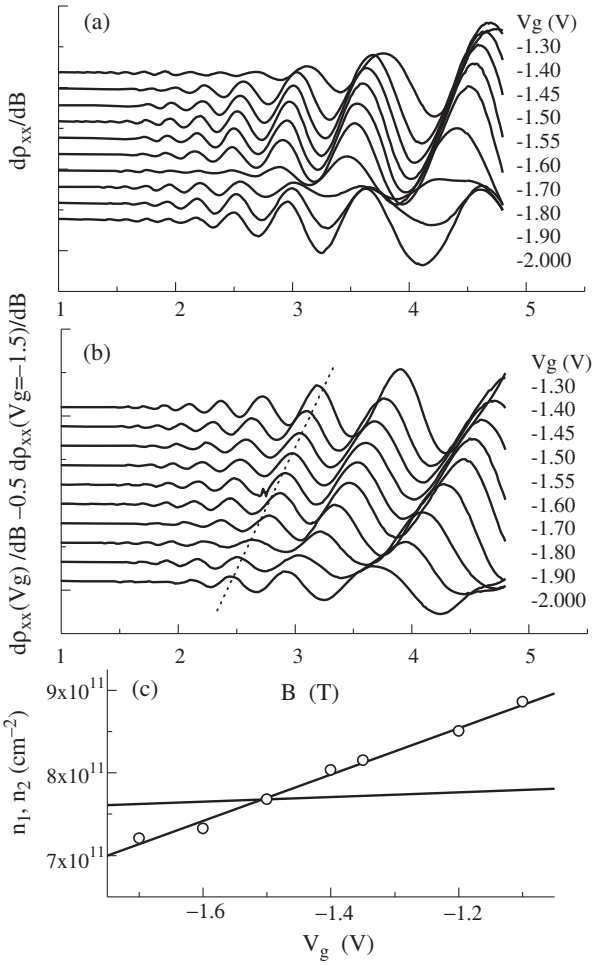

Fig. 1. (a) — The oscillations of $d\rho_{xx}/dB$ measured experimentally for different gate voltages. (b) — The oscillations for different gate voltage coming from the upper quantum well 2 obtained by subtraction of the oscillations coming from the lower well 1 (see text). (c) — The gate voltage dependence of the electron densities in the wells 1 and 2.

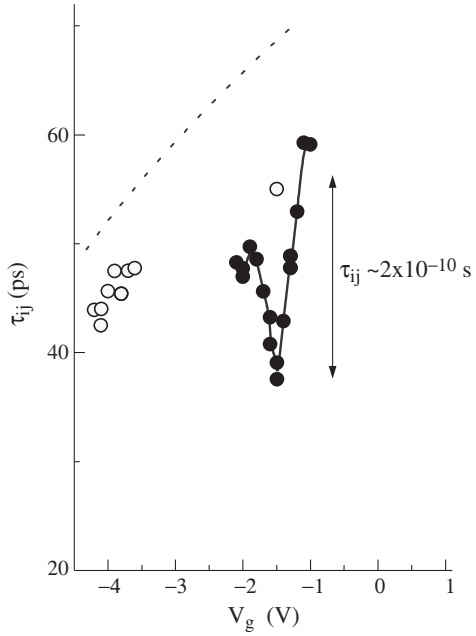

Fig. 2. The gate voltage dependence of $\tau^{\rm fit}$; open symbols — the case when only the well 1 is occupied: solid symbols — near the resonance. The dotted line is the theoretical dependence, the solid line is a guide for the eye.

oscillations in each well $\rho_{xx}(B) = \rho_{xx}^{(1)}(B) + \rho_{xx}^{(2)}(B)$ and at the "resonance" gate voltage, $V_g^{\rm res}$, $\rho_{xx}(B) = 2\rho_{xx}^{(1)}(B)$ for the close values of the mobility in the wells. Because the gate voltage changes the density only in the upper well 2, one can separate these oscillations for any V_g as follows: $\rho_{xx}^{(2)}(B, V_g) = \rho_{xx}(B, V_g) - 0.5\rho_{xx}(B, V_g^{\rm res})$. The results of such a data treatment presented in Fig. 1(a) show that the oscillations period decreases monotonically with the gate voltage and, what is more important, the oscillations amplitude changes little. Such a behavior unambiguously shows that the values of the mobility in the wells are close to each other near the "resonance".

The negative magnetoresistance caused by suppression of the WL correction was studied within a wide gate voltage range including the regimes when both 1 and 2 wells are occupied and when the upper well 2 is empty. The detailed analysis shows that reliable determination of the phase relaxation time is possible for two cases: (i) at the gate voltage close to the "resonance" and (ii) at $V_g < -3.5$ V, when only the well 1 is occupied. Theoretically, the negative magnetoresistance in double-well structure was studied in [1]. Our analysis, however, shows that the use of the results of this paper for the fit of the data in our case when $\tau_{ij} > \tau_\phi$ is impossible. At once, one can show that the fit of the data by the standard expression [2] gives the parameter $\tau^{\rm fit}$, which is very close to $(\tau_\phi^{-1} + \tau_{ij}^{-1})^{-1}$. The results of such a data treatment are presented in Fig. 2. It is clearly seen that the value of $\tau^{\rm fit}$ has sharp minimum at $V_g = -1.5$ V, when $n_1 = n_2$. The amplitude of the minimum gives the τ_{ij} value at the "resonance" about $(1.5–2.0)\times10^{-10}$ s, which is four-five times larger than the τ_ϕ value. The width of the minimum shows that τ_{ij} strongly increases when the difference between the Fermi energies in the wells becomes large than (2–3) meV. This value is close to the value of $\hbar/\tau_q$ that means that the interwell transitions are really resonance transitions. The data in Fig. 2 show that τ_ϕ near the resonance is very close to that at $V_g < -3.5$ V when only the well 1 is occupied. It is very surprising because the inter-well distance is about the Bohr radius. It means that inelasticity of the interaction of electrons in one quantum well with electrons in another one should decrease the phase relaxation time. The estimations show that this decrease should be about 40%, that is significantly larger than uncertainty in determination of the τ_ϕ value. The farther theoretical study of the phase relaxation mechanisms in double quantum wells is needed.

Acknowledgements

This work has been supported in part by the RFBR (Grant Nos. 08-02-00662, 09-02-00789, and 10-02-00481).

References

[1] O. E. Raichev *et al*, *J. Phys.: Condens. Matter* **12**, 589 (2000).
[2] S. Hikami *et al*, *Progr. Theor. Phys.* **61**, 707 (1980).

18th Int. Symp. "Nanostructures: Physics and Technology"
St Petersburg, Russia, June 21–26, 2010

Role of electron-electron interactions in microwave-induced resistance oscillations in high mobility quantum Hall systems

M. A. Zudov[1], A. T. Hatke[1], L. N. Pfeiffer[2] and K. W. West[2]

[1] School of Physics and Astronomy, University of Minnesota, Minneapolis, Minnesota 55455, USA
[2] Princeton University, Department of Electrical Engineering, Princeton, NJ 08544, USA

Abstract. When a high mobility two-dimensional electron system is illuminated by microwave radiation, its resistivity exhibits pronounced oscillations with the magnetic field. We have studied the temperature dependence of these oscillations and found that the oscillation amplitude decays exponentially with increasing temperature, as $\exp(-\alpha T^2)$, where α scales with the inverse magnetic field. This observation indicates that the temperature dependence originates *primarily* from the modification of the single particle lifetime, entering the square of the dingle factor, which we attribute to the electron-electron interaction effects.

Introduction

When a clean 2D electron system is subject to a weak magnetic field and microwave radiation, the resistance will oscillate dramatically [1], depending on the ratio of microwave and cyclotron frequencies, $\epsilon_{ac} = \omega/\omega_c$. Remarkably, at the minima of these microwave-induced resistance oscillations (MIRO) the resistance can virtually vanish forming exotic zero-resistance states [2,3]. Theoretically, MIRO were discussed in terms of the "displacement" model [4], which is based on the impurity scattering, and the "inelastic" model [5], stepping from the oscillatory electron distribution function. The correction to the resistivity due to either mechanism can be written as [5]:

$$\delta\rho = -4\pi\rho_0\tau_{tr}^{-1}\mathcal{P}_\omega\epsilon_{ac}\bar{\tau}\delta^2\sin(2\pi\epsilon_{ac}). \qquad (1)$$

Here, $\rho_0 \propto 1/\tau_{tr}$ is the Drude resistivity, τ_{tr} is the transport scattering time, $\mathcal{P}_\omega$ is a dimensionless parameter proportional to the microwave power, and $\delta = \exp(-\pi\epsilon_{ac}/\omega\tau_q)$ is the Dingle factor. In the "displacement" model $\bar{\tau} = 3\tau_q^{im}$ (impurity quantum lifetime) and in the "inelastic" model $\bar{\tau} = \tau_{in} \sim \varepsilon_F T^{-2}$ (inelastic time), where ε_F is the Fermi energy. The "inelastic" mechanism is usually favored over the "displacement" because one usually expects $\tau_{in} \gg \tau_q^{im}$, and because it can naturally explain the high temperature decay of MIRO. In this work we show that the decay of MIRO with increasing temperature originates from electron-electron interactions modifying the quantum lifetime entering the Dingle factor.

1. Experimental details

While similar results were obtained from samples fabricated from different GaAs/$Al_{0.24}Ga_{0.76}$As quantum well wafers, all the data presented here are from the sample with density and mobility of $\simeq 2.8 \times 10^{11}$ cm^{-2} and $\simeq 1.3 \times 10^7$ cm^2/V s, respectively. Measurements were performed in a ^{3}He cryostat using a standard low frequency (a few hertz) lock-in technique. The sample was continuously illuminated by microwaves of frequency $f = 81$ GHz. The temperature was varied from 1 to 5.5 K and monitored by calibrated RuO_2 and Cernox sensors.

2. Results and discussion

In Fig. 1 we present resistivity ρ as a function of magnetic field B acquired at different temperatures, from 1.0 to 5.5 K in 0.5 K increments. Vertical lines, marked by integers, label harmonics of the cyclotron resonance. The low temperature data reveal well developed MIRO extending up to the tenth order. With increasing T, the zero-field resistivity exhibits monotonic growth reflecting the crossover to the Bloch–Grüneisen regime due to excitation of acoustic phonons. Concurrently, MIRO weaken and eventually disappear. Since MIRO appear in the second order of the Dingle factor, this disappearance is not due to the thermal smearing of the Fermi surface, known to govern the temperature dependence of the Shubnikov–de Haas oscillations.

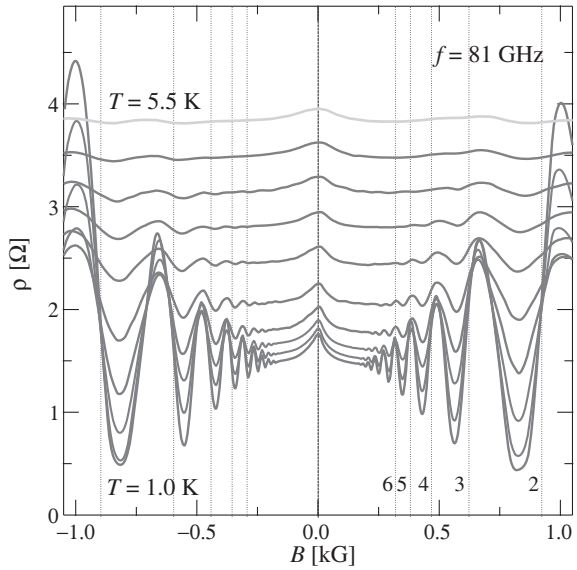

Fig. 1. Resistivity ρ vs. B under microwave irradiation at T from 1.0 to 5.5 K (as marked), in 0.5 K steps. Integers mark the harmonics of the cyclotron resonance.

We start our analysis of the temperature dependence by constructing Dingle plots and extracting the quantum lifetime τ_q for different T. We limit our analysis to $\epsilon_{ac} \gtrsim 3$ for the following reasons. First, this ensures that we stay in the regime of the overlapped Landau levels, $\delta \ll 1$. Second, we satisfy, for the most part, the condition, $T > \omega_c$, used to derive Eq. (1). Finally, we can ignore the magnetic field dependence of $\mathcal{P}_\omega$ and assume $\mathcal{P}_\omega \equiv \mathcal{P}_\omega^{(0)}\epsilon_{ac}^2(\epsilon_{ac}^2+1)/(\epsilon_{ac}^2-1)^2 \simeq \mathcal{P}_\omega^{(0)} = e^2\mathcal{E}_\omega{}^2 v_F^2/\omega^4$, where $\mathcal{E}_\omega$ is the microwave field and v_F is the Fermi velocity.

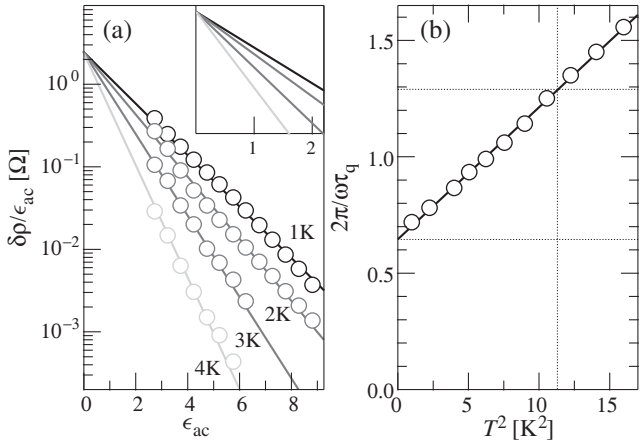

Fig. 2. (a) Normalized MIRO amplitude $\delta\rho/\epsilon_{ac}$ vs. ϵ_{ac} at $T = 1.0$, 2.0, 3.0, 4.0 K (circles) and fits to $\exp(-2\pi\epsilon_{ac}/\omega\tau_q)$ (lines). Inset shows that all fits intersect at $\epsilon_{ac} = 0$. (b) Normalized scattering rate $2\pi/\omega\tau_q$ vs. T^2. Horizontal lines mark $\tau_q = \tau_q^{im}$ and $\tau_q = \tau_q^{im}/2$, satisfied at $T^2 = 0$ and $T^2 \simeq 11$ K^2, respectively.

Using the data presented in Fig. 1 we extract the normalized MIRO amplitude, $\delta\rho/\epsilon_{ac}$, which, regardless of the model, is expected to scale with $\delta^2 = \exp(-2\pi\epsilon_{ac}/\omega\tau_q)$. The results for $T = 1$, 2, 3, 4 K are presented in Fig. 2(a) as a function of ϵ_{ac}. Having observed exponential dependences over at least two orders of magnitude in all data sets we make two important observations. First, the slope, $-2\pi/\omega\tau_q$, monotonically grows with T by absolute value, marking the increase of the quantum scattering rate. Second, all data sets can be fitted to converge to a single point at $\epsilon_{ac} = 0$, indicating that the pre-factor in Eq. (1) is essentially temperature independent [cf. inset of Fig. 2(a)].

After repeating the Dingle plot procedure for other temperatures studied we present the extracted $2\pi/\omega\tau_q$ vs. T^2 in Fig. 2(b). Remarkably, the quantum scattering rate follows quadratic dependence over the whole range of temperatures studied. Since such temperature dependence of is characteristic of electron-electron scattering we assume $1/\tau_q = 1/\tau_q^{im} + 1/\tau_q^{ee}$, where τ_q^{im} and τ_q^{ee} are the impurity and electron-electron contributions, respectively. Using the well-known estimate for the electron-electron scattering rate, $1/\tau_q^{ee} = \lambda T^2/\varepsilon_F$, where λ is a constant of the order of unity, we perform the linear fit to the data in Fig. 2(b) and obtain $\tau_q^{im} \simeq 19$ ps and $\lambda \simeq 4.1$. As indicated in Fig. 2(b) the electron-electron contribution approaches the impurity contribution at $T^2 \simeq 11$ K^2 or $T \simeq 3.3$ K. At this temperature $1/\tau_q(\bar{T}) = 1/\tau_q^{ee}(\bar{T}) + 1/\tau_q^{im} \simeq 2/\tau_q^{im} = 2/\tau_q(0)$.

To summarize our observations, the MIRO amplitude as a function of T is found to conform to a simple expression:

$$\delta\rho(T) \simeq A\epsilon_{ac}\exp\left[-2\pi/\omega_c\tau_q(T)\right]. \qquad (2)$$

Here, A is roughly independent on T, but τ_q is temperature dependent due to electron-electron interactions:

$$\frac{1}{\tau_q} = \frac{1}{\tau_q^{im}} + \frac{1}{\tau_q^{ee}}, \qquad \frac{1}{\tau_q^{ee}} \simeq \lambda\frac{T^2}{\varepsilon_F}. \qquad (3)$$

These equations suggest alternative approach to extract parameter λ. At each magnetic field B one can fit the normalized MIRO amplitude $\delta\rho/\epsilon_{ac}(T)$ with $\exp(-\alpha T^2)$ and then use $\alpha = (2\pi\lambda/\omega\varepsilon_F)\epsilon_{ac} \propto B^{-1}$. We have confirmed that this approach also leads to $\lambda \simeq 4.1$.

We now comment on a possible reason for the apparent temperature independence of A, which we can treat as a sum of the "displacement" and the "inelastic" contributions, $A = A_{dis} + A_{in}$. According to Eq. (1), at low T $A_{dis} < A_{in}$ but at high T $A_{dis} > A_{in}$. Therefore, there should exist a crossover temperature T^*, such that $A_{dis}(T^*) = A_{in}(T^*)$. Assuming $\tau_{in} \simeq \tau_q^{ee} \simeq \varepsilon_F/\lambda T^2$ we obtain $T^* \simeq 2$ K and conclude that the "displacement" contribution cannot be ignored down to the lowest temperature studied. Next, we notice that Eq. (1) contains transport scattering time, τ_{tr}, which varies roughly by a factor of two in our temperature range. If this variation is taken into account, A_{in} will decay considerably slower than $1/T^2$ and A_{dis} will grow with T, instead of being T-independent, leading to a weak temperature dependence of A within the studied range.

3. Summary

To summarize, we have studied MIRO temperature dependence in a high-mobility 2DES. We have found that the temperature dependence is exponential and originates from the temperature-dependent quantum lifetime entering the square of the Dingle factor. The corresponding correction to the quantum scattering rate obeys T^2 dependence, consistent with the electron-electron interaction effects. At the same time we are unable to identify any significant temperature dependence of the pre-factor in Eq. (1), which can be partially accounted for by the interplay between the "displacement" and the "inelastic" contributions in our high-mobility 2DES. Since this observation might be unique to our structures [6], further systematic experiments in samples with different amounts and types of disorder are highly desirable. Another important issue is the influence of the electron-electron interactions on single particle lifetime entering the square of the Dingle factor appearing in MIRO (which are different from the Shubnikov–de Haas oscillations where the Dingle factor does not contain the $1/\tau_q^{ee} \propto T^2$ term [7]). We note that such a scenario was considered a few years ago [8] and found experimental support in the recent studies of temperature evolution of phonon- and Hall field-induced resistance oscillations [9, 10]. Taken together, our findings suggest that sensitivity to electron-electron interactions is a generic property of magnetoresistance oscillations appearing in the second order of the Dingle factor.

Acknowledgements

The work at Minnesota was supported by the NSF Grant No. DMR-0548014.

References

[1] Zudov *et al*, *Phys. Rev. B* **64**, 201311(R) (2001).
[2] Mani *et al*, *Nature* **420**, 646 (2002).
[3] Zudov *et al*, *Phys. Rev. Lett.* **90**, 046807 (2003).
[4] Vavilov and Aleiner, *Phys. Rev. B* **69**, 035303 (2004).
[5] Dmitriev *et al*, *Phys. Rev. B* **71**, 115316 (2005).
[6] Hatke *et al*, *Phys. Rev. Lett.* **102**, 066804 (2009).
[7] Martin *et al*, *Phys. Rev. B* **68**, 241309(R) (2003).
[8] Ryzhii, Chaplik, and Suris, *JETP Lett.* **80**, 363 (2004).
[9] Hatke *et al*, *Phys. Rev. Lett.* **102**, 086808 (2009).
[10] Hatke *et al*, *Phys. Rev. B* **79**, 161308(R) (2009).

18th Int. Symp. "Nanostructures: Physics and Technology"
St Petersburg, Russia, June 21–26, 2010

Photogalvanic effects in (001)- and (013)-grown HgTe/CdHgTe quantum well structures

S. N. Danilov[1], B. Wittmann[1], S. A. Tarasenko[2], V. V. Bel'kov[2], E. G. Novik[3], H. Buhmann[3], C. Brüne[3], L. W. Molenkamp[3], Z. D. Kvon[4], N. N. Mikhailov[4], S. A. Dvoretsky[4], N. Q. Vinh[5], A. F. G. van der Meer[5], B. Murdin[6] and S.D. Ganichev[1]

[1] Terahertz Center, University of Regensburg, 93040 Regensburg, Germany
[2] Ioffe Physical-Technical Institute, St Petersburg, Russia
[3] Physikalisches Institut, Universität Würzburg, 97074 Würzburg, Germany
[4] Institute of Semiconductor Physics, 630900 Novosibirsk, Russia
[5] FOM Institute for Plasma Physics "Rijnhuizen", P.O. Box 1207, NL-3430 BE Nieuwegein, The Netherlands
[6] University of Surrey, Guildford, GU2 7XH, UK

Abstract. We report on the observation of the circular and linear photogalvanic effects in HgTe/CdHgTe quantum wells grown on substrates of different crystallographic orientations in mid-infrared as well as terahertz spectral ranges. The photocurrent behavior upon variation of the radiation polarization state, radiation wavelength, and temperature is studied. The experimental data are discussed in terms of phenomenological theory.

Introduction

The two-dimensional electron states in HgTe quantum well (QW) structures are characterized by a highly specific energy spectrum with an inverted band structure and large spin splitting, attracted growing attention as a potentially interesting material system for spintronics. A most efficient tool to study nonequilibrium processes in QWs yielding information on their symmetry, details of the band spin splitting, momentum and energy relaxation, etc. is the study of photogalvanic effects, in particular, the circular photogalvanic effect (CPGE) [1].

In this work we investigate photogalvanic effects in HgTe/CdHgTe structures as a function of the radiation polarization, wavelength, and temperature. We present the phenomenological theory of the effect in two-dimensional systems with point-group symmetry corresponding to (001)- and (013)-oriented structures and compare the results with experimental data.

1. Samples and experimental technique

The experiments were carried out on MBE-grown n-type $Hg_{0.3}Cd_{0.7}Te$/ HgTe/$Hg_{0.3}Cd_{0.7}Te$ QWs of (001) and (013) crystallographic orientations with two pairs of ohmic contacts in the temperature range 4.2–300 K. The (001)-oriented structures were grown on a $Cd_{0.96}Zn_{0.04}Te$ substrate and have quantum well width $L_W = 8$ and 22 nm. The (013)-oriented structures were grown on a GaAs substrate and have either 1 or 30 QWs with $L_W = 21$ nm.

For optical excitation in mid-infrared (MIR) and THz ranges we used a frequency tunable free electron laser "FELIX" at FOM Institute "Rijnhuizen" and the pulsed molecular terahertz laser [1], respectively. To measure photocurrent polarization dependences we applied $\lambda/4$ plates (or Fresnel rhomb in MIR range) which modifies the radiation helicity P_{circ} according to $P_{circ} = \sin 2\varphi$, where φ is the angle between the initial plane of polarization and the optical axis of the $\lambda/4$ plate. The geometry of the experiment is sketched in the insets in Figs. 1 and 2.

2. Experimental results

Circular (photon-helicity dependent) photocurrents, which reverse the direction upon switching the sign of P_{circ}, were observed in (001)-grown HgTe QW structures in a wide spectral and temperature range. The photocurrents are excited only at oblique incidence of radiation, reverse the sign upon inverting the incidence angle θ_0 (see inset on Fig. 1), and flow perpendicular to the incidence plane. The polarization dependence of the photocurrent is well described by $J_y = J_0 \sin 2\varphi \propto P_{circ}$. In the longitudinal geometry no helicity dependent photocurrent was observed.

The spectral dependence of the circular photocurrent, $J_{circ} = (J_{\varphi=45^\circ} - J_{\varphi=135^\circ})/2$, is shown in Fig. 1. For spectral range 6–12 μm the signal is almost independent, which can be attributed to the spectral behavior of the interband absorption. In THz range the photocurrent signal is substantially smaller and rises significantly with increasing wavelength as expected for Drude absorption.

In (013)-grown samples, helicity dependent photocurrents were detected not only at oblique incidence of radiation but also at normal incidence. Depending on the sample type, wavelength and/or temperature the currents in both x' and y' directions can be fitted simply by $J = J_0 \sin 2\varphi \propto P_{circ}$ or by more complex dependence on the angle φ (see inset on Fig. 2) given by

$$J = A \sin 2\varphi + B \sin 4\varphi + C \cos 4\varphi + D \qquad (1)$$

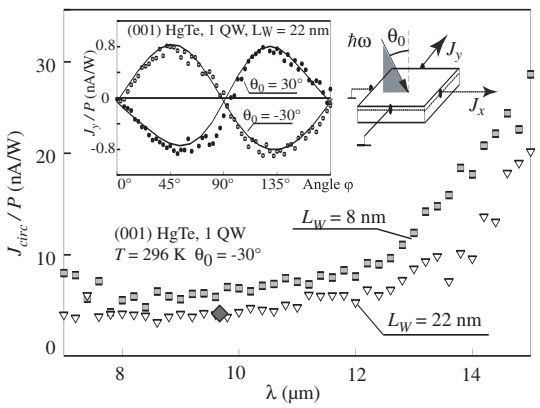

Fig. 1. CPGE spectra, geometry of experiment and the polarization dependence of the photocurrent in (001)-grown sample.

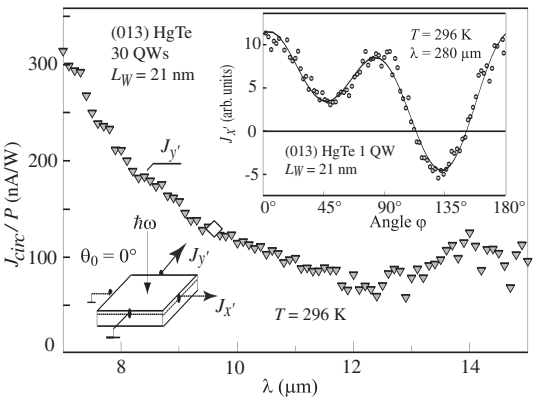

Fig. 2. MIR CPGE spectra, geometry of experiment and the polarization dependence of the photocurrent in (013)-grown sample.

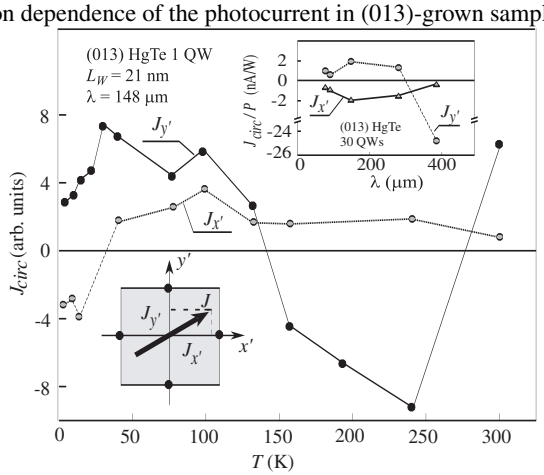

Fig. 3. CPGE temperature and spectral (inset) dependences in THz range in (013)-grown sample.

We note that the circular photocurrent $J_{\rm circ}$ is proportional to A.

Unlike (001)-grown QWs, where $J_{\rm circ}$ can only be excited by oblique incidence, its direction is always perpendicular to the incidence plane, and only the photocurrent magnitude and sign are functions of angle, temperature and wavelength, in the (013)-grown structure, $J_{\rm circ}$ can be produced by normal incidence and can flow in any direction as shown in Fig. 3, where it can be seen that $J_{x'}$ and $J_{y'}$ behave differently and change their sign depending on the wavelength and temperature.

3. Phenomenological description

In the framework of phenomenological theory, the photogalvanic current density $\mathbf{j}$ can be written as a function of the electric component $\mathbf{E}$ of the radiation field and the light propagation direction $\hat{\mathbf{e}}$ as [2,3]

$$j_\lambda = \sum_\beta \gamma_{\lambda\beta}\hat{e}_\beta P_{\rm circ}|E|^2 + \sum_{\mu,\nu}\chi_{\lambda\mu\nu}(E_\mu E_\nu^* + E_\mu^* E_\nu)/2\,, \quad (2)$$

where the first term on the right hand side is proportional to the radiation helicity $P_{\rm circ}$ and represents the CPGE, while the second term corresponds to the linear photogalvanic effect (LPGE) [3], which may be superimposed on the CPGE. The second rank pseudotensor $\hat{\gamma}$ and the third rank tensor $\hat{\chi}$ are material parameters. Their indices run over the coordinate axes.

The (001)-grown HgTe QW structure corresponds to the C_{2v} point group and there are only 4 non-zero and linearly independent components of $\hat{\gamma}$ and $\hat{\chi}$. Optical excitation of such structures at angle of incidence θ_0 in the (xz)-plane generates electric current whose x- and y-components are given by

$$j_x/P = C_x(\omega)\sin\theta_0\cos\theta_0\,(1-\cos 4\varphi)\,, \quad (3)$$

$$j_y/P = S_y(\omega)\sin\theta_0\sin 2\varphi - C_y(\omega)\sin\theta_0\sin 4\varphi\,, \quad (4)$$

where P is the radiation intensity, $S_y(\omega)$, $C_x(\omega)$ and $C_y(\omega)$ can be consistently expressed by components of the tensors $\hat{\gamma}$ and $\hat{\chi}$ defined in Eq. (2). Thus, CPGE ($S_y(\omega)\sin\theta\sin 2\varphi$) can only be generated at oblique incidence and in the direction normal to the plane of incidence, as observed in the experiments.

The (013)-oriented QWs belong to the trivial point group C_1 lacking any symmetry operation except the identity. In this case, all components of the pseudotensor γ and the tensor χ may be different from zero and are independent. For the C_1-symmetry group, the photogalvanic current for the normal excitation with elliptically polarized light is given by

$$j_\lambda/P = S_\lambda(\omega)\sin 2\varphi + b_\lambda(\omega)\sin 4\varphi + c_\lambda(\omega)\cos 4\varphi + d_\lambda(\omega). \quad (5)$$

where $S_\lambda(\omega)$, $b_\lambda(\omega)$, $c_\lambda(\omega)$ and $d_\lambda(\omega)$ can be also expressed by components of the tensors $\hat{\gamma}$ and $\hat{\chi}$ defined in Eq. (2). Exactly this polarization dependence is encapsulated in Eq. (1) and observed in experiment (the inset on Fig. 2).

Shown in Fig. 3 are the temperature and wavelength dependences for (013)-grown QW structure. All components of $\hat{\gamma}$ and $\hat{\chi}$ contribute substantially and the CPGE photocurrent direction is arbitrary and not forced to a definite crystallographic axis.

Conclusions

Our experiments show that helicity-driven photogalvanic currents can effectively be generated in HgTe quantum wells of about an order of magnitude larger than that observed in GaAs, InAs and SiGe low dimensional structures [2]. Our results reveal that photogalvanic measurements open a rich field for investigation of microscopic properties of this novel and promising material.

Acknowledgements

We thank E. L. Ivchenko for helpful discussions. The financial support of the DFG (programs WE2476/9-1 and AS327/2-1), the BMBF and RFBR is gratefully acknowledged.

References

[1] S. D. Ganichev and W. Prettl. Intense Terahertz Excitation of Semiconductors, Oxford University Press, 2006.

[2] E. L. Ivchenko and S. D. Ganichev, *Spin Photogalvanics* in *Spin Physics in Semiconductors*, ed. M. I. Dyakonov, (Springer, Berlin, 2008).

[3] E. L. Ivchenko, *Optical Spectroscopy of Semiconductor Nanostructures* (Alpha Science International, Harrow, UK, 2005).

18th Int. Symp. "Nanostructures: Physics and Technology"
St Petersburg, Russia, June 21–26, 2010

Optically active acoustical plasmons in a gated two-dimensional electron system with lateral contacts

V. V. Popov and O. V. Polischuk
Kotelnikov Institute of Radio Engineering and Electronics (Saratov Branch) RAS, 410019 Saratov, Russia

Abstract. We designed a transistor structure ensuring strong coupling between incoming terahertz radiation and acoustical plasmons in two-dimensional electron channel. Acoustic plasmon resonances with strong intensity and vanishing radiative linewidth are excited in such a structure.

Plasmons in two-dimensional electron gas (2DEG) with gate electrode (so called gated plasmons) can be used for creating compact frequency-selective and electrically tunable detectors of terahertz (THz) radiation. For small separation between the gate electrode and 2DEG, the gated plasmons exhibit acoustical (linear) dispersion [1]

$$\omega_{\rm p} = \left(\frac{eU_0}{m^*}\right)^{1/2} q, \qquad (1)$$

where $\omega_{\rm p}$ and q are the plasmon frequency and the plasmon wavevector, respectively, U_0 is the difference between the gate voltage and the threshold voltage of the 2DEG depletion, e and m^* are the electron charge and effective mass, respectively. The plasmon wavevector q is determined by geometrical length of the gate electrode l, which is typically three orders of magnitude shorter than the THz wavelength.

Resonant enhancement of the plasmon electric field in 2DEG at the plasmon resonance triggers various types of 2DEG nonlinearities, which can be used for detection of THz radiation with tunable detection frequency. One of the promising plasmon-nonlinearity mechanisms in 2DEG is hydrodynamic nonlinearity [1]. Detection of THz radiation at the plasmon resonance in transistor structures with 2DEG channels have been experimentally demonstrated in [2,3]. Since the plasmon phase velocity considerably (by two orders of magnitude) exceeds the electron transfer velocity in 2DEG, plasmonic detectors are much faster than electronic THz detectors [4].

Electrical tunability of the gated plasmon frequency makes this type of plasmons very attractive for frequency tunable detection of THz radiation. Along with a broadband tunability, an important parameter of such a detector is the plasmon resonance linewidth which determines the selectivity of the plasmonic detector. The plasmon resonance linewidth is determined by all possible mechanisms of the plasmon damping in 2DEG. The electron scattering contribution to the total linewidth of the plasmon resonance (at a half-maximum of its amplitude) is equal to $1/2\pi\tau$, where τ is the electron scattering time, which yields 0.01–0.1 THz at temperatures 4–77 K in 2DEG with high electron mobility. Radiative broadening of the plasmon resonance linewidth is related to emission of the electromagnetic waves from 2DEG by plasma oscillations, which is determined by the oscillator strength of a respective plasmon mode. Hence, excitation of narrow while intensive plasmon resonances is a controversial task because large oscillator strength of a plasmon mode, which is required for strong coupling between this mode and incoming THz radiation typically leads to considerable radiative broadening of the plasmon resonance. The gated plasmon modes have vanishing radiative damping due to acoustic (quadrupole) nature of those modes. Therefore, the excitation of intensive gated plasmon modes by incoming THz radiation is a challenging problem of coupling a tiny quadrupole to a plane THz wave.

In previous studies, the gated plasmon resonances have been observed mainly in commercial high-frequency heterotransistors with 2DEG channels. Typically, such a heterotransistor has a short gate electrode with length about 50–200 nm while there is much longer distance (of an order of the micron) between the source and drain lateral contacts [2,3]. The intensity of excitation of the gated plasmon resonances in such a structure by incoming THz wave is very weak. Therefore, the gated plasmon resonances are not exhibited in the THz absorption spectrum of such a heterotransistor since weak gated plasmon resonances merge into the background of much stronger absorption caused by resonances of the inter-contact plasmons (having much greater oscillator strength) as well as by the Drude free-electron absorption in long ungated access regions of the 2DEG channel [7]. Nevertheless, the gated plasmon resonances can be observed in the THz photoresponse spectrum of a heterotransistor. Because the photovoltage induced between the source and drain contacts of a heterotransistor by incoming THz wave appears due to nonlinear properties of the gated region of the 2DEG channel, peaks of the photovoltage are exhibited at the gated plasmon resonance excitation frequencies [2,3]. As demonstrated in [3], the gated plasmon resonance linewidth in the photoresponse spectrum of the heterotransistor with 2DEG channel exceeds the contribution caused by the electron scattering in the channel by an order of magnitude. This broadening of the plasmon resonance linewidth can be explained by the scattering of the gated plasmons at the ends of the gated portion of the channel, which results in excitation of the inter-contact plasmons in long ungated access regions of the 2DEG channel (so called inter-mode plasmon-plasmon scattering) [5,8]. Naturally, such tremendous broadening of the plasmon resonance linewidth might vastly deteriorate potentially high frequency selectivity of THz plasmonic detectors.

In this paper, we theoretically show that strong gated plasmon resonances can be excited by incoming THz wave if the entire 2DEG between the lateral (source and drain) contacts is screened by the gate electrode (see the inset in the Figure). In such a structure, the plasmon resonance linewidth shrinks down to the minimal value determined by the electron scattering in 2DEG.

We calculated the THz absorption spectrum in the structure shown in the inset of the Figure using the first-principle electromagnetic approach developed in [7] for parameters typical for InAlAs/InGaAs/InP heterotransistor structure with 2DEG

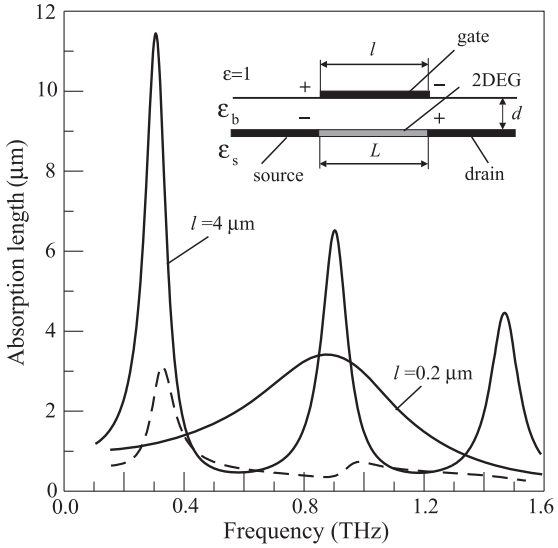

Fig. 1. The characteristic absorption length of the screened 2DEG with lateral contacts as a function of the incident THz wave frequency for different lengths of the gate electrode. Parameters of the structure are specified in the text. Dashed curve corresponds to the structure with an infinite 2DEG (without side contacts) for $l = 4$ μm. The structure under consideration is schematically shown in the inset, where the electric charges induced at the edges of the metal contacts of the structure by incident THz wave are marked. External THz wave is incident upon the structure from the top.

density $N = 3 \times 10^{12}$ cm^{-2} and geometrical dimensions $L = 4$ μm, $d = 40$ nm. We consider the normal incidence of a plane uniform THz wave upon the gated 2DEG with the electric field of this wave directed across the gate-electrode strip (i.e., in the source-to-drain direction). In this approach, the plasmon energy dissipation in 2DEG is taken into account by introducing a phenomenological electron scattering time $\tau = 2.3 \times 10^{-12}$ s in the expression for a Drude-type high-frequency sheet conductivity of 2DEG, while the radiative damping of plasmons is taken into account self-consistently by solving the equations of electromagnetism.

Figure shows the calculated characteristic absorption length as a function of the THz wave frequency. For the gate length much shorter than the length of the entire 2DEG channel between the source and drain contacts ($l \ll L$), a broad absorption resonance line originating from excitation of the inter-contact plasmons [7] in the entire 2DEG channel between the source and drain contacts emerges (the curve corresponding to $l = 0.2$ μm in the Figure). Since the contribution of the electron scattering to the total linewidth of the plasmon resonance is $1/2\pi\tau \approx 0.08$ THz, almost the entire linewidth of the inter-contact plasmon resonance ($\Delta f \approx 0.65$ THz) is caused by the radiative broadening of the plasmon resonance.

The plasmon resonance line moves toward low THz frequencies with increasing the gate length because the longer gate electrode stronger screens the plasma oscillations in the channel. Intensity of the fundamental plasmon resonance increases by a factor of three in the totally screened 2DEG as compared to that for $l = 0.2$ μm. Also, strong higher-order plasmon resonances appear at the high frequency side of the fundamental plasmon resonance line. The plasmon resonance lines become narrower with increasing the gate length. In the structure with the totally screened 2DEG ($l \approx L$), the plasmon resonance linewidth shrinks down to the value $1/2\pi\tau$ determined by the electron scattering in the 2DEG channel.

It is worth mentioning that the absorption length at the plasmon resonance in the structure with the totally screened 2DEG channel with lateral contacts exceeds a geometrical length of the channel, L, roughly by a factor of three. However, the absorption length at the plasmon resonance in a similar structure without side lateral contacts (i.e., in the structure with infinitely long 2DEG channel) is shorter than a geometrical length of the channel roughly by a factor of 1.5 (dashed curve in the Figure).

The fundamental as well as higher-order plasmon resonances are effectively excited in the totally screened 2DEG with side lateral contacts because the symmetry of electric charges induced at the edges of the metal contacts in such a structure by incident THz wave is the same as that in the gated plasmon mode (see the inset in the Figure). This principle of a quadrupole-plasmon-mode excitation can be possibly realized in a design of the transistor structure with lateral contacts in the form of bow-tie antenna [9].

In conclusion, we have shown that strong and narrow plasmon resonances can be excited in the totally screened 2DEG with side lateral contacts at THz frequencies. These results pave the way to fabrication of compact electrically tunable THz plasma-wave detectors with high selectivity and high sensitivity.

Acknowledgements

This work has been supported by the GDR-E project "Semiconductor Sources and Detectors for Terahertz Frequencies", by the Russian Foundation for Basic Research (Grant Nos. 08-02-92497 and 09-02-00395), and by the Russian Academy of Sciences Program "Fundamentals of Nanotechnology and Nanomaterials".

References

[1] M. Dyakonov *et al*, *IEEE Trans. Electron Devices* **43**, 380 (1996).
[2] W. Knap *et al*, *Appl. Phys. Lett.* **80**, 3433 (2002).
[3] A. El Fatimy *et al*, *Appl. Phys. Lett.* **89**, 131926 (2006).
[4] V. M. Muravev *et al*, *JETP Letters* **90**,197 (2009).
[5] V. V. Popov *et al*, *J. Appl. Phys.* **98**, 033510 (2005).
[6] V. V. Popov *et al*, *Int. J. High Speed Electronics and Systems* **17**, 557 (2007).
[7] V. V. Popov *et al*, *J. Appl. Phys.* **104**, 024508 (2008).
[8] V. V. Popov *et al*, *Appl. Phys. Lett.* **93**, 263503 (2008).
[9] A. A. Eldek *et al*, *Microwave Opt. Technol. Lett.* **43**, 123 (2004).

18th Int. Symp. "Nanostructures: Physics and Technology"
St Petersburg, Russia, June 21–26, 2010

Terahertz electroluminescence of surface plasmon-polaritons from nanostructured InN

T. V. Shubina[1], A. V. Andrianov[1], V. A. Shalygin[2], N. A. Gippius[3,4], A. O. Zakhar'in[1], V. N. Jmerik[1], I. P. Soshnikov[1], T. A. Komissarova[1], A. A. Usikova[1], A. N. Sofronov[2], D. A. Firsov[2], L. E. Vorob'ev[2], J. Leymarie[4], X. Wang[5], A. Yoshikawa[6], P. S. Kop'ev[1] and S. V. Ivanov[1]

[1] Ioffe Physical-Technical Institute, St Petersburg, Russia
[2] St Petersburg State Polytechnical University, St Petersburg 195251, Russia
[3] General Physics Institute RAS, Moscow 119991, Russia
[4] LASMEA-UMR 6602 CNRS-UBP, 63177 AUBIERE CEDEX, France
[5] Peking University, Beijing 100871, China
[6] Chiba University,1-33 Yayoicho, Inage-ku, Chiba 263-8522, Japan

Abstract. InN possessing electron concentrations of $10^{18} - 10^{19}$ cm^{-3} behaves at terahertz frequencies as a metal in an optical range; it makes possible supporting of surface plasmon modes in thin layers. We report on terahertz radiation with the maximum at the 2.8–5 THz recorded under electrical pumping from InN epilayers, where structural imperfections, such as nanocolumns, pores, and In clusters, are situated with a certain periodicity. The THz spectra are well consistent with the spontaneous emission of surface plasmon polaritons, which are excited thermally and coupled with electromagnetic field at these imperfections.

The electrically pumped compact sources of terahertz (THz) radiation could be useful for many applications in medicine, defect diagnostics and antiterrorism control. However, currently developed systems possess certain shortcomings that hampers their commercial production [1]. This implies a search of new approaches and materials suitable for the THz generation. Among others, there is a certain interest to InN which must possess superior carrier mobility and saturation drift velocity, in accordance with theoretical predictions [2]. The THz radiation from InN under optical pumping has been recently demonstrated and ascribed to a photo-Dember effect [3].

We report on terahertz radiation under electrical pumping from nanostructured InN. Our approach exploits the inherent properties of InN, namely: the high electron concentration and its tendency to formation of structural imperfections, such as nanocoloumns, trenches, metallic clusters, which are frequently situated with a certain periodicity. Due to the high carrier concentrations of $10^{18} - 10^{19}$ cm^{-3}, surface plasmon polaritons can be excited in thin InN layers and transformed into THz radiation at these imperfections. The thermal excitation of the plasmons by electrical pumping follows the increase of electron temperature.

The extended surface plasmons in InN differs from the localized plasmons in metallic In nanoparticles, whose resonance energies are in visible and near infrared ranges [4]. In general, the surface plasmons cannot radiate because their wave vector q is always much larger than that of photon of same frequency. Plasmon coupling with an electromagnetic wave requires the momentum exchange that can be done at spontaneous gratings formed by the imperfections. The coupling condition corresponds to $q \approx 2\pi m/a$, where a is the grating period. Modeling based on solving the Maxwell equations for a multiple-layer system [5] shows that the thickness of a plasmonic layer, d, should be as thin as 5–25 nm to support the plasmon-polaritonic modes. In this case, the conditions $[qd, qa] \ll 1$ are fulfilled to provide the emission characteristic frequencies in the range of 1–10 THz, recorded in our experiments. It might be realized if the plasmons are excited in a surface ("accumulation") layer or thin conducting regions inside a damaged InN matrix.

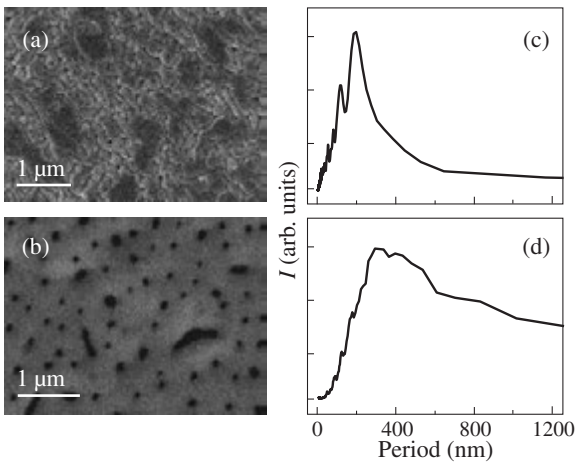

Fig. 1. Scanning electron microscopy images (a,b) with respective distributions of the distance between imperfections (c,d) in two representative InN samples.

Wurtzite InN epilayers with thickness of 1–3 μm were grown by plasma-assisted molecular beam epitaxy on c sapphire atop GaN buffers. These layers have morphology abundant in different structural imperfections. The trenches between nanocolumns and pores, frequently decorated by metallic nanoparticles, are common objects (Fig. 1). The Fourier transformation of images obtained by scanning electron microscopy (SEM) has shown that the statistical distribution of the distance between these imperfections has a peak which corresponds to a most frequent period varied from 0.15 to 1.20 μm along an axis in different samples.

The THz electroluminescence spectra were measured at 8 K as described elsewhere [6]. The emission was excited by the series of packets of rectangular pulses (15 V pulse height, 10 μs duration, 71.5 Hz reputation rate) passing through contacts formed on top surface of 4–6 mm long samples. The registered spectra has a complicated shape with the frequency of their maximum changed in the 2.8–5 THz range [7,8]. This frequency variation is an important feature, since the energies

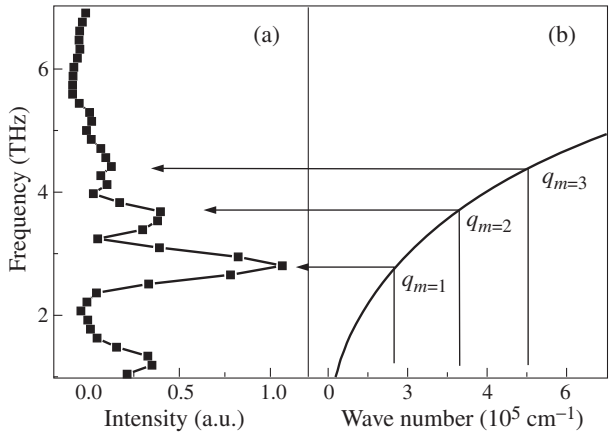

Fig. 2. (a) Spectrum of THz radiation measured in a sample with the grating period $a \sim 0.4$ μm; (b) plasmon frequency dispersion calculated assuming electron effective mass $m^* = 0.07m_0$, permittivity $\varepsilon_0 = 14\varepsilon$, and the thickness of the interior plasmonic layer $d \sim 0.01$ μm (for the surface layer, d should be ~ 0.005 μm). The electron concentration $N = (1.2 - 1.5) \times 10^{18}$ cm^{-3} is taken twice higher than the averaged Hall concentration measured in this sample.

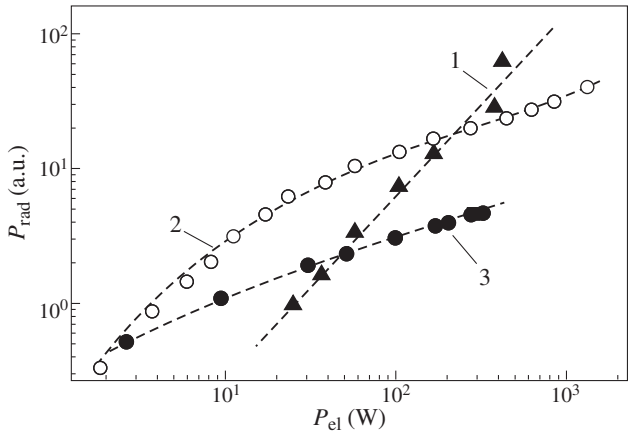

Fig. 3. The dependences of the THz radiation power (collected in the 3–5 THz range) on applied electric power in different structures: 1 — 1.3-μm thick InN sample [7]; 2 — 4-μm thick GaN layer [9]; 3 — n-doped structure with GaAs/AlGaAs quantum wells [10].

of the THz emission induced, e.g., by the electron transitions between levels of impurities are stable [6,9]. In our samples, the emission frequency increases with the decrease of the average period and the increase of the carrier concentration. Such a behavior is well consistent with the emission of grating-coupled surface plasmons. Figure 2 illustrates that presenting a THz spectrum measured in an InN sample together with the calculated plasmon frequency dispersion. This spectrum contains the series of well pronounced peaks. For the sake of demonstrativeness, we connect these peaks with the dispersion curve. The corresponding wave vectors are well consistent with the values calculated for the m-order scattering with $a \sim 0.4$ μm determined by the SEM study. As a rule, the spontaneously formed gratings and, hence, THz spectra are more complicated; variation of a along a layer provides additional peaks. Nevertheless, these spectra can be successfully modeled as well, taking into account the statistical distribution of the grating periods.

It is interesting to compare the dependence of the integral THz luminescence intensity on the applied electric power in the nanostructured InN with that in other material systems. Such a comparison with n-GaN epilayers and n-GaAs/AlGaAs quantum well structures is illustrated by Fig. 3. The comparative measurements were performed in the same conditions at $T = 4.2$ K with similar pulse excitation [7–10]. The same Ge:Ga photoresistor sensitive in the 60–110 μm spectral range was used; and the sizes of active region were almost equal for all the samples. In the n-GaN epilayers, the THz electroluminescence is mostly caused by the intracenter $2p$-$1s$ donor transitions at electric powers less than 20 W [9]. This mechanism provides more intensive THz electroluminescence in n-GaN than plasmon-related mechanism in n-InN. At powers exceeding 50 W, intraband optical transitions of hot electrons contribute mostly to THz emission in n-GaN with the power dependence of the integral THz luminescence intensity being $P_{\rm el}^{1/3}$. The n-GaAs/AlGaAs quantum well structures exhibit the similar dependence but with weaker intensity [10]. On the other hand, we observed much stronger power dependence of the THz luminescence intensity in n-InN; it was roughly proportional to $P_{\rm el}^{3/2}$. That is well consistent with the thermal excitation model described in [11]. As a result, the THz radiation from n-InN exceeds in intensity that from other structures at high enough applied electric power (>200 W). It is worth noting that the thermally-induced plasmonic radiation in polar materials can be enhanced by several orders of magnitude as compared with emission involving hot individual electrons and keeps coherence up to room temperature [12].

In conclusions, we have shown that surface plasmon polaritons can radiate in the THz range in nanostructured n-InN layers possessing certain periodicity in position of various structural imperfections. Spectra shape and characteristic frequencies are influenced by structure morphology. We believe that the yield of the radiation could be increased using specially designed periodical structures. Our findings make InN promising for portable THz emitters.

Acknowledgements

We thank S. Mihailov for fruitful discussions and W. J. Schaff for reference sample supplying. This work has been supported in part by the RFBR (grants 10-02-00633, 10-02-91767, 08-02-00162, and 07-02-91021) and the Program of the Presidium of RAN.

References

[1] M. Tonouchi, *Nature Photonics* **1**, 97 (2007).
[2] S. K. O'Leary *et al*, *Appl. Phys. Lett* **88**, 152113 (2006).
[3] R. Ascazubi *et al*, *Appl. Phys. Lett.* **84**, 4810 (2004).
[4] T. V. Shubina *et al*, *Phys. Rev. B* **79**, 153105 (2009).
[5] E. N. Economou *et al*, *Phys. Rev.* **182**, 539 (1969).
[6] A. V. Andrianov *et al*, *JETP Letters* **79**, 448 (2004).
[7] T. V. Shubina *et al*, *Physics-Uspekhi* **179**, 1007 (2009).
[8] T. V. Shubina *et al*, *Bulletin of the Russian Academy of Sciences: Physics* **74**, 61 (2010).
[9] V. A. Shalygin *et al*, *J. Appl. Phys.* **106**, 123523 (2009).
[10] V. A. Shalygin *et al*, *Bulletin of the Russian Academy of Sciences: Physics* **74**, 86 (2010).
[11] R. A. Hopfel *et al*, *Phys. Rev. Lett.* **49**, 1667 (1982).
[12] J.-J. Greffet *et al*, *Nature* **416**, 416, 62 (2002).

18th Int. Symp. "Nanostructures: Physics and Technology"
St Petersburg, Russia, June 21–26, 2010

Manifestation of resonant impurity states in terahertz photoconductuvity of GaAs/AlGaAs quantum wells

D. A. Firsov[1], V. A. Shalygin[1], V. Yu. Panevin[1], G. A. Melentyev[1], *A. N. Sofronov*[1], M. Ya. Vinnichenko[1], L. E. Vorobjev[1], A. V. Andrianov[2], A. O. Zakharyin[2], V. S. Mikhrin[2], A. P. Vasil'ev[2], A. E. Zhukov[3], L. V. Gavrilenko[4], V. I. Gavrilenko[4], A. V. Antonov[4] and V. Ya. Aleshkin[4]

[1] St Petersburg State Polytechnical University, 195251 St Petersburg, Russia
[2] Ioffe Physical-Technical Institute, St Petersburg, Russia
[3] St Petersburg Academic University, St Petersburg, Russia
[4] Institute for Physics of Microstructures, 603950 Nizhny Novgorod, Russia

Abstract. The spectra of lateral photoconductivity under terahertz excitation and the emission spectra of terahertz radiation at lateral electric field were studied in GaAs/AlGaAs quantum well structures. It was shown that the features in emission spectra are connected with the electron transitions involving the resonant donor states. Spectral and polarization dependencies of photocurrent also reveal the features related to electron transitions from the ground impurity state to the resonant one. Calculations of electron energy spectrum and optical matrix elements confirm these suggestions.

Introduction

Resonant impurity states in semiconductors and semiconductor nanostructures are promising in the development of solid-state emitters of infrared and terahertz radiation. For the first time it was demonstrated in the laser on stressed p-Ge [1] where terahertz emission related to optical transitions of holes between localized and resonant acceptor states was observed. In this case resonant impurity states arise due to external mechanical stress. Resonant states can also appear in quantum wells [2–4] as a result of size quantization. Experimentally, the existence of the resonant donor states in quantum wells were demonstrated in the measurements of terahertz absorption in superlattices [5].

The present work is devoted to the studies of lateral photoconductivity and spontaneous emission at lateral electric field in terahertz spectral range in GaAs/AlGaAs quantum wells. Much attention is given to the influence of the resonant impurity states on these phenomena.

1. Experimental details

Samples for photoconductivity studies were MBE grown and consisted of 50 layers of 300 Å GaAs quantum wells separated with 70 Å $Al_{0.3}Ga_{0.7}As$ barriers. Quantum wells were doped in the central region, 40 Å doped layer was shifted from the center of the well to 60 Å. Electron surface density was 3×10^{10} cm^{-2}.

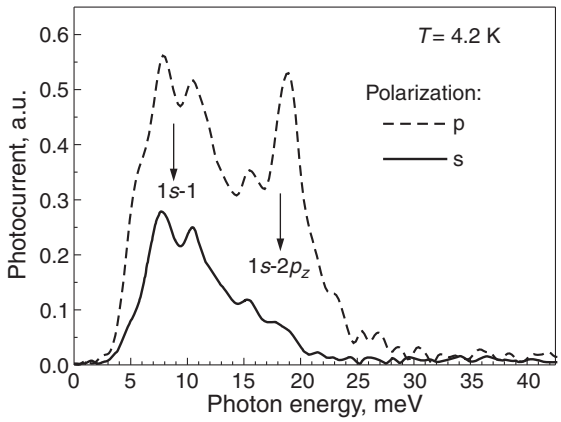

Fig. 1. Spectral dependencies of photocurrent for two polarizations of excitation. Energies of electron transitions calculated for symmetrically doped wells are shown by arrows.

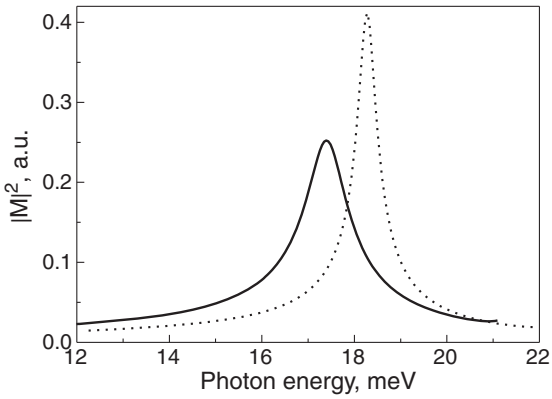

Fig. 2. Spectral dependencies of squared optical matrix element for $1s \rightarrow 2p_z$ dipole transitions and z-polarized light. Impurity shift from the well center is equal to 8 nm (solid line) and 4 nm (dotted line).

Photoconductivity spectra were obtained using Bruker Vertex 80v FTIR spectrometer operated in step-scan mode. Terahertz radiation from Hg lamp was focused on the sample using pipe waveguide and metal cone. Polyethylene film with 1200 lines/mm metal grating served as a polarizator. The sample was immersed in liquid helium. Terahertz radiation illuminated the 45° inclined sample side, so both p- and s-polarized terahertz radiation can be used for photoconductivity excitation. Light of s-polarization is polarized in the (x, y) plane of the structure, whereas polarization vector of p-polarized light contains both in-plane and z-components.

2. Results

Spectral dependencies of photocurrent are presented in Fig. 1. The relative values of photocurrent for p- and s-polarizations are determined with different intensities of excitation for these polarizations. Spectra for both p- and s-polarized light contain the wide peak with the center at 9 meV. We associate this peak with light absorption under electron transitions from donor $1s$ ground state to the first subband of size quantization $1s \rightarrow 1$. Absorption of this type should be polarized in the plane of the

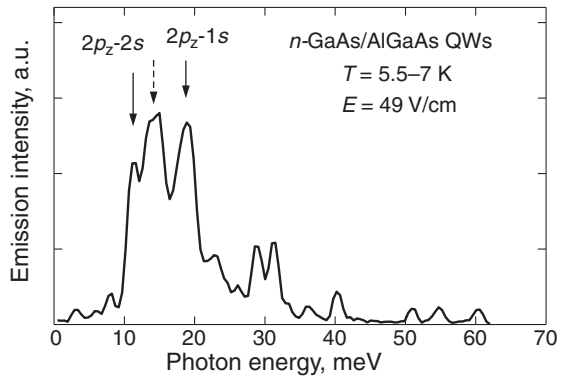

Fig. 3. Spectrum of spontaneous terahertz emission at lateral electric field.

structure due to the same symmetry of the wavefunctions of initial and final states. Calculations of electron energy spectrum in the structure with the central position of impurity atoms give the close value of 8.8 meV for the energy of this transition.

Photoconductivity spectrum for p-polarized light contains strong additional feature located close to 19 meV. It is apparent that this peak is related to the absorption of z-polarized light. Spectral position and polarization dependence of this peak indicate that it can be associated to optical electron transitions $1s \rightarrow 2p_z$ from the $1s$ ground state to resonant state $2p_z$ connected to second subband. It should be noted that the shift of impurity position from the center of quantum wells reduces the symmetry of electron states and allows the weak absorption of s-polarized light for the same $1s \rightarrow 2p_z$ transitions.

We also calculated optical matrix elements $|M|^2$ for electron transitions involving resonant impurity states. Results of the calculations of $|M|^2$ for z-polarized light are shown in Fig. 2. Calculation were carried out for two different positions of impurity atom in quantum well corresponding to boundaries of doped region in our sample. These data corresponds well to the experimentally obtained photoconductivity spectra.

It should be noted that X-ray analysis of our structure gives the value of well width of 28.8 ± 0.3 nm. It was taken into account under calculations.

Manifestation of the resonant states was also found in terahertz emission spectra. Spontaneous terahertz emission at different values of lateral electric field was studied in the structure with the same parameters but doped in the 100 Å layer in the center of each quantum wells. Number of wells in this structure was 200. Electron surface density in this structure was 10^{11} cm^{-2}.

The emission spectra (see Fig. 3) were measured using a Fourier spectrometer operating in step-scan mode, as described in [6]. Along with the feature connected with radiative electron transitions from the first subband to the ground impurity state (dashed arrow in Fig. 3) the spontaneous emission spectra reveal the peaks related to electron transitions from $2p_z$ resonant state to localized states $2p_z \rightarrow 1s$ and $2p_z \rightarrow 2s$ (solid arrows in Fig. 3). The latter peaks arise at high enough electric field corresponding to filling the resonant state. Spectral positions of these peaks correlate well with the results of calculations. To conclude, we reported the observation of resonant impurity states in photoconductivity and spontaneous emission spectra of GaAs/AlGaAs quantum well structures at lateral electric field.

Acknowledgements

Authors are grateful Yu. N. Drozdov for performing X-ray studies. This work was supported with the grants of Russian Foundation of Basic Researches and Russian Ministry of Education and Science. Support from the Linkage Grant of IB of BMBF at DLR is gratefully acknowledged.

References

[1] I. V. Altukhov, M. S. Kagan, V. P. Sinis, *JETP Lett.* **47**, 136 (1988).
[2] A. Blom, M. A. Odnoblydov, I. N. Yassievich, K. A. Chao, *Phys. Rev. B* **68**, 165338 (2003).
[3] V. Ya. Aleshkin, L. V. Gavrilenko, *JETP* **98**, 1174 (2004).
[4] N. A. Bekin, *Semiconductors* **39**, 439 (2005).
[5] M. Helm, *Phys. Rev. B* **43**, 13983 (1991).
[6] A. V. Andrianov, A. O. Zakhar'in, I. N. Yassievich, N. N. Zivov'ev, *JETP Lett.* **79**, 365 (2004).

18th Int. Symp. "Nanostructures: Physics and Technology"
St Petersburg, Russia, June 21–26, 2010

Coexistence of two types of microwave-induced resistance oscillations in 2D electron gas at large filling factors

A. A. Bykov[1], A. V. Goran[1] and S. A. Vitkalov[2]

[1] Institute of Semiconductor Physics, 630090 Novosibirsk, Russia
[2] The City College, City University of New York, New York 10031, USA

Abstract. The influence of microwave radiation (1–140 GHz) on resistance of 2D electron gas in GaAs quantum wells is studied. Two distinct series of microwave-induced magnetoresistance oscillations periodic in inverse magnetic field were observed under microwave radiation. The period of oscillations of first group is determined by the microwave frequency whereas the second group demonstrates a period, which depends on microwave power. We found that these two types of the microwave-induced resistance oscillations coexist in the 2D electron systems.

Introduction

Microwave-induced magnetoresistance oscillations of 2D electron gas in GaAs/AlGaAs heterostructures were recently discovered at large filling factors [1]. It was found that these oscillations are periodic in $1/B$ and oscillation peaks position is determined by ω/ω_c, where ω — microwave frequency and ω_c — cyclotron frequency in magnetic field B. This kind of oscillations was theoretically considered over 30 years ago [2]. However the experimental progress become to be possible mainly due to advances in technology of fabrication of high-quality modulation doped semiconductor structures. Moreover in high-mobility electron systems magnetoresistance oscillations was recently found with the period determined by microwave power [3], as opposed to [1] where the period is determined by ω/ω_c. This kind of microwave-induced oscillations at large filling factors was qualitatively explained by Zener tunneling between tilted Landau levels [4,5]. We found that these two types of the microwave-induced resistance oscillations coexist in the 2D electron systems.

1. Experimental setup

Our samples were cleaved from the wafers of the high-mobility GaAs quantum wells grown by solid source molecular beam epitaxy on semi-insulating GaAs substrates. The width of the GaAs quantum wells was 13 nm. AlAs/GaAs type-II superlattices served as barriers, which made it possible to obtain a high-mobility 2D electron gas with high electron density. In dark, the electron density and mobility of the 2D electron gas in our samples were $n_e = 1.18 \times 10^{16}$ m^{-2} and $\mu = 91$ m^2/V s, respectively. After brief light illumination, the electron density and mobility of the 2D electron gas in our samples were $n_e = 1.28 \times 10^{16}$ m^{-2} and $\mu = 111$ m^2/V s, respectively. Measurements were carried out at $T = 4.2$ K in magnetic field B up to 1 T on 50 μm wide Hall bars with distance of 250 μm between potential contacts. Microwave radiation in frequency region of (1–12) GHz was supplied to the sample through a coaxial cable and was fed to the 2D electron gas through current contacts of the Hall bars. Microwave radiation in frequency region of (37–140) GHz was supplied to the sample through a waveguide. The longitudinal resistance was measured using 1 μA current at frequency of (0.3–1) kHz.

2. Results und discussion

In Fig. 1 we present $R_{xx}(B)$ in the presence of microwave radiation of different power and frequency 140 GHz. It is clearly seen that the amplitude of Shubnikov–de Haas (SdH) oscillations is damped by microwave radiation. From the other hand, microwave radiation produces gigantic resistance oscillations. The analysis of the positions of these oscillations maxima shows that they are periodic in inverse magnetic field. Also, it is seen that there are several areas where the curves almost intersect. Two such areas are determined by the conditions: $\omega = \omega_c$ and $\omega = \omega_c/2$.

The stars in Fig. 1 denote the position of the highest maximum. Its position depends weakly on the microwave power. The weak dependence of the positions of the minima and the maxima in $R_{xx}(B)$ on the microwave power, as well as the intersection of the curves in the magnetic field determined by condition $\omega = \omega_c$, indicate that the oscillations shown in Fig. 1 are of the same nature as observed in [1]. This conclusion is also in full agreement with the observed dependence of the po-

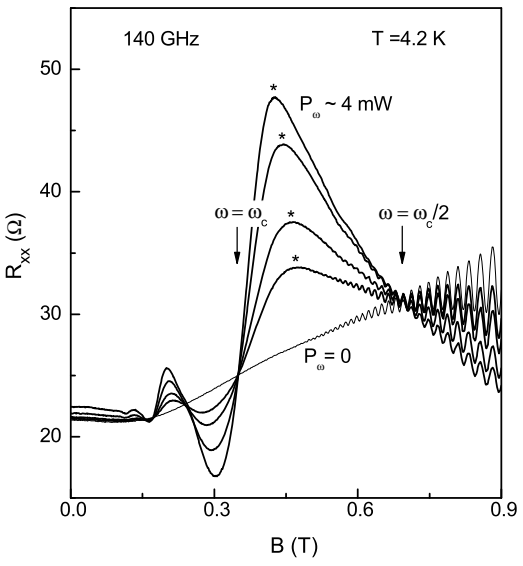

Fig. 1. Magnetoresistance R_{xx} with microwave (140 GHz) illumination on (thick line) and off (thin line) at $T = 4.2$ K for different levels of the oscillator output powers P_ω. The asterisks mark the highest maximum.

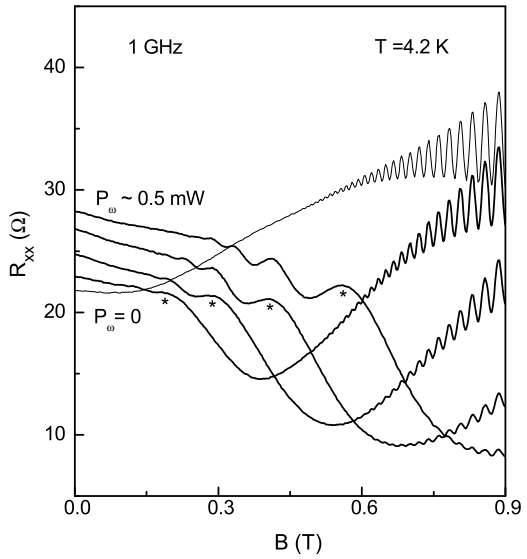

Fig. 2. Magnetoresistance R_{xx} with microwave (1 GHz) illumination on (thick line) and off (thin line) at $T = 4.2$ K for different levels of the oscillator output powers P_ω. The asterisks mark the highest maximum.

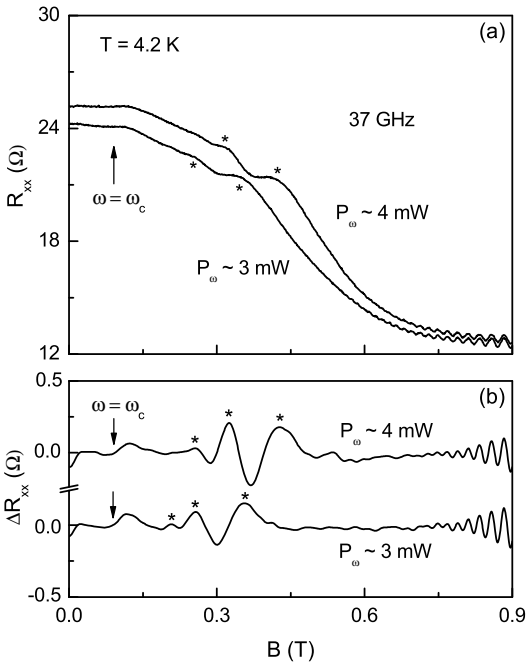

Fig. 3. (a) Magnetoresistance R_{xx} with microwave (37 GHz) illumination on at $T = 4.2$ K for two different levels of the oscillator output powers P_ω. The asterisks mark the maxima. (b) Dependences with subtracted monotonic component.

sitions of minima and maxima in magnetic field on microwave frequency. At temperature 4.2 K the lowest microwave frequency, at which this kind of the oscillations is detected in our samples, was 37 GHz.

In Fig. 2 we present $R_{xx}(B)$ for different power of the microwave radiation of frequency 1 GHz. It is seen that microwave-induced resistance oscillations appear at large filling factors, and their positions in magnetic field depend on the microwave power. The position of the highest maximum depends on the microwave power and is denoted by stars. These oscillations are periodic in $1/B$ similarly to the oscillations observed in microwave radiation of frequency 140 GHz.

In Fig. 3a we present $R_{xx}(B)$ dependence for two values of microwave power at frequency 37 GHz. Fig. 3b shows a coexistence of two kinds of oscillations at frequency 37 GHz. The position of the minimum and the maximum in magnetic field near $\omega = \omega_c$ (denoted by arrow) depends on the microwave frequency and does not depends on the power, while the position of the maxima denoted by stars move to higher magnetic fields with the power increasing.

In conclusion, we have shown the coexistence of two kinds of radiation induced $R_{xx}(B)$ oscillations in high-mobility 2D electron systems.

Acknowledgements

This work was supported by the Russian Foundation for Basic Research, INTAS and NSF.

References

[1] M. A. Zudov *et al*, *Phys. Rev. B* **64**, 201311(R) (2001).
[2] V. I. Ryzhii, *Fiz. Tverd. Tela (Leningrad)* **11**, 2577 (1969) [*Sov. Phys. Solid State* **11**, 2078 (1970)].
[3] A. A. Bykov *et al*, *Pis'ma Zh. Eksp. Teor. Fiz.* **81**, 348 (2005) [*JETP Lett.* **81**, 284 (2005)].
[4] C. L. Yang *et al*, *Phys. Rev. Lett.* **89**, 076801 (2002).
[5] A. A. Bykov *et al*, *Phys. Rev. B* **72**, 245307 (2005).

18th Int. Symp. "Nanostructures: Physics and Technology"
St Petersburg, Russia, June 21–26, 2010

Impurity photoconductivity relaxation in GaAs/InGaAsP and Ge/GeSi quantum well heterostructures

S. V. Morozov, K. V. Marem'yanin, A. V. Antonov, A. N. Yablonskiy, *L. V. Gavrilenko*, E. E. Orlova, I. V. Erofeeva, V. V. Rumyantcev and V. I. Gavrilenko

Institute for Physics of Microstructures RAS, 603950 Nizhny Novgorod, Russia

Abstract. In n-GaAs/InGaAsP and p-Ge/GeSi quantum well heterostructures excited by nanosecond narrow band pulses of THz radiation the relaxation times of the impurity photoconductivity were measured under different bias voltage.

Introduction

In last decades spectral characteristics and speed properties of impurity semiconductor far-infrared photoresponse have been investigated in details as applied to photodetectors. Nowadays there is a growing interest to the nonequilibrium phenomena and possibilities to produce the intraband population inversion in semiconductor nanostructures doped with shallow impurities. In order to design THz laser operating at the optical transitions involving shallow impurity states direct information on lifetimes of carriers both excited into continuum and captured by impurity excited states is required. In this paper we study the relaxation of impurity photoconductivity signal in n-GaAs/InGaAsP and p-Ge/GeSi quantum well (QW) heterostructures at $T = 4.2$ K excited by narrow band (0.2 cm^{-1}) tunable THz pulses of nanosecond duration.

1. Experimental details

GaAs/InGaAsP heterostructure under study (#4236) was pseudomorphically grown by MOCVD technique on GaAs(001) semi-insulating substrates and contained 30 periods of GaAs QWs 90 Å wide separated by 400 Å wide $In_{0.1}Ga_{0.9}As_{0.8}P_{0.2}$ barriers. The donor concentration measured by Hall effect was 3.3×10^{10} cm^{-2} per QW. Strained Ge/$Ge_{1-x}Si_x$ heterostructures with residual acceptors were CVD grown on Ge(111) substrates [1]. The structure #306 ($x = 0.12$) contained 162 Ge QWs 200 Å wide separated by 260 Å wide barriers and #308 one ($x = 0.09$) contained 81 Ge QWs 355 Å wide separated by 160 Å wide barriers. The residual acceptor concentration was about 10^9 cm^{-2} per QW.

The photoconductivity spectra were measured using BOMEM DA3.36 Fourier-transform spectrometer at $T = 4.2$ K. Two strip ohmic contacts 4 mm apart were deposited onto a sample surface 5 × 5 mm in size. The samples were biased by a d.c. voltage. Impurity photoconductivity spectra of GaAs/InGaAsP sample contain a broad band in between 30 and 100 cm^{-1} corresponding to transitions from the ground donor state into excited states and to the continuum (Fig. 1a). In the photoconductivity spectra of Ge/GeSi samples #306 and #308 broad band in between 20 and 40 cm^{-1} and around 60 cm^{-1} respectively were observed (Fig. 1b). The binding energy of shallow impurity is known to depend on the impurity position in QW [1, 2]. Due to the built-in strain in the Ge/GeSi heterostructures and the quantum confinement effect these spectra differ significantly from the impurity photoconductivity spectrum of bulk p-Ge where the maximum is located nearby 100 cm^{-1}.

Investigations of impurity photoconductivity relaxation kinetics were carried out at the excitation by THz pulses. The narrow-band THz difference frequency radiation was generated in GaP nonlinear crystal by mixing of two near IR laser beams [3]. The photoconductivity signal was registered with averaging by a digital oscilloscope with temporal resolution of 1 ns.

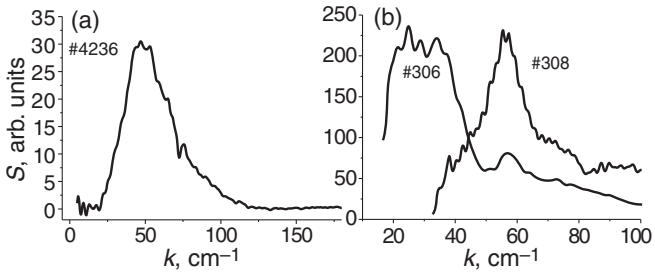

Fig. 1. Impurity photoconductivity spectra of GaAs/InGaAsP sample (a) and Ge/GeSi samples (b).

2. Results and discussions

Dependence of the photoresponse decay time on applied voltage in GaAs/InGaAsP sample and Ge/GeSi samples are given in Fig. 2–4. For all samples the increase of the bias voltage at first results in the rise of the decay time. We relate this effect within the mechanism of the cascade carrier capture by an ionized impurity due to emission of acoustical phonons with the carrier heating by the applied electric field as well as with the destruction in the electric field the excited impurity states [5]. The cascade acoustic phonon emission model of the carrier capture by ionized impurities [5] does not take into account the effect of impact ionization of shallow impurities. Note that in [4] we have not observed the relaxation time increase with the electric field prior to the impurity breakdown in n-GaAs/InGaAsP samples that can be attributed to broad-band THz excitation.

In the electric field exceeding the impurity breakdown one free hole concentration significantly increases and so the unperturbed concentration is rather high. Therefore relaxation time is determined by ionization rate that leads to the relaxation time drop with the further increase of the electric field [6, 7] that is just clearly seen in #306 sample (Fig. 3).

A detailed study of the relaxation time on the radiation frequency was undertaken in p-Ge/GeSi samples using tunable narrow-band THz difference frequency radiation pulses [3]. One can see in Fig. 3 that the observed decay time dependencies in the case of monochromatic excitation correspond fairly well to that obtained at the excitation by the broad band THz radiation [4]. As easy to see in Fig. 3 the maximum (versus bias voltage) relaxation time increases from 9 to 14 ns at the

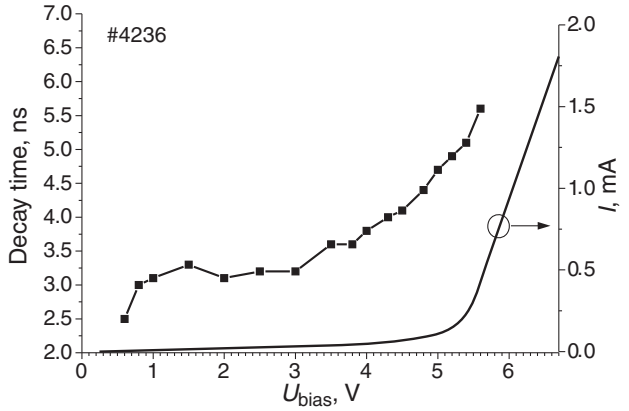

Fig. 2. I-V characteristics and photoresponse relaxation time for GaAs/InGaAsP sample versus bias voltage at $\nu = 60$ cm^{-1}.

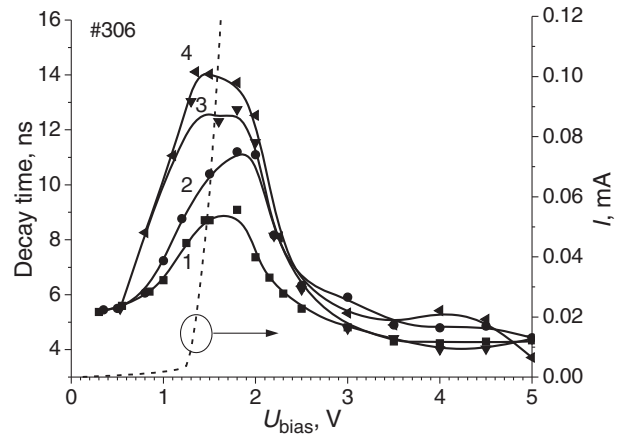

Fig. 3. Photoresponse relaxation time dependencies on narrow-band THz emission frequency (cm^{-1}) for Ge/GeSi sample (#306) versus bias voltage: (1) — 61 cm^{-1}; (2) — 42 cm^{-1}; (3) — 34 cm^{-1}; (4) — 25 cm^{-1}. The dashed line presents I-V characteristic.

radiation frequency decrease from 60 cm^{-1} down to 25 cm^{-1} for #306. This fact can be explained by a dispersion of shallow acceptor binding energies [1]. The frequency of 60 cm^{-1} nearly corresponds to the binding energy of acceptors situated nearby Ge QW center while that of 25 cm^{-1} corresponds to ionization energy for the hole (in Ge QW) bound with a remote acceptor ion in the center of GeSi barrier. We explain the observed larger relaxation time for the acceptor with lower binding energy (3 meV) by excited impurity states destruction in the electric field that results in fast cascade capture cancellation and switching to slow direct capture. Excitation frequency dependence is weaker in the sample #308 (from 6 to 9 ns at the radiation frequency decrease from 60 cm^{-1} down to 42 cm^{-1}) that can be explained by greater compensation for this sample. The compensation seems to be responsible for the narrower impurity band for the sample #308 if compared with #306.

Note that in the vicinity of impurity breakdown photoconductivity decay for sample #308 becomes more complicated than one-exponential decay and the second time scale (>100 ns) appears. As it was shown in [6] the excited states are responsible for second time scale of photoconductivity relaxation. More detailed on the long scale relaxation in #308 are given in [7].

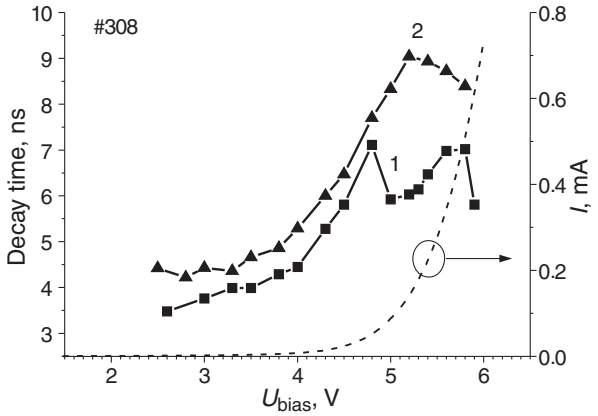

Fig. 4. Photoresponse relaxation time dependencies on narrow-band THz emission frequency (cm^{-1}) for Ge/GeSi sample (#308) versus bias voltage: (1) — 60 cm^{-1}; (2) — 42 cm^{-1}. The dashed line presents I-V characteristic.

Acknowledgements

This work has been supported by RFBR (Grant 10-02-00966), Russian Academy of Sciences, F.A.S.I. (Contract 02.518.11. 7133).

References

[1] V. Ya. Aleshkin, V. I. Gavrilenko, I. V. Erofeeva, A. L. Korotkov, D. V. Kozlov, O. A. Kuznetsov, M. D. Moldavskaya, *Phys. Stat. Sol.* (b) **210**, 649 (1998).

[2] A. A. Reeder, J.-M. Mercy, B. D. McCombe, *IEEE J. Quant. Electron.* **24**, 1690 (1998).

[3] V. Ya. Aleshkin, A. A. Antonov, S. V. Gaponov, A. A. Dubinov, Z. F. Krasil'nik, K. E. Kudryavtsev, A. G. Spivakov and A. N. Yablonskiy, *JETP Letters* **88** 787 (2009).

[4] S. V. Morozov, K. V. Marem'yanin, D. I. Kuritsin, S. M. Sergeev, A. V. Antonov, L. V. Gavrilenko, E. E. Orlova, I. V. Erofeeva, M. S. Joludev, V. I. Gavrilenko, *Journal of Physics: Conference Series* **193**, 012087 (2009).

[5] V. N. Abakumov, L. N. Kresshchuk and I. N. Yassievich, *Sov. Phys. Semicond.* **12**, 152 (1978).

[6] W. Quade, G. Hupper, E. Scholl, K. Kuhn, *Phys. Rev. B* **49**, 13408 (1994).

[7] S. V. Morozov, V. I. Gavrilenko, L. V. Gavrilenko, A. V. Antonov, K. V. Marem'yanin, A. N. Yablonskiy, D. I. Kuritsin, I. V. Erofeeva, S. M. Sergeev, V. V. Rumyantcev, *Proc. of Symposium "Nanophysics and Nanoelectronics 2010" Nizhniy Novgorod, Russia*, to be published.

18th Int. Symp. "Nanostructures: Physics and Technology"
St Petersburg, Russia, June 21–26, 2010

Negative refraction in one-dimensional photonic crystals

I. Iorsh[1], M. A. Kaliteevski[1,2], R. A. Abram[2] and S. Brand[2]

[1] St Petersburg Academic University, St Petersburg, Russia
[2] Durham University, UK

Abstract. We investigated the case of plane wave incident on the side-edge of semi-infinite Bragg reflector. We demonstrated the cases of positive refraction, negative refraction and normal channeling of light in high contrast PC. The effect of Poynting vector oscillation has been demonstrated in low contrast PC

Introduction

Negative refraction of light is widely discussed now both as an original physical phenomena and as a tool for creating new photonic devices. There are present discussions as to how negative refraction could be achieved for visible light. A few natural candidates for achieving this include metamaterials, plasmonic modes and photonic crystals [1]. Photonic crystals (PC) are artificial structures that show an extraordinary strong nonlinear dispersion at wavelengths close to the bandgap. Under certain conditions, they abnormally refract the light as if they had a negative refractive index [2]. Negative refraction has been observed in two-dimensional PC (2D-PC) into the microwave and infrared region [3]. Extensive numerical and experimental studies [4] have provided better understanding of negative refraction in photonic crystals. For instance, when light propagation in strongly modulated, 2D-PC becomes refraction-like in the vicinity of the photonic bandgap. Such a crystal behaves like a material having an effective refractive index controllable by the band structure. Boedecker and Henkel [5] found that the simple one-dimensional(1D) Kronig–Penney model provided an exactly soluble example of a photonic crystal with negative refraction. Recently it has been theoretically shown that negative refraction in 1D-PC may occur near the low frequency edge of the second and fourth bandgaps [6]. Moreover creating photonic crystals that exhibit negative refraction for visible light remains a major challenge because of fabrication difficulties and, up to today. In this paper we perform rigorous analysis of the electromagnetic field incident on the side edge of the infinite 1D-PC and show the possibility of negative refraction in the second photonic band for the high-contrast photonic crystals. We also demonstrate the new effect of normal channeling of light in the photonic crystals.

1. Problem formulation

We are considering plane, E-polarized electromagnetic wave incident on the side edge of the semi-infinite one-dimensional photonic crystal (Fig. 1). To solve the problem we should match the amplitudes of the incident, reflected and refracted waves at the interface. To describe the reflected wave we use the Rayleigh expansion and get the series of the plane waves (both propagating and evanescent). For electromagnetic wave in the PC we are considering the dispersion relation for the Bloch waves:

$$\cos(\mu d_1)\cos(\gamma d_2) - \frac{1}{2}\Big(\frac{\mu}{\gamma}+\frac{\gamma}{\mu}\Big)\sin(\mu d_1)\sin(\gamma d_2) - \cos(K_0 D) = f(\beta^2) = 0, \quad (1)$$

where $\mu^2 = n_1^2 k_0^2 - \beta^2$, $\gamma^2 = n_2^2 k_0^2 - \beta^2$, $k_0 = \omega/c$.

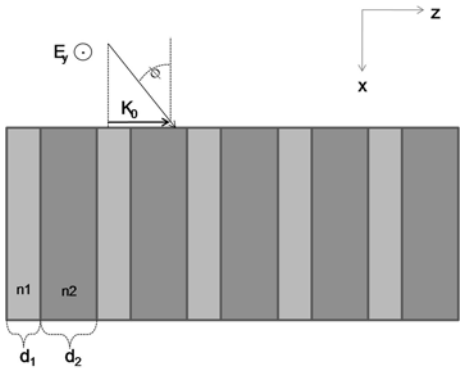

Fig. 1. $E(-)$polarized plane wave incident on the side edge of the semi-infinite Bragg reflector.

We then show (following [7]) that the solutions of this equation form the infinite set of real β^2 and that these solutions form the full set of the eigenvalues of the problem. We then construct the set of eigenfunctions corresponding to these eigenvalues and show that these eigenfunctions are the orthogonal basis in the solutions space. We derive the amplitudes of the modes of reflected and refracted waves by matching the fields at the interface and solving truncated linear system of equations. It is shown that if the frequency of the incident light lies in the second photonic band of the PC there will be only 2 eigenfunctions with real β. We further show that in the high contrast PC one mode is dominant over others (see Fig. 2).

2. Negative refraction and normal channeling

We are calculating component of the Poynting period perpendicular to the layers averaged over the period of the PC:

$$S_z = -\frac{1}{2}\Re\Big[\int_0^D [E_y H_x^*]dz\Big]. \quad (2)$$

We first consider the case of high contrast PC. In this case only one mode is dominant and we can include only one mode in the calculation of the Poynting vector. It makes the calculation simple and we get:

$$S_z = \frac{1}{2}\frac{c}{\omega}|a_{\rm m}|^2 \frac{\sin K_0 D}{\gamma\cos\mu d_1 \sin\gamma d_2 + \mu\sin\mu d_1\cos\gamma d_2}, \quad (3)$$

where $a_{\rm m}$ is the amplitude of the corresponding mode. We are interested in the function M which is a product of the Poynting vector and the Bloch vector K_0. The plot is of this function is depicted on Fig. 3.

The wave propagating from the interface corresponds to the real β. It can be seen on Fig. 2 that for the real β, product of

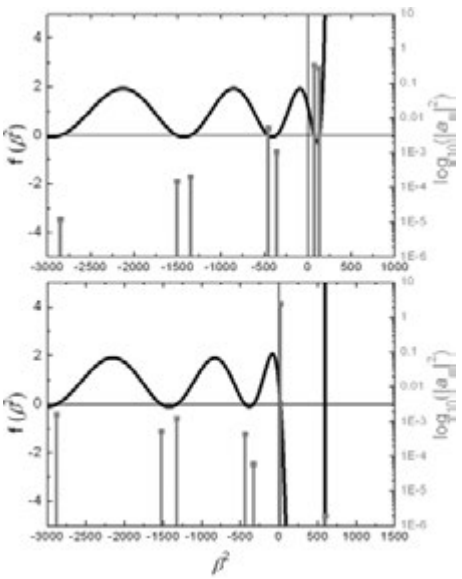

Fig. 2. Distribution of eigenvalues. gray lines show the relative amplitude of the according eigenmode. Upper image — low contrast PC, lower image — high contrast PC.

Poynting vector and Bloch vector can be positive negative or equal to zero. We have performed the FDTD simulations for all 3 cases. The results of simulations are depicted on Fig. 4. We can see that for the case of positive M we observe conventional positive refraction. In the case of negative M PC demonstrates left-handed material behavior and we observe negative refraction. In the case of $M = 0$ we can see that the light propagates normally to the interface along the layers of PC. We called this effect "resonant normal channeling". In the case of lower contrast both modes with real contribute to the field distribution in PC. So we should count 2 modes when we calculate the average Poynting vector. We show that the Poynting vector expression in this case will consist of 4 terms — 2 diagonal terms which are described by equation (3) for each mode accordingly and 2 intersection terms which will contain harmonic functions of x-coordinate and which phase will be proportional to the difference of eigenvalues of the 2 modes. We performed the FDTD simulation for the case when both diagonal terms are equal to zero. (since as it is clear from equation (3) roots of function M are equal for all modes) The result of calculation is depicted on Fig. 5.

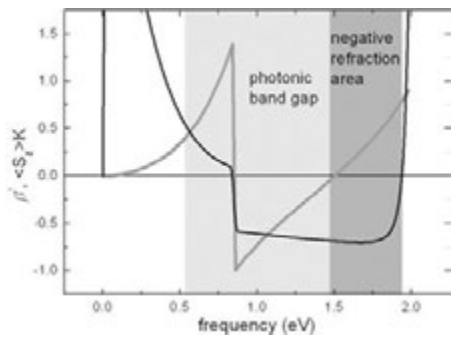

Fig. 3. Product of Bloch and Poynting vectors over frequency for high contrast PC. Eigenvalue is depicted with gray line.

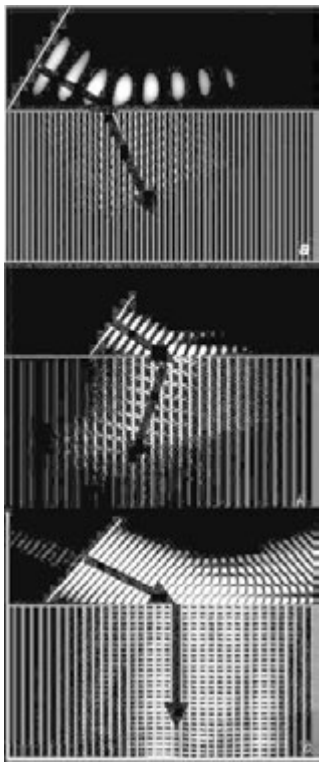

Fig. 4. FDTD simulations for high contrast PC. (a) — positive refraction case, (b) — negative refraction, (c) — resonant normal channeling. Arrow shows the direction of the Poynting vector.

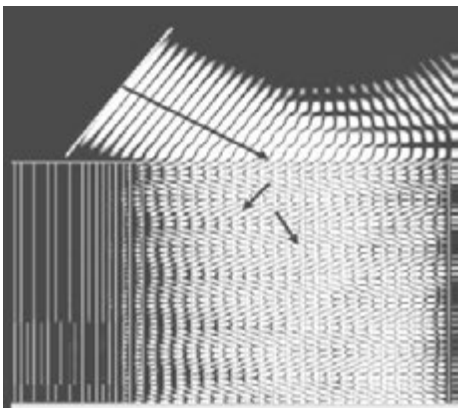

Fig. 5. FDTD simulation for low contrast PC. Arrows show the direction of Poynting vector.

3. Conclusion

It has been shown that the effect of negative refraction can be observed in 1D PC in high contrast PC — analytical conditions for observing this effect have been derived. New effect of resonant normal channeling of light has been predicted and observed. In the lower contrast PC effect of Poynting vector oscillation has been explained.

References

[1] A. V. Kavokin *et al*, *Phys. Lett. A* **339**, 387–392 (2005).
[2] P. V. Parimi *et al*, *Phys. Rev. Let.* **92**, 127401 (2004).
[3] E. Cubukcu *et al*, *Nature* **423**, 604 (2003).
[4] M. Notomi *et al*, *Opt. Quantum Electron* **34**, 133 (2002).
[5] G. Boedecker and C. Henkel, *Opt. Express* **11**, 1590 (2003).
[6] R. Srivastava *et al*, *Solid State Commun.* **147**, 157–160 (2008).
[7] I. C. Botten *et al*, *Journal of Modern Optics* **28**, 413–428 (1981).

18th Int. Symp. "Nanostructures: Physics and Technology"
St Petersburg, Russia, June 21–26, 2010

Terahertz plasmons in graphene nanoribbon arrays

V. V. Popov[1,2], T. Yu. Bagaeva[1], T. Otsuji[2,3] and V. Ryzhii[4,3]

[1] Kotelnikov Institute of Radio Engineering and Electronics (Saratov Branch), Saratov 410019, Russia
[2] Research Institute of Electrical Communication, Tohoku University, Sendai 980-8577, Japan
[3] Japan Science and Technology Agency, CREST, Tokyo 107-0075, Japan
[4] Computational Nanoelectronics Laboratory, University of Aizu, Aizu-Wakamatsu 965-8580, Japan

Abstract. We show that the plasmon frequencies in a one dimensional dense array of doped graphene nanoribbons can be changed through the entire terahertz range depending on the angle between the plasmon wavevector and the nanoribbon direction.

Graphene, a two-dimensional (2D) monolayer of graphite, has received a great deal of interest recently due to its unique electronic properties stemming from a linear (Dirac-type) gapless carrier energy spectrum in graphene $E = \pm V_F|\mathbf{p}|$, where E and $\mathbf{p}$ are the electron (hole) energy and momentum, respectively, and V_F is a band parameter (the 2D Fermi velocity, which is a constant for graphene), and upper and lower signs refer to the conduction and valence bands, respectively, [1,2]. Plasmons in intrinsic and doped graphene have been investigated lately [3–8]. The plasmon frequency is proportional to the square root of the plasmon wave vector for ungated graphene [4,6,7] and varies lineary with the plasmon wavevector for gated graphene [3,8] similar to plasmons in conventional (mostly semiconductor based) 2D electron systems (see, e.g., [9] in references therein). This is a consequence of general properties of the long-range Coulomb interaction defining the plasmon frequency in both types of 2D electron systems. However, in distinction from a conventional semiconductor 2D electron layer, the plasmon "inertia" in massless graphene is determined by a fictitious "relativistic" effective mass $m_F = E_F/V_F$, where E_F is the Fermi energy [6,8]. Because of that, the plasmon frequency in massless graphene is proportional to $N_s^{1/4}$, where N_s is the sheet electron density, whereas in conventional 2D electron systems the plasmon frequency is proportional to $N_s^{1/2}$. In intrinsic undoped graphene, plasma waves can exist only due to thermionic generation [5,7] or photogeneration [8,10] of free carriers in graphene.

When graphene is patterned into narrow ribbons, the carriers are confined in quasi-one-dimensional (1D) graph- ene nanoribbons (GNR) [11–13]. Although the band structure of a GNR differs for different, either armchair or zigzag types of the GNR [13], a common feature of the GNR is an energy gap opened due to carrier confinement. This band gap can be easily estimated for a relatively wide GNR under a hard-wall boundary condition. In this idealized case the energy spectrum is

$$E = \pm V_F\sqrt{p_\parallel^2 + n^2\left(\frac{\pi\hbar}{w}\right)^2} = \pm\frac{\Delta}{2}\sqrt{n^2 + \frac{2p_\parallel^2}{m^*\Delta}}, \qquad (1)$$

where $p_\parallel$ is the electron (hole) momentum along the GNR and w is the GNR width, $\Delta = 2\pi V_F\hbar/w$ is the energy gap between the conduction and valence bands, $m^* = \Delta/2V_F^2$ is the effective mass, and $n = 1, 2, 3, \ldots$ is the index of 1D subband in the GNR. Near the bottom of the conduction band and the top of the valence band ($n = 1$) the spectrum given by Eq. (1) is virtually quadratic $E = \pm(\Delta/2 + p_\parallel^2/2m^*)$. For $V_F \approx 10^8$ cm/s [1], formula $\Delta = 2\pi V_F\hbar/w$ reasonably well describes the experimental observations of $\Delta = (300-30)$ meV for GNR with the width of 15–90 nm [12]. Those energy band values correspond to the effective electron masses $(0.01 - 0.002)m_0$, where m_0 is the free electron mass. For narrower GNR with the width of nanometer order, this simple model yields $m^* \approx 0.1m_0$, which is very close to the effective mass of zigzag GNR calculated in a first-principle approach [13].

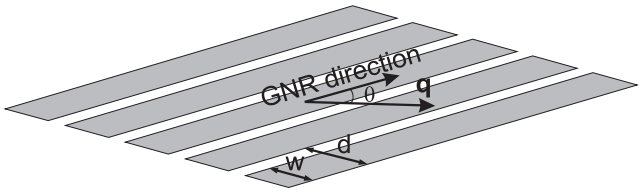

Fig. 1. Schematic of a graphene nanoribbon array.

Plasmons in GNRs, like plasmons in semiconductor nanowires [14], could be observed in optical experiments. A pertinent structure in this case could be a periodic array of GNR enhancing coupling between plasmons in GNR and electromagnetic field. In this paper, we consider plasmons in a 1D dense array of doped GNR. We show that the plasmon dispersion in such a system has a 2D plasmon form but the plasmon frequency depends on the angle between the plasmon wavevector and GNR with reducing the plasmon frequency by an order of magnitude and more at oblique angles.

Due to spatial confinement of carriers in GNRs, the macroscopic current in GNR array can flow only in the GNR direction (Fig. 1). In an actual optical experiment, the plasmon wavelength is dictated by the sample length, which is typically much longer than the period of GNR array and the width of GNR. In this case, the GNR array can be considered as a homogeneous 2D plane with anisotropic (tensor) sheet conductivity. Choosing the Cartesian coordinate system with x-coordinate axis directed along the plasmon wavevector, the sheet conductivity, $\hat{\sigma}$, of such dense GNR array can be described by a tensor

$$\hat{\sigma} = \sigma\begin{pmatrix}\cos^2\theta & \cos\theta\sin\theta\\ \cos\theta\sin\theta & \sin^2\theta\end{pmatrix}, \qquad (2)$$

where θ is the angle between the plasmon wavevector and the GNR direction and

$$\sigma = i\frac{e^2 N_{2D}}{m^*(\omega + i\nu)} \qquad (3)$$

is the Drude-type conductivity of the GNR array subject to the oscillating electric field $E\exp(-i\omega t)$ with ν being the electron

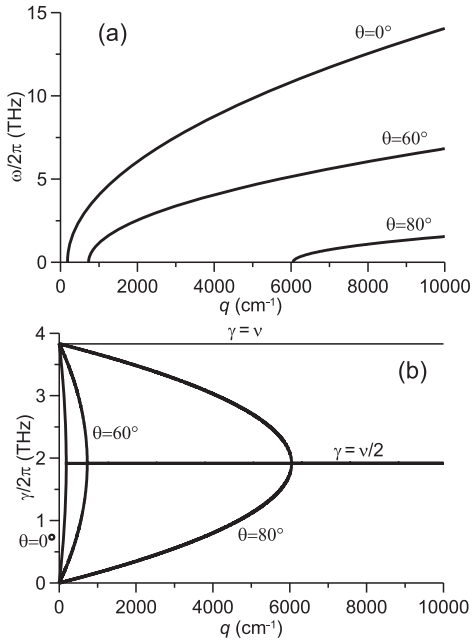

Fig. 2. (a) Plasmon dispersion $\omega/2\pi$ and (b) decay rate $\gamma/2\pi$ as functions of the plasmon wavevector for different values of angle θ and $\nu = 1.32 \times 10^{13}$ s^{-1} (electron mobility is 36000 cm^2/V s). Thin line $\gamma = \nu$ is given as the guide for an eye. Parameters of the GNR array are as follows: $m^* = 0.002m_0$, $N_{2D} = 10^{12}$ cm^{-2}.

relaxation rate in the GNR array. The sheet electron density in the GNR array is $N_{2D} = N_{1D}/d$, where N_{1D} is the 1D electron density in each GNR and d is the period of the GNR array. Because the energy gap inherent in GNR is typically much greater than the plasmon energy, the plasmons in the GNR array are not subject to interband absorption and, hence, the plasmon absorption is determined only by the intraband electron scattering rate entering Eq. (3).

In a quasi-electrostatic approximation, the dispersion relation for plasmons can be obtained by solving the Poisson equation and continuity equation with conventional boundary conditions. Such approach yields the following dispersion relation for plasmons in the GNR array

$$\widetilde{\omega} = \omega - i\gamma = \sqrt{\frac{2\pi e^2 N_{2D}}{\varepsilon m^*} q\cos^2\theta - \frac{\nu^2}{4}} - i\frac{\nu}{2}, \qquad (4)$$

where q is the plasmon wavevector and $\gamma = \nu/2$ is the plasmon relaxation rate due to its dissipation in the GNR array. The spectrum Eq. (4) is similar to that of 2D plasmons in a homogeneous 2D system with the sheet electron density N_{2D}. The plasmon frequency in the GNR array, however, vanishes for $\theta \to \pi/2$ according to the factor of $\cos\theta$. For typical parameters of GNR, $N_{2D} = 10^{12}$ cm^{-2} and $m^* = 0.002m_0$, formula Eq. (4) yields plasmon frequency about 6 THz for $\theta = 0$ (which decreases with increasing θ) for the plasmon wavelength about 30 microns.

In a quasi-electrostatic approach, the in-plane electric field E_{in} in the plasma wave is directed along the plasmon wavevector (i.e., at angle θ in respect to the GNR direction). The component of the in-plane electric field parallel to the GNR, $E_\parallel = E_{in}\cos\theta$, defines the restoring Coulomb force $eE_\parallel$ for electrons in GNR. Decrease of the restoring Coulomb force accounts for decreasing the plasmon frequency at oblique angles θ. Plasmons become overdamped [this corresponds to a purely imaginary plasmon eigen-frequency $\widetilde{\omega}$ in Eq. (4)] when $q < q_c$, where

$$q_c = \frac{1}{8\pi}\frac{\nu\varepsilon}{\sigma_0\cos^2\theta} \qquad (5)$$

with $\sigma_0 = e^2 N_{2D}/m^*\nu$.

Figure 2 demonstrates the plasmon frequencies and decay rates as functions of the plasmon wavevector. The cut-off plasmon wavevector q_c corresponds to the zero-frequency point of a dispersion curve $\omega(q)$. It is seen in Fig. 2 that the frequency of plasmons with the wavelength longer than ten microns can be tuned from 1 to 10 THz by changing the plasmon propagation angle θ. Experimentally, such plasmons could be excited in GNR arrays with tens-of-micron area by incident terahertz radiation with the electric field polarized in the plane of the GNR array. The plasmon frequency can be varied by changing the polarization of the electric field in incident terahertz wave in respect to the GNR direction.

In conclusion, we have shown that the plasmon frequency in a dense GNR array can reach terahertz range for relatively long plasmon wavelength comparable with terahertz wavelength. The frequency of plasmons in GNR array excited by incoming polarized terahertz radiation can be tuned through the entire terahertz-frequency band by changing the angle between the plasmon wavevector and the GNR direction.

Acknowledgements

This work has been supported by the Russian Foundation for Basic Research through grants 09-02-00395 and 08-02-92497 and by the Russian Academy of Science Program "Fundamentals of Nanotechnology and Nanomaterials". The work at Tohoku University and University of Aizu was supported by the Japan Science and Technology Agency, CREST and the Japan Society for Promotion of Science, Japan.

References

[1] K. S. Novoselov *et al*, *Nature* **438**, 197 (2005).
[2] M. I. Katsnelson, *Mater. Today* **10**, 20 (2007).
[3] V. Ryzhii, *Jpn. J. Appl. Phys.* **45**, L923 (2006).
[4] B. Wunsch *et al*, *New Journal of Physics* **8**, 318/15 (2006).
[5] O. Vafek, *Phys. Rev. Lett.* **97**, 266406 (2006).
[6] E. H. Hwang and S. Das Sarma, *Phys. Rev. B* **75**, 205418 (2007).
[7] L. A. Falkovsky and A. A. Varlamov, *Eur. Phys. J. B* **56**, 281 (2007).
[8] V. Ryzhii *et al*, *J. Appl. Phys.* **101**, 024509 (2007).
[9] V .V. Popov *et al*, *J. Appl. Phys.* **98**, 033510 (2005).
[10] F. Rana, *IEEE Trans. Nanotechnol.* **7**, 91 (2008).
[11] Y.-W. Son *et al*, *Nature (London)* **444**, 347 (2006).
[12] M. Y. Han *et al*, *Phys. Rev. Lett.* **98**, 206805 (2007).
[13] L. Yang *et al*, *Phys. Rev. Lett.* **99**, 186801 (2007).
[14] T. Demel *et al*, *Phys. Rev. Lett.* **66**, 2657 (1991).

18th Int. Symp. "Nanostructures: Physics and Technology"
St Petersburg, Russia, June 21–26, 2010

Terahertz luminescence under electron heating in modulation-doped AlGaN/GaN heterostructure

V. A. Shalygin[1], L. E. Vorobjev[1], D. A. Firsov[1], *A. N. Sofronov*[1], G. A. Melentyev[1], W. V. Lundin[2], A. E. Nikolaev[2], A. V. Sakharov[2] and A. F. Tsatsulnikov[2]

[1] St Petersburg State Polytechnic University, 195251 St Petersburg, Russia
[2] Ioffe Physical-Technical Institute, St Petersburg, Russia

Abstract. Emission of terahertz radiation from modulation-doped AlGaN/GaN heterostructures has been observed in lateral electric fields. Current-voltage characteristics measured at different temperatures have revealed significant electron heating of two-dimensional electrons at the AlGaN/GaN interface. The observed terahertz emission is considered in terms of the theory of blackbody-like radiation and the emissivity assuming a classical Drude conductivity of hot two-dimensional electrons.

Introduction

The development of effective and low-cost terahertz (THz) emitters is widely acknowledged as essential for the advancement of terahertz diagnostic and information technology applications in medicine and biology, chemistry and physics, nanotechnology, and other areas. In the past decade, gallium nitride has attracted much attention for applications in the electrically pumped terahertz THz emitters due to the unique combination of the high value of the electron drift velocity saturation, large energy of optical phonons, strong interaction of electrons with polar optical phonons, high electrical strength, high temperature stability, and good chemical resistance. The Monte Carlo simulation of the transit-time resonance in bulk zinc blende and wurzite GaN was performed in [1] and it has been demonstrated that this wide-gap semiconductor is very promising for generation of THz radiation, but as far as we know all experimental attempts to realize the transit-time resonance in bulk *n*-GaN have been unsuccessful due to deficient quality of the material. Recently THz electroluminescence from *n*-GaN epilayers was observed under conditions of impurity breakdown [2] when THz emission is mostly caused by the intracenter donor transitions. On the other hand, there is an opportunity to achieve intense THz emission from the same material by means of electron heating in high electric fields. From this point of view, two-dimensional electron gas (2DEG) in AlGaN/GaN heterostructures is very promising object for such studies because it demonstrates a large enhancement of electron mobility in comparison with bulk GaN [3] and therefore a significant electron heating can be realized.

In the present paper we report on the observation and study of spontaneous THz emission from modulation-doped AlGaN/GaN heterostructures under conditions of electron heating of 2DEG in lateral electric field. Complementary transport measurements were carried out to determine the dependence of effective electron temperature T_e on electric field.

1. Experimental technique

Samples were grown in standard AIX2000HT MOVPE reactor equipped with *in-situ* optical reflectance monitoring system. Ammonia, TMGa, TMAl, and SiH_4 were used as precursors, and H_2, N_2 and H_2:N_2 mixture were used as a carrier gas for various stages of growth as described below. Both samples were grown on (0001) sapphire substrates using low-temperature GaN nucleation layer.

Sample A is a standard HEMT structure consisting of 4 μm insulating GaN buffer, 1 nm AlN interface layer, 20 nm of modulation-doped $Al_{0.3}Ga_{0.7}N$ barrier, and 5 nm undoped GaN cap layer. For suppressing formation of a conductive layer at GaN/sapphire interface, GaN nucleation layer was annealed under hydrogen-free ambient, which results in quasi-2D growth mode of high-temperature GaN buffer from the beginning of growth [4]. Growth regimes for top of GaN buffer and AlN interface layer were optimized for suppression of interface erosion due to GaN-hydrogen interaction [4].

Design and growth regimes for sample B are chosen to increase electron mobility as high as possible. Five 2D-electron channels similar to one in sample A with reduced Al content and doping level were grown consequently with 100 nm period. For crystal quality improvement standard GaN growth technique developed for LED applications with nucleation layer annealing in NH_3/H_2 gaseous mixture was used. Dislocation density in sample B is approximately 5×10^8 cm^{-2} while in sample A it is about 1.5×10^9 cm^{-2}.

Surface electron concentration at the AlGaN/GaN interface in sample A is 1.6×10^{13} cm^{-2} with low-field mobility of 1500, 5200 and 5700 cm^2/V s at the temperature of 300, 77 and 4.2 K,

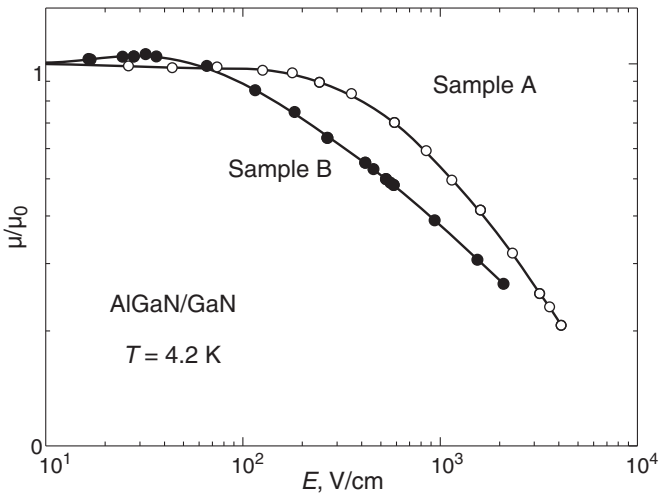

Fig. 1. Field dependence of electron mobility for 2DEG in AlGaN/GaN heterostructures.

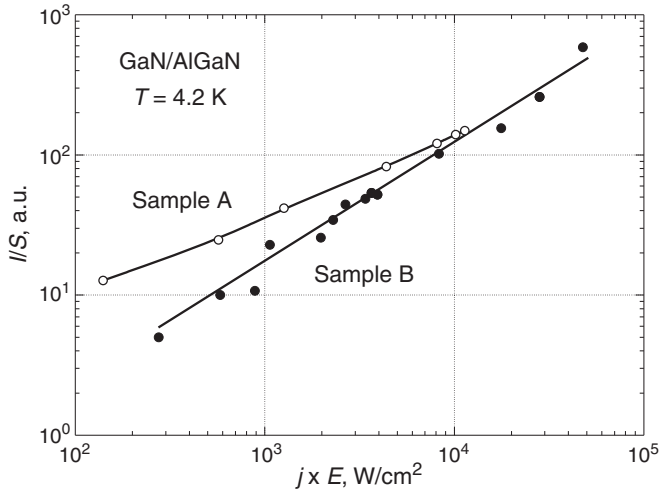

Fig. 2. Applied power dependence of integral intensity of THz radiation emission (experiment, lines are guided by eye).

respectively. In sample B the total concentration (for all five channels) is 3.0×10^{13} cm^{-3} with mobility of about 2000, 8100 and 8900 cm^2/V s at 300, 77 and 4.2 K, respectively.

The current-voltage characteristics were measured in a wide range of electric fields with samples immersed in liquid helium or liquid nitrogen and at room temperature as well. Two Ti/Au electrical contacts of a few mm length with a distance of 1–2 mm were pattern on the top surface. To avoid overheating the samples, we used 2 μs voltage pulses with a repetition rate of 1 Hz. The integral THz emission intensity was measured in the same pulse regime using a liquid-helium-cooled Ge:Ga photodetector equipped with a cold black polyethylene filter to prevent unwanted interference of near-infrared and visible radiation. The detector sensitivity range extended from 41 to 134 μm (from 9.3 to 30.4 meV).

2. Experimental results and discussion

Current-voltage characteristic were measured up to electric field of 5000 V/cm at three above-mentioned temperatures. The most pronounced features of electron heating were observed in all the samples at the lattice temperature $T = 4.2$ K. Sublinear dependence of the current upon voltage is totally explained by 2DEG mobility decrease with electric field strength because sheet electron concentration at the AlGaN/GaN interface is expected to be independent on the lattice temperature (see, for example, [5]) and hot electron temperature as well. The electron mobility normalized to its low-field value is shown in Fig. 1 as a function of applied electric field E for different samples. Sharp decrease of the electron mobility starts when *electron heating* in lateral electric field is strong enough ($T_e > 100$ K) and polar optical phonon scattering begins to play significant role. Similar behavior was earlier observed for the dependence of low-field electron mobility on the *lattice temperature* T [5] in the range of 100–300 K. It is quite natural that in the sample B with a large value of the low-field electron mobility ($\mu_0 = 8900$ cm^2/V s) the process of electron heating becomes significant at lower electric fields compared to the sample A ($\mu_0 = 5700$ cm^2/V s). In accordance with our analysis, at $T = 4.2$ K the electron temperature exceeds 300 K at electric fields above 2000 V/cm even in the sample A.

In conditions of such strong electron heating, there is an opportunity to observe the thermal radiation from 2DEG at the AlGaN/GaN interfaces. This radiation is expected to be especially intense in THz range. Indeed it was detected by means of Ge:Ga photoresistor for applied fields exceeding 100 V/cm. The dependence of integral intensity of THz electroluminescence per unit area (I/S) as a function of input specific electric power (jE) is presented in Fig. 2.

The classical model of 2DEG conductivity was applied to calculate the emissivity of AlGaN/GaN interface. This consideration was carried out after [6] where the model was developed for AlGaAs/GaAs heterojunction. We calculated the thermal emission spectra of AlGaN/GaN interfaces using the values of $T_e(E)$ determined from field dependence of electron mobility. Then the integral signal of the Ge:Ga photodetector response was simulated taking into account its sensitivity spectrum. Comparing the experimental dependence of integral intensity of THz radiation on applied electric power with the calculated dependence we conclude that the experimental results are well described within the framework of the applied theory of blackbody-like thermal emission of hot two-dimensional electrons.

Acknowledgements

This work is supported by the Russian Foundation for Basic Research and Ministry of Education and Science of Russian Federation. Support from the Linkage Grant of IB of BMBF at DLR is gratefully acknowledged.

References

[1] E. Starikov *et al*, *Journ. Appl. Phys.* **89**, 1161 (2001).
[2] V. A. Shalygin *et al*, *Journ. Appl. Phys.* **106**, 123523 (2009).
[3] M. Shur *et al*, *Journ. Electronic Materials* **25**, 777 (1996).
[4] W. V. Lundin *et al*, *Proceedings of the 13th Workshop on Metalorganic Vapour Phase Epitaxy* (Ulm, Germany, June 7–10, 2009), Inv. 2.
[5] Z. Dziuba *et al*, *Journ. Appl. Phys.* **82**, 2996 (1997).
[6] K. Hirakawa *et al*, *Phys. Rev. B* **47**, 16651 (1993).

18th Int. Symp. "Nanostructures: Physics and Technology"
St Petersburg, Russia, June 21–26, 2010

Rectification of electromagnetic wave in a semiconductor superlattice

A. V. Shorokhov[1], N. N. Khvastunov[1,2], T. Hyart[3] and K. N. Alekseev[4]

[1] Institute of Physics and Chemistry, Mordovian State University, 430005 Saransk, Russia
[2] M. E. Evsev'ev Mordovian State Pedagogical Institute, 430007 Saransk, Russia
[3] Department of Physical Sciences, University of Oulu P.O. Box 3000, 90014 Oulu, Finland
[4] Department of Physics, Loughborough University, Loughborough LE11 3TU, UK

Abstract. We study an effect of the generation of direct current which may arise in semiconductor superlattices due to a mixing of coherent electromagnetic radiations of commensurate frequencies. The physical nature of the rectified current and its connection with absorption are discussed.

Introduction

Harmonic mixing of ac electromagnetic field in various nonlinear media can leads to the effect of rectification of ac field. This effect is well-known in semiconductor physics beginning from 60-th [1,2]. The physical nature of this effect concludes in the different types of nonlinearity (as a rule it is a nonparabolicity of conduction band [3] or (and) the electron's heating by the field [2]) which can result in the dc current at harmonic mixing. In the bulk semiconductors the effect of the dc generation has been mainly considered for the mixing of microwaves, while for the semiconductor superlattice (SSL) the main interest is paid to the THz frequency domain. The interest to this problem is stipulated by the connection between the effect of rectification of ac field and the effect of amplification of THz radiation in SSL. Terahertz spectral range is the borderline of optics and electronics, and there still exists a technological gap in construction of compact and reliable sources, amplifiers and detectors. SSL have been proposed as a candidate for active material in such kind of devices.

One of the most perspective suggestions concludes in the use of strong ac pump field instead of dc bias to get an amplification of THz radiation. Negative absorption of a probe field arises if its frequency and the frequency of ac pump field are commensurate [4–13]. Parametric amplification of the even harmonics in superlattices due to the parametric resonance caused by the oscillations of electron's effective mass in miniband [8] leads to the generation of dc current. This effect is well-known for the parametric systems. First, an appearance of dc current in SSL under simultaneous action of ac electric field and its second harmonic has been shown in the papers [14–16].

In this paper we study the effect of rectification of THz radiation in SSL in the most general case of commensurate frequencies of the probe and pump fields taking into account the phase shift between ac fields and demonstrate the connection between the rectified current and components of absorption.

1. The rectification in the general case of commensurate frequencies

We suppose that the total electric field $E(t)$ acting on electrons is a sum of the pump $E_p = E_0 + E_1\cos(\omega_1 t)$ (E_0 is the dc bias) and probe $E_{\rm pr} = E_2\cos(\omega_2 t + \varphi_0)$ fields. In a real device, $E_{\rm pr}$ may be a cavity mode tuned to the desired THz frequency. We consider the most general case of commensurate frequencies $\omega_1/\omega_2 = n/m$, where n and m are integers and n/m is an irreducible fraction. Dynamics of the electrons belonging to a single miniband is well described by the semiclassical approach [17,18] based on the use of Boltzmann transport equation together with the tight-binding dispersion relation $\varepsilon(p) = (\Delta/2)[1-\cos(pd/\hbar)]$, where Δ is the miniband width, d is the SSL period, p is the quasimomentum.

The electron velocity averaged over the distribution function was calculated in [19]. Substituting the formula for $V(t)$ [19] in the definition of dc current $j_{\rm DC} = 2en_0\langle V(t)\rangle_t$ and averaging over the common period $T = 2\pi n/\omega_1 = 2\pi m/\omega_2$ of both fields, we get the following formula for dc current ($j_{\rm DC}$ is measured in the unit $j_0 = 2j_p = en_0V_0I_1/I_0$, where $V_0 = \Delta d/2\hbar$ is the peak velocity, n_0 is the electron density, I_m is the modified Bessel function of the argument $\Delta/2k_{\rm B}T$, j_p is the peak current corresponding to the critical field $E_{\rm cr} = \hbar/ed\tau$ Esaki–Tsu voltage-current characteristic [20])

$$j_{\rm dc} = \sum_{l_1,l_2=-\infty}^{\infty}\sum_{k=-\infty}^{\infty} J_{l_1}(\beta_1)J_{l_2}(\beta_2)J_{l_1-km}(\beta_1)J_{l_2+kn}(\beta_2) \times \frac{(\Omega_0 + l_1\omega_1 + l_2\omega_2)\tau\cos(kn\varphi_0) + \sin(kn\varphi_0)}{1+(\Omega_0 + l_1\omega_1 + l_2\omega_2)^2\tau^2}, \quad (1)$$

where $J_n(x)$ is the Bessel function, $\Omega_i = edE_i/\hbar$ ($i = 0, 1, 2$) and $\beta_i = \Omega_i/\omega_i$ ($i = 1, 2$).

In the case of the mixing of the pure ac fields ($E_0 = 0$), the expression for $j_{\rm dc}$ becomes

$$j_{\rm dc} = \sum_{l_1,l_2=-\infty}^{\infty}\sum_{k=-\infty}^{\infty} J_{l_1}(\beta_1)J_{l_2}(\beta_2)J_{l_1-km}(\beta_1)J_{l_2+kn}(\beta_2) \times \frac{(l_1\omega_1 + l_2\omega_2)\tau\cos(kn\varphi_0)}{1+(l_1\omega_1 + l_2\omega_2)^2\tau^2}. \quad (2)$$

Note that in this case the term which is proportional to the sine of the phase is absent.

The interesting fact follows from the Eq. (2). If the sum $n + m$ is the even number the dc current is equal to zero. In particular, the dc current is absent if we mixe the frequency and its odd harmonic or if both m and n is odd numbers. This property of the rectified current is stipulated by the breaking symmetry in the system. As a rule the rectified current arises if there exist the asymmetric periodical structure in the system. In our case the potential is symmetrical and dc current is the result of breaking the time-reversal symmetry $E(t) = -E(t + T/2)$.

In our case the common period of the probe and pump field is $T = 2\pi n/\omega_1 = 2\pi m/\omega_2$ and $E = E_1\cos[\omega_1(t + T/2)] + E_2\cos[\omega_2(t+T/2)+\varphi_0] = E_1\cos(\omega_1 t+\pi n)]+E_2\cos(\omega_2 t+$

$\pi m + \varphi_0$). Hence, if n and m are odd numbers (or $n + m$ is the even number) then the condition $E(t) = -E(t + T/2)$ is valid. In particular case of the mixing of the the pump field and its harmonics $n = 1$, and in the case when m is even number the symmetry is broken and we have the rectified current.

2. The rectification in the case of a weak probe

Let us consider the case $\omega_2 = m\omega_1$. In the limit of weak probe field ($\beta_2 \ll 1$), we need to take only the following combinations of indexes of Bessel functions in Eq. (1): (($l_2 = 0$, $j = \pm 1$), ($l_2 = \pm 1$, $j = \mp 1$), ($l_2 = 0$, $j = 0$). As a result we represent the dc current as a sum of two terms

$$j_{\rm dc} = j_{\rm dc}^{\rm stat} + j_{\rm dc}^{\rm coh} + O(\beta_2^2)\,. \tag{3}$$

Here

$$j_{\rm dc}^{\rm stat} = \sum_{l=-\infty}^{\infty} J_l^2(\beta_1) \frac{(\Omega_0 + l\omega_1)\tau}{1 + (\Omega_0 + l\omega_1)^2\tau^2} \tag{4}$$

is the static current modified by the pump field. It may be said that $j_{\rm dc}^{\rm stat}$ is a sum of several dc-curves shifted by integer multiples of the photon energy. This circumstance let us to modify the Esaki–Tsu voltage-current characteristic by the strong pump field. As a result the additional maxima arise on the VI characteristic and we can obtain the amplification of THz radiation without the formation of destructive high-field domains inside the superlattice [13,18]. In the limit $E_1 \to 0$ the current $j_{\rm dc}^{\rm stat}$ reduces to the well-known Esaki–Tsu VI characteristic for the dc-biased SSL [20] $j_{\rm dc}^{\rm stat} = \Omega_0\tau/(1 + \Omega_0^2\tau^2)$.

The second term

$$\begin{aligned} j_{\rm dc}^{\rm coh} &= \beta_2 \sum_{l=-\infty}^{\infty} J_l(\beta_1)\left[J_{l-m}(\beta_1) - J_{l+m}(\beta_1)\right] \\ &\times \frac{(\Omega_0 + l\omega_1)\tau\cos\varphi_0}{1 + (\Omega_0 + l\omega_1)^2\tau^2} \end{aligned} \tag{5}$$

has the parametric nature. It can be shown that this term is directly connected with the harmonic of electron energy.

In the case of unbiased SSL ($E_0 = 0$) the static current is equal to zero and the dc current $j_{\rm dc}$ is equal to the coherent current $j_{\rm dc}^{\rm coh}$

$$j_{\rm dc} = \left[1 + (-1)^m\right]\beta_2 \sum_{l=-\infty}^{\infty} J_l(\beta_1) J_{l-m}(\beta_1) \frac{l\omega_1\tau\cos\varphi_0}{1 + l^2\omega_1^2\tau^2}. \tag{6}$$

It follows from Eq. (6) that if we mix the pump field an its odd harmonic the dc current is absent and the dc current is not equal to zero in the case of even harmonics. Note that the even harmonics are the most perspective for the amplification of THz radiation because in this case the effect of the amplification doesn't blur by the generation of the harmonic of the pump field.

The important problem of the construction of THz amplificator is the determination of the required parameters system. We show that this problem is strongly simplified if to use the effect of the rectification of ac field. The possibility of amplification of the probe field is stipulated by the concurrence (in the case $E_{\rm dc} = 0$) the coherent and incoherent terms of the absorption $A = (\beta_2/2)(A^{\rm coh} + A^{\rm incoh})$ [8,19]. Incoherent term $A^{\rm incoh}$ plays an essential role in stabilization of space-charge instability in SSL and the coherent term $A^{\rm coh}$ describes the parametric amplification of the probe field [8]. It follows from the formulae for dc current obtained above that there are the connection between the components of the dc current and absorption. In particular, $j_{\rm dc}^{\rm stat}$ is equal to $A^{\rm incoh}$ if in the formula for $j_{\rm dc}^{\rm stat}$ we put $\Omega_0 \equiv \omega_2$. Hence if we want to find the incoherent term in the case of amplification of the m-th harmonic of the pump field we need only to measure the dc current in dc-biased ($E_0 = \hbar\omega_2/ed$) SSL placed in the pump field with the frequency $\hbar\omega_1$. We can obtain the information about the coherent term if we note that the dc current is proportional to the coherent term $\beta_2 A^{\rm coh}(m) = j_{\rm dc}^{\rm coh}(2m)$ at $\varphi_0 = 0$.

In conclusion, we have studied the effect of rectification of THz ac field in SSL in the case of commensurate frequencies of the pump and probe field. We have shown that this effect has the parametric nature and lets us to predict the possibility of amplification of THz radiation.

Acknowledgements

Our research was partially supported by the Russian Programme "Development of Scientific Potential of Universities", Grant of President of Russia for Young Scientists and AQDJJ Programme of European Science Foundation.

References

[1] Yu. K. Pozhela and H. J. Karlin, *Proc. IEEE* **53**, 1788 (1965).
[2] W. Schneider and K. Seeger, *Appl. Phys. Lett.* **8**, 133 (1966).
[3] Yu. A. Romanov, *Optika i Spektr.* (Sov. Phys. Optics and Spectroscopy) **33**, 917 (1972).
[4] V. V. Pavlovich, *Sov. Phys. Solid State* **19**, 54 (1977).
[5] Yu. A. Romanov, *Radiophysics and Quantum Electronics* **23**, 1573 (1980).
[6] Yu. A. Romanov and Yu. Yu. Romanova, *J. Exp. Theor. Phys.* **91**, 1033 (2000).
[7] T. Hyart, N. V. Alexeeva, A. Leppanen, and K. N. Alekseev, *Appl. Phys. Lett.* **89**, 132105 (2006).
[8] T. Hyart, A. V. Shorokhov, and K. N. Alekseev, *Phys. Rev. Lett.* **98**, 220404 (2007).
[9] K. N. Alekseev, M. V. Gorkunov, N. V. Demarina, T. Hyart, N. V. Alexeeva, and A. V. Shorokhov, *Europhys. Lett.* **73**, 934 (2006).
[10] Yu. A. Romanov, J. Yu. Romanova, and L. G. Mourokh, *J. Appl. Phys.* **99**, 013707 (2006).
[11] A. V. Shorokhov and K. N. Alekseev, *Physica E* **33**, 284 (2006).
[12] A. V. Shorokhov and K. N. Alekseev, *J. Exp. Theor. Phys.* **105**, 198 (2007).
[13] T. Hyart, K. N. Alekseev, and E. V. Thuneberg, *Phys. Rev. B* **77**, 165330 (2008).
[14] S. Mensa, G. M. Shmelev, E. M. Epshtein *Izvestiya Vuzov. Fizika* **6**, 112 (1988).
[15] K. Seeger, *Appl. Phys. Lett.* **76**, 82 (2000).
[16] K. N. Alekseev, M. V. Erementchouk and F. V. Kusmartsev, *Europhys. Lett.* **47**, 595 (1999).
[17] F. G. Bass and A. P. Tetervov, *Phys. Rep.* **140**, 237 (1986).
[18] A. Wacker, *Phys. Rep.* **357**, 1 (2002).
[19] A. V. Shorokhov, K. N. Alekseev *International Journal of Modern Physics B* **23**, 4448 (2009).
[20] L. Esaki and R. Tsu *IBM J. Res. Dev.* **14**, 61 (1970).

18th Int. Symp. "Nanostructures: Physics and Technology"
St Petersburg, Russia, June 21–26, 2010

Acceptor resonant states in p-type GaAs/AlGaAs narrow quantum wells

A. N. Sofronov[1], L. E. Vorobjev[1], D. A. Firsov[1],V. A. Shalygin[1], V. Yu. Panevin[1], G. A. Melentyev[1], A. E. Zhukov[2] and S. N. Danilov[3]

[1] St Petersburg State Polytechnic University, St Petersburg, Russia
[2] Ioffe Physical-Technical Institute, St Petersburg, Russia
[3] University of Regensburg, Germany

Abstract. Acceptor resonant states in narrow *p*-GaAs/AlGaAs quantum well structures were experimentally observed for the first time. Mid-IR optical absorption spectra measured at liquid helium temperature demonstrate features related to hole transitions from acceptor ground state to resonant ones, as well as to quantum well subbands. Temperature spectra evolution and modification of absorption spectra under strong lateral electric field were studied.

Introduction

In last years there has been considerable interest in resonant states of donors and acceptors in bulk semiconductors and semiconductor nanostructures due to opportunity of THz emitters development based on intracenter optical transitions of charge carriers from resonant to bound impurity states. Stimulated THz emission was observed in stressed *p*-Ge crystal at liquid helium temperature under conditions of impact ionization of impurity in a strong electric field [1]. Emission was related to population inversion of resonant acceptor states appearing due to valence band split by applied mechanical stress. Spontaneous THz emission was observed in *n*-GaAs/AlGaAs quantum wells at 4.2 K under strong lateral electric field [2]. It was shown that emission is mainly caused by optical transitions from resonant donor states attached to second quantum well subband to a localized donor states.

While donor resonant states in quantum wells were extensively studied in a number of experimental and theoretical works, resonant states of acceptor in quantum wells were not experimentally observed. In this work we report on investigations of beryllium states in GaAs/AlGaAs quantum well structures by means of optical absorption spectroscopy in mid-IR range.

1. Experimental details

Structures under investigation were grown by molecular beam epitaxy and consist of 200 periods of 38 Å GaAs quantum wells, separated by 70 nm $Al_{0.4}Ga_{0.6}As$ barriers. Doping with beryllium was provided in narrow area of 8 Å in the center of each well with surface density of 3×10^{11} cm^{-2}. The calculated ground state binding energy of beryllium in quantum well of the same width is 44 meV [3]. Samples for optical measurements were fabricated with multipass geometry.

Measuring optical absorption in a THz range is an experimental challenge, so in present work quantum well structure was designed to fit the intersubband hole transitions energies to a mid-IR range. Optical transmission spectra were measured by the Fourier spectrometer with two orthogonal light polarization. Polarization vector lies in the (x, y) plane of quantum well in the first case and contains both in-plane and z-component in the second case. Modification of absorption spectra in electric field was measured with tuned CO_2 laser. Electric field was applied to the sample with a short 2 μs pulses to avoid overheating of the sample.

2. Equilibrium absorption spectra

Equilibrium absorption spectra for z- and x-polarized light (Fig. 1 and 2 respectively) has been found from experimental data on transmission at 4.2 K. At liquid helium temperature all acceptors are frozen out and absorption may be caused only by optical transitions from beryllium ground state.

As it is known (see, for example, [4]), polarization selection rules for hole intersubband optical transitions allows absorption of x-polarized light via transitions $hh_1 \to lh_1$ and $hh_1 \to hh_3$ at nonzero hole wavevector $k_\parallel$, while z-polarized light is mainly absorbed due to $hh_1 \to hh_2$ transitions allowed at $k_\parallel = 0$. Impurity state wave functions are built from the corresponding subband wave functions so one can expect the same polarization selection rules for transitions from the ground impurity state. Due to this fact observed absorption band of z-polarized light at $\sim$ 130 meV is related to hole transitions to the states of second heavy holes subband hh_2. Absorption bands for x-polarized light can be attributed to transitions from beryllium ground state to the states of light hole subband lh_1 at photon energy of $\sim$ 80 meV and to the states of third heavy hole subband hh_3 at photon energy of $\sim$ 200 meV.

Each absorption band has a complicated shape and can be represented as a sum of the Lorentzian peaks. According to simple estimations of valence subband positions, a peak at

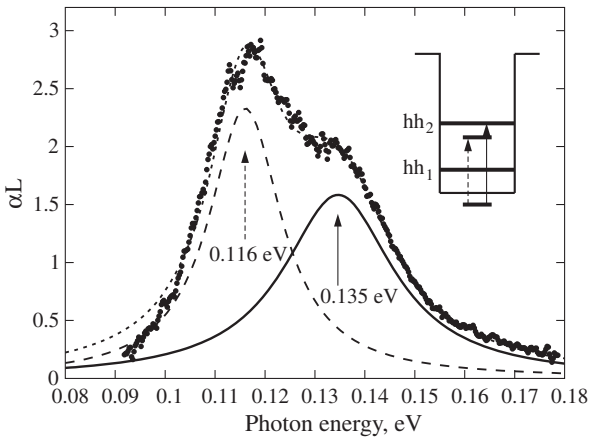

Fig. 1. Equilibrium absorption spectra for light with z-polarization (along the growth direction) at $T = 4.2$ K, L is a optical path length.

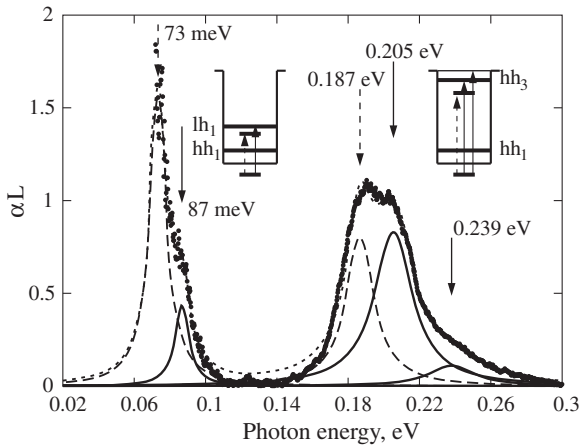

Fig. 2. Equilibrium absorption spectra for in-plane polarized light (x-polarization)at $T = 4.2$ K.

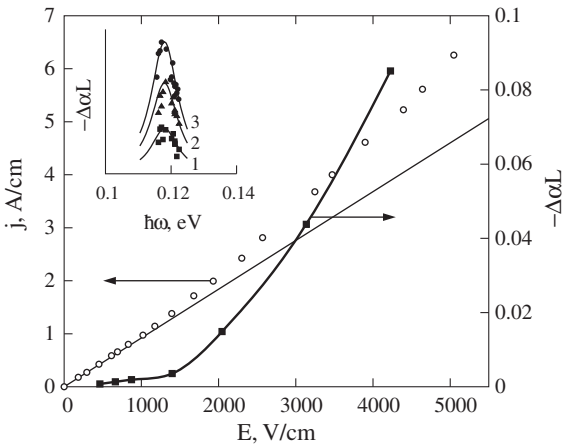

Fig. 3. Current-voltage characteristic (left axis) and field dependence of absorption modulation (right axis) at $\hbar\omega = 121$ meV. Inset shows $\Delta\alpha L$ spectrum at $E = 1440$ V/cm (1), $E = 2260$ V/cm (2), and $E = 3140$ V/cm (3).

$\hbar\omega = 135$ meV can be assigned to optical transitions to the hh_2 subband. Second peak at $\hbar\omega = 116$ meV can be attributed to intracenter transition to the acceptor resonant state attached to hh_2 subband. Schematic diagram of these transitions is presented at the inset in Fig. 1.

Longwavelength absorption band for x-polarized light consists of two peaks at $\hbar\omega = 87$ meV and $\hbar\omega = 73$ meV, herewith first one is related to hole transitions to the lh_1 subband, and second one is related to intracenter transitions to the beryllium resonant state attached to this subband.

Shortwavelength absorption band for x-polarized light can be decomposed into three peaks. The weakest one at $\hbar\omega = 239$ meV is a result of photoionization processes with hole transitions form berylium ground state to the continuum of delocalized states above the barrier. Peaks at $\hbar\omega = 205$ meV and $\hbar\omega = 187$ meV can be explained with transitions to the hh_3 subband and to resonant state attached to it.

Measured low-temperature absorption spectra allow to determine a binding energies of beryllium resonant states in a quantum well, namely 14 meV, 19 meV, and 18 meV for the states attached to lh_1, hh_2, and hh_3 subbands respectively.

Increasing the temperature leads to thermal ionization of impurities. Measured absorption spectra at several temperatures from 77 to 300 K demonstrate an appearance of additional absorption related to intersubband transitions from first heavy hole subband hh_1. Particulary, absorption band of z-polarized light at 160–200 meV related to $hh_1 \rightarrow hh_3$ transitions at $k_\parallel \neq 0$ was observed.

3. Modulation of absorption at electric field

A modification of absorption spectra at spectral range close to optical transitions energy from bound to resonant acceptor state attached to hh_2 subband at strong lateral electric field was also measured. At the presence of electric field the optical transmission of the structure increases. Modulation spectrum represents a narrow peak at the energy corresponding to optical transition from ground to resonant acceptor state. Field dependence of the change of absorption coefficient $\Delta\alpha L$ for z-polarization is presented in Fig. 3 together with current-voltage characteristic of the structure measured at liquid nitrogen temperature. Current-voltage characteristic demonstrates a weak deviation of a linear dependence at high enough electric field. Absorption modulation $\Delta\alpha L$ superlinearly increases with the increase of electric field.

At strong enough electric field processes of impurity breakdown can take place even at liquid nitrogen temperature. Observed decrease of absorption coefficient is related to impact ionization and depopulation of acceptor ground state. Measured field dependence of $\Delta\alpha L$ allows to determine directly a field dependence of free hole concentration in the first quantum well subband. Considering this dependence together with a current-voltage characteristic one can determine a field dependence of hot holes mobility in a hh_1 subband.

Investigations of resonant acceptor states in p-type quantum wells were carried out for the first time.

Acknowledgements

Authors would like to thank S. D. Ganichev (University of Regensburg, Germany) and D. V. Kozlov(Institute for Physics of Microstructures RAS, Nizhniy Novgorod, Russia). This work has been supported by Russian Foundation of Basic Research and Russian Ministry of Education and Science. Support from the linkage Grant of IB of BMBF at DLR is gratefully acknowledged.

References

[1] I. V. Altukhov *et al*, *JETP* **88**, 51 (1999).
[2] D. A. Firsov *et al*, *Bull. of the RAS: Physics* **72**, 246 (2008).
[3] W. T. Masselnik *et al*, *Phys. Rev. B* **32**, 5190 (1985).
[4] H. H. Chen *et al*, *IEEE Journ. of Quant. Elect.* **32**, 471 (1996).

18th Int. Symp. "Nanostructures: Physics and Technology"
St Petersburg, Russia, June 21–26, 2010

Crystalline properties and applications of III–V nanowires

J. Johansson[1], P. Caroff[2] and K. A. Dick[1]

[1] Solid State Physics, Lund University, Box 118, S-22100 Lund, Sweden
[2] Institut d'Electronique de Microélectronique et de Nanotechnologie, UMR CNRS 8520, Avenue Poincaré, B.P. 60069, 59652 Villeneuve d'Ascq, France

Abstract. We demonstrate that the crystal structure of gold particle-seeded III–V nanowires can be controlled by the growth parameters. In this work we focus on InAs nanowires and study the crystal structure as a function of growth temperature and nanowire diameter, but we present experimental results on crystal structure control also in other materials systems. We can explain the observed experimental trends within our classical nucleation framework. Here we use the temperature and diameter dependence of the wurtzite-zinc blende transition in InAs nanowires as a quantitative model system. Finally, we will briefly discuss a few potential applications.

Introduction

Semiconductor nanowires have made a significant impact in a great diversity of applications. Among these we mention electronic and optoelectronic devices, which includes light emitting diodes and photovoltaics (see Ref. [1] and references therein) as well as thermoelectric devices.

One major hurdle to overcome for the technologically important metal particle-seeded III–V nanowires is their high density of twin defects and stacking faults. In the extreme case and for ⟨111⟩-oriented nanowires made of materials with zinc blende (ZB) bulk crystal structure, this results in more or less random inclusions of wurtzite (WZ) when faulty stacking dominates over ordinary stacking. It is of utmost importance to be able to control and predict this polytypism, since controlling the structure means controlling the band structure, which is necessary for reproducible production of electronic and optoelectronic devices. In this investigation we present experimental results on crystal structure control in III–V materials made of InAs, GaAs, InP, and GaP. We use growth temperature, precursor molar fractions, V–III ratio, and nanowire diameter as control parameters [2].

To explain the main trends in the experimental data we have developed a classical nucleation model. To quantify the model we use the InAs experimental data. We are able to explain the temperature dependent cross-over from wurtzite to zinc blende crystal structure as the nanowire diameter is increased. Using a similar approach we have previously been able to relate the crystalline properties of GaP nanowires to the supersaturation during their growth [3]. By including the Gibbs–Thomson effect in the chemical potential, we account for the strong nanowire diameter dependence of the supersaturation. This, in turn, allows us to calculate the smooth cross-over from wurtzite to zinc blende crystal structure as the InAs nanowire diameter increases.

1. Experimental section

All nanowires used in this study were grown by metalorganic vapour phase epitaxy (MOVPE). Nanowires were grown by a particle-assisted growth mechanism using gold aerosol nanoparticles as growth seeds. Size selected particles with diameters in the range 10–80 nm were deposited on [111]B-oriented substrates in the same material as the respective nanowires.

The nanowires were grown in low-pressure MOVPE with hydrogen as the carrier gas. The precursors used were trimethylgallium (TMGa), trimethylindium (TMIn), arsine (AsH_3) and phosphine (PH_3). Growth times were selected in the range of 1–45 min to give appropriate nanowire lengths, typically between 500 nm and 2 μm. Growth temperature ranges appropriate to each material, within the range $350 - 550$ °C, were investigated

Initial morphological characterization was performed using a field-emission scanning electron microscope (SEM). Crystal structure characterization was performed using field-emission transmission electron microscope (TEM) operated at 300 kV. TEM images were recorded along the $\langle\bar{1}10\rangle$ zone axis (cubic notation), using a $2k \times 2k$ CCD camera. Samples for high resolution (HR) TEM were obtained by breaking off the nanowires from the substrate and transferring them to lacey carbon-film coated copper TEM grids. The determination of the nanowire side facet orientation was performed by combining TEM analysis with independent SEM observations of the hexagonal facet orientation of the as-grown nanowires with respect to the $\{110\}$ cleavage planes of the $\{111\}$B substrates.

2. Results and discussion

In Fig. 1, we show TEM images of InAs nanowires with different diameters grown at 460 °C. It can be seen that the fraction of WZ in the nanowires decreases with increasing diameter, in favor of ZB. The thinnest wire measured (with a diameter of 17 nm) is pure WZ, but the planar defects in the wires increase in frequency as the nanowire diameter increases. The thickest wire that is illustrated (diameter 133 nm) has a pure ZB structure with periodically occurring twin planes. InAs wires grown at the temperatures 420, 440, and 480 °C follow the same trend, with WZ at small diameters and ZB dominance at large diameters. As the growth temperature increases, the ZB phase starts to dominate at smaller nanowire diameters. At temperatures lower than about 390 °C the nanowires are however predominantly ZB (with random twinning). In this low temperature region, the fraction of WZ increases with temperature up to about 400 °C.

The pure WZ nanowires exhibit $\{\bar{1}100\}$ side facets. The nanowires containing both WZ and ZB are bounded by $\{11\bar{2}\}$ oriented side walls, which consist of alternating $\{111\}$A and $\{111\}$B microfacets [4] for twinned ZB segments and $\{\bar{1}100\}$ facets for WZ segments. We also mention that the zig-zag pattern appearing in the thickest nanowires grown at higher temperature (Fig. 1d), is an additional effect often encountered

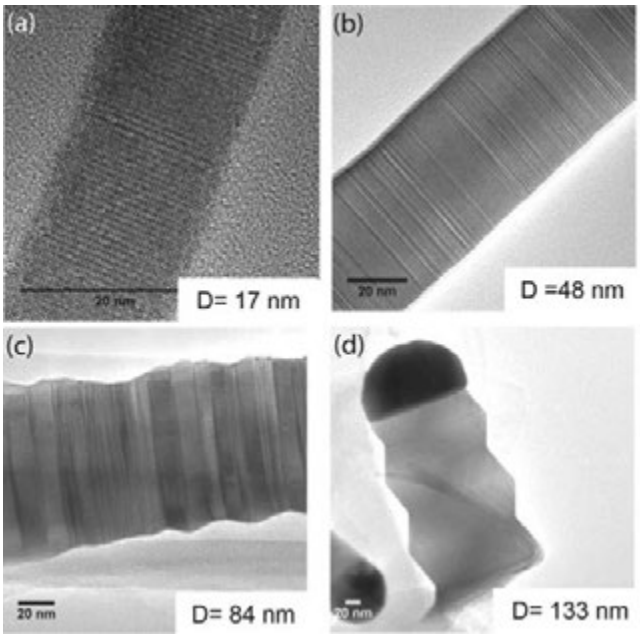

Fig. 1. TEM images of InAs nanowires with different diameters (D, indicated in the lower right corners) grown at 460 °C. The crystal structure ranges from pure WZ (a) to pure ZB (d), via the mixed phases exemplified in (b) with 85% WZ and in (c) with 25% WZ, as the diameter is increased.

in wires with pure ZB structure. This morphology arises from the alternating $\{111\}$A and $\{111\}$B facets and is a direct consequence of the periodic twinning in these nanowires [5].

The crystal structure of GaAs nanowires has been investigated over the temperature range of $350-550$ °C [2]. We have observed that nanowires grown at low temperature exhibit a ZB crystal structure with twin planes occurring in low-density. As temperature is increased, the twin plane density increases, with stacking faults (short WZ segments) first appearing around 450 °C. At sufficiently high temperature (around 550 °C), the WZ structure begins to dominate the nanowire [2]. A transition from the mixed structure to pure WZ is observed by Plante *et al* [6] over the temperature range of $500-600$ °C in MBE, showing that the same trend holds even though other growth conditions are very different. That is, the temperature dependence of the ZB-WZ transition observed in GaAs corresponds to the low temperature (about 390 °C) transition from ZB-WZ in InAs.

Another important observation is that GaAs nanowires with the predominantly WZ structure generally exhibit the ZB structure in the region directly under the particle ("neck region") [7,8]. This is usually attributed to a decrease in Ga supersaturation after the Ga precursor is turned off at the end of the growth.

The effects of temperature, molar fraction and V–III ratio have been investigated for InP nanowires [2]. We observe that the predominantly crystal structure changes from ZB at 380 °C to WZ at 430 °C, for a V–III ratio of 8. We have also observed, for InP nanowires grown at 430 °C and a V–III ratio of 207, that the total molar fraction affects the crystal structure. Nanowires grown at the highest molar fractions exhibit the mixed WZ and ZB structure, while nanowires grown at the lowest molar fractions exhibit the WZ structure. This effect was not observed for the lower growth temperature [2]. InP is also reported to exhibit a diameter dependence, with increasing WZ structure as the diameter decreases [8] in accordance with our InAs results.

We have reported a temperature effect for GaP [3] similar to the one for GaAs, namely that twin plane and stacking fault density increases with temperature. We have also shown by utilizing a pulsed growth technique that growth at low supersaturation results in predominantly ZB whereas growth at high supersaturation results in WZ dominance [2]. GaP nanowires with diameter above 100 nm also have a lower density of twin planes than thinner nanowires grown at the same conditions.

We will now introduce a classical nucleation model, which we will use to explain the experimental observations. Even if the model framework is consistent with the general experimental trends, we will restrict ourselves to explain the InAs results (the temperature and diameter dependencies).

It is well established that metal particle assisted growth of nanowires takes place by successive completion of monomolecular layers [4,8,10]. These layers nucleate at the perimeter of the nanowire-metal particle interface. The nucleation of a new plane can occur in two different positions. Either *ordinary*, resulting in zinc blende structure with ABC stacking, or *fault* position, resulting in twinning or wurtzite. Twin formation occurs if the fault plane is isolated and surrounded by ordinarily stacked layers. A segment of wurtzite structure is, on the other hand, the result of an uninterrupted sequence of fault planes [3]. This process is well described with classical nucleation theory. If a hemi-circular shape is assumed for the nuclei, the nucleation barriers read,

$$\Delta G^* = \frac{\Gamma^2}{2\pi\,\Delta\mu/s} \quad \text{and} \quad \Delta G = \frac{\Gamma_f^2}{2\pi(\Delta\mu/s - \sigma_f)} \qquad (1)$$

for ordinary and fault plane, respectively. In Eq. (1), Γ and Γ_f are the step energies of the nuclei, $\Delta\mu$ is the chemical potential difference, s is the molecular site area, and σ_f is the twin plane energy. The step energies are not known experimentally and thus have to be estimated. They are, however, closely related to the surface energies and should follow the same trends when the structure changes from zinc blende to wurtzite. Since surface energies of wurtzite tend to be lower than surface energies of zinc blende [10] one can argue that Γ_f should be lower than Γ. A direct consequence of this is that the inequality $\Delta G_f^* < \Delta G^*$ is fulfilled if the supersaturation, $\Delta\mu$, is high enough. At such conditions wurtzite formation can in fact be favorable [8].

The chemical potential can be written as,

$$\Delta\mu = k_{\mathrm{B}}T \ln\frac{x}{x_{\mathrm{eq}}} + \frac{2\gamma\Omega}{R}\,, \qquad (2)$$

where k_{B} is Boltzmann's constant, T is the absolute temperature, x and x_{eq} are the molar fractions of indium in the alloy particle during growth and at equilibrium, respectively. The first term in Eq. (2) is the conventional one and the second term accounts for the Gibbs–Thomson effect, which describes the increased pressure of indium in the alloy particle due to its finite size. Here, γ is the surface energy of the alloy particle, Ω is the atomic volume of indium in the particle, and R is the radius of the particle, which is approximately equal to the radius of the nanowire. Now, we can express the rates for ordinary and fault plane nucleation with the proportionalities,

$$J \propto Z\exp(-\Delta G^*/k_{\mathrm{B}}T),\;\; J_f \propto Z_f\exp(-\Delta G_f^*/k_{\mathrm{B}}T), \quad (3)$$

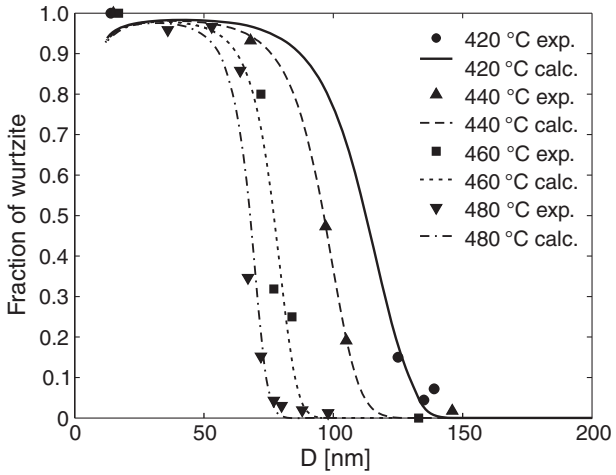

Fig. 2. The fraction of WZ as a function of nanowire diameter (D) as estimated by nucleation calculations (curves) and observed in experiments (symbols).

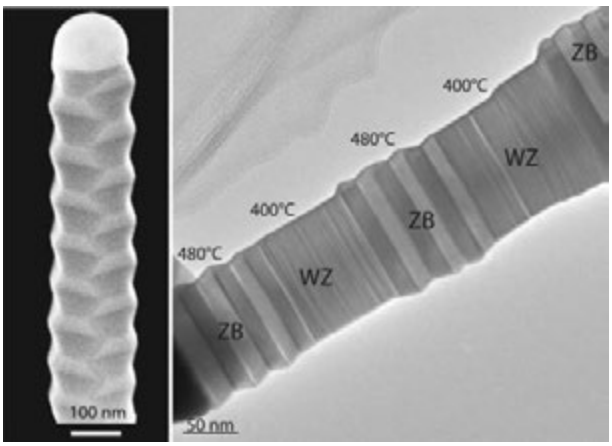

Fig. 3. (Left panel) SEM image of an InAs twin plane superlattice nanowire. (Right panel) TEM image of a ZB-WZ polytypic superlattice in an InAs nanowire. The structure was achieved by periodically varying the growth temperature.

where the exponential prefactors are the Zeldovich factors, given in [11]. The nucleation rates allow us to calculate the fault plane nucleation probability,

$$p_f = J_f/(J + J_f). \tag{4}$$

Since the nucleation is well described by a Poissonian process [3,4], the distribution of planes follows the geometric distribution. According to the statistical properties of this distribution, the probability of nucleating exactly k fault planes in a sequence before an ordinary nucleus forms is given by $p_f^k(1 - p_f)$, with $k = 0, 1, 2, \ldots$. As our criterion for WZ is two or more fault planes in a sequence, the fraction of WZ, f_{WZ}, in a nanowire can be estimated as the probability that $k \geq 2$, which reduces to $f_{\mathrm{WZ}} = p_f^2$.

In Fig. 2 we have plotted f_{WZ} as a function of InAs nanowire diameter, $D = 2R$. The parameters for the plot are given in [11]. The strong diameter dependence of f_{WZ} is explained by the R-dependence of $\Delta\mu$. In our case the supersaturation ratio, x/x_{eq}, is rather low, which makes the two terms in Eq. (2) of equal magnitude. This, in turn makes f_{WZ} strongly R-dependent. The temperature dependence of the f_{WZ}-curves is explained by the temperature dependence of the supersaturation ratio, x/x_{eq} [11].

Turning now to applications relying on crystal structure control, it is clear that most electronic and optoelectronic applications would benefit from a precisely controlled crystal structure, since a well defined crystal structure means a well defined electronic structure. In addition to such effects, we mention that the pure zinc blende wires with periodic twinning, the twin plane superlattices, (Fig. 1d) have been proposed as promising candidates for thermoelectric applications. A perspective view of such a wire made of InAs is shown in Fig. 3 (left panel).

It has recently been demonstrated by Monte Carlo simulations that the saw-tooth profile of such microfaceted wires can cause phonon backscattering [12]. This would suppress the thermal conductivity significantly, which is highly desirable for thermoelectric applications. Thermal conductivity measurements of InAs twin plane superlattice nanowires are under way.

Due to the different bandgaps of the ZB and WZ polytypes [13], an interesting idea, which could be useful for device applications as well as for fundamental physics is controlled fabrication of polytypic ZB-WZ superlattices (within the same wires). According to the data in Fig. 2 such structures should be possible to fabricate by a proper choice of nanowire diameter and temperature variation during growth. In Fig. 3 (right panel), a TEM image of a polytypic InAs superlattice is shown. The axial positioning and length of the ZB and WZ segments are directly controlled by the growth temperature sequence.

Acknowledgements

This work was performed within the Nanometer Structure Consortium at Lund University. We acknowledge financial support from the Swedish Foundation for Strategic Research (SSF), the Swedish Research Council (VR), and the Knut and Alice Wallenberg Foundation. Last, but not least, we want to thank the scientists at the Nanometer Structure Consortium in Lund for valuable discussions and input.

References

[1] K. A. Dick, *Prog. Cryst. Growth Charact. Mater.* **54**, 138 (2008).
[2] K. A. Dick *et al*, *Semicond. Sci. Technol.* **25**, 024009 (2010).
[3] J. Johansson *et al*, *Cryst. Growth Des.* **9**, 766 (2009).
[4] J. Johansson *et al*, *Nat. Mater.* **5**, 574 (2006).
[5] P. Caroff *et al*, *Nature Nanotech.* **4**, 50 (2009).
[6] M. C. Plante *et al*, *Nanotechnology* **19**, 495603 (2008).
[7] A. I. Persson *et al*, *Nature Mater.* **3**, 677 (2004).
[8] F. Glas *et al*, *Phys. Rev. Lett.* **99**, 146101 (2007).
[9] S. Paiman *et al*, *Nanotechnology* **20**, 225606 (2009).
[10] V. Dubrovskii *et al*, *Phys. Rev. B* **78**, 235301 (2008).
[11] J. Johansson *et al*, *J. Phys. Chem. C* **114**, 3837 (2010).
[12] A. L. Moore *et al*, *Appl. Phys. Lett.* **93**, 083112 (2008).
[13] A. De and C. E. Pryor, arXiv:0908.1984v1 (2009).

18th Int. Symp. "Nanostructures: Physics and Technology"
St Petersburg, Russia, June 21–26, 2010

Self-assembled InGaAs/GaAs quantum rings: Correlation of formation temperature and energy spectrum

O. S. Komkov[1], O. E. Gordyushenkov[1], A. N. Pikhtin[1], A. Aierken[2], T. Hakkarainen[2], M. Sopanen[2] and H. Lipsanen[2]

[1] St Petersburg Electrotechnical University "LETI", Prof. Popov str. 5, 197376 St Petersburg, Russia
[2] Department of Micro and Nanosciences, Micronova, Aalto University School of Science and Technology, PO Box 13500, FI-00076 Aalto, Finland

Abstract. InGaAs/GaAs quantum rings (QRs) are obtained by the transformation of InAs islands on GaAs substrate by metalorganic vapor phase epitaxy (MOVPE). Ring-shaped nanostructures are formed at 500–600 °C. The energy spectra of QRs are measured by photoreflectance technique at room temperature and at 85 K. Differential-like spectral features below GaAs energy gap are observed. Their origin can be related to optical transitions between electron and hole subbands in QRs. The dependence of these energy levels on the QR formation temperatures has been studied.

Introduction

Since the first growth of self-assembled InAs quantum rings [1], numerous theoretical and experimental studies of QRs have been reported. Due to their ring-like shape, these structures have electronic properties that differ from those of other quantum structures.

In a recent paper [2] the formation of observed here InGaAs QRs on GaAs has been investigated. The effects of growth conditions on the surface morphology were reported and low temperature photoluminescence (PL) spectra of the QRs were also observed. But it is well known that the PL generally only measures the lowest energy gap and requires the sample to be cooled to liquid helium temperatures (below 10 K) if an accurate measurement of energy is to be obtained. Sometimes the lowest energy transition can be caused by any impurities in the band gap or by narrow-gap nanostructures which exist in complicated samples. The other optical transition energies are also extremely useful for determining the full energy level spectrum of the nanostructure.

It is generally acknowledged that photoreflectance (PR) is a good non-destructive tool for the optical characterization of semiconductor nanostructures. This is a class of spectroscopy where a sample's reflectance R is probed by a spectrally-resolved light source while its dielectric function is being simultaneously externally modulated by a chopped laser pump beam with photon energy above the band-gap. The modulated component, ΔR, is detected with sensitive lock-in techniques, yielding sharp, differential-like oscillatory spectra. At room temperature photoreflectance can give equivalent energy resolution to that obtained by PL at liquid helium temperatures, and probes a far wider range of transition energies, yielding all these in a single spectrum, highlighting not only ground-state but also many higher-order interband optical transitions. In this paper, self-assembled InGaAs/GaAs quantum rings are characterized by photoreflectance technique.

1. Growth and experimental details

The samples were grown on semi-insulating GaAs(100) substrates in a horizontal MOVPE reactor at atmospheric pressure. A 100 nm thick GaAs buffer layer was grown first. InAs islands were formed by depositing a nominally 1.7 monolayer thick InAs layer on the GaAs buffer, based on the results of a previous study [3]. After stabilization, the InAs islands were transformed into QRs by capping the islands with a 2 nm thick GaAs partial capping layer followed by annealing under tertiarybutylarsine flow [2]. The annealing temperature (500–600 °C) was the same as the island growth temperature and here it will be called the formation temperature, T_f. The morphology of the QRs was characterized using contact-mode atomic force microscopy (AFM). The AFM tips were non-conductive silicon nitride tips with a diameter of 20 nm. Samples for the optical measurements were covered with a 50 nm thick GaAs barrier layer at T_f after the QR transformation was completed.

The photoreflectance measurements were realized at room and low temperature. The optical properties of the samples were modulated by a chopped He–Ne laser beam ($\lambda = 632.8$ nm). The probe beam was provided by a halogen lamp and a computer-controlled grating spectrometer. The energy of this beam was scanned as a function of photon energy from 1.12 to 1.80 eV. A high-quality silicon p-i-n photodiode and standard lock-in techniques were used to record the PR spectra.

When the laser was on, photo-generated carriers were captured by traps, thus reducing the inbuilt/surface electric field. When the laser was off, the trap population, and hence the field, were restored [4]. This mechanism modulated the Stark shift of the quantum ring energy levels which modulates the dielectric function, and thus the relative reflectivity, $\Delta R/R$. Uninteresting broad background and system-response features in R were removed.

2. Results and discussion

Fig. 1 shows atomic force microscopy images of InGaAs QRs fabricated at four different temperatures (500, 530, 550 and 570 °C). Due to the different size of the initial InAs islands at different growth temperatures, the lateral dimension of the InGaAs QRs is increased when the growth temperature increases. However, the camel-hump shape of the QRs is more obvious at lower growth temperatures (Fig. 1(a) and (b)) while the QRs are closer to a perfect ring shape at higher growth temperatures (Fig. 1(c) and (d)) [2]. The main reason for the anisotropy of the rings is the different diffusion rate of indium atoms in different directions at different temperature [5].

Due to the large size of InAs islands when the growth temperature was 600 °C, most of the islands were not completely

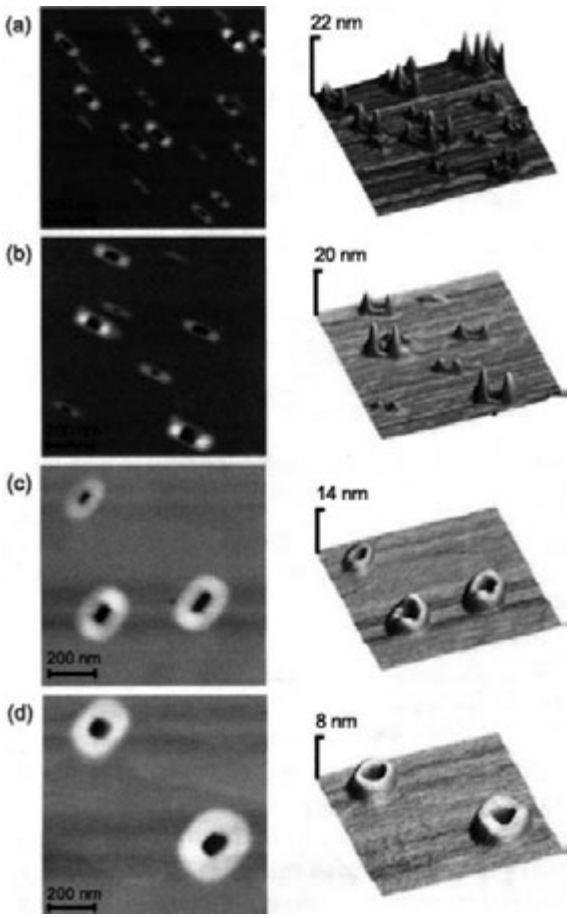

Fig. 1. 2D and 3D AFM images of InGaAs QRs fabricated at different temperatures: a) 500 °C, b) 530 °C, c) 550 °C and d) 570 °C.

transformed into rings. That is why these samples have not been taken into consideration.

Room-temperature photoreflectance spectra yielded information about only one excitonic transition in the samples. For the QRs, formed at 530–570 °C, a differential-like spectral feature below GaAs energy gap was observed. Its energy decreased with increasing T_f. To avoid a PR signal firstly observed in a bulk semi-insulating GaAs [6] in the same energy region, a back side of each investigated sample have been roughened to remove that signal [7]. In the QR sample with $T_f = 500$ °C, the PR spectrum demonstrated only the signal from GaAs. To decrease the homogeneous broadening of lineshape, photoreflectance measurements at low temperature were applied.

Fig. 2 shows low temperature (85 K) PR spectra of the same quantum ring samples. The photoreflectance spectra can be divided into two parts: the first one (from 1.5 to 1.62 eV) and the second part (from 1.38 to 1.5 eV). The first part is due to GaAs and exhibit well-defined Franz–Keldysh oscillations (FKOs). Using the method observed in [8] the internal electric field in the area of the quantum rings were determined from the period of these FKOs.

The most interesting features were observed in the second part of our PR spectra (below GaAs energy gap). Their differential-like lineshape indicates their low-dimensional nature. Precise energy of these optical transitions was determined by Kramers–Kronig method [9]. The energy of the first PR signal decreases from 1.460 eV (sample formed at 500 °C) to

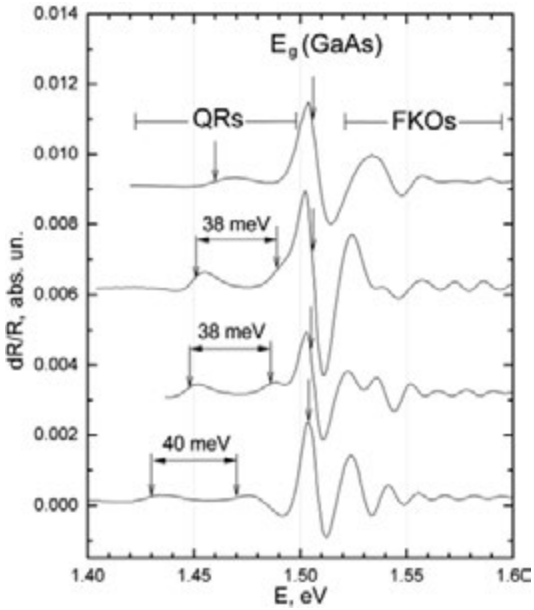

Fig. 2. Photoreflectance spectra of InGaAs quantum rings samples shown in Fig. 1, measured at 85 K.

1.430 eV (sample formed at 570 °C). This phenomenon can be explained by increasing lateral dimension of QRs with increasing T_f. The situation is similar as in the simple rectangular quantum well (QW) model — the wider the QW, the lower its ground state. The second PR signal also increases in energy with T_f. This signal can be due to excited states in QRs. At the same time, the energy interval between the above-mentioned features is increased which can not be explained with the help of the simple QW model.

In conclusion, a strong correlation between the formation temperature of InGaAs quantum rings and corresponding energy spectra was observed by using photoreflectance technique. Moreover, the magnitude of internal electric field was obtained from the period of Franz–Keldysh oscillations, which can be useful for further theoretical modeling of the quantum ring energy spectrum.

Acknowledgements

This work was partially supported by the project 2.1.2/652 of the program "Development of scientific potential of Higher School (2009-2010)".

References

[1] J. M. Garca *et al*, *Appl. Phys. Lett.* **71**, 2014 (1997).
[2] A. Aierken *et al*, *Nanotechnology* **19**, 245304 (2008).
[3] A. Aierken *et al*, *Appl. Surf. Sci.* **254**, 2072 (2007).
[4] H. Shen *et al*, *Appl. Phys. Lett.* **52**, 2058 (1998).
[5] D. Granados and J. M. Garca, *Appl. Phys. Lett* **82**, 2401 (2003).
[6] A. N. Pikhtin, V.-M. Airaksinen, H. Lipsanen and T. Tuomi, *J. Appl. Phys.* **65**, 2556 (1989).
[7] A. N. Pikhtin and M. T. Todorov, *Semiconductors* **28**, 616 (1994).
[8] A. N. Pikhtin, O. S. Komkov and K. V. Bazarov, *Semiconductors* **40**, 592 (2006).
[9] T. J. C. Hosea, *Phys. Status Solidi B* **189**, 531 (1995).

18th Int. Symp. "Nanostructures: Physics and Technology"
St Petersburg, Russia, June 21–26, 2010

Quantum antidot in graphene

V. A. Volkov, V. V. Enaldiev and I. V. Zagorodnev
V. A. Kotel'nikov Institute of Radio Engineering and Electronics of RAS, Mokhovaya 11-7, Moscow, 125009, Russia

Abstract. Effect of edge states of the Tamm-type on electron energy in graphene sheet with circular hole (antidot) is considered. The Weyl–Dirac equation with (or without) magnetic field with boundary conditions that were derived by authors earlier is solved. We compare two geometries of graphene sample: antidot and half-sheet. The Tamm states running around antidot are quantized even without magnetic field. The energies of these states undergo oscillations periodic on magnetic field, which can explain experimental results on the Aharonov–Bohm effect in ultrathin graphite with columnar defects.

Introduction

Periodic oscillations of magnetoresistance of ultrathin monocrystals of graphite with columnar defects were observed in Ref. [1]. The effect resembles the Aharonov–Bohm effect. However, the mechanism of its occurrence is not clear yet. In the present work a possible mechanism of the system is proposed. It may explain the results of [1]. We begin by considering the linear edge of graphene.

1. Energy spectrum for linear edge of graphene

Electrons in graphene behave as if they are massless "relativistic" particles near two nonequivalent points in the first Brillouin zone. Such band structures can be described by an equation which is formally equivalent to a couple of the 2D Weyl equations:

$$\tau\vec{\sigma}\,\vec{p}\Psi_\tau = E\Psi_\tau\,, \qquad (1)$$

where $\Psi = (\psi_1, \psi_2)^T$ is envelope wave function, $\vec{\sigma} = (\sigma_x, \sigma_y, \sigma_z)$ is Pauli matrices in standard presentation, the valley number $\tau = \pm 1$. The Fermi velocity (or group velocity of low-energy excitations) and the Planck's constant are set equal to unity.

Boundary conditions (BCs) for an envelope wave function were derived in our previous work [2,3] in the case of neglecting inter-valley scattering at the boundary (Γ):

$$\left(\psi_{1\tau} + ia^\tau e^{-i\alpha}\psi_{2\tau}\right)\Big|_\Gamma = 0\,. \qquad (2)$$

a is a real parameter defined at the boundary. The vector normal to the boundary is $(\cos\alpha, \sin\alpha)$. For edge states (ESs) of semi-infinite sample with the parameter a being constant at the boundary we found the dispersion relation:

$$E_\tau(k_y) = \frac{2ak_y\tau}{a^2+1}, \quad k_y\left(1 - a^{2\tau}\right) > 0\,, \qquad (3)$$

where k_y is the momentum along the linear boundary. The ESs band is represented with the rays beginning at the center of each valley and located in one of the quadrants of $E(k_y)$ plane, depending on the parameter a.

We applied the Hamiltonian (1) in the presence of a magnetic field — the momentum $\vec{p}$ was replaced by $\vec{p} + |e|\vec{A}/c$, where $\vec{A}$ is the vector potential. Then we derived dispersion equation and solved it numerically. The results are shown on Fig. 1.

If $a = 0$ the ESs magnetic spectra for graphene half-plane, Fig. 1a, are consisted with the known results [4,5,6] for zigzag edge. The energies of positive (negative) Landau levels (LLs) increase (decrease) as one approaches the boundary and the zeroth LL is twice degenerate in the valley $\tau = +1$, see the solid curve on Fig. 1a, and is nondegenerate in the valley $\tau = -1$, see the dotted curve. When $a \neq 0$ there is region where the energies of positive (negative) LLs decrease (increase) as one approaches the boundary and LLs beside zeroth have minimum or maximum, Fig. 1b. The spectrum can be obtained as a result of superposition of the spectrum (3) and the spectrum of the usual magnetic edge states taking the anticrossing into account.

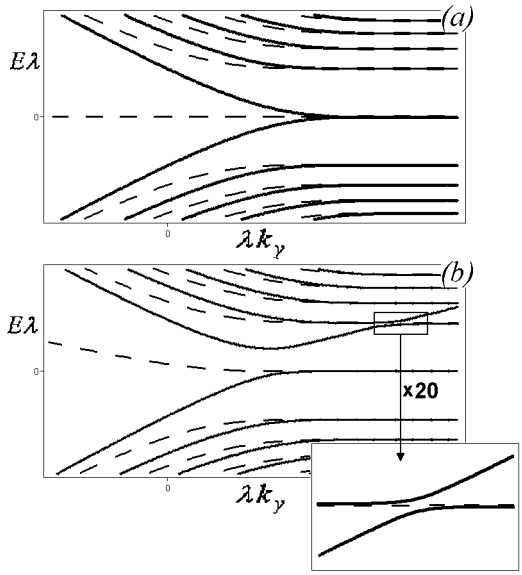

Fig. 1. Electron energy spectrum for linear graphene edge for $\tau = +1$ (the solid curve) and for $\tau = -1$ (the doted curve) valleys for different meanings of the parameter a: (a) $a = 0$, (b) $a = 0.1$. k_y is the momentum along the linear boundary of graphene, λ is the magnetic length.

2. Energy spectrum for graphene antidot without B

Now we discuss electron energy spectrum of an infinite graphene sheet with a circular hole with radius R_0, Fig. 2. We define this very system as antidot in graphene. We solve the system of equations (1),(2) with the parameter a being constant at the boundary of the hole. In polar coordinates (r, ϕ) wave function is proportional to $exp(il\phi)\mathrm{H_l}(Er)$, where $\mathrm{H_l}$ is the

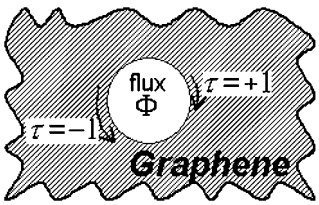

Fig. 2. Graphene antidot of radius R_0 threaded by magnetic flux Φ. The edge states of different valleys ($\tau = \pm 1$) are occupied by electrons rotating clockwise or counter-clockwise around the antidot.

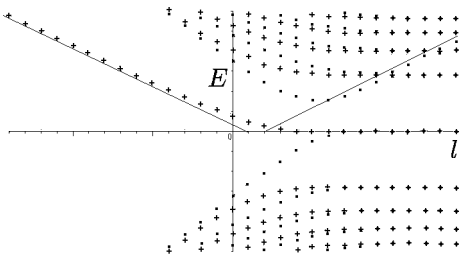

Fig. 3. The spectrum of graphene antidot in perpendicular magnetic field for $a = 0.2$, $\Phi/\Phi_0 = -2$. Crosses correspond to $\tau = -1$ valley, squares corresponds to $\tau = +1$. Solid lines are the asymptotes of the edge states.

Hankel functions [7]. For ESs we obtain dispersion relation:

$$E_\tau(l) = \frac{2\tau a^\tau}{R_0}\left(l - i\pi\left(\frac{(la^\tau)^l}{(l-1)!}\right)^2\right). \qquad (4)$$

It is applicable if $0 < \tau a^\tau l \ll 1$, $l = 1, 2, 3\ldots$ The real part of the equation (4) can be obtained from the ESs spectrum (3) for semi-infinite graphene plane if azimuthal component of the momentum is quantized, $k_y = 2\pi l/2\pi R_0$. Imaginary part corresponds to quasistationary states, i.e. $\mathrm{Im}(E) < 0$ and $|\mathrm{Im}(E)/\mathrm{Re}(E)| \ll 1$. So spectrum of ESs is quantized and forms a series of the quasidiscrete states numbered by orbital quantum number l. In this sense graphene antidot is a quantum object. This feature essentially differs graphene from usual semiconductors ("not relativistic") like GaAs or Si, in which electrons have the square law of a dispersion and are not localized by an antidot.

3. Energy spectrum of graphene antidot in magnetic field

Finally, we consider graphene antidot in a perpendicular magnetic field. Again in (1) we make substitution $\vec{p} \to \vec{p} + \frac{|e|}{c}\vec{A}$ and reduce to the confluent hypergeometric equation. We choose the solution, which corresponds to finiteness of the wave function. Substituting it in the BCs (3) and considering orbital angular momentum quantum number $l > 0$ we obtain the dispersion relation:

$$\frac{\tau E R_0}{a^\tau} U\left(l+1-\frac{cE^2}{|e|B}, l+1, \frac{|e|BR_0^2}{2c}\right)$$
$$-\frac{|e|BR_0^2}{c} U\left(l+1-\frac{cE^2}{|e|B}, l+2, \frac{|e|BR_0^2}{2c}\right) = 0, \qquad (5)$$

where $U(a, b, z)$ is the Kummer's function [7].

For $l \gg 1$ the ESs has asymptotes, Fig. 3:

$$E_\tau = \frac{2\tau a}{(1+a^2)R_0}\left(l + \frac{\Phi}{\Phi_0} + \frac{1-\tau}{2}\right). \qquad (6)$$

Φ is the magnetic flux through the hole, $\Phi_0 = hc/|e|$ is the magnetic flux quantum. The dispersion relation differs from (3) not only in the quantization of the azimuthal component of the momentum $k_y \to l/R_0$, but also in change of $l \to l + \Phi/\Phi_0$. Suppose that the Fermi level $E_F \neq 0$. It means that periodically (with the period Φ_0) the ESs level crosses the Fermi level. That is why when electrons pass through antidot in a magnetic field, electrical resistance of graphene antidot may undergo periodic oscillation as a function of the enclosed magnetic flux Φ.

References

[1] Yu. I. Latyshev *et al*, *JETP Letters* **90**, 526 (2009).
[2] V. A. Volkov, I. V. Zagorodnev, *FNT* **35**, 5 (2009).
[3] V. A. Volkov, I. V. Zagorodnev, *Journal of Physics: Conference Series* **193**, 012113 (2009).
[4] L. Brey, H. A. Fertig, *Phys. Rev. B* **73**, 195408 (2006).
[5] D. A. Abanin *et al*, *Phys. Rev. Lett.* **96**, 176803 (2006).
[6] L. Brey, H. A. Fertig, *Phys. Rev. B* **73**, 235411 (2006).
[7] M. Abramowitz, I. Stegun, *Handbook of Mathematical Functions with Formulas, Graphs, and Mathematical Tables*, New York: Dover, 1965.

18th Int. Symp. "Nanostructures: Physics and Technology"
St Petersburg, Russia, June 21–26, 2010

Continuous models of semiconductor heterojunctions and surfaces

A. A. Gorbatsevich
St Petersburg Academic University, St Petersburg, Russia

Abstract. Recently developed theory of interrelation of micro- and macroscopic description of heterojunctions is described. This theory is based on the extraction procedure of envelop function boundary condition parameters from scattering data calculated in microscopic model. A novel "dark matter"-like object in crystals is explicitly constructed — a hidden quantum well which transparency coefficient equals unity without any phase-factor. By explicit deduction of surface boundary conditions it is shown that Shockley's interpretation of Tamm's surface states as states originating in continuous model with quantum well potential at the surface is incorrect. A supersymmetric continuous model of surface states is presented.

Introduction

The problem of interrelation of microscopic structure of inhomogeneous semiconductors and their description in continuum limit (effective mass model) is by no means a new one. In semiconductor heterostructures it is directly related to the problem of establishing boundary conditions for envelope functions. Recently a new extraction procedure for envelope function boundary conditions was proposed [1] based on a direct comparison of scattering data in both microscopic and continuum models. This procedure appeared to be capable of deducing not only the boundary conditions for envelope functions but the exact location of the heterojunction in continuum model as well. The analogous approach can be well applied to the description of defect location. It was shown that in systems without spatial inversion symmetry location of a heterojunction or a defect in the continuum model can differ considerably from its real location in the microscopic model. As the verification of this statement extended microscopic objects was constructed (hidden defect pairs) invisible in the continuum (effective mass) limit. It was shown that effective size of such objects in continuum limit turns into zero. In this report we present the construction of another solid state object of "dark matter" type — one-dimensional quantum well with foreign atoms at the heterojunction. The transparency amplitude of this hidden quantum well turns into unity without any phase factor which differs this object from reflectionless potentials. Bound states are absent as well.

Historically the problem of interrelation of microscopic and continuum models was put forth by Shockley [2] who claimed that Tamm's surface states [3] originated from the quantum well introduced at the surface by an improper choice of surface location in the Kronig-Penney model considered by Tamm. In this report we extend our extraction procedure and apply it to surfaces. It is shown that quantum well do exist in Tamm's model but the condition of surface states formation doesn't coincide with the condition of the existence of localized states in asymmetric quantum well. It is shown that one should take into account both conduction and valence bands to describe surface states in the continuum model. Desrete periodic potential in this model manifests itself in the existence of valence band with negative effective mass. Semiconductor surfaces in continuum limit can be considered as inverse contacts resembling supersymmetric potentials in quantum field theory which are known to possess zero-energy localized states.

1. "Dark-matter"-like objects in semiconductors

Consider heterojunction in one-band model. Generalized boundary conditions for envelop wave functions was proposed in [4]

$$\begin{pmatrix} \Psi(+0) \\ \partial_z \Psi(+0) \end{pmatrix} = \begin{pmatrix} T_{11} & T_{12} \\ T_{21} & T_{22} \end{pmatrix} \begin{pmatrix} \Psi(-0) \\ \partial_z \Psi(-0) \end{pmatrix}. \quad (1)$$

In Ref. [5] it was shown that this form of boundary conditions emerges as a result of Hermiticity requirement for the Hamiltonian. Generalization for multi-band case is tedious but straightforward. Matrix T_{ij} is called a transfer matrix. Its diagonal form with $T_{12} = T_{21} = 0$ corresponds to the so called standard boundary conditions. Nonzero element T_{21} can be attributed to the existence of a potential located at the heterojunction (a barrier for $T_{21} > 0$ and a well for $T_{21} < 0$ [6]. Off-diagonal element describes interband mixing at the heterojunction [5]. The main idea of extraction procedure for deducing transfer matrix elements from scattering data is to compare decompositions of reflection coefficients in powers of quasimomentum calculated in envelope function approximation (1) and in a given microscopic model. In this formulation it is assumed that explicit analytical expression for reflection coefficient in the microscopic model is available, i.e. microscopic model is not very complicated, e.g., tight-binding model or continuous potential Kronig–Penney-like model. However this approach can be applied to the extraction of envelop function boundary condition parameters from scattering data for heterojunction obtained from *ab initio* calculations as well.

The origin of hidden objects in one-dimensional scattering problems can be described as follows. Consider a quantum well of width L with both heterojunctions described by generalized boundary conditions (1). Material in the well (barrier) is denoted correspondingly by index 1(2). For the quantum well reflection coefficient the following expression can be obtained:

$$r = A(k_2)\,\frac{N}{D}\,, \quad (2)$$

where $A(k_2)$ is a smooth factor which doesn't turn into zero. Numerator N and denominator D can be written as:

$$N = \sin(k_1 L)\left(1 - k_1^2 \Pi \Pi'^*\right) + k_1 \cos(k_1 L)\left(\Pi + \Pi'^*\right), \quad (3)$$

$$D = \sin(k_1 L)\left(1 - k_1^2 \Pi \Pi'\right) + k_1 \cos(k_1 L)\left(\Pi + \Pi'\right). \quad (4)$$

Here auxiliary parameter for left heterojunction Π is intro-

duced:

$$\Pi = \frac{T_{22} - ik_2T_{12}}{T_{21} - ik_2T_{11}}\,.$$

Primed quantities in (3), (4) stand for right heterojunction. In the case of physically identical left and right heterojunctions and standard boundary conditions $\Pi = -\Pi'^*$ and reflection coefficient $r \propto \sin(k_1L)$ turns into zero at $k_2L = n\pi$. This is the well-known Ramsauer–Townsend resonance. However in studying microscopic models we have discovered that in the case of generalized boundary conditions with nonzero off-diagonal matrix elements the condition $\Pi = -\Pi'^*$ can still hold but the parameter L becomes momentum dependent $L = L(k_1)$. In envelop function approximation L has a unique sense of quantum well size. So generally one should consider L as *effective quantum well size*. This effective size can turn into zero at some momentum k_{01}: $L(k_{01}) = 0$ and hence reflection coefficient (2) $r = 0$. Thus we have a new type of resonance in one-dimensional scattering theory. If $k_{01} = 0$ then effective quantum well size in the envelope function approximation equals zero identically and quantum well becomes a hidden ("dark matter"-like) object whose reflection coefficient identically equals zero in the long-wavelength limit (in the continuous approximation).

2. Surface boundary conditions and supersymmetry

The conjecture of Shockley that abrupt change of potential at the surface in continuous (envelop function) approximation can result in the emergence of quantum well potential was confirmed by Volkov and Pinsker [7]. They showed that surface boundary condition for envelope function in one-band approximation has the form

$$(1 + R\nabla)\,\Psi = 0\,, \tag{5}$$

where parameter R can be associated with delta-function attractive potential located at the surface. However the interrelation of the parameter R with parameters of microscopic model wasn't established. It is easy to verify that surface boundary conditions (5) can be considered as a particular case of generalized boundary conditions (1) with $T_{21} \neq 0$ and vacuum wave function going to zero. So one can apply extraction procedure [1] described above to the deduction of surface boundary condition parameters. The specific point here is that imaginary vacuum momentum is large and only crystal momentum near the band edge can be used to construct decomposition of scattering data. Hence the number of relations between the parameters of microscopic model and envelop function approximation parameters is reduced in comparison with real heterojunction case. It limits the available information but is still enough to analyze some physical properties. E.g. the condition for the existence of the states localized on heterojunction [5,6]

$$-\frac{T_{21}}{T_{11}} > \kappa\,, \tag{6}$$

(here κ is a vacuum decrement of localized state) contains only the ratio of the parameters T_{21} and T_{11}. It can be shown that in Kronig–Penney model this ratio takes the form

$$\frac{T_{21}}{T_{11}} = -\zeta \tan\left(\zeta\left(\Delta - \frac{1}{2}\right)\right)\,. \tag{7}$$

Here $\zeta = a\sqrt{2m_0E/h^2}$, a is lattice period, E is an energy and Δ is parameter determining the location of the surface. One can easily verify that condition (6) with *l.h.s.* given in (7) *doesn't* coincide with the well known condition for the existence of Tamm states [3]. Therefore Shockley statement is not exact and the real nature of Tamm states is not reduced to the existence of surface quantum well though this quantum well does exist. It deserves mention that in Shockley model [2] $\Delta = 1/2$, $T_{21} = 0$ and there is no attractive quantum well at the surface. Shockley attributed the emergence of surface states to the discreteness of crystal potential explicitly been taken into account and stated that this discreteness is an essential point in treating surface states. However we show that it is not necessary to introduce explicitly discrete crystal potential in the problem to describe surface states. Surface states can be well described in continuous model *without* any effective surface quantum wells but where the period crystal potential manifests itself in the multi-band nature of energy spectrum. In our model the principal point is that vacuum electrons possess energy spectrum as well though it lies far above their energy in crystal. It was established long ago [8,9] that localized states do emerge at the inverse contact where conduction and valence band change places. The nature of localized states at the inverse contact is directly related the supersymmetric properties of such two-band quantum mechanical model which allows for the existence of zero-energy mode [9]. In fact to get localized states at an interface it is not necessary to treat real supersymmetric potential but it is enough to have effective mass sign reversal. At the surface such mass reversal is realized if we consider valence band with negative effective mass and vacuum free electrons. E.g. surface states in continuous approximation exist already in the case of simple boundary condition

$$\frac{1}{m^*_{\text{valence}}}\nabla\Psi_{\text{valence}} = \frac{1}{m_0}\nabla\Phi_{\text{vacuum}}\,,$$

where $m^*_{\text{valence}} < 0$. In the case of generalized boundary conditions transfer matrix determinant should be negative $\det||\hat{T}|| < 0$. The situation is complicated by the existence of other band but it can be shown that localized states related to such formal band reversal retain. The characteristics of surface states in a specific semiconductor are determined by the interaction of zero-energy mode states with other bands of semiconductor.

Acknowledgements

This work was supported by Russian Fund for Basic Researches and RAS.

References

[1] A. A. Gorbatsevich, *JETP Letters* **84**, 593 (2006).
[2] W. Shockley, *Phys. Rev.* **56**, 317 (1939).
[3] I. Tamm, *Phys. Z. Soviet Union* **1**, 733 (1932).
[4] T. Ando and S. Mori, *Surf. Sci.* **113**, 124 (1982).
[5] I. V. Tokatly, A. G. Tsibisov and A. A. Gorbatsevich, *Phys. Rev. B* **65** 165328 (2002).
[6] Q.-G. Zhu and H. Kroemer, *Phys. Rev. B* **27**, 3519 (1983).
[7] V. A. Volkov and T. N. Pinsker, *ZhETF* **70**, 2268 (1976).
[8] R. A. Suris, *Sov. Phys. Semicond.* **20**, 1258 (1986).
[9] B. A. Volkov and O. A. Pankratov, *JETP Lett.* **42**, 145 (1995).

18th Int. Symp. "Nanostructures: Physics and Technology"
St Petersburg, Russia, June 21–26, 2010

Strong coupling and entanglement of two coupled quantum dots

Elena del Valle
School of Physics and Astronomy, University of Southampton, SO17 1BJ Southampton, UK

Abstract. I present a theoretical study of the strong and weak coupling of two quantum dots, considered as two-level systems. Under an incoherent continuous excitation, new regimes are found where the effective coupling is reinforced, causing the standard dressed states and Rabi doublet to split in four. In this regime, entanglement is enhanced above the previously reported values for thermal excitation. Finally, I consider the case where the dots are coupled through another mode: a cavity mode (harmonic oscillator) or a third two-level system.

Introduction

Strong light matter coupling with self-assembled quantum dots in microcavities has been achieved by many groups. Anti-bunching in the dot emission has been observed [1,2], evidencing its quantum nature and opening a broad range of quantum applications for these semiconductor devices, such as efficient single and two photon sources. Quantum dots, as two-level systems (or qubits), have the advantage of a solid state system, such as the possibility of optical and electrical manipulation, scalable implementations, etc. Disadvantages, as compared to atomic transitions or superconducting qubits, are, for instance, the high degree of dephasing caused by interaction with the environment [3]. Another specificity of typical experiments with quantum dots that has proved to be more relevant [4,5], is the incoherent continuous excitation. In the present model, I include both elements together with dissipation, in order to fully account for the incoherent processes that may hinder, but also, surprisingly, enhance the coherent coupling.

The study of the coupling and entanglement of two quantum dots (or two-level systems), subject to decoherence, is interesting for many reasons. The system represents an analytically solvable example of entanglement in an open quantum system. Regarded as a fundamental problem, it has been theoretically investigated in the past, but only in the presence of thermal noise [6–9]. Moreover, with the rapid progress of growth and control of quantum dots in microcavities, the possibility of coupling strongly two quantum dots has become a reality. Recently, Laucht *et al* have observed clear signatures of two dots coupling with and through a cavity mode [10]. Hints of inter-dot tunneling have also been reported previously [11].

1. Theoretical description

The quantum dots are considered as two-level systems with lowering operators σ_i ($i = 1, 2$), frequencies ω_i and coupled with strength g. They may also couple to a third intermediate mode σ_3 that can be fermionic (another quantum dot) or bosonic (a cavity mode $\sigma_3 \to a$) and provides the reference energy ($\omega_3 \equiv 0$). The Hamiltonian reads:

$$H = \sum_{i=1}^{2} \left[\omega_i \sigma_i^\dagger \sigma_i + g_i \left(\sigma_3^\dagger \sigma_i + \sigma_i^\dagger \sigma_3 \right) \right] + g \left(\sigma_1^\dagger \sigma_2 + \sigma_2^\dagger \sigma_1 \right). \quad (1)$$

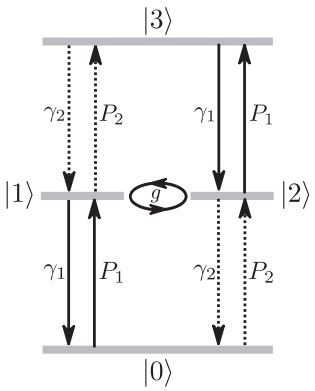

Fig. 1. Level scheme and parameters of the system under study: two coupled two-level systems with pump and decay.

The total density matrix matrix of the system, $\tilde{\rho}$, follows a master equation including all incoherent processes [4,12]:

$$\partial_t \tilde{\rho} = i[\tilde{\rho}, H] + \sum_{i=1}^{3} \left[\frac{\gamma_i}{2} \mathcal{L}_{\sigma_i} + \frac{P_i}{2} \mathcal{L}_{\sigma_i^\dagger} + \frac{\delta_i}{2} \mathcal{L}_{\sigma_i^\dagger \sigma_i} \right] \tilde{\rho}. \quad (2)$$

The parameters γ_i, P_i and δ_i are the rates of decay, pumping and pure dephasing of the modes, which appear in the equation as Lindblad terms ($\mathcal{L}_O \tilde{\rho} \equiv 2O\tilde{\rho}O^\dagger - O^\dagger O\tilde{\rho} - \tilde{\rho}O^\dagger O$). I investigate the steady state of the bipartite system, ρ, by solving exactly the equation $\partial_t \tilde{\rho} = 0$ and tracing over the intermediate mode, if present. The steady state is a mixture of all the four possible states, sketched in Fig. 1.

The strong coupling regime, determined by the appearance of dressed states, can be investigated by means of the *photoluminescence* or *power spectrum* of one of the dots, $S_1 \propto \Re \int_0^\infty \langle \sigma_1^\dagger(t)\sigma_1(t+\tau)\rangle e^{i\omega\tau} d\tau$. The required two-time correlator follows from the *quantum regression formula* [13]. The degree of entanglement in a mixture of two quantum dot states is given by the *concurrence* [14], C, equal to 0 for completely separable states and 1 for an entangled pure state. Closely related is the degree of purity in the mixture, given by the *linear entropy* [15], S_L, equal to 0 for a pure state and 1 for a maximally mixed state.

2. Strong coupling of two quantum dots

The problem of two directly coupled quantum dots with pump and decay can be fully solved analytically [16]. This allows for a detailed analysis of the physics of strong and weak coupling and the different dressed states arising in the system. For configurations with dissipative environments ($\gamma_i > P_i$), which include the thermal baths, or gain environments ($P_i > \gamma_i$),

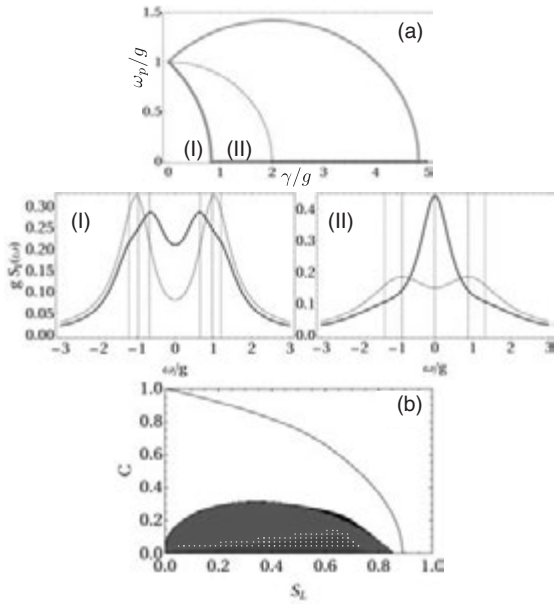

Fig. 2. (a) Double splitting (positive part only) of two coupled quantum dots (solid) and standard Rabi splitting of a four-level system (dashed), in the optimally pumped configuration. The resulting spectra of emission is a quadruplet (I) or triplet (II) instead of the standard Rabi doublet (in dashed). (b) Distribution of C and S_L for all possible two quantum dot configurations (shaded region). The thin line corresponds to the maximum concurrence for a given linear entropy in a general bipartite system. The thick dashed line corresponds to the optimally pumped configuration. In dotted, the particular case of thermal reservoirs [8].

the strong coupling is *standard*, featuring only two dressed states. More importantly, in the case where one quantum dot is in contact with a gain medium ($P_1 > \gamma_1$), and the other with a dissipative medium ($\gamma_2 > P_2$), new coupling regimes arise, that I call *second order strong coupling* (SSC) and *mixed coupling* (MC). They are characterized by the appearance of four — instead of two — dressed states, that undergo a double anticrossing. This is shown in Fig. 2(a) (at positive energies) for the optimally pumped case: $\gamma_1 = P_2 = 0$, $\gamma_2 = P_1 = \gamma$. In SSC, the spectrum of emission (I) has a quadruplet structure (with peaks positioned on the vertical solid lines) and in MC, a triplet one (II) due to the saturation of one pair of dressed states. This is to be compared with the standard results of a four level system (such as a single quantum dot with a biexciton state), superimposed in dashed. The reason for this exotic coupling regimes is to be found in the enhancement of coherence induced by the links that pump and decay establish between diagonal transitions $|0\rangle\langle i|$ and $|j\rangle\langle 3|$ ($i \neq j$). A coherence circulation loop appears in the system that accompanies and complements the Rabi oscillations between $|1\rangle \leftrightarrow |2\rangle$, producing new dressed states.

It is remarkable that the optimally pumped configuration provides also the maximum entanglement available in this system [17]. This is shown in Fig. 2(b), where the region that our system can access in the concurrence-linear entropy plane is shaded in grey/black. The optimally pumped configuration (dashed thick line) encloses most of this region, providing in good approximation the maximum entanglement for a given linear entropy. In any case, it also includes the absolute maximum entanglement, $C_{\max} = (\sqrt{5}-1)/4 \approx 0.31$, at $\gamma_{\max}/g = 1+\sqrt{5}$. These high values of entanglement are possible thanks to the inversion of population in the driven quantum dot, which reduces S_L while the coherent coupling is still effective between the dots. This should be compared with previous results [8,9] with thermal noise at resonance. I find that higher values of entanglement can be still obtained in those cases by allowing some detuning between the quantum dots (dotted region).

3. Coupling mediated by a third mode

Theoretically, the simplest element to mediate the coupling between two quantum dots is another two-level system (a resonator or a third quantum dot). Analytical solutions can still be found and directly compared with the direct coupling results. I find that entanglement is completely lost in the optimally pumped configuration although some concurrence can be obtained by having the mediator pumped and the two dots only decaying [17]. Following a different scheme, entanglement is also possible by forcing the system into an entangled state, such as the singlet (Bell) state $|1\rangle - |2\rangle$. This can be achieved if the two quantum dots are fed by the same pumping reservoirs [18].

A second possibility is that the coupling between dots is mediated by a cavity mode (harmonic oscillator). Analytical results are not available in general, and Eq. (2) must be numerically solved to obtain entanglement and emission properties. The same scheme of entanglement by the effect of a common dot reservoir is still feasible [19]. From another point of view, the cavity emission is largely modified by the strong coupling with the dots, increasing its lasing efficiency [19] or even leading to two-photon lasing [20].

Acknowledgements

This work is supported by the Newton International Fellowship Program (UK). The results from Refs. [18–20] were obtained in collaboration with F. P. Laussy, F. Troiani, C. Tejedor, S. Zippilli, A. Gonzalez-Tudela and G. Morigi.

References

[1] K. Hennessy *et al*, *Nature* **445**, 896 (2007).
[2] D. Press *et al*, *Phys. Rev. Lett.* **98**, 117402 (2007).
[3] A. Laucht *et al*, *Phys. Rev. Lett.* **103**, 087405 (2009).
[4] E. del Valle, *Microcavity Quantum Electrodynamics* (VDM Verlag, 2009).
[5] F. P. Laussy *et al*, *Phys. Rev. Lett.* **101**, 083601 (2008).
[6] M. B. Plenio *et al*, *Phys. Rev. A* **59**, 2468 (1999).
[7] D. Braun, *Phys. Rev. Lett.* **89**, 277901 (2002).
[8] J.-B. Xu and S.-B. Li, *New J. Phys.* **7**, 72 (2005).
[9] L. Hartmann *et al*, *Phys. Rev. A* **74**, 052304 (2006).
[10] A. Laucht *et al*, arXiv:0912.3685(2010).
[11] B. D. Gerardot *et al*, *Phys. Rev. Lett.* **95**, 137403 (2005).
[12] G. W. Gardiner, *Quantum Noise* (Springer-Verlag, Berlin, 1991).
[13] E. del Valle *et al*, *AIP Conf. Proc.* **1147**, 238 (2009).
[14] W. K. Wootters, *Phys. Rev. Lett.* **80**, 2245 (1998).
[15] W. J. Munro *et al*, *Phys. Rev. A* **64**, 030302 (2001).
[16] E. del Valle, arXiv:1001.2201(2010).
[17] E. del Valle, in preparation.
[18] E. del Valle *et al*, *Europhys. Lett.* **80**, 57001 (2007).
[19] E. del Valle *et al*, *Phys. Rev. B* **76**, 235317 (2007).
[20] E. del Valle *et al*, *Phys. Rev. B* **81**, 035302 (2010).

18th Int. Symp. "Nanostructures: Physics and Technology"
St Petersburg, Russia, June 21–26, 2010

Acceptor states in semiconductor quantum wells

M. A. Semina and R. A. Suris
Ioffe Physical-Technical Institute, St Petersburg, Russia

Abstract. We study the states of a hole localized on the charged acceptor in quantum well by means of the variational method. The trial function being applicable for calculating acceptor binding energy in wide range of quantum well parameters, smoothly interpolating between bulk and strictly two-dimensional limits with physically justified variational parameters is suggested. We demonstrate that the binding energy of a hole on the acceptor is, in general, non-monotonous function of a quantum well width.

Introduction

In the vicinity of the fundamental absorption the optical properties of bulk semiconductors and low-dimensional systems are controlled by the electrons and holes bound together by Coulomb interaction and localized on the impurities and imperfections of the heterostructure.

Special interest is paid to the holes localized on acceptors and A^+ centers [1–5]. Although this problem may seem trivial at first glance, the hole states in most diamond and zinc-blende lattices are described by multicomponent wave functions thus making calculations of the localized hole states a complex problem even in the bulk material [1,3]. There are few calculations of the hole states localized on acceptors in quantum wells made under some simplifying assumptions [5]. In this work we use variational method to calculate binding energies of a hole localized on the charged acceptor in quantum well.

1. Model

The states of the hole localized on the acceptor are described by Luttinger Hamiltonian

$$H = \left(1 + \frac{5\gamma_2}{2\gamma_1}\right) k^2 - \frac{2\gamma_2}{\gamma_1} \sum_i J_i k_i - \frac{2\gamma_3}{\gamma_1} \sum_{i' \neq i} \{J_{i'} J_i\}_s k_{i'} k_i - \frac{2}{r} + V(z), \quad (1)$$

where the Coulomb attraction of the hole to acceptor as well as the quantum well confinement potential $V(z)$ are included, $r = \sqrt{x^2 + y^2 + z^2}$. Here γ_i $(i = 1 \ldots 3)$ are Luttinger parameters, J_α $(\alpha = x, y, z)$ are the matrices of the angular momentum 3/2, k_α are the components of the wave vector, and we used $Ry^* = m_0 e^4 / 2\gamma_1 \varepsilon^2 \hbar^2$ as a unit of energy and $a_B^* = \hbar^2 \gamma_1 \varepsilon / m_0 e^2$ as a unit of length, with m_0, e and ε being the free electron mass, the electron charge and the dielectric constant. For simplicity, the confinement potential is chosen to be parabolic: $V(z) = \kappa z^2$, where stiffness κ is related with the localization length of the hole $L \propto \kappa^{-1/4}$.

We follow the general method developed in [6] to construct the trial function for a localized hole. Firstly we separate the two opposite limiting cases where the general shape of the wave function is known from physical arguments. In first case the quantization energy of the hole in quantum well is small compared to the Coulomb energy of the bulk acceptor and quantum well potential can be considered as a perturbation. The second case corresponds to the two-dimensional limit, where the in-plane motion of hole and its motion along the growth axis can be separated.

In the bulk limit the acceptor wave function reads [1]

$$\Psi_{3D}(\mathbf{r}) = f(r)|L=0,\ J=3/2,\ F=3/2,\ F_z=\pm 3/2\rangle + g(r)|L=2,\ J=3/2,\ F=3/2,\ F_z=\pm 3/2\rangle, \quad (2)$$

where $f(r)$ and $g(r)$ are certain radial functions to be defined from Eq. (1) with $V(z) = 0$, and $|L, J, F, F_z\rangle$ denotes the angular part possessing the orbital momentum L, spin J, total momentum (spin and orbital) F and its z projection F_z. Note that each hole state is two-fold degenerate with respect to F_z. Such a wave function is exact in the spherical limit where $\gamma_2 = \gamma_3$ [1,3] and is a good approximation with allowance for the valence band wrapping, $\gamma_2 \neq \gamma_3$. In this work we calculate functions $f(r)$ and $g(r)$ by means of the variational method with the following trial functions:

$$f(r) = C_1 \exp\left(-\alpha_1 r^2\right), \quad g(r) = C_2 r \exp\left(-\alpha_2 r^2\right), \quad (3)$$

where C_1, C_2, α_1, α_2 are trial parameters. The applicability of the chosen functions $f(r)$ and $g(r)$ is demonstrated below.

The acceptor wave function in the limit of strong confinement has a certain spin projection on the growth axis and takes the form

$$\Psi_{2D}(\mathbf{r}) = e^{-\rho/a_{2D}^*} e^{-\frac{\sqrt{\kappa}}{2}\left(\frac{\gamma_1}{\gamma_1 - 2\gamma_2}\right)^{1/2} z^2} |J_z = \pm 3/2\rangle, \quad (4)$$

where $a_{2D}^* = a_B^*(\gamma_1 + \gamma_2)/(2\gamma_1)$ is the 2D Bohr radius for the heavy hole, and $|J_z = \pm 3/2\rangle$ is the wave function corresponding to the spin projection J_z on the growth axis. Hereafter normalization constants are omitted.

The trial function was constructed in a way similar to that suggested in [6]. In our case, the trial function has four components each of those has to interpolate smoothly between the forms corresponding to the limiting cases of bulk acceptor and the acceptor in the 2D quantum well. In order to improve the accuracy, we take into account the admixture of the lowest excited states to the trial function corresponding to the two-dimensional limit, Eq. (4).

2. Results

We remind that the acceptor binding energy is a difference between ground energy levels of acceptor (E_A) and a hole, placed in the same external potential (E_h): $E_b = E_A - E_h$.

Before we proceed to discussing our results, it is necessary to estimate the applicability of the function Eq. (3) that we chose as the wave function of the bulk acceptor. To do so we compare the results of the variational calculation with the trial function Eq. (3) (solid curve in the Fig. 1) and the results of the

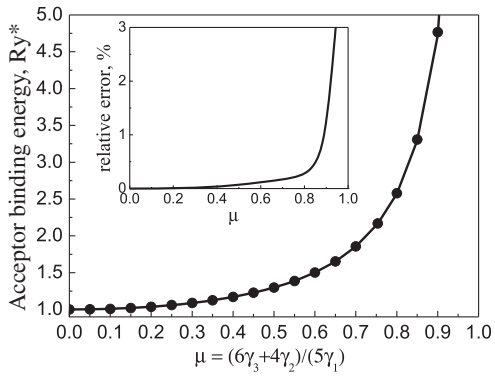

Fig. 1. Binding energy of the bulk acceptor as a function of the parameter $\mu = (6\gamma_3+4\gamma_2)/5\gamma_1$. Solid curve and circles correspond to results of variational "exact" calculation. The inset shows the relative error of the variational calculation.

"exact" calculation made by means of the method, described in [1] with using the basis containing 80 elements (circles in the Fig. 1). The acceptor binding energy is shown as a function of the parameter $\mu = (6\gamma_3 + 4\gamma_2)/5\gamma_1$ as it is the only parameter determining the binding energy of the bulk acceptor in the spherical approximation [1]. The inset to Fig. 1 shows the relative error of the variational calculation of the binding energy. One can see from Fig. 1 that the accuracy of our trial function is very high: it is $\leq 3\%$ in the relevant range of parameter μ.

In opposite limit of ultra-narrow quantum well ($\kappa \gg 1$) acceptor binding energy can be calculated analytically:

$$E_b = 4\gamma_1 Ry^*/(\gamma_1 + \gamma_2). \qquad (5)$$

Fig. 2 shows the acceptor binding energy, calculated for different values of the Luttinger parameters, as a function of quantum well potential stiffness. The dotted curves are calculated in the spherical approximation while the solid curves are calculated with allowance for the valence band wrapping. If the parameter μ is small, the difference between the light and heavy hole effective masses is also small and the dependance of the binding energy on the potential stiffness is monotonous (see Fig. 2a). In such a case the effects of the complex band structure are weak: the localization along z axis increases the Coulomb attraction between the hole and the acceptor and the binding energy increases.

The dependence of the binding energy on the potential stiffness becomes non-monotonous with an increase of μ, i.e. with an increase of light and heavy hole mass difference. If κ is small, the acceptor binding energy increases with an increase of κ since hole is pressed closer to the charged center. Further increase of κ results in the transformation of the hole state: from bulk-like, Eq. (2) it becomes more and more two-dimensional, Eq. (4). Correspondingly, in-plane hole mass reduces and binding energy decreases. Such a decrease is most pronounced when the wrapping $\gamma_2 \neq \gamma_3$ is allowed for, see Fig. 2(b) (this set of Luttinger parameters corresponds to GaAs). In very narrow quantum wells the acceptor binding energy starts to increase again. Note that the difference between the binding energies in bulk case and in the strictly 2D case can be either negative or positive depending on the value of parameter μ, see Fig. 2(c) (these parameters correspond to InAs).

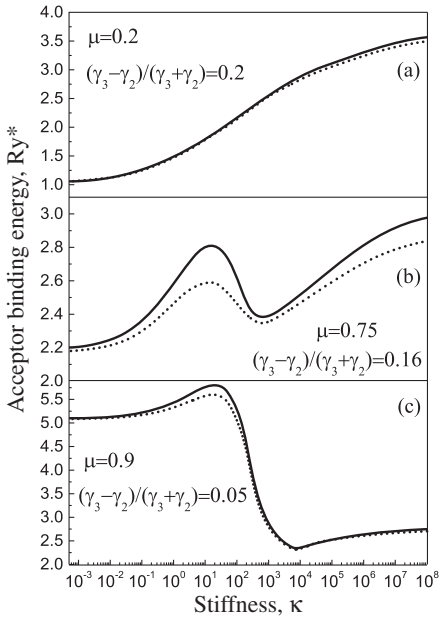

Fig. 2. Acceptor binding energy as a function of quantum well potential stiffness κ. Figures (a), (b) and (c) corresponds to different Luttinger parameters shown in each panel. The dotted curves are calculated in the spherical approximation while the solid curves are calculated with allowance for the valence band wrapping.

3. Conclusions

We demonstrate that the binding energy of hole localized on the acceptor is the non-monotonous function quantum well potential stiffness that is related to the hole localization length along the growth axis $L \propto \kappa^{-1/4}$. This result is in the contrast to the case of simple (non-degenerate) band structure, where the acceptor binding energy monotonically increases with decrease of the quantum well width. The non-monotonic dependence is most pronounced in the physically realistic well width range ($L \sim a_B^*$).

The variation of the acceptor binding energy between two limiting cases of wide and narrow quantum well is smaller as compared with the case of simple band structure. Moreover, the binding energy in narrow quantum wells can be smaller than in a bulk material. It is important to note, that the application of the spherical model of the hole dispersion can result in the incorrect binding energies in limit of the narrow wells and in intermediate case.

Acknowledgements

The work is supported by RFBR, grant 08-02-01337-a, and Federal program on support of leading scientific schools grant 4369.2010.2

References

[1] A. Baldereschi, N. O. Lipari, *Phys. Rev. B* **8**, 2697 (1973).
[2] Q. X. Zhao *et al*, *Phys. Rev. B* **63**, 195317 (2001).
[3] A. V. Efanov, *Semicond. Sci. Technol* **24**, 035017 (2009).
[4] N. S. Averkiev *et al*, *Semiconductors* **32** (2), 217 (2004).
[5] S. Fraizzoli and A. Pasquarllo, *Phys. Rev. B* **44**, 1118 (1991).
[6] M. A. Semina *et al*, *Semiconductors* **40** (11), 1338 (2006).

18th Int. Symp. "Nanostructures: Physics and Technology"
St Petersburg, Russia, June 21–26, 2010

Application of a hydrostatic technique for research of spectra of absorption of quantum dots PbI_2

V. A. Gaisin[1], B. S. Kulinkin[2] and V. A. Maruchuk[2]

[1] Faculty of Physics, St Petersburg State University, 198504 St Petersburg, Russia
[2] St Petersburg State Medical, St Petersburg University, 197022 St Petersburg, Russia

Abstract. Application of a hydrostatic technique for research of spectra of absorption of quantum dots PbI_2 in a polyvinyl spirit solution have been investigated. A change in spectra was not revealed in the interval of pressure 0–30 kbar at 77 K. It is allows make a conclusion that contact besides microcrystal's and a matrix no exist. This supervision can be used for specification of theoretical calculations.

Introduction

Nowadays interest in researching low dimensional structures steadily grows. Successes of modern technology allow receiving crystal materials of high optical quality. This effect leads to occurrence in optical spectra of absorption and a luminescence of a series narrow (in a limit having nuclear radiating semi width) lines. Structures of this kind are perspective both in purely scientific plan, and in connection with possibility of their to use at designing electronic devices. Structures of various types are studied: the quantum dots (QDs) in a glass, polymeric matrixes, in porous structures and crystal matrixes, various type getero-structures and so on. Measurements depending on structure temperature, under the influence of electric and magnetic fields at action of unidirectional and hydrostatic pressure are conducted. For finding physical characteristics of such materials and possibility of their practical application complex researches of optical spectra of absorption and photoluminescence, photoconductivity and spectrum of excitation of photoluminescence under various conditions, are carried out, temperature dependences and various influences (electric and magnetic fields under influence of the unidirectional and hydrostatic pressure) are investigated.

1. Experimental and discussion of results

In this report results of research under the influence of hydrostatic pressure are described. As it is known the hydrostatic technique in case of volume materials allows to receive a number of unique information about zone structures. Under the influence of hydrostatic pressure change of crystal structure is possible. One of essential advantages of this technique is the possibility to establish of experimental data without destruction of the investigated material. Earlier the hydrostatic technique was successfully applied by us at studying of the QDs placed in glass matrixes, and at studying various low dimensional structures-QDs which have been grown up in crystal matrixes. In case of the QDs placed in glass matrixes it has been shown that hydrostatic technique researches allow to receive not only the data about character of change zone structures but also to establish presence or absence of contact of a QDs with substance surrounding it. Character of contact QD with a matrix can be established studying influence hydrostatic pressure on QDs. Earlier the presence of contact in case of CdS CdSe, CdTe and Cu_2O placed in glass matrixes has been established. Contact was absent in case of quantum points CuCl [1] and CuBr [2]. It is necessary to emphasize that the hydrostatic technique is the unique technique allowing without destruction of the investigated material the data about its contact with environment to obtain. In the given message the analysis of structure of spectra of absorption of QDs PbI_2 in a polymeric matrix is carried out. Data on presence or absence of contact are of great importance. In the first they allow to reveal the optimal conditions of synthesis of quantum structures. In the second they are necessary both for the analysis of experimental results, and at carrying out of theoretical calculations of structure of spectra of optical transition. Polyvinyl spirit of a film were created from sated water solution PbI_2 with addition of 0.5 percent of polyvinyl spirit by a technique [3]. In a spectrum three strips - the most intensive with a maximum of 408 nm (3.04 eV) and weaker strips with maxima of 450 nm (2.75 eV) and 488 nm (2.564 eV)were observed. According to the x-ray structural analysis the average sizes of inclusions PbI_2 — 3 nm in a direction (110) and less 1 nm in a direction (001). The most intensive line with a maximum of 408 nm (3.04 eV) has been interpreted in model of quantum restriction of carriers in small particles of anisotropic semiconductors [3]. To interpret weaker on intensity of feature it was not possible. The analysis of spectra of absorption has shown that sizes QDs did not depend on conditions of synthesis. It follows from a constancy of their spectral position. Depending on conditions of synthesis their relative contribution to spectra of absorption changed only. In the given work for an establishment of the possible nature of lines the following has been made: (i) Influence of hydrostatic pressure is investigated. (ii) Decomposition of all measured spectra of absorption on components is made. Pressure was created by the high pressure box. The box allowed to create pressure in a range from 0 to 30 kbar and to carry out measurements of absorption spectrum at temperature 77–300 K [2]. In all interval of the enclosed pressure 0–30 kbar in a temperature interval 300–77 K did not change about spectral position of lines and their relative intensity. According to the data of x-ray analysis QDs have the form of thin plates with a order parity of a thickness to the linear size one to ten. It is possible to assume that three types of contacts QDs with a matrix are possible: (i) — thin side, (ii) — a plane and (iii) — all surfaces. In the latter case hydrostatic pressure can not be transmitted on QDs because of porosity of a matrix. From the literature it is known that from the presence of the contact QDs to a matrix can change electronic and hole energy. Change can be caused from two factors (i) — deformation QDs as a result of distinctions of lattices and power constants of a matrix and QDs and (ii) — fall of energy of transitions owing to penetra-

tion of wave functions of power levels QDs into a barrier .In the first case at contact QD to a matrix the thin side from outside matrixes can be neglected effect. At the analysis of power levels QDs it is possible to start with a classical case of a barrier of infinite size. In the second case — dense unilateral contact by the most developed party QDs to a matrix change owing to deformation of energy of levels (increase is possible or reduction) and reduction of energy of transitions owing to the second factor — penetration of function of a wave into a material of a barrier [4]. In the third case it is possible to expect the maximum change of power structure. Within the limits of a contour of each of lines three narrower lines have been allocated. For the most long-wave line (3.04 eV) this lines are located at the energy 2.560, 2.615 and 2.667 eV. The relative contribution of narrow lines and their width were identical within the limits of each of wide lines (2.564, 2.75 and 3.04 eV). They coincided as well for all three component of absorption. Their relative contribution to spectra of absorption did not depend on conditions of synthesis. It has been established, that except for three basic lines in a spectrum of absorption there should be at least two more short-wave lines at 3.5 and 3.8 eV. It was revealed also, that from conditions of synthesis changes only the relative contribution a component in a spectrum. Spectral position and their form do not vary. On the basis of all above stated it is possible to draw following conclusions: (i) — the basic lines (2.564, 2.75 and 3.04 eV) are connected with set QDs having the close sizes and forms — square a plate thickness of the order 1 nm and width 3 nm. (ii) — the thin lines is connected with crystal splitting of a valent zone. It follows that the size of splitting 55 meV is close to size of crystal splitting a valent zone 45 meV. (iii) — all basic line (2.564, 2.75 and 3.04 eV) are caused by transitions in the bottom electronic and hole condition. Distinction of energy of transitions is caused by various influence of a matrix. The most short-wave line (2.564 eV) corresponds to free condition QDs (a case (i)). A line at (2.75 eV) to a case (ii) — of the unilateral contact. Reduction of energy is caused by compression QDs of lengthways most developed side. Equivalent size of hydrostatic pressure of the order 15 kbar. The lines at 3.04 eV it is possible to explain a line in two ways. (i) as result of dense contact to a matrixa (case (iii)). Equivalent size of hydrostatic pressure of the order 30 kbar. (ii) — as result of display in QDs of conditions of a volumetric crystal. Such features are observed in QDs of some crystals of CdS and CdSe.

Acknowledgements

The work has been supported by the Russian Foundation for Basic Research, Grant No. 08-02-00954.This work has been supported in part by the Deutsche Forschungsgemeinschaft through SFB 410.

References

[1] B. S. Kulinkin *et al*, *FTP* **23**, 470 (1989).
[2] B. S. Kulinkin *et al*, *Fisika and Khimiya Stekla* **24**, 1470 (1988).
[3] I. H. Akopyan *et al*, *Vest. St Peter. Univer.* **3**, 96 (2003).
[4] U. Banin *et al*, *J. of Chem. Phys.* **109**, 2306 (1998).

18th Int. Symp. "Nanostructures: Physics and Technology"
St Petersburg, Russia, June 21–26, 2010

Simple quantum model of electrons accumulation in nanoscale semiconductor films

V. A. Gergel', A. V. Verhovtseva and N. M. Gorshkova
Kotel'nikov Institute of Radio Engineering and Electronics RAS, Russia

Abstract. The quantum model of electrons accumulation in positively charged boundary of semiconductor film is proposed. Model uses known ideas about the quantization of transverse electron motion in the uniform electric field near the high energy barier. The equation of surface potential from resulting boundary electric field is obtained.

Introduction

The quantum model of electrons accumulation in positively charged boundary of semiconductor film is proposed. Model uses known ideas about the quantization of transverse electron motion in the uniform electric field near the high energy barier [1]. In this case the wave functions are the semi-infinite segments of Airy's function. According to Fermi statistics the electrons are placed on these quasi-discrete states with the surface density equal to the concentration of surface donors. With the reasonable concentrations all electrons of accumulation layer are occupied mainly the first level of spatial quantization. The beginning of filling of the third level corresponds the superhigh built-in fields of the atomic order (10^8 V/cm). This feature of electronic filling is caused by an increase in energy gap between the levels with an increase of the electric field.

1. Potential profile

The profile of the potential which describes the interaction of the accumulation layer electrons with other charged particles, including holes, is found from integration of Poisson's equation where charge density is equal to the squares of the corresponding segments of Airy's functions. Its boundary value (surface potential) describes the influence of the layer of electronic accumulation on the external electrical chain (Fig. 1). The dependence of surface potential versus resulting boundary electric field, including induced by the built-in charge, is simply transformed into voltage-capacitance characteristics. It is shown that because of the well known decrease of the characteristic depth of surface states (with an increase in the electric field) both complete and differential capacities of the accumulation layer increase with an increase of the voltage. It should be noted that although the total capacity dependence on the voltage is continuous, the differential one demonstrates the expected slight jump according to the potential value corresponding the beginning of the second quantization level filling (Fig. 2) [2].

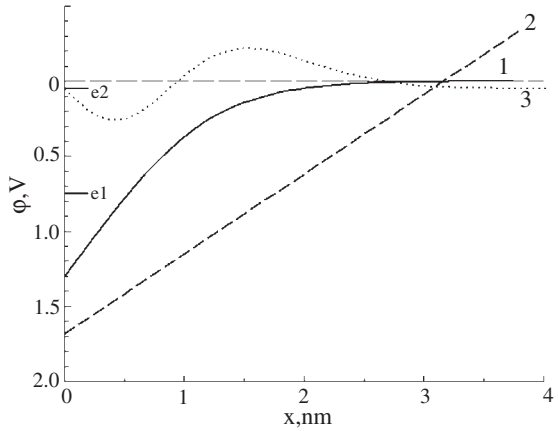

Fig. 1. Typical distribution of the surface potential (1) in the accumulation layer; the effective attractive potential of electrons (2) and a form of the wave functions of the second bound state (3).

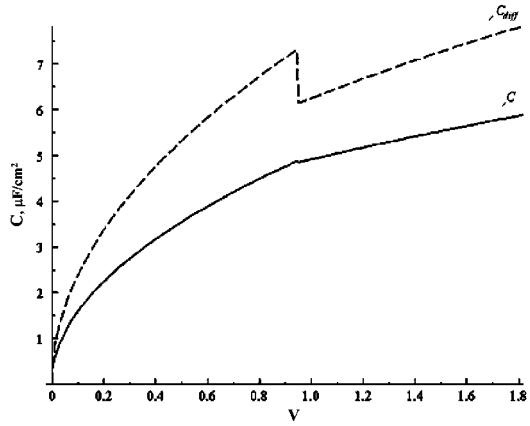

Fig. 2. The capacitance-voltage characteristics of full and differential (dashed line) capacitances of accumulation layer (C — solid line, C_{diff} — dashed line).

2. Experiment

In connection with the experimental study of photoluminescence in the films with the electronic accumulation, for example InN, the essential long-wave displacement of the peak of photoluminescence observed in them is easily explained within the framework developed model. It is due by tunneling nonequilibrium holes from the volume to the surface through the energy barrier of near-surface potential and their subsequent radiative recombination with the electrons of accumulation layer which occupy the first level of transverse quantization with the small lateral pulses. In the frames of the model involved the observed displacement of the peak from 1.9 eV in the bulk material to 0.7 eV in nano-dimensional InN films with the accumulation makes it possible to obtain the reasonable estimation for the of surface charge magnitude and corresponding electric field, proven to be of order 10^7 V/cm.

3. Conclusion

In conclusion, let us formulate our considerations about the adequacy of the purely quantum (without selfconsistance potential procedure) formulation of the problem of the accumulation of electrons in the heavily doped films. The matter is that in our problem practically entire electronic charge is concentrated in the narrow (quantum) layer by thickness $h = 2a(E_B/E)^{1/3}$, with the surface density $\sigma = \varepsilon E/4\pi e$, there a — Bohr radius, $E_B = e/\varepsilon a^2$ — Bohr electrical field. Consequently, in the unit cell of such spatial distribution — cube with the side h — it is located the $\sigma h^2 = 1/\pi(E_B/E)^{1/3}$ electrons. This number remains less or order of unity in the entire range of boundary eclectic field $E < 10^7$ V/cm. We suppose therefore that in the problem involved the use of potential selfconsistance would be serious error, because in this situation the selfconsistance leads to the fictitious energy of the Coulomb interaction of the electron with the field induced itself.

Acknowledgements

We would like to thank D. of Sci. P. N. Brunkov for helpfull discussions.

References

[1] L. Calakerol *et al*, *Phys. Rev. Lett.* **97**, 237601 (2006).
[2] Hai Lu, W. J. Schaff, L. F. Estman, *Appl. Phys. Lett.* **82**, 1736 (2003).

18th Int. Symp. "Nanostructures: Physics and Technology"
St Petersburg, Russia, June 21–26, 2010

Surface photovoltage spectroscopy and photoluminescences characterization of $GaAs_{0.7}Sb_{0.3}$/GaAs type-II quantum well with an adjacent InAs quantum-dot layer composite structure

J. D. Wu[1], Y. J. Lin[1], *Y. S. Huang*[1], Y. R. Lin[2] and H. H. Lin[2]

[1] Department of Electronic Engineering, National Taiwan University of Science and Technology, Taipei, 106, Taiwan
[2] Department of Electrical Engineering and Graduate Institute of Electronics Engineering, National Taiwan University, Taipei 106, Taiwan

Abstract. The optical properties of a $GaAs_{0.7}Sb_{0.3}$/GaAs type-II quantum well (QW) with an adjacent InAs quantum dot (QD) layer composite structure are studied by using surface photovoltage spectroscopy (SPS) and photoluminescence (PL) techniques. The room temperature SPS spectra exhibit the features originated from QDs, QW, wetting layer and GaAs cap-layer. The low-temperature PL band of the modulated potential wells in $GaAs_{0.7}Sb_{0.3}$ QW shows a large redshift as compared with the $GaAs_{0.7}Sb_{0.3}$ QW reference sample at low excitation level. At higher temperature, the composite structure reveals stronger PL intensity than that of QW, indicating the potential of the applications to laser diodes.

Introduction

Due to the type-II band alignment, the electron and hole in a GaAsSb/GaAs strained quantum well (QW) are spatially separated. This configuration leads to the fundamental transition energy of QW being lower than the band gaps of the barrier and well. This is a great advantage in application to long wavelength lasers [1]. However, the spatial separation of the electron and hole wavefunctions results in a low optical matrix element which leads to high threshold current density in GaAsSb/GaAs QW 1asers. One way to increase the matrix element is to enhance the confinement of the active medium. A composite structure consisting of a GaAsSb/GaAs QW and an adjacent InAs/GaAs self-assembled quantum dot (QD) has been proposed to improve the performance of the type-II laser diodes [2]. In this composite structure, $GaAs_{0.7}Sb_{0.3}$ QW and a GaAs spacer layer were grown beneath InAs QDs. Since the strain exerted by InAs QDs on their bottom is tensile below the dots and compressive under the edge of the dots, the band diagram of the GaAs spacer and GaAsSb QW are modulated to form potential wells in the growth plane. As a result, both electrons and holes are trapped in the potential wells induced InAs QDs. Along the growth direction, the type-II $GaAs_{0.7}Sb_{0.3}$/GaAs heterostructure provides the confinement of the third dimension. In this work, a detailed optical characterization of this composite structure was carried out by using by using surface photovoltage spectroscopy (SPS) and photoluminescence (PL) techniques. The results demonstrate the enhancement on the optical properties of $GaAs_{0.7}Sb_{0.3}$/GaAs QW, resulting from the strain-induced potential wells, which is of great importance to laser applications.

1. Experimental

The composite structures and control samples were grown on (100) n^+-GaAs substrates by gas-source molecular beam epitaxy. The growth of the composite structure began with a 500 nm GaAs buffer layer followed by the $GaAs_{0.7}Sb_{0.3}$ QW, GaAs spacer layer, and InAs QDs. The thickness of the QW is 4 nm and the nominal thickness of the QD is 2 ML. A 500 nm GaAs cap layer was then overgrown on the structure. The

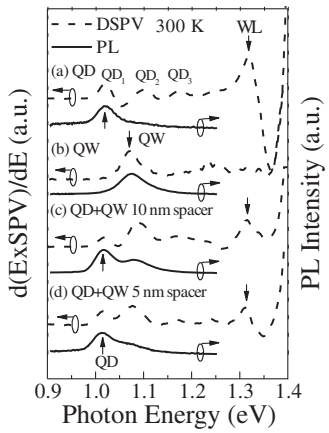

Fig. 1. Room temperature DSPV and PL spectra of (a) InAs QD, (b) GaAsSb QW, (c) the composite structure with 10 nm spacer, and (d) the composite structure with 5 nm spacer.

growth temperature for the QW and QDs was 490 °C, while all the rest layers were grown at 590 °C. The growth rate of the InAs QD layer was 0.085 ML/s. Two composite structures with different spacer thickness, t and 10 nm, respectively, were grown. Besides the two structures, two control samples, a sample with 2 ML InAs QDs and a sample with 4 nm $GaAs_{0.7}Sb_{0.3}$ QW only, were grown using the same growth conditions.

In SPS, the contact potential difference between the sample and a reference grid electrode is measured in a capacitive manner as a function of the photon energy of the probe beam by holding the grid fixed and chopping the probe beam at 200 Hz. The light from a 150 W quartz-halogen lamp was passed through a 0.2 m grating monochromator and focused onto the sample. The incident light intensity was maintained at a constant level of 10^{-4} W/cm^2. The induced surface photovoltage (SPV) on the metal grid was measured with a metal bottom as the ground electrode, using a buffer circuit and a lock-in amplifier. For PL measurements, the signal was collected by an Ocean Optics NIR 512 spectrometer. A 100 mW Nd-YAG 532 nm green laser was employed as the excitation source. A CTI-Cryogenics Cryodyne Model 22 refrigeration

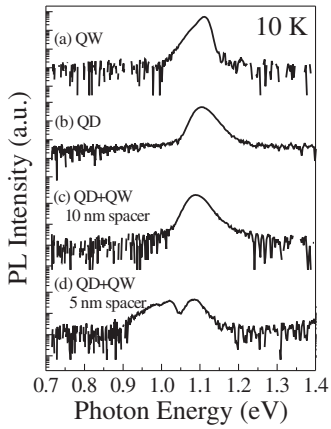

Fig. 2. PL spectra of (a) InAs QD, (b) GaAsSb QW, (c) the composite structure with 10 nm spacer, and (d) the composite structure with 5 nm spacer at an excitation level of 10 mW/cm^2.

system equipped with a model 32B digital temperature controller was used for temperature-dependent measurements.

2. Results and discussion

Figure 1 shows that the room temperature derivative SPV and PL spectra of the two control samples and the two composite structures. As can be seen in Fig. 1(a), in addition to signal from the 2D wetting layer, three QDs related transitions QD1-QD3 are presented in DSPV spectrum of the QD control sample. The transition energy of the QD1 feature corresponds well with the peak position of the PL spectrum. The DSPV spectrum of the QW control sample, as displayed in Fig. 1(b), shows the ground- and excited-state transitions. The ground state transition energy agrees well with that determined from PL feature. Figures 1(c) and 1(d) show the spectra of the composite structure with 10 and 5 nm spacer, respectively. The DSPV spectra are consisted the features originated from QD, QW and WL. The main peak of the PL spectrum, close to the QD1 position of the QD sample, is ascribed to the InAs QDs, while the feature located at higher energy side is attributed to the QW.

Figure 2 shows the 10 K PL spectra of the four samples with an excitation level of 10 mW/cm^2. As can be seen in Fig. 2(a), the emission band of the QD control sample is from one QD ensemble with the peak energy determined from a Gaussian fit of 1.11 eV. The spectrum of the QW control sample, as displayed in Fig. 2(b), shows a single band peak at 1.106 eV. The pronounced low energy tail is attributed to an exponential tail of localized states resulting from the potential fluctuation [3]. Figure 2(c) shows the spectrum of the composite structure with 10 nm spacer. The peak at 1.089 eV, slightly lower than that of to the QW emission peak, however the lineshape is similar to that of QD. The feature can be attributed to the QD related luminescence. It is known that the electron capture cross sections of InAs QDs can be as large as 10^{-10}/cm^2 [4]. Therefore, most of the electrons reaching the QD layer would be trapped into the QDs. The charged QDs may enhance the trapping of holes, resulting in the strong QD band. The PL spectrum of the composite structure with 5 nm spacer, as can be seen in Fig. 2(d), shows a longer luminescence peak at 1.021 eV, which is lower than the main peak of the QW control sample by 89 meV, suggesting that the luminescence is from the modulated potential minimum in GaAsSb QW. In the 5 nm spacer

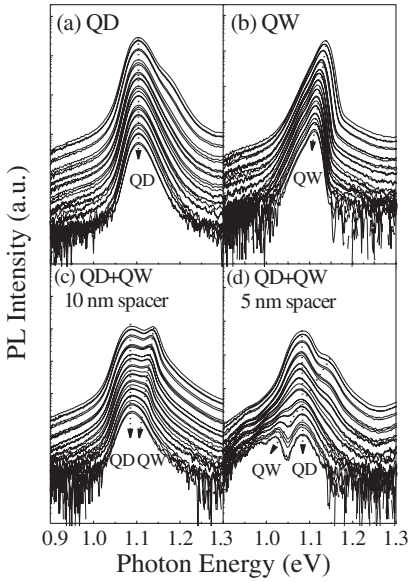

Fig. 3. Power dependent PL spectra of (a) InAs QD, (b) GaAsSb QW, (c) the composite structure with 10 nm spacer, and (d) the composite structure with 5 nm spacer at 10 K.

structure, the hole trapped in the QDs could tunnel into the modulated potential minimum in the GaAsSb QW, leading to QW related luminescence. Note that the electron and hole trapped in the potential minimum are spatially separated because of the inherent type-II band lineup of the $GaAs_{0.7}Sb_{0.3}$/GaAs.

To elucidate the behavior of this type-II transition, we performed power dependent PL measurements on these samples. As shown in Fig. 3, the peak energies of the InAs QD control sample is virtually invariant of the excitation level, indicative of the behavior of type-I band alignment. However, the QW control sample and the composite structures all show a blueshift in the peak energy relevant to either the QW or the stain modulated QWs as the excitation level increase. Due to the increment in carrier density, the space-charge file across the type-II junction is enhanced and thus upraises the quantized electron state at the interface. Hence the emission wavelength blueshifts.

Acknowledgements

This work was supported by the National Science Council of Taiwan under Project No. 98-2221-E-011-015-MY2.

References

[1] N. N. Ledentsov *et al*, *IEEE J. Sel. Top. Quantum Electron.* **6**, 439 (2000).
[2] Y. R. Lin *et al*, *Electron. Lett.* **45**, 682 (2009).
[3] M. Dinu *et al*, *J. Appl. Phys.* **94**, 1506 (2003).
[4] O. Engström *et al*, *Appl. Phys. Lett.* **85**, 2908 (2004).

18th Int. Symp. "Nanostructures: Physics and Technology"
St Petersburg, Russia, June 21–26, 2010

Electromagnetically induced transparency in double tunneling-coupled quantum wells

A. N. Litvinov[1], G. A. Kazakov[1], D. K. Loginov[2] and B. G. Matisov[1]

[1] St Petersburg State Polytechnic University, St Petersburg, Russia
[2] Institute of Physics, St Petersburg State University, St Petersburg, Russia

Abstract. In the work the possible of the observing of the electromagnetically induced transparency (EIT) effect in solid nanostructures is investigated. We propose a using double tunneling-coupled quantum wells at EIT effect condition for the creation of the long-lived quantum memory.

Now the big attention of researchers direct to electromagnetically induced transparency effect (EIT) because this effect has the wide applications at development of the devices for saving, storage and processing of quantum information and also at development of quantum logical keys. The EIT effect is appeared as the changing of medium characteristics when the medium interacts with dual-frequencies laser field. [1]. As a result, the translucence of medium takes place for laser field what is the consequence of appearing of the other quantum effect — coherent population trapping [2]. It is known that the coherent population trapping phenomenon conclude in appearance of specific ($<$ dark $>$) superposition quantum state of systems which do not interact with laser field acting on the medium. The frequency area of such enlightenment can be less in thousand and more times in comparison with the natural width of optical transition. Arising of the dark state leads to arising (induction) of low-frequency coherence. This coherence has long lifetime. It is allow to use the EIT effect for realization of long-lived quantum memory.

Recently on the base of EIT effect in atoms located in optical lattice the methods of saving and processing qubits with high accuracy was realized. However the amount of atoms which is needed for the realization of full-fledged of the memory cell does not possible to locate in optical lattice without destruction of quantum bit. But the amount of the atoms in solids is more by some orders in comparison with atoms which one can locate in optical lattice without destruction quantum bit. In other words, in this case we can realize full-fledged the memory cell which will have high accuracy at processing of information from this quantum memory. Therefore the creation of the quantum memory based on solids have advantages in comparison with atoms located in optical lattice. On the other hand, the realization of the quantum interference effect in solids (nanostructures) leads to the problems associated with the fact that the width of the optical line is big and the lifetime of coherences is small in quantum wells (quantum dots).

First (less than 10 years ago) the possibility of the observing of the EIT effect in nanostructures (quantum wells) was demonstrated experimentally in [3]. This work caused a numbers of theoretical and experimenat works devoted to investigation of the EIT effect in solids [4–9].

In present work we study the structure in which one realizes the EIT effect in nanostructures to create long-lived quantum memory. We consider the interaction of dual-frequency (Rabi frequencies are V_1 and V_2 respectively) laser field with nanostructure which consist is dual tunneled coupled quantum wells, Fig. 1. First laser field (V_1) is resonant to $1 \leftrightarrow 3$ transition and the second laser field is detuned from $2 \leftrightarrow 4$ transition by Ω_2.

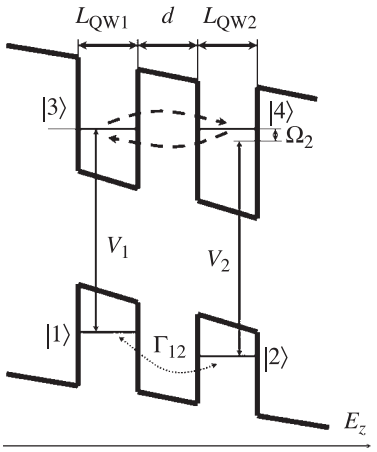

Fig. 1. Energetic scheme of levels of double tunneling-coupled quantum wells on basis of GaAs/AlGaAs in electric field E. L_{QW1}, L_{QW2} are the widths of the first and second quantum wells, d is the width of barrier layer. V_1 and V_2 are the Rabi frequencies, Ω_2 is the detuning of the laser field from the $2 \leftrightarrow 4$ transition.

In our calculation we have used parameters of nanostructure which are close to quantum wells (QW) GaAs/AlGaAs. The thicknesses of first and second GaAs quantum wells was chosen to be $L_{QW1} = 3$ nm and $L_{QW2} = 4$ nm respectively and thickness of AlGaAs was taken to be $d = 1.8$ nm. The electron effective mass in QW and barriers layers is $m_e^{GaAs} = m_e^{AlGaAs} = 0.06m_0$ (m_0 is a free electron mass) [10]. It is supposed in considered model that tunneling between halls levels $|1\rangle$ and $|2\rangle$ does not occur. This approximation is proved by the fact that the hall mass $m_e^{GaAs} = 0.35m_0$ [11] is great in comparison with electron effective mass which result in strongly decay of tunneling effect between $|1\rangle$ and $|2\rangle$ levels. Al number density in AlGaAs-layers is chosen so that the height of barriers for electron is 0.68 eV.

Lifetime of states $|3\rangle$ and $|4\rangle$ is taken to be 10 ps and it is supposed that the relaxation rate of low-frequency coherence inducted besides states $|3\rangle$ and $|4\rangle$ is approximately one microsecond. It is possible to vary the EIT resonance contrast by varying of tunneling coefficient k between states $|3\rangle$ and $|4\rangle$ by external electrical field. It is results in possibility to operate quantum coherent effect such as the EIT with external field and certainly it is interesting for practical realization of quantum logical elements.

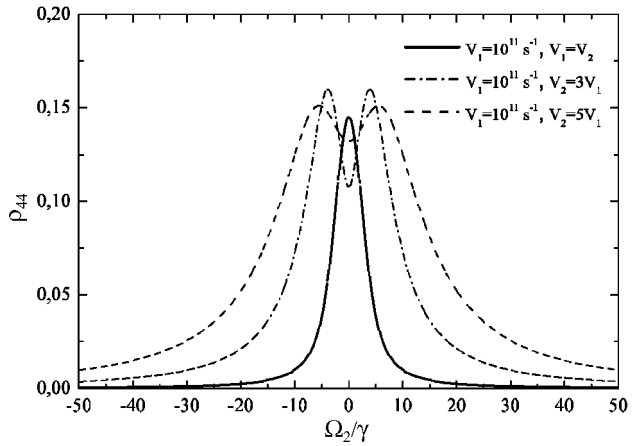

Fig. 2. The dependence of the population of $|4\rangle$ level on Ω_2/γ, where γ is the spontaneous relaxation rate of $|3\rangle$ and $|4\rangle$ levels.

Our theory is based on the density matrix formalism . The calculation results are presented on Fig. 2 which demonstrate the dependence of state $|4\rangle$ population on the laser field detuning Ω_2 and on the second laser field Rabi frequency V_2. From this figure we can see that if Rabi frequencies (intensities) V_1 and V_2 are equal than the EIT effect on $|4\rangle$ level is not take place. However if the intensity of second laser field is increase than one can see that the EIT effect (dip of population at $\Omega_2 = 0$) takes place. It should be emphasized that width and contrast of the EIT resonance are strongly depend on the width of tunneling barrier (tunneling coefficient). If the tunneling coefficient is about 1 than the EIT resonance takes place at the same intensities of the laser field. Whereas with the increasing of the width of tunneling barrier the EIT resonance takes place only for asymmetric conditions on laser field intensities.

So in this work we study the electromagnetically induced transparency effect in double tunneling-coupled quantum wells. We propose a using the EIT effect in such structure for the creation of long-lived quantum memory.

Acknowledgements

This work was supported by Federal Special-purpose Program "Science and Science-pedagogical personnel of Innovation Russia on 2009–2013" (contract П2326), by grant RFBR-09-02-90465_Ukr_f_a, Rosnauka (project 02.740.11.0214).

References

[1] S. Harris, *Physics Today* **50**, 36 (1997).
[2] B. G. Agapyev, M. B. Gorniy, B. G. Matisov and Yu. V. Rozhdestvensky, *Uspekhi Fizicheskih Nauk* **163**, 1 (1993).
[3] G. B. Serapiglia, E. Paspalakis, C. Sirtori, K. L. Vodopyanov, and C. C. Phillips, *Phys. Rev. Lett.* **84**, 1019 (2000).
[4] J. F. Dynes, M. D. Frogley, J. Rodger *et al*, *Phys. Rev. B* **72**, 085323 (2005).
[5] S. M. Sadeghi, W. Li, X. Li *et al*, *Phys. Rev. B* **74**, 161304 (2006).
[6] A. Joshi, *Phys. Rev. B* **79**, 115315 (2009).
[7] C. W. Groth, B. Michaelis, C. W. J. Beenakker, *Phys. Rev. B* **74**, 125315 (2006).
[8] S. Marcinkevicius, A. Gushterov, J. P. Reithmaier, *Appl. Phys. Lett.* **92**, 041113 (2008).
[9] V. Yannopapas, E. Paspalakis, N. V. Vitanov, *Phys. Rev. B* **80**, 035104 (2009).
[10] P. Lawaetz, *Phys. Rev. B* **4**, 3460 (1971).
[11] X. Yang, M. Yu, D. L. Kwong *et al*, *Phys. Rev. Lett.* **102**, 173902 (2009).

18th Int. Symp. "Nanostructures: Physics and Technology"
St Petersburg, Russia, June 21–26, 2010

Features of photoluminescence spectra of InAs/GaAs and InAs/AlAs quantum dots and the GaAs/AlGaAs heterostructure containing thick GaAs layer

S. V. Poltavtsev[1], V. A. Gaisin[1], B. S. Kulinkin[2], V. A. Maruchuk[2] and T. S. Shamirsaev[3]

[1] Institute of Physics, St Petersburg State University, Ulyanovskaya 1, Petrodvorets, St Petersburg, 198504, Russia
[2] St Petersburg State Medical University, Academician I. P. Pavlov, ul. L.Tolstoy, 6/8, St Petersburg, 197022, Russia
[3] Institute of Physics, Novosibirsk, 630090, Russia

Abstract. In the temperature range 4.5–300 K photoluminescence spectra of InAs/GaAs and InAs/AlAs heterostructures containing quantum dots and reflection spectra of epitaxial GaAs/AlGaAs heterostructure are investigated. For the first time the fine structure of a photoluminescence of quantum dots InAs/AlAs was observed. The spectrum consisted of five bands located in the range of energy 1.4–1.8 eV. Temperature dependence of a photoluminescence spectra was observed. The reflectivity spectrum of epitaxial GaAs/AlGaAs heterostructure containing 333 nm GaAs layer was measured. In a spectral range 1.5–1.7 eV the a regular series of narrow lines was observed. The structure of reflection spectrum is interpreted by a model involving polariton waves in a wide quantum well.

Introduction

Earlier we have investigated photoluminescence (PL) spectra of the heterostructures containing ten layers of InAs quantum dots (QD) located on a plane (100) GaAs. Measurements were done in a wide temperature interval of 80–300 K with application of a hydrostatic pressure (P = 0–16 kbar) [1]. In PL spectra three types of features were observed: (i) Two most short-wave lines $E_1 = 1516$ meV and $E_2 = 1498$ meV, appearing from radiative recombination of free and localized exitons in GaAs, (ii) located in short-wave area of a spectrum (1.3–1.4 eV) bands resulting from electron-hole recombination in isolated QD, (iii) the bands located in long-wave area (1.0–1.2 eV), related to QD arrays.

Dependence of QD spectra on laser excitation power, temperatures of heterostructure and hydrostatic pressure was observed. As a result of the performed analysis it was shown that a spectrum can be described as a composition of several Gauss contours, with different intensities, positions of maxima and semiwidths. Upon temperature rise from 80 to 300 K long-wave shift of all features and reduction of PL intensity were observed, most prominent for isolated QD. Activation energies of transitions have been defined, the possible schema of energy levels was constructed.

1. Photoluminescence

In the present work results of the further analysis of the PL spectra are given. Calculation of temperature shifts of maxima of all features for the most differing hydrostatic pressures $P = 0$ and $P = 16$ kbar is performed. The tendency of increase of temperature shift for lower energy radiating transitions has been found out. Earlier similar effect was observed in single-layered heterostructures in which QD have been located on vicinal GaAs surfaces (001) offset by 7°. As a result of the performed analysis the observable effect follows from our previous finding of considerable dependence of the baric factor B of PL spectra of QD on the transition energy under the general conditions. B changed from the value $B = 10$ meV/kbar at $E = 1.4$ eV (which coincides with the B value for bulk GaAs crystal) to $B = 6$ meV/kbar for the most long-wave QD.

For the further studying of the optical properties of both arrayed and isolated QD we present in this work results of research of the heterostructures consisting of five layers of InAs QD embedded between barrier AlAs layers. Besides, this structure contains three layers of GaAs: GaAs cap, thickness 13 nm, GaAs buffer, thickness 200 nanometers and GaAs substrate of the thickness of 200 micrometers.

Complex structure of PL spectra consisting of narrow lines and bands was observed. PL spectra depended on wavelength of exciting light, excitation laser power and temperature of heterostructure. Under excitation by a helium — neon laser PL lines have been located near the edge of excitonic absorption of bulk GaAs. Under green excitation ($\mathcal{E} = 2.2$ eV) also some bands in the range of $1.4 < E < 1.6$ eV were observed. Using the semiconductor laser with energy of $\mathcal{E} = 2.8$ eV for excitation results in the complex structure of a spectrum with wide bands in the area of $1.4 < E < 1.9$ eV and also a series of narrow lines in the same spectral range were observed. The most short-wave of these lines is located at $E = 1.7$ eV ($T = 4.5$ K). From comparison with spectrum of excitonic absorption of bulk GaAs ($E = 1.516$ eV) it is obvious that this line gets into the area of excitonic and interband transitions and therefore it can't be interpreted in model of electron-hole transitions in bulk GaAs. The performed analysis of PL spectra has allowed us to assume that in the heterostructures investigated by us the spectrum includes all four types of features: radiation of arrayed and isolated QD, GaAs buffer and GaAs substrate. To separate the possible contribution to spectra of each component a relative comparison of optical spectra of heterostructures containing InAs/AlAs QD with similar spectra of epitaxial GaAs/AlGaAs heterostructure has been done.

2. Reflection

The sample under investigation is epitaxial GaAs/AlGaAs heterostructure containing undoped 333 nm thick GaAs layer enclosed between two GaAs/AlAs superlattices, 30 nm GaAs

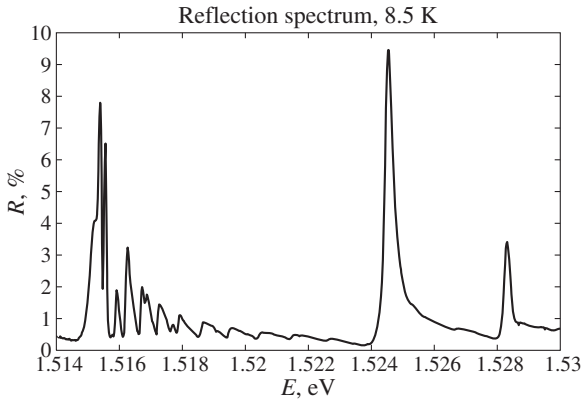

Fig. 1. Reflection spectrum of the sample with thick quantum well.

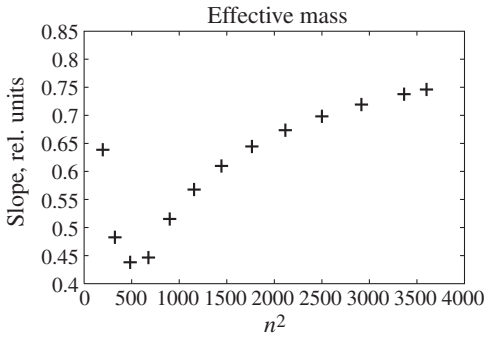

Fig. 2. Effective mass of the confined quasiparticle as finction of the square of quantum nimber n.

layer enclosed between two GaAs/AlAs superlattices and GaAs buffer layer of 30000 nm in thickness.

The reflectivity spectrum (see Fig. 1) was measured using femtosecond Ti:sapphire laser Tsunami produced by Spectra-Physics as wideband light source in Brewster geometry with subsequent normalizing by the spectrum of incident light. In this geometry laser beam is focused at sample surface under angle of about 74° in p-polarization into the spot of approximately 50 × 150 μm in size. That almost totally suppress nonresonant light scattering off the sample surface. Spectrometer used is based on MDR-23 monochromator combined with Hamamatsu CCD-photodetector and has resolution of 80 μeV.

We have chosen GaAs/AlGaAs heterostructure containing epitaxial layers of GaAs whose parametres are close to parametres of epitaxial GaAs layers in heterostructures InAs/GaAs with QD.

In the reflection spectra of epitaxial heterostructures it is possible to allocate two types of features: (i) located in short-wave area of a spectrum a maximuma at $x = 1.52455$ eV and $x = 1.52835$ eV. These features result from dimensional quantization of electrons in a condiction band and light and heavy holes in a valence band in thin GaAs layers. (ii) Oscillating structure located in long-wave area 1.516–1.530 eV. Spectral positions of maximum $E = 1.5136$ eV and minimum $E = 1.5154$ eV of the most intensive feature coincide with spectral positions of similar features in a reflection spectrum of bulk GaAs. This structure contains optical transitions in undoped GaAs layer of 333 nm in width enclosed between two GaAs/AlAs superlattices.

From comparison of reflection spectra of GaAs/AlGaAs epitaxial heterostructure and reflection and PL spectra of InAs/AlAs QD we managed to interpret observed features in PL spectra of InAs/AlAs QD as follows: (i) Structure in the PL spectra at energies above bandgap (lines at 1.650 and 1.655 eV) are related to transitions in GaAs cap. (ii) Features near the excitonic absorption edge are related to transitions in GaAs buffer layer.

This conclusion was based on two observed facts: (i) spectral positions of the basic minima of compared heterostructures coincide with each other and (ii) the majority of thin features of GaAs/AlGaAs epitaxial heterostructure reflection spectrum are located within a contour of a band in InAs/GaAs heterostructure reflection spectrum.

Rather big extents of InAs/GaAs reflection spectrum has been interpreted as a result of strong inhomogeneous broadening of the thin features forming its contour probably due to the lattice stress caused by QD.

3. Discussion

Presently there are three theories to explain the fine structure of reflection spectra of thick epitaxial layers: (i) Quantum confinement of the electrones and holes in the conduction and valence bands respectively; (ii) Quantum confinment of the excitonic states; (iii) Interference of the polariton waves in thick layers of bulk GaAs without consideration of carriers quantum confinement.

The latter was successfully applied in works to explain features in the reflection spectra of the thick heterostructures under general conditions and under uniaxial stress and magnetic field. However satiscfactory explanation was possible only in a limited spectral range. Utilizing high quality of our heterostructures (and hence narrow reflection lines), we were able to perform independent interpretation of the reflection spectra. Energy positions E of each feature in the reflection spectrum were accurately measured and analysed with respect to their quantum number n. The latter was determined independently assuming quadratic dependence $E(n)$ for high enough n in any of the three models mentioned above (see Fig. 2). It was found that for small quantum numbers $3 \le n \le 20$ there are substantial deviations of the $E(n^2)$ dependence slope $dE/n\,dn$ from the value 5 in $3 \le n \le 7$ range to almost zero ($dE/n\,dn \approx 0.2$) in $7 \le n \le 15$ range and back to 3 for $n \ge 15$. By analysis of this data we made a conclusion that fine structure of the reflection spectra of thick heterostructures should be described using polariton model.

References

[1] V. A. Gaisin *et al*, *Proc. 16th Int. Symp. "Nanostructures: Physics and Technology"*, St Petersburg, 80–81 (2008).

[2] D. K. Loginov, *Excitonic polaritons in wide GaAs/AlGaAs and CdTe/CdZnTe quantum wells*, PhD thesis, St Petersburg 2008 (in Russian).

18th Int. Symp. "Nanostructures: Physics and Technology"
St Petersburg, Russia, June 21–26, 2010

Scattering processes in a two-dimensional semimetal

E. B. Olshanetsky[1], Z. D. Kvon[1,2], M. V. Entin[1], L. I. Magarill[1,2], N. N. Mikhailov[1], I. O. Parm[1] and S. A. Dvoretsky[1]

[1] Institute of Semiconductor Physics, SB RAS, pr. Akademika Lavrent'eva 13, Novosibirsk 630090, Russia
[2] Novosibirsk State University, ul. Pirogova 2, Novosibirsk 630090, Russia

Abstract. The scattering mechanisms in a two-dimensional semimetal based on a HgTe quantum well, where the electron and hole densities are controlled over a wide range by applying the gate voltage, have been studied. It is shown that impurity scattering prevails in this system at low temperatures. Inter-particle scattering (in this case, electrons and holes) has been observed to directly affect the resistance of the metal.

It has been recently shown [1] that a two-dimensional semimetal exists in undoped HgTe based quantum wells with an inverse band structure and a (013) surface. The technolgy of low temperature deposition (about 100 °C) of silicon oxide (SiO_2) and nitride (Si_3N_4) on these structures made it possible to create a field-effect transistor based on the HgTe quantum well with the two-dimensional semimetal, which, by applying voltage to the sample, allows the system properties to be studied at an almost arbitrary density ratio of the two-dimensional electron and hole densities in the quantum well. In this study, this allowed us to reveal some scattering features inherent only in the two-dimensional semimetals and caused by the interaction of the two-dimensional electrons and holes. The experimental 20.5 nm CdHgTe/HgTe/ CdHgTe QWs with the (013) surface were prepared by MBE. The details of the structure growth process are described in [2,3].

Fig. 1 presents the $\rho_{xx}(B)$ and $\rho_{xy}(B)$ curves at the gate voltages -1.5 and $+1.5$ V. By fitting the dependences similar to those presented in Fig. 1 using the formulas of the standard classical transport model in the presence of two groups of carriers of opposite signs, we can determine the types of charge carriers involved in transport, as well as their mobilities and densities. Figure 2 presents these parameters as functions of the gate voltage. We first consider the gate voltage dependences of the electron and hole densities shown in Fig. 2a. As expected, $N_s(V_g)$ is linear with a slope of 8.7×10^{14} m^{-2}V^{-1} corresponding to the capacity of the dielectric. For $V_g \leq 0.5$ two types of carriers, electrons and holes, should be taken into account. As the negative gate bias increases, the hole density increases and the electron density decreases linearly with slopes 8.1×10^{14} and 0.7×10^{14} m^{-2}V^{-1}, respectively.

Now, we consider the behavior of the electron and hole mobilities (see Fig. 2b). In the range $+1 \leq V_g \leq +2$ V the electron mobility shows the typical dependence $\mu_e \sim N_s^{3/2}$. At $0 \leq V_g \leq +0.5$ V a sharp jump in the electron mobility is observed. A further increase of the negative gate bias slightly reduces μ_e and leads to a weak linear increase in μ_h. The mobility jump coincides with the V_g range where N_s and P_s are almost the same. This fact allows us to attribute this jump to the screening effect of the impurity scattering of electrons by holes.

In the system with two types of charge carriers, momentum relaxation can be caused, in addition to other factors, by their mutual scattering [4]. Figure 3a presents the gate voltage dependences of the structure resistance in zero magnetic field at $T = 0.195$–4.1 K. Each $\rho(V_g)$ curve has a pronounced maximum located close to the charge neutrality point. The curves show asymmetric temperature dependence with respect to the gate voltage. While at $V_g \geq 0.5$ V the resistance is almost independent of temperature, at $V_g \leq 0.5$ V a considerable increase in resistance is observed as the temperature increases. We believe that this behavior can be explained by momentum relaxation mechanism in the system with two types of charge carriers. In this case, the resistance is independent of temperature for $V_g \geq 0.5$ V, because only electrons are charge carriers in the system at these gate voltages. At $V_g \leq 0.5$ V, we use our formula obtained for the temperature dependence of resistance in a system with two types of charge carriers when momentum relaxation is due to their mutual scattering,

$$\rho(T) = \rho_0 \frac{1 + (\eta/e)(N_s\mu_p + P_s\mu_n)}{1 + (\eta/e)(N_s - P_s)^2 \mu_n\mu_p/(N_s\mu_n + P_s\mu_p)}. \quad (1)$$

Here, η is the electron-hole friction coefficient determined by the scattering of electrons by holes. The probability of this process depends on temperature as $\eta = \Theta T^2$, where Θ is a certain constant.

Closed symbols in Fig. 3b indicate the $\rho(T)$ dependences obtained from the experimental curves in Fig. 3a for $V_g = -1$,

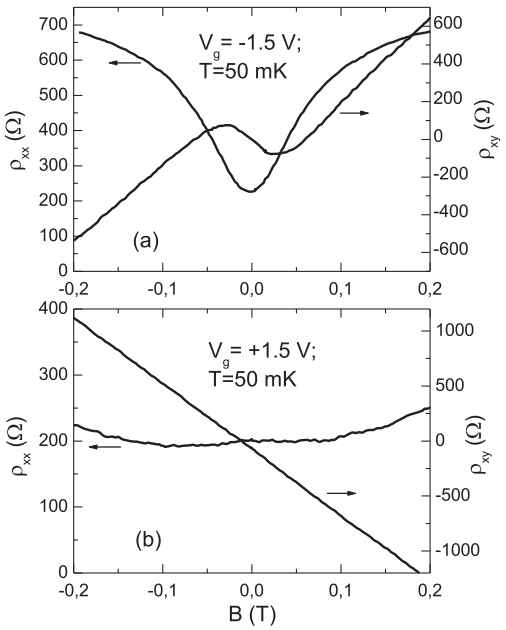

Fig. 1. Magnetic field dependences $\rho_{xx}(B)$ and $\rho_{xy}(B)$ for the electron-hole system in the HgTe quantum well at $T = 50$ mK and gate voltage $V_g = -0.5$ V (a) and $V_g = +0.5$ V (b).

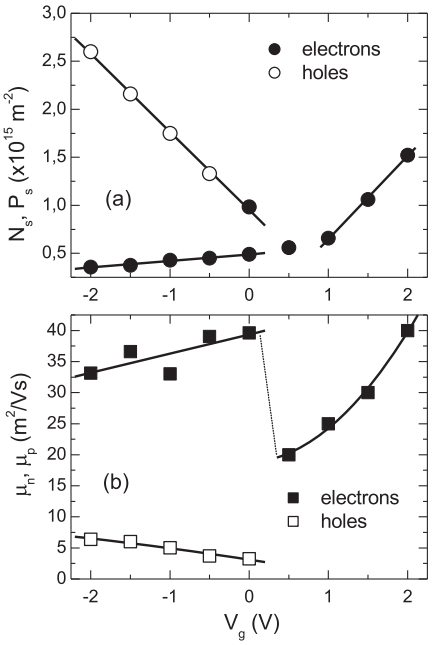

Fig. 2. Gate voltage dependences of (a) the densities of (closed circles) electrons N_s and (open circles) holes P_s and (b) the mobilities of (closed squares) electrons μ_n and (open squares) holes μ_p at $T = 200$ mK.

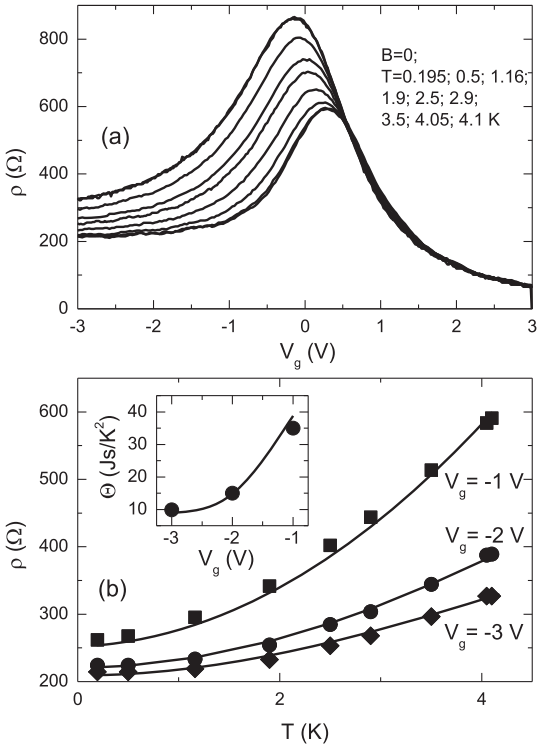

Fig. 3. (a) Gate voltage dependences $\rho(Vg)$ at $B = 0$ and various temperatures $T = 0.2$–4.1 K (from bottom to top). (b) Temperature dependences $\rho(T)$ obtained from Fig. 3a for $V_g = -1, -2, -3$ V. The lines are the fitting by formula (1) (see the text). The inset shows the experimental points and theoretical curve [obtained by Eqs. (2), (3)] for the gate voltage dependence of the fitting parameter Θ.

-2, and -3 V. At these three gate voltages, the temperature dependence of the resistance is saturated at $T \leq 0.5$ K. This allows us to use the values of the electron and hole mobilities and densities corresponding to these temperatures when fitting the curves in Fig. 3b. These parameters can be independently obtained as is described in the above discussion of curves in Fig. 1a. Therefore, the fitting procedure for each curve depends on a single parameter Θ in the expression for η. The fitting results are presented in Fig. 3b by lines. The points in the inset in Fig. 3b show the fitting parameter Θ as a function of the gate voltage. Assuming the neutral character of the inter-particle scattering and the quadratic isotropic spectrum of the electrons, we can present η as follows:

$$\eta = (k_B T)^2 \times \frac{D}{N_s P_s} F\left(\sqrt{\frac{N_s g_h}{P_s}}\right), \qquad (2)$$

where

$$F(x) = \int_0^\infty r dr J_0^2(xr)(J_0^2(r) - J_1^2(r)), \qquad (3)$$

$g_h = 2$ is the number of hole valleys, $J_n(r)$ are the Bessel functions, and the constant D is determined by the peculiarities of the interaction between electrons and holes and is independent of their densities. The line in the inset in Fig. 3b was obtained by formulas (2) and (3), which imply that $\Theta = k_B^2 D F(\sqrt{N_s g_h / P_s})/N_s P_s$. In this case, we used some experimental data on the electron and hole densities and $k_B^2 D \approx 4.5 \times 10^3$. The good agreement between the theory and experiment indicates the validity of our assumption that the observed temperature dependence of resistance is due to the mutual scattering of electrons and holes. We note that our results are the first observation of the direct effect of inter-particle scattering on the transport time in metals. In a normal situation, for example, in bismuth or antimony, this observation is complicated because the given type of scattering does not change the total momentum of the system due to the equal mobilities of electrons and holes. Moreover, even an indirect manifestation of this mechanism appears to be ambiguous owing to the competing effect of scattering on phonons, [6].

Acknowledgements

This work was supported by the Russian Foundation for Basic Research (project Nos. 09-02-00467 and 08-02-00152).

References

[1] Z. D. Kvon, E. B. Olshanetsky, D. A. Kozlov *et al*, *JETP Lett.* **87**, 502 (2008).

[2] N. N. Mikhailov, R. N. Smirnov, S. A. Dvoretsky *et al*, *Int. J. Nanotechnology* **3** 1, 120 (2006).

[3] E. B. Olshanetsky, S. Sassine, Z. D. Kvon, N. N. Mikhailov, S. A. Dvoretsky *et al*, *JETP Lett.* **84**, 565 (2006).

[4] N. N. Berchenko and M. V. Pashkovskii, *Sov. Phys. Usp.* **19**, 462 (1976).

[5] V. F. Gantmakher and I. B. Levinson, Carrier Scattering in Metals and Semiconductors (Nauka, Moscow, 1984; North Holland, New York, 1987).

[6] V. F. Gantmakher and V. T. Dolgopolov, *Sov. Phys. JETP* **33**, 1215 (1971).

18th Int. Symp. "Nanostructures: Physics and Technology"
St Petersburg, Russia, June 21–26, 2010

Coupled CdSe/ZnSe quantum dots: optical spectra and interdot energy transfer

A. Reznitsky[1], A. Klochikhin[1,2], S. Permogorov[1], V. V. Korenev[1], I. Sedova[1], S. Sorokin[1], A. Sitnikova[1] and S. Ivanov[1]

[1] Ioffe Physical-Technical Institute, St Petersburg, Russia
[2] B. P. Konstantinov Nuclear Physics Institute,188350, St Petersburg, Russia

Abstract. We have studied the emission spectra and structural properties of double CdSe/ZnSe quantum well (QW) structures grown by molecular beam epitaxy in order to elucidate the mechanisms of electronic and strain field interaction between quantum dots (QD) in QW planes. The thicknesses of ZnSe barrier separating the CdSe sheets in samples studied were in the range of 10–60 monolayers (ML). We have found that the coupling between the QDs in adjacent layers becomes relatively strong in structures with barrier thickness less than 25–27 ML, while it is rather weak for barrier thickness exceeding 30 ML. We have found that the electronic coupling occurs between the vertically stacked QDs.

Introduction

The coherent CdSe insertions in ZnSe with CdSe nominal thickness in the range of 1–3 ML are known to generate arrays of CdSe-enriched QDs incorporated into the body of ZnCdSe QW (see e.g. [1,2] and references therein). Insertion of several sheets of electronically coupled QDs in the active region of optically or electron-beam pumped lasers improves significantly the laser performance enhancing the optical confinement factor, increasing the quantum efficiency and decreasing the threshold power [3]. In this paper the photoluminescence (PL), excitation of PL spectra (PLE) and structural properties of double CdSe QD sheet structures have been studied to elucidate the mechanisms of electronic and strain field interactions between the QD planes. Some preliminary results of this work were published in [4].

1. Samples: growth and characterization

Three sets of CdSe/ZnSe nanostructures A, B and C have been grown Pseudomorphically by molecular beam epitaxy (MBE) on (001) GaAs substrates at $T = 280\,^{\circ}$C. Samples have a similar design and include a 40–60 nm thick ZnSe buffer layer followed by two CdSe QWs (QW_1 and QW_2) separated by ZnSe spacers of different thickness in the range of 10–60 MLs. The 10–20 nm cap layers of ZnSe were deposited on the top of the structures. Insertion of CdSe was performed in conventional MBE mode with nominal thicknesses t_{QW} given in the second column of Table 1. Spacer thickness t_{sp} is given in the third column of the Table. The structures of the three sets of samples were different in the sequence of the shallow and deep QW (the shallow QW was the first in A series while the deep QW was the first in B and C series).The QD morphology for most of the samples was characterized by transmission electron microscopy. The most important result of these measurements is that two QWs remain spatially separated for spacer thicknesses down to 10 ML.

2. PL and PLE spectra

Emission spectra have been studied at $T = 2$ and 77 K at above ZnSe band gap excitation by 442 nm line of He-Cd laser and at resonant excitation by different Ar^+ laser lines in spectral range 454–514 nm.

At above barrier excitation the PL spectra of samples with largest spacer thicknesses in all series (A50, B34 and C63) exhibit two bands of the exciton recombination from self-organized QDs formed in two different QWs. At the decrease of the spacer thickness two clear trends in the PL emission should be noted: (i) the drastic decrease of PL from the shallow QW in the samples of all series (PL band from shallow QW becomes practically undetectable already at $t_{sp} < 25$ ML), and (ii) the high energy shift of the PL band maximum in the emission spectra of deep QW, (see column E_{PL} of Table 1). We explained the decrease of PL intensity from the shallow QW as a result of electronic coupling between the vertically stacked quantum dots leading to the energy transfer between them [4].

The high energy shift of the PL band at the decrease of the spacer thickness was observed also in [6] and [7]. In former paper this behavior was assigned to the propagation of elastic dot-induced strain fields from one QW to another, while in the latter it was attributed to the increase of intermixing of Zn and Cd induced by strain in the coupled QWs. Both effects naturally must increase with the spacer thickness decrease.

The PLE spectra allow one to find the position of ground exciton states E_{abs} in QDs and the exciton mobility edge E_{ME} (see Table 1) which separates exciton states localized in QDs and the states spreading over all QW plane [5]. The difference $E_{ME} - E_{abs}$ gives the depth of quantum dot potential, which

Table 1. Parameters of samples. Estimations of nominal thicknesses (in ML) of CdSe insertions and ZnSe spacers are based on calibration of the growth rates. The characteristic energies of the PL and PLE spectra E_{PL}, E_{abs}, and E_{ME} are given in eV.

Sample		CdSe, t_{QW}	ZnSe, t_{sp}	E_{PL}	E_{abs}	E_{ME}
C63	QW_1	2.5	63	2.41	2.46	2.59
	QW_2	1.9		2.50	2.54	2.65
A50	QW_1	1.5	50	2.60	2.64	2.71
	QW_2	2.3		2.46	2.52	2.65
B34	QW_1	2.4	34	2.44	2.48	2.58
	QW_2	1.5		2.59	2.62	2.69
C26	QW_1	2.5	26	2.45	2.49	2.63
	QW_2	1.9		2.60	2.63	—
B18	QW_1	2.4	18	2.50	2.54	2.66
	QW_2	1.5		—	—	—
B14	QW_1	2.4	14	2.480	2.520	2.66
	QW_2	1.5		—	—	—
B10	QW_1	2.4	10	2.485	2.525	2.67
	QW_2	1.5		—	—	—

can be used for calculation of energy spectra of QDs.

3. PL spectra at resonant excitation

More information about the electronic coupling between the vertically stacked quantum dots can be obtained from the PL spectra at resonant excitation. We have performed the resonant excitation of exciton states above and below the mobility edge of shallow QW in the samples with spacer thickness $t_{sp} \leq$ 25 ML, for which PL band at above ZnSe barrier excitation is undetectable. As an example, we shall consider the PL spectra of the sample B18 at excitation by Ar^+ laser lines 2.727, 2.707 and 2.661 eV. The excitation by 2.727 eV should populate the states above E_{ME} in shallow QW, the excitation by 2.707 eV populates the states in the vicinity of E_{ME} while the excitation energy 2.661 eV practically corresponds to E_{abs} of the QDs in shallow QW. Experiments show that (i) the shape of the exciton recombination from the deep QW does not depend on the excitation energy, and (ii) no emission was detected from the shallow QW even at direct excitation of the ground exciton state E_{abs} at energy 2.661 eV. These results indicate that for samples with $t_{sp} \leq 18$ ML the rate of tunnelling from the ground state of QD of shallow QW to QD of deep QW exceeds by far that of radiative recombination. We will show that this conclusion is in good agreement with the model calculations.

4. Model description

Data on high-resolution TEM for samples grown in similar MBE mode show that the Cd distribution in the growth direction z is symmetric with respect to the middle point of the QW [1, 2]. We approximate the potential well shape in the growth direction z both within and between QDs by the function [8]

$$U(z) = C_i \Delta E_G / \cosh^2(z/l)\,, \qquad (1)$$

where $z = 0$ corresponds to the middle point of the distribution, $\Delta E_G = (2810 - 1750)$ meV is the difference of band gaps of ZnSe and cubic modification of CdSe. The characteristic parameter l defines the width of the CdSe distribution, and C_i are the CdSe concentrations in the center of the deep quantum dots (C_{dd}), in the deep QW between quantum dots (C_{dw}), in the quantum dots of the shallow QW (C_{sd}), and in the shallow QW between quantum dots (C_{sw}).

The ground confinement levels of quantum dots are set equal to E_{abs} while the ground states of QW between quantum dots are taken to be equal to E_{ME}. The parameter l in model calculations was chosen in such a way that for both QWs the total amount of CdSe within shallow and deep QWs was equal to that of deposited materials assuming that QD concentration is equal to 10^{11} cm^{-2} [2].

Under this assumption the halfwidth of the QWs has proved to be equal to 10 ML, which is in good correspondence with the results of HRTEM measurements [2]. The developed approach allows to calculate the energy spectrum and wave functions of confined exciton states in both QDs and QWs. The results of the calculation are shown in Fig. 1 for the sample C26. Using these wave functions we calculated the rates of cross relaxation between stacked shallow and deep QDs. In the right panel in Fig. 1 are presented the transition probabilities from the states n_{sd} of shallow QD to all states n_{dd} of the deep QD with lower energies. The calculations are based on the estimation of the overlap integrals not taking into account

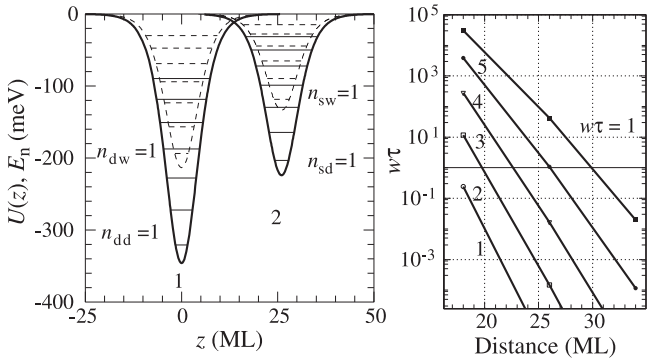

Fig. 1. Left panel: potential curves and exciton confinement levels for deep (1) and shallow (2) QDs (solid lines) and QWs (dashed lines). Confinement levels of exciton in these potentials are denoted by n_{dd}, n_{dw}, and n_{sd}, n_{sw}, respectively. Right panel: number of transitions during the exciton lifetime 300 ps from the shallow QD states n_{sd} to all lower in energy states of deep QD n_{dd} as a functions of the inter-well distances 18, 26, and 34 ML. Numbers 1–5 denote the initial states n_{sd} of shallow QDs. Results of calculation are shown by symbols.

the possible resonant enhancement of transition rates. As it is seen from these estimations, for t_{sp} less than 26 ML the rate of cross relaxation becomes comparable with rate of radiative recombination, which means that the QDs should be considered as electronically coupled.

5. Conclusions

A series of samples consisting of two layers of CdSe quantum dots separated by ZnSe spacers of different thicknesses have been grown and studied by PL and PLE. We have found that at spacer thicknesses $t_{sp} \geq 34$ there is no evidence of electronic coupling between the states in two QW sheets, while at $t_{sp} <$ 26 ML the inter-dot coupling in adjacent layers is relatively strong.

Acknowledgements

This work was partly supported by the Russian Foundation for Basic Research in frames of project 09-02-00837 and by the Program of Presidium of Russian Academy of Science "Foundations of Fundamental Investigations of Nanotechnology and Nanomaterials"

References

[1] N. Peranio *et al*, *Phys. Rev. B* **61**, 16015 (2000).
[2] D. Litvinov *et al*, *Phys. Rev. B* **61**, 16819 (2000).
[3] S. V. Ivanov *et al*, *phys. stat. sol. (a)* **204**, 251 (2007).
[4] A. Reznitsky *et al*, *phys. stat. sol. (c)* **6**, 2695 (2009).
[5] A. Klochikhin *et al*, *Semicond. Sci. & Technol.* **23**, 114010 (2008.)
[6] X. Liu *et al*, *Physica E* **32**, 65 (2006).
[7] H. S. Lee *et al*, *Appl. Phys. Lett.* **81**, 3750 (2002).
[8] A. Klochikhin *et al*, Phys. Rev. B **69**, 085308 (2004).

18th Int. Symp. "Nanostructures: Physics and Technology"
St Petersburg, Russia, June 21–26, 2010

Suppression of Auger recombination in semiconductor quantum dots at low temperatures

D. M. Samosvat, A. S. Shkolnik, V. P. Evtikhiev and G. G. Zegrya
Ioffe Physical-Technical Institute, St Petersburg, Russia

Abstract. It was shown that Auger recombination mechanism in quantum dots is divided on two parts: non-treshold process and quasi-treshold process. When all ground states are fully occupied, quasi-treshold process is fully supressed.

Introduction

The investigation of nonradiative Auger recombination in quantum dots (QDs) attracts a big interest [1]. Due to the high space localization of nonequilibrium carriers the effectiveness of Auger processes could be very high. The two Auger mechanisms very specific for QDs are theoretically described: nonthreshold and quasithreshold. Non-threshold process consist of electron- hole recombination and transferring energy to the third particle(electron or hole). The required quasipulse momentum it receives due to the scattering on the heterojunction. The quasithreshold process include electron- hole recombination and transferring energy to the third particle. The required quasipulse appear after the Heisenberg law. For the realization of both processes the three particles are enough. In our paper we envistigate the situation when all ground states are occupied (two electrons and two holes) and show that in this case the spin influence stay very important. Fig. 1. shows the schematic diagram of Auger recombination process. For both Auger processes electron can choose hole with any spin. So, this fact leads to suppression of the quasithreshold process due to its symmetry and weak influence on the non-threshold process.

1. Experimental

InAs QD single layer arrays were grown simultaneously in the same process using the Stransky–Krastanow method using molecular beam epitaxy (MBE) on GaAs substrate. The average thickness of the InAs layer was 2.9 monolayer (ML). Dependences of the lifetime of the non-equilibrium carriers and internal quantum efficiency on the incident power density for the sample C at the temperatures 77 and 5 K are shown in Fig. 2 and Fig. 3, respectively. The dependence of the internal quantum efficiency on the incident power density at the $T = 77$ K turned out to be qualitatively close to the same dependence measured at the $T = 5$ K. At the small concentrations of injected carriers (in contrast to the $T = 5$ K, where the value of the internal quantum efficiency is practically equal to 100% and the decreasing is due the band filling effect [7]) internal quantum efficiency increases withthe incident power density increasing. At the injected carriers concentrations closed to the filling of the ground state the internal quantum efficiency achieves the value of 100% whereupon it starts to decrease. At the same time there is a great difference in carrier life-time versus incident power density dependences measured at $T = 5$ K and $T = 77$ K. The value of the charge carriers life-time τ and the internal quantum efficiency η are bounded with radiative/non-radiative charge carriers life-times by the following equations:

$$\tau^{-1} = \tau_{\mathrm{RR}}^{-1} + \tau_{\mathrm{NR}}^{-1}, \quad \eta = \frac{\tau_{\mathrm{RR}}^{-1}}{\tau_{\mathrm{NR}}^{-1} + \tau_{\mathrm{RR}}^{-1}}, \qquad (1)$$

where τ_{RR} — radiative charge carriers life-time and τ_{NR} — non-radiative charge carriers life-time. Using experimental internal quantum efficiency and life-time dependencies on the injected carriers concentration ($\tau_{\mathrm{RR}}(n)$ and $\tau_{\mathrm{NR}}(n)$) we can obtain the dependencies of the radiative/non-radiative life-times on the incident power density $\tau_{\mathrm{RR}}(n)$ and $\tau_{\mathrm{NR}}(n)$, correspondingly. The first part of the dependence-increasing of the non-radiative life-time is due to the saturation of the Shokley–Reed nonradiative recombination channel and the following decreasing is the evidence of the new non-radiative channel turning on. It is necessary to point out the fact that those experiments allow us to measure the time of the non-radiative recombination process. As it can be seen the turning on of the new non-radiative

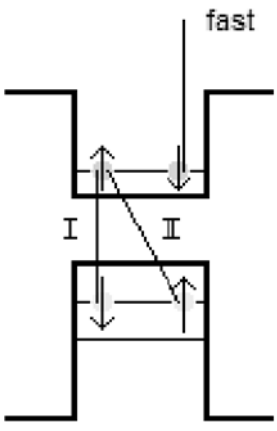

Fig. 1. Schematic of Auger process. Arrows shows the spin projection.

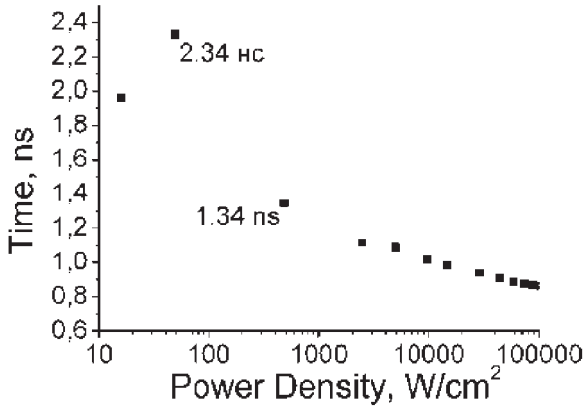

Fig. 2. Auger process in Quantum dots at T=77 K.

channel occurs while temperature changes from 5 up to 77 K. Additionally performed experiments (for example, constancy of the internal quantum efficiency and FWHM of the PL spectra from the ground state up to 100 K and so on) allow us to exclude the influence of the thermal escape of the charge carriers from the ground state. We supposed that predicted earlier Auger non-radiative recombination [2,3] is the reason of the internal quantum efficiency decreasing at the ground state filling.

2. Fundamental equations for Auger recombination

In this paper we use carriers wavefunctions localized on ground state. For simplicity, we consider parabolic bands neglecting Kane model. In quantum dots there are two carriers each sign on ground state. So, radial part of wavefunction and wavefunction charge carriers can given by:

$$\psi_e(\mathbf{r_1}, \nu_1, \mathbf{r_2}, \nu_2) = R_e(\mathbf{r_1})R_e(\mathbf{r_2})Y_{00}(\Omega_\mathbf{1})Y_{00}(\Omega_\mathbf{2})$$
$$\times\frac{1}{\sqrt{2}}\left(\left|\tfrac{1}{2}, \tfrac{1}{2}\right\rangle_1\left|\tfrac{1}{2}, -\tfrac{1}{2}\right\rangle_2 - \left|\tfrac{1}{2}, -\tfrac{1}{2}\right\rangle_1\left|\tfrac{1}{2}, \tfrac{1}{2}\right\rangle_2\right),$$
$$\psi_h(\mathbf{r_3}, \nu_3, \mathbf{r_4}, \nu_4) = R_h(\mathbf{r_3})R_h(\mathbf{r_4})Y_{00}(\Omega_\mathbf{3})Y_{00}(\Omega_\mathbf{4})$$
$$\times\frac{1}{\sqrt{2}}\left(\left|\tfrac{3}{2}, \tfrac{3}{2}\right\rangle_3\left|\tfrac{3}{2}, -\tfrac{3}{2}\right\rangle_4 - \left|\tfrac{3}{2}, -\tfrac{3}{2}\right\rangle_3\left|\tfrac{3}{2}, \tfrac{3}{2}\right\rangle_4\right).$$

At ground state angular momentum is equal to zero. We can write matrix element of transitions in Auger recombination process from initial to final state

$$M_{i\to f} = \int d\mathbf{r_1}\int d\mathbf{r_2}\int d\mathbf{r_4}\psi_e(\mathbf{r_1}, \nu_1, \mathbf{r_2}, \nu_2)$$
$$\times\psi_h(\mathbf{r_1}, \nu_3, \mathbf{r_4}, \nu_4)\frac{e^2}{|\mathbf{r_1}-\mathbf{r_2}|}\psi_h(\mathbf{r_4}, \nu_4)\psi_f(\mathbf{r_2}, \nu_f).$$

Here the initial state represented by two electron-hole pairs and final — electron in exited state and one hole on ground state. For radial part of matrix element $f(l, l_4)$ we obtain:

$$f_l = \int r_1^2 dr_1 \int r_2^2 dr_2 R_e(r_1)R_e(r_2)F_l(r_1, r_2)R_h(r_1)R_f(r_2). \quad (2)$$

Summarizing all parts of matrix element yields:

$$M = 2\left(\sqrt{1/5} + \sqrt{4/5}\right)(f(2, 2) - f(1, 2)). \quad (3)$$

Earlier [1] it was shown that matrix element of Auger process is divided by two parts due to different physical mechanisms of Auger process. Such division associated with electron(or hole) scattering on heterojunction in non-threshold matrix element and its proportional to enegry difference on heterojunction. Quasithreshold matrix element involves only wavefunctions integrals by quantum dot area.

We can do it in our case:

$$M \approx M^{(1)} + M^{(2)}. \quad (4)$$

Finally we obtain that $f(1, 2)^{(2)} = f(2, 2)^{(2)}$ and radial part of matrix element $f(1, 2)^{(2)}$ can given by:

$$f(l, 2)^{(2)} \approx \frac{\sqrt{4\pi}}{k_f^2}\int_0^R r_1^2 dr_1(R_e(r_1)R_e(r_2)R_h(r_1)R_f(r_1)) \quad (5)$$

for $l = 1, 2$. So, its vanishing the final expression of quasithreshold matrix element. Non-threshold matrix element does not vanishing and have equation. Because non-threshold matrix element is less quasithreshold matrix element in most cases, it supress the total process.

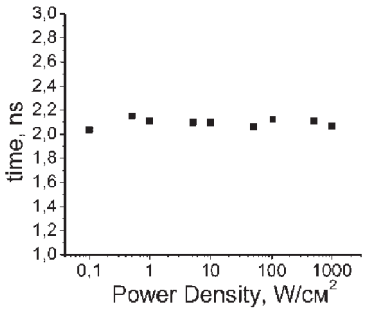

Fig. 3. Auger process in Quantum dots at $T = 5$ K.

3. Discussion

We obtain, that quantum interference between two ways of Auger recombination leads to only non-treshold mechanism can occur in QD. One can see that non-treshold and quasi-treshold mechanism occurs in different ways which is responsible for only quasitreshold mechanism vanishing by quantum interference. Quasitreshold process depends on overlap integral between electron and holes wavefunctions. So, in this case, two electrons acts as one unit and there are no distiguish between one or other electron recombination. However, the hole wavefunction have antisymmetric representation, so electron recombination with one hole eliminates with other. Now, we can analyse non-treshold mechanism. This process is due to electron(or hole) scattering on heterojunction. In this case, electron recombines with a hole and transfer energy to a high energy state. We can see that this process is asymmetric to electrond in QD in general. In this process there are scattering asymmetry. One electron scatters on heterojunction and it means that it transfer momentum to bound. In this process matrix element depends on direction of momentum transfer. So, changing momentum sign changes matrix element sign. That is, electron wavefunction asymmetry compensates scattering asymmetry. Now, consider hole wavefunctions. Though hole wavefunctions have antysymmetric representation, in case of non-treshold process, tranitions to states with different spins are in generally different due to selection rules. So, finally, we have nonvanishing part in non-treshold process. So, changing QD parameters we can supress Auger process at a higer temperatures. That is, we can essentially increase quantum efficiency of QD devices.

References

[1] G. G. Zegrya, D. M. Samosvat, *JETP* **104** 6, 954 (2007).
[2] A. S. Shkolnik, V. P. Evtihiev, G. G. Zegrya, *Technical Physics Letters* **32**, 51 (2006).
[3] D. I. Chepic *et al*, *J. Luminescence* **47** , 113 (1990).

18th Int. Symp. "Nanostructures: Physics and Technology"
St Petersburg, Russia, June 21–26, 2010

Electron-phonon effect on the ground-state binding energy of hydrogenic impurity in parabolic quantum-well wire in presence of an electric and magnetic fields

A. L. Vartanian, M. A. Yeranosyan and A. A. Kirakosyan
Department of Physics, Yerevan State University,375025 Yerevan, Armenia

Abstract. Using a variational approach, the binding energy of shallow hydrogenic impurities in a parabolic quantum wire is calculated within the effective mass approximation. The polaron effects on the ground-state binding energy in electric and magnetic fields are investigated by means of Pekar–Landau variation technique. The results for the binding energy as well as polaronic correction are obtained as a function of the applied fields and the impurity positions.

Introduction

Since semiconductor quantum wires (QWR) are usually manufactured from polar materials, the electron-LO phonon (ELOP) interaction must be taken into account for reliable description. Experimental progress through spectroscopic techniques makes possible a detailed analysis of the effects of confinement as well as electron-phonon coupling on electronic states in low-dimensional quantum systems [1–4]. Polaron effects become more interesting in the presence of external electric and magnetic fields [5–7]. A detailed knowledge of impurity effects on electronic and optical properties of low-dimensional quantum systems is crucial for interpreting experimental findings such as photoluminescence spectra, absorption and emission spectra, and also in designing new nanostructured electronic and optoelectronic devices. Recently there has been a considerable number of theoretical studies on the electron-phonon effect on impurity energies in quantum wells, wires and dots in presence of electric and magnetic fields [8–13].

In the present paper, we consider both the effects of the electric and magnetic fields and the ELOP coupling on hydrogenic impurities in a cylindrical semiconductor QWR embedded in a dielectric medium assuming a parabolic confinement potential. For simplicity, we choose the electron-phonon interaction Hamiltonian to be the bulk Fröhlich Hamiltonian. The Pekar–Landau [14] variational procedure has been used in the investigation. The binding energy of the hydrogenic donor impurity in QWR in the presence of an electric field applied perpendicular to the wire-axis and magnetic field applied parallel to the wire-axis and in the presence of ELOP interaction is given by

$$E^{\mathrm{B}}_{\mathrm{el-ph}} = E_0 - E_{\mathrm{e-ph}}(\lambda_1) \qquad (1)$$

where E_0 is the eigenvalue of the system Hamiltonian without Coulomb impurity as well as ELOP interaction and

$$E_{\mathrm{el-ph}} = E_0 - \frac{\alpha\hbar\omega_{LO}}{2}\left(\frac{\hbar}{2m^*\omega_{LO}}\right)^{1/2} \times |N|^4 \int\int d\vec{r}d\vec{r'}|\Phi_0(x,y)|^2|\Phi_0(x',y')|^2\frac{e^{(-2\lambda(r+r'))}}{|\vec{r}-\vec{r'}|}, \qquad (2)$$

where α is the electron-phonon coupling constant λ_1 is the value of λ which minimizes $E_{\mathrm{el-ph}}(\lambda)$. The polaronic shift in the binding energy is given as the difference of binding energies with and without the electron-phonon coupling.

$$\Phi_0(x,y) = \frac{1}{\rho_0\sqrt{\pi}} exp\left(-\frac{1}{2\rho_0}\left(\left(x+\rho_0^4 F\right)^2 + y^2\right)\right)$$

is the ground-state wave function of a hydrogenic impurity in quantum wire with an applied electric and magnetic fields when ELOP interaction is not considered, where F is the value of the electric field, $\rho_0 = \ell_0/\left(1+\omega_m^2/4\omega_0^2\right)^{1/4}$ and $\ell_0 = (\hbar/m^*\omega_0)^{1/2}$ is oscillator length, $\omega_m = eB/m_*c$ is ciclotron frequency, B are the value of the magnetic field.

As an illustration, we calculate the ground-state binding energy of Coulomb impurity with and without ELOP interaction in $GaAs$ QWR for which the electron-phonon coupling strength $\alpha = 0.0681$, $\varepsilon_0 = 12.7$, $\varepsilon_\infty = 10.9$, $\hbar\omega_{LO} = 36.7$ meV, and $m^* = 0.067m_0$, where m_0 is the electron bare mass. To study the dependence of binding energy and the polaronic shift of the binding energy on all interesting physical quantities, calculations for fixed parabolic potential $\hbar\omega_0 = 50$ meV were performed. In Fig. 1a dependence of impurity binding energy on the magnetic field are shown with (soled line) and without (doted line) ELOP interaction. In Fig. 1b the polaronic shift at various values of electric field of an-axis impurity is shown. It should be noted that in all considered cases both the binding energy and polaronic shift grow with the increase of magnetic field. It is a direct consequence of condensation and therefore of strengthened localization of electronic charge in the ground state around the axis of the cylinder on which the impurity is located. For position of an impurity (0, 0) (Fig. 1a) there is an inversion of the relevant curves as the greater electric field shifts the maximum of electronic probability density even more from the Coulomb centre. In all considered cases, the increase of polaronic shift of the binding energy with the increase of magnetic field is explained by the enhancement of localization of an electron. The curves of the polaronic shift (Fig. 1b), corresponding to the essentially different values of electric field practically coincide. This fact is obviously caused by a cancellation effect. The degree of diminishing of Coulomb confinement due to the shift of electronic charge by electric field from the impurity centre is cancelled by the increase of Stark confinement because of the squeeze of the electron to the opposite QWR barrier. For a considered position of impurity and at electric field $F = 0$, the contribution of ELOP interaction to the binding energy changes from 7.4% at $B = 0$ up to 10% at $B = 15$ (T). At

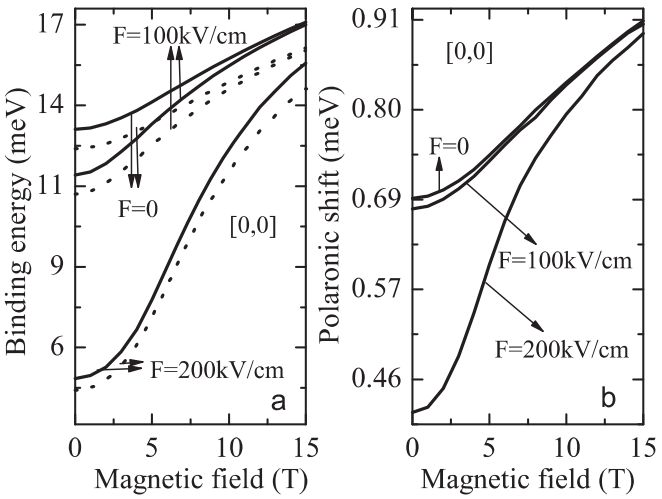

Fig. 1. Reduced binding energy (a) and polaronic shift (b) as a function of magnetic field for the on-axes impurity position.

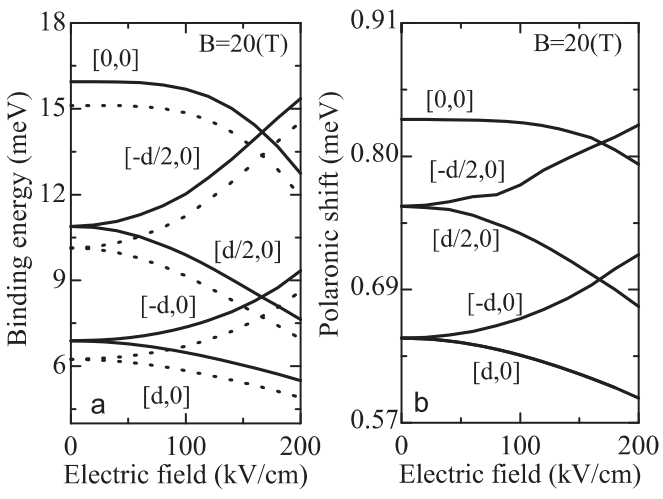

Fig. 2. Reduced binding energy (a) and polaronic shift (b) as a function of electric field for dmagnetic field $B = 2$ (T) and for the different impurity positions.

electric field $F = 100(200)$ kV/cm, these contributions constitute 7.5%(10%) to 13%(10%) respectively.

In Fig. 2a the electric field dependence of the ground-state binding energy with (solid lines) and without (dotted lines) ELOP interaction for various impurity positions along the electric field and for fixed value of magnetic field ($B = 20$ T) is shown. In Fig. 2(b), we display the appropriate polaronic shift of the binding energy. We can see that for zero electric field the degeneracy of the binding energy for the impurity states corresponding to symmetrical positions of the impurity: $(-d, 0)$ and $(d, 0)$ remains if the ELOP interaction is taken into account. In an applied electric field the degeneracy of the bound polaron binding energy is resolved and the difference in energies increases with the field. It is clearly seen from the Fig. 2a that for the impurity positions $(0, 0)$, $(d/2, 0)$ and $(d, 0)$ the binding energy decreases with the increase of an electric field, as the electric field shifts the maximum of electronic probability density from the impurity. The value of polaronic shift of binding energy for these impurity positions decrease also (Fig. 2a), with the increase of the electric field. It will be noted that for considered cases the polaronic shift decrease also, when the electric field increases. However the contribution of ELOP interaction in the binding energy increases from 8.5%(11.3%) at $F = 0$ up to 10.7%(13%) at $F = 200$ kV/cm for impurity position $(d/2, 0)$ and $(d, 0)$ respectively. Because of the strong quantum confinement of electron in QWR, the electric field only pushes a maximum of electronic probability density towards an impurity, when impurity is located at $(-d/2, 0)$ and $(-d, 0)$. Therefore the binding energy with and without ELOP interaction and polaronic shift of the binding energy increases with the increase of an electric field. The contribution of ELOP interaction for impurity positions $(-d/2, 0)$ and $(-d, 0)$ decreases from 8.5 to 6.7%, and 11.3 to 8.3% respectively, when the value of electric field increase from $F = 0$, to $F = 200$ kV/cm. The monotonic growth of polaronic shift, as in case of Fig. 2b, is caused by strengthening the electron confinement because of Stark effect.

By means of the effective-mass approximation and within a variational procedure, we have first presented a systematic study of the ground-state binding energy of a Coulomb impurity in parabolic QWR subjected to both external fields (electric and magnetic) and electron-polar optical phonon interaction. We obtained analytical expression for the bound polaron ground-state energy, which allowed a calculation of the impurity binding energy and its polaronic shift as functions of the electric and magnetic fields as well as of the impurity position and the length of QWR. We have shown that in presence of electric and magnetic fields the electron effective confinement increases and therefore increases the binding energy polaronic shift. According to our results the effect of ELOP interaction on the impurity binding energy in QWR is crucial in understanding of the optical properties of these systems associated with impurity states. This is conditioned by the fact that in some cases the electron-polar optical phonon interaction significantly changes the bound polaron energy. Although to our knowledge, there are no available experimental data to compare with our theoretical results, we believe the present calculation will be of importance in the understanding of future experimental work in this subject.

References

[1] P. Roussignor, *Phys. Rev. Lett.* **62**, 312 (1989).
[2] L. R. Wilson *et al*, *Phys. Rev. B* **57**, R2073 (1998).
[3] A. S. Bhatti *et al*, *Phys. Rev. B* **60**, 2592 (1999).
[4] R. Heitz *et al*, *Phys. Rev. Lett.* **83**, 4654 (1999).
[5] L. Jacak *et al*, *Phys. Rev. B* **67**, 035303 (2003).
[6] K. D. Zhu *et al*, *Phys. Rev. B* **47**, 12941 (1993).
[7] K. D. Zhu *et al*, *Phys. Lett. A* **190**, 337 (1994).
[8] A. L. Vartanin *et al*, *Phys. E* **27**, 447 (2005).
[9] A. L. Vartanin *et al*, *Phys. B* **390**, 256 (2007).
[10] H.-Y. Zhou *et al*, *Phys. Rev. B* **50**, 17180 (1994).
[11] C.-Y. Chen *et al*, *Phys. Rev. B* **56**, 14913 (1997).
[12] H.-Y. Zhou *et al*, *Phys. Rev. B* **50**, 17180 (1994).
[13] A. L. Vartanin *et al*, *Phys. Lett. A* **360**, 649 (2007).
[14] L. D. Landau *et al*, *Zh. Eksp. Teor. Fiz.* **16**, 341 (1946).

18th Int. Symp. "Nanostructures: Physics and Technology"
St Petersburg, Russia, June 21–26, 2010

Polarization dependence of Fano resonance in the impurity photoconductivity of quantum wells doped with shallow donors

V. Ya. Aleshkin[1], A. A. Antonov[1], *M. S. Zholudev*[1], V. Yu. Panevin[2], L. E. Vorobjev[2], D. A. Firsov[2], A. P. Vasil'ev [2] and A. E. Zhukov[3]

[1] Institute for Physics of Microstructures RAS,603950, Nizhny Novgorod, Russia
[2] St Petersburg State Polytechnic University, 195252 St Petersburg, Russia
[3] Ioffe Physical-Technical Institute, St Petersburg, Russia

Abstract. The Fano resonance caused by the electron-phonon interaction is described in the case when the resonant states interacts with two size quantization subbands and the impurity photoabsorption spectrum is calculated for two different polarizations of the incident radiation. The impurity photoconductivity spectrum for two polarizations has been measured in AlGaAs/GaAs quantum well heterostructure and the predicted strong polarization dependence of the Fano resonance has been observed.

Introduction

The specific states in which an electron occupies the ground state of the impurity and an optical phonon presents can occur in semiconductors doped with shallow donors [1]. The energy of this state equals to the energy of the impurity ground level plus the optical phonon energy $\hbar\omega_0$. If it falls into the continuous spectrum range this state becomes a quasistationary (resonant) that. In this case an asymmetric peak or dip can occur in the photoabsorption spectrum. This feature is called Fano resonance [2].

This work is focused on the study of Fano resonance dependence in the impurity photoconductivity spectrum of AlGaAs/GaAs heterostructure with quantum wells doped with shallow donors on the incident radiation polarization. The parameters of the system had been chosen so as the resonant state appears above the bottom of the second size quantization subband. This provides mixing of the resonant state with the second subband which allows the electron transition from the ground donor state to this state under the influence of radiation with an electric field normal to the quantum well plane.

1. Model for calculation

In order to calculate the resonance parameters a generalization of the Fano method [2] had been developed. The generalization makes it possible to calculate the wave functions of the resonant states and the transition probabilities in systems where a set of discrete levels with similar energies interacts with set of continuums. In this case the Fano resonance is a superposition of simple resonances and each of them is described by the following expression [2]:

$$f(\varepsilon) = |C|^2 \frac{(Q-\varepsilon)^2}{1+\varepsilon^2}.$$

The number of such terms equals to the degeneracy order of continuous spectrum nearby the resonance.

The Hamiltonian of the regarded system is

$$H = H_{\rm e} + H_{\rm phon} + H_{\rm e-ph}\,,$$

where

$$H_{\rm e} = \frac{\mathbf{p}^2}{2m_{\rm e}} + U(z) - \frac{e^2}{\kappa_0|\mathbf{r}-\mathbf{r}_0|^2}$$

is the Hamiltonian of an electron in a doped quantum well, $m_{\rm e}$ is the effective mass of the electron, $U(z)$ is the quantum well potential, e is the electron charge, κ_0 is the dielectric constant of the crystal at zero frequency, $\mathbf{r}_0$ is the impurity position;

$$H_{\rm phon} = \sum_{\mathbf{q}} \hbar\omega_0 \left(b_{\mathbf{q}}^{+} b_{\mathbf{q}} + 1/2\right)$$

is the Hamiltonian of phonon system, ω_0 is the optical phonon frequency, $b_{\mathbf{q}}^{+}$, $b_{\mathbf{q}}$ are the optical phonon creation and annihilation operators;

$$H_{\rm e-ph} = \sum_{\mathbf{q}} \left[V(q)\exp(-i\mathbf{qr})b_{\mathbf{q}}^{+} + V^*(q)\exp(i\mathbf{qr})b_{\mathbf{q}}\right]$$

is the electron-phonon interaction Hamiltonian, where

$$V(q) = \frac{ie}{q}\sqrt{\frac{2\pi\hbar\omega_0}{\mathcal{V}\overline{\kappa}}},$$
$$\overline{\kappa} = \frac{\kappa_0\kappa_\infty}{\kappa_0-\kappa_\infty},$$

κ_∞ is the dielectric constant at the frequency higher than the optical phonon frequency, $\mathcal{V}$ is the crystal volume.

The continuum wave functions had been represented in the form

$$\Psi_m(\rho,\phi,z) = e^{im\phi}\sum_{s=1}^{3}\psi_s(\rho)\varphi_s(z),$$

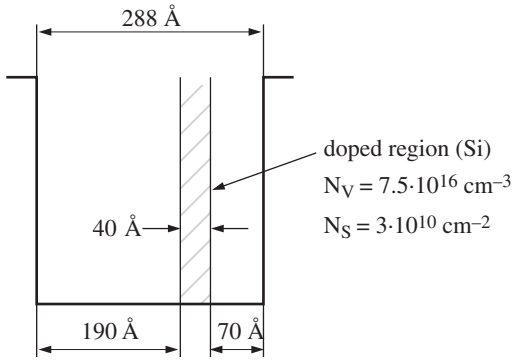

Fig. 1. Quantum well doping scheme.

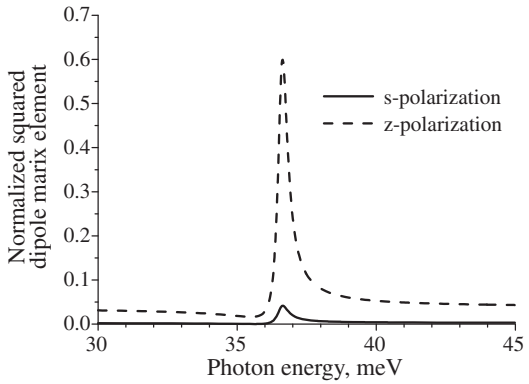

Fig. 2. The calculated squared matrix element of dipole transition operator in delta doped quantum well. The impurity locates at distance of 0.7 well width from one of it's sides. The curves are normalized on the probability of the electron transition from the donor ground state to edge of the first subband.

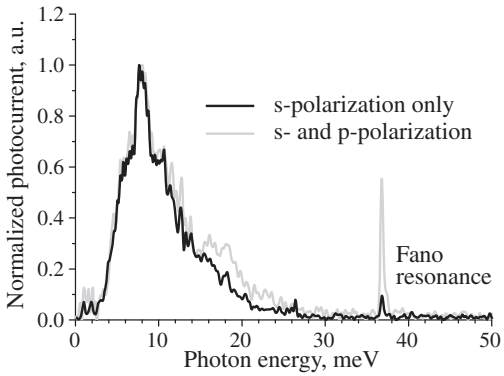

Fig. 4. Photoconductivity spectrum for different polarizations of the incident radiation. The curves are normalized on the maximum concerned with the electron transition from the donor ground state to the first subband.

where m is z-component of angular momentum, $\varphi_s(z)$ describes the electron transversal motion in the s size quantization subband.

Schrodinger equation with Hamiltonian H_e produces the differential equation system for $\psi_s(\rho)$ which had been solved numerically for the functions $f_s(\rho) = \psi_s(\rho)\rho^{-m}$ which has nonzero initial condition at $\rho = 0$ for any m:

$$f_s(0) = A_s, \quad f_s'(0) = 0,$$

where A_s is a constant determined by the normalization condition. Using generalization of the Fano theory [2], Ψ_m and wave function of the resonant state, the correct wave functions in the continuums were calculated.

The probability spectrum of the electron dipole transition from the ground donor state to continuum had been calculated for two polarizations of the incident radiation. For s-polarization the electric field lies in the quantum well plane. For z-polarization the electric field is normal to this plane.

The calculation had been carried out for structure grown by MBE which contains 50 GaAs quantum wells separated with $Al_{0.3}Ga_{0.7}As$ barriers. The quantum wells are doped with donors (Si). The doped region width is 40 Å and it's location is shown on the Fig. 1. The 200 Å GaAs cap layer was grown over the structure. According to the X-ray analysis the quantum well width is 288 ± 3 Å, the barrier width is 63 ± 3 Å.

Calculation shows that the first three size quantization level energies are 5, 20 and 44 meV, the impurity ground state ionization energy is 8 meV.

The calculation results for squared matrix element of dipole transition operator are presented on the Fig. 2 for different incident radiation polarization. It is supposed that the impurity locates in the center of the doped region.

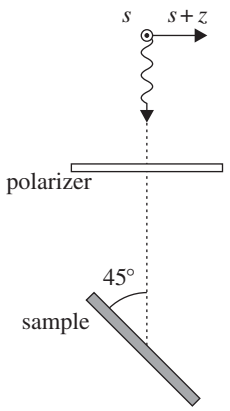

Fig. 3. Experiment scheme.

2. Experiment

In the experiment the radiation was passed trough a polarizer and fell on the sample at angle of about 45 degrees to the growth direction (see Fig. 3). The measurement had been carried out for s- and p-polarization. The last one contains z-polarized component.

The measurement results are presented on the Fig. 4. One can see that the peak height strongly depends on the polarization and appears to be much greater in the case when z-polarized component presents in the radiation.

Thus a strong polarization dependence of the impurity photocurrent in the spectral region corresponding to the optical phonon energy was predicted and experimentally observed.

Acknowledgements

The work has been supported by RFBR (grant 10-02-00311).

References

[1] V. Ya. Aleshkin, L. V. Gavrilenko, M. A. Odnoblyudov and I. N. Yassievich, *Semiconductors* **42**, 880–904 (2008).
[2] U. Fano, *Phys. Rev.* **124**, 1866 (1961).

18th Int. Symp. "Nanostructures: Physics and Technology"
St Petersburg, Russia, June 21–26, 2010

Novel system of GaAs quantum dots in GaP matrix

T. S. Shamirzaev, A. K. Gutakovskii and M. A. Putyato
Institute of Semiconductor Physics, pr. Lavrentieva 13, 630090 Novosibirsk, Russia

Abstract. Novel system of GaAs self-assembled quantum dots (QDs) embedded in GaP matrix has been studied by transmission electron microscopy, steady-state and transient photoluminescence (PL). Unusually the QDs are fully unstrained but its have no any nonradiative centers introduced by dislocations at GaAs/GaP heterostructure. The band alignment in the QDs is shown to be of type I.

1. Introduction

Self-assembled semiconductor quantum dot (QDs) with very strong three-dimensional confinement is currently considered for fabrication of novel optoelectronic devices [1]. The majority of the studies reported so far have concentrated on QDs in GaAs matrix, emitting in the near infrared spectral region such as InAs/GaAs [1], InP/GaAs [2], GaSb/GaAs [3] while the QDs emitting in visible spectral region based on others III–V compound semiconductors have received much less attention. The use of GaP as the substrate has further potential advantages of larger then GaAs band gap with, allowing more flexibility in varying the emission wavelength. Additionally, structures on GaP could take advantage of well-developed Al free light-emitting diode technology.

In this report, we present the results of a first study of the structure and energy spectrum of novel self-assembled GaAs QDs in GaP matrix by transmission electron microscopy (TEM) and photoluminescence.

2. Experimental

The samples of GaAs QDs in a GaP matrix studied in this work were grown by molecular beam epitaxy on p-type (001)-oriented GaP substrates. The samples consisted of one layer of the QDs sandwiched between two 50 nm thick layers of GaP. The nominal amount of deposited GaAs was equal to 3 monolayers. The QDs were formed at a temperature of 560 °C. A test sample with 50 nm GaP layer was grown at the same condition. The atomic structure of the QDs was studied by means of transmission electron microscopy (TEM) with employing a JEM-4000EX operated at 400 keV. Steady-state PL was excited by a He-Cd laser ($\hbar\omega = 3.81$ eV) with a power density of 0.1 W cm^{-2}. Transient PL was excited by a pulsed N2 laser ($\hbar\omega = 3.68$ eV) with a pulse duration of 7 ns and a peak power density of 400 W cm^{-2}. The PL detection was performed by a double diffraction grating spectrometer equipped with a cooled photomultiplier operated in the photon counting mode.

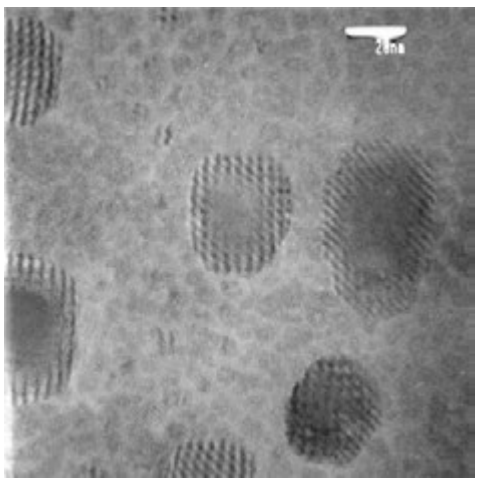

Fig. 1. TEM plane view image of the GaAs/GaP QDs.

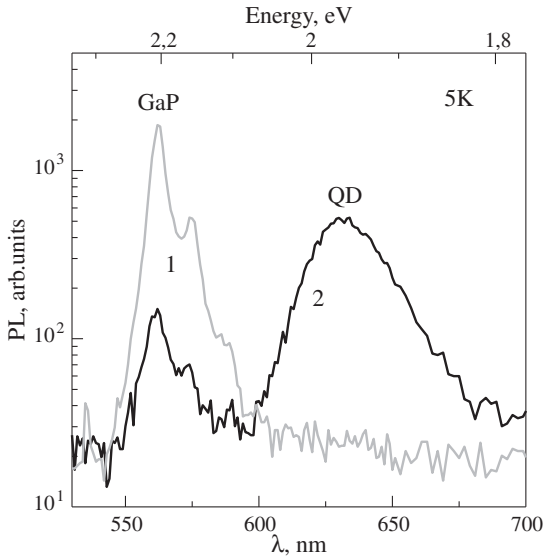

Fig. 2. PL of (1) GaP layer and (2) the structure with GaAs/GaP QDs.

3. Results

The difference in lattice parameters of GaAs and GaP is about of 4 % similar to the difference in well studied Si/Ge system [4]. So, we could expect that the atomic structure of GaAs/GaP QDs will be similar to that of Ge/Si QDs. Figure 1 demonstrates TEM plane view image of sample with GaAs/GaP QDs. In contract to strained Ge/Si QDs the GaAs QDs in GaP matrix have lattice parameter of GaAs, i.e. the strain of the QDs is fully relaxed by embedding of dislocations at GaAs/GaP heterointerface. Figure 2 demonstrates PL spectra of the GaP layer and the structure with GaAs/GaP QDs. Both the spectra contain bands connected with impurity related recombination in GaP marked in the figure as GaP. The intensity of the GaP bands is smaller in the spectrum of the structure with GaAs/GaP QDs but the spectrum contains an additional wide band related to recombination in the QDs marked in the figure as QD. It is interesting that the integrated intensity of the PL in both the spectra is similar that indicates the absence of any nonradiative centers induced by relaxation of strain in the QDs. Using the band structure parameters of GaAs and GaP taken from Ref.5 we

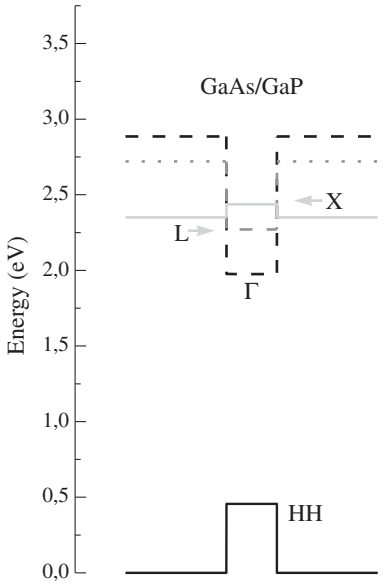

Fig. 3. Band diagrams of an unstrained GaAs/GaP heterostructure. Quantum confinement does not take into account.

calculate the band lineup of GaAs/GaP heterostructure, which is presented in Fig. 3.

Three possible energy configurations can be realized in a structure with the QDs: (i) at a small the quantum confinement lowest state of the conduction band belong to direct (Γ minimum. On the other hand, the electron states in the Γ minimum of the GaAs conduction band because of the small electron effective mass can be considerably stronger shifted by confinement than those of the L and X minima. Therefore the quantum confinement can lead to (ii) shift of the lowest state of the conduction band from direct Γ to indirect L minima within band alignment of type I, or (iii) a transition of the band alignment from type I to type II, which can happen if quantum confinement pushes the Γ and L state of conduction band above that of the matrix. In order to reveal, which energy configuration is realized in the studied QDs we measured transient PL of the structure with the QDs, which is presented in Fig. 4. One can see that the QDs demonstrate very long decay of the PL lied in millisecond region of time and its energy position practically does not shift with time after excitations.

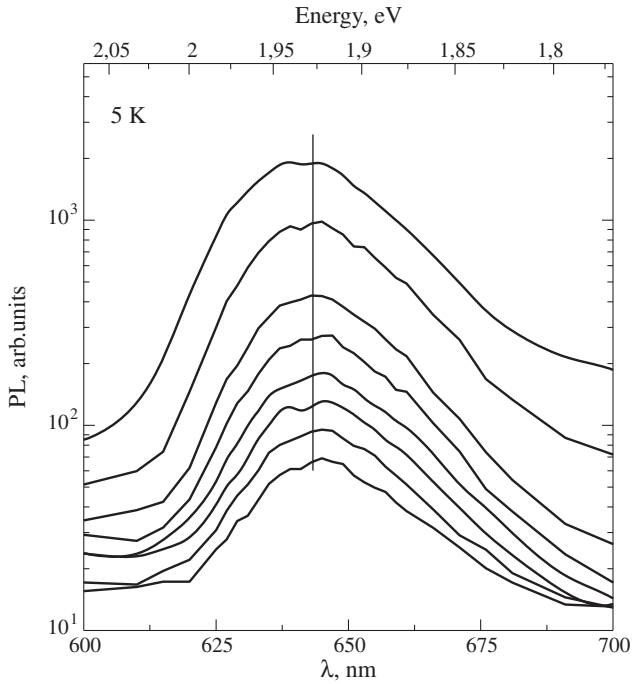

Fig. 4. Transient PL spectra of the GaAs/GaP QDs. The delays after the excitation pulse, from top to bottom (ms): 0.1, 0.3, 0.5, 0.7, 1, 1.5, 2, 3.

The observed PL decay time is too long for QDs with direct band gap structure. On the other hand, energy position of bands in spectra of the transient PL of type II heterostructures demonstrates strong red shift with time after excitation pulse [6]. Thus we conclude that structure with the GaAs/GaP QDs has the band alignment of type I but the lowest electronic level in the QDs located at the L indirect minimum of the conduction band.

Acknowledgements

This work was supported by the RFBR (grant No. 10-02-00240) and by the Program of Fundamental Studies of the Presidium of RAS (grant No. 32).

References

[1] D. Bimberg, M. Grundmann, and N. N. Ledentsov, *Quantum Dot Heterostructures* Wiley, New York, 1999.
[2] B. Wanga *et al*, *Appl. Phys. Lett.* **78**, 628 (2001).
[3] F. Hatami *et al*, *Appl. Phys. Lett.* **67**, 656 (1995).
[4] C. G. Van de Walle *et al*, *Phys. Rev. B* **39**, 1871 (1989).
[5] I. Vurgaftman *et al*, *Appl. Phys. Lett.* **89**, 5815 (2001).
[6] T. S. Shamirzaev *et al*, *Phys. Rev. B* **76**, 155309 (2007).

18th Int. Symp. "Nanostructures: Physics and Technology"
St Petersburg, Russia, June 21–26, 2010

Amplitude controlled Atomic Force Microscopy under vacuum. Principles and consequences for local observations and measurements

Paul Girard[1], Michel Ramonda[2] and Luc Girard[3]

[1] Institut d'Electronique du Sud, UMR 5214 CNRS-UM2, Université Montpellier 2, Place E. Bataillon, 34095 Montpellier Cedex 5, France
[2] Laboratoire de Microscopies en Champ Proche, Université Montpellier 2, Place E. Bataillon, 34095 Montpellier Cedex 5, France
[3] Institut de Chimie Séparative de Marcoule, UMR 5257 CEA-CNRS-UM2-ENSCM, BP 17171–30207 Bagnols sur Ceze Cedex, France

Abstract. Up to now the well established vibrating AFM concern ambient and ultra high vacuum (UHV), they are based on the control of the amplitude or frequency of vibration, respectively. Under secondary vacuum, it is shown that amplitude controlled AFM can be obtained on the basis of higher resonant modes. Then morphology as well as local voltage measurements are resulting. Since the equivalent spring mass of the real AFM sensor — a bar bringing a tip — was unknown for higher resonances, numerical simulations have been undertaken and comparisons with experiments are reported.

Introduction

Atomic Force Microscopy (AFM) is now a widely used tool for the characterizations of materials and structures down to the atomic scale. Under ambient, the intermittent contact (IC) method — or "tapping" — allows to obtain easy AFM on various materials and surfaces. Under UHV and with skilled staff, vibrating in non contact offers the possibility to obtain atomic resolution [1] on very clean surfaces.

The intermediate situation of easy AFM experiments under vacuum — and more especially secondary vacuum — was not obtained up to now. However, there are needs, especially for electrical measurements. It must be recalled that the surfaces are generally covered with a water film which: i) perturb the measurement of surface voltages [2] and ii) can snap the vibrating tip at close proximity, and close proximity between tip and surface is mandatory for well resolved measurements of potentials [3] during the examination of semiconductor nanostructures properties [4] for example. So, the extension to vacuum of the amplitude controlled and intermittent contact AFM and derived becomes questionable.

Experiments and simulations

Until now, vacuum AFM has been implemented on the basis of the control of the first resonance frequency shift of the vibrating cantilever [5]. The main reason is the following: since under vacuum the viscous damping does not occur, the quality factor Q_1 of the first resonance of period T_1 increases dramatically — i.e. by more than two orders of magnitude, referring to ambient — which in turn increases the stabilisation time duration $t_1 \approx Q_1 T_1$ of the oscillator. This makes no longer tractable the amplitude controlled AFM imaging under reasonable time durations.

Since a key point for vibrating AFM is the time $Q_n T_n$, its behaviour versus the mode order of vibration n has been examined under secondary vacuum. Both the period and quality factor of the resonances are progressively reduced which n. Thus, for resonances higher or equal to the third, an ambient like time constant — i.e. some milliseconds — can be obtained and the amplitude controlled intermittent contact (IC) AFM is becoming possible when using standard sensors [6]. The extension to vacuum of the simple and popular ambient intermittent contact AFM is then achievable. It allows to easily obtain 3D morphology (Fig. 1) — signal to thermal noise ratio

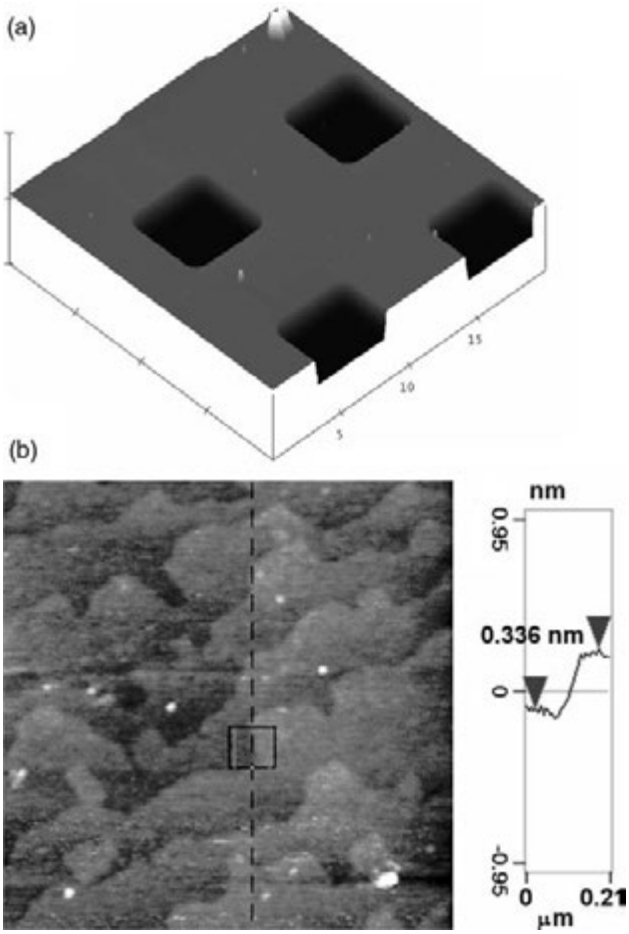

Fig. 1. Secondary vacuum morphology of: a) a cell test (20 × 20 μm^2), b) atomic steps of a MBE grown semiconductor surface (5 × 5 μm^2).

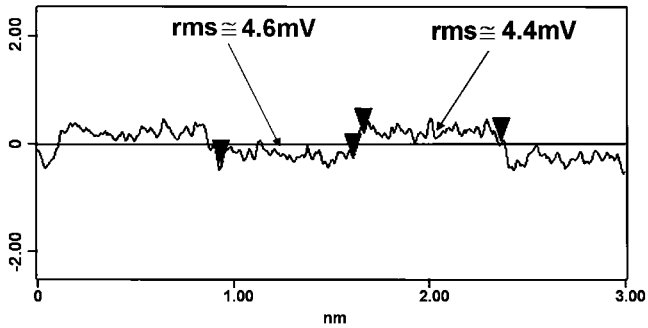

Fig. 2. Voltage measurements (20 mV p.p.) under vacuum, the rms noise is indicated.

is improved referring to ambient conditions — and, of course, it opens the way to the choice of the area of interest before the carrying out of other SPM methods.

To obtain local voltage observations and measurements — i.e. the Kelvin method — based on the gradient method [2], the phase shift of the vibrating tip is examined. The best measurement conditions are obtained with the second resonance [7,8] (Fig. 2). Additionally, in order to avoid parasitic capacitive effects with three dimensional samples, a constant tip to sample distance is required. A suitable method concerns a double pass on the same line: first high amplitude IC AFM gives the morphology reference which, in turn, becomes the basis of the mean distance adjustment during the second pass for Kelvin achievement at low oscillation amplitude.

Since the field of AFM based on higher modes of vibration is opened, the equivalent spring mass system of the AFM sensor — a bar plus a tip at the free end — becomes questionable for at least two reasons. They concern a fundamental point as well as practical considerations, i.e. the analysis of the experiments and the definition of the best sensor configuration. On the basis of a point mass added at the free end of a constant section cantilever, the effective mass and stiffness of the sensor have been simulated. Referring to the simple bar case, it results a noticeable growing of these quantities with both the tip mass and the resonance number n (Table 1).

Experiments have been done. There concern: i) the periods of resonance T_n and their ratio between different orders, the deduced point mass is about 5% of the cantilever the mass and corresponds to the tip plus the cantilever underneath, ii) the stabilisation time duration $t_n \approx Q_n T_n$ on standard sensors and iii) the effect of an added mass on the tip as well. The validity of the harmonic oscillator model and the effect of the tip mass have been shown. Then, from simulations, guidelines for the sensor optimisation can be deduced.

Table 1. New resonance frequencies, spring stiffness and effective mass when $m_{\text{tip}}/m_{\text{cantilever}} = 5\%$, like for standard AFM sensors. The reference is the mode n with the simple bar case where: $f_1 = (k_1/m_0)^{1/2}$, $f_2 = 6.267 f_1$, $f_3 = 17.55 f_1$, $f_4 = 34.40 f_1$, etc. ..., $k_1 = k_{\text{static}}$, $k_n = (f_n/f_1)^2 k_1$ and $m_0 = 0.250 m_{\text{cantilever}}$.

Mode order n	1	2	3	4
Resonance frequency	$0.9125\, f_1$	$0.9242\, f_2$	$0.9328\, f_3$	$0.9400\, f_4$
Spring stiffness	$0.9906\, k_1$	$1.380\, k_2$	$1.823\, k_3$	$2.375\, k_4$
Effective mass	$1.190\, m_0$	$1.616\, m_0$	$2.095\, m_0$	$2.688\, m_0$

Conclusions

In summary, since vacuum amplitude controlled AFM is a new method and applications on, for example, materials and devices coming from ambient are still in the infancy. In fact, the elimination or thickness reduction of the surface liquid film by heating under vacuum must certainly improve local measurements not only of voltages but also of tip to sample currents and local temperatures. Vacuum shall make possible the extension of measurements on structures and devices under variable temperatures, i.e. on the high or low side.

Additionally, this method is simple and can be managed by non AFM specialists. Since it is really low time consuming, the way is opened towards quasi routine and well resolved characterisations of semiconductor materials and structures under clean conditions.

References

[1] F. J. Giessibl, *Rev. Mod. Phys.* **75** (3), 949 (2003).
[2] N. Gaillard, M. Gros-Jean, D. Mariolle, F. Bertin and A. Bsiesy, *Appl. Phys. Lett.* **89** 15, 154101 (2006).
[3] P. Girard, A. N. Titkov, Chapt. 9 in Applied Scanning II, B. Bhushan and E. Fuchs, Springer Verlag (2006).
[4] S. Shusterman, A. Raizman, A. Sher, A. Schwartzman, O. Azriel, A. Boag, Y. Rosenwaks, P. L. Galindo and Y. Paltiel, *Europ. Phys. Lett.* **88**, 66003 (2009).
[5] T. R. Albrecht, P. Grutter, D. Horne, and D. Rugar, *J. Appl. Phys.* **69**, 668 (1991).
[6] P. Girard, M. Ramonda and R. Arinero, *Rev. of Sci. Instr.* **77** 1, 096105 (2006).
[7] L. Portes, P. Girard, R. Arinero and M. Ramonda, *Rev. of Sci. Instr.* **77** 1, 096101 (2006).
[8] L. Portes, M. Ramonda, R. Arinero and P. Girard, *Ultramicroscopy* **107**, 1027 (2007).

18th Int. Symp. "Nanostructures: Physics and Technology"
St Petersburg, Russia, June 21–26, 2010

Nano-optical emission of single colloidal CdSe nanowires

A. M. Mintairov, J. Herzog, M. Kuno and J. L. Merz
University of Notre Dame, Notre Dame, IN 46556 USA

Abstract. We used near-field scanning optical microscopy (NSOM) having spatial resolution ∼100 nm in combination with diffraction-limited micro-photoluminescence (μ-PL) and time-resolved (TR) spectroscopy to study emission properties of single colloidal CdSe nanowires (NWs). Comparison of NSOM and wide-field μ-PL images allows observation of residual chemical and/or water drops attached to a NW, which act as a nano-lens providing efficient coupling of excited and emitted photons. At temperatures $T < 150$ K the emission spectra of a single NW reveal interference structure (period $\sim\lambda/200$) manifesting strong exciton-polariton coupling. Effects of carrier localization in wurtzite (W) and zinc-blende (ZB) sections of NW were observed in temperature dependent spectra. Type-I band alignment of ZB-W heterojunction was revealed from spectral dependence of emission decay.

Introduction

Recently the synthesis and optical properties of colloidal CdSe NWs have attracted considerable attention [1]. Sharp emission lines were observed in low-temperature micro-photoluminescence (μ-PL) spectra of single CdSe NWs [2]. Such lines manifest exciton localization on zero-dimensional potential fluctuations, which was previously studied in detail in epitaxially-grown GaAs/AlGaAs NWs using high-spatial-resolution near-field scanning optical microscopy (NSOM)) [3]. Here we use temperature-dependent NSOM having spatial resolution ∼100 nm in combination with diffraction-limited μ-PL (spatial resolution ∼1 μm) and time-resolved (TR) spectroscopy to study emission properties and exciton localization in colloidal CdSe NWs.

1. Experimental details

CdSe NWs with mean diameters 20 nm and length exceeding 1 μm were synthezised following a recently-developed solid-liquid-solid growth technique [1]. High-resolution transmission electron microscopy measurements have shown that average length of zinc blende (ZB) and wurtzite (W) sections in NW is 3 and 2 nm, respectively, and that ZB(W) lengths range from 1 to 16 nm (1 to 17 nm). Our NSOM setups based on room-temperature Multi-View 1000 NSOM (NANONICS Imaging Ltd) and low-temperature CryoSXM (Oxford Instruments) heads have been described [4,5]. A home-made inverted microscope with an oil-immersion microscope objective ($\times$100, N.A. = 1.2) was used for diffraction limited wide-field (WF) imaging of an area of $\sim 30 \times 50$ μm^2 in conjunction with NSOM imaging and time-resolved spectroscopy as described in [5].

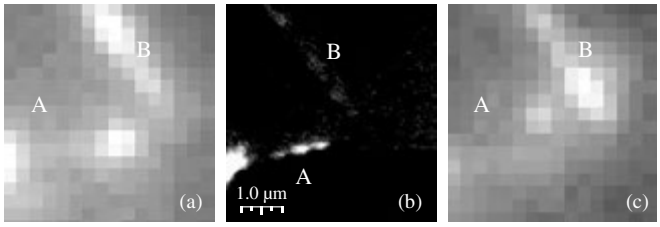

Fig. 1. Comparison of WF (a and c) and NSOM (b) images of two CdSe NWs (A and B) at 300 K. WF images a and c were taken before and after NSOM scans. Image size is $\sim 5 \times 5$ μm^2.

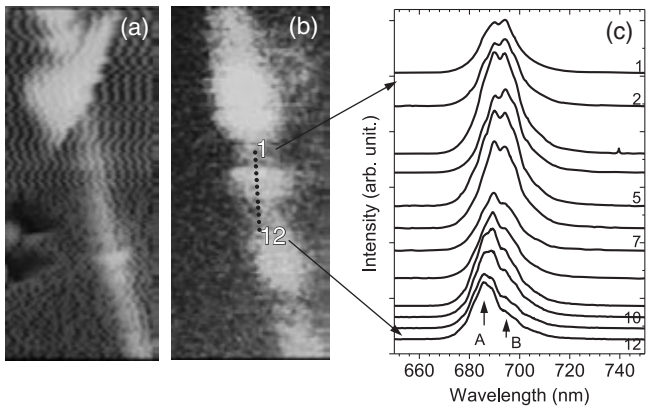

Fig. 2. Topography (a) and NSOM images (b) of CdSe NW (size 40 nm) at 50 K. Spectra (c) were taken along the NW with steps of 50 nm. Image size is 0.8×2 μm^2.

2. Near-field versus wide-field imaging

Fig. 1a–c compares NSOM and WF images of two CdSe NWs (A and B) at room temperature. WF images were taken before and after the NSOM scan. Before the scan (Fig. 1a) the WF image of NW A shows a bright, diffraction-limited circular region at each end. After the NSOM scan (Fig. 1c) the left bright spot disappears and the right one moves up by ∼1 mum. These and other observations [5] show that the NWs have a liquid drop/shell attached, which is "rearranged" by the fiber tip when it touches the wire during scanning. The shell forms a nano-lens, providing near-field coupling of incident and emitted photons, which makes colloidal nanostructures bright in far-field imaging.

3. High-spatial-resolution spectroscopy

Fig. 2a and b show 0.8×2 μm^2 topographic and NSOM images of a CdSe NW taken at 50 K. The NSOM image reveals inhomogeneity of the emission intensity on a length scale of ∼200 nm, similar to that observed at 300 K in Fig. 1b. The 12 spectra taken along the NW with 50 nm steps in Fig. 2c show that intensity variations are accompanied by variations of spectral line shape. Analysis shows that spectra consist of two overlapping bands, having width ∼15 nm, whose relative intensity changes along the NW. The bands are centred at 685(1.810) and 696(1.782) nm(eV) and can be attributed to W and ZB sections of NW as will be shown below. In Fig. 2c the spectra reveal interference structure having a modulation period of 4 nm. We found that the structure appears in NSOM

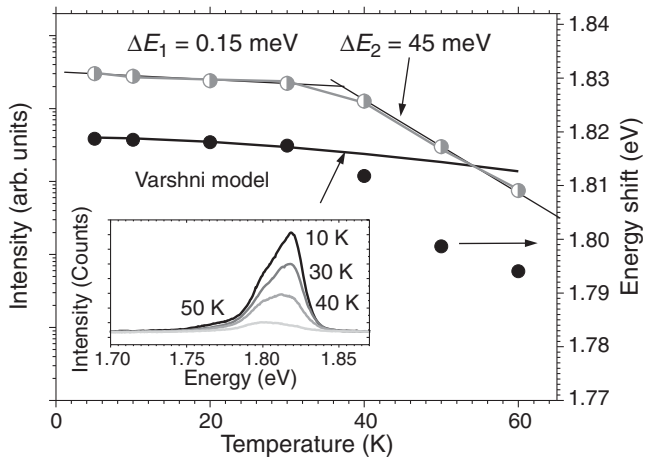

Fig. 3. Intensity and energy shift of CdSe NW PL band (see insert) versus temperature measured by NSOM (half-filled and solid circles, respectively) together with activation model fit (for intensity) and Varshni model band-gap shift (curves). Two straight lines show activation energies 0.15 and 45 meV.

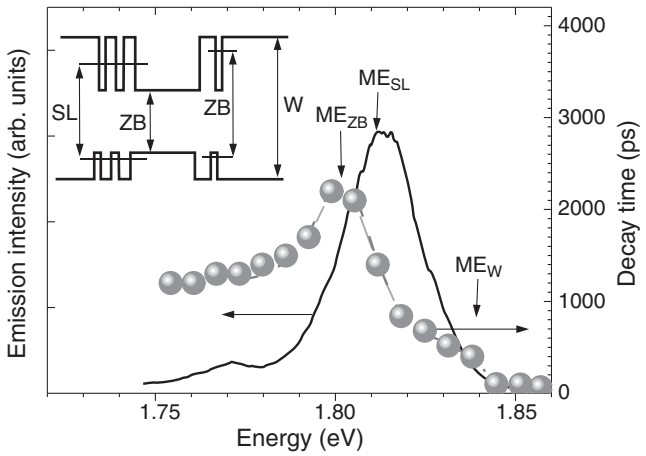

Fig. 4. Energy dispersion of emission decay time $\tau(E)$ (circles) together with time-integrated micro-PL spectra of single CdSe NW at ~10 K (solid curve). Dashed curve is fitting using band-tail model of exciton localization [9]. Insert shows energy structure and W, SL and ZB transitions of along NW.

spectra and TR μ-PL spectra at temperatures below 150 K and can be related to effects of strong exciton-polariton interaction [6].

4. Effects of carrier localization

Fig. 3 shows the temperature dependence of the integrated intensity and the peak position of a NW measured using NSOM spectra at a temperature range $T = 5-60$ K. Insert shows spectra at $T = 10$, 30, 40 and 50 K. A decrease of intensity by one order of magnitude and a red shift of peak position by ~20 meV are observed. The intensity decrease is described by two activation channels having energy $\Delta E_1 = 0.15$ and $\Delta E_2 = 45$ meV, which correspond to mobility edges for SL and W states, respectively (cf. Fig. 4). The shift value of 20 meV observed is much larger then the value of 4 meV expected for thermal expansion effects (Varshni model) [7]. In μ-PL spectra taken over a wider temperature range we observed clear S-type behaviour of the peak position, which manifests the thermal population of band-tail states [8], i.e. existence of strong one dimensional disorder along the NW. Fig. 4 shows typical spectral dependence of emission decay $\tau(E)$ of a CdSe NW together with a time-integrated spectrum. Fig. 4 also shows a cartoon describing zone structure and energy transitions of NW extracted from $\tau(E)$ curve. Similar to Fig. 2 the spectra contain two peaks — a strong one centred at 1.81 and a weak one centred at 1.77 eV. The $\tau(E)$ dependence shows increase of the decay time from 1 to 2 ns in the low energy range of emission spectra (1.75–1.8 eV) followed by a decrease at higher energies (down to $\tau = 65$ ps at 1.86 eV). Near 1.83 eV a plateau at $\tau = 700$ ps is seen. The observed behaviour can be explained assuming type-I band alignment at W-ZB heterojunction. As shown in the band diagram in Fig. 4 three types of transitions are expected for that case, which are (1) W-type transitions, corresponding to extended, tunnel-isolated (<5 nm) wurtzite sections; (2) SL-type transitions, corresponding short-period superlattice sections formed by alternation of a few nm thick, W and ZB sections, and ZB-type transitions, corresponding to isolated zinc blende sections. Since a radiation decay time is inversely proportional to a localization length one can expect a increase (decrease) of the emission decay time versus energy for ZB-type (W- and SL-type) transitions as indeed observed in experiment. We should point out that the decay increase in the low energy range of the emission spectra rule out the type-II band alignment of ZB-W heterojunction. The experimental $\tau(E)$ curve we fitted (see Fig. 4) using band-tail model of exciton localization [9] and accounting for contributions of the three W, SL and ZB transitions. The individual contribution was expressed as

$$\tau(E) = \frac{\tau_{\text{rad}}}{1 + \exp\left[\alpha(E - E_0)\right]}, \qquad (1)$$

where τ_{rad} is the radiation life-time in the strong localization regime and E_0 is a mobility edge (ME). The following values were extracted from fitting: 600 ps for $\tau_{\text{rad W}}$, 2100 ps for $\tau_{\text{rad ZB}}$ and $\tau_{\text{rad SL}}$; 1.84, 1.809 and 1.799 eV for ME_W, ME_SL and ME_ZB, respectively, and 0.004–006 eV^{-1} for α. For the ZB-transitions the "background" decay time 1200 ps, corresponding to emission of longest (16 nm) sections and negative α values, describing decay increase, were used. Our $\tau(E)$ measurements allow assignment of two peaks observed in a single NW in spectra (Fig. 2 and 4) to W and ZB section emission. In NSOM spectra in Fig. 3 we can resolve a shoulder at 1.80 eV, which is related to SL transition.

Acknowledgements
Work was supported by the National Science Foundation via NSF-NIRT grant No. ECS-0609249.

References

[1] M. Kunol, *Phys. Chem. Chem. Phys.* **10**, 620 (2008).
[2] J. J. Gelennonet *et al*, *Phys. Rev. B* **80**, 0813303(R) (2009).
[3] F. Intoni *et al*, *Phys. Rev. B* **63**, 075313 (2001); A. Feltrin *et al*, *Phys. Rev. B* **69**, 205321 (2004).
[4] A. M. Mintairov *et al*, *Phys. Rev. B* **69** 15, 155306 (2004)
[5] A. M. Mintairov *et al*, *Phys. Stat. Sol. B* (in press) (2010).
[6] F. Dubin *et al*, *Nature Physics* **2**, 32 (2006).
[7] P. Jing *et al*, *J. Phys. Chem.* **113**, 13545 (2009).
[8] A. M. Mintairov *et alSemicond. Sci. Tech.* **24**, 075013 (2009).
[9] M. Queslati *et alPhys. Rev. B* **32**, 8220 (1985).

18th Int. Symp. "Nanostructures: Physics and Technology"
St Petersburg, Russia, June 21–26, 2010

Photovoltaic properties of Au-assisted GaAs nanowire arrays grown by molecular beam epitaxy

G. E. Cirlin[1,2,3], A. D. Bouravleuv[2,3], I. P. Soshnikov[1,2], Yu. B. Samsonenko[1,2,3], V. G. Dubrovskii[2,3], E. M. Arakcheeva[3], E. M. Tanklevskaya[3] and P. Werner[4]

[1] Institute for Analytical Instrumentation, 190103 St Petersburg, Russia
[2] St Petersburg Academic University, 194021 St Petersburg, Russia
[3] Ioffe Physical-Technical Institute, St Petersburg, Russia
[4] Max Planck Institute for Microstucture Physics, D 06120, Halle/Saale, Germany

Abstract. We report on the molecular beam epitaxy (MBE) growth of Au-assisted GaAs p-type doped NW arrays on n-type GaAs(111)B substrate and their photovoltaic properties. The samples are grown at different substrate temperature within the range (520–580 °C). The conversation efficiency on the substrate temperature dependence has a maximum peaked at the substrate temperature 550 °C. For the best sample, a conversion efficiency of 1.65% and a fill factor of 25% are obtained.

Introduction

Aligned NW arrays are potential building blocks for optoelectronic devices, such as nanolasers, field-effect transistors, light-emitting diodes, field emitters etc. Compared to polycrystalline films, vertically oriented arrays are particularly advantageous for photovoltaic (PV) application because the oriented geometry provides direct conduction paths for photo-generated carriers to transport from the junction to the external electrode, thereby resulting in a high carrier collection efficiency [1]. Moreover, NW arrays have significantly smaller optical reflectance and enhanced light absorption in comparison to thin films [2]. Additionally, there is a freedom from lattice matching requirements due to strain accommodation at the nanowire surfaces, which provides greater freedom in bandgap engineering and substrate selection. In most cases, the NWs arrays can be formed via vapour-liquid-solid growth mechanism using different epitaxial techniques, such as metal organic chemical vapor deposition, molecular beam epitaxy (MBE) etc. During MBE growth, one of the most important issue is an ability to control shape, height, size and NWs density to vary the technological parameters by exploring diffusion-induced growth mode as well as monitor the formation and development of NWs in situ using reflection high-energy electron diffraction (RHEED) technique. PV properties have been investigated for different semiconductor combinations, like Si axial and core-shell single NWs [3], GaAs core-shell both single NW and NW arrays [4,5], InAs/Si(111) NW arrays [6] etc. For the GaAs-based NW arrays the conversation efficiency, to the best of our knowledge, was demonstrated at the level of 1% at room temperature. In this note we report on the growth of Au-assisted GaAs p-type doped NW arrays on n-type GaAs(111)B substrate and their photovoltaic properties depending on the substrate temperature. In our case, the highest efficiency 1.65% is obtained corresponding to the best values reported in the literature for the GaAs NWs array.

Growth experiments are carried out in EP1203 MBE reactor equipped with the effusion Au cell, on GaAs(111)B n-type ($n = 2 \times 10^{18}$ cm^{-3}) substrates. After the desorption of an oxide layer in the MBE growth chamber, ~100 nm thick GaAs Si doped ($n = 2 \times 10^{18}$ cm^{-3}) buffer layer is grown on the GaAs(111)B substrate. To promote the NW formation by the growth catalyst, the deposition of 0.3 nm thick Au layer is performed at 550 °C. The samples are then kept for 1 min. in order to form liquid drops of alloy of Au with the semiconductor material of the substrate. The MBE growth of GaAs Be-doped ($p = 1 \times 10^{18}$ cm^{-3}, as measured from a planar layer) NWs is carried out by the conventional MBE at desired substrate temperature (520–580 °C) with a GaAs growth rate 1 monolayer (ML)/s. Total NW growth time is set at 12 min. Four samples are grown at different substrate temperatures, having different morphological properties. The final NW height varies from 1.7 to 2.2 micrometers, the NWs surface density amounts to 5×10^8–1×10^8 cm^{-2}, and the average diameter is typically 50 nm.

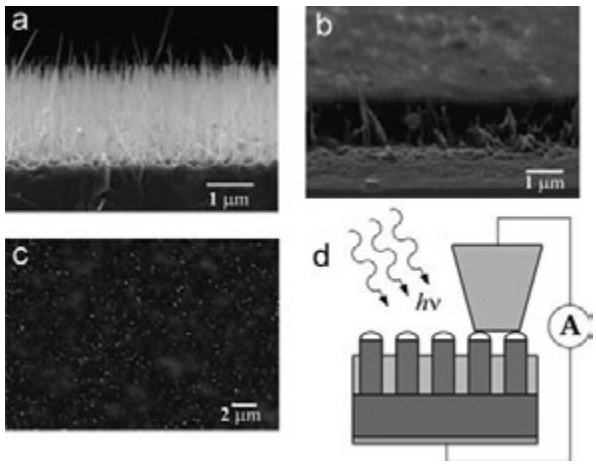

Fig. 1. SEM images taken at different stages of device structure preparation. a) — as grown GaAs NWs array, b) — after PMMA deposition, c) — top view of the resulting structure (after oxigen plasma treatment), d) — schematic view of the device structure testing.

To demonstrate the viability of our GaAs NW arrays for the use in PV application, several prototypes of solar cell devices are fabricated. To prepare the p-n junction, the spaces between the NWs are filled with insulating photoresist (PMMA) via spin coating. After photoresist deposition, the sample surface is treated in an oxygen plasma until the tips of GaAs NWs are exposed. Conventional ohmic contacts for the backside of n-type substrate are fabricated by electron-beam evaporating of AuGe (30 nm) and Ni/Au (10/150 nm) combination having resulting contact resistance ~ 1×10^{-6} Ohm/cm^2. After each

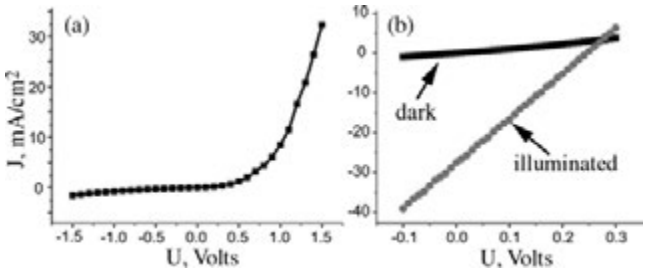

Fig. 2. a) — J-V characteristic of the device structure measured in dark, b) — J-V characteristics in dark and under illumination with an intensity of 100 mW/cm^2.

stage, the samples are studied by applying the scanning electron microscopy (SEM) technique as shown in Fig. 1(a–c), where we also present a schematics of device structure.

I-V characteristics are measured using a Keithley 238 source meter. The samples are placed on a copper base from backside; a metallic sharp tip ($D \sim 0.5$ mm) is used as top contact to the NWs/PMMA array. The energy conversion efficiency is determined by illuminating the structures using a halogen arc-lamp with the calibrated power density of $P = 100$ mW/cm^2.

Figure 2a shows typical current density-voltage (J-V) characteristic of the device structure measured in dark. The fabricated cells exhibit a clear diode behavior. Under the forward bias, an obvious turn on of the device is observed at 0.7 V. At +0.5 V bias, the forward current density is varied within the range 1.2–5.5 mA/cm^2, while the reverse leakage current density is typically about 0.01 mA/cm^2 at −0.5 V. The rectification ratio is therefore greater than 102 at +0.5 V, which demonstrates a reasonable p-n junction between the p-type GaAs NWs and n-type GaAs(111)B substrate. In Fig. 2,b we present the J-V characteristics of the best sample (with the highest NWs) in dark and under illumination. Upon illumination of the front surface with the light, the structure yields an obvious photocurrent. The short-circuit current density JSC equals 27.4 mA/cm^2 and the open-circuit voltage VOC amounts to 0.245 V. This corresponds to the conversion efficiency of 1.65% and the fill factor of 25%.

In Table 1, we summarise the conversion efficiency for different NW morphology. It is seen that the substrate temperature variation even within the range of 60°C leads to significant (up to 20 times) change in the conversation efficiency. The morphology of NW arrays therefore strongly influences the device properties. This should be due to geometrical factors as well as different Be incorporation processes at different temperatures (resulting in different doping concentration profiles). It is well established that the substrate temperature ~ 550 °C is optimal for MBE growth of GaAs NWs at the GaAs growth rate of 1 ML/s. At this temperature, GaAs NWs exhibit better homogeneity as well as the highest NW/2D growth rate ratio. When the temperature is above or below this optimal value, a rapid decrease in the NW height is observed, which is consistent with the results of previous studies. We also document the decrease of surface density as the temperature is raised to 580 °C, which can also affect the conversion efficiency. The lowest efficiency corresponds to the sample grown at lowest temperature of 520 °C, although its morphological characteristics are similar to other samples. Most probably, at this temperature Be atoms can be incorporated in different sub-lattice site leading to a higher compensation level. All abovementioned factors could influence significantly the quality of device structures. For example, the results of Ref. [4] show that the substrate temperature change of 20 °C due to the inhomogenity of substrate heater, could result in the conversion efficiency difference by a factor of 5.5, which is also in agreement with our study.

Table 1. Morphological characteristics and conversion efficiencies of different samples.

T_s, °C	NWs surface, density, cm^{-2}	NWs height, μm	Conversion efficiency, %
520	1×10^9	1.7	0.08
535	1×10^9	1.9	0.27
550	1×10^9	2.2	1.65
580	5×10^8	1.7	0.29

Acknowledgements

The authors are grateful to the financial support received from RFBR grants, scientific grant of St Petersburg Scientific Centre and different scientific programs of RAS.

References

[1] A. B. F. Martinson *et al*, *Nano Lett.* **7**, 2183 (2007).
[2] Y. J. Lee *et al*, *Nano Lett.* **8**, 1501 (2008).
[3] B. Tian *et al*, *Chem. Soc. Rev.* **38**, 16 (2009).
[4] J. A. Czaban *et al*, *Nano Lett.* **9**, 148 (2009).
[5] C. Colombo *et al*, *Appl. Phys. Lett.* **94**, 173108 (2009).
[6] W. Wei *et al*, *Nano Lett.* **9**, 2926 (2009).

18th Int. Symp. "Nanostructures: Physics and Technology"
St Petersburg, Russia, June 21–26, 2010

Confocal Raman Microscopy of the self-assembled GeSi/Si(001) nanoislands

A. I. Mashin[1], A. V. Nezhdanov[1], *D. O. Filatov*[1], M. A. Isakov[1], V. G. Shengurov[2], V. Yu. Chalkov[2] and S. A. Denisov[2]

[1] N. I. Lobachevskii University of Nizhny Novgorod, 603095, Nizhny Novgorod, Russia
[2] Research Institute for Physics and Technology, N. I. Lobachevskii University of Nizhny Novgorod, 603095, Nizhny Novgorod, Russia

Abstract. Confocal Raman Microscopy/Spectroscopy has been applied to the investigation of the composition and of the elastic strain in the self-assembled Ge_xSi_{1-x}/Si(001) nanoislands with sub-100 nm spatial resolution for the first time. The maps of the Ge molar fraction x and of the elastic strain with well resolved nanoislands and the Raman spectra of the individual nanoislands nave been obtained.

Introduction

The heterostructures with the self-assembled GeSi/Si(001) nanoislands have been being studied extensively in the last 15 years since these structures were considered to be promising for various applications in silicon photonics [1]. It is well known that the nanoislands grown by the deposition of Ge onto a Si substrate in certain conditions consist of a Ge_xSi_{1-x} alloy because of diffusion of Si from the substrate into the islands promoted by the elastic strain. For investigation of the composition and of the elastic strain in the GeSi/Si nanoislands various methods have been applied, including Double Crystal X-Ray Diffractometry (DXRD) and Raman Spectroscopy [2,3]. The main drawback of both these methods is that the measured data are averaged over the area illuminated by the probing radiation. In [4,5] Scanning Auger Microscopy (SAM) has been applied to the investigation of the composition of individual GeSi/Si(001) nanoislands. In the present work we have applied Confocal Raman Microscopy (CRM) to the investigation of the composition and of the elastic strain in the individual GeSi/Si islands for the first time.

1. Experimental

The GeSi/Si(001) islands have been grown by Sublimation Molecular Beam Epitaxy in GeH_4 ambient. The substrate temperatures T_g were 700 °C and 800 °C, the pressure of GeH_4 in the growth chamber p_g was 9×10^{-4} Torr. The GeSi islands were capped by $\approx$ 40 nm thick Si layer. The details of the growth technique as well as the results of the investigations of the islands' morphology (studied by Atomic Force Microscopy, AFM) and of their photoluminescence (PL) spectra are described in [6]. The CRM investigations were carried out using NT MDT Integra Spectra^{TM} confocal microscope at

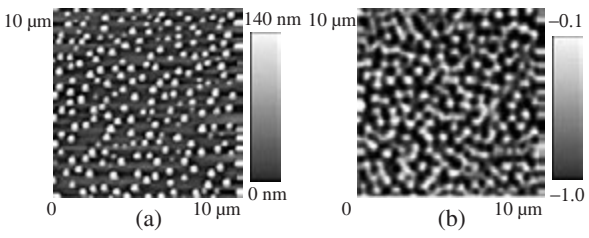

Fig. 1. AFM (a) and confocal reflection (b) images of a GeSi/Si(001) heterostructure grown at $T_g = 800$ °C and $t_g = 2$ min.

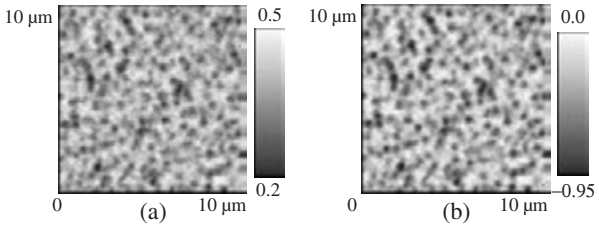

Fig. 2. The calculated maps of the Ge atomic fraction x (a) and of the elastic strain ε (b) in the GeSi/Si(001) heterostructure grown at $T_g = 800$ °C and $t_g = 2$ min.

300 K.

2. Results and discussion

In Fig. 1(b) a reflection confocal microscopic image of a structure grown at $T_g = 800$ °C is presented. The time of letting of GeH_4 into the growth chamber t_g, which determines the amount of the deposited Ge, was 2 min. The spots of 150 to 200 nm in size identified as the GeSi islands are seen. Comparing the image in Fig. 1(b) to the AFM image of the islands grown on the Si surface at the same conditions [Fig. 1(a)], one can see the surface density of the islands to be almost the same. However, the confocal image looks more fussy; the images of the adjacent islands are overlapping. According to the theory of Confocal Microscopy [7], the minimum spacing between the two adjacent points resolved according to Rayley's criterion

$$r \approx \frac{\lambda}{n}\frac{1}{NA}, \qquad (1)$$

where NA is the numerical aperture of the objective, n is the refractive index of the medium, and λ is the laser emission wavelength. For $NA = 0.95$, $n = 3.5$ (Si), and $\lambda = 473$ nm one has $r \approx 56$ nm.

In Fig. 3 and 4 the Raman spectra measured in the individual islands (a) and between the islands are presented. The peaks related to the Si–Si, Si–Ge and Ge–Ge vibration modes have been identified. The splitting of the two latter peaks was attributed to the nonuniformity of the Ge distribution inside the islands. Earlier, the SAM measurements with the depth profiling revealed that the tops of the islands were enriched with Ge [4,5].

In Fig. 2(a) and (b) the maps of x and ε, respectively are presented. These maps were calculated from the ones of the

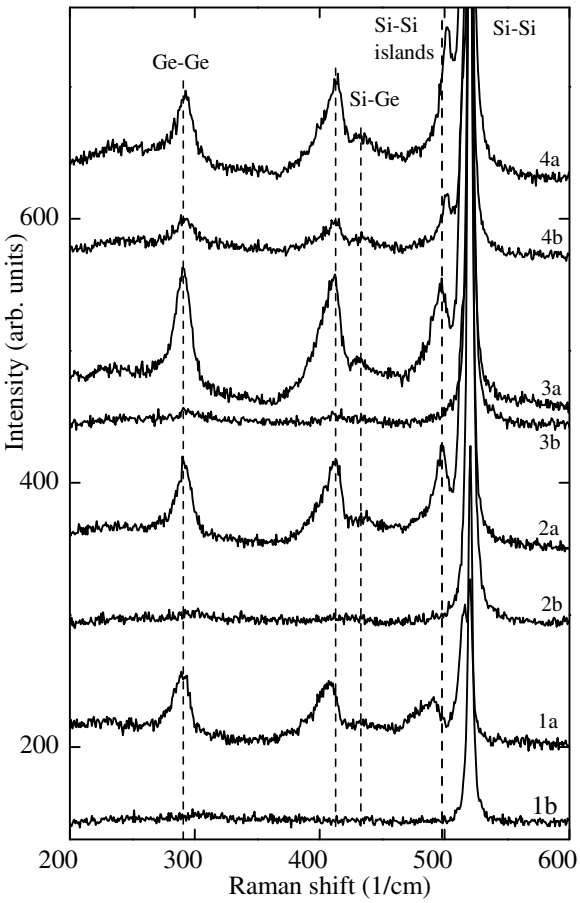

Fig. 3. The Raman spectra of the GeSi/Si(001) heterostructures grown at $T_g = 700$ °C measured in the centers of the individual islands (a) and between the islands (b). $t_g = 1$ min (1), 2 min (2), 4 min (3), and 5 min (4).

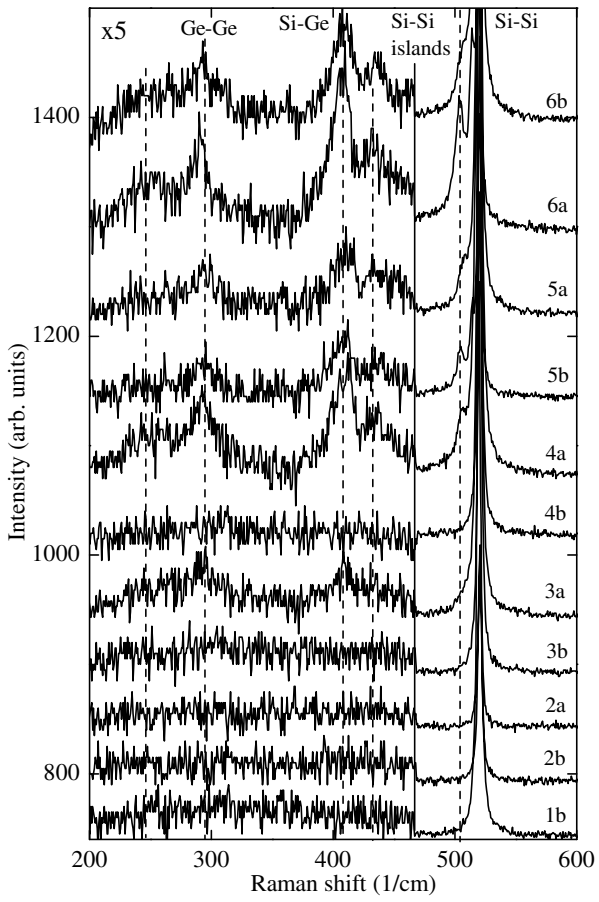

Fig. 4. The Raman spectra of the GeSi/Si(001) heterostructures grown at $T_g = 800$ °C measured in the centers of the individual islands (a) and between the islands (b). $t_g = 15$ s (1), 30 s (2), 1 min (3), 2 min (4), 4 min (5), and 5 min (6).

Raman shifts of the Ge–Ge and Si–Ge lines $k_{\mathrm{Ge-Ge}}$ and $k_{\mathrm{Si-Ge}}$, respectively following [2,8]:

$$x = 0.15k_{\mathrm{Ge-Ge}} - 0.10k_{\mathrm{Si-Ge}} - 2.17, \quad (2)$$

$$\varepsilon = (3.8k_{\mathrm{Ge-Ge}} - 4.3k_{\mathrm{Si-Ge}}) \times 10^{-3} + 0.70. \quad (3)$$

The spots with lower x and ε corresponding to the GeSi islands are seen in Fig. 2. It is worth noting that the Raman spectra presented in Fig. 3 and 4 are averaged over all the structure layers, including the cladding layer, the GeSi layer, and the buffer one. It is difficult to attribute the specific peaks in the Raman spectra to certain layers. This is a disadvantage of CRM compared to SAM with ion sputtering. From all the possible combinations of the (x, ε) pairs resulting from the positions of the Ge–Ge, Si–Ge, and Si–Si peaks, the ones satisfying the conditions $0 \le x \le 1$ and $|\epsilon| \le 1$ have been selected. For the particular structure shown in Fig. 1 and 2, $x \approx 0.94$ on the tops and $x \approx 0.24$ inside the islands were found, that agrees with the SAM results [4,5].

Acknowledgements

The authors gratefully acknowledge the financial support by Russian Federal Agency for Education (Project RNP 2.1.1. 3615).

References

[1] Y. Shiraki and A. Sakai, *Surf. Sci. Rep.* **59**, 153 (2005).

[2] Z. F. Krasil'nik, N. V. Vostokov, S. A. Gusev, I. V. Dolgov, Yu. N. Drozdov, D. N. Lobanov, L. D. Moldavskaya, A. V. Novikov, V. V. Postnikov and D. O. Filatov, *Thin Solid Films* **367**, 171 (2000).

[3] M. Ya. Valakh, R. Yu. Holiney, V. N. Dzhagan, Z. F. Krasil'nik, O. S. Lytvyn, D. N. Lobanov, A. G. Milekhin, A. I. Nikiforov, A. V. Novikov, O. P. Pchelyakov and V. A. Yukhymchuk, *Phys. Solid State* **47**, 54 (2005).

[4] G. A. Maximov, Z. F. Krasil'nik, D. O. Filatov, M. V. Kruglova, S. V. Morozov, D. Yu. Remizov, D. E. Nikolichev and V. G. Shengurov, *Phys. Solid State* **47**, 22 (2005).

[5] G. A. Maximov, Z. F. Krasil'nik, A. V. Novikov, V. G. Shengurov, D. O. Filatov. D. E. Nikolitchev, V. F. Dryakhlushin and K. P. Gaikovich, *Nanophysics, Nanoclusters and Nanodevices*, (New York: Nova Science) 87–123, 2006.

[6] D. O. Filatov, M. V. Kruglova, M. A. Isakov, S. V. Siprova, M. O. Marychev, V. G. Shengurov, V. Yu. Chalkov and S. A. Denisov, *Semicond.* **42**, 1098 (2008).

[7] R. H. Webb, *Rep. Prog. Phys.* **59**, 427 (1996).

[8] J. Groenen, R. Carles, S. Christiansen, M. Albrecht, W. Dorsch, H. P. Strunk, H. Wawra and G. Wagner, *Appl. Phys. Lett.* **71**, 3856 (1997).

18th Int. Symp. "Nanostructures: Physics and Technology"
St Petersburg, Russia, June 21–26, 2010

Kelvin probe microscopy study of charge dissipation in nano thin dielectric layers SiO_2 and Si_3N_4

P. A. Alexeev[1], M. S. Dunaevskii[1], V. A. Gritsenko[2] and A. N. Titkov[1]

[1] Ioffe Physical-Technical Institute, St Petersburg, Russia
[2] Institute of Semiconductor Physics, 630090, Novosibirsk, Russia

Abstract. In this work Kelvin probe microscopy (KPM) is proposed as a new method for visualization of charge storage and dissipation in thin SiO_2 and Si_3N_4 dielectric layers. Analysis of KPM images of charges injected from the probe allows to determine: 1) lateral size of charged area, 2) potential of charged area, 3) total amount of the charge injected in dielectric layer. It was studied also the time evolution of injected charge as a function of the temperature. It was shown, that the main mechanism of charge dissipation is lateral diffusion. The characteristic values of diffusion coefficient, mobility and activation energy were determined.

In the last decade the significant decrease of sizes of microelectronic devices occurred. For the field-effect transistors, for example, the lateral dimensions and thicknesses of gate dielectric layers decreased to the values of tenth and several nanometers, correspondingly. Thus, the processes of charge storage and charge leakage in the nano thin dielectric layers have attracted an increasing interest in the modern microelectronics. Usually, the retention and leakage of charges in dielectric layers can be controlled by measuring the current-voltage and capacitance-voltage characteristics on MOS-structures containing dielectric layers. However, these methods give information about layer properties averaged over the whole surface under MOS metallic electrode. For the devices with nano small area, when carrier diffusion length becomes comparable or even smaller then the layer lateral dimensions averaged measurements may become misleading. Thus, to be able to control the boundary effects and role of possible point defects in layers there is a need in local methods for characterization of charge behavior in nano small dielectric films.

We present a new atomic-force microscopy (AFM) method of nano local studies of charges behavior in nano thin and small dielectric layers. The method is based on local injection of carriers from AFM probe into the layer and further observation of charges spreading in the layer by Kelvin probe microscopy (KPM) analysis of surface potential around the point of local charging. With existing AFM probes locality of initial charging can be as small as 20–30 nm [1]. The time sequence of KPM images of the charged area allows studying charge evolution (see Fig. 1). The broadening of the charge spot in KPM images reflects the lateral expansion of charges in the dielectric layer and the volume of charge spot (the integral of potential over the spot area) controls the number of charges in the spot, i.e. possible leakage of charges into the substrate. For the device-quality insulating layers with open and dry surface the charged spot can demonstrate stable width and volume for tenth of hours. In case of poor oxide with large amount of defects a charge spot can disappear in minutes.

In this work we demonstrate the injected electron behavior in thin SiO_2 ($d = 20$ nm) and Si_3N_4 ($d = 10$ nm) layers on Si in the temperature range 300–400 K. To better demonstrate the abilities of the method there have been studied the samples initially exposed to atmosphere. Exposure to atmosphere leads to degradation of nano thin insulating layers and speeds up the lateral charge diffusion. However, to avoid the effect of surface liquid adsorption film on charges lateral spreading, charging procedure and Kelvin measurements have been performed on layers with dry surfaces in moderate vacuum.

Fig. 1 demonstrates the sequence of KPM images obtained with different delay after charging of SiO_2 film in the center of image $U_{\text{charging}} = 5$ V, $\tau_{\text{charging}} = 100$ ms. The cross-sectional profiles through the center of charged area are given at the Fig. 1d. One can see that the lateral size L of charged area increases with time in parallel with the decrease of electrical potential V at the center of charged area. These are evidences of lateral charge spreading and partial charge leakage to the substrate.

There are two expected mechanisms of lateral charge spreading in the case of point injection: initial electrostatic repulsion of charges which is later substituted by lateral diffusion. We have studied the dependences of charge spot broadening on time $L(t)$. The lateral size L was estimated as a FWHM of KPM profiles. In the case of predomination of diffusion mechanism one should expect a square root character of broadening dependences $L(t) = \sqrt{Dt}$.

Fig. 2a demonstrates the experimental $L^2(t)$ dependences for SiO_2 a nd Si_3N_4 layers. From the found linear $L^2(t)$ dependences, it can be concluded that at the time-scale of minutes lateral charge spreading in the studied layers is driven by diffusion mechanism. One can determine the diffusion coefficients D from these $L^2(t)$ linear dependencies $D = 10^{-11}$ cm^{2}s^{-1} for SiO_2, $D = 2 \times 10^{-12}$ cm^{2}s^{-1} and $D = 0.9 \times 10^{-11}$ cm^{2}s^{-1} for Si_3N_4 correspondingly. Using Einstein relationship $D = \mu kT/e$ one can estimate values of electron mobility for SiO_2 and Si_3N_4 layers. Since values of D and μ are extremely low it can be proposed the hopping mechanism of electron migration in the layers. It is also seen the effect of diffusion coefficient increasing in Si_3N_4 with exposure to atmosphere. Indeed, after 6 months of exposure of Si_3N_4 layer diffusion coefficient $D(Si_3N_4)$ increased and nearly reached value of that for SiO_2 (solid squares at Fig. 2a). This effect can be explained by the partial oxidation of Si_3N_4 and appearance of thin SiO_2-like film at the top of Si_3N_4 layer.

It can be also seen in Fig. 2a, that linear approximation of $L^2(t)$ to zero-time gives L of 300–400 nm these values being several times higher then the mentioned above charge injection locality of 20–30 nm. This difference occurs due to the initial rapid electrostatic repulsion process. The specially arranged fast KPM experiment permitted to reveal this process which

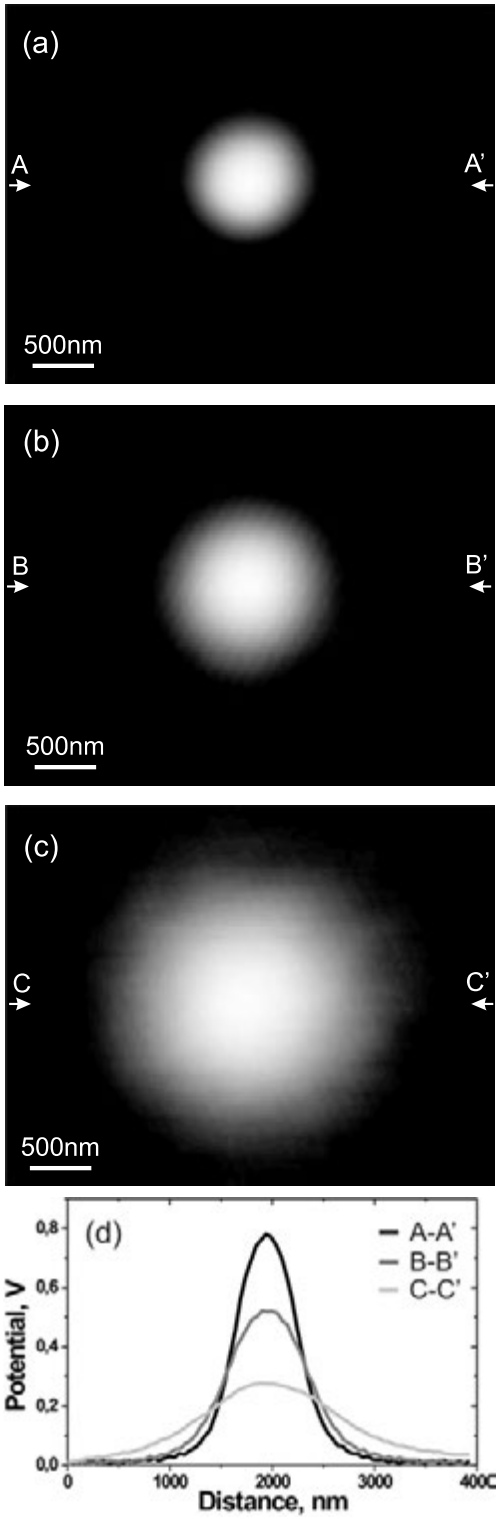

Fig. 1. KPM images of charged area taken in 5 minutes (a), 10 minutes (b) and 25 minutes (c) after electron injection at the center; (d) — KPM profiles corresponding to (a),(b) and (c).

occurs on the time-scale of few seconds.

It was also studied the temperature dependence of diffusion coefficients $D(T)$ for SiO_2 and Si_3N_4 layers (Fig. 2b). The dependences $D(T)$ can be described by the formula $D(T) = D_0 \exp(-E_a/kT)$, where E_a — activation energy for diffusion. From the plots $\ln D(1/T)$ in Fig. 2b it can be obtained the values of activation energy $E_a = 0.55$ eV for SiO_2 layer

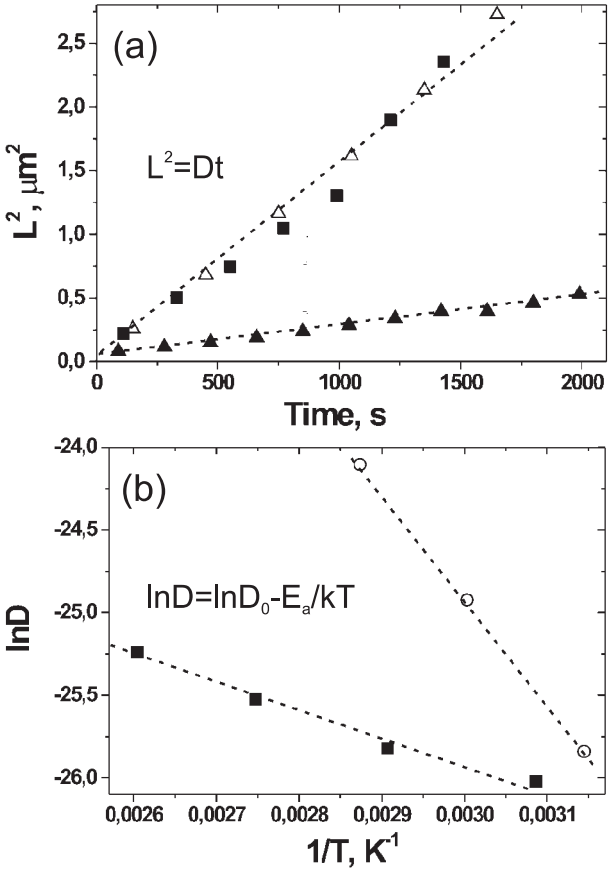

Fig. 2. (a) — Time-evolution of charged spot lateral area L^2 for SiO_2 layer (open triangles), Si_3N_4 layer (solid triangles) and Si_3N_4 layer after extra 6 months exposure to ambient atmosphere (solid squares). (b) — Dependences of logarithm of diffusion coefficient on temperature for SiO_2 layer (open circles) and Si_3N_4 layer (solid squares).

and $E_a = 0.15$ eV for Si_3N_4 layer.

To conclude, in this work there was presented the Kelvin Probe Microscopy method to study the behavior of locally injected carriers in nano thin dielectric layers. By this method it is possible to measure the diffusion coefficient (down to values of 10^{-14} cm^2s^{-1}), activation energy of diffusion and mobility of carriers in dielectric layers. The method can be applied to the studies of a wide class of dielectric layers: traditional oxides, nitrides, high-k dielectrics with the thicknesses up to 50–100 nm. As well, this method can be useful for the direct characterization of dielectric inclusions in the device structures of microelectronics.

References

[1] M. S. Dunaevskii, A. N. Titkov, S. Yu. Larkin, A. B. Speshilova, S. E. Aleksandrov, C. Bonafos, A. Claverie, R. Laiho, *Tech. Phys. Lett.* **33**, 889 (2007).

18th Int. Symp. "Nanostructures: Physics and Technology"
St Petersburg, Russia, June 21–26, 2010

Extremely sensitivity of graphene surface for HN_3 adsorption

I. V. Antonova, S.V.Mutilin, V. A. Seleznev, R. A. Soots and V. Ya. Prinz
Institute of Semiconductor Physics SB RAS, Novosibirsk, 630090, Russia

Introduction

The good sensor properties of carbon nanotubes are already known for some time. Recently, the possibility to graphene use as a highly sensitive sensor for different gases was also reported [1,2]. The gas molecules, CO, NO, NO_2 and NH_3, are all of great practical interest for industrial, environmental and medical applications. The simplest graphene-based sensor detects the conductivity change upon adsorption of analyte molecules. The change in conductivity could be attributed to the changes of charge carrier concentration in the graphene induced by adsorbed gas molecules. The ultimate aim of any detection method is to achieve such a level of sensitivity that individual quanta of a measured entity can be resolved. Graphene is strictly two-dimensional material and, as such, the highest sensor response is expected for graphene. The first-principles study of optimal absorption position, charge transfer from a molecule to graphene and adsorption energies of gas molecules on the graphene surface are realized by O. Leenaerts *et al* [3]. HN_3 was found has a maximal value of the charge transfer from a molecule to graphene ($0.027e$) among the donors and NO_2 ($-0.099e$) among the acceptors. Nevertheless, a change in the graphene resistivity due to adsorption of gas molecules not excesses then few percents [1,2,4]: typical response is about 4%. Here we report studies of the NH3 interaction with a few layer graphene resistor invested on a Si/SiO_2 substrate with the aim to find condition for the maximal sensitivity of the graphene flake for gas adsorption. It was found that 2–8 orders of magnitude of the resistance response can be provided for graphene created by electrostatic exfoliation.

1. Experimental

Graphene layers were transferred from highly oriented pyrolytic graphite (HOPG) onto the Si/SiO_2 substrate by electrostatic exfoliation. This allowed us to transfer graphene flake of typically 10 μm in size and thickness lower then 3 nm (5–7 graphene layers) or lower on a silicon substrate covered with 300 nm of SiO_2. Resistivity of silicon substrate was 350 Ohm cm and 300 nm SiO_2 layer was thermally grown on this substrate. Current-voltage characteristics or time dependence of current were measured using the Keithley picoampermeter 6485. Some parameters of the pristine structures are given in Table 1. The two structures marked as S1 and S2 had p-type conductivity and structures S3 and S4 demonstrated n-type. Conductivity type was determined based on shift of I-V curve and resistance change under HN_3 adsorption.

2. Results and discussion

Figure 1a demonstrates a change in resistance of structures S1 and S2 with a time t under ammonia flow. $R(t)$ curves were normalized on the time t_0 when the minimal resistivity was attained. Value of t_0 is depended on the geometry parameters and gas flow. As was mention above, both these structures demonstrated the p-type conductivity. Under HN_3 flow resistances of these structures are strongly increase. If we use a long time of treatment in ammonia ambient the resistances of S1 and S2 are decrease again, but now the structures revealed n-type conductivity due to ammonia adsorption. K. I. Bolotin *et al* [5] were found that conductivity of graphene suspended under SiO_2/Si substrate is increased. Suspended graphene was achieved by dipping the device in buffered oxide etchant caused uniformly removal of SiO_2 across the substrate, including the area below the graphene flake. Increase in conductivity was found [5] to follow to increase in carrier mobility. The carrier mobility in graphene deposited on a substrate such as Si/SiO_2 deteriorates due to trapped charges in the oxide or to contaminants that get trapped at the graphene-substrate interface during fabrication. We have also subjected some our structures (S3, S4) to buffered oxide etch with the aim to increase the graphene conductivity. Such treatment really leads to decrease in the resistivity of this structure from 2.94 to 1.47 kOhm. But it was found that after such treatment graphene demonstrates the n-type of conductivity. Change in the resistance of S3 sample with a time in ammonia ambient is presented in Fig. 1b and Table 1. Due to low S3 resistance and the n-type conductivity the ammonia is caused a little response in S3 structure.

A statement of the graphene surface is known can be changed by employing current-induced heating, directly resulting in a significant improvement of electrical transport. S4 the structure was subjected to current-induced annealing at applied voltage of 1 V during 5 min. This annealing leads to increase in S4 resistance in 3 times. Resistance value after current-induced annealing keep stable and is not changed with a time. Sensitivity to ammonia of the structure S4 with current-improved conductivity is increased approximately in a 4 times but still is strong lower then that for structures with p-type conductivity S1 and S2.

Clean graphene sensors are known to have very little electrical response upon exposure to ammonia Adsorption of different contaminations at the surface, doping of graphene, introduction of defects (vacancies first of all) are able to change (to increase) the sensor response. We also have used some ad-

Table 1. Parameters of graphene structures. R is the resistance calculated from I-V curve as U/I. R_0 and R_1 are the resistance of the pristine structure and structure treated in ammonia ambient. $^*R$ value after etching in HF. $^{**}R$ value after etching in HF and current-annealing.

Sample	R, kΩ	Conductivity type	$(R_1 - R_0)/R_0$
S1	1.25	p-type	2.9×10^7
S2	2.25	p-type	17.5
S3	3.0 (1.45*)	n-type	−0.21
S4	3.0 (10.0**)	n-type	−0.74

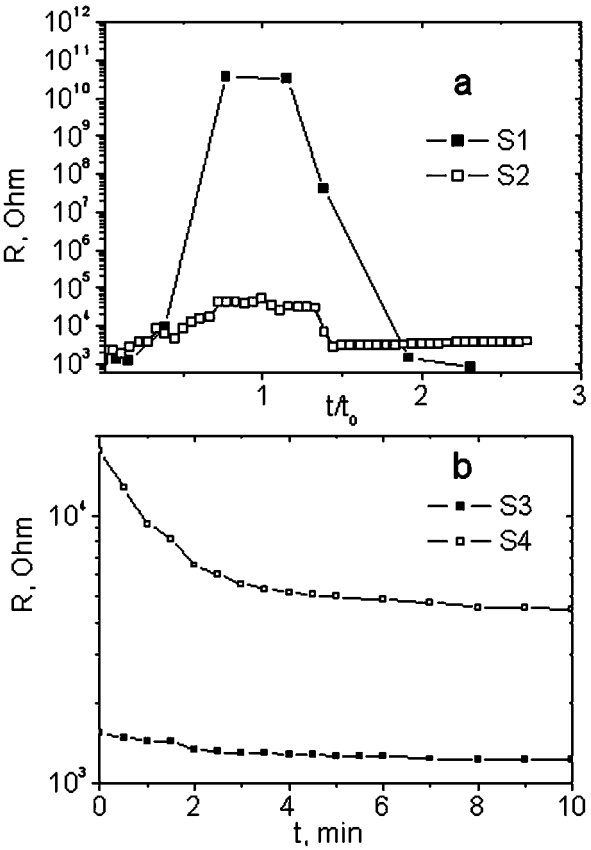

Fig. 1. Change in grapheme resistivity under HN_3 flow as a function of (a) relative time for structure S1 and S2 and (b) treatment time for structure S3 and S4. Values of t_0 are equal to 10 and 3.3 min for S1 and S2 respectively.

ditional chemical doping and/or nanostructuring with the aim to increase a resistivity modulation of the graphene layers after ammonia adsorption, especially in the case of the n-type conductivity. Different approaches for enhancement of the resistance response are analyzed in the report giving the base for development the sensors with the high sensitivity to ammonia adsorption.

Acknowledgements

This study was supported, in part, by the Russian Foundation of Basic Research (Grant 09-02-01390). The authors would like to thank A. I. Komonov and I. A. Korneev for the help with AFM measurements.

References

[1] F. Shedin *et al*, *Nature Mat.* **6**, 652 (2007).
[2] J. D. Fowler *et al*, *ACS Nano*, **3**, 301 (2009).
[3] O. Leenaerts *et al*, *Phys. Rev. B* **77**, 125416 (2008).
[4] Y. Dan *et al*, *Nanoletters* **9**, 1472 (2009).
[5] K. I. Bolotin *et al*, *Solid State Com.* **146**, 351 (2008).

18th Int. Symp. "Nanostructures: Physics and Technology"
St Petersburg, Russia, June 21–26, 2010

Could nanostructure be unspeakable quantum system?

V. V. Aristov and A. V. Nikulov
Institute of Microelectronics Technology RAS, 142432 Chernogolovka, Moscow region, Russia

Abstract. Heisenberg, Bohr and others were forced to renounce on the description of the objective reality as the aim of physics because of the paradoxical quantum phenomena observed on the atomic level. The contemporary quantum mechanics created on the base of their positivism point of view must divide the world into speakable apparatus which amplifies microscopic events to macroscopic consequences and unspeakable quantum system. Examination of the quantum phenomena corroborates the confidence expressed by creators of quantum theory that the renunciation of realism should not apply on our everyday macroscopic world. Nanostructures may be considered for the present as a boundary of realistic description for all phenomena including the quantum one.

Introduction

The progress in physics and engineering of the XX century made thanks to the quantum theory is immensely impressive. But John Bell in his famous Introductory remarks at Naples-Amalfi meeting, 1984 "Speakable and unspeakable in quantum mechanics" [1] stated that *"This progress is made in spite of the fundamental obscurity in quantum mechanics. Our theorists stride through that obscurity unimpeded... sleepwalking?"* Bell, as well as Einstein, Schrodinger and other opponents of the Copenhagen interpretation, connected this fundamental obscurity with the object of quantum description. The quantum mechanics studied during last eighty years was created on the base of the positivism point of view of Heisenberg and Bohr according to which *"any observation of atomic phenomena should include an interaction they with equipment used for the observation which can not be neglected"* [2], *"we had introduced an element of subjectivism into the theory, as if we meant to say: what happens depends on our way of observing it or on the fast that we observe it"* [3] and *"there is no way of describing what happens between two consecutive observations"* [3]. Arguing against the positivism point of view of Heisenberg, Bohr and other adherents of the Copenhagen interpretation Einstein persisted that *"it must seem a mistake to permit theoretical description to be directly dependent upon acts of empirical assertions, as it seems to me to be intended in Bohr's principle of complementarity"* [4]. Following to Einstein Bell has located the cardinal problem of the orthodox quantum mechanics: *"how exactly is the world to be divided into speakable apparatus... that we can talk about... and unspeakable quantum system that we can not talk about?"* [1].

The positivism of Heisenberg and Bohr with its necessity to refer to "apparatus" when atomic phenomena are discussed may be justified with the necessity to amplify microscopic events to macroscopic consequences, which we can observe. But we should call this necessity in question for macroscopic phenomena including the quantum one. There is no forcible reason to renounce on macroscopic realism and used the superposition principle contradicting to it [5] on the macroscopic level. The superposition principle was postulated for description of phenomena and it can not be interpreted as a realistic description without contradiction with locality principle, as the EPR paradox [6] has revealed as far back as 1935. The Bohr's reply [7] on the EPR critique [6] of quantum mechanics *"The trend of their argumentation, however, does not seem to me adequately to meet the actual situation with which we are faced in atomic physics"* witnesses that their debate on reality applied only to atomic level. Einstein was sure that *"in the macroscopic sphere it simply is considered certain that one must adhere to the program of a realistic description in space and time... No one is likely to be inclined to attempt to give up this program within the realm of the 'macroscopic'"* [4]. In accordance to the belief of the quantum theory creators the experimental evidences of the violation of realistic prediction was observed for the present only for the atomic world, i.e. for the level of elementary particles [8]. Thus, on the one hand no experimental results force us to doubt in the reality of our everyday macroscopic world but on the other hand some phenomena observed on the atomic level, such as the double-slit interference experiments and experimental evidence of the EPR correlation [9] force us to do this. Nanotechnology comes nearer to atomic level and there is important to know where may be a boundary of these phenomena. The research for this boundary is important also because of such new developments as quantum information, quantum computation, quantum cryptography, and quantum teleportation [10], base on the EPR correlation.

1. Two-slit interference experiment

Richard Feynman emphasized that the double-slit interference experiment is at the heart of quantum mechanics [11]: *"In reality, it contains the only mystery, the basic peculiarities of all of quantum mechanics"*. Indeed, this experiment demonstrates very clear both advances and defects of universally recognized quantum formalism. The wave function formalism describes very well the interference of different particles: electrons, neutrons, atoms and even molecules [9]. But it can not explain how indivisible particles manage to pass through two slits at once or, if they do not pass, why we observe the interference pattern with period $P = L\lambda/d$ corresponding to a distance d between slits, a distance L between the screen with double-slits and the detecting screen and a de Broglie wavelength $\lambda = h/p = h/mv$. The de Broglie wavelength $\lambda = h/mv \approx h/ga^3v$ increases with a particle sizes a, at the same velocity v and density g. Recently the A. Zeilinger team [12] has observed first interference of objects with nano-sizes, biomolecules and fullerenes with length, up to $a \approx 3$ nm, much larger than their de Broglie wavelength $\lambda \approx 0.004$ nm. A. Zeilinger in the talk "Exploring the Boundary between the Quantum and the Classical Worlds" [13] told on an intention to observe quantum interference viruses and possibly even nanobacteria.

In order to observe an interference of a object the period of

the interference pattern P and distance d between slits must be larger than the object size a: $P = L\lambda/d > a$; $d > a$. The object covers the distance L between screens during a time L/v. Therefore the interference experiment with a object having the size a should continue during the time

$$t_{\rm exp} > \frac{g}{h}a^5 \,. \qquad (1)$$

Since the density of all matters $g \approx 1000$ kg/m^3 in order of value $g/h \approx 10^{36}$ s/m^5 and during $t_{\rm exp} \approx 1$ s the interference of a object with size $a < 60$ nm can be observed. This size can not be increased considerably since $t_{\rm exp} \propto a^5$ (1). Thus, the level of nanostructures is boundary for a possibility of the quantum interference observation and the necessity of the superposition principle for description of such observation.

2. EPR correlation

In order to demonstrate the contradiction between the superposition principle and local realism, EPR [6] consider two particles states of which is entangled with a conservation law. For example, in the Bohm's version of the EPR paradox [14] the spin states is entangled

$$\psi = \frac{\psi_{a,\uparrow}(r_a)\psi_{b,\downarrow}(r_b) + \psi_{a,\downarrow}(r_a)\psi_{b,\uparrow}(r_b)}{\sqrt{2}} \qquad (2)$$

with the law of angular momentum conservation. Measurement of a i spin projection of the particle a must change instantaneously the quantum state of the both particles because of the superposition collapse

$$\psi = \psi_{a,\uparrow}(r_a)\psi_{b,\downarrow}(r_b) \qquad (3)$$

irrespective of the distance $r_a - r_b$ between their.

The superposition principle is used for description of the outcomes of spin projection experiments because of their paradoxicality. According to the Stern–Gerlach experiment made as far back as 1922 magnetic moment $M_{1/2}$ projection $m_{1/2,i}$ of a spin 1/2 particle seems to equal the same value independently of the measurement direction $\vec{i}$. Bell has proposed in [15] a realistic description of this paradoxical phenomenon using hidden variable. But he has revealed also in his famous theorem [16] contradictions between predictions giving with the superposition principle and any local realistic theory for the outcomes of entangled states (2) experiments. The experimental evidence [8] of Bell's inequality violation means that the EPR correlation, contradicting to the local realistic theory, is observed. But this challenge to realism can be applied only on a scale of the Bohr magneton $\mu_{\rm B}$ and the Planck's constant $\hbar$.

In accordance to the Bohr's correspondence principle a measurement of i projection gives the "classical" outcome $m \approx (\vec{M}\vec{i}) = Mcos(\varphi)$ for a macroscopic $|\vec{M}| \gg \mu_{\rm B}$ magnetic moment $\vec{M}$, but no paradoxical one $m_{1/2,i} = \pm\mu_{\rm B}$. One would think that the macroscopic quantum phenomena, superconductivity and superfluidity, violate the correspondence principle. Some authors claim on quantum superposition of macroscopic states [5,17] of molecules with magnetic moment $M \approx 200\mu_{\rm B}$ [18], ferrimagnetic nanoparticles with $M \approx 10^5\mu_{\rm B}$ [19] and superconducting loop (SQUID) with $M \approx 10^{10}\mu_{\rm B}$ [20]. But these claims on violation of macroscopic realism [5] have no valid experimental substantiation and are at variance with the fundamental law of angular momentum conservation and the universally recognized quantum formalism [21]. Thus, nanostructures may be considered for the present as a boundary between speakable and unspeakable quantum system.

Acknowledgements

This work has been supported by a grant "Possible applications of new mesoscopic quantum effects for making of element basis of quantum computer, nanoelectronics and micro-system technic" of the Fundamental Research Program of ITCS department of RAS and the Russian Foundation of Basic Research grant 08-02-99042-r-ofi.

References

[1] J. S. Bell, *Speakable and unspeakable in quantum mechanics. Collected papers on quantum philosophy*, Cambridge University Press, Cambridge, 1987, p. 169.
[2] N. Bohr, *Nature*, Suppl., **121**, 580–590 (1928).
[3] W. Heisenberg, *Physics and Philosophy*. George Allen and Unwin Edition, 1959.
[4] A. Einstein, in *Albert Einstein philosopherscientist*, ed. by P. A. Schillp, Evanston, Illinois, 1949, pp. 665–688.
[5] A. J. Leggett and A. Garg, *Phys. Rev. Lett.***54**, 857 (1985).
[6] A. Einstein, B. Podolsky, and N. Rosen, *Phys. Rev.* **47**, 777 (1935).
[7] N. Bohr, *Phys. Rev.* **48**, 696 (1935).
[8] A. Aspect *et al*, *Phys. Rev. Lett.* **47** 460 (1981); **49**, 91 (1982); **49**, 1804 (1982).
[9] G. Greenstein and A.G. Zajonc, *The Quantum Challenge. Modern Research on the Foundation of Quantum Mechanics*. Second Edition. Jones and Bartlett Publishers, Sudbury, Massachusetts, 2005.
[10] D. Bouwmeester, A. Ekert, and A. Zeilinger (Eds.), *The Physics of Quantum Information. Quantum Cryptography. Quantum Teleportation. Quantum Computation.* Springer, Berlin, Heidelberg, 2000.
[11] R. P. Feynman and A. R. Hibbs, *Quantum Mechanics and Path Integrals*, McGraw-Hill, New York, 1965.
[12] L. Hackermuller *et al*, *Phys. Rev. Lett*. **91**, 090408 (2003); S. Gerlich *et al*, *Nature Physics* **3**, 711 (2007).
[13] A. Zeilinger, *the Book of Abstract of the Conference "Frontiers of Quantum and Mesoscopic Thermodynamics"*, p. 66, Prague, Czech Republic, 26–29 July 2004.
[14] D. Bohm, *Quantum Theory*. New York: Prentice-Hall, 1951.
[15] J. Bell, *Rev. Mod. Phys.* **38**, 447 (1966).
[16] J. S. Bell, *Physics* **1**, 195 (1964).
[17] A. J. Leggett, *J. Phys.: Condens. Matter* **14**, R415 (2002).
[18] D. D. Awschalom *et al*, *Phys. Rev. Lett*. **68**, 3092 (1992).
[19] W. Wernsdorfer *et al*, *Phys. Rev. Lett*. **79**, 4014 (1997).
[20] J. R. Friedman *et al*, *Nature* **406**, 43 (2000); C. H. van der Wal *et al*, *Science* **290**, 773 (2000).
[21] A. V. Nikulov, *the Book of Abstract of the International Conference "Micro- and nanoelectronics -2009"*, p. q3-10, Moscow, Russia, 5–9 October, 2009; E-print arXiv:0907.1873.

18th Int. Symp. "Nanostructures: Physics and Technology"
St Petersburg, Russia, June 21–26, 2010

Fabrication and optical properties of porous InP crystals

V. N. Katz, *A. V. Atrashchenko*, V. P. Ulin, V. P. Evtikhiev and V. P. Kochereshko
Ioffe Physical-Technical Institute, St Petersburg, Russia

Abstract. In this paper we report results of fabrication of InP nano-porous crystals and outcome of the investigation their optical properties.

Introduction

Study of nano-composit materials is one of the most interesting tasks in the condense matter physics. The properties of such materials can be very different from the properties of bulk materials. Nano-composits can be used as a background for manufacturing of new materials with new electric, optical and other properties. Between different nano-composits an important role plays porous semiconductors and dielectrics with pore size in nanometer scale.

One of the important properties of nano-composits is low comparing to bulk dielectric permittivity that is very useful for low ε-dielectrics which useful for nano-scale devises. A very important property of these structures is a well developed surface. This allows us to fill the pores by gases and liquids and use them as sensors. Also it is very interesting to fill the pores by metals and to use them as metamaterials with negative refraction.

In this paper we have studied transmission spectra of InP nano-porous structures, refractive indexes along and perpendicular to the optical axis and Stokes parameters of the transmitted light in the spectral range close to the band of fundamental absorption.

1. Experiment

The samples of nano-porous crystals of InP were obtained by electrochemical etching of industrial n-type InP substrates ($N \sim 2 \times 10^{18}$ cm^{-2}) in chlorine electrolyte. The pores formation appears according to mechanism of nucleofilic substitution. Choosing the etching parameters, composition and concentration of the electrolyte we were able to control direction, width and deepness of the pores. As a result we have got nano-porous crystals which contains near surface transition layer of 2 microns thickness and a system of aligned pores in $\langle 100 \rangle$ direction with the average width of about 70 nm and deepness up to 150 microns. The uniformity of the deepness of the pores was controlled by homogeneity of the impurity distribution in the InP substrate. After finishing of the etching the porous layer was separated from the substrate by changes of the etching regime.

Sample #1 (Fig. 1) contains 30 micron layer of pores in $\langle 100 \rangle$ direction and 3 microns transition near-surface layer. The coefficient of porosity for this sample is of ∼70%, the average size of the pores is 70 microns, size dispersion is 22%, the ration of the deepness to diameter is 250, the thickness of the pore walls is 13–18 nm.

Figure 2 shows SEM image of the InP nano-porouse sample (sample #2) without near-surface transition layer. The thickness of the sample is 35 microns, the coefficient of porosity is 70%, the pores size is 50 nm, the dispersion of the size is 23%,

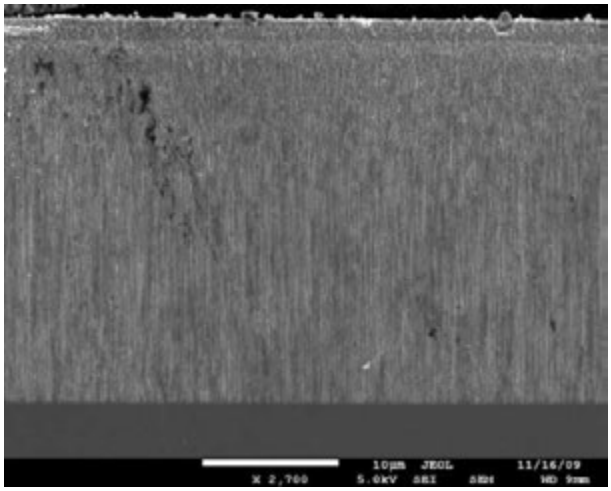

Fig. 1. SEM image of cleaved surface of sample #1 contained the system of an unidirectional $\langle 100 \rangle$ pores and near-surface transition layer of branching pores (on the top).

the ration of the deepness to diameter is 1000, the thickness of the pare walls is 13–18 nm.

Transmission spectra of these structures were measured. Broadening of the fundamental absorption edge in comparison to the bulk InP was found in the porous structures. This broadening we connect with absence of the long range order in these structures.

Below the band edge interference structure of Fabry–Perot was found in the sample of 32 microns thickness. In an oblique incidence the interferential structures in S and P polarizations are not coincide. We have used this structure to measure the effective refractive indexes perpendicular $n^{\perp}_{\text{eff}}$ and parallel $n^{\parallel}_{\text{eff}}$ to the pores.

Because the size of the pores is much smaller the light wavelength we should consider this structure in the effective media approximation. We will consider these structures as a homogeneous continuum media with an effective dielectric function.

There are numerous theoretical models to describe the dielectric function of the nano-composits [1]. Independently of the model we have to expect that the dielectric function along pores ($\varepsilon^{\parallel}_{\text{eff}}$) and perpendicular to pores ($\varepsilon^{\perp}_{\text{eff}}$) are different and $\varepsilon^{\parallel}_{\text{eff}} < \varepsilon^{\perp}_{\text{eff}}$.

From the analyses if the interference structure we have got $n^{\parallel}_{\text{eff}} = 2.7$, $n^{\perp}_{\text{eff}} = 2.8$ at 0.9 eV.

When the light propagates in an anisotropic media there are tree cases of the transformation of light polarization (i) rotation of the linear polarized light (gyrotropy), (ii) transformation of linear polarization into circular (birefringence), (iii) both

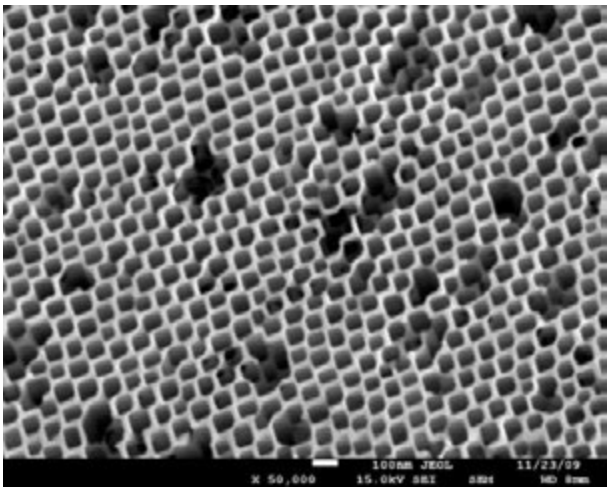

Fig. 2. SEM image of the (100) surface InP nano-porouse crystal (sample #2) without near-surface transition layer.

these effects together. To describe polarization properties of the transmitted through the sample light the Stokes parameters are used [2]. The Stokes parameters are following:

1. Degree of linear polarization in an $X - Y$ axis

$$P_{\text{lin}} = \frac{I_X - I_Y}{I_X + I_Y},$$

$I_{X,Y}$ — intensity of the light passed through the sample and polarized in X and Y directions;

2. Degree of circular polarization

$$P_{\text{cir}} = \frac{I_+ - I_-}{I_+ + I_-},$$

$I_\pm$ — intensity of the light in right and left circular polarizations;

3. Degree of linear polarizations in the axises rotated on 45 degree in relation to the X and Y

$$P_{\text{lin}}^{45} = \frac{I_{+45} - I_{-45}}{I_{+45} + I_{-45}}.$$

These parameters describe completely polarization of light $(P_{\text{lin}})^2 + (P_{\text{cir}})^2 + (P_{\text{lin}}^{45})^2 = 1$. For the completely polarized light . For partially polarized light the difference between unit and this value describes the nonpolarized component.

In our experiments we have measured these parameters as a function of the angle of incidence.

2. Data and discussion

From the experimental data we have found no gyrotropy in all our samples. For the sample #1 we have found some birefringence, but not very strong. The degree of circular polarization in the output of the sample was not exceeding of 10% at all angles. The sum of the squared Stokes parameters was only 50%. Consequently the nonpolarized component also was 50% of the intensity of the transmitted light. This depolarization can be reveled by Rayleigh scattering in the in homogeneity of the sample. Indeed the sample #1 contains near-surface transition layer which can caused this scattering.

In the sample #2 this transition layer was removed and we found that the transmitted light is 100% polarized. Absence of the light depolarization shows that the sample #2 can be considered as optically homogeneous in the studied spectral range. If we know the thickness of the sample we can also estimate the difference of the refractive indexes $n_{\text{eff}}^{\perp}$ and $n_{\text{eff}}^{\parallel}$. But because the thickness (here we mean optical thickness) of the sample is much larger the light wavelength the accuracy of this measurement is not very high. Nevertheless the obtained value is in good correlation with the values obtained from the interference structure.

3. Conclusion

In this paper we report the about the fabrication and optical properties of InP nano-porous crystals. Measuring the Stokes parameters of the transmitted light we found an anisotropy of the dielectric function along and perpendicular to the pores. From the interference structure in the thin sample we obtained the refractive indexes of the porous crystal.

Acknowledgements

This work was supported in part by a grant of the Presidium of RAS.

References

[1] L. A. Golovan *et al*,*Uspekhi Fizicheskikh Nauk* **177**, 619–638 (2007).
[2] L. Landau and E. Lifshits, Theory of fields, Moscow, 1967.

18th Int. Symp. "Nanostructures: Physics and Technology"
St Petersburg, Russia, June 21–26, 2010

Site-specific adsorption of fluorofullerene molecules on single crystalline Si surfaces

R. Z. Bakhtizin[1,6], A. I. Oreshkin[2,7], P. Murugan[3,6], V. Kumar[4,6], J. T. Sadowski[5], T. Hashizume[7], N. Fukui[7] and T. Sakurai[7]

[1] Department of Physical Electronics, Bashkir State University, Ufa 450074, Russia
[2] Moscow State University, Department of Physics, Moscow 119991, Russia
[3] Central Electrochemical Research Institute, Karaikudi 630 006, Tamil Nadu, India
[4] Dr. Vijay Kumar Foundation, 1969 Sector 4, Gurgaon 122001, Haryana, India
[5] Center for Functional Nanomaterials, Brookhaven National Laboratory, Upton NY 11973, USA
[6] Institute for Materials Research, Tohoku University, Sendai 980-8577, Japan
[7] WPI Advanced Institute for Material Research (WPI-AIMR) Tohoku University, Sendai 980-8577, Japan

Abstract. Molecular electronics using single molecules as active components is a promising technological concept with fast growing interest. Scanning tunneling microscopy has been used to spatially image single fluorofullerene $C_{60}F_{18}$ molecules on Si(100)-2 × 1 and Si(111)-7 × 7 surfaces. The images have been interpreted with the help of ab initio calculations. It is found that the polar $C_{60}F_{18}$ molecules interact with the Si(111)-7 × 7 surface with fluorine atoms pointing down towards the surface whereas the initial nucleation of deposited $C_{60}F_{18}$ molecules on the technologically important Si(100)-2 × 1 surface can occur on either sites (steps or terraces). The spectra of normalized tunneling conductivity measured above $C_{60}F_{18}$ monolayer coverage are generally consistent with its electronic structure.

Introduction

Molecular electronics is currently attracting great interest being studied as a real successor to conventional Si-based electronics technology. One its perspective is the fabrication of devices whose function is governed by single molecules so that the important step in single molecule tech-nologies is the linking of individual molecules at specific locations on Si surfaces. Fullerenes are promising candidates for the fabrication of electro-active elements in nano-science applications and can be considered as their building blocks. Therefore, the electronics based on individual molecules demands active control of the combined electronic properties of molecule and substrate [1]. An essential peculiarity of fullerenes and their derivatives used in molecular electronics is their ability to trap electrons and to keep hold them for a long time. Fullerenes can also serve as temporal electron acceptors effectively splitting excitons and generating the charge carriers — free electrons and holes. Here we present the results of scanning tunneling microscope (STM) imaging of single polar fluorofullerene molecules $C_{60}F_{18}$ deposited on the Si(111)-7 × 7 and Si(100)-2 × 1 surfaces.

1. Experimental

To prepare pure $C_{60}F_{18}$, a special procedure of fluorination of C_{60} in solid-state reactions with transition metal fluorides was employed [2]. Fluorination was conducted under Knudsen cell conditions with mass spectrometric identification of gaseous products. All experiments were carried out at room temperature using a home-built ultra high vacuum field ion-scanning tunneling microscope (base pressure 2×10^{-11} Torr) equipped with standard surface preparation facilities [3]. The deposition rate was in the range of 0.05–0.1 ML/min. A P-doped Si(100) and Si(111) wafers with resistivity of 8–15 Ω cm were used and cut into pieces of 20 × 7 × 0.5 mm^3. The surface was cleaned by outgassing overnight at 650 °C and then flashing at 1250 °C for 20 s followed by slow cooling at rates of <2°/s from 950 °C to room temperature.

2. Calculations

The details of the spatially varying charge density as observed in high-resolution STM images were analyzed from ab initio pseudopotential calculations using plane wave projector augmented wave method [4]. The exchange-correlation energy has been calculated within generalized gradient approximation (GGA) [5]. Isolated $C_{60}F_{18}$ molecule, clean Si surface as well as adsorption of $C_{60}F_{18}$ on it have been studied using a supercell with sufficient vacuum space between the molecules and surfaces. The Brillouin zone of the supercell was sampled by the k-point in the case of isolated molecules while 2 × 2 × 2 Monkhorst–Pack k-points were used for the surface calculations [6].

3. Results and discussions

The lowering of the symmetry of C_{60} by the attachment of F atoms to one part of the cage will influence the properties of the remaining part as well as the ordering and packing of the fullerene molecules on Si surface depending upon the interactions of the fullerene cage or attached atoms with the surface. The initial nucleation of the deposited $C_{60}F_{18}$ occurs on three different positions of the Si(111)-7 × 7 surface unit cell: the unfaulted half, the faulted half, and the corner hole. The corner hole adsorption site was used for the further analysis since its symmetry allows us to analyze in detail the interaction between $C_{60}F_{18}$ molecule and Si adatoms on the Si(111)-7 × 7 surface. Fig. 1a shows STM images of the filled states of a $C_{60}F_{18}$ molecule located above a corner hole of Si(111)-7 × 7 surface and Fig. 1b shows the corresponding charge isocontour calculated for this molecule by accumulating charge density from states in the energy range of $E_F - 2.25$ eV to E_F.

These results confirm well that F atoms in $C_{60}F_{18}$ molecule are oriented towards the surface. It was also found that polar fluorinated carbon fullerene has large binding energy on a corner hole site of Si(111)-7 × 7 surface due to induced polarization on the Si surface [7].

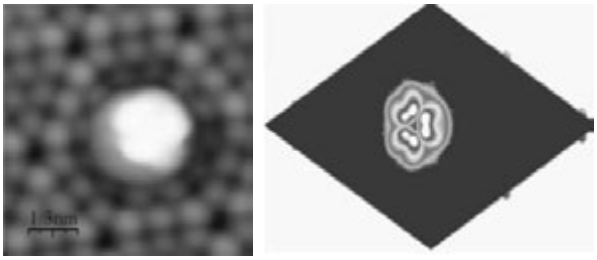

Fig. 1. Filled states STM image of single $C_{60}F_{18}$ molecule adsorbed on a corner hole site at -2.0 V (a) and its simulated STM image at -2.14 V (b).

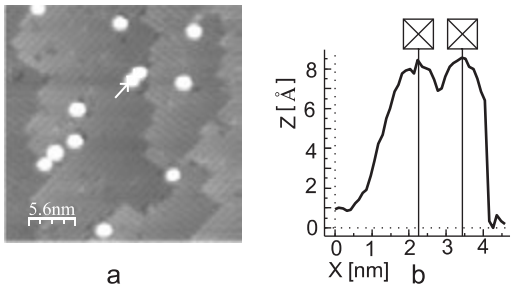

Fig. 2. Filled states STM image of the initial stage of $C_{60}F_{18}$ molecules adsorption on the Si(100)-2 × 1 surface, $U = -2.0$ V (a) and profile of surface along the line highlighted in STM image (b).

Fig. 2a shows the initial stage of $C_{60}F_{18}$ molecules adsorption on the Si(100)-2 × 1 surface and confirms clearly that the initial nucleation of deposited molecules can occur on either sites (steps or terraces). In this image two additional features can be distinguished: (I) "zigzag" buckling of dimers which form c(4 × 2) reconstruction in the vicinity of adsorbed $C_{60}F_{18}$ molecules; (II) almost all deposited molecules are located in the troughs in-between dimer rows, randomly distributed across the surface, and four-dimer or two-dimer sites in the trough were considered. The lateral size of observed $C_{60}F_{18}$ molecules is ∼ 20 Å In closer inspection, we find a tendency of molecules to form clusters even at sub-monolayer coverage. The clusters of paired molecules are seen well in Fig. 2a. Attractive electrostatic interaction between the strongly polarized $C_{60}F_{18}$ molecules is responsible for the rearrangement of the molecules. In accordance with the model of $C_{60}F_{18}$ crystal lattice [8] the shortest center-to-center distance in a molecular chain should be 9.4 Å but from Fig. 2b the average value is 11.5 Å. This is certainly a substrate effect: interaction of adsorbed molecules with a Si(100)-2 × 1 surface is more stronger than between $C_{60}F_{18}$ molecules. To estimate the influence of substrate on $C_{60}F_{18}$ film growth we deposited ∼ 1 ML coverage on Si(100) surface. STM images showed a multilayer growth while the spectra of normalized tunneling conductivity measured above $C_{60}F_{18}$ monolayer coverage (Fig. 3) were generally consistent with its electronic structure. Six distinct peaks are clearly distinguished within bias range from -4.0 to $+4.0$ V. Two of them (at -0.6 and $+0.5$ V) are related with π-bonding and π^* — antibonding states [9]. The surface state band gap is nearly 1 eV. Two others peaks at -1.6 and -3.6 V are attributed to HOMO and HOMO-1 levels of $C_{60}F_{18}$ molecule while the peaks at 1.8 and 3.2 eV — to HOMO and HOMO-1 levels respectively which agrees with the data of photoelectron spectroscopy [10]. The peaks at 1.8 and 2.8 eV are apparently related with LUMO and LUMO+1 levels respectively. From spectroscopic data obtained we can conclude that the electronic structure of fluorine fullerenes is very sensitive to substrate surface condition. Therefore some discrepancy in intermolecular distance in the molecular chain seems to be possible.

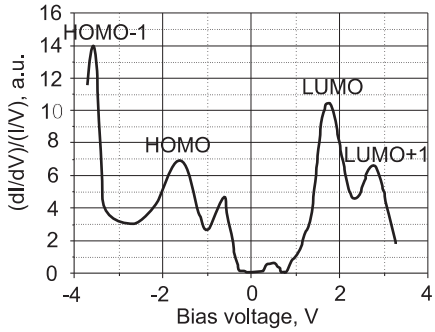

Fig. 3. Normalized tunneling conductivity measured above 1 ML of $C_{60}F_{18}$ on (2 × 1)-Si(100) surface.

Acknowledgements

Images have been processed with Nanotec Electronica WSxM software [11]. This work is supported by RFBR (Grants 08-02-97004-r_povolzh'e_a, 10-02-00575-a, 10-02-92655-IND_a).

References

[1] G. Schull, N. Neel, M. Becker *et al*, *New Journal of Physics* **10**, 065012 (2008).
[2] O. V. Boltalina, V. Yu. Markov, R. Taylor, M. P. Waugh, *Chem. Commun.* **22**, 2549 (1996).
[3] T. Sakurai, T. Hashizume, I. Kamiya *et al*, *Prog. Surf. Sci.* **33**, 3 (1990).
[4] P. E. Blöchll, *Phys. Rev.* **50**, 17953 (1994).
[5] J. P. Perdew, J. A. Chevary, S. H. Vosko *et al*, *Phys. Rev. B* **46**, 6671 (1992).
[6] H. J. Monkhorst and J. D. Pack, *Phys. Rev. B* **13**, 5188 (1976).
[7] R. Z. Bakhtizin, A. I. Oreshkin, P. Murugan *et al*, *Chem. Phys. Lett.* **482**, 307 (2009).
[8] I. S. Neretin, K. A. Lyssenko, M. Yu. Antipin *et al*, *Angew. Chem. Int. Ed.* **39**, 3273 (2000).
[9] A. W. Dunn, E. D. Svensson, C. Dekker, *Surface Scince* **498**, 237 (2002).
[10] V. M. Mikoushkin *et al*, *Journ. of Elect. Spectrosc.* **168**, 25 (2008).
[11] I. Horcas, R. Fernandez, J. M. Gomez-Rodriguez *et al*, *Rev. Sci. Instrum.* **78**, 013705 (2007).

18th Int. Symp. "Nanostructures: Physics and Technology"
St Petersburg, Russia, June 21–26, 2010

Raman scattering in short period GaN/AlN superlattices

V. Yu. Davydov[1], M. B. Smirnov[2], Yu. E. Kitaev[1], A. N. Smirnov[1], M. A. Yagovkina[1], R. N. Kyutt[1], N. A. Cherkashin[3], E. E. Zavarin[1] and W. V. Lundin[1]

[1] Ioffe Physical-Technical Institute, St Petersburg, Russia
[2] Fock Institute of Physics, St Petersburg State University, 198504, St Petersburg, Russia
[3] CEMES/CNRS, 29 rue Jeanne Marvig, 31055, Toulouse, France

Abstract. We report the first observation by Raman scattering of folded acoustic phonons and confined optical phonons in strained short-period hexagonal GaN/AlN superlattices. It is shown that such parameters of GaN/AlN superlattices as the period, built-in strain, and individual layer thicknesses can be extracted from the energy positions of optical and acoustic modes detected in Raman scattering.

Introduction

Semiconductor superlattices (SLs) are of great interest because of their unique physical properties and potential for device applications. At present, a precise non-destructive characterization of III–V nitride-based SLs is of vital importance. One of the most efficient, sensitive, and direct techniques for the quantitative characterization of SLs is Raman spectroscopy [1]. The formation of a SL leads to a folding of the Brillouin zone in the growth direction, which results in appearance of new Raman active phonon modes. However, no Raman data on observation of folded acoustic or confined optical phonons in GaN/AlN SLs are available in literature to our knowledge. The goal of our work was to show that many important parameters of GaN/AlN SLs can be extracted from Raman measurements.

1. Growth and sample characterization

GaN/AlN SLs were grown in a MOVPE system with a horizontal flow reactor on (0001) sapphire substrates at the reactor pressure of 200 mbar and temperature of 1050 °C. NH_3 flows for GaN and AlN growth were 3 SLM and 20 sccm, respectively. The GaN/AlN SL period d_p ranged from 2 to 10 nm, and the total SL thickness was in the range from 0.3 to 1 micron. To suppress effect of GaN interaction with hydrogen [2], H_2:N_2=3:10 mixture with 7 SLM total flow was used as a carrier gas for GaN growth while AlN was grown under hydrogen-free ambient conditions with 8.2 SLM N_2 carrier gas flow. The high quality of GaN/AlN SLs was confirmed by well resolved satellite peaks in X-ray diffraction rocking curves. By fitting of simulating rocking curves to the experimental ones the SL period and the strain of the alternative layers were obtained. The SL periods were estimated from of TEM measurements also (Fig. 1). Room-temperature Raman spectra were measured with a Jobin–Yvon Horiba T64000 triple Raman spectrometer equipped with a confocal microscope.

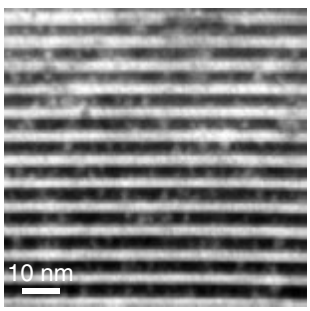

Fig. 1. TEM image of the GaN/AlN SL with $d_p \approx 5.5$ nm.

2. Discussion

Figure 2 shows Raman spectra for some of the SLs in the range of acoustic phonons. For the first time, the doublets of narrow lines were observed in the Raman spectra GaN/AlN SLs. The shift of doublets toward the exciting line with the increase of SL period is inherent for the folded acoustic phonons. The Raman shift of the doublet lines is given by $\Delta\omega^{\mp}_{n,q_z} = \omega_{n,q_z} \pm q_z s$. Here $\omega_{n,0} = 2\pi n s/d_p$ is a frequency of the folded zone center LA-phonon, q_z is the phonon wave vector projection in the folding direction, s is the LA sound velocity for averaged compound of SL, and $n = 0, 1, 2$. We have evaluated the averaged sound velocity from the Raman data presented in Fig. 2. The data for different SLs are close and the averaged velocity is equal to 9300 ± 200 m/s. The positions of the lines comprising the first folded doublet as functions of the SL period were calculated in the elastic continuum limit [3] (see Fig. 2). The results on SL periods obtained from Raman measurements are in excellent agreement with X-ray and TEM measurements.

Figure 3a shows polarized Raman spectra for a GaN/AlN SLs with different periods. Our theoretical calculations suggest

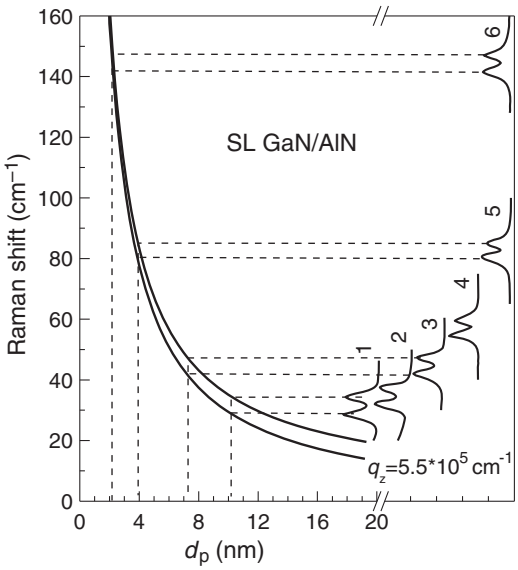

Fig. 2. Calculated frequencies of the first folded acoustic doublets (left) as a function of SL period d_p and Raman spectra (right) of GaN/AlN SLs with different d_p (d_p, nm: 1–10.1, 2–9.1, 3–7.3, 4–5.5, 5–3.9, and 6–2.1.)

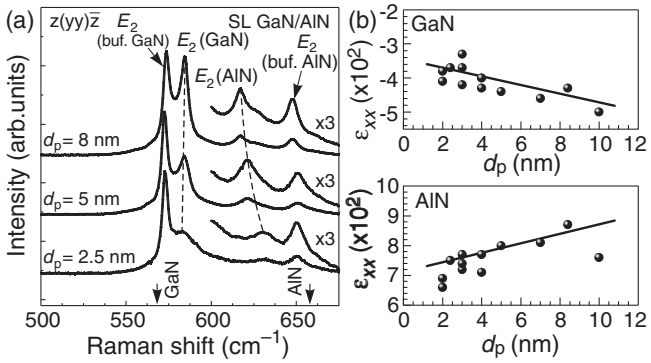

Fig. 3. (a) — Raman spectra of GaN/AlN SLs with the different periods; (b) — strains in GaN and AlN layers as a function of SL's period.

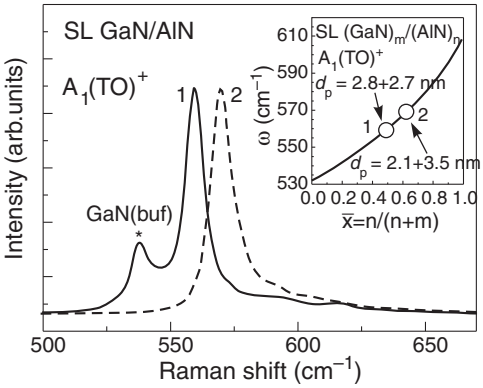

Fig. 4. Raman spectra for the A_1(TO) phonons of GaN/AlN SLs with different ratio of the layer thickness d_{GaN}/d_{AlN}, nm: 1–2.8/2.7, 2–2.1/3.5. The inset shows theoretical calculations (solid lines) and experimental data (symbols).

that phonons of the E_2 symmetry are the vibrations localized in the SL layers [4]. Indeed, the spectrum of each SL contains two E_2 lines whose frequencies are close to those of bulk GaN and AlN, but somewhat shifted. The analysis of the data leads to the conclusion that the positions of the E_2 (high) phonons can be explained by the built-in strain. The frequency positions of E_2 modes in the SLs with different periods were measured and the strain in GaN and AlN layers was inferred from Raman data by using the phonon deformation potentials from [5,6]. It has been found that the in-plane strain (ε_{xx}) is a compressive type for GaN layers and a tensile type for AlN layers. Figure 3b shows the in-plain strain as a function of the SLs period. The data on the strain in GaN and AlN layers obtained from Raman data was found to be in good agreement with the strains estimated from X-ray diffraction data.

Fig. 4 shows Raman spectra for the A_1(TO) phonons of GaN/AlN SLs with different ratio of the layer thicknesses. Only one intense line occupying a midposition between the frequencies of the A_1(TO) phonons of bulk GaN and AlN has been detected in the spectrum of SLs. It has been shown in [4] that A_1(TO) phonon is propagating throught the whole GaN/AlN SL and, therefore, reflects the average characteristics of the system. As a result, the average Al content $\bar{x}$ in the structure can be obtained from the position of the A_1(TO) phonon detected in the Raman spectra of SL. Note that the propagating phonons are supposed to be insensitive to the strain due to different signs of strains in GaN and AlN layers. The knowledge of three parameters x, $\bar{x}$ and d_p gives the possibility to estimate the individual layer thicknesses of the layers comprising the SL $\bar{x} = (d_{AlN}/d_p)x$, where $d_p = d_{GaN} + d_{AlN}$.

It was found for the first time that in GaN/AlN SLs with period less than 10 nm, the region of LO phonons of AlN contains a series of peaks, the quantity and frequencies of which varied with varying SL period. Analysis of the spectra suggested that this structure is attributable to a confined A_1(LO) phonon of AlN.

Symmetry analysis [7] shows that GaN/AlN SLs with odd and even numbers of atomic planes per primitive cell are described by different space groups, C_{6v}^4 and C_{3v}^1 respectively. As a result, the sets of normal modes and their symmetry turn out to be sensitive to a variation of the SL period by one monolayer. For a set of grown SLs with different periods, we have assigned the experimentally observed phonon modes with the symmetry modes predicted from the group-theory analysis.

Along with the group-theory analysis, we have performed the computer simulations based on the DFT theory. Relaxed structure and phonon states of GaN/AlN SLs with layers including up to 10 monolayers were studied. Raman intensities were estimated within bond polarizability model. The analysis of the results of computer simulations and experimental Raman data is in progress.

3. Conclusion

The GaN/AlN SLs with the period from 2 to 10 nm has been successfully grown by MOCVD technique on a sapphire substrate. It has been demonstrated that Raman scattering from folded acoustic modes can be used for accurate determination of the GaN/AlN SL period. The information on the behavior of optical phonons in GaN/AlN SLs provides the possibility to quantitatively estimate the type and the value of the build-in strain of the layers comprising the SLs. Combined information about acoustic and optical phonons obtained from Raman scattering allows estimation individual layer thicknesses. The further development of theory and experiment allows us to estimate the GaN/AlN SL structural parameters with an accuracy of one monolayer.

Acknowledgements

This work has been supported by RFBR(Grant 09-02-01280) NSC RFBR (Grant 08-02-92003-HHC), and the Program of RAS "The physics of new materials and structures".

References

[1] B. Jusserand and M. Cardona, in *Light Scattering in Solids V*, Ed. by M. Cardona and G. G. Guntherodt, Springer-Verlag, Berlin, p. 49 (1988).
[2] E. V. Yakovlev *et al*, *J. Cryst. Growth* **310**, 4862 (2008).
[3] M. Rytov, *Akust. Zh.* **2**, 71 (1956).
[4] M. B. Smirnov *et al*, *Phys. Solid State* **47**, 742 (2005).
[5] V. Yu. Davydov *et al*, *J. Appl. Phys.* **82**, 5091 (1997).
[6] J.-M. Wagner *et al*, *phys. stat. sol. (b)* **234**, 965 (2002).
[7] Yu. E. Kitaev *et al*, *Phys. Rev. B* **57**, 14209 (1998).

18th Int. Symp. "Nanostructures: Physics and Technology"
St Petersburg, Russia, June 21–26, 2010

Element nanodiagnostics of material surface by TXRF method with the planar waveguide-resonator application

V. K. Egorov and E. V. Egorov
IMT RAS, 142432 Chernogolovka, Moscow District, Russia

Abstract. Short description of TXRF spectrometry method and its utility for the planar nanotechnology are presented. It is shown that TXRF analysis parameters can be improved by including into X-ray optical scheme of the spectrometer a new device of X-ray nanophotonics — the planar waveguide-resonator (PXWR).

Introduction

The method of X-ray fluorescence analysis in conditions of the external total reflection of the exciting beam on the testing surface owes its origins to the pioneer work of Yoneda and Horiuchi [1]. Today TXRF spectrometry is the routine procedure for the trace element analysis of solid surfaces and liquid solutions by testing of its dry residues. Physical backgrounds of the method are described by Prof. P. Klockenkamper [2] and its experimental features are discussed in Handbook of X-ray Spectrometry [3].

TXRF spectrum shows very low intensity of the background in comparison with the conventional XRF spectrum of the same object owing to real excitation of the nanosize planar surface layer of material investigated with thickness 3–5 nanometers. Figure 1 presents TXRF and XRF spectra of the dry residue of solution contained Zn (100 mkg/L), Co (20 mkg/L) and Sr (10 mkg/L). The figure demonstrates unquestionable advantages of TXRF method. In consequence of low background deposit TXRF demonstrates super low pollution detection limits up to 10^7 atoms/cm^2. Data obtained by the method are not depended from the matrix effects. In addition to these features TXRF spectrometry is characterized by the linear relation between the target atoms content and X-ray fluorescence yield. Owing to these useful characteristics, 200 plus scientific group in the world exploits TXRF spectrometers. At the same time 5 analogical laboratories has TXRF instruments in Russia today.

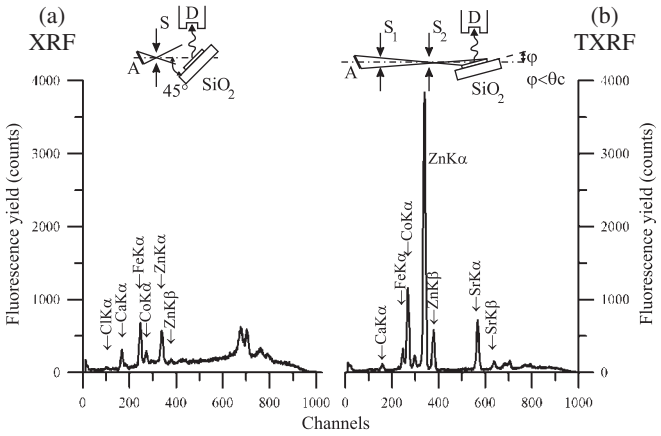

Fig. 1. Measurement geometries and X-ray fluorescence spectra collected in standard conditions (a) and at the total reflection excitation (b) for the same dry residue solution.

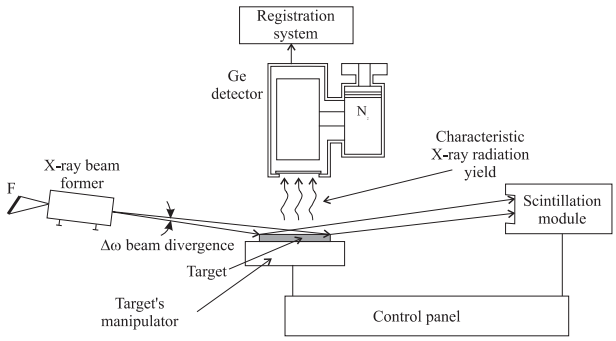

Fig. 2. Block diagram of TXRF spectrometer built in according to the conventional X-ray optics scheme.

1. TXRF spectrometer and its methodical features

The block diagram of TXRF spectrometer built on base of the conventional X-ray optic scheme is presented on Fig. 2. The spectrometer contains X-ray source (F), the exciting beam former, the system for the target orientation and the block for X-ray fluorescence yield registration. X-ray tube with the rotating, immobile or the electron transmission anodes or synchrotron channel are usually used as the X-ray source. The exciting beam former is dedicated for creation of X-ray thread form flux with minimization of its width and the angular divergence. The thread flux in conventional instruments is formed by slit-cut systems or blind assembles with including monochromators or total reflection mirrors. Standard formers produce exciting beams with the width $5 - 15$ μm and the angular divergence near 0.01°.

The target orientation system consists of the precise minigoniometer, control panel and scintillation transmitter. The system can be used for study of the nanosize depth multielement concentration profile. X-ray semiconductor detector in combination with the pulse multichannel analyzer are used for recording of the characteristical secondary fluorescence.

Conventional TXRF spectrometers X-ray optical schemes have in its arsenal three traditional ways for the analytical characteristics improving. There are X-ray source power increasing, time exposition addition and enhancing of the energy X-ray detector resolution. But the specific approach to solution this problem exists. The approach supposes the exciting beam former properties improving. The former emergent flux must be characterized by high radiation density in addition to its small width and angular divergence. The high radiation density has great significance for TXRF method since the exciting beam width in the target position is often larger than the surface target projection on flatness, which is perpendicular to the beam propagation direction. In the result, small part of the beam participates in the target excitation. So, the radiation density increasing is the important reserve for improving of TXRF analytical possibilities. This reserve can be realized with great success by application the planar X-ray waveguide-resonator

(PXWR) for TXRF exciting beam former building.

2. Exciting beam former on base of PXWR

Planar X-ray waveguide-resonator is completed by two planar dielectric polished plates positioned on small distance between them and aligned parallel to each other [4]. PXWR differs from planar monocapillary by mechanism of X-ray flux transportation. The planar monocapillary is characterized by the mechanism of multiple external total reflection of the beam in the slit clearance between planar plates. Every act of the beam reflecting is accompanied by appearing of the local interference areas of X-ray standing wave. Size of the areas, is approximately equal to value of the radiation coherence length parameter ($L = \lambda_0^2/\Delta\lambda$). When the distance between planar reflectors will be smaller as the coherence length half the uniform interference area of X-ray standing wave appears in all space of the slit clearance. The uniform interference area appearance will signal about replacement of X-ray beam propagation mechanism [4]. The device functioned in frame on the mechnism got the name: planar X-ray waveguide-resonator. So long as PXWRs are characterized by nanosize slit widths its are a very beautiful device for the nanophotonics development and can be perspective units for TXRF exciting beam former elaboration.

Figure 3 presents the comparative characteristics for X-ray exciting beams formed by double slit-cut system ($S_1 = S_2 = 15$ μm) and by simplest quartz PXWR ($s = 80$ nm). Integral intensities of the former emergent beams are approximately equivalent. It is connected with PXWR ability to increase the radiation density in the beam on 2–3 order. At the same time, the angular divergence of beam formed by the slit-cut system is smaller as the divergence of PXWR emergent beam. So, the waveguide-resonator application efficiency as the TXRF exciting beam former will increase with the distance decreasing between PXWR outlet and the testing target position.

3. TXRF measurement with competitive formers of exciting beam

We used V-Ta-C alloy target for the TXRF comparative measurements in conditions of MoK$\alpha\beta$ exciting beam formation by the slit-cut systems ($S_1 = S_2 = 15$ μm) and by PXWR with simplest construction. Figure 4 demonstrates measurement geometries and experimental TXRF spectra collected at the slitting angle of exciting beam $\Delta\psi = 0.01^\circ$. The presented spectra are characterized by almost identical set of X-ray fluorescence lines. Host metallic component lines (VKα and TaL$\alpha\beta$) demonstrate visible intensities. But spectra have additional lines belonged to Fe, Ti and Zn atoms. Fe lines present on both spectra, and we can consider that the iron is the main contamination in the alloy. At the same time, the specific calibration showed that Ti and Zn line are connected with the parasitic fluorescence radiation from lips material of output slit included into the slit-cut system. VKα line demonstrates an intensity maximum for both fluorescence patterns because the alloy composition is near $V_{0.84}Ta_{0.06}C_{0.1}$. At the same time, the intensity absolute value is higher for the spectrum collected in conditions of the exciting beam formation by PXWR. Detail experiments showed that the intensities of VKα lines for spectra collected with application of PXWR and the slit-cut systems are equal when the distance between studied target center (0) and formers output is near 60 mm. For smaller

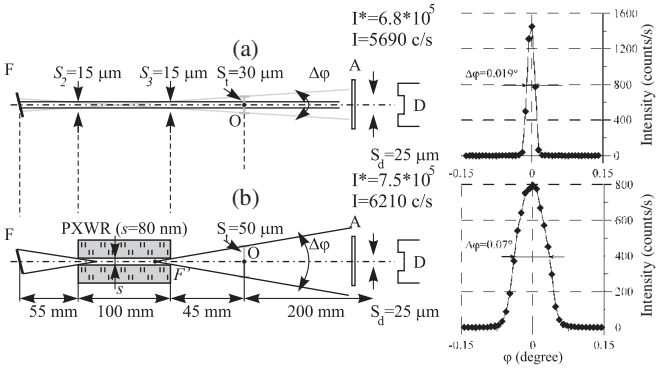

Fig. 3. Schematic design of the exciting beam fabrication by double slit-cut system (a) and by quartz PXWR with simplest construction (b) and real spatial intensity distributions for MoK$\alpha\beta$ in beams formed by these devices. X-ray source regime $U = 25$ keV, $I = 5$ mA. I is the measurement intensity and I^* is the intensity with taking into account attenuator A ($K = 120$).

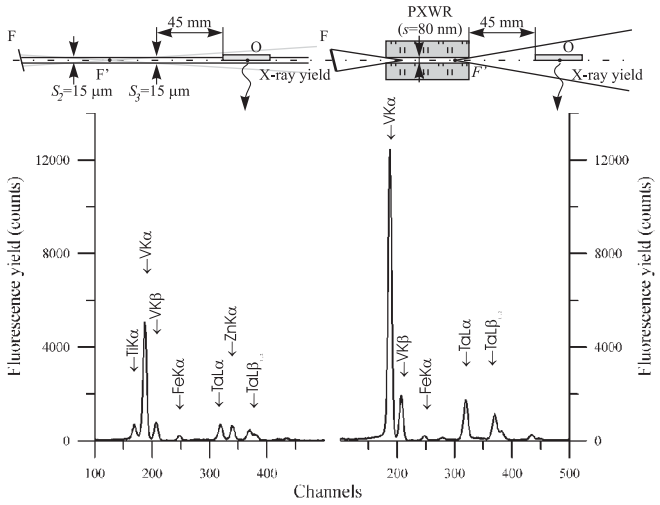

Fig. 4. Measurement geometries and TXRF spectra for V-Ta-C alloy collected at the target excitation beams formed by slit-cut system (a) and PXWR with simple construction (b). X-ray source regime $U = 25$ keV, $I = 10$ mA, collection time 300 s. Insertions show the spectra in logarithmic scale.

distances the waveguide-resonance former of TXRF exciting beam has an advantage over the slit-cut former application. Moreover, the waveguide-resonance technology presents the additional possibilities for TXRF spectrometer parameters improving by simple adaptation into its X-ray optical scheme the set of independent X-rat sourses.

References

[1] Y. Yoneda *et al*, *Rev. Sci. Inst.* **42**, 1069 (1971).
[2] R. Klockenkamper, *Total reflection X-ray fluorescence analysis*, New York: Wiley, 245 (1997).
[3] *Handbook of X-ray spectrometry, Methods and Techniques*, Eds. by R. E. Van Grieken and A. A. Markwicz, New York: Dekker, 453–487 (1993).
[4] V. K. Egorov *et al*, *Spectrochimica Acta* **B59**, 1049 (2004).

18th Int. Symp. "Nanostructures: Physics and Technology"
St Petersburg, Russia, June 21–26, 2010

Tunnel spectroscopy of the hole density of states in the GeSi/Si(001) nanoislands by Tunnelling AFM

A. A. Bukharaev[1], P. A. Borodin[1], *D. O. Filatov*[2], M. A. Isakov[2], V. G. Shengurov[3], V. Yu. Chalkov[3] and S. A. Denisov[3]

[1] Kazan' Institute for Physics and Technology, Kazan' Scientific Center, RAS, Kazan' 420029, Russia
[2] N. I. Lobachevskiy University of Nizhniy Novgorod, Nizhniy Novgorod 603950, Russia
[3] Research Institute for Physics and Technology, N. I. Lobachevskiy University of Nizhniy Novgorod, Nizhniy Novgorod 603950, Russia

Abstract. We report on the first-time investigation of the local density of states (LDOS) in the self-assembled GeSi/Si(001) nanoislands by Tunnelling Atomic Force Microscopy (AFM). The current images and the tunnel spectra of the individual islands have been obtained, which are correlated to the spatial distribution and to the energy one, respectively of the local density of the hole states in the GeSi islands.

Introduction

Scanning Tunnelling Microscopy/Spectroscopy (STM/STS) has been being used extensively for investigation of the morphology and of the atomic structure of the self-assembled semiconductor nanostructures since early 1990-s. In the recent years STM/STS in Ultra High Vacuum (UHV) has been applied also to investigation of the spatial distribution of the local density of states (LDOS) in the quantum-size semiconductor heterostructures, in particular, in the GaSb/InAs(001) quantum wells (QWs) [1] and in the self-assembled InAs/GaAs(001) quantum dots (ODs) [2,3].

Recently we have applied UHV Tunnelling Atomic Force Microscopy (AFM) [4] to the investigation of the LDOS in the In(Ga)As/GaAs(001) self assembled QDs and quantum rings [5,6]. This method allowed us to visualize the LDOS and to measure the size quantization spectrum in the QDs and rings covered by a native oxide.

In the present work we applied Tunnelling AFM to the investigation of the LDOS in the self-assembled GeSi/Si(001) nanoislands for the first time. The current images and the tunnel spectra of the individual islands reflecting the spatial distribution and the energy one, respectively of the LDOS of the hole states in the GeSi islands have been obtained.

1. Experimental

The GeSi/Si heterostructure with the self-assembled nanoislands for the Tunnelling AFM investigations had been grown by Sublimation Molecular Beam Epitaxy in GeH_4 ambient. A 200-nm thick p^+-Si (with the acceptor concentration $N_A \sim 10^{18}$ cm^{-3}) buffer had been grown on a p^+-Si(001) substrate,

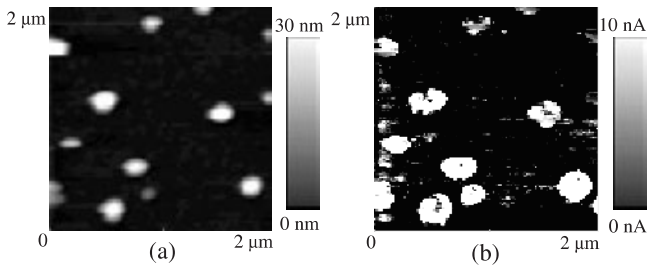

Fig. 1. The topographic (a) and current (b) images of the GeSi/Si(001) nanoislands. $V_g = 2.0$ V

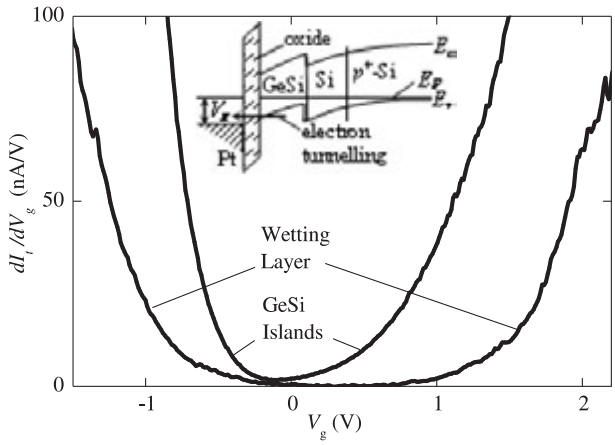

Fig. 2. The tunnel spectra dI_t/dV_g of the contact between the Pt coated AFM probe to the GeSi/Si(001) heterostructure surface.

then a 3-nm thick p-Si ($N_A \sim 10^{15}$ cm^{-3}) spacer has been deposited onto the buffer layer. Finally, the GeSi islands were grown by letting GeH_4 into the growth chamber. The substrate temperature T_g when depositing Ge was 700 °C, the pressure of GeH_4 $p_g \approx 9 \times 10^{-4}$ Torr, and the nominal thickness of Ge d_{Ge} measured by Rutherford Backscattering Spectroscopy (RBS) was $\approx$ 10 monolayers (ML). The averaged Ge molar fraction in the island material was $\approx$ 0.25 according to the photoluminescence [7] and the Raman spectroscopy [8] data.

The Tunnelling AFM investigations were carried out *ex situ* using Omicron Multiprobe P UHV system at 300 K. The sample surface covered by the native oxide formed during the sample transfer through the ambient air was scanned across by a conductive Si probe coated by Pt in the contact mode. A bias voltage V_g was applied between the AFM probe and the sample. Simultaneously with the acquisition of the topographic image, the surface distributions of the tunnel current through the contact between the probe and the sample $I_t(x, y)$ where x and y were the probe coordinates on the sample surface were acquired. In another measuring mode, the I-V curves of the probe-to-sample contact $I_t(V_g)$ were acquired in each point in the scans.

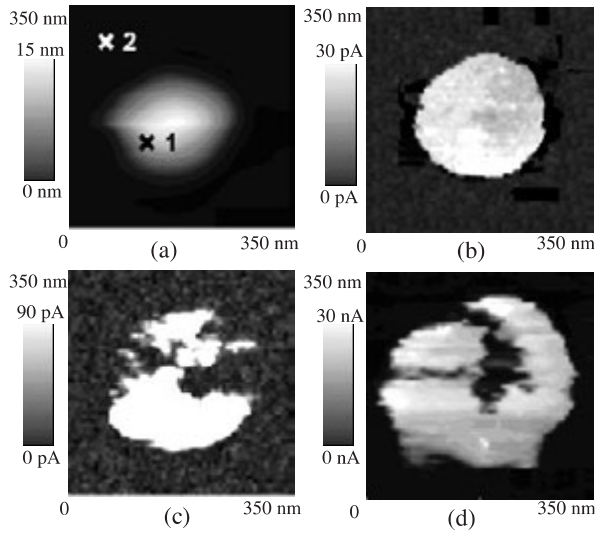

Fig. 3. The AFM (a) and the current images (b)–(d) of a GeSi/Si(001) island. $V_g = 0.1$ V (b), 0.5 V (c), and 1.0 V (d).

2. Results and discussion

In Fig. 1(a) and (b) the topographic and current images of the surface GeSi islands, respectively are presented. The islands of various sizes and shapes from the smaller dome-shaped islands to the larger pyramidal ones (so called superdomes) are seen in the topographic image [Fig. 1(a)].

In the current image [Fig. 1(b)] the spots of increased probe current I_t corresponding to the GeSi islands are seen. The increase in the probe current I_t was related to the tunnelling of the electrons from the valence band states in the GeSi islands to the free states above the Fermi level in the probe coating material (Pt, see the inset in Fig. 2).

The current images of the islands were enlarged as compared to the AFM ones that was attributed to the convolution effect due to finite apex radius of the AFM tip R_p [9]. Typical value of R_p for the Pt-coated NT-MDT NSG-01 probes was ≈ 50 nm according to the vendor's specifications.

In Fig. 2 the differential tunnel spectra dI_t/dV_g measured on the surface of an individual GeSi island and between the islands (on the surface of the wetting layer) in the points denoted by the numbers (1) and (2), respectively in Fig. 3(a) are presented. The differential tunnel spectra were calculated from the measured I-V curves by the numerical differentiating with the nonlinear 5-point smoothing. The tunnel spectra exhibited no negative differential resistance features unlike the ones of the QDs or rings [5,6]. This points to a negligible quantum size effect in the GeSi islands of relatively large size as compared to the De Broglie wavelength of the holes in the GeSi alloy.

In Fig. 3 the AFM image and the current images of an individual GeSi island measured at various gap voltages V_g are presented. The AFM image of the island in Fig. 3(a) is elongated in the horizontal (x) direction that was attributed to the creep of the scanner piezoceramics.

The general pattern of the current images was found to depend on V_g. At lower V_g corresponding to the extraction of the electrons from the electron states near the edge of the valence band in the GeSi islands, the current image has a circular symmetry [Fig. 3(b)]. At higher V_g the current image pattern transformed into the one having a twofold-like symmetry [Fig. 3(c)]. With further increasing of V_g the current image pattern took a 4-fold symmetry [Fig. 3 (d)] that could be attributed to the rising of the valence band edge due to partial elastic strain relaxation at the edges of the pyramide-shaped island.

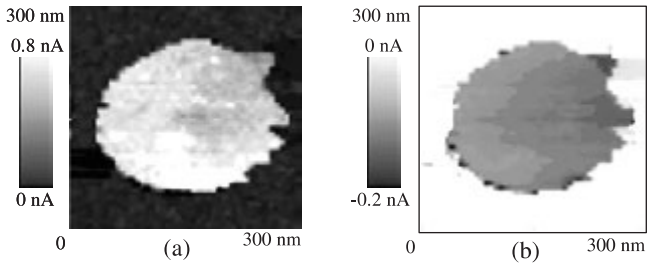

Fig. 4. The current images of a GeSi/Si(001) island. $V_g = +0.1$ V (a) and -0.1 V (b).

In Fig. 4 the current images of an individual GeSi/Si(001) island recorded at different polarities of V_g are presented. It is worth noting that the contrast in the current image inverted with the flip of the V_g immediately i.e. the surface $Ge_{0.25}si_{0.75}$/Si (001) island behaves like a heterostructure of the first type. The same conclusion follows also from the analysis of the tunnel spectra presented in Fig. 2.

Acknowledgements

The present work has been supported in part by Russian Federal Agency for Education (RNP 2.1.1.3615). The authors are grateful to P. Chernykh (Research Institute for Nuclear Physics, M. V. Lomonosov Moscow State University) for the RBS measurements.

References

[1] K. Suzuki, K. Kanisawa, C. Janer, S. Perraud, K. Takashina, T. Fujisawa and Y. Hirayama, *Phys. Rev. Lett.* **98**, 136802 (2007).
[2] B. Grandidier, Y. M. Niquet, B. Legrand, J. P. Nys, C. Priester, D. Stievenard, J. M. Gerard and V. Thierry-Mieg, *Phys. Rev. Lett.* **85**, 1068 (2000).
[3] T. Maltezopoulos, A. Bolz, C. Meyer, C. Heyn, W. Hansen, M. Morgenstern and R. Wiesendanger, *Phys. Rev. Lett.* **91**, 196804 (2003).
[4] A. Olbrich, B. Ebersberger and C. Boit, *Appl. Phys. Lett.* **73**, 3114 (1998).
[5] P. A. Borodin, A. A. Bukharaev, D. O. Filatov, D. A. Vorontsov and M. A. Lapshina, *Surf. Inv.* 2009, Issue 9, p. 71.
[6] P. A. Borodin, A. A. Bukharaev and D. O. Filatov, *J. Phys.: Conf. Series* (2010) (at press).
[7] D. O. Filatov, M. V. Kruglova, M. A. Isakov, S. V. Siprova, M. O. Marychev, V. G. Shengurov, V. Yu. Chalkov and S. A. Denisov, *Semicond.* **42**, 1098 (2008).
[8] A. I. Mashin, A. V. Nezhdanov, D. O. Filatov, M. A. Isakov, V. .G. Shengurov, V. Yu. Chalkov and Yu. A. Denisov, *Surf. Inv.* 2010 (to be published).
[9] A. A. Bukharaev, N. V. Berdunov, D. V. Ovchinnikov and K. M. Salikhov, *Scanning Microsc.* **12**, 225 (1998).

18th Int. Symp. "Nanostructures: Physics and Technology"
St Petersburg, Russia, June 21–26, 2010

Quantum dots structures quality characterization based on excitation and temperature dependencies of the photoluminescence

A. G. Gladyshev[1,2], N. V. Kryzhanovskaya[1,2], A. M. Nadtochy[1,2], A. P. Vasil'ev[2], V. N. Nevedomskiy[2], A. E. Zhukov[1], M. V. Maximov[1,2], N. N. Ledentsov[1,2] and V. M. Ustinov[1,2]

[1] St Petersburg Academic University, St Petersburg, Russia
[2] Ioffe Physical-Technical Institute, St Petersburg, Russia

Abstract. Excitation and temperature dependences of integrated photoluminescence intensity were measured for three quantum dots structures with different defect densities. We show that crystalline quality of quantum dots structures can be estimated from these dependences.

Introduction

Light-emitting devices with self-organized quantum dots (QDs) is an exciting and rapidly developing area of semiconductor physics. QDs lasers demonstrate unique characteristics that were earlier predicted by theory: a low threshold current density and high differential efficiency and temperature stability (for review, see [1]). One of the specific properties of QDs compared to quantum well (QW) structures is the possibility of attaining longer emission wavelengths in a given material system, for example, InGaAs-GaAs. To increase the emission wavelength, special growth techniques are used, such as activated alloy phase separation [2]. The growing of large QDs can be followed by the formation of dislocations in QDs and large clusters with dislocations, which gives rise to nonradiative recombination. These entities significantly deteriorate the characteristics of QDs devices. Usually transmission electron microscopy (TEM) is used for structural quality diagnostic. However this method demands much time for sample preparation. Thus, an express method of evaluation of defects density necessary during QDs properties optimization should be developed. In this work we offer a method of QD's samples structural quality characterization using PL excitation and temperature dependences. PL spectra of QD's samples with different defect densities were measured in a wide range of temperature (10–500 K) and excitation densities ($3 \times 10^{-5} - 2 \times 10^{5}$ W/cm^2) to understand influence of defects on optical properties of the samples.

1. Experimental

Three samples studied in this work were grown by a molecular beam epitaxy (MBE), on (001)-oriented GaAs substrate followed by an undoped GaAs buffer layer at 600 °C. Three layers of self-assembled InAs QDs (2.4 ML) in 50 Å thick InGaAs quantum wells (QW) and 50 Å thick GaAs spacers between them were grown at 480 °C. This active region was embedded in the middle of 2000 Å thick GaAs layer. Two 1000 Å thick AlGaAs barriers were grown on both sides of the GaAs layer to prevent carrier leakage to the substrate and the surface. A 100 Å GaAs cap layer was grown at 600 °C on the top of the structure. Samples differed only by QD's growth rate which were 0.125, 0.25 and 0.5 Å/s for samples A, B and C, respectively. The PL spectra were excited with second harmonic of CW or pulsed YAG:Nd laser (532 nm). The laser spot diameter was about 200 μm. PL signal was measured by a grating monochromator operating with a cooled Ge photodiode. Temperature dependences were measured using He close cycle cryostat (10–300 K) or home-made oven (300–500 K). The spectra were recorded using standard lock-in technique. Transmission electron microscopy studies were carried out using a Philips EM 420 electron microscope operating at 100 kV.

2. Results and discussion

According TEM images QDs were formed in all samples and have a good structural quality except sample C where many dislocations were observed. The dislocation density was less than 10^6 cm^{-2} for the samples A and B. Density of dislocation in QDs and in matrix region of the sample C was 1×10^{10} and 1×10^{9} m^{-2}, respectively. Average QDs size decreases and their density increases with QD's growth rate increasing and equal to 12, 14.5, 18 nm and 5, 3.8, 2.75×10^{10} m^{-2} for samples A, B, C, respectively. PL maximum of sample A is centered at 0.993 eV at RT and shifted to lower energy for sample B what agrees with QDs size increasing. However PL peak of sample C is shifted to higher energy. This fact can be explained by formation of dislocation in large QDs due to stress relaxation [3]. PL data at RT confirm this explanation. PL intensity of sample A is slightly lower than sample B one but PL intensity of the sample C is more than 20 times lower. These primary data showed that sample C has much poor structural quality as compared with two other samples. But the difference between samples A and B was not so considerable. So further investigation was necessary.

Dependences of integrated PL intensity (IPLI) on excitation density at 77, 300 and 500 K for all samples are shown in Figure 1. In general three regions with different slops can be marked out on these dependences. The slope (k) of the first one corresponding to low Pexc is more than 1, i.e. dependences show superlinear behavior. In this region only peak from QDs presents on PL spectra so we may get information about recombination processes in active layer. The superlinear region is changed by linear ($k = 1$) one at the higher excitation power (region 2). The third region is characterized by changing of the slope from linear to sublinear. It should be noted that the excitation density where slope changing from superlinear to linear and from linear to sublinear correspond to appearance of peaks from QW and GaAs matrix on PL spectra, respectively. So changes of the dependence slope may be connected with carrier's recombination in these parts of structures.

As one can see the dependences of sample A and B are comparable in regions 1 and 2 but different in region 3. Sample A dependence slope is higher than that for sample B in region 3. This facts allow us conclude that QDs in sample A and B have comparable structural quality but matrix structural quality of sample A is better because the excitation dependence slope of this sample in region 3 closer to 1 (linear) than those of samples B. Also we may say that QDs quality in these samples is better than that in sample C because the rate of PL signal decreasing with excitation power decreasing (region 1) is lower which corresponds to lower density of nonradiative centers. Moreover it should be noted that dependence of sample C has two different slopes in region 1 at RT and 500 K. Firstly slope is equal to

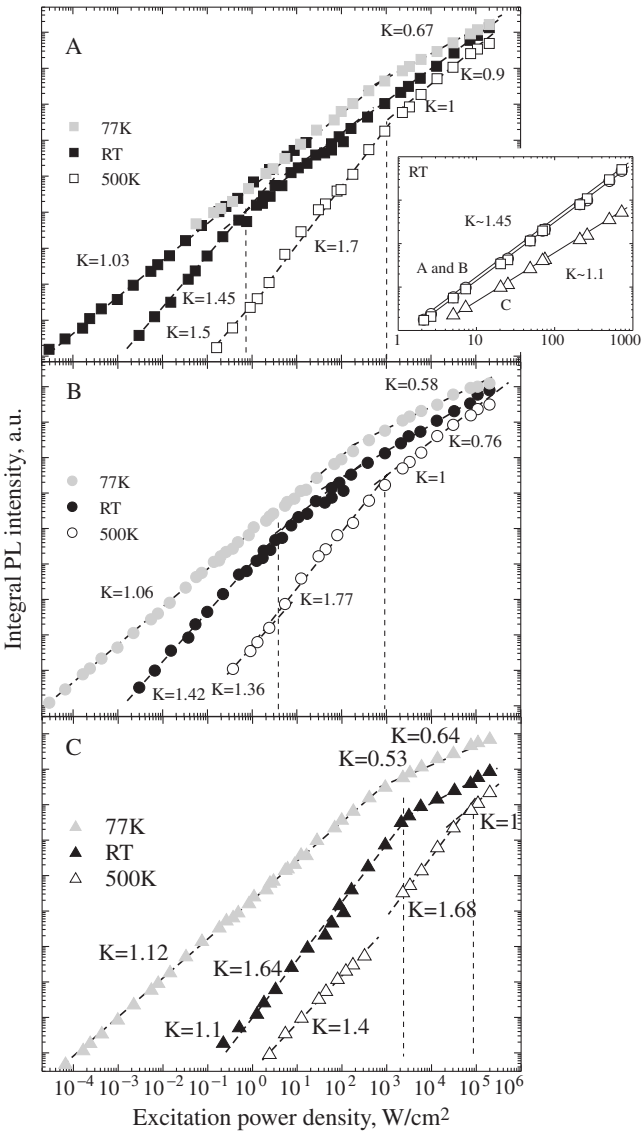

Fig. 1. Excitation dependencies of IPLI at different temperatures. The inset shows resonant PL spectra of samples A, B and C at room temperature.

about 1.1 (1.4 at 500 K) but at the higher power changes to 1.64 at RT (1.7 at 500 K). PL excitation dependences under resonant conditions using semiconductor laser emitting at 1.265 eV were measured at RT for this feature confirmation. The result of the measurement (inset in Figure 1) showed that slope of resonant dependence is the same as for the nonresonant excitation for all three samples and equal to 1.45 for samples A and B and 1.1 for sample C. This fact may be explained by effective carriers capture into defects free large size QDs at low excitation power what is confirmed by PL maximum shift from 1.01 to 0.99 eV at RT with excitation power decreasing. The results obtained shows that slopes of excitation dependence may serve as criterion for QDs samples quality characterization.

Temperature dependences of IPLI at different excitation power density are shown in Figure 2. It was observed that at the temperature range from 10 to 100 K PL intensity almost does not change with temperature and comparable for all samples so this part of dependence is not shown in Figure 2. But at the higher temperatures PL intensities gradually drops, which is attributed to thermal escape of carriers from QDs followed by nonradiative recombination in GaAs matrix. The fact that PL intensities of samples are comparable at low temperature and different at higher temperature allows use ratio

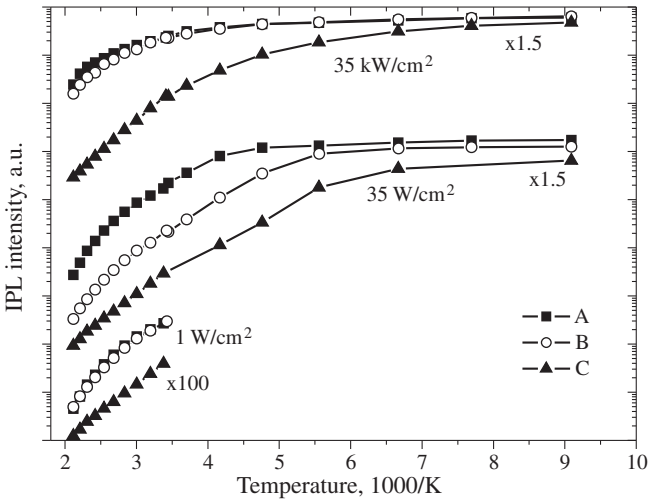

Fig. 2. Temperature dependencies of IPLI at different excitation power densities.

of IPLI at low and high temperature (for example, 77 K and RT) as a criterion of quality of different structure layers. This ratio at low excitation power give information about QDs quality, and at high one (corresponding to linear region) — about matrix layer quality. The less this ratio differs from 1 the better quality.

Temperature dependences of samples A and B at low (1 W/cm^2) excitation power are practically identical what points at the identical QDs properties. Sample A has less IPLI dropping at high (35 kW/cm^2) power what connected with higher matrix quality. More essential difference in IPLI dropping with temperature between these samples was observed at excitation density of 35 W/cm^2 corresponding to linear region of excitation dependences at RT. Such situation may be explained by increasing role of recombination in GaAs matrix with temperature growth at middle excitation power if compared with high excitation conditions when recombination in matrix has a great influence on PL process already at low temperature. IPLI temperature dropping from low to high temperature of the sample C increases with excitation power increasing what correlates with supposition that this sample has the worst matrix structural quality and efficient PL from defect free QDs at low excitation power.

3. Conclusions

It was shown that ratio between low and high temperature IPLI at different excitation power serves as sample structural quality criterion. If IPLI ratio criterion is not enough for better sample revelation that PL excitation dependences should be measured at low and high temperature and compared with each other.

Acknowledgements

This work was supported by the Federal Agency of Science and Innovation (Rosnauka).

References

[1] M. V. Maximov, N. N. Ledentsov, *Quantum Dots Lasers*, in Dekker Encyclopedia of Nanoscience and Nanotechnology, James A. Schwarz, Cristian I. Contescu, and Karol Putyera, Eds.; Marcel Dekker, Inc.: New York, 3109–3126 (2004).

[2] B. V. Volovik *et al*, *Semiconductors* **33**, 901 (1999).

[3] A. Yu. Egorov *et al*, *Semiconductors* **30**, 707 (1996).

18th Int. Symp. "Nanostructures: Physics and Technology"
St Petersburg, Russia, June 21–26, 2010

Approach to the near-field image restoration using eigenfunction expansion (computational lens)

M. U. Karelin

A. V. Luikov Heat and Mass Transfer Institute, National Academy of Sciences of Belarus, Minsk, 220072, Belarus

Abstract. For the scanning near-field imaging, use of SVD decomposition of the Green's function on full scanning geometry is described. The method is based on numerical enhancement of the raw image by its deconvolution. The proposed procedure also allows to estimate the limiting resolution of the reconstructed image. The comparison with similar approaches is briefly discussed.

Introduction

In the studies of optical and electronic properties of objects at nanoscale, various types of near-field scanning optical microscopes (NSOM) often provides the most valuable data [1]. However, both the aperture and apertureless versions of NSOM suffer from interplay between resolution and noise — smaller aperture means lower signal and higher signal-to-noise ratio (SNR) [1,2]. This leads to need of computational procedures to enhance the image; on the other hand, proper processing of NSOM image helps to obtain data not only on surface properties, but also on sub-surface structure of the sample [3].

There exists several methods for enhancement of the NSOM data [2–4] numerically ("computational lens"). However, these approaches do not include estimation of achievable resolution, rather setting it to some *ad hoc* value.

In the present paper, alternative method for numerical restoration of the NSOM data is presented. The method enables to choose the optimal resolution that is based on the scanning geometry and the detector SNR.

1. Decomposition of the Green's function

The following situation is considered (Fig. 1): the image is formed at the probe plane P (the plane of the NSOM probe movement), while the sample is situated at the plane S. x_0 is the size of the sample; y_0 is the limit of the probe movement, respectively. It is assumed that the probe has characteristic size r (typically around 10–100 nm), the distance z between the planes is much smaller than the wavelength λ. One-dimensional problem is studied to simplify the analysis.

Under these assumptions, the propagation of radiation is

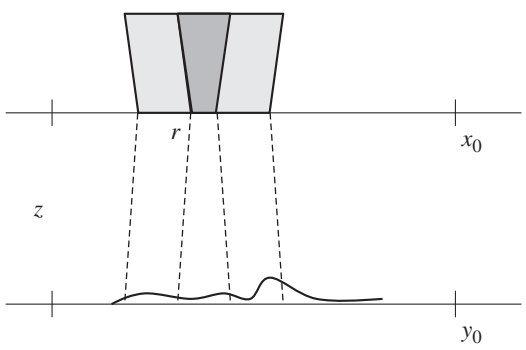

Fig. 1. The geometry of the source and registration planes and movement of the aperture NSOM probe.

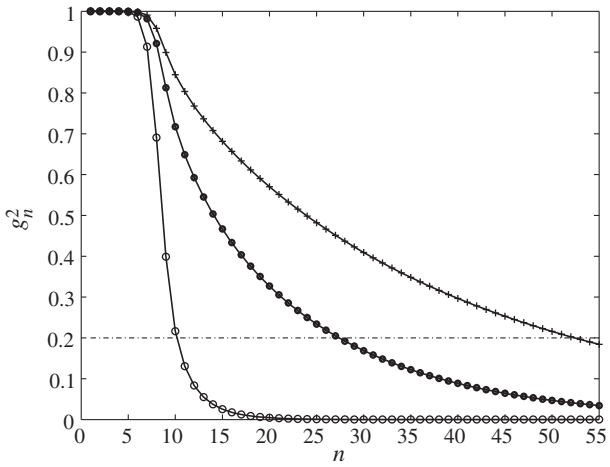

Fig. 2. Dependence of the normalized singular values of their number for $x_0 = y_0 = 1$ μm, $\lambda = 500$ nm and $z = 10$ (+'s), 20 (dots), 100 nm (circles), respectively.

described by the known Green's function [5]:

$$G(x, y) = \frac{ikz}{2} \frac{H_1^1 \left\{ k \left[(x-y)^2 + z^2 \right]^{1/2} \right\}}{\left[(x-y)^2 + z^2 \right]^{1/2}} . \qquad (1)$$

The analysis is based on a factorized representation of the Green's function with the additional orthogonality conditions (singular value decomposition, SVD, see details e.g. in [5–7]:

$$G(x, y) = \sum_{n=0}^{\infty} g_n \phi_n(x) \psi_n^*(y) , \qquad (2)$$

$$\int_{-x_0}^{x_0} dx \; \phi_n^*(x) \phi_m(x) = \int_{-y_0}^{y_0} dy \; \psi_n^*(y) \psi_m(y) = \delta_{nm} . \qquad (3)$$

From the Fig. 2 it is seen that the disctiribution of the singular values is relatively independent on the distance between planes, z, and for typical values of z the distribution has a long slowly decaying tail. It means, that in contrast with approach [6], this decomposition enables sufficient resolution enhancement.

2. SVD representation for the image enhancement

It should be noted that many NSOM systems register not the intensity of scattered radiation, but interference pattern of the scattered radiation with a plane wave source. In this case, the

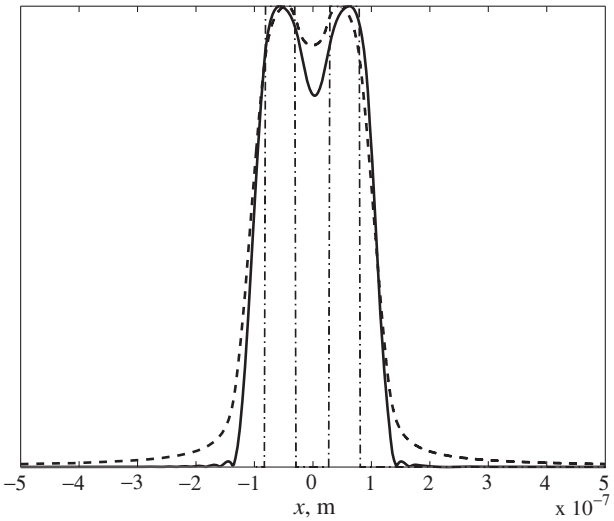

Fig. 3. Registered (dashed line) and recovered (solid line) field distributions; original object (dash-dot line).

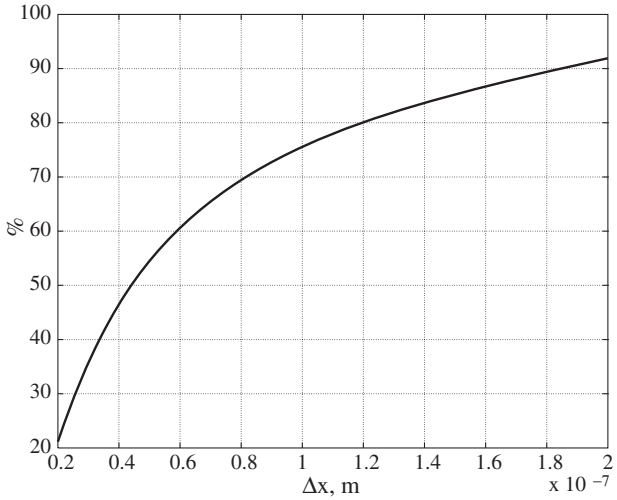

Fig. 4. Dependence of maximally allowed noise level, %, on the required resolution, m.

signal is proportional to the complex amplitude of the scattered wave, and further analysis can be performed for the complex amplitude.

Here and below, the scalar approximation is used for the electric field of light wave. In a rigorous analysis, the presence of changes in the refractive index of the subwavelength scale requires the solution of problems for vector quantities, but the scalar case can more clearly describe the main features of the image formation and treatment.

The value of the complex amplitude in ith scanning point is given by equation

$$E_i = \int_{x_i}^{x_i+r} dx a(x) \int_{-y_0}^{y_0} dy\, G(x, y) E(y)\,, \qquad (4)$$

where $a(x)$ is the probe aperture function, $E(y)$ is the field distribution at the object.

Using the SVD decomposition, it can be represented, as

$$E_i = \sum_n a_{in} g_n b_n^*\,, \qquad (5)$$

where

$$a_{in} = \int_{x_i}^{x_i+r} dx a(x) \phi_n(x)\,, \quad b_n^* = \int_{-y_0}^{y_0} dy \psi_n^*(y) E(y)\,. \qquad (6)$$

The solution, b_n, of equations (5), (6) can be found by the method of least squares. Reconstruction of the object field distribution is carried out using orthogonality of the basic functions $\psi_n(y)$. The result is presented in Fig. 3.

In the Fig. 3, the source object was two bright stripes of 25 nm width, separated by 30 nm gap, other parameters of the problem were as in Fig. 2, with $z = 10$ nm, $r = 50$ nm.

It should be noted that the limit of summation over n in the expression (5) is determined by the level of noise in the optical system and by the singular values g_n. Moreover, for large n the decomposition eigenfunctions are approximated by harmonic functions, and the limiting resolution for the given the signal to noise ratio can be calculated (Fig. 4).

To conclude, it is necessary to note, that the analysis of realistic, 2D, imaging geometry is much more demanding — full calculation of eigenfunction of Green's function requires huge amount of memory and computing capabilities. To overcome this issue, it is possible to use analogy between far-field and near-field problems and adopt products of 1D eigenfunctions as first-order approximations of their 2D counterparts. To further increase performance of calculations, massively-parallel calculation on the graphical card (GPGPU paradigm) can be naturally applied.

Acknowledgements

The work was supported by Belarusian Fund of Fundamental Research under grant No. F09K-065. Author thanks Mr. Alexander Tomko for help with the numerical simulations and analysis of AFM data.

References

[1] L. Novotny, *Progr. Opt.* **50**, (E. Wolf, Ed.), 137 (2007).
[2] J. Sun *et al*, *IEEE J. Sel. Topics Quant. Electron.* **12**, 1072 (2006).
[3] A. A. Govyadinov *et al*, *Phys. Rev. Lett.* **103**, 213901 (2009).
[4] F. Kiendl and G. Güntherodt, *Ultramicroscopy* **102**, 299 (2005).
[5] R. Pierri and F. Soldovieri, *Inverse Problems* **14**, 321 (1998).
[6] P. Martinsson *et al*, *Opt. Exp.* **14**, 11392 (2006).
[7] A. Thaning *et al*, *J. Opt. A* **5**, 153 (2003).

18th Int. Symp. "Nanostructures: Physics and Technology"
St Petersburg, Russia, June 21–26, 2010

The Raman spectra of coupled modes in heavily doped InN crystals

A. A. Klochikhin[1,2], V. Yu. Davydov[1], A. N. Smirnov[1], A. Hashimoto[3], A. Yamamoto[3] and S. Gwo[4]

[1] Ioffe Physical-Technical Institute, St Petersburg, Russia
[2] Nuclear Physics Institute, 188350, St Petersburg, Russia
[3] Department of Electronics Engineering, Fukui University, Bunkyo, Fukui 910-8507, Japan
[4] Department of Physics, National Tsing-Hua University, Hsinchu 300, Taiwan, ROC

Abstract. We have studied impurity-induced first-order resonant Raman scattering from heavily doped InN in the frequency region where LO phonons strongly interact with electron-hole excitations. The excitation energies were chosen so that the wave vectors of mixed modes fell between two Landau boundaries. We demonstrate that analysis of the resonant Raman spectra of InN at different excitation energies gives realistic estimates of such important characteristics as the Fermi wave vector and, hence, the bulk electron concentration.

Introduction

The revision of the InN band gap from 1.9 to 0.7 eV has opened new perspectives for using this material in a wide class of electronic and optoelectronic devices [1]. At the same time, special features of the electronic band structure of InN create problems in the interpretation of the results of the InN investigation as epitaxial layers or as nanostructures components . In this work we show that the unusual transformation of the InN Raman spectra at exciting energy variation results from the fundamental characteristics of the band structure of this material.

It was found earlier [2] that resonant Raman scattering can excite selectively uncoupled LO as well as LA phonons with large wave vectors. As a result, the dispersions of LO and LA phonon modes of hexagonal InN in a wide range of wave vectors have been reconstructed from experimental data. Here we present the results of studies of heavily doped InN samples in the frequency region where an LO phonon strongly interacts with an electron-hole charge density fluctuation. This region is restricted by two Landau boundaries. Below the lower boundary two phonon-plasmon modes exist. Above the upper Landau boundary pure E_1(LO) and A_1(LO) phonon modes can be observed. In between these two boundaries the continuous spectrum of mixed LO-electron-hole excitation appears. The mixed spectrum continuity within these limits is the consequence of the continuous character of the electron-hole excitations near the Fermi energy rather than decay processes. The resonant Raman process allows one to observe the dispersion of this continuous spectrum by changing the excitation energy. The realistic estimates of such important characteristics as the Fermi wave vector and, hence, the bulk electron concentration of InN can be obtained.

1. Experiment

Undoped hexagonal InN epilayers with the thicknesses from 0.2 to 0.7 microns were grown on (0001) sapphire substrates by the MOVPE technique [3]. Structural and morphological characterization of InN epilayers was performed by high resolution triple-crystal X-ray diffraction (XRD) and by atomic force microscopy (AFM). As evidenced by X-ray analysis, all the samples had a hexagonal symmetry, and no traces of other polymorphes were detected. From symmetric (0002) Bragg reflection, lattice parameter c was found to be close to $c = 5.70$ Å. The AFM measurements did not reveal any pronounced column structure of the samples studied. The Hall electron concentration ranged from 6×10^{18} to 2×10^{20} cm^{-3}, and the highest electron mobility was found to be 700 cm^2/V s. Room-tempe-rature Raman spectra for excitation energies from 1.92 to 2.71 eV were measured with a Jobin–Yvon Horiba T64000 triple Raman spectrometer with a confocal microscope. All spectra were measured in the backscattering geometry.

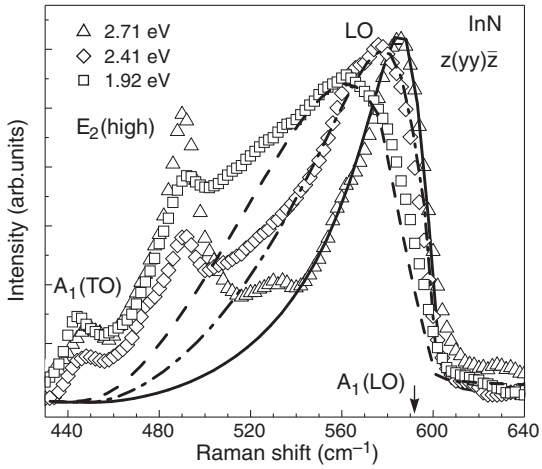

Fig. 1. Raman cross section of heavily doped InN sample as a function of energy at excitation by photons with energies 2.71, 2.41, and 1.92 eV. The symbols are the experimental data, and the solid lines are the results of model calculations at free electron concentration 1×10^{20} cm^{-3}.

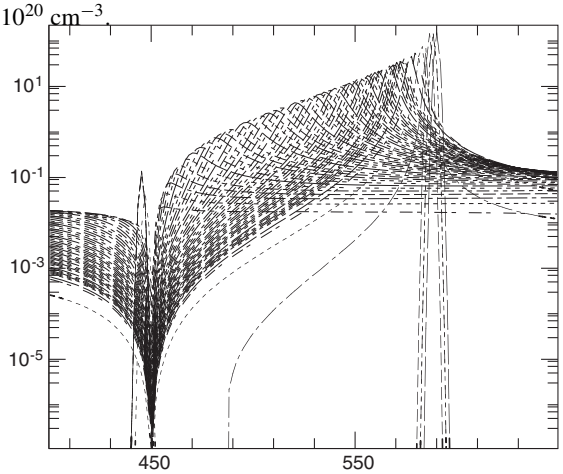

Fig. 2. Imaginary part of $1/\varepsilon(q, \omega)$ in the region of mixed modes at wave vectors from 0 to $2.5 p_F$.

Fig. 1 shows polarized Raman spectra of the InN sample

with the electron concentration close to 1×10^{20} cm^{-3} obtained at different excitation energies. It is seen that well resolved structure corresponding to Raman allowed E_2(high) and A_1(LO) phonon modes transforms into a single wide band from A_1(TO) to A_1(LO) as the excitation energy decreases from 2.71 to 1.92 eV.

2. Theory

The peculiarities of the electron band structure of InN play an important role in the Raman scattering process. Direct electromagnetic transitions from valence bands to the single conduction band with the extremum at the Γ point occur in a wide energy interval. This means that the Martin's double resonance [4,5] is realized in a wide interval of excitation photon energies.

We consider the first-order Raman scattering taking into account the wave-vector conservation law violation due to scattering of electrons and holes from charged impurity centers. The scattering amplitude contains two electromagnetic interactions with exciting and scattered photons, Fröhlich and Coulomb interactions of the photoexcited electron-hole pair with LO-phonons and electron-hole excitations $[H_F + H_C]$, and their Coulomb interaction with charged impurity centers H_i

$$A \propto \left\{ \sum_{\lambda,\lambda'} \frac{[H_{em}]_{0,\lambda}[H_F+H_C]_{\lambda,\lambda'}[H_i]_{\lambda',\lambda''}[H'_{em}]_{\lambda'',0}}{\hbar^3 (\omega-\Omega_{\lambda,0})(\omega'-\Omega_{\lambda',0})(\omega'-\Omega_{\lambda'',0})} \right\} . \quad (1)$$

Here, ω and ω' are the frequencies of incident and scattered photons, and $\Omega_{\lambda,0}$, $\Omega_{\lambda',0}$ and $\Omega_{\lambda'',0}$ are the frequencies of interband transitions.

A strong dependence of the scattering amplitude on the wave vector arises from denominators of Eq. (1) two of which can take zero value simultaneously if the scattering occurs in the region of interband absorption. Let us write the scattering amplitude neglecting the photon wave vector and preserving only the denominators that determine the amplitude dependence on the wave vector

$$\begin{aligned} A(q,\omega) \propto & \int\int\int \frac{d^3p d^3p_1 d^3p_2}{\left(\omega-\Omega_p^{eh}\right)\left(\omega'-\Omega_{p_2}^{eh}\right)\left(\omega_1-\Omega_{p_1}^{eh}-\hbar q^2/2M\right)} \\ & \times \left(\delta\left(\mathbf{p}-\mathbf{p_1}+\mathbf{q}^e\right)-\delta\left(\mathbf{p}-\mathbf{p_1}+\mathbf{q}^h\right)\right) \\ & \times \left(\delta\left(\mathbf{p_1}-\mathbf{p_2}+\mathbf{q}^e\right)-\delta\left(\mathbf{p_1}-\mathbf{p_2}+\mathbf{q}^h\right)\right) , \end{aligned} \quad (2)$$

where $\Omega_p^{eh} = E_g/\hbar + \hbar p^2/2\mu$, E_g is the band gap width, $\mu = m_e^* m_h^*/(m_e^* + m_h^*)$ is the reduced effective mass of electron and hole, M is the translational mass of the pair, $q^{e,h} = q\mu/m_{e,h}^*$, and $\hbar^2 p^2/2\mu$ is kinetic energy of relative motion of the electron-hole pair. The amplitude contains two similar terms, in the first one $\omega_1 = \omega$, and in the second term $\omega_1 = \omega'$, and we consider one of them.

The δ-functions allow us to integrate over d^3p_1 and d^3p_2. Integrating over angular variables of vector $\mathbf{p}$ and over dp^2 by using the energy conservation laws at electromagnetic transitions we consider the scattering process involving real absorption or real emission. The contribution into the scattering amplitude due to real electromagnetic transitions is given by

$$\begin{aligned} A(q,\omega) \propto & \left[\frac{2\mu\,(m_e+m_h)\,v_0}{(2\pi)^2\hbar^2 q}\right]\frac{2\mu}{\hbar(p_\omega+p_{\omega'})} \\ & \times\left[\frac{p_\omega}{(p_\omega^2-q^2/4-i\mu\gamma/\hbar)}+\frac{p_{\omega'}}{(p_{\omega'}^2-q^2/4-i\mu\gamma/\hbar)}\right]. \end{aligned} \quad (3)$$

Here, $p_\omega = \sqrt{2\mu\Delta/\hbar^2}$ and $p_{\omega'} = \sqrt{2\mu\Delta'/\hbar^2}$. Thus, the scattering cross section which is proportional to the squares of amplitude modulus of Eq. (3) will determine the wave vectors q by relating their values to the exciting or scattered light frequency by $q = 2p_\omega$ or $q = 2p_{\omega'}$. The accuracy of these values is restricted by the finite relaxation time of the photoexcited electron-hole pair τ which is related to the intermediate state broadening γ by equation $\gamma = 1/\tau$.

The Raman cross section can be written as

$$\begin{aligned} \sigma(\omega) \propto & \frac{N_i}{2\pi^2}\frac{p_\omega}{(p_\omega+p_{\omega'})^2}\int d^3q \left|\frac{4\pi\,Ze}{v_c q \varepsilon_\infty (q^2+q_{TF}^2)}\right|^2 \\ & \times \mathrm{Im}\left[\frac{1}{\varepsilon(q,\omega)}\right]\frac{2\pi}{\hbar}\left|\frac{p_\omega}{(p_\omega^2-q^2/4-i\mu\gamma/\hbar)}\right|^2 . \end{aligned} \quad (4)$$

Here, N_i and Z are the impurity center concentration and charge, respectively, v_c is the elementary cell volume, and q_{TF} is the Thomas–Fermi screening wave vector. A similar contribution arises from the second term of the amplitude given by Eq. (2) and can be obtained from Eq. (4) by substituting $p_\omega \rightleftharpoons p_{\omega'}$. The function $\mathrm{Im}[1/\varepsilon(q,\omega)]$ is the imaginary part of reciprocal dielectric function (see Fig. 2). As long as the q values are between the Landau boundaries, the scattering results in a mixed mode of longitudinal optical branch and electron-hole excitation. It is seen from Fig. 2 that the spectrum of mixed excitations is continuous. The scattering amplitude modulus squared in Eq. (4) selects the wave vectors which are defined by the excitation energies with the accuracy limited by the finite relaxation time of the photoexcited electron-hole pair $\tau = 1/\gamma$, i.e., $q = 2p_\omega \pm \sqrt{2\mu\gamma/\hbar}$ and $q = 2p_{\omega'} \pm \sqrt{2\mu\gamma/\hbar}$. The good agreement of the experimental and calculated spectra shown in Fig. 1 was obtained by fitting the bulk electron concentration (1×10^{20} cm^{-3} for the presented sample).

3. Conclusion

We show that analysis of the resonant Raman spectra of InN at different excitation energies can give realistic estimates of such important characteristics as the Fermi wave vector and, hence, the bulk electron concentration. This approach allows one to avoid the negative effect of the powerful accumulation layers of InN in Hall measurements. A more precise estimation of free electron concentrations by using the resonant Raman scattering from heavily doped InN epitaxial layers will contribute to the progress in the growth technology of high quality nanostructures based on this compound.

Acknowledgements

This work has been supported by RFBR(Grant 09-02-01280) NSC RFBR (Grant 08-02-92003-HHC), and the Program of RAS "The physics of new materials and structures".

References

[1] V. Yu. Davydov and A. A. Klochikhin, in *Indium Nitride and Related Alloys*, edited by T. D. Veal, C. F. McConville, and W. J. Schaff (CRC Press, Boca Raton) 181–241 (2009).
[2] V. Yu. Davydov *et al*, *Phys. Rev. B* (2009).
[3] A. G. Bhuiyan *et al*, *Appl. Phys. Lett.* **83**, 4788 (2003).
[4] R. M. Martin, *Phys. Rev. B* **10**, 2620 (1974).
[5] J. Menendez and M. Cardona, *Phys. Rev. B* **31**, 3696 (1985).

18th Int. Symp. "Nanostructures: Physics and Technology"
St Petersburg, Russia, June 21–26, 2010

Elemental vapor-phase synthesis of vertically aligned ZnO nanorods and heterogeneous p-n junctions fabricated on the basis of them

O. V. Kononenko[1], A. N. Red'kin[1], D. V. Matveev[2], G. N. Panin[1,5], A. A. Kovalenko[3], A. N. Baranov[4] and I. A. Khotina[6]

[1] Institute of Microelectronics Technology and High Purity Materials, RAS, 142432 Chernogolovka, Moscow Region, Russia
[2] Institute of Solid State Physics, RAS, 142432 Chernogolovka, Moscow Region, Russia
[3] Moscow State University, Department of Materials Science, 119992 Moscow, Russia
[4] Moscow State University, Chemistry Department, 119992 Moscow, Russia
[5] Quantum-functional Semiconductor Research Center, Department of Physics, Dongguk University 26, Seoul 100-715, Korea
[6] A. N. Nesmeyanov Institute of Organoelement Compounds, RAS, 119991, Moscow, Russia

Abstract. Vertically aligned ZnO nanorods were synthesized on silicon wafers. Nanorods demonstrated high structural performance and good optical characteristics. Heterogeneous p-n junctions were fabricated from aligned ZnO nanorods by deposition of NiO films or PEDOT onto nanorod tips. Measurements of I-V characteristics were performed under the UV illumination and in the dark.

Introduction

Zinc oxide is a unique functional semiconductor material with a wide forbidden band (3.37 eV), high bonding energy of the exciton (60 meV) at room temperature, and an effective ultraviolet luminescence. Materials based on ZnO can be used as components of gas sensor controls, LCD matrices, solar batteries, photocatalysts, luminescent materials, lightemitting diodes, powder lasers, and composite materials. Zinc oxide is a biocompatible material with antiseptic properties. One dimensional (1D) or quasi 1D structures on the basis of zinc oxide are a promising material for nanoelectronics. Currently the optical properties of ZnO as a semiconductor material with good luminescent properties are of greatest interest. This is due to the possibility of applying materials on the basis of zinc oxide in the creation of new effective optoelectronic devices. In recent years, there has been increasing interest in one-dimensional (1D) nanocrystalline zinc oxide (nanorods, nanowires, and nanowhiskers), motivated by its perfect crystal structure and unusual properties due to size effects. Moreover, single-crystal samples make it possible not only to raise the exciton density and create low-threshold gain media but also to reduce scattering losses [1]. In this context, aligned arrays of single-crystal nanorods 50–200 nm in diameter and several microns in length are of special interest. Aligned ZnO nanocrystal arrays on substrates are commonly grown using a thin metal film as a catalyst for 1D growth. The drawback to this method is that the nanocrystals may be contaminated with the catalyst. Moreover, catalyst particles as a rule remain on the tips of the grown zinc oxide nanocrystals. Very recently, there have been reports on the preparation of aligned zinc oxide nanorod arrays with no 1D growth catalysts, in particular, using substrates coated with polycrystalline zinc oxide. Liu *et al* obtained well-aligned ZnO nanorods on porous silicon substrates. Our previous results [2] demonstrated that aligned high-quality zinc oxide nanorod arrays can be produced by elemental vapor-phase synthesis with no 1D-growth catalysts and with no special substrate preparation steps. At the same time, the ZnO nanocrystals grown by such way were found to vary widely in shape, depending on the process conditions.

1. Experimental

Zinc oxide nanorods were grown on (001) Si substrates in a chemical vapor deposition (CVD) apparatus. The temperature in the zinc source zone was varied in our experiments from 570 to 670 °C, and the temperature in the deposition zone, was varied from 520 to 640 °C. The flow rate of the oxygen-argon mixture was 4–6 l/h. The oxygen concentration was varied from 8 to 25 vol. percent. During the process, zinc vaporized from the source, and the zinc vapor reached the growth zone and reacted with oxygen. The reaction rate in terms of zinc was 8–35 g/h, depending on the process conditions. In all our experiments, the mole fraction of zinc vapor exceeded that of oxygen. The synthesized nanorods were examined in XL 30S field emission gun high-resolution scanning electron micro-

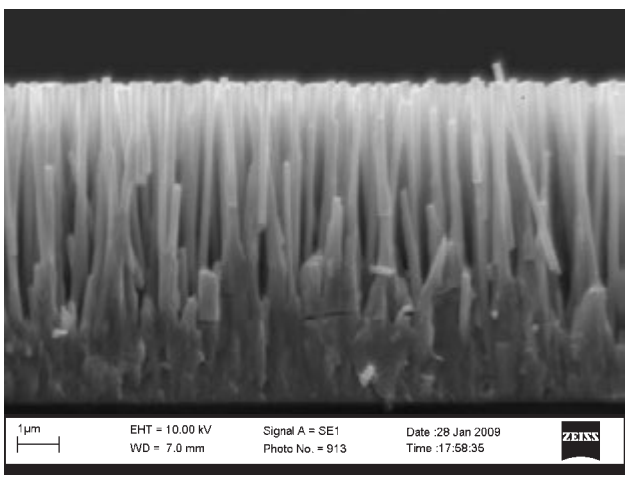

Fig. 1. SEM image of vertically oriented zinc oxide nanorods grown on silicon substrates by vapor-phase synthesis without the use of the catalyst.

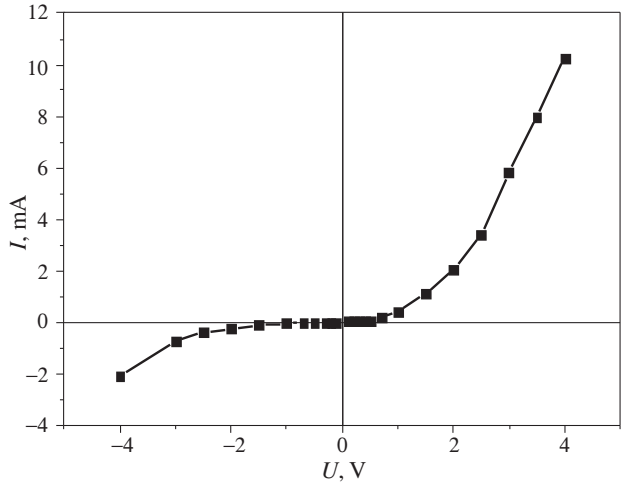

Fig. 2. I-V curve obtained on the ZnO nanorods-NiO structure.

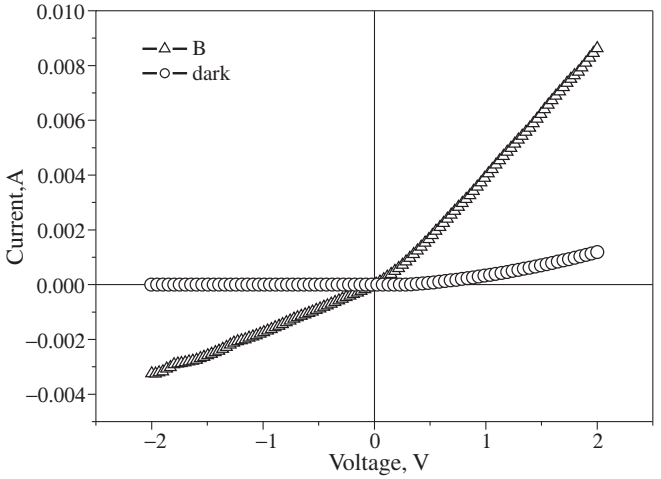

Fig. 3. I-V curves obtained in the dark and under UV illumination on the ZnO nanorods-PEDOT structure.

scope (HRSEM) with a Mono CL system for cathodoluminescence (CL) spectroscopy was used. The light emitted from the sample can be directed into the slits of the monochromator, which is mounted on the SEM. The high-resolution transmission electron microscope JEOL 4000 FX was used for structure analysis of nanorods. Heterogeneous p-n junctions were fabricated from aligned ZnO nanorods by deposition of NiO films or PEDOT onto nanorod tips. Measurements of I-V characteristics were performed under the UV illumination and in the dark.

2. Results and discussions

The shape, dimensions, and orientation of the zinc oxide nanocrystals strongly depend on the deposition conditions and the position of the substrate in the growth zone. One type of structure is a uniform array of zinc oxide nanorods identical in size and orientation (Fig. 1). Such structures grow as a rule in the upstream and central parts of the growth zone. As shown earlier, ZnO nanorods produced by this method consist of high-purity single-crystal close-to-stoichiometry material with a perfect structure. The growth of such structures is typically accompanied by the formation of a polycrystalline underlayer of variable thickness. Another type of structure is characterized by a wide diversity of shapes.

Due to the difficulties of producing zinc oxide with p-type conductivity for the formation of transparent p-n junctions, one can use wide band gap semiconductors as the p-type semiconductor. In these semiconductors their own defects are acceptors. Therefore, it is not difficult to obtain p-type conductivity there. Such semiconductors that are compatible with zinc oxide are $SrCu_2O_2$, $CuAlO_2$, and NiO [3]. It is extremely easy to produce NiO. It can be synthesized by thermal vacuum evaporation at the oxygen pressure on the order of 10-4-10-5 Torr. In addition, a hole concentration in the NiO films is high enough (on the order of 10^{20} cm^{-3}) can be obtained. We produced heterogeneous p-n junctions on the basis of the ZnO nanorods with n-type conductivity and NiO films with p-type conductivity having sufficiently good rectifying characteristics (Fig. 2).

PEDOT was deposited on ZnO nanorod tips by spin on coating. Electrical contacts were prepared to ZnO and PEDOT using conducting glue. I-V characteristic of the ZnO nanorods-PEDOT p-n junction is shown in Figure 3. The structure showed a strong, reversible response to ultraviolet light.

Acknowledgements

This work has been supported in part by the Russian Foundation for Basic Research, grant Nos. 07-08-00514 and 08-03-12109.

References

[1] A. N. Gruzintsev *et al*, *Neorg. Mater.* **42**, 508 (2006).
[2] A. N. Red'kin *et al*, *Neorg. Mater.* **43**, 301 (2007).
[3] H. Ohta *et al*, *Mater. Today* **7**, 42 (2004).

18th Int. Symp. "Nanostructures: Physics and Technology"
St Petersburg, Russia, June 21–26, 2010

Formation of GaAsN/GaN quantum dot-like nanostructure by implantation of low-energy N_2^+ ions into GaAs

V. M. Mikoushkin[1], V. V. Bryzgalov[1], Yu. S. Gordeev[1], S. Yu. Nikonov[1], A. A. Zhuravleva[1], A. P. Solonitsina[1], A. B. Ustinov[2] and M. M. Brzhezinskaya[3]

[1] Ioffe Physical-Technical Institute, St Petersburg, Russia
[2] St Petersburg State Polytechnical University, 194021 St Petersburg, Russia
[3] BESSY, German-Russian laboratory, 12489 Berlin, Germany

Abstract. Nitration of n-type GaAs (100) by low energy N_2^+ ions ($E_i = 1.5 - 2.5$ keV) has been studied by high resolution photoelectron spectroscopy with using synchrotron radiation and by Auger spectroscopy. The phase of GaAsN alloy was revealed in the nitrated nanolayer besides the dominating GaN phase. It was shown that the nitrated nanolayer has a thickness of about 5 nm and consists of the narrow band gap clusters of $GaAs_{1-x}N_x$ alloy in the GaN wide band gap matrix, which looks like a system of quantum dots.

Introduction

Nitridation by low energy N_2^+ ion beams has been revealed to be a possible way of fabrication of nitride insulating and passivating nanolayers on GaAs surface [1]– [7]. These layers were proposed for use as buffer ones for eliminating mismatch of the lattice constants of GaAs and GaN in subsequent growth of thick crystallincitee GaN films on GaAs [1,2]. Moreover, the implantation is considered to be a way of fabrication of GaN nanolayers for optoelectronic devices [4,6]. This method is relatively simple, compatible with other high vacuum techniques and gives an opportunity of in situ control of the fabricated layer by means of x-ray photoelectron spectroscopy (XPS) for elemental and chemical analysis. Creation of the phase of GaN was revealed by analysis of Ga3d photoemission spectra [1]. The conclusion was made that the implantation forms entire GaN nanolayer [1,2,4,5,6,7] or mostly GaN layer [3] on the GaAs surface. Presence of GaAs line in Ga3d spectrum was explained by the contribution of GaAs substrate observed through thing GaN layer. We report here results of sophisticated chemical analysis of nitride film fabricated by ion implantation which was conducted at completely different experimental conditions when photoelectrons of only nitrated layer were detected. Nevertheless contribution of a cluster phase of GaAsN being chemically similar to the GaAs was observed besides the phase of GaN (Fig. 1.).

1. Experimental details

The high resolution XPS experiment was carried out at the BESSY storage ring in Berlin using monochromatic synchrotron radiation of the German-Russian beamline with photoelectron spectrometer VG CLAM-4 [5]. The Auger spectroscopy experiment devoted to study of modification of nitrated layer by Ar^+ ion beam was performed using electron spectrometer

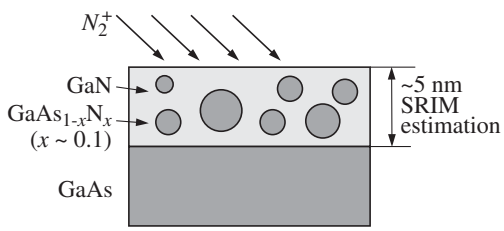

Fig. 1. Scheme of the nanostructure GaAsN/GaN formed on the GaAs surface by implantation of low-energy nitrogen ions N_2^+.

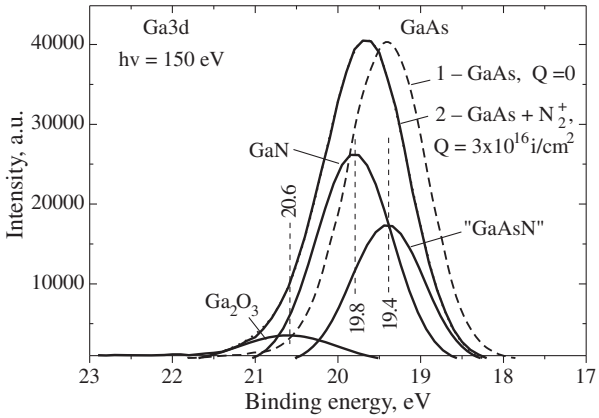

Fig. 2. Ga3d photoemission spectrum of GaAs (1) and GaAs implanted by nitrogen ions with energy $E_i = 1500$ eV (2). The last one is decomposed into different contributions.

LHS-11. GaAs (100)($n \sim 10^{18}$ cm^{-3}) wafer was taken as a sample. It was implanted at room temperature under high vacuum conditions by nitrogen ions N_2^+ with energy $E_i = 1500$ in the first experiment and $E_i = 2500$ eV in the second one. The incidence angle was normal to the surface. The dose of the implanted ions $Q \sim 3 \times 10^{16}$ cm^3 was close to the dose sufficient for saturation of the nitrogen concentration in the near-surface area [1]. The surface of the sample was preliminary cleaned by Ar^+ ions. The thickness of the nitrated layer was estimated by SRIM code to be about $d \sim 4 - 6$ nm. The peculiarity of the conducted experiments was in detecting electrons of only the nitrated layer, which was achieved by tuning the photon energy to diminish mean free path of detected electrons down to the value $\lambda \sim 0.5 - 1.0$ nm.

2. Results and discussion

The concentration of the implanted nitrogen was estimated by the analysis of line intensities. It proved to be close to the values ([N] ~ 25 at.%) obtained in Ref. [1,2,4]. The implanted nitrogen substitutes arsenic and creates chemical bonds with gallium, which is seen in the Ga3d photoemission spectra shown in Fig. 2. Curve 1 corresponds to Ga3d line of atomic clean surface of GaAs prepared by Ar^+ ion etching. Curve 2 is the spectrum of the surface implanted by nitrogen ions. Implantation shifts Ga3d spectrum to higher binding energies. Decomposition of the spectrum of the implanted surface into Gaussian

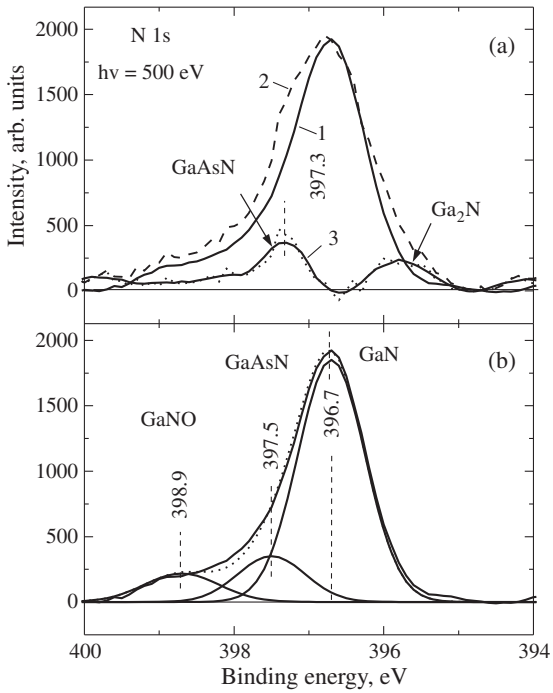

Fig. 3. N1s photoemission spectrum of GaAs implanted by nitrogen ions. The energy of implanting N_2^+ ions $E_i = 1500$ eV.

contributions shows that the phase of GaN is dominating one, but a contribution of the substance being chemically similar to GaAs is observed in the nitrated layer too. Contribution of this phase is comparable with the content of the main phase. This phase is shown below to be a GaAs alloy.

Fig. 3a shows N1s photoemission spectrum of the implanted sample (curve 1) with prominent line of the GaN phase. The binding energy of N1s core electron in GaN E_B(N1s) = 396.7 eV is in agreement with the previously published data. High energy resolution of the synchrotron beamline made it possible revealing an important peculiarity of the spectrum: an asymmetry evidencing the contribution of the additional line at higher binding energy. This additional line we assigned to the phase of GaAsN alloy. Indeed, the binding energy in alloy should be between the energies in N-Ga and N-O compounds due to lower electronegativity of As compared to O. Morover, the asymmetry becomes stronger after bombardment of the film by Ar^+ ions, which is shown below to enhance the contribution of the phase of GaAsN alloy in nitrated layer.

To confirm the spectra identification, influence of Ar^+ ion bombardment on nitric film was specially studied in additional experiment (LHS-11). Fig. 4 shows NKVV Auger spectra in the course of Ar^+ ion bombardment. The figure demonstrates increase of the relative contribution of GaAsN phase due to mixing the material by intensive cascades of secondary ions generated by heavy Ar^+ ions [11, 12]. Namely this process is responsible for enhancement of the asymmetry of the photoelectron spectrum shown in Fig. 3.

Fig. 3b demonstrates decomposition of the N1s spectrum (curve 1, Fig. 3a) of the nitrated layer into contributions of different chemical phases. The decomposition gave the N1s binding energy E_B(N1s) = 397.5 eV in $GaAs_{1-x}N_x$ alloy which turned out to be very close to the data of XPS measurements (397.6 and ~397.3 eV) of single-phase dilute alloys $GaAs_1 - xN_x$ with $x = 0.01$ and $x = 0.04$ grown by MBE in Ref. [13, 14].

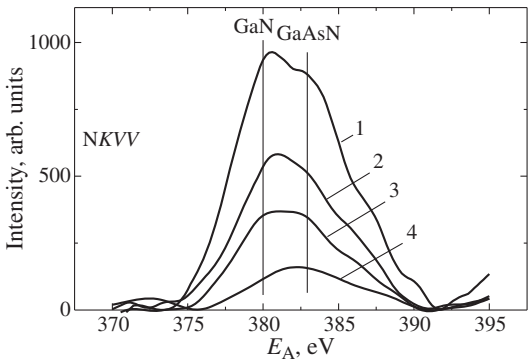

Fig. 4. NKVV Auger spectra of N-implanted GaAs in the course of bombardment by Ar^+ ions with energy $E_i = 2500$ eV.

Taking into account the total concentration of nitrogen [N] ~ 25 at.%, and the ratio of GaN and $GaAs_{1-x}N_x$ phases (Fig. 2), the content of nitrogen in alloy $GaAs_{1-x}N_x$ was estimated to be $x \sim 0.10$. This value is high enough to decrease the band gap of the alloy below the value $\Delta E = 1$ eV [15]. The revealed phase is generated on the molecular level due to segregation of molecules into clusters. The characteristic size of clusters should be less than the thickness of the nitric film. Thus we came to the conclusion that fabricated nitric nanofilm is a system of narrow band gap clusters of $GaAs_{1-x}N_x$ ($x \sim 0.10$) alloy in the wide band gap matrix of GaN.

3. Conclusions

We revealed that nitride nanolayer created by implantation of low energy N_2^+ ions into GaAs surface at is not an entire GaN layer. It consists of the narrow band gap clusters of $GaAs_{1-x}N_x$ ($x \sim 0.10$) alloy in the wide band gap matrix of GaN. This system has a sign of a system of quantum dots. N1s binding energies in $GaAs_{1-x}N_x$ ($E_B = 397.5$ eV) and GaN ($E_b = 396.7$ eV) and their difference ($\Delta E_B = 0.8$ eV) were measured in one experiment, which is important for diagnostics of the GaAs nitrides.

Acknowledgements

The research was supported by BESSY, by the RFBR (08-08-12230-ofi) and by the FAE (Contr. No. P2431).

References

[1] L. A. DeLouise, *J. Vac. Sci. Technol. A* **10** (4), 1637 (1992).
[2] L. A. DeLouise, *J. Vac. Sci. Technol. A* **11** (3), 609 (1993).
[3] J.-D. Hecht, F. Frost *et al*, *J. Appl. Phys.* **90**, 6066 (2001).
[4] Y. G. Li *et al*, *Appl. Surf. Science* **174**, 175 (2001).
[5] I. Bertoti, *Surf. Coat. Tech.* **194**, 151–152 (2002).
[6] S. Meskinis, K. Slapikas *et al*, *Vacuum* **77** (1), 79 (2004).
[7] M. Petravic *et al*, *J. Appl. Phys.* **95**, 5487 (2004).
[8] S. I. Fedoseenko *et al*, *Nucl. Instr. Meth. A* **505**, 718 (2003).
[9] B. L. Henke *et al*, *Atomic Data and Nuclear Data Tables* **54** (2), 181 (1993).
[10] X.-Y. Zhu *et al*, *J. Chem. Phys.* **97** (8), 5856 (1992).
[11] Yu. S. Gordeev *et al*, *Technical Physics* **48**, 885 (2003).
[12] V. M. Mikoushkin, V. V. Bryzgalov *et al*, *Bulletin of the Russian Academy of Sciences: Physics* **72** (5), 609 (2008).
[13] T. D. Veal *et al*, *Appl. Phys. Lett.* **85** (9), 1550 (2004).
[14] S. G. Spruytte *et al*, *J. Appl. Phys.* **89** (8), 4401 (2001).
[15] J. Sik, M. Schubert *et al*, *J. Appl. Phys.* **89** (1), 294 (2001).

18th Int. Symp. "Nanostructures: Physics and Technology"
St Petersburg, Russia, June 21–26, 2010

Plasmon-assisted effects in second-order nonlinear-optical response of core(shell) nanoparticles

T. V. Murzina, I. A. Kolmychek, A. A. Nikulin and O. A. Aktsipetrov
Department of Physics, Moscow State University, 119992 Moscow, Russia

Abstract. Nonlinear-optical properties of core(shell) γ-Fe_2O_3 (Au) nanoparticles in a polymer PMMA matrix are studied. Optical second harmonic generation (SHG) from the composite films in the absense of the external magnetic field is observed in the form of hyper-Rayleigh scattering, i.e. incoherent SHG. On the contrary, application of the magnetic field leads to the appearance of a coherent, purely magnetic SHG component from the composite. A phenomenological model of a magnetic-field induced coherence of the SHG from randomly distributed noncentrosymmetric nanoparticles is discussed.

Introduction

Plasmon-assisted effects in metal nanoparticles are known for quite a long time. Recently, the interest to such structures was increased again and was caused mostly by prospectives of their application is plasmonic devices. At the same time, composite structures containing nanoparticles are of interest from the fundamental point of view, as they can demonstrate new effects absent for the bulky materials. Resonant excitation of the surface plasmon resonance (SPR) in metallic nanostructures leads to the enhancement of the local field factor, thus resulting in the amplification of the nolinear-optical effects, such as second harmonic generation (SHG). Taking into account high sensitivity of the SHG probe to the structural, electronic and magnetic properties of a medium [1], ane can expect the appearance of novel effects in the SHG response from magnetic nanoparticles in the spectral vicinity of the LPR excitation. In this paper, nonlinear-optical response of inhomogeneous array of magnetic plasmonic core(shell) γ-Fe_2O_3 (Au) nanoparticles in polymer matrix is studied using optical second harmonic generation (SHG). It is found that in the absence of the magnetic field, the SHG from the composite structure generates is incoherent, while the application of the magnetic field leads to the appearance of a coherent magnetization-induced SHG component.

1. Experimental

Core(shell) nanoparticles consist of a ferrimagnetic γ-Fe_2O_3 core with the characteristic size of 20-25 nm, covered by the Au shell of about 2–4 nm thick. The methodic of their preparation was described elsewhere [3] The size distribution of nanoparticles is about 10%. Nanoparticles are deposited on glass substrate from their solution in PMMA, with the following heating at 110 °C for the PMMA polymerization. As the result, a solid film of about 3 μm thick is formed, the bulk concentration of randomly distributed nanoparticles being about 30%, so that the average distance between the geometrical centers of adjacent nanoparticles is about 50 nm. It is known that such a fabrication procedure results in the formation of a homogeneous film with a relatively smooth surface.

For the nonlinear-optical experiments, the output of YAG: Nd^{3+} laser with the fundamental wavelength of 1064 nm was used. The second harmonic radiation reflected (scattered) from the sample was spectrally separated by appropriate set of filters and detected by PMT and gated electronics. The PMT and related optics were placed on a computer-controlled honiometer that allowed to measure the signal scattered by the composite film in the polar angle interval from -25° to 65°. Transversal DC magnetic field of 2 kOe could be applied to the samples.

2. Results and discussion

Figure 1 shows the SHG indicatrix, i.e. the dependence of the SHG intensity on the polar angle of scattering measured at a fixed angle of incidence, the angles being counted from the normal direction to the film plane. In the absence of the applied magnetic field the SHG indicatrix demonstrates that the SHG is diffuse and scattered in a wide angular range, with no maximum in the direction of the specular reflection (Fig. 1, open circles). The observed diffuseness and depolarization of the SHG signal are the intrinsic features of the hyper-Rayleigh scattering, i.e. incoherent SHG, and is attributed to incoherent response of core (shell) nanoparticles. The approximation of the experimental dependence within the model developed in [4] allowed to estimate the correlation length of the nonlinear polarization: $L_{\mathrm{corr}} \approx 60$ nm. This value is higher than the average diameter of a single nanoparticle of approximately 30 nm and can be attributed to the existence of aggregates of NPs in the film, as well as isolated particles.

At the same time, application of the DC magnetic field results in the appearance of a maximum of the SHG intensity for the angular range that correspond to the direction of specular reflection (Fig. 1, filled circles). This is a manifestation of the

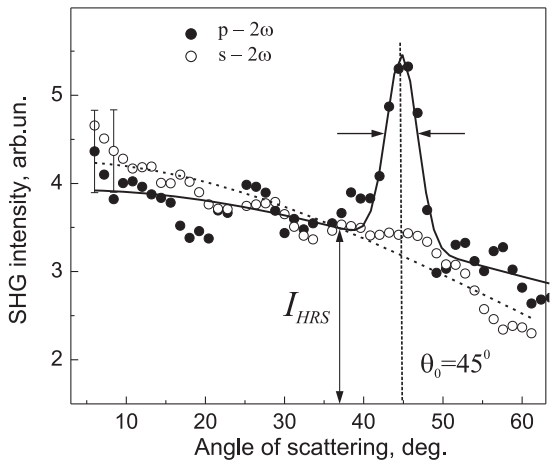

Fig. 1. Scattering indicatrices at the SHG (filled circles) and at the fundamental (open circles) wavelengths. Solid line is the the result of the approximation.

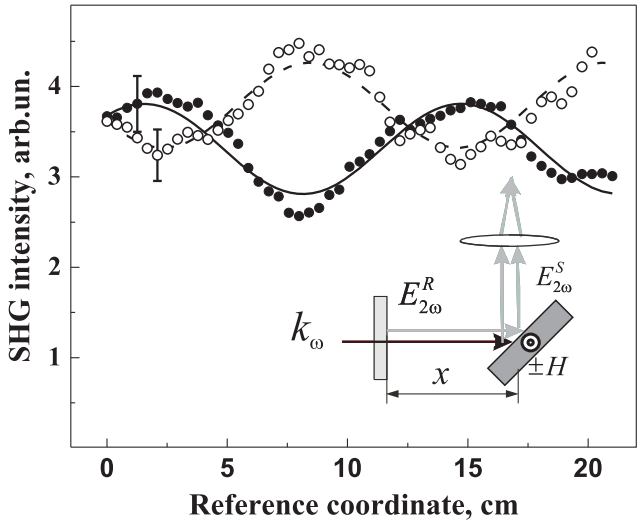

Fig. 2. SHG interferometry patterns measured for the opposite directions of the transversal magnetic field of ±2 kOe. Solid lines are the result of approximation.

appearance of a coherent SHG component.

In order to verify the coherent nature of the specular peak in the scattering indicatrices of SHG intensity in the presense of the magnetic field, SHG interferometry measurements were performed. The interferometry patterns obtained for the opposite directions of the transversal magnetic field are shown in Fig. 2. It is found that a partial coherence of the SH radiation exists, which stems from a pronounced modulation of the SHG interference patterns with a spatial period of approximately 13 cm consistent with that calculated for the dispersion of air at the SHG and the fundamental wavelengths. Moreover, an important result here is that these patterns are shifted in phase to nearly π, that is a distinct indicator that the coherent part of the SH signal is related to purely *odd* in magnetic field SH component.

The measure of the magnetization-induced effect in SHG is the magnetic contrast of the SHG intensity, $\rho_{2\omega} = I_{2\omega}(\vec{M}) - I_{2\omega}(-\vec{M})/I_{2\omega}(\vec{M}) + I_{2\omega}(-\vec{M})$, where $I_{2\omega}(\vec{M})$ and $I_{2\omega}(-\vec{M})$ are the second harmonic intensities measured for the opposite directions of the applied magnetic field. At the same time the SHG magnetic contrast is determined by the ratio of the magnetic to nonmagnetic components of the hyperpolarizability of a single nanoparticle and characterizes its magnetic properties. The SHG magnetic contrast was measured in a wide range of the scattering angle. The typical value of the magnetic contrast is about 0.2, which allows to estimate the ratio of the magnetic to nonmagnetic components of the hyperpolarizability of a single nanoparticle [2] $\hat{\gamma}_M(\vec{M})\hat{\gamma}_0^{-1} \approx 0.1$. Moreover, it is found that a narrow maximum in the magnetic contrast indicatrix appear, that can be associated with the magnetization-induced partial coherence of the SHG response in spatially inhomogeneous structure.

In summary, the appearance of a magnetization-indeuced coherent component of the nonlinear-optical response of inhomogeneous arrays of core(shell) nanoparticles are observed. This SHG component can be discussed in terms of modification of fluctuations of the nonlinear polarization in the structures under study.

References

[1] Y. R. Shen, *The principles of Nonlinear Optics* Wiley, New York, 1984.
[2] O. A. Aktsipetrov *et al*, *J. Opt. Soc. Am. B.* **22** (1), 138 (2005).
[3] P. Gangopadhyay *et al*, *IEEE Trans. Magnetics* **41** (10), 4194 (2005).
[4] A. A. Fedyanin *et al*, *Opt. Lett.* **24**, 1260 (1999).

18th Int. Symp. "Nanostructures: Physics and Technology"
St Petersburg, Russia, June 21–26, 2010

Intervalley scattering of electrons by confined and interface optical phonons in $(GaAs)_m$ $(AlAs)_n$ (001) superlattices

L. N. Nikitina[1], S. N. Grinyaev [1] and V. G. Tyuterev [2]

[1] Tomsk State University, Tomsk State Polytechnical University, [2] Tomsk State Pedagogical University, Tomsk, Russia

Abstract. Intervalley $\Gamma - M$ and $\Gamma - \Sigma$ transitions inside the conduction bands of superlattices $(GaAs)_m(AlAs)_n(001)$ caused by the optical lattice vibrations are investigated by a pseudopotential method and a phenomenological model of the interatomic bonding forces. The analysis of quantum-size effects to the electrons' and phonons' states is carried out, the interpretation of dependences of the deformation potentials versus a thickness of layers in the superlattices is given. It is shown that the intensity of intervalley scattering became maximal when the electrons' and phonon's states are both localized at the same layers of a superlattice. The interface vibrations appear in the superlattices with the layers thick enough ($m, n \geq 4$). They invoke a rather weak electronic transitions inside the higher conduction bands.

Due to multivalley character of conduction bands, mixed character of lattice vibrations and a favorable combination of phonon's and electrons' spectra parameters, a superlattice $(GaAs)_m(AlAs)_n(001)$ is of a great interest for a research and for the technical use of effects produced by the intervalley scattering of electrons by short-wave phonons. This scattering plays the important role in optical and transport properties of nanostructures, in particular, it results in leakage currents in cascade lasers, in a decrease of electrons' mobility inside the channels of transistors, in the occurrence of peculiarities in the hot photoluminescence spectra etc. [1,2]. Owing to the size quantization the electron-phonon interaction in superlattices has a complex character and it is described by the large number of deformation potentials for multiple scattering channels. The most intensive channels of scattering in superlattices are the analogues of $\underline{X}$–$\underline{X}$ transitions in GaAs, AlAs (hereafter the sphalerite's states are underlined). They involve optical vibrations confined inside layers or phonons localized near a heteroboundary.

In the present work the influence of confined and interface optical vibrations to the processes of the intervalley scattering in superlattices $(GaAs)_m(AlAs)_n(001)$ ($m, n = 1, \ldots, 8$) with the thin layers is investigated on the basis of the microscopic description of electron and phonon states.

The intensity of electron intervalley scattering from an initial state $\mu\mathbf{k}$ to the final state $\mu'\mathbf{k}\prime$ (μ, $\mathbf{k}$ label the band number and the wave vector) is determined by a deformation potential according to [3]:

$$\left| D^s_{\mu\mathbf{k},\mu'\mathbf{k}\prime} \right| = \left| \sum_{i,\alpha} \left(\frac{M}{m_\alpha} \right)^{1/2} \left(e^\alpha_i(s,\mathbf{q}) \times d^\alpha_i(\mu\mathbf{k}, \mu'\mathbf{k}\prime) \right) \right|,$$

where m_α and M are masses of α-th ion and the unit cell as a whole correspondingly, $\mathbf{e}^\alpha(s, \mathbf{q})$ is a phonon polarization vector (s — labels a phonon branch), d^α_i is a matrix element between the functions of initial and final states of a gradient of the atom potential, $\mathbf{q} = \mathbf{k}\prime - \mathbf{k}$ is the phonon wave vector. The electron states in superlattices are calculated by a method of pseudopotential [4]. The behavior of the conduction band levels for superlattices with even monolayers numbers m and n is shown at Fig. 1. The behavior of superlattice's levels correlates with those in the corresponding virtual crystals (VC). The tetragonal component of superlattice's potential results in lowering of electronic levels relative to VC levels. The greatest shifts take place for $\Gamma_1^{(1)}$, Γ_3 and M_5 conduction states located inside the $\underline{\Gamma}$ and $\underline{X}$ quantum wells. The M_1, M_4 and $\Gamma_1^{(2)}$ conduction states, being localized at anions, are shifted in much less extent.

The phonon spectra of superlattices were calculated with a phenomenological model of the bonding forces in the mass-defect approach [5].The optical branches at high frequencies $\sim$ 10–12 THz

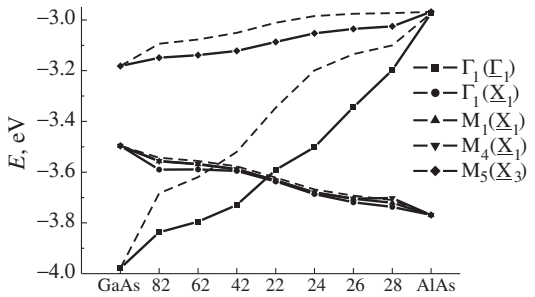

Fig. 1. Levels of a conduction band of superlattices (solid lines and symbols) for Γ, M states and solid solutions (dashed lines) for $\underline{\Gamma}$, $\underline{X}$ states in an absolute scale of energy. The figures indicate quantities of monolayers m, n.

are connected with vibrations of Al atoms. They are separated from other branches by a gap. Optical vibrations which frequencies, lying in the frequency interval of a binary component, are localized inside the corresponding layers of a superlattice.Phonons with symmetry M_5 are located in AlAs layers of a superlattice $(GaAs)_8(AlAs)_2$. They are located in GaAs layers of $(GaAs)_2(AlAs)_8$ (Fig. 2). These vibrations have a mixed LO-TO character. When thickness of layers in superlattices is large ($m, n \geq 4$) then the interface optical phonons ($\mathbf{q} \perp z$) appear in the "cavities" between acoustic and optical branches of phonon's spectrum which involves the vibration of cations near to a heteroboundary. The modules of polarization vectors $\mathbf{e}^\alpha(s, \mathbf{q}_\Sigma)$ for the interface TO-type phonon ($\omega(\mathbf{q}_\Sigma) =$ 7.40 THz) in a superlattice $(GaAs)_6(AlAs)_4$ and the interface LO type phonon ($\omega(\mathbf{q}_\Sigma) = 11.075$ THz) in a superlattice $(GaAs)_4(AlAs)_6$ are shown at Fig. 3. In the mass-defect approach the interface

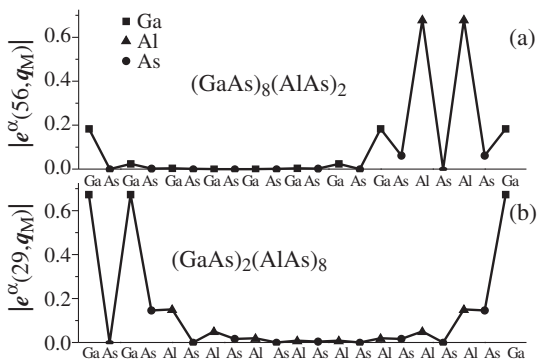

Fig. 2. Module of M_5 — phonon polarization vector $|\mathbf{e}^\alpha(s, \mathbf{q})|$: (a) of a branch with number $s = 56$ and frequency $\omega = 9.700$ THz of a superlattice $(GaAs)_8(AlAs)_2$, (b) of a branch with number $s = 29$ and frequency $\omega = 6.820$ THz of a superlattice $(GaAs)_2(AlAs)_8$.

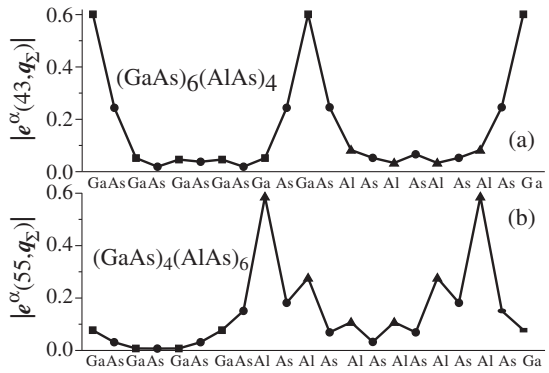

Fig. 3. Module of Σ_1-phonon polarization vector $|\mathbf{e}^{\alpha}(s, \mathbf{q})|$: (a) of a branch with number $s = 43$ and frequency $\omega = 7.402$ THz of a superlattice $(GaAs)_6(AlAs)_4$, (b) of a branch with number $s = 55$ and frequency $\omega = 11.075$ THz of a superlattice $(GaAs)_4(AlAs)_6$.

phonons appear at a wave vector in a middle point of Σ line: $\mathbf{q}_{\Sigma} = (\pi/a_0, 0, 0)$. Note, that other type of interface phonons were found at the edge of a zone Brillouine beyond the bounds of mass-defect approximation taking into account the differences of second-neighbors Ga-Al force constants from those of Ga-Ga and Al-Al [6]. These phonons of TO-type involve the vibrations of atoms Ga along [011] direction mostly, phonons of LO type involve vibrations of atoms Al in a direction [211]. Displacements in TO-type phonons are more localized near to the border due to the greater value of the imaginary part of a phonon wave vector [7].

The calculated deformation potentials for the transitions between Γ and M conduction band valleys in superlattices with a participation of phonons, confined inside the layers, are given in Table 1. The outline of bands and of the intervalley transitions are shown at Fig. 4. In superlattices with only one AlAs monolayer the scattering of electrons by vibrations of Al and Ga has approximately identical intensity due to a weak localization of wave functions of initial and final states in a narrow quantum X-well. The localization of electrons and phonons in AlAs layers enhances with a growth of a thickness of these layers. The vibrations of Al atoms begin to play the main role in $\Gamma - M$ scattering, the value of deformation potential became closer to the potential of $\underline{X}$–$\underline{X}$ scattering in AlAs.

Deformation potentials for $\Gamma - \Sigma$ transitions with the participation of interface and other phonons are given in Table 2. Phonons with low frequencies (4–5 THz) are accompanied by vibrations of atoms in both lattices. Interface phonons cause the intervalley transitions in the higher conduction bands. In a $(GaAs)_6(AlAs)_4$ superlattice the interface vibrations have TO — type vibrations of Ga atoms, in other superlattices they correspond to the LO-type vibrations of Al atoms. All channels of the scattering have a comparable value of

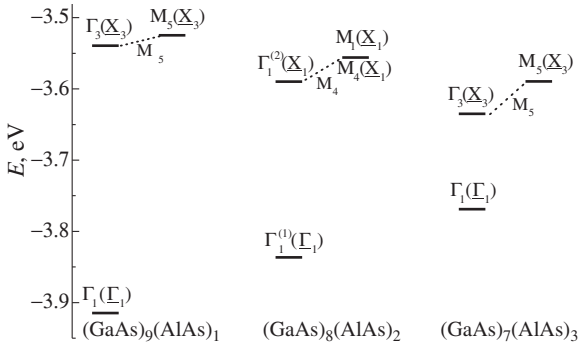

Fig. 4. Conduction band levels in superlattices with the thin AlAs layers (in the absolute energy scale). The VC states are specified in brackets. Dashed lines show the intervalley transitions with the participation of phonons confined in AlAs layers.

Table 1. Deformation potentials $|D^s_{\mu\Gamma,\mu' M}|$ for $\Gamma - M$ electron transitions in the conduction bands of superlattices $(GaAs)_m(AlAs)_n$ with thin AlAs layers. In brackets the frequencies (THz) are given of M phonons is specified. The bold font indicates the potentials due to the optical phonons confined in AlAs layers, other potentials relate to vibrations of Ga atoms

Superlattice	$m = 9$ $n = 1$	$m = 8$ $n = 2$	$m = 7$ $n = 3$
Transition,	$\Gamma_3 - M_5$	$\Gamma_1^{(2)} - M_4$	$\Gamma_3 - M_5$
energy, eV	0.014	0.032	0.046
$\lvert D^s_{\mu\Gamma,\mu' M}\rvert$, eV/Å	2.95(6.52)	2.04(5.61)	**5.30**(9.06)
	4.07(6.78)	1.46(6.26)	**7.98**(10.52)
	4.28(10.61)	1.69(6.99)	**4.71**(11.72)
		1.05(7.50)	
		9.75(9.70)	

Table 2. Deformation potentials $|D^s_{\mu\Gamma,\mu' M}|$ for $\Gamma - \Sigma$ electron transitions in the conduction band of superlattices $(GaAs)_m(AlAs)_n$. In brackets the phonon frequencies are given in THz. The bold font indicates potentials due to the interface vibrations.

Superlattice	$m = 6$ $n = 4$	$m = 8$ $n = 8$	$m = 4$ $n = 6$
Transition,	$\Gamma_1^{(2)} - \Sigma_2$	$\Gamma_1^{(1)} - \Sigma_1$	$\Gamma_1^{(1)} - \Sigma_1$
energy, eV	1.56	1.65	1.67
$\lvert D^s_{\mu\Gamma,\mu'\Sigma}\rvert$, eV/Å	1.60(4.83)	1.54(8.89)	1.46(4.99)
	1.46(5.19)	1.02(10.65)	2.09(5.41)
	1.20(5.82)	**1.52**(11.07)	4.14(9.62)
	1.04(6.95)		1.02(10.30)
	1.28(7.41)		1.73(10.63)
	2.77(9.16)		**1.90**(11.07)
	2.67(10.20)		2.45(11.56)
	2.91(11.09)		
	1.23(11.79)		

the intensity.

In a summary, in this work the deformation potentials are obtained for $\Gamma - M$ and $\Gamma - \Sigma$ intervalley transitions in a conduction band of superlattices $(GaAs)_m(AlAs)_n(001)$ with the participation of optical M-phonons confined inside the binary layers and optical Σ-phonons localized near the heteroboundary. Is shown that the intensity of $\Gamma - M$ transitions increases with a growth of a fraction of Al due to amplification of electronic density in quantum X wells. Interface phonons arise in superlattices with the layers thick enough. The $\Gamma - \Sigma$ transitions induced by them in the higher conduction bands have a rather weak intensity and are almost independent on a layers' thickness. The deformation potentials obtained here can be used for a modeling and interpretation of transport and optical properties of GaAs/AlAs(001) superlattices and heterostructures.

References

[1] X. Gao, D. Botez, I. Knezevic, *Appl. Phys. Lett.* **89**, 19191119 (2006).

[2] J. Mc Tavish, Z. Ikonic, D. Indjin, P. Harrison, *Acta Physica Polonica (A)* **113**, 891 (2008).

[3] S. N. Grinyaev, G. F. Karavaev, V. G. Tyuterev, *Physica B* **228**, 319 (1996).

[4] K. A. Mader, A. Zunger, *Phys. Rev. B* **40**, 10391 (1989).

[5] L. N. Nikitina, S. N. Grinyaev, V. G. Tyuterev, *Phys. Solid State* **48**, 120 (2006).

[6] T. Tsuchiya, H. Akera, and T. Ando, *Phys. Rev. B* **39**, 6025 (1988).

[7] C. Colvard, T. A. Gant, M. V. Klein, R. Merlin, R. Fischer, H. Morkoc, A. C. Gossard, *Phys. Rev. B* **31**, 2080 (1985).

18th Int. Symp. "Nanostructures: Physics and Technology"
St Petersburg, Russia, June 21–26, 2010

Analysis of both electron and hole subsystems in single QW by CV-profiling and self-consistent modelling

A. N. Petrovskaya and V. I. Zubkov
St Petersburg Electrotechnical University "LETI", 197376 St Petersburg, Russia

Abstract. Capacitance-voltage profiles of n-n-heterostructures with strained quantum wells $In_xGa_{1-x}As/GaAs$ have been investigated in a wide range of temperatures, test signal frequencies and biases. By fitting simulated C-V characteristics on the basis of self-consistent numerical solution of Poisson and Schrödinger equations to the experimental C-V profiles the actual lineup of both conduction and valence band edges as well as the energy spectrum in the electron and hole subsystems are derived. Effect of well width, alloy composition and dopant concentration on energies and probability of band-to-band transitions in QWs are studied.

Introduction

Among a number of various research tools used for investigations of modern semiconductor nanoheterostructures, the non-destructive electrical methods of admittance spectro-scopy (capacitance-voltage spectroscopy, temperature conductance and capacitance spectroscopy, deep level transient spectroscopy) are been efficiently applied nowadays [1].

Admittance methods cover measurements of capacitance and conductance of a structure in various modes at changing applied bias, temperature and test signal value and frequency. Thus, it is appeared possible to obtain a lot of valuable information about the electronic distribution along the heterostructure and about the energy behaviors of states inside the quantum well and in the forbidden gap.

We show here how the capacitance-voltage measurements on n-type heterostructure with quantum well (QW) together with the self-consistent simulation of Hartree potential make it possible performing a comprehensive analysis of both electron and hole subsystems.

1. Samples and measurements

The investigated samples are n-GaAs/$In_xGa_{1-x}As$/GaAs isotype heterostructures with strained single QW studied earlier in [1,2,3]. They were grown by metal-organic chemical vapor deposition (MOCVD) at temperatures 650 and 770 °C on n^+-GaAs substrate. The QW widths were 6.0 . . . 9.5 nm, and In content in QW $x = 0.065 \ldots 0.29$.

The admittance measurements were carried out using original automated measurement system, consisted of LCR-meter Agilent E4980A, closed cycle helium cryostat Janis CCS 200/204N, temperature controller LakeShore 331S and vacuum station Pfeiffer [4]. The characteristics of the computer-controlled admittance system: temperature range from 6 to 320 K with accuracy 0.1 K; frequency range from 20 Hz to 2 MHz; bias from −40 to 40 V. The wide temperature range of measurements allowed us to make comprehensive analysis of the samples.

2. Modelling capacitance-voltage characteristics

Numerical modelling the capacitance-voltage characteristics (C-V) of semiconductor heterostructures with single quantum wells proved to be an effective tool for determination of the heterostructure fundamental parameters, such as energy band lineup, band offsets, energy of bound states etc. [1,2,3,5]. The basis of a quantum well C-V simulation is a self-consistent numerical calculation of Poisson and Schrödinger equations [1,3], which is been followed by fitting the simulated carrier concentration profile to the experimental one. The output is the actual lineup of conduction band (CB) bottom and the corresponding band offset [1,2,3,5].

In our simulations the effect of elastic strains on the energy spectrum of QW heterostructures was taken into account, which arises because of the difference in lattice constants during pseudomorphical growth of InGaAs thin epitaxial layer on GaAs substrate. The resulting unit cell distortion leads to significant amendments in all energy characteristics of the strained layer: increasing the band gap, alteration of band offsets and splitting of valence band (VB) [6,7]. Note, that the valence band splitting in the investigated range of InGaAs alloy compositions ($x > 0.2$) exceeds the VB offset, so the calculations can be limited only to heavy-hole subband.

To find the quantized level energies and corresponding wave functions for single QW, the system of one-dimensional Schrödinger equations for valence and conduction bands were solved numerically in the effective mass approximation. The size of the computational matrix depends on the number of points in the mesh and is determined by the conflicting demands of accuracy and calculation speed. Obviously, calculation of a heterostructure with a QW needs using a non-uniform mesh. However, it entails destruction of the matrix symmetry. We do implement in our calculations the method of solving the Schrödinger equation using variegated step by adding an extra term in the equation and using additional matrix transformations [8]. The software was written in the graphical programming environment LabVIEW in conjunction with MatLab.

Determination of bound states energy and the corresponding wave functions for both the conduction and valence bands has been executed in one computing cycle. In Fig. 1 the results of quantization level and corresponding wave functions calculations derived from the self-consistent solution of Poisson and Schrödinger equations are shown together with the computed lineups of both energy bands.

The accumulation of large amount of charge carriers in the QW and strong Coulomb repulsion leads to the energy profile of the CB be significantly modified in comparison with a rectangular QW approximation, it forces the change of the position of bound levels.

By fitting to the experimental C-V curve the CB offset and the bottom profile of the conduction band are been determined.

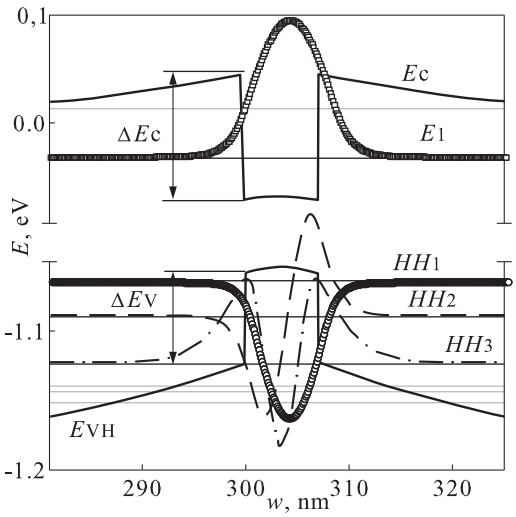

Fig. 1. Calculated quantized levels and wave functions in QW for conduction and valence bands (heavy hole subband). Well width is 7.2 nm, alloy composition $x_{\mathrm{In}} = 0.23$. CB offset is 170 meV, VB offset — 64 meV, $U = 0$ V and $T = 300$ K.

Then, based on the similarity of CB and VB lineups, the actual profile of the VB top can be determined.

3. Energy and probability of interband transitions

In proposed procedure of self-consistent solution, the bound state energies and wave functions are calculated for both conduction and valence bands in one computing cycle, including the presence of an external electric field. The calculations are been fitted to the experimental data. This allows us to estimate the energies of band-to-band transitions, as well as the overlap integral of wave functions, the square of which is directly proportional to the transition probability:

$$\int \psi^*_{e,n}(x)\psi_{h,n'}(x)dx = P_{n,n'}, \qquad (1)$$

where $\psi^*_{e,n}(x)$ is the wave function of n-state in the CB, $\psi_{h,n'}(x)$ is the wave function of n'-state in the VB, $P_{n,n'}$ is the overlap integral of the wave functions.

Thus, for the quantum well shown in Fig. 1 the derived overlap integral for E1-HH1 transition is 0.96, whereas for E1-HH2 transition is only 0.002 (HH1,2 — the first (second) level in the QW of VB for heavy holes) that fully correlates with the selection rules for even and odd states.

Then, knowing the QW level energies for conduction and valence bands, one can estimate the energies of band-to-band transitions. In Fig. 2 the energy of E1-HH1 interband transition is presented, calculated for the range of well widths and QW alloy compositions.

Increase in the well's width and depth makes it possible obtaining the smaller energy of interband transition E1-HH1. However, the depth of the well is limited by the utmost composition of pseudomorphical layer growth ($x_{\mathrm{In}} = 0.34$ for the investigated alloy). On the other hand, there is a limitation for the well width by the critical thickness of the pseudomorphical layer. For $In_{0.23}Ga_{0.77}As$ on GaAs the critical thickness is about 15 nm. The dependence of the interband transition energy E1-HH1 on the width of the active area shows saturation for wells wider than 11 nm. This is due to the appearance of

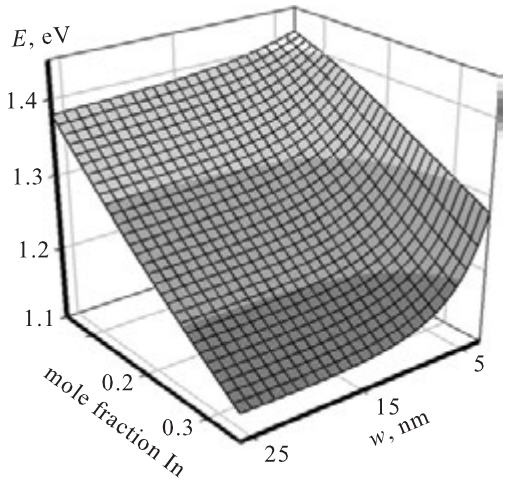

Fig. 2. Energy of band-to-band transition E1-HH1 in the range of QW widths and alloy compositions. Dopant concentration in barriers $n = 6.55 \times 10^{16}$ cm^{-3}.

the second bound level in the CB well, which shifts the energy of the first level [5].

What is worth, the carrier concentration in adjacent to the active area layers also affects significantly the value of the transition energy E1-HH1 [5]. This is only a consequence of self-consistent calculation of the Hartree potential. The rectangular QW approximation ignores the affect of the concentration in the barriers at all.

It can be concluded that the optimal QW width for given heterostructures lies within the range 8 to 11 nm, when the transition probability gets maximum and there is no second level in the CB well. To alter the necessary transition energy in this case one can vary not only the alloy composition but also the dopant concentration in barriers.

Thus, for the first time it was shown that combining the capacitance-voltage profiling of an isotype heterostructure containing a single quantum well together with numerical self-consistent simulation, one can find out both the properties of electron and hole subsystems. This opens the possibility to optimize parameters of the heterostructures before the fabrication process.

Acknowledgements

This work has been supported in parts by The Ministry of education and science (State contracts No. 02.740.11.0213 and П890) and the analytical departmental target program "Development of the Scientific Potential of Higher Schools for 2009–2010" (project No. 2.1.1/2503).

References

[1] V. I. Zubkov, *Diagnostics of Semiconductor Nanoheterostructures by Methods of Admittance Spectroscopy.* St Petersburg, 2007 [in Russian].
[2] V. I. Zubkov, *Semiconductors* **41**, 320 (2007).
[3] V. I. Zubkov *et al*, *Phys. Rev. B* **70**, 312 (2004).
[4] O. V. Kucherova *et al*, *Semiconductors* **44**, 352 (2010).
[5] A. N. Petrovskaya *et al*, *Semiconductors* **43**, 1328 (2009).
[6] P. S. Zory *et al*, *Quantum well lasers.* New Jersey: Academic Press, 1993.
[7] C. G. Van de Walle *et al*, *Phys. Rev. B* **39**, 1871 (1989).
[8] I.-H. Tan *et al*, *J. Appl. Phys.* **68**, 4071 (1990).

18th Int. Symp. "Nanostructures: Physics and Technology"
St Petersburg, Russia, June 21–26, 2010

Photoluminescent studies of the GaAs quantum dots embedded into the AlGaAs nanowires

V. N. Kats[1], V. P. Kochereshko[1], *A. V. Platonov*[1], T. V Chizhova[1], G. E. Cirlin[1,2], A. D. Bouravleuv[1,2], Yu. B. Samsonenko[1,2], J. Bleuse[3] and H. Mariette[3]

[1] Ioffe Physical-Technical Institute, St Petersburg, Russia
[2] St Petersburg Academic University, St Petersburg, Russia
[3] CEA-CNRS group Nanophysique et Semiconducteurs, CEA, INAC, SP2M, and Institut Nèel, 17 rue des Martyrs, F-38054 Grenoble, France

Abstract. We report on the photoluminescence (PL) characterization of GaAs quantum dots embedded into AlGaAs nanowires (NWs).

AlGaAs/GaAs NWs were grown on GaAs (111)B semi-insulating substrate in an MBE system equipped with solid sources supplying Ga and Al atoms, and As source to produce tetramers. Substrate surface was first deoxidized at ∼630 °C, then a 100 nm thick GaAs buffer layer was grown at 600 °C to achieve atomically flat surface. A total amount of Au equivalent to 1 nm layer was deposited without V-group flux at 550 °C using an Au effusion cell installed directly into the III–V growth chamber followed by a 1 min waiting time to achieve better homogeneity of the droplets. The substrate temperature was then set to the desired value for the growth (550 or 580 °C). This procedure results in the formation of droplets containing Au alloyed with the substrate constituents. The typical distribution of droplet sizes ranges between 40 and 50 nm. The NW growth was initiated by opening simultaneously the Al, Ga and As sources. For the samples the nominal growth rates, i.e. the growth rate on a clean and Au-free surface, were fixed at 1 monolayer (ML)/s for GaAs and AlAs 0.4 ML/s. Resulting AlxGa1-xAs growth rate was 1.4 ML/s corresponded to the Al content in the solid solution $x = 0.285$ for a planar layer.

For AlGaAs/GaAs/AlGaAs heterostructure formation, the growth started with 15 min of AlGaAs, then the Al source was closed for 5 s in order to form an GaAs segment in each NW. Then the growth of AlGaAs was performed again to produce core — shell structure. The growth was completed with 2 min deposition of GaAs at 530 °C to avoid possible oxidation of AlGaAs shell layer. We did not perform any growth interruption at the heterointerfaces. SEM and TEM characterizations were performed before the optical measurements.

We have studied the PL spectra on the set of the samples for the temperature range from 5 up to 250 K. The power dependence was also analyzed. The samples were excited by either doubled Nd:YAG laser or by doubled pulsed Ti:Sa laser. We investigated both the NWs ensemble and single NW. The PL spectra taken from the NWs ensembles demonstrated in general a very broad band in the range of 625–760 nm with irresolvable fine structure. The approach was mainly used by us for power and temperature dependence.

The mikro-PL approach was used to obtain the information on the available optical transition in the given single NW. To perform PL measurement on the single NW located on the substrate we used a microscope to focus the laser beam and collect the PL signal. The size of the laser spot we could achieve in our setup was about 1.5 μm, however the spatially resolved PL image demonstrated not more then three bright spots within the excited area with the diffraction limit size each. Assuming that every bright spot corresponds to the single NW we could select the signal from the individual one by using nanopositioner and crossed slits on the microscope output.

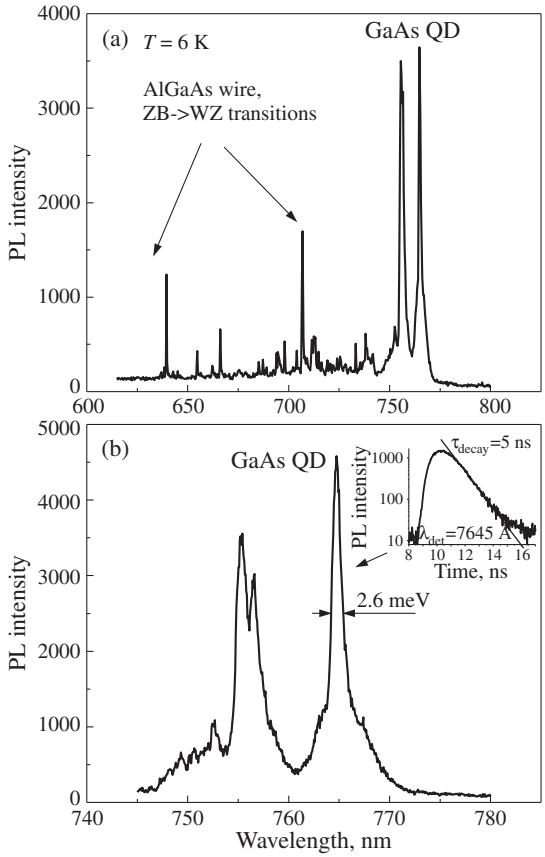

Fig. 1. Photoluminescence spectrum from the GaAs/AlGaAs QD/NW core-shell structure. Inset: Time dependence of the PL maxima of the lowest energy QD peak.

We found that mikro-PL spectra have a strong dependence on the excitation power density. Namely most of the observed optical transitions can be easily saturated and simultaneously additional lines appear in the PL spectra forming finally at high excitation a very wide PL band with extremely complex structure in the range of 625–760 nm.

At the low excitation power density PL spectra of the single NW demonstrate a structure presented on the Fig. 1a. The lines

in the range of 625–720 nm are related to the optical transitions in the AlGaAs NW and their width was limited by our resolution being below 0.2 meV.

Observation of the large amount of the optical transitions in the range of 625–720 from the single NW can be explained by taking into account the effect of the crystalline phase transition which is known to be existed in the system [1,2]. Namely in the AlGaAs nanowire the crystalline structure can switch spontaneously from zinc-blende (ZB) to the hexagonal wurtzite (WZ) structure. Since there is a difference for the band gap width for ZB and WZ AlGaAs compound the crystalline structure alternation leads to the formation of the effective superlattice along the growth direction and therefore the carries become quantized along the axis. That is the carries states are transformed into zero-dimensional instead of the one-dimensional for the case of the homogenous wire. It is clear that the quantization energy depends on the thickness of the layer with the same crystalline structure, since the thickness was uncontrollable matter in our setup we obtain the distribution for the carriers state energy. It is worth to mention that by varying growth conditions we could produce the samples that demonstrate much narrower PL band. The later probably means a cancellation of the crystalline phase transformation. However the further consideration is required to make the point clear.

We could obtain also the PL signal from the GaAs QD embedded in the NW. It can be seen in the range 750–760 nm on the Fig. 1 and presented in more details on the Fig. 1b The QD PL lines width was found to be 2.6 meV which is well above the our spectral resolution. The later probably reflects the states filling effect which is achieved at the given excitation density since the excitation was pulsed in the case.

We also performed the time resolved PL measurement with use of the fast EPD as a detector and the doubled pulsed Ti:Sa laser for the excitation. The typical transient is presented on the inset of the Fig. 1b. It demonstrates mono exponential decay that makes possible to measure the PL decay times for both AlGaAs wire and GaAs QD PL bands. In the first case it appeared to be in a range of the 20 ns, while for the second it was about 5 ns. The given decay times are pretty long in comparison to the radiative ones and therefore correspond to the relaxation and capture times.

Acknowledgements

This work has been supported in part by the international RFBR-CNRS grant.

References

[1] H. Shtrikman, R. Popovitz-Biro, A. Kretinin, and Moty Heiblum, *Nano Lett.* **9** (1), 215–219 (2009).

[2] V. G. Dubrovskii, N. V. Sibirev, G. E. Cirlin, A. D. Bouravleuv, Yu. B. Samsonenko, D. L. Dheeraj, H. L. Zhou, C. Sartel, J. C. Harmand, G. Patriarche, and F. Glas, *Phys. Rev. B* **80**, 205305 (2009).

18th Int. Symp. "Nanostructures: Physics and Technology"
St Petersburg, Russia, June 21–26, 2010

Nonlinear growth of GaAs nanowires: theory and experiment

M. A. Timofeeva[1], N. V. Sibirev[1] and V. G. Dubrovskii[1,2]

[1] St Petersburg Academic University, St Petersburg, Russia
[2] Ioffe Physical-Technical Institute, St Petersburg, Russia

Abstract. A kinetic model of growth of a semiconductor nanowires by the vapor-liquid-solid mechanism via adsorption from a gaseous medium and surface diffusion of adatoms is developed. A nonlinear equation for the rate of growth of a nanowires in the steady-state condition is derived with inclusion of the Gibbs–Thomson effect in the droplet. It is shown that, depending on the conditions of deposition, the nanowire radius, and the initial nanowires's length and temperature, six different modes of growth are possible, which is due to the nonlinearity of the equation of growth. At specified conditions of deposition, the nanowire length either infinitely increases or tends to a certain finite limit. Theory is compared to experimental data regarding the MBE growth of GaAs nanowires with Au catalyst.

1. Introduction

Semiconductor nanowires (NWs) are anisotropic nanobjects that are 10–100 nm in transverse dimensions and are grown orthogonal to the substrate surface. NWs have some unique properties that makes them promising for application in nanophotonic, nanoelectronic, nanosensing devices. The morphological properties of NWs arrays (the length, shape, and surface density) depend on the type of treatment of the activated surface and on the process of growth. NWs are grown mostly by molecular beam epitaxy (MBE) or vapor phase epitaxy (VPE) on surfaces activated with metal droplets of the catalyst of growth (e.g., Au) [1,2,3]. Fundamental studies of NW growth and physical properties are of major interest. The purpose of this study was to develop a kinetic model of growth of NWs and to analyze the problem of the maximal NWs length with consideration for various nonlinear effects [4].

2. Theoretical model

The kinetic model formulated below for the MBE growth of NWs takes into account the following processes:

- adsorption at the droplet surface with the intensity J ($J\cos\alpha = V/\Omega_s$ is the flux density for the substance flux to the surface, α is the angle of incidence of the molecular beam, V is the effective deposition rate, and Ω_s is the atomic volume in the solid phase);
- desorption from the droplet surface;
- growth of the inactivated surface;
- diffusion flux of adatoms towards the NWs top from the substrate surface and NWs sidewalls with the flux density $j_{\mathrm{diff(L)}}$.

We developed base kinetic model of nanowires growth in consideration of Gibbs–Thomson (GT) effect and various nonlinear effects of diffusion on the sidewalls. In frame of this model, we obtained kinetic equation of stationary NW growth [5]:

$$\frac{dL}{dH} = A + \frac{B\,U\left(\frac{L}{\lambda_s}\right)}{U'\left(\frac{L}{\lambda_s}\right) + 1},$$

where L is the NW length, is the effective thickness of the deposited material at the time point t, and λ_s is the diffusion length on the sidewalls, coefficient A — describes adsorption-desorption processes on the drop surface, R-depended coefficients B and C characterizes the diffusion flux from the sidewalls and substrate surface respectively. The function $U(z)$ is given by:

$$U(z) = \sin(z) + \nu\delta \times \cos(z),$$

where $\nu\delta$ depends on the properties of materials.

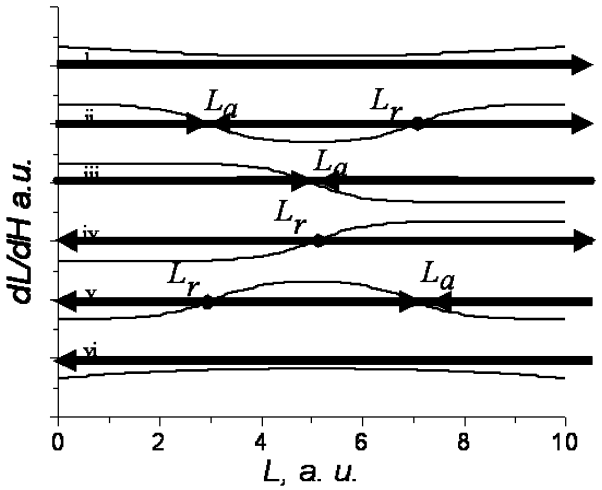

Fig. 1. Modes of growth of NWs, L_a is the attractive critical point, and L_r is the repulsive critical point.

3. Results

As a result of theoretical studies we can distinguish six possible modes of the growth of NWs (see Fig. 1 for a qualitive illustration) [4]:

(I) NWs of any initial length grow infinitely (unlimited growth).
(II) Short NWs with $L_0 < L_a$ attain the limiting length L_a and cease to grow. The suffisiently long NWs with $L_0 > L_r$ grow without limit. The NWs, whose initial length is between L_a and L_r, evaporate until they attain the length L_a (semi-limited Growth).
(III) NWs are formed with length L_a under the all droplets (limited growth).
(IV) The short NWs with $L_0 < L_r$ disappear, and the long NWs, with $L_0 > L_r$ grow without limit (continuing growth).

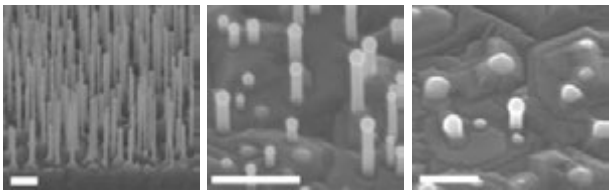

(a) (b) (c)

Fig. 2. GaAs NWs after in situ anneal under As_4. Scale bars represent 200 nm. (a) Reference sample without annealing, (b) 4 min anneal, (c) 5 min anneal.

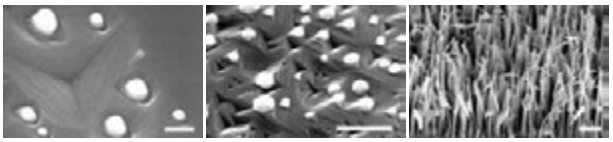

(a) (b) (c)

Fig. 3. Samples GaAs grown with a low temperature (530 °C) step of variable duration t, followed by a hight temperature step (630 °C) of 15 min. Scale bar is 400 nm. (a) $t = 0$, (b) $t = 1.5$ min, (c) $t = 15$ min.

(V) The short NWs with $L_0 < L_r$ disappear. The length of the NWs with $L_0 > L_r$ asymptotically tends to L_a (averaging growth).

(VI) The last case, the formation of NWs is impossible; i.e., no NWs grow from droplets on the substrate surface, and the NWs available on the surface break down (disappearance of NWs).

For each listed type of NWs growth we obtained bounds for radius where such type of growth can be observed, since coefficients A, B and C are the functions of NWs radius R and substrate temperature T. Summarizing on all our results we constructed growth type classification based on the main growth parameters: surface temperature, NWs radius and initial length.

4. Theory and experiment

We have developed non-linear model of NW formation and have shown that in the diffusion induced mode there are six possible scenarios of NW growth. we found experimental evidence of scenarios II and IV in the case of Au-assisted MBE of GaAs NWs on GaAs(111)B substrates. Scenario II is illustrated in Fig. 2.

Scenario IV is illustrated in Fig. 3 reveals that NWs do not grow at this relativity high temperature and the segregation of the Au particles at the substrate surface is observed [6].

Acknowledgements

This study was supported by the Federal Agency on Science and Innovations, the Russian Foundation for Basic Research. M. A. Timofeeva acknowledges the support of the "Dynasty" Foundation.

References

[1] K. Hiruma, M. Yazawa, T. Katsuyma, K. Ogawa, K. Haraguchi, and M. Koguchi, *J. Appl. Phys.* **77**, 447 (1995).

[2] Y. Cui and C. M. Lieber, *Science* **91**, 851 (2001).

[3] B. J. Ohlsson, M. T. Bjork, A. I. Persson, C. Thelander, L. R. Wallenberg, M. H. Magnusson, K. Deppert and L. Samuelson, *Physica E 13* **13**, 1126 (2002).

[4] V. G. Dubrovskii, N. V. Sibirev, and M. A. Timofeeva, *Semiconductors* **43**, 1267 (2009).

[5] V. G. Dubrovskii, N. V. Sibirev, G. E. Cirlin, A. D. Bouravleuv, Yu. B. Samsonenko, D. L. Dheeraj, H. L. Zhou, C. Sartel, J. C. Harmand, G. Patriarche, and F. Glas , *Phys. Rev B* **80**, 205305 (2009).

[6] M. Tchernycheva, G. E. Cirlin, G. Patriarche, L. Travers, V. Zwiller, U. Perinetti, and J. C. Harmand, *Nano Lett* **7**, 1500 (2007).

18th Int. Symp. "Nanostructures: Physics and Technology"
St Petersburg, Russia, June 21–26, 2010

Size quantization in graphene nanoribbon

I. V. Zagorodnev and V. A. Volkov

V. A. Kotel'nikov Institute of Radio Engineering and Electronics of RAS, Mokhovaya 11-7, Moscow, 125009, Russia

Abstract. Analytical theory of band structure of graphene nanoribbon is proposed taking into account size quantization and edge states. We solve the Weyl–Dirac equation with boundary conditions that were derived by authors earlier without specifying the microscopic structure of the translationary invariant boundary and neglecting inter-valley scattering. A simple dispersion equation that describes electron energy in one-dimensional subband is derived and solved. The resulting spectrum depends on two boundary parameters, each of that characterizes one of the boundaries of a nanoribbon. The value of these parameters can be found from comparison with the results obtained in tight-binding models or in ab initio calculations. Depending on the value of these parameters nanoribbon can be either conductor or insulator.

Electrons in graphene behave as if they are massless "relativistic" particles near two nonequivalent points in the first Brillouin zone. Such band structure can be described by an equation, which is formally equivalent to a couple of the 2D Weyl equations:

$$\tau\vec{\sigma}\,\vec{p}\psi_\tau = E_\tau\psi_\tau\,, \qquad (1)$$

where $\vec{\sigma} = (\sigma_1, \sigma_2, \sigma_3)$ is the vector of Pauli matrices in the standard representation acting on the envelope wave function $\psi_\tau = (\psi_{1\tau}, \psi_{2\tau})^T$, $\vec{p} = (p_x, p_y, 0)$ is the two-dimensional momentum operator. Band structure of graphene has two valleys which are numbered by $\tau = \pm 1$. The centers of valleys are being spaced by vector $2\vec{k}_0$ in Brillouin zone. The Fermi velocity (or group velocity of low-energy excitations) and the Planck's constant are set equal to unity.

To describe size quantization in a nanoribbon it is necessary to derive boundary conditions (BCs) for envelope wave functions. The BCs were derived in our previous articles [1,2]. We discussed translationary invariant edges. Neglecting inter-valley scattering on the boundary (S) and assuming that spatial period of the edge is smaller than the electron wavelength we found effective BCs:

$$\left(\psi_{1\tau} + ia^\tau e^{-i\alpha}\psi_{2\tau}\right)\Big|_S = 0\,, \qquad (2)$$

a is a real function defined at the boundary. The vector normal to the boundary is $(\cos\alpha, \sin\alpha)$. For edge states (ESs) or Tamm states of semi-infinite sample with the parameter a being constant at the boundary we found the dispersion relation:

$$E_\tau(k_y) = \frac{2ak_y\tau}{a^2+1}, \quad k_y\left(1 - a^{2\tau}\right) > 0\,, \qquad (3)$$

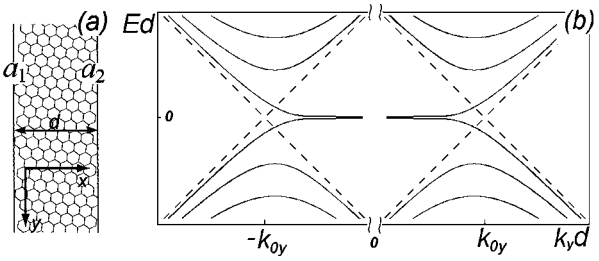

Fig. 1. (a) The geometry of graphene nanoribbon, (b) 1D subbands of size quantization $E(k_y)$ for the nanoribbon with zigzag-like model edges ($a_1 = 1/a_2 = 0$). $\pm k_{0y} = \pm k_0 \sin\alpha$ is the projections of the valley centers on the y-axis. Dotted lines denote borders of volume spectrum, $|E| = |k_y|$.

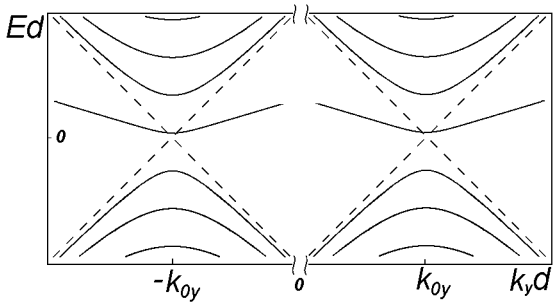

Fig. 2. Subbands $E(k_y)$ for graphene nanoribbon with symmetrical ($a_1 = a_2 = 0.15$) edges.

where k_y is the momentum along the linear boundary. The ESs band is represented with the rays beginning at the center of each valley and located in one of the quadrants of $E(k_y)$ plane, depending on the parameter a.

This work considers graphene nanoribbon (GNR) with width d. It is supposed that edges of the ribbon has different type, i.e. they are characterized by different values of the parameter a, but the value of it is constant on the left (right) edge and equals $a_1(a_2)$, Fig. 1a. We solve the equation (1) for $\tau = +1$ with BCs like (2). For solutions in the form of waves $\psi \propto e^{ik_x x + ik_y y}$ we derive the dispersion equation:

$$(1 - a_1a_2)E + (a_2 - a_1)k_y - (a_1 + a_2)k_x \cot k_x d = 0\,, \quad (4)$$

with $E^2 = k_y^2 + k_x^2$. Real k_x corresponds to a size quantization of the continuous spectrum. If $|E| < |k_y|$, k_x becomes imaginary, which corresponds to localized states near each edge. If $k_y \to \infty$ these states turn into the ESs for semi-infinite graphene with dispersion relation $E = 2a_1k_y/(1 + a_1^2)$ and $E = 2a_2k_y/(1 + a_2^2)$ on the left and the right edge respectively. Using time reversal symmetry we can obtain the size-quantized spectrum for the other valley ($\tau = -1$). The entire band structure must be invariant under change of k_y on $-k_y$.

Solutions for symmetrical ($a_1 = a_2$) and asymmetrical ($a_1 \neq a_2$) edges are shown in Figs. 2,3. Similar spectra near Fermi level were obtained by more complicated methods in [3–11].

Next we will discuss and compare electronic properties of GNRs with other theoretical models. In literature the tight-binding approximation (TBA) for armchair and zigzag edges are usually considered and the BCs are taken from the simplest consideration, that is however not well founded. GNR

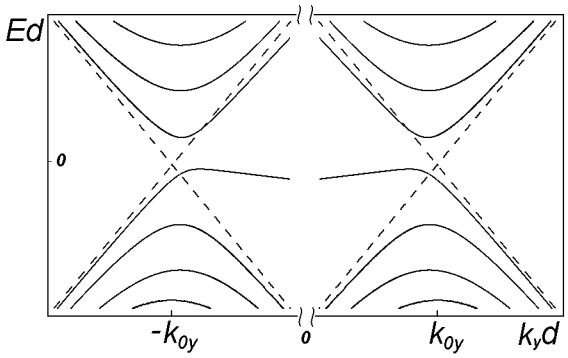

Fig. 3. Subbands $E(k_y)$ for graphene nanoribbon with asymmetrical ($a_1 = 0.6$, $a_2 = 20$) edges.

was first considered in [3] in the nearest-neighbor TBA for a certain microscopic type of its edges. It was shown that electronic properties of GNRs exhibit a strong dependence on the orientation of it edges. For zigzag edges the dispersionless ES spectrum was obtained. We can obtain this spectrum if $a_1 = 1/a_2 = 0$, Fig. 1b. In this case the BCs for the four-component envelope wave function are in agreement with [4]. According to [4] armchair edge corresponds to BCs with intervalley terms. Within our work we can not discuss this BCs. Therefore we discuss zigzag edges in details further.

For zigzag edges next nearest-neighbor TBA yield dispersive ES [6,7]. We can obtain this spectrum $E(k_y)$ near Fermi level if $a_1 \approx 0.1$, $a_2 \approx 1/0.1$ for [6] or $a_1 \approx -0.1$, $a_2 \approx -1/0.1$ for [7]. It depends on the ratio of the next nearest hopping integral (t') and the nearest one (t'). Namely $2a_1/(1 + a_1^2) = 2t'/t$ or $2a_1/(1 + a_1^2) = -2t'/t$. In these cases the ESs band are doubly degenerate.

Bearded and cove edges was discussed in the nearest-neighbor TBA by Wakabayashi [8]. We can obtain its results if $a_2 = 1/a_1 = 0$ and $a_1 = 1/a_2 = 0$ respectively.

Sasaki also considered bearded or "Klein" edge in the next nearest-neighbor TBA [9]. We can obtain this spectrum if $a_1 \approx 1/0.1$, $a_2 \approx -0.1$.

In [10] was shown that the extra edge states can be created by the decoration of edge layers. In this work was obtained similar spectra as our Fig. 2 and Fig. 3.

Our approach can be use if graphene edge passivated. There is possibility that chemical elements would interact with the edge atoms and modify properties of the edge. First-principles calculations for H-terminated zigzag ribbons confirmed the results [3]. A theoretical study of the GNR with straight edge structures different edge passivation was analyzed in [11]. Depending on the passivated atoms different spectra was obtained. We can obtain some similar spectra near Fermi level. We can not obtain edge mode connected with passivating atoms and spin effects.

There are other outstanding issues. Possible there is zigzag and armchair reconstruction [12]. Another issue is even though edges can appear macroscopically smooth and oriented at well defined angles, they are not necessarily microscopically ordered [13]. That is why our simple approach described above may be useful to analyze size quantization in GNR with straight edges with arbitrary microscopic structure, having translational symmetry. But experimental techniques are not yet able to realize exact control of the edge structures of GNRs and the edges are always very rough due to the limitation of the fabrication technology.

References

[1] V. A. Volkov, I. V. Zagorodnev, *FNT* **35**, 5 (2009).
[2] V. A. Volkov, I. V. Zagorodnev, *Journal of Physics: Conference Series* **193**, 012113 (2009).
[3] K. Nakada *et al*, *Phys. Rev. B* **54**, 17954 (1996).
[4] L. Brey, H. A. Fertig, *Phys. Rev. B* **73**, 235411 (2006).
[5] A. R. Akhmerov and C. W. J. Beenakker, *Phys. Rev. B* **77**, 085423 (2008).
[6] N. M. R. Peres *et al*, *Phys. Rev. B* **73**, 125411 (2006).
[7] K. Sasaki *et al*, *Phys. Rev. B* **75**, 235430 (2007).
[8] K. Wakabayashi *et al*, *Carbon(Elsevier)* **47**, 124 (2009).
[9] K. Sasaki *et al*, *Phys. Rev. Lett.* **102**, 146806 (2009).
[10] W. Li and R. Tao, arXiv:1001.4168 (2010).
[11] G. Lee and K. Cho, *Phys. Rev. B* **79**, 165440 (2009).
[12] P. Koskinen *et al*, arXiv:0906.0688 (2009).
[13] C. Casiraghi *et al*, *Nano Lett.* **9**, 1433 (2009).

18th Int. Symp. "Nanostructures: Physics and Technology"
St Petersburg, Russia, June 21–26, 2010

Changes of structure, electronic and magnetic properties of three dimensional disordered network of nanographites at interaction with different molecules

A. M. Ziatdinov
Institute of Chemistry, Vladivostok, Russia

Abstract. At adsorption of some molecules by nanoporous carbon materials consisting of a three dimensional disordered network of nanographites, the peripheral spin-polarized π-states of nanographites can transform because of interaction with "guest" molecules. In this work the results of investigation of influence of different adsorbed molecules on structure, electronic and magnetic properties of activated carbon fibers and their nanosized constituents are presented.

Introduction

Nanoporous carbons materials consist of a three dimensional disordered network of nanographites [1,2]. This particular structure makes them a good model system for studying nanographites. There are a few reasons for interest of scientists to nanographites. First, due to their intermediate position between the bulk graphite and aromatic molecules, nanographites are the potential source of new chemical substances with unusual electronic and magnetic properties. Second, while the fullerenes and carbon nanotubes are close shaped π-electron conjugated systems [3] which electronic properties are mainly controlled by the quantum size and surface effects, the nanographites represent the edge-open π-electron conjugated system.

Obviously, an arbitrary shaped graphene sheet comprises two kinds of edges: zigzag and armchair type edges. The calculations for the model of graphite ribbons — one dimensional graphite lattices of finite width, show that ribbons with zigzag edges possess edge states with energies close to the Fermi level [4,5]. These edge states correspond to the nonbonding molecular orbital (nonbonding π levels superimposed on the bonding π and antibonding π^* bands). In contrast, edge states are completely absent for ribbons with armchair edges. However, in a general finite graphene sheet consisting of both types of edges, even a few zigzag sites per sequence are shown to lead to non-negligible edge-state effects, resulting in an enhancement in the electronic density of states at the Fermi energy [5]. The theoretical investigations of the stacking effects in the zigzag nanographite sheets show that the edge states are sensitive to the type of the graphene layers stacking [6,7]. In last years, the reality of edge spin-polarized π-electron states was established experimentally [8–10].

In this work, the results of investigation of changes of structure, electronic and magnetic properties of activated carbon fibers (ACFs) at absorption of different molecules are presented.

1. Results and discussion

According to the X-ray data (Fig. 1) nanographites — structural blocks of ACFs, consists of 3–4 nanographene layers with the interlayer distance 0.4 nm. The mean in-plane size of nanographite is ≈2 nm. Nanosized pores divide the nanographite domains from each other. The small-angle neutron scattering data shows, that there are two kinds of pores in ACFs:

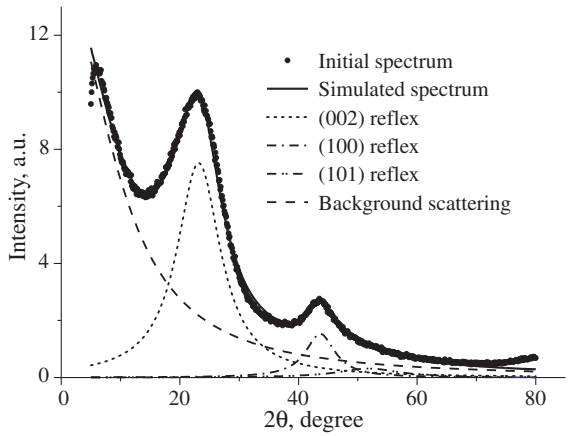

Fig. 1. X-ray diffraction spectrum of ACFs and its representation as the sum of components corresponding to the (002), (100) and (101) reflexes.

the nanopores with the sizes ≈1.2 nm and ≈10 nm.

The XPS spectrum of C1s-electrons of ACFs contains intensive peak with the binding energy 284.4 ± 0.1 eV (Fig. 2). The lineshape parameters of this peak are near the same for bulk graphite. Three less intensive peaks with the binding energies 285.9 ± 0.2, 288.6 ± 0.2 and 290.6 ± 0.3 eV are also observed near this peak. According to the literature data [11] they belong to aliphatic fragments, C-OH bond and $\pi - \pi^*$ excitations, respectively.

The ESR spectrum of ACFs consists of two weakly asymmetrical signals with different linewidth. The values of asymmetry parameter A/B and g-factor, equal for both signals, are 1.15 and 2.0027 ± 0.0001, respectively. The integral intensity of broad signal does not depend on temperature, while the integral intensity of narrow signal increases at decreasing of temperature. Therefore, the former signal corresponds to the conduction electrons and the latter signal to the localized spins. The concentration N_s of localized spins was found from the magnetic susceptibility data. Thus, by comparing the integral intensities of localized (I_s) and delocalized (I_e) spins, we can estimate the density of states near the Fermi level of nanographites: $D(E_F) = (I_e/I_s) \times (N_s/k_BT)$. Such calculations show that $D(E_F)$ for nanographites is several orders higher than the same value for the bulk graphite.

The absence of linewidth temperature dependence for narrow signal also in non-evacuated sample indicates that the lo-

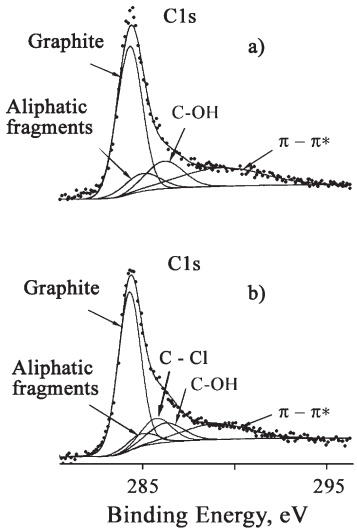

Fig. 2. XPS-spectra of C1s-electrons for initial (a) and chlorinated (b) ACFs.

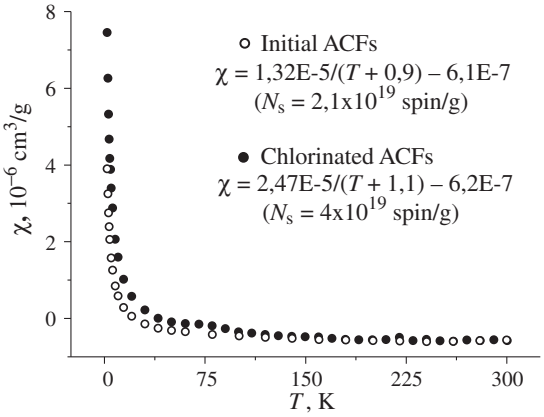

Fig. 3. Temperature dependences of magnetic susceptibility for initial and chlorinated ACFs (the theoretical expressions for approximation curves and localized spin concentrations, N_s, are presented, also).

calized spins are in the interlayer space of nanographites. Furthermore, the Curie-Weiss type temperature dependence of the magnetic susceptibility gives evidence that they are present in the nanographites in form of small clusters.

The comparison of integral intensities of ESR signal from conduction electrons in evacuated sample and in the oxygen atmosphere shows that the presence of oxygen molecules increases the number of current carriers near the Fermi level by 25–30%.

At adsorption of halogens by ACFs the intensity and linewidth of conduction electron signal decreases, while their g-factor values increase to 2.0032. Simultaneously, the concentration of localized spins is increased approximately twice (Fig. 3). The XPS data shows (Fig. 2) that at adsorption of these halogens by ACFs the part of nanographite edge carbon atoms forms the covalent bonds with them. We assume that this is the reason for the above-mentioned changes of conduction electron characteristics.

In ACFs with different sorbate the sign and quantity of the (002) X-ray diffraction peak shift, relative to its position in a spectrum of initial fibers, depend on the nature of sorbate. For example, among ACFs with spirits, the sign of this shift changes from the negative to the positive at the transferring from propanol- to isopropanol-containing fibers. In the spectrum of ACFs with water, the (002) peak is located in larger 2θ-angles, than that in a spectrum of a macroscopic graphite. In ACFs with chlorine the sign and quantity of (002) peak displacement is near for its theoretical value for chlorine molecules in nanographite interlayer space. In experiments with some sorbets, a small narrowing of the (100) peak, determining the identity period along nanographene sheets, was also observed. All above-mentioned experimental data can be interpreted as a result of intercalation, at which, simultaneously with increasing of mean distance between graphene sheets, their shift relatively to each other occurs.

2. Conclusion

The effect of different molecules adsorption on the structure, electronic and magnetic properties in a nanographite network system is investigated by using ACFs as a host material. We found that the density of electronic states near the Fermi level of nanographites — structural blocks of ACFs, is more, than that in macroscopic graphite. So, in nanographites, with random distribution of armchair and zigzag edges of graphene sheets, stable localized edge π-states, generating peak density of states near the Fermi level, are realized. It was shown that the adsorbed species of different substances are classified into the three groups with respect to the interaction with nanographites: physisorption species, charge transfer species, and covalent bonding species. Only last species destroy the edge π-states of nanographites. However, first two species can displace the Fermi level and change the concentration of delocalized spins.

Acknowledgements

The authors are grateful to Doctor Yu. M. Nikolenko and Professor V. V. Ikorskii for help in XPS and magnetic susceptibility measurements, respectively. This work has been supported in part by the Russian Foundation for Basic Research (No. 08-03-00211).

References

[1] H. Marsh, *Activated carbon compendium*, Elsevier Science, Amsterdam 2001.
[2] K. Kaneko *et al*, *Adv. Colloid Interface Sci.* **76–77**, 295 (1998).
[3] M. S. Dresselhaus *et al*, *Science of Fullerenes and Carbon Nanotubes*, Academic, San Diego 1996.
[4] M. Fujita *et al*, *J. Phys. Soc. Jpn.* **65**, 1920 (1996).
[5] K. Nakada *et al*, *Phys. Rev.* **B54**, 17954 (1996).
[6] K. Harigaya *et al*, *J. Phys.: Condensed Matter* **13**, 1295 (2001).
[7] K. Harigaya *et al*, *Chem. Phys. Lett.* **351**, 128 (2002).
[8] Y. Niimi *et al*, *Appl. Surf. Sci.* **241**, 43 (2005).
[9] Z. Klusek *et al*, *Appl. Surf. Sci.* **252**, 1221 (2005).
[10] Y. Kobayashi *et al*, *Phys. Rev.* **B71**, 193406 (2005).
[11] C. D. Wagner *et al*, *Handbook of X-ray photoelectron spectroscopy*, Perking–Elmer Corp. Phys. Electronic Division, USA 1978.

18th Int. Symp. "Nanostructures: Physics and Technology"
St Petersburg, Russia, June 21–26, 2010

SiGe-based nanostructures for LED and PD applications

Z. F. Krasilnik[1], A. V. Novikov[1], D. N. Lobanov[1], Yu. N. Drozdov[1], K. E. Kudryavtsev[1], A. V. Antonov[1], N. D. Zakharov[2] and P. Werner[2]

[1] Institute for Physics of Microstructures, Nizhni Novgorod, GSP-105, Russia
[2] Max-Planck-Institut für Mikrostrukturphysik, Weinberg 2, 06120 Halle/Saale, Germany

Abstract. The effect of structure parameters on the electroluminescence and photoconductivity of multilayer structures with self-assembled Ge(Si)/Si(001) islands has been studied. The highest intensity of the room-temperature electroluminescence in the wavelength range 1.3–1.55 μm has been observed for the islands grown at 600 °C. The observed growth of the electroluminescence signal from the islands with an increase of the Si space layer thickness is associated with a decrease of elastic strain in the structure with thicker space layers. The same diode structures with Ge(Si)/Si(001) islands have demonstrated room-temperature photoconductivity signal in the wavelength range 1.3–1.55 μm. The observed overlap of the electroluminescence and photoconductivity spectra obtained for the same structures with Ge(Si) islands makes these structures a promising material for fabrication of Si-based optocoupler.

Introduction

During the past few years, much effort has been devoted to create novel optoelectronic devices using germanium quantum dots and strained Si/Ge heterostructures [1,2] and multiquantum wells [3], because these structures are expected to allow fabrication of silicon-based optoelectronic devices by bandgap engineering [4]. The important advantage of structures with coherent Ge(Si) self-assembled island is their possibility to work in the wavelength range 1.3–1.55 μm, which is used by modern fiber communications. The bulk Si is transparent in this wavelength range that permits using the silicon-based waveguides. The last fact allows integration of optical and electronic devices within one silicon chip. In the last few years, different groups have reported on the observation of room temperature (RT) electroluminescence (EL) from the structures with Ge(Si) self-assembled islands [5–8]. The best results have been reported in the Ref. [9], where the external quantum efficiency of light emission in the wavelength range 1.3–1.8 μm was about 0.04%. Different groups have reported on the development of photodetectors based on the structures with Ge(Si) islands operating in the same wavelength range [10,11]. The observation both the EL and photoconductivity (PC) in the wavelength range 1.3–1.55 μm from the same structure with Ge(Si) islands [12] makes these structures a promising material for fabrication of Si-based optocoupler for this wavelength range. In this work we have studied the effect of the parameters of Ge(Si)/Si(001) self-assembled islands in the multilayer diode structures on the EL and PC from the islands. The parameters of Ge(Si) islands have been varied by using different growth temperatures and thicknesses of the Si space layer. The main goal of this study is the optimization of structure parameters to increase both the EL and PC signal from Ge(Si) islands in the wavelength range 1.3–1.55 μm at RT.

1. Experimental

The samples under investigation have been grown by solid source MBE on p^+ Si(001) substrates. The growth of the structures started with the deposition of 200-nm-thick contact p^+-Si layer doped by boron up to 2×10^{18} cm^{-3}. Then, a 50-nm-thick undoped Si layer was grown, followed by 20 periods of Ge(Si) islands separated by Si spacer layers with the thicknesses of 7–32 nm. The growth temperature of the multilayer structures with islands was varied in the range $T_g = 550 - 700$ °C. Finally 50-nm-thick undoped Si layer and 200-nm-thick contact n^+-Si layer doped by antimony at 5×10^{18} cm^{-3} have been grown on the top of the Ge/Si multilayer. The details of the structure growth are published in [13]. The transmission electron microscopy (TEM) studies of the grown structures were performed on Philips CM20 and JEM 4010 electron microscopes with acceleration bias of 200 and 400 kV, respectively. Au/Ti 500-μm-diameter ohmic contact has been deposited on the top of the structure for the EL and PC studies. The bottom ohmic contact was formed by deposition of Al on the back side of the substrate. The PC studies have been performed with the BRUKER VERTEX 80V Fourier-transform spectrometer under zero bias on the diode structures. The EL studies have been carried out in the pulsed mode to avoid overheating of the samples. The pulse duration and repetition period were 4 and 25 ms, respectively. The EL spectra have been measured with grating monochromator and nitrogen-cooled Ge detector. The emitting power has been measured in the continuous mode using InGaAs-based power meter PD300-IRG operating in the spectral range 0.8–1.7 μm. The power of light emitted into the spatial angle restricted by the aperture of the power meter in the direction normal to the structure surface has been measured in the experiment.

2. EL from the islands grown at different temperature

The EL study has shown that all p-i-n diodes with Ge(Si) self-assembled islands grown at various temperatures demonstrate RT EL from the islands in the range 0.75–1.0 eV (1.25–1.65 μm) (Fig. 1). It was observed that the intensities of EL signal from the islands grown at different temperatures were almost the same at low measurement temperatures ($T = 77$ K). However, the islands grown at $T_g = 600$ °C have shown the highest intensity of EL signal at RT (Fig. 1). Our previous studies [14] have revealed that Ge(Si) dome islands grown at $T_g = 600$ °C demonstrate the most intensive PL signal at RT in comparison with islands grown at other temperatures. This fact is associated with the best localization of holes in the islands grown at $T_g = 600$ °C [14]. On the one hand, the increase of the growth temperature above 600 °C leads to an enhancement of the Si diffusion into the islands [15,16]. According to the results of X-ray analysis the average Ge content in the islands

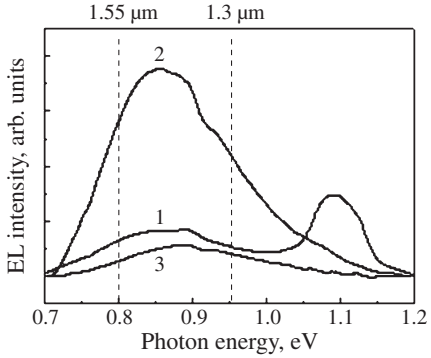

Fig. 1. EL spectra of the structure with Ge(Si) islands grown at 550 °C (1), 600 °C (2) and 650 °C (3). All spectra were recorded at room temperature and were corrected for the spectral response of the detection system. The pumping current was equal to 200 mA.

decreases from $x = 45\%$ to $x = 37\%$ with an increase of T_g from 600 to 650 °C. The growth of Si content in the islands leads to a decrease in the valence band offset on the heterojunction between silicon and Ge(Si) islands, decreasing the depth of the potential well for holes in the islands and, as a result, reducing the probability of hole localization in the islands at RT.

On the other hand, the decrease of T_g from 600 to 550 °C results in morphology transition in the growth of Ge(Si) self-assembled islands [17,18]. In this temperature range the transition of the island type, dominating on the surface, occurs from dome island growth to hut island growth [17,18]. This transition is accompanied by a dramatic decrease of the island height. Due to quantum confinement effect this leads to pushing the hole ground level in the island towards Si valence band edge, which results in a worse hole localization in the islands at RT. The latter is indicated by a presence of the intensive silicon band-edge luminescence in the RT EL spectra from the structures with hut islands (Fig. 1). Another possible reason for the decrease of the EL intensity from the islands grown at low temperatures is an increase of the point defect density and, consequently, of the nonradiative recombination centers in structures grown at low temperatures [19]. Thus, the best hole localization in the structures under investigation occurs in Ge(Si) dome islands grown at 600 °C. Together with low defect density this results in weak temperature quenching and the highest RT EL intensity from the islands, grown at this temperature.

3. Effect of space layer thickness on the EL from the islands

Another parameter of the multilayer structures, which affects the island parameters and their optical properties, is the thickness of Si spacer layer (d_{Si}) between neighboring layers of Ge(Si) islands [20,21]. The island sizes increase with an increase of the layer number, which could be attributed to an increase of the Si content in the islands due to accumulation of elastic strain in the structure [21] (Fig. 2). This effect is more pronounced in the structures with thin Si spacer due to higher elastic strain in these structures (Fig. 2).

The effect of Si spacer layer thickness on the EL of Ge(Si) islands is nontrivial. On the one hand the decrease of d_{Si} leads

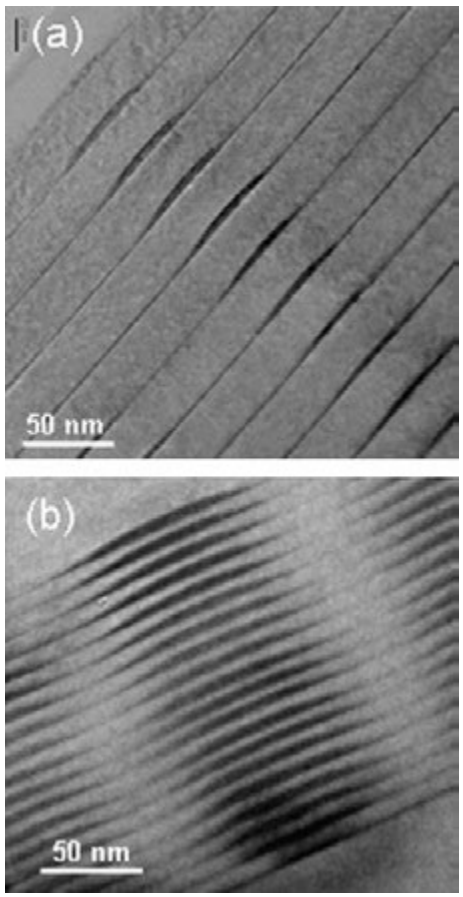

Fig. 2. TEM image of multilayer structure with Ge(Si) islands grown at 600 °C with the Si spacer layer thickness of 32 nm (a) and 7.5 nm (b).

to the increase of tensile strain of Si spacer and, as result, to the increase of potential well for electron on the heterojunction with islands [22]. The formation of miniband for charged carriers is possible in the multilayer structures with very thin ($d_{Si} < 10$ nm) Si spacer [23]. Both factors promote the increase of radiative recombination efficiency for charged carriers. However, the decrease of d_{Si} results in an increase of elastic strain in the structures [22] and, therefore, in an increase of the probability for the formation of defects in the structures, which is confirmed by TEM. Besides that, strain-induced Si diffusion into the islands of multilayer structure is more pronounced in the structures with thin Si spacer [21]. According to X-ray analysis Ge content in the islands increases from 45% to 51% with an increase of d_{Si} from 25 to 32 nm [12]. As in the case of EL intensity dependence on growth temperature, the growth of Si content in the islands with decreasing of d_{Si} leads to a smaller potential well for holes in the islands and, as a result, to a reduced EL intensity at RT. The optimization of d_{Si} value allows to reach the integral EL emitted power up to 10 μW at RT.

4. PC of multilayer structures with islands

The study of the photoconductivity spectra from the structures with Ge(Si) islands has shown the presence of PC signal at the energies below the band gap of bulk Si (Fig. 3). The intensity of PC signal from islands has the same dependencies on the

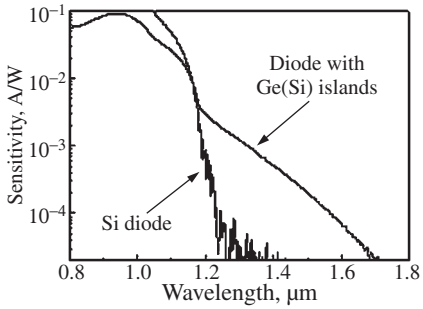

Fig. 3. PC spectra of Si diode and structure with Ge(Si) islands grown at 600 °C (with Si spacer layer thickness 16 nm). All spectra were recorded at room temperature under zero bias.

parameters of the structures as the EL signal. The intensity of the PC signal in the wavelength range 1.3–1.55 μm has a maximum for the structures with islands grown at 600 °C and has the same dependence on the Si spacer layer thickness as EL signal. The same dependencies of the EL and PC signals on the growth conditions and large overlap of the EL and PC spectra from the structures with Ge(Si) islands makes these structures a promising material for development of the Si-based optocoupler operating in the spectral range 1.3–1.55 μm.

Acknowledgements

This work was supported by the Federal Agency on Education Programs (Grant RNP.2.1.1.1370), RFBR and DFG projects.

References

[1] O. I. Dosunmu *et al*, *IEEE Photonics Technol. Lett.* **17**, 175 (2005).
[2] M. Jutzi *et al*, *IEEE Photonics Technol. Lett.* **17**, 1510 (2005).
[3] A. Splett *et al*, *IEEE Photonics Technol. Lett.* **6**, 59 (1994).
[4] E. Kasper, D. J. Paul, *Silicon Quantum Integrated Circuits*, Springer, Heidelberg (2001).
[5] W.-H. Chang *et al*, *Appl. Phys. Lett.* **83**, 2958 (2003).
[6] M. Stoffel *et al*, *Appl. Phys. Lett.* **82**, 3232 (2003).
[7] T. Brunhes *et al*, *Appl. Phys. Lett.* **77**, 1822 (2000).
[8] M. H. Liao *et al*, *IEEE Electron Device Lett.* **27**, 252 (2006).
[9] V. G. Talalaev *et al*, *Phys. Stat. Sol. (a)* **198**, R4 (2003).
[10] A. I. Yakimov *et al*, *Semiconductors* **38**, 1225 (2004).
[11] S. Tong *et al*, *Appl. Phys. Lett.* **80**, 1189 (2002).
[12] D. N. Lobanov *et al*, *Physica E* **41**, 935 (2009).
[13] Yu. N. Drozdov *et al*, *Semiconductors* **42**, 286 (2008).
[14] N. V. Vostokov *et al*, *JETP Lett.* **76**, 365 (2002).
[15] G. Capellini *et al*, *Appl. Phys. Lett.* **78**, 303 (2001).
[16] M. Floyd *et al*, *Appl. Phys. Lett.* **82**, 1473 (2003).
[17] O. G. Schmidt *et al*, *Phys. Stat. Sol. (b)* **215**, 319 (1999).
[18] A. V. Novikov *et al*, *Physica E* **23**, 416 (2004).
[19] I. A. Buyanova *et al*, *Appl. Phys. Lett.* **71**, 3676 (1997).
[20] W.-H. Chang *et al*, *Appl. Phys. Lett.* **93**, 4999 (2003).
[21] M. De Seta *et al*, *J. Appl. Rhys.* **102**, 043518 (2007).
[22] O. G. Schmidt, K. Eberl, Y. Rau, *Phys. Rev. B* **62**, 16715 (2000).
[23] N. V. Sibirev *et al*, *Semiconductors* **40**, 224 (2006).

18th Int. Symp. "Nanostructures: Physics and Technology"
St Petersburg, Russia, June 21–26, 2010

Structure and spatial distribution of Ge nanocrystals subjected by neutron irradiation

S. Levy[1], *I. Shlimak*[1], D. H. Dressler[2], T. Lu[3] and A. N. Ionov[4]

[1] Bar-Ilan Institute of Nanotechnology and Advanced Materials, Jack and Pearl Resnick Institute of Advanced Technology, Department of Physics, Bar-Ilan University, Ramat-Gan 52900, Israel
[2] Department of Chemistry, Bar Ilan University, Ramat-Gan 52900, Israel
[3] Department of Physics and Key Laboratory for Radiation Physics & Technology of Ministry of Education, Sichuan University, Chengdu 610064, P.R.China
[4] Ioffe Physical-Technical Institute, St Petersburg, Russia

Abstract. Samples of nanocrystalline Ge (NC-Ge) prepared by $^{74}Ge^{+}$ ion implantation into amorphous SiO_2 layer on the Si ⟨100⟩ surface were investigated by means of the laser Raman Scattering and High Resolution Transmission Electron Microscopy (HR-TEM). The samples were irradiated by fast neutrons in a research nuclear reactor, which results in smearing of the Raman peak at 300 cm^{-1} originated from NC-Ge. Full restoration of this peak was observed after annealing of radiation damage at 800 °C. HR-TEM pictures show, however, that the spatial and size distributions of NC-Ge in irradiated and annealed samples are changed in comparison with samples before irradiation.

Introduction

In the past few years, samples of nanocrystalline Ge (NC-Ge) embedded in silicon dioxide (SiO_2) matrix have attracted much interest due to strong visible photoluminescence and charge retention properties at room temperature [1–2]. This property has made NC-Ge the promising candidate for the creation of a new generation of nano-scale electro-optical devices.

Measurements of Raman scattering (RS) are usually used for justification of the crystalline structure because RS in solids reflects the interaction between incident photons and phonons. The bulk crystalline Ge is characterized by the Raman peak centered at 300 cm^{-1} which corresponds to the optical phonon frequency in bulk Ge crystals.

In this work, we report the results of investigation of RS spectra accompanied by images obtained by means of High Resolution Transmission Electron Microscopy (HR-TEM) in NC-Ge samples irradiated with high dose of fast neutrons in a research nuclear reactor and annealed at different temperatures. We show that high dose of neutron irradiation leads to decrease and smearing of RS peak, but after annealing of radiation damage induced by fast neutrons, the RS spectrum is fully reconstructed. However, in compliance with the HR-TEM images, the structure of NC after annealing does not coincide with initial one and reveals changes both in the average size and in the space distribution of NC.

1. Experimental details

The NC-Ge samples were prepared using $^{74}Ge^{+}$ ion implantation into 500 nm thick amorphous SiO_2 layer deposited on a silicon substrate with ⟨100⟩ oriented surface. The Ge^{+} ions were accelerated to 150 keV, with a dose of 1×10^{17} ions/cm^2. The projected range was about 100 nm and the struggle (half-width of distribution) was about 25–30 nm as predicted by SRIM [3]. These samples were labeled as "implanted" samples. After implantation, some samples were annealed at 800 °C. As a result, randomly distributed Ge atoms form nanocrystals (NC). These samples were labeled as "NC-Ge". Some of NC-Ge samples were then subjected by an intensive neutron irradiation in a research nuclear reactor with the integral dose up to 10^{20} neutrons/cm^2. These samples were labeled as "irradiated". After irradiation, some samples were annealed at 600 and 800 °C to remove the radiation damage. These samples are labeled as "semifinal" and "final" samples respectively.

The RS spectra were measured using Raman microscope LabRam HR. All measurements were conducted at room temperature using 514.5 nm laser for excitation.

HR-TEM images were obtained using the 200 kV JEOL, JEM 2100 HR-TEM. For cross-section imaging, TEM samples were prepared by focused ion beam (FIB) lift-out technique.

2. Results and discussion

Curve *a* in Fig. 1 shows RS spectra in a ^{74}Ge-implanted sample, where Ge atoms do not yet form nanocrystals. One can see a broad asymmetric unstructured band which can be attributed to separate Ge atoms or clusters [4]. The absence of NC is confirmed by analysis of TEM image (see Fig. 2a). To form nanocrystals, implanted samples were annealed at 800 °C. For-

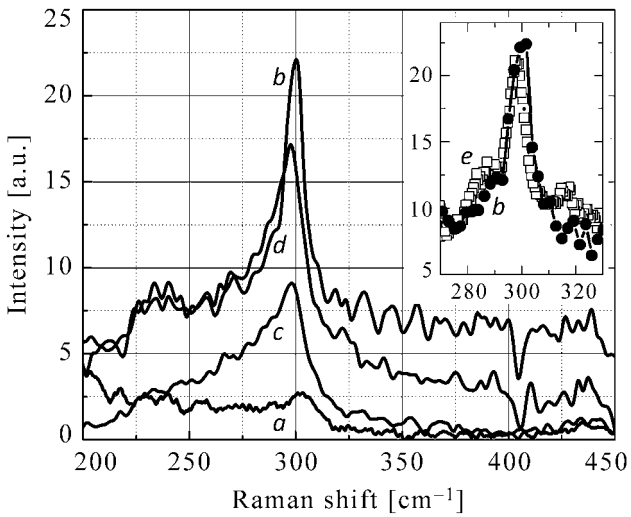

Fig. 1. Raman spectra of (*a*) "implanted", (*b*) "NC-Ge", (*c*) "irradiated" and (*d*) "semifinal" samples, inset displays RS for "initial" "NC-Ge" (*b*) and "final" (*e*) samples.

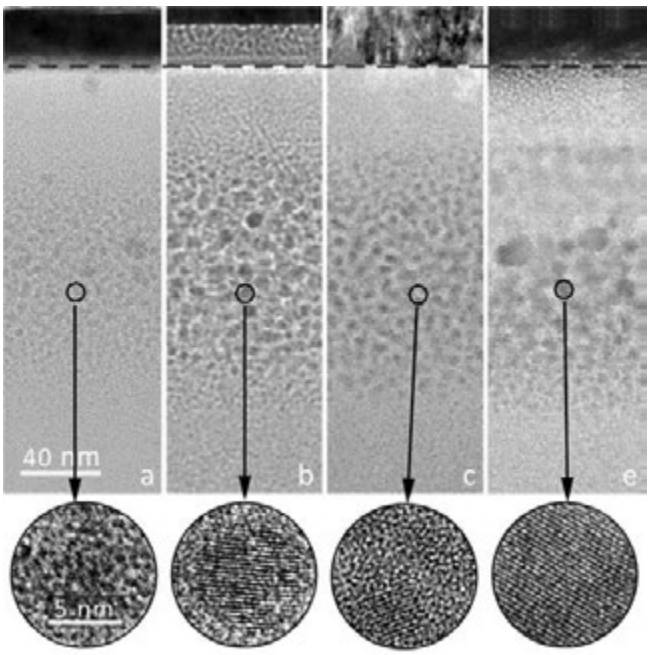

Fig. 2. HR-TEM of (*a*) "implanted" (*b*) "NC-Ge", (*c*) "irradiated" and (*e*) "final" samples. The dashed line indicates the surface of the samples covered by Pt needed for TEM cross-section preparation.

mation of NC was justified by appearance of the main RS peak centered at 300 cm^{-1} (curve *b* in Fig. 1) which is characteristic for crystalline Ge. In addition, NC-Ge were observed in HR-TEM (Fig. 2b). HR-TEM picture shows that NC-Ge regions have an almost spherical shape with diameter of about 2–8 nm. A correlation between the diameter and the depth of NC below the SiO_2 surface is observed: around the center of the projection range (100 nm), where the density of the implanted Ge atoms is maximal, NC diameter is the largest and decreases from both sides.

Then, NC-Ge samples were irradiated by an intensive neutron flux in a research nuclear reactor with integral dose up to 10^{20} cm^{-2}. As a result, the RS peak is decreased and broadened (curve *c* in Fig. 1). This can be explained by destruction of some NC due to collisions with fast neutrons and their transformation from Ge nanocrystals into amorphous clusters. The fact that RS peak does not disappear in spite of strong neutron irradiation shows that some NC have survived which makes this material proof against destructive irradiations. Existance of survived NC-Ge in irradiated samples is additionally confirmed by HR-TEM image (Fig. 2c). HR-TEM measurements also show that the density of NC is decreased.

In Fig. 1, curves *d* and *e* show the influence of annealing of irradiated samples on the RS spectrum.

For bulk Ge, disappearance of radiation damage induced by fast neutrons is achieved after annealing at 400–450 °C [5]. For NC-Ge, however, annealing even at 600 °C leads only to a partial reconstruction of the RS peak (curve *d* in Fig. 1), annealing at 800 °C is needed for full reconstruction of the initial RS peak (inset in Fig. 1).

This can be explained by the following. In irradiated bulk Ge, the destroyed areas are surrounded by crystalline matrix that serves as a seed for recrystallization. In our samples, destroyed NC are surrounded by amorphous SiO_2 which cannot promote the process of crystallization. As a result, recover of crystalline structure after the fast neutron irradiation needs the higher temperature (800 °C) which was needed for formation of NC after ion implantation.

However, HR-TEM investigations show that the reconstruction of crystallinity is not accompanied by rebuilding of the initial space distribution of NC-Ge (compare Figs. 2b and 2e). It is seen that the space distribution became asymmetric — the increased maximal size still corresponds to the center of the projection range while toward to the SiO_2 surface, the average diameter and the density of NC fall rapidly. This asymmetry may reflect influence of the near SiO_2 surface during the final annealing.

3. Conclusions

To conclude, the RS and HR-TEM measurements in NC-Ge samples subjected to irradiation by the neutron flux in a nuclear reactor show that part of NC-Ge survives even after very strong dose of irradiation which makes this material promising for fabrication of devices working in extremal conditions.

In the case of NC, annealing of radiation damage needs much higher temperatures (800 °C) than that in bulk Ge (400 °C). After annealing of radiation damage, crystallinity is recovered, but the space and size distribution of NC-Ge become asymmetric.

Acknowledgements

We are thankful to J. M. Lazebnik for irradiating the samples in a research nuclear reactor. I. S. thanks the Erick and Sheila Samson Chair of Semiconductor Technology for financial support.

References

[1] Y. Maeda, *Phys. Rev.* **B 51**, 1658 (1995).
[2] C. J. Park, H. Y. Cho, S. Kim, S.-H. Choi, R. G. Elliman, J. H. Han, C. Kim, H. N. Hwang and C. C. Hwang, *Journal of Applied Physics* **99**, 36101 (2006).
[3] J. F. Zigler, http://www.srim.org/index.htm, Copyright 1984–2006.
[4] U. Serincan, G. Kartopu, A. Guennes, T. G. Finstad, R. Turan, Y. Ekinci and S. C. Bayliss, *Semicond. Sci. Technol.* **18**, 247 (2004).
[5] I. Shlimak, A. N. Ionov, R. Rentzsch and J. M. Lazebnik, *Semicond. Sci. Technol.* **11**, 1826 (1996).

18th Int. Symp. "Nanostructures: Physics and Technology"
St Petersburg, Russia, June 21–26, 2010

Conversion of quantum states in nanostructures by acoustic soliton

I. V. Rozhansky[1], M. B. Lifshits[1,2], S. A. Tarasenko[1] and N. S. Averkiev[1]

[1] Ioffe Physical-Technical Institute, St Petersburg, Russia
[2] University of Montpellier II, Montpellier, CEDEX 5, France

Abstract. The hole states in the valence band of a large class of semiconductors are degenerate in the projections of angular momentum. We show that the switching of a hole between the states can efficiently be realized by acoustic solitons. The microscopic mechanism of such a state conversion is related to the valence band splitting by local elastic strain. The conversion is studied for the holes in a quantum dot or localized at acceptors in a quantum well.

Introduction

It is specific for semiconductor nanostructures that they allow for observation of quantum effects at high temperatures. A striking example of such a purely quantum effect is the transition between degenerate states of a system caused by a temporal perturbation. Whenever the quantum states being switched in this manner are well distinguished experimentally, this effect becomes of great interest for applications. Of particular importance especially for the spintronic devices would be the state conversion achieved in a non-magnetic way, i.e. by perturbation of electrical or mechanical origin. In this work we show that the switching between degenerate states can be realized by means of solitary strain pulse (acoustic soliton) propagating through a quantum well or quantum dot. Being a perturbation of purely mechanical origin the acoustic soliton does not interact with the carriers spin. It is therefore natural first of all to consider the effect of state conversion for semiconductor structures with negligible spin-orbit interaction (such as Si, SiC, etc). Below we focus on silicon-based quantum structures although the main conclusions can be generalized to other systems. The effect is studied theoretically the spherical Si quantum dots embedded in SiO_2 matrix and for p-type quantum wells based on silicon.

1. Conversion of a hole state in a quantum dot

We assume that in bulk material the valence-band states at the center of the Brillouin zone belong to the representation Γ'_{25} or Γ_{15} and denote the basis of Bloch amplitudes as $u_x = yz$, $u_y = xz$, and $u_z = xy$. Due to quantum confinement, the ground state of a hole in a spherical quantum dot is threefold degenerate in the projections of angular momentum [1]. In the spherical approximation for the valence band the corresponding wave functions are given by:

$$\begin{aligned}\psi_1(\mathbf{r}) &= R_1 u_x + R_2[(\chi_1+\chi_2)u_x + \varepsilon_3 u_y + \varepsilon_2 u_z],\\ \psi_2(\mathbf{r}) &= R_1 u_y + R_2[\varepsilon_3 u_x + (\chi_1-\chi_2)u_y + \varepsilon_1 u_z],\\ \psi_3(\mathbf{r}) &= R_1 u_z + R_2[\varepsilon_2 u_x + \varepsilon_1 u_y - 2\chi_1 u_z],\end{aligned}$$

where the angular parts have form

$$\chi_1 = (r^2-3z^2)/2r^2,\quad \chi_2 = 3(x^2-y^2)/2r^2,$$
$$\varepsilon_1 = 3yz/r^2,\quad \varepsilon_2 = 3xz/r^2,\quad \varepsilon_3 = 3xy/r^2,$$

and the radial parts of the envelope wavefunctions are

$$\begin{aligned}R_1(r) &= 2Cj_0(r/r_0) + Dj_0(\beta r/r_0),\\ R_2(r) &= -Cj_2(r/r_0) + Dj_2(\beta r/r_0).\end{aligned}$$

The coefficients C, D are to be found from the boundary and normalization conditions, j_0, j_2 are the spherical Bessel functions of the first kind and $\beta = \sqrt{m_h/m_l}$, m_h, m_l being the heavy and light hole masses respectively, r_0 is determined by the localization energy E: $r_0 = \hbar/\sqrt{2m_h E}$.

The solitary strain pulse resembles a perturbation which lifts the degeneracy and causes transitions of a hole between the states $\psi_1(\mathbf{r})$, $\psi_2(\mathbf{r})$ and $\psi_3(\mathbf{r})$. We consider that the acoustic soliton propagates in the x direction with velocity v inducing only one component of the strain tensor $u_{xx}(x-vt)$. The corresponding effective Hamiltonian has the form [2]

$$V = \begin{bmatrix} l & 0 & 0\\ 0 & m & 0\\ 0 & 0 & m\end{bmatrix} u_{xx}(x-vt), \qquad (1)$$

where l and m are the deformation potential constants. The strain pulse is assumed weak enough not to cause ionization of the localized hole or its transition to excited states. Then following the perturbation theory the wave function $\psi(\mathbf{r},t)$ can be expressed in terms of the non disturbed states $\psi_j(\mathbf{r})$ ($j = 1, 2, 3$). To consider transitions that are well distinguished by means of optical experiment it is convenient to change the basis so that:

$$\begin{aligned}\psi_+(\mathbf{r}) &= [\psi_1(\mathbf{r}) + i\psi_2(\mathbf{r})]/\sqrt{2},\\ \psi_-(\mathbf{r}) &= [\psi_1(\mathbf{r}) - i\psi_2(\mathbf{r})]/\sqrt{2},\\ \psi_3(\mathbf{r}) &= \psi_3(\mathbf{r}).\end{aligned}$$

The states ψ_+ and ψ_- are characterized by projections $+1$ and -1 of the orbital angular momentum, therefore, optical pumping by circularly polarized light leads to a predominant population of one of these states. The hole angular momentum can be registered in turn by analyzing the polarization of recombination radiation or the polarization change of a probe pulse. Under the perturbation induced by the strain pulse the state $\psi(\mathbf{r},t)$ evolves as

$$\psi(\mathbf{r},t) = c_+(t)\psi_+(\mathbf{r}) + c_-(t)\psi_-(\mathbf{r}) + c_3(t)\psi_3(\mathbf{r}),$$

where

$$\begin{aligned}c_+(t) &= \left[a_+\cos\Phi(t) - ia_-\sin\Phi(t)\right]e^{-i\Theta(t)},\\ c_-(t) &= \left[a_-\cos\Phi(t) - ia_+\sin\Phi(t)\right]e^{-i\Theta(t)},\\ c_3(t) &= a_3\exp[-i\Omega_3(t)].\end{aligned}$$

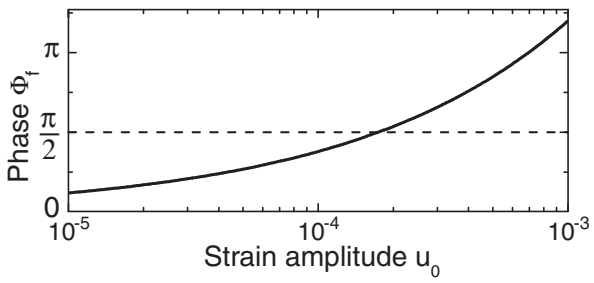

Fig. 1. Dependence of the phase shift Φ_f on the strain amplitude u_0 calculated for Si/SiO_2 spherical quantum dots. Dashed line corresponds to $\Phi_f = \pi/2$ which is optimal for the state conversion.

Here

$$\Omega_j(t) = \frac{1}{\hbar}\int_{-\infty}^{t} V_{jj}(t')dt', \quad j = 1, 2, 3,$$
$$\Theta(t) = (\Omega_1 + \Omega_2)/2, \qquad \Phi(t) = (\Omega_1 - \Omega_2)/2,$$

$V_{jj}(t)$ are the matrix elements of the perturbation (1), $a_\pm = c_\pm(-\infty)$, $a_3 = c_3(-\infty)$ denote the initial state before the soliton propagation. The phase shift $\Phi(t)$ describes the hole state time evolution due to interaction with the soliton while $\Theta(t)$ constitutes the common phase factor. In the final state, i.e., at $t = +\infty$ when the soliton has completely passed through the area of hole localization, the phase shift takes the form

$$\Phi_f = \frac{l-m}{2\hbar}\int d^3\mathbf{r}\left[R_1(r)^2 + \frac{1}{5}R_2(r)^2\right]\int_{-\infty}^{+\infty} u_{xx}(x-vt)dt.$$

Since the average value of the strain u_{xx} is non-zero within the soliton, $\Phi_f \neq 0$, and the final hole state differs from the initial one. The most efficient conversion of the hole state occurs if the soliton amplitude satisfies

$$|\Phi_f| = \pi(n + 1/2), \qquad n = 0, 1, 2, \ldots$$

In this particular case, the soliton-hole interaction results in the complete switching of the hole angular momentum: the initial state $\psi_+(\mathbf{r})$ is converted into the state $\psi_-(\mathbf{r})$ and vice versa.

In order to calculate the switching efficiency the form of the strain pulse $u_{xx}(x-vt)$ is needed. Acoustic solitons in crystals are typically approximated by solutions of the Korteweg–de Vries (KdV) wave equation [3] or the doubly dispersive equation (DDE) [4]. We consider the KdV soliton however the particular soliton shape is not crucial for our results. For the KdV soliton u_{xx} has the form

$$u_{xx}(x, t) = u_0 \cosh^{-2}\left[(x - vt)/L\right],$$

where u_0 is the strain amplitude, $L = d/\sqrt{u_0}$ is the soliton size, and d is a material constant. The phase shift is given by

$$\Phi_f = \frac{l-m}{\hbar}\frac{u_0 L}{v}\left[\frac{1}{10} + \frac{9}{10}\int R_1(r)^2 d^3\mathbf{r}\right].$$

Fig. 1 shows the dependence of the phase shift Φ_f on the strain amplitude u_0. The complete switching corresponds to the $\Phi_f = \pi/2$ and is achieved at $u_0 \sim 10^{-4}$ which appears to be within the typical range for the strain soliton pulses obtained in experiments [3, 5].

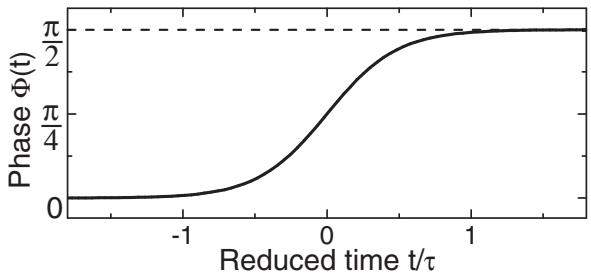

Fig. 2. Time dependence of the phase shift $\Phi(t)$ for a hole localized at an acceptor in a quantum well.

2. Conversion of the acceptor states in a quantum well

Another possibility to observe a state conversion appears for heavy holes localized at acceptors in quantum wells, where the ground state is two-fold degenerate in the projection of the angular momentum because of the complex structure of the valence band. We show [6] that the propagation of the acoustic soliton of a certain amplitude through the area of hole localization changes the projection of the hole angular momentum. The evolution of the phase shift $\Phi(t)$ with time is presented in Fig. 2. The time of complete switching of the hole state is given by $\tau = 2(L + r_0)/v$, where r_0 is the hole localization radius. It is of picosecond range being much less than the lifetime of localized holes as well as the soliton lifetime. It suggests that the effect can be studied experimentally by means of time- and space-resolved optical spectroscopy.

To summarize, we have demonstrated the possibility of switching the quantum-mechanical state of a localized carriers by an acoustic soliton. The strain amplitude required for switching the hole states in silicon-based nanostructures is found to be $\sim 10^{-4}$ which corresponds to strain pulses studied experimentally.

Acknowledgements

This work was supported by RFBR, the programs of the Russian Ministry of Education and Science, and the President Grant for young scientists (MD-1717.2009.2).

References

[1] A. S. Moskalenko, J. Berakdar, A. A. Prokofiev and I. N. Yassievich, *Phys. Rev. B* **76**, 085427 (2007).
[2] G. L. Bir and G. E. Pikus, *Symmetry and Strain-Induced Effects in Semiconductors* (Wiley, New York, 1974).
[3] H.-Y. Hao, H. J. Maris, *Phys. Rev. B* **64**, 064302 (2001).
[4] K. R. Khusnutdinova and A. M. Samsonov, *Phys. Rev. E* **77**, 066603 (2008).
[5] A. V. Scherbakov, P. J. S. van Capel, A. V. Akimov *et al*, *Phys. Rev. Lett.* **99**, 057402 (2007).
[6] I. V. Rozhansky, M. B. Lifshits, S. A. Tarasenko and N. S. Averkiev, *Phys. Rev. B* **80**, 085314 (2009).

18th Int. Symp. "Nanostructures: Physics and Technology"
St Petersburg, Russia, June 21–26, 2010

Nucleation of Ge nanoislands on pre-patterned Si substrates

P. L. Novikov, Zh. V. Smagina, V. A. Zinoviev, D. Yu. Vlasov, A. V. Dvurechenskii, D. A. Nasimov, A. S. Deryabin and A. S. Kozhukhov

Institute of Semiconductor Physics, Novosibirsk, 630090 Novosibirsk, Russia

Abstract. Joint experimental and theoretical study of Ge nanoislands growth on pre-patterned Si substrates is carried out. Si substrates that have been templated by means of electron beam lithography and reactive ion etching have been used to grow Ge by molecular-beam epitaxy. Atomic-force-microscopy studies show that at Si(100) substrate temperature 550 °C, Ge nanoislands are formed at the pits' edges, rather than between the pits. The effect is interpreted in terms of energy barrier, that is formed near the edge of a pit and prevents Ge transport inside the pit. By molecular dynamics calculations the value of energy barrier 2.1 eV was obtained. The energy barrier is shown to decrease in the case of a lower slope of the pit side walls and for Si(111) pre-patterned substrate.

Introduction

Arrays of semiconductor quantum dots (QDs) have attracted considerable interest in the last decades, as these quasi zero-dimensional systems have rich physical properties and offer great potential for device applications, such as light-emitting devices, QD-based field effect transistors, spintronics, or even quantum computation. Most of these applications require space arrangement of QDs, combined with their narrow size distribution and high density. It is a challenge to meet all these requirements simultaneously. A promising way to solve the problem of the inhomogeneous size distribution and random location of QDs is using lithographic techniques to prepare substrates with pre-patterned pits on well-defined positions. The pits serve as nucleation sites for the subsequently grown dots. However, even though extensive studies on the growth of Ge dots on pre-patterned Si substrates have been carried out, still there exists a lack of knowledge about the Ge QD formation in dependence on the pit shape. In the present paper we report on the growth of Ge dots on templated Si substrates with pre-patterned pits. We focus on the impact of a pit shape on the transport properties of Ge adatoms near the edge of a pit.

1. Experimental

The pit patterns in the Si substrates were realized by means of electron-beam lithography and subsequent reactive ion etching. Circle-shaped pits with a lateral dimension of 50 nm, a depth of 8 nm, and a periodicity of 100 nm were etched into the Si substrate. The sample growth was realized by means of solid-source molecular beam epitaxy (MBE). Prior to the deposition of Ge, the samples were chemically cleaned. To remove the thin ($\approx$ 15–20 nm) oxide film samples were treated with a slight Si flow at 700 °C. In a next step, 7 monolayers (ML) of Ge were deposited for 80 s at 550 °C. No Si buffer layer was deposited. The grown samples were analyzed by atomic force microscopy (AFM).

2. Molecular dynamics calculations

The elementary processes, promoting Ge nanoisland growth on pre-patterned surface, were studied by molecular dynamics calculations (MD). 15×15 nm mesh of Si(100)-(2×1) structure (of 20 ML thick), containing a pit, was used in calculations. The inner surface of the pit was composed by four triangle 111-oriented facets. It is assumed, that such pit geometry is self-formed during annealing, when no Si buffer layer is deposited. The pit width was 4 nm with the depth about 3 nm. Periodical boundary conditions were imposed in the lateral directions. Tersoff empirical potential was used to describe interaction between atoms. Before the calculation of surface energy the structure was allowed to relax for 10 ps at temperature 500 $^{\circ}C$. Some additional studies were carried out for pits having lower slope of side walls, and for the case of (111)-(7×7) pre-patterned surface.

3. Results and discussion

AFM image of the structure obtained after the deposition of 7 Ge MLs on pre-patterned Si(100) substrate at $T = 550$ °C is presented in Fig. 1. No Si buffer layer was deposited. It is clearly seen that most of Ge nanoislands are formed at the pits' edge, rather than in the region between the pits. On the one hand, this gives an evidence, that the surface is perfect enough to provide an effective surface diffusion of Ge adatoms. On the other hand, this points that there is an energy barrier, preventing diffusion of Ge into the pits. The value of the energy barrier was estimated from MD calculations. A deep energy minimum (-3.2 eV) was found near the edge of a pit (Fig. 2).

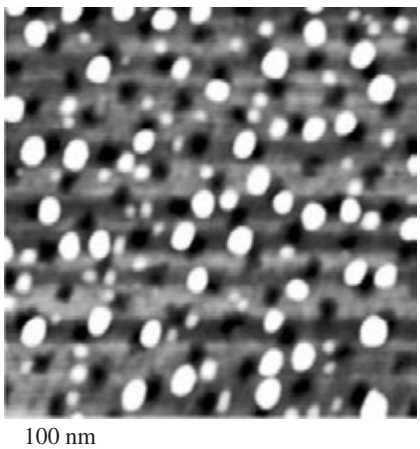

Fig. 1. AFM image of Ge nanoislands grown on Si(100) pre-patterned substrate. Black dots are the pits, white spots are Ge islands. Most of Ge islands are formed near the pit edges. Growth conditions: $T = 550$ °C, 7 Ge MLs deposited, time of deposition was 80 s; no Si buffer layer was deposited.

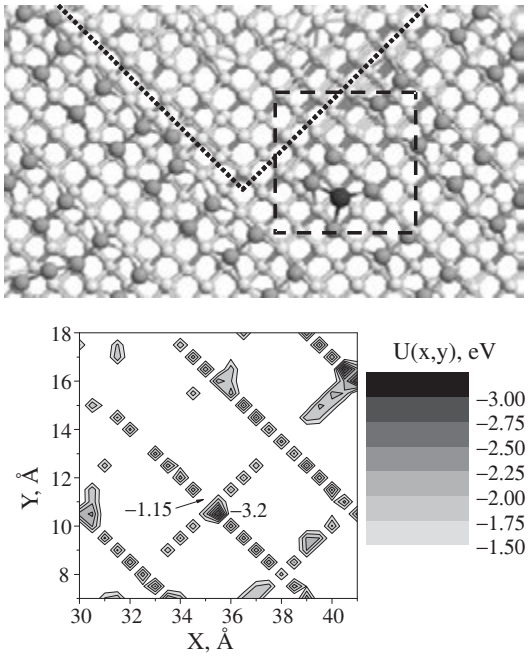

Fig. 2. Upper figure: plan view of Si(100)-(2×1) modeled structure fragment with a pit used for MD calculations. Si bulk atoms are colored in light grey, dimer rows — in grey. Dot line indicates the pit edge. Dashed square denotes a region, where the surface energy was calculated (lower figure). Ge atom (colored in black) located in the position, corresponding to the deep minimum -3.2 eV, forms three effective bonds with Si matrix. The energy in the nearest saddle point toward the pit is -1.15 eV.

The analysis shows that the vicinity of the pit edge plays the key role in deep minimum formation. Atoms at the end of a dimer row are weakly bonded to the matrix in comparison with the typical dimers. For that reason they may be shifted significantly toward a depositing Ge atom, making the interatomic attraction stronger. In the certain surface positions Ge adatom may form up to three effective bonds with the matrix. Such case is shown at the upper part of Fig. 2, where the threefold bonded Ge adatom is indicated by the black circle. The deep minima are located along the pit edge with a periodicity of 7.7 Å. The value of surface energy in the nearest saddle points is -1.15 eV. Thus, the energy barrier to escape from the minima is about 2.1 eV, which characterizes the minima points as the effective traps for Ge atoms and, consequently, as the nucleation centers for Ge nanoislands. It follows from our calculations, that the barrier height goes down to 1.8 eV after deposition of Ge wetting layer. The barrier also decreases in the case of a pit with a lower slope of side walls. This agrees with an experimental result of Rinke *et al* [1], who found, that smearing-out the pits due to the deposition of Si buffer layer promotes diffusion of Ge into the pits. Finally, we obtained the nucleation of Ge nanoislands inside the pits on the pre-patterned Si(111) substrate at the conditions of growth similar to those in case of templated Si(100) substrate. This is consistent with the results of MD calculations, which predict a lower energy barrier values near the pit edge on Si(111)-(7×7) surface.

Acknowledgements

This work was supported by RFBR (grants No. 09-02-00882, 10-02-01181), by Program of SB RAS and by Program of Nanotechnology Department of RAS.

References

[1] G. Rinke *et al*, *EPL* **85**, 58002 (2009).

18th Int. Symp. "Nanostructures: Physics and Technology"
St Petersburg, Russia, June 21–26, 2010

Monte Carlo simulation of Si-Ge nanowhisker growth

A. G. Nastovjak, I. G. Neizvestny and *N.L.Shwartz*
Institute of Semiconductor Physics SB RAS, Novosibirsk, 630090, Russia

Abstract. Composition of nanowhisker Si-Ge heterojunctions at different growth conditions and catalyst drop diameters were analyzed using Monte Carlo simulation. Maximal germanium concentration in Si-Ge heterojunction depends on the ratio between silicon and germanium flux intensities, duration of Ge deposition and nanowhisker (NW) diameter. Dependences of germanium content in NW grown during simultaneous silicon and germanium deposition on whisker diameter at different temperatures were obtained. It was found that the rise of Ge content in $Si_{1-x}Ge_x$ NW with diameter enhancement may be due to different adsorption properties of Si- and Ge-containing precursors.

Introduction

Increasing interest in Si, Ge and SiGe nanowhiskers (NWs) is due to their possible applications in electronics, photonics and the life science. These whiskers have the advantage of compatibility with conventional CMOS technology. Since chemical composition of NW grown on the base of $Si_{1-x}Ge_x$ alloys varies with changing growth conditions and catalyst drop diameter, it has to be carefully considered and precisely controlled because the chemical composition will determine the device performance. In this work formation of Si-Ge whiskers with axial heterojunctions and NWs on the base of $Si_{1-x}Ge_x$ alloy were investigated by Monte Carlo (MC) simulation.

1. Monte Carlo model and simulation results

Simulation was carried out using software developed for investigation of one-component nanowhisker growth on the base of VLS mechanism [1]. Two variants of growth are possible in the model — MBE or CVD. To adjust this program for simulation of Si-Ge NW growth seven-component system was considered: substrate and whisker material (Si); whisker material (Ge); catalyst (Au); Si- and Ge-containing precursors (P_{Si} and P_{Ge}); liquid semiconductor materials dissolved in catalyst drop (Si_L and Ge_L). Following facts were taken into consideration in the model: 1) eutectic temperatures for Si-Au and Ge-Au alloys are close; 2) concentration of semiconductor material in catalyst drop depends on temperature; 3) catalyst drop weakly wets substrate surface; 4) drop surface tension depends on temperature and concentration of dissolved semiconductor matter. Physicochemical system of catalyst-semiconductor was determined by energy parameters of the model. Suggested MC model was used for analyses of growth of Si-Ge whiskers with axial heterojunctions and NWs on the base $Si_{1-x}Ge_x$ alloy.

One of the problems of the MBE growth of axial Ge layers in a Si whisker is formation of a sharp interface of heterojunction. In Fig. 1 simulation results of axial Si-Ge heterostructures formation are presented. During the growth the constant Si and Ge fluxes amounted to 0.05 and 0.01 ML/s, were alternatively supplied. During the Ge layer deposition the Si flux was interrupted. Three Ge layers were grown, and duration of Ge deposition was increased with the layer number. One can see that the Ge layers have a triangular concentration profile (Fig. 1b).

The maximal Ge concentration increases with the layer number though in all three layers the concentration x in less than unity. The same peculiarities of Ge profile were observed in experimental work [2]. The rise of maximal concentration

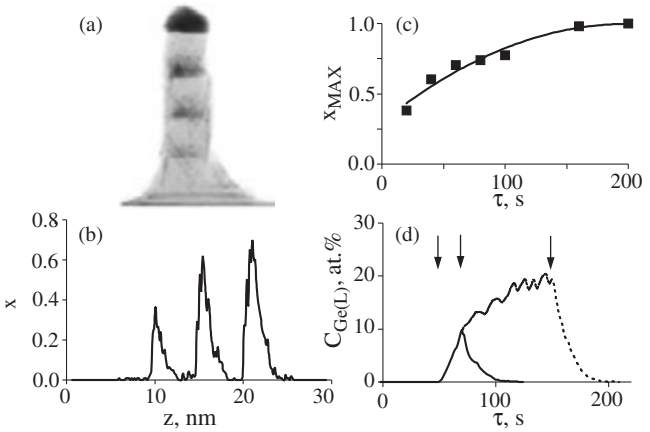

Fig. 1. Si NW with axial Ge-Si heterojunctions grown on Si(111) substrate at $T = 800$ K, $F_{Si} = 0.05$ ML/s, $F_{Ge} = 0.01$ ML/s: a) Si NW with 3 Ge layers, duration of Ge deposition $\tau_1 = 20$ s, $\tau_2 = 40$ s, $\tau_3 = 60$ s; catalyst drop diameter $d_0 = 6$ nm. Au is marked with black color, Si with light-grey color; Ge with dark-grey color; b) Ge concentration profile along the whisker; c) maximal Ge concentration in the first layer versus germanium deposition time; d) variation of Ge_L concentration in Au drop with time for different duration of Ge flux: $\tau_1 = 20$ s (solid curve), $\tau_2 = 100$ s (dotted line). Arrows indicate moments of flux switching.

with peak number in Fig. 1b is due to dependence of Ge concentration on germanium deposition time. Dependence of x_{max} in the first $Si_{1-x}Ge_x$ layer on duration of Ge flux is shown in Fig. 1c. This plot correlates with dependence of maximal concentration of liquid germanium in catalyst drop on Ge deposition time. Fig. 1d demonstrates variation of liquid germanium content in Au drop with time after switching Si and Ge fluxes for two duration of Ge flux: $\tau_1 = 20$ s, $\tau_2 = 100$ s. Composition of grown $Si_{1-x}Ge_x$ can reach pure germanium only if catalyst drop will be free of liquid silicon.

Variation of Ge concentration in the drop depends not only on deposition time of each component, the ratio of Si and Ge flux intensities but on the catalyst drop diameter as well. Fig. 2 illustrates this fact. In Fig. 2(a,b) variation with time of liquid silicon and liquid germanium concentration in Au drop after switching fluxes from Si to Ge for two catalyst drop diameter are presented. According to [3] we assume stationary concentration of semiconductor material dissolved in gold drop to be practically the same for drop diameters 6 and 12 nm. Then increasing of Ge (decreasing of Si) content to the same level in Au-Si-Ge solution needs more time in the larger drop. Vis-

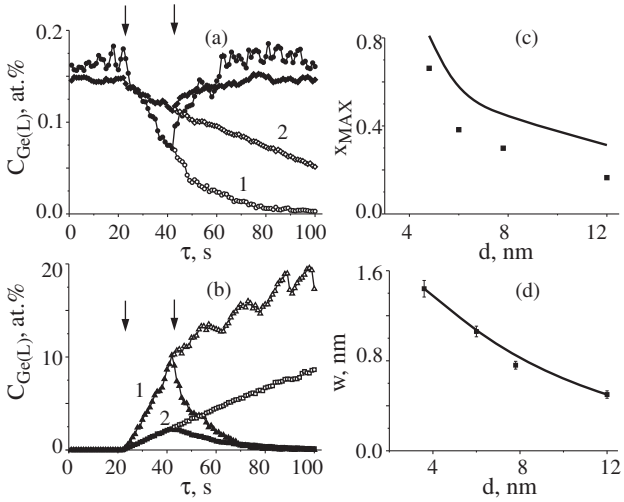

Fig. 2. Si_L concentration (a) and Ge_L concentration (b) in Au drop versus time for different d_0 and τ: 1 — $d_0 = 6$ nm, 2 — $d_0 = 12$ nm; τ_1 — 20 s (solid symbols), τ_2 — 100 s (open symbols). Arrows indicate moments of fluxes switching. Dependencies of maximal Ge concentration in the first peak (c) and thickness of Ge layer in NW (d) on drop diameter for $\tau = 20$ s.

ible fluctuations in stationary concentration of semiconductor matter in the drop are due to nucleation of new crystal layer at drop-whisker interface. For mono-nucleation process in drops with small diameter these fluctuations are more evident. Fig. 2c demonstrates dependence of maximal Ge content in the first $Si_{1-x}Ge_x$ layer on drop diameter. For given τx decreases with whisker diameter. As a characteristic of Ge layer thickness w doubled half-width of the Ge peaks in the whisker was chosen. In Fig. 2d dependence of Ge layer thickness on drop diameter is shown. Profile blurring in Si-Ge junction is due to gradual changing of Ge and Si concentration in Au drop after switching germanium and silicon fluxes during growth. For all $Si_{1-x}Ge_x$ layers considered above $x < 1$, that is why the thickness of heterojunction is equal to w. In diffusion induced mode typical for MBE the growth rate is higher for thinner whiskers. So the length of NW with larger diameter is smaller, thus thickness of Ge layer decreases with diameter. The decreasing dependence of Ge-Si heterojunction abruptness on drop diameter is predicted for short Ge deposition time not enough to achieve stationary concentration in the drop.

Effect of composition dependence on NW diameter was also found in $Si_{1-x}Ge_x$ whiskers grown at simultaneous Si and Ge deposition. The increase of Ge concentration with enlargement of NW diameter demonstrates Fig. 3. The same phenomenon for CVD grown whiskers was observed experimentally [4]. In this case rise of Ge content with whisker diameter can be explained by different adsorption properties of Si- and Ge-containing precursors (P_{Si} and P_{Ge}): if P_{Ge} is adsorbed primary on the drop, and P_{Si} — both on the drop and on the substrate, then Ge percentage in NW will be dependent on drop size. Dependence of Ge content on temperature is due to different temperature dependence of P_{Si} and P_{Ge} chemical activity and sublimation energies.

2. Summary

Characteristics of $Si_{1-x}Ge_x$ nanowhiskers were analyzed by Monte Carlo simulation. Dependences of maximal Ge concentration in axial Si-Ge junctions in Si whiskers on the ratio of Si and Ge flux intensities, duration of these fluxes and gold drop diameter were obtained. Dependence of maximal Ge concentration on time of Ge deposition is due to gradual changing of catalyst drop composition after switching Ge and Si fluxes. This delay is the main reason of heterojunction blurriness. Composition dependence of $Si_{1-x}Ge_x$ whiskers grown at simultaneous Si and Ge deposition on NW diameter can be explained by different adsorption properties of Si- and Ge-containing precursors.

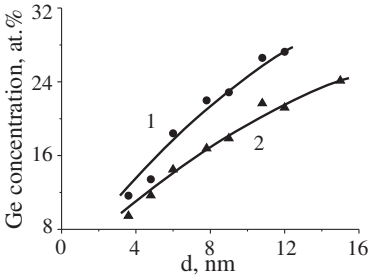

Fig. 3. Ge concentration in $Si_{1-x}Ge_x$ NW versus the diameter of the whisker grown at different temperatures: 1 — $T = 750$ K, 2 — $T = 800$ K (simultaneous Si and Ge deposition: $F_{P_{Si}} = 0.01$ ML/s; $F_{P_{Ge}} = 0.005$ ML/s).

Acknowledgements

This work was supported by RFBR grant (08-02-00068) and the project "Growth mechanisms and characteristics of Si and SiGe nanowhiskers" according to basic research RAS Presidium Program No. 27.

References

[1] A. G. Nastovjak, I. G. Neizvestny, N. L. Shwartz, *Solid State Phenomena* **156–158**, 235 (2010).
[2] N. D. Zakharov, P. Werner, G. Gerth, L. Schubert, L. Sokolov, U. Gosele, *J. Cryst. Growth* **290**, 6 (2006).
[3] E. Sutter, P. Sutter, *Nano Lett.* **8** 2, 411 (2008).
[4] X. Zhang, K.-K. Lew, P. Nimmatoori, J. M. Redwing, E. C. Dickey, *Nano Lett.* **7**, 3241 (2007).

18th Int. Symp. "Nanostructures: Physics and Technology"
St Petersburg, Russia, June 21–26, 2010

Electroabsorption spectroscopy of Ge/Si quantum dots

A. I. Yakimov, A. I. Nikiforov, A. A. Bloshkin and A. V. Dvurechenskii
Rzhanov Institute of Semiconductor Physics, SB RAS, Novosibirsk, Russia

Abstract. Using the electroabsorption spectroscopy we study effect of interdot coupling on the excitonic transitions in vertically aligned double Ge/Si quantum dots. We find that when two dots are brought closely together the oscillator strength may enlarge by a factor of about 3 as compared to the single-dot system. The experimental results are supported by theoretical considerations.

The search for the physical mechanisms that increase the efficiency of radiative recombination and the processes of the interband absorption of light in indirect band semiconductors such as silicon and germanium has been one of the topical problems of the physics of semiconductors for a long time. A significant increase in the oscillator strength for interband transitions will allow for the integration of opto- and microelectronic devices on a single silicon substrate. The spatial separation of charge carriers involved in the interband absorption or radiative recombination process in type-II Ge/Si quantum dots (QDs) prevents the development of effective Ge/Si-based optoelectronic devices. However, recently it has been demonstrated that the vertically stacked Ge islands in Si show a strong photo- and electroluminescence at a wavelength of 1.5 μm up to room temperature [1]. Probably the enhanced emission from the vertically aligned dots can be originated from the formation of collectivized or molecularlike electron and hole states in the structure due to tunnel coupling, thus making the interband transitions in Ge Si heterostuctures direct in a real space. In this work, we examine the role of vertical coupling between QDs on the excitonic transitions in double Ge/Si QDs by using electroabsorption (EA) spectroscopy.

The idea of the experiment was the following. Self-assembled Ge/Si QDs are formed in the Stranski–Krastanov growth mode. It is known that the Ge critical thickness decreases in the upper layers of a multilayer structure leading to the gradual increase of the island sizes within the island stacks from layer-to-layer [2,3]. This is due to the reduction of the strain caused by the lateral expansion of the lattice plane in the underlying island giving rise to a reduction of the effective misfit. Thus, the dots in a stack have different size, composition, and strain, and therefore different confined energy levels. As a result, electrons and holes tend to localize in individual dots with no electronic coupling between the dots. However, the state coupling would appear when an electric field brings the confined states into the resonance. Thus, the interdot coupling can be manipulated by an electric field.

For controlled tuning of the electric field, the Ge QDs are embedded in the intrinsic region of an Si $p-i-n$ diode (n^+ region uppermost), allowing fields to be applied parallel to the growth direction z (applying a reverse bias to a $p-i-n$ structure results in an electric field pointing from n^+ substrate to p^+ surface). Ge/Si heterostructures with self-assembled Ge QDs were grown by molecular-beam epitaxy on a p-Si(001) substrate with a resistivity of 150 Ω cm. The growth temperature was generally 500 °C for all layers. First, a 500 nm B-doped p^+-type Si buffer layer with doping concentration of 3×10^{18} cm^{-3} followed by a 200 nm Si undoped layer were grown. Then two Ge layers separated by Si spacer layer of

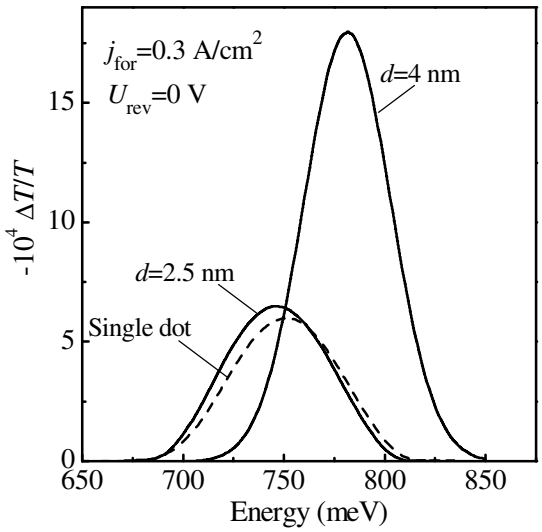

Fig. 1. Change of the absorption for the single-layer and double-layer samples in depletion mode with injected current density $j_{\rm for}=0.3$ A/cm^2 and reverse bias $U_{\rm rev}=0$ V. Here T designates transmission.

thickness d, followed by a 100 nm undoped Si layer, were fabricated at a rate of 0.02 ML/s. For all samples the Ge coverage is 6 ML. Self-assembled Ge/Si QDs with nominal separations of $d=2.5$ and 4 nm were prepared. To identify effects of dot coupling, the reference sample was grown under conditions similar to the double-dot samples, except that only a single Ge layer was deposited. Immediately after the deposition of Ge, the temperature was lowered to $T_s=350$–400 °C and the Ge islands are covered by a 1-nm Si layer. This procedure is necessary to minimize Ge-Si intermixing and to preserve island shape and size from the effect of a further higher temperature deposition. The Ge nanoislands in the first (bottom) layer act as stressors, providing preferential nucleation sites for the dots in the upper layer, directly above the underlying dot, to create the vertically aligned double QDs. The device was completed by capping a 300-nm-thick n^+-doped Si layer (Sb, 5×10^{18} cm^{-3}) to form a $p-i-n$ junction. From cross-sectional transmission electron micrographs, we observe the Ge dots to be approximately 15 nm in lateral size and about 1.5 nm in height. The scanning tunneling microscopy of a sample without the Si cap layer showed that the Ge islands have a shape of 'hut'-clusters. The density of the dots is $\sim10^{11}$ cm^{-2}.

The electroabsorption measurements were performed at temperature $T=93$ K using a VERTEX-70 Fourier transform infrared spectrometer in normal incidence geometry. The samples were forward or reverse biased to obtained the reference and the probe spectra, respectively. Under a forward applied bias,

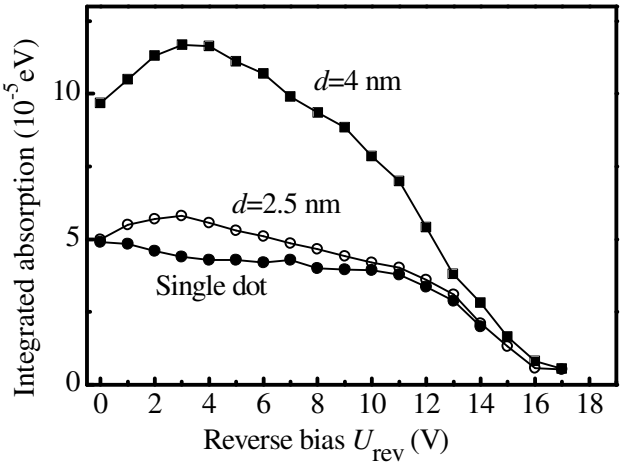

Fig. 2. The integrated EA intensity for the single-layer and double-layer samples as a function of the applied reverse bias and $j_{for} = 0.3$ A/cm^2.

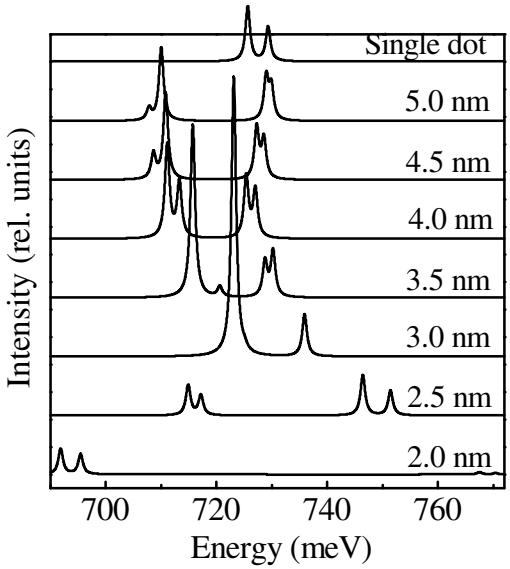

Fig. 3. Calculated optical resonances for the first four exciton states in double quantum dots versus the dot separation d. For comparison, the excitonic transitions for single quantum dot are also shown. The intensities of the resonances are normalized to the ground-state transition intensity in a single quantum dot.

the injected current, j_{for}, was selected for filling the electrons and holes into the QD states, thus blocking the excitonic transitions. The reverse bias, U_{rev}, was chosen for depleting the carriers from the QDs, thus allowing the interband absorption. Therefore, the transmission spectra of interest can be found directly as the ratio of the spectrum recorded at the reverse bias condition to the spectrum of the forward biased sample so that any spectral response not associated with the electrically modulated part of the samples is eliminated from the results. In this work, two kinds of measurements were carried out, one is the filling mode and the other is the depletion mode. The filling mode is that fixing the reverse bias U_{rev} and varying the injected current j_{for} for filling the carriers into the QD states. Alternatively, in the depletion mode we vary the U_{rev} at a fixed j_{for}.

Typical EA spectra in the depletion mode are displayed in Fig. 1. In order to accurately determine the interband transition energy of QDs, we fit the data with a Gaussian-type function which is appropriate for the inhomogeneous broadening related to the size fluctuations in QDs. A spectral line at energies ~750 meV with a Gaussian line shape and a broadening of 50–70 meV has been established to originate from the indirect excitonic transition between the hole ground state in the Ge dots with lateral size 15 nm and the electron state confined in Si near the heterojunction [4]. The intensity of the transition ia tuned by applied bias as shown in Fig. 2. For a double-dot sample with dot separation $d = 4$ nm, the integrated absorption at $U_{rev} \sim 4$ V increases by a factor of about 3 as compared to the single-layer system.

In order to understand this observation we performed calculations of oscillator strength for the $\Delta_1 - \Gamma_{25'}$ interband transition in two vertically coupled pyramidal Ge quantum dots embedded in Si [5]. A six-band $\mathbf{k} \times \mathbf{p}$ formalism was used to study the $\Gamma_{25'}$ hole states and single-band approach to obtain the Δ_1 electron state interacting with hole. The elastic strain due to the lattice mismatch between Ge and Si was included into the problem via Bir–Pikus Hamiltonian. The oscillator strength was found in dipole approximation. Calculated optical spectra are presented in Fig. 3. The most interesting result shown in Fig. 3 is an increase in the intensity of one of the possible transitions for the double QD with $d = 3.0$–3.5 nm. In particular, the probability of the exciton transition in the double QD with $d = 3.0$ nm is five times larger than the probability of this transition in the single dot. Detailed analysis showed that at $d \sim 3$ nm, the electron resides between two dots in a region where the probability to find the hole is finite due to quantum mechanical coupling between the dots. This makes the interband transition to be partially direct in the real space, thereby increasing the oscillator strength. Although this effect is less pronounced in the experiment due to the fluctuation of dot sizes in the samples, we may conclude that calculations reproduce well the experimental observation.

Acknowledgements

This work was supported by the Russian Foundation for Basic Research (Grant No. 09-02-12393).

References

[1] N. D. Zakharov, V. G. Talalaev, P. Werner, A. A. Tonkikh, and G. E. Cirlin, *Appl. Phys. Lett.* **83**, 3084 (2003); V. G. Talalaev, G. E. Cirlin, A. A. Tonkikh, N. D. Zakharov, and P. Werner, *Phys. Stat. Sol (a)* **198**, R4 (2003).

[2] J. Tersoff, C. Teichert, M. G. Lagally, *Phys. Rev. Lett* **76**, 1675 (1996).

[3] V. Le Thanh, V. Yam, P. Boucaud, F. Fortuna, C Ulysse, D. Bouchier, L. Vervoort, J.-M. Lourtioz, *Phys. Rev. B* **60**, 5851 (1999); V. Le Thanh, V. Yam, P. Boucaud, Y. Zheng, D. Bouchier, *Thin Solid Films* **369**, 43 (2000).

[4] A. Y. Yakimov, N. P. Stepina, A. V. Dvurechenskii, and A. I. Nikiforov, *Phys. Rev. B* **63**, 045312 (2001).

[5] A. I. Yakimov, A. A. Bloshkin, and A. V. Dvurechenskii, *JETP Letters* **90**, 569 (2009).

18th Int. Symp. "Nanostructures: Physics and Technology"
St Petersburg, Russia, June 21–26, 2010

Nucleation and self-ordering of misfit dislocations in SiGe nanoislands on Si(100)

V. A. Zinovyev[1], A. Marzegalli[2], F. Boioli[2], R. Gatti[2], F. Montalenti[2] and L. Miglio[2]

[1] Institute of Semiconductor Physics, 630090 Novosibirsk, Russia
[2] Dipartimento di Scienza dei Materiali, Universita di Milano-Bicocca, via Cozzi 53, 20125 Milano, Italy

Abstract. This work devotes to theoretical study of nucleation and spatial ordering of the misfit dislocations, which take place during heteroepitaxial growth of multi-dislocated SiGe islands on Si(100). The strain field induced by the misfit dislocations is modeled by finite-element-method in three dimensions, fully taking into account the interaction with the multifaceted free surfaces of realistic islands. It is shown that the formation of parallel and evenly-spaced concentric dislocation loops at the basal plane of multi-dislocated SiGe island is energetically favorable. The distances between neighboring dislocations in SiGe island are finally obtained and successfully compared with the experimental data.

Introduction

Misfit dislocation nucleation and further evolution in heteroepitaxial three dimensional (3D) islands are substantially different from the case of continuous flat films, because of the reduced size of the islands (up to some hundred nanometers in lateral size), the large and multifaceted free surface, and the significant compressive strain gradients, increasing from the island top to the bottom [1]. In particular, it is interesting to investigate phenomena of the dislocation self-ordering in nanometric island volumes for fundamental knowledge and for possible practical applications. Recently, transmission electron microscopy (TEM) analysis of SiGe dislocated islands grown on Si(100) substrates demonstrated, that misfit dislocations are self-ordered around island center in very regular "ring-like" structure composed of concentric polygons at the basal plane of the islands, with almost constant spacing between neighboring dislocations [2]. Moreover in-situ TEM observations strongly suggests that the rounded shape of dislocations is the result of the defect evolution [3]. However, the mechanism driving such unique dislocation self-ordering is unknown. In order to provide a deep insight into the dislocation ordering, we made simulation of the nucleation and evolution of misfit dislocations in heteroepitaxial islands, involving the periodic fulfilment of the critical conditions for the nucleation of a new dislocation and the guided evolution of the misfit dislocation positions by the island boundaries and the existing dislocations.

1. Modeling of the dislocated island

The finite-element method (FEM) have been used to find stress distribution in multidislocated island. We constructed in the FEM code a Si(001) substrate and a SiGe barn-shaped island with a typical aspect ratio: 0.33 [4]. In accordance with TEM observations [2,3], we suggested, that the dislocations inside 3D SiGe islands on Si(100) have a regular polygonal shape. We supply to FEM code the analytical solution of the elastic field produced, in an infinite medium, by eight dislocation segments forming a regular octagon along (110) and (100) directions. In each point the sum of the eight stress fields together with a hydrostatic compression, related to the lattice mismatch between the island and the substrate materials, is imposed as initial condition.

The FEM calculation is repeated for different island sizes and, for each size, different octagon dimensions are considered. It allows to find the critical island size for onset of the plastic relaxation and the equilibrium position of the first dislocation loop by assuming the elastic energy stored in the whole system equal to the value calculated for the coherent case. The procedure is then repeated for a second dislocation loop (same geometric characteristics). In this case we compare the energy value for each island dimensions when both the loops are present, and when it is present only the first. A second critical dimension and equilibrium position is found when the two values are equal. The procedure is iterated up to five dislocation loops.

2. Results and discussion

First, we considered case of a pure Ge barn. In Fig. 1 is shown a color map reporting the hydrostatic stress ($\sigma_{xyz} = \sigma_{xx} + \sigma_{yy} + \sigma_{zz}$) as calculated at the final stage at the interface. Dislocation equilibrium positions are equally spaced starting from the second one, as revealed by TEM images [2]. However the critical dimensions of the loops turns out to be overestimated, e.g., the critical island size for the first loop nucleation has been 73 nm, nearly doubled with respect to the theoretical prediction published in Ref. [4]. Such discrepancy may be due to the assumptions in the dislocation geometry. The non-

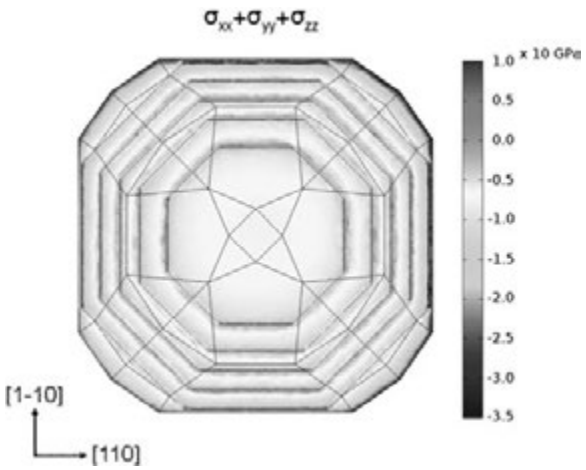

Fig. 1. (color online): Top view of a color map representing the hydrostatic stress ($\sigma_{xyz} = \sigma_{xx} + \sigma_{yy} + \sigma_{zz}$) at the interface with the substrate for a multidislocated island as calculated by FEM, considering close loop defect geometries.

uniform features of the strain field present in the island, due to the simple elastic relaxation, imply that the most effective Burgers vector relieving the deformation is different on two island sides [5]. Therefore, we propose the different dislocation evolution. We suppose two nucleation events on the two island sides, each of them creating a dislocation segment with the most favored Burgers vector. In this case the critical island base turns to be 26 nm, in better correspondence with values reported in Ref. [4]. Moreover, we constructed a barn island with uniform composition $Si_{0.64}Ge_{0.36}$ corresponding to the growth temperature about 700 °C. In this case the critical base becomes 83 nm and the average separation distance between dislocations ∼16 nm, which are in a good correspondence with the experimental values obtained from TEM observations [2,3].

On the base of analysis of simulation results and experimental data, we propose the following scenario of dislocation evolution in SiGe nanoislands. Dislocations nucleate at the island edges as straight segments, then the island expands rapidly in the perpendicular direction allowing the segment to be elongated. Reaching the surface the dislocations bends following the island perimeter [3]. The island lateral expansion and dislocation bending are easily explained as the most effective evolution in order to relax the deformation stored in the island due to the lattice mismatch with the substrate. The first process causes the placing of the dislocation in its equilibrium position inside the island that allows the overall best relaxation, while the second process allows to relieve the strong compression present along the island edges. Each new dislocation is pulled inside the island in order to maximize the strain release but it is simultaneously repelled by the previous dislocations. The changing rate of both terms turns out to be almost independent of the island volume. So, while the critical island dimensions are defined by the elastic budget stored in the island, i.e. by the balance between the energy gain and energy cost for the dislocation introduction, the actual dislocation position depends mainly on a local equilibrium arising for each new dislocation near the island edge between attractive and repulsive forces. The natural ordering of dislocations is then explained supposing that the nucleation condition for a new dislocation is reached when the island edge is far apart from the previous dislocation at an almost fixed distance.

Acknowledgements

This work has been supported by Russian Foundation of Basic Research (grant 09-02-00882).

References

[1] G. Vastola, R. Gatti, A. Marzegalli, F. Montalenti, Leo Miglio, *Self-Assembled Quantum Dots* (Berlin: Springer) 421–438, (2008).
[2] A. Portavoce, R. Hull, M. C. Reuter, F. M. Ross, *Phys. Rev. B* **76**, 235301 (2007).
[3] F. M. Ross, J. Tersoff, M. C. Reuter, F. K. LeGoues, R. M. Tromp, *Microsc. Res. Tech.* **42**, 281 (1998).
[4] R. Gatti, A. Marzegalli, V. A. Zinovyev, F. Montalenti, Leo Miglio, *Phys. Rev. B* **78**, 184104 (2008).
[5] B. J. Spencer and J. Tersoff, *Phys. Rev. B* **63**, 205424 (2001).

18th Int. Symp. "Nanostructures: Physics and Technology"
St Petersburg, Russia, June 21–26, 2010

Spin dynamics of electrons and holes in InGaAs/GaAs quantum wells at milliKelvin temperatures

D. R. Yakovlev[1,2], L. V. Fokina[1], I. A. Yugova[3], M. M. Glazov[2], I. A. Akimov[1,2], A. Greilich[1], D. Reuter[4], A. D. Wieck[4] and M. Bayer[1]

[1] Experimentelle Physik II, Technische Universität Dortmund, D-44221 Dortmund, Germany
[2] Ioffe Physical-Technical Institute, St Petersburg, Russia
[3] Physical Faculty of St Petersburg State University, 198504 St Petersburg, Russia
[4] Angewandte Festkörperphysik, Ruhr-Universität Bochum, D-44780 Bochum, Germany

Abstract. The carrier spin dynamics in a *n*-doped (In,Ga)As/GaAs quantum well has been studied by time-resolved Faraday rotation at temperatures down to 430 milliKelvin. The mechanisms of long-lived spin coherence generation are discussed for the cases of trion and exciton resonant excitation. Carrier localization leads to a saturation of spin relaxation times at 45 ns for electrons below 4.5 K and at 2 ns for holes below 2.3 K. The underlying spin relaxation mechanisms are discussed.

Introduction

The spin physics of semiconductor heterostructures attracts considerable attention nowadays due to the emerging fields of semiconductor spintronics, quantum computation and quantum information. One of the evident goals is to optimize material properties and heterostructure design to achieve the longest possible spin relaxation time so that sufficient room is left for implementing protocols for spin manipulation and read-out.

Carrier localization quenches the particle orbital motion and is one of the ways to suppress efficient spin-relaxation mechanisms related to the spin-orbit interaction. Spin relaxation of electrons localized on donors in bulk GaAs can exceed 100 ns [1,2]. In quantum well structures localization of the two-dimensional electrons at liquid helium temperatures is required to demonstrate relaxation times in the order of tens of nanoseconds [3,4]. Under these conditions spin relaxation times of few nanoseconds have been reported for resident holes [6,7,8].

In this paper we apply time-resolved Faraday rotation (FR) technique to study the carrier spin dynamics in *n*-doped (In,Ga)As/GaAs quantum well. We focus on the long-lived spin dynamics of resident electrons and photogenerated holes measured in the regime of resonant spin amplification (RSA) at very low temperatures down to 430 mK.

1. Experimental

We study a heterostructure with two coupled 8 nm thick $In_{0.09}Ga_{0.91}As$/GaAs quantum wells (QWs) separated by a thin (1.7 nm) GaAs barrier, for details see Ref. [4]. The two-dimensional electron gas density in the QWs provided by the modulation doping of barriers is about 10^{10} cm^{-2}. In photoluminescence spectrum two emission lines separated by 1.4 meV are observed which we attribute to exciton (X) and negatively charged trion (T) recombination. Their full width at half maximum of 1 meV is caused by trion and exciton localization on alloy and QW width fluctuations.

For pump-probe Faraday rotation mode-locked Ti:Sph laser with pulse duration of 1.5 ps and a repetition frequency of 75.6 MHz was used [4]. The laser wavelength was tuned in resonance with either the QW exciton or trion transitions. The excitation density was kept close to the lowest possible limit at 0.5 W/cm^2. A sensitive balanced photodiode scheme was used for recording the Faraday rotation and ellipticity signals. The sample was mounted in a cryostat with a split-coil superconducting magnet which allowed us to perform experiments in the Voigt configuration with the magnetic field $\mathbf{B} \parallel \mathbf{x}$ oriented in the quantum well plane perpendicular to the light propagation direction (coinciding with the structure growth axis, denoted as z-axis). The sample temperature was varied from 0.43 to 80 K. For milliKelvin measurements the cryostat had a ^{3}He insert, instead of a ^{4}He variable temperature insert.

2. Results and discussion

Measuring Faraday rotation signal in a magnetic field of 0.5 T under both resonant excitation of exciton and trion resonances the long-living electron spin beats have been observed. Their decay time exceeds the laser repetition period of 13.2 ns and the signal has been clearly observed at the negative delays. For this regime the dephasing time can be evaluated by the resonant spin amplification technique (RSA) [1].

The spin amplification signals measured on the exciton and trion resonance qualitatively differ from each other, see [4,5]. For the trion resonance the signal amplitude is strongly suppressed at zero magnetic field and the amplitude increases with growing field strength. For the exciton resonance the signal has a complicated shape, which results from a combination of the typical RSA signal and the trion bat-like signal. The bat-like signal at the trion resonance allows us to use the procedure suggested very recently in Ref. [4] to evaluate both the electron and the hole spin relaxation times in *n*-doped QWs.

The electron and hole spin relaxation times measured at different temperatures are collected in Fig. 1. The temperature dependencies of spin relaxation times for electrons and holes are qualitatively similar. The times are almost constant at at very low temperatures, which shows that the spin dynamics in these regimes are controlled by temperature independent mechanisms. At elevated temperatures the times drop by more than an order of magnitude. As can be seen from the solid lines in Fig. 1 these behaviors can be well fitted by the following function describing thermal activation from the ground state with a long relaxation time to an excited state with a shorter relaxation time:

$$\frac{1}{T_s^{e(h)}} = \frac{1}{T_0^{e(h)}} + \frac{1}{T_{exc}^{e(h)}} \exp\left(-\frac{\Delta E_{e(h)}}{k_B T}\right). \qquad (1)$$

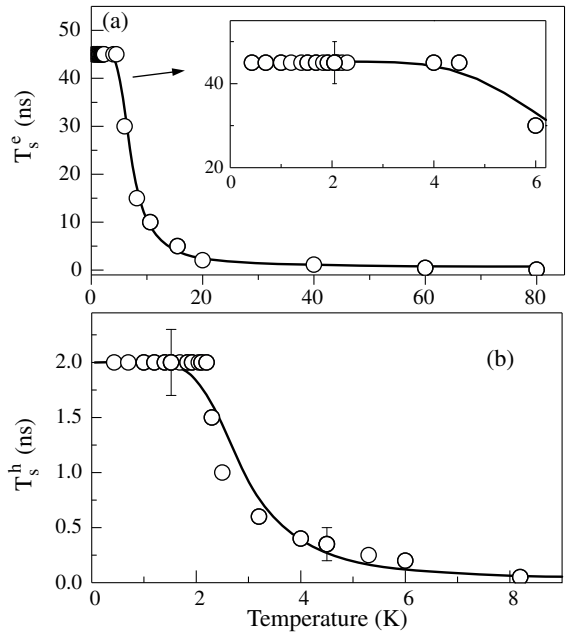

Fig. 1. Temperature dependencies of electron (a) and hole (b) spin relaxation times in an (In,Ga)As/GaAs QW. Symbols are experimental data and lines are fits with Eq. (1) using the following parameters: $T_0^e = 45$ ns, $T_{exc}^e = 0.5$ ns and $\Delta E_e = 3$ meV for electrons in panel (a), and $T_0^h = 2$ ns, $T_{exc}^h = 10$ ps and $\Delta E_h = 1.4$ meV for holes in panel (b).

Here $T_0^{e(h)}$ are the spin relaxation times in the electron (hole) ground states, $T_{exc}^{e(h)}$ are constants characterizing the transitions between the ground and excited states which depend on the electron-phonon interaction, $\Delta E_{e(h)}$ are the characteristic activation energies, and k_B is the Boltzmann constant.

The electron spin relaxation time, T_s^e, is constant in the temperature range from 0.43 to 4.5 K at an extremely large value of 45 ns. At these temperatures the resident electrons are localized and their spin relaxation is provided by the hyperfine interaction with the nuclei spins, which is almost temperature independent. At temperatures above 5 K the resident electrons are thermally activated to the delocalized states and the Dyakonov–Perel relaxation mechanism [9] which is very efficient for free electrons starts to act. As a result the relaxation time drops to 1.1 ns at 40 K and further down to 110 ps at 80 K. Such a behavior is typical for n-doped QWs with a diluted concentration of the resident electrons [3,4].

Let us turn now to the temperature dependence of the hole spin relaxation time, T_s^h, in Fig. 1(b). Below 2.2 K T_s^h saturates at a value of 2 ns. At the moment it is not clear to us what relaxation mechanism is controlling the hole spin dynamics in the range 0.43. . . 2.2 K. Most probably it is due to the admixture of the light-hole to the heavy-hole states, enhancing strongly the possibility for the spin-flip.

The hyperfine interaction with the nuclei is significantly weaker for the holes than for the electrons. This has been confirmed by the recent report on ultralong hole spin relaxation with about 70 ns relaxation time, measured in the range from 0.4–1.2 K for a p-doped 4-nm GaAs/$Al_{0.3}Ga_{0.7}As$ QW [10]. Our experimental situation differs from the one in p-doped samples with resident holes, as in n-doped samples we detect the spin dynamics of photogenerated holes bound in negatively charged trions. However, in the trion ground state, which is a singlet state, the two electrons have antiparallel spin orientations and flip-flop electron-hole process are not possible without exciting the trion complex into a triplet state, which requires an energy similar to the trion binding energy of 1.4 meV. In fact this energy is in very good agreement with the activation energy $\Delta E_h = 1.4$ meV, which has been obtained from fitting the experimental data in Fig. 1(b) by Eq. (1). Therefore we suggest that the strong decrease of the hole spin relaxation time at temperatures above 2.2 K is either due to trion thermal dissociation, which excites the hole into the continuum of free states with a strong spin-orbit interaction leading to a fast spin relaxation, or due to flip-flop process involving the trion triplet state.

Acknowledgements

This work has been supported in part by the Deutsche Forschungsgemeinschaft, RFBR, President grant for young scientists and the "Dynasty" Foundation — ICFPM.

References

[1] J. M. Kikkawa *et al*, *Phys. Rev. Lett.* **80**, 4313 (1998).
[2] R. I. Dzhioev *et al*, *Phys. Solid State* **39**, 1765 (1997).
[3] E. A. Zhukov *et al*, *Phys. Stat. Sol. B* **243**, 878 (2006).
[4] I. A. Yugova *et al*, *Phys. Rev. Lett.* **102**, 167402 (2009).
[5] L. V. Fokina *et al*, arXiv:1001.3228 (2010).
[6] X. Marie *et al*, *Phys. Rev. B* **60**, 5811 (1999).
[7] M. Syperek *et al*, *Phys. Rev. Lett.* **99**, 187401 (2007).
[8] M. Kugler *et al*, *Phys. Rev. B* **80**, 035325 (2009).
[9] *Spin Physics in Semiconductors*, Ed. M. I. Dyakonov (Springer-Verlag, Berlin, 2008).
[10] T. Korn *et al*, arXiv:0909.3711v [cond-mat.mes-hall] 21 September 2009.

18th Int. Symp. "Nanostructures: Physics and Technology"
St Petersburg, Russia, June 21–26, 2010

Spin dynamics of free electrons in (110)-oriented quantum wells

S. A. Tarasenko
Ioffe Physical-Technical Institute, St Petersburg, Russia

Abstract. It is shown that the spin dynamics of free carriers in quantum wells on (110) substrate is unusual and qualitatively differs from that in conventional (001)-grown structures. In asymmetric (110) quantum wells, the in-plane and out-of-plane spin components are coupled and, therefore, the relaxation of electron spin initially oriented along the growth axis leads to the appearance of an in-plane spin component. The interplay of the cyclotron motion and the Larmor precession in an external magnetic field in Faraday geometry results in a non-monotonic field dependence of the spin density. We also demonstrate that the energy relaxation of hot unpolarized carriers in asymmetrical (110) quantum wells should lead to their partial spin polarization.

Introduction

The long and controllable spin lifetime of carriers is a crucial factor for spintronic applications. Of particular interest in this context are semiconductor quantum wells (QWs) grown on (110)-oriented substrates. It was observed that the electron spin lifetime in such QWs drastically depends on the confinement potential symmetry and, therefore, can be tuned in a wide range by the gate voltage or by modifying the doping profile [1]. In symmetric QWs, the lifetime of electron spin along the QW normal can be as long as tens nanoseconds [2], which is caused by the suppression of D'yakonov–Perel' spin relaxation mechanism for this crystallographic orientation [3]. If, however, the QW is asymmetric, structure inversion asymmetry leads to the Rashba effective magnetic field speeding up the spin dephasing.

In this communication, we study the electron spin dynamics in asymmetric (110)-oriented QWs. We show that the low space symmetry of such structures (point group C_s) gives rise to a number of spin effects which are forbidden in conventional (001)-grown structures. In asymmetric (110) QWs, the growth direction does not coincide with a principle axis of the spin-relaxation-rate tensor. Therefore, the relaxation of electron spin initially oriented along the QW normal is described by a sum of exponential functions with different decay rates and leads to the appearance of an in-plane spin component. We also show that the partial spin polarization of carriers in asymmetric (110) QWs can be achieved by simple electron gas heating.

1. Spin relaxation

The relaxation of electron spin $\mathbf{S}$ is generally described by equation

$$\frac{dS_\alpha(t)}{dt} = -\sum_\beta \Gamma_{\alpha\beta} S_\beta(t)\,, \qquad (1)$$

where $\Gamma_{\alpha\beta}$ are components of the spin-relaxation-rate tensor, and α, β are the Cartesian coordinates. Asymmetric (110)-grown QWs contain only one non-trivial symmetry element: the mirror plane, which is normal to the in-plane axis $x \parallel [1\bar{1}0]$ and contains the in-plane axis $y \parallel [00\bar{1}]$ and the QW normal $z \parallel [110]$. The symmetry analysis shows that non-zero components of the spin-relaxation-rate tensor in such structures are Γ_{xx}, Γ_{yy}, Γ_{zz}, and $\Gamma_{yz} = \Gamma_{zy}$. The presence of the off-diagonal components Γ_{yz} and Γ_{zy} indicates that both the in-plane axis y and the QW normal z are not principle axes of the tensor $\mathbf{\Gamma}$. The principle axes $\tilde{x}$, $\tilde{y}$, $\tilde{z}$ and eigen values γ_i of the tensor $\mathbf{\Gamma}$ are found from the equation $\det(\mathbf{\Gamma} - \gamma\mathbf{I}) = 0$, which yields [4]

$$\begin{aligned} \gamma_{\tilde{x}} &= \Gamma_{xx}\,, \\ \gamma_{\tilde{y}} &= \left[\Gamma_{yy} + \Gamma_{zz} + \sqrt{(\Gamma_{yy} - \Gamma_{zz})^2 + 4\Gamma_{yz}^2}\right]/2\,, \\ \gamma_{\tilde{z}} &= \left[\Gamma_{yy} + \Gamma_{zz} - \sqrt{(\Gamma_{yy} - \Gamma_{zz})^2 + 4\Gamma_{yz}^2}\right]/2\,, \end{aligned} \qquad (2)$$

where the axes $\tilde{x}$, $\tilde{y}$, $\tilde{z}$ are obtained from x, y, z by rotating the coordinate frame around the axis x by an angle θ,

$$\tan\theta = \frac{2\Gamma_{yz}}{\Gamma_{yy} - \Gamma_{zz} + \sqrt{(\Gamma_{yy} - \Gamma_{zz})^2 + 4\Gamma_{yz}^2}}\,, \qquad (3)$$

see inset to Fig. 1.

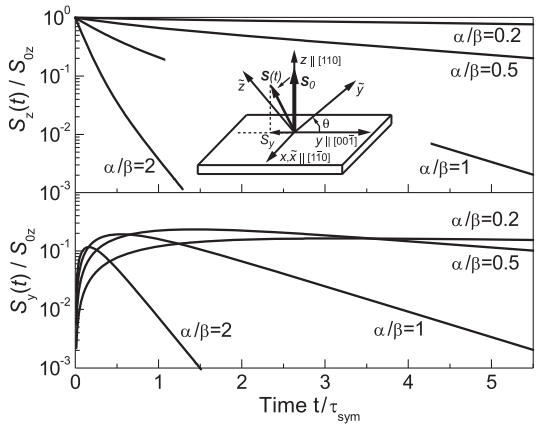

Fig. 1. Time evolution of the spin components $S_z(t)$ and $S_y(t)$ calculated for the initial spin $\mathbf{S}_0$ oriented along the QW normal z. The inset shows arrangement of the principle axes $\tilde{x}$, $\tilde{y}$, and $\tilde{z}$ of the spin-relaxation-rate tensor.

The non-coincidence of the QW growth direction with a principle axis of the tensor Γ means that the relaxation of electron spin initially directed along the QW normal is described by two different rates $\gamma_{\tilde{z}}$ and $\gamma_{\tilde{y}}$. Moreover, the relaxation leads to the rotation of spin in the (yz) plane resulting in a non-zero value of S_y, see inset to Fig. 1

Shown in Fig. 1 are the time dependences of the spin components $S_z(t)$ and $S_y(t)$ calculated for different ratios between

the Rashba and Dresselhaus contributions α/β and $\mathbf{S}_0 \parallel z$. It is assumed that the D'yakonov–Perel' mechanism determines the spin relaxation and the Larmor frequency corresponding to the effective magnetic field in (110) QWs has the form $\mathbf{\Omega_k} = (2/\hbar)(\alpha k_y, -\alpha k_x, \beta k_x)$, which implies

$$\begin{aligned} \Gamma_{xx} &= \left(\alpha^2+\beta^2\right) C\,, \quad \Gamma_{yy} = \left(\alpha^2+\beta^2\right) C\,, \\ \Gamma_{zz} &= 2\alpha^2 C\,, \quad \Gamma_{yz} = \Gamma_{zy} = \alpha\beta C\,, \end{aligned} \tag{4}$$

where the parameter C depends on the temperature and carrier density. The time t is measured in Fig. 1 in units of the in-plane relaxation time in symmetric QWs, $\tau_{\rm sym} = \beta^2 C$. The plotted dependences demonstrate that $S_z(t)$ cannot be described by one exponential function and S_y can be comparable to S_z even in the case of spin pumping along the QW normal. We also note that the sign of S_y is determined by the sign of the product $\alpha\beta$. Therefore, one can control the in-plane spin component by tuning the Rashba field, e.g., by the gate voltage.

We also study the effect of an external magnetic field on electron spin relaxation in (110)-grown QWs and show that it is unusual. Here, the interplay of the cyclotron motion of carriers, which suppresses the D'yakonov–Perel' spin relaxation mechanism, and the Larmor precession results in a non-monotonic dependence of the electron spin on the magnetic field even in the Faraday geometry. Such a behavior originates from the non-coincidence of the QW normal with a principle axis of the spin-relaxation-rate tensor.

2. Thermal orientation of electron spin

The low point-group symmetry of (110)-grown QWs gives also rise to another spin effect which is forbidden in structures of higher space symmetry. In asymmetrically-grown (110) QWs, the spin orientation of free electrons in the interface plane along the x axis occurs as soon as the the electron gas is driven out of thermal equilibrium with the crystal lattice. The mechanism of such a thermal orientation of electron spins is based on spin dependence of the electron-phonon interaction, which tends to restore equilibrium [5]. In the steady-state regime, when the electron temperature $T_{\rm e}$ and the lattice temperature T_0 are maintained slightly different from each other, the steady electron spin is proportional to the temperature difference $(T_{\rm e} - T_0)$.

Microscopically, the thermal orientation of electron spins is a two-stage process illustrated in Fig. 2. In the first stage (Fig. 2a), the carriers lose a part of their kinetic energy by emitting phonons. Such energy relaxation processes shown by curved arrows are spin-dependent: Electrons with the spin $+1/2$ along the z axis predominantly vacate the excited states with positive k_x while electrons with the spin $-1/2$ vacate the excited states with negative k_x. This leads to a nonequilibrium distribution where the spin-up hot carriers occupy mainly the left-hand branch of the dispersion curve while the spin-down carriers occupy mainly the right-hand branch. In the second stage (Fig. 2b), a net spin orientation of the electron gas appears as a result of the spin precession of nonequilibrium carriers in the spin-orbit coupling-induced effective magnetic field, which has an in-plane component due to the Rashba effect. Such a spin precession of nonequilibrium carriers is shown in Fig. 2b. Note that electrons with the spin $-1/2$ and wave vector $k_x > 0$ are acted upon by the effective field with the Larmor frequency $\mathbf{\Omega_k}$, while particles with the spin $+1/2$ and the negative wave

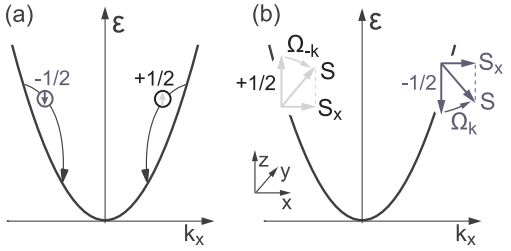

Fig. 2. Microscopic model of the thermal orientation of electron spins. Spin-dependent asymmetry of the electron energy relaxation followed by spin precession in the effective magnetic field leads to the partial spin polarization of carriers.

vector feel the field with the Larmor frequency $\mathbf{\Omega_{-k}}$. The effective magnetic field is an odd function of the wave vector, therefore, $\mathbf{\Omega_{-k}} = -\mathbf{\Omega_k}$, and the spins of particles with positive and negative values of k_x rotate in opposite directions. This leads to the appearance of the in-plane spin component $S_x > 0$ for all electrons in the subband and, thus, the net spin polarization of the electron gas.

The calculation shows that, in the case of electron energy relaxation due to interaction with bulk acoustic phonons, the electron spin density has the form

$$S_x \propto \frac{m^*\xi}{\rho a^3}\,\frac{\alpha\,\Xi_{\rm c}\Xi_{\rm cv}}{\alpha^2+\beta^2}\,\frac{T_{\rm e}-T_0}{k_{\rm B}T_{\rm e}^2}\,N_{\rm e}\,, \tag{5}$$

where m^* is the effective mass, ρ is the crystal density, a is the QW width, $\Xi_{\rm c}$ and $\Xi_{\rm cv}$ are the intraband and interband deformation-potential constants, $N_{\rm e}$ is the electron density, ξ is a coefficient given by $\xi = i\hbar P_{\rm cv}\Delta_{\rm so}/[3E_{\rm g}m_0(E_{\rm g}+\Delta_{\rm so})]$, $P_{\rm cv}$ is the interband matrix element of the momentum operator, m_0 is the free electron mass, $E_{\rm g}$ is the band gap energy, and $\Delta_{\rm so}$ is the energy of spin-orbit splitting of the valence band. An estimation for the spin density gives $S_x \sim 10^6$ cm^{-2} for the electron temperature $T_{\rm e} = 100$ K, the ratio $(T_{\rm e}-T_0)/T_{\rm e} \approx 1$, the quantum well width $a = 100$ Å, the carrier density $N_{\rm e} = 10^{11}$ cm^{-2}, and band parameters $m^* = 0.07m_0$, $\xi = 0.4$ Å, $\alpha/\hbar = 10^5$ cm/s, $\Xi_{\rm c} = -8$ eV, $\Xi_{\rm cv} = 3$ eV corresponding to GaAs-based QW structures. The estimated spin density is well above the experimental resolution.

Acknowledgements

This work was supported by the RFBR, President grant for young scientists (MD-1717.2009.2), and the Foundation "Dynasty" — ICFPM.

References

[1] O. Z. Karimov *et al*, *Phys. Rev. Lett.* **91**, 246601 (2003); V. V. Bel'kov *et al*, *Phys. Rev. Lett.* **100**, 176806 (2008).
[2] Y. Ohno *et al*, *Phys. Rev. Lett.* **83**, 4196 (1999); G. M. Müller *et al*, *Phys. Rev. Lett.* **101**, 206601 (2008).
[3] M. I. D'yakonov and V. Yu. Kachorovskii, *Sov. Phys. Semicond.* **20**, 110 (1986).
[4] S. A. Tarasenko, *Phys. Rev. B* **80**, 165317 (2009).
[5] S. A. Tarasenko, *Semicond.* **42**, 967 (2008).

18th Int. Symp. "Nanostructures: Physics and Technology"
St Petersburg, Russia, June 21–26, 2010

Quantum phenomena in the electron transport of InAs nanowires

D. Grützmacher, Ch. Volk, K. Sladek, K. Weis, S. Estevez Hernandez, H. Hardtdegen, N. Demarina and Th. Schäpers

Institute of Bio- and Nanosystems (IBN-1), Forschungszentrum Jülich and Jülich Aachen Research Alliance on fundamentals of future information technology (JARA-FIT), 52425 Jülich, Germany

Abstract. We investigated the quantum transport in InAs nanowires. From the universal conductance fluctuations at 0.5 K a phase-coherence length of 300 nm was extracted. By averaging the gate-dependent conductance fluctuations a magnetoconductance peak due to weak antilocalization was found indicating the presence of spin-orbit coupling. In a nanowire quantum dot formed by three gate fingers single electron tunneling was confirmed.

Introduction

Fundamental quantum effects in the electron transport of InAs nanowires have been studied. InAs nanowires assemble a number of remarkable features, thus the effective electron mass is very low and the surface accumulation layer due to Fermi-level pinning in the conduction band leads to the formation of a tubular shaped 2-dimensional electron gas (2DEG) on the surface (Fig. 1). Electrons in this surface accumulation layer are subject to strong spin-orbit coupling. Furthermore the radial macroscopic electric field related to the confining potential of the surface 2DEG lifts the spin-degeneracy for propagating electrons. This so-called Rashba effect is of relevance for spin electronic devices, since it can be employed for gate-controlled spin manipulation.

1. Experimental

The InAs nanowires were selectively grown on a pre-patterned GaAs (111)B substrate by low-pressure metalorganic vapor phase epitaxy in a N_2 atmosphere at a temperature of 600 °C. The wires have a diameter d of approximately 100 nm and a length L of about 5 μm (Fig. 2). After separating the InAs nanowires from their substrate, they were transferred on an n-type doped Si substrate covered by a 100-nm-thick SiO_2 layer. The nanowires were contacted individually by a pair of Ti/Au electrodes. The substrate was used as a back-gate to control the electron concentration. Additional top gates were formed by stacking a dielectric layer, either a $GdScO_3$ or a $LaLuO_3$, and a Ti/Au metal contact layer. Here we studied the electron transport at low temperatures in 2-terminal devices in the diffusive regime as well as in gated transistor structures.

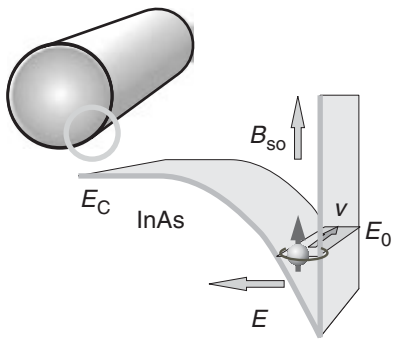

Fig. 1. Schematic illustration of a surface 2DEG in an InAs nanowire.

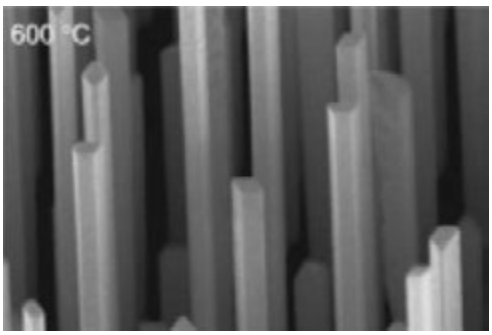

Fig. 2. Scanning electron micrograph of InAs nanowires grown by MOVPE.

2. Results and discussion

At low temperature the electron transport in small individual InAs nanowires is governed by electron interferences. If the length of the nanowire is comparable to the phase-coherence length l_ϕ magneto transport measurements reveal that the conductance fluctuates with an amplitude in the order of e^2/h. In spite of the fact that the low-temperature magneto-conductance strongly fluctuates the basic transport parameters, e.g. l_ϕ or the spin-orbit scattering length l_{so} can be extracted. Information on l_ϕ at various temperatures is obtained from the average fluctuation amplitude as well as from the correlation field. In Fig. 3 the magneto-conductance is plotted for various temperatures ranging from 0.5 to 30 K.

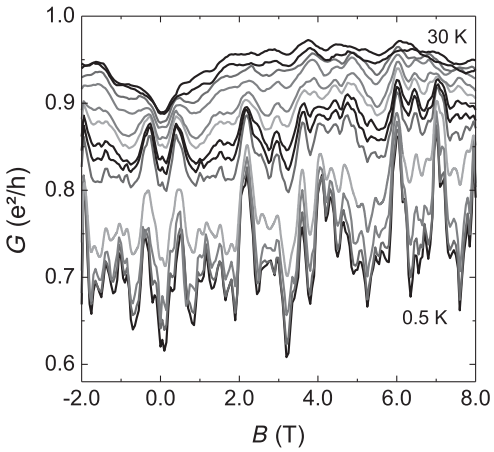

Fig. 3. Fluctuating magneto-conductance in units of e^2/h at temperatures of 0.5, 1, 2, 3, 4, 5, 6, 8, 10, 15, 20, 25, and 30 K.

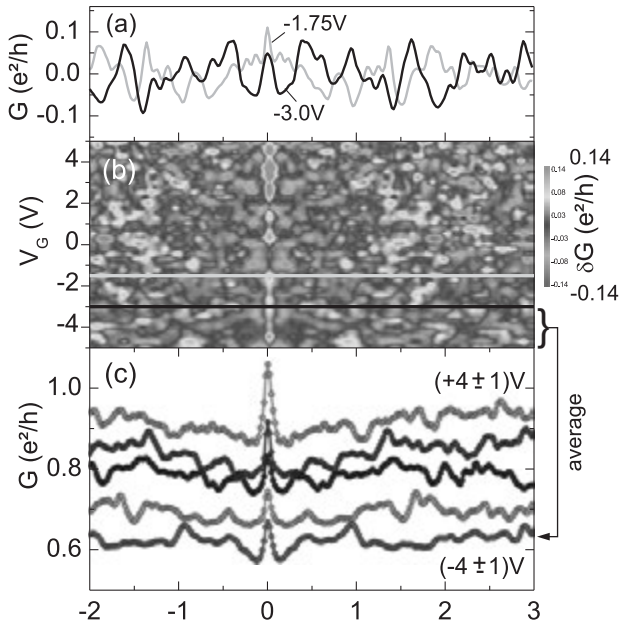

Fig. 4. (a) Magneto-conductance at 0.5 K at $V_G = -1.75$ V (red curve) and at -3.0 V (blue curve). (b) Color-scaled conductance as a function of magnetic field and gate voltage at 0.5 K. The trace of the conductance fluctuations shown in (a) are indicated by the horizontal lines. (c) Averaged magneto-conductance corrections for fluctuation measurements within a 2 V-wide gate voltage interval. The range for used for the -4 V center-gate-voltage is indicated by the arrow.

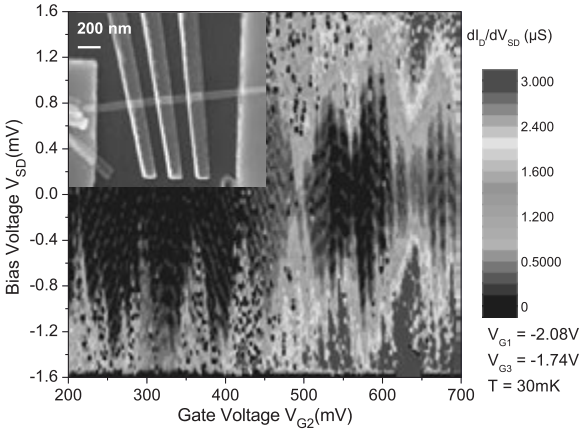

Fig. 5. Color-coded differential conductance as a function of the plunger gate voltage V_{G2} and the source-drain bias voltage V_{SD}. The inset shows a scanning electron micrograph of a InAs structure with three gate fingers. The scale bar corresponds to 200 nm.

At low temperature the conductance is strongly fluctuating, these universal conductance fluctuation (UCF) decrease in amplitude for increasing temperatures. The measurements of the UCF as a function of magnetic field can be used directly to obtain information on the phase-coherence length l_ϕ. At temperatures below about 2 K l_ϕ has its maximum value at about 300 nm, while at higher temperatures l_ϕ decreases proportional to $T^{-0.35}$ to a value of slightly above 100 nm at $T = 30$ K. Since for electrons confined in the surface potential well of InAs wires a strong spin-orbit coupling is present, a maximum of the magnetoconductance at zero field due to weak antilocalization is expected. Due to the strong conductance fluctuations in our magnetotransport experiments weak antilocalization could not be unambiguously observed directly. However, this effect is clearly resolved by averaging the conductance with respect to the gate voltage. The expected pattern for weak antilocalization is a distinct peak positioned at $B = 0$ independently of the gate voltage, whereas the position and intensity of peaks of the UCF will depend on the carrier density thus on the gate voltage. This is illustrated in Fig. 4 where the magnetoconductance fluctuations $\Delta G(B)$ at a temperature of 0.5 K are plotted for different back-gate voltages.

The color contour plot in Fig. 4(a) shows the UCF in dependence of the magnetic field and the gate voltage. Clearly, it is visible that the peaks related to UCF scatter in position and intensity depending on the gate voltage. Whereas for all gate voltages there is a peak at $B = 0$. Thus averaging the $G(B)$ curves over a range of gate voltages leads to the vanishing of the UCF signature and only the peak at $B = 0$ which is attributed to the weak antilocalization remains. This averaging procedure has been applied to several 2 V wide segments within the full spread of gate voltage variation from -5 to $+5$ V. The obtained peaks at $B = 0$ were fitted using the Kettemann model [1] describing the weak-antilocalization effect in quasi 1-dimensional conductors. The values of spin-orbit scattering length l_{so} extracted from this analysis showed almost no change in the whole gate voltage range and a spin-orbit scattering length of 160 nm was determined. Finally three top gates, each wrapping about 3/4 of the circumference of the nanowire have been fabricated. The two outermost gates are used to deplete the surface 2DEG underneath them to form barriers and a quantum dot in between them. The gate ($G2$) in the middle is used to control the potential of the dot (plunger gate). The inset of Fig. 5 depicts the SEM image of a nanowire with three top gate fingers. Fig. 5 itself shows the color-coded differential conductance as a function of the plunger gate voltage V_{G2} and the source drain voltage V_{SD} at a bath temperature of 30 mK. As one can clearly see, the differential conductance pattern shows typical Coulomb diamond structures, indicating single electron transport in the Coulomb-blockade regime.

References

[1] M. Akabori, K. Sladek, H. Hardtdegen, T. Schäpers, and D. Grützmacher, *J. Cryst. Growth* **311**, 3813 (2009).
[2] S. Kettemann, *Phys. Rev. Lett.* **98**, 176808/1 (2007).

18th Int. Symp. "Nanostructures: Physics and Technology"
St Petersburg, Russia, June 21–26, 2010

Anisotropic exchange interaction in the structures with Ge/Si quantum dots

A. F. Zinovieva, A. V. Nenashev and A. V. Dvurechenskii
Institute of Semiconductor Physics, 630090 Novosibirsk, Russia

Abstract. Anisotropic exchange interaction and its contribution in spin relaxation of carriers in the structures with Ge/Si quantum dots was analyzed on the base of the theoretical and experimental data. A probability of decoherence due to anisotropic exchange was estimated. A quantum dot arrangement, free from decoherence induced by anisotropic exchange interaction, was proposed for quantum computation schemes.

Spin physics in low-dimensional structures is very sensitive to symmetry of the object. It is clear visible in the extreme case of low-dimensional structures, quantum dots (QDs). In this case the longest spin relaxation times are predicted. However, the expected long spin lifetimes can be obtained only in the system with high symmetry. The low symmetry of nanostructures can lead to appearance of additional spin relaxation mechanisms, which takes place in the arrays of tunnel-coupled QDs with structure-inversion-asymmetry. At high density of QDs the overlapping between localized states is sufficient for coming in force the most efficient Dyakonov–Perel mechanism of spin relaxation [1]. In this case the spin relaxes during series of random tunneling events (in hopping transport) through precession in the effective magnetic field whose direction can be changed after each tunneling event. There are two ways to increase the spin relaxation time. The first follows from origin of the effective magnetic field. It relates to spin-orbit interaction and can vanish in more symmetrical structures. The second way is related to the suppression of probability of tunneling between QDs. The electron transitions between QDs provide the appearance of the effective magnetic field, then the creation of well-separated QD array allows to preserve the spin orientation for a longer time. There are the additional possibility of precise control of filling number of quantum dots. At filling number $\nu = 1$ the tunneling between dots is suppressed due to Coulomb interaction. In these conditions the anisotropic exchange interaction can come in force and control the spin relaxation process in QD arrays. The present paper is aimed to analyze the contribution of anisotropic exchange interaction in spin relaxation of carriers in the structures with Ge/Si quantum dots and to predict the experimental conditions under which the longest relaxation times can be achieved.

A promising way for the creation of zero-dimensional structures is the strain epitaxy. Semiconductor QDs fabricated by this technique can be controllably positioned, electronically coupled and embedded into active devices. Ge/Si QDs, grown by molecular beam epitaxy (MBE) in Stranski–Krastanow growth mode, are characterized by the high uniformity of shape and size (10–15%), and high spatial density, which can reach $\sim 10^{12}$ cm^{-2} in special growth conditions. This type of QDs is currently considered as one of the best candidates for solid state implementation of spintronics and quantum computation schemes because of the long spin lifetime in silicon, originating from weak SO coupling and extremely small concentration of nuclear spins in Si (a natural abundance of isotope ^{29}Si is less than 5%). In this heterosystem holes are localized inside Ge QDs, while electrons are localized in strain-induced potential

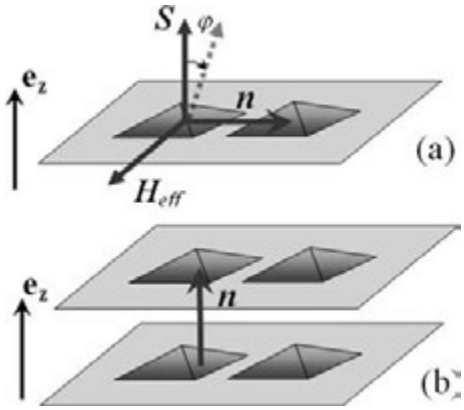

Fig. 1. Schemes of the tunneling processes with different direction n and a spin rotation around the effective magnetic field for in-plane tunneling between QDs. Here n is the tunneling direction, S is the electron spin, $H_{\rm eff}$ is the effective magnetic field, arising during tunneling between QDs, e_z is the invariant vector related to asymmetry of Ge QD.

wells near the apexes of Ge dots. Strong localization of holes allows to expect the long spin relaxation times. But the asymmetry of QD shape leads to appearance of additional terms in the spin-orbit Hamiltonian, that can be considered as analog of Rashba term [2] in two-dimensional (2D) structures. The fact is that the localization of carrier in all three dimensions leads to the uncertainty of electron momentum Δk_x, Δk_y, Δk_z. This uncertainty provides the appearance of the effective magnetic field $\mathbf{H}_{\rm eff} = \alpha_{\rm QD}(\Delta\mathbf{k}_{x,y} \times \mathbf{e}_z)/g\mu_{\rm B}$ with a random in-plane direction. Obviously, the average value of this field equals to zero for the localized state in QD. However, during tunneling between coupled QDs the preferential tunneling direction $\mathbf{n}$ appears, which defines the direction of the effective magnetic field: $\mathbf{H}_{\rm eff} = \alpha_{\rm QD}\Delta k_n(\mathbf{n} \times \mathbf{e}_z)/g\mu_{\rm B}$. Every tunneling event is accompanied by the small spin rotation in the effective magnetic field that provokes the spin flip after series of random tunneling events [3]. The tunneling (hopping) direction $\mathbf{n}$ in QD system serves as analog of the electron momentum direction $\mathbf{k}/k$ in 2D system. In the tight-binding approach we calculate the constant $\alpha_{\rm QD}$ for one-dimensional crystal, where Ge QDs serve as atoms. We obtain the spin splitting of the energy spectrum, which is linear at small k: $\Delta E_{\uparrow\downarrow} \approx \alpha_{\rm QD} \times k$, with $\alpha_{\rm QD} = 2 \times 10^{-12}$ eV cm. This value allows to estimate the value of effective magnetic field, that causes this splitting. Taking $\Delta k = 1/l$, we obtain $H_{\rm eff} \sim 100$ G (here $l = 15$ nm is typical lateral size of Ge QD). Here we use our results of

g-factor calculations [4], given in-plane g-factor $g \approx 1.5$.

For electrons localized on QDs we have the experimental data, obtained by EPR method [5]. According to these results the QD electrons give the special EPR signal with anisotropic line width. The linewidth ΔH_{pp} is about 0.8 G for the magnetic field $\mathbf{H} \parallel Z$, where Z is the [001] growth direction of the structure. On the deviation of the magnetic field from the Z-axis the ESR line becomes broader and weaker. For the in-plane magnetic field $\mathbf{H} \perp Z$ the linewidth ΔH_{pp} is approximately four times larger, than ΔH_{pp} for $\mathbf{H} \parallel Z$. The observed line width anisotropy is explained by angular dependence of transverse spin relaxation T_2 in framework of Redfield theory and confirms the existence of fluctuating effective magnetic fields in plane of QD array.

$$\begin{aligned} \frac{1}{T_1} &= \gamma^2 \left(\delta H_x^2 + \delta H_y^2 \cos^2 \theta_H \right) \frac{\tau_c}{1 + \omega_0^2 \tau_c^2}, \\ \frac{1}{T_2} &= \gamma^2 \delta H_y^2 \sin^2 \theta_H \tau_c + \frac{1}{2T_1}, \end{aligned} \quad (1)$$

where H_x and H_y are components of effective magnetic field, ω_0 is the Larmor frequency, $\gamma = g\mu_B/\hbar$ is the gyromagnetic ratio. The parameter τ_c is characteristic time of fluctuations. It was determined from angular dependence of EPR line width and consists of $\tau_c \approx 3 \times 10^{-11}$ s [5]. Taking this value and $T_2 = 0.5 \times 10^{-6}$ s (the spin echo measurements data [6]) one can estimate the effective magnetic field for electrons as $H_{\text{eff}} \approx 10$–$15$ G.

So, our theoretical and experimental results shows the existence of effective magnetic fields in the plane of the tunnel-coupled Ge/Si QD arrays. These magnetic fields strongly affects the hole (electron) spin relaxation at the tunneling transitions between QDs.

In well-ordered arrays of Ge/Si QDs at filling factor $\nu \approx 1$ the tunneling processes are suppressed and the spin relaxation is controlled by anisotropic exchange interaction. The effective magnetic field causes rotation of spins of tunnel-coupled electrons (holes) localized on adjacent QDs. Interchanging the positions of electrons (holes) is accompanied by reciprocal rotation of their spins. In other words the exchange interaction couples the tipped spins S_1' and S_2' and this leads to the following expression for the exchange Hamiltonian [7]:

$$\begin{aligned} \hat{H}_{\text{ex}} &= 2J S_1' S_2' = 2J S_1 S_2 \cos\varphi \\ &+ \left(2J/H_{\text{eff}}^2 \right) (\mathbf{S}_1 \mathbf{H}_{\text{eff}})(\mathbf{S}_2 \mathbf{H}_{\text{eff}})(1 - \cos\varphi) \\ &+ (2J/H_{\text{eff}})(\mathbf{H}_{\text{eff}}[\mathbf{S}_1 \times \mathbf{S}_2]) \sin\varphi . \end{aligned}$$

The first term is the usual scalar interaction, the second term is the scalar part of anisotropic exchange interaction and the third one is the antisymmetric interaction. For quantitative consideration of holes and electrons spin relaxation induced by anisotropic exchange interaction one needs the values of exchange integrals. They can be estimated using Heisenberg expression $J \sim 4t_0^2/U_c$, where t_0 is the tunneling constant, U_c is the charging energy of a single QD. The main difference between the values of J for electrons and holes lies in the tunneling constants. According to numerical calculations the tunneling constant for holes is 10^{-5} eV (tight-binding approach [3]), while for electrons it consists of 10^{-3} eV (effective mass approximation [8]) for the same conditions (ground states in pyramidal QDs with height $h = 1.5$ nm and lateral size $l = 15$ nm located at the distance $d = 15$ nm). The charging energies for holes and electrons have the same order of magnitude. Then the strength of exchange interaction for electrons can be several orders of magnitude higher than that for holes at the same conditions ($h = 1.5$, $d = 15$ nm). To achieve the same strength for electrons one should to increase the distance between QDs up to 25 nm, that corresponds to the experimental results discussed above [5].

The spin relaxation time depends on the correlation time τ_c. In well-ordered QD arrays τ_c is the mean correlation time of electron (hole) spin, governed by flip-flop transitions due to isotropic part of exchange interaction. Exponential dependence of tunneling constant on the distance between QDs allows to expected several orders increase of spin relaxation time in arrays with low density of QDs.

With increasing disorder degree in QD arrays the time of spin relaxation can be defined by the probability of the random jump to the empty QD. The existence of these dots can be provided by insufficient filling of QDs or deviation of the structural parameters of QDs (shape, size or composition). One random jump to this "wrong" QD can switch on the spin relaxation process in all QD array. The higher density of "wrong" QDs the higher probability of starting the spin relaxation process.

For realization of quantum computation schemes the considered anisotropic exchange interaction is very harmful, because it does not conserve the total spin of two interacting electrons (holes). One can easily estimate the probability of decoherence induced by anisotropic exchange interaction during SWAP operation, as $p_d \sim \varphi^2$. For holes $\varphi \sim 0.1$, then the probability is $p_d \sim 10^{-2}$. For electrons $\varphi \sim 0.01$, then the probability is $p_d \sim 10^{-4}$. However, for Ge QDs with vertical tunneling coupling (Fig. 1) the effective magnetic field is equal zero $\mathbf{H}_{\text{eff}} \sim (\mathbf{n} \times \mathbf{e}_z) = 0$, because in this case $\mathbf{n} \parallel \mathbf{e}_z$. Such configuration is free from decoherence induced by anisotropic exchange interaction and can be used in the future design of quantum computer.

Acknowledgements

This work was supported by RFBR (Grants 08-02-00121, 09-02-90480).

References

[1] B. I. Shklovskii, *Phys. Rev. B* **73**, 193201 (2006).
[2] A. Bychkov and E. I. Rashba, *J. Phys. C* **17**, 6039 (1984).
[3] A. F. Zinovieva, A. V. Nenashev, A. V. Dvurechenskii, *Phys. Rev. B* **71**, 033310 (2005).
[4] A. V. Nenashev, A. V. Dvurechenskii, A. F. Zinovieva, *Phys. Rev. B* **67**, 205301 (2003).
[5] A. F. Zinovieva *et al*, *Phys. Rev. B* **77**, 115319 (2008).
[6] A. F. Zinovieva *et al*, *Phys. Rev. B* (2010).
[7] K. V. Kavokin, *Phys. Rev. B* **64**, 075305 (2001).
[8] A. I. Yakimov *et al*, *Phys. Rev. B* **73**, 115333 (2006).

18th Int. Symp. "Nanostructures: Physics and Technology"
St Petersburg, Russia, June 21–26, 2010

Spin currents in diluted magnetic heterostrucures

V. V. Bel'kov[1,2], S. A. Tarasenko[2], P. Olbrich[1], W. Eder[1], D. R. Yakovlev[2,3], V. Kolkovsky[4], W. Zaleszczyk[4], G. Karczewski[4], T. Wojtowicz[4], D. Weiss[1] and S. D. Ganichev[1]

[1] Terahertz Center, University of Regensburg, 93040 Regensburg, Germany
[2] Ioffe Physical-Technical Institute, St Petersburg, Russia
[3] Experimental Physics 2, TU Dortmund University, 44221 Dortmund, Germany
[4] Institute of Physics, Polish Academy of Sciences, 02-668 Warsaw, Poland

Abstract. We study zero-bias spin separation in (Cd,Mn)Te/(Cd,Mg)Te diluted magnetic semiconductor structures. The spin current generated by electron gas heating under terahertz radiation is converted into a net electric current by applying an external magnetic field. The experiments show that the spin polarization of the magnetic ion system enhances drastically the conversion process due to the giant Zeeman splitting of conduction band and spin-dependent electron scattering by localized Mn^{2+} ions.

The generation of spin currents in low-dimensional semiconductor structures has recently attracted a lot of interest. A pure spin current is formed by oppositely directed and equal flows of spin-up and spin-down electrons. While the net electrical current is zero, the spin current is finite and leads to a spatial spin separation. Spin-dependent effects can be greatly enhanced due to exchange interaction between electrons and magnetic ions in diluted magnetic semiconductors (DMS). The strength of these effects can be widely tuned by temperature, magnetic field and concentration of the magnetic ions.

Here we report on the observation of zero-bias spin separation in (Cd,Mn)Te/(Cd,Mg)Te DMS quantum wells. We show that the free carrier absorption of terahertz radiation causes a pure spin current flow. The effect is probed in an external magnetic field which converts the spin current into a net electric current. This conversion in DMS is greatly enhanced compared to non-magnetic structures. The application of an external magnetic field results not only in a giant Zeeman spin splitting of the conduction band but evokes also spin-dependent exchange scattering free electrons by magnetic impurities. Both effects destroy the cancellation of spin-up and spin-down electron flows yielding a net electric current. We demonstrate that spin-dependent exchange scattering of electrons by magnetic impurities plays an important role in electric current generation, providing yet another handle to manipulate spin-polarized currents.

We study spin currents in *n*-type (Cd,Mn)Te/(Cd,Mg)Te single quantum well structures grown by molecular beam epitaxy on (001)-oriented GaAs substrates. Evenly spaced $Cd_{1-x}Mn_xTe$ thin layers were inserted during the growth of 10 nm wide quantum well applying the digital alloy technique.

To generate spin photocurrents we heat the electron gas by low power continuous-wave linearly polarized radiation ($\lambda = 118$ μm). Additionally we used a high power pulsed laser operating at $\lambda = 148$ μm. Terahertz photons with energies $\hbar\omega \approx 10$ meV were chosen to induce free carrier absorption only. To align the Mn^{2+} spins and to convert the spin current into a charge current an in-plane magnetic field **B** was used. The geometry of the experiment is sketched in the inset of Fig. 1. The photosignal is measured across load resistor.

The photovoltage U of DMS sample under low power cw excitation is shown as a function of the in-plane magnetic field in Fig. 1. The signal polarity reverses with the change of the magnetic field direction. The data were taken at temperatures

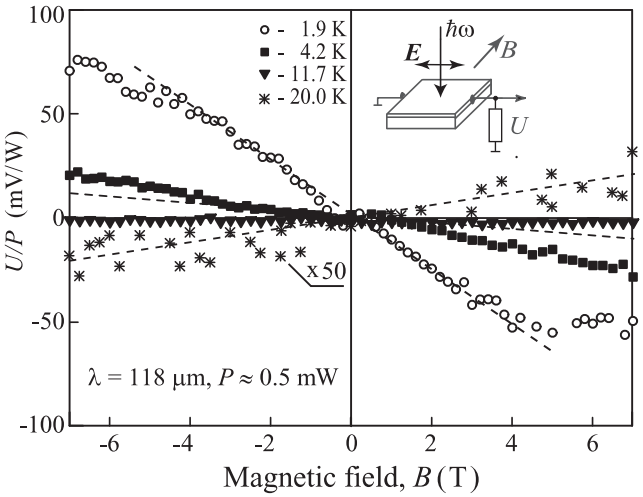

Fig. 1. Magnetic field dependence of the voltage signal U normalized by the radiation power P in response to a low excitation power applying cw laser. Inset shows the experimental geometry.

between 1.9 and 20 K. A central observation is that cooling of the sample changes the signal sign and increases its absolute values by more than two orders of magnitude. While at moderate temperatures the signal depends linearly on magnetic field, at the lowest temperature of 1.9 K the photocurrent saturates at high magnetic field. The increase of the radiation power P results in the decrease of the normalized signal U/P, indicating a reduction of the exchange enhanced spin splitting due to increased temperature of Mn-ion-system. Temperature, magnetic field and intensity dependences are typical for the magnetization of DMS and are controlled by the exchange interaction of electrons with manganese ions.

We show experimentally and theoretically that two mechanisms are responsible for the amplification of a spin current in DMS: Giant Zeeman splitting of the conduction band states and spin-dependent carrier scattering by localized Mn^{2+} spins polarized by an external magnetic field. In a degenerated electron gas at weak magnetic fields the scattering mechanism dominates the spin current conversion.

References

[1] S. D. Ganichev, S. A. Tarasenko, V. V. Bel'kov *et al*, *Phys. Rev. Lett.* **102**, 156602 (2009).

18th Int. Symp. "Nanostructures: Physics and Technology"
St Petersburg, Russia, June 21–26, 2010

Landé factor engineering and origin of magneto-gyrotropic photogalvanic effect in GaAs quantum wells

V. Lechner[1], F. Lomakina[1], S. Stachel[1], P. Olbrich[1], L. E. Golub[2], V. V. Bel'kov[2], M. Griesbeck[1], M. Kugler[1], D. Waller[1], T. Korn[1], C. Schüller[1], D. Schuh[1], W. Wegscheider[1] and S. D. Ganichev[1]

[1] Terahertz Center, Universität Regensburg, 93053 Regensburg, Germany
[2] Ioffe Physical-Technical Institute, St Petersburg, Russia

Abstract. We report on photogalvanic effects in n-modulation-doped (001)-grown GaAs/AlGaAs quantum well (QW) structures caused by terahertz laser radiation. The behaviour of both structure and bulk inversion asymmetry (SIA and BIA) induced photocurrents upon a variation of the δ-doping position at fixed QW width as well as upon a variation of the QW width at fixed δ-doping position is investigated. Our experiments demonstrate that SIA can be accurately tailored by the δ-doping layer position, which enables technicians to grow samples with almost equal degrees of SIA and BIA. Moreover the QW width dependence of the SIA induced photocurrent exhibits a strong influence of the Landé-factor.

Introduction and phenomenology

The generation, manipulation and detection of spin polarized electrons in low dimensional semiconductors are at the heart of spintronics [1]. A versatile tool to achieve these goals provides spin-orbit coupling which in quantum wells based on III–V semiconductors removes the spin degeneracy of the energy bands. The spin-splitting allows to control the spin polarization by the electric field, determines the spin relaxation rate and can be utilized for all-electric spin injection. The strength of the BIA spin-splitting depends on the QW width, temperature, and electron density. In contrast SIA originates from the inversion asymmetry of the confining potential.

Here we investigate (001)-grown GaAs QWs and demonstrate that SIA is substantially affected by the segregation during the growth of the structure. Our experiments explore the role of segregation and allow us to determine the growth conditions of structures with predetermined SIA. In this way we prepared the QWs with almost equal Rashba and Dresselhaus spin-splittings. Such structures are characterized by a drastic increase of spin relaxation times and can be applied for the development of a non-ballistic spin-field effect transistor.

The MPGE is a photocurrent generation driven by the absorption of radiation in QWs in the presence of a magnetic field. The microscopic origin of the phenomenon is explained in Refs. [1,2]. Here in order to analyze the interplay between SIA and BIA we apply the method based on the symmetry equivalence of the tensors describing the spin-splitting and MPGE [3].

Excitation of (001)-grown QWs with unpolarized radiation at normal incidence in the presence of an external in-plane magnetic field **B** provides a straight forward method to obtain the relative strengths and signs of SIA and BIA. Both MPGE and the spin-splitting are characterized by the same anisotropy in space because they are described by equivalent second rank pseudotensors, whose irreducible components differ by a scalar factor only.

In particular for an in-plane magnetic field applied along a cubic axis, e.g., y-direction, we obtain for longitudinal ($j_y \parallel [010]$) and transverse photocurrents ($j_x \parallel [100]$)

$$j_x = \gamma^{\mathrm{SIA}} B_y I , \qquad j_y = \gamma^{\mathrm{BIA}} B_y I . \tag{1}$$

Here I is the radiation intensity and γ^{SIA} and γ^{BIA} are due to SIA and BIA, respectively.

1. Experimental

In the experiments we investigated (001)-oriented Si-δ-doped n-type GaAs/$Al_{0.3}Ga_{0.7}As$ structures grown by molecular-beam epitaxy at typical temperatures in excess of 600 °C. The first part of samples has the same QW width of 15 nm but differs essentially in the doping profile. By contrast the second part of QW structures exhibits the same doping profile but varies in the QW width. In all structures apart from two, the doping layers are asymmetrically shifted off the barrier center either to the left or to the right. The impurities' Coulomb field yields an asymmetric potential profile inside the QWs. In order to describe the degree of asymmetry we introduce the parameter $\chi = (l - r)/(l + r)$, where l and r are the spacer layer thicknesses between QW and δ-layers. Square shaped samples were investigated with edges of 5 mm length oriented along the $[1\bar{1}0]$ and [110] crystallographic axes. For photocurrent measurements ohmic contacts were alloyed on the sample corners and in the middle of each sample side allowing to probe the photocurrent along different directions, as displayed in Fig. 1.

The MPGE is measured at room temperature by exciting the samples with unpolarized terahertz (THz) radiation under normal incidence, as sketched in the inset of Fig. 1. The wavelength of 280 μm was chosen to cause only free carrier absorption.

1.1. Variation of the δ-doping position

Figure 1 shows the dependence of both currents J_x and J_y on the parameter χ. The data was obtained for magnetic fields of ± 1 T applied along the y-direction. Here we normalize the data by the free carrier concentration n_s to enable a comparison of BIA and SIA in different samples.

Fig. 1 depicts that while the longitudinal current is almost independent of χ the transverse current strongly depends on χ and, moreover, changes its sign for $\chi \approx 0.1$. These results are in a full agreement with Eq. (1) demonstrating that the longitudinal current in this experimental geometry is solely due to BIA and the transverse current is caused by SIA only.

The fact that the longitudinal current in both experimental geometries is independent of χ is expected for BIA-induced effects which are obviously insensitive to the magnitude and the sign of χ. The transverse current, in contrast, is caused by SIA

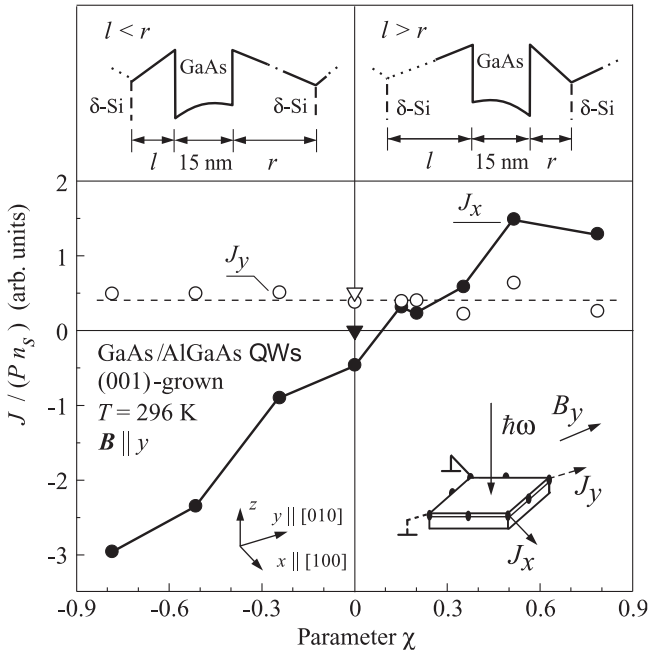

Fig. 1. Dependence of J/Pn_s on the parameter χ. The triangles show the result for the sample grown at 490 °C. Full and open circles show $J_x \propto$ SIA and $J_y \propto$ BIA, respectively for the other samples grown at 630 °C. Insets show the QW profiles, the doping positions for $l < r$ and for $l > r$ and the experimental geometry.

and is very sensitive to the impurity potential. The variation of χ affects the degree of asymmetry and even changes the sign of the transverse photocurrent due to SIA for $\chi \approx 0.1$. Our results show that for $\chi < 0.1$ the asymmetry is dominated by the potential of impurities placed on the left (substrate) side of the QW. Figure 1 demonstrates that in order to obtain a vanishing value of SIA (001)-oriented samples must be asymmetrically doped ($l > r$). This observation is attributed to the segregation of Si-impurities during molecular beam epitaxial growth and is in contrast to (110)-grown structures, where symmetrical doping results in a vanishing SIA [3]. This essential difference is caused by the difference in growth conditions. Indeed, the growth temperature of high-quality (001)-oriented QWs is typically higher than 600 °C, while (110)-structures are grown at 480 °C. In order to suppress the segregation we prepared a symmetrically doped sample with reduced temperature during the δ-doping (490 °C). We find in this case that the MPGE current perpendicular to **B**, which is caused solely by SIA, is almost equal to zero.

The next important observation is that for $\chi = 0$ and $\chi \approx 0.17$ SIA and BIA have equal strengths. In such samples the effects due to SIA and BIA cancel each other in either the $[1\bar{1}0]$ or [110] crystallographic direction depending on the relative sign of the SIA and BIA terms.

1.2. Variation of the QW width

Figure 2 shows the dependence of the current J_x on the QW width L_{QW} at fixed parameter χ. Additionally the corresponding g-factors are presented. The data depict that the SIA-induced J_x, as well as the g-factor, strongly depends on L_{QW} and, moreover, changes its sign for $L_{\mathrm{QW}} \approx 10$ nm. The g-factor equals to zero at about 6.5 nm. The L_{QW}-dependence results from the g-factor's influence on the MPGE due to the

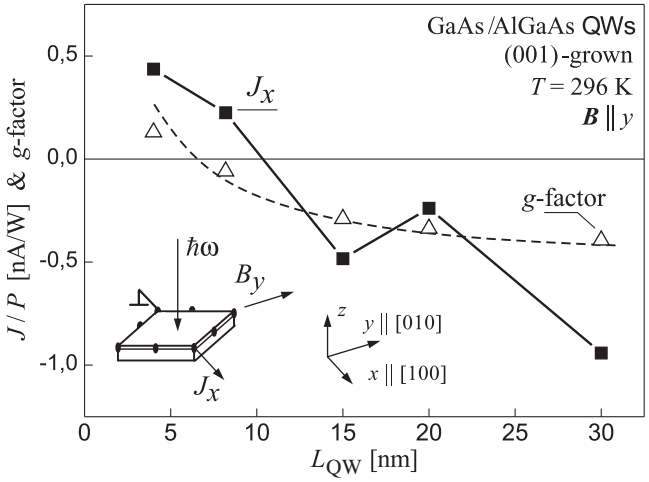

Fig. 2. Dependence of J/P on L_{QW}. The triangles show the corresponding g-factors measured with Kerr-spectroscopy.

Zeeman splitting of subbands. This verifies the spin based microscopic mechanism of the MPGE. But a further orbital, mechanism is needed to explain the difference in the two zero points.

2. Summary

The observed modulation of the SIA by a shift of the doping position demonstrates that the impurity position plays an important role in the SIA. We verified that the high growth temperatures of (001)-oriented GaAs QWs add a factor to the SIA due to impurity segregation. The monitored dependence of the transverse MPGE current on the QW width proved the influence of the g-factor and thus the spin related origin of the MPGE. The observed discrepancy in the zero points of photocurrent and g-factor is due to an additional orbital mechanism in the current formation. Our method to study SIA and BIA based on the MPGE can be applied even at room temperature, where many other methods cannot be used. The investigation of samples with different δ-doping positions led to QWs with almost equal magnitudes of Rashba and Dresselhaus constants which should exhibit extraordinary long spin relaxation times.

Acknowledgements

This work is supported by the DFG via programs SPP 1285, SFB 689, by the Linkage Grant of IB of BMBF at DLR, RFBR, Russian President grant and "Dynasty" foundation — ICFPM.

References

[1] M. I. D'yakonov, Ed., *Spin Physics in Semiconductors*, (Berlin: Springer) 2008.
[2] V. V. Bel'kov and S. D. Ganichev, *Semicond. Sci. Technol.* **23**, 114003 (2008).
[3] V. V. Bel'kov *et al*, *Phys. Rev. Lett.* **100**, 176806 (2008).
[4] V. Lechner *et al*, *Appl. Phys. Lett.* **94**, 242109 (2009).

18th Int. Symp. "Nanostructures: Physics and Technology"
St Petersburg, Russia, June 21–26, 2010

Pure spin current generation under quantum well photoionization

O. I. Utesov, A. A. Greshnov and G. G. Zegrya
Ioffe Physical-Technical Institute, St Petersburg, Russia

Abstract. A theory of pure spin current generation under photoionization of n-type quantum wells with built-in electric field has been developed. It is shown that optical transitions of the resident electrons to continuous spectrum in the presence of Rashba spin-orbit interaction result in generation of the two components of pure spin current. Important feature of the studied process is that excited carriers acquire additional degree of freedom which can be used potentially in spintronic applications.

Introduction

Spin phenomena in the low-dimensional semiconductor structures attract great interest due to possible applications of the spin systems for calculation purposes. However, a majority of the proposed schemes suggest that spin transport is accompanied by its electrical counterpart which diminishes possible advantages of the spintronic devices. Recently it was shown theoretically [1,2] that the pure spin currents can be generated via optical excitation of the resident carries in the doped quantum wells. Experimentally pure spin currents were observed in Ref. [3] under excitation of AlGaAs/GaAs quantum wells by linearly polarized light and detection of the spin accumulation near the sample edges.

In the present paper we focus on the mechanism of the pure spin current generation under the quantum well photoionization. It is non-resonant and scattering-independent in contrast to the intersubband and intrasubband mechanisms proposed earlier in Ref. [2]. In addition, the carriers excited via photoionization can move freely in the quantum well growth direction so we expect that this additional degree of freedom can be exploited in the spintronic applications. Below we present a theory of the photoionization induced pure spin currents in n-type quantum wells.

1. Theory

We start with the one-band effective Hamiltonian including Rashba spin-orbit interaction [4] with the different constants $\gamma_{1,2}$ for the resident $_{(1)}$ and excited $_{(2)}$ electron states as shown in Fig. 1,

$$\hat{H}_{1,2} = \frac{\hbar^2\hat{k}^2}{2m^*} + V(z) + \gamma_{1,2}\left(\mathbf{n}\left[\mathbf{k}\times\hat{\boldsymbol{\sigma}}\right]\right). \qquad (1)$$

Spectrum and eigenvectors of the system are given by

$$E^{\pm}_{1,2}(k_\parallel) = E_{1,2} + \frac{\hbar^2 k_\parallel^2}{2m^*} \pm \gamma_{1,2}k_\parallel, \qquad (2)$$

$$\chi^{\pm}_{1,2}(z,\boldsymbol{\rho}) = \frac{\psi_{1,2}(z)}{\sqrt{2}}\begin{pmatrix}1\\ \pm e^{i(\theta+\pi/2)}\end{pmatrix}e^{i\mathbf{k}_\parallel\boldsymbol{\rho}}. \qquad (3)$$

Here θ is defined by $\mathbf{k}_\parallel = k_\parallel(\cos\theta, \sin\theta)$. The average spin and velocity in the eigenstates $\chi^{\pm}_{1,2}$ are given by

$$\mathbf{s}^{\pm}_{1,2} = \pm\frac{1}{2}(-\sin\theta, \cos\theta, 0), \qquad (4)$$

$$\mathbf{v}^{\pm}_{1,2} = \left(\frac{\hbar k_\parallel}{m^*} \pm \frac{\gamma_{1,2}}{\hbar}\right)(\cos\theta, \sin\theta, 0). \qquad (5)$$

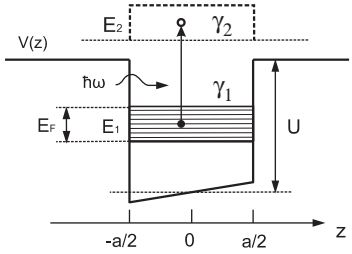

Fig. 1. Scheme of the optical transitions at $\hbar\omega > U - E_1$.

The spin flux is characterized by the pseudotensor $\hat{J}$, $J^{\alpha\beta}$ is a flow in the β direction of spins oriented along α. Also it is convenient to introduce the yx-component of the spin current pseudotensor averaged over the angle θ:

$$j^{\pm}_{1,2}(k_\parallel) = \langle s_x v_y\rangle_{1,2} = \frac{1}{4}\left(\frac{\hbar k_\parallel}{m^*} \pm \frac{\gamma_{1,2}}{\hbar}\right) = -\langle s_y v_x\rangle_{1,2}. \qquad (6)$$

In order to describe linear response of the system on the external electromagnetic field we calculate transition probabilities using the Fermi golden rule

$$M^{\pm}_{12} = \frac{2\pi}{\hbar}|V_{12}|^2\delta\left(E^{\pm}_1 + \hbar\omega - E^{\pm}_2\right), \qquad (7)$$

where $E^{\pm}_{1,2}$ are given by Eq. (2), V_{12} is the matrix element of perturbation,

$$V_{12} = A_z\frac{e\hbar}{m^*c}\int\psi_2\hat{k}_z\psi_1 dz. \qquad (8)$$

Here A_z is z-component of vector potential of the incident light. Since matrix element (8) is independent of $k_\parallel$ and spin, the overall excitation rate of an electron from the size quantization level E_1 becomes a one-parametric function of the shifted frequency,

$$P^{\pm}(\omega, k_\parallel) = \sum_2 M^{\pm}_{12} = P\left(\omega \pm \widetilde{\gamma}k_\parallel\right), \qquad (9)$$

where $\widetilde{\gamma} = (\gamma_2 - \gamma_1)/\hbar$. Within the so-called relaxation time approximation the total spin current is given by a sum of two contributions related to the emptied quantum well states and the occupied excited states, $J^{yx} = -J^{xy} = J_1 + J_2$,

$$J_1 = -\tau_1\sum_{\pm}\int\frac{k_\parallel dk_\parallel}{2\pi}P\left(\omega \pm \widetilde{\gamma}k_\parallel\right)f_0\left(E^{\pm}_1\right)j^{\pm}_1\left(k_\parallel\right), \qquad (10)$$

$$J_2 = \tau_2\sum_{\pm}\int\frac{k_\parallel dk_\parallel}{2\pi}P\left(\omega \pm \widetilde{\gamma}k_\parallel\right)f_0\left(E^{\pm}_1\right)j^{\pm}_2\left(k_\parallel\right). \qquad (11)$$

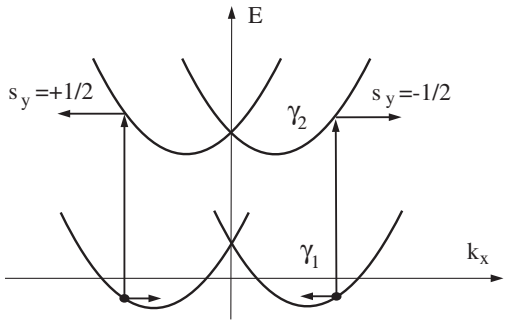

Fig. 2. Optical transitions generate J^{xy} and J^{yx} components of the pure spin current due to $\gamma_2 \neq \gamma_1$.

Here f_0 is equilibrium distribution function, $\tau_{1,2}$ stand for the relaxation times of the resident and excited carriers.

2. Results and discussion

As one can see from Fig. 2 optical transitions of the confined electrons to continuous spectrum result in generation of non-zero spin current due to $\gamma_2 - \gamma_1$ difference. To the first order in $\widetilde{\gamma}$ there are two contributions to the full spin current $J^{xy} = J_{\rm I}^{xy} + J_{\rm II}^{xy}$, where

$$J_{\rm I}^{xy} = \frac{\tau_2 n}{4}\widetilde{\gamma} P(\omega), \tag{12}$$

$$J_{\rm II}^{xy} = \frac{\pi\hbar(\tau_1 - \tau_2)n^2}{4m^*}\widetilde{\gamma} P'(\omega), \tag{13}$$

are proportional to the first and second power of 2D electron concentration n respectively. Step growth of the spin current above the photoionization threshold is accompanied by its rapid decrease, $\sim \omega^{-4.5}$ and $\sim \omega^{-5.5}$ for $J_{\rm I}^{xy}$ and $J_{\rm II}^{xy}$ respectively.

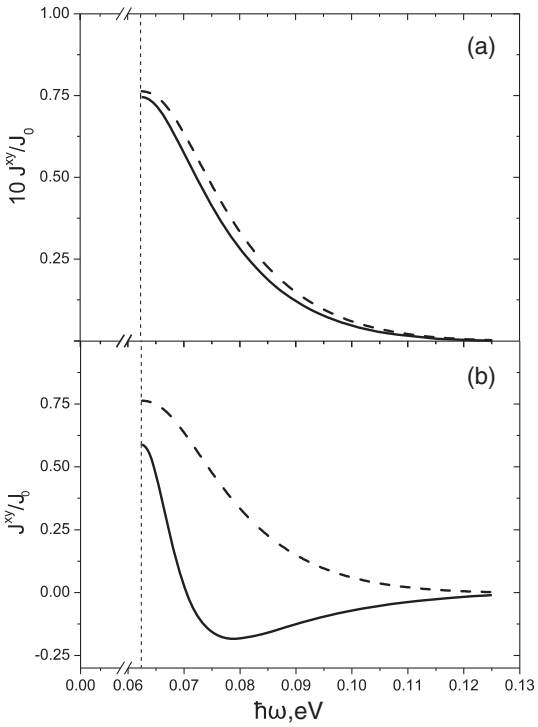

Fig. 3. Frequency dependence of spin photocurrent in GaAs/AlGaAs n-type quantum well for (a) $n = 10^{11}$ cm^{-2} and (b) $n = 10^{12}$ cm^{-2}. Here $J_0 = 2 \times 10^8$ cm^{-1}s^{-1}, solid and dashed lines are drawn for the full and partial spin currents J^{xy} and J_I^{xy} respectively.

Since usually $\tau_1 > \tau_2$ and $P'(\omega) < 0$, the second contribution, $J_{\rm II}^{xy}$, is negative. This may result in nonmonotonic behaviour of the full spin current J^{xy} provided that electron concentration is high enough.

In order to give numerical estimations of the studied effect we consider GaAs/$Al_{0.1}Ga_{0.9}$As n-type quantum well of the width $d = 10$ nm. It contains one level of size quantization, $E_1 \approx 40$ meV, and its offset $U \approx 100$ meV. For estimation we choose $\gamma_1 = 2 \times 10^{-10}$ eV cm, $\gamma_2 = 10^{-10}$ eV cm, $\tau_1 \sim 2 \times 10^{-10}$ s, $\tau_2 \sim 10^{-10}$ s and light intensity $I = 1$ kW/cm^2. Numerical curves of the spin photocurrent dependence on the photon energy $\hbar\omega$ are presented in Fig. 3 for two different electron concentrations. In the case of higher electron concentration, $n \sim 10^{12}$ cm^{-2}, one can observe non-monotonic behaviour of the full current mentioned above.

To conclude, the pure spin current generation under quantum wells photoionization has been studied. This mechanism is non-resonant and scattering-independent in contrast to the intersubband and intrasubband mechanisms proposed earlier in Ref. [2]. We expect that it is of several orders of magnitude higher than intrasubband mechanisms which is concurrent for the studied frequency range. Important feature of the studied process is that photoexcited carriers acquire additional degree of freedom which can be used potentially in spintronic applications.

Acknowledgements

This work has been supported by Russian President Grant for Young Scientists MK-1755.2009.2 and Dynasty Foundation. The authors are grateful to S. A. Tarasenko for valuable discussions.

References

[1] R. D. R. Bhat *et al*, *Phys. Rev. Lett.* **94**, 96603 (2005).
[2] S. A. Tarasenko and E. L. Ivchenko, *JETP Lett.* **81**, 231 (2005).
[3] H. Zhao *et al*, *Phys. Rev. B* **72**, 201302 (2005).
[4] Yu. A. Bychkov and E. I. Rashba, *JETP Lett.* **39**, 78 (1984).

18th Int. Symp. "Nanostructures: Physics and Technology"
St Petersburg, Russia, June 21–26, 2010

Spin current swapping

M. B. Lifshits[1,2] and M. I. Dyakonov[1]

[1] Laboratoire de Physique Théorique et Astroparticules, Université Montpellier II, CNRS, France
[2] Ioffe Physical-Technical Institute, St Petersburg, Russia

Abstract. We discuss a new spin-related transport phenomenon, consisting in a transformation (*swapping*) of spin currents, in which the spin direction and the direction of flow are interchanged. Swapping is due to the spin-orbit interaction in scattering. It originates from the correlation between the spin rotation and the scattering angle. This effect is more robust than the skew scattering, since it exists already in the first Born approximation. Swapping may lead to the spin accumulation with spin polarization perpendicular to the surface, unlike what happens in the spin Hall effect.

Introduction

Spin-orbit interaction leads to the mutual transformations of spin and charge currents [1–3]: the charge current generates the transverse spin current and *vice versa*. The family of these phenomena includes the anomalous Hall effect in ferromagnets and the direct and inverse spin Hall effect. We introduce another transport phenomenon belonging to the same family and show that because of spin-orbit interaction, a given spin current induces not only the charge current, but also a transverse *spin current* with interchanged spin direction and the direction of flow. We will refer to this transformation as the *swapping* of spin currents [4].

1. Coupling of spin and charge currents

The notion of spin current was introduced in Ref. [1]. It is described by a tensor q_{ij} where the first index indicates the direction of flow and the second one shows which component of spin is flowing. Following [3,5] we write down the phenomenological equations describing the coupling between spin and charge currents, q_{ij} and q_i (more accurately, $\mathbf{q}$ is the electron *flow* density, related to the electric current density $\mathbf{j}$ by $\mathbf{q} = -\mathbf{j}/e$, where e is the elementary charge). We consider an isotropic material with inversion symmetry. Then we have [5]:

$$q_i = q_i^{(0)} + \gamma \varepsilon_{ijk} q_{jk}^{(0)}, \quad (1)$$

$$q_{ij} = q_{ij}^{(0)} - \gamma \varepsilon_{ijk} q_k^{(0)}, \quad (2)$$

where $q_i^{(0)}$ and $q_{ij}^{(0)}$ are the primary currents, which may exist in the absence of spin-orbit interaction, ε_{ijk} is the unit antisymmetric tensor and γ is a dimensionless parameter proportional to the strength of spin-orbit interaction.

Pure symmetry considerations allow for additional terms in Eq. (2) proportional to $q_{ji}^{(0)}$ and $\delta_{ij} q_{kk}^{(0)}$, which describe transformations of spin currents. In the presence of electric field $\mathbf{E}$ and spin polarization $\mathbf{P}$, this would result in additional contributions to q_{ij} proportional to $E_j P_i$ and $\delta_{ij}(\mathbf{E} \times \mathbf{P})$, which were mentioned already in [1,2]. However the physical origin of these contributions was not understood at the time and the effect was not studied ever since.

We show that the additional terms should always enter in a combination $q_{ji}^{(0)} - \delta_{ij} q_{kk}^{(0)}$ so that Eq. (2) should be modified as:

$$q_{ij} = q_{ij}^{(0)} - \gamma \varepsilon_{ijk} q_k^{(0)} + \varkappa (q_{ji}^{(0)} - \delta_{ij} q_{kk}^{(0)}), \quad (3)$$

with a new dimensionless parameter $\varkappa$ [6]. We also show that the resulting swapping of spin currents originates from the correlation between the scattering direction and spin rotation during collisions. This effect is more robust than the spin-charge coupling: the swapping constant $\varkappa$ exists already in the Born approximation, while γ appears only beyond this approximation.

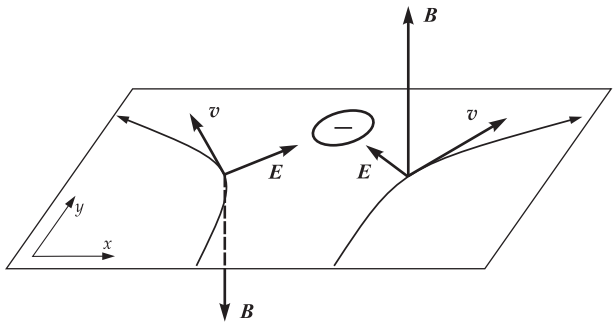

Fig. 1. Schematics of electron scattering by a negative charge. The electron spin sees a magnetic field $\mathbf{B} \sim \mathbf{v} \times \mathbf{E}$ perpendicular to the trajectory plane. Note that the magnetic field (and hence the sense of the spin rotation) has opposite directions for electrons scattered to the left and to the right.

The physical origin of the swapping effect can be readily seen from Fig. 1 illustrating the spin dependent scattering. The most important element is the magnetic field $\mathbf{B}$ existing in the electron's moving frame and seen by the electron spin. This field is perpendicular to the plane of the electron trajectory and has opposite signs for electrons moving to the right and to the left of the charged center. The Zeeman energy of the electron spin in this field is, in fact, the spin-orbit interaction.

Three spin-dependent effects can be seen:

1) The precession of the electron spin around $\mathbf{B}$ during the collision, leading to the Elliott-Yafet spin relaxation.

2) The spin asymmetry in scattering (the Mott effect, or skew scattering) resulting from the additional force proportional to the gradient of electron Zeeman energy.

3) The *correlation* between the directions of electron spin precession and scattering. Indeed, one can see that while the spin on the left trajectory is rotated clockwise, the spin on the right trajectory is rotated counterclockwise. This correlation and its consequences for spin transport were not discussed previously. We will now see that this correlation leads to a transformation of spin currents.

Suppose that the incoming electrons move in the y-direction and are polarized along y (spin current $q_{yy}^{(0)}$). The electrons scattered to the left (right) will acquire a small positive (neg-

ative) projection of spin on the x axis. This means that the initial $q_{yy}^{(0)}$ spin current is partly transformed to $-q_{xx}$. For the case when incoming (along y) electrons are polarized along x, a similar reasoning shows that the initial spin current $q_{yx}^{(0)}$ will give rise to q_{xy}. Thus in the latter case the spin direction and the direction of flow are interchanged. Summarizing, one can derive the spin current transformation law: $q_{ji}^{(0)} - \delta_{ij} q_{kk}^{(0)} \to q_{ij}$, as expressed by Eq. (3).

The reason why the terms $q_{ji}^{(0)}$ and $\delta_{ij} q_{kk}^{(0)}$ enter in such a combination can be explained as follows. Since the spin-orbit interaction is weak, the transformed currents are small compared to the primary currents. Suppose that the primary current contains only one component, say $q_{xx}^{(0)}$. In the first order in spin-orbit interaction there should be no correction to *this* component. (Similarly, when a vector **a** is rotated on a small angle, the first order correction $\delta\mathbf{a}$ is perpendicular to **a**.) The combination $q_{ji}^{(0)} - \delta_{ij} q_{kk}^{(0)}$ is the only one to meet this requirement. Generally, the terms $q_{ji}^{(0)}$ and $-\delta_{ij} q_{kk}^{(0)}$ enter with coefficients whose difference is second order in spin-orbit interaction.

2. Spin current swapping in semiconductors

We have calculated the swapping parameter $\varkappa$ for the Coulomb scattering in the Born approximation [4]:

$$\varkappa = \frac{4m}{\hbar^2}\lambda\varepsilon\,, \tag{4}$$

where λ is the spin-orbit constant and m, ε are the electron effective mass and energy. In semiconductors with the band structure of GaAs, in the limit of small effective mass, the Kane model gives [7] $\lambda = \hbar^2/4mE_g$ for $\Delta \gg E_g$ and $\lambda = (\hbar^2/3mE_g)(\Delta/E_g)$ for $\Delta \ll E_g$, where E_g is the band gap and Δ is the spin-orbit splitting of the valence band. Hence we obtain

$$\varkappa = \frac{E_F}{E_g} \quad \text{for} \quad \Delta \gg E_g\,, \tag{5}$$

$$\varkappa = \frac{4}{3}\frac{E_F}{E_g}\frac{\Delta}{E_g} \quad \text{for} \quad \Delta \ll E_g\,, \tag{6}$$

here E_F is the Fermi energy. For a bulk electron concentration of 10^{17} cm^{-3} we calculate a quite large value $\varkappa = 0.3$ for InSb (Eq. (5)) and $\varkappa = 0.003$ for GaAs (Eq. (6)).

A possible way to observe the swapping effect in semiconductors, where the exchange field is negligible, is presented in Fig. 2. The primary spin current $q_{yy}^{(0)}$ is produced by spin injection in a semiconductor 3D sample through a ferromagnetic contact. Swapping will result in the appearance of transverse spin currents $q_{xx} = q_{zz} = -\varkappa q_{yy}^{(0)}$. Those secondary currents will lead to an excess spin polarization near the lateral boundaries of the semiconductor sample, which could be detected by optical means. At the top face there will be a polarization $P_z < 0$ and at the bottom face $P_z > 0$. (Similarly $P_x < 0$ at the front face and $P_x > 0$ at the back face.) The accumulation of spins polarized perpendicular to the surface distinguishes this manifestation of swapping from the spin Hall effect, where the accumulated spins are parallel to the surface.

To summarize, we have considered a new phenomenon caused by spin-orbit interaction and consisting in swapping of spin currents. This effect originates from the correlation between the spin rotation and the direction of scattering.

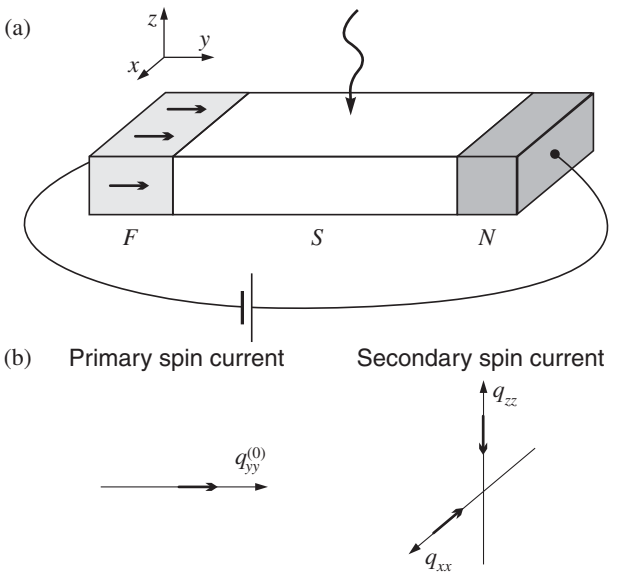

Fig. 2. Schematics of a proposed experiment revealing the swapping of spin currents. (a) The $q_{yy}^{(0)}$ spin current is electrically injected in a semiconductor (S) through a ferromagnetic contact (F) with a magnetization along the y axis. The wavy arrow symbolizes optical detection of the z-component of spin polarization near the surface. (b) The swapping effect transforms the primary spin current $q_{yy}^{(0)}$ into q_{xx} and q_{zz}. This should lead to the appearance of excess spin polarization at the lateral boundaries of the sample ($P_z < 0$ at the top face and $P_z > 0$ on the bottom one). This polarization may be detected optically.

Acknowledgements

This work was supported by RFBR, the programs of the Russian Ministry of Education and Science, and the President Grant for young scientists (MD-1717.2009.2).

References

[1] M. I. Dyakonov and V. I. Perel, *Pis'ma Zh. Eksp. Teor. Fiz.* **13**, 657 (1971) [*JETP Lett.* **13**, 467 (1971)].
[2] M. I. Dyakonov and V. I. Perel, *Phys. Lett. A* **35**, 459 (1971).
[3] M. I. Dyakonov and A. V. Khaetskii, In: *Spin Physics in Semiconductors*, M. I. Dyakonov (Ed.), Springer, Berlin (2008).
[4] M. B. Lifshits and M. I. Dyakonov, *Phys. Rev. Lett.* **103**, 186601 (2009).
[5] M. I. Dyakonov, *Phys. Rev. Lett.* **99**, 126601 (2007).
[6] Equations (1–3) are valid in the first order in spin-orbit interaction. The exact equations can be obtained from Eqs. (1–3) by replacing $q_i^{(0)} \to q_i$ and $q_{ij}^{(0)} \to q_{ij}$ in the terms containing γ and $\varkappa$.
[7] V. F. Gantmakher and Y. B. Levinson, *Carrier scattering in metals and semiconductors*, North-Holland, Amsterdam, (1987).

18th Int. Symp. "Nanostructures: Physics and Technology"
St Petersburg, Russia, June 21–26, 2010

Electron localisation effect on a spin-orbit splitting in GaAs/AlGaAs coupled quantum wells

A. V. Larionov[1], A. V. Sekretenko[1], M. M. Glazov[2] and L. E. Golub[2]

[1] Institute of Solid State Physics, RAS, 142432 Chernogolovka, Russia
[2] Ioffe Physical-Technical Institute, St Petersburg, Russia

Abstract. An effect of the localisation of electrons on their spin dynamics is studied in Schottky GaAs/AlGaAs coupled quantum wells. Electron spin dephasing is investigated by means of time-resolved Kerr rotation technique. Spin dephasing time along photoluminescence line contour is measured as a function of an external magnetic field and electrical bias. A theoretical analysis of strong dependence of electron spin relaxation time on magnetic field is developed.

Introduction

The spin-orbit splitting caused by lack of an inversion center in III–V crystals is the main factor responsible for spin relaxation processes in GaAs/AlGaAs quantum wells structures. It was recently discovered that experimentally observed electron spin relaxation anisotropy is caused by theoretically predicted "interference" of two main sources for spin-orbit splitting: a bulk inversion asymmetry (BIA) and a structure inversion asymmetry (SIA) described by the Dresselhaus and the Rashba Hamiltonians, respectively [1]. It was shown that GaAs/AlGaAs coupled quantum wells are a very suitable object for spin-orbit splitting control by electrical means [2]. This fact is very attractable for spintronics investigations.

Real semiconductors heterostructures have different types of crystal imperfection — residual impurities, interface fluctuations and others. This results in localisation of electrons in the quantum well plane. In our work we investigate via electron spin relaxation time measurements how spin-orbit splitting is modified by an electron localisation in presence of an electric field in Schottky GaAs/AlGaAs CQWs.

1. Experimental

The studied CQWs system consists of two GaAs quantum wells ($\approx$ 120 Å wide) separated by a narrow (4 monolayers) AlAs barrier. The QWs are separated from surrounding layers by 1500 Å thick $Al_{0.33}Ga_{0.67}As$ barriers. The growth axis is [001].

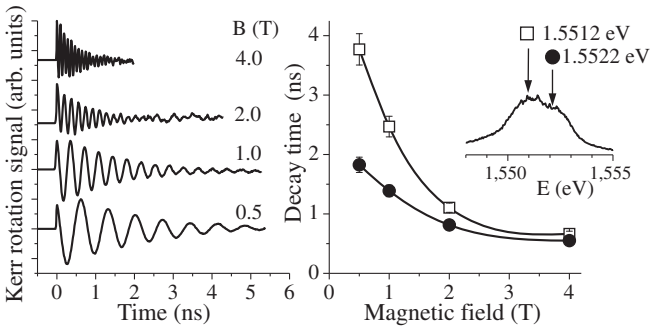

Fig. 1. (a) TRKR signal in magnetic fields from 0.5 to 4 T. Beatings were observed at temperature of $\approx$ 2 K and average pump power density $P \approx 20$ W/cm^2. (b) Magnetic field dependence of the electron spin dephasing time τ_S at two pump-probe wavelengths. The Stark shift of the indirect exciton photoluminescence line is 17.5 meV (applied bias 0.0 V). Solid lines are eye guides.

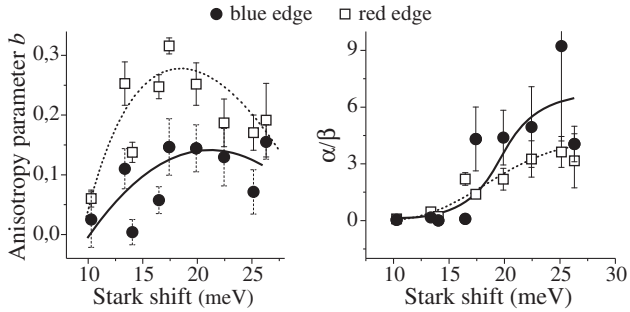

Fig. 2. The anisotropy parameter b and the ratio of Rashba and Dresselhaus constants α/β (right panel) for red and blue edges of the direct exciton PL line. Solid lines are eye guides.

An electric field was applied to the CQWs via two gates: the bottom one is a 250 Å QW modulation-doped with Si, and the top one is a 180 Å Au layer deposited on the structure forming a Schottky barrier.

The electron spin dephasing time was measured by means of the time resolved Kerr rotation (TRKR) technique employing a picosecond Ti:Sapphire laser ($\approx$ 10 ps pulse corresponding to $\approx$ 0.4 meV spectral width, 80 MHz repeating frequency). The wavelengths of pump and probe pulses were the same. We had an ability to choose different wavelengths along the contour of the direct 1sHH exciton photoluminescence line (which was $\approx$ 2 meV wide). An external magnetic field in Voigt geometry allows one to observe spin quantum beats in TRKR signal due to Larmor precession of coherently excited electron spins in CQWs around the field direction. A series of quantum beats detected in magnetic fields B from 0.5 to 4 T is presented in Fig. 1.

Experimental data presented in Fig. 1 can be fitted by exponentially damped oscillations containing the beating frequency Ω and a single decay time: $I = I_0 \exp(-t/T) \cos \Omega t$, where $\Omega = \mu_B g_e B/\hbar$, g_e is the in-plane electron g-factor. The electron-hole recombination time in CQWs in this sample is $\approx$ 6 ns under the bias of +0.4 V and longer than 10 ns at +0.3 V and lower biases. Thus the decay rate is mainly determined by the spin dephasing rate.

This sample exhibits a spin relaxation anisotropy controllable by an external electric field like the CQWs studied in our previous work [2]. A dependence of the dephasing time on the angle between the in-plane magnetic field and the [110] axis was measured in a field of 0.75 T for two wavelengths: near the blue edge of the PL line and closer to the red edge. This was

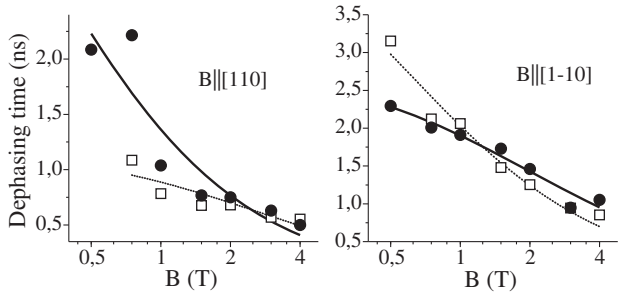

Fig. 3. Dephasing time dependencies on the magnetic field for two field directions along crystallographic axes [110] and [1$\bar{1}$0]. Solid and dashed lines correspond to fitting with Eq. (3) of data for the blue and the red edge of PL line respectively.

performed for applied biases from +0.4 to −0.4 V corresponding to indirect exciton PL line Stark shift from 10 to 26 meV, Fig. 2. The spin relaxation anisotropy strongly depends on the applied bias and is noticeably lower at the blue edge than at the red one.

Then the dephasing time in magnetic fields from 0.5 to 4 T was measured at two field orientations: along [110] and along [1$\bar{1}$0] for both the red and the blue edges of the PL line. From Fig. 3 one can see that in all cases the decay time decreases with magnetic field. These experiments were done for applied biases of +0.2, 0.0 and −0.2 V.

2. Theoretical description and discussions

In Ref. [2] the following expression for the spin dephasing time angular dependence was derived for the case of D'yakonov–Perel' mechanism:

$$\tau_s(\theta) = \frac{D}{1 + b\cos 2\theta}\,. \tag{1}$$

Experimental data can be fitted with Eq. (1) for each applied bias. This gives the values of anisotropy parameter b shown on Fig. 2. They are determined by the ratio of the Rashba (α) to the Dresselhaus (β) spin-orbit splitting constants for corresponding biases. This ratio can be calculated according to the formula [2]:

$$\left(\frac{\alpha}{\beta}\right)^{\pm 1} = \frac{3b}{1 + \sqrt{1 - (3b)^2}}. \tag{2}$$

The resulting ratio α/β is shown in Fig. 2. One can see that all important limits, $\alpha = 0$, $\alpha = \beta$, and $\alpha \gg \beta$ can be achieved in the studied structure.

The results on magnetic field dependence of the spin dephasing time presented in Figs. 1 and 3 can be explained in a following phenomenological way. Lateral localisation causes an electron g-factor spread due to dispersion of localization energy. This spread causes an additional damping of spin beatings apart from irreversible relaxation. The additional damping ratio is proportional to magnetic field. As a result, the spin decay rate is a sum of two factors. The irreversible spin relaxation is dominant in weak magnetic fields when the g-factor dispersion does not manifest itself, while the localization becomes important in stronger fields. When the Larmor frequency has a dispersion, the averaging of decaying quantum beatings gives the decaying oscillation with an average g-factor multiplied by an additional exponential damping. The expression for the full spin lifetime is

$$T_S = \frac{T_0}{1 + aB}\,, \tag{3}$$

where T_0 is the spin relaxation time in zero magnetic field, and a is related to the g-factor dispersion Δg by $\Delta g = 12.5a/T_0$ (B is measured in Teslas, and T_0 in picoseconds). Thus we can quantitatively describe an effect of electron localisation on their spin dephasing.

To summarize, an effect of the localisation on electron spin dephasing anisotropy was studied in Schottky GaAs/AlGaAs coupled quantum wells. The anisotropy is measured by means of time-resolved Kerr rotation effect at magnetic field differently orientated in the structure plane. The localisation is manifested by strong decreasing of electron spin dephasing time versus magnetic field. It can be quantitively described by an electron g-factor spreading.

References

[1] N. S. Averkiev and L. E. Golub, *Semicond. Sci. Technol.* **23**, 114002 (2008).
[2] A. V. Larionov and L. E. Golub, *Phys. Rev. B* **74**, 033302 (2008).

18th Int. Symp. "Nanostructures: Physics and Technology"
St Petersburg, Russia, June 21–26, 2010

A new mechanism of dynamic nuclear pumping evidenced by anomalous Hanle effect in InAs-GaAs quantum dots

O. Krebs[1], P. Maletinsky[2], T. Amand[3], B. Urbaszek[3], A. Lemaître[1], *P. Voisin*[1], X. Marie[3] and A. Imamoglu[2]

[1] CNRS-Laboratoire de Photonique et de Nanostructures, 91460 Marcoussis, France
[2] Institute of Quantum Electronics, ETH-Zürich, Switzerland
[3] Université de Toulouse, INSA-CNRS-UPS, LPCNO, 135 Avenue de Rangueil, 31077 Toulouse, France

Abstract. We report on experimental observations of an anomalous Hanle effect in individual self-assembled InAs/GaAs quantum dots. A sizable electron spin polarization photo-created under constant illumination is shown to persist in transverse magnetic fields as high as ∼1 T, up to a critical field where it abruptly collapses. This results in striking anomalies of the Hanle curve which point to a novel mechanism of dynamic nuclear spin polarization: an effective magnetic field, or Overhauser field, is generated perpendicular to the optically injected electron spin polarization and cancel out the external field.

Introduction

The hyperfine interaction between electron and nuclei in self-assembled InAs/GaAs QDs acts like an effective magnetic field, the Overhauser field, whose fluctuations are responsible for electron spin dephasing. However, under experimental conditions of optical pumping with cw circularly polarized light, a strong static Overhauser field B_n can develop due to dynamic nuclear polarization (DNP): under such conditions, electron spin dephasing can be substantially suppressed, even in zero external field. Conversely, if an external field $B_{\rm ext}$ is applied in a transverse direction, it is expected that spin precession about $B_{\rm ext}$ prevents the construction of nuclear polarization. We have studied the depolarization of optically oriented electron spins by a transverse magnetic field B_x (or Hanle effect), in individual InAs/GaAs QDs charged by a single hole, and evidenced a new, counter-intuitive mechanism of DNP where nuclear polarization builds-up antiparallel to the transverse field [2].

1. Hanle depolarization curves

The QDs are excited quasi-resonantly by a circularly polarized laser propagating parallel to the QD growth axis, to form a positively charged trion (X^+) in a given spin state $|\Uparrow\Downarrow\downarrow\rangle$. We observe that the strong electron spin polarization of X^+ achieved in zero magnetic field ($P_c^0 \approx 80\%$) is not destroyed

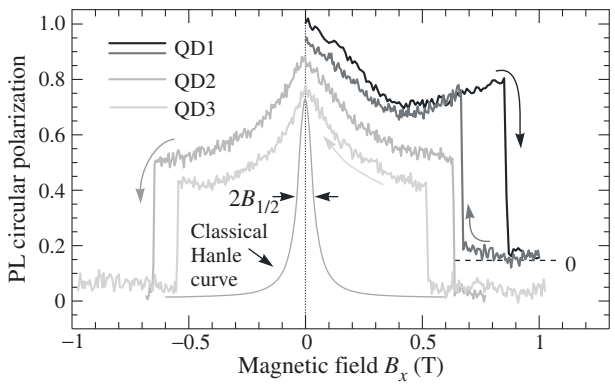

Fig. 1. Hanle depolarization curves of positive trions under continuous wave circularly polarized quasi-resonant excitation in three QDs. The experimental result is contrasted with the expected Hanle curve (black solid line).

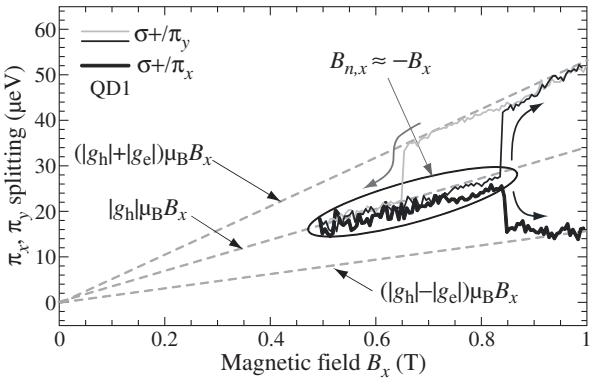

Fig. 2. Splittings of the trion transitions of QD1 under the same excitation conditions, resolved in a basis of linear polarizations (π_x, π_y).

but only slowly reduced when the transverse field increases up to a threshold value where polarization collapses. This corresponds to strong distortions of the expected Hanle curve (a Lorentzian with HWHM $B_{1/2} \approx 30$ mT determined from the measured electron g-factor) consisting of a 20–30 times broadening, an abrupt drop at a critical field and an hysteresis upon sweeping back the field (see Fig. 1). This anomalous Hanle effect evidences the persistence of a nuclear polarization B_n.

2. Transverse Overhauser field

To prevent the Hanle depolarization of electron spin, there are only two possible scenarios. (i) Either a nuclear field B_n, stronger than the applied one, remains oriented along the optical axis like in zero field. This nuclear field could persist in transverse magnetic field thanks to large strain-induced quadrupolar splittings of the nuclear spin states, as proposed in Ref. [1]. (ii) Or, a nuclear polarization develops antiparallel to the applied field, so that it hampers the Hanle depolarization. A similar phenomenon is observed in a magnetic field parallel to the optical axis, where it gives rise to pronounced nonlinearities of the Overhauser field [5,3,6,4] and feedback on the electron spin polarization [4]. Thanks to the high spectral resolution of single QD spectroscopy we could measure directly the Overhauser field, through the Zeeman splitting of the trion line. Our result indicates that the longitudinal component $B_{n,z}$ vanishes rapidly with increasing B_x, whereas a transverse com-

ponent $B_{n,x}$ develops against B_x. The $B_{n,x}$ component cancels out the total magnetic field and the resulting electron Zeeman splitting, and prevents electron spin depolarization: in the field range where X^+ circular polarization is conserved, we indeed find that the X^+ Zeeman splitting is determined by the sole hole g-factor (see Fig. 2). This "transverse Overhauser effect" evidences a novel DNP mechanism. The detailed scenario of this counter-intuitive mechanism is not yet fully understood, but it is rather likely that the strain-induced quadrupolar splitting of nuclei plays a crucial role. We suggest that this could be tested by reproducing this experiment in strain-free quantum dots.

References

[1] R. I. Dzhioev and V. L. Korenev, *Phys. Rev. Lett.* **99**, 037401 (2007).
[2] O. Krebs, P. Maletinsky, T. Amand, B. Urbaszek, A. Lemaître, P. Voisin, X. Marie and A. Imamoglu, *Phys. Rev. Lett.* **104**, 056603 (2010).
[3] A. I. Tartakovskii *et al*, *Phys. Rev. Lett.* **98**, 026806 (2007).
[4] O. Krebs *et al*, *C. R. Phys.* **9**, 874 (2008), arXiv:0904.1548.
[5] P.-F. Braun *et al*, *Phys. Rev. B* **74**, 245306 (2006).
[6] P. Maletinsky, C. W. Lai, A. Badolato, and A. Imamoglu *et al*, *Phys. Rev. B* **75**, 035409 (2007).

18th Int. Symp. "Nanostructures: Physics and Technology"
St Petersburg, Russia, June 21–26, 2010

Optically detected nuclear magnetic resonance in InGaAs quantum dots

K. Flisinski[1], I. Ya. Gerlovin[2], I. V. Ignatiev[2], M. Yu. Petrov[2], S. Yu. Verbin[2], D. R. Yakovlev[1,3] and M. Bayer[1]

[1] Experimentelle Physik II, Technische Universität Dortmund, D-44221 Dortmund, Germany
[2] Physics Department, St Petersburg State University, 198504 St Petersburg, Russia
[3] Ioffe Physical-Technical Institute, St Petersburg, Russia

Abstract. The peculiarities at the dependence of photoluminescence polarization of InGaAs quantum dots on the transverse magnetic field were observed under applying of radio frequency (RF) field. It is shown that these peculiarities result from the suppression of dynamical polarization of ^{71}Ga and As nuclei by the RF field. The effect of quadrupole splitting on nuclear spin dynamics has been evaluated.

Optically detected nuclear magnetic resonance (ODNMR) is considered as an effective tool for study of the dynamics of nuclear polarization in semiconductors [1, 2, 3]. The optical detection of nuclear spin states is possible due to strong coupling of the electron and nuclear spins in such materials via hyperfine interaction. Due to the interaction, optical orientation of electron spin is accompanied by dynamic nuclear polarization (DNP). In turn, the DNP affects the electron spin as an effective magnetic field, which changes the electron spin polarization. Application of a RF field resonant to the transitions between nuclear spin sublevels can depolarize the nuclei and thereby change the electron spin polarization. Optical registration of the changes allows one to detect the nuclear magnetic resonance.

ODNMR was observed in bulk semiconductors [1, 2] and semiconductor quantum wells [2, 3, 4]. High sensitivity of the optical registration makes the ODNMR promising for study of semiconductor quantum dots (QDs), which contain relatively small number of nuclei. At the same time, there are no experimental data related to ODNMR in such structures.

In this communication we present the first results of experimental study of nuclear magnetic resonances in InGaAs/GaAs QDs detected in polarization of their PL in transverse magnetic field (Voigt geometry). In particular, the obtained data give clear evidence of the DNP in a relatively strong transverse field of hundreds of mT. Analysis of the experimental results allowed us to identify types of the nuclei responsible for the DNP formation at the magnetic field range 0–10 mT.

We studied the sample with self-assembled InAs/GaAs QDs annealed at temperature 980 °C. In the structures studied, each QD contains one resident electron on average, which is supplied by the delta-doped barrier layers. Optically oriented electron spin interacts with nuclear spins thus efficiently polarizing the nuclei. At the same time, the electron spin polarization degree can be used as the indicator of nuclear spin polarization.

The electron spin polarization was detected via negative photoluminescence (PL) polarization [5]. The PL was excited by a cw Ti-sapphire laser, whose wavelength was tuned to the wetting layer optical transition. The PL polarization was detected using a photoelastic modulator and a photon counting system. All the experiments were done at 2 K. A split-coil superconductive magnet was used for applying the magnetic field to the samples.

We have studied the PL polarization degree as a function of the magnetic field applied perpendicular to the optical pumping direction (Hanle effect) at different optical excitation powers. It was found that the increase of pump power results in the growth of polarization degree and in the drastic increase of half width at half maximum (HWHM) of the Hanle curves. Each curve has a W-shape in its central part, which is similar to that observed earlier for *positive* PL polarization [1,6]. According to Ref. [6], the optically created nuclear spin is directed along the total field acting on the nuclei, which is the sum of external field and of effective electron field (Knight field [2]). Under strong enough optical pumping, the nuclear spin polarization is efficiently developed and its effective magnetic field affecting the electron (Overhauser field [1, 2]) may be considerably larger than the external magnetic field. The Overhauser field becomes tilted with the total field when the external magnetic field increases, which gives rise to depolarization of electron spin and causes the dips in Hanle curve near the central peak. Further increase of the external field gives rise to decrease of the nuclear field followed by partial recovery of electron spin polarization. This simplified picture of physical processes qualitatively explains the appearance of W-shape.

Although the observed evolution of the Hanle curve can be satisfactorily explained by nuclear spin polarization, the experiments performed give no direct proof for that. To verify the nuclear spin polarization experimentally and to identify the nuclei responsible for the nuclear field, we applied an RF excitation, which directly affects the nuclear spin system. We have studied the dependence of the Hanle curves on the RF field frequency. Results of the experiment are shown in Fig. 1.

As seen from the figure, application of RF field is accompanied by the appearance of clearly observed resonances. The resonance position is linearly depending of RF within experimental error. We suppose that the two observed resonances correspond to $+1/2 \leftrightarrow -1/2$ transitions in ^{71}Ga and As nuclei subject to the change of gyromagnetic ratio due to the quadrupole splitting of nuclear states. The source of the splitting is the strain-induced electric field gradient, ∇V, which lifts off the degeneracy of nuclear spin states with different absolute values of projections of nuclear spin on the principal axis of tensor ∇V [7].

To illustrate the quadrupole interaction effect on Zeeman splitting, we have done a simple estimate. The Hamiltonian of interaction of nuclear spin $\hat{\mathbf{I}}$ with external magnetic field $\mathbf{B}$ in the presence of quadrupole splitting aligned along z axis can be written as [7]

$$\hat{\mathcal{H}} = -\gamma\hbar\left(\hat{\mathbf{I}} \times \mathbf{B}\right) + \frac{h\nu_Q}{2}\left(\hat{I}_z^2 - \frac{I(I+1)}{3}\right), \qquad (1)$$

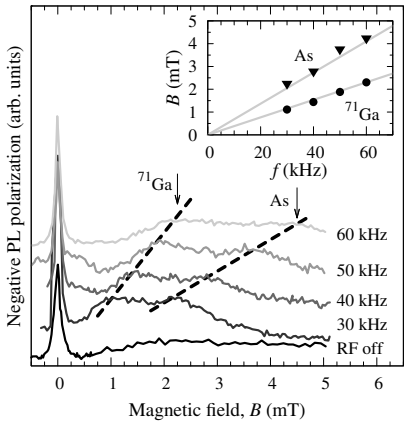

Fig. 1. Effect of RFy field on Hanle curve in the range of W-shape. The RF frequencies are given near each curve. "RF-off" indicates the curves measured in the absence of RF field. The curves are shifted vertically for clarity of presentation. Arrows and dashed lines indicate the magnetic field position of NMR for ^{71}Ga and As nuclei. Inset shows frequency dependence of resonances extracted from the experiments (symbols). Solid lines are the expected dependencies for the case of strong quadrupole splitting (see text).

where γ is the nuclear gyromagnetic ratio, h is Planck constant and $\hbar = h/(2\pi)$. The quadrupole splitting is determined by the only frequency

$$\nu_Q = \frac{3eV_{zz}Q}{2I(2I-1)h}. \qquad (2)$$

Here e is the elementary charge, Q is the nuclear quadrupole momentum, and $V_{zz} = S_{11}\varepsilon_{zz}$ is the strain-induced electric field gradient at the nuclear site.

Using a cylindrically symmetric model of QD [8] and the transversal isotropic approximation in the framework of continuum elasticity theory [9] we have estimated the value of strain ε_{zz} to be not exceeding 0.02 (two percent) in QD annealed at 980 °C. One can also easily estimate the magnitude of ν_Q using values of quadrupole momenta Q and S-tensor for different isotopes extracted from experimental data on nuclear acoustic resonance [10, 11]. The results of such calculations for gallium, arsenic, and indium nuclei are presented in Tab. 1.

Table 1. Nuclear quadrupole parameters. The values Q are taken from Ref. [10] and the values of S_{11} are taken from Ref. [11]. Quadrupole frequencies ν_Q are calculated for the value of strain $\varepsilon_{zz} = 0.01$.

Isotope	I	Q (mbar)	S_{11} (stat C/cm^3)	ν_Q (kHz)
^{71}Ga	3/2	107	9.1×10^{15}	353
^{69}Ga	3/2	171	9.1×10^{15}	564
^{75}As	3/2	314	1.31×10^{16}	1490
^{113}In	9/2	759	1.67×10^{16}	388
^{115}In	9/2	770	1.67×10^{16}	383

Results of calculations of Zeeman splitting of different sublevels $\pm1/2$ and $\pm3/2$ for ^{71}Ga nuclei obtained by direct diagonalization of the Hamiltonian given by Eq. (1) are shown in Fig. 2(a). As seen, for relatively small magnetic field (a few mT), when the quadrupole splitting is considerably larger than the Zeeman one for $\pm1/2$ sublevel, the $\pm3/2$ level is almost not split. At the same time, the splitting of $\pm1/2$ sublevels is twice larger than it should be for zero quadrupole splitting. Similar situation also appears for other types of nuclear spins.

Figure 2(b) shows the dependence of the Zeeman splitting of $\pm1/2$ and $\pm3/2$ sublevels on the angle between x axis (which is perpendicular to the principal axis of the gradient) and the

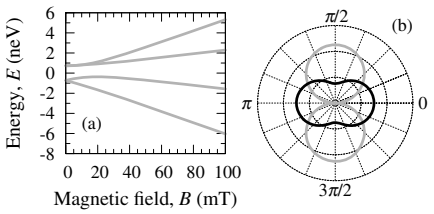

Fig. 2. (a) Zeeman splitting of ^{71}Ga nuclear spins in magnetic field applied transversally to the strain-induced quadrupole splitting of nuclear sublevels. (b) Dependencies of effective splitting of $I_z = \pm1/2$ (black line) and $I_z = \pm3/2$ (gray line) sublevels on the angle between the magnetic field and quadrupole axis. Zero angle corresponds to perpendicular orientation of these axes.

magnetic field direction for the case of strong quadrupole splitting (or weak magnetic field). As seen, if the magnetic field is applied along the quadrupole axis, there is a normal Zeeman splitting when $\Delta E_{\pm3/2} = 3\Delta E_{\pm1/2}$. When the magnetic field is transverse to the quadrupole axis, the nuclear spin doublet $\pm1/2$ is splitted twice larger and the doublet $\pm3/2$ is not splitted at all. As seen from the inset in Fig. 1, the positions of observed resonances well corresponds to the latter case for ^{71}Ga and As nuclei.

In conclusion, we have optically detected the nuclear magnetic resonance, which is the direct proof of the DNP formation in the ensemble of InGaAs quantum dots. Resonances are detected as relatively wide peaks in the magnetic field dependence of the PL polarization degree, which appear when the radio-frequency field is applied. The reason of these effects is the suppression of the dynamical nuclear polarization by the resonant field.

Acknowledgements

The authors thank V. K. Kalevich, K. V. Kavokin, and V. L. Korenev for fruitful discussions. This work has been supported by the Deutsche Forschungsgemeinschaft, by the Russian Foundation for Basic Research, by the Russian Ministry of Education, and by the "Dynasty" foundation (MYP).

References

[1] *Optical Orientation*, ed. by B. P. Zacharchenia and F. Meier (North-Holland, Amsterdam 1984).
[2] V. K. Kalevich, K. V. Kavokin, and I. A. Merkulov, In: *Spin Physics in Semiconductors*, edited by M. I. Dyakonov, Springer series in solid state science, Vol. 157 (Springer, Berlin 2008).
[3] *Semiconductor Spintronics and Quantum Computation*, ed. by D. D. Awschalom, D. Loss, and N. Samarath (Springer, Berlin 2002).
[4] G. Salis *et al*, *Phys. Rev. Lett.* **86**, 2677 (2001).
[5] R. V. Cherbunin *et al*, *Phys. Rev. B* **80**, 035326 (2009).
[6] D. Paget *et al*, *Phys. Rev. B* **15**, 5780 (1977).
[7] A. Abragam, *The Principles of Nuclear Magnetism* (Oxford Science Publications, Oxford UK 1961).
[8] M. Yu. Petrov *et al*, *Phys. Rev. B* **78**, 045315 (2008).
[9] J. Even *et al*, *Appl. Phys. Lett.* **91**, 122112 (2007).
[10] P. Pyykkö, *J. Mol. Phys.* **106**, 1965 (2008).
[11] R. K. Sundfors, *Phys. Rev. B* **10**, 4244 (1974).

18th Int. Symp. "Nanostructures: Physics and Technology"
St Petersburg, Russia, June 21–26, 2010

Magnetic-field induced second and third harmonics generation in epitaxial films of magnetic semiconductors EuTe and EuSe

B. Kaminski[1], M. Lafrentz[1], R. V. Pisarev[2], D. R. Yakovlev[1,2], *V. V. Pavlov*[2], V. A. Lukoshkin[2], A. B. Henriques[3], G. Springholz[4], G. Bauer[4], E. Abramof[5], P. H. O. Rappl[5] and M. Bayer[1]

[1] Experimentelle Physik II, Technische Universität Dortmund, D-44221, Germany
[2] Ioffe Physical-Technical Institute, St Petersburg, Russia
[3] Instituto de Física, Universidade de São Paulo, 05315-970 São Paulo, Brazil
[4] Institut für Halbleiter- und Festkörperphysik, Johannes Kepler Universität Linz, 4040 Linz, Austria
[5] LAS-INPE, 12227-010 São José dos Campos, Brazil

Abstract. Epitaxial films of magnetic semiconductors EuX (X = Te, Se) are investigated by the nonlinear optical spectroscopy using the second and third harmonics generation (SHG and THG) in the vicinity of the conduction band formed by the electronic transition $4f^7 5d^0 \rightarrow 4f^6 5d^1$ in magnetic Eu^{2+} ions. Crystal structure of EuX is centrosymmetric with the point group $m3m$,in which the SHG is strictly forbidden in the electric-dipole approximation, however the odd-order THG process is allowed. Surprisingly, in applied magnetic field the SHG has been observed revealing a novel nonlinear optical susceptibility of the magnetic-dipole type. The THG appears in applied magnetic field at the photon energies 2.2–2.4 eV close to the excitonic band-edge.

Introduction

Harmonics generation is associated with higher order optical susceptibilities, and it has a great potential for disclosing microscopic mechanisms of nonlinear interaction of light with matter and for getting unique information about the crystallographic, electronic and magnetic structure which is inaccessible in linear optics [1,2,3].

Second harmonic generation (SHG) has attracted vivid interest in fundamental physics because of its exceptional sensitivity to space and time symmetry violations [3]. Another strong point of this phenomenon is its specific sensitivity in the studies of surfaces and interfaces [4,5,6]. Various technological applications of SHG are based on materials with high second order nonlinear susceptibility combined with the possibility to fulfill phase matching conditions.

Among different optical effects the third harmonic generation (THG) is the simplest nonlinear optical phenomenon which is allowed in the electric-dipole (ED) approximation in all media. External magnetic field breaks the time-reversal symmetry enabling new third order nonlinear components [7, 8, 9].

Europium chalcogenides EuX (X = O, S, Se, and Te) form the group of magnetic semiconductors, which are well known from 60's of the last century. EuX possess unique magnetic, transport, and magneto-optical properties [10]. These properties are determined by the strongly localized $4f^7$ electrons of Eu^{2+} ions with spin $S = 7/2$. Due to competition between exchange integrals of the nearest and next-nearest neighbors the magnetic phase diagram can include antiferro-, ferri-, and ferromagnetic ordering as well as paramagnetic phase at low temperatures. Current interest in EuX magnetic semiconductors is caused by achievements in growing high quality epitaxial films of these materials and their potential applications for spintronics and magneto-optical devices [11,12].

Here we present results on magnetic-field-induced second and third harmonic generation in epitaxial films of europium chalcogenides EuTe and EuSe. The induced SHG allowed us to introduce a novel type of nonlinear optical susceptibility caused by the magnetic-dipole contribution combined with spontaneous or induced magnetization. It was found that THG is strongly enhanced in the vicinity of the excitonic band-edge at 2.2–2.4 eV when an external magnetic field is applied. By the rotation anisotropy experiments, temperature and magnetic field dependencies of magnetic-field-induced SHG and THG it is clearly shown that only the ferromagnetic component of magnetic structure is responsible for observed magneto-optical nonlinearities.

1. Second harmonic generation in EuTe and EuSe

A strong laser radiation with the electric field $\mathbf{E}(\omega)$ at the fundamental frequency creates in a medium a nonlinear polarization $\mathbf{P}(2\omega)$ at doubled frequency. As the crystal structure of EuTe and EuSe is centrosymmetric with the point group $m3m$, the SHG can be only observed in quadrupole or magnetic-dipole approximation [13,14]. A new type of nonlinear polarization can be induced if the parent crystal symmetry is broken by either magnetic field or magnetic ordering, both of which we introduce by the magnetic parameter $\mathbf{M}$. This kind of symmetry breaking does not violate the space-inversion symmetry operation. The crystallographic (eem) and induced magnetic dipole ($eemm$) nonlinear polarizations can be written as

$$\mathbf{P}(2\omega) \propto i\boldsymbol{\chi}^{\mathrm{eem}}\!:\mathbf{E}(\omega)\mathbf{B}(\omega) + \boldsymbol{\chi}^{\mathrm{eemm}}\!:\mathbf{E}(\omega)\mathbf{B}(\omega)\mathbf{M}\,,$$

where $\mathbf{E}(\omega)$ and $\mathbf{B}(\omega)$ are the electric and magnetic fields at the fundamental light wave, respectively. $\boldsymbol{\chi}^{\mathrm{eem}}$ is an axial third-rank tensor, $\boldsymbol{\chi}^{\mathrm{eemm}}$ is a polar forth-rank tensor [15].

The experimental technique is described in Ref. [16]. SHG spectra were recorded in transmission geometry using 8 ns laser pulses with a 10 Hz repetition rate. EuTe and EuSe layers were grown by molecular-beam epitaxy on (111)-oriented BaF_2 substrates [17]. Figure 1 shows the SHG spectra of EuTe recorded at different magnetic fields. At zero field, no SHG signal was detected in a wide temperature range below and above T_N. However, SHG appears at finite field in the vicinity of the

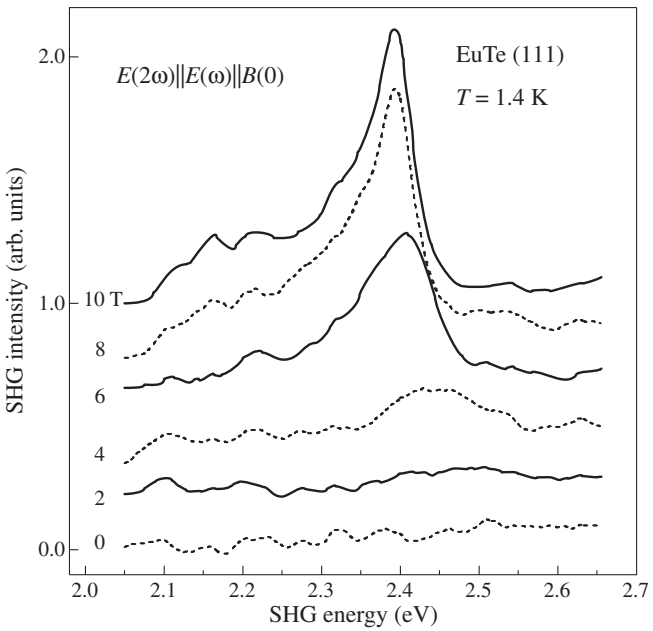

Fig. 1. SHG spectra of EuTe in magnetic fields. Spectra are offset by 0.2 relative to each other.

band gap, and its structure with a maximum at 2.4 eV and a shoulder at 2.2 eV is in good agreement with EuTe absorption spectra [17].

The rotational anisotropy of the SHG intensity detected for simultaneous rotation of linear polarizers for the fundamental and SHG light is a characteristic feature of the coherent SHG process. Corresponding diagrams for EuTe and EuSe are shown in Fig. 2 for the parallel ($\mathbf{E}(2\omega)\|\mathbf{E}(\omega)$) and perpendicular ($\mathbf{E}(2\omega)\perp\mathbf{E}(\omega)$) configuration. For EuTe the rotational anisotropies are twofold. In EuSe the rotational anisotropy is twofold in the parallel configuration but is transformed into a distorted fourfold anisotropy for the perpendicular geometry.

The observed SHG is due to the ferromagnetic component of the spin system in EuX. The role of the external magnetic field is to induce the ferromagnetic component. SHG signals are observed also above the Néel temperature, when the magnetic field polarizes the Eu^{2+} spins in a paramagnetic phase. Thus, application of the magnetic field to EuX leads to a new type of MD nonlinearity. It can be treated as a counterpart to electric field application to centrosymmetric media which breaks space-inversion symmetry and allows ED-SHG processes.

2. Third harmonics generation in EuTe and EuSe

In the ED approximation the third-order nonlinear optical polarization $\mathbf{P}(3\omega)$ can be written as

$$\mathbf{P}(3\omega) \propto \chi^{\mathrm{eeee}}\colon \mathbf{E}(\omega)\mathbf{E}(\omega)\mathbf{E}(\omega) + i\chi^{\mathrm{eeeem}}\colon \mathbf{E}(\omega)\mathbf{E}(\omega)\mathbf{E}(\omega)\mathbf{M},$$

where the first term describes the leading order ED-THG contribution and the second one describes the THG contribution with the magnetic parameter $\mathbf{M}$. χ^{eeee} is a polar forth-rank tensor, χ^{eeeem} is a axial fifth-rank tensor. It was found, that the THG is strongly enhanced in applied magnetic field at the photon energies 2.2–2.4 eV close to the excitonic band-edge.

Acknowledgements
This work was supported by the DFG, RFBR, Spintronics, FoNE, FAPESP, CNPq, and FWF.

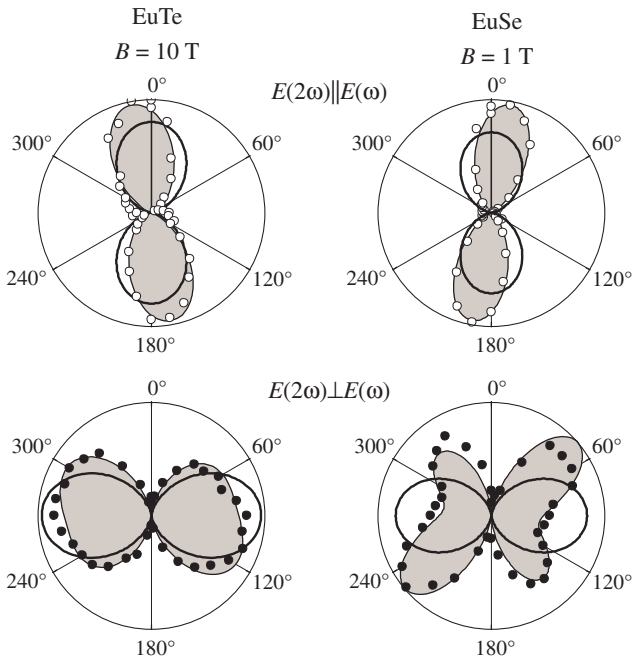

Fig. 2. Polar plots of experimental SHG intensity data (dots) in EuTe and EuSe measured at 2.4 eV. Best fits are shown by solid lines (shaded areas).

References

[1] Y. R. Shen, *The Principles of Nonlinear Optics* (New York: Wiley), 1984.
[2] R. W. Boyd, *Nonlinear Optics* (San Diego: Academic Press), 1993.
[3] M. Fiebig, V. V. Pavlov, and R. V. Pisarev, *J. Opt. Soc. Amer. B* **22**, 96 (2005).
[4] T. F. Heinz, C. K. Chen, D. Ricard, and Y. R. Shen, *Phys. Rev. Lett.* **48**, 472 (1982).
[5] P. Guyot-Sionnest, W. Chen, and Y. R. Shen, *Phys. Rev. B* **33**, 8254 (1986).
[6] P.-F. Brevet, *Surface Second Harmonic Generation*, (Presses polytechniques et universitaires romandes), 1997.
[7] V. V. Pavlov, R. V. Pisarev, M. Fiebig, and D. Fröhlich, *Phys. Solid State* **45**, 662 (2003).
[8] J. Shimura, S. Ohkoshi, and K. Hashimoto, *Appl. Phys. Lett.* **82**, 3290 (2003).
[9] O. A. Aktsipetrov *et al*, *J. Opt. Soc. Am. B* **22**, 138 (2005).
[10] P. Wachter, *Handbook on the Physics and Chemistry of Rare Earths*, **11**, Eds. K. A. Gschneider and L. R. Eyring (Amsterdam: North Holland) 507, 1979.
[11] A. Schmehl *et al*, *Nature. Mat.* **6**, 882 (2007).
[12] G. Springholz, A. Raab, R. T. Lechner, and V. Holy, *Appl. Phys. Lett.* **79**, 1225 (2001).
[13] M. Fiebig, D. Fröhlich, Th. Lottermoser, V. V. Pavlov, R. V. Pisarev, and H.-J. Weber, *Phys. Rev. Lett.* **87**, 137202 (2001).
[14] B. Kaminski, M. Lafrentz, R. V. Pisarev, D. R. Yakovlev, V. V. Pavlov *et al*, *Phys. Rev. Lett.* **103**, 057203 (2009).
[15] R. R. Birss, *Symmetry and Magnetism* (Amsterdam: North Holland), 1967.
[16] V. V. Pavlov *et al*, *Phys. Rev. Lett.* **94**, 157404 (2005).
[17] A. B. Henriques *et al*, *Phys. Rev. B* **72**, 155337 (2005).

18th Int. Symp. "Nanostructures: Physics and Technology"
St Petersburg, Russia, June 21–26, 2010

A problem of the effective g-factor in the n-HgTe/$Cd_xHg_{1-x}Te$ quantum well with inverted band structure

M. V. Yakunin[1], S. M. Podgornykh[1], N. N. Mikhailov[2] and S. A. Dvoretsky[2]

[1] Institute of Metal Physics, RAS, Ural Branch, S. Kovalevskaya Str. 18, GSP-170, Ekaterinburg 620041, Russia
[2] Institute of Semiconductor Physics, RAS, Siberian Branch, Novosibirsk, Russia

Abstract. An effective g-factor (g^*) in the conduction band of the inverted band structure of the 20 nm wide HgTe quantum well is measured by different ways: from the structure of Shubnikov–de Haas oscillations and the quantum Hall effect (QHE), from their activation development with temperature; from the coincidence effect in tilted magnetic fields and from the activation analysis of the coincidence feature taken at constant temperature as a function of the parallel magnetic field component at the fixed filling factor. Probably we present the first observation of the coincidence effect in the QHE regime that is possible due to $g^*m^*/m_0 > 1$ in the HgTe layer. Shown is that while under pure perpendicular magnetic fields the obtained $|g^*| = 50$–60, considerably smaller values are deduced from the experiments that include parallel field component. This could be described by the g-factor anisotropy of $g_\perp/g_\parallel \approx 5$. We believe that the main source of the anisotropy is a quasi-two-dimensional nature of the spin splittings in the HgTe conduction band of p-like character although the zero field spin splittings due to strong spin-orbit interaction should also be considered.

Introduction

In a HgTe quantum well (QW) within the HgTe/$Cd_xHg_{1-x}Te$ heterosystem, a unique inverted band diagram is realized when the well width d_w is larger than the critical value of 6.3 nm so that the conduction band is formed of the p-like wave functions [1,2]. Properties of the p-type conduction band differ considerably from those of a traditional s-like conduction band, in particular, due a strong spin-orbit interaction [3].

HgTe is characterized by a rather large Lande g-factor ($-g =$ 20–25 for bulk material [4]) that makes it attractive for spintronics. Actual is finding the g-factor for two-dimensional HgTe structures, which may differ considerably from the bulk value. Using the coincidence effect in tilted magnetic fields for HgTe QW [5] gave the effective g-factor $|g^*|$ between 15 and 35. For simple interpretation of this effect in terms of an s-like band, the phase reversals of Shubnikov–de Haas oscillations (SHO) should be observed at the angles θ_r to the sample normal corresponding to the relation

$$g^*m^*/m_0 = 2r\cos\theta_r, \qquad (1)$$

with $r = 1, 2, \ldots, m^*$ — the effective mass, m_0 — free electron mass. For most of the traditional heterosystems, $g^*m^*/m_0 \ll 1$ and the effect is only observed at field configurations very close to orientation parallel to the layers. This implies only small achievable values of perpendicular field component $B_\perp$ relating to the field range of SHO with large numbers. On the contrary, for the HgTe bulk parameters, $g^*m^*/m_0 \approx 0.75$ that imply angles θ_r not so close to 90° and a possibility to reach the range of $B_\perp$ corresponding to the quantum Hall effect (QHE) regime.

The purpose of the paper is an overall study of spin splittings in HgTe QW with special attention paid to specificity of the coincidence method in this material under QHE conditions.

1. The sample and experimental results

We study QHE in the HgTe/ $Cd_xHg_{1-x}Te$ (013) oriented QW, $x = 0.6$–0.73, $d_w = 20.3$ nm, doped on both sides with 10 nm spacers, with electron density 1.5×10^{15} m^{-2} and mobility of 20 m^2/ V s at liquid helium temperatures.

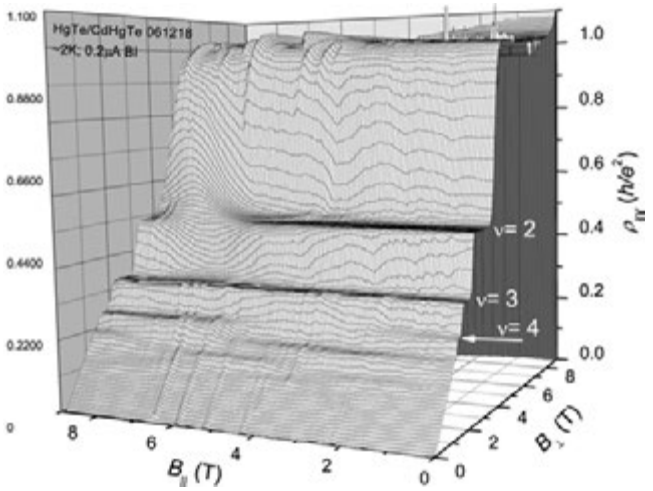

Fig. 1. Development of QHE with addition of $B_\parallel$: $\rho_{xy}(B_\perp, B_\parallel)$ as a continuous surface. Temperature $T = 1.8$ K. Note the local smoothing the plateaus away.

A traditional QHE structure in perpendicular magnetic field is seen on the right facet of Fig. 1. To study transformations of the QHE with addition of the field component $B_\parallel$ parallel to the layers we used our specific technique of sample rotation [6] with results for magnetoresistivity components presented as $\rho_{xx,xy}(B_\perp, B_\parallel)$ functions of two variables either in the form of surfaces (an example in Fig. 1) or as their maps projected onto the $(B_\perp, B_\parallel)$-plane (Fig. 2).

2. Discussion

QHE structure in the sample investigated is characterized by that the odd numbered features prevail over the even-numbered ones. This means that spin splittings are larger than the remnants of the orbital gaps between neighboring Landau levels and put the limits to the g^*-factor value

$$1 < g^*m^*/m_0 < 2. \qquad (2)$$

Assuming $m^*/m_0 = 0.024$, as obtained from cyclotron resonance on a similar sample [7] with close electron density, it yields $42 < g^* < 84$.

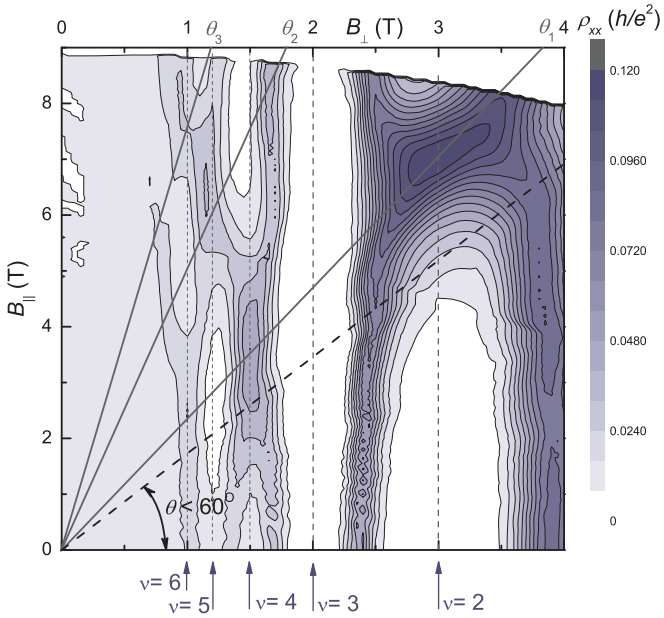

Fig. 2. Development of QHE with addition of $B_\parallel$: $\rho_{xx}(B_\perp, B_\parallel)$ presented as a map.

Another way for estimations is to compare the fields for onsets of SHO ($B_1 = 0.45$ T) and of their splitting ($B_2 = 1$ T). Considering that the onset of SHO corresponds to spin gaps the relation could be deduced: $g^*m^*/m_0 = 2B_2/(B_1 + B_2) = 1.38$, in agreement with (2), yielding $g^* = 58$ for $m^*/m_0 = 0.024$.

The gaps may also be obtained from the activation temperature dependencies of $\rho_{xx}(B)$ minima that yields $g^* = 50.4$ as deduced from the line slope through the odd numbered points and $m^*/m_0 = 0.022$ from the line slope through the even-numbered points, which is close to the cyclotron result [7].

With addition of $B_\parallel$ the $\rho_{xx}(B_\perp)$ minimum for filling factor $\nu = 2$ evolves into a sharp maximum (Fig. 2) accompanied by local smoothing the ρ_{xy} plateau away in the same $(B_\perp, B_\parallel)$ range (Fig. 1). The same happens for other even numbered QHE features with $\nu = 4, 6, 8$ although not so brightly. All of these peaks are located on the straight beam stemming from 0 on the $\rho_{xx}(B_\perp, B_\parallel)$ map with the slope of $\theta_1 = 67^\circ$ (Fig. 2) that is the $r = 1$ coincidence angle.

The self-consistent behavior of ρ_{xx} and ρ_{xy} indicates closings of the gaps between magnetic levels within corresponding field ranges confirming the applicability of the coincidence model in the QHE regime. The other coincidence angles could be determined from (1) as $\cos\theta_r = \cos\theta_1/r$: see two beams for $r = 2$ and 3 on the map Fig. 2. The beam for $r = 2$ goes close to the peaks emerging in the gaps for $\nu = 5$ and 7 and the beam for $r = 3$ goes through a weakly resolved peak in the $\nu = 6$ minimum. Thus the overall picture of the coincidence model is realized here with the effect being much sharper within the QHE range of fields. On the other hand serious quantitative discrepancies should be mentioned. First, the specific structure of QHE that establishes the relation (2) leads to a condition for the $r = 1$ coincidence as $\cos\theta_1 > 1/2$, i.e. $\theta_1 < 60^\circ$. Thus the sharp coincidence peak at $\nu = 2$ as well as other $r = 1$ peaks should lie on some radius below the 60° beam (see the dashed beam on Fig. 2). But it is above, at 67°! This leads to a discrepancy in the obtained g^* value: as follows from (1), $g^*m^*/m_0 = \cos\theta_1 = 0.786 < 1$, which falls below the range (2), and with $m^*/m_0 = 0.024$ yields $g^* = 33$.

Table 1.

Structure of QHE	$42 < g^* < 84$
Onsets of SHO and splittings	$g^* = 57.5$
$\rho_{xx\,\min}(T)[\nu]$	ν-odd: $g^* = 50.8$
	ν-even: $m^*/m_0 = 0.022$
Coincidence method	$g^* = 33$
$\rho_{xx}(B_\parallel)[\nu = 2]$	$g^* = 8$

Using advantages of our experimental technique we suggest a way to extract the bare g^* value, but not the value of the g^*m^* product as it is in a traditional coincidence method, from the activation analysis of the coincidence feature taken at constant temperature as a function of $B_\parallel$ in the cross-section of the $\rho_{xx}(B_\perp, B_\parallel)$ surface at the fixed ν ($\nu = 2$, see Fig. 2). The value so obtained is $g^* = 8$, much smaller than the values found under pure perpendicular fields, that constitutes the second discrepancy.

The obtained g^* values are summarized in the Table indicating that self-consistent values $|g^*| = 50$–60 are obtained from different measurements under pure perpendicular fields, but considerably smaller and much smaller ones — from experiments with addition of $B_\parallel$.

To resolve the discrepancies found the following things should be additionally taken into account while analyzing the results under tilted fields: (i) Possible quasi-two-dimensional character of spin splittings in the band built of p-type wave functions. It was found for valence bands of traditional heterosystems [8] and in certain cases led to that oscillations didn't change their structure with tilt at all. As we do have changes, but insufficiently fast, we may have some intermediate case. (ii) Zero field spin splittings that might be considerable in the band of p-states [3].

Acknowledgements

The work was done within RAS program 01.2.006 13395 with partial support of RFBR, projects 08-02-00222 and 09-02-96518.

References

[1] M. Konig *et al*, *J. Phys. Soc. Jpn* **77**, 031007 (2008).
[2] Z. D. Kvon *et al*, *Low Temperature Phys.* **35**, 6 (2009).
[3] X. C. Zhang *et al*, *Phys. Rev. B* **63**, 245305 (2001).
[4] S. Uchida *et al*, *J. Phys. Soc. Jpn.* **40**, 118 (1976).
[5] X. C. Zhang *et al*, *Phys. Rev. B* **69**, 115340 (2004).
[6] M. V. Yakunin *et al*, *JETP* **105**, 214 (2007).
[7] Z. D. Kvon *et al*, *Physica E* **40**, 1885 (2007).
[8] R. W. Martin *et al*, *Phys. Rev. B* **42**, 9237 (1990); R. J. Warburton *et al*, *Semicond. Sci. Technol.* **6**, 359 (1991); N. A. Gorodilov *et al*, *JETP Lett.* **56**, 394 (1992).

18th Int. Symp. "Nanostructures: Physics and Technology"
St Petersburg, Russia, June 21–26, 2010

The effect of Mn delta-doping on circularly polarized luminescence of InGaAs/GaAs quantum-size heterostructures

Yu. A. Danilov[1], *M. V. Dorokhin*[1], V. D. Kulakovskii[2], M. M. Prokof'eva[1], S. V. Zaitsev[2] and B. N. Zvonkov[1]

[1] Physical Technical Research Institute of Nizhniy Novgorod State University, 603950 Nizhniy Novgorod, Russia
[2] Institute for Solid State Physics, 142432 Chernogolovka, Moscow Region, Russia

Abstract. A quantum well luminescence of InGaAs/GaAs heterostructures with a ferromagnetic Mn delta-layer inserted into the GaAs barrier at a distance of 2–12 nm has been investigated in a wide range of magnetic fields and temperatures. A ferromagnetic behavior of circular polarization of the quantum well emission has been observed below a Curie temperature of the Mn delta-layer and explained by an s,p-d exchange interaction of QW carriers with Mn delta-layer.

Introduction

The discovery of ferromagnetism in the (Ga,Mn)As diluted magnetic semiconductor (DMS) has opened future trends for realizing semiconductor spintronics devices [1]. The feasibility of integrating ferromagnetic properties into semiconductors has resulted in a considerable interest to these materials. It has already been demonstrated that the mutual influence of magnetic ions and free carriers results in drastic changes in the hole spin polarization in the (Ga,Mn)As DMS [2]. Although the origin of ferromagnetism in (Ga,Mn)As is still under discussion [3] it is known that the magnetic behavior of the hole system strongly depends on the magnetic state realized in the DMS structures. One of the promising techniques for the formation of magnetic semiconductor structures is fabrication of quantum well (QW) heterostructures with nearby Mn-doped magnetic layer. It has already been demonstrated that the incorporation of delta-Mn doped layer into the barrier near to GaAs/p-AlGaAs [4] or InGaAs/GaAs [5] QWs allows obtaining the ferromagnetic properties in such structures. Applying the delta doping technique one can separate the location of holes in QWs and Mn ions in GaAs barrier. This decreases the effect of Mn impurity on the non-radiative recombination rate in the QW [6]. The variation of the GaAs layer thickness separating the Mn delta-layers should allow the control the spin polarization of carriers in the InGaAs QWs. The effect of the ferromagnetic layers on the spin polarization of carriers is of particular importance for applications of DMS QW structures in spintronic devices. In the present work, the circular polarization of QW electroluminescence of undoped InGaAs/GaAs QW structures with a ferromagnetic Mn delta-layer in the GaAs barrier is investigated in a wide range of magnetic fields and temperatures.

1. Experimental

The InGaAs/GaAs QW structures were fabricated by three-stage epitaxial growth method. A 0.5 μm-thick buffer GaAs layer (doped with Si up to 1×10^{17} cm^{-3}), delta-C doped layer and a 3 nm thick undoped GaAs layer were grown sequentially at 650 °C on GaAs (001) substrates by metal-organic vapor phase epitaxy (MOVPE) at atmospheric pressure. Then the $In_xGa_{1-x}As$/GaAs QW ($x = 0.1$–0.2; width $d_{QW} = 10$ nm) and thin ($d_s = 2$–12 nm) undoped spacer GaAs layer were grown at 550 °C. At the next stage the delta-Mn doped layer and the GaAs cap layer were grown at 400 °C in the same reactor by the laser sputtering of Mn and GaAs targets, respectively. The nominal densities of Mn and C in delta-layers were $\sim(0.6 - 2) \times 10^{14}$ and $\sim(2 - 3) \times 10^{12}$ cm^{-2}, respectively. For the fabrication of the diode structures an Au Schottky contact was formed at the top of the sample by vacuum thermal evaporation of metal. Back ohmic contact was formed by sparkling of Sn foil.

The schematic sketch of investigated structures is shown in Fig. 1a, and the technological details were described elsewhere [5]. The nonmagnetic reference sample contains a C delta-doped instead of Mn delta-doped layer. Also the samples with the same structure were grown on semi-insulating GaAs substrates with undoped buffer layer for transport measurements in magnetic field. The transport measurements have shown that structures with Mn delta-layer demonstrate a ferromagnetic behavior with Curie temperature $T_C \sim 30$–35 K [5]. Electroluminescence was measured at $T = 2$–80 K under the forward bias of Schottky diode (positive potential relatively to base). The operating current was varied in range of 1–30 mA. For the measurements of luminescence in the magnetic field the samples were placed into a liquid He cryostat with the superconducting magnet. The field $B = 0$–5 T was normal to the QW plane (Faraday geometry). The degree of circular polarization was evaluated by formula: $P_c = (I^+ + I^-)/(I^+ - I^-)$, where $I^{+(-)}$ are the intensities of the right(left)-hand polarized QW emission spectrum.

2. Results and discussion

It was found that in the magnetic field the EL become circularly polarized. The dependence of P_c on B has two regions: fast increase of P_c (at 0–0.4 T) and saturation at $B > 0.4$ T. The

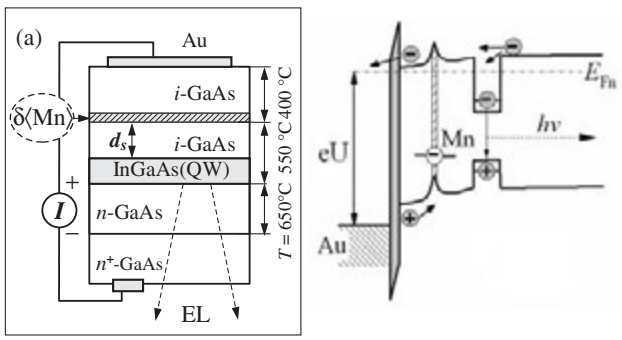

Fig. 1. The schematic diagram of investigated samples (a), a zone diagram of investigated diodes at forward bias (b).

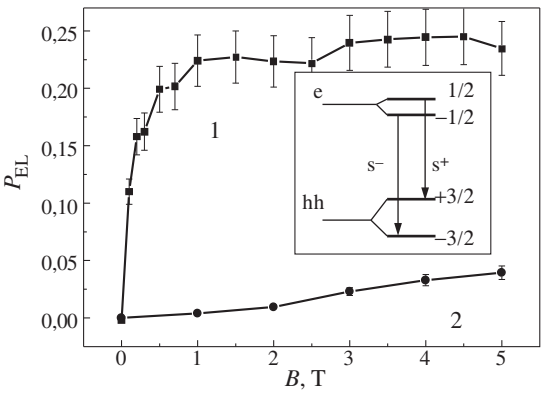

Fig. 2. The dependence of circular polarization degree of QW EL on the magnetic field for sample with delta-Mn (1) and reference sample (2). The inset shows a schematic diagram of QW electron-hole transitions at the magnetic field.

degree of circular polarization strongly exceeds the value obtained for the reference sample in the whole range of magnetic fields.

The temperature dependence of Pc shows a typical ferromagnetic behavior with the Curie temperature of 30–35 K. Below these temperatures the polarization degree changes very weakly. With the increase of T to ∼30 K it drops down. The determined Curie temperature is in good agreement with our previous investigations of the same samples grown on semi-insulating substrate [5]. The degree of circular polarization and its magnetic field dependence were found to depend on the spacer layer thickness between delta-Mn (d_s) and the QW or In content in the quantum well (x). The maximum circular polarization degree in investigated samples was 0.24 for the sample with the spacer layer thickness of 2 nm. With the increase of spacer layer thickness the ferromagnetic contribution to Pc decreases turning to zero for the sample with $d_s = 12$ nm. The circular polarization of the EL is determined by Zeeman splitting of energy levels in the quantum well. We suppose that in case of delta-Mn and QW system Zeeman splitting of heavy holes in the QW could be increased due to s,p-d-exchange interaction of QW holes with Mn ions (insert to Fig. 2). The intensity of a s^+ transition is defined by the population of carriers at the majority hole and minority electron levels. Vise versa the intensity of a s^- transition is defined by the population of carriers at the minority hole and majority electron levels. We suppose that the energy splitting of electron levels at $B < 0.4$ T is small in comparison to that of hole levels [7,8]. A spin relaxation of electrons is also small, which is related to a typical for nonmagnetic QWs slowing down of the spin relaxation with increasing B. Thus the electron population at both energy levels is approximately same. In such case high circular polarization degree that we observe is determined by Zeeman splitting of heavy hole levels in the QW enhanced due to s,p-d exchange interaction of holes with Mn ions in delta-layer. The efficiency of interaction and, as a consequence, circular polarization degree depends on the distance between QW and Mn delta-layer. The suggested theory may not be valid for the samples with deeper QW (higher x) in which Zeeman splitting of electron levels is higher due to higher g-factor [8]. There appears a noticeable difference in population of majority and minority electron levels that decreases slightly circular polarization degree at higher magnetic fields (>2 T). Thus, we have investigated a quantum well luminescence of InGaAs/GaAs heterostructures with a ferromagnetic Mn delta-layer inserted into the GaAs barrier. It was suggested that a ferromagnetic type of behavior of luminescence circular polarization observed below a Curie temperature of the Mn delta-layer could be explained by s,p-d exchange interaction of QW carriers with Mn delta-layer.

Acknowledgements

The work was supported by RFBR 08-02-00548 and 08-02-97038, RNP (No. 2.2.2.2/4297) and CRDF (grant BP4M01).

References

[1] G. A. Prinz, *Science* **282**, 1660 (1998).
[2] S. A. Wolf, D. D. Awschalom, R. A. Buhrman *et al*, *Science*, **294**, 1488 (2001).
[3] H. Ohno, D. Chiba, F. Matsukura *et al*, *Nature* **408**, 944 (2000).
[4] A. M. Nazmul, T. Amemiya, Y. Shuto *et al*, *Phys. Rev. Lett.* **95**, 017201 (2005).
[5] S. V. Zaitsev, M. V. Dorokhin, A. S. Brichkin *et al*, *JETP letters* **90**, 658 (2009).
[6] M. Poggio, R. C. Myers, N. P. Stern *et al*, *Phys. Rev. B* **72**, 2353135 (2005).
[7] G. Hendorfer and J. Schneider, *Sem. Sci. Technol.* **6**, 595 (1991).
[8] R. Kotlyar, T. L. Reinecke, M. Bayer, and A. Forchel, *Phys. Rev. B* **65**, 195314 (2004).
[9] M. M. Glazov, *Phys. Rev. B* **70**, 195314 (2004).

18th Int. Symp. "Nanostructures: Physics and Technology"
St Petersburg, Russia, June 21–26, 2010

Magnetic and magneto-optical properties of two-dimension arrays of Co nanoparticles in CaF_2/Co/CaF_2/Si(111) heterostructures

S. V. Gastev[1], D. A. Baranov[1], V. V. Fedorov[1], B. B. Krichevtsov[1], V. I. Sakharov[1], I. T. Serenkov[1], S. M. Suturin[1], A. V. Nashchekin[1], N. S. Sokolov[1] and T. Shimada[2]

[1] Ioffe Physical-Technical Institute, St Petersburg, Russia
[2] Department of Chemistry, The University of Tokyo, Japan

Abstract. Two-dimension arrays of cobalt nanoparticles in CaF_2/Co/CaF_2/Si(111) heterostructures have been fabricated by molecular beam epitaxy. Characterization of morphology and magnetization of the arrays has been carried out by AFM, SEM, MEIS methods, and SQUID magnetometery. Magneto-optical polar and longitudinal Kerr effect in heterostructures has been investigated by laser polarimetric set-ups. Spectral dependences of polar Kerr effect and reflectivity spectra have been measured in the spectral range 1.5–5 eV. It was found that the magnitude, sign and shape of spectral dependence of magneto-optical Kerr effect drastically depend on density and dimensions of magnetic nanoparticles in array.

Introduction

Magneto-optical Kerr effects (MOKE) (polar, longitudinal, and transversal) are widely used for investigations of thin and ultra-thin ferromagnetic films [1]. High sensitivity, the possibility to carry out "in-situ" measurements and relative simplicity make MOKE methods very attractive for study of both static and dynamic film magnetization behavior. Nevertheless the microscopic mechanisms responsible for the magnitude and sign of MOKE are not well established up to now especially for granular magnetic systems. Studies of polar Kerr effect (PKE) carried out by Kalska *et al* [2]. have shown that the sign of PKE in arrays of Co nanoparticles on different substrates is opposite to the bulk Co samples and Co thick films in wide spectral range. The reasons for such drastic change of PKE still remain unclear.

Optical and magneto-optical properties of nano-hetero-structures involving magnetic and dielectric layers can considerably depend on magnetic layer morphology [3,4]. The influence of morphology can manifest itself due to (i) different properties of nano-layers consisting of separate and connected magnetic particles and (ii) a change of interference conditions for light waves reflected by the substrate and dielectric layers, and originated from magnetic layer when morphology of magnetic layer is transformed from continues film to an array of separate particles. In this work we investigate magnetic, optical and magneto-optical properties of CaF_2/Co/CaF_2/Si(111) heterostructures with different types of cobalt layer morphology.

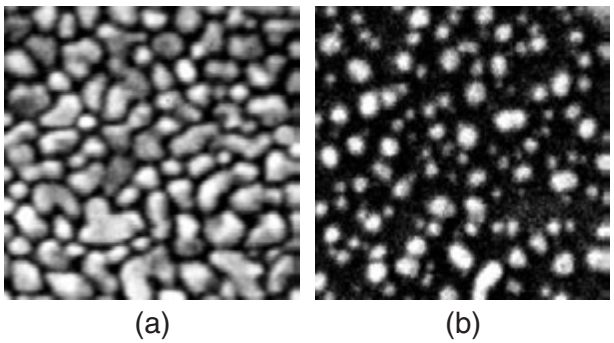

Fig. 1. SEM images of Co island arrays grown at the same deposition time and growth temperatures $T_{gr} = RT$ (a), and 300 °C (b).

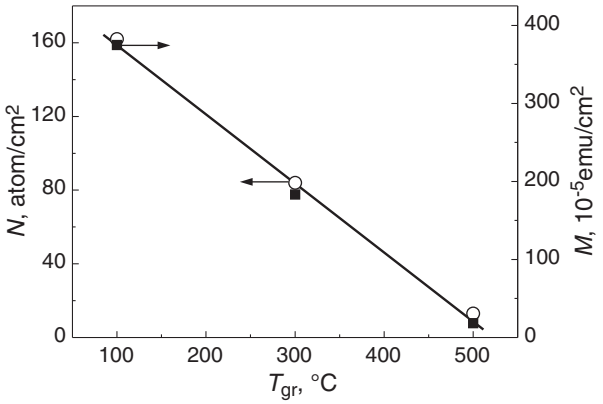

Fig. 2. Magnetization of structures and surface density of cobalt atoms as functions of T_{gr}.

1. Experimental

Heterostructures were prepared by MBE technology on Si(111) substrates. Co films were grown on 30 monolayers (ML) thick CaF_2 buffer layer and covered by 20 ML thick CaF_2 protective layer. The growth of Co layer was carried out at different substrate temperatures T_{gr} and different deposition times t_d. Two series of structures were studied. Samples of series I have been grown at different substrate temperatures and at constant deposition time which correspond to continuous film with effective thickness $d_{eff} \approx 8$ nm. Samples of series II were grown at constant growth temperature $T_{gr} = 294$ K and different t_{exp} corresponding to $d_{eff} = 3, 5, 8$ nm. At initial stages of Co layer growth a separate cobalt nanoparticles appear on CaF_2 buffer layer, which at following stages conglomerate providing a quasi-continuous film. The surface density of Co atoms has been determined by Middle Enegry Ion Scattering (MEIS) method. Magnetization of Co arrays has been measured by SQUID magnetometer (MPSM system) with in-plane orientation of magnetic field. Both polar and longitudinal Kerr-effects were studied by laser polarimetric technique at wavelengths $\lambda = 633$, 650 and 532 nm. Spectral dependence of rotation

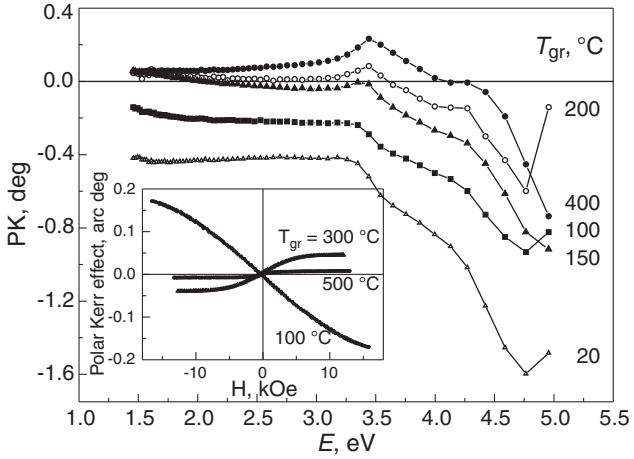

Fig. 3. Spectra of polar Kerr effect for structures of series I ($d_{\text{eff}} \sim$ 8 nm). Inset shows magnetic field dependence of PK for $E =$ 1.96 eV ($\lambda = 633$ nm) for structures grown at $T_{\text{gr}} = 100$, 300, and 500 ° C.

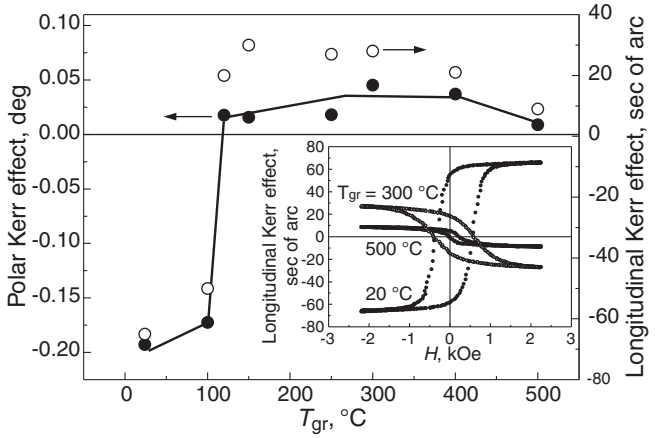

Fig. 4. Polar and longitudinal Kerr effect measured in saturation at $\lambda = 633$ nm as a function of T_{gr}. Inset shows magnetic field dependence of LK effect for structures grown at $T_{\text{gr}} = 20$, 300 and 500 °C.

angle in polar Kerr-effect and reflectivity spectra were measured in 1.5–5 eV spectral range.

2. Results

Investigations of heterostructures by scanning electron microscopy (SEM) and atomic force microscopy (AFM) show that both the morphology and effective thickness of magnetic layer considerably depend on the growth temperature. The structures grown at $T_{\text{gr}} = (20 - 100)$ °C with $d_{\text{eff}} = 8$ nm show quasi-continuous cobalt layer but at higher temperatures an arrays of single nano-islands with lateral dimensions of (10–40) nm separated by distance of (20–30) nm (Fig. 1). The height of particles estimated by means of AFM is about (5–20) nm.

Both the magnetization of structure M and surface density of Co atoms N in array considerably decrease with increase of T_{gr} (Fig. 2). Correlation between M and N and estimation of magnitude of magnetic moment per atom ($\sim 2\mu_{\text{B}}$) shows that practically all Co atoms are in ferromagnetic state and contribute to the magnetization.

It was found that the spectra of polar Kerr effect for magnetization-saturated Co arrays grown at low ($T_{\text{gr}} < 150$ °C) and high ($T_{\text{gr}} > 150$ °C) temperatures T_{gr} have opposite signs in very wide spectral range (Fig. 3).

Fig. 4 presents the measured rotation angles in polar and longitudinal Kerr effects at $\lambda = 633$ nm as functions of T_{gr} for Co structures grown at a constant t_{d}. One can see that the magnitude of Kerr rotation is large at $T_{\text{gr}} < 120$ °C, changes its sign in step-like manner at $T_{\text{gr}} \approx 120$ °C and stays small in modulus at $T_{\text{gr}} > 300$ °C.

The change of signs of polar and longitudinal Kerr-effects was also observed for structures grown at the same temperature $T_{\text{gr}} = RT$ and different deposition times t_{d}. Decrease of t_{d} results in decrease of both Co amount deposited onto CaF_2 and Co islands density.

Kerr rotation changes its sign for Co film effective thickness $d_{\text{eff}} \approx 3.5$ nm.

3. Summary

Reversible magnetic field dependence of PKE and irreversi-ble (hysteretic) one of LKE indicate that Co arrays have in-plane magnetic anisotropy. This is caused by flat two-dimensional shape of arrays, shape of particles, and magnetic dipole interaction between them. Decrease of the particle number in array results in decrease of in-plane magnetic anisotropy due to decrease of magnetic dipole interaction.

Decrease of particles density is followed by step-like change of sign and magnitude of polar and longitudinal Kerr effect and transformation of PKE shape and reflectivity spectral dependence. This behavior may be attributed to manifestation of local field effects in arrays of closely packed magnetic particles due to electromagnetic interaction between particles [5] and change of interference conditions for the light reflected from the substrate and Co nanoparticle arrays.

Acknowledgements

This work has been supported in part by using Foundation of Basic Research and programms of Russian Academy of Sciences.

References

[1] A. K. Zvezdin, V. A. Kotov, *Modern Magnetooptics and Magnetooptical Materials* (IOP, Bristol), 1997.

[2] B. Kalska *et al*, *J. Appl. Phys.* **92**, 7481 (2002); **95**, 1343 (2004); **98**, 0044318 (2005).

[3] L. Pasquali, B. P. Doyle, F. Borgatti, A. Giglia, N. Mahne, M. Pedio, S. Nannarone, A. K. Kaveev, A. S. Balanev, B. B. Krichevtsov, S. M. Suturin and N. S. Sokolov, *Surface Science.* **600**, 4170–4175, (2006).

[4] N. Yakovlev, A. Kaveev, N. Sokolov, B. Krichevtsov, A. Huan, *Current Applied Physics.* **6**, 575–578, (2006).

[5] V. A. Kosobukin, B. B. Krichevtsov, *Fiz. Tverd. Tela*, **52**, 759 (2010).

18th Int. Symp. "Nanostructures: Physics and Technology"
St Petersburg, Russia, June 21–26, 2010

Spin splitting in HgTe/CdHgTe(013) quantum well heterostructures

A. V. Ikonnikov[1], K. E. Spirin[1], S. S. Krishtopenko[1], V. I. Gavrilenko[1], S. A. Dvoretckiy[2] and N. N. Mihailov[2]

[1] Institute for Physics of Microstructures RAS, 603950 Nizhny Novgorod, Russia
[2] Institute of Semiconductor Physics, SB RAS, Novosibirsk, Russia

Abstract. Beating of Shubnikov–de Haas oscillations and cyclotron resonance line splitting have been observed in single side selectively doped n-type HgTe/CdHgTe(013) quantum well heterostructures the inverted band structure at $T = 4.2$ K. Both effects are attributed to a large (about 30 meV) spin splitting at $B = 0$ of the lowest heavy hole like subband in the conduction band.

Introduction

In recent years there has been a significant interest to spin-related phenomena in semiconductor heterostructures with large spin-orbit interaction stimulated by the proposition of electron wave analog of electro-optic modulator [1]. A typical value of the spin splitting at zero magnetic field due to say Rashba effect [2] in the conduction band of A3B5 heterostructures is few meV only. However in HgTe/CdHgTe heterostructures it can reach several tens of meV in the electric fields about 10^5 V/cm that corresponds to the 2D electron density about 10^{12} cm^{-2} [3]. The large spin splitting takes place in HgTe/CdHgTe heterostructures with so-called inverted band structure when HgTe quantum well (QW) width exceeds 6.3 nm. In that case the bottom of the conduction band is formed by wave functions of the p-type, that leads to a larger spin-orbit interaction, as compared with the normal conduction band formed by the wave functions of s-type. This work is devoted to the investigation into energy spectrum spin splitting in asymmetric HgTe/CdHgTe(013) heterostructures.

1. Experimental

The sample under study was grown by molecular beam epitaxy on semi-insulating GaAs(013) substrate and relaxed CdTe buffer [4]. The active part of the structure consists of a lower barrier $Cd_xHg_{1-x}Te$ ($x \sim 0.6$) 30 nm wide, a 15 nm HgTe QW, an upper $Cd_xHg_{1-x}Te$ barrier (similar to the lower one) and CdTe cap layer 40 nm wide. Lower barrier was selectively doped with In 11.5 nm apart from QW. The impurity sheet concentration was 4×10^{12} cm-2. The concentration mobility of 2D electrons in the QW at $T = 4.2$ K were 2×10^{12} cm^{-2} and 2×10^5 cm^2/V s respectively. In this paper we investigated Shubnikov–de Haas (SdH) oscillations and cyclotron resonance (CR) absorption at $f = 0.693$ THz in the magnetic fields up to 3 T.

2. Results and discussions

Fig. 1 shows a typical dependence of the longitudinal magnetoresistance versus the inverse magnetic field where the beatings of SdH oscillations are clearly seen. These beatings are not observed in similar samples with a symmetric selective doping below and above the QW. In Fig. 2 the results of Fourier transform of SdH oscillations in the inverse magnetic field is presented. Here H_{1-} and H_{1+} peaks correspond to concentrations of carriers in the spin split first (heavy hole type) subband of size quantization in the conduction band. E_2 peak corresponds to the half of carrier concentration in the second (electron type) subband where the spin splitting is small [3].

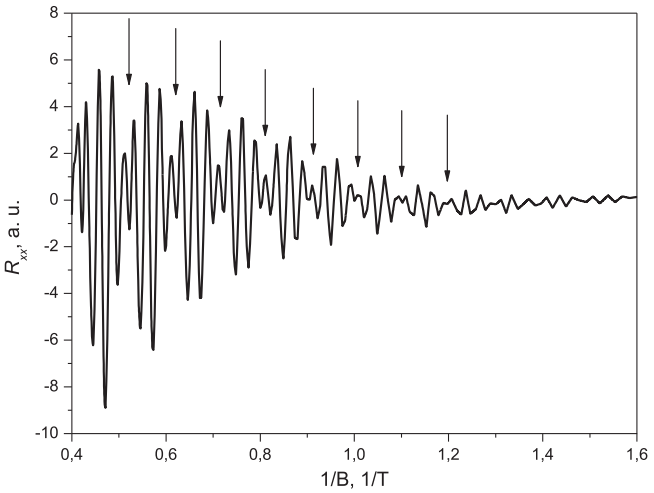

Fig. 1. Shubnikov–de Haas oscillations versus the inverse magnetic field. The arrows indicate nodes of the oscillation beating.

The value of the spin splitting in the H_1 subband can be determined directly from the analysis of the SdH oscillations beating (cf. [3]). In the quasiclassical approximation in the magnetic field the areas of 2D electron orbits in k-space corresponding to different Landau levels are quantized: $S = (\nu + \lambda)\Delta S$, where $\Delta S = 2\pi eB/(\hbar c)$, $\nu = 0, 1, 2\ldots$ and λ is ν-independent.

Harmonic analysis of the observed SdH oscillations shows that the nodes of the beats occur in the magnetic fields corresponding to maxima of the oscillations in H_{1-} subband with a lower concentration and minima of the oscillations in H_{1+} one. This means that in these fields the Fermi level is located at the n-th Landau level of H_{1-} subband and in middle of m-th and (m-1)-th Landau levels of H_{1+} subband. The value of δ determined at $B = 0$ as the splitting of the subbands at $k = k_F$ (where k_F is the wavevector at the Fermi energy) can be represented as the difference between the energies of n-ths Landau levels from different subbands

$$\delta = E_{n^-} - E_{n^+} = \hbar\omega_{c^+}\left(m - n - \frac{1}{2}\right). \qquad (1)$$

Here $\omega_{c^+} = eB/(m_{c^+}c)$, where $m_{c^+} = 0.044m_0$ (see below). Harmonic analysis of SdH oscillations shows that the observed beat nodes (Fig. 1) correspond (from left to the right) to numbers $n = 11, 14, 17, 20, 23, 26$ and $m = 16, 20, 24, 28, 32,$

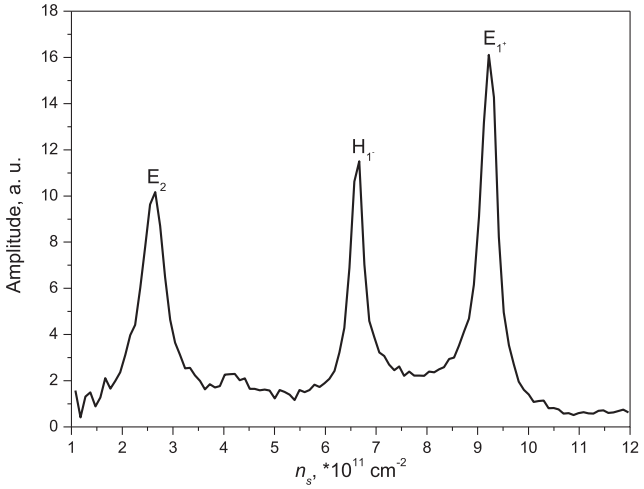

Fig. 2. Fourier analysis of the Shubnikov–de Haas oscillations at 4.2 K.

36, that, in accordance with expression (1), gives the value of δ about 30–32 meV. This value is close to that obtained in [3] for samples with similar 2D concentrations.

Spin splitting of the energy spectrum can result in a nonequidistant spacing of Landau levels in two subbands at the Fermi level (see, for example, [2]). In the paper [5] in the undoped HgTe/CdTe heterostructures with the electron density in QW up to 10^{12} cm^{-2}, induced by applied voltage to the gate electrode, along with SdH oscillation beating a remarkable (∼4%) splitting of the CR line was observed. The effect was associated with the spin splitting of subbands at $B = 0$, but the results obtained were interpreted in terms of a linear splitting dependence on k (cf. [2]). At the same time in HgTe QW with the inverted band structure the spin splitting of H1 subband at small k is proportional to k^3, gets maximum and even decreases at larger k values (see, for example, [3]). In present study we found a large (∼12%) CR line splitting ($m_{c^+} = 0.039m_0$, $m_{c^+} = 0.044m_0$, see Figure 3), which was not observed in samples with a symmetrical profile of QW.

The cyclotron mass at the Fermi level is given by the expression

$$\frac{1}{m_c} = \frac{1}{\hbar^2}\left(\frac{1}{k}\frac{\partial E}{\partial k}\right)_{k_F}, \qquad (2)$$

where $E = E_0(k) \pm \delta(k)/2$. To get the cyclotron masses from the expression (2) one should substitute the appropriate values of k_F for each subband which can be determined from the concentration of carriers in the subbands: $k_{F\pm} = (4\pi n_\pm)^{1/2}$. The observed splitting of the cyclotron resonance line can be attributed both to a nonparabolic dispersion law $E_0(k)$ and to the $\delta(k)$ dependence. However, as shown in [3], for the carrier concentration about 2×10^{12} cm^{-2} the $\delta(k)$ dependence gets a maximum near $k \sim k_F$ and the derivative $\partial\delta/\partial k$ is small. At the same time, the band nonparabolicity leads to a noticeable m_c dependence on k_F. For the estimations we used the "Kane" dispersion law (see, e.g., [5])

$$E_0(k) = -\frac{E_g}{2} + \sqrt{\left(\frac{E_g}{2}\right)^2 + E_g\frac{\hbar^2k^2}{2m^*}}, \qquad (3)$$

where E_g is the effective bandgap, $m^* = 0.02m_0$ — effective mass at the bottom of the H_1 subband [5]. Substituting $E_0(k)$

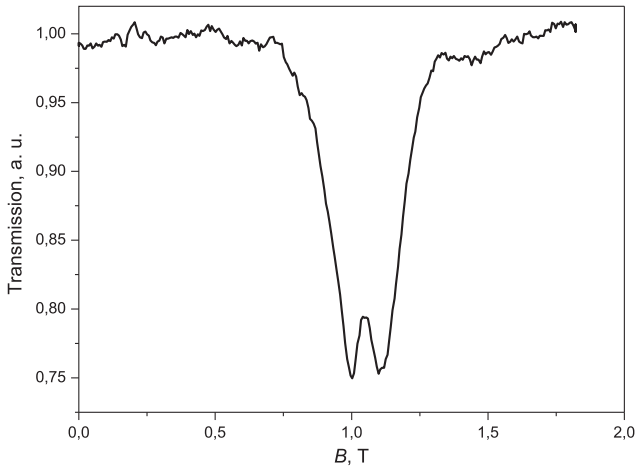

Fig. 3. Cyclotron resonance spectrum obtained at $T = 4.2$ K, $\hbar\omega_c = 2.864$ meV.

in the expression (2) and assuming $k_{F\pm} = k_F \pm \Delta k$ ($\Delta k \ll k_F$), we obtain

$$\frac{1}{m_{c\pm}} = \frac{1}{m_{c0}}\left[1 \mp \frac{2E_F^*}{E_g}\left(\frac{m^*}{m_{c0}}\right)^2\frac{\Delta k}{k_F}\right]. \qquad (4)$$

Here

$$\frac{1}{m_{c0}} = \frac{1}{2}\left(\frac{1}{m_{c^+}} + \frac{1}{m_{c^-}}\right), \quad E_F^* = \hbar^2{k_F}^2/2m^*.$$

The value of E_F^*/E_g is easy to find from the expression $(m^*/m_{c0})^2 = (1 + 2E_F^*/E_g)^{-1}$ resulting in an obvious way from (2) and (3), where $m_{c0} = 0.042m_0$ is the experimentally obtained average cyclotron mass value.

From the obtained concentrations in H_{1+} and H_{1-} subbands (see Fig. 2) we readily get $k_{F^+} = 3.4 \times 10^6$ cm^{-1}, $k_{F^+} = 2.9 \times 10^6$ cm^{-1} and $\Delta k_F = 0.25 \times 10^6$ cm^{-1}, that gives $(1/m_{c\pm}) = (1/m_{c0})(1 \mp 0.06)$. The latter just corresponds to 12% cyclotron mass difference observed in the experiment (Fig. 3). This allows us to conclude that the observed splitting of the CR line results mainly from the band nonparabolicity and therefore from k_F difference in the two subbands rather from $\delta(k)$ dependence.

Acknowledgements

This work was financially supported by RFBR (grant 09-02-00752), Russian Academy of Sciences and the Dynasty foundation.

References

[1] S. Datta, B. Das, *Appl. Phys. Lett.* **56**, 665 (1990).
[2] Yu. A. Bychkov, E. I. Rashba, *JETP Lett.* **39**, 78 (1984).
[3] Y. S. Gui *et al*, *Phys. Rev. B* **70**, 115328 (2004).
[4] N. N. Mikhailov *et al*, *Int. J. Nanotechnology* **3**, 120 (2006).
[5] M. Schultz *et al*, *Semicond. Sci. Technol.* **11**, 1168 (1996).

18th Int. Symp. "Nanostructures: Physics and Technology"
St Petersburg, Russia, June 21–26, 2010

Magnetic moment of one-dimensional ring with spin-orbit interaction

V. A. Margulis and V. A. Mironov
Institute of Physics and Chemistry, Mordovian State University, 430005 Saransk, Russia

Abstract. An explicit analytic expression is obtained for the magnetic moment and the persistent current of the electron gas in an one-dimensional ring taking into account the spin-orbit interaction in the Rashba model with $T = 0$. The cases of the constant chemical potential and number of electrons are investigated. Dependencies of the magnetic moment and the persistent current on the magnetic field are analyzed.

Introduction

Nanostructures with the ring geometry are of considerable interest, because they offer unique possibilities to investigate quantum interference effects, such as the persistent current and the Aharonov–Bohm effect. It should be noted that the simplest one-dimensional (1D) model has played an important role in the understanding of quantum interference effects. In this model, variation of the magnetic field strength leads to the modification of electron phases, which leads to periodic oscillations of electronic properties (Aharonov–Bohm oscillations) and the persistent current. The persistent current of free spinless electrons in the 1D ring was theoretically studied in [1]. Periods and shapes of the current oscillations were found.

The interplay between spin-orbit interaction (SOI) and quantum confinement have attracted considerable attention. It is stipulated by the possibility to manipulate the spin degree of freedom of electrons by coupling to their orbital motion and vice versa. There are two different types of SOI in two-dimensional semiconductor structures due to the effective internal electric field. One of them, Dresselhaus SOI [2] appears as a result of the inversion asymmetry present in the crystal lattice of the semiconductor structure. Another type of SOI is Rashba model [3]. It arises due to the structural inversion asymmetry. This case is the most interesting because of the ability to control electrically the strength of this interaction [4].

1. Evaluation of the magnetic moment

We consider the electron gas in 1D ring, of radius r, in the xy plane. The ring is placed in an external magnetic field **B** directed along the z axis. The electron energy spectrum of the system with Rashba SOI is determined by the formula [5,6]

$$E_{m,s} = \varepsilon_0 \left(m + \eta + 1/2\right)^2 + \frac{\varepsilon_0}{4} + s\sqrt{\frac{\alpha^2}{r^2}\left(m+\eta+\frac{1}{2}\right)^2 + \left[\varepsilon_0\left(m+\eta+\frac{1}{2}\right) - \varepsilon_z\right]^2}, \quad (1)$$

where $m = 0, \pm1, \pm2, \ldots, s = \pm1, \alpha$ is the SOI constant, $\varepsilon_0 = \hbar^2/(2m^*r^2)$, m^* is the effective electron mass, $\varepsilon_z = g\mu_B B/2$, g is the electron g-factor, μ_B is the Bohr magneton, $\eta = \Phi/\Phi_0$, Φ_0 is the magnetic flux quantum, $\Phi = \pi r^2 B$ is the magnetic flux threading the ring. It is seen that the spectrum consists of two systems ("staircases") of levels ($E_{m,+}$ and $E_{m,-}$).

We have evaluated the magnetic moment of the ring for the case of the constant chemical potential μ and for the case of the constant number N of electrons in the system at $T = 0$

$$\frac{M}{\mu_B^*} = -\frac{1}{2}\sum_{s=\pm1}\left(\left(m_1^s + m_2^s + 2\eta + 1\right)\left(m_2^s - m_1^s + 1\right) + \sum_{k=m_1^s}^{m_2^s} \frac{s\left((k+\eta+1/2)(\gamma^2+1-\delta) - \delta\eta(1-\delta)\right)}{\sqrt{\gamma^2(k+\eta+1/2)^2 + (k+\eta+1/2-\delta\eta)^2}}\right), \quad (2)$$

where $\delta = gm^*/m_0$, m_0 is the free electron mass, $\gamma = \alpha/r\varepsilon_0$, $\mu_B^* = e\hbar/2m^*c$ is the effective Bohr magneton. Note, that $m_{1,2}^s$ is the integer part of x determined by the equation $E_{x,s} = E_F$ (E_F is the Fermi energy), i.e. $m_{1,2}^s = [x_{1,2}^s]$, for the case of the constant chemical potential. For the case of the constant number of electrons, the $m_{1,2}^s$ are the upper filled levels, where m_1^s is negative and m_2^s can be either positive or negative number.

We have obtained a persistent current of the ring for the case of the constant chemical potential μ and for the case of the constant number N of electrons

$$I = \frac{c}{\pi r^2} M, \quad (3)$$

where c is the light velocity and M is given by the formula (2).

2. Conclusion

The magnetic field dependence of the magnetic moment M_μ has the shape of sawtooth oscillations with an amplitude that

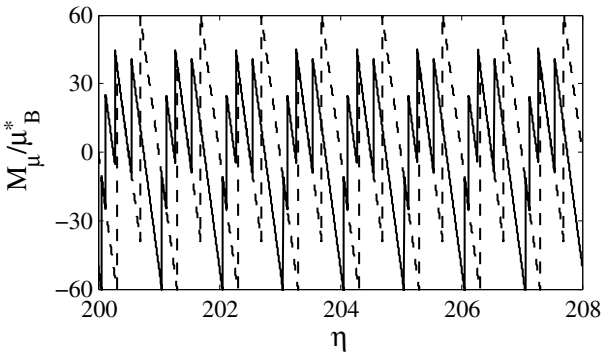

Fig. 1. Dependencies of the magnetic moment on the number of the magnetic flux quantum for a constant chemical potential. Dashed line corresponds to spinless electrons ($\alpha = 0$, $g = 0$), while solid lines correspond to SOI with $\alpha = 2.5 \times 10^{-10}$ eVcm and $g = -1.1$. These dependencies were calculated for $\mu = 2.5 \times 10^{-14}$ erg, $m^* = 0.067m_0$ and $r = 300$ nm.

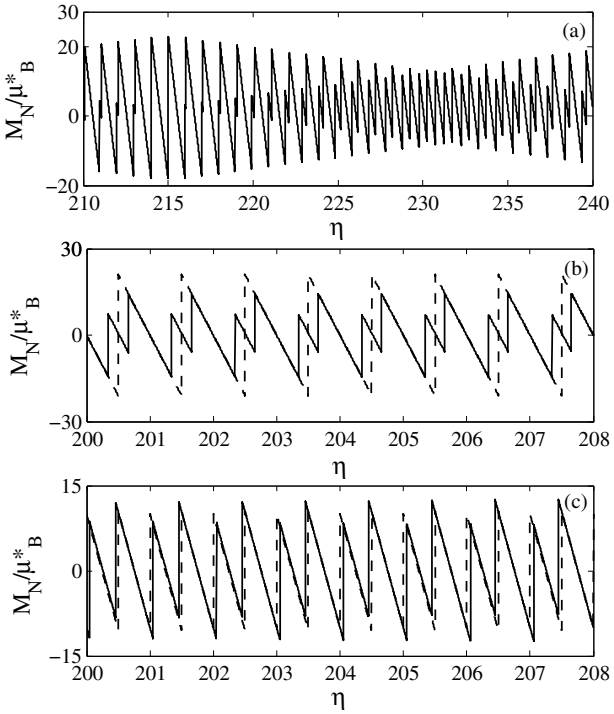

Fig. 2. Dependencies of the magnetic moment on the magnetic flux for a constant number of electrons. Dashed lines correspond to absence of the spin splitting ($\alpha = 0$ and $g = 0$) and the solid lines correspond to the presence of spin splitting $\alpha = 2.5 \times 10^{-10}$ eVcm: (a) $N = 42$, $g = 5$, (b) $N = 42$, $g = -1.1$, (c) $N = 41$, $g = -1.1$. $m^* = 0.067m_0$, $r = 300$ nm.

depends on the magnetic field (Fig. 1). It is stipulated by the fact that the degenerate Landau level splits into two levels due to the spin splitting. Crossing of the Fermi energy with these levels leads to appearance of oscillations. Oscillations of the varying amplitude arise as a result of superposition of oscillations from electrons with two spin directions. We have compared the magnetic moment of the spinless electron gas with the moment calculated taken into account Rashba SOI (Fig. 1). It is obviously that the spin splitting gives additional jumps of the magnetic moment. In addition, our analysis shows that SOI and the Zeeman splitting of levels lead to break of periodicity of oscillations.

Magnetic moment oscillations for $N = \text{const}$, as well as in the previous case, are non-periodic sawtooth oscillations with the varying amplitude (Fig. 2). In this case, the jump of the magnetic moment occurs every time when the upper filled energy level intersects with the empty level. As a result, transfer of an electron from the occupied level to the empty level arises. The electron can transfer to the level of its spin staircase or the level of the other staircase, due to the complicated dependence of the spectrum on the magnetic field. As a result jumps of the magnetic moment of electrons with the one spin direction are combined with jumps of electrons with the other spin direction. Therefore, the amplitude of oscillations has non-monotonic dependence on the magnetic field (Fig. 2a).

The persistent current undergoes oscillations of the same type, as follows from (3). We can compare results of our calculations of the persistent current of the ring with experimental results for a single semiconductor ring [7]. By averaging of different measurements, the authors of [7] have found a typical current amplitude of 4 ± 2 nA. We have constructed a graph of the persistent current I_N (for $N = \text{const}$) in Fig. 3, using the parameters of the experiment [7] ($r \simeq (r_{\text{inner}} + r_{\text{outer}})/2 \simeq 1.35$ μm, $N \simeq 2\pi r\sqrt{n_s} \simeq 506$, here n_s is the electron density of the two-dimensional electron gas at the heterointerface) and the value of the constants of SOI for the heterostructure AlGaAs/GaAs $\alpha = 7.5 \times 10^{-11}$ eVcm, $g = -1.1$ [8]. It can be seen the amplitude of the current calculated in our work has the same order of magnitude as the experimental value.

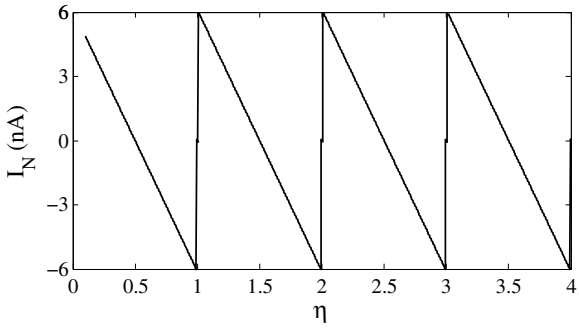

Fig. 3. The persistent current at a constant number of electrons versus magnetic flux. $N = 506$ and $r = 1.35$ μm [7], $g = -1.1$ and $\alpha = 2.5 \times 10^{-10}$ eVcm [8], $m^* = 0.067m_0$.

It should be noted that oscillations can be observed when two conditions are satisfied. The width of energy levels should be considerably smaller than the spacing between the neighboring levels, $\Delta E \gg T$. Energy levels should not be substantially smeared by scattering, i.e. $\Delta E \gg \hbar\tau$, where τ is the relaxation time.

References

[1] Ho-Fai Cheung *et al*, *Phys. Rev. B.* **37**, 6050 (1988).
[2] G. Dresselhaus, *Phys. Rev.* **100**, 580 (1955).
[3] E. I. Rashba, *Sov. Phys. Solid State* **2**, 1109 (1960).
[4] J. Nitta *et al*, *Appl. Phys.* **105**, 122402 (2009).
[5] J. Splettstoesser *et al*, *Phys. Rev. B.* **68**, 165341 (2003).
[6] Hong-Yi Chen *et al*, *Phys. Rev. B.* **78**, 073407 (2008).
[7] D. Mailly *et al*, *Phys. Rev. Lett.* **70**, 2020 (1993).
[8] M. A. Wilde *et al*, *Phys. Rev. B.* **79**, 125330 (2009).

18th Int. Symp. "Nanostructures: Physics and Technology"
St Petersburg, Russia, June 21–26, 2010

Circularly-polarized photoluminescence InSb/InAs type II heterostructure control by excitation power

M. S. Mukhin[1,2], Ya. V. Terent'ev[1], V. A. Solov'ev[1] and S. V. Ivanov[1]

[1] Ioffe Physical-Technical Institute, St Petersburg, Russia
[2] St Petersburg Academic University, St Petersburg, Russia

Abstract. InSb/InAs heterostructure with a type II band alignment has been fabricated by molecular-beam epitaxy. Nearly 100% σ^- optically induced polarization has been observed at the low excitation power. The polarization value remains high enough even at $T = 70$ K.

Introduction

Spin is the only electron internal degree of freedom, and utilizing it in the new generations of semiconductor devices is the semiconductor spintronics main goal. Recent achievements in material fabrication made it possible to introduce the nonequilibrium spin in the novel class of systems. Today spintronics focuses on three types of materials: ferromagnetic metallic alloys, ferromagnetic semiconductors and non-magnetic materials where spin polarization can be achieved through the Zeeman effect in large magnetic fields with low temperatures. Ferromagnetic metallic alloys are currently used for magnetoelectronic devices. Ferromagnetic semiconductors and nonmagnetic materials, however, are of primary interest. Most of the work in making semiconductors ferromagnetic has been focused on II–VI semiconductors such as CdTe or ZnSe. In this systems the semiconductors are doped with magnetic ions (such as manganese) to create magnetic character small pockets resulting in a diluted magnetic semiconductor (DMS). More recent investigation has been focused on doping III–V semiconductors such as GaAs into a DMS state. With III–V semiconductors, however, the magnetic elements are much less soluble than in II–VI semiconductors making their injection into a material like GaAs or InAs much more difficult [1,2].

In the paper magneto-optical studies of non-magnetic heterostructures type II InSb quantum dots in a matrix InAs, which demonstrate nearly 100% σ^- optically induced polarization at a low excitation power are reported. The InAs/InSb material system has recently attracted much attention either due to self-organization phenomena or quantum dots (QDs) strain-induced formation. The type II QDs structures might be helpful of spintronics applications, especially for spin storage devices, because of their long carrier lifetimes and long electron spin relaxation times [3]. Besides, these material system possible applications can be attributed to the field of mid-IR optoelectronics [4].

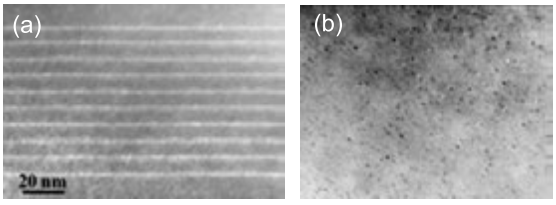

Fig. 1. (a) Dark-field (002) cross-sectional TEM image of ten-period InSb/InAs nanostructure; (b) plan-view TEM image of single InSb insertion.

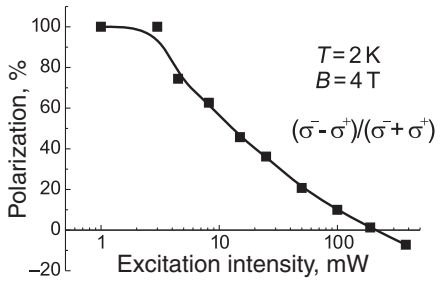

Fig. 2. Polarization in magnetic field $B = 4$ T and temperature 2 K versus excitation power.

We have proposed and fabricated by molecular beam epitaxy a type of In(Sb,As) nanostructures incorporating thin InSb insertion layers in a InAs matrix. The samples with either a single InSb insertion layers or an InAs/InSb superlattice demonstrated bright photoluminescence (PL) below the InAs band gap. It was attributed to type II transitions between holes confined in the strained InSb and electrons in the surrounding InAs. Furthermore cross-sectional electron microscopy images clearly showed the QDs strain-induced formation when the InAs layer thickness did not exceed 1.5–2.0 monolayers [5].

We presented structural and magneto-optical studies of InSb QDs in a InAs matrix. The studied samples were fabricated by MBE. The samples differed in InSb nominal thicknesses and growth regimes. X-ray diffraction and TEM studies were presented to analyze the structure morphology. Magneto-PL spectra were measured as a function of the external magnetic field, excitation power and temperature. The assignment of the PL peaks was fulfilled by the calculation utilizing the Keynes model. Unfortunately the ultra-thin insertion layers exceed the limits of the Keynes model, which is the confirmed lack of good agreement with spectra. At present the work on a tight-binding the holes localization calculation was organized.

1. Experimental samples: design and fabrication

The InSb/InAs nanostructures were grown on n-InAs (001) substrates using a RIBER 32P setup. Conventional solid source effusion cells were used to produce In, Al and Sb_4 fluxes, whereas the As_4 flux had a VAC-500 cracking cell as a source. The structures active region consists of a 0.1 μm thick InAs layer centered with an InSb/InAs multiple structure with a ranging period for different samples.

The InSb sub-monolayers (SML) were formed by the InAs growth surface exposure to the Sb_4 flux. Such process is expected to be possible due to the very efficient As-Sb anion

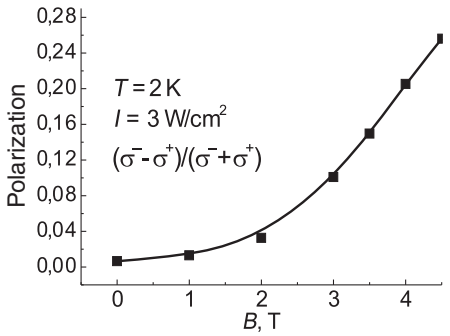

Fig. 3. Polarization versus magnetic field B, temperature $T = 2$ K and excitation power $I = 1$ W/cm^2.

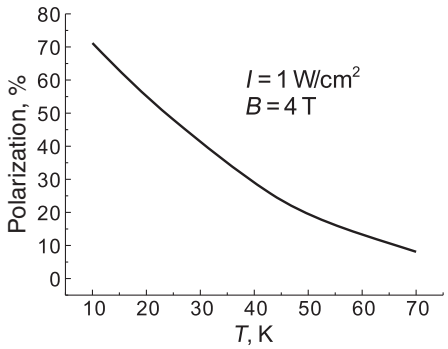

Fig. 4. Polarization in magnetic field $B = 4$ T and excitation power $I = 1$ W/cm^2 versus temperature.

exchange reaction observed earlier for a GaSb/GaAs system at the similar temperatures. It has been shown that the As surface atoms are replaced by the Sb ones just during a few second exposure of the InAs surface to the Sb_4 flux, as confirmed by changing the (2×4)As-stabilized RHEED surface reconstruction to the (1×3)Sb one [6]. The As-by-Sb exchange efficiency is confirmed by X-ray diffraction (XRD) data obtained on the InSb/InAs multiple structures grown under the same conditions. The InSb insertion nominal thickness estimated from the simulation of the experimental XRD rocking curve increases from 0.6 to $\sim$1.3 ML as the temperature decreases from 485 to 430 °C, respectively.

The InSb insertions good structural quality and flatness are directly observed in a cross-section (002) darkfield transmission electron microscopy (TEM) image (Fig. 1a). TEM studies were performed using an EM-420 Philips microscope operating at 100 keV. In the cross-section TEM micrograph, the InSb sheets resemble ultra-thin planar layers with faint thickness or composition inhomogeneities. The plan-view TEM image obtained for the structure with a single InSb sub-monolayer reveals an existence of quantum-dot-like InSb-rich islands (Fig. 1b). The islands characteristic lateral size and their sheet density are estimated as approximately 2.5 nm and 10^{12} m^{-2}, respectively.

2. Experiment

For magneto-PL measurements the samples were immersed in superfluid helium in the cryostat with a split-coil superconducting magnet. The emission circular polarization was analyzed using a NaCl Fresnel rhomb followed with a linear polarizer. PL spectra were detected by a grating monochromator with a nitrogen-cooled InAs photodiode. Circularly-polarized PL spectra in a magnetic field applied in the Faraday geometry were measured in a variable temperature in the range 2–80 K. The samples were excited by the 809 nm line injection laser diode. The excitation power was in range of 0.3–40 W/cm^2, the excitation spot size on the sample was in the range of 0.5–1 mm.

Figure 2 shows general polarization behavior in a magnetic field $B = 4$ T under the temperature 2 K depends on the excitation power in the 0.3–40 W/cm2 range power. It is clear that the photoluminescence from quantum dots InSb has nearly 100% σ^- optically induced polarization at the lowest excitation power. σ^- polarization corresponds to a spin electron projection to magnetic vector equals +1/2. Increasing of the excitation density leads to exponential-like reduction of the polarization degree. The polarization changes the sign to σ^+ at power nearly 10 W/cm^2. Further increasing the optical injection power results in weak subsequent growth σ^+ polarization reached nearly 20% by excitation power equals 40 W/cm^2.

Magnetic field dependence of the PL peak energy follows the electron cyclotron energy in the InAs conduction band (see Fig. 3) and the polarization sign meets the selection rules for optical transitions involving heavy holes. These facts indicate that Zeeman splitting of the conduction band electrons plays the dominant role in the observed phenomenon, but the origin of the sign inversion at high excitation densities is still unclear.

Figure 4 demonstrates that the increase in sample temperature results in polarization reduction, however the polarization value remains high enough ($\sim$10% σ^- polarization by the lowest excitation power) even at $T = 70$ K.

The detailed effect mechanism is being examined yet, but, it is obvious, that the large Zeeman splitting of the InAs conducting band and optical transmissions selection rules assistance of heavy and lights holes of InSb are underlay that phenomenon. As it follows from an estimation performed in the weak-coupling limit, light-hole and heavy-hole states are split in InSb/InAs strained QDs, with the light-hole level lying lower. The hole localization energy detailed calculation in the ultra-thin InSb insertion layers are required for development correct physical model. As mentioned before, to date authors carry on a tight-binding calculation of energy-band structure InSb/InAs heterostructure (in comparison with the Keynes model, tight-binding theory works with widths equal a few monolayers and takes into account splitting of valence band under elastic stress).

References

[1] Sigma-Aldrich company, http://www.sigmaaldrich.com.
[2] T. T. Chen *et al*, *J. Appl. Phys.* **93**, 9655 (2002).
[3] H. Gotoh *et al*, *Appl. Phys. Lett.* **72**, 1341 (1998).
[4] Y. S. Chiu *et al*, *Appl. Phys. Lett.* **81**, 4943 (2002).
[5] S. V. Ivanov *et al*, *Bulletin of the Russian Academy of Sciences: Physics* **23**, 1119 (2005).
[6] S. V. Ivanov *et al*, *Elsivier Science* (2003).

18th Int. Symp. "Nanostructures: Physics and Technology"
St Petersburg, Russia, June 21–26, 2010

Dynamics of nuclear spin polarization in quantum dots in transverse magnetic field: A graded box model approach

M. Yu. Petrov, S. V. Yakovlev, D. K. Loginov and I. V. Ignatiev
Physics Department, St Petersburg State University, 198504 St Petersburg, Russia

Abstract. We report on the numerical modeling of the dynamics of nuclear spin polarization in a QD in external magnetic field applied in Voigt geometry. We show that the nuclear spin polarization is tilted from the axis of optical excitation due to the coherent exchange of angular momentum between the electron-nuclear spin system and the external magnetic field.

Introduction

The dynamics of nuclear spin polarization in quantum dots (QDs) is intensively investigated in recent years [1]. In the typical scenario of experiments, a series of pumping pulses of one helicity creates the spin polarization of localized electrons. This polarization appears to be a source of angular momentum, which can be transferred to a nuclear spin bath via electron-nuclear hyperfine interaction [2, 3]. Usually, the experimental technique for detecting the dynamic nuclear polarization (DNP) in QDs requires an additional external magnetic field, which is typically applied along to the electron spin orientation axis (Faraday geometry) [3,4,5]. Only a few works are related to study the effect of DNP in the Voigt geometry where the external magnetic field is applied perpendicular to the axis of optical excitation [6, 7].

Usual explanation of the DNP creation in a transverse magnetic field is based on the nuclear spin temperature approach [8]. In this approach, the nuclear spin dipole-dipole interaction leads to the nuclear spin cooling and creating the nonzero component of DNP along the magnetic field axis. However, the nuclear spin temperature approach is based on the assumption of *short* correlation time, which is the time of coherent evolution of electron-nuclear spin system. This assumption is not valid for negatively charged QDs where the electron spin is localized and interacts with the nuclei for a long time so that its precession angle about the nuclear hyperfine field can be large [2]. It is this regime, which we consider in this work.

A model comprising of one electron spin coupled to a nuclear spin bath with a few tens of nuclear spins can give exact quantum mechanical solution of spin dynamics qualitatively similar to that in real QD even with no an allowance for quantitative comparison between them. In such modeling, one can investigate the dynamics of electron and nuclear spin polarization and their dependencies on different external conditions, which is usually not possible in experiments with real QDs.

Here, we report on investigation of electron-nuclear spin dynamics in framework of graded model [9]. We extend this approach to the case of external magnetic field applied perpendicularly to the axis of injected electron spin polarization. We will show that even without dipole-dipole interaction, there is a possibility to create nonzero DNP in plane perpendicular to the axis of electron spin initialization.

1. Model

We consider a system comprising of one electron spin $\hat{\mathbf{S}}$ coupled to N elementary nuclear spins $\hat{\mathbf{I}}^j$ by hyperfine interaction. In external magnetic field $\mathbf{B} = [B, 0, 0]$, the Hamiltonian of this system can be written as

$$\hat{\mathcal{H}} = \mu_\mathrm{B} g_\mathrm{e} B \hat{S}_x + v_0 \sum_{j=1}^{N} A^j |\psi(\mathbf{R}_j)|^2 \left(\hat{\mathbf{S}} \times \hat{\mathbf{I}}^j\right), \quad (1)$$

where μ_B and g_e are the Bohr magneton and electron g factor, v_0 is the unit cell volume, A^j and $|\psi(\mathbf{R}_j)|^2$ are the hyperfine coupling constant and the electron density at the nuclear position $\mathbf{R}_j$ of jth nucleus, respectively. We ignore here a slow precession of nuclear spins in the magnetic field.

The graded model approach allows one to consider relatively large number of nuclear spins [9]. The approach consists in approximation of electron density distribution $|\psi(\mathbf{r})|^2$ by a step-like function $|\psi_k|^2$ where k labels the nuclear groups. To be specific, we can consider all the hyperfine constants to be the same for all nuclei. In this case, Eq. (1) can be rewritten in the basis of collective momenta $\hat{\mathcal{I}}^k = \sum_{j\in(k)} \hat{\mathbf{I}}^j$ of each kth group of nuclei so that, for number of nuclear groups $n \ll N$, the Hamiltonian matrix is block-diagonal with size of each block drastically smaller than the size of total Hamiltonian matrix.

To model the optical pumping of resident electron, we suppose that, at time momenta, T_m, short laser pulses create spin-oriented electron state $|\uparrow_z\rangle$ with density matrix $\rho_\mathrm{e} = |\uparrow_z\rangle\langle\uparrow_z|$. Each pulse is so short that it does not change the nuclear spin state so that the nuclear density matrix is continuous $\rho_N(T_\mathrm{m} - 0) = \rho_N(T_\mathrm{m}) = \rho_N(T_\mathrm{m} + 0)$. Between the pump pulses, the electron-nuclear spin dynamics evolves with the Hamiltonian given by Eq. (1) and the total density matrix of coupled spin system is

$$\rho(T_\mathrm{m} + t) = \exp\left[-\frac{i}{\hbar}\mathcal{H}t\right][\rho(T_\mathrm{m}) \otimes \rho_\mathrm{e}] \exp\left[+\frac{i}{\hbar}\mathcal{H}t\right]. \quad (2)$$

From the numerical solution of Eq. (2) obtained by the use of the eigenvalue decomposition of each block of the Hamiltonian matrix, the electron spin polarization $\langle\hat{S}_z\rangle$ and the effective nuclear magnetic field

$$\mathbf{B}_N = \frac{v_0}{\mu_\mathrm{B} g_\mathrm{e}} \left\langle \sum_j A^j |\psi(\mathbf{R}_j)|^2 \hat{\mathbf{I}}^j \right\rangle$$

can be calculated. Here, $\langle \ldots \rangle$ denotes averaging over the density matrix ρ.

2. Results and discussion

First, we consider separately the electron spin dynamics either in the presence of hyperfine interaction or in an external magnetic field B. Figure 1(a) shows the time evolution of nonzero components of electron spin polarization in these two well-known cases. The electron spin precession is characterized

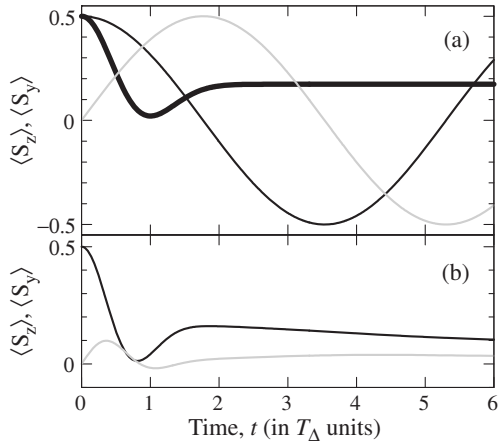

Fig. 1. Dynamics of z (black lines) and y (gray lines) components of electron spin polarization calculated for model with $N = 48$ nuclear spins divided in two groups. (a) Electron spin dynamics in NSF (thick line) and in magnetic field $B = 2\pi\hbar/(\mu_B g_e 7T_\Delta)$ (thin lines). (b) Electron spin dynamics calculated for the joined action of hyperfine interaction with NSF and of magnetic field B.

by frequency $\omega = \mu_B g_e B/\hbar$. The electron spin dephasing in the frozen nuclear spin fluctuations (NSF) is characterized by time $T_\Delta = \hbar/(\mu_B g_e \Delta_B)$, i. e., the time when the electron spin polarization reaches its minimum [2]. Here, Δ_B is the variance of the distribution of NSF for unpolarized nuclear spins $W(\mathbf{B}_N) = \exp[-\mathbf{B}_N^2/\Delta_B^2]/(\sqrt{\pi}\Delta_B)^3$ [2]. In both the cases, there is an electron spin precession about a magnetic field. However, the difference is that, due to a random distribution of NSF, mean electron spin $\bar{S}_z(t) = (1/t)\int_0^t \langle \hat{S}_z(\tau)\rangle d\tau$ reaches in the NSF field a constant value of $S_0/3$ at large time. In the case of free electron spin precession about external magnetic field, all the components of mean spin are zero.

At zero magnetic field, due to the coherent motion of electron-nucear spin system, the total angular momentum of the system $\hat{\mathbf{F}} = \hat{\mathbf{S}} + \sum_j \hat{\mathbf{I}}^j$ is conserved and belongs to both the subsystems. The coherent motion is interrupted at the momenta of a new polarization pulses leading to violation of the angular momentum conservation law and saving a portion of total angular momentum in the nuclear spin bath. In the presence of external magnetic field, the z and y components of the total angular momentum are not conserved. As seen from Fig. 1(b), this results in appearance of nonzero y component of mean electron spin polarization $\bar{S}_y$. In fact, this component is obtained from external magnetic field. If the coherent motion of electron and nuclear spins is interrupted by excitation, this y component also appears in nuclear spin bath.

Figure 2(a) demonstrates the dynamics of effective nuclear field accumulation in the case when the pulse-repetition period is $6T_\Delta$ at fixed external magnetic field $B = 0.2B_N^{\max}$ where $B_N^{\max}$ is the magnetic field of totally polarized nuclei. The magnetic field dependences of different components of nuclear field are shown in Fig. 2(b). As seen, the model calculations clearly demonstrate the appearance of all three components of nuclear spin polarization at non-zero external field. After first pump pulse, due to the precession of electron spin in external magnetic field, the component of electron spin polarization and, correspondingly, the nuclear polarization in y direction appear to the moment of second pump pulse. As a result, the electron spin feels, besides the external field, the created

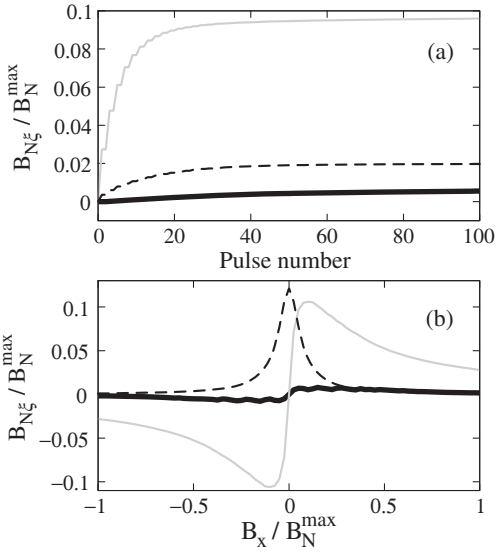

Fig. 2. (a) Dynamics of components of nuclear spin polarization (x — black line, y — gray line, z — dashed line) at fixed magnetic field $B = 0.2B_N^{\max}$. (b) Dependencies of components of nuclear spin polarization accumulated at 100th pump pulse on external magnetic field.

nuclear polarization and precesses in the total field, $\mathbf{B}_T = \mathbf{B}_N + \mathbf{B}$, which is tilted from x direction. Next pump pulse restores the electron spin and, during this polarization event, the nuclear polarization in x direction appears. After many pump pulses, these effects are accumulated, so that all three components of nuclear magnetic field may grow up to noticeable values. These values sensitively depend on external magnetic field, as it shown in Fig. 2(b). Such non-trivial dynamics demonstrate a possibility of nuclear polarization tilted from the direction of injected spins even in the absence of dipole-dipole interaction.

In conclusion, we have studied the dynamics of electron-nuclear spin system of a model QD consisting of one localized electron coupled to a nuclear spin bath by the hyperfine interaction in the presence of external magnetic field. We have shown, the appearance of nuclear spin polarization tilted from the direction of electron spin polarization, which is due to the coherent exchange of angular momentum between the coupled electron-nuclear spin system and external magnetic field.

Acknowledgements

The work has been partially supported by the Russian Ministry of Science and Education, the Russian Foundation for Basic Research, and by the "Dynasty" foundation (M.Y.P.).

References

[1] *Spin Physics in Semiconductors,* edited by M. I. Dyakonov (Springer-Verlag, Berlin 2008).
[2] I. A. Merkulov *et al*, *Phys. Rev. B* **65**, 205309 (2002).
[3] D. Gammon *et al*, *Phys. Rev. Lett.* **86**, 5176 (2001).
[4] C. W. Lai *et al*, *Phys. Rev. Lett.* **96**, 167403 (2006).
[5] A. I. Tartakovskii *et al*, *Phys. Rev. Lett.* **98**, 026806 (2007).
[6] R. I. Dzhioev and V. L. Korenev, *Phys. Rev. Lett.* **99**, 037401 (2007).
[7] O. Krebs *et al*, *Phys. Rev. Lett.* **104**, 056603 (2010).
[8] *Optical Orientation*, ed. by F. Meier and B. P. Zacharchenia (North-Holland, Amsterdam 1984).
[9] M. Yu. Petrov *et al*, *Phys. Rev. B* **80**, 125318 (2009).

18th Int. Symp. "Nanostructures: Physics and Technology"
St Petersburg, Russia, June 21–26, 2010

Random spin-orbit coupling and spin relaxation in multiple (110)-grown quantum wells

M. A. Semina[1], M. M. Glazov[1] and E. Ya. Sherman[2]

[1] Ioffe Physical-Technical Institute, St Petersburg, Russia
[2] Department of Physical Chemistry, The University of the Basque Country, 48080 Bilbao, Spain & IKERBASQUE Basque Foundation for Science, Alameda Urquijo 36-5, 48011, Bilbao, Bizkaia, Spain

Abstract. We address theoretically the relaxation of electron spin in multiple (110) GaAs quantum wells. In symmetric systems the growth axis component of the spin is not affected by the D'yakonov–Perel' spin relaxation mechanism. The sources of spin relaxation are the random Rashba spin-orbit coupling due to the electric field of donors and spin-flip collisions of electrons from different quantum wells. The strong enhancement of the spin relaxation time is predicted. It is demonstrated that even a minor asymmetry of the system can result in the spin relaxation rates observed in the state-of-the-art (110)-grown structures.

Introduction

One of the hopes at a possible realization of a very long spin relaxation time system is related to the GaAs quantum wells grown along $z \parallel [110]$. In these structures the form of the bulk inversion asymmetry (Dresselhaus) spin-orbit coupling prevents relaxation of the spin component parallel to the growth axis [110]. Here the effective field is always collinear with this axis [1] and, therefore, the spin, oriented along it, experiences no torque. However, the experiment clearly demonstrates finite spin coherence lifetime [2,3] causing the discussion of its origin.

The possible mechanism can be related to the intrinsic randomness in the spin-orbit coupling. The electric field of the ionized donors causes a random Rashba field [4]. The corresponding effective magnetic field is directed in the structure plane, and, therefore, can influence the growth-direction component of the spin. Its randomness causes random spin precession and leads to the finite spin relaxation rate. Multiple quantum wells bring about two new physical effects disregarded previously. First, Coulomb forces can be strongly reduced by the screening due to the presence of conduction electrons. Second effect in these structures is the spin-flip scattering of electrons from different quantum wells. We focus on these two spin relaxation processes, inherent for multiple quantum wells and limiting the spin relaxation time there.

1. Model

Figure 1a shows a scheme of a multiple quantum well structure similar to that studied in Ref. [3]: relatively thin conducting layers separated by wide barriers. To reduce the structure asymmetry-induced Rashba field, each quantum well is located in a macroscopically symmetric environment. The electrons in the conducting layers come from ionized donors located between them. A typical building element of a multiple quantum well is a three-well structure presented in Fig. 1b. The central and the side quantum wells are separated by the distance L, typically on the order of 50–100 nm. The donor layers are inserted symmetrically at the distance $|z_{\rm ext}|$ to prevent the appearance of the macroscopic Rashba field in the central well, hence the structure in Fig. 1b maintains macroscopic symmetry with respect to the $z \longleftrightarrow -z$ reflection.

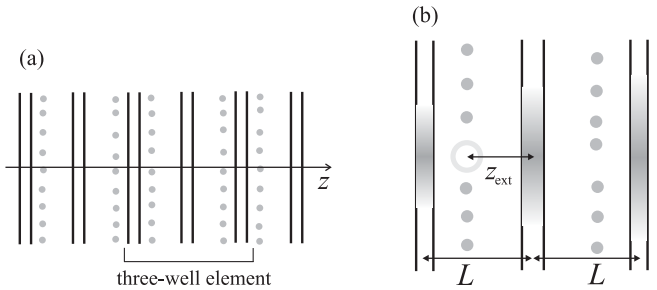

Fig. 1. (a) Multiple quantum well structure. Dopant layers are shown as filled circles. (b) Three-layer building element. The non-uniformly filled rectangles sketch the electron density distributions induced by the selected ion (empty circle) in each well.

The fluctuating Rashba field can be described by the effective spin precession frequency

$$\mathbf{\Omega}_{\mathbf{k}}(\boldsymbol{\rho}) = \frac{2\alpha_{\rm R}(\boldsymbol{\rho})}{\hbar}\left(k_y, -k_x, 0\right), \qquad (1)$$

which depends on the electron in-plane position, $\boldsymbol{\rho}$, and its wave vector $\mathbf{k} = (k_x, k_y)$, where x, y are the in-plane axes, and the Rashba constant

$$\alpha_{\rm R}(\boldsymbol{\rho}) = \xi e E_z(\boldsymbol{\rho}) \qquad (2)$$

is directly proportional to the z-component of the electric field caused by the donors, $E_z(\boldsymbol{\rho})$ with ξ being structure-dependent constant. Electrons are free to move in the quantum well plane but cannot move along the growth direction, making screening of the z-axis and lateral field components drastically different. In multiple quantum wells z-component is reduced due to the redistribution of the electron density in the side wells (see Fig 1b). The Fourier transform of the z field component has a form [5]

$$E_z(q) = -\frac{z_{\rm ext}}{|z_{\rm ext}|}\frac{2\pi e}{\varkappa}\frac{(q+q_s)e^{-q|z_{\rm ext}|} - q_s e^{-2qL+q|z_{\rm ext}|}}{q+q_s\left(1-e^{-2qL}\right)}, \qquad (3)$$

where $\varkappa$ is the static dielectric constant and q_s is the Thomas–Fermi screening wave vector. If the charge is close to the central quantum well, the induced field of the side layers can be neglected, and, therefore, the screening does not play a role. By contrast, if the external charge is close to the side plane, the

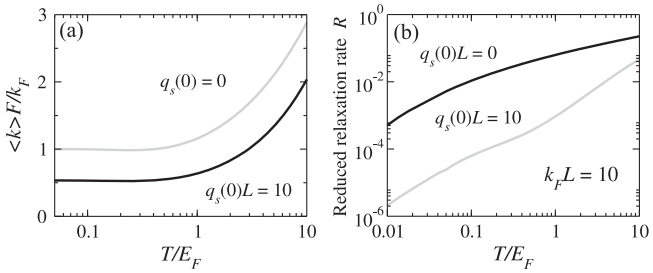

Fig. 2. The temperature dependence of $(\langle k \rangle / k_{\rm F})F$ for different screening parameters (their values at $T = 0$ are marked near the plots). The donors are located at $|z_{\rm ext}| = L/2$. Temperature dependence of the reduced spin relaxation rate R due to the electron-electron scattering for different screening parameters marked near the plots.

resulting field can be to a good approximation described by a dipole formed by the external charge and the opposite charge induced at the nearest side plane.

2. Spin relaxation

The spin relaxation rate for the case of the random spin-orbit coupling can be estimated as

$$\frac{1}{\tau_s} \sim \langle \Omega_{\mathbf{k}}^2 \rangle \tau_{\rm d} \sim \frac{1}{\hbar^2} \langle \alpha_{\rm R}^2 \rangle k^2 \tau_{\rm d}, \tag{4}$$

where $\langle \Omega_{\mathbf{k}}^2 \rangle$, $\langle \alpha_{\rm R}^2 \rangle$ are the mean square fluctuations of the spin precession rate and spin-orbit coupling constant, respectively, and $\tau_{\rm d}$ is the passage time of the correlated domain for the spin-orbit coupling, $\tau_{\rm d} \sim |z_{\rm ext}|/v$ where v is the electron velocity.

In the quasi-classical limit where $k|z_{\rm ext}| \gg 1$, $k/q_s \gg 1$ the spin relaxation rate is proportional to the autocorrelation function of the spin precession frequencies. As a result for the ensemble-averaged electron spin relaxation rate due to the interaction with donors one has [5]:

$$\frac{1}{\tau_{\rm d}^{[s]}} = 16\pi \frac{\xi^2 k_{\rm F} m}{\hbar^3} \frac{e^4}{\varkappa^2 L} n_{\rm d} \frac{\langle k \rangle}{k_{\rm F}} F, \tag{5}$$

where $n_{\rm d}$ is the concentration of donors per layer, $k_{\rm F}$ is the Fermi wave vector at the temperature $T = 0$ and F is the temperature-dependent factor. The angular brackets stand for: $\langle k \rangle = \sum_{\mathbf{k}} k\,(\partial f_k/\partial E)/[\sum_{\mathbf{k}} (\partial f_k/\partial E)]$, with f_k being the electron distribution function and E being the electron energy. There are two main causes for the temperature dependence of $\tau_{\rm d}^{[s]}$: the wave vector dependence of the spin precession frequency, and the fact that screening wave vector q_s decreases with the temperature. The calculated dependence of $(\langle k \rangle / k_{\rm F})F$ on T is presented in Fig. 2a. At low temperatures $T \ll E_{\rm F} = \hbar^2 k_{\rm F}^2/(2m)$ the spin relaxation rate saturates at a constant value which depends on the screening. For the non-degenerate gas $1/\tau_{\rm d}^{[s]}$ increases as $T^{1/2}$: due to competition of the enhancement of the mean square of the spin splitting $\propto T$ and decrease of the domain passage time $\tau_{\rm d} \propto 1/T^{1/2}$.

So far, the effects of electron-electron interaction were neglected. The z-component of electron spin is conserved in the process of collision of two electrons in the same well provided that the well is symmetric, however, the collisions between the electrons in different wells result in the spin relaxation. Physically, this process can be interpreted as the random spin precession of a given electron in the fluctuating spin-orbit field caused by the other electron. It can be shown that the electron-electron contribution to the spin relaxation rate is given by [5]

$$\frac{1}{\tau_{\rm ee}^{[s]}} = \frac{16}{\pi} \frac{me^4}{\hbar^3 \varkappa^2} k_{\rm F}^4 \xi^2 R, \tag{6}$$

where the dimensionless factor R depends on the temperature, electron density, screening wavevector, and interwell distance. Its temperature dependence is plotted in Fig. 2b. At low temperatures, $T \ll E_{\rm F}$, $R \propto (T/E_{\rm F})^2$ showing Fermi-liquid behavior, while for the non-degenerate electrons $R \propto T^{1/2}$ similarly to the donor-induced spin relaxation. It is worth noting that in the case of the ionized donor scattering the spin relaxation rate can be reduced to Eq. (6) with the parameter $R = \pi \langle k \rangle F/(2k_{\rm F}^2 L)$. If donors are positioned near the side wells, $|z_{\rm ext}| \approx L$, the electron-electron collisions and spin precession caused by random doping make the same contributions to the spin relaxation rate at $T \gg E_{\rm F}$.

3. Discussion

The spin lifetimes can be estimated taking into account that for the low temperatures the main contribution comes from the ions. Eq. (5) with the typical parameters of GaAs-based quantum wells, and $\xi = 5$ Å^2 yields the value of τ_s close to 400 nanosecond at $|z_{\rm ext}| = L/2$. Such a long time is considerably attributed to the screening; in a single well geometry with the same $|z_{\rm ext}|$ it would be smaller by approximately a factor of 2, see Fig. 2a.

The experiment reveals the times an order of magnitude shorter [3]. The difference can be related to the nonprecise information about the material and structure parameters and possible structure asymmetry resulting in a very weak but regular Rashba field on the spatial scale comparable or larger than the electron free path. For the single-electron momentum relaxation time τ_p^* on the order of 1 ps, it is sufficient to have a very weak asymmetry and, hence, very small spin splitting at the Fermi level on the order of 0.01 meV to ensure the times observed in the experiment.

Acknowledgements

Partial support from RFBR, President grant for young scientists and the "Dynasty" Foundation — ICFPM, UPV-EHU grant GIU 07/40 and MCI grant FIS2009-12773-C02-01 is acknowledged.

References

[1] M. I. Dyakonov and V. Yu. Kachorovskii, *Fiz. Tekh. Poluprovodn* (St Petersburg) **20**, 178 (1986) [Sov. Phys. Semicond. **20**, 110 (1986)].

[2] V. V. Belkov, P. Olbrich, S. A. Tarasenko, D. Schuh, W. Wegscheider, T. Korn, C. Schüller, D. Weiss, W. Prettl, and S. D. Ganichev, *Phys. Rev. Lett.* **100**, 176806 (2008).

[3] G. M. Müller, M. Römer, D. Schuh, W. Wegscheider, J. Hübner, and M. Oestreich, *Phys. Rev. Lett.* **101**, 206601 (2008).

[4] E. Ya. Sherman, *Appl. Phys. Lett.* **82**, 209 (2003); M. M. Glazov and E. Ya. Sherman, *Phys. Rev. B* **71**, 241312(R) (2005).

[5] M. M. Glazov, M. A. Semina, and E. Ya. Sherman, Pre-print arXiv:0911.1444 (2009); M. M. Glazov, M. A. Semina, and E. Ya. Sherman, *Phys. Rev. B* **81**, in print.

18th Int. Symp. "Nanostructures: Physics and Technology"
St Petersburg, Russia, June 21–26, 2010

Spin waves in 2D diluted magnetic semiconductors

P. M. Shmakov, A. P. Dmitriev and V. Yu. Kachorovskii
Ioffe Physical-Technical Institute, St Petersburg, Russia

Abstract. We study collective spin excitations in two-dimensional diluted magnetic semiconductors, placed into external magnetic field B. We calculate analytically the spectrum of the spin waves taking into account both the electron-electron and electron-ion exchange interactions. We demonstrate that the interplay between these interactions leads to novel phenomena, such as the anti-crossing between two spin-wave branches in a certain range of magnetic fields and the inversion of the group velocity sign with the increasing of B.

Introduction

Effective manipulation of spin degree of freedom in a semiconductor device by external electric and magnetic fields is one of the primary goals of spintronics [1,2]. A possible way to increase coupling of electron spin to external magnetic field is to use semiconductor-based materials, which incorporate magnetic elements, typically Mn ions. Such materials are called diluted magnetic semiconductors (DMS). Many remarkable features of DMS are induced by the exchange interaction between the localized electrons on d-shells of Mn ions and delocalized band carriers. Recently, the homogeneous ($k = 0$) collective spin excitations in $Cd_{1-x}Mn_xTe$ quantum wells were studied experimentally [3,4] and theoretically [4,5]. Two collective modes $\omega_{1,2}(0)$ were observed and attributed to the electron and ion spin excitations (Fig. 1). It was also found that the anti-crossing between these modes occurs at a ceratin value of magnetic field $B = B_{\rm res}$. This result was interpreted theoretically in frame of mean-field approximation [4]. As was shown later, both experimentally and theoretically [5], other spin excitations (decoupled modes) are allowed in this system, which are not captured by mean-field picture.

Our goal is to generalize the theory of these collective excitations for inhomogeneous case and find the spectrum of spin waves $\omega_{1,2}(k)$ in the system.

In inhomogeneous case the electron-electron exchange interaction comes into play. It is well known that such interaction leads to renormalization of spin characteristics of electron gas, so one could expect small changes of the spectrum. We demonstrate that in fact the situation is much more interesting, and the simultaneous presence of two types of exchange interaction leads to a number of novel phenomena the most remarkable one being the anti-crossing of two spin-wave branches at non-zero wave vector, which occurs in a wide range of magnetic fields (see Fig. 2).

1. Theory

We consider the 2D electron gas interacting with the magnetic ions randomly distributed with 2D concentration n_J, which is typically much higher than electron concentration n_e. The system is placed into magnetic field **B** which leads to Zeeman splitting of both electron and ion spin levels with frequencies ω_e and ω_J, respectively. We assume that **B** is parallel to the well plane, thus affecting only the spin degrees of freedom. The electron-ion exchange interaction significantly increases electron spin precession frequency: $\Omega_e = \omega_e + \alpha n_J J_\parallel/\hbar a$, where α is exchange interaction constant, $J_\parallel$ is the equilibrium polarization of the ion spins, and a is the quantum well width.

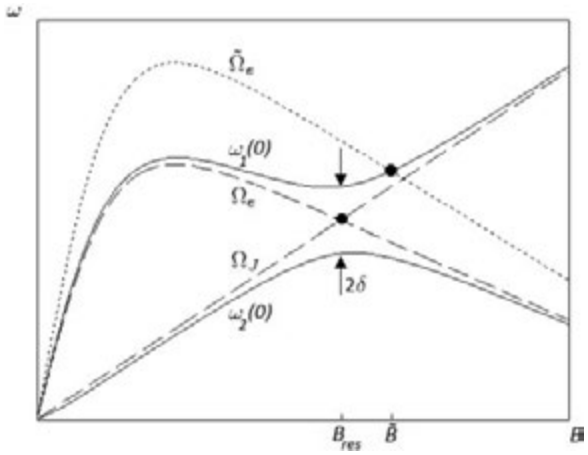

Fig. 1. Dependence of frequencies of the collective modes on external magnetic field B in the homogeneous case ($k = 0$). Dashed lines represent effective Zeeman splittings of electrons (Ω_e) and ions (Ω_J). $\widetilde{\Omega}_e$ is the edge of the Stoner continuum. The interaction between $\mathbf{s}_\perp$ and $\mathbf{J}_\perp$ leads to the anti-crossing of electron and ion precession frequencies at "resonant" magnetic field $B = B_{\rm res}$ at $k = 0$. In a case $B < B_{\rm res}$, the anti-crossing shifts to $k > 0$ (see Fig. 2). In a case $B > \widetilde{B}$, the ion spin wave branch appears above the Stoner continuum (see Fig. 3).

Typically, $\alpha n_J J_\parallel/\hbar a \gg \omega_e$, and consequently, $\Omega_e \gg \omega_e$. As for ion spin precession frequency, it remains almost unchanged for typical situation $\alpha n_e s_\parallel/\hbar a \ll \omega_J$: $\Omega_J = \omega_J + \alpha n_e s_\parallel/\hbar a \approx \omega_J$, where $s_\parallel$ is equilibrium electron spin polarization.

We study the excitations of spin components, perpendicular to the external field: $\mathbf{s}_\perp$, $\mathbf{J}_\perp$. Just as in the homogeneous case [4,5], there are two types of collective excitations (electron and ion spin waves) and a number of decoupled modes, which can not be described based on mean-field picture. One can show that dispersion of decoupled modes is negligibly small, so that we focus on dynamics of electron and ion spin waves. In the mean-field approximation, these excitations are described by the following system of coupled quasiclassical kinetic equations:

$$\frac{\partial s}{\partial t} + \left(v_F \mathbf{n}\nabla + i\widetilde{\Omega}_e\right)(s + Gs_0) = i\delta_1 J\,, \qquad (1)$$

$$\frac{\partial J}{\partial t} + i\Omega_J J = i\delta_2 s_0\,. \qquad (2)$$

Here $s(\mathbf{r}, \varphi, t) = s_\perp^x + is_\perp^y$ and $J(\mathbf{r}, t) = J_\perp^x + iJ_\perp^y$ are complex electron and ion spin densities, v_F is Fermi velocity, φ is the velocity angle in the well plane, $\delta_1 = \alpha n_J s_\parallel/\hbar a$,

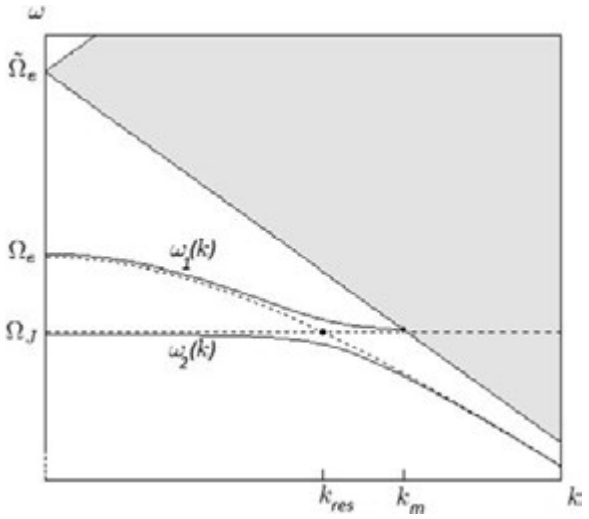

Fig. 2. Spin waves spectra for $B < B_{\rm res}$. Dashed lines represent the case $\delta = 0$ (Fermi-liquid spin waves and independent precession of ion spins). Solid lines correspond to $\delta > 0$. The greyed area is the Stoner continuum (single-particle excitations). The interaction between electron and ion spins leads to the anti-crossing of spin wave branches.

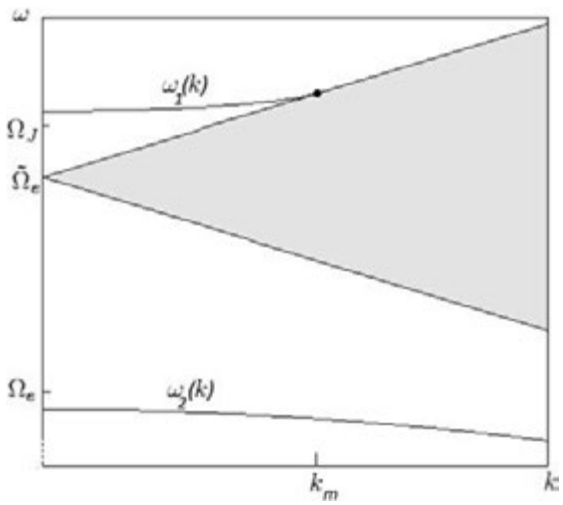

Fig. 3. Spin waves spectra for $B > \widetilde{B}$. In this case the ion spin-wave branch appears above the Stoner continuum and its dispersion is positive.

$\delta_2 = 3\alpha n_{\rm e} J_\parallel/2\hbar a$, $\mathbf{n} = (\cos\varphi, \sin\varphi)$, and $s_0 = \int_0^{2\pi} s d\varphi/2\pi$. In these equations both electron-ion and electron-electron exchange interactions are taken into account. The electron-electron exchange interaction is described in the framework of Landau Fermi-liquid theory and characterized by dimensionless constant G. This interaction leads to renormalization of the electron Zeeman splitting: $\Omega_{\rm e} \to \widetilde{\Omega}_{\rm e} = \Omega_{\rm e}/(1+G)$. In the homogeneous case ($k = 0$), the constant G drops out from Eqs. (1),(2) and the frequencies of two collective modes are given by equations derived in Ref. [4]: $\omega_{1,2}(0) = (\Omega_{\rm e} + \Omega_J)/2 \pm \sqrt{(\Omega_{\rm e} - \Omega_J)^2/4 + \delta^2}$, where $\delta = \sqrt{\delta_1\delta_2}$.

Next we discuss the case $k \neq 0$. Solving Eqs. (1),(2), one can show that the excitation spectrum consists of two spin-wave branches $\omega_{1,2}(k)$, decoupled branches, and the Stoner continuum (single-particle excitations), which is defined by inequality $|\omega - \widetilde{\Omega}_{\rm e}| \leq v_{\rm F}k$.

We assume ferromagnetic coupling, $G < 0$, and consider the case $|G| < 1$ (the case $G < -1$ corresponds to the Stoner instability). The behavior of the collective modes strongly depends on the relation between the parameters $\delta/\Omega_{\rm e}$ and $|G|$. For $\delta/\Omega_{\rm e} \ll |G|$ (this was the case in the experiment [5]) the anti-crossing occurs when $\Omega_{\rm e} > \Omega_J$, (see Fig. 2) which corresponds to the case $B < B_{\rm res}$ (see Fig. 1). This point can be clarified by considering the case $\delta = 0$ (electron-ion spin coupling is turned off). In this case, there are two branches of the spectrum, corresponding to Fermi-liquid spin waves with negative dispersion and dispersionless excitations of ion spins (dashed lines on Fig. 2). For $B < B_{\rm res}$ these two branches intersect each other at $k = k_{\rm res}$. For B close to $B_{\rm res}$ and $G \ll 1$, the anticrossing point is given by $k_{\rm res} = \sqrt{2\Omega_{\rm e}(\Omega_{\rm e} - \Omega_J)}/v_{\rm F}$. Turning on electron-ion spin coupling leads to the anti-crossing of two branches with the splitting of frequencies $\omega_1(k_{\rm res}) - \omega_2(k_{\rm res}) \approx 2\delta$.

As seen from Fig. 2 the upper branch of the spectrum reaches the Stoner continuum for $k = k_m$. For $k > k_m$ the corresponding ion-type excitations slowly decay in time due to electron-ion exchange coupling with the characteristic time scale of the order of $v_{\rm F}k^2/(\delta^2\sqrt{k^2 - k_m^2})$. This type of decay is similar to the well-known Landau damping in plasma.

Another phenomenon is the change from negative dispersion of the ion spin-wave branch to positive one at the magnetic field $B = \widetilde{B}$ corresponding to $\Omega_J = \widetilde{\Omega}_{\rm e}$. In the case $B < \widetilde{B}$ both spin-wave branches are below the Stoner continuum and have negative dispersion. While B increases approaching $\widetilde{B}$, the ion spin-wave branch becomes shorter ($k_m \to 0$) and disappears when $B = \widetilde{B}$. For larger magnetic fields, the ion branch appears above the Stoner continuum and has positive dispersion (Fig. 3). It is worth noting that the dispersion can also change sign for the case $\Omega_{\rm e} > \Omega_J$ provided that $\delta/\Omega_{\rm e} \gg G$.

Acknowledgements

The work was supported by RFBR, by grant of Russian Scientific School, by programmes of the RAS and by grant of RosNauka (project number 02.740.11.5072).

References

[1] Semiconductor Spintronics and Quantum Computation, eds. D. D. Awschalom, D. Loss, and N. Samarth, in the series "Nanoscience and technology", eds. K. von Klitzing, H. Sakaki, and R. Wiesendanger (Springer, Berlin, 2002).

[2] J. Cibert and D. Scalbert "Diluted Magnetic Semiconductors: Basic Physics and Optical Properties", in "Spin Physics in Semiconductors", ed. by M. I. Dyakonov (Berlin, Springer, 2008) chap. 13.

[3] F. J. Teran *et al*, *Phys. Rev. Lett.* **91**, 077201 (2003).

[4] M. Vladimirova *et al*, *Phys. Rev. B* **78**, 081305 (2008).

[5] J. Konig and A. H. MacDonald *Phys. Rev. Lett.* **91**, 077202 (2003).

18th Int. Symp. "Nanostructures: Physics and Technology"
St Petersburg, Russia, June 21–26, 2010

Magnetic and transport properties of 2D GaAs/InGaAs/GaAs structures with δ-doped Mn layer

B. A. Aronzon[1], V. V. Rylkov[1,3], M. A. Pankov[1], E. Z. Meilikhov[1], O. Drachenko[2], A. B. Davydov[1], N. B. Zvonkov[4] and *A. S. Vedeneev*[3]

[1] RRC Kurchatov Institute, 123182 Moscow, Russia
[2] Institute of Ion Beam Physics and Materials Research, Forschungszentrum Dresden-Rossendorf, 01314 Dresden, Germany
[3] V. A. Kotel'nikov Institute of Radio Engineering and Electronics of RAS, Fryazino branch, 141190 Fryazino, Moscow distr., Russia
[4] Physicotechnical Research Institute, Nizhnii Novgorod State University, Nizhnii Novgorod 603950, Russia

Present study of the diluted magnetic semiconductors (DMS) properties is actually focused on III-Mn-V materials for different heterostructure creation as a base for future spintronic devises [1]. Main attention was given to analyses the 3D (films) III-Mn-V material properties [1]. In works devoted to low-dimensional III-Mn-V structures, the authors provided achievement of the Curie temperature maximum value, T_C, at increased hole density in vicinity of the Mn ions [2]. However, such spatial "separation" of magnetic impurity and charge carriers results (according with exchange strengthening) stringing the Coulomb scattering on Mn ions and, accordingly, low values of the hole mobility, ($\leq$ 10 cm^2/V s [2]). In the case the structures could not be considered as two-dimensional because the quantum level tailing, ($\Delta E \approx \hbar/\tau$), exceeds the inter-level energy value. In the paper, the quantum well (QW) GaAs/In$_x$Ga$_{1-x}$As/GaAs structures with separated δ-doped Mn layer with the hole mobility in QW $\approx$3000 cm^2/V s at 5 K have been studied as an example. The structures show the ferromagnetic ordering in 2D III-Mn-V systems at $T_C \approx 40$ K. Observation of the resistance temperature dependence maximum and anomalous Hall effect (AHE) with value correlated to results calculated for ferromagnetic 2D III-Mn-V systems [3], also proof the ferromagnetic ordering of the structures.

In$_x$Ga$_{1-x}$As (x = 0.16–0.23) structures with $\approx$ 10 nm QW have been grown by MOCVD (B. N. Zvonkov, SRPhTI, Nizhny Novgorod). QW and surrounding GaAs layers (buffer, bottom and top spacer layers) have been grown up at temperature 600 °C while the δ-doped Mn and top GaAs layers were grown at 450 °C. The δ-doped Mn layer with concentration of N_{Mn} = 0.2–1 ML separated on QW by the spacer, $\approx$3 nm thickness, has been created by laser sputtering of Mn target. Details of QW structural properties analyzed by X-ray method have allowed defining the Mn atom spatial distribution and also to show practical absence of Mn in QW (the Mn impurity thick distribution is characterized by $\approx$ 2–3 nm) [4]. The QW electron transport properties have been studied in a temperature range 5–100 K and magnetic field up to 12 Tl using the double Hall cross mesa structures.

Fig. 1 illustrates the temperature dependences of R_{xx} resistance for GaAs/In$_x$Ga$_{1-x}$As/GaAs structures with different Mn concentration. Feature of the $R_{xx}(T)$ curves is different for samples with quasi-metallic (curves 2, 3) and activation (1) conductance type: there are maxima and knee-bend regions (curve 1) at T = 25–40 K and absence of similar features for the sample when Mn — impurity is absent (curve 4). The

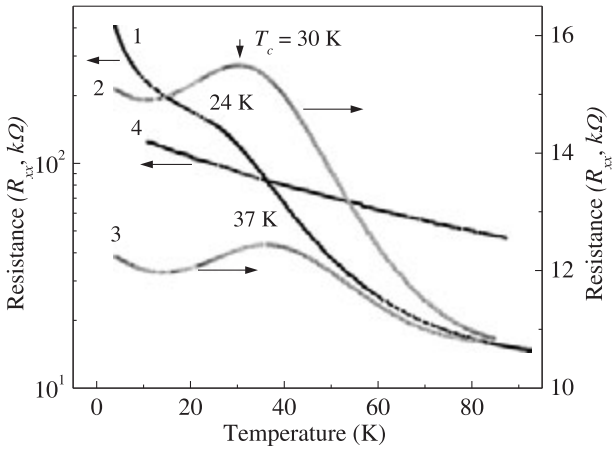

Fig. 1. Temperature dependences of structures with different Mn maintenance, M: 1.2 (1); 0.51 (2); 0.4 (3), and 0 (4).

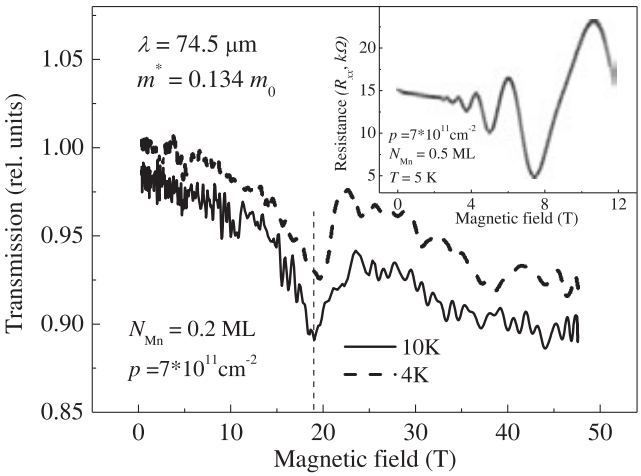

Fig. 2. Magnetic field dependence of optical radiation transmission (λ = 74.5 μm) for structure with quasi-metallic conductivity (p = 7 $\times$ 10^{11} cm^{-2}) at 4 and 10 K. The insert: Shubnikov–de Haas oscillations for the structure with same hole concentration at 5 K.

resistance rising with the T decreasing (down to $T \approx T_C$) and presence of the $R_{xx}(T)$ maximum is caused by ferromagnetic transition and illustrates a general property of III-Mn-V structures including heterostructures [2]. Notice that the structure resistance at temperatures $\leq$ 100 K is practically caused by quasi-2D holes in QW confirmed by observation of cy-

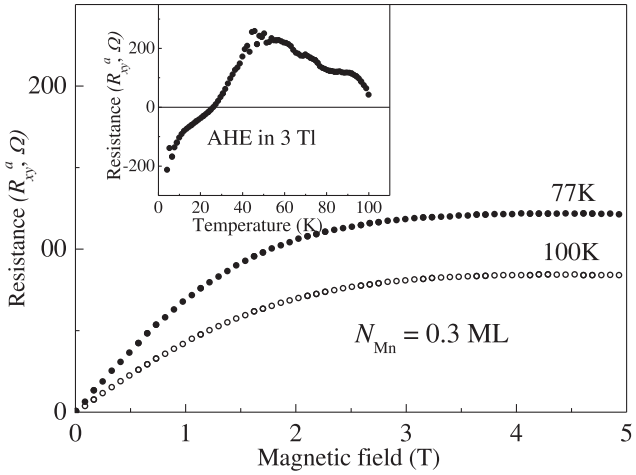

Fig. 3. Field dependence of the Hall effect anomaly components for structure with $N_{\mathrm{Mn}} = 0.3$ ML ($x = 0.16$) at 77 and 100 K. The insert: the AHE temperature dependence at 3 Tl.

clotron resonance and Shubnikov–de Haas oscillations (ShdH) in structures with quasi-metallic conductivity type (the hole concentration is $p = 7 \times 10^{11}$ cm^{-2}, Fig. 2) and absence of these effects in the case of longitudinal geometry. Effective hole mass found by CR measurements $m = 0.134m_0$ is smaller compared to heavy hole mass and corresponds to strained GaAs/In$_x$Ga$_{1-x}$As/GaAs QWs. The 2D hole concentration obtained by Shubnikov–de Haas oscillations coincides with accuracy $\approx 2\%$ with the data of the Hall effect measurements in weak field.

For structures with quasi-metallic conductivity type ($p \approx 7 \times 10^{11}$ cm^{-2}, $N_{\mathrm{Mn}} \approx 0.5$ ML) we have compared the T_{C} values found by maxima of $R_{xx}(T)$ curves and Curie temperature calculated for hetero-structures with indirect exchange interaction through 2D hole channel, and shown that experimental T_{C} values coincide with calculated results within a factor of ≤ 2 [4]. It testifies an essential role of QW holes in the structure ferromagnetic ordering, and the hole spin polarization also.

Hence notice recently developed different model explaining the carrier spin polarisation nearby the magnetic impurity δ-doped layer in usual semiconductors [5]. The model is based on assumption that the central part of this layer forms native FM, the band FM, and ferromagnetic order is accompanied by appearance of quasi-2D spin-polarized states in the semiconductor forbidden band. The band FM implies interaction through these states with QW holes followed by the spin polarization [5]. Underline that both mechanisms [4,5] lead to 2D hole spin polarization. Also obvious that relative contribution of these mechanisms can be revealed by study of QW structures with various spacer thicknesses, that is planed for in further.

Spine polarization of holes in our case is also proved by observation of the AHE in structures [4]. The AHE conductance, $\sigma_{xy}^a = (0.1 - 0.2)e^2/h$, well corresponds to results calculated for 2D III-Mn-V ferromagnetic systems [3], where the intrinsic AHE mechanism is predicted as dominant and σ_{xy}^a does not dependent on the carrier scattering time τ. Considered conditions assume that anomaly Hall effect component income is rising with the hole mobility decreasing (relation of the σ_{xy}^n to the normal Hall effect component conductance is proportional to τ^{-2}). The latter have been proved by results of the AHE measurements in samples with relatively low hole mobility, $\mu \approx 700$ cm^{-2}/V s at $T \approx 30$ K (Fig. 3 see). Observation of the AHE at temperature up to 100 K is visible for the case. Also notice the AHE sign reversion at $T \leq 30$ K associated with AHE skew-scattering mechanism starting as dominant in a region of the carrier mobility recession at temperatures less then 30 K.

Acknowledgements

The work has been supported by RFBR (#08-02-00719, 09-07-00290, 09-07-13594).

References

[1] T. Jungwirth *et al*, *Rev. Mod. Phys.* **78**, 809 (2006).
[2] A. M. Nazmul *et al*, *Phys. Rev. Lett.* **95**, 17201 (2005).
[3] S. Y. Liu *et al*, *Phys. Rev. B* **72**, 195329 (2005).
[4] M. A. Pankov *et al*, *JETP* **136**, 346 (2009).
[5] V. N. Men'shov *et al*, *Phys. Rev. B* **80**, 35315 (2009).

18th Int. Symp. "Nanostructures: Physics and Technology"
St Petersburg, Russia, June 21–26, 2010

CVD-diamond grown on porous alumina template

A. S. Vedeneev[1], M. P. Dukhnovskii[2], I. A. Leontiev[2], A. Yu. Mityagin[1], A. K. Ratnikova[2], Yu. Yu. Fedorov[2], O. Yu. Kudryashov[1,2] and A. S. Bugaev[1]

[1] V. A. Kotel'nikov Institute of Radio Engineering and Electronics RAS, Fryazino branch, 141190 Fryazino, Moscow distr., Russia
[2] FSUE "FPC ISTOK", 141190 Fryazino, Moscow distr., Russia

CVD-diamond is emerging material for modern electronic technology as perspective wide-gap semiconductor or high-performance heat-sink substrate. Unique properties permit a leap rise of operation frequency, power-carrying capacity and operating temperature, and thus mark out the diamond compared to other useful semiconductors for application in UHF- and power electronics [1]. The CVD-diamond film growth is actually performed by UHF activation of the methane-hydrogen gas mixture using the diamond nano-powder sown silicon wafer as the substrate [1]. The growth is initiated there by diamond nano-crystals and grown film thus doesn't have any prior crystallographic direction.

In the paper we demonstrate possibility of CVD-diamond growth on porous alumina templates. Alumina film obtained by anodic oxidation proves itself out as a self-organized nanostructured material containing cylindrical pore array with the pore concentration $\sim 10^{12}$ cm^{-2} and diameter varied in a range of $\sim$10 up to $\sim$100 nm by anodic voltage variation [2]. Moments of nano-modified alumina surface creation by anodic aluminum film oxidation are presented. The (100) Si wafers of 57 mm diameter and 0.3 mm thick with sputtered 0.1 μm thick titanium and 2 μm thick aluminum films have been taken as the substrate. Anodic oxidation has been carried out in 1.5 M oxalic acid water solution at 50–70 V anode voltage (see [2]). Topology analysis of alumina surface by AFM (Solver) has revealed the porous array with a period of 110–120 nm and pore diameter of 40–60 nm.

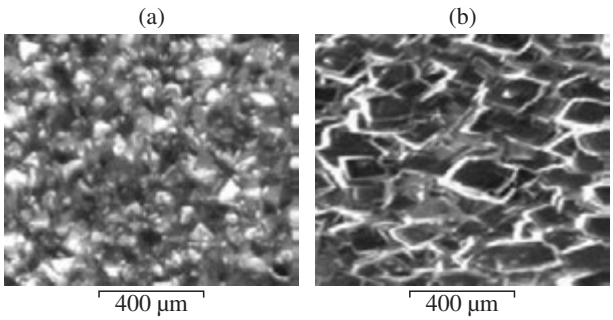

Fig. 1. CVD-diamond surface SEM image.

The 0.4 mm thick CVD-diamond films have been grown using the ASTeX system and modified alumina surface or diamond sown Si wafer as the substrate (the diamond growth rate was 5.0 μm/hour). In contrast to films grown on the diamond sown Si wafers (Fig. 1a) the surface of diamond films on modified alumina have shown clearly-marked (100) crystallographic direction and large-scale, 150–200 μm, crystalline grains (Fig. 1b). Supplementary study has shown that initial stage of CVD-diamond growth could be associated with carbon penetration inside the pores followed by formation of thin amorphous sublayer.

Results reveal new moments for technology development in the case of CVD-diamond growth on semiconductor or insulating substrates including self-organization and nanopatterning process.

Acknowledgements

The work has been partly supported by RFBR (#09-07-00290) and RNP (#2.1.1.4639).

References

[1] P. W. May, *Phil. Trans. Royal Soc. Lond. A* **358**, 473 (2000); *Endeavour Mag.* **19** (3), 101 (1995).
[2] J. M. Xu *et al*, *J. Appl. Phys.* **91**, 2544 (2002); *Appl. Phys. Lett.* **75**, 367 (1999).

18th Int. Symp. "Nanostructures: Physics and Technology"
St Petersburg, Russia, June 21–26, 2010

Site-selective plasmonic enhancement of emission in semiconductors

A. A. Toropov[1], T. V. Shubina[1], K. G. Belyaev[1], V. Kh. Kaibyshev[1], V. N. Jmerik[1], S. V. Ivanov[1], P. S. Kop'ev[1], Y. Ogawa[2] and F. Minami[2]

[1] Ioffe Physical-Technical Institute, St Petersburg, Russia
[2] Department of Physics, Tokyo Institute of Technology, Meguro, Tokyo 152-8551, Japan

Abstract. We report on systematic studies of the light-amplification effect in epitaxial semiconductor structures, induced by resonant interaction of emitting excitons with plasmons excited in gold nanoparticles. Near-field scanning optical microscopy was employed to place the particle near the surface of an InGaN film or a CdSe/ZnSe quantum dot heterostructure. Strong local enhancement (up to 50 times at 300 K) of the emission of excitons located in the near-field of the plasmonic particle could be observed subject to the precise compliance with polarization selection rules. The light-enhancement is identified as the Purcell effect and the realistic conditions of its observation are formulated.

Introduction

In the recent years, there has been a revival of long-standing experimental efforts to control the spontaneous emission dynamics by a Purcell-like effect in metal nanostructures [1–5]. The interest is mostly stimulated by the advances in modern nanotechnology allowing fabrication of well-defined metal nanostructures supporting localized plasmons and single quantum emitters. In particular, it is well established now that the rate of spontaneous recombination of the coupled "emitter-plasmon" system can be increased above that of an isolated emitter, owing to a significant local increase in the photonic mode density near the small metallic particle. This mechanism, which is in many aspects equivalent to the Purcell effect in optical microcavities, has been detected for single organic molecules and colloidal quantum dots (QDs) [1–4] as well as for localized excitons in the epitaxial films of InGaN [5]. In principle, this effect can be useful for designing novel single-photon devices with the improved efficiency [4]. The obstacle in this way is strong dissipation of confined plasmonic modes in absorptive metals. As a result, the commonly achieved enhancement factors are quite moderate and precise optimization of the structures is an important prerequisite for substantial improvements of the radiative properties [6].

Another trend in the studies and applications of the plasmon-assisted phenomena is engineering of metal-semiconductor light-emitting structures with an increased brightness [7–10]. The simplest proposed design involves a semiconductor heterostructure with a quantum well (QW) buried in the vicinity of the surface covered by a patterned metal film [7,8]. Note that the surface plasmon polariton spreading in a smooth thin metal film is usefulness for the enhancement of the emission, since it cannot interact with radiative emission modes [11]. The coupling to the external radiation can be facilitated either by ruling the semiconductor-metal interface with a grating [7] or making the interface randomly rough [8]. Recently, the plasmon-enhanced electroluminescence has been reported in light-emitting diodes based on InGaN/GaN QWs [9] and Si DQs [10] with embedded silver nanoparticles.

Here we investigate the plasmon-induced enhancement of the excitonic emission in epitaxial semiconductor structures, performed on a *microscopic level*, when just a few localized excitons, or even a single exciton, interact with the plasmons confined in a single metallic nanoparticle. Most of the results are obtained using apertureless near-field scanning optical microscopy (NSOM). The comparative studies of different structures, InGaN films and ZnCdSe/ZnSe QDs, have allowed us to identify the observed strong local enhancement of the emission (up to 50 times) as a purely electromagnetic plasmon-induced phenomenon, and to formulate the conditions required for its realization.

1. Samples and experimental techniques

The samples chosen for these studies are $In_xGa_{1-x}N$ ($0.2 < x < 0.5$) films and ZnCdSe/ZnSe QD heterostructures, fabricated by molecular-beam epitaxy (MBE). 200 nm thick layers of InGaN were deposited by plasma-assisted MBE above a GaN buffer layer grown on a c-oriented sapphire substrate. The samples were grown under N-rich conditions to provide a nano-columnar film morphology with the surface roughness on the scale of 100 nm [12]. In the ZnCdSe/ZnSe heterostructure the plane sheet of the ZnCdSe QDs is buried within the ZnSe matrix 10 nm below the surface. The morphology of the structure is generally flat besides the sites where extended defects meet the surface, disturbing the surface flatness. Strong localization of excitons occurs in the structures of both types due to either the compositional fluctuations enhanced by phase separation in InGaN, or the strain-driven formation of ZnCdSe QDs. The conventional spectra of excitonic photoluminescence (PL) there are inhomogeneously broadened, whereas employment of the techniques with high spatial resolution has allowed one to extract PL narrow lines attributed to the emission of single excitons [13]. In our experiments, the PL spectra were excited by a 532 nm laser line, which corresponds to the resonant excitation of localized excitons just below the fundamental band edge.

The near-field optical experiments were carried out by using a low-temperature NSOM system (Nanonics Cryo-View 2000). The illumination of the tip of the NSOM probe placed in the near-field of the sample surface, as well as PL detection, were performed via a confocal optical microscope. A noticeable PL enhancement was obtained only with apertureless probes produced from glass fibers, with an attached single gold nanoparticle of 100–200 nm in diameter. The plasmon resonance frequency for these particles corresponds to the spectral range of the excitonic emission in the investigated samples.

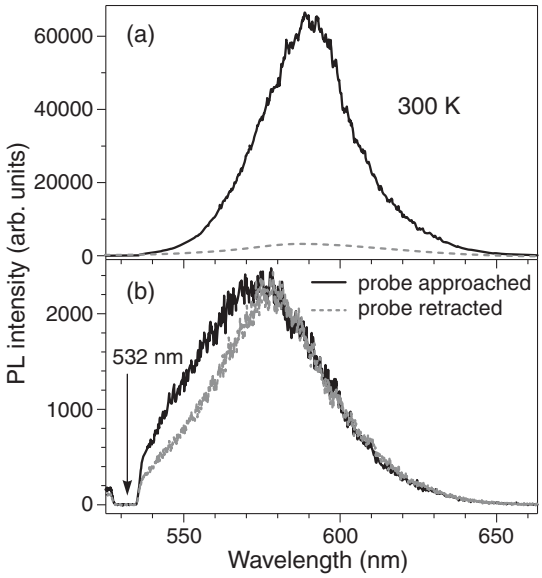

Fig. 1. Typical PL spectra measured in an $In_{0.25}Ga_{0.75}N$ film at 300 K with the NSOM probe either approached (solid lines) or retracted (dashed lines). Figure a) corresponds to the probe located within a pit of the topographical relief of the surface, while Fig. b) corresponds to a protrusion.

More details of the experimental setup have been published elsewhere [5].

2. Results and discussion

It was found that the effect of the tip with the attached gold particle on the shape and intensity of the PL spectrum strongly depends on the local morphology of the investigated surface [5]. Figure 1 illustrates this observation, demonstrating the typical spectra measured in an $In_{0.25}Ga_{0.75}N$ film at room temperature with the tip of the NSOM probe located within a pit (Fig. 1(a)) and protrusion (Fig. 1(b)) of the surface relief with the probe either approached to the surface (solid curves) or retracted (dashed curves). The PL signal is collected from the circle of about 2 μm in diameter, centered near the tip of the probe. The spectra measured with the retracted probe are only weakly dependent on the position of the measurement. It means that the PL spectrum is perfectly averaged over the spectra of many involved excitons. The location of the gold particle within the pit gives rise to a drastic (typically 20–50 times) increase in integral intensity of the emission and some variation of the line shape. On the other hand, the effect of the tip placed above a protrusion or a flat area is negligibly small. This observation is in agreement with theoretical considerations predicting much stronger plasmon-dipole interaction for the radial polarization of the dipole with respect to the metal surface than for the tangential one [6,11,14]. This condition cannot be efficiently fulfilled in the geometry of a confocal optical microscope, if the metal particle is placed above a flat surface or certain protrusion of the excitonic medium. However, when the plasmonic nanoparticle is positioned within the pit and the amplified exciton is localized somewhere in the film surrounding this pit, the optimal configuration for the detection of the plasmonic enhancement can be readily realized.

Figure 2 presents similar spectra measured at the low temperature (15 K), when the temperature-induced broadening of the excitonic lines is negligibly small. Again the spectra measured with the retracted probe are generally smooth and only weakly dependent on the position on the sample surface. Contrary to that, the shape of the spectrum is extremely sensitive to the location of the approached tip. The emission line consists now of a number of superimposed peaks with different spectral widths. This behavior can be understood as the selective enhancement of a part of the inhomogeneously broadened emission spectrum by affecting only a limited number of localized excitons emitting within the near-field of the gold particle. Note that the tip-induced PL enhancement observed at 15 K is much weaker than at room temperature, being typically in the range of 1–5 times, when the tip is located within a pit. The tip position above a protrusion usually leads to a PL quenching.

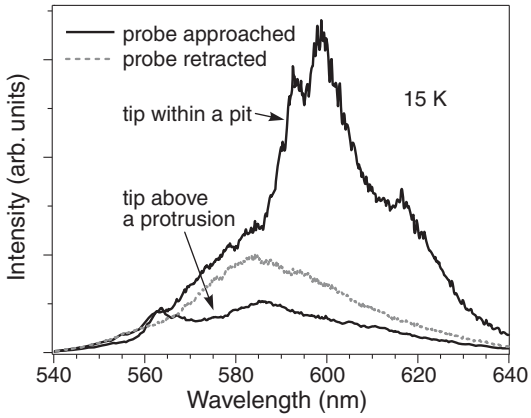

Fig. 2. Typical PL spectra measured in an $In_{0.25}Ga_{0.75}N$ film at 15 K with the NSOM probe either approached (solid lines) or retracted (dashed lines). The location of the tip is identified in the figure for each spectrum.

Similar experiments were performed with the ZnCdSe/ZnSe QD structures. A very moderate tip-induced enhancement can be observed there only in rather rare locations on the surface, presumably corresponding to some disturbances of the surface due to the emergence of extended defects. For the most area of the sample the approach of the tip results in the PL quenching rather than enhancement.

To analyze the data, we have employed a simple phenomenological model of rate equations based on the formalism of Gersten and Nitzan [14,15]. In this model, the localized exciton is considered as a two-level system. Each level is characterized by the radiative and nonradiative decay rates $\Gamma_{i,r}$ and $\Gamma_{i,nr}$ ($i = 1, 2$). The total decay rates are $\Gamma_i = \Gamma_{i,r} + \Gamma_{i,nr}$. The first (ground) level corresponds to the exciton emission frequency $\omega_{\rm em}$, while the second level is responsible for the absorption of the external radiation exciting the system at $\omega_{\rm ex}$ ($\omega_{\rm em} < \omega_{\rm ex}$). The energy relaxation from the second level to the first one is described by the decay rate $\Gamma_{2,1}$. Then the emission enhancement ratio can be obtained as

$$R_{\rm PL} = \frac{I_{\rm PL}}{I_{\rm PL,0}} = |A(\omega_{\rm ex})|^2\,|A(\omega_{\rm em})|^2 \times$$
$$\times \frac{\Gamma_2}{\Gamma_2+\Gamma_{2,p}}\,\frac{\Gamma_2+\Gamma_{2,1}}{\Gamma_2+\Gamma_{2,1}+\Gamma_{2,p}}\,\frac{\Gamma_1}{\Gamma_1+\Gamma_{1,p}}\,.$$

Here $I_{\rm PL,0}$ and $I_{\rm PL}$ are the PL intensities of an isolated exciton and the exciton coupled to a plasmon and $A(\omega)$ is the field amplification factor describing the local enhancement of the electromagnetic field, induced by the metal particle at the position of the exciton. The quantities $\Gamma_{i,p}$ represent the ad-

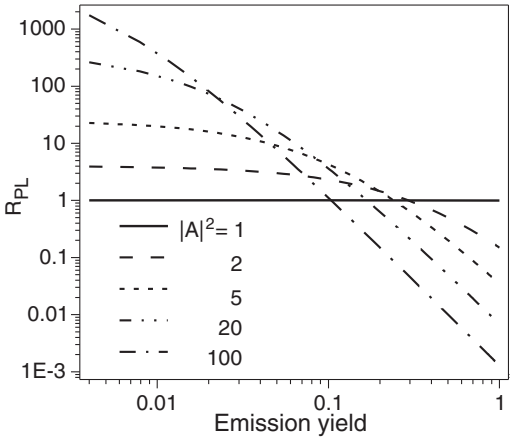

Fig. 3. Emission enhancement ratio versus emission yield, calculated for different field amplification factors.

ditional decay rates emerging due to the energy transfer from the exciton to the plasmon. They can be estimated within formalism of an electromagnetic theory [6,16].

Figure 3 shows the calculated emission enhancement factor versus the emission yield $Y = \Gamma_{1,r}/(\Gamma_{1,r}+\Gamma_{1,nr})$ for different values of $|A|^2$. In this calculation we chose $\Gamma_{1,r} = 1$ ns as estimated from the performed time-resolved PL measurements for both types of structures. Is is assumed that $\Gamma_{2,1} \gg \Gamma_i$ and the fraction of the energy coupled to the plasmon mode that is reradiated is $1/2$. The latter estimation is valid for the gold sphere of $\sim$150 nm in diameter [5].

The curves in Fig. 3 together with the experimentally measured emission enhancement factors allow rough estimation of the emission yield and effective field amplification factors. In the experiments with the InGaN samples with the tip located within pits of the surface the emission enhancement factors typically scatter within the range of 20–50 for 300 K and 1–5 for 5 K. It was obtained from temperature-dependent cw PL measurements that the average PL intensity and, hence, the emission yield drops by $\sim$50 times with the increase of the temperature from 15 to 300 K. Comparing these data with the curves shown in Fig. 3 one can estimate the emission yield of the InGaN structures as 0.2–0.4% at 300 K and 10–20% at 15 K. This corresponds to the possible values of $|A|^2$ between 5 and 10. For the ZnCdSe/ZnSe structures the emission yield corresponding to the optimal position of the NSOM tip can be estimated as 3–6% at 300 K and 50–90% at 15 K, whereas $|A|^2$ does not exceed 1–2. The smaller values of the field amplification factor in the ZnCdSe/ZnSe structures result most probably from worth compliance with the polarization selection rules for the gold particle located above the generally flat surface and separated from the emitting QDs by the 10 nm thick ZnSe layer. The rough surface of the InGaN films appears to be much more promising for the implementation of the plasmonic enhancement. Besides, as can be seen from Fig. 3, the sizeable emission enhancement factor can be observed only for the structures with a relatively low initial emission yield.

3. Conclusions

We demonstrate that under certain conditions the plasmon-induced enhancement of the emission in semiconductors can be a useful phenomenon allowing noticeable improvements of the radiative properties. In particular, for the InGaN films with the low-temperature emission yield $\sim$20% the 50-times decrease in the quantum yield due to the rise of the temperature up to 300 K can be nearly overcome by the proper employment of the plasmonic enhancement. One should note, nevertheless, that the device implementation of this scheme can be intricate since the interacting metal-semiconductor structures should comply with many strict requirements, including the fulfillment of the resonance between the frequencies of the emitting dipoles and the plasmon and of the polarization selection rules, realization of high enough values of the field enhancement factors, and accurate engineering of the balance between the radiation and dissipation in the metal structures.

Acknowledgements

This work has been supported in part by the RFBR (grants 09-02-01305a and 10-02-00633a) and the Program of the Presidium of RAS.

References

[1] R. M. Amos, and W. L. Barns, *Phys. Rev. B* **55**, 7249 (1997).
[2] J. R. Lakowicz, *Anal. Biochem* **298**, 1 (2001).
[3] J. N. Farahani, D. W. Pohl, H. -J. Eisler, and B. Hecht, *Phys. Rev. Lett.* **95**, 017402 (2005).
[4] A. V. Akimov, A. Mukherjee, C. L. Yu, D. E. Chang, A. S. Zibrov, P. R. Hemmer, H. Park, and M. D. Lukin, *Nature* **450**, 402 (2007).
[5] A. A. Toropov, T. V. Shubina, V. N. Jmerik, S. V. Ivanov, Y. Ogawa, and F. Minami, *Phys. Rev. Lett.* **103**, 037403 (2009).
[6] H. Mertens, A. F. Koenderink, and A. Polman, *Phys. Rev. B* **76**, 115123 (2007).
[7] N. E. Hecker, R. A. Hoepfel, N. Sawaki, T. Maier, and G. Strasser, *Appl. Phys. Lett.* **75**, 1577 (1999).
[8] K. Okamoto, I. Niki, A. Shvartser, Y. Narukawa, T. Mukai, and A. Scherer, *Nature Mat.* **3**, 601 (2004).
[9] M.-K. Kwon, J.-Y. Kim, B.-H. Kim, I.-K. Park, C.-Y. Cho, C. C. Byeon, and S.-J. Park, *Adv. Mat.* **20**, 1253 (2008).
[10] B.-H. Kim, C.-H. Cho, J.-S. Mun,'M.-K. Kwon, T.-Y. Park, J. S. Kim, C. C. Byeon, J. Lee, and S.-J. Park, *Adv. Mat.* **20**, 3100 (2008).
[11] W. L. Barnes, *J. Mod. Opt.* **45**, 661 (1998).
[12] V. N. Jmerik, A. M. Mizerov, T. V. Shubina, M. Yagovkina, V. B. Listoshin, A. A. Sitnikova, S. V. Ivanov, M.-H. Kim, M. Koike, B.-J. Kim, *J. Crystal Growth*, **301–302** 469 (2007).
[13] J. H. Rice, J. W. Robinson, A. Jarjour, R. A. Taylor, R. A. Oliver, G. A. D. Briggs, M. J. Kappers, and C. J. Humphreys, *Appl. Phys. Lett.* **84**, 4110 (2004).
[14] J. Gersten and A. Nitzan, *J. Chem. Phys.* **75**, 1139 (1981).
[15] D. A. Weitz, S. Garoff, J. Gersten, and A. Nitzan, *J. Chem. Phys.* **78**, 5324 (1983).
[16] A. O. Govorov, G. W. Bryant, W. Zhang, T. Skeini, J. Lee, N. A. Kotov, J. M. Slocik, and R. R. Naik, *Nano Lett.* **6**, 984 (2006).

18th Int. Symp. "Nanostructures: Physics and Technology"
St Petersburg, Russia, June 21–26, 2010

Zeeman effect on trions in a dense 2DEG

V. P. Kochereshko[1], L. Besombes[2], H. Mariette[2], T. Wojtowicz[3], G. Karczewski[3] and J. Kossut[3]

[1] Ioffe Physical-Technical Institute, St Petersburg, Russia
[2] Institut Neel, CNRS, Grenoble, France
[3] Institute of Physics Polish Academy of Sciences, PL-02608 Warsaw, Poland

Abstract. Reflectivity and photoluminescence spectra from CdTe/CdMgTe modulation doped quantum well structures were studied. We have found that in reflectivity spectra the value and the sign of the Zeeman splitting of the trion lines depend on the electron concentration in the quantum well, whereas the value and sign of the exciton line splitting are constant for all studied electron concentrations. On the other hand, in the photoluminescence spectra the sign and value of the Zeeman splitting are the same for trion and exciton. Such "renormalization" of the trion g-factor is explained in the model of combined exciton-electron processes.

Introduction

Trions in semiconductor quantum wells (QW) have been under study for a relatively long time [1] but there are still many unclear features. Most surprising is the properties of the trion in the presence of a dense electron gas. Very unusual is the behavior of the exciton and trion spectra in the presence of magnetic fields. In magnetic fields new lines emerge in absorption, reflection and photoluminescence spectra of doped QWs [3,4].

In the present paper we study the concentration dependence of the Zeeman splitting on the 2DEG density using reflectivity and photo luminescence in magnetic fields.

1. Experiment

We studied modulation-doped CdTe/($Cd_{0.7}Mg_{0.3}$)Te quantum well structures with 2DEGs of different densities (from $n_e \sim 10^{10}$ up to $n_e \sim 10^{12}$ cm^{-2}). The structures contained a 100 Å single quantum well (SQW) and were δ-doped in the barriers at 100 Å distance from the QW. A special design of the structures made it possible to control the electron concentration keeping all other parameters constant with high accuracy.

In this study we compare Reflectivity and PL spectra taken from the QWs with different electron densities in magnetic fields from 0 to 7.5 T.

At very low electron concentration in the QW only the exciton reflection line (X) is present in the spectra. At the higher electron concentrations the exciton reflection line loses its intensity, and the trion line (T) emerge in the spectra. In relatively high magnetic field, the trion line becomes strongly polarized. This polarization is due to the singlet character of the trion ground state. As a result, in high enough magnetic field the trion can be created in one circular polarization of photons only [1]. In magnetic fields, additionally to the exciton and trion lines, new lines, signed ExCR and TrCR appear in the spectra. These lines were analyzed in our publications [3,5]. At the highest electron concentration the exciton line disappears from the spectra and the trion line conserves its amplitude.

The exciton and trion lines show a normal quadratic diamagnetic shift to high energies with increasing magnetic field. At the same time lines ExCR and TrCR shift linearly with increasing magnetic field.

Additionally all these lines are split in magnetic field. At low electron concentrations the value and the sign of the exciton and trion Zeeman splittings are equal. But at high concentrations the sign of the trion Zeeman splitting becomes opposite to that of the exciton and other lines.

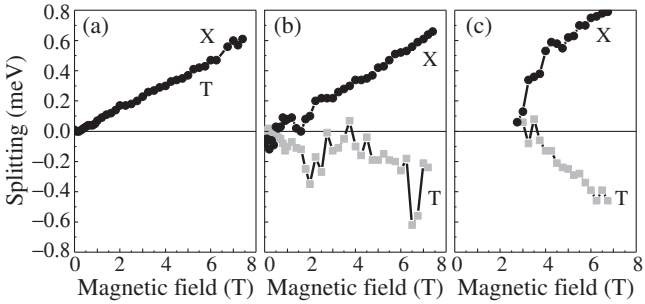

Fig. 1. Exciton (X) and trion (T) Zeeman splitting as a function of electron concentration. Electron concentration is 2×10^{10} cm^{-2} (a); electron concentration is 8×10^{10} cm^{-2} (b); electron concentration is 3×10^{11} cm^{-2} (c).

Figure 1 shows the dependences of the exciton and trion Zeeman splitting on magnetic field for the samples with different electron concentrations. One can see that at low electron concentrations the exciton and the trion splitting coincide, but with increase in electron concentration the exciton splitting is conserved but the trion splitting changes its value and even its sign.

We have also recorded PL spectra from these samples. We found that in the PL spectra the value and the sign of the trion Zeeman splitting are exactly the same as for the exciton and do not depend on the electron concentration.

Such a concentration dependence of the trion Zeeman splitting could be interpreted as a renormalization of the trion g-factor. But in this case it is not clear why this effect is absent for the exciton and why it is absent in PL spectra.

We will explain the observed effect in the framework of the model of combined exciton/trion electron processes which was applied successfully to the ExCR and TrCR transitions.

2. Discussion

Let us consider the trion formation in detail. The trion absorption (reflectivity) line corresponds to the binding of one photo-created exciton and one electron from the 2DEG. In the initial state of this process we have an electron e and in the final state we have a singlet trion Tr^s. The scheme of such a process is the following:

$$e + ph \rightarrow Tr^s . \quad (1)$$

The energy of this transition is therefore:

$$E_{\rm ph} = E_{\rm Tr} - E_{\rm e}\,.$$

As electrons in the 2DEG have energies (measured from the bottom of conduction band) in the range from zero to the Fermi energy: $0 \le E_{\rm e} \le E_{\rm F}$, the trion absorption (reflection) band should be spread within the energy range from $(E_{\rm Tr} - E_{\rm F})$ to $E_{\rm Tr}$.

In magnetic fields the background electrons occupy Landau levels which are below the Fermi level. When the filling factor $\nu \le 1$ the trion can form by binding of an exciton and a resident electron from the lowest Landau level. The energy of the corresponding optical transition is:

$$E_{\rm ph} = E_{\rm Tr}(H) - \hbar\omega_{\rm c}/2\,.$$

Because the second electron is bound very weakly to the exciton, in high enough magnetic fields the magnetic field dependence of the trion energy is:

$$E_{\rm Tr}(H) \propto \hbar\omega_{\rm c}/2\,.$$

Consequently, the energy of the optical transition corresponding to trion formation is constant with magnetic field (omitting the diamagnetic shift) as is observed in the experiment.

$$E_{\rm ph} = \text{ const}\,.$$

It is easy to see that the value and sign of the Zeeman splitting of the trion absorption line is exactly the same as the value and sign of the Zeeman splitting of the exciton line [1].

At higher filling factors, when $2 > \nu > 1$, electrons can occupy two Landau levels. In such conditions one can observe the phenomenon of Combined Trion Cyclotron Resonance TrCR [5]. In this effect, the incident photon creates a trion and simultaneously initiates a transition of an additional electron from the lowest to one of the higher Landau levels. The scheme of the corresponding process is:

$$e_1^{\uparrow} + e_1^{\uparrow} + ph \rightarrow Tr^{\rm s} + e_2^{\uparrow}\,. \qquad (2)$$

Here $e_1^{\uparrow}$ is an electron on the first Landau level with spin $\uparrow$, $e_2^{\uparrow}$ is an electron on the second Landau level with spin $\uparrow$. The energy of the optical transition in magnetic fields in this case is:

$$E_{\rm ph} = E_{\rm Tr}(H) + \frac{1}{2}\hbar\omega_{\rm c}\,.$$

Consequently the absorption line shifts with increase of magnetic fields to higher energies as $\hbar\omega_{\rm c}$. It is obvious that, because the initial and the final spin state of the additional electron are the same, the value and the sign of the observed Zeeman splitting will be the same as for the exciton line.

In these conditions $(1 < \nu < 2)$ another process is also possible. In this process, an incident photon creates a virtual trion in the triplet state [6,7]. This trion produces a spin-flip with one of the electrons on the first Landau level. As a result, in the final state, we get a trion in the singlet state plus an electron on the second Landau level with opposite spin. This is possible if the second level is only partially filled. The process is:

$$e_1^{\uparrow} + e_2^{\uparrow} + ph \rightarrow Tr^{\rm t} + e_1^{\uparrow} \rightarrow Tr^{\rm s} + e_2^{\downarrow}\,. \qquad (3)$$

The energy of the optical transition in this case is the same as for singlet trion formation. It is easy to see that the sign of the Zeeman splitting of the absorption line for this process is opposite to the Zeeman splitting of the singlet trion line in the normal process (1) and (2). Indeed, because the initial and the final spin state of the additional electron are different it will give a double contribution to the observed Zeeman splitting.

Consequently, the process (3) can explain the observed paradoxes related to the trion Zeeman splitting without any g-factor renormalizations.

3. Conclusion

In the reflectivity spectra of modulation doped QW structures, it has been found that the value and sign of the trion line's Zeeman splitting depend strongly on the electron concentration whereas the exciton Zeeman splitting does not depend on electron concentration. We found also that the Zeeman splitting of the trion and exciton are absolutely equal in the PL spectra. The observed phenomena are explained by trion triplet-singlet conversion with simultaneous transition of an additional electron between Landau levels.

Acknowledgements

This work received partial financial support from a grant of the Presidium of Russian Academy of Sciences, from grant RFBR-CNRS. We thank also Ronald Cox for help with this paper.

References

[1] K. Kheng, R. T. Cox *et al*, *Phys. Rev. Lett.* **71**, 1752 (1993); A. J. Shields, M. Pepper *et al*, *Phys. Rev. B* **52**,7841 (1995); G. Finkelstein, H. Shtrinkman, I. Bar-Joseph *et al*, *Phys. Rev. B* **53**, R1709 (1996).

[2] G. V. Astakhov, V. P. Kochereshko, D. R. Yakovlev, W. Ossau, J. Nürnberger, W. Faschinger and G. Landwehr, *Phys. Rev. B* **62**, 10345 (2000).

[3] D. R. Yakovlev, V. P. Kochereshko *et al*, *Phys. Rev. Lett* **79**, 3974 (1997).

[4] K. J. Nash, M. S. Skolnick, M. K. Saker and S. J. Bass, *Phys. Rev. Lett.* **70**, 3115 (1993).

[5] V. P. Kochereshko, G. V. Astakhov, D. R. Yakovlev, W. Ossau, G. Landwehr, W. Faschinger, T. Wojtowicz, G. Karczewski and J. Kossut *Physica E* **17**, 197–200, (2003).

[6] D. Andronikov, V. Kochereshko *et al*, *Phys. Rev. B* **71**, 165339 (2005).

[7] A. B. Dzyubenko, H. A. Nickel, T. Yeo, B. D. McCombe and A. Petrou *Phys. Stat. Sol. (b)* **227**, 365 (2001).

18th Int. Symp. "Nanostructures: Physics and Technology"
St Petersburg, Russia, June 21–26, 2010

Photoluminescence of GaAs nanowires of different crystal structures

B. V. Novikov[1], S. Yu. Serov[1], N. G. Filosofov[1], *I. V. Shtrom*[1], V. G. Talalaev[1], O. F. Vyvenko[1], E. V. Ubyivovk[1], A. S. Bondarenko[1], Yu. B. Samsonenko[2,4], A. D. Bouravleuv[2,3], I. P. Soshnikov[2,3], N. V. Sibirev[2], V. G. Dubrovskii[2,3] and G. E. Cirlin[2,4]

[1] St Petersburg State University, Physical Faculty, St Petersburg, Russia
[2] St Petersburg Academic University, St Petersburg, Russia
[3] Ioffe Physical-Technical Institute, St Petersburg, Russia
[4] Institute for Analytical Instruments RAS, St Petersburg, Russia

Abstract. GaAs nanowires grown by Au-assisted molecular beam epitaxy (MBE) on the GaAs(111)B and Si(111) substrates were investigated. Low temperature photoluminescence (PL) bands corresponded to the exciton emission of zinc blende (ZB) and wurtzite (WZ) phases were identified.

Introduction

Nanowires (NW) of semiconductor compounds attract now an increased interest due to their potential application in nanoelectronics and nanophotonics. Lasers, photodetectors, solar cells and others devices can be fabricated on their base. Depending on the growth conditions the crystal structure of GaAs NW's can be varied from cubic type zinc blende (ZB) to hexagonal type wurtzite (WZ) or their mixuture [1,2]. Besides regular lattice twin-type defects were found both within ZB as well as within WZ segments in many cases. It was found previously that exciton photoluminescence (PL) spectra of GaAs NWs depended on their phase content as well as on their diameters [1,2]. However, not all of the registered PL-lines were identified reliably.

In this work the arrays of GaAs NWs were studied by means of PL and transmission electron (TEM) techniques. The samples with predominately single phase structure were selected to identify exciton PL bands related to ZB or to WZ. Temperature behavior of the bands as well as their degradation under the intense laser radiation were investigated as well.

1. Experimental

NWs were grown with molecular beam epitaxy (MBE) on the GaAs(111)B and Si(111) substrates using gold droplets as precursor. Other details of the NWs growth technique, their electron-microscopic characteristics and PL measurements can be found elsewhere [1].

2. Result and discussion

TEM investigation of our samples showed that NWs which were grown during 30 min. exhibited predominately ZB structure with numerous rotation twins and narrow bands of WZ along their length. The samples which were grown during 15 min. had predominately WZ structure. These is in concordance with the results obtained with CVD technique [2].

Figs. 1 and 2 show the results of our PL investigation of NWs with predominant ZB (Fig. 1) or WZ (Fig. 2) modification grown on GaAs substrate. Fig. 1 represents the spectra of GaAs substrate and ZB NW. PL spectrum of substrate at 5 K consists of the main band marked as I_c and a weak band E_{ex} at 1.513 eV that corresponds well with the position of free exciton in bulk GaAs. The spectrum of ZB NWs exhibits similar features except the free exciton band is shifted NW by 2–3 nm to higher energy with respect to free excitons in the substrate. This shift might be attributed to the quantum confinement effect. Since PL band I_c is present in the spectra both of the substrate and NWs we believe is due to the impurity-band optical transition and is associated with carbon. The presence of carbon in NW

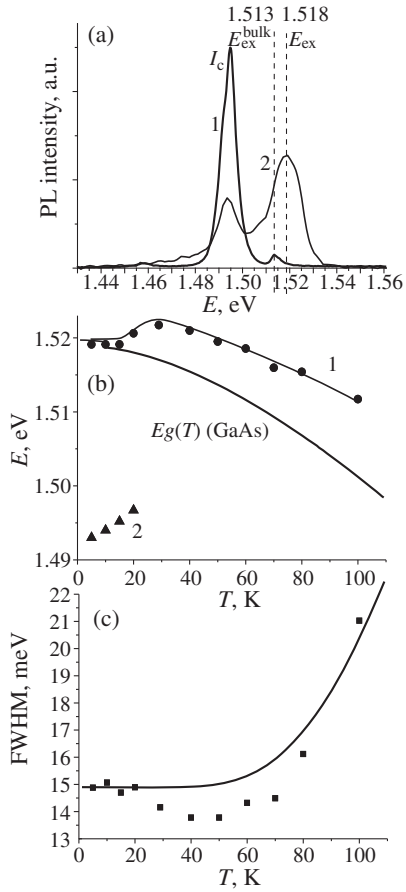

Fig. 1. (a) PL specta of NW's sample with ZB form at 5 K (1) and substrate GaAs(111) (2); (b) The shift of maximum of the PL band E_{ex} (1) and impurity band I_c (2) from the temperature for the sample with ZB phase; (c) The changing of FWHM of PL band E_{ex} from the temperature for the sample with ZB phase and theoretical curves of broadening.

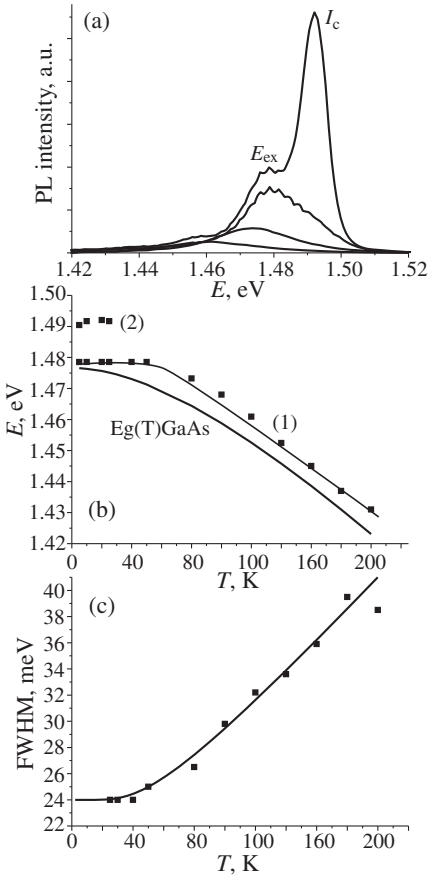

Fig. 2. (a) PL specta of NW's sample with WZ form at different temperature 5,25,80 and 120 K; (b) The shift of maximum of the PL band E_{ex} (1) and impurity band I_c (2) from the temperature for the sample with WZ phase; (c) The changing of FWHM of PL band E_{ex} from the temperature for the sample with WZ phase and theoretical curves of broadening.

is caused probably by the diffusion of carbon from substrate during the growth process. This band is absent in NW, grown on the Si(111) substrate. The bands E_{ex} and I_c show anomalous temperature behavior Fig. 1b in comparison with the band gap of bulk GaAs. We attribute this behavior to the non-uniformity of NW sample structure. FWHM of E_{ex} as a function of the temperature exhibits also extraordinary behavior Fig. 1c. We explain the existence of minimum close 50 K by the migration of the energy along NW, by the ionization of shallow and filling of deeper quantum states [3].

Fig. 2a represents PL spectra from array of NWs with predominant hexagonal structure of NWs taken at diverse temperatures. Beside carbon-related band I_c a new band marked as E_{ex} is clearly seen in the PL spectrum. The intensity of this band changed slowly with the temperature increase. It could be detected at the temperature as high as 259 K. The positions of both bands didn't change with increasing of laser pumping.

It should be noted that the PL bands with the energies below I_c band are interpreted conventionally as some impurity bands. However the impurity bands vanish usually at the temperature as low as 30 K and their spectral positions depend strongly on the intensity of the excitation. Thus, we ruled out impurities as the origin of E_{ex} band in WZ NWs. The temperature dependence of the position of E_{ex} band differed from that known for E_g in GaAs Fig. 2b. Such dependence of FWHM for E_{ex} band

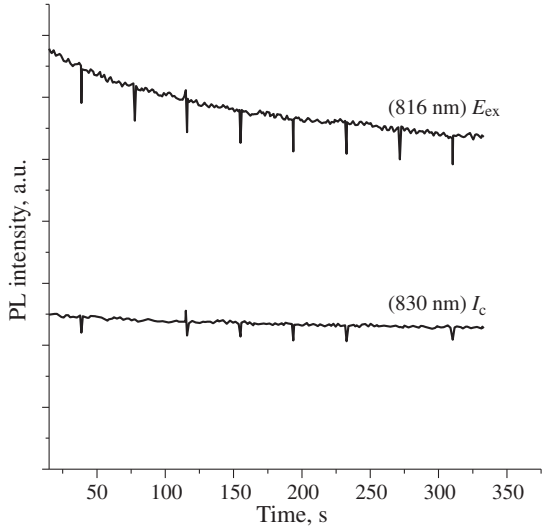

Fig. 3. The time dependence of PL intensity of the sample grown on Si(111) substrate under the action of Nd-laser (530 nm) with excitation power 100 meV, at 5 K. The top curve is E_{ex} (816 nm), bottom curve is impurity band I_c (830 nm).

was found to be exponential with activation energies of 18 and of 35 meV for WZ and ZB respectively.

It is well known that in A_3B_5 as well as in A_2B_6 compounds the band gap for WZ structure is always larger than that for ZB. This trend was recently confirmed for GaAs by theoretical calculations [4]. We suppose that appearence of PL maximum at 1.48 eV corresponds to direct and indirect transitions between the electronic states in ZB and WZ closely spaced nanoregions. Similar explanation was purposed for InP NW's [5].

The degradation of PL intensity of GaAs NW's was investigated under continuous laser excitation at 5K with the wavelength of 530 nm.

Fig. 3 shows the time dependence of E_{ex} and I_c bands under the action of the laser radiation. The intensity of E_{ex} band decreased noticeably and non-reversibly while the intensity of I_c band remained relatively stable. The electron-microscopic observations showed that the form of NW's was changed under the action of laser light. Firstly, the NW's bent and touched each other with their tops [6], then they fell down to the substrate and transformed to the pyramids.

References

[1] B. V. Novikov *et al*, *17th Int. Symp. "Nanostructures: Physics and Technology"* 186–187 (2009).
[2] K. Hiruma *et al*, *J. Appl. Phys.* **74(5)**, 3162–3171 (1993).
[3] M. B. Smirnov *et al*, *Phys. St. Sol(B)* **247** 2, 347 (2010).
[4] Z. Zanolli *et al*, *Phys. Rev. B* **75**, 245121 (2007).
[5] J. Bao *et al*, *Nanoletters* **8(3)**, 836–841 (2008).
[6] O. A. Neutcheva *Thechnical Phys. Letters* **33**, 21 (2007).

18th Int. Symp. "Nanostructures: Physics and Technology"
St Petersburg, Russia, June 21–26, 2010

Effect of external electric fields and internal charges on resonant light reflection by excitons in GaAs/$Ga_{0.7}Al_{0.3}As$ quantum well

V. G. Davydov, V. V. Ovsyankin, B. V. Stroganov and S. V. Poltavtsev
Institute of Physics, Physical Faculty, St Petersburg State University, Ulyanovskaya ul. 1, Petrodvorets, St Petersburg, 198504, Russia

Abstract. Linear and nonlinear resonant coherent optical properties of excitons in GaAs/GaAlAs quantum wells are explored to evaluate their applicability as an active media for information processing and optical computing. Strong effect of the charge state of the sample on the excitons and their interaction with light is observed. Nature of this effect is studied and two possible mechanisms are proposed.

Introduction

Semiconductor heterostructures are rather promising in a role of active media in various fields of optoelectronics and all-optical information processing [1]. Particularly, excitons in the single quantum well off sufficiently high quality can be considered as an approximate model for an ensemble of ideal two-level systems in a sense that all imperfections, such as homogeneous and inhomogeneous broadening etc., can be weaker (in terms of matrix element's magnitude and/or characteristic energy scale) than main functional interaction, that is interaction with light — information carrier.

Of course, quality and applicability of this model depends both on the physical properties of the given sample and on the details of it's intended use. GaAs/GaAlAs heterostructures are rather stable in the typical laboratory environment, so their physical properties can be divided in two classes: those which have been formed during the manufacturing process and are embedded within the sample (such as composition of the structure layers, doping concentrations, spatial roughness of the hetero-junctions etc.) and those affected by an external environment (temperature, electric and/or magnetic fields, spectrum and intensity of light, both functional and stray etc.). Despite of the great variety of the physical factors, their effects on the excitons as an ideal model can be viewed on a very simple single-dimension basis: away from (or, more rarely, toward) perfection. All important working characteristics (except wavelength range which is always near infrared for GaAs-based structures), such as speed, elements density, energy consumption etc., are determined by a single value — relation between oscillator strength and some effective broadening. The higher this ratio, the better physical model is. This provides one by a natural scale of importance: as soon as an effect of a single factor on a total line width (or on an intensity of the resonant exciton's spectral line in, say, reflection spectrum) can be isolated (separately measured), the feasibility of efforts to eliminate this factor becomes obvious.

In course of manufacturing and investigation of many samples it was found that thorough and accurate technical measures during the MBE growth can yield samples with inhomogeneous broadening low enough to see other effects, such as caused by an exciton-exciton interaction, free charge carriers and electric fields. The latter can lead to a behaviour which depends on the sample prehistory (because carriers easily accumulate between the nearly perfectly insulating layers of the structure), weak illumination by an ambient light (which can create additional carriers and/or shunt insulating layers by photocurrent) and other environment. Anyway, the given fragment of a given sample in exactly the same controllable environment always demonstrate the same, albeit sometimes very complex, behaviour (spectral position, width and intensity of the exciton's resonant line). Other characteristics (nonlinear coefficients, time scales, spectral shape changes under intensive resonant light etc.) have been investigated elsewhere and are not a subject of this work.

1. Experimental

The experimental technique has been deliberately chosen to be as simple as possible, because this allows less space for experimental errors as well as theoretical speculations. The main observable is the magnitude of a resonant reflection coefficient of a moderately focused laser beam from the sample. To eliminate nonresonant reflection from the sample surface, light beam was directed from the Brewster's angle (which is rather big for the investigated semiconductor, about 74°) and thoroughly polarized in the plane of incidence. Light not reflected by excitons in a quantum well is absorbed by inter-band transition in bulk GaAs substrate. Undertaken measures suppress total nonresonant reflection coefficient to a value of the order of a few pro mille [2].

Intensity of the laser light is chosen small enough, so that all processes are linear with respect to it and further it's reduction doesn't lead to any observable changes in the reflection spectrum. Laser used is either tunable CW (to measure the peak reflection coefficient), or wide-band femtosecond Ti:sapphire, properly filtered by a multi-layer interference filter and/or a monochromator to measure the integral intensity of the spectral line without sensing other resonances (such as free excitons in the substrate, light-hole excitons in the same quantum well or heavy-hole excitons in another quantum wells embedded in the same sample).

Temperature of the sample is maintained by a two-stage closed cycle helium cryostat on a predetermined level (usually 8.25 K, for the sake of consistency with numerous previous experiments with the same samples [3,4]). Electric field is applied by means of an electrode located in a vacuum near the surface of the sample (with grounded substrate). This arrangement prevents one from applying DC field and/or steady DC current, but leaves the sample surface optically clean. Discharge

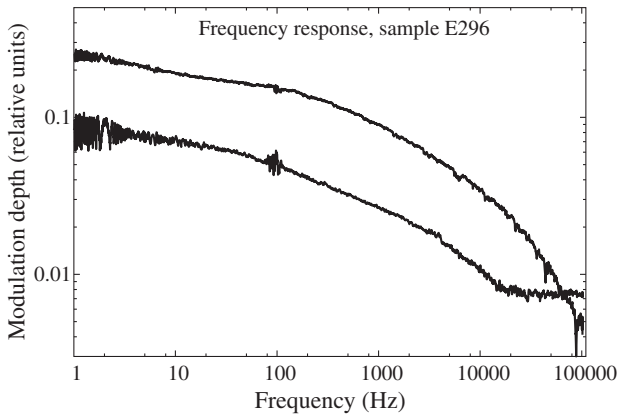

Fig. 1. Reflection modulation of the resonant light wiht (upper trace) and without (lower trace) auxilliary wideband illumination. Spurious features around 2 and 100 Hz are produced by cryostat vibration and rectified mains voltage respectively and don't relate to the sample itself.

of the internal electric fields is performed via illumination by a wide-band "white" light, which causes photoconductivity in all layers of the structure.

To increase sensitivity, accumulation technuques are applied, such as lock-in detection (under sinusoidal AC excitation) and time-resolved accumulation (when a sample is excited by a repetitive electric pulses).

2. Results

As an example we present here some representative data obtained on the sample E296, which contains a quantum well of a rather decent quality [4]. Due to the later fact, this sample was studied most comprehensively and stability of it's characteristics has been verified for several years.

In Figure 1 frequency responses of the resonant reflection change caused by illumination with 100%-modulated resonant light of moderate intensity (much stronger than the probe light, but much weaker with respect to intensities which cause significant line broadening, biexciton formation and similar strong nonlinearities) are shown. Exact intensity of the excitation light does not matter in this experiment because observed effet depend roughly logariphmically on it (note the logarithmic scale on both axes). The only difference between two datasets is a presence (or absence) of a weak (few lux) white ambient illumination.

From this figure one can see that there is very wide spectrum of relaxation times in the sample. Mechanisms of this relaxation, whatever they could be, strongly depend on the external illumination. Note that two traces intersect each other at some frequency, suggesting that there are at least two different mechanisms with opposite properties with respect to white light.

3. Discussion

Physical nature of observed effect can be described from two points of view. Firstly, electric field can distort excitonic quantum states, relax some kind of symmetry and allow excitons to interact more effectivly with their immediate environment. And secondly, electric fields are inextricably tied with layers of charged carriers, who interact with excitons by analog of chemical bonding, forming trions etc. Probably, these two approaches are indeed mere different views of the same physics.

In some samples the effect of the electric field is rather prominent: fraction of typical photovoltaic potential can cause change in reflection by tens of percent. This opens possible applications for various types of electrooptical light modulators, either of phase and amplitude types, with ability to develop spatial resolution.

Another possible application of such a strong effect can be in the field of sensitive infrared and terahertz detectors, including imaging ones.

References

[1] K.-H. Brenner, Alan Huang, *J. Opt. Soc. Am.* **A 3**, 62 (1986).
[2] V. Davydov, S. Gavrilov, G. Kozlov, B. Stroganov, S. Poltavtsev, V. Ovsyankin, *Optics and Spectroscopy* **107** 6 (1 December 2009), pp. 981–986.
[3] V. G. Davydov, S. V. Poltavtsev, V. V. Ovsyankin, B. V. Stroganov, *Temperature anomaly in the polarization relaxation of 2D excitons and droplet-type e-h condensation in GaAs SQWs*, OECS9 and ICSCE2 Abstracts, Southampton, UK, p. 114 (2005).
[4] Sergey V. Poltavtsev, Vladimir V. Ovsyankin, and Boris V. Stroganov, *Physica Status Solidi (c)* **6** 2, 483 (2009).

18th Int. Symp. "Nanostructures: Physics and Technology"
St Petersburg, Russia, June 21–26, 2010

Calculation of optical matrix elements in carbon nanotubes made simple

S. V. Goupalov[1,2], A. Zarifi[3] and T. G. Pedersen[4]

[1] Department of Physics, Jackson State University, Jackson, MS 39217, USA
[2] Ioffe Physical-Technical Institute, St Petersburg, Russia
[3] Department of Physics, Yasouj University, Yasouj, Iran
[4] Department of Physics and Nanotechnology, Aalborg University, Aalborg, Denmark

Abstract. Analytical expressions for dipole matrix elements describing interband optical transitions in carbon nanotubes are obtained for arbitrary light polarization and nanotube chiralities. The effect of the symmetry with respect to the time reversal on the dependences of the optical matrix elements on the quantum numbers of electronic states in carbon nanotubes is studied.

Introduction

The dependences of matrix elements for optical transitions in carbon nanotubes (CNTs) on quantum numbers of the electronic states and on the nanotube chiral indices are essential for both the study of the fundamental optical phenomena in CNTs and the application of optical methods for their characterization.

Two different approaches have been used to calculate the dipole optical matrix elements within the tight-binding (TB) method. The first approach [1] succesfully applied for the case of the *parallel* polarization is based on the introduction of the so-called atomic dipole vectors. In the case of *perpendicular* polarization it becomes quite complicated. The results of calculations reported in [1] turn out to be inconsistent with the symmetry requirements. Recently the method of [1] was further developed in [2] and the numerical results for perpendicular polarization have been corrected. However, the derivation of [2] was quite laborious while the final result was obtained in a rather complicated form.

An alternative method was proposed in [3]. There it was applied to calculate matrix elements of optical transitions within the effective mass (EM) scheme accounting for a few lowest (uppermost) subbands of the conduction (valence) band of a CNT. In the present paper we show that extension of this method to account for all possible interband transitions yields an elegant and straightforward derivation of the optical matrix elements for arbitrary polarizations and nanotube chiralities.

1. Perpendicular polarization

Let's direct the z axis along the CNT. The expression for the y-component of the *coordinate* interband matrix element was found in [3] in the form:

$$\langle v, \mathbf{k}'|y|c, \mathbf{k}\rangle = i R\, \frac{\delta_{\mu',\mu-1} - \delta_{\mu',\mu+1}}{2}\, \delta_{K_2,K_2'} \times \sum_{b=A,B} C_b^*\left(v, \mathbf{k}'\right) C_b(c, \mathbf{k})\,. \quad (1)$$

Here $\mathbf{k}$ refers to the electron two-dimensional wave vector in graphene and has the components K_1 along the nanotube's circumference and K_2 along the nanotube's cylindrical axis. In a nanotube the wave vector K_1 becomes quantized: $K_1^\mu = \mu/R$, where R is the nanotube's radius; $C_b(s, \mathbf{k})$ are the coefficients of the TB method for the s-band. The key idea in deriving Eq. (1) was to use the fact that the periodic in z Bloch functions belonging to the same K_2 but different band indices s ($s = c, v$) and μ_s form a complete set of functions.

Within the zone-folding scheme the column coefficients of the TB method $\hat{C}(c, \mathbf{k})$ and $\hat{C}(v, \mathbf{k})$ are found to be [1,2,4]

$$\hat{C}(c, \mathbf{k}) = \frac{1}{\sqrt{2}} \begin{pmatrix} e^{i\varphi_c} \\ 1 \end{pmatrix},\ \hat{C}(v, \mathbf{k}) = \frac{1}{\sqrt{2}} \begin{pmatrix} -e^{i\varphi_v} \\ 1 \end{pmatrix}, \quad (2)$$

where $\varphi_{c,v} = \arctan \frac{\mathcal{B}}{\mathcal{A}} + \pi/2 - \pi/2\,\mathrm{sgn}(\mathcal{A})$,

$$\mathcal{A} = 2\cos\left(k_x a/2\sqrt{3}\right)\cos\left(k_y a/2\right) + \cos\left(k_x a/\sqrt{3}\right),$$
$$\mathcal{B} = 2\sin\left(k_x a/2\sqrt{3}\right)\cos\left(k_y a/2\right) - \sin\left(k_x a/\sqrt{3}\right),$$

$k_x = K_1^\mu \cos\alpha - K_2 \sin\alpha$, $k_y = K_1^\mu \sin\alpha + K_2 \cos\alpha$, a is the lattice constant of graphene, and the angle α is related to the nanotube chiral angle θ by $\alpha = \pi/6 - \theta$.

Substituting Eqs. (2) into Eq. (1) we obtain

$$\left|\langle v, \mathbf{k}'|y|c, \mathbf{k}\rangle\right| = R\delta_{K_2,K_2'} \left|\frac{\delta_{\mu',\mu+1} - \delta_{\mu',\mu-1}}{2}\right| \times \left|\sin\left[\left(\varphi_v' - \varphi_c\right)/2\right]\right|\,. \quad (3)$$

The corresponding *velocity* matrix element is

$$\left|\langle v, \mathbf{k}'|v_y|c, \mathbf{k}\rangle\right| = \frac{R}{\hbar}\delta_{K_2,K_2'}\left[E_{c,\mu}(K_2) - E_{v,\mu'}(K_2)\right] \times \left|\frac{\delta_{\mu',\mu+1} - \delta_{\mu',\mu-1}}{2}\right| \left|\sin\left[(\varphi_v' - \varphi_c)/2\right]\right|\,, \quad (4)$$

where $E_{s,\mu}(K_2)$ is the electron energy in the s-band. Eqs. (3) and (4) are original and constitute our main result.

In Fig. 1 matrix elements of the *velocity* operator for all possible interband transitions in a (4,2) CNT calculated using Eq. (4) are shown (for the sake of brevity, we use the notation $|v_y| \equiv \left|\langle v, \mu, K_2|v_y|c, \mu+1, K_2\rangle\right|$; T is the length of the nanotube's translational vector [4]).

One can see from Fig. 1 that (a) the figure is symmetric with respect to the line $K_2 = 0$ and (b) all the curves intersect pairwise at the edges of the CNT one-dimensional Brillouin zone. These features are due to (i) the fact that there is a mirror-like symmetry between the energies of the conduction

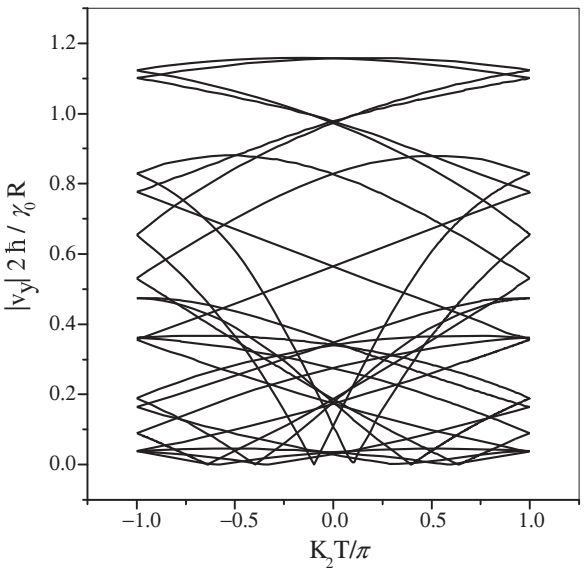

Fig. 1. Velocity matrix elements for all possible interband optical transitions in a (4,2) CNT. Incident light is polarized perpendicular to the nanotube axis, z. γ_0 is the transfer integral of TB method.

and valence-band electronic states of the nanotube [5], and (ii) the symmetry with respect to time reversal. We will limit our discussion to transitions of the type $v, \mu \to c, \mu + 1$.

In Fig. 2 are shown the 29 replicas of the Brillouin zone of a (4,2) carbon nanotube (corresponding to the $N = 28$ subbands in the conduction or valence band) superimposed upon the reciprocal lattice of graphene. The origin of the **k**-space of graphen is chosen in a Γ-point. The spin-orbit interaction in CNTs is negligible. For such systems one can neglect the electron spin, and the time reversal operation relates states with the opposite wave vectors. This rule can be applied to CNTs if the origin in the reciprocal space of graphene is moved to the point with $\mu = N/2$, $K_2 = 0$, where N is the number of hexagons in the one-dimensional unit cell of the CNT [4]. This point corresponds to a **M** point in the reciprocal space of graphene (see Fig. 2). Then it follows that the curves in Fig. 1 corresponding to the pairs of interband transitions $v, \mu' = N/2 + l \to c$, $\mu = N/2 + l + 1$ and $v, \mu' = N/2 - l - 1 \to c, \mu = N/2 - l$ are related to one another by reflection with respect to the line $K_2 = 0$ (l is an integer modulo $N/2$). This conclusion holds for CNTs of arbitrary chiralities.

The situation described above for the (4,2) CNT is typical for all *chiral* nanotubes. For *achiral* nanotubes one has $|v_y(K_2)| = |v_y(-K_2)|$ and, therefore, the two curves $|v_y(K_2)|$, related by the reflection with respect to the line $K_2 = 0$ and representing two different transitions, will coincide [6]. For a (m, m) armchair nanotube such pairs of interband transitions are $v, \mu' = m + n \to c, \mu = m + n + 1$ and $v, \mu' = m - n - 1 \to c, \mu = m - n$. We would like to emphasize that this coincidence is not a consequence of some fundamental symmetry of the physical system under study but merely a property of the model which neglects the overlap integral of the TB method.

It is worth to note that the (4,2) CNT possesses some extra symmetry peculiar for this particular nanotube. Namely, the states with $\mu = 11$, $K_2 = \pi/T$; $\mu = 25$, $K_2 = \pi/T$; $\mu = 3$, $K_2 = -\pi/T$, and $\mu = 17$, $K_2 = -\pi/T$ correspond to the **M** points in the reciprocal space of graphene

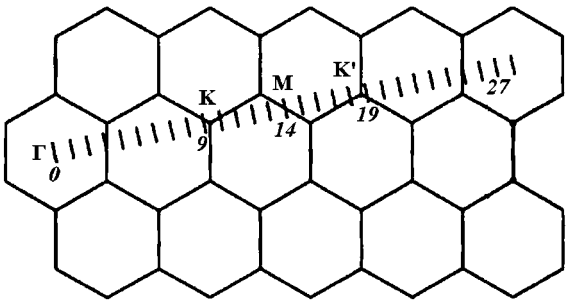

Fig. 2. The 29 replicas of the Brillouin zone of a (4,2) CNT (corresponding to the 28 subbands in the conduction or valence band) superimposed upon the reciprocal lattice of graphene. The 0-th and the 28-th replicas correspond to the same subband. The points indicated as **K** and **K**′ serve as the origins of the reciprocal space for the corresponding valleys within the EM description.

(see Fig. 2). This means that the points in the **k**-space corresponding to $\mu_1 = 11 - m$, $K_2^{(1)} = \pi/T$ and $\mu_2 = 11 + m$, $K_2^{(2)} = \pi/T$ are symmetric with respect to the **M** point. But we have already seen that such a symmetry is related to the time reversal operation (all the **M** points are equivalent). Therefore, within our model (neglecting the overlap integral), the values of $|v_y(K_2 = \pi/T)|$ coincide for the pairs of transitions v, $\mu' = 10 - m \to c$, $\mu = 11 - m$ and $v, \mu' = 11 + m \to c$, $\mu = 12 + m$. The same is true for the pairs of transitions v, $\mu' = 24 - m \to c$, $\mu = 25 - m$ and $v, \mu' = 25 + m \to c$, $\mu = 26 + m$, where all the values of μ should be taken modulo 28. Similar relations take place at $K_2 = -\pi/T$.

2. Parallel polarization

The interband *coordinate* matrix element for *parallel* polarization was found in Ref. [3] in the form

$$\langle v, \mathbf{k}'|z|c, \mathbf{k}\rangle = i\delta_{\mu,\mu'}\delta_{K_2,K_2'} \sum_{b=A,B} C_b^*(v, \mathbf{k}') \frac{\partial C_b(c, \mathbf{k})}{\partial K_2}. \quad (5)$$

Starting from this expression it is easy to reproduce the analytical result first obtained in [1].

Acknowledgements

The work of SVG was supported by the NSF under grant No. HRD-0833178.

References

[1] J. Jiang, R. Saito, A. Grüneis, G. Dresselhaus, and M. S. Dresselhaus, *Carbon* **42**, 3169 (2004).
[2] A. Zarifi and T. G. Pedersen, *Phys. Rev. B* **80**, 195422 (2009).
[3] S. V. Goupalov, *Phys. Rev. B* **72**, 195403 (2005).
[4] R. Saito, G. Dresselhaus, M.S. Dresselhaus, *Physical Properties of Carbon Nanotubes* (Imperial College, London, 1998).
[5] As a consequence of the overlap integral of the tight-binding method being neglected. See Ref. [4].
[6] This is not the case of Fig. 6 in Ref. [1] describing optical transitions in a (10, 10) armchair nanotube.

18th Int. Symp. "Nanostructures: Physics and Technology"
St Petersburg, Russia, June 21–26, 2010

Non-parabolicity of exciton dispersion in nanostructure containing thick GaAs/AlGaAs quantum well

D. K. Loginov
Physics Department, St Petersburg State University, 198504 St Petersburg, Russia

Abstract. A theory of non-parabolicity of excitonic dispersion related to the mixing of states of exciton at its motion is developed. The model is applied to calculation the polaritonic spectra of a nanostructure containing thick GaAs/AlGaAs quantum well.

Introduction

The most publications devoted to the phenomena related to the motion of exciton in both bulk crystals and nanostructures consider the energy and wave functions of exciton in framework of the model based on the effective mass approximation [1,2,3]. Such approximation results in parabolic dispersion of exciton energy. However, there is a physical mechanism, which gives rise to the deviation of excitonic dispersion from the parabolic law. Present work is devoted to investigation of non-parabolicity of excitonic dispersion related to the mixing of its ground and excited states due to the exciton translational motion in thick quantum well (QW) by the square-law terms of Luttinger Hamiltonian for hole and electron. In this work, we also present the results of calculations of reflectivity spectra for a nanostructure containing thick QW.

1. Effect of non-parabolicity

The effect under discussion is considered for a nanostructure containing the thick GaAs/$Al_{0.3}Ga_{0.7}As$ QW. We suppose that the direction of growth axis (z axis) coincides with [001] crystallografical axis. The direction of exciton propagation coincides with this axis too, i.e., $K_z = K$ and $K_x = K_y = 0$, where K is the exciton wave vector. The reflectivity spectra are calculated for normal incidence of light on the surface of nanostructure, i.e., the light propagation coincides with z axis. To calculate the reflectivity spectra, we use the model of interference of polariton waves in QW [5] generalized for the case of non-parabolic effects.

For exciton movement along z axis, the projection of generalized wave vector of electron and hole can be presented in the form:

$$\hat{k}_z^{\mathrm{e}} = \hat{p}_z/\hbar + \frac{m_{\mathrm{e}}}{M}\hat{K}\,,$$
$$\hat{k}_z^{\mathrm{h}} = -\hat{p}_z/\hbar + \frac{m_{\mathrm{h}}}{M}\hat{K}\,.$$

Here $\hat{p}_z = -i\hbar\partial/\partial z$ is the operator of momentum of relative motion of the electron and hole, where z is the z-component of distance between the electron and hole in exciton. The operator of wave vector of exciton is: $\hat{K} = -i\partial/\partial Z$, where Z is the coordinate of excitonic center of mass. $M = m_{\mathrm{e}} + m_{\mathrm{h}}$ is the exciton mass, where m_{e} and m_{h} are the electron and the hole masses, respectively.

Using expressions for generalized wave vector in excitonic Hamiltonian [2,4], it is possible to get, apart of standart terms

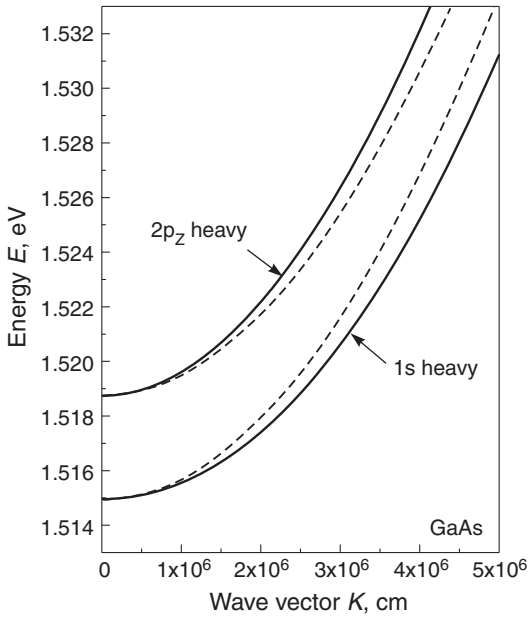

Fig. 1. Dispersion of $1s$ and $2p_z$ heavy excitons calculated with and without considering their mixing (solid and dashed curves, accordingly).

of Hamilton operator, also operator:

$$\hat{V} = \frac{2\hbar\hat{K}\,\hat{p}_z}{M}\,,$$

which gives rise to the non-parabolicity of excitonic dispersion. Calculations show that the matrix element of operator $\hat{V}$ is maximal in the case of mixing $1s$- and $2p_z$- excitonic states and has the form:

$$V = 0.28\left(\frac{\hbar^2}{a_{\mathrm{B}}M}\right)K\,, \qquad (1)$$

where a_{B} is the Bohr radius of exciton and K is the exciton wave vector. Numerical coefficient 0.28 is determined by the straightforward calculation of matrix element of operator $\hat{V}$ at hydrogen-like wave functions of $1s$ and $2p_z$ exciton states. For any other excited states such matrix element is equal to zero or negligibly small. The approximation used allows us to obtain the equation for dispersion of $1s$ and $2p_z$ excitonic states with taking into account their mixing:

$$E_{1s,2p_z} = \frac{1}{2}\left\{\left(E_{1s}^{(0)} + E_{2p_z}^{(0)}\right) \mp \sqrt{\left(E_{1s}^{(0)} - E_{2p_z}(0)\right)^2 + 4|V|^2}\right\}, \quad (2)$$

where

$$E^{(0)}_{1s,2p_z} = E_g - R^{1s(2p_z)}_{ex} + \hbar^2 K^2/(2M)$$

are the energies of non-mixed $1s$ and $2p_z$ states of exciton. Here E_g is the band gap and $R^{1s(2p_z)}_{ex}$ is the Ridberg energy for $1s$ and $2p_z$ excitonic states, accordingly. As seen from Eq. (2), the wave-vector dependence of excitonic energy is non-parabolic.

The dispersion curves are calculated using material parameters of GaAs crystal taken from the literature: $\varepsilon_0 = 12.56$ [7], $m_{hh} = 0.45m_0$ [8], and $m_e = 0.066m_0$ [9]. The Bohr radius and exciton mass calculated by the use of these parameters are: $a_B = 11.5$ nm and $M_h = 0.52m_0$, respectively. We have calculated the dispersion curves near the Γ point of Brillouin zone ($K = 0$).

The results of calculations of non-parabolicity effect are presented in Fig. 1. As seen, the mixing of $1s$ and $2p_z$ states leads to noticeable modification of dispersion. The dispersion curve for $1s$-exciton becomes more flat and the dispersion for $2p_z$-exciton becomes more sharp comparing to that calculated without taking into account the mixing of excitonic states. It also seen from the figure that the deviation of dispersion curves calculated with and without mixing $1s$ and $2p_z$ states reaches 2 meV in the spectral range considered.

2. Reflectivity spectra

To calculate the reflectivity spectrum with taking into account the non-parabolicity, it is necessary to include the excitonic contribution into the crystal polarizability as it was done, e.g., in Ref. [4]:

$$p(\omega, K) = \frac{E_{2p_z}\varepsilon_0\hbar\omega_{LT}}{E_{1s}E_{2p_z} - |V|^2}, \qquad (3)$$

where $\hbar\omega_{LT}$ is the longitudinal-transverse splitting of exciton and ε_0 is the background dielectric constant. For calculation of reflectivity spectra we have used this expression and the dispersion equation for normal modes [5]:

$$\varepsilon(\omega, K) = (cK/\omega)^2,$$

where $\varepsilon(\omega, K) = \varepsilon_0 + p(\omega, K)$, c is the light velocity, and ω is the frequency of incident light. To calculate the interference of polariton waves in many layer nanostructure, one should use the Maxwell's boundary conditions (BC) and the additional boundary conditions (ABC) of Pekar [5]. The Maxwell's BC is related to the continuity of electrical and magnetic fields of light at each interface of nanostructure. According to ABC of Pekar [5], the sum of contributions of excitonic states to polarizability of crystal should be zero at the interfaces of QW because the exciton can not escape from the QW layer.

To estimate the influence of this effect on spectrum of reflectivity of nanostructure we have performed the calculation of such spectra with and without mixing of ground and excited states for the nanostructure GaAs/AlGaAs, which consists of a GaAs layer with thickness 200 nm sandwiched between the AlGaAs barrier layers. One of the barriers has the thickness 100 nm and another one is semi-infinite. Similar to Ref. [5], we use the approximation of infinitely high barriers. The value of the longitudinal-transverse splitting for GaAs is $\hbar\omega_{LT} = 0.09$ meV [10].

Results of these calculations are presented in Fig. 2. It is seen that there is a noticeable shift of spectral oscillations

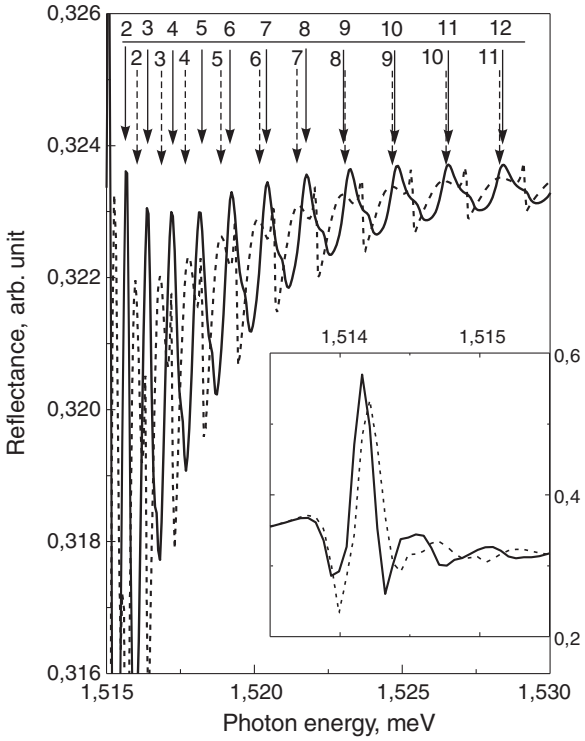

Fig. 2. Reflectivity spectra of nanostructure GaAs/AlGaAs calculated with and without considering the non-parabolisity effect (solid and dashed curves, accordingly). Dashed and solid arrows show the spectral positions of maxima of oscillations in these spectra. The inset shows a fragments of these spectra in spectral range near the main maxima of reflectivity.

with the same number. E.g., the spectral position of the 11-th oscillation differs in both the spectra at about one quasi-period of the oscillations. Hence, the effect of non-parabolicity is sufficient and could be observed experimentally.

Acknowledgements

The author thanks I. V. Ignatiev for fruitful discussions. This work has been supported by the Russian Foundation for Basic Research and by the Russian Ministry of Science and Education.

References

[1] R. S. Knox, *Theory of excitons* (Rochester, New York 1963), 219.
[2] M. Altarelli, Nunzio O. Lipari, *Phys. Rev. B* **7**, 3798 (1973).
[3] A. P. Silin, *Phys. Solid State* **13**, 1789 (1971).
[4] D. K. Loginov, *Phys. Solid State* **52**, 70 (2010).
[5] S. I. Pekar, *Kristallooptika i dobavochnye svetovye volny*, (Nauk Dumka, Kiev 1982) 178–84 (in Russian).
[6] V. M. Agranovich and V. L. Ginzburg, *Kristallooptika s uchetom prostranstvennoi dispersii* (Nauka, Moskava 1965) 58 (in Russian).
[7] M. S. Skolnik, A. K. Jain, R. A. Stradling, J. Leotin, J. C. Ousset, S. Askenazy, *J. Phys. C: Solid State Phys.* **9**, 2809 (1976).
[8] R. Romestain and C. Weisbuch, *Phys. Rev. Lett.* **45**, 2067 (1980).
[9] P. Lawaetz, *Phys. Rev. B* **4**, 3460 (1971).
[10] G. Fishman, *Solid State Commun.* **27**, 1097 (1978).

18th Int. Symp. "Nanostructures: Physics and Technology"
St Petersburg, Russia, June 21–26, 2010

STM images of sub-surface acceptors in GaAs: importance of hybridization with surface states and splitting due to surface strain

J.-M. Jancu[1], J.-Ch. Girard[1], M. O. Nestoklon[1,2], A. Lemaître[1], F. Glas[1], Z. Z. Wang[1] and *P. Voisin*[1]

[1] CNRS-Laboratoire de Photonique et de Nanostructures, route de Nozay, F-91460, Marcoussis, France
[2] Ioffe Physical-Technical Institute, St Petersburg, Russia

Abstract. We report on tight binding simulations of Scanning Tunneling Microscopy images of neutral acceptor states associated with subsurface Mn dopant in GaAs. Calculations evidence the role of hybridization of the impurity state with surface states, and the splitting of the fourfold degenerate acceptor state due to surface buckling.

Recently, observation of individual sub-surface acceptor states in various III–V semiconductors has attracted considerable attention, due to the result novelty and the completely unexpected triangular or butterfly-like shapes revealed by the experiments. Understanding in full details the observations turned out to be a real challenge for theory, since both the atomic-scale texture of the images and their overall shape must be explained. There is so far a general consensus with Terzov and Hamann's theory stating that STM measures the local density of state (LDOS) at the tip position (a fraction of a nm from the sample surface), at the tip Fermi energy. However, implementing the theory for specific cases in semiconductor physics is difficult. It is known from surface physics studies performed in the 90's, combining STM and ab initio modelling, that a few specific surface states (involving dangling bonds) extend in the vacuum and dominate the LDOS at the tip position. These studies also revealed the importance of the (110)-surface elastic relaxation known as the "buckling": surface atoms near a (110) surface are displaced by more that 10% from their nominal position in the bulk crystal, under the effect of a surface stress that is analogous to a $[1\bar{1}0]$ uniaxial stress. On the other hand, ab initio methods cannot handle the large (10^4 to 10^5 atom) supercells (SC) needed to account for a relatively large object such as an acceptor state.

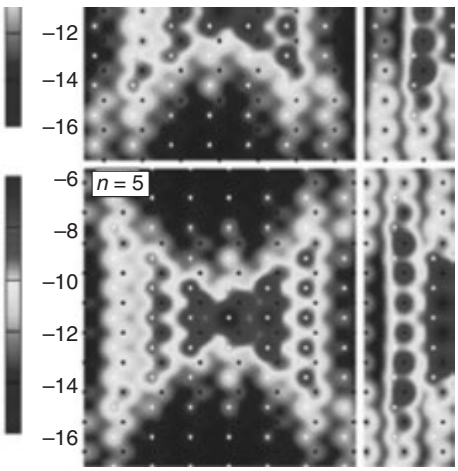

Fig. 1. Bulk impurity cross section (BICS) (left), simulated STM images (SSTM) (center), and experimental STM images (right) of a Mn neutral acceptor located n monolayers ($n = 3$ to 5) below the (110) surface. BICS is calculated in a (110) plane, n atomic planes away from the impurity, and SSTM 2 Å above the surface. SSTM LDOS is multiplied by 10^4 with respect to BICS. As (white) and Ga (black) positions on the surface are indicated.

In brief, theory must be able to account precisely for bulk and surface properties at an atomistic level, and to handle large supercells. We have applied the advanced spds* tight-binding (TB) model to this problem. It is known that this model has not only a unique ability to reproduce the full band structure of bulk semiconductors, but also the potential to describe vacuum states, as a result of "numerical completeness" of the spds* basis. As a happy surprise, we found that it reproduces the ab initio calculation of surface states, provided that the buckled atomic positions are taken into account: in stark contrast with ab initio methods, atomistic methods like TB do not provide atomic positions and need them as an input. Next, we solved the bulk acceptor state problem by considering a large supercell with a single dopant atom near the center. Acceptor binding energy results from the cooperation of the Coulomb potential and a localized potential known as the "central cell correction". The minimum supercell size increases roughly as the cube of the Bohr radius. For GaAs:Mn, the binding energy (Bohr radius) is of the order of 100 meV (1 nm) and a 10^4 atom SC is confortable, while for an hydrogenic acceptor like GaAs:Be (binding energy of 30 meV), a 10^5 atom SC is required. The corresponding increase of TB hamiltonian size is x1000, and the latter case is still slightly beyond the limits of our code capability. Interestingly, we are able to determine the TB on-site energies and two-center transfer integrals for the dopant atom from comparisons of TB and ab initio band structures of binary compounds (e.g. parameterizations of GaAs and MnAs provide all the information for GaAs:Mn, except for a single "band offset" parameter). The full atomic configuration of the dopant is taken into account, but so far we did not include details of the exchange interaction responsible for the magnetic properties of Mn-doped semiconductors. In the crudest approximation, exchange simply adds a 20 meV spin-dependent contribution to binding energy, that can be renormalized in the central-cell potential. The left column in Fig. 1 shows the calculated cross section of the 4-fold degenerate Mn acceptor state LDOS in the bulk material, in (110) planes at various distances from the impurity center, while the right column shows STM images measured on different acceptors located at corresponding depths below the surface. The central column shows our simulated STM images, calculated for a supercell including a free surface. While the overall shape and size of the images are similar, one can note important differences: the atomic texture of bulk acceptor LDOS shows contributions of both Ga and As atoms forming zig-zag chains along the $[1\bar{1}0]$ direction, with a clear predominance of As (70% of LDOS). This is what should be expected for any localized state formed out of low-lying

valence states in a III–V polar semiconductor. In contrast, the STM images reveal only the sub-lattice of Ga atoms on the surface, which (under extreme simplification) simply points to the fact that only surface states associated with empty Ga dangling bounds have a significant LDOS in the vacuum. The simulation reproduces the experimental trend, proving that the image is actually formed by hybridization of the surface and impurity states: what is measured experimentally is the LDOS of the surface state component of an hybrid state. The second major difference between left and right columns concerns the asymmetry of the butterfly: in bulk, it has a stronger left wing, and the opposite in STM images. This astonishing feature (similar shape but opposite symmetry) reflects a strong difference in electronic structure: the bulk neutral acceptor state has fourfold degeneracy, which is lifted by the interaction with the surface strain field. In the STM image simulation, we find a very large splitting (40 meV) between the ground and excited acceptor state, reflecting the important role of the surface buckling. Even at room temperature, only the ground state can be occupied by a hole and seen via tunnel injection of an electron. Interestingly, the simulated STM image of the ground state ressembles the experimental image, while the sum of ground and excited state LDOS is nearly identical to the bulk acceptor LDOS.

References

[1] G. Mahieu *et al*, *Phys. Rev. Lett.* **94**, 026407 (2005).
[2] A. M. Yakunin *et al*, *Phys. Rev. Lett.* **92**, 216806 (2004).
[3] J.-M. Jancu *et al*, *Phys. Rev. Lett.* **101**, 196801 (2008).

18th Int. Symp. "Nanostructures: Physics and Technology"
St Petersburg, Russia, June 21–26, 2010

Vibrationally-assisted tunneling and STM-controlled motions and reactions of single adsorbates

S. G. Tikhodeev[1] and H. Ueba[2]

[1] A. M. Prokhorov General Physics Institute, Moscow, Russia
[2] Division of Nanotechnology and New Functional Material Science, Graduate School of Science and Engineering, University of Toyama, Toyama 930-8555, Japan

Abstract. A recently proposed mechanism of vibrationally-assisted tunneling (VAT) to control the motions and reactions of single adsorbates with the scanning tunneling microscope tip is discussed and illustrated on several experimental examples. It is found that the VAT mechanism can play a key role in the adsorbate dynamical motion when the energy of the relevant vibrational excitation is lower than the barrier for motion or reaction.

With the tip of a scanning tunneling microscope, it is possible to move a single molecule on a surface or to control a few molecules chemical reaction. This revolutionary discovery of the early 1990's [1] caused an avalanche of beautiful experiments, theoretical work, and practical implementations (see reviews, e.g., in [2,3]). An important mechanism of the motion is the vibrational ladder climbing in the potential well [4,5,6]. This involves a heating of the molecule through inelastic electron tunneling from tip to substrate through the molecule. This mechanism allows the molecule to overcome the energy barrier leading to motion.

An analysis [7] of the recent experiments on water/heavy water dimer motions [8] and cobalt hopping on Cu surfaces [9] shows that in order to describe quantitatively the tip induced adsorbate motion, rather than simply considering above barrier motion, it is important to include single atom or molecule quantum tunneling through the barrier.

Figure 1 explains the main idea of VAT. The left potential well is the initial position of the reactant (adatom or molecule). It is separated by a potential barrier from another potential well, or just from the onset of a free motion. In a simple truncated harmonic potential, the reaction occurs when the reactant reaches a vibrational level n_c just above the barrier [6].

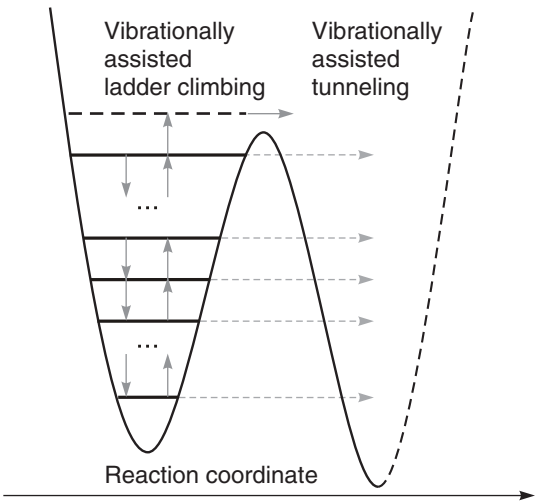

Fig. 1. Ladder climbing and descending (up and down arrows) in a truncated harmonic potential. Also shown are the quantum tunneling processes from the ground state as well as from the higher excited levels (dashed arrows).

If, however, the barrier is semi-transparent for quantum tunneling, there will be a tunneling component in the overall reaction rate. In the equilibrium situation at low temperatures, although the tunneling rates γ_m are expected to grow exponentially with vibrational level number m because of a lower and a narrower barrier, the role of tunneling from the higher levels is quenched by their exponentially decreased population. Under the STM tip, with the overheating by inelastic electron tunneling, their population grows, and the tunneling from higher excited states can make a significant impact into the overall reaction rate, thus enabling *vibrationally assisted tunneling*.

The transitions between the different vibrational levels are usually described in a truncated harmonic potential approximation by a Pauli master equation [6]. We now add tunneling processes from all levels and rewrite the Pauli master equation in a form

$$\frac{dP_0}{dt} = -\gamma_0 P_0 + \Gamma_\downarrow P_1 - \Gamma_\uparrow P_0, \quad (1)$$

$$\frac{dP_m}{dt} = -\gamma_m P_m + (m+1)\Gamma_\downarrow P_{m+1} + m\Gamma_\uparrow P_{m-1} - \left[m\Gamma_\downarrow + (m+1)\Gamma_\uparrow\right] P_m\,, \quad (2)$$

where $P_m(t)$ is the probability of finding the reactant in the vibrational state m at time t. The main quantities here are the vibrational excitation $\Gamma_\uparrow$ and deexcitation $\Gamma_\downarrow$ rates between the nearest-neighboring levels and the tunneling rates γ_m from the m-th level. The latter are assumed to grow fast with m because of narrower and lower barriers for higher levels. Here, we assume no backward tunneling.

Within the so-called adsorbate induced resonance model for electron-vibration coupling, the excitation and deexcitation rates are given by [6]

$$\Gamma_\uparrow = n_{\rm T}(\hbar\Omega)\gamma_{\rm v} + \Gamma_{\rm iet},\ \Gamma_\downarrow = [n_{\rm T}(\hbar\Omega)+1]\gamma_{\rm v} + \Gamma_{\rm iet}, \quad (3)$$

where $n_{\rm T}(\omega) = (e^{\hbar\omega/k_{\rm B}T}-1)^{-1}$ is the stationary phonon distribution function in the absence of bias voltage, and $\gamma_{\rm v}$ is the vibrational damping rate. Here the vibrational generation rate $\Gamma_{\rm iet}$ is given in the low-temperature limit $k_{\rm B}T \ll \hbar\Omega$ by [11]

$$\Gamma_{\rm iet}(V) \simeq \frac{\Gamma_{\rm t}}{\Gamma_{\rm s}}\,\gamma_{\rm eh}\,\frac{eV-\hbar\Omega}{\hbar\Omega}\,\theta(eV-\hbar\Omega), \quad (4)$$

where $\gamma_{\rm v} \approx \gamma_{\rm eh} \approx 2\pi\chi^2\rho_{\rm a}^2(E_{\rm F})\hbar\Omega$ is the vibrational damping due to electron-hole pair excitations in the substrate (metal),

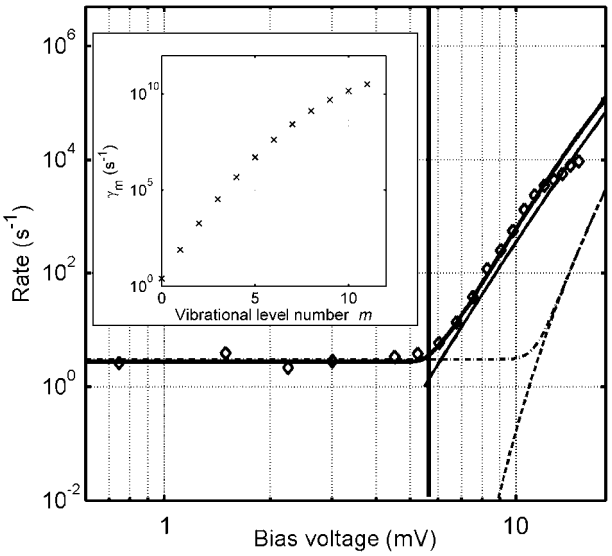

Fig. 2. Bias voltage dependence of cobalt fcc to hcp sites hopping on Cu(111) at $T = 2.3$ K. Diamonds are the experimental data [9]. Dashed line is the low temperature ladder climbing process, $R \propto (eV - \hbar\Omega)^{n_c}$, dash-dotted line is a sum of this ladder climbing process with the tunneling rate from the ground state only. Black solid line is $R \propto (eV)^{n_c}$ as in [9,10]. Grey solid curve shows the result of our simulation within the VAT model. Vertical solid line is the vibrational energy $\hbar\Omega$. Insert shows the assumed tunneling rates γ_m for Co on Cu(111).

χ is the vibrational-adsorbate coupling constant. The general condition for validity of our model is $\gamma_v \gg \Gamma_{iet}(V)$.

In case if the tunneling γ_m is negligibly small, terms with γ_m in Eq. (1) are omitted, and the quasistationary solution of the Pauli master equation gives the Arrhenius type formula for reaction rate, governed by the effective temperature due to the vibrational overheating [6]. In the low-temperature limit $k_B T \ll \hbar\Omega$ this gives a power-law dependence for the reaction rate

$$R(V) \propto \left(|eV| - \hbar\Omega\right)^{n_c} \theta\left(|eV| - \hbar\Omega\right). \qquad (5)$$

However, if the barrier is thin, and the vibration levels can be emptied via atomic quantum tunneling as described in Eqs. (1,2), the power law Eq. (5) no longer holds. There is no simple Arrhenius-type solution in this case. The master equation can be easily solved numerically if the tunneling rates γ_m are known (or can be estimated).

An example of a situation when tunneling from many excited levels may be involved arises as a result of reinterpretation of results on the hopping rate for cobalt adatoms on a Cu(111) surface [9], see in Fig. 2. The nonlinear hopping rate between the fcc and hcp site as a function of bias voltage has been explained using the vibrational heating mechanism, which seems to reproduce [9, 10] the power-law dependence of a reaction rate on bias voltage. Below the threshold voltage corresponding to excitation of the vibrational mode responsible for the lateral movement, the constant transfer rate of about 10 s^{-1} has been observed in [9], independent on the bias voltage, suggesting the quantum tunneling in spite of the large mass of the Co atom.

Figure 2 shows the measured Co transfer rate $R(V)$ between hcp and fcc sites on the substrate at $T = 2.3$ K (diamonds). The black solid line shows the over-barrier motion rate $R \propto (eV)^{n_c}$ with $n_c = 11$ as in [10]. It seemingly reproduces the experiment but fails to account for a finite $\hbar\Omega = 5.4$ meV. Such power law holds only in the limit $eV \gg \hbar\Omega$. This was the case of Xe hopping between a substrate and tip [6], but it cannot be applied here. The correct dependence Eq. (4) $R \propto (eV - \hbar\Omega)^{n_c}$ is shown as the dashed line and it is very far from the experimental data. Adding the constant tunneling rate from the ground state (dash-dotted line) does not still improve the situation.

However, the VAT mechanism can nicely reproduce the experimental results (thick solid grey line in Fig. 2). The following parameters were used: $\gamma_{eh} \approx 10^{10}$ s^{-1} [10] $\hbar\Omega = 5.4$ meV [9,10], $\Gamma_s = 18$ meV, $\Gamma_t = 6$ meV (providing a correct tunneling resistance of the STM contact), $\varepsilon_a = -70$ meV, $\chi = 14.8$ meV. As to the tunneling rates used (see inset in Fig. 2), we estimated them using a simple WKB formula $\gamma_m = \nu \exp\{-d_m/\hbar\sqrt{(2MV_{B,m}}\}$ (M, d_m and $V_{B,m}$ are the mass of a Co atom, distance and barrier for tunneling from all the vibrational states $m = 0, 1, \ldots, n_c - 1$, respectively; the prefactor ν was chosen to fit the experimental value [9] of γ_0).

It can be understood from Fig. 2, that single over-barrier climbing just cannot reproduce the measured $R(V)$ dependence in the vicinity of the threshold (if not to decrease $\hbar\Omega$ from 5.4 to ≈ 2 meV, which contradicts to many other data), whereas VAT works surprisingly well.

Acknowledgements

This work has been supported in part by the Russian Foundation for Basic Research and the Russian Academy of Science (program #27).

References

[1] D. M. Eigler and E. K. Schweizer, *Nature* **344**, 524 (1990).
[2] W. Ho, *J. Chem. Phys.* **117** 11033 (2002).
[3] H. Ueba *et al*, *Chapter 3 in book "Current-Driven Phenomena in Nanoelectronics"*, ed. T. Seideman, World Scientific, Singapore, 2010.
[4] S. Gao *et al*, *Solid State Commun.* **84**, 271 (1992).
[5] R. E. Walkup *et al*, *Phys. Rev. B* **48**, 1858 (1993).
[6] S. Gao *et al*, *Phys. Rev. B* **55**, 4825 (1997).
[7] S. G. Tikhodeev and H. Ueba, *Phys. Res. Lett.* **102** 246101 (2009).
[8] T. Kumagai *et al*, *Phys. Rev. Lett.* **100**, 166101 (2008).
[9] J. A. Stroscio and R. J. Celotta, *Science* **306**, 242 (2004).
[10] K. Liu and S. Gao, *Phys. Rev. Lett.* **95**, 226102 (2005).
[11] S. G. Tikhodeev and H. Ueba, *Phys. Rev. B* **70**, 125414 (2004).

18th Int. Symp. "Nanostructures: Physics and Technology"
St Petersburg, Russia, June 21–26, 2010

Conductivity of polymers with charge injection doping

A. N. Ionov[1] and R. Rentzsch[2]

[1] Ioffe Physical-Technical Institute, St Petersburg, Russia
[2] Institut für Experimentalphysik, Freie Universität Berlin, 14195 Berlin, Germany

Abstract. We discuss different models of conduction, which could explain the occurrence of superconducting current in polymer.

Introduction

The importance of conductive polymers is based on such properties as their high conductivity (nearly metallic conductivity at room temperature), plasticity, low weight, small energy consumption for production, simple processing technology, and low cost. At the moment, the main technological process for producing high conductivity in conjugated polymers is by chemical and/or electrochemical doping. The induced electrical conductivity is permanent, until the carriers are chemically compensated or until they are purposely removed by "undoping" [1]. At first sight, there is every reason to be optimistic about achieving metallic conductivity or even superconductivity with this technology. This is because upon doping, the bond lengths change so that charge can be stored in solitons, polarons, or bipolarons. Thus the electron-phonon interaction that is responsible for superconductivity in conventional metals can also be an important effect in metallic polymers. Doubly charged bipolarons can be thought of as analogous to real-space Cooper pairs and are able to produce superconductivity [2]. However, superconductivity has not yet been observed in doped conjugated polymers. The reason for this may be connected with the strong disorder of the polymer macromolecules due to chemical doping and/or electrochemical doping with a high concentration of the dopants. High doping levels may play a destructive role there by spatial segregation of polymer chains. As a result, the metallic islands may be surrounded by a dielectric matrix. Probably for this reason, true metallic conductivity is not yet observed at low temperatures.

1. Experimental

However, there exists another possibility for doping, which is based on charge injection from metallic electrodes into the polymer. There are two techniques for charge doping. In the first case, in an ideal polymer structure, electrons reside in the LUMO (lowest unoccupied molecular orbital) and/or holes reside in the HOMO (highest occupied molecular orbital) bands only, as long as a biasing voltage is applied. In the second one, charge doping occurs due to electrification effect [3]. It is well known that all isolators and non-conducting polymers always accept a charge when they are in contact with metals. It has been shown that polymer electrification occurs due to the localized energy states situated in the polymer in an energy interval close to the Fermi energy of the majority of the metals [3,4]. Negative charge is captured by empty traps which are located close to the polymer surface, whereas positive charge appears if filled traps deliver electrons to the metal electrodes. The traps are the result of various kinds of defects, such as chemical groups, cavities and entanglements, unsaturated bonds. Polarization of the polymer matrix by randomly distributed localized charges causes both a shift and a broadening of the orbital energies, so that some HOMO-levels lie above the Fermi level of the contact metal and some LUMO-levels below it. This means that contact between a metal and a polymer causes electrons from the metal to transfer to the LUMO of the polymer, or electrons may transfer from the HOMO to the metal [5]. As a result, energy states with energies close to the Fermi energy of most metals form between HOMO and LUMO orbitals of macromolecules. Since the depth of charge penetration due to electrification may reach several micrometers, the energy states should extend to the same depth within polymer films. Thus, the appearance of metallic conductivity in polymers is inevitably linked to this electrification process; consequently, the high conductivity in metal-polymer-metal structures occurs only over a length scale of up to some micrometers in zero fields. Experiments have shown that the higher the plasticity of the polymer material, the greater the thickness of the polymer film in which the effect of metal conductivity makes itself evident. Electrification of polymers is not possible if the polymer has a permanent conductivity, for example due to doping. Effective electrification of polymers for switching to the metallic state is possible only if they are nonconductive before the metal-polymer contact is made.

2. Low temperature conductivity

Fig. 1 shows the temperature dependence of the polyamidine film placed between different electrodes. As is seen from Fig. 1, there is no difference between $R(T)$-dependences with polymer and without one.

In the case of superconducting electrodes supercurrent flows through the polymer. Earlier it has been shown that the classical

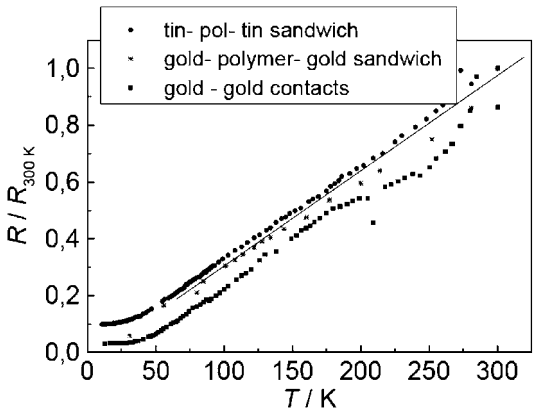

Fig. 1. $R(T)$-dependence for polyamidine with film thickness about one micron placed between different electrodes in relative units and $R(T)$-dependence for a Au/Au electrodes; $\rho_{\mathrm{Me}}(300\ \mathrm{K}) \approx 10^{-6}\ \Omega/\mathrm{cm}$; $\rho_{\mathrm{Me}}(4.2\ \mathrm{K}) \approx 10^{-8}\ \Omega/\mathrm{cm}$.

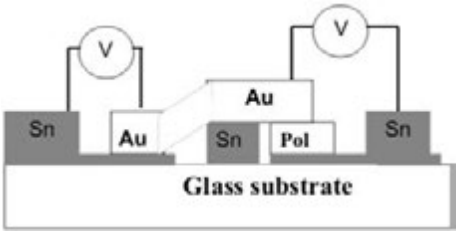

Fig. 2. Experimental set-up. Spreading resistances between Au/Sn and Au/Pol/Sn are dominant resistances and rule the $R(T)$-dependences.

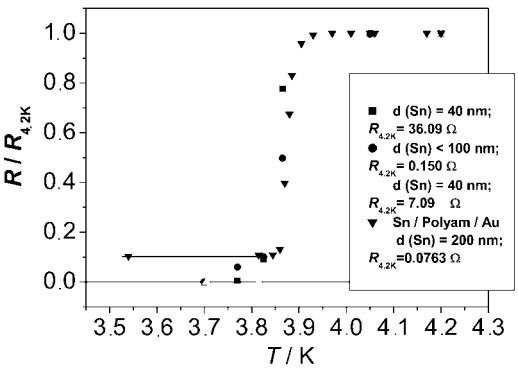

Fig. 3. $R(T)$-dependences for tin films in planar geometry with different thicknesses; $R(T)$-dependence of Sn/Pol/Au sandwich construction.

theory of the proximity effect explaining an induced superconductivity in normal metals will not agree with experimental results observed on Sn-polyamidine-Sn structures [6].

3. Discussion of the ballistic transport

In the ballistic transport regime, the mean free path of the charge carriers should be greater than the distance between the electrodes. The ballistic transport connected with coherent resonance tunneling of charge carriers through localized states in insulating barriers has been observed in different structures [7]. If the localized states are distributed uniformly in energy and are located in the middle of the band gap energy of the insulator then a Josephson current may flow through it in superconductor-insulator-superconductor structuress with linear dependence versus T [8]. At resonance tunneling effect the Cooper pairs from the superconductor should penetrate into the normal metal and conversely in superconductor-polymer-normal metal structure (S-P-N), free electrons from the normal metal should penetrate into the superconductor as has been observed in a direct contact between a metal and a superconductor. If the thickness of the superconducting metal is much less than the thickness of the normal metal, suppression of its superconductivity should be observed [9]. For detection of ballistic transport in polymer channels, we compared the T_c suppression of tin films with different thicknesses in the range of 40–800 nm in direct contact with a gold electrode which had a thickness of 30 μm, to those in a sandwich of tin through a polyamidine film with a thickness of about 2 μm and a back electrode of gold of 30 μm thickness (Fig. 2).

The value of T_c for Sn-Pol-Au sandwich sandwiches is the same as for Sn films (Fig. 3). The thickness of the tin films evaporated in vacuum was verified by means of an atomic-force microscope. Typical experimental $R(T)$-dependences in

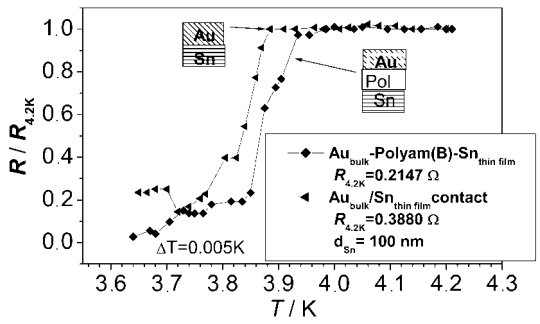

Fig. 4. Experimental results of the comparison of structures described in Fig. 2. Film thickness Sn is 100 nm. For Au/Sn contact T_c shift is about 0.05 K versus Au/Pol/Sn sandwich construction.

the vicinity of T_c for Sn-Au and for Sn-Pol-Au sandwiches are shown in Fig. 4. The figure shows that with direct contact of the gold electrode to Sn, the beginning of the transition to the superconducting state is strongly shifted to lower temperatures, which is not observed in Sn-Pol-Au sandwiches. The shift of T_c increases with decreasing thickness of the superconducting film, as it should be for a direct contact of a superconductor with a normal metal [9]. On the other hand, if a polyamidine film was placed between the normal metal and the superconductor, the change in T_c was not observed (Fig. 4). The experimental results obtained contradict the model of ballistic transport due to resonance tunneling in polymer channels if we consider that the amount of normal electrons which arrive at the superconductor tin film is comparable to the amount of Cooper pairs. In the opposite case, its influence would be too small and therefore the T_c shift is inappreciable in superconductor-polymer-normal metal sandwich structures.

But it yet not argued that the polymer has intrinsic superconductivity. The reason is that a number of facts consistent with the model of resonant tunneling. For example there is the dependence of the absolute value of the critical current on the magnitude of the order parameter of superconducting electrodes. This, for example, may be connected with to polymer-metal interface. The more theoretical and experimental work needs to be done for a complete understanding the existing of superconducting properties in the polymer.

Acknowledgements

We thank Prof. M. Yu. Kupriyanov and Prof. W. D. Brewer for discussion of the experimental results.

References

[1] A. J. Heeger, *Rev. Mod. Phys.* **73**, 681 (2001).
[2] D. M. Eagles, *Phil. Mag.* **85**, 1931 (2005).
[3] J. Lowell and A. C. Rose-Innes, *Adv. Phys.* **29**, 947 (1980).
[4] C. B. Duke and T. I. Fabish, *Phys. Rev. Let.* **37**, 1075 (1976).
[5] C. B. Duke *et al*, *Phys. Rev. B* **18**, 5717 (1978).
[6] A. N. Ionov and R. Rentzsch, *Ann. Phys.* **18**, 963 (2009).
[7] V. V. Kuznetsov *et al*, *Phys. Rev. B* **54**, 1502 (1996).
[8] A. A. Golubov *et al*, *Rev. Mod. Phys.* **76** (2), 411–469 (2004).
[9] J. J. Hauser *et al*, *Phys. Rev.* **136**, A637–A641 (1964).

18th Int. Symp. "Nanostructures: Physics and Technology"
St Petersburg, Russia, June 21–26, 2010

Spatial effects of Fano resonance in local tunneling conductivity in the presence of impurity on semiconductor surface

V. N. Mantsevich and N. S. Maslova
Moscow State University, Faculty of Physics, Chair of Quantum Electronics, Moscow, 119991, Russia

Abstract. We report the results of local tunneling conductivity spatial distribution detailed theoretical investigations in the presence of impurity atom for a wide range of applied bias voltage. We observed Fano resonance in tunneling conductivity as a result of interference between resonant tunneling channel through impurity energy level and direct tunneling channel between the tunneling contact leads. It was shown that interference between tunneling channels leads to modification of tunneling conductivity form measured by the scanning tunneling microscopy/spectroscopy (STM/STS) depending on the distance value from the impurity.

Introduction

Localized states formed by individual impurity atoms play an important role in tunneling processes in small size junctions and usually determine the behavior of tunneling characteristics in STM/STS contacts. Influence of different impurities on the tunneling conductivity was widely studied experimentally and theoretically [1,2,3]. Most of the experiments were carried out with the help of STM/STS technique [4,5], but experimental measurements provides no information weather electron transport occurs coherently or incoherently. Answer to this question can be found from the comparison between experimental and theoretical results. Usually theoretical calculations of interference effects between resonant and direct tunneling channels correspond to the case when metallic STM tip is positioned above the impurity atom [6,1]. However experimentally tunneling conductivity can be measured far away from the impurity [7] and just this case is quite of great interest because it gives an opportunity to initialize impurities types. So in our work we present formula, which describe spatial distribution of local tunneling conductivity in vicinity of impurity in the case of interference between tunneling channels.

1. The suggested model and main results

We shall analyze tunneling processes between semiconductor surface and metallic STM tip. We model semiconductor surface by 1D atomic chain which consists of similar atoms with energy levels ε_1 and similar tunneling transfer amplitudes $\Im$ between the atoms. Distance between the atoms in the atomic chain is described by the parameter a. Atomic chain includes impurity with energy ε_d, tunneling transfer amplitude from impurity atom to the nearest atoms of the atomic chain is τ. Tunneling conductivity is measured by the STM tip. Direct tunneling between the surface continuous spectrum states and tip states is described by the transfer amplitude t. Tunneling from the impurity energy level to the tip is described by tunneling transfer amplitude T.

The model system can be described by the Hamiltonian $\hat{H}$:

$$\begin{aligned}\hat{H} &= \hat{H}_0 + \hat{H}_{\text{imp}} + \hat{H}_{\text{tun}} + \hat{H}_{\text{tip}}\\ \hat{H}_0 &= \sum_k \varepsilon_k c_k^+ c_k + \sum_k \Im c_k^+ c_k + \text{h.c.}\end{aligned}$$

$$\begin{aligned}\hat{H}_{\text{tun}} &= \sum_{k,d} \tau c_k^+ c_d + \sum_{d,p} T c_d^+ c_p + \sum_{k,p} t c_k^+ c_p + \text{h.c.}\\ \hat{H}_{\text{imp}} &= \sum_d \varepsilon_d c_d^+ c_d; \quad \hat{H}_{\text{tip}} = \sum_p \varepsilon_p c_p^+ c_p \end{aligned} \tag{1}$$

Indices k and p label the states in the left (semiconductor) and right (tip) lead, respectively. Index d indicates that impurity electron operator is involved. $\hat{H}_0$ is a typical Hamiltonian for atomic chain with hoppings without any impurities. $\hat{H}_{\text{tun}}$ describes resonant tunneling transitions from the impurity state to the semiconductor and metallic tip and direct transitions between the tunneling contact leads. $\hat{H}_{\text{imp}}$ corresponds to the electrons in the localized state formed by the impurity atom in the atomic chain, $\hat{H}_{\text{tip}}$ describes conduction electrons in the metallic tip.

We shall use non-equilibrium diagram technique in our investigation of tunneling conductivity spatial distribution [8]. Tunneling current from the right lead in this formalism can be determined as (we set charge $e = 1$):

$$I(V) = \text{Im}\left(i \sum_{k,p} \int d\omega \left(T G_{pd}^{<} + t G_{pk}^{<} \right) + \text{h.c.} \right). \tag{2}$$

Substituting the correspondent expressions for the $G^<$ functions to the tunneling current equation 2, performing summation over k and k' and taking imaginary part we get the expression for the local tunneling conductivity:

$$\begin{aligned}\frac{dI}{dV} &= \sqrt{\gamma_{kp}\gamma_{kd}\gamma_{pd}\nu_k^0}\, Re G_{dd}^{\text{R}} \cos(2k(\omega)x)\\ &+\gamma_{kp}(\gamma_{kd}+\gamma_{pd})\nu_k^0 \text{Im} G_{dd}^{\text{R}} \cos(2k(\omega)x)\\ &+\frac{\gamma_{kd}\gamma_{pd}}{\gamma_{kd}+\gamma_{pd}} \text{Im} G_{dd}^{\text{R}} + \frac{\gamma_{kd}^2\gamma_{pd}\gamma_{kp}(\omega-\varepsilon_d)\cos(2k(\omega)x)}{((\omega-\varepsilon_d)^2+(\gamma_{kd}+\gamma_{pd})^2)^2}\\ &+\gamma_{kp}\nu_k^0\left(1+\frac{(\omega-\varepsilon_d)^2+\gamma_{kd}^2-\gamma_{pd}(\omega-\varepsilon_d)}{(\omega-\varepsilon_d)^2+(\gamma_{kd}+\gamma_{pd})^2}\right)\\ &\times\left(\frac{(\omega-\varepsilon_d)^2+(\gamma_{kd}+\gamma_{pd})^2(1-\cos(2k(\omega)x))}{(\omega-\varepsilon_d)^2+(\gamma_{kd}+\gamma_{pd})^2}\right.\\ &\left.+\frac{\gamma_{pd}(\gamma_{pd}+\gamma_{kd})\cos(2k(\omega)x)}{(\omega-\varepsilon_d)^2+(\gamma_{kd}+\gamma_{pd})^2}\right),\end{aligned} \tag{3}$$

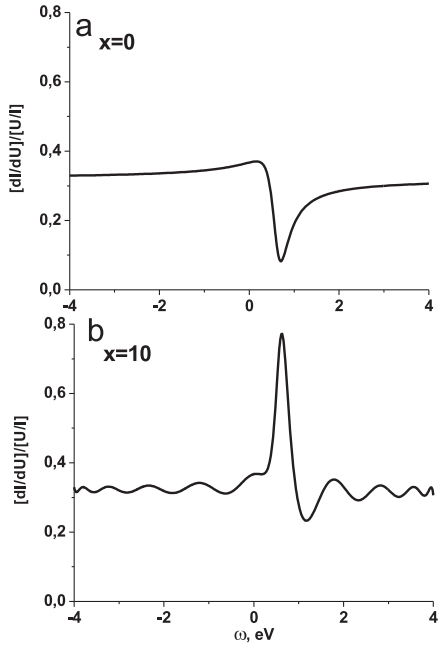

Fig. 1. Local tunneling conductivity as a function of applied bias voltage calculated for different values of the distance x from the impurity atom along the atomic chain. For all the figures values of the parameters $a = 1$, $t = 0.40$, $T = 0.25$, $\tau = 0.35$, $\Im = 1.00$, $\varepsilon_d = 0.60$, $\nu_k^0 = 1$ are the same.

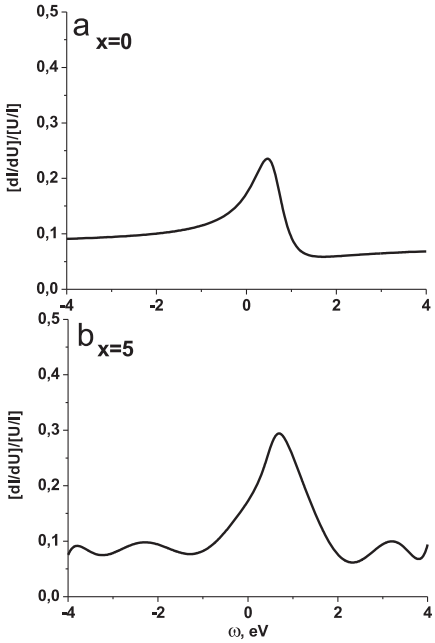

Fig. 2. Local tunneling conductivity as a function of applied bias voltage calculated for different values of the distance x from the impurity atom along the atomic chain. For all the figures values of the parameters $a = 1$, $t = 0.20$, $T = 0.40$, $\tau = 0.50$, $\Im = 1.00$, $\varepsilon_d = 0.60$, $\nu_k^0 = 1$ are the same.

where impurity retarded Green's function is defined by the expression:

$$G_{dd}^{\mathrm{R}} = \frac{1}{\omega - \varepsilon_d - i(\gamma_{kd} + \gamma_{pd})}. \qquad (4)$$

Relaxation rates γ_{kd}, γ_{pd} are determined by electron tunneling transitions from localized states to the leads k and p continuum states and relaxation rate γ_{kp} corresponds to direct tunneling transitions between k and p continuum states $\sum_p T^2 \mathrm{Im} G_{pp}^{0\mathrm{R}} = \gamma_{pd}$; $\sum_p t^2 \mathrm{Im} G_{pp}^{0\mathrm{R}} = \gamma_{kp}$; $\sum_k \tau^2 \mathrm{Im} G_{kk}^{0\mathrm{R}} = \gamma_{kd}$.

ν_k^0 is unperturbed density of states in semiconductor. Expression for $k(\omega)$ is determined from the dispersion law of the 1D atomic chain.

Tunneling conductance as a function of applied bias voltage for different values of distance from the impurity and different values of tunneling transfer amplitudes is shown on Figures 1 and 2. Figure 1 corresponds to the case when direct tunneling channel transfer amplitude t exceeds resonant tunneling channel transfer amplitudes through the impurity energy level T and τ. In this case tunneling conductivity calculated above the impurity (Fig. 1a) shows Fano line shape due to interference between resonant and nonresonant tunneling channels. Dip is formed in tunneling conductivity when applied bias voltage is equal to the impurity energy level position.

Figure 2 shows tunneling conductance as a function of applied bias voltage in the case when resonant tunneling channel transfer amplitudes through the impurity energy level T and τ exceed transfer amplitude of direct tunneling channel t. Formation of asymmetric peak in tunneling conductivity calculated above the impurity (Fig. 2a) in the resonance can be seen in the tunneling conductivity in this case. With increasing of distance value resonant peak still exists but it's shape changes due to the effects caused by the interference between tunneling channels (Fig. 2b).

In this work we have studied the influence of interplay between the resonant tunneling channel through the impurity energy level and direct tunneling channel between the leads of tunneling contact on local tunneling conductivity form. It was found that value of the distance from the impurity leads to formation of special features in tunneling conductivity (resonant dip or peak). When direct tunneling channel transfer amplitude exceeds resonant tunneling channel transfer amplitudes through the impurity energy level tunneling conductivity calculated above the impurity has Fano line shape. With increasing of the distance from the impurity a series of dips are formed in local tunneling conductivity in spite of a dip or a peak exists in the resonance. We derived replacement of the dip by the peak as a result of interference between the direct and resonant tunneling channels.

Acknowledgements

This work was supported by RFBR grants and by the National Grants for technical regulation and metrology.

References

[1] J. Konig *et al*, *Phys. Rev. Lett.* **76**, 1715 (1996).
[2] U. Fano, *Phys. Rev.* **1244**, 1866 (1961).
[3] J. Gores *et al*, *Phys. Rev. B* **62**, 2188 (2000).
[4] R. Dombrowski *et al*, *Appl. Phys. A* **66**, S203–S206 (1998).
[5] J. Inglesfield *et al*, *Condens. Matter* **12**, L489–L496 (2000).
[6] W. Hofstetter *et al*, *Phys. Rev. Letters* **87**, 156803 (2001).
[7] V. Madhavan*et al*, *Science* **280**, 567 (1998).
[8] L. V. Keldysh, *Sov. Phys JETP* **20**, 1018 (1964).

18th Int. Symp. "Nanostructures: Physics and Technology"
St Petersburg, Russia, June 21–26, 2010

MgB_2-based tunnel junctions and their characteristics

V. E. Shaternik[1], S. Yu. Larkin[2], M. A. Belogolovskii[3] and A. P. Shapovalov[1]

[1] G. V. Kurdyumov Institute for Metal Physics, National Academy of Sciences of Ukraine, Kiev, Ukraine
[2] Scientific and Industrial Concern 'Nauka', 03148 Kiev, Ukraine
[3] Donetsk Institute for Physics and Engineering, National Academy of Sciences of Ukraine, 83114 Donetsk, Ukraine

Abstract. Experimental data for Josephson junctions based on MgB_2 and Mo-Re thin superconducting films as well as their theoretical analysis are presented and discussed in the context of the device practical applications.

Perspective [1] as qubits, Josephson MgB_2–oxide–Mo-Re alloy, Mo-Re alloy–oxide–Pb, and Mo-Re alloy–normal metal–oxide–normal metal–Mo-Re alloy junctions have been fabricated and studied. Thin (50–100 nm) Mo-Re superconducting films were deposited on Al_2O_3 substrates by using a dc magnetron sputtering of Mo-Re target. MgB_2 superconducting layers of the 50–100 nm thickness are deposited on the Al_2O_3 substrates as well but in this case e-beam evaporation of boron and thermal coevaporation of magnesium was used. Normal metal (Sn, Al, Mg) thin films were deposited on the Mo-Re films surfaces by thermal evaporation of metals in vacuum and oxidized to form oxide barriers within the junctions. Quasiparticle I-V curves of the fabricated junctions have been measured in a wide range of voltage biases. To investigate the transparency spread of the device barriers, computer simulations of the measured quasiparticle I-V characteristics have been performed in the framework of a model taking into account multiple Andreev reflections at double-barrier junction interfaces. It is shown that the junctions studied can be modelled as highly asymmetric double-barrier Josephson junctions with a great difference between the two barrier transparencies [2,3,4]. The main features of the numerical simulation of I-V curves and their comparison with measured characteristics are presented and discussed.

The $I_c(T)$ characteristics, measured for the Josephson heterostructures with different thicknesses of a metal layer s and exposure dose E, essentially deviate from well-known Ambegaokar–Baratoff and Kulik–Omelianchuck $I_c(T)$ theoretical curves due to the proximity effect caused by a comparatively high value of s (up to 100 nm). We study theoretically two extreme limits: a clean and a dirty limit for the interlayer between superconducting electrodes and discuss thermal stability of the junctions characterizing it with the temperature derivative $dI_c(T)/dT$. A combined experimental and theoretical analysis of the problem provides a way for understanding, controlling and improving the design of Josephson devices based on MgB_2 and Mo-Re thin superconducting films in order to enhance their reliability.

Additionally, we have studied an effect of a microwave 60 GHz irradiation on the measured I-V characteristics. We have observed clear Shapiro steps in the curves and present their theoretical interpretation.

References

[1] A. I. Braginski *et al*, *J. Appl. Phys.* **60**, 2058 (1986).
[2] V. Shaternik *et al*, *J. Phys.: Conf. Ser.* **97**, 012243 (2008).
[3] V. Shaternik *et al*, *Int. J. Modern Phys.* **23**, 3520 (2009).
[4] I. P. Nevirkovets *et al*, *Appl. Phys. Lett.* **88**, 212504 (2006).

18th Int. Symp. "Nanostructures: Physics and Technology"
St Petersburg, Russia, June 21–26, 2010

The Kondo effect and coherent transport in stacking-faults-free wurtzite InAs nanowires grown by VLS-MBE

A. V. Kretinin[1], R. Popovitz-Biro[2], D. Mahalu[1], M. Heiblum[1] and H. Shtrikman[1]

[1] Braun Center for Submicron Research, Weizmann Institute of Science, Rehovot, 76100, Israel
[2] Electron Microscopy Unit, Weizmann Institute of Science, Rehovot, 76100, Israel

Abstract. A combination of high crystalline quality of wurtzite InAs nanowires grown by the VLS-MBE technique and a careful fabrication of nanowire-based FET devices allowed us to observe a variety of phenomena associated with mesoscopic coherent transport. For a weakly pinched conducting channel the conductance exhibits well-pronounced Kondo peaks some of them reaching the conductance unitary limit. Also Kondo effect with even number of electrons attributed to a zero-magnetic field singlet-triplet transition of the ground state has been observed. At higher gate voltages when the channel is fully open we observe the Fabry–Pérot type conductance oscillations. The length of the coherent conductance channel deduced from the period of the oscillations is in agreement with the physical length of the device.

Introduction

Rapidly expanding field of semiconductor nanowires grown by the gold-assisted vapor-liquid-solid (VLS) mechanism [1] brings promises of new materials and devices into the fields of quantum transport [2] and photonics [3]. The semiconductor nanowires synthesized by VLS are unique for their large aspect ratio which normally exceeds 100 and makes them interesting objects for studying 0D and 1D mesoscopic transport [2, 4]. InAs nanowires have gained particular interest partially due to the relative simplicity of formation of reliable ohmic contacts but mainly due to large expected electron mobility and strong bulk spin-orbit coupling. Despite of all advantages InAs nanowire-base devices suffer common problem — strong disorder which reduces the mean free path and limits the possible application area of such devices to diffusive 1D conductors [5].

Because of this unfortunate limitation imposed by the disorder great deal of effort is taken to find its sources and eliminate them. Some of the disorder such as unintentional doping with contaminating elements and stacking faults are inherent to the growth process, others such as surface states and atoms/molecules adsorbed on the surface are most likely to originate from the device fabrication. The best way to avoid the unintentional doping is to use controlled clean growth environment of MBE in combination with optimal growth conditions. In addition to clean growth, extra attention should addressed to the device fabrication in order to eliminate the influence of the substrate and various molecules trapped in the vicinity of the conductance channel. This is usually achieved by fabricating the device suspended in vacuum away from the substrate [6] along with extensive postprocess cleaning.

In this report we present the results of transport measurements performed on freely suspended stacking faults-free wurtzite (WZ) InAs nanowires grown by VLS-MBE. The measured coherent transport manifests itself through the Kondo effect reaching its unitary limit [7, 8] and the Fabry–Pérot conductance oscillations [9].

1. Experimental

The stacking faults-free InAs nanowires were grown by gold-assisted VLS-MBE, on the (110) InAs substrate (Fig. 1). The fact that the grown nanowires are free of stacking-faults is confirmed by careful TEM study. After short nucleation at 500 °C growth temperature was reduced to 400 °C in order to minimized the possibility of Au incorporation during wires growth and enhance wires growth with respect to the bulk growth. As/Ga ratio was kept low to assure slow growth rate. Our intuitive explanation for the improved results is based on the individual role of In and As atoms in the growth process. We speculate that In mobility is affected by the surface roughness, while As arrival is not. Relatively uniform/flat bulk growth on (110) provides longer migration length and stability in supply of In. Low As over pressure determines a slow and stable growth rate. Under these conditions the preferred nucleation of WZ at the perimeter is maintained all along the wire growth [1].

For the single nanowire FET fabrication we used a p-type doped Si substrate with 150 nm of dry thermal SiO_2 grown on top. The nanowires were deposited from ethanol solution across narrow (490 nm) and long (20 μm) grooves chemically etched in SiO_2 so that the central part of the wire is suspended across the groove over the Si substrate and its ends are lying on the surface of the SiO_2. The Ni/Au ohmic contacts were deposited using e-beam lithography on top of the two ends of the nanowire leaving the central suspended part unaffected. The heavily p-doped substrate was used to apply the backgate voltage V_g to control the carrier density.

Transport experiments were carried out in the He^3 system at 350 mK and in the dilution refrigerator with the base temperature of about 10 mK using standard lock-in technique. During

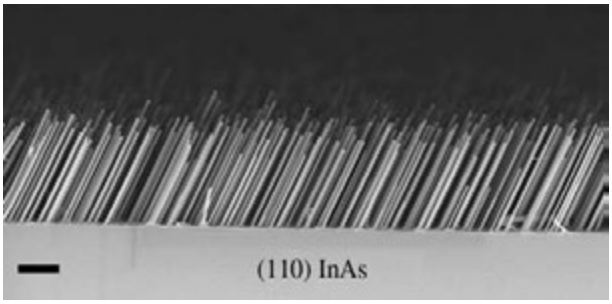

Fig. 1. SEM micrograph of InAs nanowires grown by VLS-MBE on InAs (110) substrate. The scale bar is 1 μm.

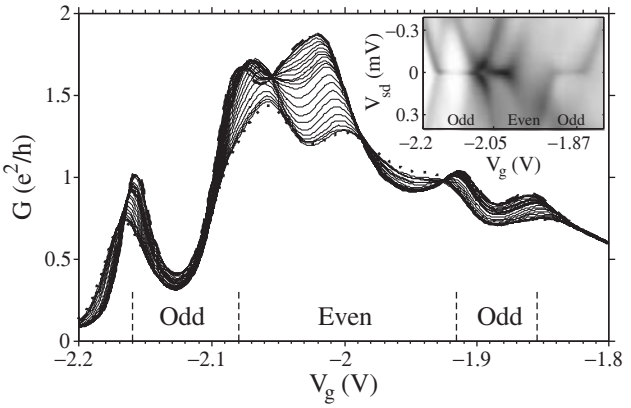

Fig. 2. The conductance G as a function of the backgate voltage V_g in the range of temperatures from 10 mK (dashed line) to 620 mK (dotted line). Insert: The greyscale plot of the conductance in $V_g - V_{\rm sd}$ plane (white corresponds to $0.2e^2/h$, black corresponds to $2.1e^2/h$).

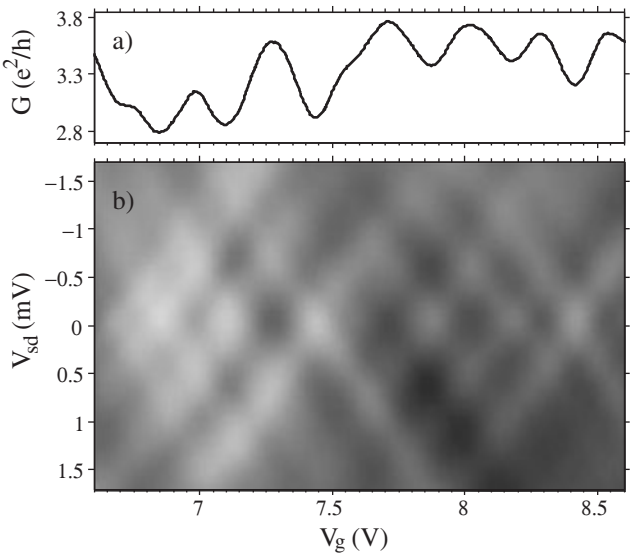

Fig. 3. a) The conductance G at positive values of backgate voltage V_g at 350 mK shows quasi-periodic conductance oscillations. b) The greyscale plot of the conductance in $V_g - V_{\rm sd}$ plane illustrates crisscrossed pattern typical for Fabry–Pérot interference in the conducting channel (white corresponds to $2.5e^2/h$, black corresponds to $4.3e^2/h$).

the experiment the sample was mounted inside the inner vacuum chamber at below 10^{-5} Torr.

2. Observation of Kondo effect

At low temperature and zero applied gate voltage V_g almost all of our nanowire devices have conduction of about $2e^2/h$. We believe that the reason for this non-zero conduction is the surface accumulation layer for electrons which is a well-known feature of InAs. As shown in Fig. 2 at negative applied gate voltage the conductance through the nanowire exhibits Coulomb blockade oscillations modified by the Kondo effect.

In addition to usual Kondo effect seen for odd number of confined electrons we observed a Kondo feature at an even filling for V_g from -2.08 to -1.99 V with significantly higher Kondo temperature as compared to neighboring odd electron number Kondo effect (see Insert in Fig. 2) with the conductance reaching its unitary limit. This even electron number Kondo is similar to one observed in lateral quantum dots at zero magnetic field [10] it also has a non-monotonic temperature dependence attributed to so-called two-stage Kondo effect [11]. We conclude that this strong even-electron Kondo effect is formed due to the gate voltage controlled singlet-triplet transition of the ground state of the nanowire quantum dot [12].

3. Fabry–Pérot type conductance oscillations

At positive voltages on the backgate the conductance of the nanowire shows an increase with quasi-periodic oscillations superimposed on it (Fig. 3a). The conductance plotted as a function of the gate voltage and source-drain bias revealed crisscrossed pattern of bright lines corresponding to minima of the conductance (Fig. 3b). This pattern originates from the Fabry–Pérot interference of electrons at the Fermi level bouncing between weakly backscattering ohmic contacts. Similar pattern is usually observed in ballistic carbon nanotubes [9]. The estimate of the length L of the interferometer from the gate voltage period of oscillations $\Delta V_g \approx 0.25$ V and the capacitance of the backgate $C_g^{\rm L} \approx 8.2$ pF/m gives $L \approx 320$ nm, which is of the order of the lithographically defined length of the nanowire device (490 nm). Similar oscillations but with longer period in V_g were observed on devices with shorter (280 nm) conducting channel. It is worth mentioning that the backgate capacitance $C_g^{\rm L}$ is taken from the electrostatic simulation made for a metallic nanowire device without taking into account the finite density of states in the nanowire and it is most likely that $C_g^{\rm L}$ is overestimated, resulting in underestimation of L. Observation of well-pronounced Fabry–Pérot conductance oscillations is a direct proof of the phase coherent transport with very small if any difference in the length of the electron's forward and backward paths along which the phase is acquired. From this fact we can conclude that the transport is not diffusive otherwise the oscillations would be smeared out.

References

[1] V. G. Dubrovskii *et al*, *Phys. Rev. B* **78**, 235301 (2008).
[2] L. Samuelson *et al*, *Phys. E* **25**, 313 (2004).
[3] E. D. Minot *et al*, *Nano Lett.* **7**, 367 (2007).
[4] J. Xiang *et al*, *Nature* **441**, 489 (2006).
[5] S. Dhara *et al*, *Phys. Rev. B* **79**, 121311 (2009).
[6] J. Nygård and D. H. Cobden, *Appl. Phys. Lett.* **79**, 4216 (2001).
[7] T. S. Jespersen *et al*, *Phys. Rev. B* **74**, 233304 (2006).
[8] W. G. van der Wiel *et al*, *Science* **289**, 2105 (2000).
[9] W. Liang *et al*, *Nature* **411**, 665 (2001).
[10] A. Kogan *et al*, *Phys. Rev. B* **67**, 113309 (2003).
[11] W. G. van der Wiel *et al*, *Phys. Rev. Lett.* **88**, 126803 (2002).
[12] M. Pustilnik and L. I. Glazman, *Phys. Rev. Lett.* **87**, 216601 (2001).

18th Int. Symp. "Nanostructures: Physics and Technology"
St Petersburg, Russia, June 21–26, 2010

Electronic transport through contact of correlated quantum wire with leads of higher dimension

S. N. Artemenko and P. P. Aseev

V. A. Kotel'nikov Institute for Radioengineering and Electronics of Russian Academy of Sciences, Moscow, Russia

Abstract. We study theoretically electronic transport through a contact of a quantum wire with 2D or 3D leads and find that if the contact is not a smooth and adiabatic one, then the conduction is strongly suppressed, and above a threshold voltage the DC current $\bar{I}$ is accompanied by coherent oscillations with frequency $f = \bar{I}/e$. The effect is related to inter-electronic repulsion and interaction of the DC current with Friedel oscillations near the sharp contacts.

In contrast to 2D and 3D systems where basic electronic properties are usually well described by Fermi-liquid picture, 1D systems of interacting electrons are better described in terms of the Luttinger liquid (LL) with bosonic excitations. LL is an alternative to Fermi liquid in 1D (for a review see Ref. [1]). Interaction greatly affects electronic transport in 1D systems, in particular, even isolated impurities strongly suppress conductivity resulting in power-law I-V curves [1]. This was confirmed experimentally in various 1D systems including semiconductor quantum wires [2] and was described in terms of macroscopic tunneling between different minima of a periodic potential inclined by external bias. The periodic potential is associated with Friedel oscillations (FO) induced by impurity. It was shown recently [3] that the power-law regime takes place only at small enough voltages, while above a threshold voltage a dynamical regime of conduction starts in which the DC current is accompanied by oscillations with frequency $f = \bar{I}/e$. The effect is induced by the inter-electronic repulsion. Interesting effects can be expected also at the contacts between quantum wires and electrodes of higher dimension, that is between the Fermi liquid and electrons in strongly correlated state. This problem is not still studied and, typically, the boundary conditions derived by Egger and Grabert [4] for ideal adiabatic contacts are used. These conditions were derived only for expectation values and cannot be used to study fluctuations which are very important in 1D systems. Further, real contacts are not necessarily adiabatic, and one can expect that reflections of electrons from the contacts may result in FO and, hence, in effects similar to the case of impurities. Here we derive boundary conditions for the non-adiabatic contacts, study conditions for formation of the FO near the contacts, and show that conductivity is affected by FO resulting in the dynamic regime of conduction that resembles the Josephson effect and the Coulomb blockade.

We derive boundary conditions using the ideas of the scattering approach (for a review see Ref. [5]). We describe a 1D conductor by a potential well at $|x| < l/2$ with a channel forming a quantum wire along the x-axis. The wire is attached to two symmetric 2D or 3D metallic leads. The region of the conducting wire is considered as a scattering barrier. Since the results are very similar for both contacts we consider here for brevity the left lead only. In the leads we, without loss of generality, assume that longitudinal, along the x axis, and transverse motion are separable. The longitudinal and transverse motion in the left lead is characterized by the wave vectors k and the energy $\varepsilon_1 = \frac{k^2}{2m}$, the total energy being $\varepsilon = \varepsilon_1 + \varepsilon_n$ where n is an index labeling transverse energies. We assume that electrons in the leads do not interact. Then we solve equation of motion for electronic field operators in the leads with the boundary conditions at $|x| = l/2$ demanding the continuity of both the field operators and their derivatives. This enables us to express the solution for the n-th transverse channel in terms of the field operator $\hat{\psi}_\mathrm{b}$ at the boundary

$$\hat{\psi}(x) = \hat{\psi}_\mathrm{b} \cos kx + \frac{1}{k}\,\partial_x \hat{\psi}_\mathrm{b} \sin kx\,. \qquad (1)$$

This expression contains the incident and outgoing waves. The incident wave, $\hat{\psi}_\mathrm{in}(x)$ is determined by the state of the lead far from the barrier. Therefore, $\hat{\psi}_\mathrm{in}(x)$ must not depend on the properties of the barrier and must have an equilibrium form. Equating the incoming part of Eq. 1 to the equilibrium form we find

$$\hat{\psi}_\mathrm{b} - \frac{i}{k_1}\partial_x \hat{\psi}_\mathrm{b} = \frac{4\pi}{\sqrt{L}} \sum_{k>0} \hat{c}_{n,k}\,\delta\left(\varepsilon - \varepsilon_n - \frac{k^2}{2m}\right), \qquad (2)$$

where $k_1 = \sqrt{2m(\varepsilon - \varepsilon_n)}$ and $\hat{c}_{n,k}$ is an annihilation operator of the electron in the lead with the longitudinal momentum k in the transverse channel n of the lead.

Equation (2) relates the field operator at the boundary to the equilibrium states of the transverse channel n at energy ε in the lead. But what we need is a relation between the boundary value of the field operator of the lowest transverse eigenstate of the conducting wire and the incident states of the lead. Therefore, we project relations (2) to the eigenstates of the wire. But as the transverse states of the lead are not the eigenstates of the wire we obtain an infinite system of linear equations for boundary values of the field operators $\hat{\psi}_j$ of transverse eigenstates j of the wire

$$\hat{\psi}_j - \sum_{j'} i r_{jj'} \partial_x \hat{\psi}_{jj'} = \hat{Z}_j\,, \qquad (3)$$

where Z_j is the projection of the l.h.s. of Eq. (2) to the transverse state j of the wire. We need to find a solution of Eq. (3) for the state $j = 0$ describing the lowest subband that is responsible for electronic transport in the wire, while the states $j > 0$ with higher transverse energies do not contribute to transport. It can be shown that the relation we need has a form

$$A(\varepsilon)\hat{\psi}_0 + B(\varepsilon)\partial_x \hat{\psi}_0 = \frac{1}{\sqrt{V}} \sum_{\mathbf{n}=n,k>0} \gamma(k)\hat{c}_\mathbf{n} 2\pi\,\delta\,(\varepsilon - \varepsilon_\mathbf{n})\,, \qquad (4)$$

where exact expressions for coefficients in Eq. (4) depend on the shape of the contacts.

Coefficients in (4) are not arbitrary. As the fields $\hat{\psi}_0$ must obey the commutation relations we can find a relation between the coefficients. Further, it is instructive to relate the coefficients to such physical parameters of the system as a transmission probability t for the incident electrons. Therefore, we consider the system of non-interacting electrons for which we can solve easily equations for field operators inside the wire and demand fulfilment of commutation relations and calculate conductivity. This enables us to reduce the number of undetermined constants. Then we transform the equations to time representation taking into acount that we consider the states close to the Fermi energy, ε_F. As it is more convenient to express boundary conditions in terms of physical values, we multiply Eq. (4) and its Hermitian conjugate and find

$$\frac{v_F}{t}\hat{\rho} \pm \hat{j} + v_F f \hat{\rho}_F = \frac{1}{V}\sum_{\mathbf{n},\mathbf{n}'} \hat{c}^+_{\mathbf{n}'}\hat{c}_{\mathbf{n}} e^{i(\varepsilon_{\mathbf{n}'}-\varepsilon_{\mathbf{n}})t}\,, \qquad (5)$$

where $\hat{j}$ and $\hat{\rho}$ are operators of current and of perturbations of smooth part of charge density, $\hat{\rho}_F$ is the $2k_F$-component of charge density (FO), f is a number of order unity if the transmission probability t is not close to unity and $f \simeq \sqrt{2(1-t)}$ if $1-t \ll 1$. Thus FO disappear if the contacts are adiabatic.

In order to check conditions (5) we considered a wire with non-interacting 1D electrons with contacts of simple nearly adiabatic geometry with a potential step at the contact. In this case we can use adiabatic approximation in the leads and matched the solution in the leads with the exact solution in the wire. It was found that condition (5) yields correct result for conductivity $G = tG_0$ in accordance with Landauer formula ($G_0 = e^2/h$ is the conductivity quantum).

To take into account interaction we consider a spinless repulsive LL characterized by parameter $K_\rho < 1$ ($K_\rho = 1$ for non-interacting electrons) measuring strengh of the short-range interaction that describes gated quantum wires where the long-range part of the interaction is screened by 3D gate electrodes. As the LL theory is valid when all energies of the problem are small compared to the Fermi energy, we consider nearly adiabatic contacts, $1-t \ll 1$, then $f \ll 1$ and the energy related to the FO in (5) is small compared to the Fermi energy. Further, following Ref. [4] we take into account screening of the potenial of the leads by 3D gates. Then we express Eq. (5) in terms of the bosonic displacement field $\hat{\Phi}(t,x)$ of the LL theory. This field determines operators of charge density and current in the wire

$$\hat{\rho} = -\frac{1}{\pi}\frac{\partial\hat{\Phi}}{\partial x} + \frac{k_F}{\pi}\cos\left(2k_F x - 2\hat{\Phi}\right), \quad \hat{I} = \frac{e}{\pi}\partial_t\hat{\Phi}\,.$$

Finally, we obtain for the left and right contacts

$$\frac{v_F}{K_\rho^2}\partial_x\hat{\Phi}_\rho \mp \partial_t\hat{\Phi}_\rho + f\varepsilon_F\cos\left(2\hat{\Phi}_\rho \mp k_F l\right) = \hat{P}_{L,R}\,. \qquad (6)$$

The last term in the l.h.s. of (6) is related to FO.

The average value $\langle\hat{P}_A\rangle$ is related to the voltage bias $U_{L,R}$ at the respective contact and the boundary conditions for expectation value $\phi \equiv \langle\hat{\Phi}\rangle$ reads

$$\frac{v_F}{K_\rho^2}\partial_x\phi \mp \partial_t\phi + d\sin\left(2\phi_{L,R} + \alpha\right) = U_{L,R}\,, \qquad (7)$$

where $d = f\varepsilon_F\sqrt{\langle\cos 2\hat{\varphi}\rangle^2 + \langle\sin 2\hat{\varphi}\rangle^2}$, $\alpha = \arctan\frac{\langle\cos 2\hat{\varphi}\rangle}{\langle\sin 2\hat{\varphi}\rangle}$. In case of an adiabatic contact $t = 1, d = 0$ and the equation reduces to boundary conditions derived by Egger and Grabert [4].

Correlation function for the operator $\langle P_A\rangle$ with A=R,L has the form

$$\langle\{P_A(\omega),\, P_{A'}(\omega')\}\rangle = 4\pi^2\delta_{AA'}\omega\coth\frac{\omega}{2T}\,\delta\left(\omega+\omega'\right)\,. \qquad (8)$$

The operator $\hat{\Phi}(t,x)$ obeys wave equation (see [1]) with velocity of excitations $v = v_F/K_\rho$. Now, having equation of motion and conditions (6–8) we can calculate current through the wire. This is not simple in a general case because the boundary conditions contain the term which is non-linear in $\hat{\Phi}$. We solve the problem using the Gaussian model for fluctuations. Strictly speaking, the fluctuations are not Gaussian, but our approach can be justified strictly in the limit of strong inter-electronic repulsion and in the limit of large voltages/currents when the non-Gaussian part of fluctuations is small. This can be shown similarly to the case of the current passing through an impurity in a 1D conductor [6].

We found that at low voltages $V < V_T \simeq f^{\frac{1+K_\rho}{1-K_\rho}}\varepsilon_F$ applied to the contacts the linear conductivity in long quantum wires is suppressed by FO provided $K_\rho < 1$. Within the Gaussian approximation for fluctations we obtain zero current at such voltages, but if one takes into account fluctuations of solitonic type responsible for macroscopic tunneling then in analogy to the case of impurity one gets power-law I-V curves. This regime is destroyed by thermal fluctuations at temperatures $T > T_0 \simeq eV_T/k_B$ and does not exist in short wires $l < l_0 \simeq \frac{\hbar v_\rho}{eV_T}$.

At voltages $V > V_T$ the dynamic regime of conduction resembling the Josephson effect starts. Current in the dynamic regime was calculated in the limit of large voltages. It was found that in this limit the regime of coherent generation takes place if the electronic repulsion is strong enough, $K_\rho < 1/3$, the critical value here is different from that at low voltages and from the critical value 1/2 in the case of impurity. The current contains the DC part $\bar{I} = VG_0 - I_{nl}$, and the AC part oscillating with frequency $\omega_0 = \frac{2\pi\bar{I}}{e} \approx \frac{eV}{\hbar}$

$$I_{ac} \simeq 2\pi G_0 d_0 K_\rho^2/\left(K_\rho^2 + \tan^2\frac{\omega_0 t_l}{2}\right),\; I_{nl} \simeq 2\pi\left(\frac{V_T}{V}\right)I_{ac}\,.$$

Oscillations of both non-linear part of DC current and of AC current on voltage are induced by multiple reflections of current pulses from the contacts.

References

[1] T. Giamarchi, *Quantum Physics in One Dimension*, Clarendon Press, Oxford (2003).
[2] O. M. Auslaender *et al*, *Science* **308**, 88 (2005).
[3] S. N. Artemenko, S. V. Remizov, D. S. Shapiro, *Pis'ma v ZhETF* **87**, 792 (2009) [*JETP Lett.* **87**, 692].
[4] R. Egger, H. Grabert, *Phys. Rev. B* **58**, 10761 (1998).
[5] Ya. M. Blanter, M. Buttiker, *Phys. Rep.* **336**, 1 (2000).
[6] S. N. Artemenko, D. S. Shapiro, R. R. Vakhitov, S. V. Remizov, *Journal of Physics: Conference Series* **193**, 012119 (2009).

18th Int. Symp. "Nanostructures: Physics and Technology"
St Petersburg, Russia, June 21–26, 2010

Photo-induced conductance fluctuations in mesoscopic Ge/Si systems with quantum dots

N. P. Stepina[1], E. S. Koptev[1], A. V. Dvurechenskii[1], I. V. Osinnyukh[1], A. I. Nikiforov[1], D. Gruetzmacher[2], J. Moers[2] and J. Gerharz[2]

[1] Institute of Semiconductor Physics, 630090 Novosibirsk, Russia
[2] Institute of Bio- and Nanosystems, Forschungszentrum Julich GmbH 52425 Julich, Germany

Abstract. We studied the evolution of electron transport in a strongly localized quantum dot system under small photon flux. Mesoscopic fluctuations of conductance in hopping regime via two-dimensional array of Ge/Si-quantum dots were observed in samples patterned laterally in the decananometer range. This phenomenon enables the detection of single photoexcited carriers in a wide wavelength range. The distribution function of the fluctuations in ln G was analyzed in a frame of the model of conduction via exponentially rare, quasi-one-dimensional chains of hops.

Introduction

The aim of this work is to show the proof of working principle of a single photon detector (SPD) based on a dense array of Ge quantum dots (QD), which is operating at the telecommunication wavelength between 0.9 and 1.55 μm. Self-organizing growth techniques that includes a carefully controlled strained layer epitaxy at low (300 °C) temperature allows the formation of high density array of QDs with nanometer dimensions and homogeneous size distribution. The areal density of nanoclusters (4×10^{11} cm^{-2}) is large enough for the charge transport through such a system at low ($\leq$ 20 K) temperatures being dominated by hole hopping between dots [1]. The idea of the SPD is based on the discovery that the hopping conductance in a densely packed array of Ge islands crucially depends on these occupation of the QDs by holes [2]. It was shown that the conductance is changed non-monotonously by more than six orders of magnitude upon variation of the average QD filling factor ranging from 0.5 to 6 holes per dot. Thus, changing the QD charge state by illumination should cause a change in the conductance of the array. In macroscopic samples with Ge/Si QDs both negative and positive photoresponce depending on dot filling factor were observed [3] under illumination with wavelength between 0.9–1.55 μm. Long-time conductance dynamics (typically, 10^2–10^4 seconds at $T = 4.2$ K) has been revealed as well as after switch on and switch off the illumination, displaying a sluggish temporal dependence. It was found that the residual photoconductance could persist for several hours after the light switching off. Using these phenomena for mesoscopic samples when the sample size is too small for self-averaging taking place, one can observe the physical processes corresponding to the unit events of network transformation. It is well known that the particular arrangement of localization centers within a sample produces conductance fluctuations as a function of external influences which are unique to each mesoscopic sample. Thus, under weak illumination, a step-like change in the hopping conductance should be expected due to the charge changing by one carrier in one of the dots.

We present the experimental results of photo-induced conductance fluctuations in nanometer size QDs structures with different width and length of conductance channels. To observe significant changes of the conductance under variation the dot occupancies during illumination, initial number of holes per dot was chosen to be 1.75. To supply holes to the dots, a boron δ-doped Si layer was inserted 5 nm below the Ge QDs layer. Electron-beam lithography was used to create the conductance channel, with their width and length being changed in the range of 50–1500 nm. Quasi-one-dimensional, square and short samples were prepared and measured. The system was excited by fiber coupled laser with 1.55 μm wavelength and 1 mW power value. To get extremely small light intensity, initial laser power was attenuated up to 60 dB. Four-point scheme was used to measure the resistance traces. The temperature stability was controlled using Ge thermometer. Time-resolved measurements were carried out using transport dewar at temperature 4.2 K and small currents (10^{-12}–10^{-14} A) allowing to be in Ohmic regime.

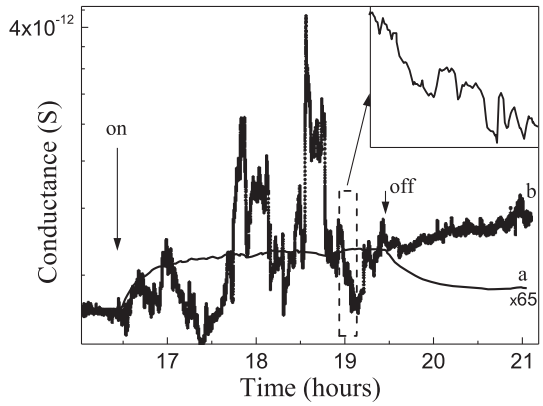

Fig. 1. Conductance evolution of the mesoscopic sample (l = 100 nm, w = 70 nm) under illumination with 1.55 μm light wavelength at 30 dB attenuation. Line a) depicts the conductance vs time for corresponding macroscopic sample. Inset is enhanced part of conductance curve.

1. Results and discussion

Fig. 1 shows the typical conductance traces for mesoscopic sample with w = 70 nm width and l = 100 nm length of the conductive channel under 30 dB attenuation of laser light. In the large-area sample measured in parallel (curve a), illumination causes a monotonic change of the conductance with time. Unlike macroscopic structures, in small-area samples, where conduction takes place through a mesoscopic size hopping network, the conductance evolves with time (curve b) in discrete

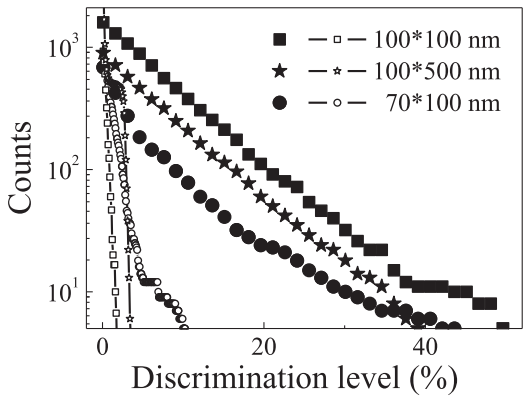

Fig. 2. Counts per 10000 seconds of conductance tracks at different discrimination levels for the samples with different channel size in dark (open symbols) and under illumination with 30 dB laser attenuation (full symbols).

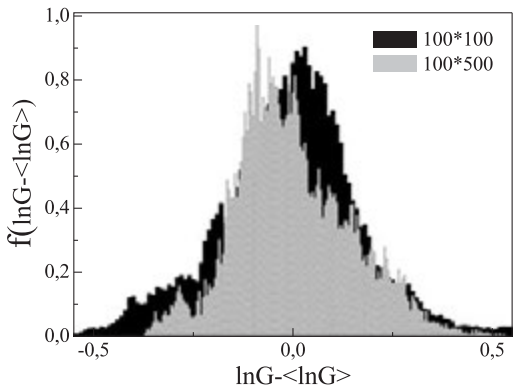

Fig. 3. Distribution functions of the $\ln G - \langle \ln G \rangle$ for two samples with different channel length under illumination.

steps (inset to Fig. 1). We suggest that these steps correspond to changing of the individual QDs filling factor due to absorption of a single photon. Under 1.55 μm wavelength illumination, every photon absorbed in QD excites one electron from the dot, caused the addition of a single positive charge into dot. Generated electrons can be captured by another dot; as the result, the redistribution of carriers among different QDs occurs. New potential landscape leads to a new conductive path providing change of the conductance with time. Due to non-monotonic dependence of hopping conductance on QD occupancy, we observed both positive and negative steps in the conductance traces. Relaxation processes that are usually responsible for the appearance of downward steps [4], have negligible contribution due to persistent photo-conductance effect, which is a characteristic feature for the structures under study [3].

Experimental kinetics data for dark and photo-excited parts of the time-resolved conductance were analyzed in the frame of count rates at different threshold (discrimination) level. The rate of steps was estimated by the following simple procedure. We found the extrema of the current derivative (with respect to time) responsible for the fluctuations and than determined the value of ΔG between every two extrema. The results of such procedure for three samples with different conductive channel sizes under 30 dB attenuation of the laser light are shown in Fig. 2. The range of conductance tracks was chosen to be 10000 seconds. The sample a) corresponds to the quasi-one-dimensional structure ($l = 500$ nm, $w = 100$ nm), sample b) is a square one ($l = 100$ nm, $w = 100$ nm) and sample c) has a smallest channel width ($l = 100$ nm, $w = 70$ nm). One can see that the dark noise doesn't exceed 4–10% (open symbols in Fig. 2) whereas the conductance fluctuations under illumination reach more than 50% of magnitude. The largest number of fluctuations is observed in square sample. This sample is also characterized by the average conductance which is one order of magnitude higher that in the long channel case ($l = 500$ nm). This result is the evidence that localized states which shunt the infinite cluster appear at small chanell length. Since the probability for the formation of such a chain is an exponential function of l, a small change in the channel length should lead to a substantial change in conductance.

To understand the geometric structure of percolation network responsible for the conductance fluctuations, ensemble distribution of the resistance should be analyzed. When the channel length is reduced becoming less than the correlation radius of the critical network, the conduction proceeds via variable-range hopping along exponentially rare, almost rectilinear isolated chains of hops. Owing to the exponential spread of resistance of different chains, only a limited number of channels will carry the main part of current. The conductance is determined by so-called 'optimal chains', i.e. chains for which the product of their conductance and probability of formation is maximum [5]. If the sample area is so small that average number of optimal chains over its area is less than unity, the mesoscopic phenomena are observed in conductance measurements. As the channel length increases, the probability for the appearance of a chain with high conductance decreases. The current flow through a structure becomes determined by the set of the lowest-resistance chains. As a results, the peak position of the distribution function of the conductance among various structures should shifts toward low conductance. Indeed, such a shift of the peak position is observed when the channel length changes from 100 to 500 nm (Fig. 3).

Acknowledgements

This work was supported by RFBR (Grant No. 08-02-12095-OFI, Grant No. 10-02-00618).

References

[1] A. I. Yakimov, A. V. Dvurechenskii, V. V. Kirienko, Yu. I. Yakovlev, A. I. Nikiforov, C. J. Adkins, *Phys. Rev.* **B 61**, 10868 (2000).

[2] A. I. Yakimov *et al*, *JETP Letters* **77**, 376 (2003).

[3] N. P. Stepina, A. I. Yakimov, A. V. Nenashev, A. V. Dvurechenskii, N. A. Sobolev, J. P. Leitao, V. V. Kirienko, A. I. Nikiforov, E. S. Koptev, L. Pereira, *Journal of Experimental and Theoretical Physics* **103** 269 (2006).

[4] J. C. Blakesley, P. See, A. J. Shields, B. E. Kardynal, P. Atkinson, I. Farrer, and D. A. Ritchie, *Phys. Rev. Lett.* **94**, 067401 (2005).

[5] M. Pollak, J. J. Hauser, *Phys. Rev. Lett.* **31**, 1304 (1973).

18th Int. Symp. "Nanostructures: Physics and Technology"
St Petersburg, Russia, June 21–26, 2010

Polarization-dependent photocurrents in graphene

M. M. Glazov[1], S. A. Tarasenko[1], E. L. Ivchenko[1], J. Karch[2], P. Olbrich[2], M. Schmalzbauer[2], C. Brinsteiner[2], U. Wurstbauer[2], D. Weiss[2], J. Eroms[2] and S. D. Ganichev[2]

[1] Ioffe Physical-Technical Institute, St Petersburg, Russia
[2] Terahertz Center, University of Regensburg, 93040 Regensburg, Germany

Abstract. Polarization-dependent dc photocurrents are observed in graphene under terahertz irradiation both at normal and oblique incidence. The phenomenological analysis shows that in ideal infinite graphene layers the photoresponse can only be caused by the photon drag effect revealing a remarkable polarization dependence. Moreover, in addition to the conventional longitudinal drag current, the radiation induces a transverse drag current sensitive to both linear and circular polarizations. The photocurrent observed at normal incidence arises due to the edges of the sample, which reduce the symmetry and cause photogalvanic effects. Microscopic theories of the photon drag effect and the edge photocurrents in graphene are developed.

Introduction

Graphene, a monolayer sheet of carbon, has been synthesized quite recently and revealed plenty of fascinating effects. The equivalence of the electron dispersion law in graphene to that of a massless relativistic particle has created enormous excitement, since relativistic experiments in a solid state environment became feasible, see e.g. Ref. [1].

Here we report that the illumination of graphene flakes by polarized radiation of a terahertz (THz) laser causes directed electric currents without any applied bias. The photoresponse reveals effects driven solely by the radiation helicity as well as those related to the linear polarization of the incident wave. Such photocurrents being well known in nanostructures have proven to be a versatile tool for studies of non-equilibrium processes yielding information on the symmetry, band structure, kinetic properties, etc. [2].

We demonstrate that the helicity driven photocurrent in graphene has two contributions of different nature. One of them appears at oblique incidence only and is an odd function of the angle of incidence. The performed theoretical analysis shows that it is caused by the circular photon drag effect, which stems from the simultaneous transfer of the linear and angular momenta of photons to free carriers. Another contribution has its maximum at normal incidence and cannot be attributed to the properties of infinite graphene. We conclude that the currents at normal incidence, both helicity-sensitive and generated by linearly polarized radiation, are related to edge effects of the finite-size samples.

1. Experimental results

The studied samples are all single-layer graphene flakes with linear sizes of $1 - 30$ μm. The structures have free carrier concentrations $n \lesssim 2 \times 10^{12}$ cm^{-2}, Fermi energies $E_F \lesssim 165$ meV, and mobilities at room temperature of the order of 2.5×10^3 cm^2/V s. The photocurrents are excited at room temperature by polarized THz radiation with the wavelength $\lambda = 118$ μm (photon energy $\hbar\omega = 10.5$ meV) and the power $P \simeq 20$ mW. The light polarization state is varied by a $\lambda/4$ plate, whose rotation results in the change of the degree of circular polarization according to $P_{\rm circ} = \sin 2\varphi$, where φ is the angle between the polarization vector of the initial laser radiation and the plate c-axis. In Fig. 1(b) the schemes of the studied samples 1 and 2 are shown. Details on samples and experiment are presented in Ref. [3].

Figure 1(a) shows the dependence of the photoresponse of sample 1 on the polarization for three different angles of incidence. The inset illustrates the experimental geometry. One can see that the substantial contribution to the total photocurrent changes its sign upon switching the radiation helicity from right- to left-handed circularly polarized light, depicted by the two arrows in Fig. 1(a).

The dependence of the photon-helicity sensitive contribution to the photoresponse on the incidence angle θ_0 is presented in Fig. 1(c). The photocurrent measured in the longitudinal geometry is almost independent on the angle of incidence. The transverse current evidently represents a superposition of two effects, even and odd in the incidence angle. An important feature of the odd contribution is that its direction is determined by the light propagation plane, the radiation helicity and the sign of θ_0, irrespective to the orientation of the sample edges by contrast to the photocurrents being even functions of the angle θ_0.

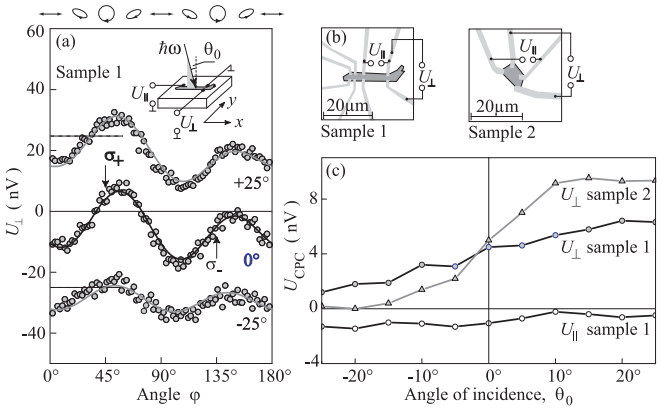

Fig. 1. (a) Photosignals $U_\perp$ in a single graphene sheet as a function of the angle φ, which determines the radiation helicity. The signals are measured perpendicularly to the light propagation direction. The data for the incidence angles $\theta_0 = \pm 25^\circ$ are shifted by ± 25 nV. The inset shows the experimental geometry. (b) Schemes of the samples 1 and 2. (c) Photon-helicity sensitive signal $U_{\rm CPC} = [U(\varphi = 45^\circ) - U(\varphi = 135^\circ)]/2$ measured as a function of the incidence angle θ_0. Full circles and triangles show the transversal response $U_\perp$ for samples 1 and 2, respectively. Open circles show the signal obtained in the longitudinal geometry $U_\parallel$ for sample 1.

2. Model and discussion

Symmetry analysis carried out for the honeycomb lattice of graphene (point group D_{6h}) demonstrates that the photocurrent in the ideal structure can be generated at oblique incidence only. In addition, for graphene, the optical transitions involving a normal component of the radiation electric field are suppressed in the studied frequency range. Hence, for the light incidence in the (xz) plane, where z is the graphene normal, the photocurrent is described by the phenomenological expressions

$$\begin{aligned} j_x &= q_x \left[T_1 |\mathbf{E}_\parallel|^2 + T_2 \left(|E_x|^2 - |E_y|^2 \right) \right], \\ j_y &= q_x \left[T_c P_{\rm circ} |\mathbf{E}_\parallel|^2 + T_2 \left(E_x E_y^* + E_y E_x^* \right) \right], \end{aligned} \quad (1)$$

where $\mathbf{q} = (q_x, 0, q_z)$ is the photon wave vector and $\mathbf{E}_\parallel$ the in-plane projection of the light-wave electric field with the components E_x and E_y. The coefficients T_1 and T_2 describe the linear, and T_c the circular drag effect. The directions of the photon drag currents are depicted in Fig. 2. They are in agreement with the experimental data where the circular photocurrent odd in θ_0 is observed in the transversal geometry only, cf. Figs. 1(c) and 2(a). In contrast, the linear photocurrent odd in θ_0 has both longitudinal and transverse components, see Figs. 2(b) and (c). The appearance of a helicity-driven drag current is a specific feature of two-dimensional systems like graphene, this effect is forbidden in bulk materials of the cubic symmetry.

The microscopic theory of the photon drag effect is developed in the framework of the Boltzmann kinetic equation valid in the classical frequency range $\hbar\omega \ll E_F$ relevant for our samples. The contributions to the photocurrents (1) can appear either due to the gradient of electric field (qE^2-mechanism) or to a combined action of the electric and magnetic fields of the light wave (EB-mechanism or high-frequency Hall effect) [4, 5]. The calculation shows that the parameter T_c describing the photon-helicity sensitive contribution in n-type samples is given by [3]

$$T_c = \sum_{\mathbf{k}} \frac{e^3 v^4 \tau_1^2 (1+\tau_2/\tau_1)}{\left[1+(\omega\tau_1)^2\right]\left[1+(\omega\tau_2)^2\right]} \left(\frac{d\tau_1}{d\varepsilon_k} - \frac{\tau_1}{\varepsilon_k} \right) \frac{df_0}{d\varepsilon_k}, \quad (2)$$

where e ($e < 0$) is the electron charge, $\mathbf{k}$ the wave vector, $\varepsilon_k = \hbar v k$ the electron dispersion in graphene, v the effective velocity, and $f_0 \equiv f_0(\varepsilon_k)$ the equilibrium distribution function, τ_1 and τ_2 are the relaxation times of the first and second angular harmonics of the nonequilibrium contribution to distribution function. The expressions for the linear photon drag constants, T_1 and T_2, are presented in Ref. [3]. Figure 2 shows frequency dependences of the circular (d) and linear (e) drag currents calculated for short-range scatterers, where $\tau_1 = 2\tau_2 \propto \varepsilon_k^{-1}$. At $\omega\tau_1 \ll 1$, the linear drag current approaches a constant value while the circular drag current vanishes. At high frequencies, $\omega\tau_1 \gg 1$, the linear current decreases as ω^{-3}, while the circular one is proportional to ω^{-4}. For the samples under consideration, the linear and circular photocurrents are estimated as 0.1–1 nA at the radiation intensity 1 W/cm^2, which corresponds to the currents measured in the experiments.

The photon drag effect, however, cannot be responsible for photocurrents observed at normal incidence. They are a clear evidence of the symmetry reduction in our samples, which is most likely caused by the edges. Indeed, the presence of an edge breaks the space inversion symmetry and can result in diffusive scattering (at least partial) of electrons from the edge. Under excitation by polarized radiation, such a scattering asymmetry gives rise to a dc electric current along the sample boundary in a narrow stripe of the width $l = v\tau_1$, similarly to surface photocurrents observed in bulk materials [5, 6]. We develop the microscopic theory of the edge photocurrents assuming the diffusive scattering of electrons at the edges. Both linear and circular photocurrents appear in this model for $\hbar\omega \ll E_F$ [3]. The obtained polarization dependences of the photocurrent are in agreement with the ones observed experimentally, see Fig. 1.

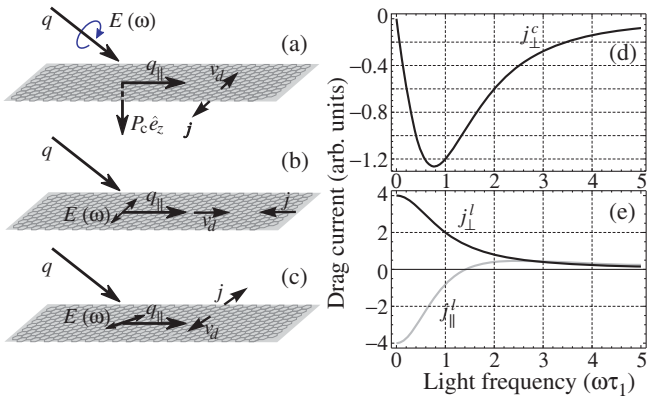

Fig. 2. Schematic illustration of the photon drag effects. Panel (a): circular photon drag effect with the photocurrent generated perpendicularly to the light incidence plane. Panels (b) and (c): longitudinal and transverse contributions to the linear photon drag current, respectively. Calculated frequency dependences of (d) circular photon-drag current $j_\perp^c$ and (e) longitudinal $j_\parallel^l$ and transversal $j_\perp^l$ contributions to the linear photon-drag current. The short-range scattering is assumed in the calculation.

In conclusion, we have demonstrated that the irradiation of graphene flakes results in directed electric currents of different origins. While the contribution from oblique incidence results from the transfer of the photon angular and linear momenta to free carriers, the effect at normal incidence is caused by the sample edges. The proposed theory describes both the helicity driven and the linear-polarization dependent photocurrents.

Acknowledgements

The support from the DFG, the Linkage Grant of IB of BMBF at DLR, RFBR, FASI, President grant for young scientists and the "Dynasty" Foundation — ICFPM is acknowledged.

References

[1] A. K. Geim and K. S. Novoselov, *Nature Mat.* **6**, 183 (2007).
[2] E. L. Ivchenko, *Optical Spectroscopy of Semiconductor Nanostructures* (Alpha Science Int., Harrow, UK, 2005).
[3] J. Karch *et al*, preprint arXiv:1002.1047 (2010).
[4] V. I. Perel' and Ya. M. Pinskii, *Sov. Phys. Solid State* **15**, 688 (1973).
[5] V. L. Gurevich and R. Laiho, *Phys. Rev. B* **48**, 8307 (1993); *Phys. Solid State* **42**, 1807 (2000).
[6] L. I. Magarill and M. V. Entin, *Sov. Phys. Solid State* **21**, 743 (1979); V. L. Alperovich, V. I. Belinicher, V. N. Novikov, and A. S. Terekhov, *JETP Lett.* **31**, 547 (1980).

18th Int. Symp. "Nanostructures: Physics and Technology"
St Petersburg, Russia, June 21–26, 2010

Destructive phase in ultra small superconducting cylinders

I. Sternfeld[1], Hadas Shtrikman[2], A. Tsukernik[3], M. Karpovski[1] and *A. Palevski*[1]

[1] School of Physics and Astronomy, Tel Aviv University, Tel Aviv 69978, Israel
[2] Department of Condensed Matter, Weizmann Institute of Science, Rehovot 76100, Israel
[3] The Center for Nanoscience and Nanotechnology, Tel Aviv University, Tel Aviv 69978, Israel

We report the recent unpublished results of our investigation of a metal-superconductor quantum phase transition in ultra small cylinders. As the diameter of the cylinder made of superconductor, d, becomes smaller than the superconducting coherence length, ξ_S, the superconducting state is destroyed in some small range of magnetic fields, when the magnetic flux through the cylinder is close to $\Phi = \Phi_0/2$, ($\Phi_0 = h/2e$). Although the reason for this phase transition can be understood from a simple phenomenological model, the nature and properties of the anomalous dissipative state occurring in such ultra small systems remains an unsolved, controversial problem. So far this quantum phase transition has been observed in 150 nm Al cylinders, only by a single experimental group [1], where Al is known to have a very large superconductor coherence length. Our experimental groups in TAU and WIS developed a new technology to fabricate and to make electrical contacts to metallic nanocylinders with diameters as small as 50 nm. The smaller size of the cylinder makes the conditions of $d \ll \xi_S$, much stronger then in previously reported experiments [1] and therefore the new properties of the so-called destructive phase are expected to be revealed.

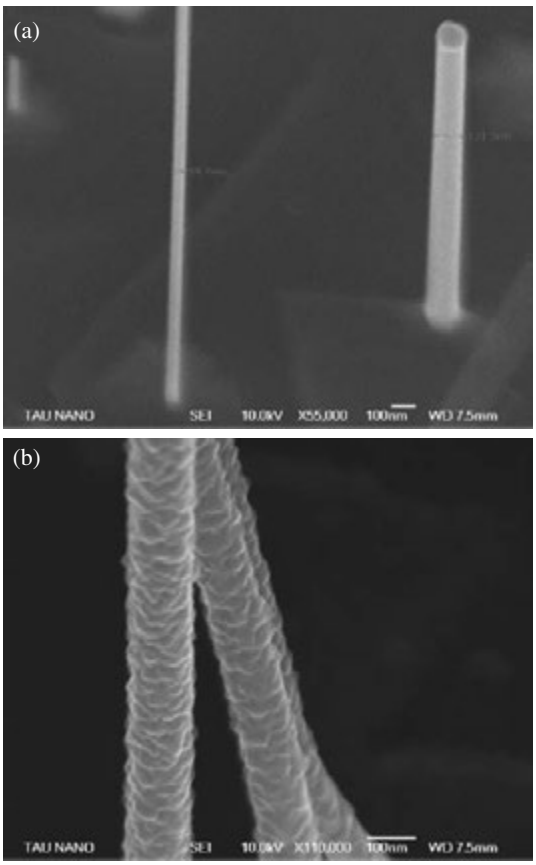

Fig. 1. SEM micrograph of InAs nanowires: (a) as grown by MBE, (b) after coating with Al.

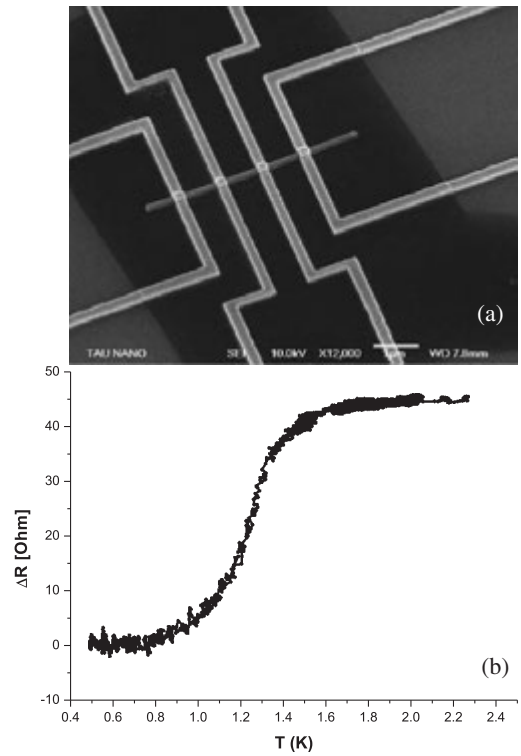

Fig. 2. (a) Al nano cylinder connected for 4-terminal measurement using e-beam lithography. (b) superconducting transition of thin walled Al nano cylinder.

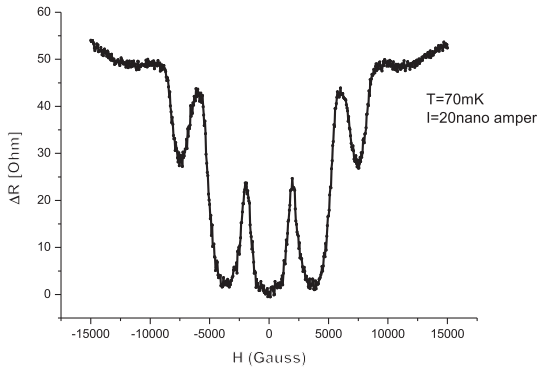

Fig. 3. Magnetoresistance curve of 80 nm diameter Al nano cylinder.

The fabrication of superconductor nanocylinders consists of three major procedures: 1) MBE growth of GaAs nanowires or InAs nanowires, which form the adjustable mold for, 2) deposition of a superconductor film over the nanowire and finally, 3) harvesting and nanofabrication of the electrical contacts.

Figure 1(a), (b) and Figure 2(a) show typical results the as grown wires, Al coated nanowires and processed sample with the electric leads, respectively. The fabricated Al nanocylinders become superconducting, with somewhat broader transition region than in planer films of similar thickness, as evident from Figure 2.

The new destructive phase of Al is clearly observed in Figure 3, as the magnetic flux attains half integer values of flux quanta $\Phi = \Phi_0(n+1/2)$ and the sample remains in its dissipative state even at 70 mK. The temperature variation of this state in our experiments will be compared to that expected from the theoretical models.

References

[1] Y. Liu, Yu. Zadorozhny, M. M. Rosario, B. Y. Rock, P. T. Carrigan, and H. Wang, *Destruction of the Global Phase Coherence in Ultrathin, Doubly Connected Superconducting Cylinders*, Science **294**, 5550 (2001), 2332–2334.

18th Int. Symp. "Nanostructures: Physics and Technology"
St Petersburg, Russia, June 21–26, 2010

Low-field hole mobility in rolled-up Si/SiGe heterostructures

N. V. Demarina[1,2] and D. A. Grützmacher[2]

[1] Radiophysics Department, Nizhny Novgorod State University, 603950 Nizhny Novgorod, Russia
[2] Institute of Bio- and Nanosystems (IBN-1), Forschungszentrum Jülich and Jülich Aachen Research Alliance on fundamentals of future information technology (JARA-FIT), 52425 Jülich, Germany

Abstract. We report a Monte Carlo study of the low-field hole transport in scrolled Si/SiGe heterostructures. We reveal that the interface roughness scattering substantially reduces the hole mobility and this is the main scattering mechanism limiting its magnitude in the SiGe scrolled structures. However, increase in the width of the SiGe layer is accompanied by substantial increase in the hole mobility which reaches the value of 10^4 cm^2/V s. The study delivers criteria for development of a building block for a tube-like field-effect transistor.

Introduction

Rolled-up structures fabricated due to self-scrolling of a sequence of Si and SiGe layers grown on a Si substrate and detached from it by selective etching, are fascinating nano-objects with balanced complex strain distribution which might demonstrate unique transport phenomena in both conduction and valence bands [1]. As it has been recently shown, p-type modulation doping can be implemented in those structures [2]. This in the case of the appropriate doping level might result in the formation of two-dimensional hole gas in the Ge_xSi_{1-x} layer which density can be controlled via an electric field applied perpendicular to the layers. The hole mobility in the modulation-doped scrolled structures can be substantially enhanced due to the separation of the charge carriers from the scattering centers as well as the reduction of the effective mass in the strained semiconductor layers.

1. Object of the study and method

We consider a scrolled structure reported recently in Ref. [2] which was formed by a bi-film consisting of Si and $Si_{1-x}Ge_x$ layers of width h_{Si} and h_{SiGe} correspondingly grown on (001) Si-substrate. In our theoretical treatment we assume that the structure is cylindrically rolled containing only one layer of the bifilm and doping is applied to the layer of Si located at the inner surface of the tube with the width of 2 nm as it is shown in Fig. 1, inset. This model of the doping approximately corresponds to the delta-doping of the structure. For the calculation of the hole mobility in the structure we first determine the strain in a stationary configuration of the tube making use of the linear elasticity theory. Following Grundmann [3], strain components in the tube grown on (001) oriented substrate can be written as functions of the tube internal radius R (Fig. 1a) and the lattice constant on the inner (Si) surface of the tube. Minimization of the total elastic energy enables to determine the values of the radius and lattice constant of the tube in the equilibrium state. We note that the radius value calculated using this model is in a good agreement with the available experimental data [4]. The strain distribution strongly affects position of the conduction and valence band, namely hydrostatic strain shifts the energy position of bands and biaxial strain splits the degenerate bands. First, we calculate the position of the conduction (E_{c0}) and valence (E_{v0}) band edges in scrolled structures taking into account only the strain contribution to the band bending following the expressions from Ref. [5]. The dash-dotted line in Fig. 1b shows the calculated position of the valence and

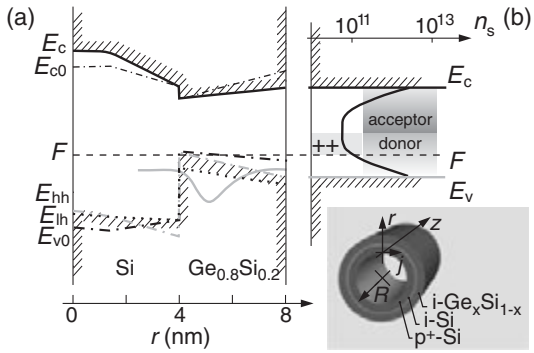

Fig. 1. (a) Conduction (E_c) and valence (E_v) bands and Fermi level (F) in the $Si/Si_{0.2}Ge_{0.8}$ scrolled structure calculated neglecting (thin dot-dashed line) and taking into account (thick lines) the surface states and doping; dashed and dot lines indicate position of the Γ-point of the heavy and light-hole states correspondingly; the width of the both Si and $Si_{0.2}Ge_{0.8}$ layers is 4 nm; (b) Surface state density n_s at the SiO_2/p-Si interface; Inset: sketch of a scrolled Si/SiGe heterostructure which consists of Si and SiGe layers.

conduction bands' edges for the $Si/Si_{0.2}Ge_{0.8}$ scrolled structure. The band offset is mainly restricted to the valence band and the $Si_{0.2}Ge_{0.8}$ layer is a potential well for holes.

Second, we take into account the additional electrostatic potential ($V(r)$) emerging due to the electric charge accumulated in the volume of the structure due to the modulation doping and charged surface states formed after the oxidation of the Si and $Si_{1-x}Ge_x$ surfaces. Therefore, the position of the conduction and valence bands fulfils $E_{c(v)} = E_{c(v)0} - qV(r)$, where q denotes the positive elementary charge. We find the electrostatic potential by the self-consistent solution of Poisson and Schroedinger equations. The Schroedinger equation has been solved for the envelope functions within the effective mass approach for both heavy- and light-hole states. We note that for the typical layer thicknesses of the scrolled structures the radius of the latter exceeds 50 nm which eliminates quantization of the hole spectrum for the momentum quantum number, thus the hole gas in rolled-structures has two-dimensional features. We perform integration of the Poisson equation neglecting the free electron charge and assuming that the doping atoms are fully ionized and the hole density is determined by the corresponding wave functions and occupation of the energy states. The total density of charged surface states at the inner surface determines the magnitude of the electric field normal to the

surface thus the required boundary condition for the Poisson equation. The full band bending is determined by the condition that the total space charge in a scrolled structure is equal and opposite to the charge accumulated by the surface states.

We describe the density of surface states on the inner and external structure surfaces as a function of energy W by the well-known U-type dependence (Fig. 1b), which for the (001) Si surface after oxidation at room temperature is presented in Ref. [6]. The charge of the surface states depends on the type of the state and its occupation by electrons. Note that in accordance with the conventional model [7] the states lying above the middle of the gap are acceptor-type and below are donor-type. Fig. 1a displays the calculated position of the bands for the $Si/Si_{0.2}Ge_{0.8}$ structure with the p-doping density in the Si layer of 10^{12} cm^{-2} and the total surface density at the each surface of 10^{12} cm^{-2}. The corresponding function of the surface state density at the Si surface is presented in Fig. 1b. In this particular case the Fermi level near the surfaces is approaching the valence band edge thus leading to the positive charge of the both Si and SiGe interfaces. This together with the modulation doping gives rise to the down-ward tilt of the bands near the $Si_{0.2}Ge_{0.8}$ layer surface and consequent accumulation of the hole gas at the $Si_{0.2}Ge_{0.8}$ interface.

2. Results

We perform calculation of the low-field hole mobility in the scrolled structures subject to a static electric field applied along the structure axis at low temperature by means of the three-dimensional single-particle Monte Carlo method. We treat inelastic hole interplay with optical phonons and elastic interaction with acoustic phonons via deformation-potential coupling for bulk material. We also take into account interface roughness scattering using the scattering potential due to the roughness given by δ-function at a perfect interface [8] assuming that the interface exhibits small thickness fluctuation of 0.4 nm and the surface roughness correlation length in the direction parallel to the surface is about 2.5 nm [9]. The scattering rates for every structure are calculated numerically using the hole wave functions and energy levels obtained due to the solution of the coupled Poisson and Schroedinger equations.

In the hole transport simulations we always assume that the surface state density at the both structure surfaces was about 10^{10} cm^{-2} and choose the modulation doping level which gives the hole density in the SiGe channel of about 10^{11} cm^{-2}. First, we calculate the hole mobility as a function of Ge content in the $Si/Si_{1-x}Ge_x$ rolled structure with the equal width of both layers, namely 2, 4, 6 and 10 nm (Fig. 2a). The mobility dependence displays pronounced minimum for the value of the Ge content of about 0.5. The decrease of the mobility at the low Ge content we attribute to the hole scattering at the Si/SiGe interface roughness which is dominating among other scattering processes at low temperature and getting more intensive with larger Ge content. Substantial reduction of the hole effective mass in the SiGe layer with the larger Ge content ensures the mobility growth for Ge content above 0.5. We note that the mobility also substantially drops with decrease in layers thicknesses which can be attributed to the stronger penetration of the hole wave function tail into the Si layer when the both layers are relatively thin, therefore leading to the stronger interplay between holes and imperfections of the surface between Si and

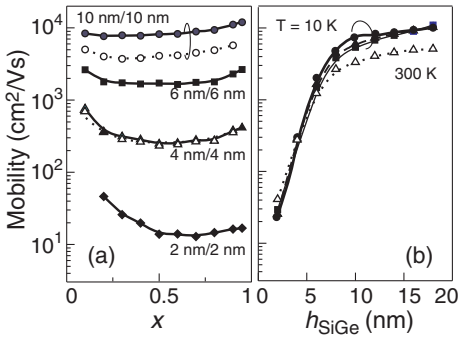

Fig. 2. (a) Low-field hole mobility along the rolled structure axis as a function of Ge content x in the $Si_{1-x}Ge_x$ layer; the thicknesses of the Si and $Si_{1-x}Ge_x$ layers are equal and of 2, 4, 6, and 10 nm; (b) Low-field hole mobility along the $Si/Si_{0.5}Ge_{0.5}$ structure axis vs the $Si_{0.5}Ge_{0.5}$ layer thickness. The calculations are performed for low (solid lines) and room (dot lines) temperature.

SiGe layers. Presence of the strong interface scattering in the rolled structures with thin layers is also validated by the mobility calculation performed at room temperature (Fig. 2a). In the scrolled structures with the wide SiGe wells (width above 8 nm) the holes at room temperature are also undergoing strong scattering at optical phonons yielding decrease in the mobility by factor of two in comparison with the value at low temperature. In the structures with the narrow quantum well the interface roughness scattering always dominates thus the mobility does not change with temperature.

Fig. 2b displays low-field hole mobility growth with the width of the SiGe layer width while the width of the Si layer holds 4 (squares), 6 (triangles), and 10 nm (circles). As we have already discussed above the interface roughness scattering becomes less intensive with increasing width of the SiGe quantum well causing substantial increase in mobility from 20 till 1000 cm^2/V s. The same curves show that the width of the Si layer affects the mobility value only slightly as the holes are manly confined in the SiGe layer. Comparison of the mobility calculated for low and room temperature enables us to conclude that the optical phonon scattering affects hole transport only in the scrolled structures with the layer width larger than 5 nm.

References

[1] V. Ya. Prinz *et al*, *Physica E* **6**, 828 (2000).
[2] J. Yukecheva *et al*, *Semicond. Sci. Technol.* **23**, 105007 (2008).
[3] M. Grundmann, *Appl. Phys. Lett.* **83**, 2444 (2003).
[4] S. V. Golod *et al*, *Appl. Phys. Lett.* **84**, 3391 (2004).
[5] F. Schaeffler, *Semicond. Sci. Technol.* **12**, 1515 (1997).
[6] M. H. White *et al*, *IEEE Trans.* **ED-19**, 1280 (1972).
[7] H. Lueth, *Solid surfaces, interfaces and thin films.* (Springer).
[8] G. Etemadi *et al*, *Solid State Commun.* **86**, 739 (1993).
[9] S. Tsujino *et al*, *Appl. Phys. Lett.* **84**, 2829 (2004).

18th Int. Symp. "Nanostructures: Physics and Technology"
St Petersburg, Russia, June 21–26, 2010

Valley-orbit photocurrents in graphene

L. E. Golub and S. A. Tarasenko
Ioffe Physical-Technical Institute, St Petersburg, Russia

Abstract. We show that the optical excitation of graphene with linearly polarized light can lead to the pure valley-orbit current: Photoexcited electrons in different valleys move in opposite directions while the total electric current does not appear under the light absorption. The direction of the electric current in each valley is determined by the light polarization with respect to the crystal lattice. Microscopically, the generation of the pure valley-orbit photocurrent in graphene originates from the warping of electron energy spectrum.

Introduction

Graphene, an one-atom-thick layer of carbon with the honeycomb crystal lattice, has been attracting rapidly growing attention due to its unique electronic properties. The electron excitations in graphene are similar to massless Dirac fermions with the Dirac points situated at the points K and K' of the Brillouin zone edge [1]. The interplay of two equivalent valleys K and K' gives raise to new transport phenomena, which are absent in systems with simple electron dispersion, and underlies the novel research area called "valleytronics" [2]. In particular, in multi-valley structures one can construct peculiar electron distribution where particles from different valleys flow predominantly in different directions [3].

Here, we show that the valley-orbit current can be optically injected in graphene. We demonstrate that the excitation of a graphene by normally-incident linearly polarized light leads to the electron flux $\mathbf{j}^{(v)}$ in each valley ($v = K, K'$), which direction is determined by the light polarization. However, the electron fluxes in the valleys, $\mathbf{j}^{(K)}$ and $\mathbf{j}^{(K')}$, respectively, are always directed oppositely, so that the total electric current $\mathbf{j}^{(K)} + \mathbf{j}^{(K')}$ vanishes.

1. Phenomenological theory

Phenomenologically, the emergence of the valley-orbit photocurrent is related to the low point-group symmetry of individual valleys. In contrast to honeycomb lattice of graphene, which possesses the center of space inversion, the valleys K and K' are described by the point group D_{3h} lacking the space inversion [see Fig. 1]. It follows from symmetry analysis that the group D_{3h} allows for the photocurrent induced by normally incident linearly polarized light. The polarization dependences of the current components in the valley K are given by

$$j_x^{(K)} = \chi (e_x^2 - e_y^2) I\,, \quad j_y^{(K)} = -2\chi e_x e_y I\,. \qquad (1)$$

Here, χ is a parameter, e_x and e_y are components of the light polarization unit vector, I is the light intensity, and the coordinate frame is chosen in such a way that the plane (xz) coincides with one of the valley mirror planes [see Fig. 1]. The photocurrent in the valley K' is obtained from Eq (1) by the replacement $x \to -x$, which gives $\mathbf{j}^{(K')} = -\mathbf{j}^{(K)}$. We note that the absence of the total electric current is in agreement with the symmetry of infinite honeycomb lattice which is centrosymmetric and does not allow for any photocurrent in the geometry of normal incidence.

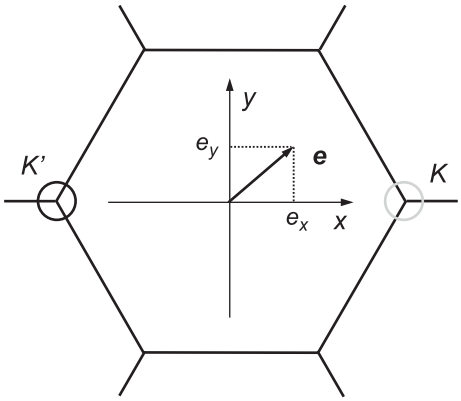

Fig. 1. Brillouin zone of graphene. The circles indicate neighborhood of the K and K' points where the electron states have trigonal symmetry allowing for the photocurrent.

2. Microscopic theory

The electron states at the K and K' valleys are related by the time inversion. Therefore, the pure valley-orbit current in graphene is dissipationless. It means that the parameter χ in Eq. (1) is invariant under the time inversion operation. This distinguishes the valley-orbit current excited by linearly polarized light from the linear photogalvanic current which is described by a tensor containing an odd number of dissipative values. In the framework of kinetic theory the electric current caused by nonequilibrium carriers in the K valley is given by

$$\mathbf{j}^{(K)} = 2e \sum_{\mathbf{k}} \left(\mathbf{v}_{\mathbf{k}}^{\mathrm{c}} f_{\mathbf{k}}^{\mathrm{c}} + \mathbf{v}_{\mathbf{k}}^{\mathrm{v}} f_{\mathbf{k}}^{\mathrm{v}} \right), \qquad (2)$$

where e is the electron charge, the factor "2" accounts for spin degeneracy, the velocities are $\mathbf{v}_{\mathbf{k}}^{\mathrm{c,v}} = \hbar^{-1} \partial \varepsilon_{\mathrm{c,v}}(\mathbf{k}) / \partial \mathbf{k}$, $\varepsilon_{\mathrm{c,v}}(\mathbf{k})$ are the electron energy dispersions in the conduction (c) and valence (v) bands, and $f_{\mathbf{k}}^{\mathrm{c,v}}$ are the distribution functions in the c- and v-bands. Under interband absorption the nonequilibrium corrections to populations in both bands are opposite:

$$f_{\mathbf{k}}^{\mathrm{c}} = -f_{\mathbf{k}}^{\mathrm{v}},$$

and the velocities are opposite due to electron-hole symmetry. Therefore, we have for the interband photocurrent in the K valley:

$$\mathbf{j}^{(K)} = 4e \sum_{\mathbf{k}} \mathbf{v}_{\mathbf{k}}^{\mathrm{c}} f_{\mathbf{k}}^{\mathrm{c}}. \qquad (3)$$

The steady-state nonequilibrium correction to the distribution function is found from the kinetic equation

$$\sum_{\mathbf{k}'} W_{\mathbf{k}\mathbf{k}'} \left(f_{\mathbf{k}}^{\mathrm{c}} - f_{\mathbf{k}'}^{\mathrm{c}} \right) = G_{\mathbf{k}}, \qquad (4)$$

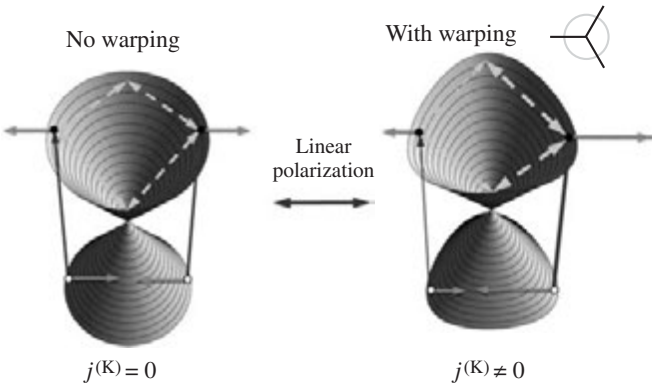

Fig. 2. Illustration of the photocurrent generation in one valley. Warping results in three sources of valley-orbit current: (i) the velocities at $\mathbf{k}$ and $-\mathbf{k}$ are not equal (horizontal arrows), (ii) the interband excitation rates $G_{\mathbf{k}}$ and $G_{-\mathbf{k}}$ are different (vertical arrows), and (iii) the elastic scattering rates from the points $\mathbf{k}$ and $-\mathbf{k}$ are different (dashed arrows), which leads to photocurrent under linearly-polarized excitation.

where, $W_{\mathbf{k}\mathbf{k}'} = W_{\mathbf{k}'\mathbf{k}}$ is the probability of electron scattering, and $G_{\mathbf{k}}$ is the optical generation rate.

Microscopically, the photocurrents in the valleys emerge due to warping of the energy spectrum at K and K' points, which reflects the trigonal symmetry of the graphene sublattices. We assume that the warping of the energy cones is relatively small and, therefore, calculate the valley-orbit current in the first order in warping. In this approximation, the energy spectrum in the vicinity of the K point is given by

$$\varepsilon_{\mathrm{c,v}}(\mathbf{k}) = \pm\left(v\hbar k - \mu k^2 \cos 3\varphi_{\mathbf{k}}\right), \tag{5}$$

where $\varphi_{\mathbf{k}}$ is an angle between $\mathbf{k}$ and the x axis.

3. Contributions to valley-orbit photocurrent

The warping of energy spectrum gives rise to linear in μ terms in (i) velocity, (ii) optical generation rate, and (iii) elastic scattering probability, see Figure 2.

Taking into account μ-linear terms in the velocity we obtain the following contribution to the photocurrent in the K-valley:

$$\chi^{(\mathrm{vel})} = \frac{5}{2}\frac{\mu e}{\hbar} k_\omega \tau_2(k_\omega)\frac{\eta}{\hbar\omega}. \tag{6}$$

Here, $k_\omega = \omega/(2v)$ is the absolute value of the photogenerated carrier wavevector, τ_n $(n = 1, 2\ldots)$ are the elastic relaxation times of the n-th angular harmonics of the distribution function, possible dependence of the relaxation time on the wavevector, $\tau_2(k)$, is taken into account, and $\eta = \pi e^2/\hbar c$ is the interband absorbance for normally-incident light calculated in the isotropic approximation.

The contribution to the photocurrent due to warping-induced corrections to the optical generation rate is given by

$$\chi^{(\mathrm{gen})} = -\frac{\mu e}{\hbar}\left\{4k\tau_1(k) + \frac{k}{2}\frac{d}{dk}\left[k\tau_1(k)\right]\right\}\frac{\eta}{\hbar\omega}, \tag{7}$$

while the contribution due to warping induced change of scattering has the form

$$\chi^{(\mathrm{sc})} = \frac{\mu e}{2\hbar} k\tau_2\left[13\frac{\tau_1}{\tau_2} - 5\frac{\tau_1}{\tau_3} - 9 + \tau_1 k\frac{d}{dk}\left(\frac{1}{\tau_1} - \frac{1}{\tau_2} - \frac{1}{\tau_3}\right) + 2k\frac{d}{dk}\left(\frac{\tau_1}{\tau_2}\right)\right]\frac{\eta}{\hbar\omega}. \tag{8}$$

Here all values should be taken at $k = k_\omega$.

4. Discussion

The total photocurrent in the K valley is given by Eq. (1) where the coefficient χ is the sum

$$\chi = \chi^{(\mathrm{vel})} + \chi^{(\mathrm{gen})} + \chi^{(\mathrm{sc})}. \tag{9}$$

Since these expressions are determined by explicit dependences of the relaxation times on the energy, the photocurrent occurs to be sensitive to the dominating scattering mechanism. For scattering by unscreened Coulomb impurities, the following relations take place:

$$\tau_1 \sim k, \quad \tau_2 = 2\tau_1, \quad \tau_3 = 3\tau_1. \tag{10}$$

As a result, in this case

$$\chi = -\frac{13\eta}{6}\frac{\mu e\tau_1(k_\omega)}{\hbar^2 v} \propto \omega.$$

For electron scattering by short-range static defects

$$\tau_1 \sim \frac{1}{k}, \quad \tau_2 = \tau_3 = \frac{\tau_1}{2}, \tag{11}$$

we obtain

$$\chi = -\frac{7\eta}{8}\frac{\mu e\tau_1(k_\omega)}{\hbar^2 v} \propto \frac{1}{\omega}.$$

These results demonstrate that the excitation spectrum of the valley-orbit photocurrent is determined by dominant scattering mechanism.

For relaxation time $\tau_1 = 1$ ps, $\mu = 2.5\,\mathrm{eV\AA}^2$, $v = 10^8$ cm/s the theory yields $\chi \approx 0.2$ mA cm/W. This estimation shows that just 5% disbalance in the currents $\mathbf{j}^{(K)}$ and $\mathbf{j}^{(K')}$ results in electric photocurrent with magnitude 10 nA/cm at excitation intensity $I = 1$ W/cm^2, which is of the same order or even larger than signals meausered in traditional 2D semiconductor systems.

Acknowledgements

This work was partially supported by RFBR, "Dynasty" Foundation — ICFPM and President grant for young scientists.

References

[1] A. H. Castro Neto *et al*, *Rev. Mod. Phys.* **81**, 109 (2009).
[2] A. Rycerz, J. Tworzydlo, and C. W. J. Beenakker, *Nature Phys.* **3**, 172 (2007).
[3] E. L. Ivchenko and S. A. Tarasenko, *Semicond. Sci. Technol.* **23**, 114007 (2008).

18th Int. Symp. "Nanostructures: Physics and Technology"
St Petersburg, Russia, June 21–26, 2010

Crossover between weak field and strong field magnetoresistance

A. A. Greshnov, O. I. Utesov and G. G. Zegrya
Ioffe Physical-Technical Institute, St Petersburg, Russia

Abstract. The problem of crossover between weak field magnetoresistance (weak localization) and strong field magnetoresistance (integer quantum Hall effect) has been studied using impurity diagrammatic technique and direct numerical calculations. It is shown that conventional weak localization contribution of the first order in $(k_\mathrm{F}l)^{-1}$ is overcome by the second order contribution $\delta\sigma_2$ provided that magnetic field is strong enough, namely $a_\mathrm{H}/l < (L_\phi/l)^{1/(\pi k_\mathrm{F}l)}$ while $\omega_\mathrm{c}\tau \ll 1$. In higher magnetic fields, $\omega_\mathrm{c}\tau \gg 1$, impurity diagrammatic technique is feeble against the problem of quantum corrections to conductivity while numerical study shows that peaks of the longitudinal conductivity grow with Landau level number n, in contrast to Pruisken–Khmelnitskii hypothesis of two-parameter scaling. Arguments in favour of reliability of the numerical results are presented.

Introduction

While the phenomena of weak localization and the integer quantum Hall effect are known for more than thirty years and basic physical pictures behind these effects are comprehended well, a general theory unifying regimes of the low and high magnetic fields is still lacking. On the other hand, a few principal problems arise in both regimes which deserve a minute study. First of all, it is generally believed but never proved that conductivity of a two-dimensional electronic system obeys whether one-parameter or two-parameter scaling as proposed in Refs. [1,2]. Moreover, violation of scaling in some specific model of disorder was claimed in Ref. [3]. Substantial controversy between the values of the second-order quantum correction to conductivity reported in Refs. [4,5,6] restrict fully reliable results to the first order in $(k_\mathrm{F}l)^{-1}$. Also it seems unlikely that various explanations of the integer quantum Hall effect exploiting localization in the bulk, edge states, electrostatics of compressible and incompressible strips, Chern–Simons field theory, Chalker–Coddington network model and non-linear σ-model are fully consistent with each other. Though our understanding of all these problems is far from being complete, we are delighted to report on some progress achieved from both the low-B and high-B sides.

1. Moderate magnetic fields

Let us concentrate on a non-interacting two-dimensional electron system with sufficiently large $k_\mathrm{F}l$ parameter and negligible spin-orbit interaction. The first-order quantum correction to its classical (Drude) conductivity $\sigma_0 = ne^2\tau = k_\mathrm{F}l(e^2/h)$ is due to so-called Cooperon channel resulting in the infrared logarithmical divergence [7],

$$\delta\sigma_1(T, B) = -\frac{2\ln\left(\min(L_\phi, a_\mathrm{H})/l\right)}{\pi}\frac{e^2}{h}, \qquad (1)$$

where phase-breaking length $L_\phi \propto T^{-p}$ with some inelastic scattering mechanism dependent exponent p and magnetic length is given by $a_\mathrm{H} = \sqrt{\hbar c/eB}$. It is easy to see from Eq. (1) that initially large zero-field value of $|\delta\sigma_1|$ is almost fully suppressed when magnetic length a_H approaches transport scale l resulting in the well-known negative magnetoresistance.

However, let us show that the treatment above loses its validity before $a_\mathrm{H} = l$ if quantum corrections of the second order in $(k_\mathrm{F}l)^{-1}$ depicted in Fig. 1 are taken into account.

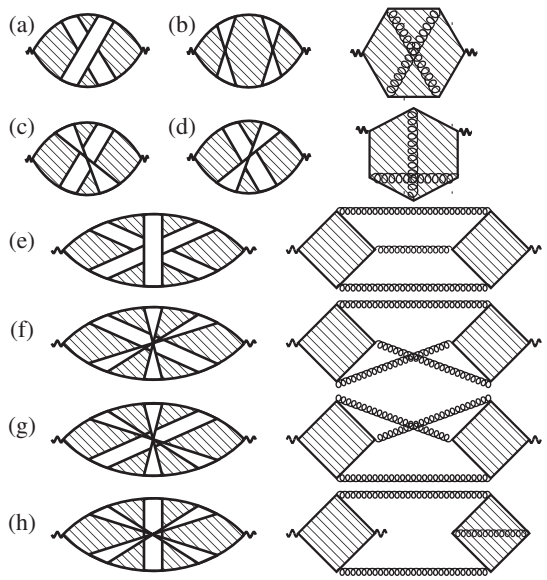

Fig. 1. Second order quantum corrections to conductivity $\delta\sigma_2$ in the conventional representation (on the left) and Hikami representation (on the right). Straight and crossed blocks stand for Diffusons and Cooperons correspondingly, hatched regions cover additional dressings ("hats" and "boots").

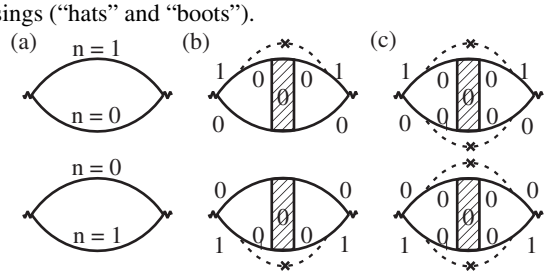

Fig. 2. Relevant contributions to conductivity in the ultraquantum limit of strong magnetic field, $n = 0$, $\omega_\mathrm{c}\tau \gg 1$. Hatched blocks denote the full two-particle propagators projected on the ground Landau level $n = 0$. Both RA and RR(AA) contributions should to be taken into account.

Generally speaking, individual diagrams presented in Fig. 1 show stronger infrared divergence than that of $\delta\sigma_1$. In particular, the skeleton diagram (h) from Fig. 1 diverges like

$\sim \int dq/q^3$. However, this disastrous power divergence vanishes when all three diagrams forming (h) are summed up. Similar cancellation occurs with the squared logarithmical terms $\sim \ln^2(L/l)$ as discussed in Ref. [7] and only simple logarithm survives (this confirms scaling hypothesis up to the second order in $(k_\mathrm{F}l)^{-1}$). In order to estimate $\delta\sigma_2$ near $a_\mathrm{H} = l$ we focus on the diagrams (a) and (e) since all the other contributions contain Cooperons so they are suppressed substantially. These two sets of diagrams, (a) and (e), consist of 16 and 9 diagrams correspondingly which show ultraviolet divergence until the proper counter-terms are added [8]. Our answer for $\delta\sigma_2(T)$ derived using conventional impurity diagrammatic technique,

$$\delta\sigma_2(T) = -\frac{2}{\pi^2}\frac{\ln(L_\phi/l)}{k_\mathrm{F}l}\frac{e^2}{h}, \qquad (2)$$

is in agreement with Ref. [5] and 4 times greater than that of Ref. [6] while Ref. [4] gives $\delta\sigma_2 = 0$. Comparing r.h.s. of Eq. (2) with that of Eq. (1) we see that $|\delta\sigma_2|$ becomes greater than $|\delta\sigma_1|$ when

$$a_\mathrm{H} = l\left(\frac{L_\phi}{l}\right)^{1/(\pi k_\mathrm{F}l)}. \qquad (3)$$

Thus we argue that only taking into account both ballistics [9] and second-order contribution $\delta\sigma_2$ allows for correct evaluation of the quantum corrections to conductivity in the intermediate range of magnetic fields ($a_\mathrm{H} \lesssim l$, $\omega_\mathrm{c}\tau \ll 1$).

2. Strong magnetic fields

It is generally believed [10] that opposite case of high magnetic fields, $\omega_\mathrm{c}\tau \gg 1$ (well separated and spin-splitted Landau levels), can be treated using a formula due to Ando [11]

$$\sigma_0 = \sigma_{xx}^{(n)} = D_n^2(E_\mathrm{F})\frac{2n+1}{\pi}\frac{e^2}{h}, \qquad (4)$$

for "Drude" conductivity and Eq. (2) for relevant quantum correction to σ_0 as long as $\delta\sigma_2 \ll \sigma_0$. Here $D_n(E)$ is reduced density of states equal to 1 at the center of n-th Landau level and effective "$k_\mathrm{F}l$" parameter is equal to $2(2n+1)/\pi$. This approach provides simple estimation for the so called unitary localization length,

$$\xi_U \approx \exp\left[(2n+1)^2\right] a_\mathrm{H}, \qquad (5)$$

which points out impossibility to observe localization (and accompanying integer quantum Hall effect) above $n = 0$, since it is extremely hard to realize $L_\phi \gg \xi_1$ (which is about $10^4 a_\mathrm{H} \approx 0.1$ mm) in real or numerical experiments.

However, it is well known that rules of the game change in the case of $\omega_\mathrm{c}\tau \gg 1$, and in the ultraquantum limit $n = 0$ only the diagrams depicted in Fig. 2 are of the principal order in $(\omega_\mathrm{c}\tau)^{-1}$. This set of diagrams includes all orders in the effective "$k_\mathrm{F}l$" parameter but none of the skeleton diagrams from Fig. 1. This circumstance points out substantial discrepancy between the low field and strong field diagrammatics. In order to check if Eq. (2) really describes quantum correction to Eq. (4) as stated in Ref. [10], we compare dependence of the σ_{xx} peak values on the sample size L obtained by direct numerical simulation [12] in the cases of short-range and medium-range disorder presented in Fig. 3 and that given by Eq. (2) ("Hikami law"). It is clearly seen that numerical curves have nothing common with "Hikami law" and revision of the theory is needed for the $\omega_\mathrm{c}\tau \gg 1$ case. On the other hand, inapplicability of Eq. (2) to strong magnetic field and absolutely flat numerical $\sigma_{xx}(L)$ curves evidence against two-parameter scaling proposed in Ref. [2].

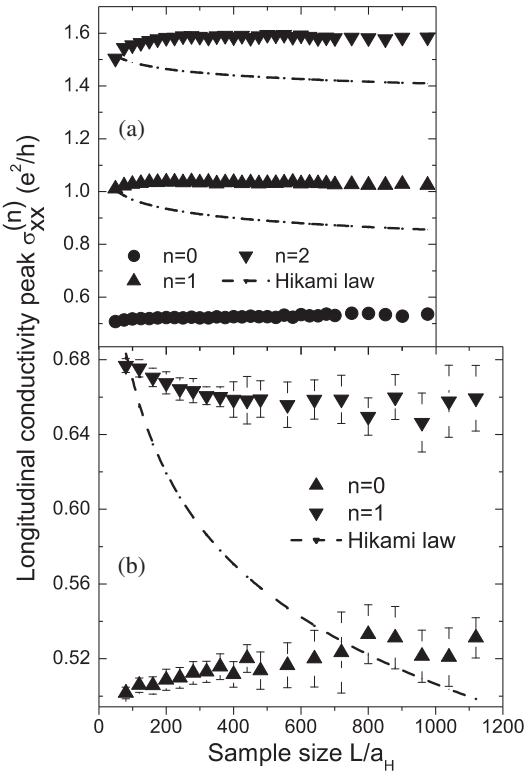

Fig. 3. Dependance of the longitudinal conductivity peaks on the sample size L under conditions of the integer quantum Hall effect ($\omega_\mathrm{c}\tau \gg 1$). The cases of short-range disorder ($\lambda = 0.25a_\mathrm{H}$) and medium-range disorder ($\lambda = a_\mathrm{H}$) are shown in (a) and (b) correspondingly.

Acknowledgements

This work has been supported by Russian President Grant for Young Scientists MK-1755.2009.2 and Dynasty Foundation. A. A. Greshnov is grateful to V. Yu. Kachorovskii and I. V. Gornyi for valuable discussions.

References

[1] E. Abrahams *et al*, *Phys. Rev. Lett.* **42**, 673 (1979).
[2] D. E. Khmelnitskii, *JETP Lett.* **38**, 454 (1983).
[3] K. B. Efetov, *JETP Lett.* **41**, 508 (1985).
[4] K. B. Efetov *et al*, *JETP* **52**, 568 (1980).
[5] S. Hikami, *Phys. Rev. B* **24**, 2671 (1981).
[6] A. A. Golubenzev, *JETP Lett.* **41**, 644 (1985).
[7] L. P. Gor'kov *et al*, *JETP Lett.* **30**, 248 (1979).
[8] A. A. Greshnov *et al*, *Physica E*, (in press).
[9] V. M. Gasparyan, A. Yu. Zyuzin, *Phys. Sol. St.* **27**, 999 (1985).
[10] B. Huckestein, *Rev. Mod. Phys.* **67**, 357 (1995).
[11] T. Ando, *J. Phys. Soc. Jpn.* **37**, 1233 (1974).
[12] A. A. Greshnov *et al*, *JETP* **107**, 491 (2008).

18th Int. Symp. "Nanostructures: Physics and Technology"
St Petersburg, Russia, June 21–26, 2010

Vertical transport in InAs/AlSb superlattices

M. S. Kagan[1], I. V. Altukhov[1], A. N. Baranov[2], N. D. Il'inskaya[3], S. K. Paprotskiy[1], V. P. Sinis[1] and A. A. Usikova[3]

[1] V. A. Kotel'nikov Institute of Radio Engineering and Electronics, RAS, Moscow, Russia
[2] IES, Université Montpellier 2, CNRS, Montpellier, France
[3] Ioffe Physical-Technical Institute, St Petersburg, Russia

Abstract. The negative differential conductivity and electric instabilities are found to appear in type-II InAs/AlSb superlattices. The origin of the nonlinear effects is discussed.

Introduction

In recent years, much attention has been focused on studies of InAs-based type-II heterostructures due to a high conduction band offset and a small electron effective mass of $0.023m_0$ in InAs. The studies have been performed mainly on InAs/AlSb structures aimed for mid-IR (see, e.g., [1] and references within) and THz [2] photodetectors, quantum cascade lasers operating in the spectral range of 2.3 to 5 μm (e.g., [3]) and, recently, fast hot-electron transistors [4]. Transport properties of superlattices (mainly GaAs-based SLs) have been investigated in details in connection with expected Bloch wave amplification. It was found that negative differential conductivity (NDC) causes the formation of electric domains, which makes it difficult to observe the Bloch oscillations. InAs-based SLs are also very attractive for studies of these nonlinear phenomena. In this report we present studies of vertical transport in InAs/AlSb SLs.

1. Experimental

The InAs/AlSb SL samples have been grown on InAs substrate by molecular beam epitaxy at Montpellier University. The SL consists of 85 periods of 4 nm InAs/2 nm AlSb between n^+ top contact layer of InAs doped with Si ($n = 1 \times 10^{19}$ cm^{-3}) and n^+ Si-doped InAs substrate ($n = 2 \times 10^{18}$ cm^{-3}). The Si doping level of SL was $(1-2)\times 10^{17}$ cm^{-3}. The structures have been processed by means of standard wet etching techniques as well as classical lithography. The last step was a metal (gold) deposition. Different mesa structures have been designed, with areas from 10^{-3} to 10^{-2} cm^2. Voltage pulses of 0.2 to 10 μs duration were applied to the sample and the load resistance connected in series. The time dependences of voltages on the sample and load resistance were recorded.

2. Results and discussion

Fig. 1 shows the current-voltage characteristics of a SL sample measured at the end of sufficiently long (several μs) voltage pulse when both voltage and current saturated. The region with NDC is clearly seen. Of course, the NDC is only imaginary because the domain formation should destroy the field uniformity. The arrow in Fig. 1 shows the current jump resulted from matched load resistance.

Kinetics of the sample voltage and current is presented in Fig. 2 for maximal applied voltage. It is rather complicated. The damped oscillations arisen at the time moments 0.48 and 0.77 μs are due to parasitic resonant circuits and indicate the appearance of NDC. Time averaging over the oscillations shows the jumps in the sample resistance. Two such kinks are seen in Fig. 2. They are likely connected with field domain formation.

The current rise with time constant of the order of 1 μs can be a result of drift-diffusion relaxation to a steady state. The origin of so long times will be discussed.

The current evolution at different voltages is shown in Fig. 3. The time positions of the current kinks move to the start simply due to increasing voltage with time; the jumps (and the following parasitic oscillations) appear at the same instantaneous voltage.

In summary, the studies of vertical transport in type-II InAs/AlSb superlattices reveal the appearance of NDC and field do-

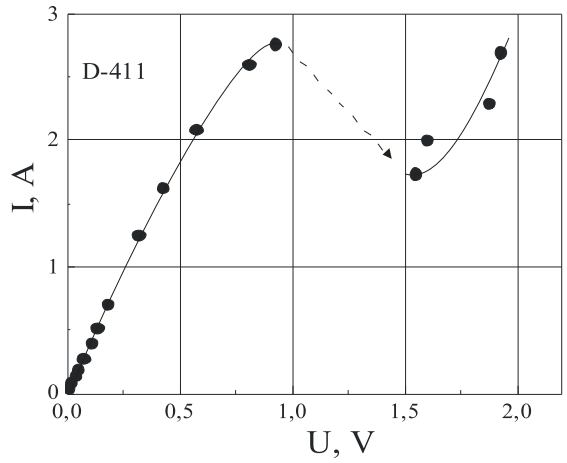

Fig. 1. I-V characteristic of InAs/AlSb SL at 77 K.

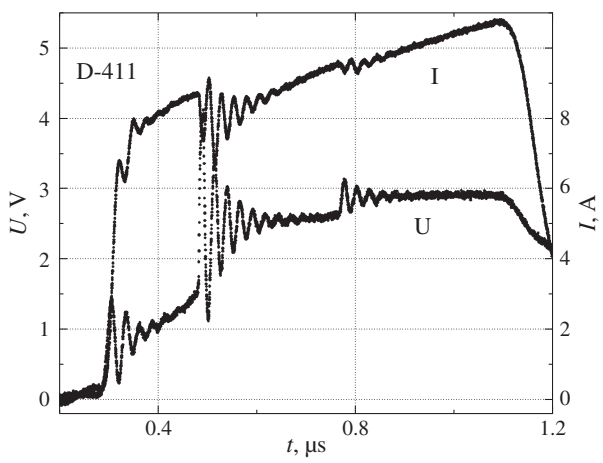

Fig. 2. Current and voltage pulse shapes. $T = 77$ K.

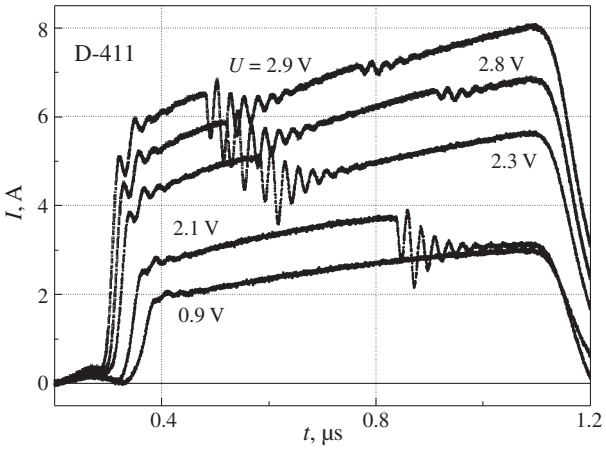

Fig. 3. Current pulses at different applied voltages.

mains in this system.

Acknowledgements

The work is supported by RFBR grants 07-02-00857, 08-02-01464, 08-02-91323 and RAS programs "Basic research in nanotechnology and nanomaterials" and "Modern problems of radiophysics".

References

[1] J. Hoffmann, T. Lehnert, D. Hoffmann and H. Fouckhardt, *Semicond. Sci. Technol.* **24**, 065008 (2009); Jie Guo *et al*, *Infrared Physics & Technology* **52** 124 (2009); J. B. Rodriguez, E. Plis, G. Bishop *et al*, *Appl. Phys. Lett.* **91**, 043514 (2007).

[2] L. L. Li *et al*, *Microelectronics Journal* **40**, 812 (2009).

[3] A. N. Baranov, N. Bertru, Y. Cuminal, G. Boissier, C. Alibert and A. Joullié, *Appl. Phys. Lett.* **71**, 735 (1997); A. A. Popov, V. V. Sherstnev, A. N. Baranov, C. Alibert, Y. P. Yakovlev, *Electronics Letters*, **34**, 1398 (1998); J. Devenson, R. Teissier, O. Cathabard, and A. N. Baranov, *Appl. Phys. Lett.* **90**, 111118 (2007).

[4] T. Daoud, G. Boissier, J. Devenson, A. N. Baranov and R. Teissier, *Journal of Physics: Conference Series*, **193**, 012014 (2009).

18th Int. Symp. "Nanostructures: Physics and Technology"
St Petersburg, Russia, June 21–26, 2010

Acoustoelectric effect in quasi-one-dimensional quantum wire with spin-orbit interaction

I. A. Kokurin and V. A. Margulis
Mordovian State University, 430005 Saransk, Russia

Abstract. The acoustoelectric (AE) effect in ballistic quasi-one-dimensional (Q1D) quantum wire with Rashba spin-orbit interaction (SOI) is investigated. The sound wave is presented as the phonon flux and the calculation approach [V. L. Gurevich *et al*, *Phys. Rev. Lett.* **77**, 3881 (1996)] is updated for the case when there is the SOI in the wire. Both charge and spin currents are generated in the system. Their dependencies on the chemical potential, applied magnetic field, sound frequency and strength of SOI are studied. The possibility of pure spin AE current generation is discussed.

Introduction

The two-dimensional electron gas (2DEG) and the systems of reduced dimensionality based on 2DEG (quantum wires (QWs) and dots) attract much attention due to spin-orbit interaction (SOI). The SOI allows to manipulate spin degrees of freedom by means of electric field that can be used for application in spintronics [1]. The spin currents (SCs) generation is one of the important purposes of spintronics as well. There are two principal mechanisms of SOI in 2DEG-based systems: (i) the first one is the so-called Rashba SOI [2] that is due to structure inversion asymmetry of quantum well producing 2DEG, (ii) the second one is the so-called Dresselhaus SOI [3] that deals with the lack of inversion symmetry in bulk material. It is important for application that the SOI strength for 2DEG structures can be tunable [4,5]. Note that for InAs-based structures Rashba SOI mechanism is dominant [5]. The corresponding Hamiltonian is given by

$$H_{\rm R} = \frac{\alpha}{\hbar}(\sigma_x p_y - \sigma_y p_x), \qquad (1)$$

where σ_i are the Pauli matrices, $\mathbf{p} = (p_x, p_y)$ is the electron momentum, and α is the Rashba SOI strength parameter.

The acoustoelectric (AE) effect in quasi-one-dimensional (Q1D) systems is the powerful tool to supply the information about electron energy spectrum. The AE current was investigated experimentally in QW defined by split-gate in GaAs-$Al_xGa_{1-x}As$ heterostructure [6]. A number of theoretical descriptions of AE effect in QWs were suggested where the electron spin is not taken into account.

The aim of present work is the theoretical investigation of the AE effect in Q1D QW with Rashba SOI under the ballistic transport regime. We are interested by the case of long QW [7] ($qL \gg 1$ with L and q being the QW length and the sound wavenumber, respectively). Note that AE current calculated in Ref. [7] (in system of spinless electrons) vanishes at sound frequencies $\omega_{\mathbf{q}}$ less than threshold frequency $\omega_{\rm th} = 2m^*w^2/\hbar$, with m^*, w being effective mass and sound velocity, respectively.

1. Model and Hamiltonian

We consider QW with the parabolic confinement potential. The system is placed into in-plane magnetic field $\mathbf{B} = (B_x, B_y, 0)$. It is well-known that QW Hamiltonian with SOI can not be diagonalized analytically even for simple confinement potentials [8,9]. Here we use exactly solvable model of quantum wire with Rashba SOI [10] neglecting the first term in Eq. (1). This model can be applied for narrow wires. The simplified QW Hamiltonian with Rashba SOI is given by

$$H = \frac{\mathbf{p}^2}{2m^*} + \frac{m^*\omega_0^2 y^2}{2} - \frac{\alpha}{\hbar}\sigma_y p_x + \frac{1}{2}g^*\mu_{\rm B}(\sigma_x B_x + \sigma_y B_y), \quad (2)$$

where ω_0 is the frequency of parabolic potential that determines the character transverse size of the wire, $l_0 = \sqrt{\hbar/m^*\omega_0}$; g^*, $\mu_{\rm B} = |e|\hbar/2m_0c$ are effective g-factor and Bohr magneton, respectively.

The energy spectrum and wave functions in such a model are given by

$$\begin{aligned} E_{ns}(k) &= \hbar\omega_0(n+1/2) + \frac{\hbar^2k^2}{2m^*} \\ &+ s\sqrt{(\alpha k - g^*\mu_{\rm B}B_y/2)^2 + (g^*\mu_{\rm B}B_x/2)^2}, \quad (3) \end{aligned}$$

$$|nsk\rangle = \frac{e^{ikx}}{\sqrt{L}}\Phi_n(y)\frac{1}{\sqrt{2}}\begin{pmatrix} se^{i\varphi(k)} \\ 1 \end{pmatrix}. \qquad (4)$$

Here $\Phi_n(y)$ is the harmonic oscillator eigenfunction, $\varphi(k) = \arctan[-B_y/B_x + 2\alpha k/(g^*\mu_{\rm B}B_x)]$, $n = 0, 1, 2, \ldots$, $s = \pm 1$. The spin projection expectation values are $\langle nsk|\sigma_x|nsk\rangle = s\cos\varphi(k)$ and $\langle nsk|\sigma_y|nsk\rangle = -s\sin\varphi(k)$.

The QW energy spectrum is plotted in Fig. 1a. Note that if we take into account the first term in SOI Hamiltonian (1) then the interaction between adjacent subbands leads (after numerical diagonalization of QW Hamiltonian) to transformation of crossings labelled by arrows in Fig. 1a into anticrossings due to $\langle n's'k'|\sigma_x p_y|nsk\rangle \neq 0$ at $n' = n \pm 1$, $s' \neq s$.

2. AE current calculation

For AE current calculation we update the kinetic approach that was developed for Q1D spinless electrons with simple parabolic dispersion in Ref. [7]. The sound wave is assumed to propagate along the wire, $\mathbf{q} = (q, 0, 0)$. At low temperatures the interaction of electron with ultrasound can be treated as the direct absorption of acoustic phonon.

The charge AE current I^c is given by

$$I^c = e\sum_{n,s}\int_{-\infty}^{\infty}\frac{dk}{2\pi}v_{ns}(k)\Delta f_{ns}(k), \qquad (5)$$

where $v_{ns}(k) = \partial E_{nsk}/\partial(\hbar k)$ is the electron velocity. In presence of the SOI $v_{ns}(k) \neq \hbar k/m^*$. The velocity operator is given by $v_x = p_x/m^* - (\alpha/\hbar)\sigma_y$. Non-equilibrium distribution function is $f = f_0 + \Delta f$, where at equilibrium it is equal

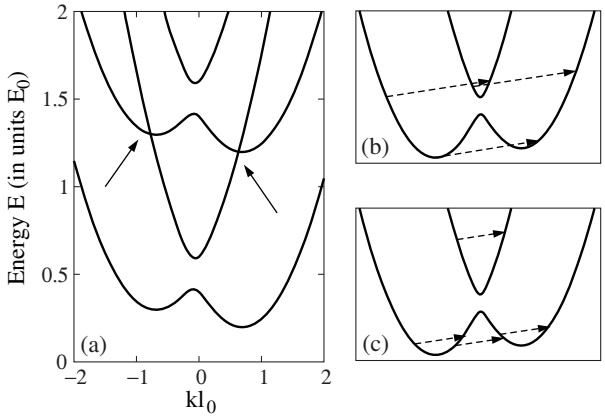

Fig. 1. a) The QW energy spectrum, $k_{so}l_0 = 0.7$, $E_Z/\hbar\omega_0 = 0.2$, $\theta = \pi/6$ ($k_{so} = \alpha m^*/\hbar^2$, $\theta = \arctan(B_y/B_x)$, $E_0 = \hbar\omega_0$). The arrows indicate the crossings that transform into anticrossings if the total Rashba Hamiltonian will be taken into account. b), c) The possible electron transitions for phonon absorption.

to f_0 being the Fermi distribution function, and Δf denotes non-equilibrium correction ($\Delta f \ll f_0$). The kinetic equation is given by [7]

$$v\frac{\partial(\Delta f)}{\partial x} = I[f]. \tag{6}$$

Here $I[f]$ is the electron-phonon collision term. We use simple boundary condition: $\Delta f = 0$ at $x = \mp L/2$ for an electron velocity $v > 0$ ($v < 0$), that corresponds to the presence of electron-phonon interaction inside the wire only and electrons in reservoir obey the equilibrium distribution f_0.

The solution of kinetic Eq. (6) with mentioned boundary conditions has the form

$$\Delta f = \left[x + \mathrm{sgn}(v)\frac{L}{2}\right]\frac{1}{v}I[f]. \tag{7}$$

The electron-phonon collision term can be written in usual manner using the matrix elements of electron-phonon interaction operator H^{e-ph}. The above matrix elements have the form

$$|\langle n's'k', 0|H^{e-ph}|nsk, \pm\mathbf{q}\rangle|^2 = |C_\mathbf{q}|^2\left(N_\mathbf{q} + \frac{1}{2} \mp \frac{1}{2}\right)$$
$$\times\delta_{k',k\pm q}\delta_{n'n}\frac{1}{2}\{1 + ss'\cos[\varphi(k) - \varphi(k \pm q)]\}. \tag{8}$$

Here the sign $\pm$ corresponds to the absorption (emission) of the acoustic phonon. The non-equilibrium phonon distribution function is $N_\mathbf{q} = N_0\delta_{\mathbf{q},\mathbf{q_0}}$ ($N_0 = SV_0/\hbar w^2 q_0$, S is the sound intensity, V_0 is the normalization volume). Here $C_\mathbf{q}$ is the electron-phonon coupling constant, that for the case of unscreened piezoelectric (PE) interaction (PE interaction dominates in $A^{III}B^V$ structures at comparatively low frequencies about 1–3 GHz that is typical for AE experiment [6]) is given by

$$C_\mathbf{q}^{\mathrm{PE}} = M_\lambda(\mathbf{e}_q)(\hbar/2\rho_0 V_0\omega_\mathbf{q})^{1/2},$$

where ρ_0 is the mass density, $M_\lambda(\mathbf{e}_q)$ is the PE interaction tensor, that depends on phonon propagation direction $\mathbf{e}_q$ and polarization λ, and in our case it is the constant.

The electrons carry spin as well as charge therefore we can write for the components of SC I_j^s ($j = x, y$) in analogy to charge current

$$I_j^s = \sum_{n,s}\int_{-\infty}^{\infty}\frac{dk}{2\pi}\langle nsk|\sigma_j|nsk\rangle v_{ns}(k)\Delta f_{ns}(k). \tag{9}$$

3. Discussion

There are both charge and spin currents in the wire. Both types of the current undergo nonmonotonic dependencies on sound frequency and SOI strength. In Ref. [7] the momentum and energy conservation for phonon absorption (emission) processes leads to the transitions between states with the following momentum in each subband $\hbar k_{1,2} = m^* w \pm \hbar q/2$. The presence of the SOI in the system leads to the complex structure of the energy spectrum and to possibility of inter-subband phonon-induced transitions and therefore the new features appear in AE current behavior. The numerically calculated possible transitions determined by conservation laws in QW with SOI are depicted on Fig. 1b,c. The number of possible transition in a pair of spin-split subbands is greater than in absence of SOI. Therefore the dependence of charge AE current on the chemical potential differs from giant oscillations of AE current in system of spinless electrons [7]. Moreover, the charge AE current can change the sign as the chemical potential increases.

Note that the transitions conserving the velocity direction do not contribute to the current as well as in SOI absence case [7]. This fact leads to mentioned limitation on the sound frequency. The above limitation is lifted if there is SOI in the system due to complex structure of the energy spectrum. In contrast to the charge current, the transitions conserving the velocity direction give the contribution to AE SC. The AE SC components are non-uniform in QW (x-dependent). The components of SC are sufficiently different at left (right) QW edge ($x = \mp L/2$).

It is worth mentioning that the special situation can be achieved by tuning of external parameters when there is the pure spin AE current in the wire (without charge current).

Acknowledgements

This work has been supported by the program 'Development of scientific potential of the Higher School' of Russian Ministry of Education and Science (project No. 2.1.1/2656) and by the Russian Foundation for Basic Research (grant No. 08-02-01035).

References

[1] I. Žutić, J. Fabian, and S. Das Sarma, *Rev. Mod. Phys.* **76**, 323 (2004).
[2] Yu. A. Bychkov, E. I. Rashba, *JETP Lett.* **39**, 78 (1984).
[3] G. Dresselhaus, *Phys. Rev.* **100**, 580 (1955).
[4] J. Nitta, T. Akazaki, H. Takayanagi, T. Enoki, *Phys. Rev. Lett.* **78**, 1335 (1997).
[5] D. Grundler, *Phys. Rev. Lett.* **84**, 6074 (2000).
[6] J. M. Shilton, V. I. Talyanskii, M. Pepper *et al*, *J. Phys.: Condens. Matter* **8**, L531 (1996).
[7] V. L. Gurevich, V. B. Pevzner, and G. J. Iafrate, *Phys. Rev. Lett.* **77**, 3881 (1996).
[8] J. Knobbe, Th. Schäpers, *Phys. Rev. B* **71**, 035311 (2005).
[9] C. A. Perroni, D. Bercioux, V. M. Ramaglia, V. Cataudella, *J. Phys.: Condens. Matter* **19**, 186227 (2007).
[10] Y. V. Pershin, J. A. Nesteroff, V. Privman, *Phys. Rev. B* **69**, 121306 (2004).

18th Int. Symp. "Nanostructures: Physics and Technology"
St Petersburg, Russia, June 21–26, 2010

Photoluminescence and photoexcitation transport in silicon-rich nitride films with amorphous Si nanoclusters

V. A. Stuchinsky[1], T. T. Korchagina[1], V. A. Volodin[1,2] and M. Vergnat[3]

[1] Institute of Semiconductor Physics of SB RAS, Lavrenteva ave., 13, Novosibirsk 630090, Russia
[2] Novosibirsk State University, Pirogova str., 2, 630090, Novosibirsk, Russia
[3] Laboratoire de Physique des Matériaux, Nancy-Université, CNRS, Boulevard des Aiguillettes B.P. 239, 54506 Vandœuvre lés Nancy, France

Abstract. In the present paper, we give a detailed analysis of the temperature dependence of photoluminescence intensity in a nanoscale system formed by a-Si nanoclusters embedded within a silicon nitride matrix. Our experimental data suggest that (i) the photoluminescence (PL) in this system obeys the quantum-confinement rather than band-tail PL model and (ii) the temperature quenching of the photoluminescence involves two nonradiative paths, one path being the nondissociative migration of photoexcitations to nonradiative sites and the other, their dissociative migration to those sites.

Introduction

In our previous study [1], we examined the temperature dependence of the PL intensity I in silicon-rich nitride (SRN, $Si_{3+x}N_4$:H) films deposited onto Si substrates from a flow of silane-ammonia mixture diluted with nitrogen. The films of different stoichiometries ($x = 0.08 - 3.7$) were grown at two different temperatures, 100 and 380 °C (sample series 611–615 and 621–625, see Table 1). According to Raman scattering data, the Si nanoparticles in our films were a-Si nanoclusters (nc's). The curves of $I(T)$ plotted in semi-log scale exhibited a distinct change of their slope at $T^* \approx 200$ K (see Fig. 1), thus pointing to the fact that two different nonradiative processes were involved in the PL thermal quenching phenomenon. By fitting our I-vs-T data with the expression

$$I \sim \left(1 + f_1\, e_r^{-1}(T)\, e^{-\frac{E_{a1}}{kT}} + f_2\, e_r^{-1}(T)\, e^{-\frac{E_{a2}}{kT}}\right)^{-1} \qquad (1)$$

in which the Calcott formula for the temperature-dependent radiative recombination rate $e_r(T)$ was used [2], we were able to evaluate the thermal activation energies E_{ai} and the frequency factors f_i ($i = 1, 2$) of the two processes. Since the activation energy of the process which accelerated the rate of PL thermal quenching at $T > 200$ K, $E_{a2} \approx 0.13 - 0.15$ eV, was close to the binding energy of a Si nanoparticle confined exciton, this process was identified as the thermally stimulated exciton dissociation proceeding in the system when the most mobile carrier (hole) hopped into a neighboring a-Si nc to subsequently migrate into more remote a-Si particles. The activation energy of this process was interpreted as the polarization energy due to partial exciton dissociation. The low-temperature process with relatively low activation energy, $E_{a1} \approx 0.03 - 0.04$ eV, was identified as exciton recombination at nonradiative sites in the system, mediated by the tunneling migration of excitons as complex particles without (or with negligible) electrical polarization.

Table 1. Specifications, growth conditions, thickness d and stoichiometry parameter x of examined SiN_x films

Sample	T, °C	NH_3/SiH_4 flow ratio	d, nm	Stoichiometry parameter x
611	100	5	∼240	∼0.08
612	100	2.6	∼400	∼0.33
613	100	1.5	∼400	∼1.0
614	100	0.9	∼450	∼2.7
615	100	0.5	∼450	∼3.7
621	380	5	∼280	∼0.08
622	380	2.6	∼430	∼0.33
623	380	1.5	∼430	∼1.0
624	380	0.9	∼510	∼2.7
625	380	0.5	∼510	∼3.7

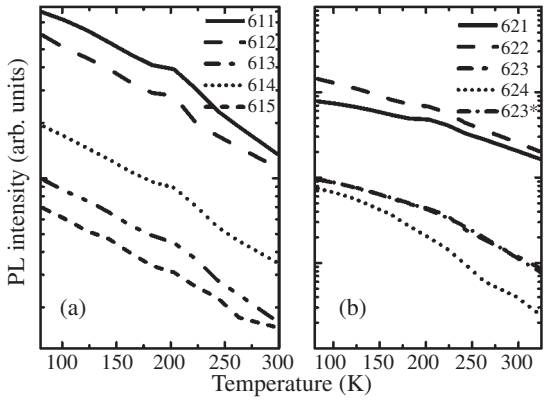

Fig. 1. Maximum PL intensity versus temperature in the spectra of samples grown at temperatures $T = 100$ °C (a) and 380 °C (b). The fitting quality ensured by the developed model is illustrated by curve 623*, which was calculated by formula (1) to fit the experimental data for sample 623.

In the present report, we give a detailed analysis of our $I(T)$ data that confirms the interpretation of these data previously advanced in [1]. Based on this analysis, we make some further conclusions concerning the PL mechanism in the nanoscale system of interest and describe the manifestation of photoexcitation transport processes in its photoluminescent properties.

1. Analysis

The analysis was made considering the experimental values of f_2/f_1 since these values turned out to be rather insensitive to the parameter values used in the Calcott formula for e_r. In our model, the ratio f_2/f_1 was assumed to be defined by the tunneling rates of holes and excitons making hops into

neighboring a-Si clusters:

$$\frac{f_2}{f_1} \approx \frac{n^{-1}\nu_{\rm h}\exp\left(-\frac{2}{\hbar}\int\limits_0^{R_t}\sqrt{2m_{\rm h}^{\rm Si_3N_4}V^*(x)}dx\right)}{m^{-1}\nu_{\rm ex}\exp\left(-\frac{2}{\hbar}\int\limits_0^{R_t}\sqrt{2m^*V_{\rm b}^{\rm ex}}dx\right)}. \qquad (2)$$

In (2), $\nu_{\rm h}$ and $\nu_{\rm ex}$ are the characteristic frequencies of the internal motion of the thermally excited hole and ground-state exciton inside a-Si nc's; $m^* = (m_{\rm h}^{\rm Si_3N_4} + m_{\rm e}^{\rm Si_3N_4})$; n is the mean number of hops into neighboring a-Si nc's the holes makes prior to the complete dissociation of exciton; m is the mean number of hops the tunneling exciton makes prior to its nonradiative recombination in one of nearby a-Si nc's; R_t is the tunneling distance, or the width of the tunnel barrier between neighboring nc's; and $V^*(x) = (V_{\rm b}^{\rm h} - E_{act2} + E_{\rm pol}\frac{x}{R_t})$, where $E_{\rm pol} \approx E_{a2}$ is the electrical polarization energy, and $V_{\rm b}^{\rm h}$ and $V_{\rm b}^{\rm ex}$ are the tunnel barriers for holes and excitons in zero electric field.

The right-hand side of (2) being a sharply increasing function of R_t, this allows us, with some values of n and m assumed, to evaluate the typical separation between neighboring a-Si nc's in our SRN films. The obtained values of R_t proved to be quite realistic, falling into the range from 0.3 to 1.7 nm. As it could be expected, the experimental values of E_{a2}, if plotted against R_t, give a linearly increasing function (see Fig. 2a). This function, available in the interval $0.37 < R_t < 0.57$ nm (for $m/n = 1$) can be fitted with a straight line, going through origin, whose slope gives a proportionality-factor value 2.87×10^6 eV/cm that compares well (within a factor of ten) to the coefficient $(4q/\varepsilon\varepsilon_0 R_{\rm nc}^2) \approx 1.6 \times 10^7$ eV/cm ($R_{\rm nc}$ is the nc size) which appears in a simple electrostatic formula relating the electrostatic energy in a plane capacitor formed by two circular capacitor plates of diameter $R_{\rm nc}$ charged with charges $\pm q$, with capacitor gap R_t. The agreement is not bad considering the fact that the capacitor offers only a very crude approximation to the real system formed by an electron and a hole localized at neighboring a-Si nc's. The main difference between the plane capacitor and the two-nanocluster system in the present context consists in that, for quantum-mechanical reasons, the electron and hole wave functions in the latter system cannot be localized at adjacent nc surfaces to the same relative degree as the surface charges in the ideal capacitor can.

Since the polarization energy $E_{\rm pol}$ between the parting hole and electron grows in value with increasing the electron-hole separation, it can be expected, in view of the strong dependence of the right-hand side of (2) on R_t, that some correlation could also be traced between the experimental values of f_2/f_1 and E_{a2}. As it is demonstrated by Fig. 2b, such a correlation is indeed displayed by our experimental data. The curve in Fig. 2b was calculated by formula (2) with $m/n = 1$, R_t [cm] $= E_{\rm pol}$ [eV]$/2.87\times10^6$ and with the values of $R_{\rm nc}$ and $E_{\rm PL}$ fixed to 1.4 nm and 2.52 eV, respectively. The deviation of the experimental points from the calculated curve presumably results from the difference between the actual values of m/n, $R_{\rm nc}$ and $E_{\rm PL}$ in individual samples and the values of m/n, $R_{\rm nc}$ and $E_{\rm PL}$ the curve was calculated with, and also from disregard of resonance phenomena and finite-size effects for tunneling excitons. Although the values of f_2 and f_1 (and also f_2/f_1) in the examined samples show no regular tendency, or a universal behavior common for both sample series, if considered as function of x (see [1])[1], a clear correlation between the experimental values of f_2/f_1 and E_{a2} *in all samples*, quite consistent with the adopted model, is evident. This correlation provides further impressive support for the proposed interpretation of our experimental data.

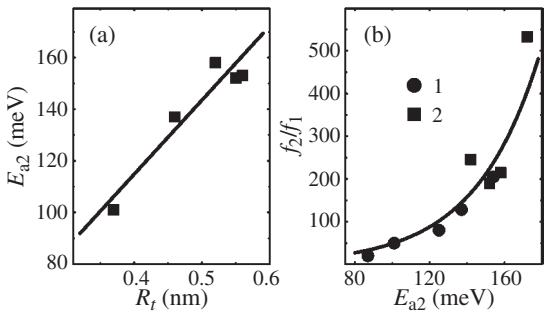

Fig. 2. a) The activation energy E_{a2} versus the tunneling distance R_t. The values of R_t are values obtained assuming $m/n = 1$. b) The ratio f_2/f_1 versus the energy E_{a2}. 1 and 2 — data for sample series 611–615 and 621–625, respectively. The curve is the dependence calculated by the developed model for $m/n = 1$, $R_{\rm nc} = 1.4$ nm, and PL emission energy $E_{\rm PL} = 2.52$ eV.

2. Conclusions

The obtained data strongly suggest that it is the quantum-confinement rather than band-tail PL model that should to be accepted for a-Si nc's in SRN films grown by the present PECVD process [3,4]. If considered in a more general context, these data provide a clear picture that shows in which form photogenerated electrons and holes exist and migrate in nanoscale systems formed by "weakly amorphous" (and crystalline) Si nanoparticles hosted in a wide-gap dielectric matrix.

References

[1] T. T. Korchagina *et al*, *17-th International Symposium "Nanostructures: Physics and Technology"*, 266–267 (2009).
[2] P. D. J. Calcott *et al*, *J. Phys.: Condens. Matter*, **5**, L91 (1993).
[3] M. J. Estes *et al*, *Phys. Rev. B* **54**, 14633 (1996).
[4] Nae-Man Park *et al*, *Phys. Rev. Lett.* **86**, 1355 (2001).

[1] The latter seems to be a result of the interplay of the following two factors. First, as it is evidenced by the PL data, with increasing x larger nc's form in the samples, and the confinement energy of charge carriers in the nc wells decreases; this factor acts to increase the effective barrier height for tunneling particles. On the other hand, the width of the tunnel barriers between neighboring nc's can be expected to decrease with x. The two factors act in opposition in defining the value of the exponents in (1). Yet, the proportion between these factors is not defined by the value of x rigidly since our samples contained, along with a-Si nc's, a considerable fraction of "dissolved" silicon, whose content could be affected by subtle details of the growth processes held at different conditions. In addition, there could be lateral nonuniformity of film structure/composition in the samples, also contributing to the scatter of data. As a consequence, the behavior of f_2, f_1, and f_2/f_1 versus x has appeared different in the two sample series. Yet, the data taken from the various samples demonstrate a distinct correlation between f_2/f_1 and E_{a2}, reflecting the fact that the two nonradiative processes were not independent as both were underlied by one and the same nanoscale structure.

18th Int. Symp. "Nanostructures: Physics and Technology"
St Petersburg, Russia, June 21–26, 2010

InGaAs tunnel-injection nanostructures: transport via nanobridge states versus drift

V. G. Talalaev[1,2], A. V. Senichev[2], B. V. Novikov[2], J. W. Tomm[3], N. D. Zakharov[4], P. Werner[4], Yu. B. Samsonenko[5,6] and G. E. Cirlin[5,6]

[1] Martin-Luther-Universität Halle-Wittenberg, ZIK "SiLi-nano", 06120 Halle, Germany
[2] St Petersburg State University, Fock Institute of Physics, 198504 St Petersburg, Russia
[3] Max-Born-Institut für Nichtlineare Optik und Kurzzeitspektroskopie, 12489 Berlin, Germany
[4] Max-Planck-Institut für Mikrostrukturphysik, 06120 Halle, Germany
[5] Ioffe Physical-Technical Institute, St Petersburg, Russia
[6] St Petersburg Academic University, St Petersburg, Russia

Abstract. Tunnel-injection nanosructures containing an upper InGaAs quantum well (QW) layer, as injector of carriers, and a lower layer of InAs quantum dots (QDs), as light emitter, spaced by GaAs barrier have been investigated by optical spectroscopy and electron microscopy. The drastic reduction of the electron transfer time from QW to QDs for barrier thickness lower than 6 nm is found to be related to the formation of InGaAs nanobridges between QD apexes and QW layer. The competition between hole eigen-states of nanobridges and electric field built up in barrier by carrier separation caused by electron tunneling from QW to QDs is considered.

Tunnel-injection structures have special relevance for the design of the gain region in diode lasers due to the spatial separation of carrier injector and light emitter. This factor also produces a strong dependence of efficiency of such lasers on the carrier tunneling conditions between injector and emitter. We showed earlier for InGaAs system [1] that the sequence of layers: quantum dots-quantum well (QDs-QW), separated by a thin GaAs barrier, results in non-classical reduction of the electron transfer time for barrier thicknesses <6 nm. This phenomenon was attributed to the formation of the InGaAs nanobridges between QD apexes and QW layer. In this work we study the influence of hole eigen-states of nanobridges and electric field induced by carrier separation caused by tunneling of electrons through barrier on the transport and emission properties of QW-QDs tunnel-injection nanostructures (TINs).

TINs are grown by molecular beam epitaxy with the following sequence of layers: InAs QDs (2 monolayers), GaAs spacer with different thickness, and an 11-nm thick $In_{0.15}Ga_{0.85}As$ QW. Reference samples containing exclusively QDs or QW layers are grown as well.

Data on structural parameters and chemical composition of TINs are provided by transmission electron microscopy. For GaAs barrier thinner than 6 nm point contacts (nanobridges) between QD apexes and QW layer are detected. The nanobridges had a 2 nm size and variable indium content.

On a basis of this information the calculations within the framework of the effective mass approximation were performed. These calculations and Arrhenius analysis give the conduction band structure of TINs presented in Fig. 1a. The calculations have shown that nanobridge cross-section is not sufficient for confined electron state. Nevertheless cylinder-like nanobridge with a cross-section of 2 nm and an average indium content of 15% can have one confined heavy hole state as long as the barrier part of nanobridge is longer than 4 nm.

Emission and tunnel properties of TINs are investigated by photoluminescence (PL) spectroscopy. At low temperature and low (cw) excitation power the typical PL spectrum of TINs includes QD0 band (1.2 eV) and QW line (1.3 eV) attributed to the optical transitions between ground states in QDs and QW, respectively [1]. Higher power density was achieved by pulse excitation. In these conditions QD1 band appeared near 1.27 eV which is assigned to the radiative recombination between excited states in QDs. For TINs with barrier thickness from 4 to 6 nm a new spectral band NB was detected at 1.3 eV. Its origin is attributed to a transition involving a hole eigen-state of nanobridge and an electron ground state of QD (see Fig. 1).

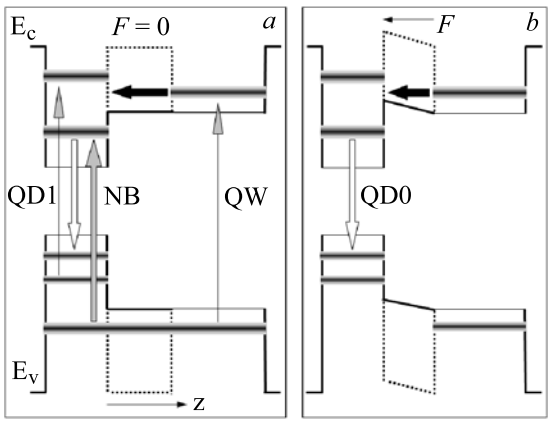

Fig. 1. Energy structure with optical and tunnel transitions for two TINs with different nanobridges: a — nanobridge with hole state; b — empty nanobridge (thin barrier). Axis z has a growth direction. Solid line shows z-axis going through the nanobridge; dashed line is for z-axis outside the nanobridge. The direction of vertical transitions is related to the PL excitation mode (Fig. 2).

Such transition should have large oscillator strength. Above barrier interaction between the hole states of QD and QW takes place in a similar way as Breit–Wigner resonance. The contribution of different states in the emission properties of QDs is quite evident in PL excitation spectra of TINs (Fig. 2). It can be seen how much it depends on the barrier thickness. In this way, the studied TINs can be separated into three groups: 1) without nanobridges (thick barrier); 2) with nanobridges having a hole state (optimal barrier); 3) with "empty" nanobridges, i.e. without confined states (thin barrier).

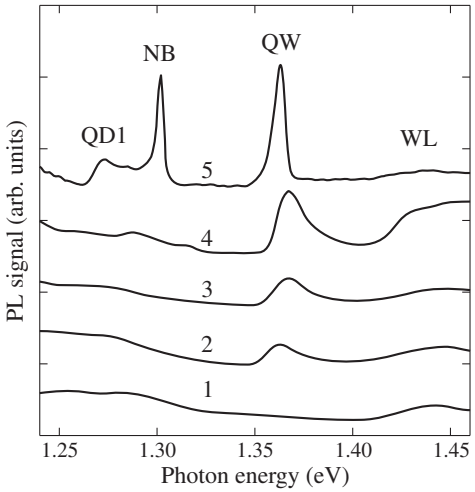

Fig. 2. PL excitation spectra for different barrier thickness, B (nm): 1 — referent sample (single QD layer); 2 — 9.5 nm; 3 — 6.5 nm; 4 — 3.1 nm; 5 — 4.4 nm. PL signal was detected at 1.2 eV (QD0).

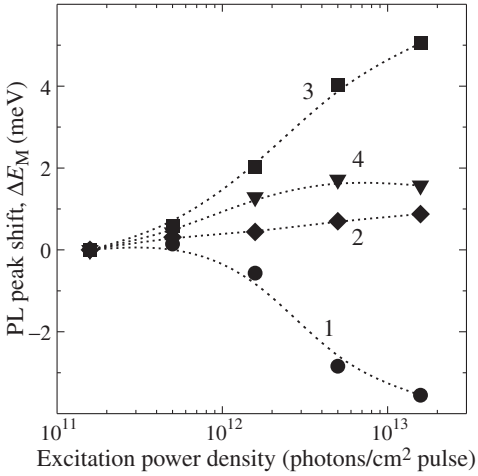

Fig. 3. Dependence of the QW peak shift energy on the PL excitation power density for TINs with different barrier thickness B: 1 — 3.1 nm; 2 — 4.4 nm; 3 — 7.4 nm; 4 — 9.5 nm.

The barrier thickness of TINs (B) also determines the dependence of PL peak shift $\Delta E_M(B)$ on the excitation power density. This dependence was studied for the QW PL line under pulse excitation (Fig. 3). "Red" energy shift for the thin barrier ($B = 3.1$ nm, curve 1 was replaced by the "blue" shift for the thicker barriers (curve 3 for 7.4 nm). The "blue" shift for TIN with the barrier thickness of 4.4 nm (curve 2) was below 1 meV. The dependences for TIN with extremely thick barrier ($B = 9.5$ nm, curve 4) and for reference sample (single QW) were close to each other in the region of weak "blue" shifts.

For thick and thin barriers (groups 1 and 3) the tunnel transfer of excitation from QW to QD primarily affects the electron subsystem. It means that QD gets additional resident electrons, and QW — excessive positive charge of holes. An intrinsic tunneling-induced electric field F is built up (Fig. 1b) and drift appears. The strength F is determined by excess carrier concentration, i.e. by the PL excitation power density. We believe that "red" PL QW peak shift for TINs with thin barrier (group 3, Fig. 3, curve 1) originates from Stark effect. "Blue" PL QW peak shift for TINs with thick barriers (group 1, Fig. 3, curve 3) is likely to be explained by the prevalence of a competing process over the weak intrinsic field. Such process is, e.g. screening of exciton states in the QW. In Fig. 2 the pronounced exciton resonance of QW is clearly visible.

In TINs with optimal barrier (group 2, Fig. 3, curve 2) no charge separation take place, because simultaneously with the tunneling of electrons into the QDs a transfer of holes occurs, ensured by the hole eigen-state of nanobridge. As a result neutrality of all TIN components is ensured and no intrinsic field is induced. In this case the screening is also weak, because it is supported by low density of the residual neutral electron-hole plasma. It causes a small reduction of exciton binding energy and, as a consequence, a slight "blue" shift of QW peak in TINs with an optimal barrier.

The fault of built-up electric field caused by hole states within the nanobridges gives an answer to the question: in what way and how much nanobridges influence the dependence of tunneling time between QW and QDs on the barrier thickness $\tau_T(B)$. This dependence has been studied before in [1] for low excitation density, where the influence of intrinsic field was negligible (Fig. 3). In order to determine the electron tunneling time the transient PL profiles were analyzed. For thick barriers (group 1) the $\tau_T(B)$-dependence is well described by the semi-classical WKB-approximation. When the barrier thickness becomes smaller than 6 nm (group 2), the tunneling character is changing. The exciton passes through such barrier as a whole, $\tau_T(B)$-dependence deviates from WKB-model.

In this work the tunneling time dependence on the barrier thickness is studied for high PL excitation density, where the excitation light itself modifies the charge conditions in active region of TINs (Fig. 3): for a thick barrier the QW exciton states are screened, and for a thin barrier an electric field is induced (Fig. 1b). A quantitative evaluation is carried out for the tunneling-induced field strength ($F = 2 \times 10^4$ V/cm) and the InGaAs/GaAs interface charge density (10^{11} cm^{-2}) for 3.1-nm GaAs barrier. Thus the application of nanobridges with particular hole states can has a high potential for novel TINs-based laser.

Acknowledgements

This work was supported by the Russian Foundation for Basic Research (080200954), Programs of RAS on Nanotechnologies and Nanomaterials and the German Federal Ministry of Education and Research (03Z2HN12).

References

[1] V. G. Talalaev *et al*, *Appl. Phys. Lett.* **93**, 031105 (2008).

18th Int. Symp. "Nanostructures: Physics and Technology"
St Petersburg, Russia, June 21–26, 2010

Quantum transport in GaAs/$Al_xGa_{1-x}As$ superlattices with weak barriers

A. A. Andronov, E. P. Dodin, Yu. N. Nozdrin and *D. I. Zinchenko*
Institute for Physics of Microstructures RAS, Nizhny Novgorod GSP-105 603600, Russia

Abstract. In [1], the THz Wannier–Stark laser based on GaAs/$Al_xGa_{1-x}As$ superlattices with weak barriers had been proposed. The amplification in this laser is due to population inversion between the first and the second Wannier–Stark levels located several SL periods apart in the electric field region of *positive* differential conductivity. Such lasers could well compete with existing quantum cascade lasers due to simplicity of the superlattices used and high tunability. In this report we discuss mechanisms of electric transport in Wannier–Stark lasers and present different approaches to model it.

Introduction

Terahertz technology is under intensive development all over the world during the last years. The idea of using semiconductor superlattices (SL) to generate electromagnetic radiation with frequency tunable by changing applied electric field appeared long ago [2,3]. For easily fabricated superlattice parameters this frequency can be tuned to Terahertz region. However, it was soon established that the field configuration in such structure will be unstable due to existence of low-frequency (static) negative differential conductivity (NDC) in the working region of proposed device, leading to formation of domains of inhomogenious electric fields. To prevent field instabilities, different schemes were put forward, and one of them led to creation of Quantum Cascade Lasers (QCLs) [4] which can now operate in the Terahertz range [5].

In [1], alternative design of laser based on SLs with weak barriers was presented. In this case, lasing should appear due to natural inversion between population of 1st and 2nd Wannier–Stark (W.–S.) levels in different wells of the superlattice (cf. [3]), and the frequency of such transition depends on the voltage drop on one period of SL, that makes it possible to tune the laser frequency substantially wider as compared to QCLs. The estimations of amplification for such lasers [1] show higher values compared to Terahertz QCL design.

To make more accurate amplification calculations, the nature of quantum transport in such structures has to be taken into account. In this report we discuss mechanisms of transport in SLs with weak barriers and show different approaches to model it.

1. Experimental

In this work, several different SL samples with weak (short ~1–1.5 nm and low <100 meV) potential barriers and minigap not exceeding 20 meV have been studied [6]. Here the results for 2 such SLs, samples 426 and 816, are presented. Table 1 shows some properties of these samples, here E_1 is the bottom of the first miniband, ΔE_1 is the width of 1-st miniband, $E_{\rm gap}$ is the width of the 1-st minigap, E_2 is the bottom of the 2-nd miniband, ΔE_2 is the width of 2-nd miniband, d, w and b are SL period, well and barrier widths, correspondingly, and N is the number of SL layers.

In Fig. 1, the experimentally observed I-V curves (studied on n^+-SL-n^+ mesas) for these SL samples are presented. In the rising part of the I-V curve, there are some pronounced peculiarities (arrows) that are attributed to resonant tunneling between Wannier–Stark levels of different wells, located several SL periods apart [6].

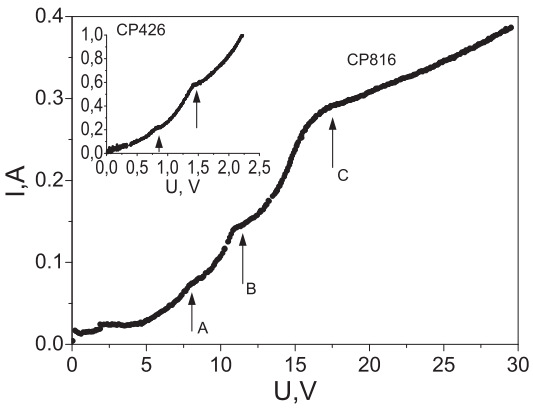

Fig. 1. I-V curves for samples SL 426 and SL 816.

2. Wannier–Stark laser

The peculiarities in I-V curves and their identification as due to inter-Wannier–Stark level tunneling [6] point to the existence of long-range (several SL periods) tunneling of electrons in superlattices studied. This implies that the wavefunctions of W.–S. levels in such structures can be extended to long distances near the resonance values of electric field which correspond to aligning of W.–S. levels originating from different minibands. In such resonant situation matrix elements of transitions between aligned levels become large due to long distance between wells where these levels are located. On the other hand, there is natural inversion between levels of first W.–S. ladder (originating from first miniband) and levels of second ladder, when the level of first ladder lies higher than the level of second ladder located in another well (Fig. 2, arrow labeled ω_3). This

Table 1. Sample parameters.

Sample	426	816
E_0 (meV)	3.2	7.4
ΔE_1 (meV)	11.2	9.8
E_1 (meV)	14.4	17.2
$E_{\rm gap}$ (meV)	7.1	16.8
E_2 (meV)	21.3	33.9
ΔE_2 (meV)	34.9	32.5
$d = w + b$ (μm)	185 + 10	160 + 20
N	100	1000

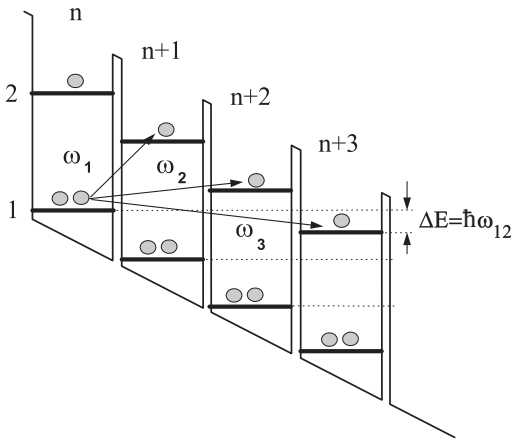

Fig. 2. Scheme of energy levels in SL and transitions between them; circles represent relative population of levels.

leads to the existing of lasing transition with high amplification coefficient [1].

3. Quantum transport in Wannier–Stark laser

To calculate amplification coefficient in W.–S. laser more accurately, one has to consider transport mechanism in such structures. The transport in superlattices has been studied extensively [7], and it has been shown that the nature of transport processes depends on the SL parameters and the considered field region. Most of the transport calculations use either tight-binding models where only neighboring wells are taken into account (which cannot be applied here since in our experimental data we see traces of resonances between levels in distant wells) or miniband approach (which cannot be applied since in our structures the miniband width is less then the voltage drop on one SL period in the considered field region).

Our first approach to calculate I-V curve for our structures is to use quasiclassical Monte-Carlo simulation [8]. It can be used to simulate miniband transport and effect of Zener tunneling without additional fitting parameters, but it fails to reproduce the effects of Wannier–Stark levels alignment since it essentially treats the SL as an effective homogenious medium and doesn't include level quantization.

The density matrix formalism allows to take into account the important properties of considered structures. It has been shown already in [3] that the current density around the resonance can be calculated using the formula

$$J = edN\eta\left(1 - e^{-\frac{\Delta}{kT}}\right)\frac{2|\Omega|^2\tau_\perp}{1+\epsilon^2\tau_\perp^2+4|\Omega|^2\tau_\parallel\tau_\perp}, \qquad (1)$$

where $\hbar\epsilon = eFd - \Delta$ is the energy detuning from resonance, Ω is the anticrossing gap, $\tau_\parallel$ is the frequency of electron transitions from the excited to the ground state, $\tau_\perp$ is the mean free path when the transverse momentum is dissipated, Δ is the distance between levels in a well, N is the electron concentration and η is a constant of the order of unity. However from this formula it follows that the region to the right of the resonance has NDC, while in our experiments the current remains monotonic around resonances. The density matrix approach was also applied in [9] to the case of superlattices with strong interminiband tunneling, resembling our case, and their result also exhibits strong NDC regions after the peaks.

As a first attempt to include quantum effects to our transport calculation we used formula (1) for current around the resonance, and we took into account transitions from ground state in one well to first and second excited states in other wells and added several resonance curves together, basing on calculated W.–S. levels anticrossing parameters [6]. The resulting curve strongly depends on τ parameters appearing in (1), but for some values the calculated curve can be made monotonically rising, like experimental curve. In the report an attempt to fit the above calculation to the experimental I-V curve will be made by choosing optimal scattering parameters.

Another problem that has to be taken into account is the importance of coherence in SL transport [cf. 10]. We have to distinguish between short-range and long-range tunneling transitions, in the short-range case (neighboring wells) the Rabi oscillations frequency (anticrossing gap) for resonantly coupled levels is high and there is no coherence loss during the tunneling event, while for distant levels the decoherence becomes important and it becomes more and more difficult for electrons to tunnel through the barriers as the distance increases. As was shown in [10], for resonances with strong decoherence it's better to use localized basis instead of extended one used for amplification calculations in [1] as it gives more physical description of tunneling processes in this case.

In the report the density matrix transport calculation will be presented which takes into account the above points.

Acknowledgements

The authors are thankful to A.A. Padalitsa and A.A. Marmalyuk for growing the SL samples, M. N. Drozdov and Yu. N. Drozdov for SIMS and X-Ray characterization of the samples and to I. Yu. Shuleshova for samples processing. The work is supported by RFBR Project 09-02-00380-a.

References

[1] A. A. Andronov, D. I. Zinchenko, E. P. Dodin, Yu. N. Nozdrin, *Proc. of 17th Int. Symp. "Nanostructures:Physics and Technology" (Minsk, 2009)*, Ioffe Institute, p. 23, 2009.
[2] L. Esaki and R. Tsu, *IBM J.Res.Dev.* **14**, 61 (1970).
[3] R. F. Kazarinov, R. A. Suris, *Sov. Phys. Semicond.* **5**, 707 (1971).
[4] J. Faist *et al*, *Science* **264**, 553 (1994).
[5] R. Kohler, A. Tredicucci, F. Beltram, H. E. Beere, E. H. Linfield, A. G. Davies, D. A. Ritchie, R. C. Iotti, F. Rossi, *Nature* **417**, 156 (2002).
[6] A. A. Andronov, E. P. Dodin, Yu. N. Nozdrin, D. I. Zinchenko, *Semiconductors* **43**, 228 (2009).
[7] L. L. Bonilla, H. T. Grahn, *Rep. Progr. Phys.* **68**, 577 (2005).
[8] A. A. Andronov, I. M. Nefedov, and A. V. Sosnin, *Semiconductors* **37**, 360 (2003).
[9] L. K. Orlov, Yu. A. Romanov, *Fiz. Tekhn. Poluprov.* **19**, 1877 (1985).
[10] H. Callebaut, Q. Hu, *J. Appl. Phys* **98**, 104505 (2005).

18th Int. Symp. "Nanostructures: Physics and Technology"
St Petersburg, Russia, June 21–26, 2010

Could dissipationless current be observed at non-zero resistance?

V. L. Gurtovoi, A. I. Ilin, *A. V. Nikulov* and V. A. Tulin
Institute of Microelectronics Technology RAS, 142432 Chernogolovka, Moscow region, Russia

Abstract. The persistent current, i.e. the equilibrium direct electric current circulating in realistic rings, some authors interpreted as dissipationless in spite of non-zero resistance of the rings, whereas the other one suppose that this current can not decay at dissipation. The observation of potential difference connected with the persistent current may give new important information about paradoxical nature of this quantum phenomena observed in nanostructures.

Introduction

The mesoscopic phenomenon predicted as far back as 1970 [1] could be at last observed with confidence [2,3] thanks to nanotechnology progress. The persistent current has been the focus of considerable theoretical and experimental work, but its basic properties remain a topic of controversy. The direct circular current is observed at equilibrium condition in realistic normal metal rings containing atomic defects, grain boundaries, and other kinds of static disorder. The main problem may be put into the question: "How can the persistent current contrive to do not decay in the absence of an applied voltage and a nonzero electrical resistance?" The dictums of different authors concerning a possible answer on this question are contradictory. The authors of [2] and also [4] are sure that a dissipating energy is absent in spite of non-zero resistance and interpret the persistent current as a dissipationless current. Contrary to this confidence I.O. Kulik, who predicted first the persistent current, accentuated in [1] that the taking into account of dissipation should not result in the current disappearance. The experimental results presented in this work testify in favour for the Kulik's opinion.

1. Could familiar analog in atomic physics be complete?

The author [4] writes that *The idea that a normal, nonsuperconducting metal ring can sustain a persistent current — one that flows forever without dissipating energy — seems preposterous*. And it is written in [2] that *"A dissipationless equilibrium current flowing through a resistive circuit is counterintuitive"*. It is correct. The authors [2,4] and all others can not explain how an electric current passing through resistors can be dissipationless. The authors [2] limit oneself to *"a familiar analog in atomic physics: Some atomic species' electronic ground states possess nonzero orbital angular momentum, which is equivalent to a current circulating around the atom"*. Indeed, the possibility of the persistent current is described with the Bohr–Sommerfeld quantization

$$\oint_l dl\hbar\nabla\varphi = \oint_l dlp = 2\pi\hbar n \qquad (1)$$

as well as of the stationary electron orbits of atom. But the wave function $\Psi = |\Psi| \exp i\varphi$ describing a electron state in realistic metal ring can not be stationary in time in contrast to the one in atom. Electrons have a finite mean free path in realistic metal ring and the experimental results [2] conform to the theory [5] considering this real case. This experimental result [2] contradict to the statement of their authors that the persistent current, which they observe, is dissipationless.

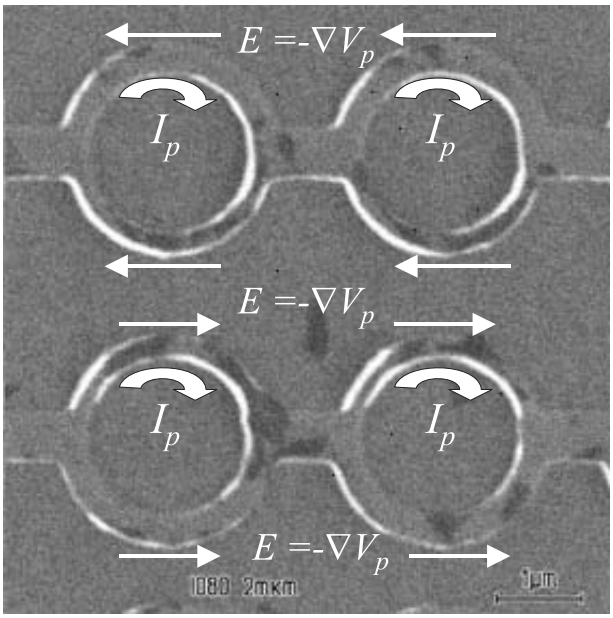

Fig. 1. A fragment of the system of 1080 series-connected asymmetric aluminum rings with the same diameter $2r \approx 2\ \mu$m. The sign of the potential difference V_p and the electric field $E = -\nabla V_\mathrm{p}$ direction depend on the I_p direction in the narrow half-ring $w_n \approx 0.3\ \mu$m, having higher resistance $R_n > R_\mathrm{w}$. In the wide half-ring $w_\mathrm{w} \approx 0.4\ \mu$m the persistent current flows against the electric field $E = -\nabla V_\mathrm{p}$.

2. Persistent current and conventional circular current

On the other hand I. O. Kulik did not explain how the persistent current can not decay at dissipation without an applied electric field. Conventional circular current I can not decay $RI = -d\Phi/dt$ in a ring with non-zero resistance $R > 0$ only at a non-zero Faraday's electromotive forcee $-d\Phi/dt \neq 0$. The persistent current is observed at a magnetic flux inside the ring $\Phi \neq n\Phi_0$, $\Phi \neq (n+0.5)\Phi_0$ constant in time $d\Phi/dt = 0$ [2,3]. Its direction and value change periodically in Φ with period equal the flux quantum $\Phi_0 = 2\pi\hbar/q$, $I_\mathrm{p}(\Phi/\Phi_0)$ because of the Aharonov–Bohm effect, $\hbar \bigtriangledown \varphi = p = mv + qA$. This difference between the persistent current and conventional circular current is obviously the principal motive to interpret the first as the dissipationless current.

3. Persistent current in realistic ring with different resistance of half-rings

It is well known that the conventional circular current I induced by the Faraday's electromotive force $-d\Phi/dt \neq 0$ should

cause the potential difference

$$V = 0.5(R_n - R_w)I \qquad (2)$$

on the half-rings with different resistance $R_n > R_w$. The I direction corresponds to the electric field $E = -\nabla V - dA/dt$ direction in the both half-rings in this case in accordance with the Ohm's law $E = \rho j$. In the case of the persistent current non-potential electric field $-dA/dt$ is absent $-dA/dt = l^{-1}d\Phi/dt = 0$. Experimental investigations of the possibility to observe a potential difference like (2) on the half-rings with different resistance and non-zero persistent current $I_p \neq 0$ could have decisive importance for the understanding of the nature of the persistent current.

Modern nanotechnology allows to make a system of rings, similar the one used in the works [2,3], with different resistance $R_n > R_w$ of the half-rings. But, as the authors [2,4] note justly, detection of the persistent currents in normal metal ring is extremely difficult, first of all because of its very small magnitude. One may expect that the potential difference (1) should be also very small. The persistent current has much larger magnitude in superconductor ring. Therefore it was detected first at non-zero resistance $R > 0$ as far back as 1962 [6]. The persistent current in normal state of superconductor and non-superconductor (semiconductor and normal metal) has seminar nature and the theorists demonstrate this likeness. I. O. Kulik made the theory of the persistent current in non-superconductor nano-structure [1] just after the work [7] on this phenomenon in normal state of superconductor. In twenty years F. von Oppen and E. K. Riedel have calculated the flux-periodic persistent current in mesoscopic superconducting rings close to T_c [8] after the calculation of the disorder-averaged persistent current for a non-superconductor mesoscopic ring [9]. The magnetisation induced by the $I_p(\Phi/\Phi_0)$ is observed both in normal metal rings [3] and in normal state of superconductor rings [10].

In order to verify the possibility of the potential difference $V_p(\Phi/\Phi_0) \propto I_p(\Phi/\Phi_0)$ we used a system of 1080 series-connected asymmetric aluminum rings. A fragment of the system is shown on Fig. 1. All 1080 rings have the same diameter $2r \approx 2$ μm and half-ring widths $w_n \approx 0.3$ μm and $w_w \approx 0.4$ μm. Without controlled external electric current and depressed uncontrolled electric noise we can observe the voltage oscillations $V_p(\Phi/\Phi_0) \propto I_p(\Phi/\Phi_0)$ with amplitude up to $V_A \approx 0.1$ μV (on one ring $V_{A,1} = V_A/1080 \approx 0.1$ nV) in the temperature region $T = 1.358$–1.372 K corresponding to the lower part $R(T)/R_n = 0.01$–0.25 of superconducting resistive transition, Fig. 2, at our possibility to see the $V_p(\Phi/\Phi_0)$ oscillations with the amplitude down to $V_A \approx 0.02$ μV. The magnetisation measurements [10] and our observation of the Little–Parks [6] oscillations of resistance $R(\Phi/\Phi_0) = V(\Phi/\Phi_0)/I_{ext}$, Fig. 2, give evidence of non-zero persistent current at higher temperatures up to $R(T)/R_n \approx 1$, in accordance with the fluctuation theory [7,8]. Therefore one may expect that the $V_p(\Phi/\Phi_0)$ oscillations can be also observed at higher temperatures on a system with lager number of the rings.

The author [4] notes that the persistent current can not be detected with help of an ammeter. According to the result of our measurements it can be detected with help of the voltmeter. It is important. The direct voltage can be added in system of series-connected rings. Even if the voltage $V_p(\Phi/\Phi_0) \propto I_p(\Phi/\Phi_0)$ is very small in single asymmetric normal metal rings it can be observed with help of a system containing enough big number of rings. The observations $V_p(\Phi/\Phi_0) \propto I_p(\Phi/\Phi_0)$ reveal that the persistent current can flow against the force $F_E = qE$ of the direct electric field $E = -\nabla V_p$, Fig. 1. Because of this result the interpretation [2,4] of the persistent current as dissipationless phenomenon can not solve the problem of force balance.

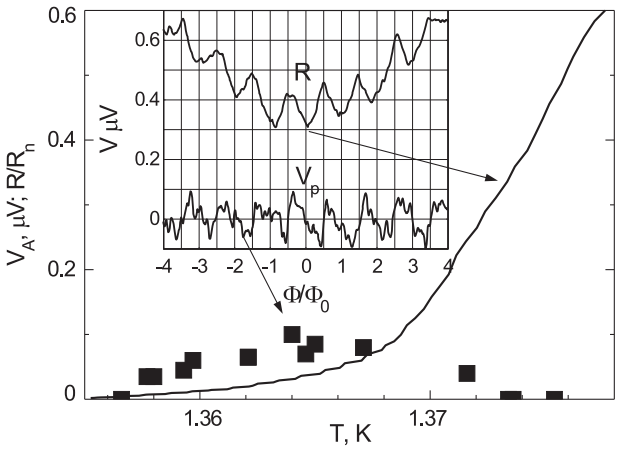

Fig. 2. Temperature dependence of the amplitude V_A of the potential difference oscillations $V_p(\Phi/\Phi_0) \propto I_p(\Phi/\Phi_0)$ (indicated by squares) observed without external electric current on 1080 series-connected asymmetric aluminum rings, shown on the background of the superconducting resistive transition R/R_n of this system. The inset shows (V_p) these oscillations $V_p(\Phi/\Phi_0) \propto I_p(\Phi/\Phi_0)$ observed at $T = 1.364$ K and (R) the Little–Parks oscillations of resistance $V = R(\Phi/\Phi_0)I_{ext} \propto I_p^2(\Phi/\Phi_0)$ observed at $T = 1.374$ K and very low measuring current $I_{ext} = 0.1$ nA.

Acknowledgements

This work has been supported by a grant "Possible applications of new mesoscopic quantum effects for making of element basis of quantum computer, nanoelectronics and micro-system technic" of the Fundamental Research Program of ITCS department of RAS and the Russian Foundation of Basic Research grant 08-02-99042-r-ofi.

References

[1] I. O. Kulik, *Pisma Zh. Eksp. Teor. Fiz.* **11**, 407 (1970) (*JETP Lett.* **11**, 275 (1970)).
[2] A. C. Bleszynski-Jayich *et al*, *Science* **326**, 272 (2009).
[3] H. Bluhm *et al*, *Phys. Rev. Lett.* **102**, 136802 (2009).
[4] N. O. Birge, *Science* **326**, 244 (2009).
[5] E. K. Riedel and F. von Oppen, *Phys. Rev. B* **47**, 15449 (1993).
[6] W. A. Little and R. D. Parks, *Phys. Rev. Lett.* **9**, 9 (1962).
[7] I. O. Kulik, *Zh. Eksp. Teor. Fiz.* **58**, 2171 (1970).
[8] F. von Oppen and E. K. Riedel, *Phys. Rev. B* **46**, 3203 (1992).
[9] F. von Oppen and E. K. Riedel, *Phys. Rev.Lett.* **66**, 587 (1991).
[10] N. C. Koshnick *et al*, *Science* **318**, 1440 (2007).

18th Int. Symp. "Nanostructures: Physics and Technology"
St Petersburg, Russia, June 21–26, 2010

Optical and magnetic properties of Co films deposited on colloidal crystal

M. V. Sapozhnikov[1], S. A. Gusev[1], V. V. Rogov[1], O. L. Ermolaeva[1], B .B. Troitskii[2], L. V. Khokhlova[2] and D. A. Smirnov[2]

[1] Institute for Physics of Microstructures RAS, Nizhny Novgorod, GSP-105, Russia
[2] G. A. Razuvaev Institute of Organometallic Chemistry RAS, Nizhny Novgorod, Russia

Abstract. We report here on the magnetic and optical properties of nanocorrugated Co films deposited on the top of PMMA colloidal crystal. Optical reflectance spectra were studied in the range of near UV, IR and visible light for p- and s-polarizations. Valleys were observed in the reflectance spectra and their positions scale with the PMMA sphere diameter. In explanation of the above scenario, not only the surface plasmon resonance but also the dipole resonance of single Co nanocaps should be considered. Magnetooptic measurements showed the qualitative change of the magnetization curve and enhancement of magnetooptic rotation at wavelength $\lambda = 632$ nm in comparison with flat control Co film.

The main idea of quickly developing plasmonics is to enhance and manipulate optical phenomena at the nanoscale dimension by plasmonic mechanisms [1]. Nowadays plasmonic systems using magnetic materials attracts growing interest. Recently the enhancement of magnetooptic effects by resonant scattering of the light in nanostructured magnetic materials has been predicted theoretically [2], some works are devoted to the experimental study of SPR effect on the optical transmission through a subwavelength hole array in magnetic films [3], and on magneto-optical effect in magnetic periodic nanostructures [4].

Here we report on the study of surface plasmon resonance (SPR) effects on the optical properties of Co films deposited on the surface of polymethyl methacrylate (PMMA) colloidal crystals. The investigations of reflection spectra carried out separately for s- and p- polarization of the incident light and for different film thicknesses allowed to distinguish the effects of the propagating and localized surface plasmons. The measurements of the magnetization curves demonstrated the increase of the magnetooptic rotation of the nanocorrugated film in comparison with the control flat Co film. Magnetic force microscopy (MFM) investigations of the magnetization distribution in the samples were carried out to explain the peculiarities of the magnetization curves.

The initial colloidal crystals of PMMA were prepared by emulsion polymerization with the potassium peroxodisulfate as catalyst followed by careful drying in a chamber at room temperature. Characterization of the colloidal crystal was made by scanning electron microscopy (SEM) and by AFM microscopy (Fig. 1). The SEM images showed that PMMA particles are densely packed in a hexagonal structure. The main defects in the structure are single particles upon the surface of the colloidal crystal, vacancies in the upper layer and the boundaries between crystallites with different orientations of the crystal axes.

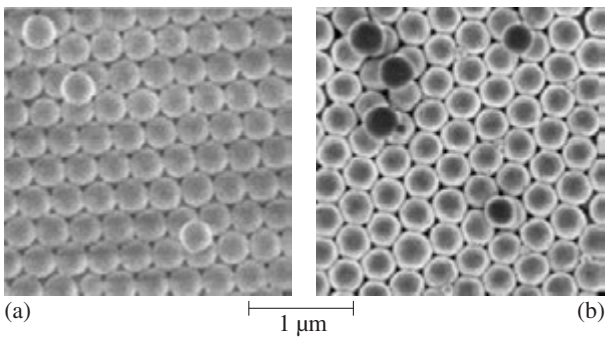

Fig. 1. SEM images of the PMMA colloidal crystal: A) before deposition of the Co film, B) after deposition of the film. The single particles are seen on the surface in both cases.

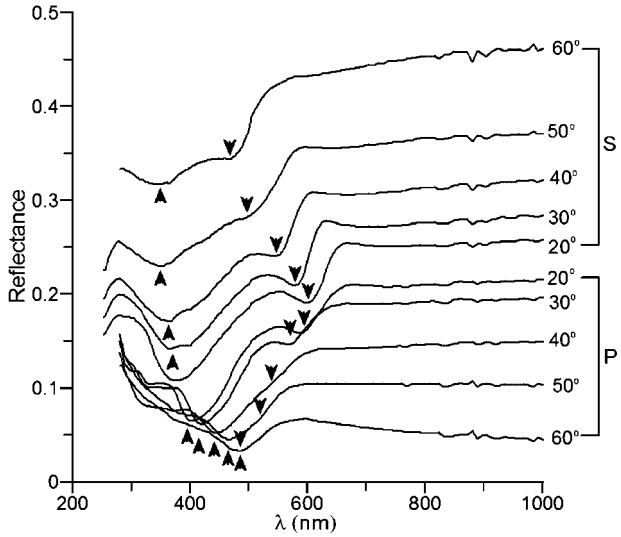

Fig. 2. Measured optical reflectance spectra of 30 nm thick nanocorrugated Co film (particle size of initial PMMA colloidal crystal is 290 nm) for s- and p-polarization of the incident light and for different angles of the light incidence. Down arrows indicate minima due to propagative SPP mode, up arrows indicate minima due to localized plasmon modes.

The Co film was deposited on the surface of PMMA colloidal crystal by using magnetron sputtering. As the thickness of the films (30 and 60 nm) was sufficiently less than the diameter of the particles, the film became corrugated in two dimensions. The optical reflection spectra of the nanocorrugated Co films, control Co films and initial colloidal crystals were obtained at room temperature by using high pressure xenon lamp, diffraction spectrometer and precision silicon photodiodes designed as detector for 200–1100 nm wavelength range.

The typical mirror reflection spectra for the 30-nm Co film deposited on the surface of the colloidal crystal are represented

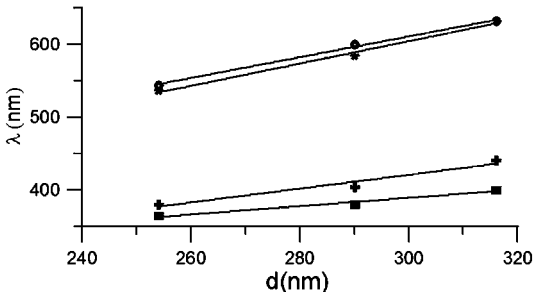

Fig. 3. Scaling of the reflectance spectra of 30 nm nanocorrugated films with the diameter of the PMMA particles. The positions of long-wave and short-wave reflectance minima for samples with different diameters are shown for the incident angle 20°: circles and squares — s-polarization, stars and crosses — p-polarization.

in Fig. 2. The measurements were performed in the angle range from 20 to 60° (measured from the structure surface normal) both for s- (TE) and p- (TM) polarizations.

Two minima were observed in the mirror reflection spectra of 30-nm films and their position are scaled with PMMA particle diameter (Fig. 3) while the reflection spectrum of a flat Co film had monotonic shape. The long-wave (lw) minimum blue-shifted with the increase of the angle of light incidence in the same manner for s- and p- polarizations. On the contrary the short-wave (sw) minimum red-shifted for p-polarization and almost did not shift for s-polarization. Besides in the case of 60nm Co film the sw-minimum remained similar to 30 nm thick Co films while the lw-minimum almost disappeared.

Obviously, these minima caused by different mechanisms. Qualitatively the shape of spectra can be explained in the following way. The angular dependence of the long-wave-length minimum and its position scaling with the period of the structure points on the propagating plasmons excitation in the system. Due to two-dimensional structuring of the system they can be excited both by s-and p-polarized incident radiation. The disappearance of the minimum for the 60 nm film suggests that it is associated with the plasmons excitation on the inner boundary between the metal and dielectric.

In its turn the appearance of the sw-minimum in the reflection spectrum can be attributed to the excitation of localized dipole resonances on structure defects, presumably in PMMA particles separately lying on the surface of the colloidal crystal and coated with cobalt hemispheres. Indeed, due to the cylindrical symmetry of the defect, it has two eigen modes of the dipole oscillations — with the dipole lying in the plane of the system or with the dipole perpendicular to the plane of the system. Generally, this oscillation will have different frequencies. Obviously, s-polarized incident wave will excite only longitudinal dipole resonance, independently of the angle of incidence. As for p-polarized incident radiation it will excite parallel dipole oscillation at small incident angles, so the positions of minima in spectrum for p- and s- polarizations are close for 20°. On the contrary, at tangent incident angles the p-polarized incident radiation will excite a perpendicular dipole oscillation with a different frequency. With the increase of the incident angle of p-polarization the amplitude of the parallel dipole mode will decrease while the amplitude of the perpendicular mode will increase. If the resonances width is comparable with the distance between them one will observe only one minimum in the reflection spectrum, but its position

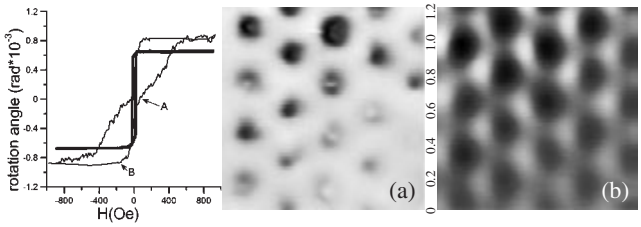

Fig. 4. Magnetization curve of the nanocorrugated Co film (thin line) on the top of PMMA colloidal crystal (particle diameter 290 nm) measured by longitudinal magnetooptic Kerr effect. Thick line is a magnetization curve of the flat 30 nm Co film obtained in the same deposition process. A) MFM image of the sample at $H = 0$, magnetization state of Co hemispheres looks like magnetic vortex. B) MFM image of the sample at $H = 800$ Oe, hemispheres are in the single domain state. The corresponding states are indicated on the magnetization curve.

will depend on the incident angle. So, while the lw-minima in the reflectance spectrum are caused by the excitation of the propagating plasmon, the sw-minima are caused due to localized dipole resonances.

The magnetic properties of the nanocorrugated Co films were also studied. The magnetization curve was investigated by the measurement of longitudinal magnetooptic Kerr effect (Fig. 4) with the use of He-Ne laser $\lambda = 632$ nm. Two main facts should be mentioned. First — the magnetization curve is similar to that of magnetic nanoparticles with the vortex distribution of magnetization [4]. This was verified by MFM measurements. As the lattice is hexagonal some of the vortices are frustrated. Second — all measured nanocorrugated Co films had a higher coefficient of the magnetooptical rotation in saturation for $\lambda = 632$ nm than the corresponding control flat Co films deposited in the same process.

Acknowledgements

This research was supported by RFBR, FTP "Scientific and scientific-pedagogical personnel of innovative Russia" in 2009–2013 and byAgency for Education of the Russian Federation (project No. RNP 2.1.1/2833).

References

[1] V. I. Belotelov *et al*, *Phys. Rev. Lett.* **98**, 077401 (2007).
[2] F. Przybilla *et al*, *J. Opt. A: Pure Appl. Opt.* **8**, 458 (2006).
[3] Z. Liu *et al*, *Appl. Phys. Lett.* **95**, 032502 (2009).
[4] R. P. Cowburn *et al*, *Phys. Rev. Lett.* **83**, 1042 (1999).

18th Int. Symp. "Nanostructures: Physics and Technology"
St Petersburg, Russia, June 21–26, 2010

The behavior of composite InN/In nanostructures in the crossed electrical and magnetic fields

T. A. Komissarova[1], M. A. Shakhov[1], V. N. Jmerik[1], R. V. Parfeniev[1], P. Paturi[2], X. Wang[3], A. Yoshikawa[4] and S. V. Ivanov[1]

[1] Ioffe Physical-Technical Institute, St Petersburg, Russia
[2] Wihuri Physical Laboratory, Turku University, Turku, Finland
[3] Peking University, Beijing 100871, China
[4] Chiba University, Chiba, Japan

Abstract. The magnetic field dependences of the Hall coefficient (R_H) and resistivity (ρ) of spontaneously formed InN/In composite nanostructures are investigated. The abnormal magnetic field dependence of R_H and significant variation of ρ with the magnetic field have been observed. Both effects have been found to be related to the effect of the indium nanoparticles.

Introduction

Recent studies of the optical properties of InN epitaxial films have shown that this material should be considered as a semiconductor/metal composite nanostructure rather than a conventional semiconductor [1]. It involves both the InN semiconductor matrix and the metallic indium nanoparticles. The latter can arise spontaneously during the InN epitaxial growth due to its small heat of formation, existence of In precipitates on the growth surface and large density of extended defects which are able to accumulate excessive In from the InN surface. These In nanoparticles influence strongly the optical properties of InN layers leading to discrepancy between characteristic energies of different optical processes (absorption, emission, photo-carriers generation) [1].

It would be reasonable to assume that it is also possible to show up the existence of In nanoclusters from studies of electrical properties of the InN epilayers. To the best of our knowledge, there are only few works devoted to the investigation of this problem [2]. However, the electrical measurements (Hall effect and resistivity) in these works were performed at a single value of low magnetic field (<1 T) and no significant influence of the In nanoclusters has been revealed. This paper reports on the dependence of transport properties of spontaneously formed InN/In composite nanostructures on magnetic field up to 30 T.

1. Experimental

InN films were grown by plasma-assisted molecular beam epitaxy under the slightly different stoichiometric conditions on GaN buffer layers deposited on c-sapphire substrates prior to InN growth. The magnetic field was applied parallel to the *c*-axis of the films and normal to the electric current. The magnetic field dependences of the Hall coefficient (R_H) and the resistivity (ρ) were measured in the wide temperature range (1.6–300) K in the pulsed magnetic fields up to 30 T.

It has been found that the absolute value of the Hall coefficient increases with the magnetic field in the whole temperature range (Fig. 1), while in a conventional semiconductor R_H should decrease or be independent of the magnetic field. We have also observed strong variation of the ρ with the magnetic field. The value of the magnetoresistance at 25 T $\Delta\rho/\rho_0 = (\rho(B) - \rho_0)/\rho_0$ achieves 600% at 4.2 K and 350%

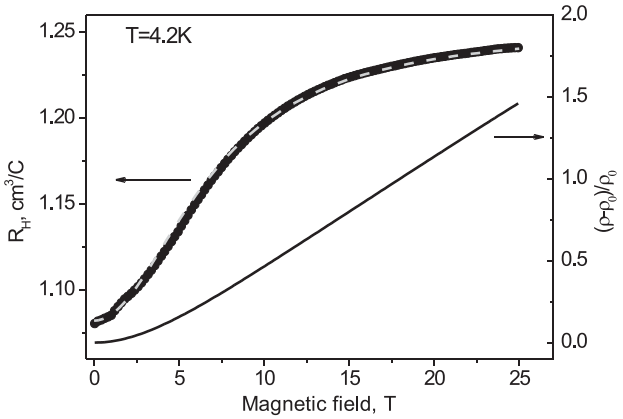

Fig. 1. Experimental magnetic field dependences of R_H and MR (black curves) and the approximation of the former in the frames of the model [5] (grey curve).

at 300 K in one of the samples. The magnetoresistance (MR) effect can occur in a non-magnetic conventional semiconductor due to action of the Lorentz force on the charge carriers if the latter are distributed in energy. However, the InN semiconductor matrix is a degenerate semiconductor with the typical electron concentration of about 10^{18}–10^{19} cm^{-3}. Since only the electrons with the Fermi energy participate in the conductivity, the MR effect should not be observed in this case. Another possibility of appearance of the MR effect in a semiconductor is an existence of the several types of charge carriers. Indeed, it has been previously reported that the electron accumulation layer exists at the surface of InN bulk epilayer [3]. However, the MR effect associated with the change of the electron mean free path should have a square-law dependence on the magnetic field and saturate in high magnetic fields ($B\mu_{1,2} > 1$), while the experimental magnetic field dependences of MR are almost linear and do not saturate up to 30 T for all the investigated samples.

2. Discussion

The experimental dependences of the R_H and MR cannot be explained by considering only the InN semiconductor matrix. We should take into account the existence of the In nanoparticles inside the InN semiconductor matrix in the investigated composite films, that was proved previously by studying the

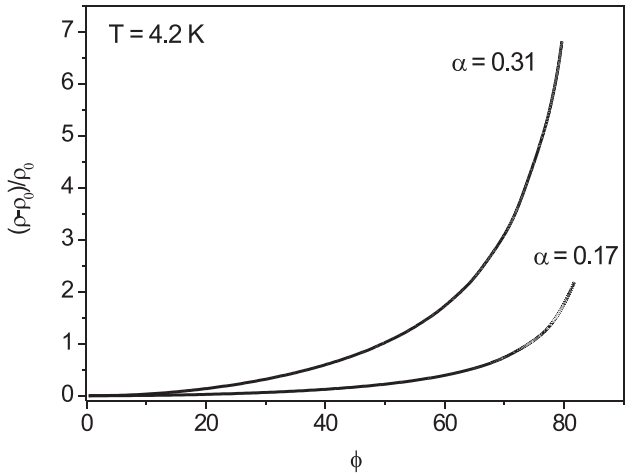

Fig. 2. The Hall angle dependences of the MR in the InN/In composite nanostructures with the same electron parameters of the semiconductor matrix but different α values.

magnetic field and temperature dependences of onset of a superconducting transition in the InN epilayers [4]. The Hall coefficient can increase with B in a semiconductor involving inhomogeneities with the conductivity strongly exceeding that of the surrounding matrix [5]. The following geometrical consideration can explain the increase of R_{H} and ρ with the magnetic field [6]. Since the surface of the highly conducting inhomogeneity is the equipotential surface, the vector of electric field $\mathbf{E}$ is always normal to this surface. At zero magnetic field, the electric current $\mathbf{j} = \sigma\mathbf{E}$ is parallel to $\mathbf{E}$, which causes the current lines to be focused on the inhomogeneities acting as "short-circuits". Therefore at low B the measured values of the R_{H} and ρ are governed by both the parameters of the conducting inhomogeneities and the semiconductor matrix rather than the matrix itself. With the B increase, the $\mathbf{j}$ vector is deviated from $\mathbf{E}$ by the Hall angle $\mathrm{tg}\phi = \mu B$, the current lines being pushed out the conducting inhomogeneities, leading to the increase in R_{H} and ρ. In the limit of high B the Hall angle tends to 90° and the current should flow only through the matrix, i.e. the R_{H} and ρ values are defined only by the semiconductor transport characteristics.

We have approximated the experimental dependences of the Hall coefficient in the frame of the model of the semiconductor matrix with the conducting inhomogeneities [5]. There are three adjustable parameters: the electron concentration n and mobility μ in the semiconductor matrix and α coefficient which is the ratio between the volume of the conducting inhomogeneities and the total volume of the semiconductor. The approximation of the experimental dependences shows good correlation between the experimental and theoretical data (Fig. 1).

The value of the magnetoresistance $\Delta\rho/\rho_0$ at the certain magnetic field should depend on the Hall angle and the relation between the conductivity of the InN semiconductor matrix and In nanoparticles in the frame of this consideration. In turn, the total conductivity of the indium nanoparticles is governed by the relative amount of the nanoparticles α. Figure 2 presents the comparison of the MR for two InN structures with the same conductivity of about 10^3 $(\Omega\,\mathrm{cm})^{-1}$ but different α. One can see that indeed the large amount of In nanoparticles leads to the higher value of MR at the same value of the Hall angle.

Summarizing, it has been found that the In nanoparticles in the composite InN/In semiconductor/metal structures influence strongly the measured electrical parameters and result in the abnormal magnetic field dependence of the Hall coefficient and the strong geometrical magnetoresistance effect. The proposed approach allows one to derive the real transport parameters (μ and n) of InN semiconductor matrix as well as an amount of metallic In incorporated.

Acknowledgements

The work has been supported in part by RFBR and the Program of Presidium of RAS.

References

[1] T. V. Shubina *et al*, *Phys. Rev. B* **79**, 153105 (2009).
[2] T. A. Komissarova *et al*, *Semiconductors* **43**, 285 (2009).
[3] C. H. Swartz *et al*, *J. Crystal Growth* **269**, 29 (2004).
[4] T. A. Komissarova *et al*, *Appl. Phys. Lett.* **95**, 086101 (2009).
[5] C. M. Wolfe *et al*, *Appl. Phys. Lett.* **18**, 205 (1971).
[6] T. Thio *et al*, *Appl. Phys. Lett.* **72**, 3497 (1998).

18th Int. Symp. "Nanostructures: Physics and Technology"
St Petersburg, Russia, June 21–26, 2010

Observation of anti-vortex states in cross-like nanomagnets

S. A. Gusev, O. L. Ermolaeva, B. A. Gribkov, A. A. Fraerman, V. L. Mironov and E. V. Skorohodov
Institute for Physics of Microstructures RAS, Nizhny Novgorod, 603950, GSP-105, Russia

Abstract. In the paper we report results of experimental study of heterogeneous states in cross-like ferromagnetic nanostructures. The arrays of asymmetrical cobalt crosses with 1 μm branches, 100 nm widths of the branches and 40 nm thicknesses were fabricated using e-beam lithography. Each branch of the cross was tapered at one end and bulbous at the opposite. The formation of anti-vortex magnetic states in these nanostructures during magnetization reversal was demonstrated experimentally using magnetic force microscopy.

Introduction

Practical applications as well as fundamental investigations of magnetic nanostructures (nanomagnets) require well-controlled magnetic states. One of the method to control the magnetic states at the nanometer scale is the well adjusted topology and dimensions of magnetic nanoelements. A range of interesting phenomena take place in the intermediate ("mesoscopic") range of 10–1000 nm, where electron-beam lithography allows for "magnetic nano-engineering" with fine defined geometry of nanostructures. Highlights are the realization of vortex states in ferromagnetic nanodisks [1], and spiral (helical) states in laterally confined magnetic multilayers [2], and prediction of a novel type of magnetic walls in nanoconstrictions [3]. In this paper we report on an experimental study of another fundamental magnetization structure, the anti-vortex [4–6], which is a topological counterpart of a magnetic vortex. Besides being a remarkable magnetic structure the anti-vortex is expected to show unusual transport properties in an applied external magnetic field, namely a spectacular new phenomenon, the so-called "topological" Hall effect [7]. Unlike a vortex, the realization of an anti-vortex, i.e. preparation of a nanostructure that contains only a single anti-vortex, is a challenging task. The anti-vortex possesses a "magnetic charge" resulting in additional, in comparison with a vortex, magnetostatic energy. A few years ago, an anti-vortex structure was created at a cross junction of four connected rings [6] with vortex distribution in each of the rings; however this complicated design does not allow for transport measurements, especially in an external magnetic field. In this work a single anti-vortex state has been realized in asymmetric cross-like nanoelements (nanomagnets) suitable for Hall measurements. The anti-vortex state we prepared by means of a specific procedure of magnetization reversal stimulated by the shape asymmetry.

1. Experimental results

The theoretical grounds of our experiments in details are presented in the paper [8]. First of all we have produced computer modeling of magnetization distribution in cross-like nanomagnets with different shapes, and in this computer experiments also we have studied the possibility to manipulate a residual magnetization of nanostructures by an external magnetic field applied in different directions in the preliminarily magnetization. The micromagnetic modeling of magnetic states was performed using software based on solutions to the Landau–Lifshitz–Gilbert (LLG) equation. In the model we have taken into account the dependence of coercivity of magnetic elements on their shape and considered as a symmetrical, as an asymmetrical cross shown in Fig. 1. The arrays of Co crosses were fabricated using electron-beam lithography (EBL) from cobalt films. We have used both usual EBL method (with positive PMMA resist and lift-off technique), and nanolithographic process developed by us with DUV resists which are sensitive to electron exposure too (positive tone FP 9120 and FP 051). The e-beam exposure was done using the ELPHY PLUS system based on the scanning electron microscope SUPRA 50VP. The magnetic states in the Co crosses were studied using a multimode scanning probe microscope "Solver-HV". The scanning probes were cobalt-coated with a thickness of 30 nm. Before measurements the tips were magnetized along the symmetry axes (Z) in 10 kOe external magnetic field. The MFM measurements were performed in the non contact constant height mode.

The first set of measured samples was consisted of symmetric crosses. Their magnetic structure depended on the aspect ratio ($g = a/b$, a — the length of the crosses arms, b — the width of the segments), as expected. Crosses with relatively small aspect ratio g showed spontaneous quasi-uniform states. The crosses with larger aspect ratio g could go into vortex states. Spontaneous quasi-uniform states with two types of symmetry, A and B were observed in the crosses with lateral size $a = 600$ nm and $b = 100$ nm. A characteristic feature of A and B uniform states is the quadrupole symmetry of the MFM contrast distribution (on the Fig. 2a presented type A only). For the crosses with $a = 600$ nm and width of branch $b = 200$ nm quasi-vortex states were registered. The experimental MFM image of a quasi-vortex state is represented on the Fig. 2b. To realize the anti-vortex state we fabricated asymmetrical crosses (Fig. 1b). The lateral size of the crosses was $a = 1$ μm, the width of the branch was $b = 100$ nm and size

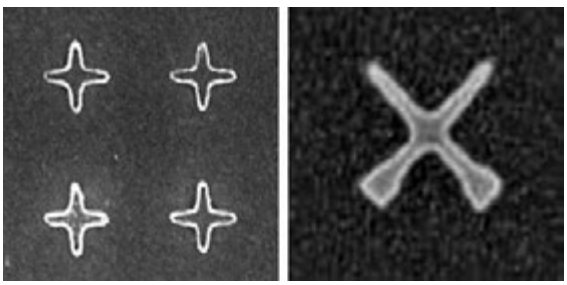

Fig. 1. SEM images of Co nano-crosses produced by e-beam lithography. The white scale bar is 1 μm.

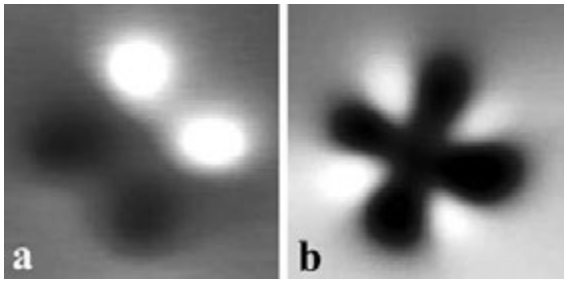

Fig. 2. The experimental MFM contrast distributions corresponding to the A type of quasi-uniform state (a) and quasi- vortex (b) distribution of magnetization.

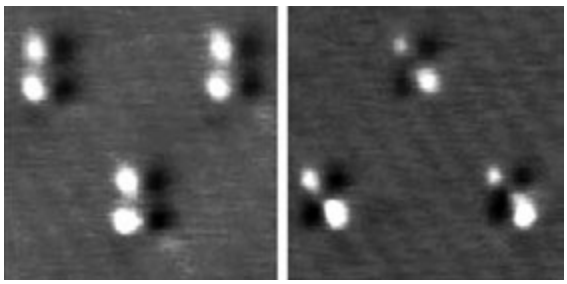

Fig. 3. Transformation of magnetic states in asymmetric Co crosses from quasi uniform states to anti-vortex states in an external magnetic field. The frame size is 6×6 μm.

of the bulb was 150 nm. Fig. 3 shows the results of MFM investigation of asymmetric crosses. Magnetization in a strong (800 Oe) magnetic field directed along the diagonal of the cross results in quasi uniform magnetization (Fig. 3a). A weak reversed magnetic field with magnitude of 250 Oe leads to the transition some of the particles into anti-vortex state with characteristic quadrupole symmetry of MFM contrast. An increase of the external magnetic field to 400 Oe leads to the creation of anti-vortexes in all crosses (Fig. 3b). The observed dispersion of switching fields from 250 Oe to 400 Oe can be connected with the dispersion in particle coercive forces due to shape differences.

2. Conclusions

It was shown that shape control based on electron-beam lithography allows for practical "nano-engineering" of magnetic states in cross-like nanostructures. We demonstrated that symmetric Co nano-crosses can be put into spontaneous quasi-uniform and quasi-vortex states depending on their size and aspect ratio. The asymmetrical Co crosses where each branch is tapered at one end and bulbous at the other showed the stable formation of anti-vortex states during magnetization reversal. These structures with controllable quasi-uniform and anti-vortex states are very promising for the investigations of transport peculiarities and magneto-dynamical phenomena in inhomogeneous magnetic systems. Finally we have fabricated first nanostructures for the study "topological" Hall effect (Fig. 4). Large electrical contacts and ferromagnetic cross in the centre of structure had been produced with the EBL by means lift-off technique. For the fabrication of fine nanocontacts (length is 1.5 μm, width — 75 nm, thickness — 50 nm) we have used local deposition of Pt from the vapor stimulated by ions (FIB CVD) by means NEON 40 cross-beams station.

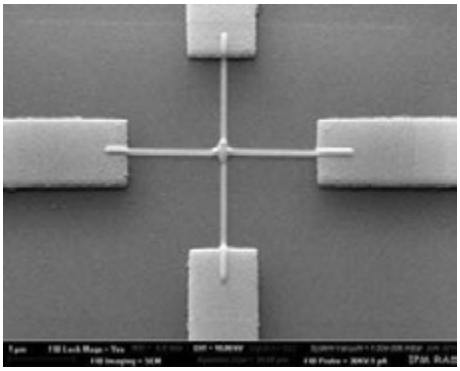

Fig. 4. SEM microphotography of trial nanostructure for the electrical measurements of "topological" Hall effect.

Acknowledgements

This work was supported by the Russian Foundation for Basic Research and Russian Federal Educational Agency.

References

[1] R. P. Cowburn, D. K. Koltsov, A. O. Adeyeye, M. E. Welland, and D. M. Tricker, *Phys. Rev. Lett.* **83**, 1042 (1999).
[2] A. A. Fraerman, B. A. Gribkov, S. A. Gusev, A. Yu. Klimov, V. L. Mironov, D. S. Nikitushkin, V. V. Rogov, S. N. Vdovichev, B. Hjorvarsson, and H. Zabel, *J. Appl. Phys.* **103**, 073916, (2008).
[3] P. Bruno, *Phys. Rev. Lett.* **83**, 2425 (1999).
[4] S. Gliga, M. Yan, R. Hertel, and C. M. Schneider, *Phys. Rev. B* **77**, 060404(R), (2008).
[5] H. Wang, C. E. Campbell, *Phys. Rev. B* **76**, 220407(R) (2007).
[6] K. Shigeto, T. Okuno, K. Mibu, T. Shinjo, T. Ono, *Appl. Phys. Lett.* **80**, 4190, (2002).
[7] A. Neubauer, C. Pfleiderer, B. Binz, A. Rosch, R. Ritz, P. G. Niklowitz and P. Boni, *Phys. Rev. Lett.* **102**, 186602 (2009).
[8] arxiv.org-ftp-arxiv-papers-0909-0909.5134.

18th Int. Symp. "Nanostructures: Physics and Technology"
St Petersburg, Russia, June 21–26, 2010

Plasmon-assisted enhancement of nonlinear refraction and absorption in core (shell) γ-Fe_2O_3 (Au) nanoparticles

I. A. Kolmychek, T. V. Murzina and O. A. Aktsipetrov
Department of Physics, M. V. Lomonosov Moscow State University, 119992 Moscow, Russia

Abstract. Spectra of the nonlinear refraction and absorption coefficients of core (shell) γ-Fe_2O_3 (Au) nanoparticles' film are measured in the spectral vicinity of the plasmon mode. Resonant features of plasmon-assisted enhancement of nonlinear effects are revealed.

Introduction

Metallic structures with dimensions smaller than the wavelength of light demonstrate fascinating optical properties which are highly dependent on the particle material, size and shape [1]. Plasmon resonance leads to the amplification of the local field within the structure resulting in the enhancement of nonlinear-optical processes [2, 3]. Materials possessing high nonlinearities have been thought to be good candidates for new optical and electronic devices, optical signal processing and optical limiting [4].

Studying such processes as nonlinear absorption and refraction of light, propagating in a medium allows us to estimate imaginary and real parts of nonlinear susceptibilities. Although there are a plenty of theoretical and experimental works devoted to nonlinear-optical properties of plasmonic systems like "polymer-noble metal nanostructures" [5,4,6], no detailed spectroscopy of such effects till now have been performed.

In this paper, self-defocusing effects and nonlinear absorption are experimentally studied in core (shell) γ-Fe_2O_3 (Au) nanoparticles. The plasmon-assisted changes in nonli-near-optical properties are studied in the spectral interval of plasmon excitation.

1. Experimental

Synthesis of core (shell) nanoparticles has been reported previously [7]. The nanoparticles consist of γ-Fe_2O_3 core 20–25 nm in diameter, and of the Au shell of the thickness of about 2–4 nm. The size distribution of nanoparticles is narrow, being about 10%. The resulting dry nanoparticle powder was resuspended in polymethylmethacrylate (PMMA) and deposited on a glass substrate. The thickness of the solid film was about 3 μm. The absorption spectrum of these structures demonstrates the existence of the plasmon resonance in the gold shell at the wavelength of about 560 nm, that is the edge of the gold absorption band.

The atomic force microscopy studies of the core (shell) nanoparticles prove that the average diameter of isolated nanoparticles is several tens of nanometers, the particles are randomly distributed on the substrate and that there are single nanoparticles and bunches of particles.

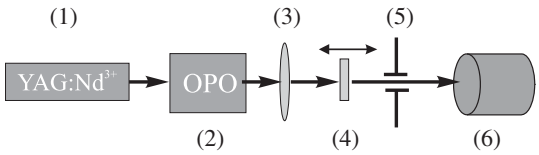

Fig. 1. Schematic picture of the experimental setup for the Z-scan technique.

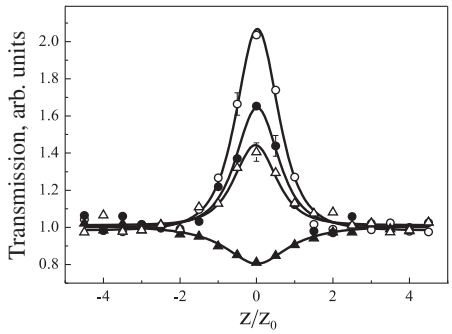

Fig. 2. Experimental data of open aperture Z-scan at fundamental wavelength 570 nm and intensities: 8 MW/cm^2 (filled triangles), 16 MW/cm^2 (open triangles), 19 MW/cm^2 (filled circles) and 25 MW/cm^2 (open circles).

The experiment was performed using the Z-scan technique, described in details in [8]. A scheme of the setup is shown at the Fig. 1. The third harmonic output of YAG:Nd^{+3} laser (1) at the wavelength 354.6 nm, power 100 mJ/pulse, repetition rate 10 Hz, pulse duration 15 ns, pumped the optical parametric oscillator (OPO) (2), which was used for fundamental radiation at tunable from 490 to 530 nm wavelength. A lens (3) focused the radiation onto the sample (4), moving along the beam's propagation. The light, transmitted through the sample, was detected by the photodiode (6). During the experiment, studying nonlinear refraction, the diaphragm (5) was partially closed (closed aperture scheme). So the experimental data were the dependencies of the transmission coefficient T on the sample's position z. The point $z = 0$ corresponds to the focal plane. All dependencies, presented below, were normalized to the transmission far from the focus, where nonlinear effects can be neglected. It should be noted that pure PMMA performs neither nonlinear absorption, nor refraction [4]. So all observed effects are associated with nanoparticles.

2. Nonlinear absorption

To reveal the mechanism of the nonlinear absorption, the dependencies $T(z)$ were measured in the open aperture scheme at the fundamental wavelength 570 nm and different intensities of incident radiation (Fig. 2). It was found that in the case of low fundamental intensity a minimum at $T(z)$ in the focal plane was observed (Fig. 2, filled triangles). But the picture changes drastically with increasing of the laser intensity. Is was experimentally shown that when the intensity of light in the focal plane lies in the range from 16 to 25 MW/cm^2, the transmission increases near the point $z = 0$.

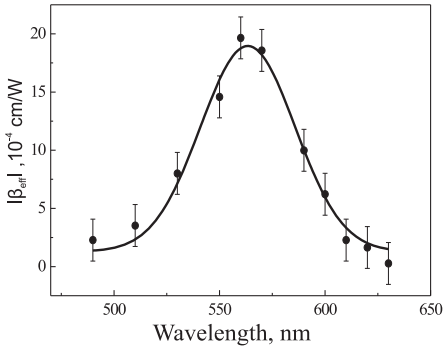

Fig. 3. The spectrum of the effective nonlinear absorbtion coefficient, observed at the fundamental intensities of about 20–25 MW/cm^2.

Experimental data showed that at low fundamental intensities the main contribution to the nonlinear absorption is due to the two-photon absorption, corresponding to the electronic transition from the ground state of the conduction band to the continuum of states. At high fundamental intensities the saturable absorption dominates. Although the saturable absorption is not strictly third-order nonlinear effect, we analyse only cubic contribution, high-order susceptibilities are neglected due to their relatively small magnitude.

Dependencies $T(z)$ in the open aperture scheme were measured at different wavelengths and high intensities of incident radiation (20–25 MW/cm^2). Using these data the coefficients of effective cubic saturable absorption β_{eff} were calculated at different wavelengths (Fig. 3). It was found that the value of β_{eff} reaches a maximum at the wavelength about 560–570 nm, i.e. in the spectral vicinity of the plasmon resonance.

3. Nonlinear refraction

In the closed aperture scheme both effects, nonlinear absorption and nonlinear refraction, are measured. Example of a typical dependence $T(z)$ in such case for the fundamental wavelength 580 nm is shown at the Fig. 4. Dividing the data of the closed aperture Z-scan to those of the open aperture Z-scan the picture, corresponding self-defocusing of light in the nanoparticles' film, was got (Fig. 4, dot curve).

Analyzing the experimental data at different fundamental wavelengths, the nonlinear refraction coefficient n_2 was calculated. Self-defocusing effect argues that $n_2 < 0$. The spectrum of the $|n_2|$ (Fig. 5) proves the resonant enhancement of nonlinear refraction effect due to the plasmon excitation.

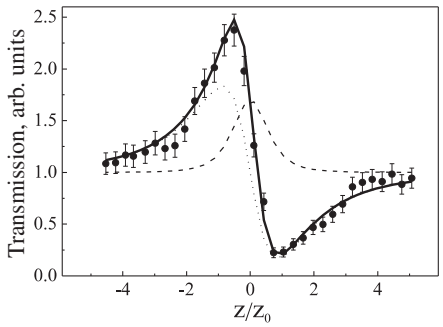

Fig. 4. Experimental data of closed aperture Z-scan at fundamental wavelength 580 nm (filled circles). Dashed curve — nonlinear absorption, dot curve — self-defocusing, solid curve — both effects.

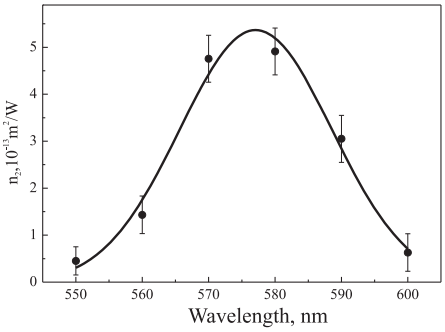

Fig. 5. The spectrum of the cubic refraction coefficient's absolute values.

4. Conclusion

In conclusion, the measurements of nonlinear absorption and refraction can provide us information of the nonlinear properties of the sample under study. It was experimentally proved that saturable absorption and self-defocusing can be enhanced in the spectral vicinity of the plasmon resonance of core (shell) γ-Fe_2O_3 (Au) nanoparticles due to the large enhancement of the local electric field near the nanoparticle's surface.

Acknowledgements

Authors are thankful to J. Wouters, Katholieke Universiteit Leuven, Belgium, for the samples' preparation and A. A. Nikulin, Moscow State University, Russia, for fruitful discussions.

References

[1] D. A. Smith *et al*, *J. Appl. Phys.* **97**, 10M504 (2005).
[2] A. Wokaun *et al*, *Phys. Rev. B.* **24**, 849. (1981).
[3] S. Kim *et al*, *Nature* **453**, 757 (2008).
[4] Y. Deng *et al*, *Physica E* **40**, 911 (2008).
[5] M. Kodirov *et al*, *Optics and Spectroscopy* **102** (1), 73 (2007).
[6] D. Kohlgraf-Owens *et al*, *Optics Express* **16** (14), 10823 (2008).
[7] P. Gangopadhyay *et al*, *IEEE Trans. Magnetics* **41** (10), 4194 (2005).
[8] M. Sheik-Bahae *et al*, *J. Quantum Electron.* **QE-26**, 760 (1990).

18th Int. Symp. "Nanostructures: Physics and Technology"
St Petersburg, Russia, June 21–26, 2010

Magneto-optic Kerr effect in dense single layers of magnetic nanoparticles

V. A. Kosobukin
Ioffe Physical-Technical Institute, St Petersburg, Russia

Abstract. A theory of polar magneto-optic Kerr effect in single layers of nanoparticles is developed. An array of magnetic ellipsoids occupying a rectangular lattice in a dielectric is considered as a model. Local-field effect due to interparticle interactions of both optic and magneto-optic dipoles is taken into account. It is shown that when the in-layer particle concentration increases the sign of the Kerr rotation angle for Co particles changes in a wide spectral range as compared with that for a single particle.

Introduction

Magneto-optic properties of nanoparticle layers were shown to depend considerably on the morphology of a magnetic system [1]. In this respect, of interest are recent observations of inversion of Kerr rotation sign in rather broad (a few eV) spectral range [1] when in-layer concentration of Co particles increases so that single islands transform to a system of close-packed islands. The related problem was theoretically treated in [2] for square lattices of magnetic particles.

In this work a theory is developed for magneto-optic Kerr effects in anisotropic arrays of nanoparticles occupying a rectangular lattice whose limiting cases are a square lattice and a single chain of particles. For magnetic ellipsoids, the local-field effects due to optic and magneto-optic dipole-dipole interactions between the particles is self-consistently treated within the Green function technique. The analysis shows that for ferromagnetic Co particles the local field can actually result in changing the Kerr rotation sign, details of the transition depending on the lattice parameters and on the shape and size of particles.

1. Model and general expressions

Consider a two-dimensional array of magnetic nanoparticles embedded in a transparent dielectric, the magnetization-free permittivities of the two media being ε and ε_1, respectively. Magnetic particles are assumed to be ellipsoids with semiaxes a, b, c along Cartesian axes. The ellipsoids are centered at the sites $\boldsymbol{\rho}_{\mathbf{n}} = A_x n_1 \mathbf{e}_x + A_y n_2 \mathbf{e}_y$ of rectangular lattice with the periods A_x, A_y and $\mathbf{n} = n_1 \mathbf{e}_x + n_2 \mathbf{e}_y$, where n_1, n_2 are the integers. For polar magneto-optic Kerr effect, the magnetization of particles $\mathbf{M} = M\mathbf{e}_z$ is perpendicular to the layer and the magnetization-induced components of dielectric tensor are $\varepsilon_{xy} = -\varepsilon_{yx} = ig$, where $g \sim M_z = M$.

A linearly polarized monochromatic wave $\mathbf{E}^0(z) = \mathbf{e}_x E^{\mathrm{inc}} \exp(-ik_1 z)$ with $k_1 = k_0\sqrt{\varepsilon_1}$ and $k_0 = \omega/c$ is normally incident onto the layer. The field $\mathbf{E}^0$ induces the dielectric polarization of the layer

$$\mathbf{P}(\mathbf{r}) = \sum_{\mathbf{n}} \left(p_x \mathbf{e}_x + p_y \mathbf{e}_y\right) \delta\left(\boldsymbol{\rho} - \boldsymbol{\rho}_{\mathbf{n}}\right) \delta(z), \tag{1}$$

expressed here in terms of optic and magneto-optic dipole moments of a particle with components p_x and p_y, respectively. In Eq. (1), delta-functions imply the smallness of particles ($a \sim b \sim c \ll 1/k_1$), in which case the quasi-electrostatic approximation is used.

Given Eq. (1), the problem is to study polar magneto-optic Kerr effect. The field components for the normally reflected wave with elliptic polarization are expressed as

$$E_\alpha(z) = \delta_{\alpha x} E_x^0(z) + \frac{1}{A_x A_y} G_{\alpha\alpha}^0(z, 0) \chi_{\alpha x} E_x^0(0), \tag{2}$$

if A_x, $A_y \ll 2\pi/k_1$. In Eq. (2), $G_{\alpha\alpha}^0(z, z')$ and $\chi_{\alpha x}$ with $\alpha = x$, y are, respectively, the components of the tensor Green function and of the effective particle polarizability in the external field $E_x^0(z)$. Note that $\chi_{yx} = 0$, if $\mathbf{M} = 0$.

From Eq. (2) one obtains the following asymptotic expressions

$$E_\alpha^{\mathrm{r}}(z) = r_{\alpha x} E^{\mathrm{inc}} e^{ik_1 z} \tag{3}$$

for normally reflected waves. The wave with the orthogonal polarization components (3) is elliptically polarized, and its Kerr rotation angle (orientation angle of the polarization ellipse) is expressed as follows

$$\theta = \mathrm{Re}\left(E_y^{\mathrm{r}}/E_x^{\mathrm{r}}\right), \tag{4}$$

where the condition $|E_y^{\mathrm{r}}| \ll |E_x^{\mathrm{r}}|$ is implied. Next, the Kerr rotation angle θ is explicitly calculated.

2. Effective polarizabilities of nanoparticles

For a single ellipsoid, the polarizability tensor in a uniform external field is known to be diagonal with the components

$$\chi_{\alpha\alpha}^0 = \frac{abc}{3} \frac{\varepsilon - \varepsilon_1}{\varepsilon N_\alpha - \varepsilon_1 (1 - N_\alpha)}, \tag{5}$$

where N_α is the depolarizing factor along the principal axis α. In a layer of such ellipsoids, the external field induces the effective dipole moments $\mathbf{p}_{\mathbf{n}'}$ at the sites $\boldsymbol{\rho}_{\mathbf{n}'}$. As a result, the local field acting the dipole $\mathbf{p}_{\mathbf{n}}$ is a sum of $\mathbf{E}^0$ and the field, induced by the other ($\mathbf{n}' \neq \mathbf{n}$) dipoles $\mathbf{p}_{\mathbf{n}'}$ of the layer. In the quasi-static approximation (A_x, $A_y \ll 2\pi/k_1$) this local-field effect is described by the equation of coupled dipoles

$$p_x = \chi_{xx}^0 \left(E_x^0 + \frac{S_x}{\varepsilon_1 A_x^3} p_x\right). \tag{6}$$

Here, S_x stands for the dipole sum defined by the relation

$$\sum_{\mathbf{n}(\neq 0)} \frac{3\rho_{\mathbf{n},\alpha}^2 - \rho_{\mathbf{n}}^2}{\rho_{\mathbf{n}}^5} = \frac{S_\alpha(\eta)}{A_\alpha^3} \tag{7}$$

with $\alpha = x$. The sums $S_\alpha(\eta)$ were derived in [3] depending on the parameter $\eta = A_x/A_y$ of a rectangular lattice and estimated as $S_\alpha(1) \cong 4.52$. From Eq. (6) one obtains the effective polarizability

$$\chi_{xx} = \chi_{xx}^0 \left(1 - \frac{\chi_{xx}^0 S_x(\eta)}{\varepsilon_1 A_x^3}\right)^{-1} \tag{8}$$

of the dipole $p_x = \chi_{xx} E_x^0(0)$ entering Eq. (1).

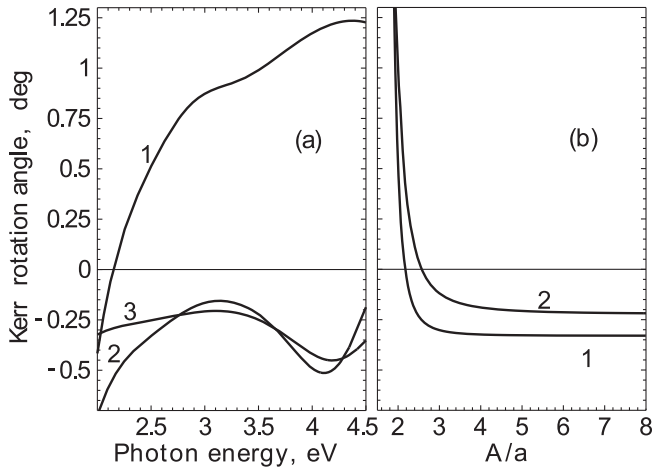

Fig. 1. (a) Spectra of the Kerr rotation angle for Co-based nanostructures embedded in dielectric CaF_2: 1 — a square lattice of ellipsoids with $a = b = 5$ nm, $c/a = 2.5$, $A = 10$ nm, 2 — a single Co ellipsoid, 3 — semi-infinite Co. (b) Kerr rotation dependence on the ratio A/a for the lattice of ellipsoids at the following photon energies: 1 — 2.5 eV, 2 — 3.5 eV.

For non-zero magnetization $\mathbf{M} = M\mathbf{e}_z$, the effective magneto-optic dipoles p_y induced by the internal field $\widetilde{E}_x^{(i)}$ in the particles are defined by the equation

$$p_y = -\frac{abc}{3} ig \widetilde{E}_x^{(i)} + \chi_{yy}^0 \frac{S_y(\eta)}{\varepsilon_1 A_y^3} p_y, \tag{9}$$

analogous to Eq. (6), with $S_y(\eta) = S_x(1/\eta)$ from Eq. (7). Since $\widetilde{E}_x^{(i)} = \chi_{xx} E_x^{(i)} / \chi_{xx}^0$ and $E_x^{(i)} = \varepsilon_1 E_x^0 / [\varepsilon N_x - \varepsilon_1 (1 - N_x)]$ [2], one obtains

$$\chi_{yx} = \frac{ig\varepsilon_1}{\varepsilon_1 - \varepsilon} \chi_{xx} \left(1 - \frac{\chi_{yy}^0 S_y(\eta)}{\varepsilon_1 A_y^3} \right)^{-1} \tag{10}$$

for magneto-optic polarizability of the dipoles $p_y = \chi_{yx} E_x^0$ in Eq. (1).

From Eq. (4) written in the form $\theta = \mathrm{Re}(\chi_{yx}/\chi_{xx})$ with Eqs. (8) and (10) taken into account, one obtains for the Kerr rotation of the reflected wave

$$\theta = \mathrm{Re} \left(\frac{ig\varepsilon_1}{\varepsilon_1 - \varepsilon} \left[1 - \frac{\chi_{yy}^0 S_y(\eta)}{\varepsilon_1 A_y^3} \right]^{-1} \right). \tag{11}$$

This equation shows that the magneto-optic local-field effect in a layer is defined by interaction of magneto-optic dipoles p_y given by Eq. (9). The local-field effect vanishes in the limit $A_y \to \infty$, when Eq. (11) goes to that corresponding to a single ellipsoid.

3. Discussion

Spectrum of the Kerr rotation angle (11) calculated for a lattice of Co spheroids with $a = b \neq c$ in surrounding dielectric CaF_2 is presented by curve 1 in Fig. 1(a). For comparison, the Kerr rotation is also shown for a single Co ellipsoid (curve 2) and a single plane surface of Co (curve 3). Fig. 1(a) demonstrates that in a wide spectral range the Kerr rotation θ for a dense layer of Co particles has the opposite sign than for a single Co ellipsoid or bulk Co.

Spectrum of the Kerr rotation (11) depends strongly on the interparticle distances (lattice periods). For a square lattice with $A_x = A_y = A$ ($\eta = 1$), the Kerr rotation angle as a function of the period A is shown in Fig. 1(b) at a few photon energies. It is seen that for $A \gg a$, when the dipole-dipole interaction between ellipsoids with the semiaxes $\sim a$ is weak, the Kerr rotation is close to that of a single ellipsoid. On the contrary, in decreasing the lattice period A the Kerr rotation spectrum changes, getting opposite sign at $A \gtrsim 2a$. Details of such transition depend on photon energy, and so does the value of A corresponding to inversion of the Kerr rotation sign.

The condition $A \approx 2a$ of the sign inversion means that real particles are very close to each other or even touching. Then, the dipole approximation adopted in Eqs. (6) and (9) can be thought of as questionable because formally it implies smallness of the particle size $2a$ as compared with the interparticle distance A. Indeed, the acting field between touching particles is non-uniform, and multipole interactions are important. However, it was demonstrated [4] that this effect can be phenomenologically described by Eq. (6) assigned to the dipoles of effective particles allowed to intersect. Introducing Eq. (9), we generalize this idea to magneto-optics of multiple particles, in which case the relation $\pi a^2 = A^2$ between the model parameters is taken to define the lower boundary $A/a = \sqrt{\pi}$ in Fig. 1(b) in analogy with [4].

Turning to ellipsoids with $a = b \neq c$ and $\eta = 1$, dependence of the Kerr rotation spectra on the ratio c/a, i.e. on the magnetic particle shape, shows the following tendency in the range 2 to 4.5 eV. If $c/a \ll 1$ (oblate spheroids), the local-field effect is weak because $(c/a)(a/A)^3 \ll 1$ in the denominator of Eq. (11), and the Kerr rotation spectrum has the same sign for a layer and for a single particle. If $c \sim a$, the Kerr rotation angles can be of different signs in different parts of the spectral range. At last, if $c/a \gg 1$ (prolate spheroids), the Kerr rotation sign for a layer becomes opposite to that typical of a single particle. For a chain of magnetic spheroids ($A_y \sim 2a \ll A_x$), it is concluded from Eq. (11) that the magneto-optic local-field effect is not weaker than for a dense two-dimensional array of the same spheroids, while the local-field effect vanishes in the usual reflection.

In conclusion, a theory is developed for polar magneto-optic Kerr effect in dense arrays of nanoparticles. Optic and magneto-optic local-field effects are treated for ordered arrays of magnetic ellipsoids where the acting and external fields differ owing to interparticle dipole interactions. The sign of Kerr rotation spectrum at normal light incidence onto a layer is shown to be inverted in increasing the particle concentration (decreasing the interparticle distance) in the layer. Thus, the inversion of the Kerr rotation sign in a wide spectral range can be assigned to a fundamental electromagnetic interaction which is expected to be effective in both periodic and disordered nanostructures.

Acknowledgements

This work is supported by the RFBR, grant 10-02-00783.

References

[1] B. Kalska, J. J. Paggel, P. Fumagalli, M. Hilgendorff, M. Giersig, *J. Appl. Phys.* **92**, 7481 (2002); B. B. Krichevtsov, A. G. Banshchikov, S. V. Gastev, A. V. Nashchekin, S. M. Suturin, V. A. Kosobukin, N. S. Sokolov, T. Shimada, *Proc. Int. Conf. "New in magnetism and magnetic materials"*, Moscow Univ., 189, 2009.

[2] V. A. Kosobukin, B. B. Krichevtsov, *Phys. Solid State* **52**, No. 4 (2010).

[3] V. L. Berkovits, A. B. Gordeeva, V. A. Kosobukin, *Phys. Solid State* **43**, 1018 (2001).

[4] E. M. Purcell, C. R. Pennypacker, *Astrophys. J.* **186**, 705 (1973); B. T. Drane, *Astrophys. J.* **333**, 848 (1988); V. M. Shalaev (Ed.), *Optical Properties of Nanostructured Random Media. Topics Appl. Phys.* **82**, 93 (2002).

18th Int. Symp. "Nanostructures: Physics and Technology"
St Petersburg, Russia, June 21–26, 2010

Multiway spin valve based on uniaxial exchange-coupled (211)MgO/(210)[Fe/Cr]$_N$ superlattices

V. V. Ustinov, *T. P. Krinitsina*, M. A. Milyaev and L. N. Romashev
Institute of Metal Physics, Ural Branch RAS, Ekaterinburg, 620990, Russia

Abstract. The structure, magnetic and magnetoresistive properties of antiferromagnetically coupled superlattices [Fe/Cr]$_N$ grown on (211)MgO substrate have been investigated. It is shown that (211)MgO substrate is appropriate for the growth of (210) Fe/Cr multilayer with a strong uniaxial in-plane magnetic anisotropy. The stepwise behavior of magnetization $M(H)$ and magnetoresistance $\Delta R(H)/R$ is revealed in the case when the magnetic field is applied along the easy axis in the film plane of the superlattice. The steps on the $M(H)$ and $\Delta R(H)/R$ dependences are caused by the flip of magnetic moments of individual Fe layers.

Introduction

It was established [1,2] that the magnetic structure of Co-Pt-Ru and Fe-Au multilayers with out-of-plane anisotropy could exist as a set of collinear magnetic states. In such multilayers the transitions between these magnetic states occur as a spin-flip (or meta-magnetic) phase transitions. Magnetization reversal processes in the materials result in the appearance of stepped anomalies on a magnetization curve detected mainly by MOKE measurements and sometimes by SQUID/VSM magnetometry [1,3]. The stepped magnetic field dependences of both magnetization and magnetoresistance were investigated in Co-Pd-Ru multilayers [3].

In paper [4] (as well as in [1]) it is pointed out that the unusual reorientation and multidomain effects revealed are unknown both in bulk magnetics and in easy-plane antiferromagnetic (AF) superlattices. At the same time there are no physical restrictions forbidding the similar reorientation effects in multilayers with in-plane anisotropy. In order to prepare a multilayer with stepped in-plane magnetization it is necessary to create in a multilayer the strong uniaxial in-plane anisotropy, the energy of which is comparable or stronger than interlayer exchange coupling.

In many multilayers consisting of ferromagnetic (FM) and nonmagnetic metals (Fe/Cr, Co/Cu, Co/Ru, etc.) the strength of the exchange coupling and the value of the in-plane anisotropy energy depend on thickness of nonmagnetic and FM layers, respectively. It means that it is possible to find the appropriate combination of layers thickness of magnetic and nonmagnetic materials, and to grow multilayer with relatively strong uniaxial in-plane anisotropy.

Two types of MgO substrates are used most often for the growth of Fe/Cr multilayers with in-plane anisotropy, (100)MgO and (110)MgO. The first of them in used for the growth of AF-coupled multilayers with four-fold anisotropy in the film plane. The second one is a well known substrate for the growth of (211)Fe/Cr superlattices [5], in which the surface spin-flop transition was observed [6]. The (211)Fe/Cr multilayers have the uniaxial two-fold in-plane anisotropy. We have discovered that there exists another substrate suitable for preparation of Fe/Cr multilayers with strong uniaxial in-plane anisotropy. The substrate is found to be (211)MgO.

The main goals of the present study are the following: i) to demonstrate the appropriateness of (211)MgO substrates for the growth of Fe/Cr superlattices with strong uniaxial in-plane anisotropy, ii) to investigate the structure, magnetic and magnetoresistive properties of Fe/Cr superlattices grown on (211)MgO substrates, and iii) to study the peculiarities of multiple spin-flip transitions in these samples as the base for multiway spin valve.

1. Experimental

The [Fe(85 Å)/Cr(t_{Cr})]$_{12}$ superlattices consisting of twelve pairs of relatively thick Fe layers and Cr layers the thickness of $t_{Cr} = 12.44$ and 13.6 Å were MBE-grown on (211)MgO substrates with the Cr(80 Å) buffer layer. The typical deposition rate of Fe and Cr layers was about 1.5 Å/min. The substrate temperature during the buffer layer deposition was $T_{sub} = 300$ °C, whereas for the multilayer growth it was $T_{sub} = 180$ °C. The thicknesses of Fe and Cr layers were chosen to create the uniaxial in-plane anisotropy energy which could be comparable or stronger than the interlayer exchange coupling.

The structures were characterized by TEM and X-ray diffraction. The in-plane anisotropy and magnetization curves were studied at room temperature by vibration sample magnetometer. Magnetic properties at low temperatures were measured by superconducting quantum interference device (SQUID) magnetometry. Magnetoresistance was studied by the standard four-probe technique (PPMS, Quantum Design).

2. Results and discussion

Figure 1a shows an electron diffraction pattern (EPD) of the (211)MgO/[Fe/Cr]$_{12}$ superlattice. The EPD includes reflections from both MgO substrate and Fe/Cr multilayer. According to the standard identification procedure [7], these reflections correspond to (211)MgO and (210)Fe/Cr planes.

The TEM study has shown that the Fe/Cr multilayer is a pseudo-single-crystal with the preferable orientation of (210) Fe/Cr. The epitaxial orientations in this sample are [100]Fe/Cr$\|$[110]MgO and [210]Fe/Cr$\|$[11$\bar{1}$] MgO. The lattice constants for MgO and Fe/Cr are 4.21 and 2.87 Å, respectively. The distance between the nearest atoms in MgO (fcc structure) in the [11$\bar{1}$] direction is $\sqrt{3}a_{MgO} = 7.30$ Å, whereas the distance between the nearest atoms in the parallel direction of [210]Fe/Cr (bcc structure) is $\sqrt{5}a_{Fe} = 6.41$ Å. The lattice mismatch of [210]Fe/Cr with [11$\bar{1}$]MgO is about 12%. The similar calculation for [100]Fe/Cr gives the 3.7% lattice mismatch. Thus, the nearest atoms form the rectangle the sizes of 2.87 and 6.41 Å in the (210)Fe plane. The crystal symmetry in the (210)Fe layers causes apparently the uniaxial in-plane anisotropy revealed in the sample (Fig. 1b). According to magnetic measurements the easy axis is directed along [001]Fe/Cr, whereas the hard axis is directed along [120]Fe/Cr.

Large lattice mismatch (12%) for the [210]Fe/Cr direction, obviously, stimulates internal strains, which usually relax during a multilayer growth when the total film thickness increases. Due to the strains relaxation the anisotropy constant could be different in Fe layers, which have the nominal equal thickness. Therefore Fe

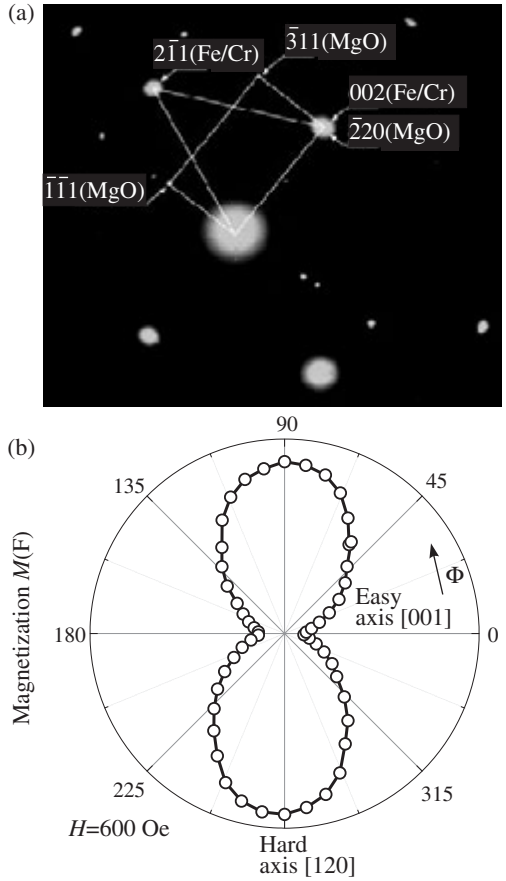

Fig. 1. (a) Electron diffraction pattern of the (211)MgO/[Fe(85 Å)/Cr(13.6 Å)]$_{12}$ superlattice; the reflections from MgO substrate and Fe/Cr superlattice are shown; (b) Angle in-plane dependence of the superlattice magnetization $M(\Phi)$ at $H = 600$ Oe.

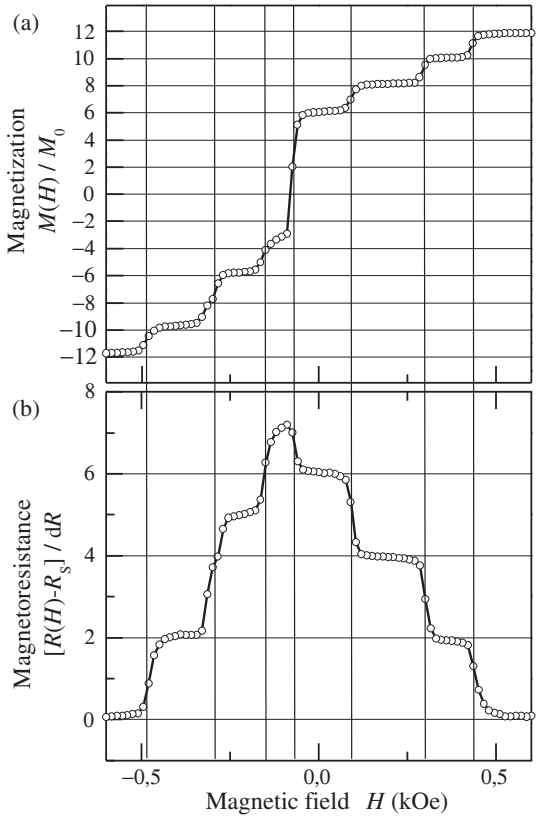

Fig. 2. Normalized descending branch of magnetization hysteresis loop (a) and corresponding branch of GMR curve (b). Magnetic field is applied along the easy axis in the film plane.

layers could be nonequivalent in the multilayer stack. The interface roughness could also depend on the magnetic layers index. The growth induced reduction of the interface roughness was discussed by Willekens *et al* [3] for the interpretation of the stepped hysteresis loops in Co-Pd-Ru multilayers. The thicknesses of Cr and Fe layers in our superlattices were chosen on the base of the well-known properties of Fe/Cr multilayers. The Cr layer thickness of $t_{Cr} \approx 9$–10 Å corresponds to the strong antiferromagnetic interlayer coupling, whereas $t_{Cr} \approx 18$–20 Å corresponds to ferromagnetic one. The exchange coupling in the $t_{Cr} \approx 12$–14 Å superlattices is still antiferromagnetic but it is "weak" (the constant of the bilinear exchange coupling is nearly zero in the $t_{Cr} \approx 9$–10 Å superlattice). The in-plane anisotropy energy is known to be proportional to the thickness of Fe layers, while the saturation field has the inverse dependence on the Fe layer thickness. We have increased the Fe layer thickness up to $t_{Fe} = 85$ Å. Due to that it became possible to reduce the saturation fields H_s of our samples up to the range of $|H| < 1$ kOe, where the uniaxial in-plane anisotropy plays important role in the formation of collinear magnetic states.

Figures 2a,b demonstrate the step-like behavior of magnetization and magnetoresistance when the magnetic field is applied along the easy axis. Corresponding curves are smooth for field H oriented along the hard axis.

Magnetization M is expressed in Fig. 2a in units of the magnetic moment M_0 of a single Fe layer. The total magnetic moment of the superlattice changes discretely with steps proportional to $\Delta M = 2M_0$. The change of magnetization direction of a single magnetic layer leads to magnetoresistance variation. One can separate the effects of the surface (external) spin-flip transition and the internal transition occurred inside the superlattice: the δR step-change corresponds to a surface spin-flip transition, and the $2\delta R$ — to a spin-flip transition inside the superlattice. The flip of the magnetic moment M_i located between two anti-parallel M_{i+1} and M_{i-1} moments will not change the superlattice resistance.

3. Conclusions

We have grown the (211)MgO/(210)[Fe/Cr]$_{12}$ superlattices with strong uniaxial in-plane anisotropy. The multi-stepwise magnetization and magnetoresistance behavior is observed when the magnetic field is applied along the easy axis in the film plane. These giant magnetoresistance peculiarities may be used as the base for a multiway spin valve.

Acknowledgements

This research has been supported in part by Grants of RFBR and RAS.

References

[1] O. Hellwig *et al*, *Nature Mater.* **2**, 112 (2003).
[2] M. Zoładz *et al*, *J. Magn. Magn. Mater.* **272–276**, 1253 (2004).
[3] H. J. Lugauer *et al*, *J. Crystal Growth* **175/176**, 619 (1997).
[4] L. Hansen *et al*, *Appl. Phys. Lett.* **79**, 3125 (2001).
[5] W. Y. Yu *et al*, *Phys. Rev. B* **51**, 9722 (1995).
[6] J. A. Gaj *et al*, *Solid State Commun.* **29**, 435 (1979).
[7] B. E. Larson *et al*, *Phys. Rev. B* **37**, 4137 (1988).
[8] D. R. Yakovlev *et al*, *Phys. Rev. Lett.* **88**, 257401 (2002).

18th Int. Symp. "Nanostructures: Physics and Technology"
St Petersburg, Russia, June 21–26, 2010

The model of electric field assisted dissolution of metal nanoparticles in glass

A. A. Lipovskii[1], *M. I. Petrov* [2], V. G. Melehin[3] and Yu. P. Svirko [4]

[1] St Petersburg State Polytechnical University, St Petersburg, 195251, Russia
[2] St Petersburg Academic University, St Petersburg, 194021, Russia
[3] Ioffe Physical-Technical Institute, St Petersburg, Russia
[4] University of Eastern Finland, Joensuu, 80101, Finland

Abstract. The model of electric field assisted dissolution (EFAD) of metal nanoparticles in glass-metal nanocomposite (GMN) is presented. Ion and electron emission under the high electric field formed beneath the GMN surface jointly result in full dissolution of metal nanoparticles. Calculations based on the developed model show that the nanoparticles are charging in the course of the dissolution process due the differing structures of the potential barriers and the mechanisms of electrons and ions emission and that there exists a frontier of the dissolution going from the nanocomposite anodic surface to the bulk. The EFAD process was applied to form in the GMN diffraction gratings with periods of 400, 600, and 800 nm.

Introduction

Glass-metal nanocomposites (GMN) are prospective materials for photonics applications due to their unique optical properties [1]. Existence of surface plasmon resonance with high localization of electric field dramatically enhances optical properties of media embedded with metal nanoparticles. Latest investigations showed that silver [2,3], gold [4] and copper [5] nanoparticles could be removed from glass matrix via so-called electric field assisted dissolution (EFAD) process under external electric field applied. This phenomenon opens new possibilities to produce submicron scale photonic structures based on the GMN, for the EFAD allows controlling local distribution of nanoparticles along the sample surface and, consequently, optical density of GMN. In particular, two-dimensional profile of optical transmittance can be formed. In spite of the usability of this phenomenon the model of the dissolution process, which should provide formation of EFAD-produced structures possessing given characteristics was not developed until now. Here we present the model of the EFAD process.

1. High electric field formation

The dissolution of metal nanoparticles is mainly due to the high electric field formed in the subanodic surface of GMN. The origin of this field is similar to the origin of electric field formation in the course of thermal poling of glasses [2]. It is usually associated with originated from atmosphere slow hydrogen ions which are penetrating into the glass during poling. However, the origin of these hydrogen ions in glass and in GMN is different. Specifically, when we apply the electric field to a virgin glass, the enrichment of the glass with hydrogen species takes place in the course of the poling. Contrary, the hydrogen ions were incorporated into the GMN during metal nanoparticles formation via reduction of the metal by hydrogen, i.e. before the electric filed was applied. Thus after an external field is applied the strong (up to 1 V/nm) local electric field in the subanodic region is formed. The tunneling of electrons and repeatable emission of metal ions driven by this field results in complete dissolution of the nanoparticles.

2. Electron and ion emission from nanoparticle

The dissolution of metal nanoparticles in the presence of the electric field resembles the electric field stimulated diffusion of metal film in glass, the important difference being that in GMN, there is no a direct contact of dissolving metal entity with anodic electrode. This similarity allowed us estimating thermal activated transition energy of silver atoms into glass matrix ($Ag^0 \rightarrow Ag^+$) for observed dynamic of metal film diffusion: $E_{Ag} \sim 1.2$ eV.

Available data [6] on photoconductivity spectra of soda-lime glasses and the results of numerical calculations of band structure of fused silica, sodium disilicate and sodium-calcium-silicate glass [7] enable evaluating the position of electron mobility edge in soda-lime glass at the energy of $\simeq 1.2$ eV below vacuum level and the glass bandgap of $\simeq 6$ eV.

The bent of the glass band structure in strong electric field is sufficient to permit a direct tunneling of electrons from silver Fermi level E_f (4.6 eV below vacuum level) to the glass conductivity band. Polarization of the nanoparticles in the external electrical field and tunneling of electrons thermally distributed above the Fermi level increase probability of tunneling through the barrier depicted in Fig. 1. The total electron current from

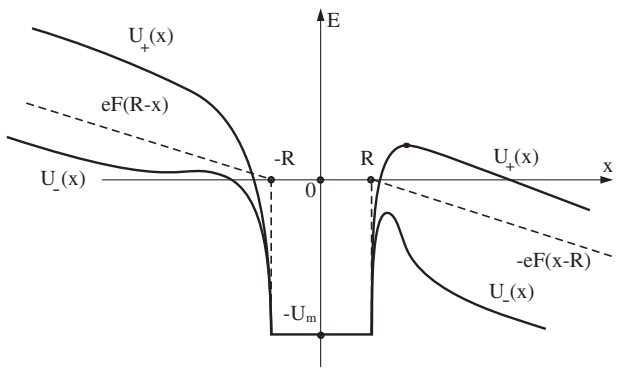

Fig. 1. Profile of potential barrier for electrons in case of positively (U_+) and negatively (U_-) charged spherical nanoparticle. Here x is a coordinate along the sphere axis parallel to the vector of electrical field **F**, R is the radius of the nanoparticle, U_m is electron energy inside the nanoparticle.

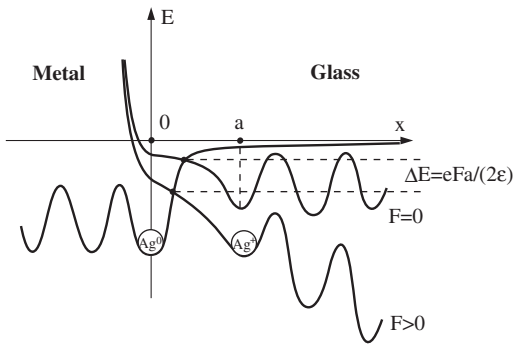

Fig. 2. Energy terms of neutral (inside metal) and ionized (inside glass) silver atoms for $\theta = 0$ direction. High local electrical field decreases the height of potential barrier for ΔE. F is electric field intensity, a is a mean distance of ion jump in glass.

the nanoparticle is given by the expression

$$J = \frac{emkT}{2\pi^2\hbar^3}\int_{E_{\rm cm}}^{\infty} \ln\left(1+\exp\left(-\frac{E-E_{\rm f}}{kT}\right)\right)D(E)dE, \quad (1)$$

where $E_{\rm cm}$ is the edge of metal conductivity band and $D(E)$ is tunneling probability that is determined by the profile of potential barrier $U(r,\theta)$. Treating metal nanoparticle as a metal sphere of radius R we can derive expression for profile of the electron potential barrier in uniform external electrical field:

$$U(r,\theta) = -\frac{eF\cos(\theta)(r-R)}{\epsilon} + \frac{eQ}{\epsilon}\left(\frac{1}{r}-\frac{1}{R}\right)$$
$$+\frac{eF\cos(\theta)R^3}{\epsilon}\left(\frac{1}{r^2}-\frac{1}{R^2}\right) - \frac{eR}{\epsilon}\frac{1}{(r^2-R^2)},\ r > R. \quad (2)$$

Here θ is angle between radius-vector $\mathbf{r}$ and electrical field vector $\mathbf{F}$; Q is possible charge of the sphere and ϵ is dielectric permittivity of the glass. There are four main contribution in the local field near the surface of metal sphere which correspond to the components of potential energy U: homogeneous external electric field, electric field of a charged sphere, field of the polarized sphere and the field of image correspondingly in the expression (2). The potential energy inside the sphere ($r < R$) equals to $-U_m$.

On the other hand the high electrical field decreases the height of the potential barrier for ions and activates ion emission from nanoparticles (Fig. 2). Thus the ion current from the nanoparticle is proportional to:

$$J_i(\theta) \sim \exp(eF\cos(\theta)a/(2\epsilon kT)). \quad (3)$$

Both ion and electron emission processes jointly result in full dissolution of metal nanoparticles.

The differing structures of the potential barriers and the mechanisms of electrons and ions emission make probabilities of ion and electron transitions different and hence should result in charging of nanoparticles in EFAD process. Our calculations based on the developed model show that this charge could be about +5 elementary charges for 2 nm in radius nanoparticle under electric field $F/\epsilon \approx 0.5$ V/nm.

Joining our model and the model of charge transport during field modification of GMN show that there exists a frontier of the dissolution going from the GMN anodic surface to the bulk. Appearance of this frontier is mainly related with the formation of the frontier of mobile charges (alkali ions) in the glass matrix. It is worse to mention that the magnitude of the additional charge of nanoparticles is influenced by surrounding glass matrix.

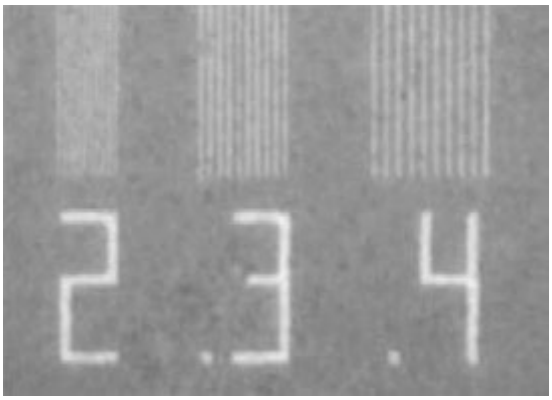

Fig. 3. Optical microscope image of the diffraction gratings formed in the GMN. Numbers 2, 3 and 4 correspond 400, 600 and 800 nm period, respectively.

The EFAD process was used to produce subwavelength transmission gratings with equal spacing and line width (Fig. 3) having periods 400, 600 and 800 nm. Further experiments will be aimed at the study of the interaction of overcrossing spatial Bragg-like resonance in the periodic structures and surface plasmon resonance in silver nanoparticles.

The presented model makes possible design and control of GMN characteristics in EFAD process and opens new possibilities for photonic structures formation.

Acknowledgements

This work has been partly supported by RFBR (grant #08-02-00522) and Russian Ministry of Science and Education (project #2.1.1/988).

References

[1] G. Schmid, *Clusters and Colloids, From Theory to Applications*, (Wiley-VCH) 556, 1994.
[2] M. Halonen, A. A. Lipovskii, Y. P. Svirko, *Opt. Express* **15**, 6840 (2007).
[3] U. Kreibig, M. Vollmer, *Optical Properties of Metal Clusters*, (Springer: Berlin) 532, 1995.
[4] A. Podlipensky *et al*, *J. Phys. Chem. B* **108**, 17699 (2004).
[5] O. Deparis, P. G. Kazansky, A. Abdolvand, A. Podlipensky, G. Seifert, H. Graener, *Appl. Phys. Lett.* **85(6)**, 872–874 (2004).
[6] L. B. Glebov, *Proc. of SPIE* **4347**, 343 2001.
[7] E. Ellis *et al*, *Phil. Magazine B* **40**, 105 (1979).

18th Int. Symp. "Nanostructures: Physics and Technology"
St Petersburg, Russia, June 21–26, 2010

Localized surface plasmon resonance of metal nanoparticles in photo-thermo-refractive glasses

O. A. Usov[1], A. I. Sidorov[2], A. V. Nashchekin[1], O. A. Podsvirov[3], A. I. Ignatev[2], A. V. Vostokov[3] and V. N. Nevedomskiy[1]

[1] Ioffe Physical-Technical Institute, St Petersburg, Russia
[2] St Petersburg ITMO State University, Kronverkskii 49, 194021 St Petersburg, Russia
[3] St Petersburg Polytechnical State University, Polytechnicheskaya 29, 194021 St Petersburg, Russia

Abstract. Metal nanoparticles (MNP) embedded in a glass matrix exhibit an intense color related to the localized surface plasmon resonance. Silver nanoparticles were shown to be fabricated of subsurface multilayer structure in the photo-thermo-refractive glasses after high electron beam irradiation with subsequent heat treatment. The shape, size distribution and MNP concentration depend on irradiation dozes and heat treatment temperatures. The report will present the technology of MNP fabrication, experimental measurements of optical absorption spectra and TEM images which used for characterization of MNP size distribution.

Introduction

Noble metals such as Ag, Au and Cu are widely used for fabrication of metal-dielectric photonic nanostructures [1–3] named metamaterials with unusual optical properties permitted for manipulation, guiding and localization of light at nanoscale. Metal nanoparticles (MNPs) embedded in a glass matrix exhibit a very intense color related to the resonance oscillation of the free conduction electrons known as localized surface plasmon resonance (LSPR). Due to high sensitivity of LSPR to dielectric properties of surrounding media such structures have a great application potential in high sensitive chemical and biomolecular detection. From the application point of view, optimization of the plasmonic device efficiency requires an investigation of the quantum size effect of MNPs and its interaction with the environment which have strong influence on the spectral characteristics of LSPR. The report will present the technology of fabrication of MNPs in the photothermorefractive (PTR) glasses, optical absorption spectra, TEM images that used for characterization shape and size of nanoparticles. Experimental spectral characteristics of obtained structures were shown to be in a good agreement with calculated ones using Mie model for light scattering on spherical MNPs in the PTR glasses in a quasi-static (dipole) approximation.

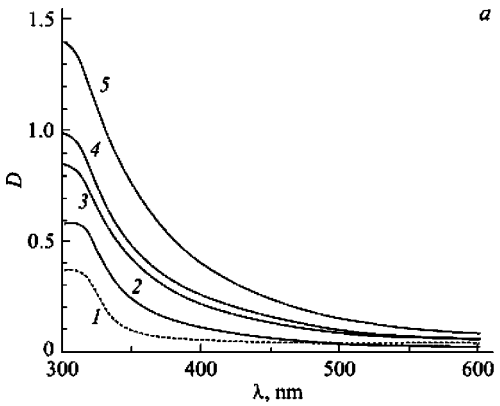

Fig. 1. Optical density of initial sample and dependences on e-beam irradiation dozes in the range between 10 and 50 mCcm^{-2} before heat treatment.

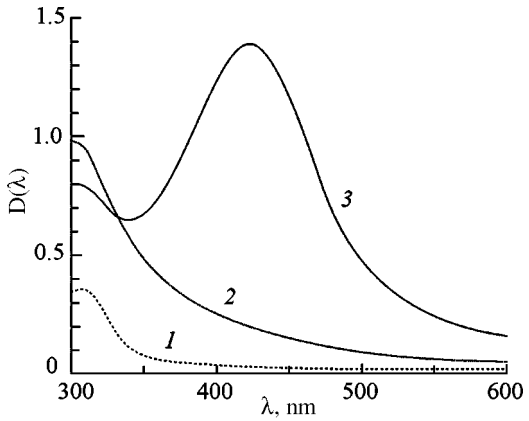

Fig. 2. Spectral dependence of optical density: 1 — initial glass, 2 — after 40 mCcm^{-2} e-beam irradiation, 3 — after e-beam irradiation and heat treatment at 540 °C during 4 hours.

1. Technology and fabrication

The MNPs in the PTR glasses were fabricated using technology described by authors earlier [1–3]. The size, shape and concentration of MNPs (Ag, Cu, Au etc.) precipitated in a glass subsurface layers depend on glass composition, type and intensity irradiation (UV, electron etc.) and thermal treatment. The samples were exposed at RT using scanning electron microscope CamScan Series 4 DV100 with electron energy 5–30 keV, current 2 nA, the size of exposed area being as large as 270×350 nm^2 and dose of irradiation about 11.4 mCcm^{-2} [1–3]. The electron beam energy 20 keV applied to all regions of the sample 4, the diameter of electron beam being equal to 2 mm. This processes are supposed to initiate nucleation of subnanometer metal clusters with density depending on the deposited energy. Such clusters form a so-called latent image that take place in the strong analogy with photographic processes [4]. Subsequent heat treatment at 540 °C unlike photography promotes diffusion of silver ions from volume to the charged cluster region, transfer electrons silver ions in the vicinity of a stable clusters and the neutral atoms being aggregated due to diffusion into colloidal particles with subsurface multilayer space distribution [1–3].

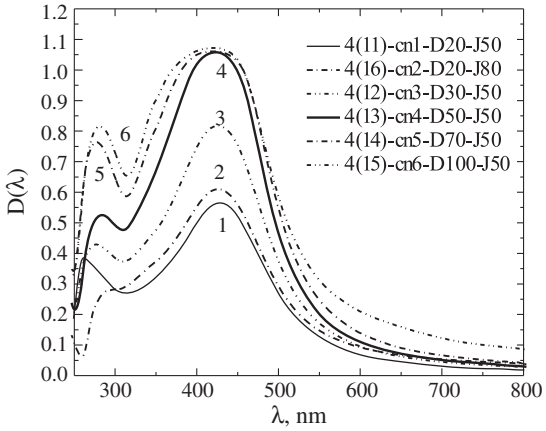

Fig. 3. Spectral dependence of optical density $D(\lambda)$ of 6 irradiated regions of sample 4 assigned by curve number in accordance with description of the Table 1.

2. Results and discussion

The optical density spectra of the PTR glass samples with Ag NPs showed in Figs. 1–3 display a specific LSPR peaks in the range between 400–450 nm. The optical spectra shown were obtained with Cary 500 (Varian) UV-vis-NIR spectrophotometer in the range 200–1000 nm. From spectra in Figs. 1–2 it is evident that an initial and irradiated PTR glass samples do not show LSPR peak absorption. But after thermal treatment the latent images developed and silver LSPR optical absorption peaks appear as shown in Figs. 2–3. The intensity and LSPR peak positions depend on heat treatment time: at initial stage LSPR peaks are in the range 390–420 nm, but with increase time they are redshift to 440–450 nm. The LSPR linewidths (FWHM) and line shapes dependence on irradiation electron energy and dozes are described in Table 1 and shown in Fig. 3. From HRTEM image shown in Fig. 4 it is supposed that the shape of MNPs are close to the spherical ones and the estimatedNP diameters are distributed between 5–10 nm. The average MNP diameters evaluated from optical density shown in Fig. 3 were obtained in the range about 2–6 nm using the Mie model of light scattering on spherical NPs in a quasistatic (dipole) approximation. The size underestimation obtained from optical data analysis is supposed to be overcome by extension the Mie model by taking into account the nonspherical (spheroidal) shape of MNPs using so-called Mie-Gans model.

Table 1. Experimental data of 6 irradiated region of the sample No. 4 assigned to curve number in the first column and the results of analysis of the spectral dependence of the optical density shown in Fig. 3, which relates to LSPR of the Ag NPs.

	Irradiation		LSPR peak	
Curve	Doze(D), mCcm^{-2}	Time, s	λ, nm	FWHM, nm
1	20	400	425	142
2	20	250	427	132
3	30	600	424	138
4	40	1000	419	142
5	50	1400	415	162
6	60	2000	407	166

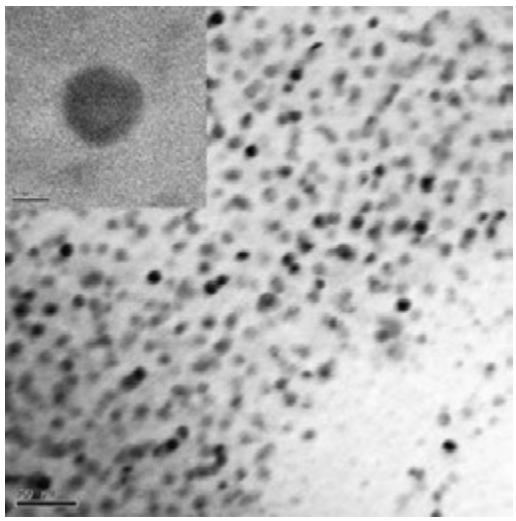

Fig. 4. TEM image of Ag nanoparticles in photothermorefractive glass after 50 mCcm^{-2} electron beam irradiation that relates with curve number 4 in Fig. 3.

3. Conclusions

The technology of fabrication of Ag NPs with average diameter about 2–10 nm in the subsurface layers of PTR glasses has been developed, the thickness of the layer being varied in the range 0.1–1.5 nm. The specific peaks in the optical absorption spectra were observed in the range of 405–430 nm corresponding to the localized SPR of silver NPs. The peak position and shape were shown to be strongly defined by the technological parameters such as electron beam energy, irradiation fluence, current density and the thermal treatment. So for applications such structures can be optimized by decreasing of the irradiation dozes and increasing of the current density which promote the decrease of linewidth of the LSPR at the selected beam energy and heat treatment temperatures.

Acknowledgements

This work is supported in part by the grant #10155 "Fundamental Science for Medicine" of the Presidium of the RAS, by the President of the RF grant #3306.2010.2 and RFBR grant #09-02-92009.

References

[1] N. V. Nikonorov *et al*, *Tech. Phys. Let.* **35** 7, 35 (2009).
[2] A. V. Vostokov *et al*, *Tech. Phys. Let.* **35** 7, 58 (2009).
[3] O. A. Usov *et al*, *Proc. SPIE* **7394**, 73942J (2009).
[4] R. E. Lamaestre *et al*, *Phys. Rev.* **76**, 205431 (2007).

18th Int. Symp. "Nanostructures: Physics and Technology"
St Petersburg, Russia, June 21–26, 2010

Excitonic polaritons in planar microcavities: polariton-polariton scattering and Bose condensation

V. D. Kulakovskii
Institute of Solid State Physics, RAS, Chernogolovka, Moscow reg. 142432, Russia

Abstract. Effect of polariton-polariton scattering on the polariton condensation is investigated with the use of polarization-dependent studies of the emission kinetics from the scalar and spinor polariton systems in GaAs MCs excited into a low polariton branch far from the inflection point with the use, respectively, of circularly and linearly polarized ns-long pulses. The effect of magnetic field on the polarization and Zeeman splitting of the Bose condensate of polarions is discussed.

Introduction

Microcavity (MC) exciton polaritons, composite quasiparticles consisting of quantum well exciton and MC photon components, have been proposed as candidates for Bose–Einstein condensation (BEC) [1,2]. Due to their low mass, the critical temperature for BEC is expected to be high. The confinement in two dimensions, along with the dual exciton-photon character of polaritons, enables interesting optical effects. Several characteristic signatures of dynamical condensation have been reported in recent years. The final energy distribution of polaritons is usually compared to the Bose–Einstein one [3]. However, the system is inherently dynamical because of the short lifetime of polaritons, on the order of a few ps in investigated samples [4]. Further complications are introduced by the polariton spin degree of freedom that leads to the interplay between energy and spin relaxation [5,6].

1. Polariton condensation at zero magnetic field

We present results of experimental polarization-dependent studies of the kinetics of polariton condensation in the scalar and spinor polariton systems in GaAs MCs excited into a low polariton (LP) branch far from the inflection point with the use, respectively, of circularly and linearly polarized ns-long pulses. The results give the insight on the energy and spin relaxation mechanisms of LPs and their condensation in momentum space.

No pronounced bottleneck effect is observed in MCs at positive detunings of the cavity and exciton modes $\delta = E_C - E_X >$ 1 meV ($E_X - E_{LP}(k = 0) < 2$ meV). At low excitation densities, P, the photoexcited LPs lose their polarization during the energy relaxation as it is expected in the case of dominated phonon-assisted LP scattering. The absence of the bottleneck in these MCs is well expected as only 1–2 phonon assisted scatterings are enough for the energy relaxation of exciton-like LPs to the LP band bottom. The polarization of $k = 0$ LPs increases monotonously with P due to enhanced contribution of LP-LP scatterings in the LP relaxation. The LP spin is retained in the process of scattering of two circularly polarized LPs with identical spins. As a result the macrooccupied mode at the LP band bottom under circularly polarized pumping acquires the polarization of the exciting pulse. In the case of the linearly polarized excitation, the rotation of the linear polarization axis by 90° is observed between the pump and condensate. Such a rotation is a specific for a LP-LP scattering of two linearly polarized LPs. Thus the condensate emission features are similar to those observed in a parametric oscillator experiment using the excitation near the inflection point of the LP dispersion and connected to spin-asymmetric LP-LP interaction. Thereby we conclude that the macrooccupation of the $k \sim 0$ states is provided by the direct LP-LP scattering in the excited mode.

A well pronounced bottleneck effect in the LP relaxation at low P appears with increasing LP band depth. The increase in P leads to the suppression of the bottleneck due to enhanced contribution from LP-LP scatterings. As the latter do not disturb the polarization of circularly polarized LPs, a nearly 100% circular polarization of the condensate is observed under the circularly polarized excitation. In contrast, no marked polarization is observed under the linearly polarized pumping. That is a direct proof of the Bose condensation in the LP system via multiple LP-LP scatterings.

2. Effect of magnetic field

The effect of magnetic field, B, on the LP condensation is investigated in high-Q MCs under the excitation well above the band gap. The condensate emission at $B = 0$ is linearly polarized. The effect originates from the fact that LPs with the same spin repel each other, while there is weak attraction between the LPs with opposite spins. At low magnetic fields, Zeeman splitting of LP levels has been found to cause an elliptical polarization of the ground condensate state rather than its splitting. Above some critical magnitude of B, the ground condensate state splits into two elliptically polarized components whose polarization transforms to circular one with a further increase in the magnetic field.

References

[1] C. Weisbuch, M. Nishioka, A. Ishikawa, and Y. Arakawa, *Phys. Rev. Lett.* **69**, 3314 (1992).
[2] A. Imamoglu, R. J. Ram, S. Pau, and Y. Yamamoto, *Phys. Rev. A* **53** 4250 (1996).
[3] H. Deng, G. S. Solomon, R. Hey, K. H. Ploog, and Y. Yamamoto, *Phys. Rev. Lett.* **99** 126403 (2007).
[4] T. D. Doan, H. T. Cao, D. B. Tran Thoai, and H. Haug, *Phys. Rev. B* **72** 085301 (2005).
[5] K. V. Kavokin, I. A. Shelykh, A. V. Kavokin, G. Malpuech, and P. Bigenwald, *Phys. Rev. Lett.* **92** 017401 (2004).
[6] Yu. G. Rubo, A. V. Kavokin, and I. A. Shelykh *Phys. Lett. A* **358** 227 (2006).

18th Int. Symp. "Nanostructures: Physics and Technology"
St Petersburg, Russia, June 21–26, 2010

Spin and transport effects in quantum microcavities

L. E. Golub and M. M. Glazov
Ioffe Physical-Technical Institute, St Petersburg, Russia

Abstract. We study theoretically spin-dependent transport of exciton-polaritons in quantum microcavities. Microscopic symmetry of the structure is taken into account by allowing for both the longitudinal-transverse and anisotropic splitting of polariton states. Such a splitting is equivalent to an effective magnetic field acting of polariton pseudospin and results in various phenomena, e.g. polarization conversion. In addition to the classical effects, the interference of polaritons is taken into account by the generalization of kinetic equation.

Introduction

Cavity polaritons being light-matter mixed states are formed as a result of the strong coupling between the photonic mode of a microcavity with excitons in a quantum well embedded into the structure. An interplay of the exciton spin and photon polarization degrees of freedom results in a number of spectacular phenomena widely studied nowadays.

The polaritonic spin states are described by two quantum numbers: an in-plane wave vector $\mathbf{k}$ and a projection of the angular momentum on the growth axis z, which can be either $+1$ or -1. The states with a definite angular momentum projection correspond to the circularly polarized light, and their linear combinations correspond to the elliptically polarized light. The polarization description is most conveniently described by using the concept of the pseudospin Bloch vector $\mathbf{S}_\mathbf{k}$ whose components are related with the Stokes parameters of radiation as

$$P_\mathrm{c}(\mathbf{k}) = \frac{S_{\mathbf{k},z}}{f_\mathbf{k}}, \quad P_1(\mathbf{k}) = \frac{S_{\mathbf{k},x}}{f_\mathbf{k}}, \quad P_{1'}(\mathbf{k}) = \frac{S_{\mathbf{k},y}}{f_\mathbf{k}}. \qquad (1)$$

where $f_\mathbf{k}$ is the mean occupation of the state $\mathbf{k}$, circular polarization degree P_c, and linear polarization degrees in two pairs of orthogonal axes rotated relative to each other by 45°, P_1 and $P_{1'}$.

Similarly to the quantum well electrons the polariton spin dynamics is driven by the the spin splitting of their energy dispersion which acts as a magnetic field with the $\mathbf{k}$-dependent Larmor frequency $\Omega_\mathbf{k}$. The Optical spin Hall effect, i.e. the linear-to-circular polarization conversion in microcavities, is a convenient way to visualize spin dynamics and precession frequency yielding important information on the magnitude and the direction of an effective magnetic field acting on the polariton spin [1].

Here we present a theory of the polarization conversion in microcavities with allowance for both longitudinal-transverse and anisotropic splittings of the polariton energy spectrum. We consider also the interference phenomena in microcavities which are shown to be strongly affected by the polarization splitting. The developed theory is compared with recent experimental findings [2].

1. Kinetic theory

The polarization dynamics in the linear regime is described by a kinetic equation for the pseudospin density of the polaritons

$$\frac{\mathbf{S}_\mathbf{k}}{\tau_0} + \mathbf{S}_\mathbf{k} \times \mathbf{\Omega}_\mathbf{k} + \frac{\mathbf{S}_\mathbf{k} - \langle \mathbf{S} \rangle}{\tau_1} = \mathbf{g}_\mathbf{k}, \qquad (2)$$

where τ_0 and τ_1 are the lifetime and elastic scattering times of exciton-polaritons, respectively, $\mathbf{g}_\mathbf{k}$ is the generation rate, and the angular brackets denote averaging over directions of $\mathbf{k}$. The effective Larmor precession vector $\mathbf{\Omega}_\mathbf{k}$ lies in the cavity plane and is described by two contributions, one with a fixed direction results from the structural anisotropy, another containing the second angular harmonics describes TE–TM splitting of the eigenmodes in ideal microcavities:

$$\mathbf{\Omega}_\mathbf{k} = \mathbf{\Delta} + \Omega_0(\cos 2\varphi, \sin 2\varphi). \qquad (3)$$

Here φ is an angle between $\mathbf{k}$ and x-axis, and it is assumed in what follows, that $\mathbf{\Delta} \parallel x$. Quantities Ω_0 and Δ describe TE–TM and anisotropic splittings, respectively, they are some functions of the wave vector absolute value k, which is assumed hereafter to be fixed: $k = k_0$ since we neglect inelastic processes. The angular distribution of the vector $\mathbf{\Omega}_\mathbf{k}$ is plotted in Fig. 1 for three important cases: $\Delta = 0$, $\Delta = \Omega_0$, and $\Delta > \Omega_0$. One can see that the precession frequency is anisotropic where both Ω_0 and Δ are nonzero.

There are two important limiting cases where the spin dynamics in microcavities is most brightly pronounced and studied experimentally: the excitation of a given state $\mathbf{k}_0$ [1] which corresponds to the standard Rayleigh scattering geometry, and the case of isotropic rate $\mathbf{g}_\mathbf{k} = \mathbf{g}$ [2]. In the first case only one state on the elastic circle is excited, and the polarization in scattered states is detected. For $\Delta = 0$ the problem was studied in detail in Ref. [3]: in this case the angular distribution of the circular polarization degree is described by the second angular harmonics and is zero on average, $\langle P_\mathrm{c} \rangle = 0$.

The situation changes if the anisotropic splitting is taken into account. We focus here on the experimentally important case where the generation is isotropic [2]. In the case of $\mathbf{g} \parallel \mathbf{\Delta}$ the angular averaged circular $\langle P_\mathrm{c} \rangle$ and linear $\langle P_{1'} \rangle$ polarizations vanish from the symmetry arguments. The linear polarization $\langle P_1 \rangle$ is partially lost for $\Omega_\mathbf{k} \neq 0$. An increase of Δ results in the increase of S_x and, accordingly, $\langle P_1 \rangle$, since its relaxation is reduced similarly to the suppression of the D'yakonov–

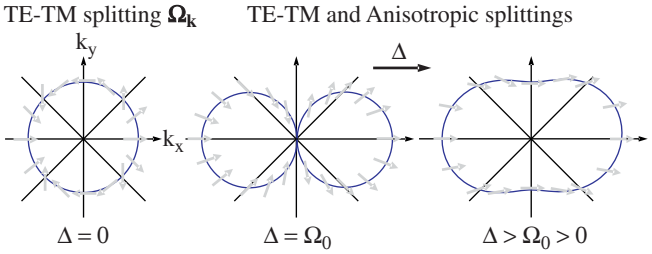

Fig. 1. The angular distribution of the effective magnetic fields in $\mathbf{k}$ space. The arrows show the directions of $\mathbf{\Omega}_\mathbf{k}$ for different orientations of the wave vector, and the curves show the absolute value $\Omega_\mathbf{k}$.

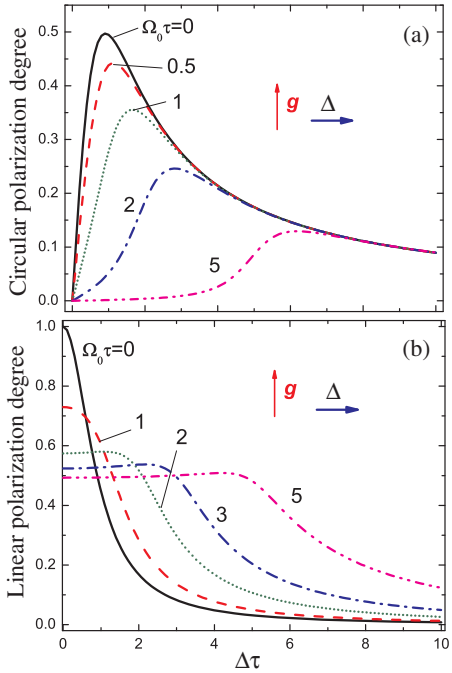

Fig. 2. Dependences of circular polarization degree $\langle P_c \rangle$ (a) and linear polarization degree $\langle P_{l'} \rangle$ (b) on the anisotropic splitting Δ at isotropic excitation with $\mathbf{g} \perp \mathbf{\Delta}$, $\tau/\tau_1 = 0.1$.

Perel' spin relaxation by the Larmor effect of the magnetic field. Hence the linear polarization degree $\langle P_l \rangle$ reaches one at $\Delta\tau \gg 1$, $\Delta \gg \Omega_0$.

If vectors $\mathbf{g}$ and $\mathbf{\Delta}$ are no longer parallel the situation strongly changes. Most importantly, the angular-averaged values of circular, $\langle P_c \rangle$ and linear, $\langle P_{l'} \rangle$ polarization appear. Their dependence on the system parameters is plotted in Fig. 2 for the case of $\mathbf{g}$ and $\mathbf{\Delta}$ being perpendicular.

Panel (a) presents the circular polarization degree, $\langle P_c \rangle$, and panel (b) shows the linear polarization degree $\langle P_{l'} \rangle$. Figure 2(a) demonstrates that the angular-integrated circular polarization degree is a non-monotonous function of the anisotropic splitting Δ. First, it increases with an increase of Δ, because the anisotropic splitting acts as a constant magnetic field and induces the conversion of perpendicular to $\mathbf{\Delta}$ in plane pseudospin component to its out of plane component. Further increase of Δ results in suppression of the circular polarization degree due to the spin precession. The linear polarization degree $\langle P_{l'} \rangle$ monotonously decreases as function of $\Delta\tau$, Fig. 2(b), since it is converted to the circular polarization and partially lost due to the spin precession around $\Omega_{\mathbf{k}}$.

The detailed analysis of the angular distribution of the circular polarization degree is given in Ref. [4]. In addition to the zeroth angular harmonics the distribution contains other even harmonics.

2. Interference effects

The classical kinetic theory presented in the previous Section describes well the available experimental data on the Optical spin Hall effect in microcavities [4]. However, exciton-polaritons keep their coherence while propagating over large distances [1]. As a result, interference effects can come into play. The most important of those are the coherent phenomena leading to weak localization of polaritons [3].

The description of the spin dynamics of the exciton-polaritons with account for the interference effects is reduced to the solution of the kinetic equations for the particle number density ($f_{\mathbf{k}}$) and spin density ($\mathbf{S}_{\mathbf{k}}$) where the scattering terms in Eq. (2) acquire the corrections like

$$\frac{\mathbf{S}_{\mathbf{k}} - \langle \mathbf{S} \rangle}{\tau_1} \to \frac{\mathbf{S}_{\mathbf{k}} - \langle \mathbf{S} \rangle}{\tau_1} - \widehat{W} \left(\mathbf{S}_{-\mathbf{k}} - \langle \mathbf{S} \rangle \right), \qquad (4)$$

where the tensor $\widehat{W}$ and a corresponding scalar W in the similar equation for $f_{\mathbf{k}}$ describe spin-dependent return probabilities are calculated by Greens function method [3,4].

The interference effects are most pronounced in the multiple scattering regime, $\tau_1 \ll \tau_0$ where the polariton experiences many scattering acts during its life time in a cavity. It results in the corrections to kinetic coefficients such as diffusion constants, spin relaxation rates, and polarization conversion efficiencies of the order of $(k_0 l)^{-1} \ln(\tau_0/\tau_1)$, $(k_0 l)^{-1} \ln(\tau_s/\tau_1)$, where l is the mean free path, and $\tau_s \sim 1/\langle \Omega_{\mathbf{k}}^2 \tau_1 \rangle$ [3]. The analytical and numerical results for anisotropic microcavities are presented in Ref. [4]. The presence of both anisotropic and longitudinal-transverse splittings results in a specific interference of polaritons. For instance with an increase of $\Delta\tau$ the particle return probability, W_0, and parallel to the Δ spin component return probability, W_{xx}, approach the values for $\Omega_0 = 0$, $\Delta = 0$ despite the presence of the spin splittings.

3. Conclusions

We have studied in detail the exciton-polariton spin dynamics with allowance for both the longitudinal-transverse splitting ($\propto \Omega_0$) and the anisotropic splitting ($\propto \Delta$) which coexist in real structures. The presence of the anisotropic splitting changes dramatically the polarization conversion in microcavities as compared with the case of ideal isotropic system where only longitudinal-transverse splitting is present. The emission of the microcavity excited by linearly polarized light becomes, in general, elliptically polarized. The efficiency of the linear to circular polarization conversion depends strongly on the relation between the longitudinal-transverse splitting, the anisotropic splitting and the polariton radiative and scattering rates.

We have analyzed the effects of anisotropic splitting on the interference of polaritons caused by the weak localization/antilocalization phenomena. The spin-dependent return probabilities are shown to be strongly sensitive to the anisotropic splitting of polariton states.

Application of our model to recent experimental data on Optical spin Hall effect in microcavities [2] showed a good agreement with the experiment.

Acknowledgements

This work was partially supported by RFBR, "Dynasty" Foundation — ICFPM and President grant for young scientists.

References

[1] C. Leyder *et al*, *Nature Physics* **3**, 628 (2007).
[2] A. Amo *et al*, *Phys. Rev. B* **80**, 165325 (2009).
[3] M. M. Glazov and L. E. Golub, *Phys. Rev. B* **77**, 165341 (2008).
[4] M. M. Glazov and L. E. Golub, *arXiv:*0912.2519 (2009).

18th Int. Symp. "Nanostructures: Physics and Technology"
St Petersburg, Russia, June 21–26, 2010

Linear and nonlinear coupling of quantum dots in microcavities

F. P. Laussy,[1] E. del Valle,[1] A. Gonzalez-Tudela,[2] E. Cancellieri,[2] D. Sanvitto[2] and C. Tejedor[2]

[1] School of Physics and Astronomy, University of Southampton, SO171BJ, Southampton, UK
[2] Universidad Autónoma de Madrid, 28049, Madrid, Spain

Abstract. We discuss the topical and fundamental problem of strong-coupling between a quantum dot an the single mode of a microcavity. We report seminal quantitative descriptions of experimental data, both in the linear and in the nonlinear regimes, based on a theoretical model that includes pumping and quantum statistics.

Introduction

After its pioneering observation in micropillars [1] and in photonic crystals [2] in 2004, strong-coupling of light and matter is now commonplace in zero-dimensional nanostructures [3–8]. This physics is primordial both for fundamental research and technological applications, from thresholdless lasers and new light-sources to quantum information processing. We have given the first quantitative description of experimental data [9] (see Fig. 1), by providing a general model of quantum modes coupling [10]. Our model extends the atomistic description, that limits to the excited state of the atom in an empty cavity as an initial condition. In semiconductor microcavities, however, photoluminescence measurements are typically made in the steady state established by a continuous, incoherent pumping. We take these specificities into account and: i) recover the spontaneous emission case of an arbitrary initial state in the limit of vanishing pumping, thereby providing a complete, self-consistent and general description of light-matter coupling, and ii) include dynamical effects of quantum statistics for non-vanishing pumping, such as Bose stimulation and Pauli blocking.

1. Linear regime

When pumping is very small, so that the system is most of the time in vacuum, and occasionally excited, its photoluminescence spectrum is that of spontaneous emission of the state that results from the averaged excitation. In a microcavity, excitation is typically sought to be of the quantum dot itself, by mean of electron-hole pairs relaxation from off-resonant pumping [11]. As such, its photoluminescence spectrum would recover that of the atomic literature [12], up to a technical correction that consists in computing the cavity mode spectrum (for a microcavity) rather than the direct atomic de-excitation (for an optical cavity). However, various mechanisms result in an effective microcavity pumping, where photons are directly injected into the coupled light-matter system. One vivid scenario is that the quantum dot of interest, in strong-coupling with the cavity, is a "lucky" one — well positioned in the optical field, with adequate coupling strength, etc. — but is surrounded by many other dots, less efficiently coupled to the cavity (in weak-coupling). These are also excited by electron-pairs ideally intended for the strongly-coupled dot only. The other dots can release efficiently (by Purcell enhancement) and with no correlations (in a Markovian approximation) their excitation in the cavity mode and as such bath the light-matter system of interest in a photonic environment. As the initial state (and effective quantum steady state) affects dramatically the spectral shapes, it is important to take into account both excitation channels to reproduce experimental data, in particular as effects of pumping are known to produce nontrivial phenomenology even at a qualitative level [13]. Most strikingly, at resonance, neither a doublet is a guarantee of strong-coupling nor a singlet is an evidence of weak-coupling. The analysis should be done at the level of spectral shapes rather than for the anticrossing of the maxima, for which there is no closed expression [14].

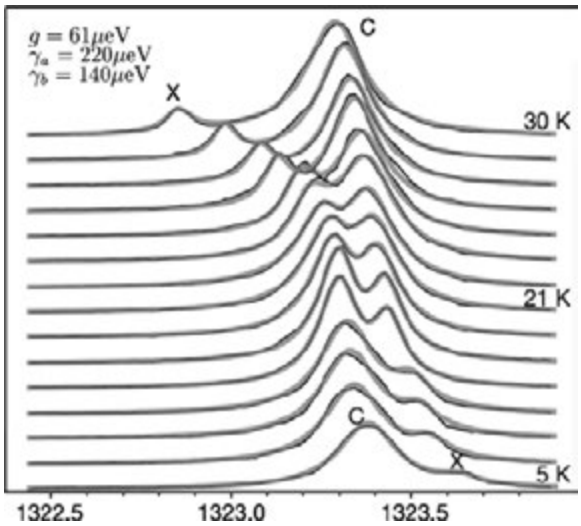

Fig. 1. Fit in the linear regime: data of Reithmaier *et al* [1] with — superimposed in red — our global fit [9].

2. Nonlinear regime

When pumping is non-negligible, quantum statistics is to be added to the previous considerations. In the case of a large or elongated quantum-dot, where the electron and hole can bind as an exciton, the underlying statistics is that of Bose–Einstein [15]. This results in stimulated emission and line narrowing with increasing pumping (Schallow–Townes effect). If, on the other hand, the electron and hole are quantized separately in a small quantum dot, Pauli exclusion prevents other electrons and holes to populate the already excited dot, and the statistics of Fermi–Dirac rules the dynamics. As a conclusion, increasing excitation can lead to a variety of rich nonlinear effects, in the wake of Jaynes–Cummings physics (strong coupling of a boson and fermion). An important expected manifestation is full-field quantization, that results in a series of peaks at anharmonic frequencies $\pm(\sqrt{n} \pm \sqrt{n-1})$ when n excitations are in the system [16]. State of the art technology does not yet allow to resolve clearly this fine-structure in semiconduc-

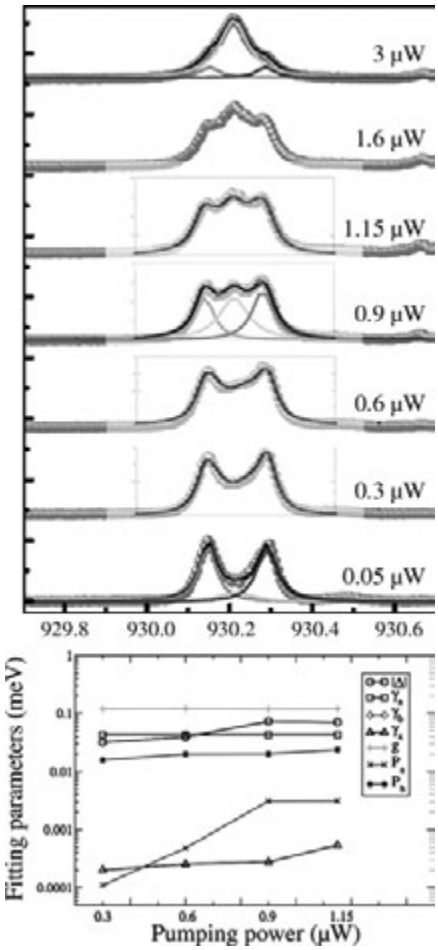

Fig. 2. Fit in the nonlinear regime: data of Ota *et al* [19] with — superimposed in blue for the four central panels — our global fit (fitting parameters appear below) with a fermion model [17] including dephasing [21].

tors, although we find that a careful analysis in a situation with significant cavity pumping, could evidence manifestations of nonlinearities at the quantum level [17].

Another important expected manifestation of a two-level system brought in the nonlinear regime by high pumping is lasing. Recently, the transition from vacuum strong-coupling to lasing has indeed been reported [18]. In another, related work [19], this transition was observed to pass through a stage where a triplet is formed by appearance of a peak at the cavity mode frequency that subsequently overtakes the polariton modes as the system enters into lasing (see Fig. 2). Various explanations have been advanced for spectral triplets of this type [3,19]. We offer one that, including a term of dephasing — which has been demonstrated to play a key role with increasing pumping [8] — explains the appearance of the triplet as a melting of the inner transitions between rungs of the Jaynes–Cummings ladder. Such a transition, if confirmed, would provide a striking crossover from the quantum realm, where single quanta rule the dynamics of the system [20], to the classical world, where a continuous field (the lasing mode) takes over a small number of quantum correlators. We have confronted our theory with the experimental data, again by fitting, but the situation in the nonlinear regime is significantly more complicated, owing to the lack of closed expressions for the spectral lineshapes. We have used genetic algorithm methods to do a global fitting of the data. We find our proposition to be consistent with the supposed parameters of this experiment, beside with a neat contribution due to a drift in detuning more than to dephasing. Beyond supporting claims of quantum nonlinearities, our work also provides the first quantitative description of strong-coupling experimental data but now in the nonlinear and fermionic regime.

References

[1] J. P. Reithmaier, G. Sek, A. Löffler, C. Hofmann, S. Kuhn, S. Reitzenstein, L. V. Keldysh, V. D. Kulakovskii, T. L. Reinecker, and A. Forchel, *Nature* **432**, 197 (2004).

[2] T. Yoshie, A. Scherer, J. Heindrickson, G. Khitrova, H. M. Gibbs, G. Rupper, C. Ell, O. B. Shchekin, and D. G. Deppe, *Nature* **432**, 200 (2004).

[3] K. Hennessy, A. Badolato, M. Winger, D. Gerace, M. Atature, S. Gulde, S. Fält, E. L. Hu, and A.İmamoğlu, *Nature* **445**, 896 (2007).

[4] D. Press, S. Götzinger, S. Reitzenstein, C. Hofmann, A. Löffler, M. Kamp, A. Forchel, and Y. Yamamoto, *Phys. Rev. Lett.* **98**, 117402 (2007).

[5] M. Nomura, Y. Ota, N. Kumagai, S. Iwamoto, and Y. Arakawa, *Appl. Phys. Express* **1**, 072102 (2008).

[6] C. Kistner, T. Heindel, C. Schneider, A. Rahimi-Iman, S. Reitzenstein, S. Höfling, and A. Forchel, *Opt. Express* **16**, 15006 (2008).

[7] A. Dousse, J. Suffczyński, R. Braive, A. Miard, A. Lemaître, I. Sagnes, L. Lanco, J. Bloch, P. Voisin, and P. Senellart, *Appl. Phys. Lett.* **94**, 121102 (2009).

[8] A. Laucht, N. Hauke, J. M. Villas-Bôas, F. Hofbauer, G. Böhm, M. Kaniber, and J. J. Finley, *Phys. Rev. Lett.* **103**, 087405 (2009).

[9] F. P. Laussy, E. del Valle, and C. Tejedor, *Phys. Rev. Lett.* **101**, 083601 (2008).

[10] F. P. Laussy, E. del Valle, and C. Tejedor, *Phys. Rev. B* **79**, 235325 (2009).

[11] N. Averkiev, M. Glazov, and A. Poddubny, *Sov. Phys. JETP* **135**, 959 (2009).

[12] H. J. Carmichael, R. J. Brecha, M. G. Raizen, H. J. Kimble, and P. R. Rice, *Phys. Rev. A* **40**, 5516 (1989).

[13] L. V. Keldysh, V. D. Kulakovskii, S. Reitzenstein, M. N. Makhonin, and A. Forchel, *Pis'ma ZhETF* **84**, 584 (2006).

[14] A. Gonzalez-Tudela, E. del Valle, C. Tejedor, and F. Laussy, *Superlatt. Microstruct.* **47**, 16 (2010).

[15] F. P. Laussy, M. M. Glazov, A. Kavokin, D. M. Whittaker, and G. Malpuech, *Phys. Rev. B* **73**, 115343 (2006).

[16] F. P. Laussy and E. del Valle, *AIP Conference Proceedings* **1147**, 46 (2009).

[17] E. del Valle, F. P. Laussy, and C. Tejedor, *Phys. Rev. B* **79**, 235326 (2009).

[18] M. Nomura, N. Kumagai, S. Iwamoto, Y. Ota, and Y. Arakawa, *Nat. Phys.* (2010), AOP, doi:10.1038/nphys1518.

[19] Y. Ota, N. Kumagai, S. Ohkouchi, M. Shirane, M. Nomura, S. Ishida, S. Iwamoto, S. Yorozu, and Y. Arakawa, *Appl. Phys. Express* **2**, 122301 (2009).

[20] G. Khitrova, H. M. Gibbs, M. Kira, S. W. Koch, and A. Scherer, *Nat. Phys.* **2**, 81 (2006).

[21] A. Gonzalez-Tudela, E. del Valle, C. Tejedor, E. Cancellieri, D. Sanvitto, and F. P. Laussy, *Opt. Express* (to appear in Vol. 18, No. 7), arXiv:0907.1302 (2010).

18th Int. Symp. "Nanostructures: Physics and Technology"
St Petersburg, Russia, June 21–26, 2010

Resonant Bragg structure mediated by the quantum well excitons at the second quantum state

V. V. Chaldyshev[1], A. P. Vasil'ev[1], Z. Chen[2] and Z. Liu[2]

[1] Ioffe Physical-Technical Institute, St Petersburg, Russia
[2] Brooklyn College of the City University of New York, New York, USA

Abstract. A periodic multiple quantum well GaAs/AlGaAs structure was designed, grown and characterized in order to reveal resonant features in optical spectra when the Bragg resonance was tuned to the second quantum state x-e2-hh2 of the heavy-hole exciton-polaritons in the quantum wells. The fine tuning and detuning of the resonance was achieved by changing of the incident angle of the light and the sample temperature. A significant enhancement of the light-matter interaction was observed through strong optical reflection and electroreflection under the resonant conditions.

Introduction

The resonant Bragg structure (RBS) is a special type of one-dimensional photonic crystals where the electromagnetic waves resonantly interact with quasi-two-dimensional excitons in a periodic system of quantum wells (MQW). Multiple diffraction of the exciton-polaritons impacts the optical properties of the medium in a vicinity of the resonant frequency when the periodicity of the structure, d, is tuned to the Bragg condition $d = \pi c/(\omega n)$, where ω is the frequency of the exciton-polaritons in the QWs, n is the refraction index of the barrier, c is the speed of light in vacuum. This phenomenon was first considered in Ref. [1] and extensively studied in theory in subsequent publications (see, for instance, [2,3] and references there). It has been shown that the large number of quantum wells enhances the light-matter interaction and significantly increases the width of the polariton band gap, giving rise to a superradiant optical mode.

The experimental research has been done on the CdTe/CdMgTe [4], GaAs/InGaAs [5,6] and GaAs/AlGaAs [7,8] MQW structures. These works demonstrated in experiment the feasibility of the coherent exciton-photon coupling in MQW with a large number of periods. This phenomenon makes the RBS attractive for applications to a variety of photonic devices that may benefit from a flexible Bragg reflection.

All the above mentioned research was focused on the lowest energy state of the exciton-polaritons in the QWs. However, the resonant reflection does not require any population of the excitonic or electronic state and can be realized for higher quantum confinement levels.

In this paper we report the results of optical study of a novel resonant Bragg structure based on the GaAs/AlGaAs MQW system. In this structure the Bragg reflection resonance is tuned to the frequency of the heavy-hole excitons at the second quantum level e2-hh2.

1. Experimental

The RBS consisted of 60 GaAs QWs separated by AlGaAs barriers. It was grown by molecular beam epitaxy (MBE) in a Riber 32 system on a semi-insulating 2-inch GaAs substrate with (001) orientation. The samples were not intentionally doped. The optical spectra of the fabricated RBS were measured at various angles and polarizations of the incident light in the temperature range from 4 to 300 K. The reflectance was measured using a grating monochromator equipped with a Si linear array photodetector. The electroreflectance was studied by the contactless technique with modulation voltages in the range of 200–1200 V.

2. Results

Figure 1 shows the reflection spectra of the RBS recorded at 4.2 K at different angles of the light incidence, *theta*, and polarizations (s, p). The spectra demonstrate one major reflection band in the range of 740–780 nm accompanied by a large number of interference fringes on the background reflection. The latter corresponds to what is expected for a dielectric material with the refraction index $n = 3.6$. The background reflection diminishes in p-polarization when the incident angle approaches the Brewster's angle. The shift of the reflectance band center, λ_m, as the function of the incident angle follows the Bragg diffraction equation:

$$\lambda_m = 2d\sqrt{n^2 - \sin^2\theta}\,. \qquad (1)$$

The fine structure of the reflection spectra relates to the excitonic transitions, which are marked in Fig. 1 by arrows. It should be noted that the strongest reflection is observed at the incidence angle of about 23° when the center of the Bragg reflection band coincides with the wavelength of the QW exciton-polariton band x-e2-hh2.

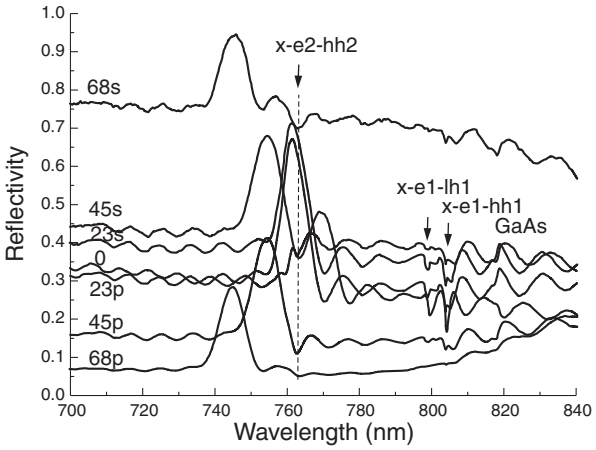

Fig. 1. Reflectivity of the GaAs/AlGaAs RBS at 4.2 K for s- and p-polarizations of the light at the angle of incidence of 68°, 45°, 23°, and 0°. Arrows mark the features related to the excitonic transitions in the quantum wells (x-ehh1, x-elh1, and x-ehh2) and in the bulk GaAs substrate.

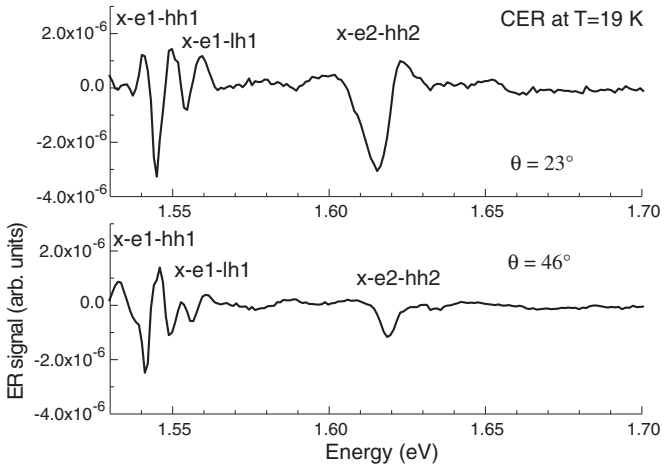

Fig. 2. Contactless electro-reflectivity of the GaAs/AlGaAs RBS at 19 K at the incident angles of 23° and 45°.

Plotted in Fig. 2 are the contactless electro-reflection (CER) spectra recorded at 19 K with modulation voltage of 500 V and two different angles of incidence. Since the background index of refraction is not sensitive to the weak modulating electric field, the major features in the CER spectra originate from different excitonic states in the quantum wells. A strong signal related to the GaAs substrate was also observed (not shown in Fig. 2), which indicated a very low screening of the electric field by free carriers. The CER features were fitted in the first derivative approximation with Gaussian line shape. The peak energies in the CER spectra were quantitatively consistent with quantum mechanical calculations based on the sample design. The most important observation in Fig. 2 is an increase in both the magnitude and the width of the electro-reflection related to the x-e2-hh2 exciton, when the angle of incidence is tuned from 46° to 23°. The full width at half maximum for the x-e2-hh2 peak, Δ, changes from 5.3 to 9.4 meV, whereas for the x-e1-hh1 ground exciton level it always remains equal to 3.9 ± 0.1 meV. Alternatively, the enhancement of the x-e2-hh2 peak was realized by variation of the sample temperature.

3. Discussion

The experimental observations described above give the evidence for the super-radiant mode of the RBS. Formation of this mode occurs when the sample temperature is below 30 K and the incident angle is about 23°. According to Equation (1) this angle provides the Bragg condition at 762 nm, which corresponds to the energy of 1.62 eV of exciton-polaritons at the second quantum state e2-hh2. The broadening of the exciton-polariton reflection band due to the electro-magnetic coupling in MQW system under the Bragg conditions can be described as [1,2]

$$\Delta = 2\,(N\Gamma_0 + \Gamma)\,, \qquad (2)$$

where Γ_0 is the radiative broadening parameter for the exciton-polariton in a single quantum well; Γ represents the non-radiative broadening; and $N = 60$ is the number of QWs in the system. Because the systems of x-e1-hh1 and x-e1-lh1 exciton-polaritons are far away from the resonance conditions, they give an estimate of the non-radiative broadening $2\Gamma = 3.9$ meV for our MQW sample. According to Equation (2) this gives $\Gamma_0 = 45$ μeV, which is close to the expected values [7] for the GaAs/AlGaAs system.

4. Conclusions

We demonstrated for the first time the double resonance due to the coupling of the Bragg diffraction and the second quantum state e2-hh2 of exciton-polaritons in a MQW structure. Our experiments show a substantial enhancement of the exciton-photon interaction in the RBS by fine tuning of the Bragg wavelength via variation of the incident angle of the light. or by changing the exciton frequency via the sample temperature. Parameters of the optical features in reflection and electro-reflection spectra are evaluated in- and out of resonance conditions.

Acknowledgements

This work has been supported in part by the Russian Foundation for Basic Research, grant #09-02-12313, and by the Russian Academy of Sciences.

References

[1] E. L. Ivchenko *et al*, *Phys. Solid State* **36**, 1156 (1994).
[2] L. I. Deych *et al*, *Phys. Rev. B* **69**, 75308 (2004).
[3] E. L. Ivchenko *et al*, *Phys. Rev. B* **70**, 195106 (2004).
[4] E. L. Ivchenko *et al*, *Phys. Solid State* **39**, 1852 (1997).
[5] M. Hubner *et al*, *Phys. Rev. Lett*. **83**, 2841 (1999).
[6] J. P. Prineas *et al*, *Phys. Rev. B* **61**, 13863 (2000).
[7] V. V. Chaldyshev *et al*, *J. Mater. Sci.: Materials in Electronics*, **19**, 699 (2008).
[8] D. Goldberg *et al*, *Nature Photonics* DOI: 10.1038/NPHOTON.2009.190.

18th Int. Symp. "Nanostructures: Physics and Technology"
St Petersburg, Russia, June 21–26, 2010

Multiple diffraction of light and interference effects in spectroscopy of 3D photonic crystal films

V. G. Fedotov[1,2] and A. V. Sel'kin[2,1]

[1] Faculty of Physics, St Petersburg State University, 198504 St Petersburg, Russia
[2] Ioffe Physical-Technical Institute, St Petersburg, Russia

Abstract. New interference patterns in Bragg reflection and transmission spectra of three-dimensional opal-like photonic crystal films are found to be due to multiple diffraction of light. Typical spectra of reflectance and transmittance are calculated making use of the dynamical diffraction theory generalized to the case of high dielectric contrast. An analysis is made of the complicated spectral structure in the Bragg reflection and transmission contours, which shows that the additional short-periodic Fabry–Pérot-like interference structure (interference "comb") arises as a result of the interference between additional low-group-velocity waves.

Introduction

Photonic crystals (PhCs) are spatially periodic solid-state structures whose permittivity is modulated with a period comparable to the wavelength of light. These structures attract much attention in up-to-date studies. Considerable interest to PhCs is stimulated by currently emerging applications in laser technology and optoelectronics utilizing nanostructured materials [1, 2] and by the fundamental scientific problems which come about in attempting to explain PhC mediated optical phenomena [3].

One of the striking phenomena is the multiple Bragg diffraction appearing when two or more families of crystal planes with different plane indices are involved in Bragg reflection at the same frequency. It is worth noting that the methods and the models used when examining the effects of multiple diffraction for X-rays [4, 5] are often inapplicable to PhC structures because of their high dielectric contrast (strong spatial modulation of refraction index).

This paper studies Bragg reflection and transmission spectra formed by resonant diffraction of light from a three-dimensional (3D) opal-like PhC slab for the case when the multiple diffraction effects are of importance. Here, we focus on new interference effects which are expected to be observed for thin PhC films.

Particular attention is paid to the analysis of the complex spectral structure governing the Bragg reflection contour which is shaped due to the interference of light on two plane boundaries of the PhC slab and strongly depends on structural perfection of PhC.

1. Results

The eigenmode dispersion curves and zero-order diffraction (reflection and transmission) spectra were calculated, for reference, in the three- and two-band mixing approximations [6]. The incidence angle $\theta = 57^\circ$ for *s*-polarized light was taken in our numerical calculations. The case of the three-band mixing model corresponds to the 3D situation and takes into account simultaneous diffraction from two systems of crystal planes, (111) and $(11\bar{1})$, with $(11\bar{1})$ being non-parallel to the reflecting lateral surface of the slab. The Bragg reflection and transmission spectra are depicted for this case in Fig. 1 by solid lines. Dashed lines in the figure are referred to the two-band mixing model (one-dimensional (1D) situation) and describe the light diffraction from the only one system of crystal planes, (111), parallel to the lateral surface plane. We see, comparing the two models, that the spectra calculated qualitatively differ to each other in the spectral range of the photonic band gap (PBG) where maximum (minimum) values of reflectance (transmittance) take place. Outside the PBG resonant region, classic

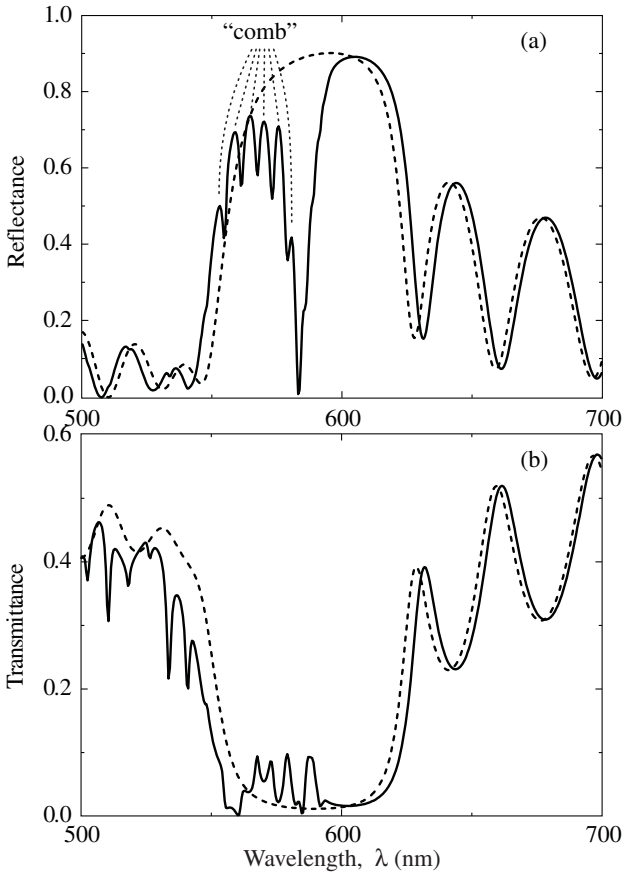

Fig. 1. Calculated Bragg reflection (a) and transmission (b) spectra of an opal-like photonic crystal film (assembled from polystyrene spheres of 300 nm in diameter) with the 20 monolayers thickness. The dashed curve describes the light diffraction from the only one system of crystal planes (111) parallel to the lateral surface plane. The solid curve corresponds to the simultaneous diffraction from two systems of crystal planes, (111) and $(11\bar{1})$, with $(11\bar{1})$ being inclined to the reflecting surface of the specimen.

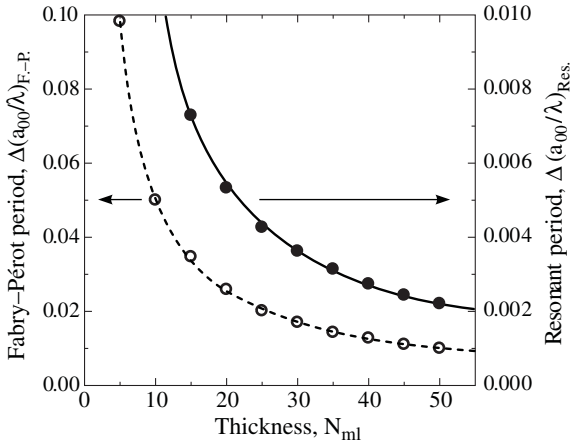

Fig. 2. Fabry–Pérot-like oscillation periods in the off-resonant (dashed curve, open circles) and resonant (solid curve, black circles) spectral ranges as a function of the monolayer count. The symbols are the distances between the neighboring interference peaks in the reflection spectra, the dashed curve is calculated by using Eq. (1), and the solid curve is obtained by using reciprocal rational function, Eq. (2). a_{00} is the neighboring spacing between spheres of the opal-like PhC structure and λ is the wavelength of light in vacuum.

Fabry–Pérot interference fringes are observed.

Calculations performed in the framework of 3D model show that an additional short-periodic Fabry–Pérot-like interference structure (interference "comb") appears in the resonant range. It should be noted that such a "comb" disappears with increasing the imaginary part of permittivity [7], which corresponds usually to the deterioration of the PhC structural quality. Thus, in order to register the interference "comb" one needs to use PhC specimens of high enough perfection.

2. Discussion

Period of Fabry–Pérot oscillations can be estimated in the continuous medium approximation when a PhC film is considered as a homogeneous dielectric slab. In such a case, the period of oscillations is given by

$$\Delta\left(\frac{a_{00}}{\lambda}\right)_{\text{F.–P.}} = \frac{1}{2\sqrt{\varepsilon_0 - \sin^2\theta}\left(\sqrt{2/3}(N_{\text{ml}} - 1) + 1\right)}, \quad (1)$$

where $\varepsilon_0 = \varepsilon_a f + \varepsilon_b(1-f)$ is the average permittivity of PhC assembled of the spheres with permittivity ε_a (for polystyrene $\varepsilon_a = 2.522$) and pores with permittivity ε_b (for vacuum $\varepsilon_b = 1$), and f is the filling fraction of sphere material in the PhC structure.

In Fig. 2, the dashed curve shows the calculated (using Eq. (1)) spectral oscillation period $\Delta(a_{00}/\lambda)_{\text{F.–P.}}$ against the film thickness expressed in the monolayer count N_{ml}, the thickness of each monolayer being equal to 300 nm. In this figure, the open circles represent the oscillation periods taken from the calculated off-resonant Bragg reflection spectra similar to those shown in Fig. 1(a) (solid curve). As can be seen, the dashed curve plotted with Eq. (1) fits the open circles well.

As indicated above, the additional interference "comb" is exclusively due to the multiple 3D diffraction of light. In the two-band mixing approximation (1D periodic structure), such a structure does not occur (Fig. 1, dashed curves). Short-periodic spectral oscillations observed in the resonant range allow one to find their period as a function of the film thickness N_{ml} (Fig. 2, black circles). This dependence is hyperbolic (Fig. 2, solid curve) and scaled with that depicted for the off-resonant region, i.e.

$$\Delta\left(\frac{a_{00}}{\lambda}\right)_{\text{F.–P.}} / \Delta\left(\frac{a_{00}}{\lambda}\right)_{\text{Res.}} = \text{const}.$$

In order to describe analytically the short-periodic oscillations appearing in the reflection and transmission spectra within the resonant region (the interference "comb"), we need a more detailed eigenmode spectrum inside the PBG region. The finite thickness of the PhC plate gives rise to the spatial quantization of the additional low-group-velocity modes [6], which determines the corresponding oscillation period,

$$\Delta\left(\frac{a_{00}}{\lambda}\right) = \frac{\partial\omega}{\partial k_z}\frac{1/(2c)}{\sqrt{2/3}(N_{\text{ml}} - 1) + 1}, \quad (2)$$

where ω is the frequency of light, k_z is the projection of the eigenmode wavevector onto the normal to the surface and c is the velocity of light in vacuum.

In conclusion, we would like to note that the phenomena discussed in this paper are in some sense similar to those observed in the media possessing spatial dispersion [8]. In both situations, additional electromagnetic waves are involved into consideration and the problem of the additional boundary conditions for the field amplitudes should be solved. However, unlike the media with spatial dispersion, PhC structures do not necessarily are characterized by a non-local dielectric response. Therefore, PhCs cannot be related, in general, to the systems with spatial dispersion, even though the multi-wave propagation regime takes place inside PhC as well.

Acknowledgements

This work was supported in part by the Russian Foundation for Basic Research under Grant No. 08-02-00642-a and by the State Contract No. 02.740.11.0384.

References

[1] M. Mizeikis, S. Juodkazis, A. Marcinkevičius, S. Matsuo, and H. Misawa, *J. Photochem. and Photobiol. C* **2**, 35 (2001).
[2] C. López, *Adv. Mater.* **15**, 1679 (2003).
[3] K. Sakoda, *Optical Properties of Photonic Crystals* (Springer, Berlin-Heidelberg-New York, 2001).
[4] B. W. Batterman and H. Cole, *Rev. Mod. Phys.* **36**, 681 (1964).
[5] S.-L. Chang, *Multiple Diffraction of X-Rays in Crystals* (Springer, Berlin-Heidelberg-New York, 1984).
[6] V. G. Fedotov, A. V. Sel'kin, A. Yu. Men'shikova, N. N. Shevchenko, and A. V. Yakimanskiy, *Proc. of 17th Int. Symp. "Nanostructures: Physics and Technology"*, Minsk, Belarus, 2009, p. 109.
[7] A. G. Bazhenova, A. Yu. Men'shikova, A. V. Sel'kin, V. G. Fedotov, N. N. Shevchenko, and A. V. Yakimanskiy, *High Energy Chemistry* **42**, 527 (2008).
[8] V. M. Agranovich and V. L. Ginzburg, *Crystal Optics with Spatial Dispersion, and Excitons* (Springer, Berlin-Heidelberg-New York, 1984).

18th Int. Symp. "Nanostructures: Physics and Technology"
St Petersburg, Russia, June 21–26, 2010

Sensitive analysis of 2D photonic bandgaps using boundary integral equations

L. I. Goray

St Petersburg Academic University, St Petersburg, Russia
Institute for Analytical Instrumentation, RAS, Rizhsky Prospect 26, St Petersburg 190103, Russia

Abstract. A boundary-integral-equation-based method is proposed to calculate sensitive diffraction properties of various photonic crystal slabs (PCS). The numerical results presented demonstrate the significant impact of rod shapes and sizes on diffraction in metallic 2D PCS supporting the polariton-plasmon excitation, particularly close to resonances and at high filling ratios.

Introduction

In the recent decades, we have been witnessing unwaning interest, both of theoreticians and experimenters, in the properties of photonic crystal slabs (PCS) and metamaterials. Progress in the technology of nanostructures with a characteristic surface relief of the order of 10–100 nm has stimulated production of 2D and 3D periodic structures with periods shorter than the wavelength of visible light, i.e. subwavelength diffraction gratings. Nowadays considerable effort is devoted to the investigation of polariton-plasmon PCS with metallic or semiconducting nanostructures supporting strong light-matter interaction. Large photonic band gaps, extraordinary light transmission properties, negative refraction, and strong coupling between the electronic and photonic resonances can be supported in such structures.

Though surface plasmon excitation plays a predominant part in metallic subwavelength PCS, other types of electromagnetic resonances can also exist in complex structures: Rayleigh anomalies, Fabry–Perot resonances, waveguiding anomalies, cavity modes, etc. In some cases it is difficult to distinguish among these phenomena, owing to their gradual mutation from one into another, and determine which is which even using electromagnetic field map distributions inside the grating structure. There is therefore a growing need for methods based on a rigorous theory which would be both accurate and fast enough [1]. Most of the theoretical investigations applied to PCS have been performed using the plane wave method (scattering-matrix formalism), but this method suffers from poor convergence and needs large computation times, especially for the TM-polarized incident light, because of its main accuracy parameter scaling cubically with time [2,3]. Recently a modeling tool without such limitations has been developed on the basis of the rigorous single-boundary integral equations for conical diffraction [4] and the scattering matrix approach applied to off-plane multilayer gratings [5].

The motivation for the present communication is to introduce the new method as an exact and universal approach to be applied in areas where rapid design and analysis of the most sensitive PCS cases would be at a premium. The aim of this work is to investigate the influence of rod (nanowire) shapes and rod filling ratio on diffraction in metallic 2D PCS supporting the polariton-plasmon excitation, particularly close to resonances.

1. Theory

We employed the boundary integral equation method for a theoretical description of the optical properties of PCS. The theory is covered here necessarily very briefly because its main parts have been described at considerable length in Refs. 4,5. The electromagnetic formulation of diffraction by gratings, which are modeled as infinite periodic structures, can be reduced to a system of Helmholtz equations for the z-components of the electric and magnetic fields in $\mathbf{R^2}$, where the solutions have to be quasiperiodic in the x-direction, subject to radiation conditions in the y-direction, and satisfy certain jump conditions at the interfaces between different materials of the diffraction grating. In the case of classical diffraction, when the incident wave vector is orthogonal to the z-direction, the system splits into independent problems for the two basic polarizations of the incident wave, whereas in the case of conical diffraction the boundary values of the z-components, as well as their normal and tangential derivatives at the interfaces, are coupled. Thus the unknowns are scalar functions in the case of classical diffraction, and two-component vector functions in the conical case.

A grating diffracts the incoming plane wave into a finite number of outgoing plane waves, the so-called reflected and transmitted modes. The program computes the energies and polarizations of these modes for an arbitrary number of layers with different profile types including closed boundaries (i.e. inclusions). The boundary profiles of the layers must be strictly separated, i.e. the maximal y-value of a given profile is strictly less than the minimal y-value of the next profile above. In this case, it is possible to determine the diffracted field of the grating by computing the scattering matrix separately for any profile. The computation of the scattering amplitude matrices is based on the solution of a 2×2 system of singular integral equations at each interface between two different materials. The integral equations are discretized with a collocation method, the unknowns are sought as trigonometric polynomials which in the case of profiles with edges are partially replaced by splines to improve the approximation of the solution near the edges.

2. Numerical experiment and discussion

In this Section, we are going to analyze numerically the optical response of PCS with different cross sections of nanowires invariant with respect to the z axis and different number of gratings stacked one upon the other. The geometric model under study approaches the description proposed for rectangular PCS

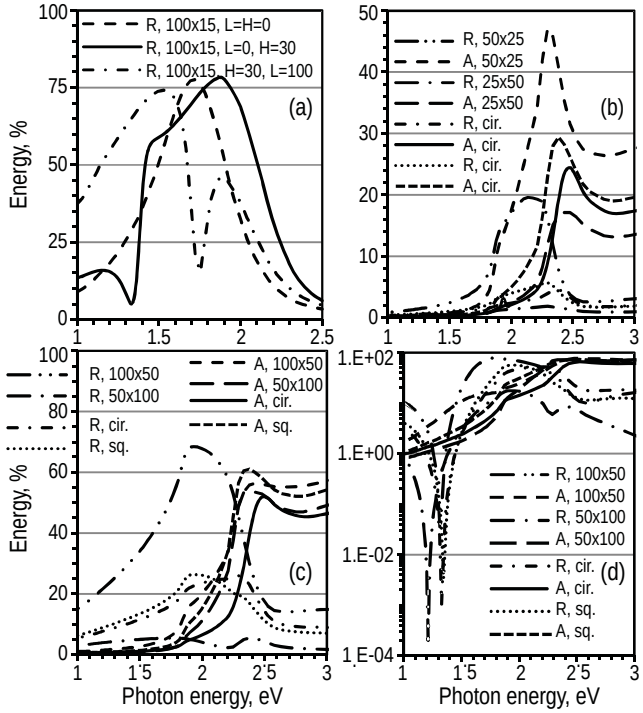

Fig. 1. Calculated reflection (R) and absorption (A) spectra of Si-embedded $d = 200$-nm gratings with Au nanowires of rectangular ($a \times b$ in nm^2), circular (cir.), and square (sq.) shapes and vertical, H, and horizontal, L, displacements in nm are plotted vs. photon energy for normal incidence and TM polarization.

(Ref. [6], Fig. 1). The model contains M identical gratings of arbitrary cross section displaced vertically (by H_m) and horizontally (by L_m) relative to one another and embedded in a homogeneous medium with dielectric permittivity ϵ_1 and magnetic susceptibility μ_1. We are going to deal here only with materials with $\mu_m = 1$, although the model is applicable to other cases as well, including metamaterials [4]. The dependence of the dielectric permittivity ϵ_2 of the material of nanorods on the incident photon frequency is assumed to be known. The lower medium (substrate) and the upper one are likewise assigned pairs of material constants, but one may conceive of more complicated cases of multilayer structures as well. The model allows also arbitrary incidence of, in the general case, elliptically polarized radiation on PCS, which is prescribed by two angles of incidence and two angles of polarization.

In Fig. 1a, calculated spectra of reflected energy for PCS with Au nanowires of rectangular cross section, measuring 100×15 nm^2 and $M = 1$ ($H = L = 0$) or $M = 2$ ($H =$ 30 nm, $L = 0$ and $H = 30$ nm, $L = 100$ nm) are compared with similar spectra derived in Ref. [6] (Fig. 3a) by the plane-wave approach. We consider here TM-polarized radiation (the plane of polarization is perpendicular to the lines) incident normally with respect to the x-z plane) on a grating with a period $d = 200$ nm and refractive indices of Au taken from [7]. To eliminate interference effects, the Au nanorods are embedded in an infinite homogeneous Si matrix with dielectric permittivity $\epsilon_1 = 2.13$. Examining the two figures, we see a very good agreement, which evidences applicability of both rigorous numerical methods to analysis of such PCS.

Figure 1b displays for comparison theoretical spectra of energy reflected from, and absorbed by, a PCS with Au nanowires of circular, square, and rectangular cross sections of the same area and with $M = 1$ studied in the 1–3-eV range. In this and subsequent examples we consider light normally falling on Au nanowires with $d = 200$ nm embedded in a Si matrix with refractive indices of Au taken from [8]. The $a \times b$ dimensions of the rectangular rods selected for this example are 50×25 nm^2 or 25×50 nm^2 and the width of the squares and diameter of the circles were chosen so as to obtain equal areas. As seen from Fig. 1b, reflection and, particularly, absorption spectra exhibit a strong difference near the plasmon-polariton anomaly among the four shapes of nanowire cross section chosen. These differences amount to several hundred percent for the rectangles because of their different width-to-height ratio (2 and 0.5) compared with the square and the circle (1). One observes also a noticeable difference in the positions of the absorption and reflection maxima among different grating profiles.

Figure 1c presents energy spectra similar to those displayed in Fig. 2 but for a cross sectional area 4 times that of the preceding example. In this case, $a \times b = 100 \times 50$ nm^2 or 50×100 nm^2. We readily see that the differences in the reflection and absorption spectra among gratings of different profiles increase with increasing filling ratio and are observed now not only close to the plasmon resonances. Near the resonances, they amount to a few tens of absolute percent.

Figure 1d shows spectra similar to those depicted in Fig. 1c but for $M = 2$, $H = 50$ nm, and $L = 0$. In the case of two gratings, the plasmon-polariton resonance frequencies are subtracted or summed [6], and one may expect still larger differences in the spectra of reflected and absorbed energy among crystals with lattice cells of different shape. Indeed, Fig. 1d drawn on a log scale reveals enormous differences, up to an order of magnitude, throughout the spectrum studied. Thus, the simple effective medium theory cannot be applied to design and analysis of such PCS. The minimum reflectance of $\sim 10^{-6}$ is observed for a photonic bandgap with a rectangular cross section which is the most sensitive shape due to its lower symmetry and different absorption. The relative error calculated from the energy balance for absorption gratings is $\sim 0.01\%$ and the computation time is shown to scale quadratically with the main accuracy parameter. The code developed and tested is found to be very accurate and fast for solving complex PCS diffraction problems with any rods including nanowires with real profiles, the cases that should be studied experimentally.

Acknowledgements

The author feels indebted to Gunther Schmidt (WIAS, Germany) for the information provided.

References

[1] G. Kobidze *et al*, *Phys. Rev. E* **72**, 056702 (2005).
[2] A. Christ *et al*, *Phys. Rev. B* **70**, 125113 (2004).
[3] D. Maystre, *Pure Appl. Opt.* **3**, 975 (1994).
[4] L. I. Goray *et al*, *J. Opt. Soc. Am. A* **27**, 585 (2010).
[5] L. I. Goray, *Proc. SPIE* **7390**, 73900V (2009).
[6] A. Christ *et al*, *Phys. Rev. B* **76**, 201405 (2007).
[7] P. B. Johnson *et al*, *Phys. Rev. B* **37**, 4137 (1988).
[8] E. D. Palik, ed., *Handbook of Optical Constant of Solids* (Academic, Orlando, 1985).

18th Int. Symp. "Nanostructures: Physics and Technology"
St Petersburg, Russia, June 21–26, 2010

Emission of an oscillating point dipole from a periodic array of dielectric nanopillars

S. V. Lobanov[1,2], T. Weiss[3,4], N. A. Gippius[1,3] and S. G. Tikhodeev[1,2]

[1] A. M. Prokhorov General Physics Institute, Moscow, Russia
[2] M. V. Lomonosov Moscow State University, Moscow, Russia
[3] LASMEA, University Blaise Pascal, 24 Avenue des Landais, F-63177 Aubière Cedex, France
[4] 4th Physics Institute, University of Stuttgart, Pfaffenwaldring 57, D-70550 Stuttgart, Germany

Abstract. We employ the Fourier modal method to investigate numerically the interaction of an oscillating point dipole with a periodic array of dielectric nanopillars in the weak coupling limit. It is shown that the coupling of the dipole with Fabry–Perot resonances of photonic crystal eigenmodes produces the dominating effect on the emission. The radiation pattern depends strongly on the position, orientation and oscillation frequency of the dipole.

Nanophotonics has been developing very quickly in recent years. One of its promising directions is the theoretical and experimental investigation of the electromagnetic emission of a quantum dot (or a molecule) placed inside a two-dimensional photonic crystal slab (PCS). The exact description of photon radiation from a quantum emitter placed in some dielectric environment is very difficult. A reasonable approximation is the model of an oscillating point dipole that oscillates with constant frequency and magnitude fixed by the external source (so-called weak coupling limit). In other words, the emission of a current $\vec{j}(\vec{r},t) = \vec{j}_0 \times \delta(\vec{r}-\vec{r}_0) \times \mathrm{e}^{-i\omega t}$ placed in an environment with spatially modulated permittivity has to be calculated. Thus, the system is purely classical and can be described by Maxwell's equations. In this work we use the scattering matrix formalism [1,2] in order to solve Maxwell's equations numerically.

The structure of interest is shown schematically in Fig. 1. It consists of an infinite number of nanocylinders arranged in a square lattice with period $d = 660$ nm. Each nanocylinder has a radius $r = 200$ nm, height $h = 3$ μm and permittivity $\varepsilon = 10$. The propagation of light in this layer is described by a superposition of eigenmodes which are characterized by their specific electromagnetic field distribution (in the (x, y)-plane) and momentum eigenvalue K_z. In this paper we investigate emission of the dipole in a frequency range when only a few number of modes can transfer energy from one border of the layer to another.

Let us consider the propagation of an eigenmode inside the photonic crystal layer (see Fig. 2). If the eigenmode propagates upwards, it is partially reflected at the boundary to the top

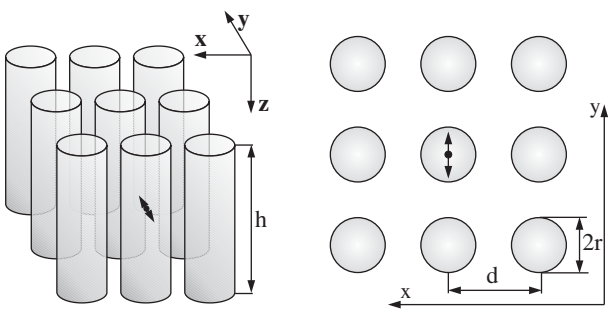

Fig. 1. The lateral (left panel) and top (right panel) views of a photonic crystal slab consisting of dielectric nanopillars. The dot with arrows marks the dipole and its polarization director.

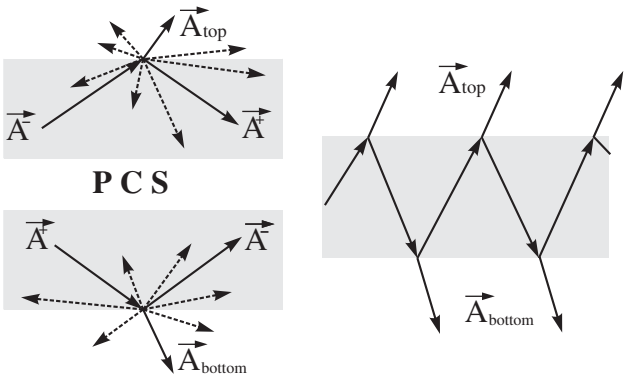

Fig. 2. The eigenmode scattering at PCS' boundaries (left panel) and the Fabry–Perot resonance formation (right panel).

layer, whereas some parts are transmitted or scattered. If all the scattered part is damped strongly, then the reflected and transmitted modes only participate in the energy transfer. The reflected eigenmode moves downwards and, once more, it is partially reflected at the bottom interface producing an upgoing mode. This process is repeated multiply (see the right panel in Fig. 2). As a result the so-called Fabry–Perot resonances appear in the transmission and reflection spectra of the PCS. If an oscillating point dipole is placed exactly in the center of the photonic crystal layer, it can excite only even Fabry–Perot modes that correspond to eigenmodes with wavenumber $K_z = (\pi/h)\,2n$, $n = 1, 2, \ldots$, because odd Fabry–Perot modes have

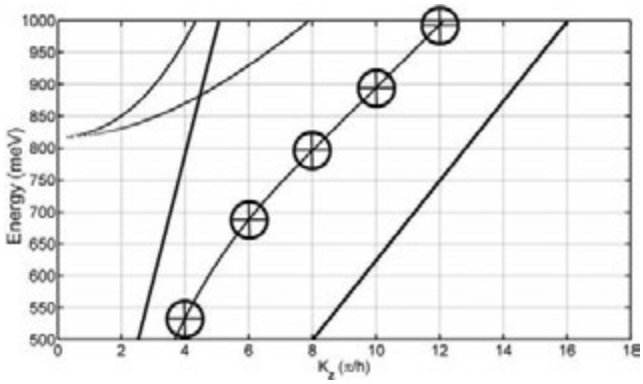

Fig. 3. The calculated dispersions of eigenvalues K_z for propagating eigenmodes which can transfer energy along z-axis. Circles mark even Fabry–Perot resonances of the first eigenmode.

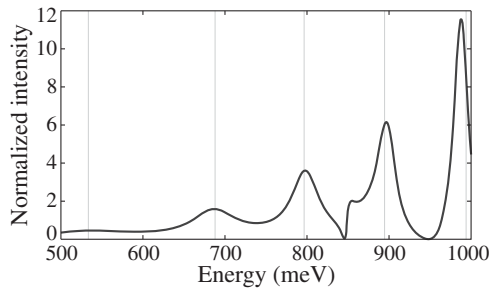

Fig. 4. The calculated emission spectrum to the top for the y-oriented oscillating point dipole placed in the center of a single nanopillar. Vertical lines mark energies of even Fabry–Perot resonances of the first eigenmode (circles in Fig. 3).

a knot surface with zero amplitude in the center of the layer.

The calculated dispersions of eigenvalues K_z for eigenmodes which can transfer energy through the PCS and radiate along z-axis are shown in Fig. 3. One can see that the energy transfer at photon energy less than 800 meV is due to one eigenmode only. We will call it henceforth the first eigenmode. The circles in this figure mark the even Fabry–Perot resonances of this eigenmode.

The calculated emission spectrum of the y-oriented dipole placed in the center of a single nanopillar is shown in Fig. 4. The emission intensity in this and next figures is normalized to the maximum radiated intensity of a dipole in free-space. The vertical lines mark energies of the even Fabry–Perot resonances of the first eigenmode (circles in Fig. 3). As expected, the peaks in the radiation intensity spectrum correspond to the discussed even Fabry–Perot resonances.

Let us consider the radiation of a dipole at the energy of the second Fabry–Perot resonance (the second vertical line in Fig. 4). The calculated directional pattern of the emission is shown in Fig. 5. The total emission intensity equals approximately to the total emission intensity of an equivalent dipole in free-space but the radiation is directed mainly along the z-axis.

It is interesting to investigate also the radiation at energies of minima in the emission spectrum, i.e. at energies of the odd

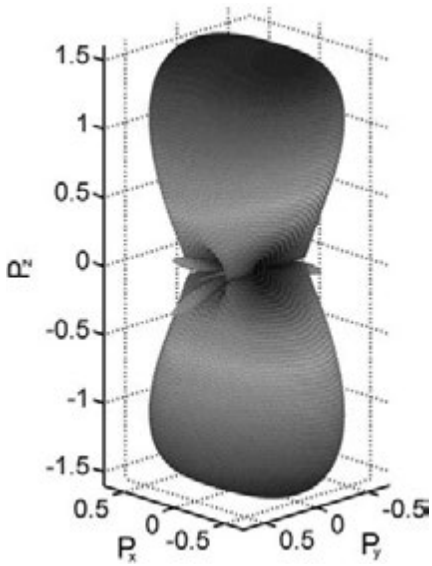

Fig. 5. The calculated radiation pattern of the y-oriented oscillating point dipole placed in the center of a single nanopillar at the energy of the sixth Fabry–Perot resonance of the first eigenmode.

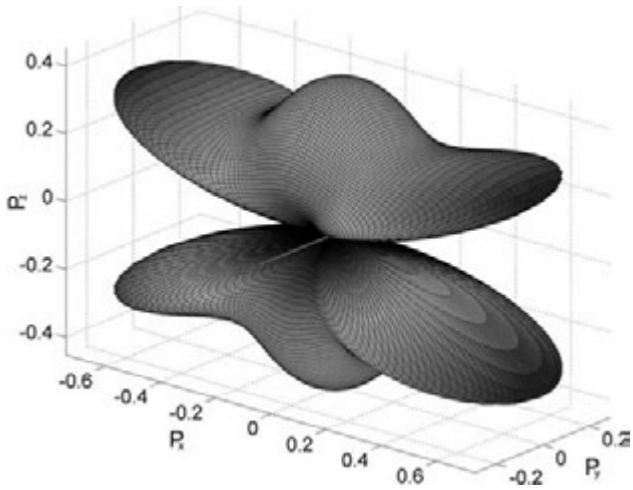

Fig. 6. The calculated radiation pattern of the y-oriented oscillating point dipole placed in the center of a single nanopillar at energy of the odd fifth Fabry–Perot resonance of the first eigenmode.

Fabry–Perot resonances. Such a calculated directional pattern of emission is shown in Fig. 6. It can be easily understood from this picture that the radiation along z-axis is suppressed in this case.

To conclude, the Fabry–Perot resonances of the eigenmodes make a considerable impact on the radiation of the oscillating point dipole placed in the PCS. It is possible to control the total intensity and the directional pattern of emission by changing parameters of the structure, the dipole location and the frequency domain. It opens the way to manipulate an excited-state lifetime of an emitter and to fabricate nanoantennas in the optical domain.

Acknowledgements

This work has been supported in part by the Russian Foundation for Basic Research and the Russian Academy of Science (Program # 27).

References

[1] D. M. Whittaker and I. S. Culshaw, *Phys. Rev. B* **60**, 2610 (1999).
[2] S. G. Tikhodeev *et al*, *Phys. Rev. B* **66**, 045102 (2002).

18th Int. Symp. "Nanostructures: Physics and Technology"
St Petersburg, Russia, June 21–26, 2010

Resonant Wood anomalies in photonic quasicrystals

A. N. Poddubny
Ioffe Physical-Technical Institute, St Petersburg, Russia

Abstract. We present a general theory of light diffraction from resonant scatterers arranged in the planar quasicrystalline array. Rich structure, absent in periodic case, is found in specular reflection spectra, and interpreted as a novel kind of Wood anomalies, characteristic for quasicrystals. Theory is applied to the specific cases of Penrose tilings of quantum dots and metallic nanoparticles.

Introduction

Discovery of quasicrystals [1] initiated new fields of research in solid-state photonics. These deterministic objects allow Bragg diffraction of light, like conventional photonic crystals, but are not restricted by the requirement of periodicity, and so can be easier tailored to the desired optical properties. It is especially important for control of light-matter interaction in *resonant* photonic structures, where the constituent materials possess elementary excitations, like excitons or plasmons. For example, one-dimensional (1D) polaritonic Fibonacci quasicrystal based on quantum-well (QW) excitons has been realized in [2], while the 2D plasmonic deterministic aperiodic structures of metallic nanoparticles have been fabricated in Ref. [3]. On the other hand, it is well known that interference between different processes of light diffraction from arbitrary grating (see Fig. 1) can lead to the so-called Wood anomalies in optical spectra [4]. However, no systematical study of Wood anomalies in *quasicrystalline* gratings has been performed yet, although their high importance for light transmission through aperiodic hole arrays has been mentioned in Ref. [5].

Here we develop the general theory of light diffraction from the 2D resonant photonic quasicrystals and show, that lattice Wood anomalies of novel type, completely absent in periodic case, are manifested in their optical spectra.

1. Problem definition

The structure under consideration consists of QDs, arranged in the canonical Penrose tiling [6] in the plane (xy) and embedded in the dielectric matrix. To construct this tiling, shown on Fig. 2(a) we first define five basic vectors $\mathbf{e}_n$ as $\mathbf{e}_n = [\cos(2\pi n/5), \sin(2\pi n/5)]$, $n = 0\ldots4$. Then we introduce five sets of the parallel lines $\mathbf{r}_n$, each set normal to the corresponding vector: $\mathbf{r}_{n,j} \times \mathbf{e}_n = j + (2/5)$ $(j = 0, \pm1\ldots)$ Finally, each cell in the grid bounded by the lines $\mathbf{r}_{0,j_0}$, $\mathbf{r}_{0,j_0+1}$, $\ldots$ $\mathbf{r}_{4,j_4}$, $\mathbf{r}_{4,j_4+1}$ is mapped to the point $\mathbf{r} = a_r \sum_{n=0}^{4} j_n \mathbf{e}_n$ belonging to the Penrose lattice with the rhombus side equal to a_r. The structure factor of this lattice

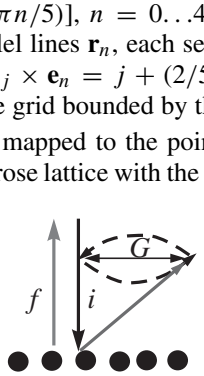

Fig. 1. Schematic illustration of the interference processes, leading to the Wood anomalies. In-plane diffraction vector $\mathbf{G}$ is shown. The incident wave i can be reflected either directly ($i \to f$), or after double diffraction by the vector G and back.

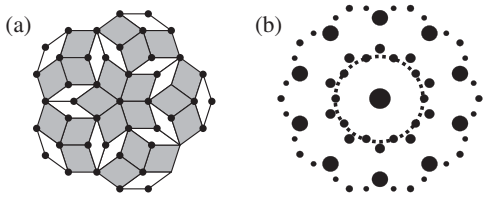

Fig. 2. (a) Canonic Penrose tiling. (b) Calculated diffraction image of this tiling. The diameter of each spot, located at the point corresponding to the Bragg diffraction vector $\mathbf{G}$, is proportional to the absolute value of the structure factor $|f_{\mathbf{G}}|$. Only the spots with $|f_{\mathbf{G}}| > 0.15$ are shown. Dashed circle indicates ten diffraction vectors with $|\mathbf{G}| \equiv G^* \approx (2\pi/a_r) \times 1.05$.

$$f(\mathbf{q}) = \lim_{N\to\infty} \frac{1}{N} \sum_{j=1}^{N} e^{2i\mathbf{q}\mathbf{r}_j} = \sum_{h_1h_2h_3h_4} f_{\mathbf{G}} \delta_{2\mathbf{q}-\mathbf{G}_{h_1h_2h_3h_4}} \quad (1)$$

illustrated in Fig. 2(b) consists of the Bragg peaks at the 2D diffraction vectors $\mathbf{G} \equiv \mathbf{G}_{h_1h_2h_3h_4} = G^* \sum_{n=1}^{4} h_n \mathbf{e}_n$, where $G^* = 4\pi\tau^2/(5a_r)$ and $\tau = (\sqrt{5}+1)/2$ is the golden mean. The star of each vector $\mathbf{G}$ consists of ten vectors distributed over two five-vector stars $\mathbf{G}_{n,\pm} = \pm G\mathbf{e}_n$, where $n = 0\ldots4$.

Wave equation for the electric field $\mathbf{E}$ is

$$\mathrm{rot\ rot}\, \mathbf{E}(\mathbf{r}) = \left(\frac{\omega}{c}\right)^2 \mathbf{D}(\mathbf{r}), \quad (2)$$

where the displacement vector $\mathbf{D}(\mathbf{r}) = \varepsilon_b \mathbf{E}(\mathbf{r}) + 4\pi \mathbf{P}_{\mathrm{exc}}(\mathbf{r})$ includes nonresonant contribution characterized with background dielectric constant ε_b and excitonic polarization $\mathbf{P}_{\mathrm{exc}}$. The material relationship between the excitonic polarization $\mathbf{P}_{\mathrm{exc}}$ and the electric field reads [7]

$$4\pi \mathbf{P}_{\mathrm{exc}}(\mathbf{r}) = \chi(\omega) \sum_{\mathbf{a}} \Phi(\mathbf{r}-\mathbf{a}) \int d^3r' \Phi(\mathbf{r}'-\mathbf{a}) \mathbf{E}(\mathbf{r}'), \quad (3)$$

where the resonant susceptibility is $\chi(\omega) = \pi\varepsilon_b a_B^3 \omega_{LT}/(\omega_0 - \omega - i\Gamma)$. Eq. (3) contains summation over excitonic polarizations in all QDs, centered at the points $\mathbf{a}$, and characterized by excitonic envelope functions $\Phi(\mathbf{r}-\mathbf{a})$. Other excitonic parameters in Eq. (3) are: longitudinal-transverse splitting ω_{LT} and Bohr radius in the corresponding bulk semiconductor a_B, resonance frequency ω_0 and phenomenological nonradiative damping Γ. In our calculations we took the exciton envelope wavefunction in the Gaussian form $\Phi(r) = \Phi_0(\pi R)^{-3/2} \exp(-r^2/R^2)$, where R is the characteristic radius of QD. Note, that the same equations can describe resonant responce of the cluster of small metallic spheres with the

raduis $R \ll 1/q$. In this case the functions $\Phi(r)$ are constant for $r < R$ and zero for $r \geq R$ and, while the function χ should be replaced by the resonant susceptibility of the metallic sphere near the plasmon resonance.

2. Calculation and discussion

Our approach to the calculation of the reflection coefficient under the normal incidence of the plane wave $\mathbf{E}\exp(iqz)$ generalizes results of Refs. [7,8]. Electric field dependence on the coordinates x and y is described in plane wave basis, $E(x, y) \propto \exp(iG_x x + iG_y y)$. Different plane waves are coupled due to the Bragg diffraction, with the strength determined by the structure factor coefficients. We keep in the plane wave expansions only the diffraction vectors $\mathbf{G}$ with largest values of $f_{\mathbf{G}}$, shown in Fig. 2(b). Reflection coefficient from the 2D lattice of QDs can be presented in a simple form only if all harmonics excepting $G = 0$ are neglected,

$$r(\omega) = \frac{i\Gamma_0}{\omega_0 - \omega - i(\Gamma + \Gamma_0)}, \qquad \Gamma_0 = \frac{\pi q a_{\mathrm{B}}^3 \omega_{\mathrm{LT}} (\Phi_0)^2 \mathrm{e}^{-(qR)^2/2}}{2\bar{S}}, \tag{4}$$

here $\bar{S} \approx 0.81 a_r^2$ is the mean area per QD in the Penrose tiling, and Γ_0 is exction radiative decay rate. This expression is similar to the reflection coefficient from the quantum-well exciton and holds only for inter-QD distances small as compared to the light wavelength, $a_r \ll 1/q$. In general case coupling with another diffraction vectors $G \neq 0$ must be takein into account. The results of calculation are presented in Fig. 3. The structure was almost exactly tuned to the lattice resonance at the diffraction vector $|\mathbf{G}| \equiv G^*$:

$$\omega_0 = \omega_{\mathrm{G}^*} - 10\Gamma_0, \quad \omega_{\mathrm{G}^*} = cG^*/n_{\mathrm{b}}. \tag{5}$$

Dashed curve was calculated taking into account only one diffraction vector $G = 0$ and shows only one Lorenzian peak (4). Dotted curve was calculated with 11 diffraction vectors, namely $G = 0$ and $G = G^*$. We see that allowance of non-zero diffraction vectors leads to the splitting of the single resonance (4). Since the structure is closely tuned to the specific resonance (5), the spectrum is not changed considerably when extra diffraction vectors with $G \neq 0$, $G \neq G^*$ are taken into account (see solid curve).

This splitting of the reflectivity spectrum due to existence of multiple grating resonances is the characteristic property of the quasicrystalline lattice. It is related to the fact that the structure-factor coefficients are less then unity. To illustrate this idea let us for simlicity ignore light polarization and consider just two diffraction vectors, 0 and G^*, coupled by the structure factor $f \equiv f_{\mathrm{G}^*}$. Similar to the two-wave approximation in 1D case [8], the eigenstates of such system are found from coupled equations

$$\begin{aligned} (\omega_0 - \omega - i\Gamma)\, E_0 &= i\Gamma_0 \,(E_0 + f E_{\mathrm{G}^*}) \\ (\omega_0 - \omega - i\Gamma)\, E_{\mathrm{G}^*} &= i\Gamma_{\mathrm{G}^*} \left(E_{\mathrm{G}^*} + f^* E_0\right), \end{aligned} \tag{6}$$

where characterisitic decay rate of the wave with wavevector G is $\Gamma_{\mathrm{G}^*} \propto \Gamma_0/\sqrt{\omega - \omega_{\mathrm{G}^*}}$. Note, that for $\omega_0 < \omega_{\mathrm{G}^*}$ coefficient Γ_{G^*} is pure imaginary, $\Gamma_{\mathrm{G}^*} = i|\Gamma_{\mathrm{G}^*}|$. It means that the wavevector G^* is outside the light cone and no diffracted wave

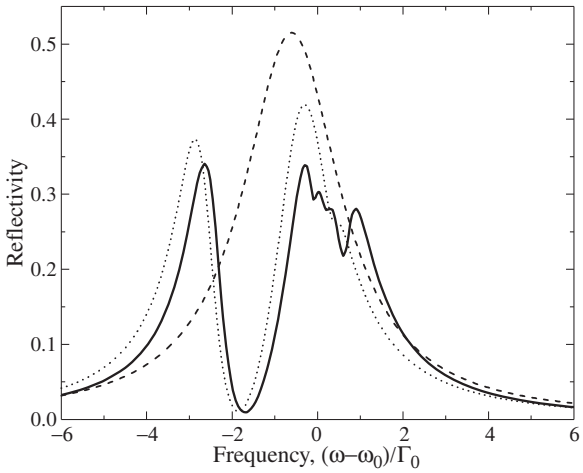

Fig. 3. Specular reflection coefficient for a Penrose quasicrystal. Calculated for $\Gamma_0/\omega_0 = 10^{-2}$, $\Gamma/\Gamma_0 = 0.2$. Solid, dotted and dashed curve were calculated taken into account 61,11 and 1 diffraction vectors from Fig. 2(b), respectively. Other parameters are indicated in text.

is evanescent. In the periodic lattice, where $|f| = 1$, only one of the two solutions

$$\omega_{1,2} = \omega_0 - i\Gamma - i\frac{\Gamma_0 + \Gamma_{\mathrm{G}^*}}{2} \pm i\sqrt{\frac{(\Gamma_0 + \Gamma_{\mathrm{G}^*})^2}{4} - |f|^2 \Gamma_0 \Gamma_{\mathrm{G}^*}}$$

of (6), with $\omega_1 = \omega_0 - i(\Gamma + \Gamma_0 + \Gamma_{\mathrm{G}^*})$ corresponds to the "bright" mode. The second, "dark", mode has eigenfrequency $\omega_2 = \omega_0 - i\Gamma$ independent on Γ_0, i.e. does not interact with the normally incident wave. Thus, in in the periodic lattice additional diffraction vectors lead only to renormalization of the exciton resonance frequency, $\omega_{\mathrm{res}} \to \omega_{\mathrm{res}} - i\Gamma_{\mathrm{G}^*}(\omega)$, in agreement with [7]. Conventional Wood anomalies are then described by the inverse square root dependence of Γ_{G^*} on ω, and are manifested as a notch in reflectivity spectrum for $\omega_{\mathrm{G}^*} > \omega_0$ and as a sharp spike for $\omega_{\mathrm{G}^*} < \omega_0$. However, in the quasicrystalline case both solutions of (6) become "bright", which leads to the splitting of the resonance reflectivity, in accordance with Fig. 3. This result can be also straightforwadly applied to the slightly distorted periodic resonant structures [8].

In conclusion, we demonstrate that in 2D quasicrystalline case the interplay between the specular reflection and in-plane light diffraction lead to the unusual specular reflection spectra.

Acknowledgements

We acknowledge the support by RFBR and the "Dynasty" Foundation — ICFPM.

References

[1] D. Levine, P. J. Steinhardt, *Phys. Rev. Lett.* **53**, 2477 (1984).
[2] J. Hendrickson *et al*, *Opt. Express* **16**, 15382 (2008).
[3] A. Gopinath *et al*, *Opt. Express* **17** (2009).
[4] N. García and A. A. Maradudin, *Optics Communications* **45** 301(1983).
[5] N. Papasimakis *et al*, *Appl. Phys. Lett.* **91**, 081503 (2007).
[6] M. A. Kaliteevski *et al*, *J. Phys.: Condens. Matter* **13**, 10459 (2000).
[7] E. L. Ivchenko *et al*, *Phys. Solid State* **42** 1756 (2000).
[8] A. N. Poddubny *et al*, *Phys. Rev. B* **80**, 115314 (2009).

18th Int. Symp. "Nanostructures: Physics and Technology"
St Petersburg, Russia, June 21–26, 2010

Bloch terahertz waves on the mesoscopic structures of $A^{III}B^{III}C_2^{VI}$ crystals

R. M. Sardarli[1], E. K. Huseynov[2], A. A. Bayramov[2] and A. P. Abdullayev[1]

[1] Institute of Radiation Problems Azerbaijan National Academy of Sciences, Baku, AZ1143 Azerbaijan
[2] Institute of Physics Azerbaijan National Academy of Sciences, Baku, AZ1143 Azerbaijan

Abstract. In layered crystals of the $A^{III}B^{III}C_2^{VI}$ family the presence of wide temperature ranges is indicated, in which on the primitive translation of the lattice of the initial phase superlattices with periods of 5–15 nm are superimposed. At that, the neutron-diffraction patterns show the presence of superstructural reflections: both reflections that are multiple of the initial translation of the lattice and incommensurable superstructural ones. Our research showed that layered crystals of the $TlInS_2$ family are crystallized with the formation of both incommensurable and commensurate superlattices and could be used for the generation of terahertz waves.

Introduction

A number of works [1,2] have been devoted to the creation of the terahertz Bloch generator on the basis of semiconductor superlattices [3–12]. Both at the improper phase transitions (accompanied by quadrupling cells and by incommensurable phases) and in the polytypic modifications of layered ferroelectric semiconductors of the $A^{III}B^{III}C_2^{VI}$ family, a periodically spatially changing superlattice (in this case, direction (001)) with the period of 5–15 nm is superimposed to the initial translation of the lattice. Such a structure develops additional periodic potential, which leads to partitioning of the quasi-impulse Brillouin zones and allowed energy bands of the electron of the initial phase into the collection of relatively narrow (10^5–10^7 cm^{-1}) Brillouin mini-zones and narrow (10^{-3}–10^{-1} eV) allowed energy mini-bands and mini band gaps. Due to the small sizes of these mini-zones in the superlattices, Bloch electron oscillations appear along with the Wannier–Stark levels [2] in already relatively weak static electric fields (10^2–10^4 V/cm). In superlattices with the period of 00 Å in the E_C fields equal to 4 kV/cm, the frequency of Bloch oscillations is: $f_c \equiv \Omega_c/(2x\pi) \approx 1$ THz (where Ω_c is angular frequency).

The presence of Bloch oscillation in the superlattices has been cogently confirmed in a number of experimental works. This makes the idea of creation of a terahertz Bloch generator based on semiconductor superlattices and with a frequency that would be continuously retuned by the static electric field extremely attractive.

1. Results

We considered the low-energy spectrum of a $TlGaSe_2$ crystal which is a structural analog of a $TlInS_2$ crystal. We investigated the dispersion relationships for the transverse acoustic phonons in $TlGaSe_2$ and the low-frequency phonons which are active in the infrared and Raman spectra of the $TlGaSe_2$ compound [13–16]. The frequency of acoustic phonons in the direction (001), which is perpendicular to layers, is considerably lower than in the direction (100) which lies inside the layer. Such behavior is typical for layered crystals, and it confirms that intra-layer bonding among ions is considerably stronger than interlayer bonding. To clarify the structure of polytypic modifications of $TlGaSe_2$, we carried out neutron-diffraction measurements of several samples of the compound. The measurements resulted in two diffraction patterns. This enabled us to draw a conclusion that here we have two polytypic modifications which will be called below 'α-$TlGaSe_2$' and 'β-$TlGaSe_2$'. The neutron-diffraction pattern indicates only the reflections that are relevant to the monoclinic structure. In addition to regular monoclinic reflections (hol), strong superstructural reflections of the (hol$+\frac{1}{2}$) type are also observed as well as weak satellites of the (hol$+m\,\frac{1}{10}$) type. Both types of additional reflections are observed at $h = 2xn + 1$ and disappear at $h = 2xn$. Analysis allows us to draw the conclusion that in β-$TlGaSe_2$ there is lattice modulation which results in the formation of long-period structure with the period of modulation of $C_{mod} = 10xc_{pr} = 160$ Å, where c_{pr} is the lattice constant of a primitive cell.

We have carried out neutron-diffraction measurements of α- and β-$TlGaSe_2$ in the temperature range of 4–600 K. The neutron-diffraction measurements of α-$TlGaSe_2$ showed that below 100 K phase transition (FT) occurs along with quadrupling of the unit cell volume.

So, we have researched two-dimensional distribution of scattering intensity in planes (110) and $(\overline{110})$, close to reflections $(111\frac{1}{4})$ and $(11\overline{1}\frac{1}{4})$, respectively. It has been discovered that in the temperature range of 216–200 K there is a disproportionate phase with $\overrightarrow{q_{inc}} = (\delta\delta\frac{1}{4})$. This vector is transferred into a four-beam star $(\bar{\delta}\delta\frac{1}{4})$, $(\overline{\delta\delta}\frac{1}{4})$, $(\delta\bar{\delta}\frac{1}{4})$ by means of the point group symmetry operations. Reflections corresponding to all four beams of the 'star' were experimentally measured. The value of δ was equal to 0.012 ± 0.003. Within the resolution limits, the value of δ between FT1 and FT2 remained constant. Below 200 K, reconstruction of the structure modulation occurred in presence of a proportional structure with $\overrightarrow{q_1}$ and a new disproportion, the value and the direction of which could not have been determined, apparently, due to the fact that this disproportion does not lie in the plane where measurements were conducted.

We also carried out a study on temperature dependence of scattering intensity at (1,1;1.25) while heating and cooling. In both cases it is evident that the superlattice appears at a temperature of 216 K. Thus, in the $TlInS_2$ compound, in the temperature range of 216–200 K there is a disproportionate phase with $q_{ink} = (\delta\delta\frac{1}{4})$.

In relaxed ferroelectrics based of layered crystals of the $TlInS_2$ family [16–18] in the temperature range between T_f and T_d (where T_f represents Vogel–Fulcher temperature — the

temperature of transition from the nano-domain state to the ordered macro-domain state, and where T_d represents Burns temperature, the temperature of transition from the vapor phase to the nano-domain state), a crystal is in disproportionate superstructural state. This is characterized by the section where weak temperature dependence of conductivity (210–240 K) is observed.

It should be noted that such kind of conductivity at low temperatures ($T < 170$ K) is typical of crystals of this class and indicative of presence of non-activation hopping conductivity at which carrier hops within the localized zone occur with emission of phonon. In our opinion, the mechanism of attenuation of temperature dependence of the conductivity section in the $T_f - T_d$ temperature range is fundamentally different for this temperature range. It is known that this temperature range is characterized by the disturbance in the translation invariant periodicity of the crystal lattice of $TlInS_2$ and by the appearance of the superlattice aliquant of the initial translation of the lattice. In this case, parabolic zones split into mini-zones which in turn are divided by small band-gaps and have a Brillouin zone determined by the period of the superlattice.

Author's studies theoretically examine the flow of current in the structures with superlattices. They show that the flow is determined by resonance tunneling through the potential barriers dividing wells. In this case, we must take it into account that the defects formed by radiation exposure have a radius of localization of 10 nm, i.e., they can quantize spatially and form structures with charge carriers geometrically constrained in all three dimensions (quantum points). The lower limit for the size of a quantum point is determined from the condition when at least one electron level exists at the quantum point. This size must not be less than 4 nm.

When measuring $\sigma(T)$ in the region of the disproportionate phase, due to certain conditions, energy levels of the quantum point turn out to be in potential wells caused by the superlattice of the $TlInS_2$ crystal. Resonance tunneling is achieved from the electron levels of the quantum point through potential barriers, which eventually leads to the observed attenuation of the temperature dependence of conductivity in the domain of existence of the relaxed state.

Our research showed that layered crystals of the $TlInS_2$ family are crystallized with the formation of both incommensurable and commensurate superlattices and could be used for the generation of terahertz waves.

2. Conclusions

In layered crystals of the $A^{III}B^{III}C_2^{VI}$ family the presence of wide temperature ranges is indicated, in which on the primitive translation of the lattice of the initial phase superlattices with periods of 5–15 nm are superimposed. Our research showed that layered crystals of the $TlInS_2$ family are crystallized with the formation of both incommensurable and commensurate (of the initial translation) superlattices and could be used for the generation of Terahertz radiation.

References

[1] F. Bloch, *Z. Phys.* **52**, 555 (1928); C. Zener, *Proc. Royal Soc.* (London) Ser. A, **145**, 523 (1934).

[2] G. H. Wannier, *Rev. Mod. Phys.* **34**, 645 (1962).

[3] J. Feldmann, K. Leo, J. Shah, D. A. B. Miller, J. E. Cunningham, T. Meier, G. von Plessen, A. Schulze, P. Thomas, S. Schmitt Rink, *Phys. Rev. B* **46**, 7252 (1992).

[4] M. Sudzius, V. G. Lyssenko, F. Löser, K. Leo, M. M. Dignam, K. Köhler, *Phys. Rev. B* **57**, R12693 (1998).

[5] F. Löser, Y. A. Kosevich, K. Köhler, K. Leo, *Phys. Rev. B* **61**, R13373 (2000).

[6] A. A. Andronov, M. N. Drozdov, D. I. Zinchenko, A. A. Marmalyuk, I. M. Nefedov, Yu. N. Nozdrin, A. A. Padalisa, A. V. Sosnin, A. V. Ustinov, V. I. Shashkin, *UFN* (in Russian) **173** 7, 780 (2003).

[7] R. M. Sardarly, O. A. Samedov, A. A. Bayramov, A. P. Abdullayev, F. T. Salmanov, *Fizika* (in Russian) **14** 3, 80–84 (2008).

[8] Yu. A. Romanov, Yu. Yu. Romanova, *Physics of the Solid State* **46** 1, [Translated from *Fizika Tverdogo Tela* **46** 1, 162 (2004)].

[9] L. Esaki, R. Tsu, *IBM J. Res. Dev.* **14**, 61 (1970).

[10] Yu. A. Romanov, E. V. Demidov, *Physics of the Solid State* **41** 9, [Translated from *Fizika Tverdogo Tela* **41** 9, 1698 (1999).

[11] Yu. A. Romanov, Yu. Yu. Romanova, *Physics of the Solid State* **43** 3, [Translated from *Fizika Tverdogo Tela* **43** 3, 520, (2001)].

[12] Yu. A. Romanov, *Physics of the Solid State* **45** 3, [Translated from *Fizika Tverdogo Tela* **45** 3, 529 (2003).

[13] S. B. Vahrushev, B. E. Kvatkovski, N. M. Okuneva, K. R. Allahverdiyev, R. M. Sardarly, *Neutron diffraction investigations of $TlGaSe_2$ crystals*, Leningrad 12 p. (Preprint No. 886 Ph. Tech. Inst.) (1984).

[14] R. M. Sardarly, *Oscilating spectrums of $A^{III}B^{VI}$ and $A^{III}B^{III}C_2^{VI}$ compounds*. ELM, Baku, 225 p. (2004).

[15] R. M. Sardarly, O. A. Samedov, I. Sh. Sadykhov, A. I. Nadzhafov and F. T. Salmanov, *Physics of the Solid State*, **47** 9, 1729–1733 (2005).

[16] R. M. Sardarly, N. T. Mamedov, K. Wakita, Y. Shim, O. A. Samedov, A. I. Nadzhafov and E. A. Zeynalova, *Phys. Stat. Sol.* **203** 11, 2845–2851 (2006).

18th Int. Symp. "Nanostructures: Physics and Technology"
St Petersburg, Russia, June 21–26, 2010

Resonant elastic scattering of light from rough interfaces of Bragg structures (photonic crystals)

A. V. Sel'kin[1], V. A. Kosobukin[1], Yu. N. Lazareva[2] and A. K. Zharinov[1]

[1] Ioffe Physical-Technical Institute, St Petersburg, Russia
[2] D. F. Ustinov Baltic State Technical University "Voenmekh", 190005 St Petersburg, Russia

Abstract. A theory is developed for resonant elastic scattering of light from Bragg structures (one-dimensional photonic crystals) whose interfaces are randomly rough. The study is mainly focused on the spectral and angle dependences of radiation giving information about static disorder responsible for the elastic scattering. The diffuse reflection spectra for polarized light are computed and analyzed in detail. Angle dependent suppressing the reflection diffuse component for p -polarized light and strong dependence of the scattering spectrum on the location of single rough interface are demonstrated. A resonant enhancement of the scattering cross-section is found to be manifested in the vicinity of the photonic stop-band edges.

Introduction

Surface roughness is one of the most important reasons for appearance of diffusive component of light reflected from a condensed medium. The intensity and angle distribution of diffusively scattered light are directly defined by the geometrical parameters of the surface roughness [1,2]. Of great interest for spectroscopy is the resonant elastic scattering of light from surface and interface roughness. Such a scattering is significantly enhanced in exciting of inherent resonant states as was demonstrated for excitons excited at both semiconductor surfaces [2] and quantum wells [3]. For dielectric multilayers and semiconductor multiple quantum wells, the role of the surface or interface roughness becomes much more important. This makes actual to solve the problem for diffusive scattering of light from multiple rough interfaces at resonant excitation. Earlier the effect of this kind was not studied.

In this work the spectra of diffusive scattering of polarized light from the Bragg structures with randomly rough interfaces are investigated. The spectral features under study are associated with the Bragg electromagnetic modes of a plane spatially periodic dielectric structure (1D photonic crystal). The model is expected to be applicable to the photonic crystals whose representatives are prepared by either layer-by-layer growth of one-dimensional dielectric Bragg structures or by filling with a substance the voids in three-dimensional opal-like photonic crystals.

1. Model and theoretical background

A theory is developed for the steady-state elastic scattering of light via Bragg electromagnetic modes in the structure whose interfaces are randomly rough. Fig. 1 shows schematically a one-dimensional array of dielectric layers with such rough interfaces alternating along the z-axis. The rough interfaces between the media are assumed to be plane on the average and thicknesses of the alternating slabs are a and b, and dielectric constants are ε_a and ε_b. The structure includes N interfaces, and its period, $d = a+b$, is comparable with the wavelength of light, so that the condition for Bragg diffraction is satisfied. It is assumed that a monochromatic wave with linear polarization s or p is incident onto the Bragg structure at an angle of θ (S_0 in Fig. 1) and both reflected I_R and scattered I'_σ waves of the same polarization are observed at the angles of θ and θ', respectively,

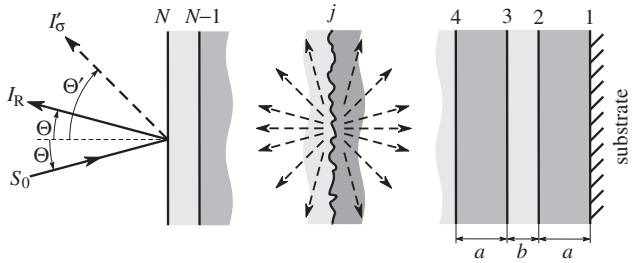

Fig. 1. Scheme of scattering of light from the j-th rough interface in the Bragg structure under study.

in backward direction.

The perturbative theory of resonant scattering of light is developed in two steps. In zero-order approximation, reflectivities of s and p polarized waves are studied for the average Bragg multilayer with the planar interfaces. Next, resonant scattering of light is treated in the Rayleigh approximation following [1,2] assuming the roughness profiles to be described by the random functions $z = \zeta_j(x)$, where j enumerates the interfaces (Fig. 1). For concreteness, the Gaussian correlation function is used for the interfaces

$$\langle \zeta_j(x)\zeta_k\left(x'\right)\rangle = \delta_{ik}h_j^2 g_j\left(|x-x'|\right). \qquad (1)$$

Here, the Kroneker delta δ_{ik} stands for the interface correlation coefficient and

$$g_j\left(|x-x'|\right) = \exp\left(\frac{-|x-x'|^2}{\Lambda_j^2}\right). \qquad (2)$$

It is assumed that the mean-square roughness height $h_j = \langle\zeta_j^2(x)\rangle^{1/2}$ of j-th interface, being a plane on the average, is small as compared with both the wavelength λ of light ($h_j \ll \lambda$) and the transverse correlation length Λ_j ($h_j \ll \Lambda_j$).

Then, the cross-sections are derived for scattering of linearly polarized light to the lowest (Born's) approximation in $\zeta_j(x)$ satisfying the Gaussian statistics, Eqs. (1) and (2). The dimensionless cross-section is obtained following [2,3] as

$$\sigma(\theta,\theta') = \frac{I'_\sigma(\theta')\cos\theta'}{S_0(\theta)}. \qquad (3)$$

Considered below are the spectral and angle dependences of scattering of light when the incident and scattered waves have

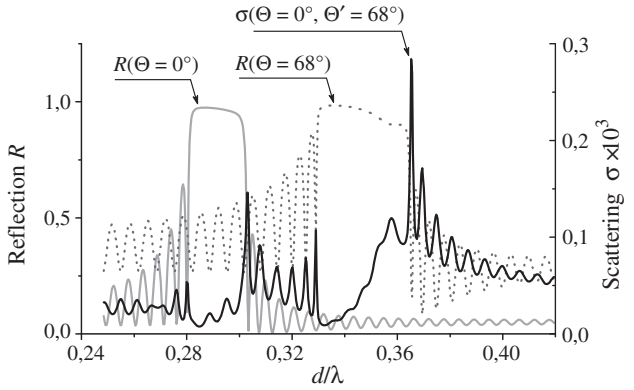

Fig. 2. Spectrum of dimensionless cross-section $\sigma(\theta, \theta')$ for diffusive scattering $s \to s$ at the angles of incidence $\theta = 0^\circ$ and scattering $\theta' = 68^\circ$ (the planes of incidence and scattering coincide) in comparison with the spectra R of specular reflection at the incidence angles $\theta = 0^\circ$ and $\theta' = 68^\circ$. Calculations are performed for a Bragg structure with 101 interfaces whose roughness heights are $h_j = 2$ nm; d is its period, λ is the wavelength of light in vacuum.

s or p polarization. Spectral dependences of the cross-sections $\sigma(\theta, \theta')$ are analyzed for $s \to s$ and $p \to p$ backward scattering channels, where the incidence, θ, and scattering, θ',angles are counted off the external normal to the plane surface of the Bragg structure.

2. Numerical calculation and discussion

Our study is mainly focused on the angle dependences of radiation giving direct information about the static disorder responsible for the elastic scattering. In what follows we present, in short, the results of the spectral study of diffusive reflection of light from a Bragg structure with randomly rough interfaces.

The spectral and angle dependencies of scattering intensity from the Bragg structure were analyzed numerically with Gaussian correlation function in the absolute-value scaled interface roughness. Dielectric permittivities of the media (Fig. 1) are the following: $\varepsilon_0 = 2.25$ (substrate), $\varepsilon_a = 3.2 + i0.02$ and $\varepsilon_b = 2.5 + i0.02$. The correlation length of rough interfaces in Eqs. (1) and (2) is $\Lambda_j = 300$ nm. The Bragg structure with the identity period $d = a + b$ consists of the alternating slabs with $a = 140$ nm and $b = 80$ nm.

Figure 2 presents a typical spectrum $\sigma(\theta, \theta)$ of diffusive scattering of light from the Bragg structure to vacuum (Fig. 1). Compare the spectra of diffusive scattering σ and resonant Bragg reflection R shown at two incidence angles ($\theta = 0^\circ$ and $\theta = 68^\circ$). It is seen from Fig. 2 that scattering intensity σ is essentially enhanced at the edges of the stop-band (photonic bandgap) which appears as the spectral range of nearly total reflectivity R depending on the angle θ. The estimated intensity of the scattering signal $\sigma(\theta, \theta')$ is completely accessible for experimental measurement for even rather small interface roughness ($h < 2$ nm). In addition to the scattering $s \to s$, the diffusive scattering $p \to p$ is studied showing the effect of suppressing the diffusive component.

It is seen from Fig. 3 that the diffusive scattering from single interface strongly depends on its depth in the Bragg structure both in intensity and spectral shape. Such a dependence can be used to get information about the distribution of the Bragg electromagnetic mode along the axis of the Bragg structure.

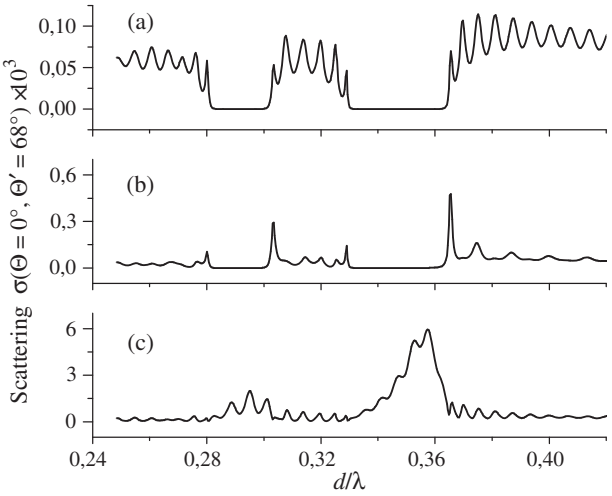

Fig. 3. Spectra of dimensionless cross-sections σ for diffusive scattering $s \to s$ from single rough interfaces placed at different depths in the Bragg structure (Fig. 1). The depth is specified by the interface numbers $j = 1$ (a), $j = 50$ (b) and $j = 101$ (c) with $h_1 = h_{50} = h_{101} = 20$ nm.

3. Conclusion

A theory is presented for resonant elastic scattering of light from Bragg structures with randomly rough interfaces between constituents. For linearly polarized light waves the spectra of diffuse scattering are analyzed in terms of statistical parameters of interface roughness in comparison with the spectra of Bragg reflection. The scattering cross-section is found to be resonantly enhanced in the vicinity of the photonic stop-band edges, that allows to observe the scattering signal from rather small roughness. The scattering spectra are demonstrated to depend drastically on the depth location of a single rough interface in the Bragg structure. As well, an angle-dependent suppressing the reflection diffuse component in p-polarized light is found.

Acknowledgements

The work was supported by the Russian Federation State Contract No. 02.74011.0384.

References

[1] A. A. Maradudin, D. L. Mills, *Phys. Rev.* **B11**, 1392 (1975).
[2] V. A. Kosobukin, A. V. Sel'kin, *Solid State Commun.* **66**, 313 (1988).
[3] V. A. Kosobukin, A. V. Sel'kin, *Phys. Solid State* **42**, 1914 (2000); *Physica E* **18**, 452 (2003).

18th Int. Symp. "Nanostructures: Physics and Technology"
St Petersburg, Russia, June 21–26, 2010

Nonmonotonic behaviour and scaling of light attenuation length in one-dimensional disordered photonic crystals

A. A. Greshnov[1], O. I. Utesov[1], *G. G. Zegrya*[1], M. A. Kaliteevski[1,2], R. A. Abram[2] and S. Brand[2]

[1] Ioffe Physical-Technical Institute, St Petersburg, Russia
[2] Department of Physics, Durham University, Durham, DH1 3LE, UK

Abstract. The influence of disorder on propagation of light in one-dimensional periodic structures is studied analytically using so-called phase formalism and Fokker–Planck equation. It is shown that light attenuation length obeys one-parameter scaling and shows non-monotonic behaviour as a function of the effective parameter given by the ratio of the disorder amplitude to the square root of dielectric contrast, $\delta/\sqrt{\eta}$. This kind of behaviour is explained by the crossover between weak disorder regime corresponding to gradual destruction of reflecting properties of a photonic crystal and strong disorder regime when the periodic component of refractive index can be almost fully neglected.

Introduction

Since Yablonovitch [1] pointed out that photonic crystals can possess photonic band gaps which can be used to inhibit spontaneous emission from potentially radiative centers located within such structures, the physics of photonic crystals has developed very rapidly. In particular, the basic electromagnetic theory of the structures has been formulated, real photonic crystals fabricated and their properties demonstrated for various regions of the electromagnetic spectrum from radiowaves [2] to visible light [3]. Further, a number of optoelectronic devices making use of photonic crystal, such as lasers, waveguides and photonic circuits have been produced. However, perfect photonic crystals cannot be fabricated, and the imperfections in their structure result in the appearance of states within the photonic band gaps which are detrimental to the properties required for optoelectronic device applications. Recently it was proposed to use so-called phase formalism for description of the density of states inside the photonic band gaps [4]. In this paper we develop this theory to include some possible correlations between components of disorder and study attenuation length reflecting localization properties of the one-dimensional photonic crystals. It is shown that localization length being nonmonotonic function of disorder amplitude obeys scaling.

Theory

Let us consider a one-dimensional two-component basically periodic photonic system with an average refractive index $n_0 = \overline{(n_1 + n_2)}/2$, dielectric contrast $\eta = \overline{(n_1 - n_2)}/(2n_0)$ and a period $D = \overline{d_1 + d_2}$ disturbed by moderate amount of disorder as sketched in Fig. 1. We suppose both dielectric and geometrical components of disorder to be uncorrelated among the different periods which is quite reasonable for the actual technologies of the photonic crystal formation. This model still permits us to consider arbitrary correlations inside a period of the structure. Focusing on the universal characteristics we assume that the structure is long enough so that self-averaging takes place. Solving one-dimensional wave equation ($c = 1$)

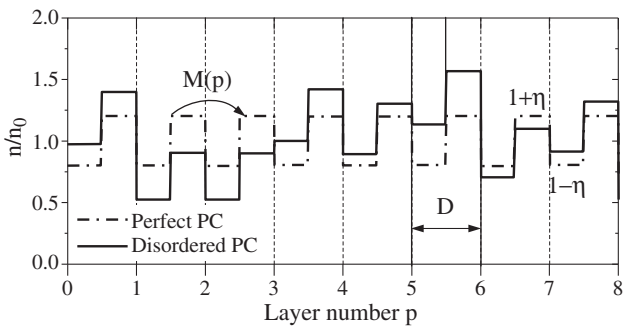

Fig. 1. A schematic diagram of one-dimensional disordered photonic crystal. The case of dielectric disorder correlated inside a period is shown.

$$\frac{d^2E}{dz^2} = -n^2(z)\omega^2 E, \tag{1}$$

for a given period p of the photonic crystal, we come readily to the transfer matrix description with the transfer matrix $M(p)$ of the form

$$M(p) = \begin{pmatrix} C_1C_2 - \frac{n_1}{n_2}S_1S_2 & \frac{1}{n_1}S_1C_2 + \frac{1}{n_2}C_1S_2 \\ -n_1S_1C_2 - n_2C_1S_2 & C_1C_2 - \frac{n_2}{n_1}S_1S_2 \end{pmatrix}, \tag{2}$$

which acts on the two-component electric field related vector $V(p)$ so that

$$M(p)V(p) = M(p)\begin{pmatrix} E(z_p) \\ \omega^{-1}E'(z_p) \end{pmatrix} = V(p+1). \tag{3}$$

Here $E' = dE/dz$, z_p are boundary coordinates, $C_{1,2} = \cos\phi_{1,2}$, $S_{1,2} = \sin\phi_{1,2}$, $\phi_{1,2} = n_{1,2}(p)\omega d_{1,2}(p)$. It is convenient to introduce the logarithmic derivative of electric field $L = E'/(\omega E)$ whose evolution over a period is given by

$$L(p+1) = \frac{M_{22}L(p) + M_{21}}{M_{11} + M_{12}L(p)}. \tag{4}$$

Following the standard procedure described in Refs. [5], we obtain the stationary Fokker–Plank type equation for the distribution function of the phase $\Psi = 2\mathrm{arccot}(L)$:

$$\frac{d}{d\Psi}\left\{\frac{d}{d\Psi}\left[\left(1+\gamma_n\sin^2\Psi\right)F\right] + \left[\beta\cos\Psi - \alpha(G+\sin\Psi)\right]F\right\} = 0, \tag{5}$$

where the three basic parameters α, β and γ_n given by

$$\alpha = \frac{2\eta}{\pi^2\delta^2},\ \beta = \frac{1}{\pi}\frac{\xi_n}{\delta^2},\ \gamma_n = \frac{4}{\pi^2}\frac{\delta_n^2 - \xi_n}{\delta^2},\ \delta^2 = \delta_n^2 + \delta_d^2,$$
$$\delta_n^2 = \frac{\overline{(\delta n_1 + \delta n_2)^2}}{4n_0^2},\ \delta_d^2 = \frac{\overline{(\delta d_1 + \delta d_2)^2}}{D^2},\ \xi_n = \frac{\overline{\delta n_1 \delta n_2}}{n_0^2},$$

describe total amount of disorder and correlations. At center of the photonic band gap ($G = 0$) the 2π-periodic solution of Eq. (5) is given by

$$F(\Psi) = \frac{N\exp(-\Lambda)}{1+\gamma_n \sin^2\Psi}, \tag{6}$$

$$\Lambda = \frac{\operatorname{arctanh}(\sqrt{\frac{\gamma_n}{\gamma_n+1}}\cos\Psi)}{\sqrt{\gamma_n(\gamma_n+1)}}\alpha + \frac{\arctan(\sqrt{\gamma_n}\sin\Psi)}{\sqrt{\gamma_n}}\beta. \tag{7}$$

In the case $\gamma_n = 0$ (i.e. $\delta n_1 = \delta n_2$) the distribution function simplifies to

$$F(\Psi) = \frac{1}{2\pi I_0(\sqrt{\alpha^2+\beta^2})}\exp\left(-\alpha\cos\Psi - \beta\sin\Psi\right). \tag{8}$$

Let us define inverse attenuation length $\gamma = D/\xi$ as

$$\gamma = \overline{\ln\left(\frac{E_{p+1}}{E_p}\right)^2} = \overline{\ln(M_{11}+M_{12}L)^2}. \tag{9}$$

It is convenient to partition γ into three parts,

$$\gamma = \gamma_1 + \gamma_2 + \gamma_3, \tag{10}$$

$$\gamma_1 = \int F(L)\ln|1+4\eta-\pi^2\delta^2|dL, \tag{11}$$

$$\gamma_2 = \int F(L)\ln|1-2\pi^2\delta^2\beta L|dL, \tag{12}$$

$$\gamma_3 = \int F(L)\ln|1-\pi^2\delta^2L^2|dL. \tag{13}$$

The first term, γ_1, is trivial,

$$\gamma_1 = \ln|1+4\eta-\pi^2\delta^2| \approx 4\eta-\pi^2\delta^2 = -\pi^2\delta^2(1-2\alpha). \tag{14}$$

Relevant contributions to $\gamma_{2,3}$ come from $|L| \lesssim 1$, therefore similar expansion of the logarithms can be applied to Eqs. (12,13) but with some care since $\overline{L}$, $\overline{L^2}$ diverges at large $|L|$ due to slow decrease of $F(L) \sim L^{-2}$. After separation of slowly decreasing part of the distribution function,

$$F^{(0)}(\Psi) = \frac{1}{2\pi I_0(\sqrt{\alpha^2+\beta^2})}\exp(-\alpha\cos\Psi), \tag{15}$$

the integrals appearing in Eqs. (12,13) can be evaluated resulting in the following answers for γ_2 and $\gamma_3 = \gamma_3^{(0)} + \gamma_3^{(1)}$:

$$\gamma_2 = \frac{2\sqrt{\pi}\beta\delta^2}{I_0(\sqrt{\alpha^2+\beta^2})}\sum_{n=0}^{\infty} C_{2n}\left(-\frac{\alpha}{2}\right)^n, \tag{16}$$

$$C_{2n} = \sum_{p=0}^{n}(-1)^p\frac{\Gamma(p+\frac{1}{2})\Gamma(n-p+\frac{3}{2})}{p!(n-p)!\Gamma(\frac{n+2}{2})\Gamma(\frac{n+3}{2})}$$

$$\times {}_2F_3\left(p+\frac{1}{2}, n-p+\frac{3}{2}; \frac{3}{2}, \frac{n+2}{2}, \frac{n+3}{2}; \frac{\beta^2}{4}\right), \tag{17}$$

$$\gamma_3^{(0)} = \frac{\pi^2\delta^2}{I_0(\sqrt{\alpha^2+\beta^2})}[(1-2\alpha)I_0(\alpha)+2\alpha I_1(\alpha)], \tag{18}$$

$$\gamma_3^{(1)} = -\frac{\delta^2}{2\pi^{1/2}I_0(\sqrt{\alpha^2+\beta^2})}\sum_{n=0}^{\infty} C_{3n}\left(-\frac{\alpha}{2}\right)^n, \tag{19}$$

$$C_{3n} = \sum_{p=0}^{n}(-1)^p\frac{\Gamma(p+\frac{1}{2})\Gamma(n-p+\frac{5}{2})}{p!(n-p)!\Gamma(\frac{n+3}{2})\Gamma(\frac{n+4}{2})}$$

$$\times {}_3F_4\left(1, p+\frac{1}{2}, n-p+\frac{5}{2}; \frac{3}{2}, 2, \frac{n+3}{2}, \frac{n+4}{2}; \frac{\beta^2}{4}\right). \tag{20}$$

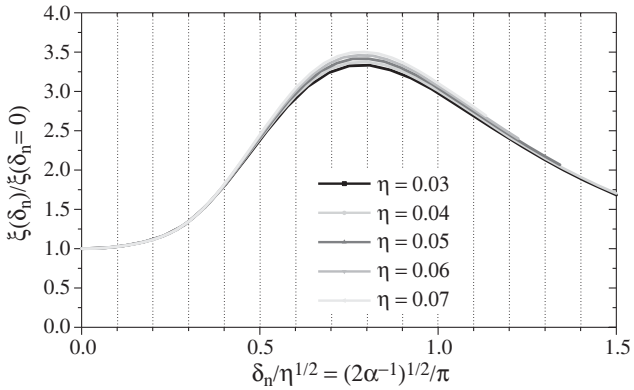

Fig. 2. Attenuation length vs. normalized disorder amplitude.

Although the obtained expressions seem to be rather cumbersome, they show that the normalized attenuation length $\xi\delta^2/D$ is a function of the only parameter $\alpha^{-1} = \pi^2\delta^2/(2\eta)$ provided that dielectric-to-geometrical disorder ratio described by $\beta = \delta_n^2/(\pi\delta^2)$ is fixed, i.e. scaling takes place. It is straightforward to obtain low α (strong disorder) asymptotics of the attenuation length at fixed β, say $\beta = \pi^{-1}$, i.e. fully dielectric disorder, which reads

$$\alpha \approx [(2\pi\beta+\pi^2-3/4)I_0^{-1}(\beta)-\pi^2]\delta^2 \approx 0.98\delta^2. \tag{21}$$

High α (small disorder) asymptotics can be obtained as well using asymptotic version of the distribution function (8), $F(\Psi) \approx \delta(\Psi)$,

$$\alpha \approx 4\eta - \pi^2\delta^2. \tag{22}$$

Comparison of the two asymptotics given by Eqs. (21-22) shows that localization length must be a nonmonotonic function of the disorder amplitude. This kind of behaviour and scaling are clearly seen from Fig. 2 obtained by direct numerical calculations of the localization length. Both asymptotics given by Eqs. (21-22) as well as their extended versions are in excellent agreement with the numerical results presented in Fig. 2.

To conclude, a theory of light localization in one-dimensional photonic crystals has been developed using a phase variable stochastic approach proposed earlier. It is found that localization length obeys scaling and shows non-monotonic behaviour as a function of disorder amplitude. This kind of behaviour is due to crossover between weak disorder regime corresponding to gradual destruction of reflecting properties of a photonic crystal and strong disorder regime when the periodic component of refractive index can be almost fully neglected.

Acknowledgements

This work has been supported by Russian President Grant for Young Scientists MK-1755.2009.2 and Dynasty Foundation.

References

[1] E. Yablonovitch, *Phys. Rev. Lett.* **58**, 2059 (1987).
[2] W. M. Robertson *et al*, *Phys. Rev. Lett.* **68**, 2023 (1992).
[3] T. F. Krauss *et al*, *Nature* **383**, 699 (1996).
[4] A. A. Greshnov *et al*, *Solid State Comm.* **146**, 157 (2008).
[5] H. Risken, *The Fokker–Planck Equation: Methods of Solutions and Applications* (Springer, Berlin, 1989).

18th Int. Symp. "Nanostructures: Physics and Technology"
St Petersburg, Russia, June 21–26, 2010

Tuning the crystal structure of III–V nanowires

V. G. Dubrovskii
St Petersburg Academic University, St Petersburg, Russia

Abstract. Rotational twins and highly faulted zinc blende (ZB)–wurtzite (WZ) mix-ups persist as one of the most challenging constrains in III–V nanowire (NW) fabrication technologies. In this talk, we present an overview of recent achievements in the tuning and controlling the crystal structure of III–V NWs. We first consider the major physical reasons for the formation of WZ phase in NWs and the conditions under which such NWs can actually grow. The role of surface energies, triple line (TL) nucleation and supersaturation is discussed. Surface energies of different sidewall planes of ZB and WZ III–V NWs with regular hexagonal cross section are compared and it is shown that the surface energy decreases only for three of four possible transitions, of which only one is not associated with the 30° rotation. Next, different possibilities to tune the crystal phase and to obtain stacking fault free ZB or WZ NWs are discussed. Among these, we consider: (i) changing the growth conditions in Au-assisted epitaxy, i.e., different supersaturation during the growth; (ii) changing the Au nanoparticle size; (iii) changing the growth catalyst and (iv) pure WZ crystal structure of catalyst-free nanoneedles (NNs), whose growth is rather different from NWs. Theoretical models and experimental data supporting the models and featuring the stacking fault free structure are presented and analyzed.

III–V semiconductor NWs are very attractive one-dimensional nanostructures with many promising applications in nanoelectronics, nanophotonics and nanosensing devices as well as from the viewpoint of fundamental physics. Using modern epitaxy techniques such as molecular beam epitaxy (MBE) or metal organic chemical vapor deposition (MOCVD), NWs with diameters of order of tens of nanometers and length up tens of micrometers can be obtained. These NWs are usually grown in a bottom up manner via the vapor-liquid-solid (VLS) mode [1] with metal (Au) catalyst nanodrops. By organizing Au nanoparticles before growth, regular NW arrays can be fabricated [2]. This is an obvious advantage for technological applications as compared to self-organized nanostructures, where such precise control over the position, diameter and shape cannot be achieved. Another important feature of NWs with sufficiently small footprint is their ability to accumulate strain in two dimensions [3,4], enabling unique opportunity for growing dislocation free NWs (and heterostructures within NWs) in highly mismatched material systems, e.g., III–V compounds on silicon.

Perhaps on of the most surprising and fundamental features of III–V NWs is that, unlike under bulk form, they often adopt hexagonal WZ structure [4–9], the effect which never happens in 2D layers or quantum dots. This phenomenon has been observed for most III–V NWs and epitaxy techniques on different substrates. Unfortunately, WZ structure is not stable and highly faulted WZ-ZB mix-ups exist [5,6]. Since stacking faults introduce unwanted defects, the control over phase purity is now considered as one of the most important issues in NW fabrication technology.

As suggested in Refs. [10–14], the positive difference in bulk cohesive energies between WZ and ZB structure (24 meV per pair in GaAs) can be outbalanced by the gain in the effective surface energy (which contribution into the overall formation enthalpy becomes important for smaller diameters), decreasing in the ZB-WZ transition. Without such gain, WZ structure can never be formed. We therefore analyze the number of dangling bonds on different sidewalls planes of ZB and WZ NWs [15]. In the case of regular hexagonal cross-section, there are two pairs of relevant parallel planes: $(2\bar{1}\bar{1})$ ZB and $(1\bar{1}00)$ WZ, and $(1\bar{1}0)$ ZB and $(11\bar{2}0)$ WZ sidewalls. These two ZB-WZ counterparts differ by 30° angular rotation of the entire NW. In the first-order approximation, the surface energy of the lateral facets is proportional to the density of dangling bonds created by the dissection of crystal by the corresponding vertical planes. Simple counting of dangling bonds, together with the known surface energies of ZB planes, yields the results summarized in Table 1, where $\tau = \gamma_{WZ}/\gamma_{ZB}$. The end result can be formulated as follows: The maximum surface energy gain of 25% at $\tau = 0.75$ relates to the direct $(2\bar{1}\bar{1}) \rightarrow (11\bar{2}0)$ transition without rotation, which is exactly the result of Ref. [11]. The indirect $(2\bar{1}\bar{1}) \rightarrow (11\bar{2}0)$ and $(1\bar{1}0) \rightarrow (1\bar{1}00)$ transitions, associated with the rotation by angle of 30°, give a lower gain of 13.3% at $\tau = 0.867$. The direct $(1\bar{1}0) \rightarrow (11\bar{2}0)$ transition does not gain any energy.

Table 1. Surface energies of sidewall facets and the ratios τ related to the ZB to WZ transitions.

Facet type	Surface energy, J/m^2	Transition	τ
$(2\bar{1}\bar{1})$	1.73	$(2\bar{1}\bar{1}) \rightarrow (1\bar{1}00)$	0.75
$(1\bar{1}0)$	1.50	$(2\bar{1}\bar{1}) \rightarrow (11\bar{2}0)$	0.867
$(1\bar{1}00)$	1.30	$(1\bar{1}0) \rightarrow (11\bar{2}0)$	1
$(11\bar{2}0)$	1.50	$(1\bar{1}0) \rightarrow (1\bar{1}00)$	0.867

Whenever is smaller than one, the supersaturation becomes decisive for the observed crystal structure: ZB phase should be prevalent at low supersaturation, and WZ phase should form at high supersaturation [12–14]. *The first method* to control the crystal structure is therefore the growth parameters tuning. We discuss relevant TL nucleation models and very important experimental results of Refs. [7–9,16], showing that the use of appropriate growth temperature, fluxes ratio, substrate orientation enable to obtain continuous low supersaturation in the vicinity of growing NWs resulting in phase perfection in different III–V NWs. One example from Ref. [16] is presented in Fig. 1. GaAs NWs were fabricated by Au-assisted MBE on the GaAs(111)B substrate via a special two-step procedure with temperature ramping, where the foot of NW was obtained at usual conditions and the upper pure ZB section was grown at a very high temperature of 630 °C. A non-linear growth model is presented which elucidates the growth behavior and the experimentally observed temperature dependence of the crystal

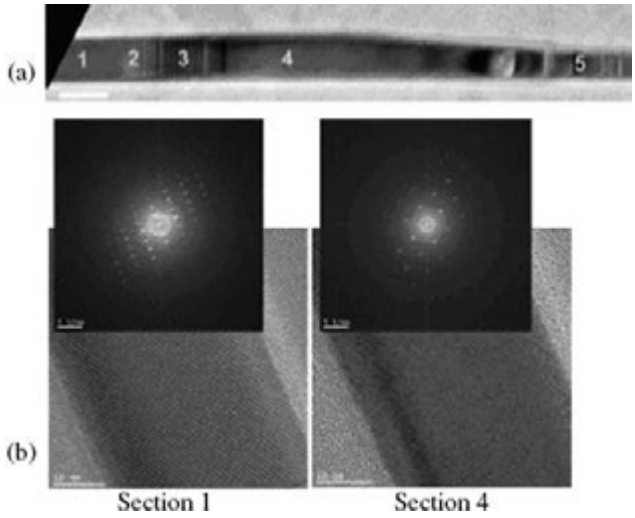

Fig. 1. (a) TEM image of a NW grown with two temperature steps showing phase transitions along the NW length. From left to right: pure WZ phase corresponding to 530 °C growth (1), WZ with twins (2) and highly faulted WZ/ZB mix up (3) corresponding to temperature ramping, pure ZB phase corresponding to 630 °C (4), significant reduction of the diameter followed by phase mixing (5); (b) High resolution TEM close-ups of pure WZ (section 1) and ZB (section 4) GaAs NW.

phase.

As the diameter of NW increases, TL nucleation (which can only favor ZB phase due to a lower surface energy of a portion of island perimeter at the TL) must be suppressed by the polynuclear growth [14]. This provides *the second method* to grow stacking fault free WZ NWs with sufficiently small and ZB NWs with sufficiently large footprints, dictated by the initial Au drop size. The example from Ref. [17] is given in Fig. 2. The results obtained demonstrate pure WZ structure of InP NWs (grown by Au-catalyzed MOCVD on the GaAs(111)B substrate) with 12 nm diameter and twinning defects in a larger diameter 45 nm NW. It is noteworthy that the TL nucleation can be also suppressed at very high supersaturations due to much higher nucleation probabilities. In this respect, we will discuss the results obtained in Ref. [18], where pure ZB phase of MOCVD grown GaAs NWs (with Au catalyst) was obtained at very high NW growth rate of 10 nm/s.

All above considerations apply only to the case of Au-catalyzed growth. We now note that the necessary condition for WZ phase formation is a lower nucleation barrier at the TL. According to Ref. [12], this condition for a WZ NW growing via the VLS mechanism can be written down as

$$\gamma_{\mathrm{IV}} - \gamma_{\mathrm{IL}} - \gamma_{\mathrm{LV}} \sin\beta < 0\,. \qquad (1)$$

Here, γ_{IV} is the surface energy of lateral sidewall plane in contact with the vapor (created by the TL nucleation), γ_{IL} is the surface energy at the lateral solid-liquid boundary, γ_{LV} is the surface energy of (liquid) drop and β is the contact angle of the drop seated at the NW top. The term $\gamma_{\mathrm{LV}} \sin\beta$ gives the surface energy of pre-existing liquid-vapor interface eliminated by the TL nucleation. The corresponding illustration from Ref. [12] is presented in Fig. 3. From Eq. (1), TL nucleation is preferred when the liquid-vapor surface energy γ_{LV} is large enough. Estimates of Ref. [14] show the validity of inequality given by

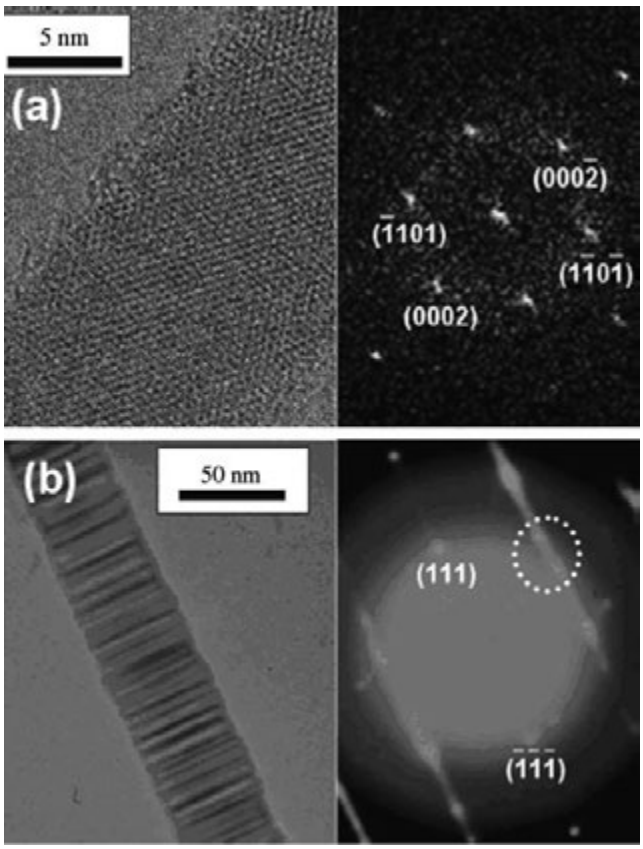

Fig. 2. TEM images of InP NWs showing a pure WZ phase of 12 nm NW (a) and twining defects in 45 nm NW (b).

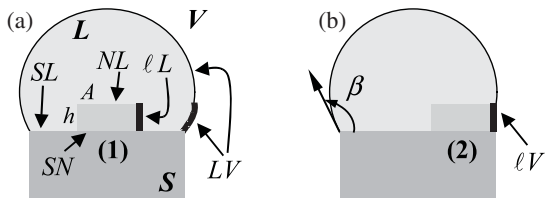

Fig. 3. Nucleation in the centre of liquid-solid interface (a) and at the TL (b) with the parameters described in the text.

Eq. (1) in the case of Au-assisted MBE growth of GaAs NWs. Under the assumption of a low As solubility in Au, the value of γ_{LV} must be between the surface energies of pure liquid Ga and Au (0.72 and 1.14 J/m^2, respectively) [19]. For a diluted alloy, the surface energy would become close to that of liquid Au, so the assumption given by Eq. (1) looks reasonable for many Au alloys. We note, however, that changing the catalyst to another metal with a lower surface energy (e.g., Ga in the case of self-catalyzed GaAs NW growth) may break the condition (1) and therefore completely suppress the WZ phase formation at the TL. We will present some experimental data on the MBE growth of self-catalyzed GaAs NWs on the Si(111) substrate to support this argument. Thus, changing the growth catalyst and decreasing γ_{LV} may provide *the third method* to obtain stacking fault free ZB III–V NWs.

Finally, we present some experimental data and a nucleation model for the catalyst-free MOCVD growth of GaAs NNs on sapphire, the material system with extreme lattice mismatch of 46% [20]. The GaAs NNs have almost atomically sharp tip, stepwise tapered sidewalls consisting of $(1\bar{1}00)$ and (0001) terraces, taper angle of typically 6–11°, length and base di-

mension scalable with time and, surprisingly, single crystalline WZ phase even for submicron base dimensions. The nucleation model attributes this unusual growth to extreme lattice mismatch which favors large aspect ratio of the order of ten due to a more efficient elastic stress relaxation in taller islands. Since the catalyst-free stress-driven NN growth is rather different from the VLS case, the condition for the nucleation of WZ NN now has the form

$$\Delta\mu_0 > \psi/(1-\omega\tau)\,. \qquad (2)$$

Here, $\Delta\mu_0$ is the difference in chemical potentials in the vapor (or adatom) and solid GaAs phase, $\psi = 24$ meV is the difference in bulk cohesive energies between WZ and ZB GaAs, $\tau = \gamma_{\rm WZ}/\gamma_{\rm ZB} = 0.75$ and ω of the order of one. Similar to the cases discussed in Refs. [12–14,16], NNs would tend to adopt WZ phase at large enough supersaturations; however, the form of condition (2) is different. With the above parameters, we arrive at the estimate $\Delta\mu_0 >$ meV. The critical supersaturation is therefore even lower than in the VLS case (typically few hundreds of meV [12,14]) so NNs should systematically nucleate in WZ phase. Once the WZ NN seed forms, it serves as a fully-relaxed WZ template for the subsequent core-shell mode growth, and nothing prevents the continuation of the bulk-quantity, WZ-phase growth thereafter. This gives *the fourth example* of pure crystal phase of highly anisotropic nanostructures grown on dissimilar substrates.

Acknowledgements

This work was partially supported by different grants of Russian Foundation for Basic Research, Presidium of RAS and the Russian Federal Agency for Science and Innovation.

References

[1] R. S. Wagner, W. C. Ellis, *Appl. Phys. Lett.* **4**, 89 (1964).
[2] B. J. Ohlsson *et al*, *Appl. Phys. Lett.* **79**, 3335 (2001).
[3] G. E. Cirlin *et al*, *Phys. Stat. Sol. RRL* **3**, 112 (2009).
[4] L. C. Chuang *et al*, *Appl. Phys. Lett.* **90**, 043115 (2007).
[5] A. I. Persson *et al*, *Nature Mater.* **3**, 677 (2004).
[6] I. P. Soshnikov *et al*, *Phys. Solid State* **47**, 2213 (2005).
[7] K. A. Dick *et al*, *Semicond. Sci. Technol.* **25**, 024009 (2010).
[8] H. Shtrikman *et al*, *Nano Lett.* **9**, 215 (2009).
[9] H. J. Joyce *et al*, *Nano Lett.* **10**, 908 (2010).
[10] A. A. Stekolnikov and F. Bechstedt, *Phys. Rev. B* **72**, 125326 (2005).
[11] V. G. Dubrovskii and N. V. Sibirev, *Phys. Rev. B* **77**, 035414 (2008).
[12] F. Glas *et al*, *Phys. Rev. Lett.* **99**, 146101 (2007).
[13] J. Johansson *et al*, *Cryst. Growth and Design* **9**, 766 (2009).
[14] V. G. Dubrovskii *et al*, *Phys. Rev. B* 7**8**, 235301 (2008).
[15] N. V. Sibirev *et al*, *Phys. Solid State* **52**, 1428 (2010).
[16] V. G. Dubrovskii *et al*, *Phys. Rev. B* **80**, 066940 (2009).
[17] M. Moewe *et al*, *J. Appl. Phys.* **104**, 044313 (2008).
[18] H. Huang *et al*, *Nano Lett.* **10**, 64 (2010).
[19] A. Zangwill, *Physics at surfaces*. Cambridge University Press, Cambridge (1988).
[20] L. C. Chuang *et al*, submitted to *Nature Materials*.

18th Int. Symp. "Nanostructures: Physics and Technology"
St Petersburg, Russia, June 21–26, 2010

MOCVD growth of BInAs/GaAs quantum dots and the PL spectrum enhancement by Boron-incorporation

Xiaomin Ren, Qi Wang, Hui Huang, Jiajian Li, Yue Yang, Qiongfang Ma, Yongqing Huang, Xia Zhang, Yisu Yang, Xian Ye and Shiwei Cai

Key Laboratory of Information Photonics and Optical Communications
(Beijing University of Posts and Telecommunications), Ministry of Education,
Zh. I. Alferov Russian-Chinese Joint Laboratory of Information Optoelectronics and Nanoheterostructures
P.O. Box 66, #10 Xitucheng Road, Haidian District, Beijing 100876, China

Abstract. The growth of BInAs/GaAs quantum dots and the relevant measurement results are reported. The PL spectrum enhancement by Boron-incorporation has been observed by the comparison between BInAs/GaAs quantum dots and InAs/GaAs ones.

Introduction

III–V semiconductor quantum dots (QDs) and related QD lasers have been intensively studied due to their intrinsic advantages in electronic and photonic properties and attractive potential of applications. Many significant achievements have been obtained in this area [1,2]. However, further investigations to improve their properties and performances, for example, to extend their emitting wavelength and to realize more precise control of the morphology of QDs, are still needed. In our laboratory, we have tried to grow Boron-incorporated III–V semiconductor materials not only in bulk form [3] but also in the form of QDs. We hope the latter efforts may provide new possibilities for the design and fabrication of specially required QDs. The relevant experimental works are presented as follows.

1. Sample growth

The epitaxial growth of the InAs/GaAs and BInAs/GaAs QDs was performed by MOCVD with a Thomas Swan CCS-MOCVD system at a pressure of 100 Torr. TMGa, TMIn, TEB and AsH_3 were used as the precursors. For each sample, the complete growth procedure is as follows: Firstly, 500 nm-thick GaAs buffer layer was grown after GaAs (100) substrate was heated up to 650 °C under AsH_3 protection. Then it was cooled down to 500 °C and InAs or BInAs QDs were formed in Stranski–Krastanow mode (typical growth time was chosen as 20 s). Subsequently, after 30 s growth interruption (GRI) under AsH_3 flow, the QDs were capped with 5 nm-thick GaAs overgrown layer at the same temperature (500 °C). Then another 30 s GRI was implemented. Finally, the growth temperature was increased to 600 °C and the sample was covered with a 50 nm-thick GaAs cap layer. Actually, for the purpose of experimental investigation, we made a series of samples including those without the 50 nm-thick GaAs cap layer or even without the 5 nm-thick GaAs overgrown layer.

2. Measurement results

Fig. 1(a) and Fig. 1(b) show respectively the PL spectra of the InAs/GaAs QDs and the BInAs/GaAs QDs with the same top structure that only a 5 nm-thick GaAs overgrown layer was formed. The corresponding PL peaks in the two figures appear at the wavelength of 1440 and 1380 nm, respectively, while the peak in each figure at 1060 nm indicates the existence

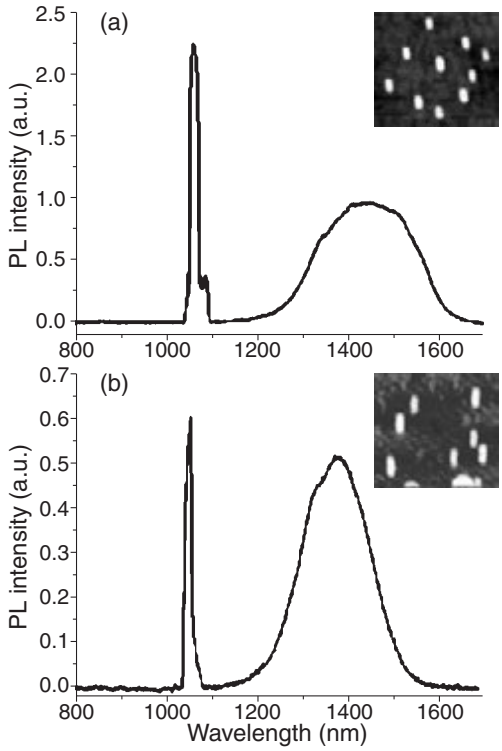

Fig. 1. PL spectrum of the QDs structure with a 5 nm-thick GaAs overgrown layer (a) InAs/GaAs QDs; (b) BInAs/GaAs QDs.

of the incident light of excitation for the PL measurements. The inserts are the AFM images of the surface morphology of the structures. It can be found that the PL intensity of the BInAs/GaAs QDs is approximately as twice higher as that of the InAs/GaAs QDs and the FWHM linewidth of the PL peak of the BInAs/GaAs QDs is obviously narrower than that of the InAs/GaAs QDs.

The situation shown in Fig. 2 is similar to that in Fig. 1. However, it should be noted that each of the QDs structures corresponding to Fig. 2 has one more layer, i.e. a 50 nm-thick GaAs cap layer than that corresponding to Fig. 1. In this case, even bigger difference in PL intensity between the InAs/GaAs QDs and the BInAs/GaAs QDs as shown in Fig. 2(a) and Fig. 2(b), respectively, can be observed. The wavelengths of the two PL peaks are 1171 and 1113 nm, respectively. The FWHM linewidth of the PL peak of the BInAs/GaAs QDs (71 meV) is now a little bit broader than that of the InAs/GaAs QDs

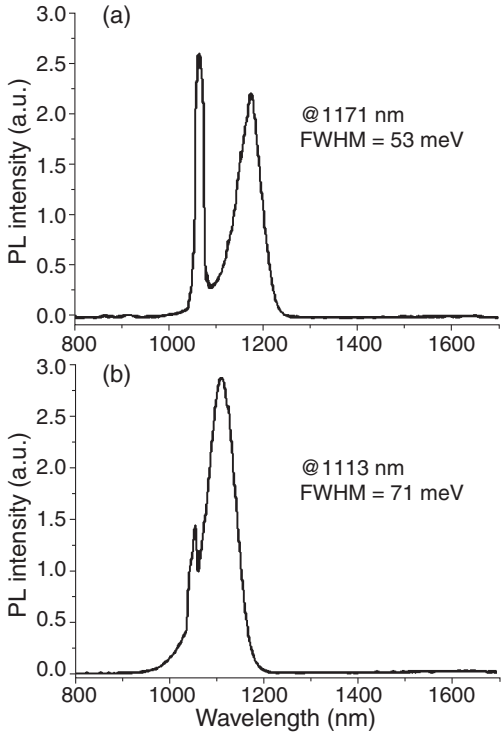

Fig. 2. PL spectrum of the QDs structure with a 5 $nm - thick$ GaAs overgrown layer and then a 50 nm-thick GaAs cap layer (a) InAs/GaAs QDs; (b) BInAs/GaAs QDs.

(53 meV).

3. Conclusion

In summary, the experimental observations show that the Boron-incorporation can remarkably enhance the PL spectrum of the InAs/GaAs QDs and further investigation on the growth and properties of the BInAs/GaAs QDs is very interesting and rather important for future optoelectronics.

Acknowledgements

This work was supported by grants from National Basic Research Program of China (Nos. 2003CB314900 and 2010CB 327600), the 111 Program of China (No. B07005), Program of Key International Science and Technology Cooperation Projects, MOST of China (No. 2006DFB11110), National Natural Science Foundation of China (Nos. 60576018 and 90201035), Program of China for New Century Excellent Talents in University (Nos. NCET-05-0111 and NCET-08-0736), and the Program of China for Changjiang Scholars and Innovative Research Team in University (No. IRT0609). The authors sincerely thank Prof. Zh. I. Alferov for his support to this work and are grateful to Profs. V. G. Dubrovskii, A. E. Zhukov, V. M. Ustinov and A. A. Gorbatsevich for tutorial presentations and helpful discussions.

References

[1] V. M. Ustinov, A. E. Zhukov, A. Yu. Egorov, N. A. Maleev *et al*, *Quantum Dot Lasers*, Oxford University Press (2003).

[2] Dieter Bimberg *et al*, *Semiconductor Quantum Dots, Optical Fiber Telecommunications V A: Components and Subsystems*, Elsevier Inc. 23 (2008).

[3] X. Ren, Q. Wang, H. Huang, Y. Huang *et al*, *16th International Symposium on Nanostructures: Physics and Technology*, July 14–18, Vladivostok, Russia, 263 (2008).

18th Int. Symp. "Nanostructures: Physics and Technology"
St Petersburg, Russia, June 21–26, 2010

The growth of semiconductor nanostructures on lattice-mismatched substrates

N. V. Sibirev[1], Xu Zhang[1,2] and V. G. Dubrovskii[1,3]

[1] St Petersburg Academic University, 194021, St Petersburg, Russia
[2] Key Laboratory of Information Photonics and Optical Communications (Ministry of Education), Beijing University of Posts and Telecommunications P.O. Box 66, Beijing 100876, China
[3] Ioffe Physical-Technical Institute, St Petersburg, Russia

Abstract. Theoretical study of semiconductor growth on the lattice-mismatched substrates is presented. The effects of elastic strain relaxation and wetting energy are taken into account simultaneously. The aspect ratio of 3D islands as a function of lattice mismatch and technologically controlled growth conditions is obtained and analyzed. Based on the latter, we demonstrate different growth modes, e.g., Frank–van der Merwe, Stranski–Krastanow, Volmer–Weber mechanisms, as well as the surprising effect of catalyst free ZnO nanoneedle formation on the sapphire (the system with 21% lattice misfit).

Lattice mismatch is one of the major constraints which limits the growth of high-quality thin film on a foreign substrate. The universally recognized reason for 2D to 3D growth transformation is the strain energy relaxation in an island [1,2]. Generally, the 3D growth is observed when the lattice mismatch is greater than 2%. For a mismatch less than 10.5%, the growth in the Stranski–Krastanow mode occurs. For example, the Ge/Si system (4% mismatch) is grown in the Stranski–Krastanow mode and the critical thickness is about 5 monolayers [3]. For mismatch greater than 10%, the Volmer–Weber mode is realized. The InAs quantum dots growth on the Si substrate (10.6% mismatch) proceeds in the Volmer–Weber mode [4]. In Ref. [5], the lattice mismatch of 22% is hypothesized as the driving force for the formation of ZnO nanoneedles on sapphire.

Here we propose a nucleation model for island growth on a lattice-mismatched substrate. We assume that the shape of an island is determined at the nucleation stage and does not change at the follow up stages of growth. Under this assumption, it is sufficient to determine the shape of the critical island. Formation enthalpy of 3D island with a given radius R and aspect ratio $\beta = L/2R$ (with L as the island height), considered below as two independent variables, can be presented in the form

$$\Delta G_{3D} = -\frac{8}{3}\beta\frac{\Delta\mu}{\Omega}R^3 + 8\left(\beta\gamma_F + \Delta\gamma\right)R^2. \qquad (1)$$

Here, Ω is the elementary volume, $\gamma_F F$ is the surface energy of vertical facets (formed due to the nucleation), $\Delta\gamma = \gamma_W + \gamma_B - \gamma_S$, γ_W is the surface energy of in-plane facets (formed due to the nucleation), γ_B is the surface energy of solid-solid interface at the island base (also formed due to the nucleation) and γ_S is the surface energy of pre-existing substrate surface (eliminated by the nucleation). The vapor-solid difference of chemical potentials in a lattice mismatched material system is given by $\Delta\mu = \Delta\mu_0 - w(\beta)$. The elastic energy is presented in the form $w(\beta) = w_{2D}z(x)$, where $w_{2D} = \lambda\varepsilon_0^2\Omega$ is the specific elastic energy of a 2D layer, $z(x)$ is the elastic energy relaxation and $x = \beta/\beta_0$. Hereinafter, we used a simplified formula for the elastic relaxation in the form $z(x) = 1/(1+x)$.

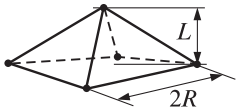

Fig. 1. Model shape of nanoisland.

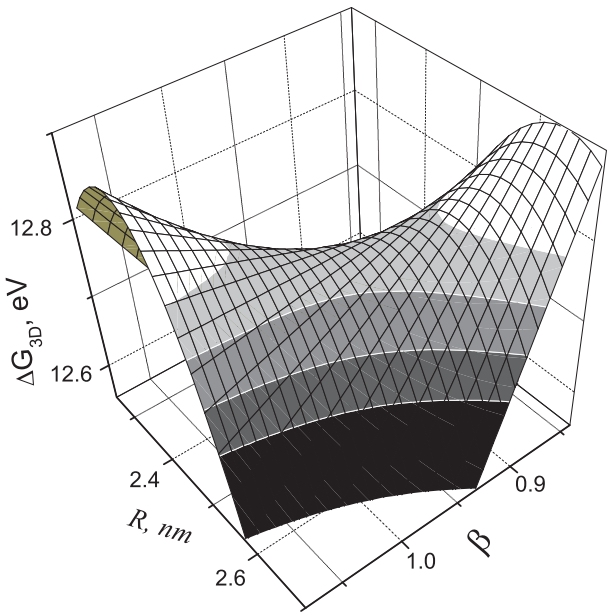

Fig. 2. Formation enthalpy of three dimensional island.

The shape and the nucleation barrier of the critical 3D island is determined by the saddle point of formation enthalpy, as shown in Fig. 2. This follows from the classical theory of nucleation adopted to the case of two independent variables. The nucleation barrier ΔG^*_{3D} for 3D growth is now determined by the minimum of ΔG^β_{3D} in β. Here, ΔG^β_{3D} is the β -dependent maximum of enthalpy given by

$$\Delta G^\beta_{3D} = \Delta G_0\frac{(\beta+a)^3}{\beta^2\left(\chi - bz(\beta)\right)^2}. \qquad (2)$$

With $\chi = h\Delta\mu_0/2\Omega\gamma_F$ as the normalized chemical potential, $a = \Delta\gamma/2\gamma_F$ at the normalized difference of surface energy, $b = hw_{2D}/2\Omega\gamma_F$ as the constant related to the elastic energy and h as the height of a monolayer.

The formation enthalpy of 2D island is given by

$$\Delta G_{2D} = -\left(\frac{\Delta\mu}{\Omega}h - \Delta\gamma\right)4R^2 + 4Rh\gamma_F. \qquad (3)$$

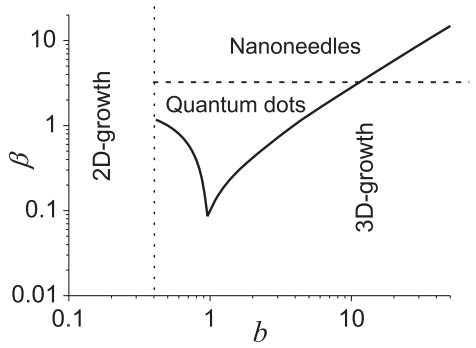

Fig. 3. b — dependences of aspect ratio of critical island, at $a = 0$, $\chi = 1$, $\beta_0 = 0.1$.

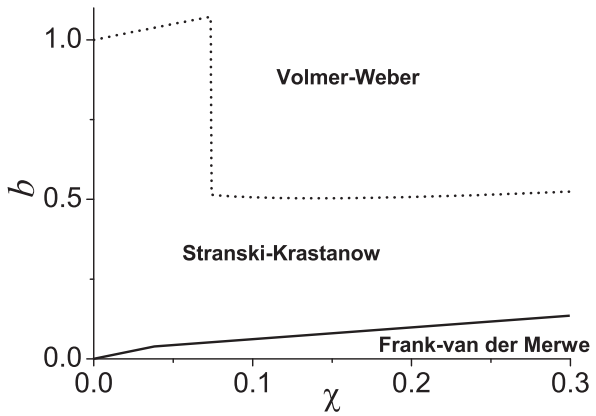

Fig. 4. Typical growth diagram phase diagram at $a = -1$, $\beta_0 = 0.1$.

Relation (3) yields the following expression for the 2D nucleation barrier:

$$\Delta G_{2D} = \Delta G_0 \frac{0.75}{\chi - \beta - a}. \qquad (4)$$

Comparing Eqs. (2),(4), 3D nucleation is preferable if the corresponding nucleation barrier ΔG^*_{3D} is less than ΔG^*_{2D}. Therefore, the Volmer–Weber mode is realized at $\Delta G^*_{2D} > \Delta G^*_{3D}$. The aspect ratio in the saddle point determines the shape of critical island, as demonstrated by Fig. 3. Smaller aspect ratios at modest b relate to the case of quantum dots, while the increase in b leads to more elongated objects like nanoneedles.

In the case of $\Delta G^*_{2D} < \Delta G^*_{3D}$, the first 2D layer must be formed. On the other hand, after the formation of the wetting layer and the difference of surface energy a becomes zero. This changes the nucleation barriers on the wetting layer compared to the initial case of a foreign substrate, making it possible to distinguish the Frank–van der Merwe and the Stranski–Krastanow growth modes. In the case of layer-by-layer growth, the 2D nucleation barrier remains lower than the 3D one; the opposite inequality relates to the Stranski–Krastanow mode. The corresponding growth diagrams are presented in Fig. 4.

In conclusion, the presented model allows us to predict the growth mode of semiconductor nanoislands on a lattice mismatch substrate and the dependence of the quantum dot or nanoneedle aspect ratio on the growth conditions and the material constants. This work was partially supported by different grants of Russian Foundation for Basic Research, Presidium of RAS and the Russian Federal Agency for Science and Innovation.

References

[1] O. P. Pchelyakov, Y. B. Bolkhovityanov, A. V. Dvurechenskii, L. V. Sokolov, A. I. Nikiforov, A. I. Yakimov, B. Voigtlander, *Semiconductors* **34** 1229 (2000).

[2] D. Bimberg, M. Grundmann, N. N. Ledentsov. Quantum dot heterostructures. New York: Wiley, 1999.

[3] V. G. Dubrovskii, A. A. Tonkikh, G. E. Cirlin, V. M. Ustinov, P. Werner, *Techinical physics letters* **30** 920 (2004).

[4] Z. M. Zhao, O. Hul'ko, H. J. Kim, J. Liu, T. Sugahari, B. Shi, Y. H. Xie *J. Crystal Growth* **271** 450 (2004).

[5] J. Y. Park, J. M. Lee, J. H. Je, S. S. Kim *J. Crystal Growth* **281** 446 (2005).

18th Int. Symp. "Nanostructures: Physics and Technology"
St Petersburg, Russia, June 21–26, 2010

Cobalt nanoparticles epitaxially grown on CaF_2 (111)

N. S. Sokolov[1], S. M. Suturin[1], V. V. Fedorov[1], Yu. Yu. Illarionov[1], A. A. Sitnikova[1], A. V. Nashchekin[1], I .T. Serenkov[1], V. I. Saharov[1], N. V. Sibirev[2] and V. G. Dubrovskii[1,2]

[1] Ioffe Physical-Technical Institute, St Petersburg, Russia
[2] St Petersburg Academic University, St Petersburg, Russia

Abstract. Cobalt growth on atomically clean CaF_2(111) surface is studied in a wide range of growth conditions: 1–20 nm exposure at 100–500 °C. Cobalt nanoparticles are shown to have well ordered fcc lattice oriented identically to the underlying lattice of CaF_2. Size, shape and surface density of the Co nanoparticles are shown to be well controllable by an appropriate choice of growth conditions. A theoretical model is developed describing the nucleation and growth of Co nanoparticles on the CaF_2 surface, and a reasonable agreement with the experiment is achieved.

Introduction

Development of novel materials for ultrahigh density magnetic memories is closely related to the problem of overcoming the superparamagnetic limit and decreasing the magnetic bit size [1]. Fabricating ferromagnetic-on-antiferro-magnetic heterostructures and exploiting the exchange bias effect is a promising approach whereas Co on antiferromagnetic fluoride (MnF_2, NiF_2) can be a suitable materials choice. In heteroepitaxy of fluorides on silicon, CaF_2 is often used as a buffer or capping layer and serves as a convenient modeling material. Therefore it is attractive to study growth, structural and magnetic properties of Co on CaF_2. Few attempts have been made so far to study Co growth on CaF_2. Very high (4×10^{12} cm^{-2}) concentration of Co islands not dependent on the growth temperature was observed in Ref. 2 and was likely due to a high density of surface defects. The first approach to study electron structure and magnetic properties of higher crystal quality Co islands on CaF_2(111) is described in Ref. [3]. In this work, the arrays of epitaxial Co nanoparticles on CaF_2(111) were studied in detail for a wide range of Co exposures (1–20 nm) and temperatures (100–500 °C). Concentration of cobalt nanoparticles, their geometrical parameters and crystal structure were studied as functions of growth parameters.

1. Experimental

Cobalt/fluorite heterostructures were grown on Si(111) by molecular beam epitaxy. Planar 6 nm thick layer of calcium fluoride was grown on Si at 750 °C to prevent reaction between Si and Co. Cobalt was deposited on CaF_2(111) surface from an e-beam source providing flux of ∼0.2 nm/min. Since Co/CaF_2 sticking coefficient was found to be less than unity for elevated temperature, cobalt exposure in nm (flux multiplied by the growth time) will be indicated instead of coverage. Samples with Co exposure of 1–20 nm grown at 100–500 °C were characterized by NT-MDT ambient air atomic force microscope (AFM), JEOL scanning electron microscope (SEM), JEOL 2100F transmission electron microscope (TEM) and Medium Energy Ion Scattering (MEIS).

It was shown that the concentration of Co nanoparticles, their shape and size depend drastically on the growth parameters. It was demonstrated that by choosing appropriate growth conditions the nanoparticles may be organized in various patterns on the CaF_2 surface. By changing the cobalt exposure, one can observe gradual transformation from chains of small islands at CaF_2 step edges to arrays of facetted islands 20–50 nm in lateral size (Fig. 1).

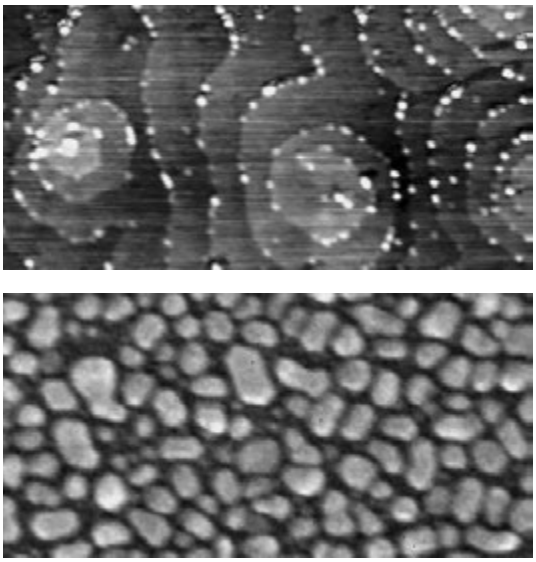

Fig. 1. Co nanoparticles grown at 300 °C: cobalt exposure 1 nm (top AFM) and 20 nm (bottom SEM). Image size 850 × 425 nm^2.

It was shown that the growth temperature not only affects the crystal structure (as will be discussed below) but also influences the size-to-surface-density ratio, as illustra-ted by the cross-section TEM images in Fig. 2. A 20 nm exposure at 100 °C results in the coalescence of individual flat-top nanoparticles, giving rise to almost continuous film. The same amount of cobalt deposited at 300 and 500 °C produces separated particles of two different shapes: wide flat-top islands and faceted round-shape islands. It becomes clear from Fig. 2 that the total volume of Co is considerably lower for the 500 °C sample, though all three samples have the same cobalt exposure. This is most probably due to the decrease in Co/CaF_2 sticking coefficient at elevated temperature.

An estimate of the sticking coefficient at various growth temperatures was carried out by measuring the amount of Co atoms per unit area by means of MEIS. It was shown that for 20 nm exposure the percentage of Co atoms remaining at the surface is ∼ 100% at 100 °C, ∼ 50% at 300 °C and just 8% at 500 °C.

To gain a quantitative understanding of the mechanisms inducing the diffusion of Co adatoms, nanoparticle nucleation and growth, the nanoparticle density may be analyzed as a function of exposure and temperature (Fig. 3). It is readily

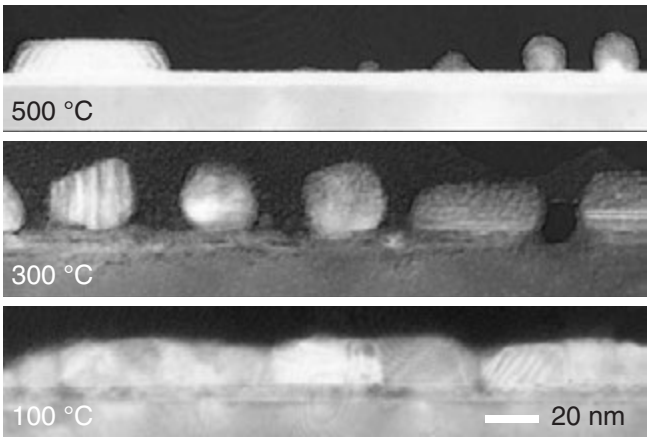

Fig. 2. Cross-section TEM images of 20 nm cobalt exposure at 100, 300 and 500 °C.

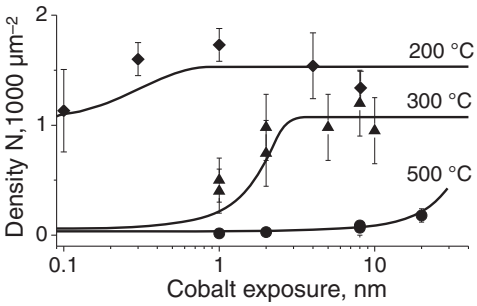

Fig. 3. Density of nanoparticles vs. cobalt exposure at different growth temperatures: experimental data (symbols) and theoretical simulation (lines).

seen that the density increases rapidly with the coverage, as the nanoparticles emerge and grow. At a certain exposure, the density saturation is reached, the maximum density being higher for a lower temperature. A slow density decrease after the saturation most probably corresponds to the coalescence of the nanoparticles.

The experimental curves were simulated using the kinetic model for the stress driven nanoparticle formation, which predicts the following time dependence of density:

$$n(t) = N\left(1 - \exp\left[-\exp\left(c[h - h_*]\right)\right]\right) . \qquad (1)$$

Here, N is the particle density at the end of the nucleation stage, c is the parameter of classical nucleation theory, h is the cobalt exposure in monolayers and h_* is the critical thickness. It has been found that the Co growth proceeds in a kinetically controlled mode. In this case the maximal density of islands is given by [4]:

$$N \propto \exp\left(3T_{\mathrm{D}}/2T\right) , \qquad (2)$$

where T is the growth temperature. The characteristic diffusion temperature T_{D} describes the temperature behavior of the stress-driven diffusion. Calculations were made by means of Eqs. (1),(2) for the following parameters: $T_{\mathrm{D}} = 642$ K, $c = 5.76 - T/135$ K.

It has been demonstrated that, in the wide range of growth parameters considered, fcc is the dominating lattice structure of Co nanoparticles. The highest lattice ordering is observed for 500 °C growth, where bright RHEED patterns (Fig. 4) indicate that the majority of nanoparticles have fcc lattice co-oriented

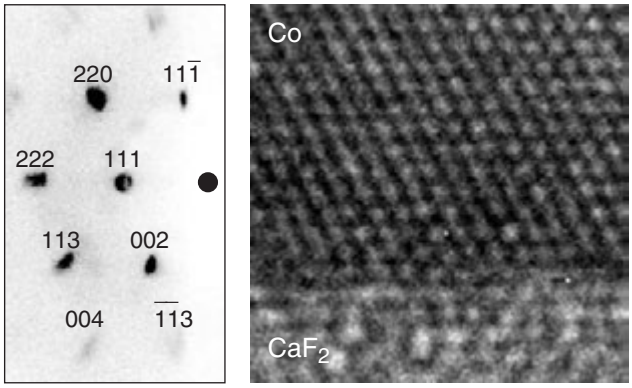

Fig. 4. On the left: fcc RHEED pattern (exposure 20 nm at 500 °C). On the right: 4×4 nm^2 HRTEM image of Co nanoparticle (exposure 20 nm at 100 °C).

with the lattice of underlying CaF_2. Additional analysis of RHEED and TEM diffraction patterns revealed unusual features that were ascribed to the stacking faults.

Samples grown at 100 °C showed less distinct diffraction patterns because of smaller size of nanoparticles. However, high resolution TEM (Fig. 4) and MEIS/channeling measurements confirmed that individual particles still have a well ordered fcc lattice and sharp interface with $CaF_2(111)$.

2. Conclusion

It is shown that, in a wide range of growth conditions, deposition of Co on $CaF_2(111)$ produces epitaxial Co nanoparticles with a well ordered fcc lattice. The geometrical parameters can be controlled by an appropriate choice of temperature and cobalt exposure. The nanoparticle density may be well described by the kinetic model proposed.

Acknowledgements

The work was partly supported by RFBR grants and programs of RAS and was performed in part at the regional Collective Use Center "Materials Science and Diagnostics in Advanced Technologies".

References

[1] J. Nogues and I. K. Schuller, *J. Magnetism and Magn. Materials* **192**, 203(1999).
[2] K. R. Heim *et al*, *J. Appl. Phys.* **80** (2), 1161 (1996).
[3] L. Pasquali *et al*, *Surf. Sci.* **600**, 4170 (2006).
[4] V. G. Dubrovskii *et al*, *Phys. Rev. B* **68**, 075409 (2003).

18th Int. Symp. "Nanostructures: Physics and Technology"
St Petersburg, Russia, June 21–26, 2010

Fluctuation-induced spreading of size distribution during nanoparticle growth stage

M. V. Nazarenko[1] and V. G. Dubrovskii[1,2]

[1] St Petersburg Academic University, St Petersburg, Russia
[2] Ioffe Physical-Technical Institute, St Petersburg, Russia

Abstract. This work addresses theory condensation based on the continuous Zeldovich equation for the size distribution of supercritical nanoparticles with keeping the second derivative with respect to the invariant size. The fluctuation-induced spreading of nanoparticle size spectrum at the growth stage is studied. The increase of dispersion depends on the growth index m as well as on the growth condition. In particular, we find that the spreading effect on 2D nanoislands growing at a constant material influx is huge at $m = 1$, but almost absent at $m = 2$. Dependence of InAs quantum dots optical properties on growth condition is demonstrated.

Introduction

Classical nucleation-condensation theory is based on the kinetic Zeldovich equation in partial derivatives of the second order for the distribution of nanoparticles over sizes [1–4]. This equation is obtained as a continuous approximation of finite-difference master equations in the monomer limit, where the growth-evaporation rates are related via the detailed balance with the known minimum work of nanoparticle formation [5]. Since the growth equation contains unknown supersaturation of a metastable phase, one should also consider the material balance [2–4]. In an open system with pumping, the supersaturation changes in time due to the monomer consumption by the growing nanoparticles and the material influx into the system [1–3]. Analytical or numerical studies of a particular condensing system therefore requires a solution of two connected equations for the time-dependent size distribution and the supersaturation: the differential Zeldovich equation and the integral equation of material balance [2,3]. Steep exponential dependence of nucleation rate on the supersaturation [1,2] makes the whole system strongly non-linear. The non-linearity of the equations, the fluctuation-induced effects and many other factors make the nucleation-condensation theory rather complex for the analysis. Such analysis is of great importance however in connection with thin films and surface islands [1,4], semiconductor quantum dots (QDs) [6], freestanding nanowires [7] and many other applications.

In the past, the common approach in analytical studies was to neglect either the non-linearity [5] or the second derivatives [2,4,6] in the growth equation at different stages of nucleation-condensation process. Neglect of fluctuations for supercritical nanoparticles (i.e., omitting second derivative with respect to size in the Zeldovich equation) leads to the time invariance of size distribution in terms of a certain invariant size, which can be defined for any particular condensing system [1,2,4,6,7]. As a consequence, the size spectrum evolves in time as a whole as the particles grow, with only the mean size changing. Recently it has been shown that the mentioned time invariance at the growth stage is the exception [3]. Fluctuation-induced spreading of size distribution is a result of keeping the term with second derivative in the Zeldovich equation.

1. System of growth equations

We consider the size-dependent growth rate of quite general form [1–4]:

$$W_i^+ = \frac{m(\zeta+1)}{\tau} i^{(m-1)/m},$$

where W_i^+ is growth rate of nanoparticle containing i monomers, ζ is the supersaturation, τ is characteristic microscopic time of nanoparticle growth, and m is the growth index that depends on the space dimensions of the nanoparticle and the metastable environment and nanoparticle growth regime; m normally lies between 1 and 3. For condensation of 2D nanoislands from adatom sea $m = 2$ corresponds to ballistic regime and $m = 1$ to diffusion regime. Ideal supersaturation $\Phi(t)$ is considered to be

$$\Phi(t) = \begin{cases} t/t_\infty & \text{if } 0 \le t \le t_0 \\ t_0/t_\infty \equiv \Phi_0 & \text{if } t > t_0 \end{cases},$$

where the macroscopic time t_∞ determines the characteristic rate of material influx and t_0 is stabilization time when the pumping is stopped. All calculations are performed in terms of invariant size ρ given by $\rho = i^{1/m}$, so that

$$\frac{\mathrm{d}\rho}{\mathrm{d}t} = \frac{\zeta}{\tau}.$$

Following Kuni [2], new time-dependent variable $z(t)$ is defined as the most representative invariant nanoparticle size at time t. The Zeldovich equation for the nanoparticle distribution function $f(\rho, z)$ in supercritical region can be written as

$$\frac{\partial}{\partial z} f(\rho, z) = -\frac{\partial}{\partial \rho}\left[f(\rho, z) - \frac{\varphi(z)}{m\rho^{m-1}} \frac{\partial}{\partial \rho} f(\rho, z) \right], \quad (1)$$

where $\varphi = \frac{1}{2} + \frac{1}{\zeta}$.

2. Green function of Zeldovich equation

Assuming that the nucleation stage is already completed and the nanoparticle density has reached its maximum value N_∞, we introduce the normalized size distribution $g(\rho, z) = f(\rho, z)/N_\infty$. We search for the asymptotic solution to Eq. (1) for $g(\rho, z)$ at large z (and ρ) in the form of Gaussian with z-dependent dispersion $\psi(z)$:

$$g(\rho, z) = \frac{1}{\sqrt{2\pi\psi(z)}} \exp\left(-\frac{(\rho - z)^2}{2\psi(z)} \right). \quad (2)$$

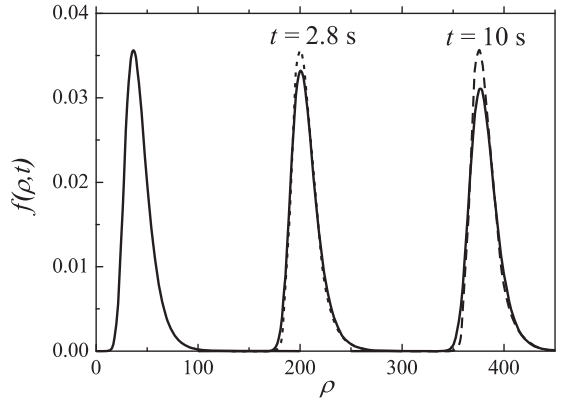

Fig. 1. Time evolution of 2D nanoislands size spectrum in $m = 2$ case. Dashed line show time-invariant spectrum.

In this asymptotic case Eq. (2) gives us the following condition for $\psi(z)$:

$$\frac{\mathrm{d}\psi}{\mathrm{d}z} = \frac{2\varphi(z)}{mz^{m-1}}. \tag{3}$$

Equation (3) should be solved with the boundary condition $\psi(z_0) = 0$, where z_0 is the most representative size at the end of nucleation stage. Solving Eq. (3) we can obtain Green function and, consequently, solution of Eq. (1) for any initial condition.

3. Results of numerical calculations

Eq. (3) was solved numerically for 2D nanoislands growing from the adatom sea in typical conditions InAs growth condition: $\tau = 3 \times 10^{-3}$ s, $t_\infty = 6 \times 10^{-2}$ s (corresponds to the deposition rate of 0.1 monolayers per second). Both $m = 2$ and $m = 1$ cases were considered (Fig. 1 and Fig. 2 respectively). Maximum time corresponds to formation of the continuous monolayer.

It is easy to see that broadening of the size distribution is almost negligible for the ballistic regime ($m = 2$, see Fig. 1). On the contrary, for diffusion regime ($m = 1$, see Fig. 2) the diffusion-induced spreading is huge. In that regime the spectrum spreads immediately after the nucleation stage so that the difference between the fluctuational and time-invariant cases becomes significant already at $t = 0.60$ s. At the end of the growth stage, the spectrum converts to a rather broad Gaussian which forgets completely about the initial condition.

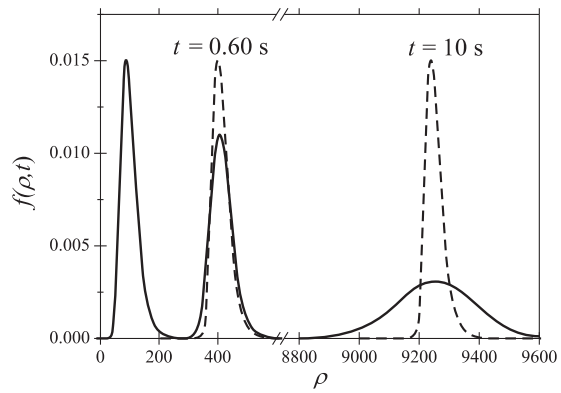

Fig. 2. Time evolution of 2D nanoislands size spectrum in $m = 1$ case. Dashed line show time-invariant spectrum.

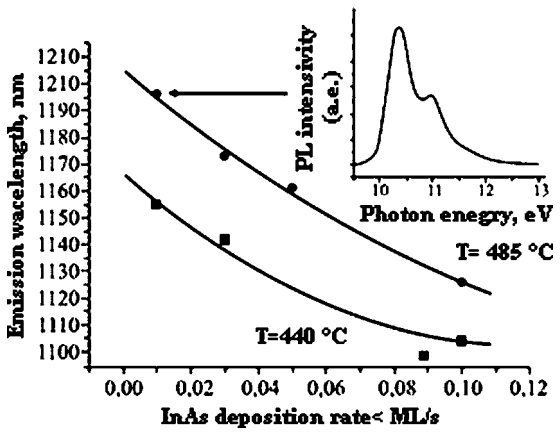

Fig. 3. Dependence of QD photoluminescence wavelength on the temperature and deposition rate. Inset shows sample photoluminescence spectrum.

4. Influence of growth conditions of QD properties

Based on the above model, it has been shown that for Stranski–Krastanov QD formation, a higher deposition rate and a lower growth temperature lead to smaller QDs with higher density [9]. Fig. 3 demonstrates the dependence of InAs QDs photoluminescence wavelength experimentally obtained at two different temperatures and deposition rates between 0.01 and 0.1 ML/s. This shows a possibility for a kinetically controlled engineering of QD arrays with the desired properties for different applications.

Acknowledgements

This work has been supported by the Russian Foundation for Basic Research. Authors would like to thank R. A. Suris, A. K. Shchekin, L.T. Adzhemyan, S.A. Kukushkin and A.V. Osipov for helpful discussions.

References

[1] D. Kashchiev, *Nucleation: Basic Theory with Applications* (Oxford: Butterworth Heinemann), 2000.
[2] F. M. Kuni, *Colloid J.* **46**, 791 (1984).
[3] V. G. Dubrovskii, *J. Chem. Phys.* **131**, 164514 (2009).
[4] S. A. Kukushkin, and A .V. Osipov, *Prog. Surf. Sci.* **51**, 1 (1996).
[5] D. Kashchiev, *J. Chem. Phys.* **129**, 164701 (2008).
[6] A. V. Osipov, S. A. Kukushkin, F. Schmitt, and P. Hess, *Phys. Rev. B* **64**, 205421 (2001).
[7] V. G. Dubrovskii, N. V. Sibirev, J. C. Harmand, and F. Glas, *Phys. Rev. B* **78**, 235301 (2008).
[8] V. G. Dubrovskii, G. E. Cirlin, and V. M. Ustinov, *Phys. Rev.* **B** 68, 075409 (2003).

18th Int. Symp. "Nanostructures: Physics and Technology"
St Petersburg, Russia, June 21–26, 2010

Step-terraced morphology formation on patterned GaAs(001) substrates

I. O. Akhundov[1], D. V. Sheglov[1,2], A. S. Kozhukhov[1,2], N. S. Rudaya[1], *V. L. Alperovich*[1,2], A. V. Latyshev[1,2] and A. S. Terekhov[1,2]

[1] Institute of Semiconductor Physics, 630090 Novosibirsk, Russia
[2] Novosibirsk State University, 630090 Novosibirsk, Russia

Abstract. The technique for preparing "step and terrace" GaAs(001) surfaces by annealing in the conditions close to equilibrium is further developed. Experiments on the mesa-structured GaAs substrates allowed us to evaluate the closeness of the annealing conditions to the equilibrium. The kinetics of surface flattening is measured. It is shown that the length of monatomic steps, which is a suitable characteristic of the "step and terrace" morphology, decreases inversely with the annealing duration. The influence of antimony, a potential surfactant, on the process of GaAs(001) surface flattening is studied. It is found that antimony hinders rather than facilitates surface flattening, presumably due to the formation of a robust Sb-stabilized reconstruction on the Sb/GaAs(001) surface.

Introduction

Atomically clean and flat semiconductor surfaces are needed for both fundamental surface science and device applications. Such surfaces yield opportunities for reproducible fabrication of nanoscale structures by means of atomic-probe techniques or due to self-assembling phenomena. Despite small values of the root mean square (rms) roughness, crystal surfaces prepared by standard chemo-mechanical polishing are disordered on a microscopic scale. By allowing surface migration at elevated temperatures, such surfaces can be brought to an ordered step-terraced morphology, which corresponds to a regular set of atomically flat terraces separated by monatomic steps. Almost perfect step-terraced silicon surfaces are obtained by annealing in vacuum [1, 2]. However, the application of this method to III–V semiconductors is hindered by high and different evaporation rates of the III and V components. Recently we demonstrated an opportunity to obtain step-terraced GaAs(001) surfaces by annealing in the conditions close to equilibrium between the surface and arsenic and gallium vapors [3]. The equilibrium conditions are provided by the presence of the saturated Ga-As melt. This technique was proved to be efficient and cost-effective as compared to the time- and resource-consuming earlier experiments in the MBE and MOCVD growth chambers [4, 5]. However, a number of questions related to this technique are still open. Firstly, the closeness of the conditions to the equilibrium is not determined. The deviation of the conditions towards growth or sublimation may lead to kinetic instabilities which hinder the process of flattening. Secondly, the kinetics of flattening should be measured in order to open the opportunity of comparing the experimental results with a theory and determination microscopic parameters which govern the flattening process. Thirdly, the annealing temperatures $T = 550$–650 °C, at which the GaAs flattening takes place, are too high for device applications. Therefore, the search of ways, such as using surfactants, which may help to reduce the flattening temperatures, is a topical question for device technologies. The present study is aimed at solving the above mentioned problems by annealing experiments on the preliminary patterned GaAs(001) substrates.

1. Experimental

The experiments were performed on the epi-ready GaAs(001) substrates. Square-shaped 5×5 μm^2 mesas were confined by grooves, ~10 nm in depth and ~100 nm in width. The grooves were made with the help of GaAs(001) oxidation induced by atomic force microscope (AFM) tip [6] and subsequent chemical removal of the oxide [7]. The mesas served as marks which allowed us to spot the same areas on the sample after subsequent anneals. The details of annealing in quasi-equilibrium conditions and *ex situ* AFM measurements are described earlier [3].

2. Results and discussion

Figure 1(a–d) shows the AFM image of a GaAs(001) substrate around a 5×5 μm^2 mesa before (a) and after (b–d) consecutive anneals at $T = 625$ °C. No traces of "step and terrace"

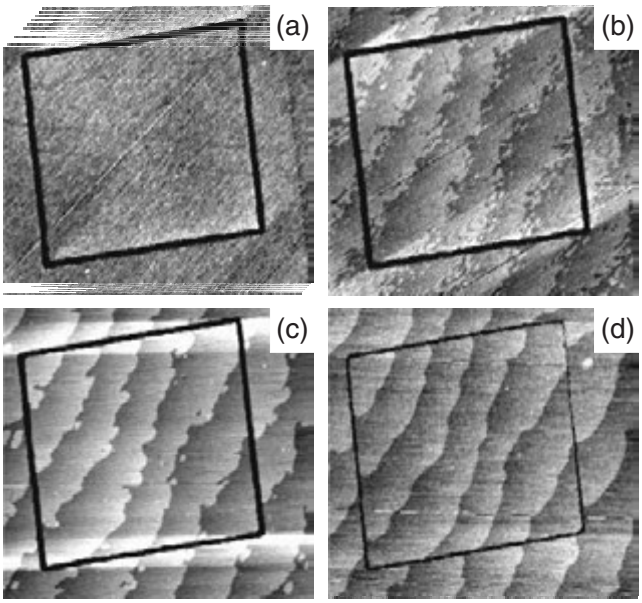

Fig. 1. 8×7 μm^2 AFM images of the mesa-structured epi-ready GaAs(001) substrate before (a) and after thermal smoothing in quasi-equilibrium conditions at $T = 625$ °C for 10 (b), 40 (c), and 100 minutes (d).

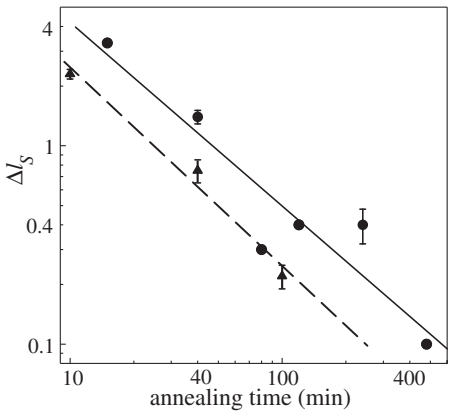

Fig. 2. Excess of the normalized step length Δl_S versus annealing time for two sets of measurements (circles and triangles). The straight lines are the linear fits to the experiments (see text).

morphology is observed before the anneals (Fig. 1a). Distinct terraces bounded by jagged steps are seen on the AFM image after annealing for 10 minutes (Fig. 1a). On the terraces there is a substantial concentration of two-dimensional "positive" and "negative" islands of monatomic height and depth, respectively.

The increase of the annealing time led to step smoothing, to the increase of the average lateral size of the islands, and to the decrease of their concentration (Fig. 1c). As a result of annealing for 100 minutes at $T = 625$ °C (Fig. 1d), the surface morphology approached that of an "ideal" vicinal surface with a regular set of atomically flat terraces of $\sim$1 μm in width separated by monatomic steps. The width of the terraces corresponds to the misorientation angle of $\sim$0.02 °.

To detect the deviations of the annealing conditions from the equilibrium toward the growth or sublimation, we analyzed the position of monatomic steps after consecutive anneals. In the cases of growth or sublimation one would expect the movement of the steps toward lower or higher lying terraces, respectively. Detailed comparison of the AFM images measured on patterned GaAs(001) substrates after anneals for various durations did not reveal any significant shift of the mean positions of steps. The accuracy of the step position measurements allowed us to estimate the upper limit of the growth (or sublimation) rate to be well below 3×10^{-5} monolayers per second. It should be also noted that step-flow growth (or sublimation) would lead to flattening of mesas into step-free facets, similar to the phenomenon observed during epitaxial growth on mesa-structured GaAs substrates [8]. However, as it is seen from Fig. 1(b–d), each step inside the mesa is a continuous extension of the step outside the mesa, with the uppermost and the lowest terraces on the mesa having approximately the same width as compared to other terraces. Thus, within the experimental accuracy, the annealing conditions are close to equilibrium.

It is seen from Fig. 1 that step smoothing, along with the decrease of island concentration, is the basic process of the step-terrace morphology formation. Consequently, the evolution of the Fourier transform of the step deviations from straight lines would be a useful characteristic of surface flattening. However, the Fourier analysis is complicated by the "overhangs" in the shape of steps, which are clearly seen in Fig. 1b. Therefore, in the present study we analyzed the kinetics of an integral parameter, the total length of monatomic steps L_S. As it was shown earlier [3], the evolution of the surface morphology during thermal flattening can be more adequately characterized by the step length than by the rms roughness R_q. Indeed, in course of flattening, L_S decreases by an order of magnitude and approaches the ultimately small value equal to the length L_0 of straight steps at an ideal vicinal surface, while R_q changes by less than a factor of 2. Figure 2 shows the excess Δl_S of the normalized length of steps $l_S = L_S/L_0$ over unity $\Delta l_S = (l_S - 1)$ as a function of the annealing time t for two sets of experiments. It is seen that both experiments yielded similar results: Δl_S decreases with the increase of the annealing time. In the double logarithmic scale both experimental dependences $\Delta l_S(t)$ can be approximated by straight lines. This approximation corresponds to power function $\Delta l_S(t) = \beta t^{-\alpha}$, with the power $\alpha = 1 \pm 0.15$ and coefficient $\beta = 0.85 \pm 0.15$. Thus, the excess of the step length Δl_S is inversely proportional to the annealing time. This experimental dependence should be compared with a quantitative theory, which, to our knowledge, is not yet available.

In an attempt to reduce the temperatures at which the smooth step-terraced GaAs surfaces can be prepared, we studied the influence of antimony, as a potential surfactant, on the process of surface flattening. To this end, antimony was added to the Ga-As melt. Under annealing, the Ga-As-Sb melt served as a source of Sb vapor, and, thus, Sb adsorbed on the GaAs surface. It was found that in the range of annealing temperatures $T = 550$–650 °C and Sb molar concentrations $x_{Sb} = 0.1\%$–5%, antimony led to the deterioration rather than improvement of the surface morphology (not shown). This deterioration revealed itself as a substantial increase of step length and island concentration. Thus, in these conditions antimony hinders rather than facilitates flattening. A possible reason for the Sb-induced deterioration of the surface morphology is the formation of a robust Sb-stabilized reconstruction GaAs(001)-(2×4) [9], which reduces the mobility of surface atoms.

Acknowledgements

This work was supported by the Russian Foundation for Basic Research (Grant No. 08-02-01236) and by the Russian Academy of Sciences.

References

[1] A. V. Latyshev, A. L. Aseev, A. B. Krasilnikov and S. I. Stenin, *Surf. Sci.* **213**, 157 (1989).
[2] H.-C. Jeong and E. D. Williams, *Surface Sci. Reports* **34**, 171 (1999).
[3] V. L. Alperovich *et al*, *Appl. Phys. Lett.* **94**, 101908 (2009).
[4] Z. Ding *et al*, *Phys. Rev. Lett.* **90** 216109 (2002).
[5] J. E. Epler, T. A. Jung and H. P. Schweizer. *Appl. Phys. Lett.* **62**, 143 (1993).
[6] D. V. Sheglov *et al*, *Phys. Low-Dim. Struct.* **5/6**, 239 (2002).
[7] V. L. Alperovich *et al*, *Appl. Surf. Sci.* **235**, 249 (2004).
[8] H. Weishart, E. Bauser, M. Konuma, and H.-J. Queisser, *J. Crys. Growth* **137**, 335 (1994).
[9] F. Maeda, Y. Watanabe and M. Oshima, *Phys. Rev. B* **48**, 14733 (1993).

18th Int. Symp. "Nanostructures: Physics and Technology"
St Petersburg, Russia, June 21–26, 2010

Quantum-size dependence of optical properties of dielectric films with Ge nanoclusters: scanning and spectral ellipsometry studies

E. Gorokhov[1], T. Easwarakhantan[2], D.V. Marin[1], V.A. Volodin[1], *K.N. Astankova*[1], I.A. Azarov[1] and M. Vergnat[2]

[1] Institute of Semiconductor Physics of SB RAS, Lavrenteva av., 13, Novosibirsk 630090, Russia
[2] Institute Jean Lamour, Nancy-Université, Boulevard des Aiguillettes B.P. 239, 54506, France

Introduction

The express and contactless method for determination of phase composition and sizes of semiconductor nanoclusters in dielectric matrix was claimed in [1]. It is needed non-destructive certification, which can be performed in real time of synthesis heterolayers in different conditions. For that purpose, it is expected to obtain contactless the data that characterize the main structural parameters of Ge:GeO_2 heterofilms, using only the spectral and scanning ellipsometry and PL. Such measurements have preliminary been "calibrated" on the basis of structural data of heterolayers obtained by the methods of HRTEM, Raman scattering and IR-spectroscopy. Actuality of the present work is supported by perspectives of applying of Ge quantum dots (QDs) in GeO_2 films in nanooptics and nanoelectronics [1,2].

The present thesis is aimed at definition of optical parameters (E_g^{eff}, ε, n and k) dependence on both quantum size effect and phase composition effect for Ge-QDs in GeO_2 films. Effective permittivity (ε) of a dielectric film with embedded semiconductor nanoclusters is depended on permittivities ($\varepsilon_{\text{matrix}}$ and ε_{QD}) of both materials and is depended on quantum-size effect. So, effective permittivity depends on shape and size (for spherical shapes diameter — D) of semiconductor nanoclusters. Taking into account dependences $n_{\text{QD}}(D)$ and $k_{\text{QD}}(D)$ into the well-known Bruggeman formula (1) allows to calculate the effective optical constants more accurate. In some cases it allows from measured n and k of the heterolayer calculate average sizes of QDs, its dispersion and concentration, its phase composition.

$$f_{\text{Ge}_a}\frac{\varepsilon_{\text{Ge}_a}-\varepsilon}{\varepsilon_{\text{Ge}_a}+2\varepsilon}+f_{\text{Ge}_c}\frac{\varepsilon_{\text{Ge}_c}-\varepsilon}{\varepsilon_{\text{Ge}_c}+2\varepsilon}+f_{\text{GeO}_2}\frac{\varepsilon_{\text{GeO}_2}-\varepsilon}{\varepsilon_{\text{GeO}_2}+2\varepsilon}=0$$
$$f_{\text{Ge}_a}+f_{\text{Ge}_c}=M_{\text{Ge}},\quad f_{\text{Ge}_c}=0. \qquad (1)$$

It is easier to realize such structural analysis of the studied heterostructures Ge-QD in GeO_2, due to known molar composition. The studied films of solid germanium monoxide are metastable and can be easily decomposited using relatively weak thermal treatments according to reaction (2GeO(s)$\longrightarrow$ GeO_2+Ge). It should be noted, that the mole composition ratio of Ge and GeO_2 is exactly equal to 1:1 independently of decomposition conditions. So, due to difference in density of germanium and glassy GeO_2, the volume part of Ge nanoclusters is $\sim$ 30.7%. The concentration of Ge nanoclusters is determined by its average sizes and one can find the average distance between them (l), using relation $l \sim 0.5D$. It should be noted, that the nanoclusters are distributed in matrix quite homogeneously. One can ignore the influence of quantum-size effect on optical properties of GeO_2 barriers, because the electron wave functions in wide-gap dielectrics are strongly localized, . So we have an ideal case for definition of the average sizes of Ge nanoclusters from measurements of optical constants of the Ge-QD in GeO_2 heterolayers and the dependences $n_{\text{QD}}(D)$ and $k_{\text{QD}}(D)$ can be obtained experimentally. The accuracy of such dependencies will be better if use spectral studies $n(\lambda, D)$ and $k(\lambda, D)$. The additional structural information can be obtained from studies of optical gap dependence of Ge-QD in GeO_2 heterolayers: $E_g^{\text{eff}} \sim f(D)$.

1. Experiments and results

A uniformly thick homogeneous film of metastable stoichiometric GeO(s) was deposited on cleaned Si substrate using reevaporation process [3] in a vacuum $\sim 10^{-4}$ Pa of heterolayers Ge:GeO_2 from another silicon wafer on which this layer has previously been condensed from the vapor GeO by LP CVD method in a flow reactor. Then the initial GeO(s)/Si structure was 5 minutes annealed at temperatures 260, 290 and 320 °C in high vacuum $\sim 10^{-6}$ Pa. Due to such "soft" annealing condition the very first stages of decomposition of metastable GeO(s) film on heterostructure Ge:GeO_2 were studied.

The changes of optical parameters $n(\lambda, D)$, $k(\lambda, D)$ and (E_g^{eff}) of decomposited GeO(s) film after each annealing procedure were studied. The analysis of these data allows us: (a) — to confirm the conclusions of work [1] that one should takes into account the quantum-size effect in Ge nanoclusters when calculate it's optical parameters from Bruggeman formula; (b) — to obtain the quantitative data about influence of the quantum size effect on optical parameters of Ge nanoclusters.

The measurements of $n(\lambda, T_i^{\text{an}})$ and $k(\lambda, T_i^{\text{an}})$ of GeO(s) film (Fig. 1) were carried out using spectral ellipsometer Jobin Yvon in University of Nancy, France, and spectral ellipsometers in ISP SB RAS and Science and Education Complex "Nanosystem and modern materials" Novosibirsk state university, Russia. The original computer programs for interpretation of experimental data were used. The results obtained using different ellipsometers were in good alignment. Additionally in Fig. 1 the experimental dependences $n(\lambda)$ and $k(\lambda)$ are shown: a) for Ge:GeO_2 heterolayer deposited in quarts tube flowing reactor using LP CVD method; b) calculated from Bruggeman formula dependences for Ge:GeO_2 heterolayer with the same (namely 1:1) molar ratio of Ge to GeO_2; c) for GeO_2 film grown on Ge substrate using thermal oxidation at 600 °C. The optical parameters of Ge were taken for amorphous phase. The curves 4,5,7 were obtained from both spectral ellipsometry and scanning laser multi-thickness ellipsometry data [4], so the accuracy of definition of $n(\lambda)$ and $k(\lambda)$ was very high.

The data for $k(\lambda)$ for all studied films (shown in Fig. 1) are

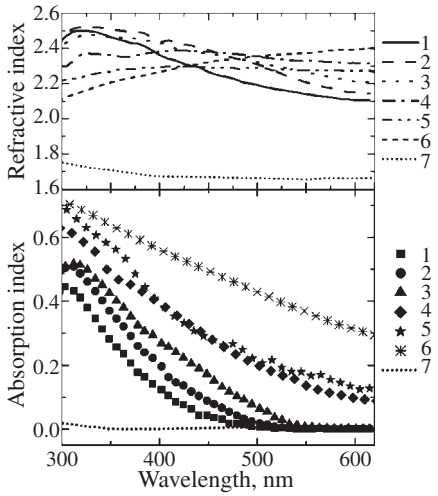

Fig. 1. Spectral dependence of optical constant in films: 1, 2, 3, 4 — GeO(s) as depos. and annel. at 260, 290, 320 °C, 5 — LP CVD Ge:GeO_2, 6 — Bruggeman model, 7 — thermal GeO_2.

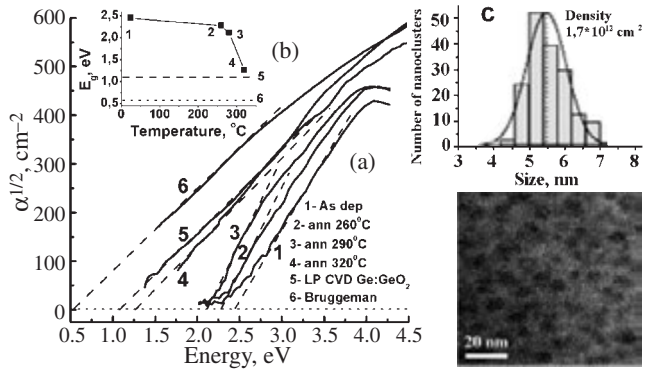

Fig. 2. (a) absorbance coefficients α for all Ge:GeO_2 films; (b) temperature dependence of E_g^{eff} for the same films; (c) HRTEM image of LP CVD Ge:GeO_2 size dispersion of Ge nanoclusters.

plotted in Fig. 2(a,b) in special Tauc coordinates. The vertical axis is square root from absorbance coefficient α. This coefficient is obtained from extinction coefficient as: $[\alpha^j(E)]^{1/2} = [2\pi k^j(E)/\lambda]^{1/2}$. Parameter j is the number of a studied film. Using well known formula for amorphous semiconductors $\alpha^{1/2} \sim (E - E_g)$, we have obtained the effective optical gap ($E_g^{j_{\text{eff}}}$) for all studied films Ge:GeO_2. The method of interpolation of linear dependences in special Tauc coordinates was used. The meaning of effective optical gap is the point of crossing of horizontal axis with that linear dependence (Fig. 2a). The changes in effective optical gap with the growth of annealing temperature T_{an} of GeO(s) film is shown in Fig. 2b. For comparing analysis and for analysis of Ge nanoclusters sizes, the E_g^{eff} for amorphous bulk germanium and for Ge:GeO_2 heterolayer deposited in quarts tube flowing reactor using LP CVD method are shown in Fig. 2b, lines 5 and 6. For the last case the E_g^{eff} is 1.15 eV. It should be noted that for this case the dispersion of sizes of Ge nanoclusters was studied using HRTEM direct data (Fig. 2c) [1]. For HRTEM studies the film was deposited on specially prepared very thin membranes that transparent for electron beam. While for Ge:GeO_2 heterofilms subjected to annealing at 320, 290 and 260 °C the Ge nanocluster's sizes should gradually become smaller.

The smallest Ge nanoclusters are in not annealed metastable GeO solid film, grown at temperature $\sim$ 25 °C. According to our hypothesis [5] the not decomposited GeO film contains tetrahedrons bonded in vertex of an angles (like $Ge(O)_4$ tetrahedrons in GeO_2). In the center of a tetrahedron is a Ge atom, which electron orbitals are 4-fold coordinated and sp^3-hybridizated. The Ge atom is bonded with two O atoms and two Ge atoms placed in vertexes. The length of Ge-Ge and Ge-O bonds is different, so tetrahedrons have not right shape and as a result are unstable. The decomposition of such structure is the reconstruction of homogenous but unstable system into more stable but heterogeneous structure. The last structure is a mixture of Ge and $Ge(O)_4$ tetrahedrons. The both tetrahedrons step by step form separate Ge and GeO_2 clusters. So, not decomposited GeO film contains Ge clusters of minimal size — namely clusters consisting from 3 Ge atoms. In Raman scattering spectrum of such film there are no peaks due to Ge-Ge vibration modes. So, surpassingly, such film does not contain Ge clusters bigger than 6–8 atoms. One can conclude that minimal D in not decomposited GeO film is not more than 2–4 Å.

2. Conclusions

(1) The spectral parameters $n(\lambda)$ and $k(\lambda)$ for heterolayers Ge:GeO_2 with molar ratio 1:1 on the first stages of decomposition of metastable GeO(s) film were studied for the first time. Analysis of both spectral ellipsometry and scanning laser multithickness ellipsometry data allows to remarkably improve the accuracy of definition of $n(\lambda)$ and $k(\lambda)$ for these films.

(2) It was shown, that for Ge nanoclusters with sizes up to $\sim$ 12–15 nm in heterolayers Ge:GeO_2, it is important to take into account the influence of quantum size effects in calculations of $n(\lambda)$ and $k(\lambda)$ using Bruggeman formula. The first data about the influence of quantum size effects on optical properties of the heterolayers Ge:GeO_2 with Ge nanoclusters with sizes from $\sim$ 0.2–0.4 up to 5.5 nm were obtained.

(3) The optical gap for not decomposited GeO(s) film was defined for the first time, it is 2.45 eV. The initial temperature of GeO(s) film decomposition to Ge and GeO_2 was $\sim$ 250 °C.

Acknowledgements

This work was carried out only due to financial support of RFBR (grant # 07-08-00438) without any RAS budget financial support. E. B. Gorokhov is grateful to University of Nancy for traveling grant.

References

[1] E. B. Gorokhov *et al*, *14th Int. Symp. "Nanostructures: Physics and Technology"*, 2006, p. 170–171.

[2] V. A. Volodin *et al*, *"Quantum Dots: Research, Technology and Applications"*, New York, 2008, p. 333–372.

[3] K. N. Astankova *et al*, *Journal of surface investigation. X-ray, synchrotron and neutron techniques*, **3**, 773 (2009).

[4] D. V. Marin *et al*, *Optics and Spectroscopy* **106**, 436 (2009).

[5] E. B. Gorokhov *et al*, *17th International Symposium "Nanostructures: Physics and Technology"*, 2009, p. 146–147.

18th Int. Symp. "Nanostructures: Physics and Technology"
St Petersburg, Russia, June 21–26, 2010

(GaMn)As nanowhiskers grown by molecular beam epitaxy

A. Bouravleuv[1,2,3], S. Novikov[2], N. Lebedeva[2], N. Sibirev[3], G. Cirlin[1,3,4] and H. Lipsanen[2]

[1] Ioffe Physical-Technical Institute, St Petersburg, Russia
[2] Helsinki University of Technology, FI-02150 Espoo, Finland
[3] St Petersburg Academic University, St Petersburg, Russia
[4] Institute for Analytical Instrumentation, 190103 St Petersburg, Russia

Abstract. (Ga,Mn)As were obtained by molecular-beam epitaxy (MBE) on GaAs(111)B substrates. The NWs obtained have lengths up to 10 μm. The crucial influence of Mn fluxes and the growth temperature on NW distribution and sizes is determined. The self-sustained excitation of (Ga,Mn)As NWs oscillations under constant electron beam of scanning electron microscope (SEM) is found.

Introduction

Diluted magnetic semiconductors (DMS) have attracted increasing attention because of their potential applications in spintronics devices [1] nowadays. The most studied DMS material is GaMnAs. In this material, the ferromagnetic transition seems to be induced by interactions between spins of Mn ions and holes from valence band. This opens up possibilities to control the ferromagnetic properties by applying not only magnetic, but also electric field. The concentration of Mn is one of the most important parameters, since Mn atoms provide on the one hand uncompensated localized spins, when they occupy Ga lattice sites, and on other holes. It should be noted, that As antisites and Mn interstitials as double donors decrease the concentration of holes and as a consequence, the Curie temperature. In equilibrium growth conditions Mn has low solubility in GaAs, therefore nonequlibrium growth techniques should be used to obtain the high Mn concentration. Among them the MBE growth of (Ga,Mn)As nanowhiskers (NW) appears to be particularly promising. Recently (Ga,Mn)As NW have been synthesized by different methods. Kim *et al* fabricated $Ga_{1-x}Mn_xAs$ NW using the vapor transport method, using the evaporation of GaAs/$MnCl_2$ [2]. The core-shell GaAs/GaMnAs have been grown by Rudolph *et al* [3]. Firstly they obtained GaAs NW using common vapor-liquid-solid technique with Au as a catalyst. Then GaMnAs shell was deposited on the side facets of GaAs NWs under low temperature conditions. The highest Curie temperature, that they reached was equal to 20 K. Sadowskii *et al* utilized another experimental approach [4]. They observed that continuing GaMnAs MBE growth in the presence of surface MnAs clusters, i.e. at phase segregation conditions, leads to formation of nanowires. The NWs obtained were tapered. At high densities of Mn flux using in experiments, fabricated NWs had a lot of side branches.

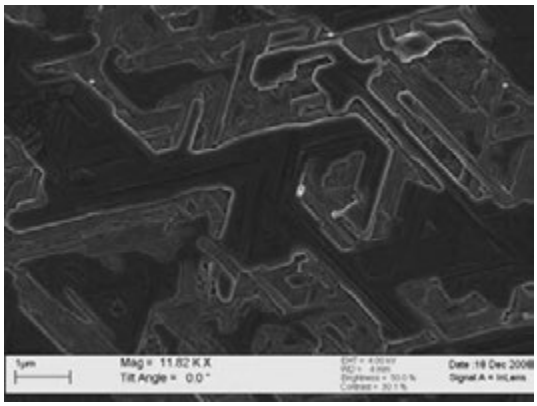

Fig. 1. SEM image of individual NWs. The scale bar corresponds to 1 μm.

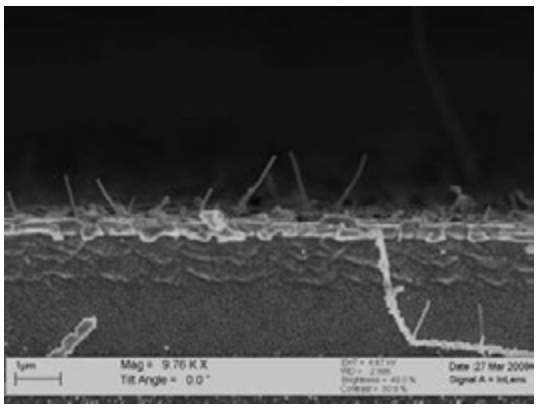

Fig. 2. SEM image of NW arrays. The scale bar corresponds to 1 μm.

Here we report on the investigation of MBE growth of (Ga,Mn)As NWs using both MnAs and GaMnAs preliminary deposited nanoclusters as a seeds for the growth.

1. Experimental

(GaMn)As nanowhiskers were grown on GaAs(111)B substrates using VG100H MBE system. Firstly, GaAs(111)B substrates were chemically cleaned prior to growth. Then they were annealed to eliminate native oxide overlayer. By opening for 15 s Ga and Mn cells, the seeds for the growth of NWs were created. Nanowhisker growth was initiated after reducing the temperature. The growth of GaMnAs nanowhiskers was performed in the temperature range from 500 to 680 °C. The duration of growth was varied from 15 to 30 min. The V/III ratio was equal to 1. The temperature of the Mn K-cell was varied in the range from 500 to 550 °C.

Sample characterization was carried out using Zeiss Supra 40 Scanning Electron Microscope (SEM).

2. Results

The NWs obtained at low Mn flux are shown in Fig. 1. As one can see, the surface density of NWs is very small. The length of NW is close to 100 nm, that can be result of insufficient

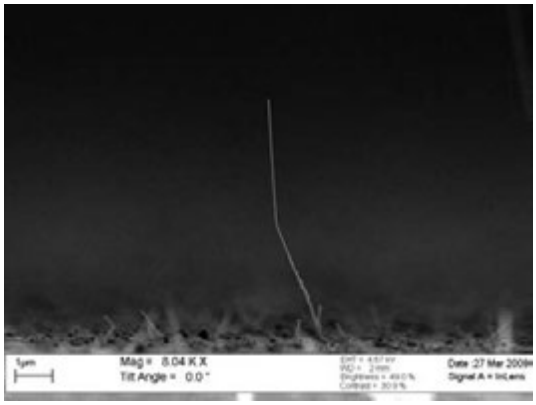

Fig. 3. SEM image of individual NWs. The scale bar corresponds to 1 μm.

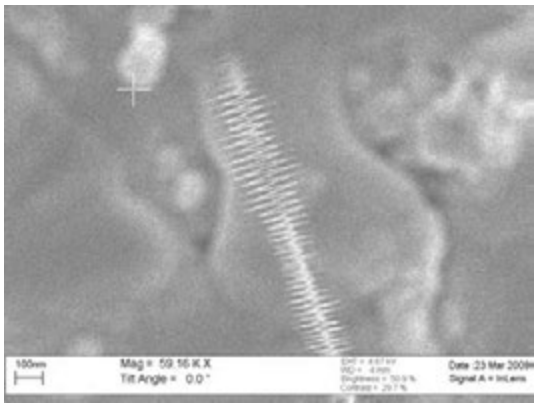

Fig. 4. SEM image of vibrating NW. The scale bar corresponds to 1 μm.

time of the growth in such growth conditions. NWs have pronounced catalytic droplet on the top indicating the formation of NW according to vapor-liquid-solid (VLS) mechanism of the growth.

Figure 2 demonstrates SEM image of the sample with (Ga,Mn)As NWs grown at 660 °C and higher Mn flux. The density of NWs obtained is higher than in the previous case. Therefore, the temperature of the Mn cell seems to be governing condition for the (Ga,Mn)As NWs growth. The arrays of NWs have average length of 1.2 μm. The average radial size of NWs is close to 40 nm. Uncommonly to the growth of GaAs NWs on GaAs(111)B surfaces, the growth directions of our NWs distinct from $\langle 111 \rangle$. Unfortunately, we have not performed high resolutions transmission electron microscopy (HRTEM) measurements yet to determine their crystallographic orientation.

Some of (Ga,Mn)As NWs obtained have length up to 10 μm as it is shown in Fig. 3. Such NWs are of importance for investigation of electric properties, since the problem of making electric contacts to such NWs can be solved much easier.

Moreover, we have found a very interesting effect, which can be attributable not to magnetic properties of (Ga,Mn)As NWs, but to their geometrical sizes. The sinusoidal function in Fig. 4 and Fig. 5 represents vibration of individual (Ga,Mn)As NW. The self-sustained mechanical oscillations of NW can be caused by the constant electron beam of a scanning electron microscope (SEM). Energy seems to be pumped into the oscillations by the beam-induced time-varying charge on NW. Similar oscillations have been already observed for SiC NWs [5,6]. But in our case, oscillations have higher modes, which to the best of our knowledge have not been observed yet. The realization observation and modeling of auto-oscillations of NW opening the way for nanometric dc to ac conversion as well as for fabrication of prototypes of NW-based radio devices.

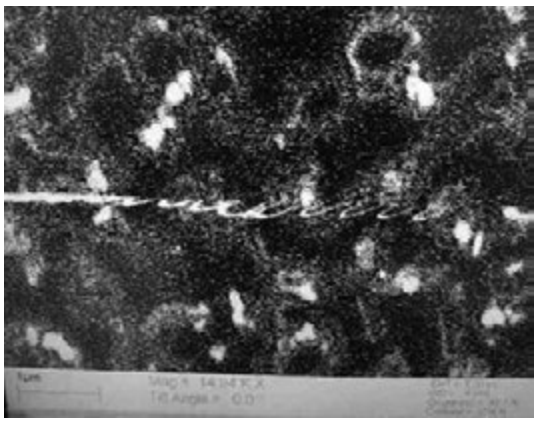

Fig. 5. SEM image of vibrating NW. The scale bar corresponds to 1 μm.

Acknowledgements

This work was supported by Academy of Finland and different grants of RFBR.

References

[1] H. Ohno, *Science* **281**, 951 (1998).
[2] H. S. Kim *et al*, *J. Chem. Mater.* **21**, 1137 (2009).
[3] A. Rudolph *et al*, *Nano Lett.* **9**, 3860 (2009).
[4] J. Sadowski *et al*, *Nano Lett.* **7**, 2724 (2007).
[5] S. Perisanu *et al*, *Phys. Rev. B* **77**, 165434 (2008).
[6] P. Vincent *et al*, *Phys. Rev. B* **76**, 085435 (2007).

18th Int. Symp. "Nanostructures: Physics and Technology"
St Petersburg, Russia, June 21–26, 2010

Light-emitting Si nanostructures formed due to reduction of SiO_2 by irradiation with swift heavy ions

G. A. Kachurin[1], S. G. Cherkova[1], D. V. Marin[1], V. G. Kesler[1], V. A. Volodin[1] and V. A. Skuratov[2]

[1] Institute of Semiconductor Physics SB RAS, 630090 Novosibirsk, Russia
[2] Joint Institute for Nuclear Research, 141980 Dubna, Russia

Abstract. Thin stoichiometric SiO_2 layers were irradiated with 167 MeV Xe ions to the dose of 10^{14} cm^{-2}. The spectroscopy of Raman scattering, photoluminescence and X-ray photoelectron spectroscopy (XPS) were used for the characterizations. Raman scattering has shown partial decomposition of the layers with formation of excess Si in the irradiated layers. XPS spectra demonstrated decrease in number of Si-Si_0 bonds (SiO_2) and appearance of Si atoms coordinated with 1–4 Si neighbors. Wide visible photoluminescence band peaked at ∼600 nm was observed after Xe bombardment and passivation by H_2. The emission at about 600 nm is usually connected with Si nanoprecipitates of different shapes and dimensions. The obtained results are ascribed to partial reduction of SiO_2 in the tracks of swift heavy ions and formation of light-emitting Si nanostructures.

The interest to quantum-size Si nanostructures is motivated by the demand for Si-based optoelectronics and non-volatile memory devices. Si nanocrystals have been conventionally fabricated by two-step processes — either ion implantation of Si^+ ions into SiO_2 layers or deposition of Si and SiO_2 followed by high-temperature annealing. In both cases Si-rich SiO_2 decomposes and self-assembly of Si nanocrystals takes place. Here we report an attempt to synthesize Si nanostructures in stoichiometric SiO_2 layers. For this purpose we employed irradiation with swift heavy ions. When such ions penetrate in solid-state targets, they form tens of microns long tracks with the diameters of 3–5 nm, where extremely high carrier concentrations, temperatures and pressure occur for 10^{-13}–10^{-11} s [1]. That may invoke thermally or ionization stimulated structural transformations, including reduction of the oxides. A few articles related to the bombardment of Si suboxide layers with SHI have been published earlier [2–5].

In our experiments 320 nm thick SiO_2 layers were thermally grown on Si substrates. Their refractive index was found to be 1.45. The irradiation was performed with 167 MeV Xe ions to the dose of 10^{14} cm^{-2}. The stopping power of the Xe ions in the layers nearly completely (>99.8%) consisted of electronic losses. Some of the irradiated samples were passivated by anneals in forming gas (94%Ar + 6%H_2) at 500 °C for 1 h. The spectroscopy of Raman scattering, photoluminescence and X-ray photoelectron spectroscopy (XPS) were used for the characterizations. Laser lines $\lambda = 514.5$ nm and $\lambda = 488$ nm were used to excite Raman scattering and photoluminescence, respectively. Photoelectrons were generated by the Al Kα X-ray line of 1486.6 eV from the Al source.

It was established, that after irradiation drastic changes in the properties of the layers occurred. Raman scattering has shown partial decomposition of the layers with formation of excess Si (Fig. 1). The wide band peaked at about 480 cm^{-1}, usually ascribed to the amorphous Si, was observed in the irradiated samples. XPS spectra demonstrated decrease in number of Si-Si_0 bonds (SiO_2) and appearance of Si atoms coordinated with 1–4 Si neighbors (Fig. 2,3). Wide visible photoluminescence band from green to red regions was observed (Fig. 4). Passivation with H_2 led to about three-fold enhancement of its intensity and to distinguishing of maximum at 600 nm (Fig. 4, circles). The emission at about 600 nm is usually connected with Si nanoprecipitates of different shapes and dimensions. The obtained results are ascribed to partial reduction of SiO_2

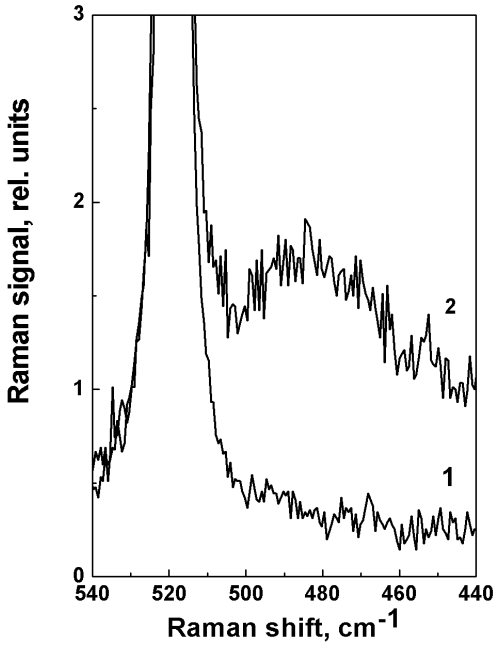

Fig. 1. Raman spectra of the layers before (1) and after (2) Xe bombardment.

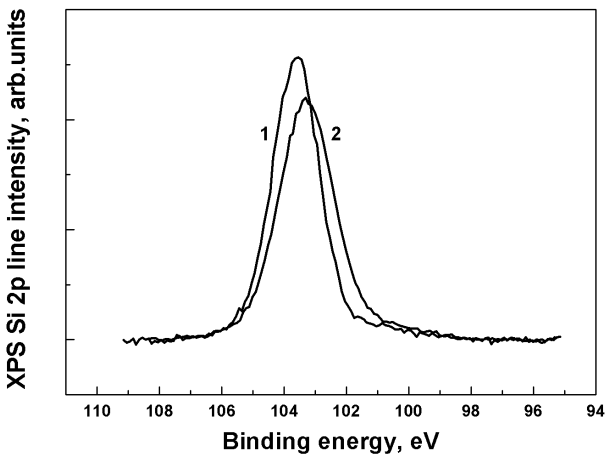

Fig. 2. XPS spectra of the layers before (1) and after Xe bombardment (2).

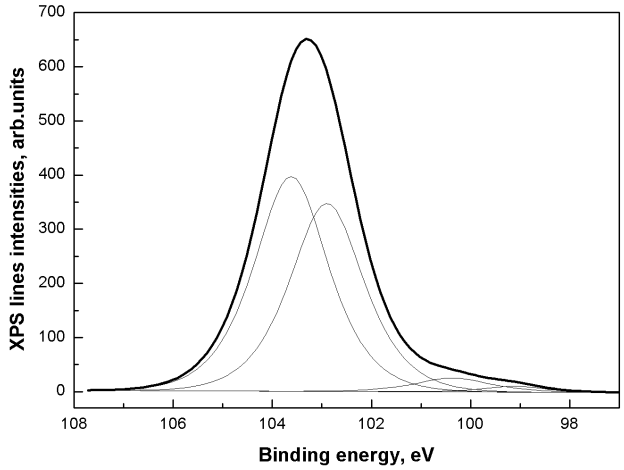

Fig. 3. Deconvolution of Si 2p XPS line after Xe bombardment in the Gaussian bands: Si-Si_0 — 103.6 eV, Si-Si_1 — 102.4 eV, Si-Si_3 — 100.9 eV, Si-Si_4 — 99.8 eV.

in the tracks of swift heavy ions and formation of light-emitting Si nanostructures. The possible mechanisms of nanostructures formation are discussed. The role of oxygen out-diffusion from the ion tracks is believed to be the most significant factor for the syntheses of quantum-size light-emitting nanoparticles.

Acknowledgements

We thank Dr. V. V. Kirienko for the anneals in forming gas. This work has been supported by the Grant # 08-02-00221 of Russian Foundation for Basic Researches.

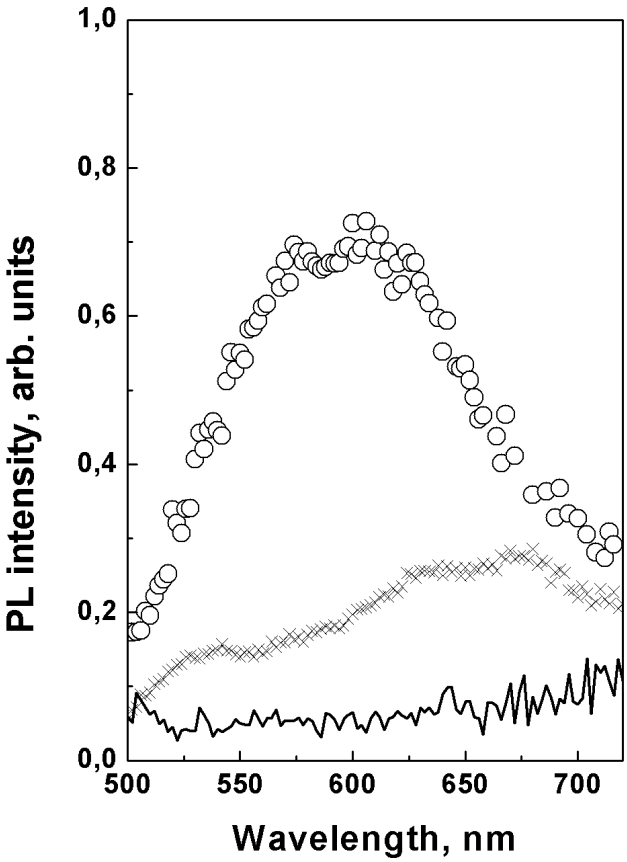

Fig. 4. PL spectra of SiO_2 layers before (solid line) and after Xe bombardment (crosses). Circles — after the passivation.

References

[1] M. Toulemonde *et al*, *Nucl. Instr. and Meth. B* **166–167**, 903 (2000).
[2] D. Rodichev *et al*, *Nucl. Instr. and Meth. B* **107**, 259 (1996).
[3] P. S. Chaudhari *et al*, *J. Appl. Phys.* **93(6)**, 3486 (2003).
[4] P. S. Chaudhari *et al*, *Instr. and Meth. B* **239**, 185 (2005).
[5] W. M. Arnoldbik *et al*, *Phys. Rev. B* **71**, 125329 (2005).

18th Int. Symp. "Nanostructures: Physics and Technology"
St Petersburg, Russia, June 21–26, 2010

Curvature control of shells containing two-dimensional electron gas

S. V. Mutilin, Yu. S. Yukecheva, A. B. Vorob'ev, M. A. Putyato and V. Ya. Prinz
Institute of Semiconductor Physics, 630090, Novosibirsk, acad. Lavrentyev Ave., 13, Russia

Abstract. InAs/AlSb/GaSb/SiO_2 shells containing two-dimensional electron gas were fabricated. It was shown that both electron concentration and electron mobility in the shells drastically depend on the depth at which the InAs quantum well is buried. Shell curvature was changed more than 3 times using electron beam exposure. Electron beam exposure does not destroy two-dimensional electron gas in the shells.

Introduction

Recent progress in technology makes possible fabrication of shells with micro- and submicrometer radii, made of semiconductor heterostructures [1]. Such systems are attractive, at first, for investigations of charge carrier transport in strong magnetic field gradient. Since electron motion in 2D system is governed by normal-to-surface component of magnetic field, electrons on a curved surface feel external uniform magnetic field as effectively non-uniform one. Magnetic field gradient causes non-uniform distrubution of current density and electric field [2], and edge states redistribution in quantizing magnetic fields [3,4]. In experiment it is revealed as, for instance, a giant asymmetry of two-dimensional electron gas (2DEG) longitudinal resistivity (up to 10^4) with respect to magnetic field direction [5]. Second, considerable strain in shells, reaching several percents, can be used for effective control of their band structure parameters. It was calculated that band gap in semiconductor shells can be tuned in the range of 1 eV [6]. Since both magnetic field nonuniformity and strain distribution depend on curvature, it seems very important to find a way to control local curvature of shells containing 2DEG.

1. Experimental

A set of heterostructures, consisting of the 15-nm-thick InAs quantum well (QW) sandwiched between AlSb/GaSb layers with thicknesses varied from 0 to 40 nm and 20-nm-thick AlSb sacrificial layer was grown by molecular beam epitaxy on GaSb (100) substrates. On the top of heterostructures, SiO_2 film was deposited by chemical vapor deposition. Using optical lithography and wet etching, a cross-shaped mesastructures were defined.

Magnetotransport measurements at $T = 4.2$ K revealed well-pronounced Shubnikov–de Haas oscillations showing presence of 2DEG; the highest mobility obtained in such structures was 1.2×10^5 cm^2/(V s) at the concentration of 10^{12} cm^{-2}. Subsequent selective etching of AlSb sacrificial layer leads to buckling of strained films [7] and formation of shells with radii of about 10 μm (Fig. 1).

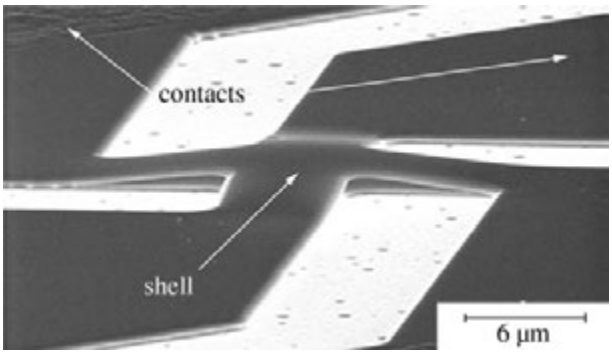

Fig. 1. InAs/AlSb/GaSb/SiO_2 cross-shaped shell with 2DEG.

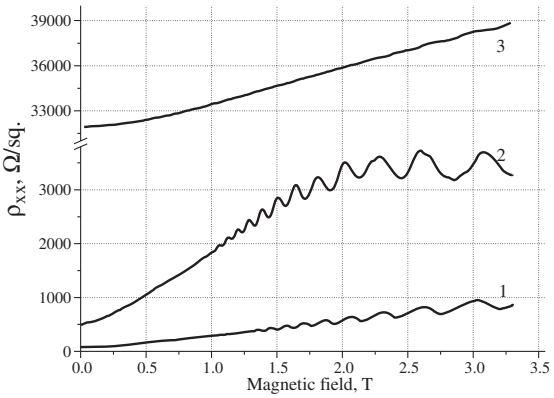

Fig. 2. Resistance of the sample with InAs QW buried at the depth of 30 nm: (1) initially flat structure, (2) shell structure. For comparison, the curve (3) represents the resistance of sample with InAs QW located on the surface of shell.

Magnetotransport measurements in shells indicated presence of 2DEG with concentrations varying from 8.6×10^{11} to 10^{12} cm^{-2}. It was shown that the mobility of 2DEG drastically falls with decreasing of the depth at which the quantum well is buried. Mobility of 2DEG buried at the depth of 30 nm was about 2.5×10^4 cm^2/(V s), while electron mobility in QW placed directly on the surface was only 200 cm^2/(V s) (Fig. 2). Presumable reason of this difference is scattering on charged surface states. In order to change InAs/AlSb/GaSb/SiO_2 shell

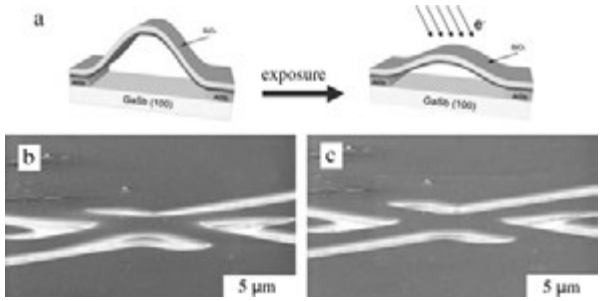

Fig. 3. Increasing of shell curvature radius caused by electron beam exposure: a) schematic drawing, b) SEM image of the shell before exposure, c) SEM image of the shell after exposure.

curvature, electron beam exposure in the electron microscope chamber was used [8]. It was shown that exposed shells increase their curvature radius more than 3 times (Fig. 3). Magnetotransport measurements demonstrated presence of 2DEG in exposed shells with the same concentration as before exposure.

2. Conclusion

We report on fabrication of shells with curvature radii of about 10 m which contain InAs QW with 2DEG. The control of shell curvature is demonstrated which does not destroy 2DEG in the shells.

References

[1] V. Ya. Prinz *et al*, *Physica E.* **6**, 828 (2000).
[2] A. V. Chaplik *et al*, *JETP Lett.* **72**, 723 (2000).
[3] A. Lorke *et al*, *Superlatt. Microstruct.* **33**, 347 (2003).
[4] S. Mendach, *Diss. Doktorgrades des Fachbereichs Physik.*, Hamburg, 2005.
[5] A. B. Voro'ev *et al*, *Phys. Rev. B* **75**, 205309 (2007).
[6] V. M. Osadchii *et al*, *Phys. Rev. B* **72**, 033313 (2005).
[7] V. Ya. Prinz *et al*, *Sci. Technol. Adv. Mater.* **10**, 034502 (2009).
[8] Yu. S. Yukecheva *et al*, *Semicond. Sci. Technol.* **23**, 105007 (2008).

18th Int. Symp. "Nanostructures: Physics and Technology"
St Petersburg, Russia, June 21–26, 2010

2D–3D and "hut"-"dome" transitions during Ge growth on the Ge_xSi_{1-x} surface

A. I. Nikiforov, V. V. Ulyanov, V. A. Timofeev and O. P. Pchelyakov
Rzhanov Institute of Semiconductor Physics SB RAS, Lavrentjeva 13, 630090 Novosibirsk, Russia

Abstract. Dependences of the critical Ge layer thicknesses on the solid solution composition and thickness were established. The observed decrease in the critical thicknesses of 2D–3D and hut-dome transitions against the growth on the pure Si(100) surface was accounted for by the accumulation of elastic strains with increasing Ge percentage or thickness of the GeSi solid solution.

The germanium on silicon heterosystem is an ideal object for studying the heteroepitaxial growth and the growth mode transition (the Stranski–Krastanow mechanism). The silicon structures with germanium quantum dots are of practical interest for optoelectronics due to their potential covering the regions from IR through the wavelengths used in fiber-optic communications.

Reflection high-energy electron diffraction (RHEED) is the most used technique in MBE. This technique enabled oscillations of the in-plane lattice constant to be detected for the Ge film growing according to the 2D mechanism on the silicon surface [1]. There are available numerous papers that report studies of early stages of Ge growth on the Si(100) surface but only few data on the influence of Ge_xSi_{1-x} layer on the wetting layer thickness and "hut"-"dome" transition [2,3]. The growth of pure Ge on the Si(100) surface is described in most detail in Refs. [4,5]. The phase diagram of the morphological state of Ge films on the Si(100) surface was obtained, the explicit dependence of the wetting layer thickness on temperature being not discovered though. Probably, that was because the attention was mainly paid there to boundaries of the formation of variously shaped islands.

A Katun-C MBE installation equipped with two electron beam evaporators for Si and Ge was used for synthesis. Diffraction patterns were monitored during the growth using a CCD camera on line with PC. The software allowed both the whole images and chosen fragments of the diffraction patterns to be monitored at the rate of 10 frames/s. Ge grew at the rate of 0.3–10 ML/min, temperature was varied from 250 to 700 °C.

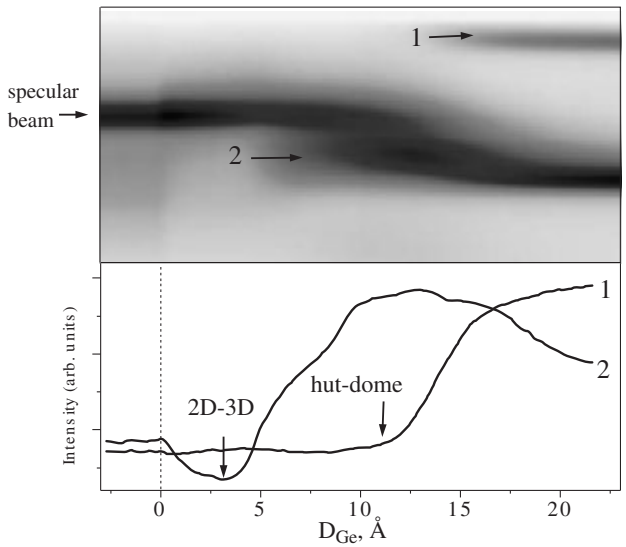

Fig. 1. Variations in the profile intensity along zero reflection in the diffraction pattern in the course of the Ge layer growth on Ge_xSi_{1-x} surface.

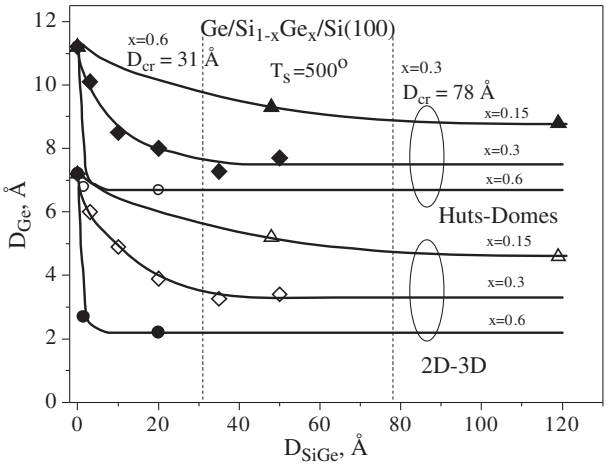

Fig. 2. 2D–3D and "hut"-"dome" transitions thickness as a function of thickness for different Ge content in Ge_xSi_{1-x} layers.

As the deposited layer thickness increases, elastic strain induced by mismatching of the Si and Ge lattice constants also increases. Starting with some critical thickness, from two-dimensional to three-dimensional growth mechanism and from "hut"-clusters to "dome"-clusters (hut-dome) transitions is observed, a part of strains being relaxed that is energetically favorable due to a decrease in the free energy of the system. Figure 1 shows variations in the profile intensity along zero reflection in the diffraction pattern in the course of the Ge layer growth on Ge_xSi_{1-x} surface. Along with oscillations of the specular reflection, a three-dimensional reflection becomes observable at a certain moment of time. The point of 2D to 3D transition (arrowed in curve 1, Fig. 1) and"hut"-"dome" (arrowed in curve 2, Fig. 1) is detected at an abrupt increase in the signal of 3D object towards reflections in the diffraction pattern.

Thus, identifying the moment of 2D–3D and hut-dome transitions at various thickness of Ge_xSi_{1-x} layer at 500 °C allowed the wetting layer and hut-dome transitions thickness to be determined as a function of thickness for different Ge content in Ge_xSi_{1-x} layers (see Figure 2).

The critical transition thicknesses are observed to decrease to reach saturation as the solid solution thickens. The observed decrease in thicknesses is accounted for by strengthening the strain deformation in the solid solution layer. As a result, the initiation of the morphological transitions by the stored elastic deformation needs ever decreasing thickness of the pure germanium layer.

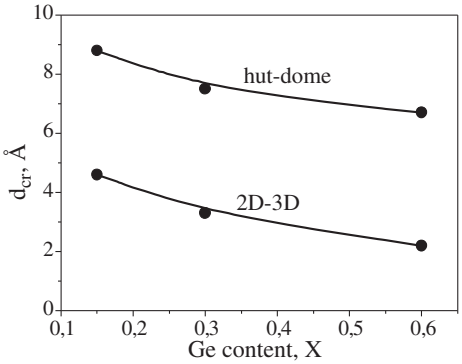

Fig. 3. Variations in the critical thicknesses of 2D–3D and "hut"-"dome" transitions depending on the solid solution composition.

Figure 3 shows variations in the critical thicknesses of 2D–3D and "hut"-"dome" transitions depending on the solid solution composition at the saturation stage. Another reason for decreasing thicknesses is, probably, strengthening of the elastic deformation with increasing germanium content in the solid solution.

Thus, morphological transformations in the Ge layer happen when a total of germanium thickness in the solid solution and in the deposited germanium layer is larger than the critical value. Changes in the critical thicknesses of 2D–3D and "hut"-"dome" transitions are accounted for by an increase in the magnitude of elastic strains with increasing thickness and germanium content in the solid solution Ge_xSi_{1-x}.

Acknowledgements

The work is supported by the Russian Foundation for Basic Research (Grants 09-02-01262 and 09-02-12421).

References

[1] A. I. Nikiforov, V. A. Cherepanov, and O. P. Pchelyakov, *Mat. Sci. Engineering B* **89**, 180 (2002).
[2] N. V. Vostokov *et al*, *Physics of the Solid State* **47**, 26 (2005).
[3] Zhensheng Tao *et al*, *Applied Surface Science* **255**, 3548 (2009).
[4] V. Cimalla and K. Zekentes, *Phys. Rev. Lett.* **77**, 1452 (2000).
[5] O. P. Pchelyakov *et al*, *Thin Solid Films* **306**, 299 (1997).

18th Int. Symp. "Nanostructures: Physics and Technology"
St Petersburg, Russia, June 21–26, 2010

Properties of silicon dioxide layers with embedded metal nanoclusters grown by pulsed laser deposition

A. Novikau[1], P. Gaiduk[1], K. Maksimova[2] and A. Zenkevich[2]

[1] Belarusian State University, prosp. Nezavisimosti, 4, 220030, Minsk, Belarus
[2] Moscow Engeneering-Physics Institute, 31 Kashirskoe road, 115409, Moscow, Russia

Abstract. A 2D layer of Me (metal) nanodots embedded in SiO_2 was produced by pulsed laser deposition followed by furnace oxidation and rapid thermal annealing. The samples were characterized structurally by using transmission electron microscopy and Rutherford backscattering spectrometry, as well as electrically by measuring C-V and I-V characteristics. It was found that the formation of a high density Me and silicide dots took place due to Me segregation induced by oxidation. Strong evidence of oxidation temperature as well as impurity type effect on charge storage in crystalline Me-nanodot layer is demonstrated by the hysteresis behavior of the high-frequency C-V curves.

Introduction

During the last decade, much attention has been focused on the investigation of semiconductor and metallic nanocrystals or nanoclusters (NC) embedded in dielectric matrices. The interest is motivated by possible applications of such nanocomposite structures. Particularly, semiconductor or metal NCs embedded in SiO_2 dielectric layer of a metal-insulator-semiconductor field-effect transistor (MOSFET) may replace SiN_x floating gate in conventional Flash memory devices, allowing for thinner injection oxides, and subsequently, smaller operating voltages, longer retention time and faster write/erase speeds [1–3]. The performance of such memory structure strongly depends on the characteristics of the NCs arrays, such as their size, shape, spatial distribution, electronic band alignment.

Several different approaches have been recently tested for formation of NCs in dielectric layers. Self-assembling of NCs in SiO_2 layers fabricated by low-energy ion implantation and different deposition techniques has been studied by several groups [4–7]. A strong memory effect in MOS devices using oxides with Si or Ge NCs was reported in [4,6]. However, implantation of Ge at the silicon — tunnel oxide interface creates trap sites and results in degradation of device performance [4]. The growth technique, using MBE deposition of 0.7–1 nm thick Ge layer, followed by rapid thermal processing was implemented in [8,9]. An alternative method for Ge NCs production has been recently proposed [10]. The method utilizes the following steps: low pressure chemical vapor deposition (LPCVD) of thin SiGe layer, thermal wet or dry oxidation, and thermal treatment in inert ambient (reduction).

In this paper a similar method is proposed to achieve a thin SiO_2 layers with embedded Au or Pt NCs. On the first step a thin Si:Me layer was grown by a pulsed laser deposition. Since Au and Si do not form any stable chemical compounds and there is no stable gold oxide, Au can be expected to precipitate in NCs during the oxidation of Si:Au alloy.

1. Experimental

Wafers of n-type (001) Si were used as substrates. The uniform SiO_2 layer of 6-nm-thick (tunnel oxide) was first grown in a dry oxygen ambiance. An amorphous Si:Me (Au, Pt) layer of 20-nm-thick was then grown by pulsed laser deposition at room temperature. The sandwiched Si:Me/SiO_2/Si samples were thermally oxidized in dry oxygen ambient at 640–725 °C for 60–540 min; i.e. at the maximum low temperatures for thermal oxidation of Si in dry oxygen. Finally, thermally oxidized structures were heated in dry nitrogen ambient at 900 °C for 30 s. A reference sample SiO_2/Si without NCs was prepared for comparison.

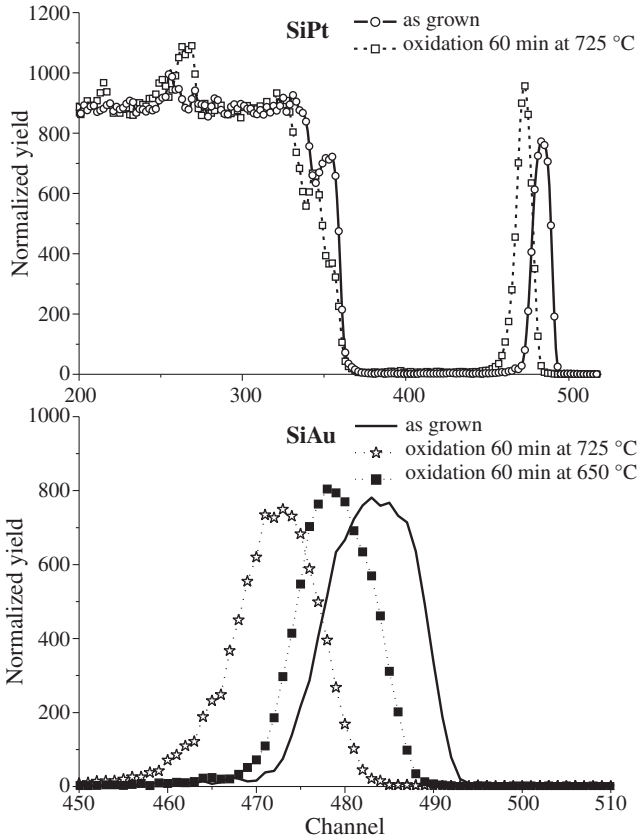

Fig. 1. RBS spectra from as grown and thermal oxidized SiMe/SiO_2/Si samples.

The composition and dopant depth distribution of the samples were measured by Rutherford backscattering spectrometry (RBS) using a 1.0–1.5 MeV He^+ beam and the spectra were analyzed by the RUMP program. The structure and phase quality were investigated by transmission electron microscopy (TEM) in plan-view and cross-section geometries with a Philips CM20 instrument operating at 200 keV. MOS capacitors with In electrodes were finally fabricated and high-frequency capacitance-

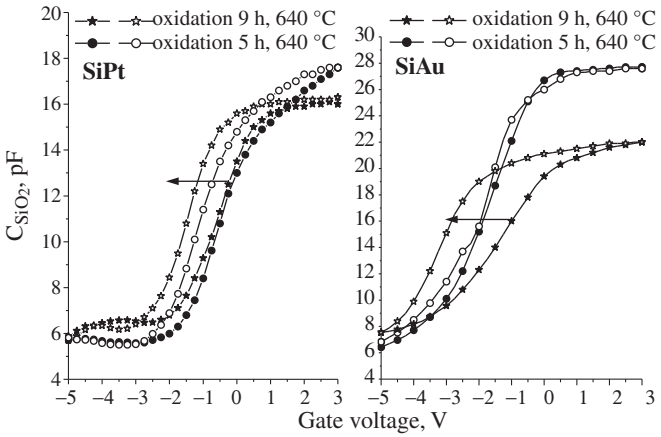

Fig. 2. High-frequency capacitance vs voltage curves of SiAu and SiPt samples oxidized in dry O_2 at 640 °C for 5–9 h.

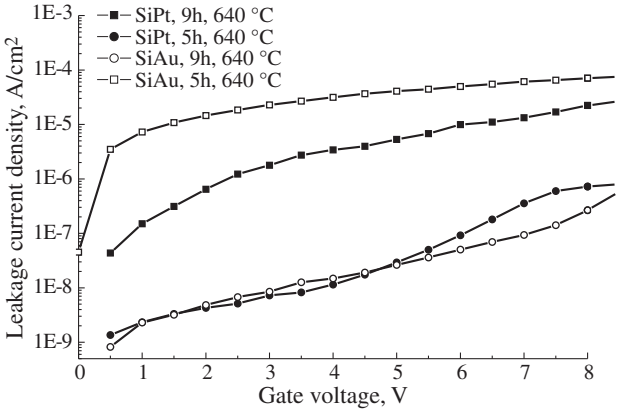

Fig. 3. Leakage current vs gate voltage characteristics obtained from SiAu and SiPt wafers oxidized dry conditions at 640 °C.

voltage (CV) measurements were carried out using a serial HP4156B instrument.

2. Results and discussion

The typical RBS spectra from the as grown and thermally treated samples are shown in Fig. 1. The RBS spectra show that the thickness of as deposited layers is about 22 nm. The layers contain Me-atoms in concentration in between 2.5–4.5%. It is clearly observed in RBS spectra, that thermal oxidation shifts the Pt peak to the region of lower energies; that corresponds pile up of Pt atoms at the SiO_2/Si interface. Thus, the transformation of concentration profiles of the Pt and Au, during thermal oxidation indicates the complete rejection of Me atoms from the oxide during the oxidation of a-Si:Me layer. The comparative analysis of RBS data (Fig. 1) reveals that Au and Pt segregation depends on oxidation conditions. In particular, neither evaporation nor diffusion of Au or Pt in SiO_2 layer takes place during thermal oxidation in dry O_2. On the contrary, oxidation at higher temperatures results in strong loss (about 30%) of Me from the SiO_2 layer, probably because of evaporation and partially diffusing into the Si substrate.

The results of our plan-view TEM investigations (published elsewhere [12]) correlate well with RBS data. Well-separated Au and PtSi clusters embedded in the SiO_2 layer are clearly observed after thermal treatment. The average size of NCs was obtained from the plan-view TEM image and estimated to be 10 - 20 nm. The conditions of oxidation and reduction were optimized taking into account Me segregation at the Si/SiO_2 interface and the highest value of charge storage capability.

The influence of oxidation temperature as well as embedded Me type on efficiency of charge storage was studied by high-frequency CV measurements. The difference in hysteresis values of the CV characteristics was found for the structures, containing Au or Pt NCs (Fig. 2).

The maximal value of a voltage shift was obtained in dry O_2 oxidation of SiAu structures and was measured to be 1.8 V for V_g shift $-5/3$ V. On the contrary, in the case of SiPt oxidation the maximum value of flat-band voltage shift is 1.2 V. High positive gate voltages force the CV curves to be shifted in the direction of stored negative charges. Thus, the charge trapping occurs through electron injection from the substrate into the oxide. Increasing of V_g sweep up to 5 V resulted in a gradual increase of the flat-band voltage shift. No flat-band voltage shift was observed for the reference sample prepared from the wafer with pure SiO_2, oxidized at 850 °C for 60 min in O_2 ambient. Thus, we assume that the effect of charge storage is related to metallic nanocrystals.

One of the major reasons for the loss of charge in the floating gate structures is the leakage current. The measured IV curves (Fig. 3) from SiAu and SiPt wafers oxidized in dry ambient reveals that the density of leakage current can be reduced to 10^{-8} A/cm^2. It is observed that the oxidation temperature effect on the level of leakage current is strong. The oxidation conditions should be optimized for each type of embedded metal NCs. We suppose that the low value of the leakage current was achieved due to high quality dry thermal growth of both tunnel and capping oxides compared to the deposited oxides, used in the alternative methods of MOS capacitor formation [13].

Acknowledgements

This work was funded by Belorussian and Russian Foundations for Fundamental Research (projects T08P-184 / 90023).

References

[1] Y. H. Kwon *et al*, *Appl. Phys. Lett.* **80**, 2502 (2002).
[2] S. Tiwari *et al*, *Appl. Phys. Lett.* **68**, 1377 (1996).
[3] S. Tiwari *et al*, *Appl. Phys. Lett.* **69**, 1232 (1996).
[4] P. Normand *et al*, *Appl. Phys. Lett.* **83**, 168 (2003).
[5] V. Beyer *et al*, *Phys. Rev. B* **77**, 014107 (2008).
[6] T. Baron *et al*, *Appl. Phys. Lett.* **83**, 1444 (2003).
[7] W. K. Choi *et al*, *Appl. Phys. Lett.* **80**, 2014 (2002).
[8] A. Kanjilal *et al*, *Appl. Phys. Lett.* **82**, 1212 (2003).
[9] A. Kanjilal *et al*, *Appl. Phys. A* **81**, 363 (2005).
[10] A. G. Novikau *et al*, *Proc. of ICMNE* **O3–O2** (2007).
[11] A. Hiraki *et al*, *J. Appl. Phys.* **43**, 3643 (1972).
[12] K. Yu. Maksimova *et al*, *Perspektivnye materialy* **2** (in press) (2010).
[13] Zerlinda Tan *et al*, *Appl. Phys. Lett.* **86**, 013107 (2004).

18th Int. Symp. "Nanostructures: Physics and Technology"
St Petersburg, Russia, June 21–26, 2010

Self-catalyzed molecular beam epitaxial growth of III–V nanowires on different substrates

Yu. B. Samsonenko[1,2,3], A. D. Bouravlev[2,3], N. K. Polyakov[1,2], V. P. Ulin[3], A. G. Gladyshev[2] and G. E. Cirlin [1,2,3]

[1] Institute for Analytical Instrumentation RAS, Rizhsky 26, 190103, Russia
[2] St Petersburg Academic University, St Petersburg, Russia
[3] Ioffe Physical-Technical Institute, St Petersburg, Russia

Abstract. The self-catalyzed molecular beam epitaxial growth of GaAs and InAs nanowires using in situ deposited III-group droplets on both GaAs and Si substrates with different treatment of the surface is investigated. The thin substrate native oxide is found to play a crucial role in the nanowire formation. The presence of the nanowires and there forms, sizes, growth directions and surface density is characterized by reflection high energy electron diffraction (RHEED) and scanning electron microscopy measurements.

Introduction

Self-standing III–V nanowires (NWs) are promising building blocks for future optoelectronic devices, in particular, LEDs, lasers, photodetectors and solar cells. NWs are usually grown by metal-organic chemical vapor deposition (MOCVD) or molecular beam epitaxy (MBE) via the so-called vapor-liquid-solid (VLS) mechanism [1,2] on the surfaces activated by the drops of a metal catalyst (e.g., Au). Due to ability relax strain in two dimensions, NW geometry is ideal for monolithic integration of materials with different lattice constants. However, it is well known that nanowires can be unintentionally contaminated by metal used as a catalyst for the growth and in many cases such contaminations can lead to the uncontrollable doping of growing crystals. Therefore, the methods of the growth of one-dimensional nanostructures without the using of any external catalysts have a great practical consequence [3]. The influence of conditions of self-catalyzed MBE growth III–V nanowires and different substrates and surface treatments on forms, sizes, growth directions and surface density was supposed to be found.

1. Experiment

NW growth experiments were carried out using EP1203 MBE setup equipped with different effusion cells including In, Ga, As at high vacuum conditions. Different treatments of the substrates were used prior to the growth. GaAs (111)B as well as Si substrates were chemically cleaned using standard technique, whereas the treatment in a 10% HF aqueous solution was applied to eliminate native SiO_2 layer from another Si substrate used in growth experiments.

GaAs NWs were grown at one technological cycle on both types of Si substrates at 590 °C. GaAs equivalent deposition rate was one monolayer per second. Ga/As_4 fluxes ratio was equal to 3. The short deposition of Ga without As flux was used to fabricated seeds for the NW growth. After this stage, the growth of GaAs NWs by the conventional MBE was initiated. The duration of the growth was 20 min.

As opposed to GaAs NW growth on Si, prior to the growth GaAs substrates were annealed to eliminate oxide overlayer. In this case, we did not deposited any Ga to create any seeds. Immediately after annealing procedure, the growth of GaAs NW was carried out at at 590 °C.

InAs NWs were grown only on Si substrates at 430 °C. The growth lasted for 10 min. InAs equivalent deposition rate was set 0.4 monolayer per second. The V/III fluxes ratio was equal to 3. Similar to the case of GaAs NW growth on Si, In seeds were fabricated before NWs growth in the absence of As flux at 475 °C.

The NW formation was characterized by in situ reflection high energy electron diffraction (RHEED). The substrate temperature was measured using an infrared pyrometer. The surface morphology of the samples was studied using scanning electron microscope (SEM) Supra 25.

2. Results and discussion

As for the most important results of the experiments, we have found the conditions that allow tuning for self-catalyzed molecular beam epitaxial growth of III–V nanowires on different substrates using EP1203 MBE setup. Although the RHEED patterns are not shown in this report, it was this method that enables us to find suitable conditions among number of experiments in initial stage.

It is easy to see from Fig. 1 the influence application of different substrates and various treatments of the surfaces on the form, density and distribution of growth direction self-catalyzed GaAs nanowires. We suppose that material, crystal structure and treatment surfaces affect first of all on the formation of seed drops or other type embryos and determine their form, size and density. Fig. 2 seems to support this statement. Since InAs NWs grow in more narrow range of parameters than GaAs NWs, we can see only the initial growth stage of InAs NWs on the part b) and only seed droplets on the part a). It can be found also reverse influence of the native SiO_2 layer in cases GaAs and InAs NWs growth.

Acknowledgements

Authors would like to thank V. G. Dubrovskii, N. V. Sibirev for helpful discussions.

This work was partially supported by different grants of Russian Foundation for Basic Research, Presidium of RAS and the Russian Federal Agency for Science and Innovation.

References

[1] E. I. Givargizov et al, Kristallografiya 18, 147 (1973).

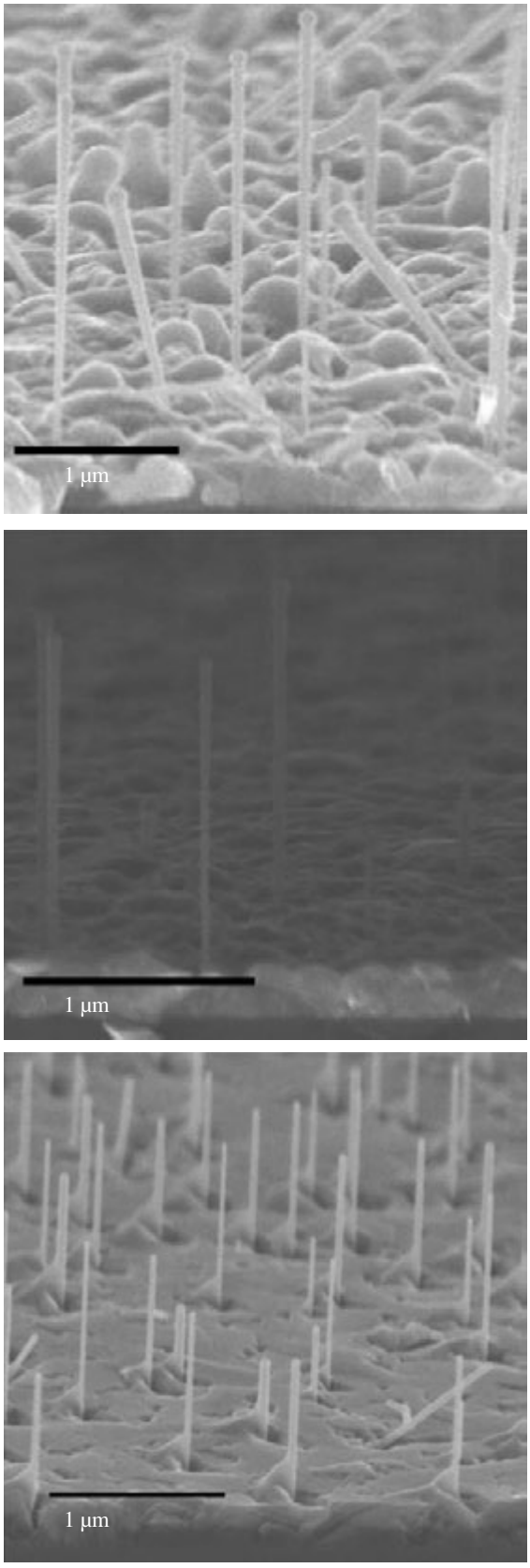

Fig. 1. Typical images of the surface after the growth process of GaAs NWs under 20° angle to the surface for three different type of substrate: (a) Si(111) covered with native SiO_2 layer; (b) Si(111) with special treatment surface; (c) GaAs(111)B substrate.

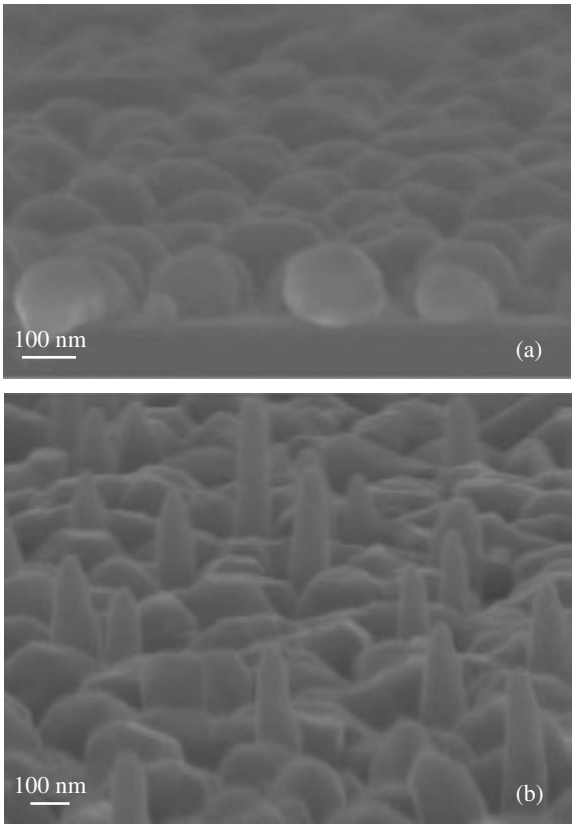

Fig. 2. Typical view on two different type of substrate after the growth process of InAs NWs under 20° angle to the surface: a) Si(111) covered with native SiO_2 layer; b) Si(111) with special treatment surface.

71, 205325 (2005).

[2] V. G. Dubrovskii, G. E. Cirlin, I. P. Soshnikov, N. V. Sibirev, A. A. Tonkikh, Yu. B. Samsonenko, V. M. Ustinov. Phys.Rev B

[3] A. Fontcuberta i Morral, C. Colombo, G. Abstreiter, Appl. Phys. Lett. **92**, 063112 (2008).

18th Int. Symp. "Nanostructures: Physics and Technology"
St Petersburg, Russia, June 21–26, 2010

A new process for fabricating carbon nanotubes

I. A. Korneev[1], V. A. Seleznev[1], V. Ya. Prinz[1], A. E. Zarvin[2], V. V. Kalyada[2] and N. G. Korobeishchikov[2]

[1] A. V. Rzhanov Institute of Semiconductor Physics SB RAS, Novosibirsk, 630090, Acad. Lavrent'ev Ave. 13, Russia
[2] Novosibirsk State University, Novosibirsk, 630090, Pirogov Str. 2, Russia

Graphene, a material appearing in the form of planar carbon monolayers, is remarkable for its unique physical properties such as, for instance, super-high mechanical strength and conductivity [1,2]. These properties make this material a promising one in the development of new nanoelectronic and nanomechanic devices [2,3]. A controlled process for forming 3D graphene shells from planar graphene layers would enable a new class of structures with unusual properties, for instance, those with giant magnetoresistance asymmetry, found in previously formed semiconductor shells [4]. A controlled transition from planar graphene layers to 3D graphene shells was first attempted in [5] using a mechanical action exercised on graphite surface with the help of an AFM probe tip. In this way, nanotubes and nanocorrugations were formed.

In the present work, like in our previous studies aimed at the formation of semiconductor nanotubes and other shells [6], we propose using the bending moment due to elastic forces, which would result in the self-rolling of graphene layers in tubes-scrolls.

For the first time we observed the formation of nanotubes from highly oriented graphite layers exposed to 500 eV Ar^+ ion bombardment. The tubes thus formed were more than 1 μm long, and their diameter was about 3 nm. Semi-contact atomic-force microscopy was employed to show that the nanotubes indeed could be formed from graphite monolayers which self-rolled from step edges on graphite surface and that the total number of turns in the obtained tubes could amount to several turns. Measurement data on the conductivity of formed tubes are reported.

The phenomenon observed in the present study may prove useful in the development of a controlled formation process for carbon nanotubes.

Acknowledgements

This work was supported by the Russian Foundation for Basic Research (Grant No. 09-02-01390-a).

References

[1] K. S. Novoselov *et al*, *Science* **306**, 666–669 (2004).
[2] K. I. Bolotin *et al*, *Solid State Comm.* **146**, 351 (2008).
[3] J. S. Bunch *et al*, *Science* **315**, 490 (2007).
[4] A. B. Vorob'ev *et al*, *Phys. Rev. B* **75**, 205309 (2007).
[5] V. Ya. Prinz, V. A. Seleznev *et al*, *Phys. Stat. Sol. B* **244**, 4193 (2007).
[6] V. Ya. Prinz *et al*, *Physica E* **6**, 1/4, 828 (2000).

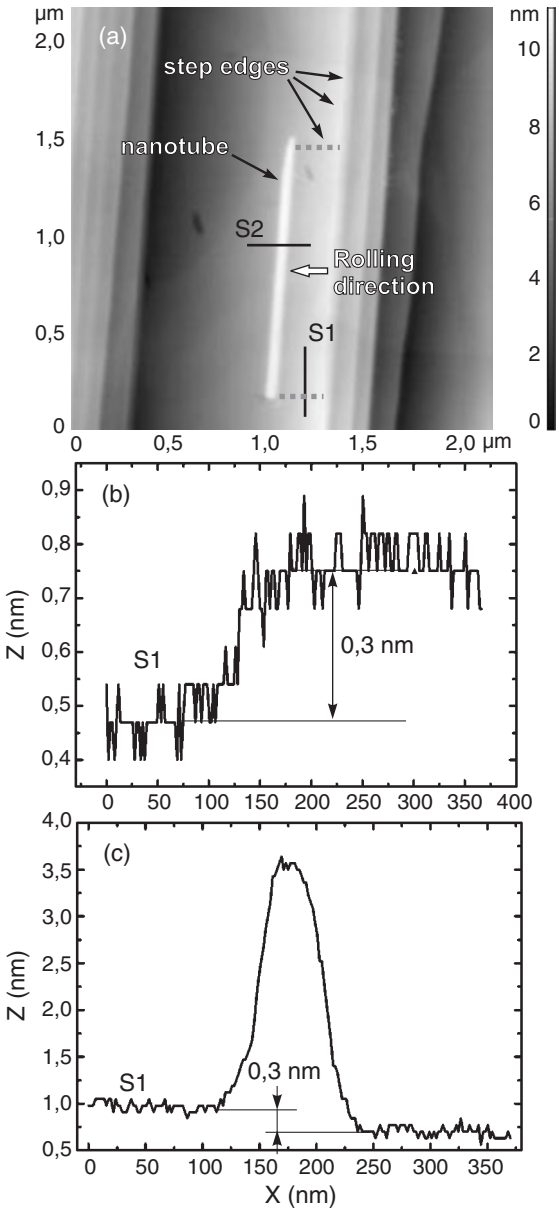

Fig. 1. Carbon nanotube was rolled from a monoatomic layer of graphite: a) AFM thopographic image of the graphite surface with monoatomic steps and carbon nanotube; b) AFM height profile along the straight line S1 marked in (a); c) AFM height profile along the straight line S2 marked in (a). It is clear from the profile lines S1 and S2 that carbon nanotube has been rolled only from the one atomic layer. Diameter of the nanotube is 2.8 nm. Number of coils is about 4. The nanotube was rolling up from the edge of step over a distance of 210 nm.

18th Int. Symp. "Nanostructures: Physics and Technology"
St Petersburg, Russia, June 21–26, 2010

GaAs nano-islands and nanowires grown by molecular-beam epitaxy on a graphite substrate

M. A. Putyato, V. Ya. Prinz, *V. A. Seleznev* and V. V. Preobrazhensky
A. V. Rzhanov Institute of Semiconductor Physics SB RAS, Novosibirsk, 630090, Acad. Lavrent'ev Ave. 13

For the first time, molecular-beam epitaxy was used to grow 3D GaAs nano-islands and nanowires on a pyrolitic graphite substrate. The nano-islands only nucleated at step edges and defect sites, with no nucleation having occurred on terraces (Fig. 1). Reflection electron diffraction data proved that the resultant nano-objects were single crystals. The size and morphology of the nano-objects were examined with the help of atomic-force microscopy. The nano-islands were faceted with (111) crystallographic planes, and their typical size was 30 nm. Following a prolonged growth, the nano-islands merged together with the formation of nanowires that delineated atomic steps on the graphite surface. Similar experiments with silicon revealed a substantial difference between the growth of GaAs and that of Si on graphite substrates. In the latter case, thin α-Si nanowires were found to grow along atomic steps.

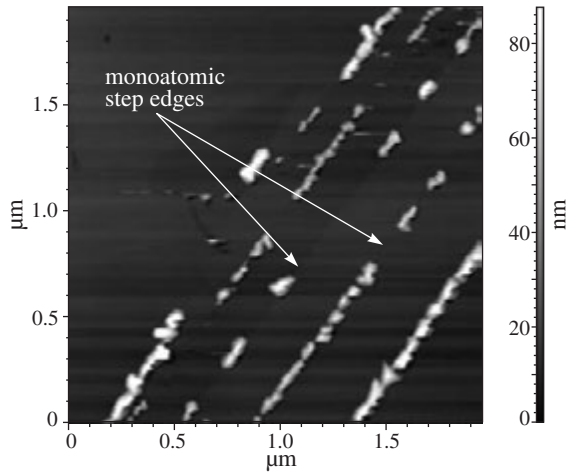

Fig. 1. AFM image of the pyrolitic graphite surface with monoatomic steps and GaAs nano-islands nucleated at step edges.

Prospects for further studies in the present field and potential applications of the process, for instance, for passivation of nanopore edges in graphene membranes are considered [1].

Acknowledgements

This work was supported by the Russian Foundation for Basic Research (Grant No. 09-02-01390-a).

References

[1] D. Jiang, V. R. Cooper, S. Dai, *Nano Lett.* **9** 12, 4019 (2009).

18th Int. Symp. "Nanostructures: Physics and Technology"
St Petersburg, Russia, June 21–26, 2010

New approaches to the elaboration of non-linear optical glasses with controlled nanostructure

V. N. Sigaev[1], S. V. Lotarev[1], N. V. Golubev[1] and G. E. Malashkevich[2]

[1] Optical Glass Center of Mendeleev University of Chemical Technology, 9 Miusskaya sq., Moscow 125047, Russia
[2] B. I. Stepanov Institute of Physics, NAS of Belarus, 68, Nezalezhnastsi Avenue, Minsk 220072, Belarus

Abstract. Two approaches to produce promising functional structures in glasses are known to be effective: via formation of phase inhomogeneities at early stages of the phase separation by heat-treatment and via spatially-selective crystallization of functional crystalline phases in the glass by laser irradiation. By example of Li_2O-ZnO-Nb_2O_5-$SiO_2(GeO_2)$ glasses we show that nano-inhomogeneous structure of the glass determines its second-order optical nonlinearity. It is also shown that $LiGa_5O_8$ nanocrystals precipitate in 0.1 mol.% NiO-doped $7.5Li_2O$-$2.5Na_2O$-$20.0Ga_2O_3$-$35.0GeO_2$-$35.0SiO_2$ glass heat-treated at 670 °C for 90 min, augmenting its luminescence efficiency. On the basis of the second approach a rapid local precipitation of $LaBGeO_5$ microcrystals with nearly monodisperse size distribution was realized in the lanthanum-boron-germanate glass using a copper vapor laser irradiation.

Progress in optoelectronics, integral optics, photonics and communications results in a rapid growth of the number of developments and studies on non-linear optical (NLO) materials. Oxide glasses possess high manufacturability, low cost, possibility to produce glassy objects of any desirable shape, good transparency and stable properties which can be gradually varied by an appropriate change of the glass composition. These advantages give rise to numerous attempts to elaborate glasses showing a high second-order optical non-linearity (SON). An efficient development of glasses possessing a SON is hindered with a poor understanding of atomic structure of multicomponent glass, as well as of nano-scale transformations producing inversion symmetry disturbance and ever-order nonlinearities origin. Nevertheless recently a number of fiber and planar devices (linear electro-optical modulators and switches, frequency converters etc.) was elaborated on the basis of thermally poled silica glass with periodically applied electrodes. These devises are shown to be efficient enough for commercial applications. Their further progress and extension of possible applications are limited with the relatively small SON characteristic of the poled silica glass.

Therefore developing approaches for systematic elaboration of the glass with a high and well-reproducible SON is a really urgent problem now. If such a glass were created then glass-based optoelectronic devises and integral optics elements could be a promising alternative to NLO crystals, subject to evident advantages of the glass in the field of fiber-optics technology.

In the present paper we represent two approaches to a generation of NLO structures in glasses: via formation of phase inhomogeneities at early stages of the phase separation by heat-treatment and via spatially-selective crystallization on NLO phases in the glass by laser irradiation.

By example of Li_2O-ZnO-Nb_2O_5-$SiO_2(GeO_2)$ glasses we show that nano-inhomogeneous structure of the glass (size, topology and chemical composition of the inhomogeneities) determines its SON and that controlled nanostructuring the glass with non-centrosymmetric phase inhomogeneities is a promising approach to the development of a new materials class — nanostructured glasses possessing a high SON for optoelectronics, integral optics and photonics.

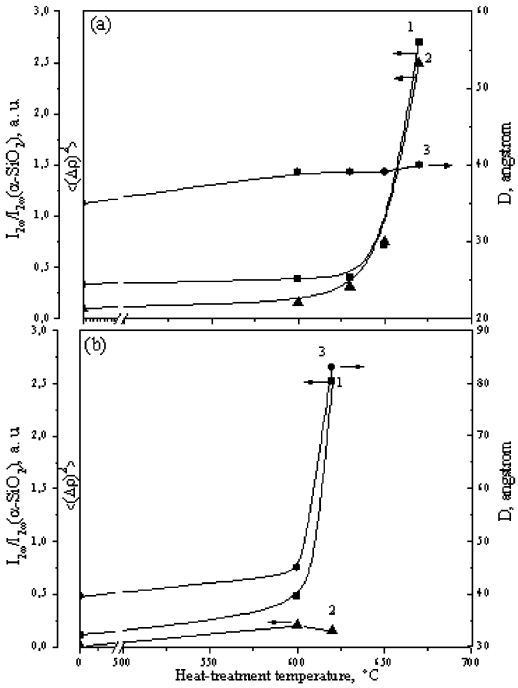

Fig. 1. Structural parameters of nanoinhomogeneities precipitated in the glass (see the text for details) and two scenarios of the SON enhancement in the nanostructured glass: precipitation of ferroelectric (a) and non-polar (b) phases.

As a result of the performed studies of nano-scale glass structure transformation and its influence on the NLO properties of the glass [1–7] together with the literature analysis a conception can be suggested that is 1) choosing a glass-forming system in which ferroelectric NLO phases can be crystallized; 2) finding a composition near a boundary of the glass-forming region or the amorphous phase separation region, or a glass-forming composition corresponding to the composition of the ferroelectric crystals; 3) initiation of a structural anisotropy in the glass by the thermal poling technique or by applying a high pressure 4) determining a narrow time-temperature region allowing a bulk nanocrystallization of the glass via the heat-treatment; 5) thermal poling of the nanostructured glass; 6) irradiating the glass by a focused laser beam resulting in

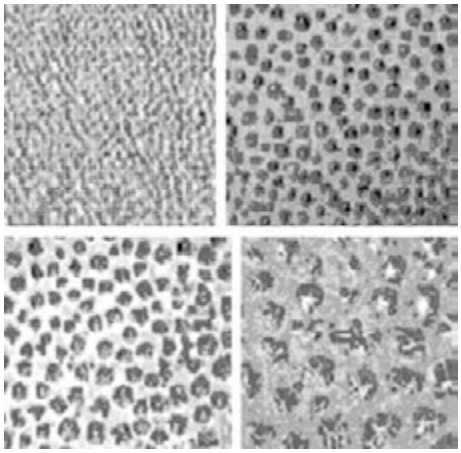

Fig. 2. Microphotographs of NLO $LaBGeO_5$ crystals precipitated in the glass bulk by copper vapor laser irradiation at different irradiation conditions. Scale: 1 cm corresponds to 20 μm.

micro- or nano-sized NLO crystals formation.

We have shown that nanoparticles which precipitate at temperatures near glass transition of glasses of appropriate compositions can manifest polar phase properties resulting in a high second harmonic generation (SHG) efficiency whereas the X-ray diffraction curve is quite smooth and characterizes the glass as fully amorphous. At nucleation stage, as the chemical differentiation increases, SHG signal grows up to 10 units of quartz powder standard and can be gradually varied even without further growth crystallites and keeping the glass transparent. This is illustrated by Fig. 1 in which difference of the electron densities $\langle(\Delta\rho)^2\rangle$ of the inhomogeneities and the glass matrix (1), relative SHG signal value $I_{2\omega}$ (2), inhomogeneities size D (3) vs. heat-treatment temperature are shown for two glasses taken as an example. Ferroelectric $LiNbO_3$ (à) precipitates in one of them and in this case SHG enhancement can be seen even at the stage characterized by fully amorphous X-ray diffraction picture. Non-polar $LiZnNbO_4$ phase precipitates in the other glass without noticeable SHG signal change.

SHG origin in glasses is determined by the nano-scale spatial modulation of the polarizability due to nano-scale chemical differentiation as well as by polarity of the precipitated nanoparticles.

Notion of slight nano-scale structural rearrangement in glasses at early stages of phase separation in the glass-forming systems which allow precipitation of polar phases is of great interest for a space-selective formation of the crystalline structures including periodical gratings, waveguides, couplers which are extremely interesting for integral optics. Laser irradiation is known to be very promising for obtaining such structures [6–10].

We have suggested a technique of local crystallization of the glass by laser irradiation [6] allowing nucleation and growth of the NLO microcrystals with nearly monodisperse size distribution in any required region of the glass within a split second. Fig. 2 shows NLO crystals of stillwellite-like $LaBGeO_5$ crystals in the lanthanum-boron-germanate glass which were obtained by irradiation with the copper vapor laser. A size and a number of crystals can be widely varied changing the irradiation conditions. This opens a way to elaboration of a new glass-ceramics materials type in which location of crystalline phase in the glass bulk is specified by the operator.

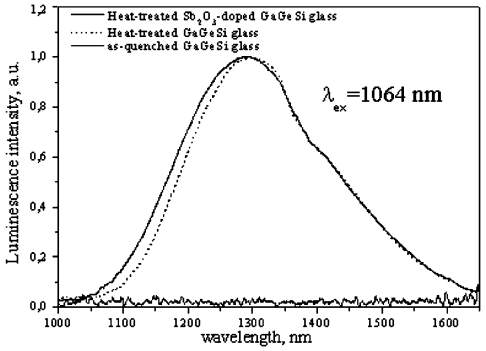

Fig. 3. Luminescence spectra of heat-treated (670 °C, 90 min) and as-quenched 0.1 mol.% NiO-doped GaGeSi glasses.

Two approaches described can be extended to some other functional properties which can be successfully improved by nanostructuring the glass. For example, it is known that luminescence efficiency in Ni-doped gallium-silicate glasses which is normally negligible due to strong nonradiative relaxation can be substantially enhanced by nanocrystallization of $LiGa_5O_8$ and Ga_2O_3 phases containing Ni^{2+} ions [11,12]. It is a key result for fiber and microchip laser applications. However, gallium-silicate glasses are difficult to obtain.

We show [13] that quantum yield of luminescence can be effectively enhanced in the 0.1 mol.% NiO-doped $7.5Li_2O$-$2.5Na_2O$-$20.0Ga_2O_3$-$35.0GeO_2$-$35.0SiO_2$ glass via heat treatment at 670 °C for 90 min (Fig. 3). Having a $\sim$ 100 °C lower melting point, this gallium-germanosilicate (GaGeSi) glass is far more manufacturable than the gallium-silicate one. It can be produced providing optical quality and keeps good transparency even after precipitation of Ni^{2+}-containing $LiGa_5O_8$ nanocrystals which is the only phase precipitating in the glass at those heat-treatment conditions.

Acknowledgements

This work is financially supported by Russian Foundation for Basic Research (FBR grant #10-03-00104), RFBR–CNRS program (grant #10-03-91056), and grant of the president of Russia MK-3594.2009.3.

References

[1] V. N. Sigaev *et al*, *J. Non-Cryst. Solid* **352**, 4142 (2006).
[2] V. N. Sigaev *et al*, *J. Non-Cryst. Solid* **353**, 1956 (2007).
[3] V. N. Sigaev *et al*, *J. Non-Cryst. Solid* **306**, 238 (2002).
[4] V. N. Sigaev *et al*, *J. Non-Cryst. Solid* **354**, 873 (2008).
[5] N. V. Sigaev *et al*, *J. Non-Cryst. Solid* **354**, 1909 (2008).
[6] N. V. Sigaev *et al*, *Glass Phys. Chem.* **35**, 13 (2009).
[7] N. V. Komatsu *et al*, *J. Amer. Ceram. Soc.* **90**, 699 (2007).
[8] T. Honma *et al*, *Opt. Mater.* **32**, 443 (2010).
[9] A. Stone *et al*, *Opt. Exp.* **17**, 582 (2009).
[10] P. Haro-Gonzalez *et al*, *Opt. Exp.* **18**, 582 (2010).
[11] T. Suzuki *et al*, *J. Luminescence* **128**, 603 (2008).
[12] T. Suzuki *et al*, *Appl. Phys. Lett.* **86**, 131903 (2005).
[13] N. V. Golubev *et al*, Proceedings of IV Int. Conf. "Actual Problems of Solid State Physics". October 20–23, 2009. Minsk, Belarus. Vol. 3. P. 360–362.

18th Int. Symp. "Nanostructures: Physics and Technology"
St Petersburg, Russia, June 21–26, 2010

Growth of ordered III–V nanowhiskers using electron lithography

I. P. Soshnikov[1,2], A. G. Gladyshev[2], Dm. Afanasyev[4], G. E. Cirlin[1,2,3], A. D. Bouravlev[1] and Yu. B. Samsonenko[1,2,3]

[1] Ioffe Physical-Technical Institute, St Petersburg, Russia
[2] St Petersburg Academic University, St Petersburg, Russia
[3] Institute for Analytical Instrumentation RAS, Rizhsky 26, 190103, Russia
[4] Physical department of St Petersburg State University, Ulyanovskaya 3, St Petersburg, 198504, Russia

Abstract. The fabrication of ordered nanowhiskers (ONWs) arrays using electron lithography is demonstrated. The influence of technological parameters on NWs morphology is studied.

Semiconductor nanowhiskers (NWs) (Si, GaAs, InP) have recently attracted an increasingly growing interest towards their applications in novel electronic and analytical devices [1–3]. Unfortunately, typical methods like fabricate non-ordered NWs that limits at investigation of different properties of individual NWs and in applying. There the work is devoted development of the fabrication of ONWs using electron beam lithography.

Prior to the growth, GaAs(111)B as well as Si(111) substrates were chemically cleaned. Then they were covered by electron resist 950 PMMA A (Microchem) using spin-coater. The thickness of the resist layer was varied from 50 to 100 nm. Electron beam exposure of PMMA was provided by scanning electron microscopes (SEM) Supra 25 C. Zeiss with special Raith Elphy kits tools. Development was done in 9% chlorobenzene solution. The ultrathin Au layer was deposited using VUP-5 chamber equipped by e-beam evaporation system. Lift off process was carried out in acetone.

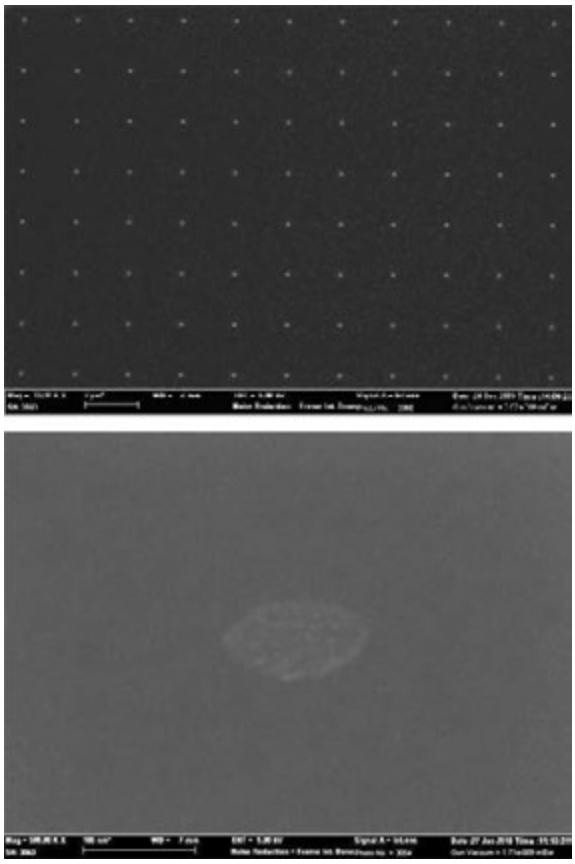

Fig. 1. SEM micrograph of plan view of array (top image) and one (bottom image) of Au nanodroplets.

Formation of AuGa nanodroplets and growth of GaAs and InAs NWs are realized by molecular beam epitaxial (MBE) set up EP1203 by methods described in [4,5]. The structure of NWs is examined in situ by reflection high energy electron diffraction (RHEED) [6].

In the work we fabricated array 100x100μ with activator (catalytical) Au — nanodroplet at step of 1, 2, 4, 6 μ. Typical SEM image of the array at step of 2 μ and individual catalytic Au nanodroplets are given on Fig. 1. Size of droplets is varied from 50 to 350 nm in result changing of electron beam energy and exposure (Fig. 2).

On the Fig. 3 we can see that NWs is grown in the region with lithographic window. In other region we can find only rare NWs while likely grown in defect of resist or spontaneous local autocatalytic activation of the surface. The density of "defective" NWs can 10^3 cm^{-2} and dependent on quality of lithographic process.

Detail studying corrected NWs demonstrated that NWs morphology dependent on specifics of substrate preparation, lithographic and growth processes, thickness and size Au droplet. Characteristic size of regular NWs is from 10 to 100 nm in diameter and before 10000 nm in length. Notice that char-

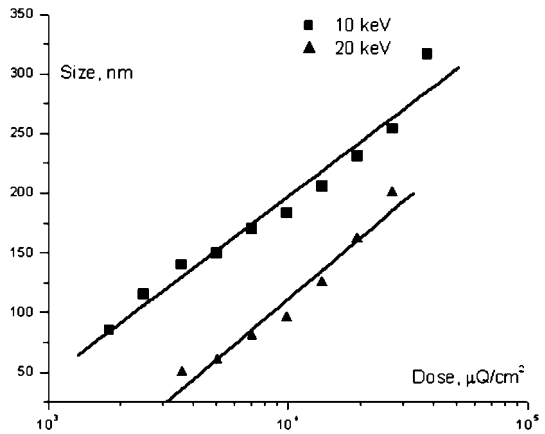

Fig. 2. Size of lithographic window vs electron beam exposure.

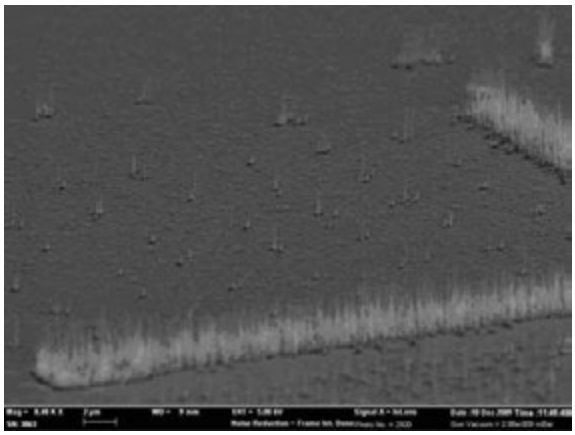

Fig. 3. SEM micrograph of lithographic Au catalytic "multiply" NWs.

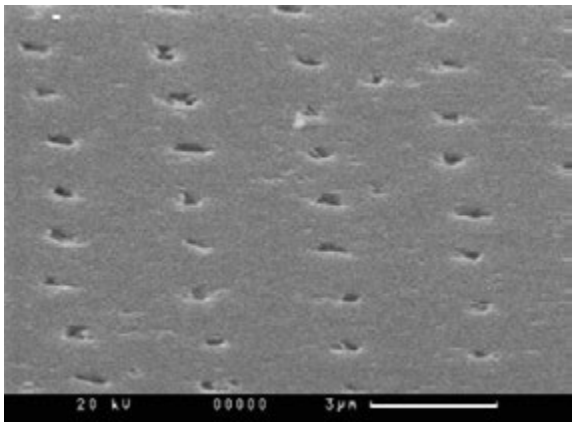

Fig. 4. SEM micrograph of "negative" NWs.

acteristic length of NWs is dependent effective thickness of deposited GaAs layer. At high thickness of Au layer and/or short time of annealing can find growth 2 and more NWs in the 1 lithographic cell (droplet) in ⟨111⟩ B direction (Fig. 3). The effect can be explained by formation of some AuGa nanodroplets. The excess of Au can effect on the growth of additional branches of NWs. Besides at optimal parameter can be fabricated regular massive of NWs with diameter about 20–30 nm and length before 10 μ and more.

Sometimes, we find "negative growth" of NWs, i.e. on the place lithographic windows is formation holes (Fig. 4). The phenomenon can be explained by effect of PMMA residue after lift off process.

Acknowledgements

Authors are greatly prof. V. G. Dubrovskii and prof. V. M. Ustinov for the helpful discussions. This work was supported by RFBR and scientific program "Quantum nanostructures" of RAS.

References

[1] C. Y. Zhi, X. D. Bai, and E. G. Wang, *Appl. Phys. Lett.* **86**, 213108 (2005).

[2] B. J. Ohlsson, M. T. Bjork, M. H. Magnusson, K. Deppert, L. Samuelson L. R. Wallenberg, *Appl. Phys. Lett.* **79** (20), 3335 (2001).

[3] T. Bryllert, L. E. Wernersson, T. Lowgren and L. Samuelson, *Nanotechnology* **17**, S227–S230 (2006).

[4] V. G. Dubrovskii, G. E. Cirlin, I. P. Soshnikov, N. V. Sibirev, A. A. Tonkikh, Yu. B. Samsonenko, V. M. Ustinov, *Phys. Rev. B* **71**, 205325 (2005).

[5] G. E. Cirlin, V. G. Dubrovskii, I. P. Soshnikov, N. V. Sibirev, A. A. Tonkikh, Yu. B. Samsonenko, V. M. Ustinov, *Semiconductors* **39**, 557 (2005).

[6] I. P. Soshnikov, G. E. Cirlin, A. A. Tonkikh, Yu. B. Samsonenko, G. Dubrovskii, V. M. Ustinov, D. Litvinov, D. Gerthsen, *Tech. Phys. Lett.* **34** (6), 538 (2008).

18th Int. Symp. "Nanostructures: Physics and Technology"
St Petersburg, Russia, June 21–26, 2010

Spectroscopic ellipsometry for characterization of MBE grown Si-whisker structures

S. N. Svitasheva, *F. N. Dultsev* and A. L. Aseev
Rzhanov Institute of Semiconductors Physics of RAS, Russia

Abstract. Silicon nanowhiskers (Si-NWs) were fabricated by the molecular beam epitaxy (MBE) with Au droplets on the top. This report is focused on the characterization of optical properties of Si- NWs structures by spectroscopic ellipsometry (SE) in visible and near UV field. Explanation of extra-ordinary optical properties NWs structures (giant absorption in the field of almost transparency of Si) is suggested here. The impacting of metallic layer of Ti and protecting layer of TiONx on optical properties of Si-NWs structures is demonstrated.

Introduction

Silicon-NWs are considered as promising candidates for post-CMOS logic elements due to their potential compatibility with the existing CMOS technology, letting to implement vertical surround-gate field-effect transistors [1]. Details of description of the molecular beam epitaxy (MBE) growth procedure are given in [2].

1. Dependence of optical properties from Si-NWs length

SE spectra of NWs structures are represented in terms of $\varepsilon_{\text{pseudo}}(E)$, as show in Figure 1.

Obviously, NWs layers are sufficiently transparent in the range of 1.5–3.0 eV so that it is possible to observe phenomenon of interference, amplitudes of which strongly depend upon NWs length (Fig. 1b) and their size distribution (Fig. 1a).

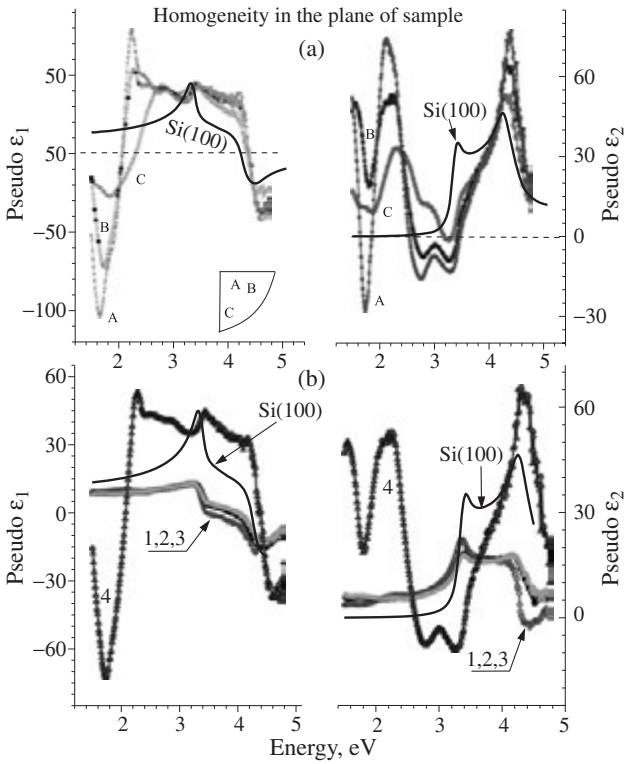

Fig. 1. a) Spectra A, B, and C of pseudodielectric functions of the sample 4 displayed non-homogeneity of the NWs distribution over the surface of sample in several points (A, B, C) on substrate as shown in the left insert of graph. b) Pseudodielectric functions of all our NWs structures differed from single crystal Si ones; NWs length for 1,2,3 and 4 are 210, 220, 240 and (580–990) nm, respectively.

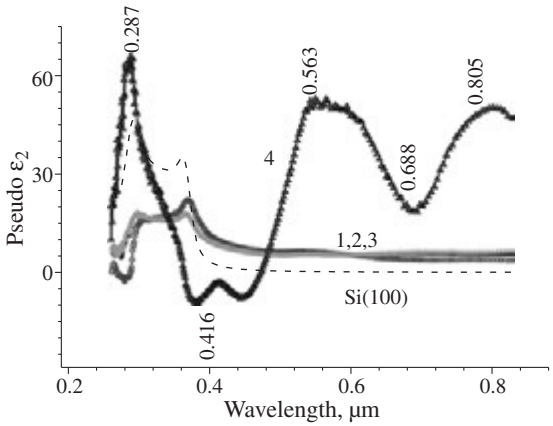

Fig. 2. Ellipsometric spectra $\varepsilon_2(\lambda)$ of Si-NWs structures (1, 2, 3, 4) and c-Si (100); and Table explaining Figure 2.

2. Explanation of extra-ordinary optical properties NWs structures . . .

Explanation of extra-ordinary optical properties NWs structures is suggested here.

Structures like our ones are now considered as metamaterial [3], optical properties of which are wonderful and their application promises to create extraordinary devices in future such as ultrahigh-resolution imaging systems and cloaking means, or optical switch using carbon nanotubes [4] and others. So it is very present-day and interesting problem to study optical properties of nanowhisker structures.

Table 1.

Whisker's length, μm	Wavelength of interference, μm		Extremum's positions (λ) in spectrum of ε_2, μm	
	λ_1 for $\Delta=\pi$	λ_2 for $\Delta=2\pi$		
$L_1 = 0.99$	1.39	0.699	—	0.688
$L_2 = 0.58$	0.82	0.41	0.805	0.416
$L_3=L_1-L_2=0.41$	0.579	0.289	0.576	0.287

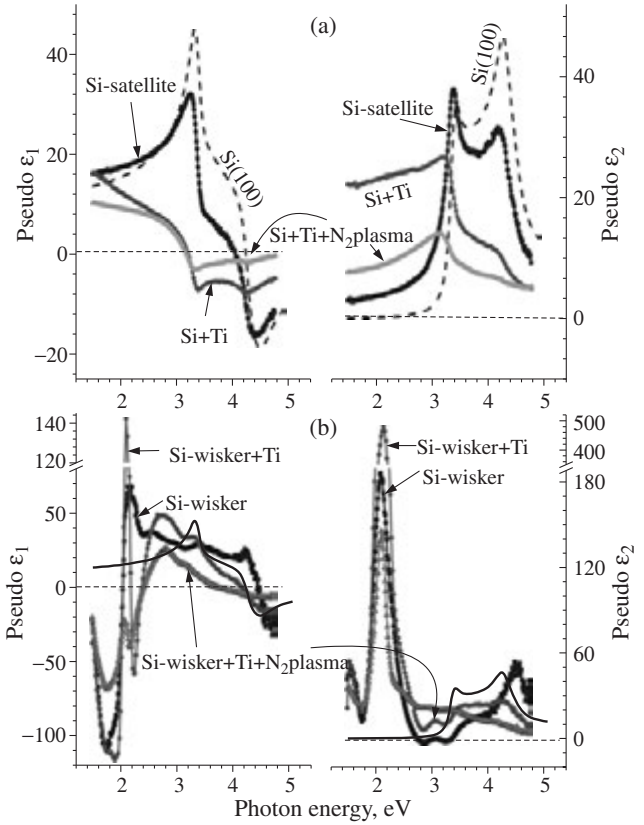

Fig. 3. Spectral dependences of optical properties (real ε_1 and imaginary ε_2 parts of pseudodielectric function) depending from films deposited: a) of satellite and b) of Si-NWs structure with great length of whiskers (580–990 nm).

3. Dependence of optical properties of NWs structures upon deposited films

In our experiment the metal Ti layer was simultaneously deposited both onto the 4-inch Si (001)-satellite wafers and onto Si NWs-structure in high vacuum (10^{-5}–10^{-7} Pa), using the e-beam sputtering technique.

Plasma-chemical nitridation of Ti nano-layers for protection nano-layers formation was carried out in plasma of nitrogen gas at pressure 0.2 Torr, with RF power 100 watt and radio frequency 13.56 MHz for 25 minutes at temperature 0 °C by several steps cyclically: nitridation for 1 minute and a cooling for 5 minutes. Parameters of a protecting layer TiONx were first studied using simplified structure of Si-satellite. With the purpose of definition of properties of a finite protecting layer, three ellipsometric spectra were successively registered in terms of pseudo-dielectric functions: 1) before and 2) after Ti film deposition and 3) after nitridation procedure of Ti film, as shown in Figure 3a.

4. Modeling and calculation of parameters of satellite

Thickness of native oxide SiO_2 was found from spectra marked in Figure 3a as Si-satellite. From the second spectra marked as Si+Ti, metal thickness and dielectric function of Ti were calculated. Dielectric function of transition metal Ti was approximated by a sum of four oscillators using as start spectra [5]. At last from the third spectra in Figure 3a marked as Si+Ti+N_2 plasma, thickness and spectral dependence of dielectric function of a protecting film were calculated by numerical method using the Marquardt-Levenberg method. As a result, 76 Å of metallic titanium were converted into 141 Å oxynitride TiONx, optical properties of which are similar to film properties described in [6–8]. The impacting of metallic layer of Ti and protecting layer of TiONx on optical properties of silicon nanowhisker's structures is demonstrated by Figure 3b. It is important to notice, that energy position of peaks of huge absorption in $\varepsilon_2(E)$ slightly depend upon deposited films, this fact confirms origin of peaks due to interference because length of whiskers is practically the same. Optical studies were carried out by spectroscopic Phase Modulated Ellipsometer UVISEL (ISA Jobin Yvon-Sofie).

References

[1] V. Smiidt, H. Riel, S. Senz, S. Karg, W. Riess, and U. Gosele, *Small* **2**, 85–88 (2006).
[2] N. Zakharov, P. Werner, L. Sokolov, U. Goesele, *Physica E* **37**, 148–152 (2007).
[3] D. R. Smith, S. Schultz, P. Markos, C. M. Soukoulis, *Phys. Rev. B* **65**, 195104 (2002); Metamaterials Publications.htm.
[4] P. Collins and P. Avouris, *Sci. American* 2000.
[5] P. B. Johnson, R. W. Christy, *Physical Review B* **9** 12, 5056–5070 (1974).
[6] E. Langereis, S. B. S. Heil, M. C. M. van de Sanden, and W. M. M. Kessels, *J. Appl. Phys.* **100** 023534 (2006).
[7] E. Langereis, S. B. S. Heil, M. C. M. van de Sanden, W. M. M. Kessels, *Phys. Stat. Sol. (c)* **2**, 3958 (2005).
[8] S. H. Mohamed, O. Kappertz, J. M. Ngaruiya, T. Niemeier, R. Drese, R. Detemple, M. M. Wakkad, M. Wuttig, *Phys. Stat. Sol. (a)* **201**, 90 (2004).

18th Int. Symp. "Nanostructures: Physics and Technology"
St Petersburg, Russia, June 21–26, 2010

Zinc oxide based nanostructures for light emitting diode applications

N. V. Tarasenko, A. P. Stupak, M. I. Nedelko and A. A. Nevar

B. I. Stepanov Institute of Physics of National Academy of Sciences of Belarus , 68 Nezalezhnasty Ave., 220072 Minsk, Belarus

Abstract. An unintentionally doped n-type and N-In codoped p-type ZnO nanoparticles were synthesized by submerged electrical discharge technique in water and in aqueous ammonium nitrate solution, respectively. The composition, morphology, absorbance and luminescent properties of the formed structures were studied. The synthesized ZnO nanostructures were employed to form the homojunction diode on Si(100) substrates. The results obtained showed that ZnO-based ultraviolet light-emitting devices could be realized using ZnO nanostructures synthesized by low cost electrical discharge technique.

Introduction

Last years, ZnO nanostructures have been found to have many novel properties and wide potential applications [1]. The specific physical and chemical properties of zinc oxide make it a promising candidate for applications in optoelectronic devices and light emitting diodes (LEDs) at room temperature (RT). Zinc oxide (ZnO) is a wide-bandgap (3.36 eV) semiconductor that has a stable wurtzite structure. ZnO has high exciton binding energy (60 meV), and it is able to operate in harsh environments, such as outer space and high radiation facilities [2]. However, a fabrication of p-ZnO materials with sufficiently high conductivity and carrier density is still a major problem, although there have been some recent reports on p-type doping in ZnO with N, As or P [3–5]. One hopes to increase the acceptor density in ZnO by co-doping method using nitrogen and a group-III element to prepare p-type ZnO [6,7]. The codoping method is expected to enhance the solubility of N in ZnO and the p-ZnO will be able to act as the source for hole injection. In this work, an unintentionally doped n-type and N-In codoped p-type ZnO nanoparticles were synthesized by submerged electrical discharge technique in water and in aqueous ammonium nitrate solution, respectively. The composition, morphology, absorbance and luminescent properties of the formed structures were studied. Electroluminescence (EL) emission from the ZnO homojunction LED structure was realized at room temperature.

1. Experimental

Several experimental conditions were tested to synthesize nanoparticles of different composition. The electrical discharge between two zinc electrodes immersed in distilled water was used to produce undoped ZnO nanoparticles. To synthesize of N-doped and In-N co-doped ZnO nanocrystals and fabricate of p-type ZnO we used electrical discharge between Zn-Zn and Zn-In electrodes immersed into the 0.001 M ammonium nitrate solutions. The experimental apparatus and experimental procedure for a preparation of nanoparticles by the electrical discharge method have been described earlier [8,9]. Metallic rods with diameters of 6 mm were employed as electrodes. The discharge was stable as long as a cathode-anode gap was less than 1 mm. The discharge current was monitored by means of the current viewing resistor. Voltage and current were recorded utilizing a digital oscilloscope. The pulsed spark discharges have been used. The discharge was initiated by applying a high-frequency voltage of 3.5 kV with a repetition rate of 100 Hz. The peak current of the discharge was 60 A with a pulse duration of 30 μs. The synthesized particles were obtained as colloidal solutions. The formed nanoparticles were characterized by optical absorption and photoluminescence spectroscopy for monitoring the changes in the absorption characteristics and luminescence properties, transmission electron microscopy (TEM) and X-ray diffraction (XRD) in order to determine the powder composition, its crystalline structure, lattice parameters and grain size. Nanopowders for XRD measurements were obtained after the drying of the colloidal solutions. The X-ray diffractometer D8-Advance (Bruker, Germany) was used for XRD measurements. The synthesized ZnO nanoparticles were deposited on Si(100) substrates to form the homojunction diode. The elemental composition of the films deposited on the substrate was detected using energy dispersive X-ray (EDX) spectrometer attached to the scanning electron microscope (SUPRA 55WDS, Carl Zeiss, Germany). The luminescence spectra of the deposited samples were measured with a spectral resolution of 1 nm on a Solar SFL-1211A spectrometer with a Xe lamp as excitation source.

2. Results and discussion

From the absorption spectra the optical band-gap (E_g) was determined using the relation $khv = (hv - E_g)^{1/2}$ ($hv > E_g$), where hv is the photon energy [10]. The optical band-gap was estimated to be approximately 3.36, 3.16, 3.0 and 3.22 eV corresponding to the ZnO, ZnO:In, ZnO:N, and ZnO:(N,In) samples. The estimated optical band-gap values for both the ZnO:N and ZnO:(In,N) samples were found to be shifted to lower energies compared to that for the undoped ZnO ($E_g = 3.36$ eV). Thus, there is an evident narrowing of the band gap after doping. Besides, the value of the bandgap for the synthesized undoped ZnO nanocrystals is lower than that of 3.38 eV [11] for the ZnO reported in the literature. This deviation is likely related to the size, defect energy levels or boundary characteristics effects [2]. The SEM investigation of the formed nanoparticles revealed loosely aggregated clusters consisting of rod-like grains with average diameter of about 30 nm and 80–100 nm in length. EDX line profile measurements supported the presence of In and N in the ZnO:(In, N) particles. As it followed from the XRD patterns the synthesized product was composed of hexagonal ZnO nanocrystals. The position of the reflection peaks were observed to be varied with the compo-

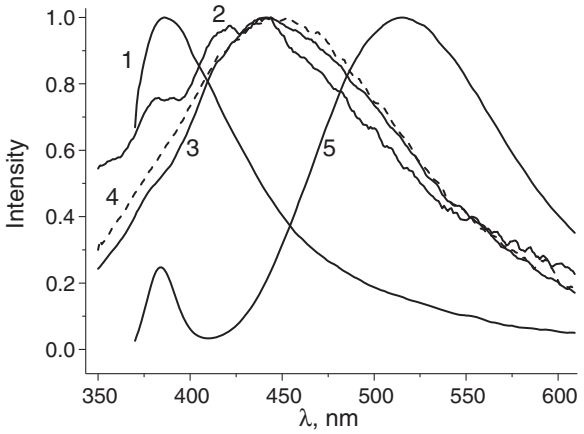

Fig. 1. Photoluminescence spectra of ZnO nanoparticles prepared in Zn-Zn discharge in water (1), Zn-In discharge in water (2), Zn-Zn discharge in NH_4NO_3 solution (3) and Zn-In discharge in NH_4NO_3 solution (4) and of commercial ZnO powder (5). The excitation wavelength used in PL measurements was 270 nm.

sition of dopants. The room-temperature luminescence spectra recorded for ZnO samples deposited on silicon substrates from the prepared solutions are presented in Fig. 1.

For comparison, a spectrum of the sample prepared from the commercial ZnO powder (bulk ZnO) with characteristic crystallite size of 0.5 μm is also shown. Before a deposition a small amount of this powder was ultrasonically dispersed in water and then dropped onto a silicon substrate. The UV emissions of different nanostructures were normalized. The luminescence spectrum of ZnO samples synthesized by electrical Zn-Zn discharge in water reveals the prominent UV-band at 380 nm and exhibits relatively weak violet emissions. For the sample prepared from the commercial ZnO powder, two peaks are observed in the PL spectrum: the relatively weaker UV band at 383 nm and a broad green emission band at about 515 nm. The PL emission of the doped ZnO samples exhibit red-shifted broad UV-violet bands with maximum around 430 nm. It is known that at room temperature, ZnO typically exhibits one emission peak in the UV region, and possibly one or more peaks in the visible spectral range (violet, blue, green, yellow and orange-red) which are attributed to defect emissions [12]. The UV photoluminescence peak can be ascribed to the near band edge excitonic emission, but the origin of different defect emissions is still not fully understood. The mechanism of visible emission is suggested mainly due to the present of various point defects, either extrinsic or intrinsic, such as oxygen vacancy, interstitial zinc, and antisite oxygen, which can easily form recombination centres [12,13]. The ratio IUV/IVIS may be used for relative evaluation of crystal quality. The low intensity of the green emission may be due to the low density of oxygen vacancies during the preparation of the ZnO samples, whereas the strong room temperature UV emission intensity should be attributed to the high purity with perfect crystallinity. In our ZnO nanoparticles prepared in Zn-Zn discharge in water, the PL spectra exhibit a strong UV emission, which confirms that the synthesized particles have good optical properties with few structural defects. The observed PL features of the doped ZnO samples can be related to the red-shift and decreasing of the UV emission band together with an appearance a violet emission band at (430 nm) which can be attributed to surface defects in the ZnO samples [13]. The red-shift of the near band edge emission band for the N-doped ZnO thin films have been observed in earlier works [3,14]. For example, an increase of N concentration in ZnO films was shown to increase both the red-shift of the near band edge peak position and the relative intensity of the visible peak of a N-doped sample [14]. Under a forward bias larger than 8 V, we observed an electroluminescence, which was composed of an ultraviolet peak centered at 390 nm and a green band around 540 nm. The results obtained prove that the electrical discharge in liquid technique is a simple, rapid, and low cost synthesis route for producing nanocrystalline ZnO powders with good crystallinity and properties. The whole procedure is cheap and could be easily extended to mass production.

Acknowledgements

The authors gratefully acknowledge the financial support of the National Academy of Sciences of Belarus (Grants #F08-077 and VET 2-16). The authors would like to thank Dr. E. I. Mosunov for his assistance in the XRD analysis and Dr. E. A. Sosnova for SEM and EDX measurements.

References

[1] Z. L. Wang, *Materials Today* **6**, 26 (2004).
[2] C. Klingshirn, *Phys. Status Solidi B* **244**, 3027 (2007).
[3] U. K. Gautam, L. S. Panchakarla, B. Dierre, X. Fang, Y. Bando, T. Sekiguchi, A. Govindaraj, D. Golberg, and C. N. R. Rao *Adv. Funct. Mater.* **19**, 131 (2009).
[4] H. von Wenckstern, G. Benndorf, S. Heitsch *et al*, *Appl. Phys. A* **88**, 125 (2007).
[5] Y. R. Ryu, T. S. Lee, J. H. Leem, H. W. White, *Appl. Phys. Lett.* **83**, 4032 (2003).
[6] H. Kim, A. Cepler, C. Cetina, D. Knies, M. S. Osofsky, R. C. Y. Auyeung, A. Pique, *Appl. Phys. A* **93**, 593 (2008).
[7] L. L. Chen, J. G. Lu, Z. Z. Ye, Y. M. Lin, B. H. Zhao, Y. M. Ye, J. S. Li, and L. P. Zhu, *Appl. Phys. Lett.* **87**, 252106 (2005).
[8] V. S. Burakov, N. A. Savastenko, N. V. Tarasenko, E. A. Nevar, *J. of Appl. Spectr.* **75**, 114 (2008).
[9] V. S. Burakov, E. A. Nevar, M. I. Nedelko, N. V. Tarasenko, *Techn. Phys. Lett.* **34**, 679 (2008).
[10] V. P. Gribkovski, *Theory of light absorption and emission in semiconductors* (Nauka, Minsk, 1974).
[11] S. J. Pearton, D. P. Norton, K. Ip, Y. W. Heo, T. Steiner, *Prog. Mater. Sci.* **50**, 293 (2005).
[12] A. B. Djurisic, Y. H. Leung, K. H. Tam *et al*, *Nanotechnology* **18**, 095702 (2007).
[13] S. Labuayai, V. Promarak, S. Maensiri, *Appl. Phys. A* **94**, 755 (2009).
[14] X. Wang, Y. M. Lu, D. Z. Shen, Z. Z. Zhang, B. H. Li, B. Yao, J. Y. Zhang, D. X. Zhao, X. W. Fan, *J. Luminescence* **122–123**, 165 (2007).

18th Int. Symp. "Nanostructures: Physics and Technology"
St Petersburg, Russia, June 21–26, 2010

Formation of α-MoO_3 (010) micropalettes for nanoarchitecture

I. B. Troitskaia, V. V. Atuchin, T. A. Gavrilova and D. V. Sheglov
Institute of Semiconductor Physics SB RAS, Novosibirsk, Russia

Abstract. α-MoO_3 micropalettes with high-quality surface are formed via recrystallization of intermediate molybdenum oxide at $T = 650$ °C. The intermediate molybdenum oxide was obtained by thermal decomposition of molybdenum formate at $T = 450$ °C under oxygen deficiency. The chemical composition, structure and micromorphology of α-MoO_3 micropalettes and intermediate products were examined by XRD, SEM, AFM, TG/DSC and IR spectroscopy methods. Results indicate the formation of α-MoO_3 micropalettes with ∼50 μm length, ∼10 μm width and ∼600 nm thickness, developed (010) crystal plane and high-quality flat surface.

Introduction

Further development of nanotechnologies demands much of top-quality of base plates [1] and their material [2]. Orthorhombic α-MoO_3 is characterized by unique layered structure which enables to form plate-like crystals with flat top-quality surface. This property gives an opportunity to use α-MoO_3 as a source material for the substrate fabrication. By virtue of layered structure, α-MoO_3 possesses such multifaced functional properties as modulation of electrical conductivity under contact with chemical gas agents, electrochemical activity, optical, photochromic and electrochromic properties. Numerous efforts were spent to prepare α-MoO_3 crystals as nanobelts, whiskers, nanorods and nanoslabs [3,4]. High-quality single crystals with up to $10 \times 2 \times 0.1$ mm^3 dimensions were obtained via the sublimation in two-zone furnace at $T = 790$ °C [5]. Present study is aimed to trace a formation of α-MoO_3 micropalettes with flat surface under thermal decomposition of molybdenum formate taken as a precursor. Significant area and high surface quality of the final micropalettes promise for creation of large-area α-MoO_3 substrate for nanoarchitecture.

1. Experimental

Synthesis of α-MoO_3 micropalettes shown in Fig. 1 was carried out by several stages. Firstly molybdenum formate was fabricated for using as a precursor. The 0.2 g $(NH_4)_6Mo_7O_{24} \cdot 4H_2O$ was dissolved in 10 ml of distilled water, then 5 ml of formic acid was added into the solution and precipitation was held at room temperature by 24 h. Microstructure of the white precursor crystals obtained was investigated by SEM with the LEO 1430 device. As it is seen in Fig. 2 molybdenum formate friable nanorods with ∼300 nm diameter and ∼5 μm length are formed by reaction. The nanocrystals can be easily dissolved in water or ethanol, therefore they were washed with acetone. The light-blue nanoplates of the intermediate molybdenum oxide were obtained by the thermal decomposition of the precur-

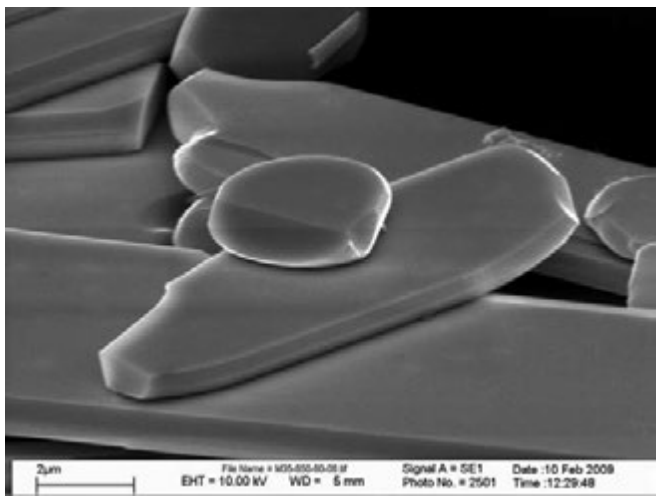

Fig. 1. SEM image of α-MoO_3 micropalettes.

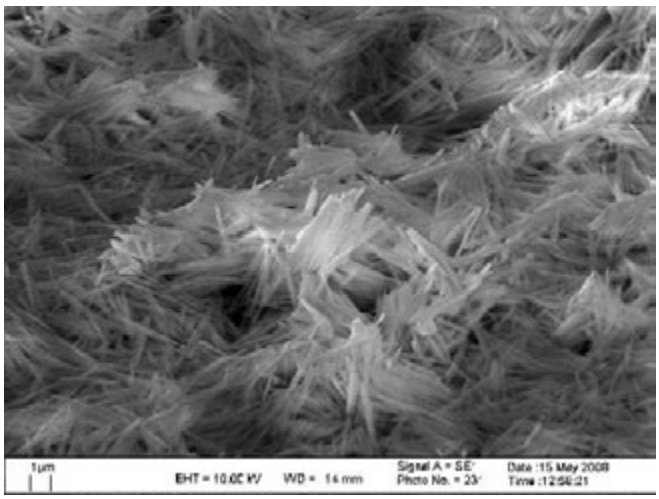

Fig. 2. SEM image of molybdenum formate nanorods.

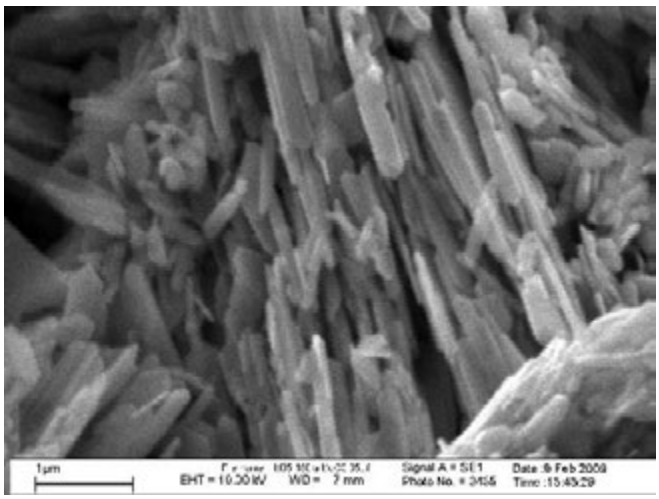

Fig. 3. SEM image of intermediate molybdenum oxide nanoplates.

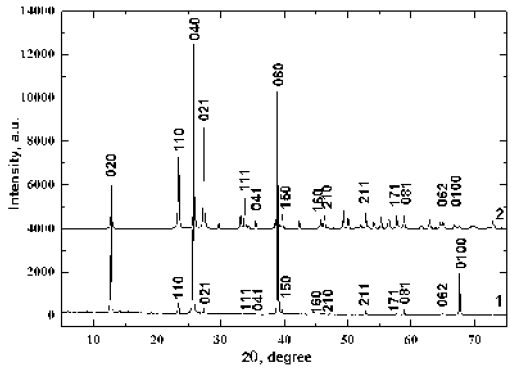

Fig. 4. XRD patterns of the micropalettes (curve 1) and calculated for α-MoO_3 (curve 2).

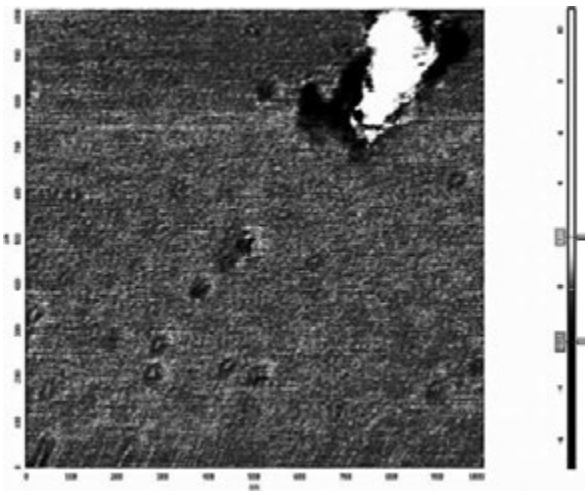

Fig. 5. AFM image of α-MoO_3 (010) micropalette surface.

sor nanorods under the oxygen deficiency and $T = 450$ °C. The nanoplates with ∼1 μm length, ∼250 nm width and up to 50 nm thickness are shown in Fig. 3. Finally the α-MoO_3 flat micropalettes were formed via recrystallization of the intermediate oxide at $T = 650$ °C during 9 h in the quartz open-type reactor in air atmosphere. As a result the pale-yellow plate-like micropalettes shown in Fig. 1 were formed. They have uniform ∼600 nm thickness, ∼50 μm length, ∼10 μm width, flat surface and sizeable surface area.

In Fig. 4 the XRD patterns are shown for the micropalettes. The experimental curve was carried out with DRON-UM1 device by 2θ scanning over 0–75° range. The recorded pattern is completely related to that calculated for α-MoO_3 phase (PDF 05-0508, sp. gr. $Pbmn$, $a = 0.0392$ nm, $b = 0.1385$ nm, $c = 0.03697$ nm). Evident change of the peak intensities in recorded XRD pattern proves the (010) primary orientation of α-MoO_3 micropalettes.

In Fig. 5 the AFM image of (010) surface of the α-MoO_3 micropalette is shown. It was obtained by SOLVER P-47H (NT-MDT) device. The surface is characterized by high general flatness with rms ∼0.16 nm. This value is comparable with α-MoO_3 cell parameter $b = 0.1385$ nm. Few local point defects are distributed over the surface and one of them is visible in the upper-right corner of the AFM image. Probably, these defects originate from the nonstoichiometric points of the intermediate oxide. These points should have specific recrystallization temperature and different recrystallization kinetic rate. On a basis of property investigations of intermediate molybdenum oxide and molybdenum formate by SEM, XRD, TG/DSC and IR spectrometry, the way to obtain the α-MoO_3 micropalettes with top-quality surface have been maped out.

References

[1] R. Waters, B. Zeghbroeck, *Appl. Phys. Lett.* **75**, 2410 (1999).
[2] I. E. Kalabin, T. I. Grigorieva, L. D. Pocrovsky, D. V. Sheglov, D. I. Shevtsov, V. V. Atuchin, *Opt. Commun.* **221**, 359 (2003).
[3] V. V. Atuchin, T. A. Gavrilova, V. G. Kostrovsky, L. D. Pokrovsky, I. B. Troitskaia, *Inorg. Mater* **44**, 622 (2008).
[4] C. V. Ramana, V. V. Atuchin, I. B. Troitskaia, S. A. Gromilov, V. G. Kostrovsky, G. B. Saupe, *Solid State Commun.* **149**, 6 (2009).
[5] H. C. Zeng, *J. Crys. Growth.* **203**, 547 (1999).

18th Int. Symp. "Nanostructures: Physics and Technology"
St Petersburg, Russia, June 21–26, 2010

Formation of Si nanocrystals and amorphous Si nanoclusters in silicon-rich nitride and oxide films using femtosecond laser pulse treatments

V. A. Volodin[1,2], T. T. Korchagina[1], A. A. Popov[3], M. Vergnat[4], J. Koch[5], B. N. Chichkov[5], J. Jedrzejewski[6] and I. Balberg[6]

[1] Institute of Semiconductor Physics of SB RAS, Lavrenteva ave., 13, Novosibirsk 630090, Russia
[2] Novosibirsk State University, Pirogova str., 2, 630090, Novosibirsk, Russia
[3] Yaroslavl Department of FTI RAS, University ave., 21, Yaroslavl, Russia
[4] Laboratoire de Physique des Matériaux, Nancy-Université, CNRS, Boulevard des Aiguillettes B.P. 239, 54506 Vandœuvre lés Nancy, France
[5] Laser Zentrum Hannover, Hollerithallee 8, 30419 Hannover, Germany
[6] Racah Institute of Physics, The Hebrew University, Jerusalem 91904, Israel

Abstract. Femtosecond laser treatments were applied for crystallization of amorphous silicon nanoclusters in silicon-rich nitride and oxide films. Regimes of crystallization of amorphous Si nanoclusters in the initial films were found. Effect of laser assisted formation of a-Si nanoclusters in the non-stoichiometric dielectric films with relatively low concentration of additional Si atoms was also observed. This approach is applicable for the creation of dielectric films with semiconductor nanoclusters on non-refractory substrates.

The interest in amorphous, nano- and microcrystalline silicon films on non-refractory inexpensive substrates and their crystallization is stimulated by demands of giant microelectronics. The enlargement of sizes of flat panel displays with active thin film transistor matrix can be described as "reverse Moor's low" [1]. Dielectric films with amorphous or crystalline Si clusters show promise as a material for optoelectronic and flash-memory applications [2]. Modern technique allows to produce the films at temperature as low as 100 °C. The problem of formation of amorphous Si nanoclusters and its crystallization is a topic of current research. The laser pulse crystallization has advantages in comparison with long time high temperature furnace annealing [3]. The present work is devoted to the development of laser assisted formation of a-Si nanoclusters in dielectric films and their crystallization.

The silicon reach nitride (SRN) films were deposited using low frequency plasma enhanced chemical vapor deposition technique. The stoichiometric parameter x in the SiN_x:H films was varied from 0.6 to 1.3 using various ratios of SiH_4 and NH_3 gases in the reactor during deposition. Some parameters of the films are described elsewhere [4]. The Si-rich SiO_2 films (SiO_x, $0 > x > 2$) were prepared using the co-sputtering from two separate Si and SiO_2 targets [5].

A Ti-Sapphire laser with a central wavelength of 800 nm and pulse duration of <30 fs was used for laser treatments of the initial films. Scanning treatments using x-y sample translation by computer-controlled motors were carried out. The pulse repetition rate was 1 kHz. We used laser fluences from 65 to 250 mJ/cm^2. Raman spectroscopy technique was used to identify the structure (amorphous or crystalline) of the Si nanoclusters in the films. Raman spectra were recorded in the back-scattering geometry with the 514.5 nm Ar^+ laser line.

According to Raman scattering data all SRN and Si-rich SiO_2 films with relatively high concentration of additional silicon contained amorphous Si clusters whose density in-creased with the concentration of the additional silicon. In the Raman spectra of nearly stoichiometric silicon nitride and silicon oxide films there were no peaks associated with vibrations of Si-Si bonds. So, one can assume that in this case the additional silicon does not form nanoclusters and the structure is close to random bonding (RB) model.

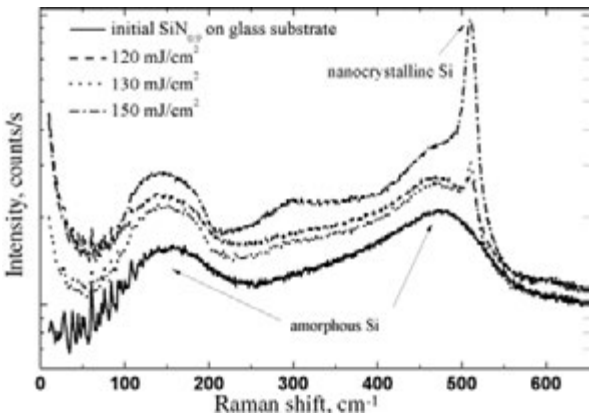

Fig. 1. Raman spectra of initial and laser treated SRN film.

In the case of femtosecond laser pulse the crystallization of amorphous Si films on glass substrates the threshold for full crystallization of the films with a thickness about 100 nm was found to be about 65 mJ/cm^2 [6]. Because of the absorption in the SRN films is lower, laser treatments with fluences up to 250 mJ/cm^2 were applied. Some Raman scattering data for initial and treated SRN films are shown in Figures 1 and 2.

The general trend in laser treatments of the SRN films is the more additional Si atoms are contained in the film — the less laser fluences were needed to crystallize or modify the silicon nanoclusters. It is obvious, because the absorbance coefficient grow with growing silicon amount in the SRN films. Even the femtosecond laser treatments with fluences up to 250 mJ/cm^2 were not enough to make visible structural changes in the $SiN_{1.3}$ film. In the $SiN_{1.2}$ film laser treatments stimulate only creation of small amorphous nanoclusters. As one can see in Figure 2 the initial $SiN_{1.2}$ film on Si substrate does not contain amorphous Si nanoclusters. The laser treatments not only

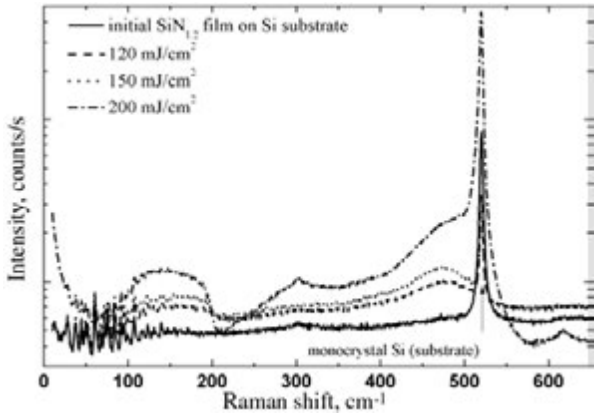

Fig. 2. Raman spectra of the initial and treated (by femtosecond laser pulses of various fluences) SRN film on Si substrates.

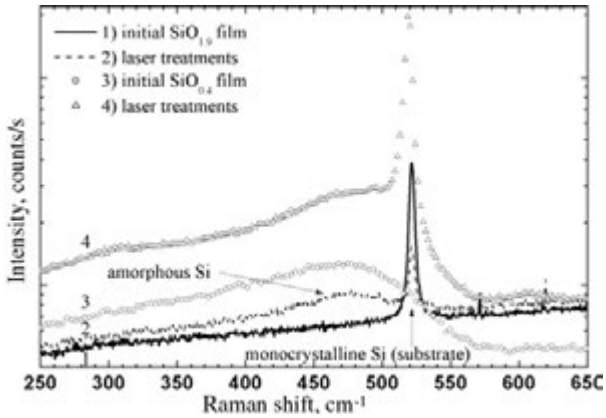

Fig. 3. Raman spectra of $SiO_{1.9}$ (curve 1) and $SiO_{0.4}$ (curve 3) initial films on Si substrates. Curves 2 and 4 are Raman spectra of $SiO_{1.9}$ and $SiO_{0.4}$ films after laser treatment with a fluence of 100 mJ/cm^2.

stimulate the growth of amorphous silicon nanocluster (amorphous peak is appeared), but also crystallize some nanoclusters ("nanocrystalline" peak is appeared). For the SRN films with stoichiometric parameter x lesser that 1.0 it was possible to crystallize all silicon nanoclusters using laser treatments with fluences of 120 mJ/cm^2 and larger. In the case of the SRN films on silicon substrates of some semitransparent films one can see in the Raman spectra a narrow peak at 520 cm^{-1} which is from the Si substrate (Figure 2). So, the femtosecond laser treatments lead not only to the crystallization of existed amorphous silicon nanoclusters, but also to growth or formation of new amorphous nanoclusters in the SRN films.

The structural changes of the SiO_x films under laser treatments were similar to those of the SRN films. From Figure 3 we see that, in the case of a low concentration of additional silicon, the laser treatment lead to the gathering of the randomly distributed silicon atoms thus yielding amorphous nanoclusters. In the case of high concentration of silicon it was possible to crystallize amorphous Si clusters with a formation of nanocrystals with sizes up to 10 nm (estimated from peak position on curve 4, Figure 3).

The measured PL spectra of initial and laser treated films were different. This is probably due to structural changes (crystallization and increasing of nanocluster's sizes) and the changes in non-radiative centers that are caused by crystallization [7].

For ultra-power femtosecond pulse impact one can assume that the non-linear effects play an important role in the light absorption. The optical gap of silicon nitride is about 5 eV while the average energy of the photons in the Ti-sapphire laser is 1.5 eV. The photon energy is not enough for effective absorbance even in a-Si:H films with an optical gap 1.5–1.9 eV [6]. Supposedly, multi-photon processes can take place. The pulse duration in our case is much lower than the time of electron-phonon interaction in semiconductors (about 1–2 picoseconds). So, that during the pulse the "hot" electron-hole plasma does not excite vibration modes in silicon and does not relax. According to some theoretical calculations, when the concentration of "hot" electrons approaches to 9–20% of the Si atoms concentration, silicon becomes unstable [8]. This meta-stable stage can relax to more stable crystalline phase without melting, but with generation of latent heat of crystallization. So, this process is similar to "explosive" crystallization. In the case of laser assistant gathering of additional silicon into cluster, surpassingly some laser assistant diffusion mechanisms take place. It can be thermal post-pulse diffusion or diffusion due to the brake up of valence bonds by multiphoton absorbance.

To summarize, the possibility of applying femtosecond laser pulses to crystallize amorphous Si nanoclusters in SRN and SiO_x films on different substrates was demonstrated for the first time to yield crystallization of amorphous silicon nanoclusters. The laser fluences for crystallization were found for the films of various non-stoichiometry. Also, the effect of laser assistant formation of amorphous Si nanoclusters in SRN films and SiO_x films with relatively low concentration of additional silicon atoms was observed. The approach developed here can be used for the creation of dielectric films with semiconductor nanoclusters on non-refractory substrates.

Acknowledgements

V.A.V is grateful to DAAD and RFBR for support.

References

[1] M. S. Shur *et al*, *10th International Symposium "Nanostructures: Physics and Technology"*, 2002, p. 618–622.
[2] Nae-Man Park *et al*, *Phys. Rev. Lett.* **86**, 1355 (2001).
[3] V. A. Volodin *et al*, *Appl. Phys. Lett.* **73**, 1212 (1998).
[4] T. T. Korchagina *et al*, *17th International Symposium "Nanostructures: Physics and Technology"*, 2009, p. 266–267.
[5] N. Karpov *et al*, *Journal of Optoelectronics and Advanced Materials* **11**, 625 (2009).
[6] V. A. Volodin *et al*, *JETP Letters* **86**, 119 (2007).
[7] M. Molinari *et al*, *Europhysics Letters* **66**, 674 (2004).
[8] J. Bok *et al*, *Phys. Letters A* **84**, 448 (1981).

18th Int. Symp. "Nanostructures: Physics and Technology"
St Petersburg, Russia, June 21–26, 2010

The growth of inclined GaAs nanowires during molecular beam epitaxy: Theory and experiment

Xu Zhang[1,2], N. V. Sibirev[2], G. E. Cirlin[2,3], C. Sartel[4], M. Tchernycheva[4], J. C. Harmand[3] and V. G. Dubrovskii[2]

[1] Key Laboratory of Information Photonics and Optical Communications (Ministry of Education), Beijing University of Posts and Telecommunications P.O. Box 66, Beijing 100876, China
[2] St Petersburg Academic University, St Petersburg, Russia & Ioffe Physical-Technical Institute, St Petersburg, Russia
[3] CNRS-LPN, Route de Nozay, 91460 Marcoussis, France
[4] Department OptoGaN, Institut d'Electronique Fondamentale, UMR 8622 CNRS, 91405 Orsay Cedex, France

Abstract. The growth mechanism of inclined GaAs nanowires during molecular beam epitaxy (MBE) is investigated theoretically. A kinetic model is proposed that account for the Gibbs–Thomson effect, the nucleation-mediated growth, the desorption from the sidewalls and the adatom diffusion from the surface to the top of nanowires. The decreasing length/diameter dependence of the inclined nanowires is obtained that fits the experimental data well. The length of the inclined nanowires as a function of radius under different thickness of the deposited material and various inclined angle is investigated by theoretically and compared to the experimental data. It is shown that the inclined GaAs nanowires grow faster than the vertical ones. By fitting our theoretical curves to the experimental data, we can deduce some important parameters of nanowire growth, in particular the diffusion lengths on different surfaces and the supersaturation.

Introduction

The growth mechanisms of III–V nanowires in different epitaxy techniques have drawn a great of interest recently. The difference between the vertical and the inclined nanowires is that they are grown on the substrates of various crystal orientations, because the preferred nanowire growth direction is [111]. The growth angle of the inclined nanowires is determined by the direction of crystal surface. In this work, the GaAs inclined nanowires grow on the GaAs (211) surface activated by Au are presented experimentally, the theoretical model is proposed under the consideration of adsorption-desorption effect, Gibbs–Thomson effect [1], and adatom diffusion from the surface to the top of nanowires. Theoretical and experimental normalized length/diameter curves are compared to each other and a good correlation between them is demonstrated.

1. Theoretical model

The model of the inclined nanowires is sketched in Figure 1. The impingement flux is defined by the effective arrival rate J, which equals the deposition rate over the atomic volume in the solid state, $J = V/\Omega \cos\alpha$. We do not consider the nonstationary growth effect and lateral growth of the nanowires.

The steady state growth model of the inclined nanowires

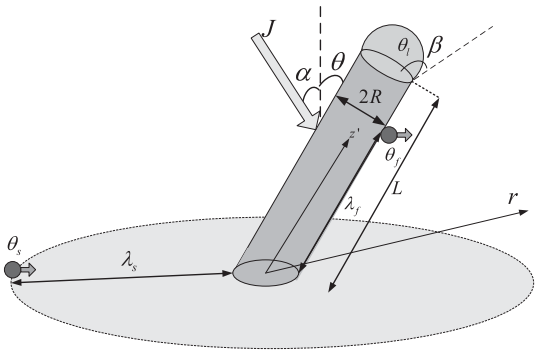

Fig. 1. Illustration of the growth model.

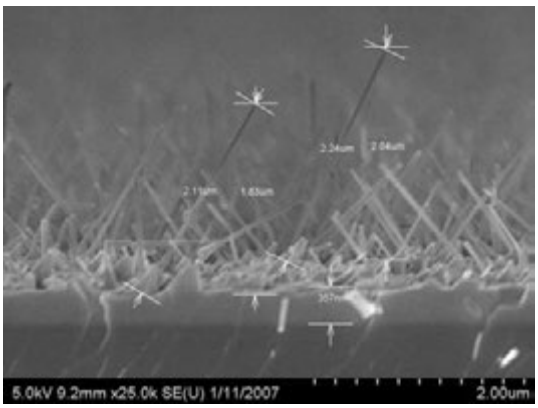

Fig. 2. The MBE grown GaAs nanowires, the inclined angle is $\theta = 25^\circ$, the substrate is GaAs(211), and the thickness of deposited material is 357 nm.

for the concentration of adatoms at the sidewall surface n_f, and at the substrate surfacen_s, satisfy the following diffusion equations:

$$D_f \frac{d^2 n_f}{dz'^2} + \frac{1}{\pi} J \sin(\alpha + \theta) - \frac{n_f}{\tau_f} = 0, \quad (1)$$

$$D_s \Delta n_s + J \cos\alpha - \frac{n_s}{\tau_s} = 0. \quad (2)$$

Here, D_f and D_s are the diffusion coefficients for adatom at the lateral surface and at the substrate surface, respectively. Δ is the two dimentional Laplace operator in the plane of the substrate. τ_f and τ_s are the average lifetime of an adatom at the lateral surface and substrate respectively. On the left hand of the above equations, the first term describe the diffusion; the second and third term describe the adsorption and desorption and/or nucleation, respectively. α and θ are the incident angle of beam and the inclined angle of the nanowires, respectively.

Following the procedure of Ref. 2 and 3, take into account the factor of the adsorpton-desorption at the droplet surface, the rate of growth of the inactivated surface, and the diffusion flux toward the top of nanowires , which contribute to the growth

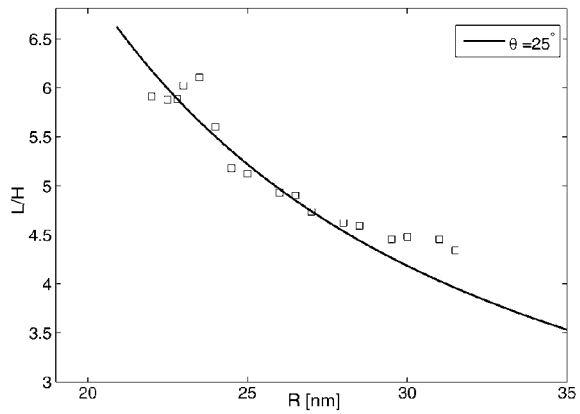

Fig. 3. The solid line is calculated from Eq. (3) at $\theta_s = 32$, $\theta_f = 9$, $R_{\mathrm{GT}} = 6.6$ nm and the squares represent the experimental data.

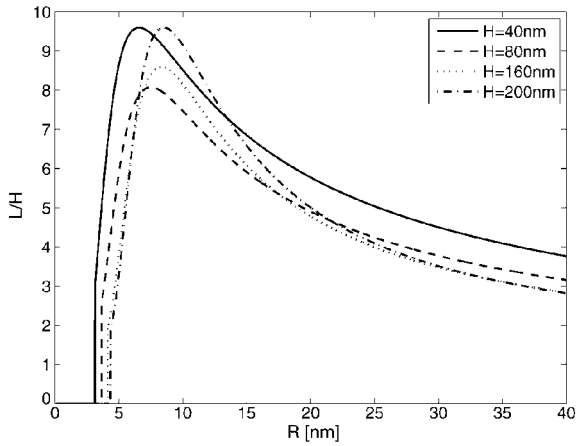

Fig. 4. The nanowire length as a function of radius, at different thickness of deposited material.

of the nanowires. The solution of the above is present in the form

$$\frac{dL}{dH} = A + \frac{2}{R\cos\alpha} \times \frac{\left(1-\frac{\theta_l}{\theta_s}\right)\lambda_s\delta\cos\alpha + \left(1-\frac{\theta_l}{\theta_f}\right)\left(\frac{\lambda_f}{\pi}\right)U\left(\frac{L}{\lambda_f}\right)\sin(\alpha+\theta)}{U'(L/\lambda_f)}. \tag{3}$$

The coefficient A describes the adsorption-desorpion at the droplet surface and the growth of the inactivated surface. $\theta_s = J\tau_s\sigma_s\cos\alpha$ is the activity of adatoms at the substrate surface; $\theta_f = \pi^{-1}J\tau_f\sigma_f\sin(\alpha+\theta)$ is the activity of adatoms at the WNC surface; $\theta_l = \exp(\mu_l^{\infty}/k_{\mathrm{B}}T + R_{\mathrm{GN}}/R)$ is the activity of the liquid solution in the droplet; R_{GT} is the Gibbs–Thomson radius; μ_l^{∞} is the chemical potential in the bulk's liquid phase; k_{B} is the Boltzmann constant; T is the surface temperature.

2. Results

Fig. 2 demonstrates SEM image of MBE grown inclined GaAs nanowires. The inclined angle of nanowire is $\theta = 25°$, the substrate is GaAs(211), and the thickness of deposited material is 357 nm. Figure 3 shows a good agreement between the proposed model and the experimental data.

Theoretical analysis about the dependence of the inclined nanowire length on the radius at different thickness of deposited material and various inclined angle is shown in Fig. 4 and Fig. 5 respectively.

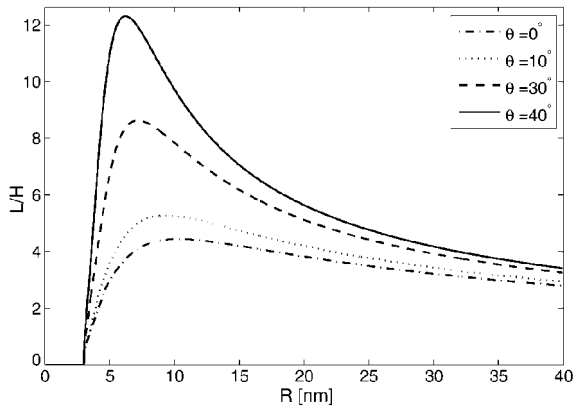

Fig. 5. The nanowire length as a function of radius, at the inclined angle of 0°, 10°, 30°, 40°, respectively, and $\theta_s = 32$, $\theta_f = 9$, $R_{\mathrm{GT}} = 6.6$ nm, $H = 357$ nm.

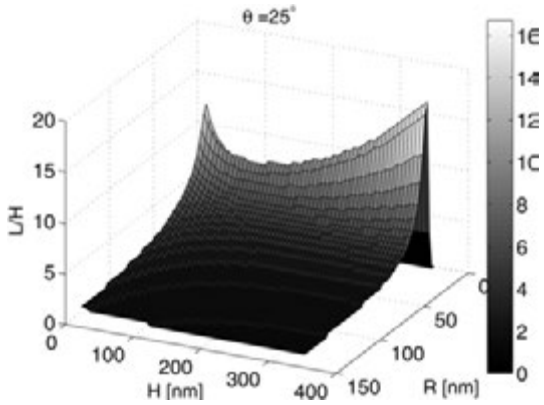

Fig. 6. The nanowire length as a function of radius and the thickness of deposited material.

We can conclude from Fig. 5 that the inclined angle affects the length of nanowire, especially the nanowire of small radius, but the angle has little effect with regard to the nanowire of large radius. Fig. 6 shows the length of nanowire as a function of both the radius the thickness of deposited material, from this figure we can deduce that there are two local maximum length of nanowire in the range of H from 40 nm to 350 nm at the radius about 8 nm. The best fit to the experimental data allows us to obtain the following values of parameters: the diffusion length of adatoms at the substrate and the lateral surface equals 100 nm and 6000 nm respectively.

Acknowledgements

This work was supported by the 111 Project (No. B07005), Program for Changjiang Scholars and Innovative Research Team in University (IRT0609) and National Basic Research Program of China (No. 2010CB327600).

References

[1] E. I. Givargizov *et al*, *Kristallografiya* **18**, 147 (1973).
[2] V. G. Dubrovskii *et al*, *Phys. Rev. B* **80**, 205305 (2009).
[3] N. V. Sibirev *et al*, *Technical Physics*, **54**, 586 (2009).

18th Int. Symp. "Nanostructures: Physics and Technology"
St Petersburg, Russia, June 21–26, 2010

Self-organized quantum dots for single photon emitters

Erik Stock[1], Anatol Lochmann[1], Waldemar Unrau[1], Andrei Schliwa[1], Askhat K. Bakarov[2], Aleksandr I. Toropov[2], Ilia A. Derebezov[2], Vladimir Haisler[2] and Dieter Bimberg[1]

[1] Institut für Festkörperphysik, TU-Berlin, 10623 Berlin, Germany
[2] Institute of Semiconductor Physics, 630090 Novosibirsk, Russia

Abstract. The development of semiconductor based single photon and entangled photon emitters with high out-coupling efficiency will be the key for quantum key distribution systems. We have developed InGaAs/GaAs quantum dot (QD) based Resonant-Cavity LEDs (RC-LED). The resonant cavity leads to an increased external quantum efficiency and due to the Purcell effect to an increased spontaneous emission rate. QDs grown on 111 GaAs substrate are a promising system for the generation of entangled photon pairs.

Introduction

A network providing communication secured by principle physical laws is possible based on quantum cryptography. One fundamental building block in a quantum cryptography network is a robust and easy to handle source of single photons or entangled photon pairs. Self-organized quantum dots (QDs) demonstrated their excellent capability for a such compact device [1]. Electrical pumping of single QDs embedded in pin-diode structures poses two main challenges: The first is the control of the current path in a way that only one QD is pumped, and the second is to assure that the QD is equally filled by electrons and holes to achieve emission from uncharged excitons. Thus the uncharged biexciton-exciton decay cascade can be used for the creation of entangled photon pairs (provided the fine-structure splitting (FSS) is small enough) or single polarized photons (for large FSS), prerequisite for the BB84 protocol. The second key specification to single photon sources for the realization of a quantum cryptography system is a high repetition rate and a low fraction of empty pulses. Both are essential for high and secure key transmission rate. The repetition rate in QD based single photon sources is limited by the exciton life time and the parasitic electrical bandwidth of the device, whereas the number of empty pulses is mainly controlled by the out-coupling efficiency.

1. High speed single photon sources

We realized a highly efficient single photon sources (SPS) operating at repetition frequencies up to 1 GHz based on well established semiconductor technology: Our device consists of a GaAs layer with low density (around 10^9 cm^{-2}) of InAs QDs, a 60 nm-thick AlGaAs aperture layer with high aluminium content and p- and n-type GaAs electrical contact layers. The aperture is used to confine the electric current in order to address a single QD. To increase out-coupling efficiency and to decrease the exciton lifetime further, this structure was embedded in a micro-cavity, consisting of 12/5 GaAs/AlAs-DBR mirror-pairs on the bottom/top of the device grown by MBE on n-doped (100) GaAs substrates. The cylindrical mesas were defined by inductively coupled plasma reactive ion etching. Oxide current apertures were created using selective oxidation of the high aluminium content aperture layers. Tapered oxide current apertures were used to enhance the stability of the oxide structure and to improve the injection characteristics of the device. (Fig. 1). The additional DBR mirrors increase the serial resistance and the capacity of our device in comparison to simpler devices slightly reducing the electrical bandwidth

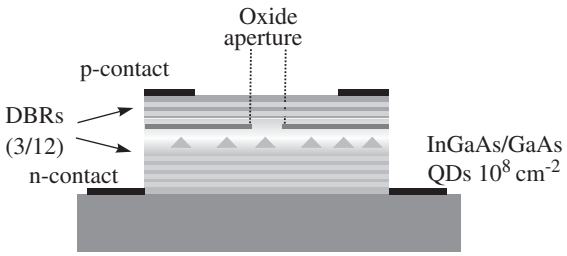

Fig. 1. Schematic picture of the resonant cavity LED.

and deforming the shape of an electrical pulse. We were able to operate our RC-LED at 1 GHz and a pulse width of 350 ps by increasing the high/low voltage to 3.1 and 1.1 V, respectively [2]. The optical response of our device to the electrical pulse agrees very well with theoretical simulations of a pulse train with a FWHM of 400 ps (Fig. 2, top). The exciton lifetime without the cavity is in the order of 1 ns and the short optical response of our device demonstrates an appreciable reduction of lifetime by at least a factor of two owing to the Purcell effect. The temporal resolution of our APD is 400 ps, thus presently still limiting the measured optical response. For photon correlation measurement, two APDs for the start and stop signal are used, thus reducing the time resolution to 700 ps. The measured correlation function (Fig. 2, bottom) looks similar to CW excitation. The measured $g^{(2)}(0)$ value of 0.25 is again limited by the time resolution of our setup. The photon correlation agrees excellently with a simulation of a pulsed ideal single photon device $g^{(2)}(0) = 0$ with 1 GHz repetition rate, taking into account the limited time resolution of 0.7 ns of our setup.

At bias conditions, where the exciton emission is saturated, the count rate of our avalanche photodiodes (APDs) is ten times higher than from previous devices without cavity under comparable bias [3]. The exciton life time is reduced by a factor of at least 2.5 to $\leq$ 400 ps due to the Purcell effect.

2. Entangled photon generation

As proposed by Benson *et al* [4] a single QD is an excellent source for entangled photon pairs if the FSS of the exciton bright states is reduced to less than the homogeneous line width. For In(Ga)As QDs on (001) GaAs the FSS will be non-zero even for perfect symmetric QDs, due to the asymmetric piezoelectric field. Post growth techniques such as magnetic field or annealing have to be applied to tune the FSS to zero. In contrast to this the piezoelectric field for QDs grown on (111) GaAs substrate is directed along the growth direction and cannot lower the symmetry below C_3V. Using 8 band $k \times p$ theory

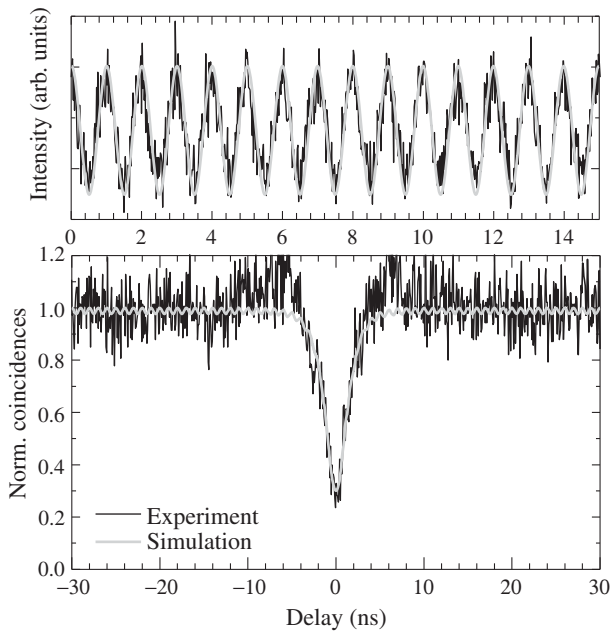

Fig. 2. Top: Optical response to a 1 GHz electrical signal. Bottom: Measured second order correlation at 1 GHz. The red line is a simulation taking in to account the time resolution of our setup and resulting in a $g^{(2)}(0) = 0$.

in conjunction with the configuration interaction method we showed that the FSS is expected to be zero [5]. As a result the biexciton to exciton recombination cascade of QDs grown on (111) GaAs can be used for the generation of entangled photons without further tuning of the FSS as long as there are not large shape anisotropies. In order to study the FSS of QDs grown on a GaAs (111) samples were grown using molecular beam epitaxy on substrates having a miscut of 3°: The QDs were grown using the droplet technique and capped with 65 nm GaAs followed by a Al_6Ga_4As layer and a 10 nm GaAs layer. The sample was excited with a frequency doubled Nd:YVO Laser in a microphotoluminescence setup. Since the wafer rotation was switched of during growth, the luminescence of the samples varies signifcantly on diferent areas of the wafers. Some parts emit spectral broad luminescence having little relation to QDs, other areas show spatially well separated luminescence centers, with spectrally sharp luminescence lines. The distance between two QDs can exceed a few μm and the spatial QD density here is signifcantly less than 10^9 cm^{-2}. Thus single QD spectroscopy without additional selection as for example mesa etching or shadow masks is possible. Second order correlation measurements proves non-classical light emission from these QDs. The measured FSS of these QDs is in the order of our spectral resolution (10 μeV) [6], making them a promising candidate for sources of entangled photon pairs.

Acknowledgements

This work was partly funded by the SfB 787 and the NATO SfP 982735.

References

[1] D. Bimberg, E. Stock, A. Lochmann, A. Schliwa, J. A. Tofflinger, W. Unrau, M. Munnix, S. Rodt, V. A. Haisler, A. I. Toropov, A. K. Bakarov and A. K. Kalagin, *IEEE Photonics Journal* **1**, 58 (2009).

[2] A. Lochmann, E. Stock, J. A. Tofflinger, W. Unrau, A. Toropov, A. Bakarov, V. Haisler and D. Bimberg, *Electron. Lett.* **45**, 556 (2009).

[3] A. Lochmann, E. Stock, O. Schulz, F. Hopfer, D. Bimberg, V. A. Haisler, A. I. Toropov, A. K. Bakarov and A. K. Kalagin, *Electron. Lett.* **42**, 774 (2006).

[4] O. Benson, C. Santori, M. Pelton and Y. Yamamoto *Phys. Rev. Lett.* **84**, 2513 (2000).

[5] A. Schliwa, M. Winkelnkemper, A. Lochmann, E. Stock and D. Bimberg, *Phys. Rev. B* **80**, 161307 (2009).

[6] E. Stock, T. Warming, I. Ostapenko, S. Rodt, A. Schliwa, J. A. Tofflinger, A. Lochmann, A. I. Toropov, S. A. Moshchenko, D. V. Dmitriev, V. A. Haisler and D. Bimberg, *Appl. Phys. Lett.* **96**, 093112 (2010).

18th Int. Symp. "Nanostructures: Physics and Technology"
St Petersburg, Russia, June 21–26, 2010

Low frequency noise and degradation of graphene transistors

S. Rumyantsev[1,3], G. Liu[2], W. Stillman[3], M. Shur[3] and A. A. Balandin[2]

[1] Ioffe Physical-Technical Institute, St Petersburg, Russia
[2] Department of Electrical Engineering, University of California, Riverside California 92521, USA
[3] Rensselaer Polytechnic Institute, Troy, New York 12180, USA

Abstract. We studied the effect of aging on the low frequency noise in single and bi-layer back-gate graphene transistors. The p-type degenerately doped Si wafers, covered with 300-nm thermally grown SiO_2, served as a substrate and back-gate for graphene layers prepared by mechanical exfoliation from the bulk highly oriented pyrolytic graphite. The mobility extracted through the Drude formula was within a range of from 2000 to 5000 $cm^2/V\,s$ for electrons and for holes. Aging at room temperature led to the shift of the Dirac point, decrease of the carrier mobility and strong increase of the noise amplitude. Noise behavior indicates noise mechanism different from that in Si MOSFETs.

Introduction

Extraordinary properties of graphene, especially its extre-mely high room temperature electron and hole mobilities [1,2] and thermal conductivity [3,4] make this material very promising for sensing, terahertz [5], and microelectronics applications. Most of these potential applications require low levels of noise including noise at frequencies, f, below 100 kHz. This kind of noise limits the sensitivity of sensors and up-converts to the phase noise of microwave oscillators or mixers. Low frequency noise is also a useful tool to study transport mechanisms, impurities and defects, and to diagnose reliability problems.

Here we report on the noise properties of single (SLG) and bi-layer (BLG) back-gate graphene transistors before and after their aging at room temperature.

1. Experimental details

Graphene layers were prepared by mechanical exfoliation from the bulk highly oriented pyrolytic graphite.

The SLG and BLG samples were selected via deconvolution of the Raman 2D band and comparison of the intensities of the G peak and 2D band [6,7]. The p-type degenerately doped Si wafers covered with 300-nm thermally grown SiO_2 served as a substrate and back-gate for exfoliated graphene. Leo1550 electron beam lithography was used to define the source and drain areas through the contact bars. The 10-nm Cr/100-nm Au source and drain contacts were deposited on graphene by electron beam evaporation, connecting the graphene to pre-deposited Cr/Au metal contact pads.

The fabricated transistors were kept at ambient conditions for more than a month. During this time, we measured I-V characteristics and electronic noise.

2. Results and discussions

Fig. 1 shows transfer current voltage characteristics of two SLG graphene transistors before degradation (solid lines) and after keeping the devices at ambient environment for 1 month (dashed lines). Assuming that the threshold voltage coincides with the Dirac voltage,V_D, the effective mobility, $\mu_{\rm eff}$, can be estimated from the output current-voltage characteristics as $\mu_{\rm eff} = (\sigma(V_g) - \sigma(V_D))/(C(V_g - V_D)$, where C is the gate capacitance per unit area, and σ is the conductivity. The mobility for our un-aged transistor varied from 2000 to 5000 $cm^2/V\,s$ for electrons and holes at room temperature. Estimates of the contact resistance indicated their potential significance in device noise.

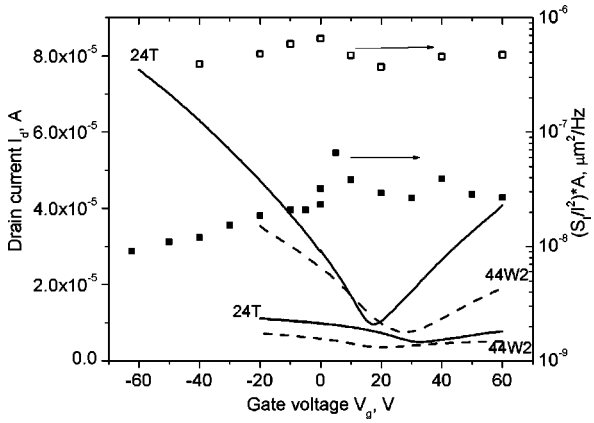

Fig. 1. Output current-voltage characteristics (drain current versus gate voltage) for two SLG graphene transistors. Drain voltage V_d = 100 mV. Symbols show noise S_I/I^2 times graphene area, A. f = 10 Hz.

As seen from Fig. 1, degradation led to the decrease of the current and slope of the I_d versus V_g dependences. Depending on the device, the Dirac voltage either increased or decreased with the aging time. Analysis showed that both contact resistance and mobility degraded as a result of aging.

The low frequency noise was measured in the frequency range from 1 to 50 kHz at different gate voltages. The noise spectra being close to the $1/f$ spectrum demonstrated weak deviation from the pure $1/f$ noise both in slope and shape for some devices. This deviation might indicate the contribution of some well defined traps to the noise in gra-phene [8].

Fig. 1 also shows the noise at f = 10 Hz (relative spectral noise density of short circuit current fluctuations) normalized to graphene area, A, as a function of the gate voltage for the sample 24 T before and after 1 month of aging, respectively. As seen, the amplitude of noise increased more than one order of magnitude as a result of aging.

Recently, Ref. [9] reported on noise decrease with the increase of the electron/hole concentration in SLG and on noise increase with the increase of the electron/hole concentration in BLG. We did not confirm this result. We found no correlation of the slope of noise versus gate voltage dependences with the number of graphene layers (see Ref [10], as well). For many devices, at small gate voltages noise increases first and than de-

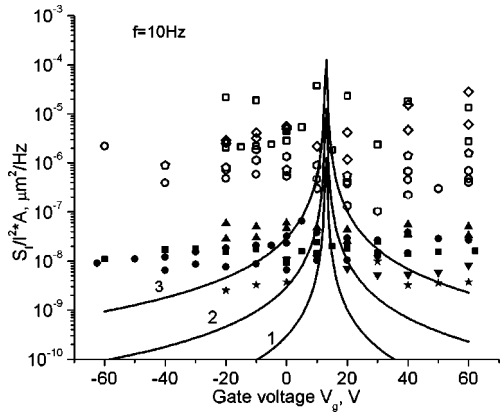

Fig. 2. Noise as a function of gate voltage. Filed and open symbols show (S_I/I^2 A) for transistors before and after the aging, respectively. Lines are calculated in accordance with McWhorter model for different oxide trap concentrations: 1 — $N_t = 10^{17}$ $(\mathrm{cm}^3\mathrm{eV})^{-1}$, 2 — $N_t = 10^{18}$ $(\mathrm{cm}^3\mathrm{eV})^{-1}$, 3 — $N_t = 10^{19}$ $(\mathrm{cm}^3\mathrm{eV})^{-1}$.

creases with the increase of the gate voltage swing. This kind of behavior is qualitatively different from that for Si MOSFETs where this kind of behavior was never observed.

Figure 2 summarizes the result of the noise measurements of all graphene transistors before and after aging. We found that, for the samples before aging, when the noise amplitude is normalized to the gate area the dispersion in noise from sample to sample is reduced significantly. This indicates the dominant contribution to noise of the graphene layer itself and minor role of contacts in noise behavior for the majority of samples.

The low frequency noise in MOSFETs is usually analyzed in the framework of the McWhorter model. In the model, noise is caused by the tunneling of the carriers from the channel to the traps in the oxide. Therefore the trap concentration in the oxide is a natural figure of merit for the noise amplitude in MOSFETs. The lines in Fig. 2 show the McWhorter model noise amplitudes calculated in graphene transistors for different trap concentrations. Lines one and two correspond to $N_t = 10^{17}$ $(\mathrm{cm}^3\mathrm{eV})^{-1}$ and $N_t = 10^{18}$ $(\mathrm{cm}^3\mathrm{eV})^{-1}$, respectively, which represent the typical range for Si n-channel MOSFETs. Line 3 corresponds to $N_t = 10^{19}$ $(\mathrm{cm}^3\mathrm{eV})^{-1}$, which is typical for Si MOSFETs with high-k dielectric. Even though noise in graphene does not comply with the McWhorter model, Fig. 2 allows us to compare the noise amplitude in graphene and MOSFETs. As seen, while at high carrier concentration the noise in graphene is higher than in typical Si MOSFETs, at low concentrations the noise is of the same order of magnitude as in Si MOSFETs.

To conclude, the low frequency $1/f$ noise in SLG and BLG was studied at atmospheric pressure and at room temperature. Since normalization of the noise to the graphene area reduces the spread of the noise amplitude from device to device we conclude that not contacts but the graphene itself plays the major role in noise behavior. Aging led to the shift of the Dirac point, decrease of the carrier mobility and contact resistance, as well as to the strong increase of the noise amplitude. Even at low carrier concentration the noise amplitude is comparable to that in MOSFETs, the gate voltage dependence of noise does not comply with McWhorter model indicating other noise mechanisms than in Si MOSFETs.

Acknowledgements

The work at UCR was supported, in part, by DARPA-SRC Focus Center Research Program (FCRP) through its Center on Functional Engineered Nano Architectonics (FENA). The work at RPI was supported by IFC seed funding. At Ioffe Inst. the work was supported by the Russian Fund of Basic Research (Grant 08-02-00010).

References

[1] K. I. Bolotin *et al*, *Sol. St. Comm.* **146**, 351 (2008).
[2] P. Blake *et al*, *Sol. St. Comm.* **149**, 1068 (2009).
[3] A. A. Balandin *et al*, *Nano Lett.* **8**, 902 (2008).
[4] D. L. Nika *et al*, *Phys. Rev. B* **79**, 155413 (2009).
[5] V. Ryzhii *et al*, *Proc. of Advanced Research Workshop Future Trends in Microelectronics (Sardinia, Italy June 2009)*, Wiley & Sons, Inc., (2010).
[6] I. Calizo *et al*, *Appl. Phys. Lett.* **91**, 071913 (2007).
[7] I. Calizo *et al*, *Appl. Phys. Lett.* **91**, 20104 (2007).
[8] Q. Shao *et al*, *IEEE El. Dev. Lett.* **30**, 288 (2009).
[9] A. N. Pal *et al*, *Appl. Phys. Lett.* **95**, 082105 (2009).
[10] G. Liu *et al*, *Appl. Phys. Lett.* **95**, 033103 (2009).

18th Int. Symp. "Nanostructures: Physics and Technology"
St Petersburg, Russia, June 21–26, 2010

Silicon Nanowire Transistor as high sensitive bio- and chemical sensor

V. A. Krupenin[1,3], D. E. Presnov[2,3], *S. V. Amitonov*[1], Y. S. Ushakova[4] and V. S. Vlasenko[1]

[1] Laboratory of Cryoelectronics, Moscow State University, 119991 Moscow, Russia
[2] Nuclear Physics Institute, Moscow State University, 119991 Moscow, Russia
[3] Institute of Nanotechnologies in Microelectronics RAS, 119991, Moscow, Russia
[4] Division of Chemical Enzymology, Moscow State University, 119991 Moscow, Russia

Abstract. In this work authors persent the results of the fabrication technology development and the experimental study of silicon nanowire field effect transistor (NW FET) as a potential sensor for application in biology and medicine. The original fabrication technology used silicon-on-insulator (SOI) material and did not involve Si doping and activation processes. Current-voltage characteristics of the experimental structures were measured in a buffer solutions over a wide range (0–10 V) of the gate voltages. The possibility of using of the silicon NW FET as a sensitive field/charge sensor was demonstrated by pH mesurements.

Introduction

Recent progress in nanoscale fabrication technologies led to appearance of great number of original devices based on nanostructures. One of them are nanowire-based field effect transistors, which can be use in physical experiments, electronic schemes and in a wide variety of biological and chemical applications. NW transistor can serve as the basis for ultra small bio- and chemical sensors [1] with femtomole sensitivity to the certain type of objects [1–5]. The sensitivity of NW FET can be very high, in some experiments devices which can detect even a single viruses or biomolecules were demonstrated [2,3]. This could be vital step in problems of early medical diagnostics, harmful biological substances detection in bioterrorism protection and biowarfare.

1. Samples fabrication

We used SOI wafer with the following parameters: top silicon layer — 110 nm thick, p-type; insulating buried oxide — 200 nm thick; Si substrate — 700 μm thick, p-type. Experimental structures were formed in a top silicon layer of SOI material. The fabrication method based on a reactive ion etching of top Si layer through the metal mask was used. After structure patterning in PMMA resist by e-beam writer a metal mask was formed by deposition of Al thin (10 nm) film. Using the reactive ion etching of Si layer through the Al mask we made nanowires from 50 nm (Fig. 1) and higher in width and 1.5–5 μm in length. After lift-off process the contact pads of the NW transistors were made by deposition of thin (30 nm) Ti film through another resist mask. As a result a Schottky barrier occured in a source/drain contacts interface with a Si nanowire. Schottky barrier NW FETs have a number of advantages including simple, low temperature processing and the elimination of doping and subsequent activation processes. Their fabrication method does not require any source and drain doping allowing to form a contact leads in a simple process without thermal annealing. To make the waterproof structures Ti electrodes were covered with an SiO_2 insulator layer (200 nm thick). Final structure is shown on Fig. 2. The backside of the Si substrate covered by metal film served as a gate electrode for all the transistor structures on the same sample.

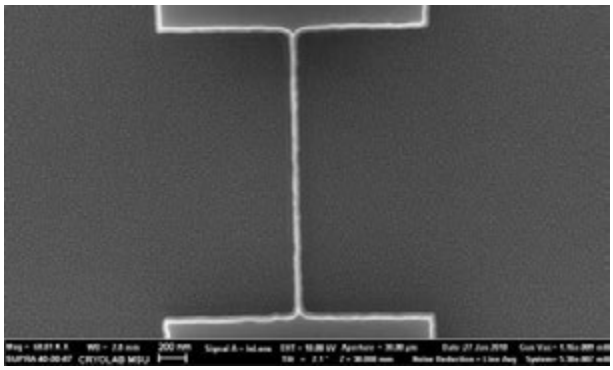

Fig. 1. Nanowire — transistor channel (SEM image).

2. Results

We have measured current-gate characteristics of the NW FET structures by applying fixed source-drain voltage and measuring the transport current through the transistor at different gate voltages. All the devices showed enhancement-mode operation for positive gate biases (inverse electron channel) with saturated drain current. Conductivity of the transistor channel depended on the electric field applied to the Si nanowire. Even a local disturbance of the electric field around the nanowire could change its conductivity noticeably. This enables to register any small charged particles which are attached to (detached

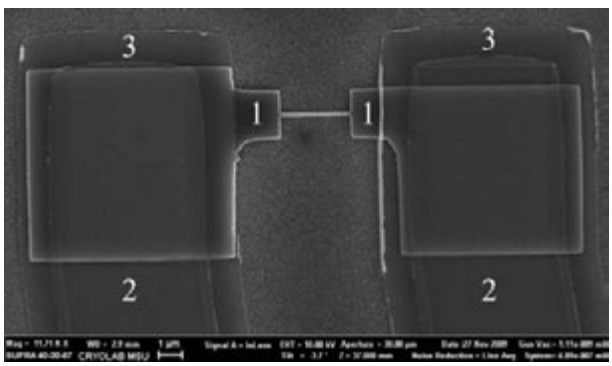

Fig. 2. Nanowire field-effect transistor structure from SOI (SEM image). 1 — Si contact pads; 2 — Ti source and drain electrods; 3 — isolation SiO_2 layer.

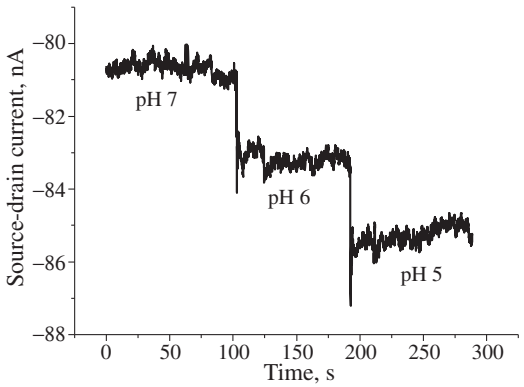

Fig. 3. Real-time response of NW transistor on pH changing. Gate voltage $V_g = 9$ V, source-drain voltage $V_{sd} = -2$ V.

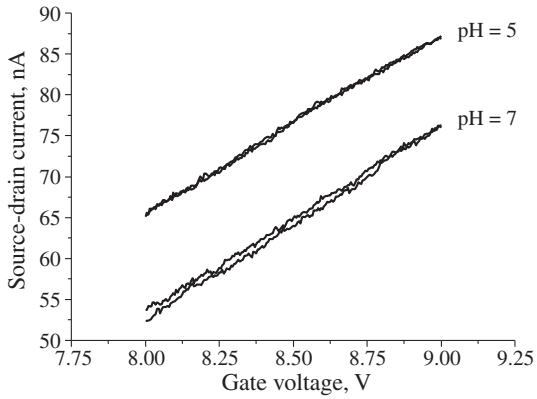

Fig. 4. Current — gate voltage characteristics of NW transistor at different pH. Source-drain voltage $V_{sd} = 2$ V.

off) the surface of Si nanowire channel: molecules, nanoparticles, viruses, DNA etc. We have tested our NW FETs in buffer solutions (MES, 10 mM) with different pH. Figures 3 and 4 have shown the responces of NW transistor on the pH changes. Further investigations are in a progress.

3. Conclusions

Introduced fabrication method offers good reproducibility and high quality of the fabricated structures. Fabricated Si nanowire FET discussed above shows the capability to serve as a very good core element of the bio- and chemical sensors. Modification of its surface with the selectively binding molecules and radicals could provide us a nanoscale femtomolar selective sensor.

Acknowledgements

This work was supported by grant 09-02-12238-ofi-m of Russian Foundation for Basic Research.

References

[1] Y. Cui, O. Wei, H. Park and C. M. Lieber, *Science* **293**, 1289 (2001).

[2] E. Stern, J. F. Klemic, D. A. Routenberg, P. N. Wyrembak, D. B. Turner-Evans, A. D. Hamilton, D. A. LaVan, T. M. Fahmy and M. A. Reed, *Nature* **445**, 519 (2007).

[3] F. Patolsky, G. Zheng, O. Hayden, M. Lakadamyali, X. Zhuang and C. M. Lieber, *PNAS* **101**, 14017 (2004).

[4] M. Curreli, R. Zhang, F. N. Ishikawa, H.-K. Chang, R. J. Cote, C. Zhou and M. E. Thompson, *IEEE Trans. Nanotechnol.* **7**, 651 (2008).

[5] E. Stern, E. R. Steenblock, M. A. Reed and T. M. Fahmy, *Nano Letters* **8**, 3310 (2008).

18th Int. Symp. "Nanostructures: Physics and Technology"
St Petersburg, Russia, June 21–26, 2010

Optical bistability in artificial composite nanoscale molecules: Towards all optical processing at the nanoscale

A. V. Malyshev[1,2] and V. A. Malyshev[3]

[1] Universidad Complutense de Madrid, Spain
[2] Ioffe Physical-Technical Institute, St Petersburg, Russia
[3] Zernike Institute for Advanced Materials, University of Groningen, The Netherlands

Abstract. Optical response of artificial composite nanoscale molecules comprising a closely spaced noble metal nanoparticle and a semiconductor quantum dot have been studied theoretically. We consider a system composed of an Au particle and CdSe or CdSe/ZnSe quantum dot and predict optical bistability and hysteresis in its response, which suggests various applications, in particular, all-optical processing and optical memory.

Introduction

Arrays of metallic nano-particles (often referred to as plasmonic arrays), are widely recognized as potential building blocks for nanoscale optical circuits [1,2,3]. Recently, a number of papers reported fascinating properties of small clusters of closely spaced semiconductor quantum dots (SQD) and metallic nano-particles (MNP) [4, 5, 6, 7]. Fano resonances [4, 6], bistability in the absorption spectrum [6], and meta-"molecular" resonances [7] have been predicted. When such systems are excited optically, the dipole moment of the excitonic transition in the SQD generates additional electric field at the MNP, which is superposed with the external field, while the induced dipole moment of the MNP generates an additional electric field at the SQD, providing a feedback. Thus, the presence of the MNP leads to a self-action of the optical transition dipole moment, which can give rise to a variety of new optical properties. In particular, if the coupling between two particles is strong the self-action can be large enough to result in optical bistability.

We consider a CdSe or CdSe/ZnSe spherical semiconductor quantum dot and a Au nano-sphere, the simplest artificial diatomic nano-molecule (see the schematic view of the system in Fig. 1). We demonstrate that optical bistability and hysteresis can be observed in the system. The two stable states of the systems have different polarizations, providing a possibility to store information in the form of the system polarization. We argue also that in addition to the traditional way of switching by the amplitude of the driving electric field, the state of such artificial diatomic molecule can be switched by the polarization of the field with respect to the molecule axis. The fact that both the SQD and the MNP can sustain high electric fields suggests such possible applications of the artificial molecule as an all-optical switch and optical memory at nano-scale.

1. Formalism

We assume that the SQD-MNP system is embedded in a dielectric host with the permeability ε_b and driven by the external electric field with the amplitude $\mathbf{E}_0$ and frequency ω. The SQD is treated quantum mechanically (as a two level system) within the framework of the Maxwell–Bloch equations while the MNP is treated classically; the response of the MNP is described by its frequency dependent polarizability within the point dipole approximation. The rotating wave approximation is used throughout the paper, so that all time dependent quantities represent amplitudes of the corresponding signals, the set

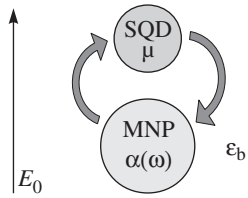

Fig. 1. Schematics of a semiconductor quantum dot — metallic nanoparticle hybrid system embedded into a homogeneous dielectric background with permeability ε_b and subjected to an external field with the amplitude $\mathbf{E}_0$.

of equations for which reads:

$$\dot{Z} = -\gamma\,(Z+1) - \frac{1}{2}\left(\Omega R^* + \Omega^* R\right), \qquad (1)$$

$$\dot{R} = -\left(i\Delta + \Gamma\right) R + \Omega Z, \qquad (2)$$

where $Z = \rho_{11} - \rho_{00}$ is the population difference, R is the amplitude of the off-diagonal density matrix element ρ_{10}, γ and Γ are relaxation rates, Δ is the detuning of the SQD resonance and $\Omega = \boldsymbol{\mu}\mathbf{E}/\hbar$ is the Rabi frequency ($\boldsymbol{\mu}$ is the optical transition dipole moment of the SQD). The total electric field $\mathbf{E}$ at the SQD is the superposition of the external field $\mathbf{E}_0$ and the scattered field produced by the MNP:

$$\mathbf{E} = \frac{1}{\varepsilon_s'}\left(\mathbf{E}_0 + \frac{\bar{\mathbf{S}}\mathbf{P}_{\mathrm{MNP}}}{d^3}\right). \qquad (3)$$

Here, $\varepsilon_s' = (\varepsilon_s + 2\varepsilon_b)$, $\varepsilon_s/3\varepsilon_b$ is the SQD dielectric constant, $\bar{\mathbf{S}} = \mathrm{diag}(-1,-1,2)$ is the angular part of the dipole field Green tensor, d is the SQD-MNP center-to-center distance and $\mathbf{P}_{\mathrm{MNP}}$ is the induced dipole moment of the MNP:

$$\mathbf{P}_{\mathrm{MNP}} = \alpha(\omega)a^3\left(\mathbf{E}_0 + \frac{\bar{\mathbf{S}}\mathbf{P}_{\mathrm{SQD}}}{\varepsilon_b\, d^3}\right), \qquad (4)$$

where $\alpha(\omega)a^3$ is the classical frequency dependent polarizability of the MNP, a being its radius and $\alpha(\omega) = [\varepsilon_M(\omega) - \varepsilon_b]/[\varepsilon_M(\omega) + 2\varepsilon_b]$ with $\varepsilon_M(\omega)$ being the dielectric function of the metal while $\mathbf{P}_{\mathrm{SQD}} = (-i/2)R\boldsymbol{\mu}$ is the SQD dipole moment amplitude. The total electric field in the SQD is therefore given by

$$\mathbf{E} = \frac{1}{\varepsilon_s'}\left[\mathbf{1} + \frac{\alpha(\omega)a^3}{d^3}\bar{\mathbf{S}}\right]\mathbf{E}_0 + \frac{\alpha(\omega)a^3}{\varepsilon_s'\varepsilon_b\, d^6}\bar{\mathbf{S}}^2\mathbf{P}_{\mathrm{SQD}}\,. \qquad (5)$$

The Rabi frequency $\Omega = \mu E/\hbar = \Omega_r - iGR$ entering Eq. (1) and (2) contains the part corresponding to the renormalized

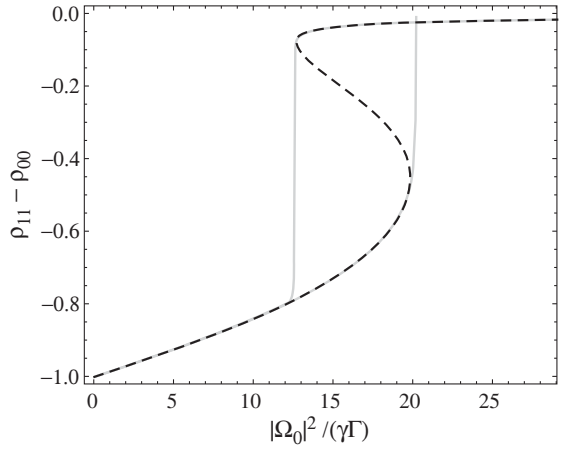

Fig. 2. Dependence of the population difference of the SQD on the external field $\Omega_0 = \mu E_0/\hbar$ manifesting optical bistability. Dashed line — the three-valued solution of Eq. (6). Solid line — solution of Eq. (6) with time dependent external field sweeping back and forth across the bistability region.

external field, Ω_r [the first term in Eq. (5)], and the self action [the second term in Eq. (5)]. The steady-state equation for the population difference Z reads:

$$\frac{|\Omega_r|^2}{\gamma\,\Gamma} = -\frac{Z+1}{Z}\,\frac{|\Gamma + i\,(\Delta + G\,Z)|^2}{\Gamma^2}\,. \qquad (6)$$

For some set of parameters and values of the driving fields this equation can have three real solutions, only two of which turn up to be stable.

2. Results

Hereafter we consider spherical CdSe/ZnSe SQD and Au MNP and use the following set of parameters: $\hbar\omega = 2.36$ eV (which corresponds to optical transition in 3.3 nm SQD), $\varepsilon_s = 6.2$, $a = 10$ nm, $d = 17$ nm, $\varepsilon_b = 1$, $1/\gamma = 0.8$ ns, $1/\Gamma = 0.3$ ns, $\Delta = 0$. We use tabulated dielectric function of gold [8] to calculate the polarizability of the MNP.

Dashed line in Fig. 2 shows the solution to Eq. (6), the dependence of the steady state population difference on the renormalized external field $\Omega_0 = \mu E_0/\hbar$ (the field is parallel to the system axis). Only the upper and lower branches of this solution are stable, resulting in optical bistability. To observe the two branches, we sweep the external field back and forth across the bistability region. Solid line in Fig. 2 shows the result of the corresponding calculation. The figure demonstrates that when the field is increasing (from 0), the population difference follows the lower stable branch until the critical field amplitude is reached. Further, the system switches abruptly to its other stable state (upper branch). When we sweep the field back the upper-to-lower branch switch occurs at a different critical field, forming the typical hysteresis loop.

The bistability of the population of the SQD results in the bistability of SQD and MNP polarizations. In Fig. 3, we present the hysteresis loop of the polarization of the SQD calculated for the same parameters as in Fig. 2. The two stable states of the SQD population correspond to two different polarization, providing the possibility for storage of information by the system polarization.

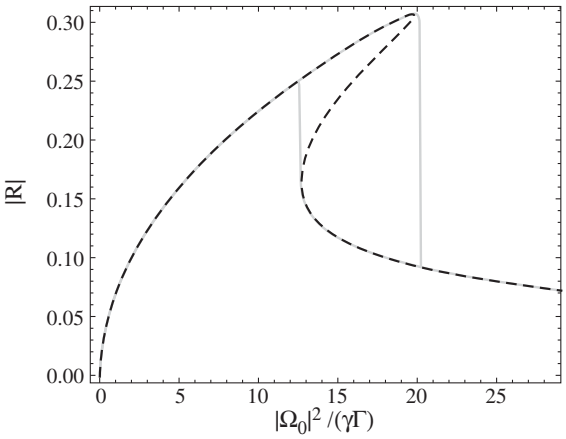

Fig. 3. Same as in Fig. 2 only for the amplitude $|R|$.

Finally, we point out that the specific feature of the SQD-MNP system is the existence of the symmetry axis; this allows us to drive the system not only by the amplitude of the external field, but also by the orientation of its polarization with respect to the axis. These are new properties which can be useful for applications.

3. Summary

We investigated theoretically the optical response of a hybrid "artificial" molecule composed of a semiconductor quantum dot, modeled as a two-level system and a metal nanoparticle, considered classically, which are coupled by the dipole-dipole interaction. The interaction results in a self-action of the SQD via MNP, leading to the dependence of the SQD optical transition frequency on the population, which provide a feedback mechanism resulting in several fascinating effects. Thus, in the strong coupling regime, we found that the system can manifest bistability and optical hysteresis, as well as switching of the polarization of both SQD and MNP by the incoming field. Such switching can be achieved not only by the traditional amplitude control but also by the polarization of the incoming field with respect to the system axis; the latter being very promising for optical memory applications at the nanoscale.

Acknowledgements

AVM acknowledges support from projects MOSAICO (FIS 2006-01485), BSCH-UCM (PR58/08-15916), the Ramón y Cajal program (Ministerio de Ciencia e Innovación de España) as well as the University of Groningen for hospitality.

References

[1] M. Quinten *et al*, *Opt. Lett.* **23**, 1331 (1998).
[2] M. L. Brongersma, J. W. Hartman, and H. A. Atwater, *Phys. Rev. B* **62**, R16356 (2000).
[3] A. V. Malyshev *et al*, *Nano Lett.* **8**, 2369 (2008).
[4] W. Zhang *et al*, *Phys. Rev. Lett.* **97**, 146804 (2006).
[5] A. O. Govorov *et al*, *Nano Lett.* **6**, 984 (2006).
[6] R. D. Artuso and G. W. Bryant, *Nano Lett.* **8**, 2106 (2008).
[7] S. M. Sadeghi, *Phys. Rev. B* **79**, 233309 (2009).
[8] P. B. Johnson and R. W. Christy, *Phys. Rev. B* **6**, 4370 (1972).

18th Int. Symp. "Nanostructures: Physics and Technology"
St Petersburg, Russia, June 21–26, 2010

Discrete spectrum of measured parameters of a superconductor nanostructure

A. V. Nikulov

Institute of Microelectronics Technology RAS, 142432 Chernogolovka, Moscow region, Russia

Abstract. The discreteness of permitted state spectrum postulated on atomic level can be macroscopic in nanostructures and larger structures because of macroscopic quantum phenomena such as superconductivity. The change by jump of measured parameters because of the macroscopic discreteness may be used for some applications. A device is proposed measured parameters of which can change by jump at a weak change of external parameters. The devise consists of two superconductor loop connected with two Josephson junctions. The macroscopic parameter — maximum value of the super-current through the two Josephson junctions — can change with the quantum number determining macroscopic angular momentum of superconducting pairs in one of the two loops.

Introduction

The distinctive feature of quantum mechanics is discreteness. Its scale on the atomic level is determined with the Planck's constant $\hbar$. For example, the discrete values of measured projection of angular momentum of atom and spin differ on $\hbar$. Discreteness in nanostrucrures may have much larger scale because of macroscopic quantum phenomena such as superconductivity. According to the Bohr's quantization $pr = n\hbar$ the difference of angular momentum $M_\mathrm{p} = pr$ between adjacent permitted states, $n + 1$ and n, of a free electron in a nano-ring with a radius $r > 1$ nm equals $\hbar$ as well as in atom. The energy difference $E_{n+1} - E_n = mv_{n+1}^2/2 - mv_n^2/2 = (2n + 1)\hbar^2/2mr^2$ is much smaller than in atom. Because of the latter the persistent current, the quantum phenomenon observed because of the discreteness of spectrum, can be observed only at very low temperature in semiconductor and normal metal rings with realistic radius from $r = 10$ nm [1] to $r = 800$ nm [2]. This phenomena can not be practically observed in the ring with the radius $r > 10$ μm. In contrast to the semiconductor and normal metal rings, in superconductor ring with such radius the persistent current is observed in the whole temperature region corresponding to the superconducting state $T < T_\mathrm{c}$ and even in some region above it $T > T_\mathrm{c}$ [3]. The energy difference $E_{n+1} - E_n$ between adjacent permitted states in superconductor ring in N_s times higher [4] then in the non-superconductor one because of the same $n\hbar$ angular momentum of all $N_s = Vn_s = \pi r^2 s n_s$ superconducting pairs containing in the ring with the volume V, the radius r and the section area s.

The angular momentum difference between adjacent permitted states of superconductor rings with uniform section area s increases also in N_s times, $M_{p,n+1} - M_{p,n} = N_s\hbar$. The density of pairs n_s in superconducting state $T < T_\mathrm{c}$ is equal in order of value 1/2 electron density in the metal. Therefore the number N_s is enormous in any ring with realistic size. The great discreteness may be useful for applications. Nanostructures may be more useful for some applications because of too great discreteness of macroscopic superconductor structures. In order to the discreteness can be used it should become apparent in measurable parameters. A device measurable parameters of which is strongly discrete is proposed in this work.

1. Discrete states of superconducting loop

The enormous discreteness in superconductor is describe very well with the Ginzburg-Landau wave function $\Psi_\mathrm{GL} = |\Psi_\mathrm{GL}| \exp i\phi$. Where $|\Psi_\mathrm{GL}|^2 = n_s$ and $V|\Psi_\mathrm{GL}|^2 = Vn_s = N_s$ are the density and the total number of superconducting pairs in the ring. But $\hbar \bigtriangledown \phi = p = mv + qA$ is canonical momentum of single pair with the charge $q = 2e$. Because of the requirement that the complex pair wave function closed in the loop must be single-valued at any its point $\Psi_\mathrm{GL} = |\Psi_\mathrm{GL}| \exp i\phi = |\Psi_\mathrm{GL}| \exp i(\phi + 2\pi n)$ the phase ϕ must change by integral multiples of 2π

$$\oint_l dl \bigtriangledown \phi = n2\pi \tag{1}$$

following a complete turn along the path of integration l. Because of the quantization (1) and the relation $\oint_l dl\hbar \bigtriangledown \phi = \oint_l dlp = m\oint_l dlv + q\Phi$ the minimum value of the permitted velocity $v = (2\pi\hbar/ml)(n - \Phi/\Phi_0)$ of superconducting pairs in a loop is periodic function of magnetic field B with the period $B_0 = \Phi_0/S$ corresponding to the flux quantum $\Phi_0 = 2\pi\hbar/q \approx 2.07 \times 10^{-15}$ T m^2 inside the loop with the area S. The two permitted states $n = k$ and $n = k+1$ have equal

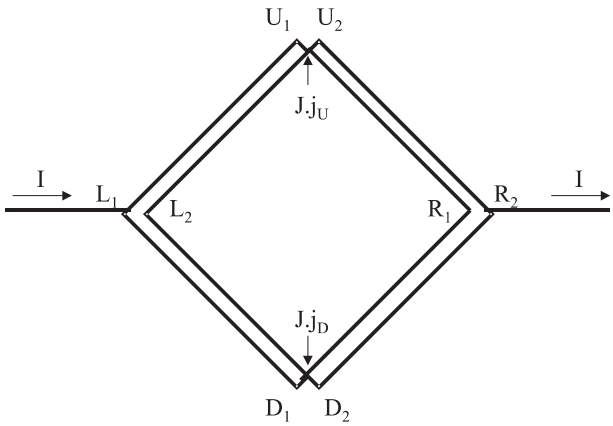

Fig. 1. A sketch of the device consisting of two superconductor loop connected with two Josephson junctions $J.j_\mathrm{U}$ and $J.j_\mathrm{D}$. The maximum value of the super-current I_s changes by jump from $I_s = 2I_\mathrm{c}$ to $I_s = 0$ at the change the the quantum number n_1 or n_2 in one of the loops. This jump can be observed as voltage $V = R(I - I_s)$ jump at applying of an external current $I < 2I_\mathrm{c}$ as shown on the figure.

minimum energy $E_k = E_{k+1} = N_s m v^2/2 = N_s \pi^2 \hbar^2/ml^2$ at $BS = \Phi = (k+0.5)\Phi_0$. Because of the great number of pairs N_s the energy difference between these states becomes high $|E_{k+1} - E_k| > k_B T$ at small deviation $\delta B = B - (k+0.5)\Phi_0/S$ of magnetic field value B from $(k+0.5)\Phi_0/S$. The angular momentum and other parameters can change by jump at small variation δB of the magnetic field B.

2. Two superconductor loop connected with two Josephson junctions

This change can be detected with help of the device, sketch of which is shown on Fig. 1. The device consists of two superconductor loops $L_1 - U_1 - R_1 - D_1 - L_1$ and $L_2 - U_2 - R_2 - D_2 - L_1$ with equal area S. The velocity of superconducting pairs in the loops $v_1 = (2\pi\hbar/ml)(n_1 - \Phi/\Phi_0)$ and $v_2 = (2\pi\hbar/ml)(n_2 - \Phi/\Phi_0)$ depends on the quantum numbers n_1 and n_2, i.e. the phase ϕ change (1) at complete turn along each of the loops. The loops are connected with two Josephson junctions in two points, as it is shown on Fig. 1. According to the current-phase relationship $I = I_c \sin(\Delta\phi)$ between the super-current I_s through the Josephson junction and the phase difference $\Delta\phi$ between the junction boundaries the maximum value of the super-current

$$I_s = I_c [\sin(\Delta\phi_U) + \sin(\Delta\phi_D)] \qquad (2)$$

through two Josephson junction should depend on the relation between the phase differences $\Delta\phi_U$ and $\Delta\phi_D$. According to the quantization relation (1) along the path of integration $L_1 - U_1 - R_1 - D_1 - L_1$, $L_2 - U_2 - R_2 - D_2 - L_2$ and $L_1 - U_1 - J.j_U - U_2 - R_2 - D_2 - J.j_D - D_1 - L_1$ the value $\Delta\phi_D - \Delta\phi_U = \pi(n_1 + n_2)$ is determined only with the quantum numbers n_1 and n_2, at any external magnetic field B and the equal area S of the loops. The maximum value of the super-current (2)

$$I_s = I_c [\sin(\Delta\phi_U) + \sin(\Delta\phi_U + \pi(n_1 + n_2))] \qquad (3)$$

should have discrete values equal $2I_c$ when the sum $n_1 + n_2$ is an even number and $I_s = 0$ when $n_1 + n_2$ is an odd number.

The persistent current $I_p = s2en_s v = (4sen_s\pi\hbar/ml)(n - \Phi/\Phi_0)$ in the states $n = k$ and $n = k+1$ with minimum energy at $BS = \Phi = (k+0.5)\Phi_0$ has the same direction in the loops when the sum $n_1 + n_2$ is an even number and the directions are opposite when $n_1 + n_2$ is odd. The change of the persistent current direction, for example, in the first loop at the change from $n_1 = k$ to $n_1 = k+1$ can be detected as the voltage $V = R_n(I - I_s)$ jump, at an external current $I < 2I_c$ applied as shown on Fig. 1. The voltage jump can mount up to the value $R_n I_c = \pi\Delta/2e = \pi 1.76 k_B T_c/2e$ [5]. For example, the maximum jump can equal 2 mV in the case on niobium loops with the critical temperature $T_c = 9.2$ K.

This jump may be observed at very weak variation $\delta B = B - (k+0.5)\Phi_0/S$ of the external magnetic field B. The energy $E_n = N_s m v_n^2/2 = I_{p,A}\Phi_0(n - \Phi/\Phi_0)^2$ difference between adjacent permitted states, for example $n = 0$ and $n = 1$ at $BS = \Phi = 0.5\Phi_0$,

$$E_1 - E_0 = 2I_{p,A} S\delta B = 2I_{p,A}\Phi_0(S\delta B/\Phi_0) \qquad (4)$$

increases with the loop area S and the amplitude $I_{p,A} = 2sen_s \pi\hbar/ml$ of the oscillations $I_p = I_{p,A} 2(n - \Phi/\Phi_0)$. The value $\delta B > (E_1 - E_0)/2I_{p,A}S$ of the magnetic field variation, at which the probability $P_{n=1} = e^{-(E_1 - E_0)/k_B T}/[1 + e^{-(E_1 - E_0)/k_B T}]$ of the $n = 1$ state, for example, changes between 0 and 1, decreases with the increase of the loop sizes, because of the relation $I_{p,A} S \propto (s/l)l^2 = sl = V$. This value is enough low already in a loop with nano-size. For example, the persistent current amplitude $I_{p,A} \approx 200\ \mu$A $(1 - T/T_c)$ observed in the aluminum ring with diameter $2r \approx 4\ \mu$m and circumference section $s \approx 1000$ nm^2 [6] corresponds to the value $2I_{p,A}\Phi_0/k_B \approx 30000$ K at $T \approx 0.5T_c$. The jump from $P_{n=1} = 0$ to $P_{n=1} = 1$ should by observed with variation $S\delta B > 0.0003\Phi_0 \approx 0.5 \times 10^{-18}$ T m^2 and $\delta B > 5 \times 10^{-8}$ T at this value of the persistent current, $T \approx 10$ K and $S = \pi r^2 \approx 12\ \mu\text{m} = 1.2 \times 10^{-11}$ m^2.

The magnetic flux variation $S\delta B = \delta\Phi > 0.0007\Phi_0 = 10^{-18}$ T m^2 can be induced with a current $I_{sw} > 2 \times 10^{-8}$ A $= 0.02\ \mu$A circulating in an additional loop with $2r = 4\ \mu$m having the inductance $L = 2 \times 10^{-11}$ H [5]. The value of the switching current I_{sw} should not depend on the loop length l, because of the proportionality $L \propto l$ and $I_{p,A} \propto 1/l$. The loop with a small l can be used as a bit, the two states $n = 0$ and $n = 1$ of which can be read in the way shown on Fig. 1. The devise Fig. 1 with a large loop length $l \gg \pi 2r \approx 12\ \mu$m can be used for measurement of very weak magnetic field $B \approx \delta B \propto 1/sl$. This very sensitive magnetometer has some advantages in comparison with the well known SQUID (Superconducting quantum interference devices) [7].

The possibility of the voltage jump at the quantum number n_1, n_2 change in one of the loop of the devise shown on Fig. 1 was corroborated experimentally in the work [8]. The voltage $V = R_n(I - I_s)$ (or the resistance V/I measured in [8]) changes by jump with magnetic field B at the change of the persistent current direction, i.e. the n_1 number in one of the loop and returns to the initial value at the same change in the other loop. The quantum numbers n_1 and n_2 change in [8] at different magnetic field values because of different section s of the loops. This circumstance may be used in the devise proposed in the present work.

Acknowledgements

This work has been supported by a grant "Possible applications of new mesoscopic quantum effects for making of element basis of quantum computer, nanoelectronics and micro-system technic" of the Fundamental Research Program of ITCS department of RAS and the Russian Foundation of Basic Research grant 08-02-99042-r-ofi.

References

[1] N. A. J. M. Kleemans *et al*, *Phys. Rev. Lett.* **99**, 146808 (2007).
[2] A. C. Bleszynski-Jayich *et al*, *Science* **326**, 272 (2009).
[3] N. C. Koshnick *et al*, *Science* **318**, 1440 (2007).
[4] A. V. Nikulov, *Phys. Rev. B* **64**, 012505 (2001).
[5] M. Tinkham, *Introduction to Superconductivity.* McGraw-Hill Book Company (1975).
[6] V. L. Gurtovoi *et al*, *Zh. Eksp. Teor. Fiz.* **132**, 1320 (2007) (*JETP* **105**, 1157 (2007)).
[7] A. Barone and G. Paterno, *Physics and Applications of the Josephson Effect*. Wiley-Interscience, New-York, 1982.
[8] I. N. Zhilyaev, S. G.Boronin, A. V. Nikulov and K. Fossheim, *Quantum Computers and Computing* **2**, 49 (2001).

18th Int. Symp. "Nanostructures: Physics and Technology"
St Petersburg, Russia, June 21–26, 2010

Optimization of S-shaped IV curves in nanosized multilayered doped heterostructures

M. N. Yakupov[1] and V. A. Gergel[2]

[1] Division of Silicon Microsystem and Nanostructure Technology, Institute of Electron Technology, 02-668 Warsaw, Poland
[2] Institute of Radioengineering and Electronics, RAS, 125009 Moscow, Russia

Abstract. We consider the problem of determining the sizes and doping profiles that maximise the microwave power density in the GaAs/AlGaAs multilayered heterostructure. Depending on the doping level in the range $(1-5)\times10^{17}$ cm^{-3}, the barrier heights in the range 0.1–0.2 eV and lengths in the range 30–70 nm of both the narrow- and wide-bandgap layers, the current-voltage characteristics exhibit the bistability loop relates to the thermal-injection instability. The computational method and results of optimisation are given for the practical examination of proposed structure.

Introduction

In our previous study [1], we applied simulation methods based on the energy-balance equation to the investigation of the electrical conductivity of nanosized multilayered heavily doped heterostructures under high electric fields (Fig. 1) and showed the such a structure exhibit the negative resistance in the current-voltage curves. In this work, we discuss the optimisation procedure to maximise the microwave power density, which is our figure-of-merit (FOM). In order to calculate this FOM we consider the negative-conductance region and evaluate the differences of applied voltages and the output current of this region (Fig. 5). The value of microwave power density depends on number of active layers, the length of each layer, doping concentration, the width of sideband layers, the height of first barrier and the abruptness of the hetero junction between the narrow- and wide-gap sections.

The physical model suggested in our study [1] interpreted these feature in terms of the cumulative effect of electrostatic reduction in the barrier heights. This mechanism provides the appearance of bistability (S-shaped) regions in the IV-curves, which one we call the thermal-injection instability. We note that the assumption of the basic possibility of the existence of S-shaped current-voltage characteristics of doped superlattice was studied for the first time by Suris and Fedirko in the well-known work [2] devoted to the heating-related photoconductivity and to the sensitivity to intense external microwave radiation.

We review the energy transport model, optimisation results and the computational mechanism which we used to obtain the S-shaped region.

1. The Energy-transport model behind the analysis

The model based on the set of Poisson, continuity equations and additional energy-balance relation, comprising the energy-transport model in Stratton's formulation [3]:

$$\begin{aligned}\frac{d^2\varphi}{dx^2} &= -\frac{q}{\varepsilon\varepsilon_0}(N-n)\,,\\ \frac{dj_n}{dx} &= 0\,,\\ \frac{dj_T}{dx} &= j_n\frac{d(\varphi+\varphi_C)}{dx}-n\frac{(T_0-T_e)}{\tau_e}\,.\end{aligned}$$

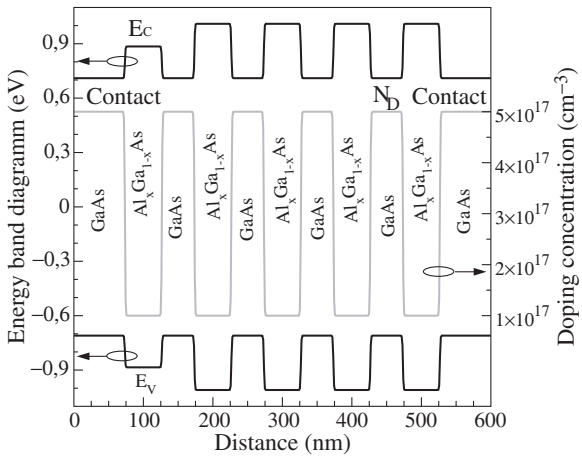

Fig. 1. Energy Band Diagram and Doping Concentration of multilayered heterostructure.

The electrostatic potential φ is supplemented with a band-edge quasi-potential term:

$$\varphi_C = -E_C(x)/q\,, \tag{1}$$

where $E_C(x)$ is the conduction band edge varying in space according to the changes in composition. The mobility and energy relaxation time of electrons are used the simplified power-low dependencies on electron temperature T_e:

$$\mu=\mu_0\left(\frac{T_0}{T_e}\right)^{\alpha},\ \tau_e=\tau_0\left(\frac{T_e}{T_0}\right)^{(1-\alpha)},\ 0.5\le\alpha\le1\,, \tag{2}$$

where the values of low-field mobility μ_0 and constant τ_0 are made consistent with saturation velocity υ_S through:

$$\upsilon_S^2=\frac{\mu_0 T_0}{\tau_0}\,. \tag{3}$$

For GaAs heterostructure we used the following numerical values for the constant:

$$\begin{aligned}\mu_0 &= 8\times10^3\,\frac{\mathrm{cm}^2}{\mathrm{V\,s}}\,,\\ \upsilon_S &= 1\times10^7\,\frac{\mathrm{cm}}{\mathrm{s}},\quad \tau_0=2\times10^{-12}\ \mathrm{s}.\end{aligned}$$

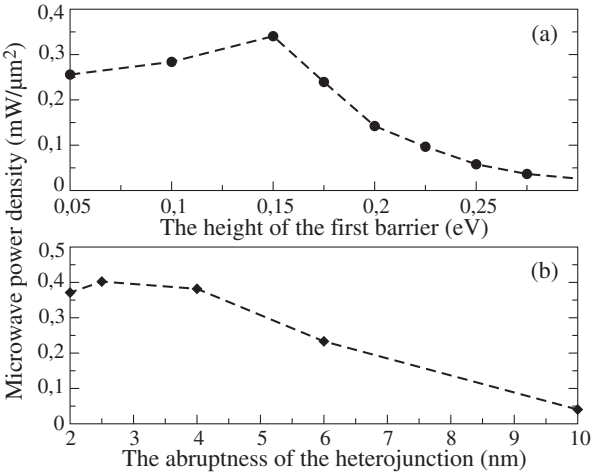

Fig. 2. Dependence of the microwave power density on the height of first barrier and the abruptness of the heterojunction.

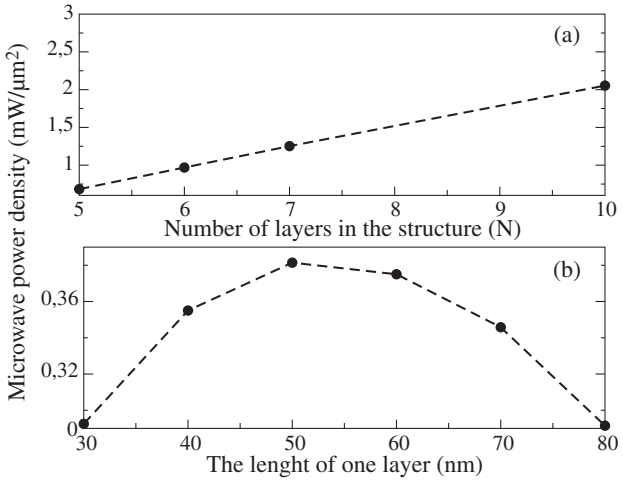

Fig. 3. Dependence of microwave power density on the number of active layers and the length of each layer.

2. Optimization results

Rather simplified analytical expression of the description the S-shaped I-V curve using the conventional drift-diffusion approximation was done given in the work [1]. This result has only qualitative description, but it gives the direction that the ration between the energy-barrier heigh φ_C and the equilibrium thermal energy T_0 plays the crucial role. The more rigorous analysis is based on numerical simulation of energy balanced model, which is used to increase the microwave power density.

First we investigate the role of the first section of the superlattice. As it is depicted Fig. 2a there is an optimal height of first barrier, which is around 0.15 eV.

From Fig. 3a we can make a conclusion that the microwave power density increases linearly with number of heterolayers.

Also there is an evidence on Fig. 4a that the lower doping level N_D in wide-band layers then greather the microwave power density.

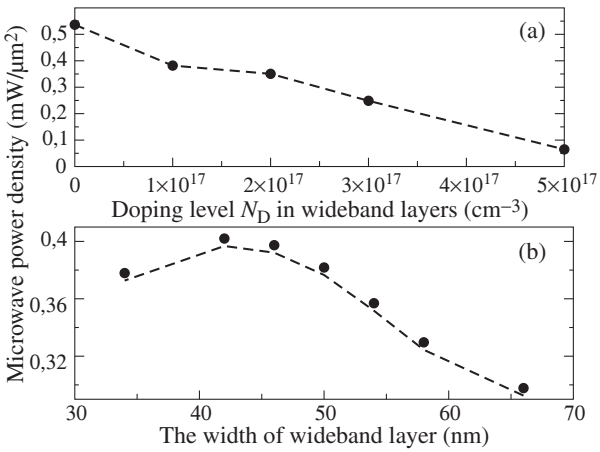

Fig. 4. Dependence of microwave power density on the doping level N_D and the width of wideband layer.

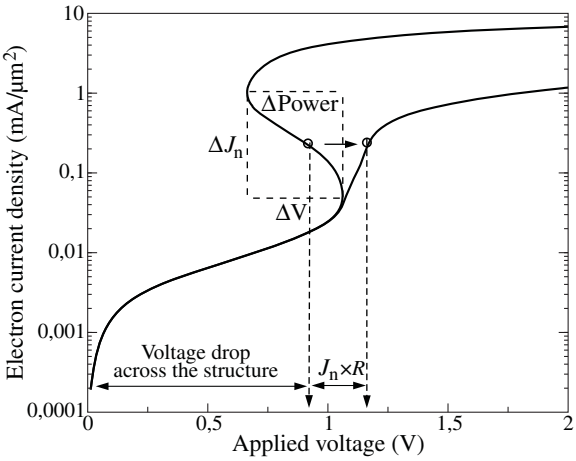

Fig. 5. The linearisation of IV curves by extra resistor to get monotonic function and determination of microwave power density.

3. Algorithm of computation of S-shaped IV curves

To make the computation of S-shaped IV curves numerically stable we introduce the extra resistor to avoid the multivalued of current voltage characteristic at given supply voltage (Fig. 5).

The next step of this work will be the development of the small-signal model to make an estimation of maximum oscillation frequency of such multilayered heterostructure.

We believe that such device, which exhibit the negative resistance, can be used to generate oscillations in the terahertz frequency range as a solid-state microwave source.

Acknowledgements

One of the author, Yakupov M. N. would like thank to the project COMON (Compact Modeling Network) FP7 PEOPLE IAPP, No. 218255.

References

[1] V. A. Gergel, A. P. Zelenyi and M. N. Yakupov, *Semiconductor* **41**, 325 (2007).

[2] R. A. Suris and V. A. Fedirko, *Fiz. Tekh. Poluprovodn.* (St Petersburg) **12** 1060 (1978).

[3] R. Stratton, *Phys. Rev.* **126**, 2002 (1962).

18th Int. Symp. "Nanostructures: Physics and Technology"
St Petersburg, Russia, June 21–26, 2010

New lighting technologies based on RGB LEDs with smart control

A. L. Zakgeim and M. N. Mizerov
Submicron Heterostructures for Microelectronics, Research & Engineering Center RAS, St Petersburg, Russia

Abstract. The key aspect of solid-state lighting (SSL) that radically distinguishes it from the conventional lamps is its high controllability. Due to the use of the principle of RGB-mixing in multichip LED modules one can easily tune spectrum, chromaticity coordinates, correlate color temperature (CCT), color rendering index (CRI), temporal modulation and spatial pattern of emitted light. This ability can make the artificial light closer to the natural one, with its daily cycles. The primary function of the artificial light sources, simulating daylight, is the support of physical and psychological human health. Further functional expandability of the smart light lies in the field of creating special illumination systems for the staff working in extreme conditions, such as air traffic controllers, the crews of autonomous objects, etc. Furthermore, the development of versatile surgical illuminators enabled to improve the visualization of biological tissues is of special interest.

Over the last decade, the light-emitting diodes keep advancing at a rapid pace, with improvements being achieved in efficacy, light quality and operating life. Today the lighting technologies based on the LEDs, or, to put it differently, a solid-state lighting, have the potential to cause a breakthrough in the lighting market through the introduction of the highly energy-efficient, longer-lasting, versatile light sources, including high-quality white light. It is safe to say that the SSL is one of the most outstanding achievements of the nanotechnology.

The implementation of the SSL has the technical-economical and biomedical aspects. The former concerns energy savings that now determine crucially the competitiveness of the economy, environmental safety and, eventually, the living conditions of the society. In this connection, the LEDs whose efficiency is 5–10 times greater than that of the traditional lamps can make a significant contribution to solving the energy problems. The fact is generally recognized now and quite a few experts are calculating the cost saved by replacing the lamps with the LEDs. For example, according to the last DOE report the United States will save, owing to the SSL, in 2030 about 130TWh of electricity or 19 billion dollars [1].

However, the advantages of the SSL lie not only in the field of efficiency but also in that of the quality of light. The light is no less important component of the environment than the air, water, food, etc. Its quality is characterized by the set of parameters: intensity, spectral distribution, chromaticity coordinates, correlated color temperature, color rendering index and temporary alternations. Still, until recently, the requirements were regulated only for the illuminance; for example, 300 lx — for crude work, 10000 lx — for delicate work.

Let us consider the issues of human light perception in some detail considering the biological evolution. Over millions of years, a human being, as a biological organism, was formed in the natural illumination. This natural (sun) light is characterized by the broad, continuum spectrum closed to Planckian radiator in the range 1800–10000 K which depends on the time of the day, season, and weather. Obviously, these properties have left a deep imprint in the functioning of our body which obeys the circadian rhythms. In this concern, a relatively new discovery of the fourth type of a photoreceptor in the eye is of special interest. It has a specific spectral sensitivity and is not responsible for the visual perception, but it controls the biochemical composition of blood, namely the amounts of melatonin (sleep hormone) and cortisol (stress hormone).

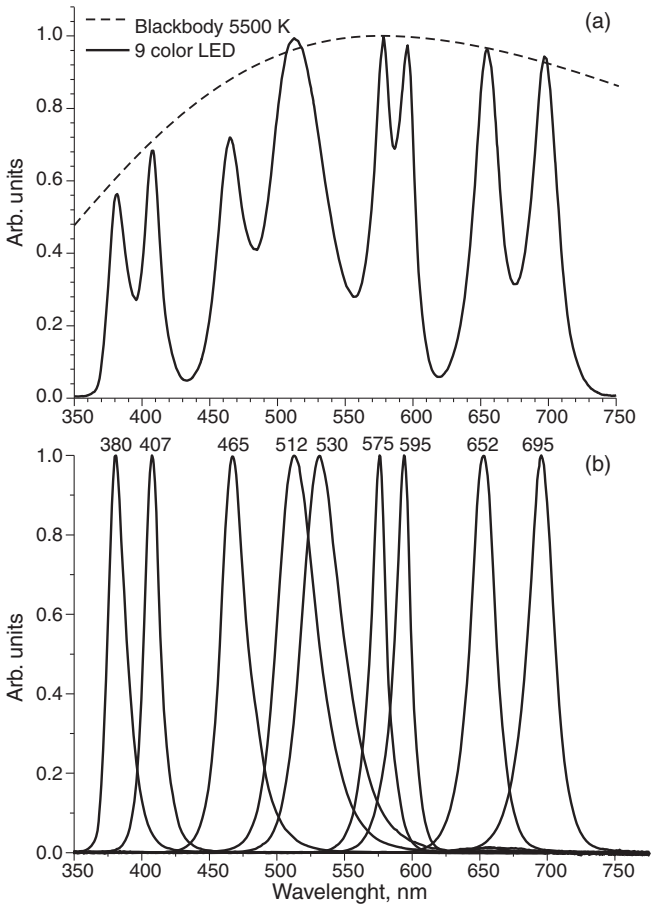

Fig. 1. (a) example of filling of blackbody spectrum at CCT = 5500 K by additive mixing of emissions from nine colored LED; (b) relative spectral power distribution for up-to-date LEDs of visible spectrum.

The era of the artificial lighting, in which the civilized part of the humanity spends more and more time, has started about a 100 years ago with the invention of the Edison incandescent lamp. Unfortunately, in the course of time, people has started to spend not only night, but a considerable part of day time in the artificial light because of the wide spread of the industrial and office buildings with no windows. Most of the light we receive now is from the discharge and fluorescent lamps, whose emis-

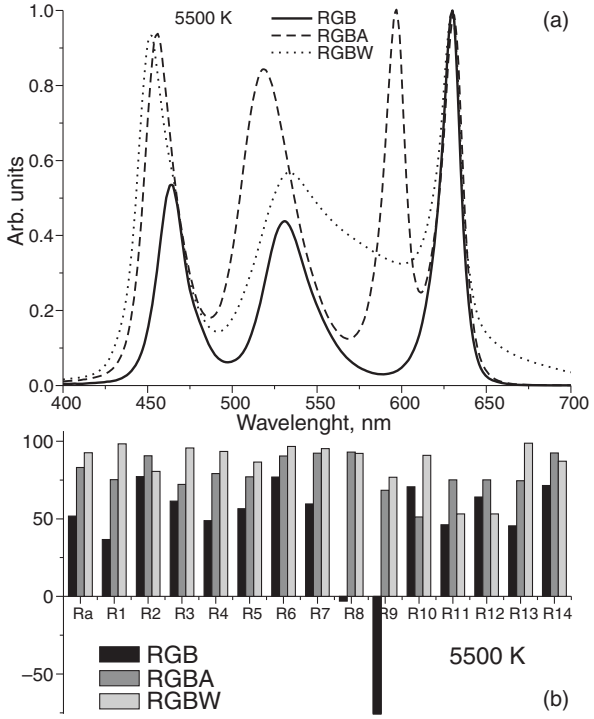

Fig. 2. (a) relative spectral power distribution and (b) color rendering indices diagrams for RGB, RGBA and RGBW versions of the synthesis of white light with a CCT = 5500 K.

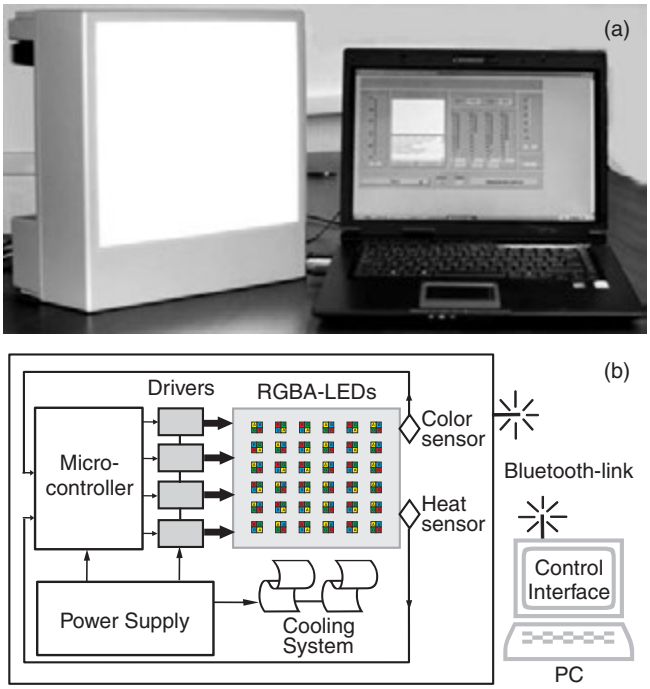

Fig. 3. (a) general view of LED module and user interface of versatile smart light source; (b) block diagram of control circuit.

sion differs greatly from the natural light. The implications of this change in the habitat are far from clear, but still they cause apprehension among the physicians and biologists. The light of the fluorescent lamps is selective with the lack of frequency bands that may be important for health, often "cold" (depressive) and static, conflicting with the cyclic processes in the human body. Numerous biomedical studies indicate that the violation of the luminous harmony can lead to various health disorders, both physical and psychophysiological.

Yet what can we say about the light of the LEDs? It is well known that there are two approaches to the creation of the white LEDs. The most commonly used method is a phosphor converted GaN LED. The light output of a blue LED excites the fluorescent material, and then the additive mixing of the unabsorbed blue light from the LED and a longer wavelength emission from the fluorescent material give the white light. This approach does not differ radically from the operation of the fluorescent lamps. The other way of producing the white light consists in the additive color mixing of the emissions from several chips having different primary colors. This method opens up fresh opportunities for creating the dynamic controlled versatile solid-state lamps with variable spectra, color coordinates and dimming that is known as the smart light [2]. Theoretically, such light control may be implemented relatively easily by the current modulation of the individual emitting chips comprising the RGB module. In practice, the control and the maintenance of the parameter stability require complex electronic circuits with a pulse-width modulation driving technique and internal digital feedback links. The latter is due to the complicated, nonlinear dependencies of the LED spectrum and brightness on current [3].

The key performance metrics of the white light sources are lumen efficacy (LE), correlated color temperature and color rendering index. LE, in the lighting language, means the efficiency of conversion of the electrical energy into the light flux. CRI, which should ideally be equal to 100, characterizes the proximity of a specific spectrum to the continuous spectrum of a blackbody with the same color temperature or, in other way, the correct color reproduction of the illuminated objects. As a rule, LE and CRI work against each other, so it is important to improve both metrics simultaneously. The up-to-day LEDs overlap the entire visible spectral range (excepting "green valley" 540–580 nm) with the high efficiency and can almost perfectly reproduce the "sun quality" light as it is depicted on the Fig. 1a,b. However, as the experimental and theoretical studies [4,5] had shown, in order to obtain the high quality white light the trichromatic RGB or quadrichromatic RGBA, RGBW systems (R: 630–640 nm, G: 530–550 nm, B: 450–460 nm, A: 590–595 nm, W: phosphor conversion white LED with a CCT = 3000–5000 K) may be quite enough. Spectral distribution and color rendering indices for the RGB, RGBA, RGBW system at CCT = 5500 K are shown on the Fig. 2. We give preference to the RGBA system as the most universal one for getting the white light with a CCT in the range of 1800–10000 K and the wide color gamut of chromaticity diagram CIE 1931.

Fig. 3 presents the general view and the block diagram of an experimental smart light source for the comprehensive biomedical research of the light influence on psychophysiological state of a human. An optical system enables the high output of ∼10000 lm, with a high degree of homogeneity in color and brightness over the emitting surface and a wide spatial radiation pattern. The source power is enough for illuminating the room of several tens square meters. The electronic control circuit and the software allows to set the lighting modes quantitatively (CCT, color coordinates, illuminance) or in a qualitative form (sunrise, sun at zenith, cloudy day, etc.). The whole process is controlled from a remote computer. Joint researches

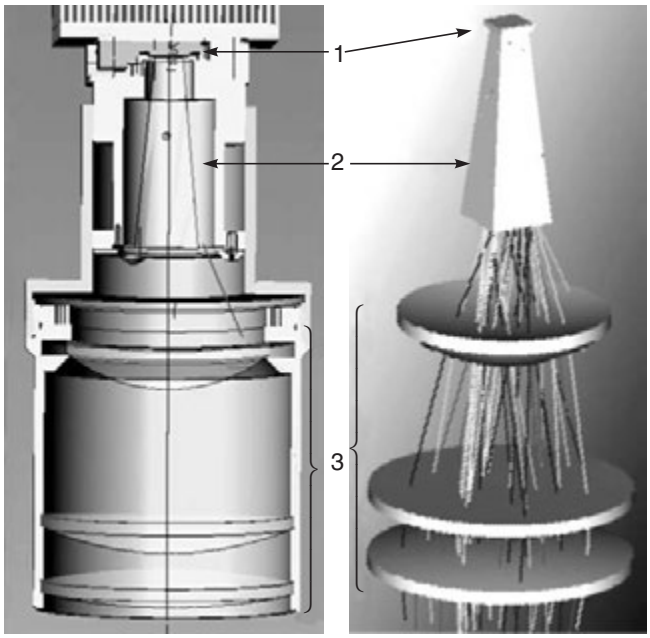

Fig. 4. Optical scheme and cross-section of surgical illuminator with variable emission spectrum. 1 — four-color LED module, 2 — prism concentrator, 3 — three-element lens.

with the specialists of the Centre of Aerospace Medicine are now conducted at a special complex, where the lighting effects are estimated by registration of the following parameters: encephalogram, cardiogram, pulse and the breathing rate, speed of test exercise, etc. The ultimate goal of the investigation is to develop the algorithms of the illumination that enable the concentration of attention (vital activity) with a subsequent relaxation of the personnel working under an extreme mental stress, such as air traffic controllers, operators of hazard installations, drivers, pilots, etc. In the future, similar (though probably simplified systems) can be used in the residential houses and offices. They could accurately simulate the natural changes of the daylight supporting the daily cycle and improving the well-being of the people.

Yet another important application of the smart light in medicine is connected with the surgery, namely, improving the visualization nerves, blood vessels and the other biological tissues located in an operation field. It is widely recognized that the appearance of an illuminated object is a result of the overlap integral between the spectral distribution of light source and the reflectance spectrum of the object. By adjusting the light spectrum, the surgeon can choose an optimal emission for a reveal currently necessary tissue against a background. The experimental model of a smart LED surgical illuminator is shown on the Fig. 4. The most important requirement to the device is the high level of illumination of the working field (>10000 lx) combined with a high color and brightness uniformity. To meet these demands we employed a superpower four-color RGBW LED (output flux up to 4000 lm), a prism concentrator for color mixing and a three-element lens for forming the illuminated field. Electronic control scheme is similar to the one considered above. At present, the smart surgical illuminator is being tested in the St Petersburg State I. P. Pavlov Medical University.

In addition to the considered applications, the smart RGB light sources have the great potential for the agrotechnology and the light signal technique (automobile, traffic lights, etc.) where the visual perception can be combined with the transmission of information.

References

[1] *Energy Savings Potential of Solid-State Lighting* in General Illumination Applications 2010 to 2030/ U.S. Department of Energy – February 2010. http://apps1.eere.energy.gov/buildings/publications/pdfs/ssl/ssl_energy-savings-report_10-30.pdf.
[2] E. Fred Schubert *et al*, *Science* **308**, 1274 (2005).
[3] A. Zukauskas *et al*, *Proc. of SPIE* **5187**, 185 (2004).
[4] A. Zukauskas, M. Shur, R. Gaska, *Introduction to Solid-State Lighting*, J. Wiley & Sons, NY, 2002.
[5] S. Chhajed *et al*, *J. Appl. Phys.* **97,** 054506 (2005).

18th Int. Symp. "Nanostructures: Physics and Technology"
St Petersburg, Russia, June 21–26, 2010

Auger recombination in InGaN nanoislands behind efficiency droop of blue light-emitting diodes

A. A. Greshnov, B. Ya. Ber, A. E. Chernyakov, D. Yu. Kazanzev, A. S. Pavluchenko, N. M. Shmidt, Z. N. Sokolova, E. B. Yakimov, A. L. Zakgeim and G. G. Zegrya
Ioffe Physical-Technical Institute, St Petersburg, Russia

Abstract. The problem of efficiency droop with injection current in InGaN blue light-emitting diodes has been studied. A series of InGaN light-emitting diodes produced by ZAO "Svetlana-Optoelectronics" have shown peak efficiencies close to the leading values ($\sim 30\%$). We speculate that efficiency droop can be due to Auger recombination in the vicinity of zero-dimensional lateral inhomogeneities and system of the extended defects. Fitting of the efficiency droop curves $\eta(j)$ shows that it falls like j^{-b}, b being between 0.2 and 0.3, which points out the non-symmetrical injection of electrons and holes.

Introduction

Droop of the external quantum efficiency η with injection current j remains the main problem retarding wide application of InGaN light-emitting diodes as the white-light sources. It is well known that nitride materials have a large number of various inhomogeneities including the point defects, single dislocations and walls, grain boundaries etc [1]. Nevertheless, well optimized InGaN light-emitting diodes of the blue spectral range show external quantum efficiency up to 35% as shown in Fig. 1 (samples Sv1-Sv4 were produced by ZAO "Svetlana-Optoelectronics", St Petersburg). Though a few mechanisms behind efficiency droop were proposed, the problem is still far from solution [2]. In this paper we present experimental and theoretical study of the efficiency droop problem focusing on the Auger recombination channel as a possible explanation of the droop at high injection currents.

Localization and Auger recombination

It is generally believed that the only reason of efficient operation of the nitride light-emitting diodes in spite of very high density of the extended defects is formation of the nanometer-size compositional fluctuations ("nanoislands") which can be imaged by means of TEM [3]. Amplitude of the corresponding random potential can be estimated as width of the electroluminescence spectra shown in Fig. 2, i.e. $U_0 \gtrsim 150$ meV. This value is almost independent of injection current which means that distribution of carriers is far from being quasi-equilibrium, convenient and widely used approximation.

It is well known that localization of carriers significantly amplify Auger channel of non-radiative recombination [4]. While bulk mechanism of Auger recombination is extremely weak due to wide band gap of the nitride materials, situation changes when dealing with the low dimensions. In order to estimate the non-radiative lifetime τ_A we exploit standard expression for the Auger recombination rate neglecting exchange contribution [5],

$$R = \frac{2\pi}{\hbar} \sum_{1,2,3,4} f_1 f_2 (1-f_3)(1-f_4) |\langle 12| \frac{e^2}{\epsilon r} |34\rangle|^2 \times \delta(E_1 + E_2 - E_3 - E_4). \quad (1)$$

Our estimation shows that $\tau_A \gtrsim 10^{-8}$ s, i.e. at least one order of magnitude higher than radiative lifetime τ_A, when considering Auger recombination in 3 nm wide $In_{0.2}Ga_{0.8}N$ quantum wells

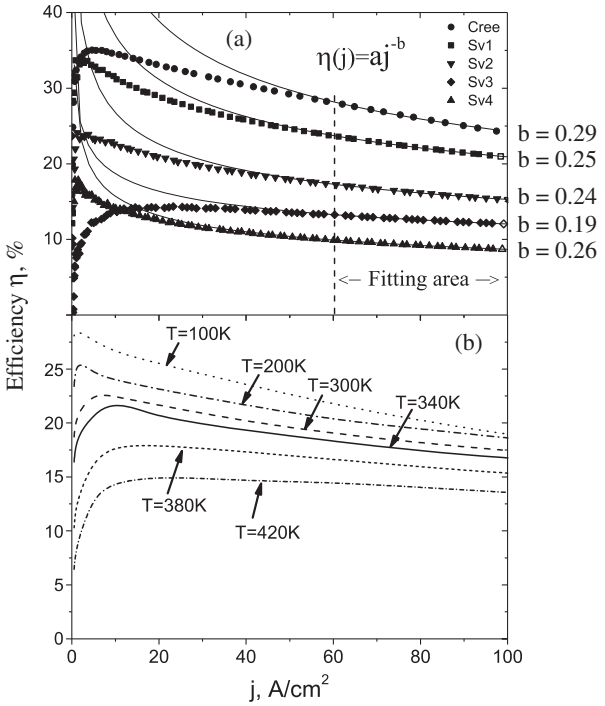

Fig. 1. External quantum efficiency vs. injection current density (a) for a series of light-emitting diodes at room temperature, (b) at different temperatures for LED #Sv2.

at injection currents up to 100 A/cm^2. Though significant enhancement of τ_R/τ_A ratio takes place in 2D case due to power law $R \propto E_g^{-6}$ instead of exponential one, it it still insufficient to explain the observed efficiency droop. Thus, standard mechanisms of Auger recombination in the homogeneous quantum wells (threshold, quasi-threshold and thresholdless) cannot be behind the droop.

However, it is well known that lateral structure of the nitride layers is far from being homogeneous and numerous compositional fluctuations and extended defects arise instead [1]. This implies formation of the In-rich nanoislands which significantly enhance Auger recombination rate, so that $R \propto E_g^{-4.5}$. Due to strong dependence of the rate on the nanoisland dimensions and wide distribution of geometrical parameters it is hard to give more or less precise answer for R so we just used a model of spherically symmetrical dots with $d = 5$ nm diameter for the sake of estimation. As a result calculated value of the non-radiative time $\tau_A \sim 0.3$ ns is about one order of magni-

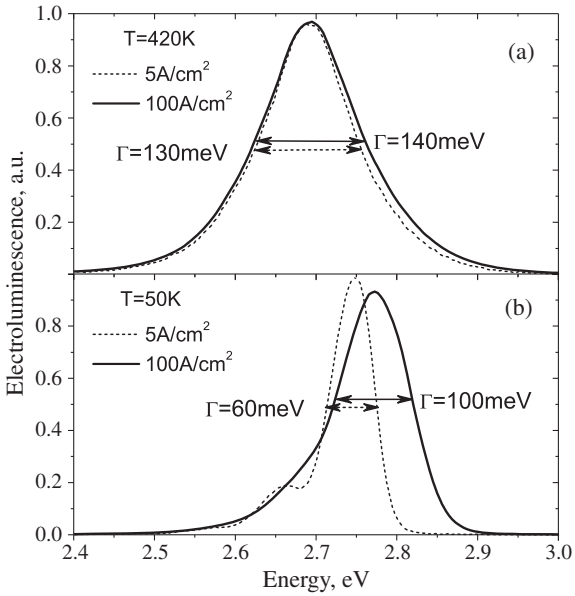

Fig. 2. Electroluminescence spectra of LED #Sv2 at (a) $T = 420$ K and (b) $T = 50$ K.

tude smaller than radiative time. Assuming 10% of the sample area to be filled with InGaN nanoislands we obtain comparable values of the effective non-radiative time τ_A^* and radiative time τ_R, resulting in $\eta \sim 50\%$. Moreover, due to strong dependence of R on E_g we can obtain the same quantity assuming only 0.1% of the narrow-bandgap InN nanoislands. While this hypothesis seems to be unlikely due to physical picture of the nitride material growth (though not disproved), we speculate that similar zero-dimensional enhancement of Auger recombination can take place in the vicinity of system of the extended defects.

Finally, efficiency droop curves have been analyzed quantitatively. While quite different behaviour of the curves presented in Fig. 1(a) takes place till $j^* \sim 50$ A/cm^2, all of them can be successfully fitted by power law

$$\eta(j) \sim j^{-b} \tag{2}$$

with index b being about 0.2–0.3 at higher currents. Naively speaking, this evidences against Auger recombination as a possible mechanism behind efficiency droop since it predicts $\eta \propto j^{-1}$. However, $b = 1$ can be easily derived only assuming equal concentrations of electrons and holes and quasi-equilibrium distribution of both types of carrier which is not the case evidently. Therefore this argument indicates to importance of the light-emitting structure design improvement [6] more than to complete exception of the Auger recombination.

In conclusion, we have shown that efficiency droop of InGaN blue LEDs can be explained by Auger recombination in the In-rich nanoislands while relatively small value of the exponent $b \sim$ (0.2–0.3) deduced from Fig. 1(a) is probably due to non-symmetrical and non-quasiequilibrium distribution of carriers in the active region. We also speculate that another possible channel of losses can be related to Auger recombination in the vicinity of system of the extended defects.

Acknowledgements

This work has been supported by RFBR (08-02-01337) and Federal Programme on Support of Leading Scientific Schools.

References

[1] A. E. Chernyakov *et al*, *Superlat. Microstr.* **45**, 301 (2009).
[2] X. Ni *et al*, *Appl. Phys. Lett.* **93**, 171113 (2008).
[3] V. Potin *et al*, *Phys. Stat. Sol. (b)* **234**, 947 (2002).
[4] A. S. Polkovnikov, G. G. Zegrya, *Phys. Rev. B* **58**, 4039 (1998).
[5] V. N. Abakumov, V. I. Perel, I. N. Yassievich, *Nonradiative Recombination in Semiconductors*, North-Holland, 1991.
[6] A. A. Greshnov *et al*, *Proceedings of 14th Int. Symp. "Nanostructures: Physics and Technologies"*, p. 242 (2006).

18th Int. Symp. "Nanostructures: Physics and Technology"
St Petersburg, Russia, June 21–26, 2010

Effects of nitride-based plasma pre-treatment prior to SiN_x passivation in AlGaN/GaN HEMTs on silicon substrate

Cheol-Koo Hahn, Ji Ha Kim, Hong Goo Choi, Min-Woo Ha, Hong Joo Song, Cheong Hyun Roh and Jun Ho Lee

Korea Electronics Technology Institute, 68 Yatap-dong, Bundang-gu, Seongnam, Gyeonggi-do 463-816, Korea

Abstract. Nitrogen-based plasma pre-treatment was applied to the AlGaN/GaN high electron mobility transistor (HEMT) before surface passivation to prevent RF current dispersion phenomena. Although the DC saturated current (IDS) was reduced from 235 to 110 mA/mm at zero gate bias by nitrogen plasma pre-treatment, RF power was increased from 15 to 18.1 dBm. Reduction of channel carrier by neutralization of surface positive charge during plasma pre-treatment is thought to be the origin of IDS reduction. Auger Electron Spectroscopy (AES) measurement revealed that the Carbon- and Oxygen-relate surface contamination was clearly removed. Elimination of surface contamination and curing of nitrogen-vacancy (VN)-related defects is believed to reduce surface trap, resulting in the elimination of RF power dispersion.

Introduction

AlGaN/GaN high electron mobility transistor is very perspective in high power RF electronics. Because of its surpassing material properties comparing to the previous Si, GaAs, SiGe, etc., higher power density at higher frequency can be realized with higher linearity and thermal stability. However some technical issues are remain to be solved for its pratical use. Among them power dispersion in RF region caused by surface trap is one of the serious one to be overcome. In this work we applied surface plasma pre-treatment to eliminate RF-dispersion phenomena. Oxygen and carbon related surface contamination and nitrogen-vacancy (VN)-related defects is believed to be cured by surface pre-treatment and RF power dispersion is reduced to less than 1%.

1. Experiments

A 17.5 nm $Al_{0.26}Ga_{0.74}N$/GaN-on-Si was used for a device fabrication. After the deep mesa etching for device isolation, Ti/Al/Ni/Au (30/100/30/100 nm) Ohmic metals were deposited and annealed by rapid thermal anneal (RTA) at 900 °C. The Ni/Au was used for Schottky gate with its length and width of 0.8 and 96 μm, respectively. Various surface pre-treatments were applied to the sample before 100 nm-thick SiN_x passivation. (wet treatment with NH_4OH or BOE, plasma treatment with N_2 or NH_3 with optimized conditions, respectively). Direct current (dc) I-V, pulsed I-V and radio frequency (rf) characteristics were measure to characterize the pre-treatment effects. For the pulsed I-V measurements (using the DIVA-D265), VDS = 15 V, VGS = -2 V were applied and the pulse width and period were 500 ns and 1 ms, respectively. Load-source-pull measurements were carried out for RF characterization.

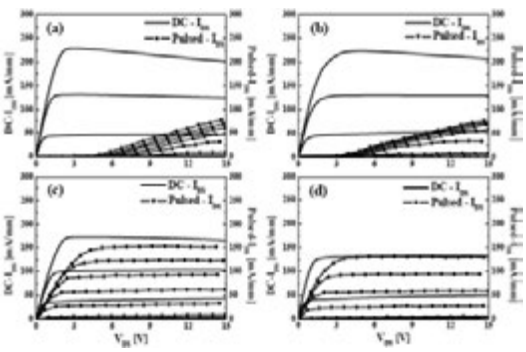

Fig. 1. The dc and pulsed I-V characteristics of the AlGaN/GaN HEMTs with various pretreatments conditions (VDS $= 0 - 15$ V and VGS $= -3 - 1$ V); (a) without pre-treatment, pre-treatment with (b) NH_4OH, (c) NH_4OH/N_2 and (d) NH_4OH/NH_3.

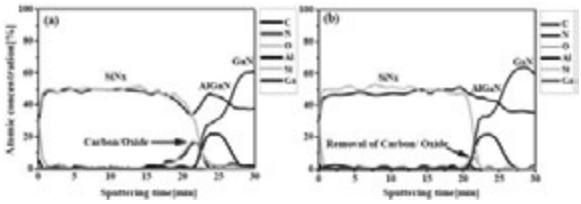

Fig. 2. Atomic concentrations of AlGaN surface by auger electron spectroscopy. With, (a) NH_4OH wet treatment and (b) NH_4OH chemical + NH_3 plasma pre-treatment prior to SiN_x passivation, respectively.

2. Results and discussion

Figure 1 is the DC I-V and pulsed I-V characteristics of the fabricated AlGaN/GaN HEMTs with various pre-treatment conditions. While the devices without pre-treatment (Fig. 1a) and with chemical pre-treatment (Fig. 1b) show wide discrepancies between DC- and pulsed I-V characteristics, caused by surface deep traps, the devices with plasma pre-treatment (Fig. 1c,d) show the recovery in the pulsed I-V curves. Especially, in the sample with NH_3 plasma pre-treatment (Fig. 1d), pulsed I-V curves show 99% of DC ones. Although the saturated drain current is reduced from 235 to 110 mA/mm, RF power is increased from 15 to 18.1 dBm. From the surface analysis with AES, it is found that carbon- and oxygen related contamination between AlGaN surface and SiN_x passivation layer is clearly removed. It is thought that the surface contamination and native oxide is effectively removed and furthermore, surface traps (mainly nitrogen vacancy) is neutralize by plasma treatment. VN neutralization is deduced from the fact that the drain saturation current is reduced from 235 to 110 mA/mm. The neutralization of surface charge results in a carrier reduction in the channel effecting the drain current. Mores on our experimental results will be discussed in detail.

Acknowledgements

This work was partly supported by the R&D program of MKE (Development of GaN power amplifier for 4G base station, KI001693) and (Development of high efficiency GaN power device for a power grid inverter system).

References

[1] R. Ventury *et al*, *IEEE Trans. Electron Devices* **48**, 560 (2001).
[2] T. Mizutani *et al*, *IEEE Trans. Electron Devices* **50**, 2015 (2003).
[3] G. Simin *et al*, *Appl. Phys. Lett* **79**, 2651 (2001).
[4] S. C. Binari *et al*, *IEEE Trans. Electron Devices* **48**, 465 (2001).
[5] S. Arulkumaran *et al*, *Appl. Phys. Lett* **84**, 613 (2004).
[6] D. J. Meyer, *Proc. of CS MANTECH*, 305, 2007.
[7] T. Hashizume *et al*, *J. Vac. Sci. Technol. B* **19**, 1675 (2001).
[8] M. F. Romero *et al*, *IEEE Trans. Electron Device Lett.* **29**, 209 (2008).
[9] A. P. Edwards *et al*, *IEEE Trans. Electron Device Lett.* **26**, 225 (2005).
[10] T. Hashizume *et al*, *J. Vac. Sci. Technol. B* **21**, 1828 (2003).
[11] T. Hashizume *et al*, *Appl. Phys. Lett.* **77**, 1499 (2004).
[12] A. Hierro *et al*, *Appl. Phys. Lett.* **77**, 1499 (2000).
[13] T. Kunii, *Proc. of IEEE Comp. Semicon. Int. Circuit Symp.* 197, 2004.
[14] J. H. Kim *et al*, *Jpn. J. Appl. Phys.* to be published.

18th Int. Symp. "Nanostructures: Physics and Technology"
St Petersburg, Russia, June 21–26, 2010

Semimetal-semiconductor transition in graphene interacted with hydrogen

A. A. Pakhnevich[1], M. A. Putyato[1], V. A. Volodin[1,2] and V. Ya. Prinz[1]

[1] Institute of Semiconductor Physics SB RAS, Acad. Lavrent'ev Ave. 13, 630090, Novosibirsk, Russia
[2] Novosibirsk State University, Pirogova St. 2, 630090, Novosibirsk, Russia

Abstract. Two new techniques of graphane fabrication are proposed and demonstrated: graphene hydrogenation in cold hydrogen electron-cyclotron resonance plasma and graphene hydrogenation by atomic hydrogen. Some features of semimetal-semiconductor transition and properties of hydrogenated graphene are investigated.

Introduction

The current interest in hydrogenated graphene properties is caused by possibility to make hydrogen saturated graphene, so-called graphane. As theoretical work [1] predicts, this novel material is a direct-gap semiconductor with energy gap of 3.6 eV. The development of graphane fabrication technique opens new prospects in graphene nanoelectronics. Firstly, it solves a problem of high leakage currents caused by graphene semimetal properties in the electronic devices. Secondly, the reversible electrochemical control of graphene hydrogenation allows one to create a new type of memory elements [2]. Thirdly, it opens up new possibilities for creation of optoelectronics devices. Fourthly, lattice-mismatch mechanical strains in graphene-graphane films can be significant, that allows making three-dimensional graphene nanoobjects by means of well-developed techniques of thin films rolling [3]. For the first time a graphane fabrication was demonstrated by hydrogen-argon dc-plasma treatment of graphene [4]; the material obtained by this technique may have many crystal structure defects because of high plasma ion energy, which can exceed 100 eV.

In this work we propose two new graphane fabrication techniques allowing one to make graphene hydrogenation more delicate due to the lower energy of hydrogen particles. The first technique implies graphene hydrogenation by cold hydrogen electron-cyclotron resonance (ECR) plasma with ion energy of 1–10 eV. In the second technique graphene is hydrogenated by atomic hydrogen with energy of about 0.1 eV.

1. Experiment details

Graphene samples were made by electrostatic exfoliation of highly-oriented pyrolytic graphite. Electric strip contacts to the samples were patterned with liquid silver paste and dried. Graphene was hydrogenated in vacuum chamber by hydrogen ECR plasma and by atomic hydrogen flow. Graphene saturation with hydrogen was achieved in 1 minute at 10^{-2} Pa pressure for ECR plasma treatment and at dose of 10^{16} units/cm^2 for atomic flow hydrogenation. For scanning tunneling spectroscopy experiments the scanning probe microscope NT-MDT SOLVER P47-PRO was used. Raman spectra were measured with Horiba Jobin Yvon T64000 spectrometer.

2. Results and discussion

Electronic properties of hydrogenated graphene samples were investigated by scanning tunnel spectroscopy. Examples of tunnel volt-ampere characteristics are shown on Fig. 1. As one can see, the graphene hydrogenation leads to formation of wide plateaus in the central parts of volt-ampere curves for both techniques that unambiguously indicates a forbidden gap appearance in the material. The plateau's width of 3–4 eV for graphene hydrogenated by atomic hydrogen is in good agreement with the theoretical value of forbidden gap width of graphane. Thus, the results have evidently proved the possibility of realization of semimetal-semiconductor transition and graphane fabrication by the proposed techniques.

The quality of graphene samples was diagnosed by Raman spectroscopy for the both hydrogenation techniques. Measured spectra are shown on Fig. 2.

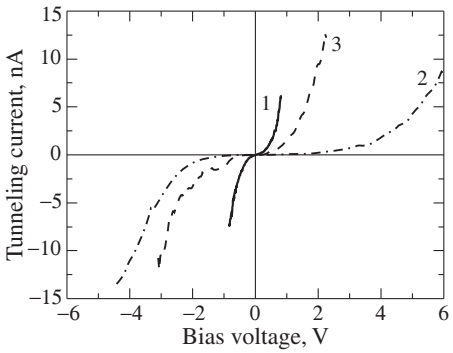

Fig. 1. Evolution of tunnel volt-ampere characteristics of graphene during hydrogenation. 1 — pristine graphene, 2 — hydrogenated by atomic hydrogen, 3 — hydrogenated by ECR hydrogen plasma.

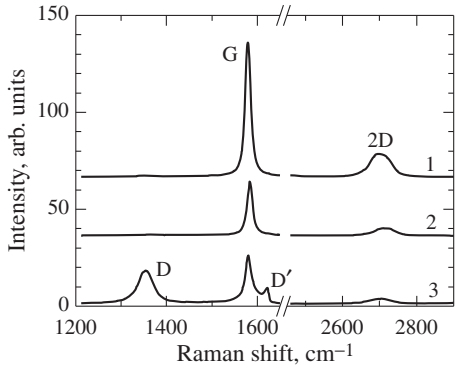

Fig. 2. Raman spectra of graphene during hydrogenation. 1 — pristine graphene, 2 — hydrogenated by atomic hydrogen, 3 — hydrogenated by ECR hydrogen plasma.

Peaks G and 2D in spectra are typical for graphene, they are attributed to the single scattering of photoelectrons on in-line phonon modes and double scattering of photoelectrons on breathing-like phonon modes respectively in Raman process. In contrary, peaks D and D′ are referred to single phonon scattering in Raman processes prohibited by selection rules for ideal graphene crystal. Peaks D and D′ appear in Raman spectrum for the graphene sample hydrogenated by ECR plasma as Fig. 2 demonstrates. It indicates that such hydrogenation leads to the formation of structural defects in significant concentration. When graphene is hydrogenated by atomic hydrogen the peaks D and D′ are suppressed, that evidently shows that the concentration of structural defects is low and this technique is very promising for fabrication of structurally perfect graphane films.

Acknowledgements

We thank Dr. V. S. Aliev for graphene treatment by ECR hydrogen plasma and E. Yu. Zhdanov for experimental assistance. This work was supported by RFBR (Grant 09-02-01390).

References

[1] J. O. Sofo *et al*, *Phys. Rev. B* **75**, 153401 (2007).
[2] T. J. Echtermeyer *et al*, arXiv:0712.2026v1.
[3] V. Ya. Prinz *et al*, *Physica E* **6**, 828 (2000).
[4] D. C. Elias *et al*, *Science* **323**, 610 (2009).

18th Int. Symp. "Nanostructures: Physics and Technology"
St Petersburg, Russia, June 21–26, 2010

Peculiarities of impact ionization of impurity Al in SiC polytypes

V. I. Sankin, N. S. Averkiev, A. M. Monakhov, P. P. Shkrebiy, P. L. Abramov and N. I. Sablina
Ioffe Physical-Technical Institute, St Petersburg, Russia

Abstract. Peculiarities of impact ionization of impurity with small atom radius in semiconductors are investigated using Al in SiC polytypes as an example. It is shown that in these conditions an impurity low temperature breakdown is realized at high impurity concentration.

Introduction

Primary investigations of hole transport in strong electrical field [1] have shown some new possibilities of p-type SiC as a material for fabrication of different effective devices. These investigations are important especially because of special effects in electronic SiC such as effects of Wannier–Stark localization in strong electric fields that can critically limit reliable functioning of electronic devices [2]. The electrical breakdown of Al acceptor impurity is related to the problem of hole transport in strong electrical fields.

1. Physical model

A quality picture shows on Fig. 1 shows the probability of ionization collisions with impurity atoms in Ge(Al) and SiC(Al). Al radius in hydrogen-like approximation for Ge and SiC is equaled 120 and 4 angstroms respectively. The probability of collisions in SiC will be noticeable at $N_a - N_d$ in three order larger than in Ge, namely, at $N_a - N_d > 10^{17}$ cm^{-3}.

2. Experiment

We have studied I-V characteristics of Al electrical breakdown in p-type 6H-SiC, 4H-SiC and 15R-SiC. The measurements were performed on P$^+$–P, N–P experimental structures and the p-type monocrystal with $N_a - N_d \sim 5 \times 10^{15}$ cm^{-3}. Each of the P-epilayers was doped by aluminum. The P layers of the 2–7 μm thickness were deposited on an n-type 6H-, 15R-SiC Lely substrate, a 4H commercial substrate and C faces of P$^+$(Al) epilayers by sublimation and CVD epitaxy. The experimental structures were analogical to ones used in [1]. Opposite to the classic works on Ge [3] we obtained a drop of breakdown field with increase of $N_a - N_d$. Based on obtained data one can say that in 4H-, 6H-, 15R-SiC the absence of low temperature impurity breakdown of Al impurity around of $N_a - N_d \sim 10^{17}$ cm^{-3} and $T = 77$ K, 4.2 K at about 130 kV/cm was observed. We failed to establish the threshold on $N_a - N_d$ with a more accuracy due to the absence of required samples with the concentration in the range of 10^{17} cm$^{-3} < N_a - N_d < 3 \times 10^{17}$ cm^{-3}. Electrical breakdown field F_b is equal to 1.6×10^6 V/cm at $N_a - N_d \sim 5 \times 10^{17}$ cm^{-3} under the $F \parallel C$ condition.

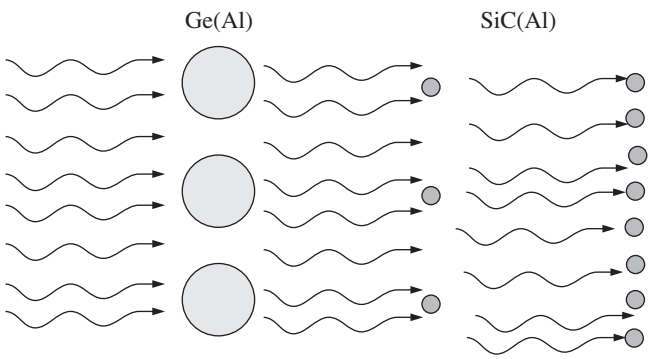

Fig. 1. The peculiarities of impact ionization of Al impurity in Ge and SiC.

3. Discussion

The impurity breakdown exists in concentration range 3×10^{17} cm$^{-3} \le N_a - N_d \le 10^{19}$ cm^{-3} and does not exist at $N_a - N_d < 10^{17}$ cm^{-3} to 130 kV/cm [2]. It is evidence of physical model (Fig. 1). The results obtained show that the breakdown field F_b in SiC(Al) increases when the concentration is decreasing from 10^{19} down to 3×10^{17} cm^{-3} in our samples. It is explained by increase of ionization energy [3] and N_d/N_a ratio increase [5]. We may suppose that increasing of phonon carrier collisions with field increasing stimulates breakdown of Al impurity. Such collisions change carrier's motion direction repeatedly and promote a higher probability of its collision with impurities. The breakdown at 300 K takes place even in the samples with the absence of low-temperature breakdown. Possibly, it is just explained by increasing of carrier scattering. Breakdown electrical field $F_b \| C$ is proved to be almost 40 times bigger than $F_b \perp C$. The calculation based on the zero-radius potential model show the substantial anisotropy of the spatial density distribution of hole localized on Al ac-

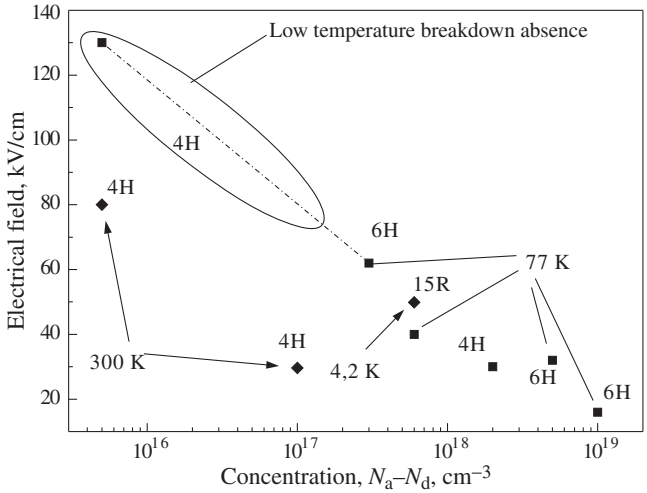

Fig. 2. The dependence of Al impurity breakdown field in 4H-,6H- and 15R-SiC on $N_a - N_d$.

ceptor in SiC, that is equivalent of ionization cross-section decrease. In this case we see breakdown because of increasing of phonon carrier collisions with field rise.

4. Conclusions

The investigation of electrical breakdown in p-type SiC(Al) polytypes has been presented and it has been shown that this effect is explained on the basis of the impact ionization of acceptors Al in SiC polytypes.

Acknowledgements

This work has been supported in part by the RFBR 08-02-00565-à.

References

[1] V. I. Sankin *et al*, *Appl. Phys.Lett.* **94** 8, 082101 (2009).
[2] V. I. Sankin *et alMater. Sci. Forum* **600–603**, 513 (2009).
[3] N. Sclar and E. Burstein, *Phys. Chem. Solids*, **2**, 1 (1957).
[4] G. A. Lomakina *et al*, *Soviet Fiz. Tverd. Tela* **12**, 2918 (1970).
[5] K Seeger, *Semiconductor Physics: An Introduction 5-th* ed. (Springer series in solid sciences: Vol. 40) Berlin , 336 (1991).

18th Int. Symp. "Nanostructures: Physics and Technology"
St Petersburg, Russia, June 21–26, 2010

Asymmetric structure GaN/1ML-InN/InGaN/GaN QWs and its application for next generation high efficiency solar cells

A. Yoshikawa, Y. Ishitani and K. Kusakabe

Graduate School of Electrical and Electronic Engineering, and VBL, Chiba University, 1-33 Yayoi-cho, Inage-ku, Chiba 263-8522, Japan

Abstract. We propose novel III-N based next generation high efficiency solar cells in this paper. A basic structure for the proposed solar cell is a tandem type, i.e. 4–6 solar cells covering different solar spectrum regions are connected in series. Each cell is consisting of a p-n junction in which asymmetric GaN/1-ML InN/InGaN/GaN-based QWs are embedded to expect photo-/thermal-sensitization effects at the 1-ML InN wells. The expected conversion efficiencies are about 10% higher than those of conventional III-N based tandem solar cells due to the photo-/thermal-sensitization effects. The asymmetric QWs play an important role of photo-/thermal-sensitization effects in the cell so that the solar spectra of wavelengths ranging from 2000 to 2500 nm can be also converted to electricity. The expected theoretical conversion efficiencies for the AM 1.5 solar spectrum are as high as 55 and 52% for 5 and 4 tandem cells, respectively, and they are increased up to 63 and 61% under 250 concentrated suns, correspondingly.

Introduction

We have recently proposed fabrication of fine structure symmetric InN/GaN QWs as well as asymmetric GaN/InN/InGaN/GaN QWs in which ∼one-monolayer-thick InN wells play an important role. In the symmetric InN/GaN QWs, though the lattice mismatch between InN and GaN is as high as 11%, the InN wells can successfully be embedded coherently since the InN well is ultimately thin, i.e. one monolayer (1-ML) [1]–[3]. The asymmetric one was developed from the symmetric one to extend and/or tune the emission/absorption wavelengths toward longer side than those of symmetric one [4]. The asymmetric QWs are composed of the following layers in succession: an ∼1-ML-thick InN well grown on a GaN barrier layer, an InGaN layer, and a GaN barrier layer again; these QWs can be used first for the development of blue-green light emitters with remarkably reduced quantum confinement Stark effect (QCSE) due to the effects of employing an ultrathin InN QW structure.

We have only recently further extended an application of the asymmetric QWs toward novel III-N based next generation high efficiency tandem solar cells, in which the asymmetric QWs are embedded around the p-n junction in each cell. The asymmetric QWs play an important role of photo-/thermal-sensitization effects in the cell so that the solar spectra of wavelengths ranging from 2000 to 2500 nm can be also converted to electricity. The expected theoretical conversion efficiencies for the AM 1.5 solar spectrum are as high as 55 and 52% for 5 and 4-tandem cells, respectively, and also 63 and 61% under 250 concentrated suns, respectively.

In this paper, we briefly report the features of proposed novel structure asymmetric GaN/1-ML InN/GaN QWs grown by rf-MBE and their application to novel photonic devices. We first describe the application of asymmetric QWs to blue-green LEDs so that one can understand what is the asymmetric structure QW and how does it work. Then, we explain the role of asymmetric QWs to increase the conversion efficiency of solar cells as being photo-/thermal-sensitizer.

Table 1. Material parameters used for the calculation of theoretical conversion efficiencies of proposed III-N based tandem solar cells.

	$In_xGa_{(1-x)}N$	GaN	InN	unit
E_g	$0.65x + 3.39(1-x)$ $-1.4x(1-x)$	3.39	0.65	eV
m_e	$1/(1+15/E_g)+0.03x$	0.18	0.04	m_0
m_h	$0.42x + 1.6(1-x)$	1.6	0.42	m_0
μ_e	$2000x + 1000(1-x)$	1000	2000	$cm^2/V\,s$
μ_h	30	30	30	$cm^2/V\,s$
n	5×10^{18}	5×10^{18}	5×10^{18}	cm^{-3}
p	$5\times10^{18}x+5\times10^{17}(1-x)$	5×10^{17}	5×10^{18}	cm^{-3}

1. Experimental

First, symmetric InN/GaN QWs for the characterization by STEM were grown at 650 °C by RF-MBE on Ga-polarity GaN/c-plane sapphire substrates prepared by MOVPE. The deposition rate of InN was 1.5 Å/sec and a total supply of 3 MLs. It has been previously reported that the thickness of the InN well is restricted to less than 2 MLs due to the self-limiting process carried out at growth temperatures higher than 600 °C, even when several MLs of InN are supplied [1]– [4].

For the fabrication of LEDs working in blue-green region, the asymmetric structure GaN/1-ML InN/$In_{0.15}Ga_{0.85}N$/GaN 5-QW active layer was grown at 610 °C on a Si-doped GaN bulk substrate. Then, a 20-nm-thick $Al_{0.15}Ga_{0.85}N$ electron-

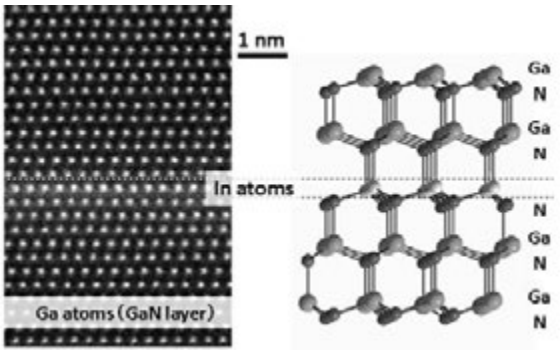

Fig. 1. The sub-Å resolution Z-contrast STEM image for ∼1-ML InN well coherently embedded in the GaN matrix comparing with corresponding crystal model.

blocking layer and a 130-nm-thick Mg-doped GaN layer were grown on the QWs. The growth sequence of a single period is as follows. First, the InN well was grown on the GaN surface at the deposition rate of 1.5 Å/sec and the total supply of 5 MLs. Second, the 2-nm-thick $In_{0.15}Ga_{0.85}N$ layer was grown with a beam flux ratio of 0.15:0.85 (In:Ga). Finally, the 10-nm-thick GaN layer was grown on the InGaN layer.

For the application of the asymmetric structure QWs to solar cells, we report just the theoretical calculation of conversion efficiencies for AM 1.5 solar spectrum [5] assuming the material parameters summarized in Table 1.

2. Results and discussion

Figure 1 shows sub-Å resolution Z-contrast image obtained by cross-sectional scanning transmission electron microscope (STEM) for the sample grown under 3 ML InN supply at 650 °C, in which fractional ML InN wells were observed [2]. It is shown that the QW is coherently embedded and no defects are generated at the hetero-interface even though the lattice mismatch is such large as 11% between InN and GaN. Please remind that thick InN films can be deposited only below 500 °C under +c-polarity growth regime, and the present growth temperatures for the InN/GaN QWs are much higher than those of the thick InN growth, which is probably due to a GaN matrix effect making an effective bonding strength of In-N atoms stronger. The raised temperature process is quite important to improve the quality of GaN matrix. Anyway, depending on these high temperature as well as immiscible nature between InN and GaN, coherent structure ∼1 ML InN well can be introduced into GaN matrix under self-limiting and self-ordering processes [1]– [3].

It has been previously reported that the emission peaks observed for the nominally 1-ML-thick InN/GaN QWs were mainly in the range of 380–430 nm depending on the growth conditions. They were principally located at about 390 and 420 nm for the 1-ML-/2-ML-thick wells, respectively, and also affected by their lateral size and local thicknesses as well [1]–[3]. This implies that it is difficult to use these InN QWs as the active layer of blue-green (450–530 nm) light emitters since their thicknesses are basically less than 2 MLs under such high temperatures as 600 − 650 °C. For achieving the longer wavelength emission, we first examined symmetric QWs consisting of InGaN barriers instead of GaN, but we suffered surface roughening due to disturbance of self-limiting and self-ordering processes by using InGaN ternary alloys. In order to overcome this problem and realize high-efficiency LEDs operating in the blue-green region by employing ∼1-ML-thick InN-based nanostructures, we have proposed the asymmetric GaN/1-ML InN/InGaN/GaN QWs where the ternary InGaN alloys are capped by binary GaN to improve the surface roughness [4].

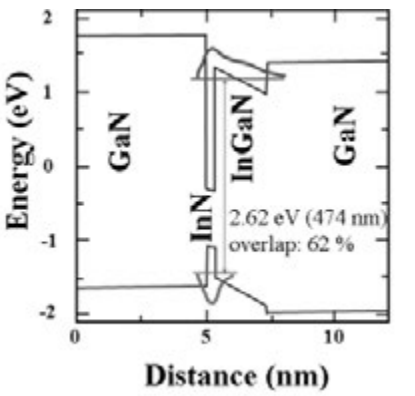

Fig. 2. Energy band profile for the proposed asymmetric GaN/1-ML InN/InGaN/GaN QW.

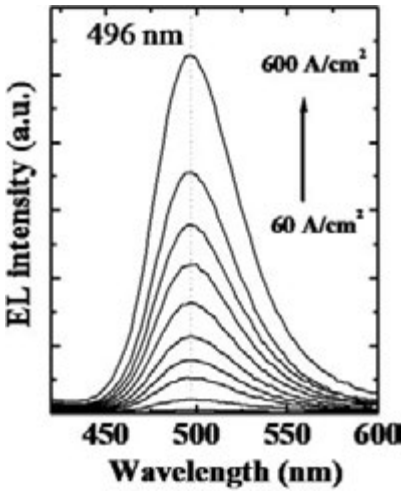

Fig. 3. EL emission spectra for the LED with asymmetric 5 QWs.

Figure 2 shows the energy band profile for the asymmetric GaN/1-ML InN/InGaN/GaN QWs. The materials parameters for deriving the band profile are shown in a previous paper [4]. It has been shown that an overlap of electron and hole wavefunctions is remarkably improved by the presence of 1-ML InN. We have examined to assure this effect by fabricating/evaluating LED structures with asymmetric QWs. Figure 3 shows the electroluminescence spectra under different injection current densities, and it is shown that the QCSE is remarkably suppressed.

Then, we explain about the proposed novel III-N based next generation solar cells. As explained above, the PL emission at RT for the 1-ML InN/GaN QW is located at about 390 nm. This indicates that the localization energy of excitons at the 1-ML InN well in GaN matrix is about 200 meV which is almost the same as that of InAs quantum dots in GaAs. Therefore, we designed novel structure solar cells which utilize photo-/thermal-sensitization effects at the 1-ML QWs in GaN and/or InGaN matrices.

Figure 4 shows the energy band diagram for the 4 tandem cells as a typical example of the proposed solar cells. The GaN/1-ML InN/InGaN/GaN QWs are inserted around the p-n junction of each cell. Of course, indium compositions of the InGaN ternary alloys must be suitably designed for dividing the solar spectrum so as to equally share photons by each cell. One important difference in the design of the QWs compared to that for LEDs shown in Fig. 2 is that the thickness of GaN layer must be quite thin so that photo-excited carriers can easily tunnel through it. As for the photo-sensitization effect, the AM 1.5 spectrum has the solar power of about 4% and the corresponding photon number of about 10% in the wavelengths from 2000 to 2500 nm, which contribute to the photo-sensitization source.

Figure 5 shows the theoretical AM 1.5 conversion efficiencies as well as those under 250-suns concentration for the proposed solar cells against the number of tandem cells. The

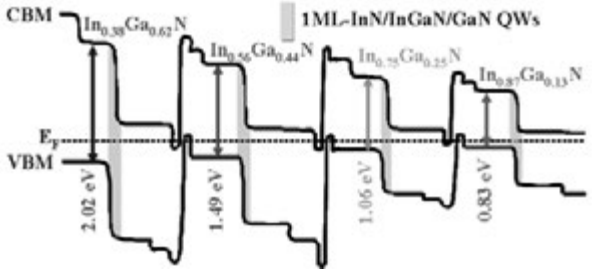

Fig. 4. Energy band diagram for the proposed III-N based tandem solar cells with photo-/thermal-sensitization regions at the each p-n junction.

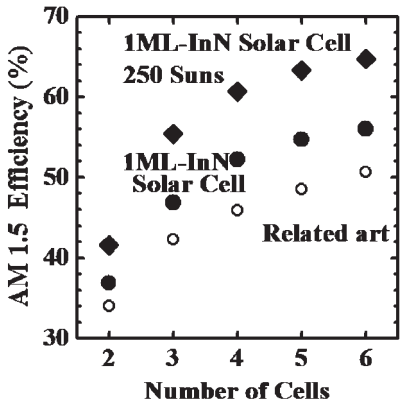

Fig. 5. Comparative display for the theoretical conversion efficiencies for several III-N based tandem solar cells with and without photo-/thermal-sensitization effects.

efficiencies for conventional III-N based tandem solar cells are also shown as their references. The efficiencies for cells with and without sensitization are 55 and 49% for 5 tandem cells, respectively, and 52 and 46% for 4 tandem cells, correspondingly. Those enhancements of the efficiencies are attributed to the voltage gain through the photo-/thermal-sensitization effects at the asymmetric QWs region. Furthermore, it is shown that the efficiencies for the cells with photo-sensitization can be increased up to 63 and 61% under 250 suns concentration for 5 and 4 tandem cells, respectively.

3. Summary

We have proposed the novel asymmetric structure GaN/1-ML InN/InGaN/GaN QWs and applied them for blue-green LEDs as well as III-N based next generation high efficiency tandem solar cells. Concerning the solar cells, the asymmetric structure GaN/1-ML InN/InGaN/GaN-based QWs play an important role of photo-/thermal-sensitization effects in the cell so that the solar spectra of wavelengths ranging from 2000 to 2500 nm can be also converted to electricity. The expected theoretical conversion efficiencies for the AM 1.5 solar spectrum are as high as 55 and 52% for 5 and 4-tandem cells, respectively, and they are increased up to 63 and 61% under 250 concentrated suns, correspondingly.

Acknowledgements

This work was partly supported by the Grant-in-Aid for Science Research on Priority Areas (#18069002, 2007). The authors greatly appreciate Prof. Pan and Dr. Chisholm measuring and analyzing the 1 ML InN QWs by STEM.

References

[1] A. Yoshikawa, S. B. Che, W. Yamaguchi, H. Saito, X. Q. Wang, Y. Ishitani, and E. S. Hwang, *Appl. Phys. Lett.* **90**, 073101 (2007).
[2] A. Yoshikawa, S. B. Che, Y. Ishitani, and X. Wang, *J. Crystal Growth* **311**, 2073 (2009).
[3] A. Yoshikawa, S. B. Che, N. Hashimoto, H. Saito, Y. Ishitani, and X. Q. Wang, *J. Vacuum Sci. Tech.* **B26**, 1551 (2008).
[4] S. B. Che, A. Yuki, H. Watanabe, Y. Ishitani, and A. Yoshikawa, *Appl. Phys. Express* **2**, 021001 (2009).
[5] AM 1.5 spectrum: "ASTM G173-03 Reference Spectra Derived from SMARTS v. 2.9.2".

Author Index